

Lecture Notes in Civil Engineering

J. N. Reddy
Chien Ming Wang
Van Hai Luong
Anh Tuan Le *Editors*

ICSCEA 2019

Proceedings of the International
Conference on Sustainable Civil
Engineering and Architecture



Lecture Notes in Civil Engineering

Volume 80

Series Editors

Marco di Prisco, Politecnico di Milano, Milano, Italy

Sheng-Hong Chen, School of Water Resources and Hydropower Engineering,
Wuhan University, Wuhan, China

Ioannis Vayas, Institute of Steel Structures, National Technical University of
Athens, Athens, Greece

Sanjay Kumar Shukla, School of Engineering, Edith Cowan University, Joondalup,
WA, Australia

Anuj Sharma, Iowa State University, Ames, IA, USA

Nagesh Kumar, Department of Civil Engineering, Indian Institute of Science
Bangalore, Bengaluru, Karnataka, India

Chien Ming Wang, School of Civil Engineering, The University of Queensland,
Brisbane, QLD, Australia

Lecture Notes in Civil Engineering (LNCE) publishes the latest developments in Civil Engineering—quickly, informally and in top quality. Though original research reported in proceedings and post-proceedings represents the core of LNCE, edited volumes of exceptionally high quality and interest may also be considered for publication. Volumes published in LNCE embrace all aspects and subfields of, as well as new challenges in, Civil Engineering. Topics in the series include:

- Construction and Structural Mechanics
- Building Materials
- Concrete, Steel and Timber Structures
- Geotechnical Engineering
- Earthquake Engineering
- Coastal Engineering
- Ocean and Offshore Engineering; Ships and Floating Structures
- Hydraulics, Hydrology and Water Resources Engineering
- Environmental Engineering and Sustainability
- Structural Health and Monitoring
- Surveying and Geographical Information Systems
- Indoor Environments
- Transportation and Traffic
- Risk Analysis
- Safety and Security

To submit a proposal or request further information, please contact the appropriate Springer Editor:

- Mr. Pierpaolo Riva at pierpaolo.riva@springer.com (Europe and Americas);
- Ms. Swati Meherishi at swati.meherishi@springer.com (Asia - except China, and Australia, New Zealand);
- Dr. Mengchu Huang at mengchu.huang@springer.com (China).

All books in the series now indexed by Scopus and EI Compendex database!

More information about this series at <http://www.springer.com/series/15087>

J. N. Reddy · Chien Ming Wang ·
Van Hai Luong · Anh Tuan Le
Editors

ICSCEA 2019

Proceedings of the International Conference
on Sustainable Civil Engineering
and Architecture



Springer

Editors

J. N. Reddy
Department of Mechanical Engineering
Texas A&M University
College Station, TX, USA

Van Hai Luong
Faculty of Civil Engineering, Ho Chi Minh
City University of Technology (HCMUT)
Vietnam National University Ho Chi Minh
City (VNU-HCM)
Ho Chi Minh City, Vietnam

Chien Ming Wang
School of Civil Engineering
The University of Queensland
St. Lucia, QLD, Australia

Anh Tuan Le
Faculty of Civil Engineering, Ho Chi Minh
City University of Technology (HCMUT)
Vietnam National University Ho Chi Minh
City (VNU-HCM)
Ho Chi Minh City, Vietnam

ISSN 2366-2557

ISSN 2366-2565 (electronic)

Lecture Notes in Civil Engineering

ISBN 978-981-15-5143-7

ISBN 978-981-15-5144-4 (eBook)

<https://doi.org/10.1007/978-981-15-5144-4>

© Springer Nature Singapore Pte Ltd. 2020

This work is subject to copyright. All rights are reserved by the Publisher, whether the whole or part of the material is concerned, specifically the rights of translation, reprinting, reuse of illustrations, recitation, broadcasting, reproduction on microfilms or in any other physical way, and transmission or information storage and retrieval, electronic adaptation, computer software, or by similar or dissimilar methodology now known or hereafter developed.

The use of general descriptive names, registered names, trademarks, service marks, etc. in this publication does not imply, even in the absence of a specific statement, that such names are exempt from the relevant protective laws and regulations and therefore free for general use.

The publisher, the authors and the editors are safe to assume that the advice and information in this book are believed to be true and accurate at the date of publication. Neither the publisher nor the authors or the editors give a warranty, expressed or implied, with respect to the material contained herein or for any errors or omissions that may have been made. The publisher remains neutral with regard to jurisdictional claims in published maps and institutional affiliations.

This Springer imprint is published by the registered company Springer Nature Singapore Pte Ltd.
The registered company address is: 152 Beach Road, #21-01/04 Gateway East, Singapore 189721,
Singapore

Committees

Member of ICSCEA International Scientific Committee

J. N. Reddy, Texas A&M University, USA
Chien Ming Wang, The University of Queensland (UQ), Australia
Chris Mannaerts, University of Twente, Netherlands
Chunwei Zhang, Qingdao University of Technology, China
Hitoshi Tanaka, Tohoku University, Japan
Jaroong Rungamornrat, Chulalongkorn University, Thailand
Jin-Ho Park, Inha University, Korea
Kok Keng Ang, The National University of Singapore, Singapore
Massimo Menenti, Delft University of Technology, Netherlands
Roderik Lindenbergh, Delft University of Technology, Netherlands
Teerapong Senjuntichai, Chulalongkorn University, Thailand
Tomoaki Utsunomiya, Kyushu University, Japan
Asif S Usmani, The Hong Kong Polytechnic University, Hong Kong
Baji Hassan, Central Queensland University, Australia
Chi Won Ahn, Korea Advanced Institute of Science and Technology, Korea
Chung Bang Yun, Ulsan National Institute of Science and Technology, Korea
Hong Hao, Curtin University, Australia
Jaehong Lee, Sejong University, Korea
Jian-Guo Dai, Hong Kong Polytechnic University, Hong Kong
Keh Chyuan Tsai, National Taiwan University, Taiwan
Kenichiro Nakarai, Hiroshima University, Japan
Kenji Kawai, Hiroshima University, Japan
Lasef Md Rian, Xi'an Jiaotong-Liverpool University, China
Li Jia, China University of Geosciences, China
Lindung Zalbuin Mase, University of Bengkulu, Indonesia
Mike Xie, RMIT University, Australia
Mitsutaka Sugimoto, Nagaoka University of Technology, Japan
Ong Wee Keong, Fyfe Asia, Singapore

Pruettha Nanakorn, SIIT, Thammasat University, Thailand
Quoc Tinh Bui, Tokyo Institute of Technology, Japan
Ryunosuke Kido, Kyoto University, Japan
Sachie Sato, Tokyo City University, Japan
Safoora Zaminpardaz, RMIT University, Australia
Salman Azhar, Auburn University, USA
Seok Hong Lee, Chung-Ang University, Korea
Sritawat Kitipornchai, The University of Queensland (UQ), Australia
Suelynn Choy, RMIT University, Australia
Takeshi Satoh, The University of Tokyo, Japan
Yeong Bin Yang, Chongqing University, China
Yuko Ogawa, Hiroshima University, Japan

Local Scientific Committee

Anh Thang Le
Anh Tuan Bui Le
Chau Lan Nguyen
Dinh Nhan Dao
Dinh Thanh Chau
Duc Hien Le
Duy Quoc Huu Phan
Hai Pham
Hong Tham Duong
Huu Phu Nguyen
Huy Cung Nguyen
Minh Tam Nguyen
Minh Truc Thi Huynh
Minh Tung Tran
Nam Tuan Tran
Ngoc Chau Dang
Ngoc Than Tan Cao
Ngoc Tri Ngo
Nguyen Thi Cao
Ninh Thuy Nguyen
Phu Cuong Nguyen
Quang Minh Nguyen
Quang Trung Nguyen
Si Lanh Ho
Tan Van Vu
Thanh Danh Tran
Thanh Nhat Tran
Thoi Trung Nguyen

Thu Huong Thi Le
Trong Phuoc Huynh
Trong Phuoc Nguyen
Trong Toan Khong
Trung Kien Nguyen
Tuan Kiet Tran
Van Hieu Nguyen
Van Phuc Le
Van Vuong Nguyen Do
Xuan Hung Nguyen

HCMUT's Scientific Committee

Thanh Phong Mai
Minh Phuong Le
Danh Thao Nguyen
Anh Tuan Le
Van Hai Luong
Xuan Loc Luu
Hoai Long Le
Thai Binh Nguyen
Phuong Trinh Bui
Ngoc Thi Huynh
Anh Thu Nguyen
Anh Thu Thi Phan
Ba Vinh Le
Bao Binh Luong
Bao Thu Thi Le
Bay Thi Nguyen
Dang Trinh Nguyen
Duc Duy Ho
Duc Hoc Tran
Hai Yen Tran
Hien Vu Phan
Hoang Hung Nguyen Tran
Hong An Nguyen
Hong Luan Pham
Hong Na Thi Le
Hong Son Vu Pham
Manh Tuan Nguyen
Nhut Nhut Nguyen
Quang Truong Nguyen
Quoc Bang Tran

Quoc Hoang Vu
Quoc Vinh Nguyen
Son Thai
Tien Dac Tran
Tien Sy Do
Tinh Nghiem Ngoc Doan
Trong Hieu Dinh Nguyen
Tuan Duc Ho
Tuyet Giang Thi Vo
Van Phuoc Nhan Le
Van Qui Lai
Van Vui Cao
Xuan Long Nguyen
Xuan Qui Lieu
Xuan Vu Nguyen

Local Organizing Committee

Chairman

A/Prof. Anh Tuan Le

Co-chairman

A/Prof. Van Hai Luong

Members

Dr. Thai Binh Nguyen
Dr. Phuong Trinh Bui
Dr. Ngoc Thi Huynh
Ms. Bich Phuong Thi Nguyen

Sponsors



Preface

On behalf of the Organizing Committee, it is our great pleasure to welcome you to the International Conference on Sustainable Civil Engineering and Architecture (ICSCEA) 2019 in Ho Chi Minh City. The conference is hosted by Ho Chi Minh City University of Technology (HCMUT), Vietnam National University Ho Chi Minh City (VNU-HCM).

The conference aims at a closer collaboration and cooperation between Vietnamese and worldwide scholars in civil engineering and architecture. The organizers expect to organize this conference biannually to create innovative space for scholars in civil engineering and architecture to share, to exchange, to connect, and to build a better world. As a developing country, Vietnam considers civil engineering and architecture as the key fields to transform the country quickly to be a developed and modern country.

The conference program includes 12 plenary and keynote lectures, and more than 120 contributions to the field of civil engineering and architecture throughout one and a half days in four sets of five parallel oral sessions. A majority of them come from universities and research institutes of countries such as Australia, Belgium, China, Dubai, Japan, Netherlands, Singapore, Korea, Taiwan, Thailand, USA, Vietnam, and so on. This proceedings of the ICSCEA 2019 contains selected papers that cover almost all the topics in civil engineering and architecture. We hope that the papers in this volume of proceedings will trigger new ideas in your professional work and research.

We would like to thank all authors for their contributions to this conference. We also would like to thank the staff members of the HCMUT, VNU-HCM for providing assistance during the preparation stage of this conference. We send our

sincere gratitude to the dedicated reviewers for their time and contribution to enhance the scientific quality of the manuscripts. Last but not least, we acknowledge the support received from the sponsors. Without all this invaluable help, it is difficult to imagine the success of this conference.

Ho Chi Minh City, Vietnam

J. N. Reddy
Chien Ming Wang
Van Hai Luong
Anh Tuan Le
Editors of the ICSCEA 2019 Proceedings

Contents

Plenary and Keynote

Floating Solutions for Challenges Facing Humanity	3
C. M. Wang and Brydon T. Wang	
Decadal Morphological Recovery of Estuaries and Coasts	
After the 2011 Tohoku Tsunami	31
Hitoshi Tanaka and Trong Hiep Nguyen	
Formal Techniques for Emergent Architectural Designs	43
Jin-Ho Park	
Research and Development of New Spaces on the Sea for Industrial and Recreational Applications	57
Kok Keng Ang, Jian Dai, and Chi Zhang	
Analytical Methods for Dynamic Interaction Between Strip Foundations and Poroelastic Soils	85
Teerapong Senjuntichai and Suraparb Keawsawasvong	
Floating Offshore Wind Turbines in Goto Islands, Nagasaki, Japan . . .	103
Tomoaki Utsunomiya, Iku Sato, and Takashi Shiraishi	

Architecture Session

Adaptive and Variable Building Envelopes: Formal Methods and Robotic Fabrication	117
Su Jung Ji, Jin-Ho Park, Se Jung Jeong, and Yang Sook Jeon	
An Analysis of Green Building Certification Systems in Vietnam	125
Le Thi Hong Na and Dang Nguyen Hong Anh	
Design Exploration and Fabrication Using Industrial Robotic Arm . . .	135
Seung Beom Park, Jin-Ho Park, You Jin Park, and Tuan Anh Nguyen Vu	

Assessment of Roof Architecture of Street Houses in Some Central Districts of Ho Chi Minh City	143
Le Thi Hong Na and Nguyen Dang Hoang Nhat Truong	
Hanoi Old Quarter with Its Historic Tube House Transition in the Vietnam Context.....	153
Minh Hung Ngo	
Identifying and Assessing the Attractiveness of Public Spaces for the Youth as a Key Factor to Help Establish Social Sustainability—Case Studies from Hanoi	159
Quang Minh Nguyen, The Trung Doan, Quynh Hoa Ta, Manh Tri Nguyen, Tien Hau Phan, Ngoc Huyen Chu, and Thi Thanh Hien Pham	
Public Park Behavior Relationship in Danang: An Impact of Physical Environment on User's Behaviors	175
Duy Thinh Do and Thi Vy Phuong Vo	
Studies on Household Water Consumption and Water-Saving Solutions for Four Cities in the Red River Delta (Hanoi, Hai Phong, Hai Duong and Nam Dinh).....	185
Quang Minh Nguyen	
The Inter-relationships Between LST, NDVI, NDBI in Remote Sensing to Achieve Drought Resilience in Ninh Thuan, Vietnam	201
Nguyen Quoc Vinh, Nguyen Trong Khanh, and Pham Thi Anh	
Urban Appearance in the Industry 4.0—In Case of Ho Chi Minh City	211
Le Thi Bao Thu	
Concrete and Steel Sessions	
A Study on Strain Contour Plots and Crack Development for Reinforcement Concrete Beams Based on the Application of DIC Technique	221
Anh Thang Le, H. T. Tai Nguyen, N. T. Hung, and Quy Duc Le	
Application of Modified D-Value Method Considering Plastic Strain Hardening Effect to Prediction of Structural Mechanics of Steel Moment Resisting Frames with New Column Support System	231
Naoki Tamura, Sachi Furukawa, and Yoshihiro Kimura	
Calibrating the K&C Material Model for Fiber Reinforced Concrete Structures	241
Duc-Kien Thai and Duy-Duan Nguyen	
Cyclic Loading Tests of Steel Pile Filled with Concrete at Pile Top Subjected to Tensile Axial Force	251
Tomoya Saito, Toshiharu Hirose, and Yoshihiro Kimura	

Effect of Indentation Strain Rate on Plastic Properties in SS400 Steel Weld Zone	259
Thai-Hoan Pham and Ngoc-Vinh Nguyen	
Elastic Buckling Load of Continuous Braced H-Shaped Beams with Fork Restraint	269
Yui Sato and Yoshihiro Kimura	
Experimental Study of Reinforced Concrete Beams Strengthened by High-Strength Fiber Reinforced Concrete	279
T. Hung Nguyen, Anh Thang Le, G. Phat Kha, and C. V. Duc Phan	
Investigating the Crack Velocity in Ultra-High-Performance Fiber-Reinforced Concrete at High Strain Rates	287
Tri Thuong Ngo, Duy Liem Nguyen, and Ngoc Thanh Tran	
Modeling of Reinforced Concrete Beam Retrofitted with Fiber Reinforced Polymer Composite by Using ANSYS Software	295
Trong Toan Khong, Quoc Tinh Tran, and Van Trinh Do	
Nonlinear Inelastic Analysis for Steel Frames	311
Phu-Cuong Nguyen, Tran-Trung Nguyen, Qui X. Lieu, Thanh-Tuan Tran, Phong Thanh Nguyen, and Trong-Nghia Nguyen	
Optimization of Steel Panel Damper Design for Seismic Moment Frames	319
Keh-Chyuan Tsai and Chu-Hung Chang	
Relationship Between the Intensity and Young's Module of Concrete Over Time	329
Phuc Binh An Nguyen, Quang Thai Bui, and Thanh Dung Ho	
Shear Resistance Behaviours of a Newly Puzzle Shape of Crest Bond Rib Shear Connector: A FEM Modelling Study to Compare with the Previous Experimental	343
Trong Toan Khong, Quoc Tinh Tran, and Van Trinh Do	
Simulation of Concrete-Filled Steel Box Columns	359
Duc-Duy Pham, Phu-Cuong Nguyen, Duy-Liem Nguyen, and Hoang-An Le	
Study on Two-Directional Seismic Deterioration of Tested Steel Columns	367
Tran Tuan Nam	
Test of a Full-Scale Two-Story Steel X-BRBF: Strong-Axis Instability of Buckling Restrained Brace Associated with Out-of-Plane Bending of Gusset Connections	375
Dinh-Hai Pham and Chung-Che Chou	

Using Deterministic Approach to Predict Compressive Strength of High-Performance Fiber-Reinforced Concrete Under Different Sizes	381
Duy-Liem Nguyen, Phu-Cuong Nguyen, Ngoc-Thanh Tran, and Tri-Thuong Ngo	
Validation of Simulated Behavior of Blast Loaded Reinforced Concrete Columns Retrofitted with Tyfo® Fibrwrap® System Through Experiments	389
J. Quek, C. L. Liu, J. V. P. Musngi, and P. B. Malalasekara	
Vibration-Based Damage Identification of Steel Moment-Resisting Frames	399
Luc-Hoang-Hiep Nguyen and Duc-Duy Ho	
Construction Materials Session	
Adiabatic Temperature Rise and Thermal Analysis of High-Performance Concrete Bridge Elements	413
Tu Anh Do, Thuan Huu Nguyen, Thanh Xuan Vu, Tuyet Thi Hoang, Tam Duc Tran, and Thanh Tien Bui	
Air Permeability of Precast Concrete Box Culvert Applying Steam Curing Condition	425
May Huu Nguyen, Kenichiro Nakarai, and Saeko Kajita	
Chloride Penetration Test of Concrete Simulating Deicing Salt Attack	431
Yuka Yoshizumi, Kenichiro Nakarai, May H. Nguyen, Norie Tada, and Masayuki Yamamoto	
Comparative Performances of Reinforced Beams Using Concrete Made from Crushed Sand and Fly Ash	437
Duy-Liem Nguyen, Van-Thuan Nguyen, Minh-Phung Tran, and Minh-Thuan Duong	
Effect of Fly Ash and Alkaline Solution on Rheology of Foamed Concrete	447
Anh Tuan Le, Thuy Ninh Nguyen, and Hyugmoon Kwon	
Effect of Sodium-Silicate Treatment for Recycled Concrete Aggregate on Slump and Compressive Strength of Concrete	457
Phuong Trinh Bui, Huynh Sang Le, Phan Phuong Uyen Nguyen, Thanh Nam Ly, Ngoc Thanh Nguyen, Yuko Ogawa, and Kenji Kawai	
Effect of Water-to-Binder Ratio on Cementing Efficiency Factor of Fly Ash Regarding Compressive Strength of Concrete	467
Phat Tan Huynh, Phuong Trinh Bui, Yuko Ogawa, and Kenji Kawai	

Effects of Fiber Type and Volume Fraction on Fracture Properties of Ultra-High-Performance Fiber-Reinforced Concrete	477
Ngoc Thanh Tran, Tri Thuong Ngo, and Duy Liem Nguyen	
Evaluate Healing Performance of Asphalt Mixture Containing Steel Slag by Using Induction and Microwave Heating.....	485
Tam Minh Phan, Dae-Wook Park, Tri Ho Minh Le, and Jun-Sang Park	
Evaluating the Effect of Steel Fibers on Some Mechanical Properties of Ultra-High Performance Concrete	493
Cong Thang Nguyen, Huu Hanh Pham, Van Tuan Nguyen, Sy Dong Pham, and Viet Hung Cu	
Evaluation of Factors of Asphalt that Influence the Dynamic Modulus of Dense Asphalt Concrete in Viet Nam.....	503
Hai Nhu Nguyen, Anh Tuan Le, Hai Viet Vo, and Hoang Minh Tran	
Experimental Study on the Response of Ultra-High Performance Fiber Reinforced Concrete Slabs Under Contact Blast Loading	513
Ba Danh Le, Duy Hoa Pham, Cong Thang Nguyen, Duc Linh Ngo, and Thi Thuy Dung Bui	
Influence of Chloride Ion in Sea Sand on Mechanical Properties of Fly Ash Concrete Exposed to Accelerated Carbonation	521
Quoc Viet Dang, Aoi Okada, Yuko Ogawa, and Kenji Kawai	
Influence of Molar Concentration of Sodium Hydroxide Solution on High Temperature Resistance of Geopolymer Paste	531
T. Azeyanagi, A. Saludung, Y. Ogawa, and K. Kawai	
Investigation of Compressive Behaviors of Geofoams Made in Vietnam	539
Hoang-Hung Tran-Nguyen and Vinh P. Phan	
Investigation of Mechanical Properties of Fly Ash/RFCC Based Geopolymer Concrete	547
Anh Tuan Le, Khoa Tan Nguyen, Thuy Ninh Nguyen, Eunseo Kim, and Kihak Lee	
Investigation of the Influence of Residue Fluid Catalytic Cracking (FCC) on Properties of Autoclaved Aerated Concrete	553
Anh Tuan Le, Khoa V. A. Pham, Ninh Thuy Nguyen, Chorong Lee, and Kihak Lee	
Investigation on Moisture Transfer in Mortar After Exposure to High Temperature	563
M. Mizoguchi, T. Kitagawa, T. Daungwilailuk, Y. Ogawa, and K. Kawai	

Lead Adsorption on Cement Paste at Various pH Values Controlled by Different Methods	573
T. Nishiwaki, M. Yamasaki, S. J. Zhou, Y. Ogawa, and K. Kawai	
Lightweight Concrete Using Lightweight Aggregates from Construction and Demolition Wastes—Production and Properties	581
Hung Phong Nguyen, Ngoc Lan Le, Cong Thang Nguyen, Van Tuan Nguyen, Tuan Trung Nguyen, and Xuan Hien Nguyen	
Possibility of Using High Volume Fly Ash to Produce Low Cement Ultra High Performance Concrete	589
Sy Dong Pham, Van Tuan Nguyen, Trung Thanh Le, and Cong Thang Nguyen	
Strength Development Properties of Core Specimens Taken from Structural Concrete Test Specimens Prepared All Over Japan	599
Sachie Sato, Yoshihiro Masuda, and Hiroyuki Tanano	
Tensile Behavior of Ultra-High-Ductile Fiber-Reinforced Cementless Composites	607
Huy Hoang Nguyen, Jeong-Il Choi, Se-Eon Park, and Bang Yeon Lee	
Geotechnical and Transportation Sessions	
An Exploratory Test of Communicative Mobility Management for Promoting Modal Shift in Ho Chi Minh City	617
Hong Tan Van, Kiyohisa Terai, and Tetsuo Yai	
Analyze Shear Strain of Inhomogeneous Soil Considering Interaction Between SFRC Foundation and Soil	627
Tran-Trung Nguyen, Phu-Cuong Nguyen, Trong-Nghia Nguyen, Ngoc-Tuan Tran, Minh-Hoang Le, and Phong Thanh Nguyen	
Application of Bailey Method in Determining Aggregate Gradation in Dense Graded Asphalt Concrete in Vietnam	637
Manh Tuan Nguyen	
Application of EPS in the Road Construction on Soft Grounds	647
Hirahara Naoyuki, Le Ba Vinh, Satoshi Kobayashi, and To Le Huong	
Back Analysis on Deep Excavation in the Thick Sand Layer by Hardening Soil Small Model	659
Quoc Thien Huynh, Van Qui Lai, Viet Thai Tran, and Minh Tam Nguyen	
Consolidation Behavior of Soft Soil with Different Sample Sizes—A Case Study of Preloading Without PVD in Ho Chi Minh City	669
Nhat-Truyen Phu and Ba-Vinh Le	

Determination of Unloading—Reloading Modulus and Exponent Parameters (m) for Hardening Soil Model of Soft Soil in Ho Chi Minh City	677
Trung Ngo Duc, Phan Vo, and Thanh Tran Thi	
Effects of SPT Numbers on Liquefaction Potential Assessment of Fine Soil	691
Tham Hong Duong	
Evaluating the Possible Use of High Modulus Asphalt Mixtures in Flexible Pavements in Vietnam	701
T. Nhan Phan and H. T. Tai Nguyen	
Experimental Studies on the Improvement of Soft Soils by Cement in Vinh Long City	709
Quang Vinh Pham, Nhat Truyen Phu, Ba Vinh Le, and Dinh Uy Vo	
Finite Element Analysis of a Deep Excavation Adjacent to the Ben Thanh—Suoi Tien Metro Tunnels	717
Le Ba Vinh, Ngoc Trieu Hoang, Hoang The Thao, and Hoang Long Hai	
Generating a 3D Point Cloud of a Small Steel Bridge Model Structure Using a Hokuyo UTM 30LX Laser Scanner	729
Ngoc Thi Huynh and Anh Thu Thi Phan	
Optimal Design for Rutting Resistance of Asphalt Concrete Pavements by Experimental Testing and Finite Element Modelling	737
Chau Phuong Ngo, Van Bac Nguyen, Ngoc Bay Pham, Thanh Phong Nguyen, Van Phuc Le, and Van Hung Nguyen	
Performance Analysis of a Combination Between D-Wall and Secant Pile Wall in Upgrading the Depth of Basement by Plaxis 2D: A Case Study in Ho Chi Minh City	745
Van Qui Lai, Minh Nhan Le, Quoc Thien Huynh, and Thanh Hai Do	
Performance Analysis of Axially Loaded Piles by Load Transfer Method: A Case Study in Ho Chi Minh City	757
Van Qui Lai, Quoc Thien Huynh, Thanh Hai Do, and Thi Gai Nguyen	
Practical Performance of Magnetostrictive Vibration Energy Harvester in Highway Bridge	767
Tuan Minh Ha, Saiji Fukada, Toshiyuki Ueno, and Duc-Duy Ho	
Quality Assessment of Field Soilcrete Created by Jet Grouting in the Mekong Delta	777
Hoang-Hung Tran-Nguyen and Nhungh H. D. Ly	
Studies on the Effects of Raft and Piles on Behavior of Piled Raft Foundations	785
Le Ba Vinh, To Le Huong, Le Ba Khanh, and Hoang The Thao	

Uncertainties in Problem of Ground Improvement Using Prefabricated Vertical Drains (PVD) and Seeking a Cost-Effective Design Applying Monte Carlo Sampling.....	795
Tham Hong Duong and Kim Truc Do Thi	
Remote Sensing, Construction Management and Water Resource Engineering Sessions	
A Proposed Model for Predicting the Risks of Contamination Intrusion in Water Distribution System	805
Thi Minh Lanh Pham and Quang Truong Nguyen	
Accuracy Assessment of 3D Point Clouds Collected by a Low Cost UAV-Based Laser Scanner System	815
Cong Bang Van Dang, Kazuyoshi Takahashi, and Anh Thu Thi Phan	
Application of Information and Communication Technology in Construction Companies in Vietnam	825
Khoa Dang Vo, Chau Ngoc Dang, Chau Van Nguyen, Hiep Trong Hoang, An Thanh Nguyen, Quan Khac Nguyen, and Long Le-Hoai	
Apply System Dynamic in Resolving the Dispute of Time Delay in Viet Nam Construction Project	835
H. L. Pham and N. T. Le	
Applying Water Footprint Model to Estimate Water Requirements of Rice Crops	849
Vu Hien Phan and Anh Tuan Nguyen	
Cost and Environmental Benefit Analysis of Solar—Panel Installation on Glass Surfaces to Reduce the Energy Consumption in High Rise Buildings	857
Trung Quang Nguyen, Duc Long Luong, Anh-Duc Pham, and Quynh Chau Truong	
Decision Scaling Approach to Assess Climate Change Impacts on Water Shortage Situation in the Ba River Basin—Vietnam.....	867
V. T. V. Anh, T. Thuc, N. Thong, and P. T. T. Duong	
Development of Africa Wild Dog Optimization Algorithm for Optimize Freight Coordination for Decreasing Greenhouse Gases.....	881
Pham Vu Hong Son and Tran Trong Khoi	
Estimating Values of the Can Gio Mangrove Ecosystem Services Using Remote Sensing	891
Nguyen Hoang Yen and Dao Nguyen Khoi	

Contents	xxi
Evaluation of Spatial Planning Solutions in Terms of Urban Water Management Using the Multi-criteria Method	903
Ngoc Tu Tong	
Investigating Partnering Performance in the Vietnamese Construction Industry	915
Khoa Dang Vo, Sy Tien Do, Thu Anh Nguyen, Chau Ngoc Dang, Thanh Huy Tran, and Long Le-Hoai	
Management of Buildings with Semantic and 3D Spatial Properties by S_EUDM Data Model	931
T. V. Phan, G. T. Anh Nguyen, and Trung Tran Do Quoc	
Monitoring the Spatio-Temporal Changes of Can Gio Mangrove Forest Using Google Earth Engine	941
Vu Hoang Dinh Phuc and Dao Nguyen Khoi	
Progress Report on the Present Conditions and Technical Cooperation Related to Bridge Maintenance Management in Kingdom of Bhutan	951
T. Kameda, S. Nii, K. Takahashi, K. Wakabayashi, and K. Konno	
Quantitative Structuring for the Strategy Map of Coastal Urban Projects Using a Hybrid Approach of Fuzzy Logic and DEMATEL	957
Truc Thi Minh Huynh, Duc-Hoc Tran, Anh-Duc Pham, and Long Le-Hoai	
Review the Vietnamese Contractor's Roles in Implementing the Prerequisites of LEED v4 BD + C Project	969
Duy Hoang Pham, Huyn Kyu Shin, and Yong Han Ahn	
Rice Crop Monitoring in the Mekong Delta, Vietnam Using Multi-temporal Sentinel-1 Data with C-Band	979
Hoang Phi Phung and Lam Dao Nguyen	
Storage Tank Inspection Based Laser Scanning	987
L. Truong-Hong, R. Lindenbergh, and P. Fisk	
Studying Wind Flow-Field Around a Triangular Building by CFD and Wind Tunnel	997
Do N. Ngo, Y. Q. Nguyen, Anh T. Tran, and Hien T. Le	
Variation Order Management in Vietnam Construction Projects	1007
Nam N. N. Tran, Sy T. Do, Thu A. Nguyen, and Long H. Le	

Structure Session

Dynamic Analysis of Multi-layer Connected Plate Resting on a Pasternak Foundation Subjected to Moving Load	1017
Tan Ngoc Than Cao, Van Hai Luong, Xuan Vu Nguyen, and Minh Thi Tran	
A Proposed Method for Inspecting and Predicting the Seismic Vulnerability of Dam Structures in Korea	1027
Anh-Tuan Cao, Thanh-Tuan Tran, Tahmina Tasnim Nahar, and Dookie Kim	
Analysis of the Relationship Between the Deflection Pattern of a Floating Plate Induced by Moving Load and the Material Angle by Using the Boundary Element-Moving Element Method	1037
Xuan Vu Nguyen, Van Hai Luong, Tan Ngoc Than Cao, and Minh Thi Tran	
Case Study on Field Application of Structural Strengthening Technique with Fire-Protection to a Commercial Building	1045
L. X. Binh, V. N. Linh, D. X. Quy, H. V. Quan, H. V. Tuan, and W. K. Ong	
Damage Detection in Plates with Different Boundary Conditions Using Improved Modal Strain Energy Method	1059
Thanh-Cao Le, Tan-Thinh Nguyen, Thanh-Canh Huynh, and Duc-Duy Ho	
Dynamic Analysis of Beams on Nonlinear Foundation Considering the Mass of Foundation to Moving Oscillator	1069
Trong Phuoc Nguyen and Minh Thi Ha	
Energy Simulation and Life Cycle Cost Analysis for Designing Energy Efficient Commercial Buildings in Pakistan	1079
Najam Us Saqib and Salman Azhar	
Evaluation of Response Variability of Euler–Bernoulli Beam Resting on Foundation Due to Randomness in Elastic Modulus	1087
Ta Duy Hien and Phu-Cuong Nguyen	
Experimental and Numerical Modal Analysis of Cabinet Facility Considering the Connection Nonlinearity	1093
Thanh-Tuan Tran, Anh-Tuan Cao, Kashif Salman, Phu-Cuong Nguyen, and Dookie Kim	
Experimental Modelling of Self-excited Responses of a Square Cylinder in Smooth Wind Flow	1101
Cung Huy Nguyen, Van Tan Vu, and Khang Thanh Huong	

Free Vibration Analysis of FG Sandwich Plates on Elastic Foundation Using a Refined Quasi-3D Inverse Sinusoidal Shear Deformation Theory	1107
Tan-Van Vu, Ngoc-Hung Nguyen, Tan-Tai Huynh Nguyen, Canh-Tuan Nguyen, Quang-Hung Truong, and Ut-Kien Van Tang	
Hydroelastic Analysis of Floating Plates Subjected to Moving Loads in Shallow Water Condition by Using the Moving Element Method	1119
Xuan Vu Nguyen, Van Hai Luong, Tan Ngoc Than Cao, and Minh Thi Tran	
Multi-patch Geometrically Nonlinear Isogeometric Analysis of Spatial Beams with Additive Rotation Updates	1129
Duy Vo, Pruettha Nanakorn, and Tinh Quoc Bui	
Optimal Compensation of Axial Shortening in Tall Buildings by Differential Evolution	1137
Duc-Xuan Nguyen and Hoang-Anh Pham	
Postbuckling Isogeometric Analysis of Functionally Graded Carbon Nanotube-reinforced Composite Shells Under Combined Loading	1145
Tan N. Nguyen, Pham Toan Thang, Dieu Thanh Thi Do, Seunghye Lee, and Jaehong Lee	
Safety of Structures in Fire	1153
Asif S. Usmani	
Stochastic Modelling for Service Life Prediction of Underground Tunnels Subjected to Water Ingress	1161
Hassan Baji and Hamid Reza Ronagh	
Structural Damage Detection in Space Frames Using Modal Strain Energy Method and Genetic Algorithm	1169
Quang-Huy Le, Van-Phuong Huynh, Minh-Tuan Ha, and Duc-Duy Ho	
Structural Damage Detection Using Model Order Reduction and Two-Stage Method	1179
Qui X. Lieu, Phu-Cuong Nguyen, Seunghye Lee, Jaehong Lee, and Van Hai Luong	
The Application of Basalt Fiber Fabric to Reinforce the Structures in the Construction Industry	1189
Thi Ngoc Quyen Nguyen	
The Impacts of Different Structural Design Alternatives on the Embodied Emissions of Flat Plate Buildings	1199
Tran Mai Kim Hoang Trinh, Sanaul Chowdhury, Jeung-Hwan Doh, and Cai Shunyao	

The Reduction of Vibration of Multiple Tuned Mass Dampers in Continuous Beam Traversed by Moving Loads	1209
Trong Phuoc Nguyen and Duy Thoai Vo	
Topology Optimization of Two-Dimensional Trusses Using Improved Particle Swarm Optimization	1219
Phirun Hou and Pruettha Nanakorn	
Transverse Galloping Analysis of a Sculptural Column	1229
Cung Huy Nguyen, Tai Dinh Truong, Kha Dinh Nguyen, and Van Hai Luong	
Two-Dimensional Truss Topology Design by Reinforcement Learning	1237
S. Sahachaisaree, P. Sae-ma, and P. Nanakorn	
Updating the Reliability of Aging Miter Gates in the Presence of Corrosion and Fatigue	1247
Thuong Van Dang, Quang Anh Mai, Pablo G. Morato, and Philippe Rigo	
Vibration Analysis in Designing Post-tensioned Slabs	1255
Ha Thu Tran and Hung Manh Tran	

Plenary and Keynote

Floating Solutions for Challenges Facing Humanity



C. M. Wang and Brydon T. Wang

1 Introduction

In 2003, Nobel Laureate Richard Smalley presented a list of top ten ‘global concerns’ that humanity had to contend with over the next half a century [27]. These global concerns (as set out in descending order of priority) are: energy insecurity and the need for alternative sources to fossil fuel; water shortages; food scarcity; environmental threats from climate change and pollution; poverty; terrorism and war; disease, the education gap, the development of democracy, and over-population [26].

Twelve years later, the United Nations General Assembly adopted resolution 70/1 that set out 17 Sustainable Development Goals or SDGs for brevity [22]. The goals provided a framework that allowed countries (both developed and developing nations) to align their efforts to, in essence, solve a similar set of problems to Smalley’s list of global concerns.

The authors suggest that how we choose to deploy infrastructure and build our cities will have a significant impact on the way we are able to respond to the global concerns and meet the SDGs. While the challenge of adopting cheap and abundant renewable energy sources is given pre-eminent position on the list of global concerns, this article considers that any infrastructure solution addressing the challenge of abundant clean energy production (or any of the remaining global concerns) must also contend with the environmental threat of rising sea levels, particularly in light of coastal urbanisation. Accordingly, this article positions the environmental threat of rising sea levels and extreme storm events on the same level of pre-eminence on the list of global concerns [18].

C. M. Wang (✉)

School of Civil Engineering, The University of Queensland, St Lucia, QLD 4072, Australia
e-mail: cm.wang@uq.edu.au

B. T. Wang

School of Law, Queensland University of Technology, Brisbane, QLD 4000, Australia

However, rather than armouring our coastlines against the increasing threat of rising sea levels, there is a need to consider the ocean as a means of providing succour to our emerging needs. Ocean exploration has fuelled advancement in drugs, food and energy; vastly improving the quality of life on earth. In fact, twenty percent of the protein we consume comes from seafood, and half of the oxygen we breathe comes from the oxygen produced by phytoplankton photosynthesis in the sea [23]. This has given rise to a constellation of different economic and socio-political activities seeking to sustainably leverage the resources of the ocean while broadly preserving and enhancing ocean ecosystems. These activities fall under the broad umbrella of the ‘Blue Economy’ which is defined by the World Bank as the ‘sustainable use of ocean resources for economic growth, improved livelihoods and jobs, and ocean ecosystem health’ [30].

In this paper, we present floating solutions in four parts to address the challenges of energy insecurity, clean water and food shortages, environmental concerns, and to support resilient communities in addressing social issues of poverty and population pressures on urban development. The authors note that the floating solutions set out in this article allow us to support the Blue Economy and meet the following SDGs:

(*SDG 7) affordable and clean energy*—through the use of floating wind turbines, floating solar farms, wave energy converters and the exploitation of ocean thermal energy conversion;

(*SDG 6) clean water and sanitation*—through the use of floating desalination plants that can be towed and deployed in crucial situations;

(*SDG 9) industry, innovation, and infrastructure*—through the use of floating structures to avail offshore fish farming and floating vegetable and dairy farms. Floating structures can also be used to support the blue economy through installations for tourism and cultural spaces;

(*SDG 13) climate action*—through the use of floating structures to access the ocean’s potential to provide abundant and clean energy, reducing dependency on fossil fuels and biomass for energy generation;

(*SDG 14) life below water*—through the use of floating structures and ecological engineering to reduce the impact of hard marine infrastructure on fragmentation of coastal environments and disruption to wave patterns, and a move away from the traditional land reclamation approach that destroys the marine ecology beneath the project footprint;

(*SDG 15) life on land*—through the potential for floating structures to enable cities to alleviate land pressures due to coastal urbanisation; and

(*SDG 11) sustainable cities and communities*—through *hybrid floating cities*, where cities expand over adjacent water bodies in an environmentally sensitive way while exploiting the ocean as a clean and abundant source of energy and site for food and clean water production.

2 Part 1: Floating Solutions for Harvesting Energy from Oceans

Smalley [26] notes that access to energy is the single most important factor that impacts the prosperity of any society. Cheap and abundant clean energy allows us to deploy technology to help us desalinate water, increase food production, reduce our impact on the environment from the use of fossil fuels and take steps to reduce our environmental footprint.

While we have met our energy demands by expanding into the oceans to exploit offshore oil and gas deposits, the oil crises of the 1970s sparked international research into offshore wind energy in the 1980s [12]. As the offshore renewable energy industry matures in certain jurisdictions and public desire for solutions to reduce carbon and greenhouse gas emissions become more urgent, a range of clean energy sources such as solar energy, wind energy, wave energy and tidal current energy are coming to the fore.

Presented in this section are floating solutions for harvesting different forms of energy from our oceans or siting sensitive energy infrastructure in the ocean to address energy insecurity and provide a means of obtaining clean and abundant energy without the use of fossil fuels and biomass.

2.1 *Floating Wind Turbines*

The ocean offers a source of cheap and abundant renewable energy. There is more wind in the oceans than on land with ‘estimates regarding global potential of wind energy capacity alone exceeding the IEA’s 2010 estimate of average global electricity generation’ [21]. Systematic Ocean Energy Resource assessment shows that offshore wind amount to more than 192,000 TWh/year [20].

This vast amount of wind energy from the ocean may be harvested using floating offshore wind turbines and made readily available to coastal populations. A significant advantage of offshore applications of wind turbines are that the actual components that make up the turbines do not have the same transportation constraints as their land-based alternatives, which allows floating wind turbines to be made at a significantly larger scale. Currently, onshore wind turbines range from 2.1 to 5.8 MW whereas offshore wind turbines range from 6.0 to 10.0 MW (Siemens Gamesa). In a recent demonstration project in Goto Island, Japan, a 2 MW spar floating wind turbine was designed and installed. It has a hybrid precast concrete and steel spar of 76 m in length that carries a 56 m tower with a rotor diameter of 80 m (see Fig. 1a). With the success of this project, plans are also underway to build another 8 larger floating wind turbines to supply electricity for the entire Goto Island. Similarly, Saitec is building concrete pontoon type floating wind turbines in Spain (see Fig. 1b) [16].

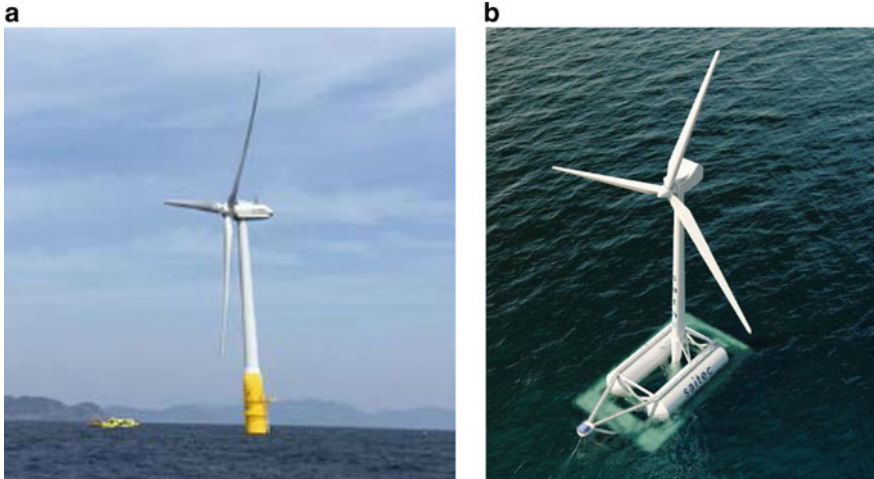


Fig. 1 **a** Floating spar wind turbine, Goto Island. **b** Saitec wind turbine on concrete pontoon off the coast of Spain

2.2 Wave Energy Converters

It is estimated that wave energy amounts to 80,000 TWh/year [20]. However, the technology extant is not at a level of maturity that readily allows the exploitation of wave energy at scale. At the heart of the operational challenges to harvesting wave energy is that the components of the converters tend to break down after a period of time due to the continual movement of their parts under enormous forces.

Pelamis was one of the first companies to commercialise ocean surface wave energy conversion. It began in 2004 with a prototype at the European Marine Energy Centre in Scotland that was followed by the Enersis Aguacadoura Wave Farm in Portugal. Unfortunately, the Portuguese installation proved to be short-lived, operating for less than half a year. Following a number of small-scale wave farms around Europe, Pelamis went into administration in November 2014 [2].

However, new technologies aimed at harvesting wave energy are still being tested. One such emerging technology is offered by Eco Wave Power where floaters that rest on the water surface are attached to an existing marine structure, such as a wharf, pier or breakwater. The technology utilises incoming surface waves through the use of floaters that pump hydraulic pistons, which in turn generates pressure that drives a hydraulic motor to create energy. The deployment of the technology along coastal installations increases accessibility and ease of maintenance. The technology has been successfully deployed in Gibraltar and in the Jaffa Port in Israel (see Fig. 2a) <https://www.ecowavepower.com/>.

Similarly, the Guangzhou Institute of Energy Conversion has developed a new form of wave energy converter based on energy absorbers mounted on a semi-submersible floating structure called the *Sharp Eagle* (see Fig. 2b). The energy

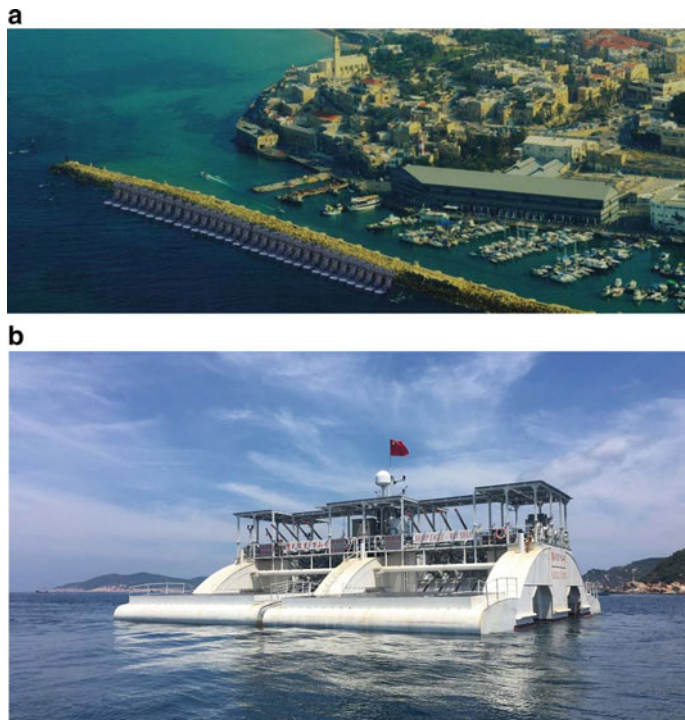


Fig. 2 **a** Eco wave power installation at Jaffa Port, Israel. **b** Sharp Eagle developed by Guangzhou Institute of Energy Conversion

production system was integrated into the grid at Dawanshan Island in 2015, and claims to have the highest average wave-to-wire efficiency recorded at 24% http://english.giec.cas.cn/ns/tn/201707/t20170725_181220.html.

2.3 *Floating Solar Farms*

Floating solar farms are installations of photovoltaic (PV) systems on floating structures. This form of siting PV arrays in the ocean is a fast-growing deployment option with over 100 installations worldwide [14]. One of the key advantages of the deployment strategy is that these floating solar farms can be located close to urban environments without the problem of overshadowing by adjacent buildings. Reservoirs, lakes, seas and oceans offer abundant space to site these floating solar farms. When deployed on reservoirs, floating solar farms help to reduce water loss via evaporation and prevent the growth of algae.

An example of such an installation is the Kagoshima Nantsujima mega solar power plant, a 70 MW floating solar plant in Kagoshima Prefecture of Southern Japan (see

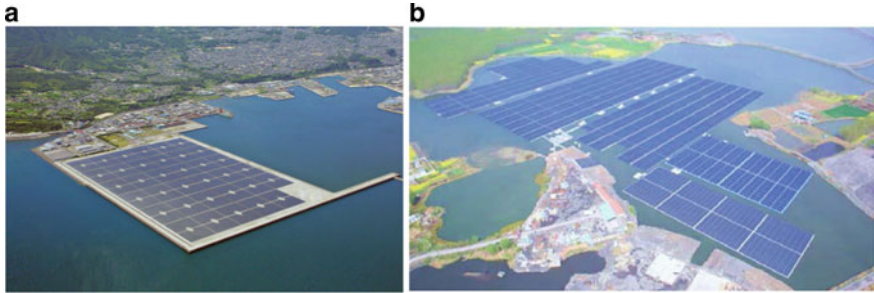


Fig. 3 **a** Floating solar plant in Kagoshima. **b** Floating solar farm in Huainan, China, which has been deployed over a flooded area that was once a coal mine

Fig. 3a) which started operation in 2013. The floating solar farm is presently the largest solar power plant in Japan with a capacity to generate enough electricity for 22,000 average households. Other examples include the floating solar farm at Yamakura dam, which houses 50,000 solar PV panels over 180,000 m² of the surface of a reservoir [32]. A large floating solar farm is found in Huainan, China, which started operation in 2017 (see Fig. 3b). It occupies a flooded area that was once a coal mine. The farm has the capacity to generate 40 MW of electricity to power 15,000 households. In Europe, London has also installed a 23,000 floating solar PV farm on a man-made reservoir near Heathrow airport [8]. Singapore has contributed significantly to the research in floating solar application on fresh water reservoirs by building the world's largest 1 MW floating solar testbed on the Tengeh Reservoir [14].

2.4 Ocean Thermal Energy Conversion (OTEC)

OTEC exploits the temperature differential between the warmer part of an ocean surface and the cooler waters deeper. Warm surface water with a temperature of around 25 °C is utilised to vaporise a working fluid that has a low-boiling point (such as ammonia). The vapour expands and spins a turbine coupled to a generator to produce electricity. By using risers (or vertical pipelines), cold water of about 4 °C is drawn from an ocean depth of 1 km to cool the ammonia vapour back to its liquid state for the power cycle. OTEC plants have yet to be built but it is envisaged that OTEC will be mankind's solution for its energy needs due to the abundance of solar energy that has been stored in the surface waters of oceans. Figure 4 shows Dr. Alfred Yee's 125 MW OTEC plant.



Fig. 4 Dr. Alfred Yee's 125 MW OTEC plant

2.5 Floating Nuclear Power Plants and Oil Storage Facilities

While not directly exploiting the ocean as a source of abundant and clean energy, the following floating solutions aim at addressing energy insecurity by locating energy infrastructure in close proximity to an urban population so as to reduce the requirement to build expensive electrical transmission infrastructure or to utilise valuable coastal land resources for energy or oil stockpiles. Such floating structures also exploit the natural moat of the surrounding ocean space that allows such sensitive installations to be securely operated despite its proximity to coastal populations.

Russia launched the world's first floating nuclear power plant in 2018 (see Fig. 5a). The 70 MW vessel christened the *Akademik Lomonosov* was towed away from

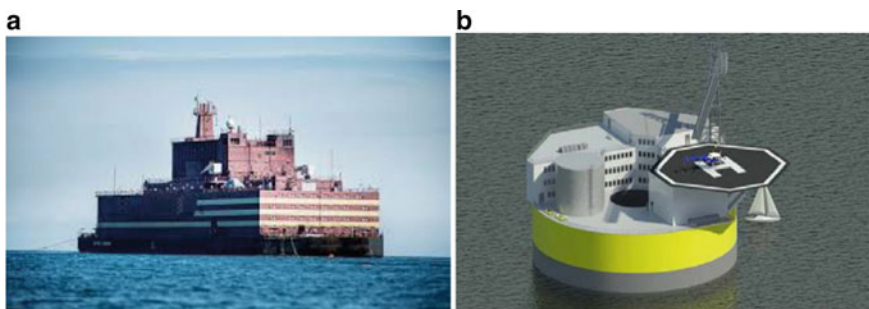


Fig. 5 **a** Russia's floating nuclear power plant. **b** Floating nuclear power plant

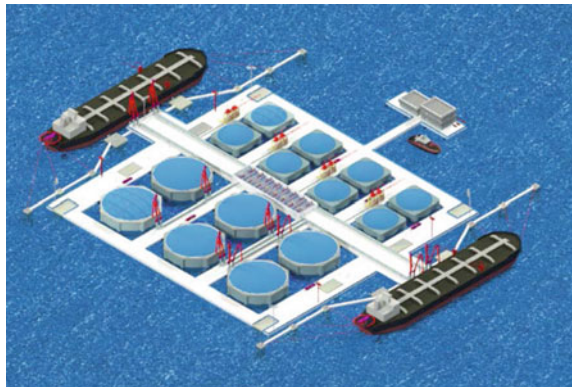
St Petersburg by two boats. It is presently deployed in the Arctic town of Pevek. A floating nuclear power plant makes economic sense where there is a need to supply power to highly remote locations. The ability to tow such energy infrastructure around is ideal as it reduces the need to construct powerlines and transmission towers to bring power to these remote locations. Currently, Russia and China are collaborating to develop other floating nuclear power plants (see Fig. 5b).

At present, oil tank farms are typically sited on land. For safety, these flammable oil tank farms could be floated out. Japan has shown that oil can be safely stored in the sea. There are large floating oil storage bases in Shirashima and in Kamigoto [31]. In Shirashima oil storage base, there are 8 large steel floating modules (each module measuring 397 m × 82 m × 25.1 m) and they can accommodate 5.6 million kL of crude oil. In the case of the Kamigoto base, there are 5 large steel floating modules (each module measuring 390 m × 97 m × 27.6 m) with a total storage capacity of 4.4 million kL (see Fig. 6). These floating oil storage bases were built over 20 years ago. Similarly, Singapore plans to build a floating hydrocarbon storage and bunker facility in its coastal waters due to lack of appropriate land space for oil tank farms. Figure 7 shows the proposed floating hydrocarbon storage and bunker

Fig. 6 Kamigoto floating oil storage base



Fig. 7 Floating hydrocarbon storage facility



facility as designed by researchers from the National University of Singapore and SINTEF [1, 36, 37].

Offshore storage facilities for the energy industry are also being considered by Deloitte Tohmatsu with offshore hydrogen storage facilities to be deployed in close proximity to offshore rigs in order to exploit and harvest the hydrogen by-product created in these installations [11].

3 Part 2: Floating Solutions to Address Water Shortages and Food Scarcity

Presented in this section are floating solutions that address water shortages and provide opportunities to increase offshore aquaculture and agricultural applications to meet increasing food demands.

3.1 *Floating Desalination Plants*

As climate change causes havoc with the world's rainfall distribution, some parts of the world like California, the Eastern Mediterranean, East Africa, South Africa and Australia have all experienced severe and in some cases unprecedented droughts in recent years. The global desalination market has expanded dramatically particularly in North America and the Middle East [11].

Kokubun noted that despite Southern California experiencing a continuous drought event that began in the early 1990s and lasting half a decade, it took until 2013 before construction began on a desalination plant at Carlsbad, California. Further, given concerns of environmental damage caused by drawing from adjacent coastal sources, land-based desalination plants are increasingly required to adopt expensive solutions to draw seawater from further out and at the bottom of the sea to avoid drawing in and killing small marine species in nearby coastal environments. These desalination plants are also expensive to operate with facilities left dormant after the particular drought event passes. In 2012, the Sydney Desalination Plant was left in a 'water security' mode after operating for two years, but was recently restarted in January 2019 (although it will take 8 months to restart the desalination facility).

Floating desalination plants offers a means of addressing water shortages in a faster, cheaper and more flexible manner. As these facilities can be floated to the urban centre at need, this flexibility of deployment to meet demand provides significant advantage. These facilities can also be located at sites further from coastal environments to 'preserve diversification of the shallow sea' environment [11].

Bowarege has developed the world's first self-contained desalination plants mounted on barges. Each barge has the capacity to produce 25,000 m³ a day of desalinated potable water from primary seawater. Barges are fitted with reverse osmosis



Fig. 8 Floating desalination plant at Jeddah

desalination plants, on-board power generators, laboratories, control rooms and staff accommodation. Since operations began in 2008, the floating desalination plants have provided emergency water supply to several Saudi Arabian cities. First moored at Shuaibah, south of Jeddah, delivering water to Makkah and Jeddah (see Fig. 8). They moved to Shuqaiq in 2009 until the Shuqaiq Independent Water and Power Project came online a year later, and since 2011 they have been at the Yanbu-Madinah desalination plants complex on the Red Sea to serve the industrial city of Yanbu and the city of Madinah. Cyprus and Thailand have similarly deployed floating desalination plants.

3.2 *Floating Fish Farms*

Despite the potential opportunity for using floating desalination plants as a means of clean water production, the existing state of play is that ‘available water resources appear insufficient for agriculture to meet the food demands’ of future populations [6]. This water shortage is exacerbated by forecast changes to the composition of diets with a shift to more meat (which consumes 10 times more water to produce per calorie) and a further ten per cent increase in calorie consumption. Coupled with the higher incidence of droughts and floods, the prospect of water shortages translates to greater food insecurity.

Fish is known to be the cheapest protein source that can be farmed to feed billions of people that will be added to the world. Fish has an excellent food conversion ratio of 1.2:1, i.e. we can expect 1.2 kg of protein from the fish by feeding it with 1 kg of protein [15]. The reason for this significant food conversion ratio is the fact that

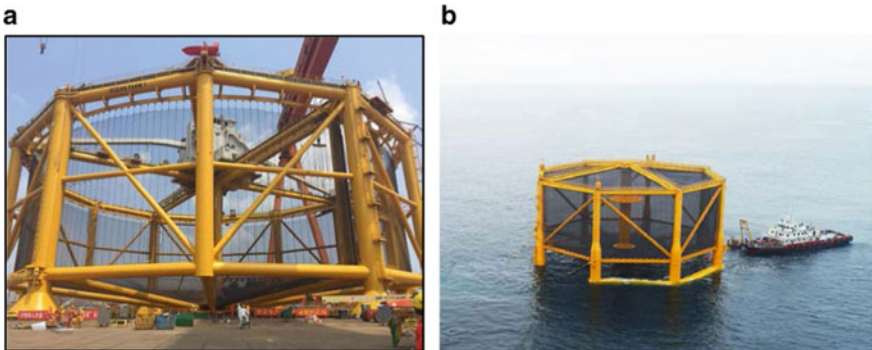


Fig. 9 **a** Norwegian's Ocean Farm 1. **b** Chinese's Shenlan 1

the fish is cold-blooded and the buoyancy force of its environment helps the fish to overcome gravity, allowing its bones to stay relatively small. Given the decline of yield in global fisheries, many countries with coastlines are now farming fish for food and for export, with aquaculture contributing to 39% of food production [6].

Duarte et al. [6] noted that fish farming in nearshore environment relies on the use of public coastal space. Accordingly, nearshore fish farms end up in direct ‘competition with other societal demands’. This leads to increased community opposition and in conflict with other usages such as shipping, fishing, tourism, conservation and recreation. Further, given the limited space available to nearshore fish farms, the farmed fish tend to be kept in crowded conditions that impact the coastal environment due to pollution caused by uneaten fish feed and fish faeces.

Conservative estimates by Duarte et al. [6] observed that an ocean shelf area of 26 million km² could support a distributed offshore fish farms production industry that would yield of 3×10^{10} to 6×10^{10} metric tonnes in fish products. The study, reported in 2009, observed that only 0.04% of shelf area was currently used for offshore fish farming. Accordingly, fish farm operators worldwide are planning to move offshore for more sea space and generally better water quality, which are needed to increase the production of healthy fish [33]. Figure 9a, b show huge offshore fish cages designed by the Norwegians and by the Chinese, respectively. These fish cages can accommodate more than 1 million salmon, and are 10 times larger than conventional open net cages in nearshore farming.

3.3 Floating Vegetable and Dairy Farms

In order to reduce transportation and energy costs in bringing food to coastal cities or cities with water bodies, floating vegetable and dairy farms have been proposed. The Barcelona-based Forward Thinking Architecture proposed a 2-tier floating farm



Fig. 10 Floating farm by Barcelona-based forward thinking architecture. <http://smartfloatingfarms.com/>



Fig. 11 Floating dairy farm in Rotterdam. Photo courtesy of Soon Heng Lim

with the first tier devoted to fish farming, the second tier for hydroponics vegetables and the roof covered with PV panels for power as shown in Fig. 10.

The first floating dairy farm in the world has been built in Rotterdam (see Fig. 11). The cows on this dairy farm produce milk which will be processed into various dairy products at the site on the water. Worldwide the idea of a floating farm is accepted as being animal friendly, economically sound and as a sustainable alternative to traditional agriculture. With this scalable and duplicable pilot, Rotterdam is testing the real possibilities for floating farms in cities.

4 Part 3: Floating Solutions to Address Environmental Concerns

4.1 Floating Solutions for Clean and Safer Water Environment

Smith-Godfrey [28] observed that the ‘inherently fluid nature’ of the ocean makes it challenging to isolate marine industries and other economic activities from impacting marine ecosystems. Burt et al. [4] note that the primacy of coastal cities in the global economy has led to considerable costs to the environment.



Fig. 12 Boyan Slat's long floating screens

The oceans have been used as rubbish dumpsites. In the Pacific Ocean, there is a garbage patch called the Pacific Trash vortex discovered in 1985. The garbage patch (a soupy mix of plastics and microplastics), now the size of Texas, is trapped by the ocean currents. In 2017, a 22-year old Boyan Slat proposed using a 2000 ft long floating plastic boom, attached to a geotextile skirt that extended about 10 ft beneath the water surface to concentrate the plastic garbage like an artificial coastline (see Fig. 12). The screens capture plastic trash as small as 1 cm and as large as discarded fishing nets. At regular intervals, a ship would transport the trash back to land where it would be recycled. By 2040, Slat promised that he could clear 90% of the trash. The removal of plastic garbage in the oceans is essential as it has been recently discovered that microplastics are found in the fish that we eat.

Rivers and coastal waters may potentially be cleaned by Vincent Callebaut's proposal of a whale-shaped floating garden that is designed to drift through the water bodies while cleaning the water by using a bio-filtration system (see Fig. 13) [17].

4.2 Floating Solutions for Protecting Fragile Shorelines, Beaches and Ports from Large Waves and Winds

Sustained coastal urbanization patterns have led to the alteration of coastal habitats to accommodate residential and commercial infrastructure. Land reclamation practices cause the complete destruction of the marine ecology below its urban footprint. This is exacerbated by the growing need to protect coastal development from the threat of sea level rises and the intensification and increased incidences of tropical storms. This has led to the prolific use of marine infrastructure such as breakwaters, seawalls, and pilings to protect the coastal urban fabric. However, these marine structures fragment the undersea environment and lead to significant loss of habitat [3].



Fig. 13 Vincent Callebaut's whale shaped floating garden

Engineering practices in respect of coastal urban development have shifted in response to growing awareness of the need to restore fragile shoreline environments. This has led to the development of ‘soft engineering’ practices that deploy the ‘wave attenuating and flood control properties of natural ecosystems such as marshlands, mangroves, and oyster reefs in order to reverse the impact of hard infrastructure changing coastal hydrodynamics and wave environments, particularly in intertidal and shallow subtidal habitats [3].

Instead of solid breakwaters breaking up littoral flows, large-scale floating breakwaters now provide a solution to shield all coastal assets from being destroyed by strong waves while ensuring that fragmentation of the undersea habitat is minimised [5]. By having a windbreak structure on the floating breakwaters, destructive wind speeds may also be reduced to manageable wind speeds. Wang et al. [35] in the University of Queensland have developed a floating forest (inspired by the mangrove forest) as part of a component of a mega floating breakwater and wind-break structure to protect fragile beaches, ports and marinas from extreme storms (see Fig. 14).

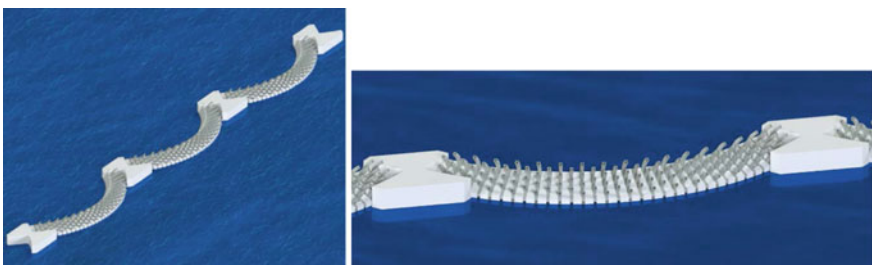


Fig. 14 Floating forest

This continues a new approach towards ‘ecological engineering’ that aims to integrate ‘theoretical and applied ecology … into the design of artificial, engineered structures in order to enhance both the environmental and human-use benefits of constructed habitats’ [4].

5 Part 4: Floating Solutions to Support Resilient Communities

5.1 *Hybrid Floating Cities: Architecture and Urban Design in Support of the Blue Economy*

Our crucial relationship with the ocean is highlighted by the significance of coastal cities where ‘80% of global trade transits through port cities and nearly two-thirds of the petroleum that powers the global growth engine … are transported via maritime networks’. This attraction to the ocean has driven coastal urbanisation such that close to 50% of global population, and two thirds of mega-cities worldwide are squeezed into the tenth of available global landmass that comprise our coasts [4].

Floating structures anchored onto the shoreline of coastal cities allow the creation of *hybrid floating cities*, where cities expand over their adjacent water bodies in an environmentally sensitive way while exploiting the ocean as a clean and abundant source of energy and site of food and clean water production. In such a manner, architecture and urban design can be harnessed to support and grow the Blue Economy.

In his germinal work on ‘Making a City’, John Montgomery noted two decades ago that the ‘sprawl, strip or edge city, more often than not planned around the automobile … is no longer considered sustainable (economically and socially as well as environmentally)’. Despite these observations, the compression of the urban form against shorelines naturally produces linear urban development that characterise strip or edge cities. By expanding over the adjacent water body, linear urban forms can be gradually reshaped to be made denser and more compact.

However, the idea of using floating solutions to shape and supplement coastal urban forms is not novel. The Japanese Metabolists and Archigram and Buckminster Fuller in the West provided sophisticated proposals that aimed to grow our cities into the adjacent ocean space, connecting floating communities back to the mainland via bridges [34].

This section surveys floating solutions, built and unbuilt, that offer key potential solutions for cities to utilise floating structures to create vibrant and new spaces for activity, bringing together disparate parts of the city through new floating infrastructure to permit greater densification of the existing urban environment.

First, given the intimate connection a floating structure offers to the water, there is a clear advantage offered by such installations to the tourism industry and for cultural activities. Montgomery notes the critical ingredient of ‘activity’ (described as



Fig. 15 Christo's floating walkway on Lake Iseo, Italy

'natural animation' or the 'city transaction base') to the success of urbanity. Where a city does not possess these spaces to 'facilitate exchange of information, friendship, material goods, culture, knowledge, insight, skills and also the exchange of emotional, psychological and spiritual support' ... the urban form of the city 'becomes progressively more lifeless, dull and inert'. Consequently, cities have also been using floating structures as a means of programming places for 'activity' into the city without subsuming existing parts of the urban fabric, and instead, utilising public ocean space.

In the summer of 2016, artist Christo deployed a 3 km long floating walkway in Lake Iseo, Italy. Comprising 220,000 high-density polyethylene cubes, the floating walkway was 16 m wide and was covered in 100,000 m² of shimmering yellow fabric (Fig. 15). Visitors who were attracted by the installation remarked that the experience had offered them the opportunity to feel like they were walking on water or the back of a whale.

This idea was duplicated as a scenic floating wooden 500 m walkway in Shiziguan, Hubei (see Fig. 16), and the world's longest boardwalk on the Hongshui River in China (see Fig. 17). Both floating solutions assisted in supporting the tourism industry in contributing significantly to the local economies.

But beyond the economic potential offered by such tourism installations, floating solutions can contribute to the vibrancy of the urban fabric of cities, contributing to the well-being of residents. In Singapore, floating wetlands were built to bring vibrancy onto the Punggol Waterway. Each floating wetland comprises hexagonal shaped HDPE modules with a hole in the middle of each module for water plants to be housed (see Fig. 18). But beyond the spaces for play and for activating the city, since the deployment of the wetlands project, the water quality in Punggol Waterway has improved and many pond animals are thriving on the wetlands. Additional floating



Fig. 16 Floating walkway in Hubei



Fig. 17 Floating boardwalk on Hongshui river

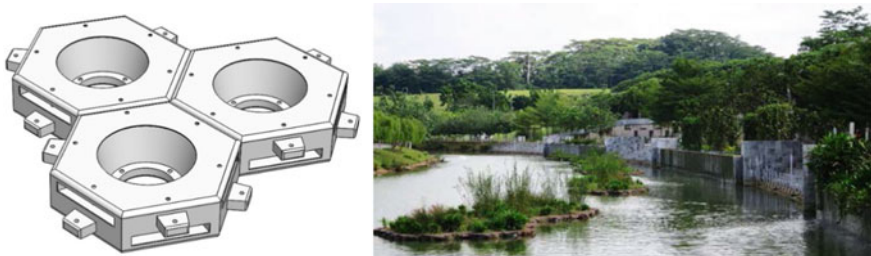


Fig. 18 Floating hexagonal shaped HDPE modules and floating wetlands on Punggol waterway

wetlands were recently constructed in Singapore's Pulau Ubin to provide additional habitats for herons.

In Seoul, three floating islands were constructed to bring vibrancy to the Han River (see Fig. 19). The islands can accommodate 6200 people. The 20,400 m² complex houses 3 cultural centres, featuring performances, water sports and aquatic events.



Fig. 19 Seoul floating Islands

Since its opening, millions of people have visited the islands and it is now a very popular tourist and local cultural activity spot.

In Europe, Paris has activated its public river spaces by creating a floating community centre (Fig. 20a) and a separate floating urban art centre (Fig. 20b). These floating solutions create new and attractive public space and to provide the preconditions for successful urban places [19, 24].

Similarly, the Dutch have built a floating pavilion in Rijnhaven (see Fig. 21) comprising 3 interlinked spheres, the largest of which has a radius of 12 m and the

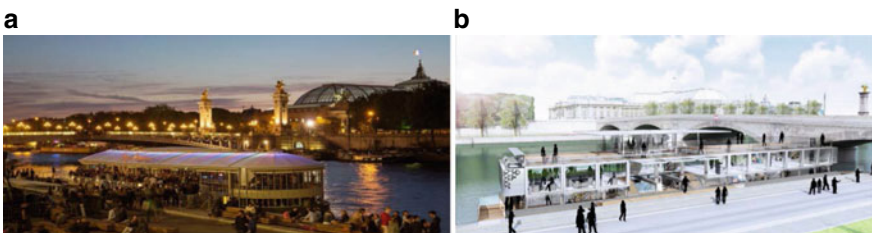


Fig. 20 **a** Floating community center in Paris. **b** Floating urban art centre in Paris



Fig. 21 Floating pavilion in Rotterdam, The Netherlands

floor space of the pavilion island is $46\text{ m} \times 24\text{ m}$. The floating pavilion currently serves as an exhibition and events venue.

Other projects that may drive activity and place making in the city are oriented on creating novelty—addressing Sherman’s [25] indicator of a successful urban place of a surprising feature in a city ‘to keep citizens awake, provide topics of conversation, [and to] prevent ennui’. In Sorenga, Oslo, a floating beach was built next to a hip condominium complex (see Fig. 22). The additional commercial benefit of the novelty was the resultant increase in property prices of the adjacent properties.

In the same vein, floating restaurants and floating hotels serve as places of surprise in cities. Their novelty create excitement for customers and city occupants. Examples of such floating solutions are seen in Fig. 23, showing the famous Jumbo restaurant in Hong Kong, and Fig. 24, showing the Le Off Paris Seine floating hotel.

Singapore has the world’s largest floating performance stage which is sited on the Marina Bay (see Fig. 25). It is a steel platform and measures $120\text{ m} \times 83\text{ m} \times 1.2\text{ m}$. A more detailed description of this floating platform is provided by Koh and Lim [10]. The National Day Parade and festival celebrations are held annually on this floating platform.

5.2 *Floating Solutions for Infrastructure*

Urban communities separated by deep rivers, lakes, fjords and straits may be joined by using floating bridges, roads and railways to generate greater economic activities and human interaction. These floating structures can be kilometres long as they



Fig. 22 Floating beach in Sørenga, Oslo, Norway. Photos courtesy of Tor Ole Olsen

Fig. 23 Jumbo restaurant in Hong Kong





Fig. 24 Le Off Paris Seine floating hotel



Fig. 25 Floating performance stage at Marina Bay, Singapore

exploit the free-of-charge buoyancy force of the water to carry the massive dead loads and traffic loads. Examples of these large floating bridges are the 2020 m long Lacey V Murrow Memorial Bridge over Washington Lake (see Fig. 26a), the 2350 m Evergreen Point Floating Bridge in Seattle over 61 m water depth atop 61 m soft silt (see Fig. 26b), the 1246 m long Nordhordland bridge at Sallhus over a fjord depth of 500 m (see Fig. 26c), the 845 m long Bergsoysund Bridge near Kristiansund over a fjord depth of 320 m (see Fig. 26d) and the 410 m Yumemai Floating Steel Arch Bridge in Osaka (see Fig. 26e). More ambitious plans are underway to build submerged floating road tunnels with either pontoon or tension-leg supports to cross the wide and deep fjords in Norway along the E-39 highway.

Where a marine site is characterised by a large tidal variation, floating piers have been built so that the required freeboard can be maintained at any time. South Korea has built two very large floating cruise ship piers in Incheon Golden harbor that has a tidal variation of 10 m [9]. One floating pier is made of steel whilst the other



Fig. 26 **a** Lacey V. Murrow Bridge. **b** Evergreen point floating bridge. **c** Nordhordland bridge. **d** Bergsoysund Bridge. **e** Yumemai floating steel arch bridge in Osaka

made from prestressed concrete (see Fig. 27). In Japan's Ujina port, there are a few floating piers which have been in operation for a few decades. Alaska has a floating prestressed concrete terminal dock. It is envisaged that many floating ports will be built in the near future as ships get larger (longer and heavier) and longer wharves and deeper water depth are needed for berthing.

The Japanese successfully demonstrated the feasibility of a floating airport by carrying out tests on a 1 km long floating runway from 1995 to 2000 [29] as part of the investigation into a second runway for Kansai International Airport (see Fig. 28). The project underscored the urban design strategy of locating sensitive infrastructure (much like the oil storage and hydrogen storage facilities identified above) in the ocean securely away from but still in close proximity to urban centres. Subsequent research in this area has also produced investigations into the feasibility of a super-scale floating airport comprising multiple floating modules [36, 37].



Fig. 27 Floating piers in Incheon Golden harbor. Photo courtesy of Kwanghoe Jung



Fig. 28 Mega-float—a 1 km long floating airplane runway test model in Tokyo Bay. Photo courtesy of M. Fujikubo

5.3 Floating Solutions for Land Scarce Coastal Mega-Cities

The phenomenon of coastal urbanisation has led to significant pressure on land-based resources. Chief among these is the quest for available land space for residential, commercial and recreational activities. While this has led to significant projects to reclaim land from the ocean, land reclamation projects are highly environmentally problematic as they destroy the marine ecosystem below their footprint and require further damage to the environment at the source of where fill materials are extracted.



Fig. 29 **a** Canoe Pass village in Vancouver. **b** Floating homes in Copenhagen

Land reclamation also becomes economically unfeasible where the site has a soft bed or where water depth exceeds 30 m. However, one of the significant issues of land reclamation is that the created space is still subject to the threat of rising sea levels.

Floating solutions utilising VLFS technology has been embraced by land-scarce countries such as Singapore, Monaco, the Netherlands and Japan. The advantages of VLFS over traditional land reclamation include the fast pace in which space for urban development can be created and utilized, lowering the cost of deployment and allowing projects to be delivered more quickly. The flexibility of deployment allows the programmed space on top of these floating structures to be towed to the area of need. Further, as these floating structures are inherently base isolated, they are not affected by seismic action and are, due to their nature, immune to rising sea levels.

Although there is no VLFS suburbs currently under construction, floating houses and villages have long been part of our history. For example, Fig. 29a shows the floating houses in Vancouver, Canada and Fig. 29b shows the floating homes (made from container boxes) in Copenhagen for students. As more examples are built in the future as solutions to tackle coastal urbanisation, the authors suggest that there will be growing familiarity and acceptance of floating structures as simply extensions of the existing urban environment. This in turn may open the way to more visionary satellite applications of floating cities, such as Vincent Callebaut's Floating LilyPad settlements (see Fig. 30a) to accommodate climate refugees and Bjarke Ingels' Oceanix City proposal to house 10,000 people (see Fig. 30b). Joseph Lim from the National University of Singapore recently explored the prospect of repurposing semi-submersible and superbarges into offshore and nearshore settlements to potentially accommodate 1.6 billion people on 6510 offshore settlements [13].

6 Concluding Remarks

Our world faces many challenging problems ahead as a result of climate change and overpopulation. Some of these challenges can be solved by looking towards the vast oceans which take up about 70% of the world's surface. By using our technological

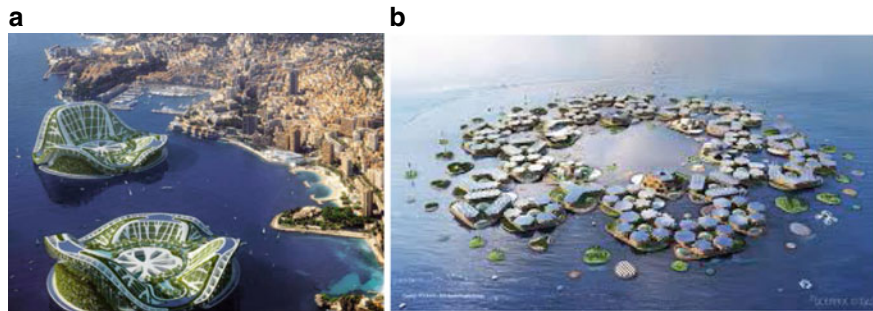


Fig. 30 **a** Floating Lily Pad city. **b** Floating city by Bjarke Ingels

advances in ocean engineering, marine and offshore structures and innovative ideas of floating solutions, we can:

- secure abundant offshore renewable energy for the world's energy needs,
- deploy mega-floating aquaculture farms and desalination plants to meet our need for clean water and food production requirements,
- create cleaner marine environments and safer urban spaces by cleaning the oceans and siting hazardous industry at sea away from urban populations,
- increase economic activity and vibrancy through the creation of businesses and jobs associated with the Blue Economy,
- construct infrastructure through the use of floating structures to create new urban corridors by connecting land parcels separated by water bodies. This will allow enhanced economic activities and population distribution through these new connections, and
- build floating villages, towns, cities and even countries to produce hybrid floating city solutions to address population pressures on land-based resources and ameliorate the linear sprawl of urban development along coastlines.

The ocean is clearly the next frontier for the future of cities. It offers itself as a resource that we must sensitively engage with in order to increase our habitable environments for us to live, work and play. It is crucial we understand our role as city builders and exercise stewardship of this resource for future generations and to ensure that we lean on (or float over) the oceans for our urban needs while preserving and celebrating our valuable marine ecosystems.

Acknowledgements The authors are grateful to the Australian Research Council in providing the research funds for Discovery Projects on Floating Forest and the Next Generation Blue Aquaculture Farms.

References

1. Ang KK, Dai J, Hellan O, Watn A, Si MBI (2019) Design and potential applications of floating structures in Singapore. In: Wang CM et al (eds) WCFS2019, proceedings of the world conference on floating solutions, lecture notes in civil engineering, vol 41. Springer Nature, Singapore, pp 135–154
2. BBC News (2014) Wave power firm Pelamis calls in administrators. 21 Nov 2014. <https://www.bbc.com/news/uk-scotland-scotland-business-30151276>
3. Bulleri F, Chapman M (2010) The introduction of coastal infrastructure as a driver of change in marine environments. *J Appl Ecol* 47(1):26–53
4. Burt J, Killilea M, Ciprut S (2019) Coastal urbanization and environmental change: opportunities for collaborative education across a global network university. *Reg Stud Mar Sci* 26: Article Number 100501
5. Dai J, Wang CM, Utsunomiya T, Duan WH (2018) Review of recent research and developments on floating breakwaters. *Ocean Eng* 158:132–151
6. Duarte C, Holmer M, Olsen Y, Soto D, Marba N, Guiu J, Black K, Karakassis I (2009) Will the oceans help feed humanity? *Bioscience* 59(11):967–976
7. Guangzhou Institute of Energy Conversion, Chinese Academy of Sciences (2017) Sharp Eagle: scientist discovered a new economic way to convert wave energy. http://english.giec.cas.cn/ns/tm/201707/t20170725_181220.html
8. Harvey F (2016) World's biggest floating solar farm powers up outside London. The Guardian 29 Feb 2016. <https://www.theguardian.com/environment/2016/feb/29/worlds-biggest-floating-solar-farm-power-up-outside-london>
9. Jung KH, Lee SH, Kim HS, Choi YH, Kang S (2019) Design and construction of the floating concrete pier in Golden Harbour, Incheon. In: Wang CM et al (eds) WCFS2019, proceedings of the world conference on floating solutions, lecture notes in civil engineering, vol 41. Springer Nature, Singapore, pp 283–297
10. Koh HS, Lim YB (2015) Floating performance stage at the Marina Bay, Singapore. In: Wang CM, Wang BT (eds) Large floating structures, ocean engineering and oceanography, vol 3. Springer, Singapore, pp 37–60
11. Kokubun T (2014) Shift to floating seawater desalination in order to reduce environmental issues and supply timely to meet demand. Deloitte Tohmatsu Consulting Co presentation slides made available to the OECD at <https://www.oecd.org/sti/ind/oecd-shipbuilding-workshop-kokubun.pdf>
12. Leary D, Esteban M (2009) Climate change and renewable energy from the ocean and tides: calming the sea of regulatory uncertainty. *Int J Mar Coast Law* 24(4):617–651
13. Lim JEM (2019) Repurposing jack-ups, semi-submersibles and superbarges into offshore and nearshore settlements. In: Wang CM et al (eds) WCFS2019, proceedings of the world conference on floating solutions, lecture notes in civil engineering, vol 41. Springer Nature, Singapore, pp 329–357
14. Liu H, Kumar A, Reindl T (2019) The dawn of floating solar—technology, benefits and challenges. In: Wang CM et al (eds) WCFS2019, proceedings of the world conference on floating solutions, lecture notes in civil engineering, vol 41. Springer Nature, Singapore, pp 373–383
15. Lovell T (1989) Nutrition and feeding of fish. Springer, Boston, USA
16. Maslin E (2017) The future floats. *Offshore Eng* 1 July 2017
17. Meinholt B (2014) Whale-shaped floating garden designed to clean the world's rivers. InHabitat 17 Apr 2014. <https://inhabitat.com/whale-shaped-floating-garden-cleans-the-worlds-rivers/>
18. Michener W, Blood E, Bildstein K, Brisson M, Gardner L (1997) Climate change, hurricanes and tropical storms, and rising sea level in coastal wetlands. *Ecol Appl* 7(3):770–801
19. Montgomery J (1998) Making a city: Urbanity, vitality and urban design. *J Urban Des* 3(1):93–116. <https://doi.org/10.1080/13574809808724418>
20. Narasimalu S (2019) Floating clean multi-energy systems towards driving blue economic growth. In: Wang CM et al (eds) WCFS2019, proceedings of the world conference on floating solutions, lecture notes in civil engineering, vol 41. Springer Nature, Singapore, pp 329–357

21. Pelc R, Fujita RM (2002) Renewable energy from the ocean. *Mar Policy* 26:471–479
22. Rahimifard S, Trollman H (2018) UN sustainable development goals: an engineering perspective. *Int J Sustain Eng* 11(1):1–3
23. Roach J (2004) Source of half earth's oxygen gets little credit. *Nat Geog* 7 June
24. Ronzatti G, Lovric P (2019) Floating infrastructure large scale public spaces on water. In: Wang CM et al (eds) WCFS2019, proceedings of the world conference on floating solutions, lecture notes in civil engineering, vol 41. Springer Nature, Singapore, pp 49–66
25. Sherman B. (1988) Cities Fit to Live In. London: Channel 4 Books
26. Smalley RE (2005) Future global energy prosperity: the terawatt challenge. *Mater Res Soc Bull* 30:412–417
27. Smalley RE (2003) Top ten problems of humanity for next 50 years. In: Energy and nanotechnology conference, 3 May 2003. Rice University, Houston, USA
28. Smith-Godfrey S (2016) Defining the blue economy. *Maritime Aff J Nat Maritime Found India* 12:58–64
29. Suzuki H (2008) Research and development of VLFS). In: Wang CM, Watanabe E, Utsunomiya T (eds) Very large floating structures. Taylor and Francis, Abingdon, UK, pp 204–227
30. The World Bank (2017) What is the blue economy. <https://www.worldbank.org/en/news/infographic/2017/06/06/blue-economy>
31. Ueda S (2015) Floating oil storage bases. In: Wang CM, Wang BT (eds) Large floating structures, ocean engineering and oceanography, vol 3. Springer, Singapore, pp 91–106
32. Vaughn A (2016) Japan begins work on 'world's largest' floating solar farm. *Guardian* 27 Jan 2016. <https://www.theguardian.com/environment/2016/jan/27/japan-begins-work-on-worlds-largest-floating-solar-farm>
33. Wang CM, Chu YI, Park JC (2019) Moving offshore for fish farming. *J Aquac Mar Biol* 8(2):38–39
34. Wang B (2019) Floating cities: the future or a washed-up idea? *The Conversation* 3 June 2019. <https://theconversation.com/floating-cities-the-future-or-a-washed-up-idea-116511>
35. Wang CM, Han MM, Lyu JW, Duan WH, Jung KH, Kang-An S (2019) Floating forest: a novel floating breakwater-windbreak structure. In: Wang CM et al (eds) WCFS2019, proceedings of the world conference on floating solutions, lecture notes in civil engineering, vol 41. Springer Nature, Singapore, pp 219–234
36. Zhang C, Magee AR, Fonseca N, Hellan O, Ang KK (2019) Hydrodynamic responses and loads of a floating hydrocarbon storage tank system for concept validation and numerical verification. In: Wang CM et al (eds) WCFS2019, proceedings of the world conference on floating solutions, lecture notes in civil engineering, vol 41. Springer Nature, Singapore, pp 155–171
37. Zhang HC, Xu DL, Xia SY, Shi QJ, Yang GY, Ding R (2019) Dynamics of super-scale modularized floating airport. In: Wang CM et al (eds) WCFS2019, proceedings of the world conference on floating solutions, lecture notes in civil engineering, vol 41. Springer Nature, Singapore, pp 155–171

Decadal Morphological Recovery of Estuaries and Coasts After the 2011 Tohoku Tsunami



Hitoshi Tanaka and Trong Hiep Nguyen

1 Introduction

The 2011 Great East Japan Earthquake and Tsunami is considered as one of the most devastating catastrophes in Japan with a record of 40 m wave height in Iwate Prefecture [12]. The tragedy brought a huge miserable damage and loss to both tangibles and people in the areas along the coast of Miyagi Prefecture from Iwate to Fukushima Prefecture.

The hazard of earthquake induced-tsunami now is not a rare problem in world since according to the global historical tsunami database [13] for the last 20 years, major earthquake generated-tsunami has occurred with the frequency at least one event a year. In the globe, a considerable amount of literature has done in regard to the impacts of tsunami on coastal areas. Concerning the 2004 Indian Ocean Tsunami, several studies about the morphology change set off by the tsunami were conducted (e.g., [2, 11, 14, 24]). Some of these researches were faced with the deficiency of topography data before the tsunami. Paris et al. [15] studied the spatial distribution of tsunami deposit at West Banda Aceh, Indonesia along 18 km of the coastline and reported a maximum coastal erosion of 123 m. Goto et al. [3] carried out the investigation of the discrepancy of bathymetry due to the tsunami along 2 km of coastline including Kirinda Harbor, Sri Lanka. This study provided that sedimentation along the shoreline occurred due to the tsunami except in the harbor, where erosion occurred, and the bathymetry data were restored to pre-tsunami levels within a year after the tsunami. And most recently, Koiwa et al. [8] indicated the barrier spit recovery at Pakarang Cape, Thailand.

Regarding the 2011 Great East Japan Earthquake and Tsunami, the multidisciplinary research of the coastal damage and recovery after the tsunami was encouraged by a great deal of support due to the sufficiency of both pre and post-tsunami data.

H. Tanaka (✉) · T. H. Nguyen

Department of Civil and Environmental Engineering, Tohoku University, 6-6-06 Aoba Aramaki, Sendai 980-8579, Japan

e-mail: hitoshi.tanaka.b7@tohoku.ac.jp

This is shown by many studies on severe erosion on coasts and complex morphology phenomena by using field data, aerial and satellite photographs [1, 16–23]. Among them, Tanaka et al. [18] reported comprehensively on the significant changes of coastal and estuarine areas in Miyagi Prefecture such as beach erosion, breaching, sand barriers and sand spits' disappearance. Recently, to focus intrinsically on the morphological change at river mouths and adjacent zones, Hiep et al. [4] learned the evolution of the sand spit in relation to the sand terrace normally fed by the ebb flow or flood discharge at the Abukuma River. Thus, the slow recovery and 70 m remaining erosion of the sandy beach adjoining to the Natori River mouth were also discussed particularly in Hiep et al. [5]. Hence, Hiep et al. [6, 7] also discusses respectively the river mouth's mechanism causing the unchangeable shape of the sand spits at the Naruse River and the Kitakami River.

This study, to make a more comprehensive and cohesive analysis on the recovery process of all estuaries in over 8 years in Miyagi Prefecture, focused on the evolution after the tsunami of four different river mouths at the Abukuma River, the Natori River, the Naruse River and the Kitakami River. By either analyzing photographs from various sources capturing the morphology of these river mouths before and after the tsunami or conducting a concurrent discussion, it demonstrates that depending on different characteristics and conditions, each river mouth recovers differently which some areas have potential to self-recover but some has still suffered from a poor recovering situation.

2 Study Area

The study area focuses on the estuarine and coastal areas at four rivers, which are the Abukuma River, the Natori River, the Naruse River and the Kitakami River. These rivers are located respectively along approximate 85 km stretch of the coastline in Miyagi Prefecture facing the Pacific Ocean (Fig. 1). Except the Kitakami River discharging to the Oppa bay, the three other rivers pour into Sendai Bay. All four rivers are categorized as class A in Japan by which the national government has the responsibility to manage operational systems and mitigate every problems regarding water resources and protection against extreme disasters. The river length and catchment of the Natori and the Naruse River are much less compared to those of the Abukuma River and the Kitakami River (Table 1).

And due to the distinguishable topographical conditions and the present of man-made constructions in each river, the sediment supply onto each river mouth is either different resulting significantly on the recovery process of them after the tsunami. In relation to coastal morphology detriment, the estuarine of these four rivers suffered the same dramatic damage that the sand spits of these river mouths were flushed away by the high-energy tsunami forcing the mouth wide open; surrounding sandy beaches eroded severely; coastal protection constructions and port areas were devastated rigorously. Particularly, in the Kitakami River, the disappearance of the entire wealthy

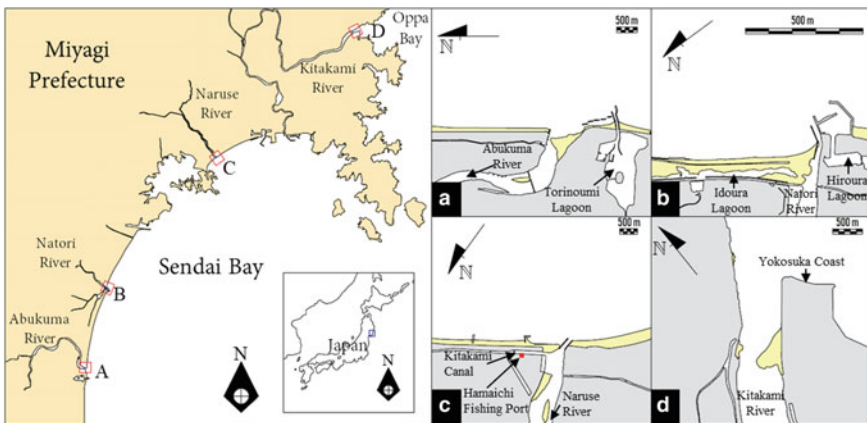


Fig. 1 Map of Miyagi prefecture and study areas

Table 1 Discrepancy of river features

River name	River length (km)	River catchment (km^2)
Abukuma	225	5396
Natori	55	933
Naruse	89	1133
Kitakami	249	10,150

Yokosuka Coast and the area behind it reflected how remarkable the topographical change was caused by the tsunami.

3 Data Collection

This study was fortunate to collect various data from multiple sources lead by the aerial photographs from Tohoku Regional Bureau of Ministry of Land, Infrastructure, Transport and Tourism (MLIT). Other sources of data include Google Earth images, UAV and GPS data taken from several field trips. All data are greatly valuable and utilized to carry on this analysis. In order to make an accurate comparison pre and post-tsunami, it is important that all images of each study area were gone through rectification process to share one specific coordinate system corresponding to the north. In addition, shoreline detection is the required work to obtain the numeral data of coastline to proceed to further detail investigation.

4 Recovery Process of River Mouths

In the first place, this section will discuss the recovery process of each river mouth individually since each river has its own certain mechanism to reflect in the recovery after the nasty disaster.

4.1 Abukuma River

The Abukuma River is a special river that the catchment is considerably big as compared to other rivers in Miyagi Prefecture. Before the tsunami occurred, the river mouth of the Abukuma River was investigated broadly and presented in many studies such as Mano et al. [9] and Mano and Sawamoto [10]. The small sand spit on the left side has a stable shape and was able to regain its formation after the 2011 Tsunami. In the meanwhile, the right sand spit, whose the form is rather large and covers almost the river mouth width, has much complex mechanism since many studies found the shape of the sand spit was constrained considerably by the interrelation among waves, tidal flow and flood actions.

Figure 2(a-2) refers to situation 2 days after the tsunami, which the long and horizontal sand spit was clearly disappeared and only some remaining portions adhered to the right embankment. Following to that, the river was wide open, allowed wave propagates further upstream, and the water depth at prior sand spit was acutely deep. This results in the intrusion of sand spit into the river as observed in Fig. 2(a-3~5).

Afterwards, the right sand spit was eventually able to retrieve its own pre-tsunami location, which it gradually developed towards downstream as indicated in Fig. 2b. Until the sand spit reached to the position as seen in Fig. 2(b-5), it turned into the state, which is under a dynamic equilibrium mechanism to retain the its shape. This finding was discussed more thoroughly in Tanaka et al. [20] and the evidence reflects

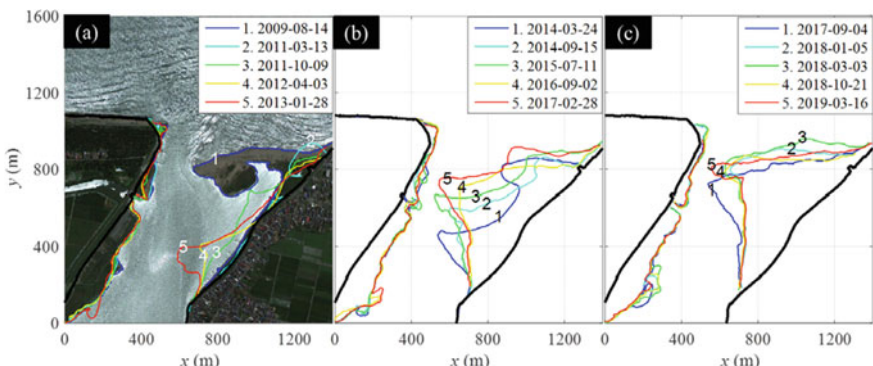


Fig. 2 Abukuma river mouth's morphology change

in Fig. 2c as the discrepancy of the sand spit is not profound. The overwhelming variation of the sand spit merely appears whether a tremendous flood widens the entrance of the river mouth and creates a sand terrace placed in front of the estuary; however, subsequently wave actions will do compensating work by transporting sediment from the sand terrace to supply the sand spit again.

A more thorough understanding of the impact of the sand terrace on the sand spit was not provided in this study but investigated in depth in Hiep et al. [4].

4.2 Natori River

The Natori River is the smallest river corresponding to length and catchment among four considered rivers. In contrast to other study areas, on the left side, the Natori River has a large sand spit and a long sandy beach accounted from the wave dissipating concrete block to the sand spit in this study. As seen in Fig. 3(a-1, 2), before the tsunami took place, the Natori River had a wealthy coast that the shape was fairly stable.

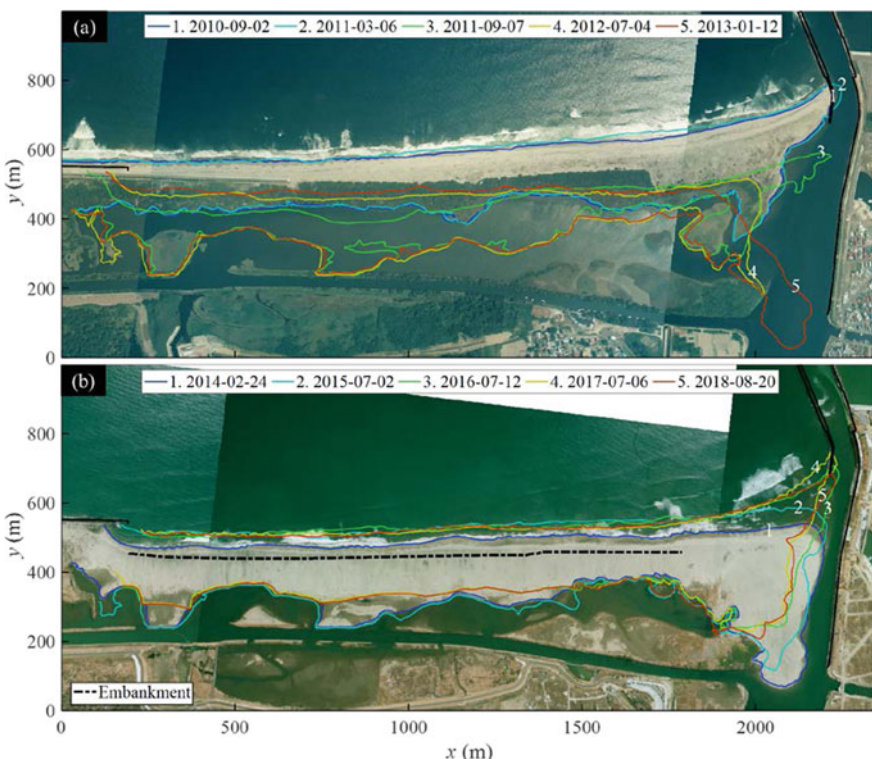


Fig. 3 Natori river mouth's morphology change

However, the entire area was change remarkably, when the tsunami demolished the sand spit and destroyed nearly the sandy beach. The remaining area was pushed further upstream as shown in Fig. 3(a-2, 3). Thereafter, the sand spit was merely a small portion and under vulnerable state, that intrusion of the sand spit happened when high waves approached. This explains the long oblique strip of sand spit pointing towards into the river [Fig. 3(a-5)]. Afterwards, the recovery process started accelerating which the shape of the sandy beach has formed again and the sand spit developed and almost reached the jetty as it used to.

Despite that, the self-recovery was not sufficient to restore the pre-tsunami position that the gap between the sand spit and the jetty had existed and been required to be addressed by nourishing work since the open route caused leakage of river discharge from the jettied main river channel [Fig. 3(b-1~3)]. Until July 2016, the nourishment to support the sand spit evolution accomplished and overall, the configuration of the entire river mouth area has been nearly regained [Fig. 3(b-4, 5)]. Nevertheless, the morphology of the Natori River has yet pictured the change caused by the 2011 tsunami, as the shoreline of the sandy beach has remained the retreat of roughly 70 m compared to the prior shoreline position. According to Hiep et al. [5], it was identified that the area of the sandy beach has been accounted for 50% of that before tsunami.

Moreover, it is also of important to keep a careful check on the erosion of the sandy beach area because to prevent sudden disasters in the future, a construction of embankment along the sandy beach was implemented. Hiep et al. [5] also claimed the risk of river inundation since river mouth width has the tendency to become smaller due to wave overtopping but in this study, it only considers the overall recovery of the river mouth.

4.3 Naruse River

Compared to other rivers, the Naruse River mouth has a special feature that the river mouth consists of not only a sand spit attached to jetty at downstream but at upstream there is an area in which sediment was deposited. As recorded before the tsunami, the morphology of the Naruse River mouth was solid and significant change was rare to happen in this area [Fig. 4(a-1~4)]. However, the sand spit was totally flushed away by the 2011 tsunami and the river entrance was analogous to other areas where was wide open and waves were able to approach further into the river as seen in Fig. 4(a-5). This phenomenon, at the beginning, dug up the sediment near the left bank's embankment and continued until a large amount of sediment was eroded and the head portion of the sediment deposit became flatter in transverse direction [Fig. 4(a-6)].

Afterwards, although the river started to recover, it faces many challenges since the westward longshore sediment movement was interrupted by the T-headline and waves transported sediment further upstream (see Fig. 1c). As presented in Hiep et al. [6], waves approach into the river remains in a certain angle to the shoreline

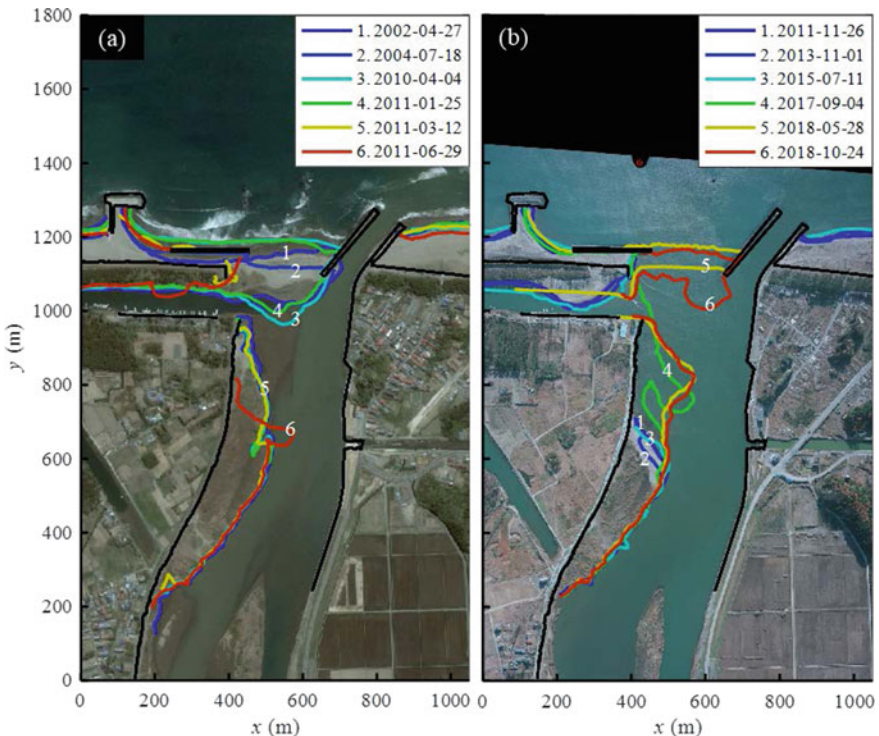


Fig. 4 Naruse river mouth's morphology change

of sediment deposit resulting in the apparent shape of the shoreline evolution of the sediment deposit and nearly no sediment was accumulated in transverse direction [Fig. 4(b-1~4)]. As seen in Fig. 1, on the left side of the Naruse River mouth, there are a canal called Kitakami Canal and a small fishing port called Hamaichi. Since sediment occupied the route of the canal with sediment carried by diffracted waves and obstructed the activities of fishing port, a construction work was implemented by dredging the sediment in the canal and transporting it to nourish the sand spit. The construction was successfully complete at the end of March 2018 and the sand spit developed bigger towards downstream by the reason of sediment contribution carried by wave overtopping [Fig. 4(b-5, 6)]. A year after the construction, both the sand spit and downstream sediment deposit area has maintained a stable state.

4.4 Kitakami River

The Kitakami River is different from other rivers since it is the only river facing the Oppa Bay. Prior to the tsunami, the Kitakami River mouth had several distinct

features, which are the Yokosuka Coast facing the Oppa Bay and a long sand spit extending from the mouth to a spot at downstream. During this period, the sand spit was stable and only small variations were observed at its head owing to river discharge, while the Yokosuka Coast was in more fluctuating condition because of high waves effect occasionally [Fig. 5(a-1~5)]. The mutual interaction between the sand spit and the coast was of greatly important and discussed broadly in past studies before the tsunami due to the operation of the longshore sediment transport and the discharge from the river.

However, the Kitakami River mouth has extremely gentle bed slope of 1/10,000, resulting remarkably severe damages due to tsunami propagation into the river and overflowing water during the 2011 Tsunami. Indeed, the energy and the distance that the tsunami could propagate and reach to far upstream were astonishingly higher in comparison with other areas. This explains the serious devastation on the riverine structures, which the whole mouth area including the land area behind the shoreline was submerged in water and the Yokosuka Coast was entirely disappeared as Fig. 5(a-6). In addition, the return flow was contributed as well to trigger significant topographical changes such as erosion of sand spit and a wide open river entrance [Fig. 5(a-7)]. Similar to three above rivers, waves were allowed to generate

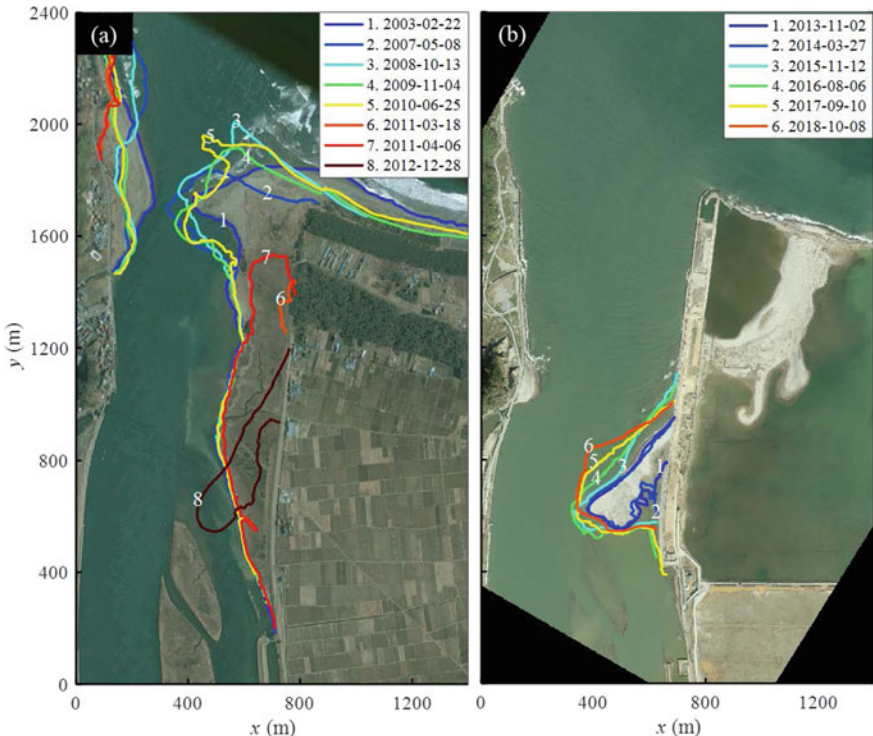


Fig. 5 Kikakami river mouth's morphology change

directly into the river and pushed the sediment forming the sand spit as captured in Fig. 5(a-8). This shape was mainly stable until 2 years recently when some variants of development have been monitored.

After the intrusion occurred, the recovery of river mouth to its own prior shape is considered as a formidable task. The water depth in the nearshore zone is rather deep after the tsunami and the sediment supply is also limited due to the condition of surrounding rocky cliffs. The special topography of the Oppa Bay in front of the Kitakima River with the surrounding mountainous terrains is the reason why waves only come into two unique directions of east and north-east. The consistency of wave incidence's approach leads the corresponding wave breaking appears parallel at the entrance after refraction as a result that sediment transport capacity to the sand spit is rather slow and slight because the shoreline coincides with wave incidence's angle. Additionally, the longshore sediment transport was obstructed by the reconstruction of the area behind the old Yokosuka Coast containing a groin near entrance. Plus, due to the deep water depth its area, the sand spit has been a solid shape and not tried to develop in transverse direction to reach the opposite site as depicted in Fig. 5b. This was explained minutely in Hiep et al. [7] by showing the wave direction data at the Oppa Bay and cross-sectional data at several positions of the sand spit. In summary, it is expected that the recovery of the sand spit will be seen as new additional layers grown onto the previous shoreline.

5 Conclusions

The 2011 Great East Japan Earthquake and Tsunami occurred and caused severe damages along the coast in Miyagi Prefecture. It has been over 8 years since the 2011 Tsunami arrived and the recovery process of four rivers was measured and analysed thoroughly within this period. It is believed that it is a big challenge for all rivers to recover to their pre-tsunami situation since the conditions are not sufficient to pursue that goal. The Abukuma River is the only river performing a fully recovery despite of the notable change of sand spit's configuration. Both the Naruse River and the Natori River were supported by human work to accelerate their recovery process; however, the sandy beach of the Natori River still requires a longer period to compensate for the erosion. And the Kitakami is expected to remain its slow recovery due to its inclement topography and wave conditions. The benchmark of 10 years after the tsunami is coming soon and it is of greatly vital to keep monitoring and observing any changes of these locations as long as the aftermath of the tsunami has not faded away completely.

Acknowledgements A genuine gratitude is expressed to the Kitakami River Lower Reach Office as well as the Sendai Office of River and National Highway, Ministry of Land Infrastructure and Transport (MLIT) for providing valuable aerial images and data utilized to conduct analysis in this study. This study was supported by the “Tohoku Ecosystem-Associated Marine Sciences (TEAMS)” project funded by MEXT.

References

1. Adityawan MB, Dao NX, Tanaka H, Mano A, Udo K (2014) Morphological changes along the Ishinomaki coast induced by the 2011 Great East Japan tsunami and the relationship with coastal structures. *Coast Eng J* 56:1450016
2. Choowong M, Phantuwongraj S, Charoentitirat T, Chutakositkanon V, Yumuang S, Charusiri P (2009) Beach recovery after 2004 Indian Ocean tsunami from Phang-nga, Thailand. *Geomorphology* 104:134–142
3. Goto K, Takahashi J, Oie T, Imaura F (2011) Remarkable bathymetric change in the nearshore zone by the 2004 Indian Ocean tsunami: Kirinda Harbor, Sri Lanka. *Geomorphology* 1–2:107–116
4. Hiep NT, Tanaka H, Tinh NT, Ito K, Yamanaka T (2019a) The recovery process of sandspit and sand terrace at the Abukuma River mouth after the 2011 Tohoku Tsunami. *J Jpn Soc Civ Eng (Coast Eng) Ser. B2* 75(2) (in Japanese, in press)
5. Hiep NT, Tanaka H, Tinh NT (2019b) Morphology change and recovery process of sandy coast and sandspit at the Natori River mouth after the 2011 Tsunami. *J Jpn Soc Civ Eng Ser. B3 (Ocean Eng)* 75(2) (in Japanese, in press)
6. Hiep NT, Tanaka H, Tinh NT (2019c) Post-Tsunami recovery and morphology change at Naruse River mouth, Japan. In: Proceedings of the 10th international conference on Asian and Pacific coast (in press)
7. Hiep NT, Tanaka H, Tinh NT (2019d) Sandspit intrusion and morphological recovery under the impact of the 2011 Tohoku Tsunami at Kitakami River mouth, Japan. In: Proceedings of the 10th international conference on Asian and Pacific coast (in press)
8. Koiba N, Takahashi M, Sugisawa S, Ito A, Matsumoto H, Tanavud C, Goto K (2017) Barrier spit recovery following the 2004 Indian Ocean tsunami at Pakarang Cape, southwest Thailand. *Geomorphology* 306:314–324
9. Mano A, Sawamoto M, Nagao M (1994) Response characteristics of river mouth topography in wide time scale range. In: Proceedings of 24th international conference on coastal engineering, pp 3126–3138
10. Mano A, Sawamoto M (1996) Interactions between a sand barrier and flood terrace at the Abukuma River mouth. In: Proceedings of 25th international conference on coastal engineering, pp 4505–4516
11. Mascarenhas A, Jayakumar S (2008) An environmental perspective of the post-tsunami scenario along the coast of Tamil Nadu, India: role of sand dunes and forests. *J Environ Manag* 89:24–34
12. Mori N, Takahashi T (2012) The 2011 Tohoku earthquake Tsunami joint survey group: nationwide post event survey and analysis of the 2011 Tohoku earthquake tsunami. *Coast Eng J* 54(1):1250001
13. National Geophysical Data Center/World Data Service: NCEI/WDS Global Historical Tsunami Database (2019) NOAA National Centers for Environmental Information. Retrieved 25 Apr 2019, from <https://doi.org/10.7289/v5pn93h7>
14. Pari Y, Murthy MVR, Kumar SJ, Subramanian BR, Ramachandran S (2008) Morphological changes at Vellar estuary, India-impact of the December 2004 tsunami. *J Environ Manag* 89:45–57
15. Paris R, Wassmer P, Sartohadi J, Lavigne F, Barthomeuf B, Desgages E, Grancher D, Baumert P, Vautier F, Brunstein D, Gomez C (2009) Tsunamis as geomorphic crises: lessons from the December 26, 2004 tsunami in Lhok Nga, West Banda Aceh (Sumatra, Indonesia). *Geomorphology* 104(1–2):59–72
16. Roh M, Tanaka H, Mitobe Y (2016) Morphological characteristics of river mouths after the 2011 Tohoku Tsunami in Miyagi Prefecture. In: Santiago-Fandino V, Tanaka H, Spiske M (eds) *Tsunamis and earthquakes in coastal environments*. Springer International Publishing, Berlin, pp 137–152
17. Suppasri A, Koshimura S, Imai K, Mas E, Gokon H, Muhari A, Imamura F (2012) Damage characteristic and field survey of the 2011 Great East Japan Tsunami in Miyagi Prefecture. *Coast Eng J* 54(1):1250010

18. Tanaka H, Tinh NX, Umeda M, Hirao R, Pradjiko E, Mano A, Udo K (2012) Coastal and estuarine morphology changes induced by the 2011 Great East Japan earthquake tsunami. *Coast Eng J* 54(1):1250010
19. Tanaka H, Adityawan MB, Mano A (2014) Morphological changes at the Nanakita River mouth after the Great East Japan Tsunami of 2011. *Coast Eng J* 86:14–26
20. Tanaka H, Hiep NT, Mitobe Y, Sato K (2017) Study on recovery process of sandspit at Abukuma River mouth after 2011 Tsunami. *J Jpn Soc Civ Eng Ser. B1 (Hydraul Eng)* 73(4):I_997-I_1002 (in Japanese)
21. Tappin DR, Evans HM, Jordan CJ, Richmond B, Sugawara D, Goto K (2012) Coastal changes in the Sendai area from the impact of 2011 Tohoku-oki tsunami: Interpretations of time series satellite images, helicopter-borne video footage and field observation. *Sed Geol* 282(30):151–174
22. Udo K, Sugawara D, Tanaka H, Imai K, Mano A (2012) Impact of the 2011 Tohoku earthquake and tsunami on beach morphology along the northern Sendai Coast. *Coast Eng J* 54(1):1250009
23. Udo K, Tojo K, Takeda Y, Tanaka H, Mano A (2016) Characteristics of shoreline retreat due to the 2011 Tohoku Earthquake Tsunami and its recovery after three years. In: Santiago-Fandino V, Tanaka H, Spiske M (eds) *Tsunamis and earthquakes in coastal environments*. Springer International Publishing, Berlin, pp 113–123
24. Umitsu M, Tanavud C, Patanakanog B (2007) Effects of landforms on tsunami flow in the plains of Banda Aceh, Indonesia, and Nam Khem, Thailand. *Mar Geol* 242:141–153

Formal Techniques for Emergent Architectural Designs



Jin-Ho Park

1 Introduction

Any architectural design appears either regularly ordered or disordered, although the two notions are deeply related to each other. Finding order in a disordered or arbitrarily collected complex design is difficult. On the contrary, finding a certain ruled order in a design that started from an order may be easy occasionally.

Various designs can be occasionally generated beyond expectations by simply articulating simple rules and principles. Unexpected or overwhelming designs can emerge by applying the rules and principles of architectural design. Some designs appear to be complicated when reading architectural floor plans. A design relies on simple rules and principles through systematic evaluation. Architects can continue to create similar designs with rules and principles, indicating that they have their own style and language.

Let us consider two architectural floor plans, namely, the Sultan al-Ashraf Barsbay Funerary Complex in Suq al-Nahhasin, Cairo and the National Assembly Building in Bangladesh. The former appears simple although its spatial order is unremarkable from its exterior. The latter, a modern structure, has a complex plan. Although the design of National Assembly Building looks an entirely disordered distribution of the building constituent, its underlying structure exhibits perfectly ordered designs. An underlying order or principle may be gradually exposed when all constituents of a design are systematically decomposed.

In this article, formal techniques are introduced into the analysis and synthesis of architectural designs. The notions of symmetry and subsymmetry and Boolean operations are delineated. The methods can be applied either straightforwardly or tactfully to generate new designs (Fig. 1).

J.-H. Park (✉)

Department of Architecture, Inha University, Incheon, Korea

e-mail: jinhopark@inha.ac.kr

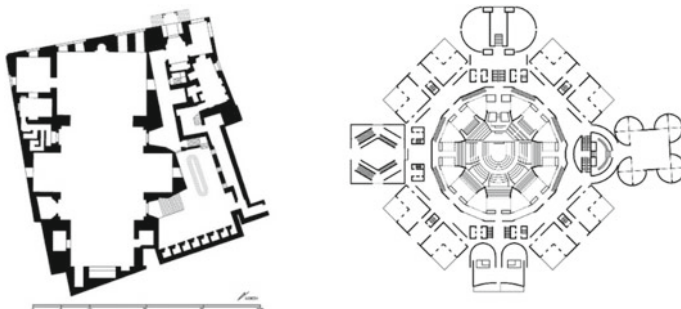


Fig. 1 Left. Sultan al-Ashraf Barsbay Funerary Complex at Suq al-Nahhasin, Cairo; Right. Louis Kahn's National Assembly building in Bangladesh

2 Subshape and Partial Ordering

Like a subgroup of a group, in shape recognition, identifying subshapes within a shape is involved to morph the larger impression into something entirely different [5]. Subshapes in a shape may not be readily recognizable at a first glance, since they are interwoven in a larger shape, and one typically addresses the shape in its entirety.

The hierarchical structure of the partial ordering is clearer when analysed mathematically [3, 12]. Let S be the finite set $\{a, b, c\}$; and $P(S) = \{\emptyset, \{a\}, \{b\}, \{c\}, \{a, b\}, \{a, c\}, \{b, c\}, \{a, b, c\}\}$. The hierarchical order of the group and subgroup of the elements is shown using a lattice diagram. All possible subgroups of the three elements set $\{a, b, c\}$ as well as the four elements set $\{a, b, c, d\}$ are illustrated in the lattice diagram in Fig. 2.

Subshapes provide a way of analysing complex architectural designs as an arrangement of integrated shapes making up the whole. The subshapes are thought to be cognitive [10] or algebraic [12]. The shapes may be analysed to show regularity in their formation of the whole. By nesting and isolating parts of the shape, their arrangement will be revealed.

The same logic applies to subsymmetries of the regular polygon to construct a hierarchical order. Subsymmetries arise from a curtailment of some symmetry operations: that is, formally selecting subgroups from the group of symmetries. As a result, it is possible to illustrate the apparent overlay of multiple subsymmetries involved in overall design. The process creates a hierarchy of partial ordering with respect to subsymmetries that parametrically represents the whole shape. When used as generative tactics, by superimposing subshapes to compose another shape, the subshapes disappear to morph into a new design.

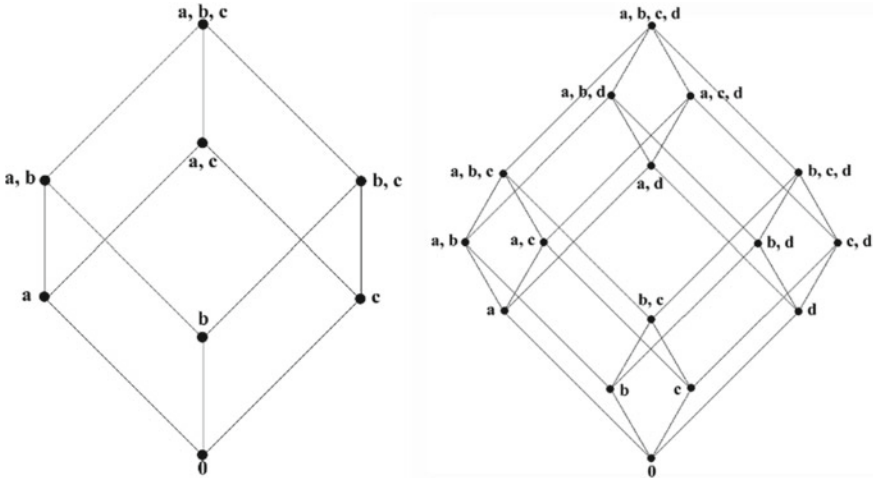


Fig. 2 Diagrams of the underlying structures of the partial ordering. Left: Lattice diagram of the set $S = \{a, b, c\}$: The set at the top of the figure, $\{a, b, c\}$, consists of all of the elements of the set. For example, sets $\{a, b\}$, $\{a, c\}$, and $\{b, c\}$ are each in the subset relation to $\{a, b, c\}$. This subset relation is the basis for partially ordering the sets. Right: Lattice diagram of the set $S = \{a, b, c, d\}$

3 Subsymmetry in Architectural Designs

Symmetry, which is derived from the Latin word *symmetria* (a portmanteau of *syn* [together] and *metria* [to measure]), indicates the appropriate arrangement of the parts of a whole to one another with regard to size and form. It clearly implies compositional balance between parts to create a harmonious whole. Architectural designs are composed of discernible components to form an overall structure. Different components in a design are integrated and connected. Although some designs show a harmonious whole, others do not. Symmetry may serve as a crucial notion that may provide insight into the balance and harmony of spatial composition in architecture.

Architectural designs are analyzed and synthesized with respect to a partial order of symmetry and classified using lattice diagrams of the symmetry [6, 7]. The approach demonstrates how different subsymmetries may be revealed in each part of the design and how various symmetric transformations combine to achieve the whole design. A partial ordering technique dissects the floor plans by showing their hierarchical subsymmetries with respect to subsymmetries when it is used to analyze architectural designs. Designers can incrementally add and remove subsymmetries to compose and decompose complex axial designs. Although the final design is not self-evident in the use of embedded subsymmetries, the designer will be able to explain how subsymmetries are utilized. At first glance, individual designs appear intricate and without obvious symmetry. However, an analysis of subsymmetries and symmetric transformations clearly exposes the underlying structure (Fig. 3).

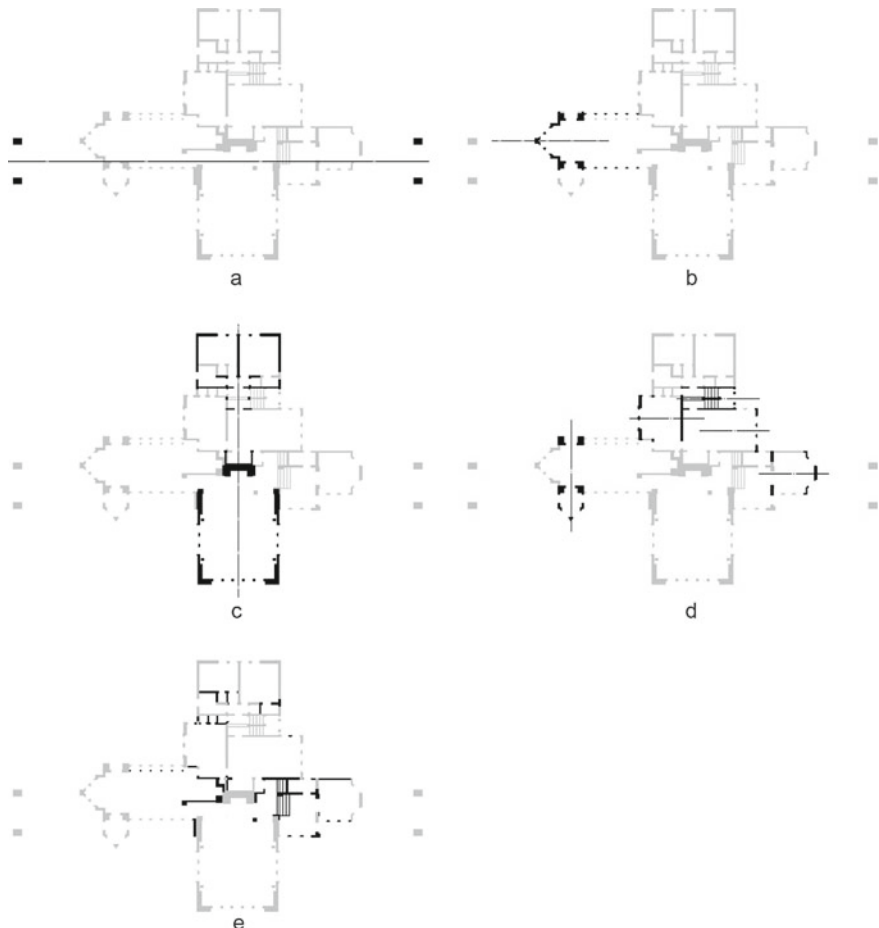


Fig. 3 Partial ordering with regard to subsymmetry drawings for the first floor plans of the Ward Willits House, 1901, Highland Park, Illinois: **a** long axis through porch piers; **b** axis through the dining room; **c** axis through the living room and hearth. A hearth facing into the living room is at its center; **d** minor axes through various parts of the plan; **e** remaining elements having no overall symmetry

Symmetries are typically defined as isometries that leave an object in a congruent figure without changing its appearance. They preserve the distances between points and angles. Planar transformations have four types, namely, translations, rotations, reflections, and glide reflections. The collection of all isometries of a figure on a plane can form a certain algebraic structure known as the symmetry group of a figure. Such an algebraic structure exhibits certain group of symmetries [1, 4].

In this section, we focus on the notion of the symmetry principle in a plane. Two types of plane group symmetry exist in two dimensions, namely, the finite and infinite groups. The former is called the point group, where isometric transformations occur

in a fixed point or line. The latter is called the frieze group, where isometric transformations occur under unidirectional translation and has two directional translations called the wallpaper group [2].

A point group symmetry is briefly considered. In the point group symmetry, two finite point groups, namely, C_n (cyclic group) and D_n (dihedral group), exist in the plane, where “ n ” represents the period of the group or the number of $360/n$ rotations. The number of elements in a finite group is called its order. The symmetry group of D_n has order $2n$ elements, whereas C_n has order n elements. The symmetry group of the square is the dihedral group D_4 of order 8. The subsymmetries of other regular polygons can be considered. For example, the symmetry group of the square consists of eight distinguishable operations, such as four four-reflections and quarter-turns. The symmetry group of the square forms 10 different subsymmetry designs.

Let us consider a simple possible element of a regular rectangular polygon. The reason for using a simple element is that it helps to readily clarify the increasing complexity and diversity encountered in designs for clearly revealing the hierarchical structure of the entire pattern. Developments in complexity rapidly occur by adding other symmetric motifs individually. The rectangle has two mirror reflections and two rotational symmetries of the order two. This shape forms five different subsymmetry designs as shown in Fig. 4.

We may stack each subsymmetry on top of each other by using the subsymmetry of the rectangle. This process indicates that the full symmetry of the rectangle is located at the ground level (a). The second floor illustrates D_1 symmetry at the vertical reflection axis (b). The third level represents D_1 symmetry at the horizontal reflection axis (c), where the fourth floor is arranged based on a half-turn rotation (d). The top-level has no symmetry, which is denoted as C_1 (e) (Fig. 5).

This mechanism illustrates the possibilities for generating diverse 3D designs depending on the assembly and stacking of each subsymmetry on top of each other. The combinatory possibilities for assembling can enormously increase, and the means that each clustering looks different from each other in 3D when additional elements are augmented in each level. In particular, independent elaboration of these arrangements into a large assembly creates various housing patterns.

Subsymmetries can be superimposed on a single floor. Each subsymmetry sometimes appears unrecognizable because various subsymmetries are mixed across a complex design at a glance. However, the underlying composition of a design is rooted in its hierarchical structure. Some architects strategically incorporate the techniques into their projects. Their designs may result in a new perspective in creating architectural spaces because of their unique ability to transcend formal and mathematical limits.

Louis I. Kahn's National Assembly Building in Bangladesh is exemplified through a detailed analysis with regard to the subsymmetries of the point group symmetry. Kahn has been known for his use of extensive geometric principles. His works are identified by his creative use of geometric shapes, such as squares, circles, and triangles. The spatial composition in his works occasionally appears primitive, but powerful forms where architectural elements are intricately arrayed through geometric systems [13].

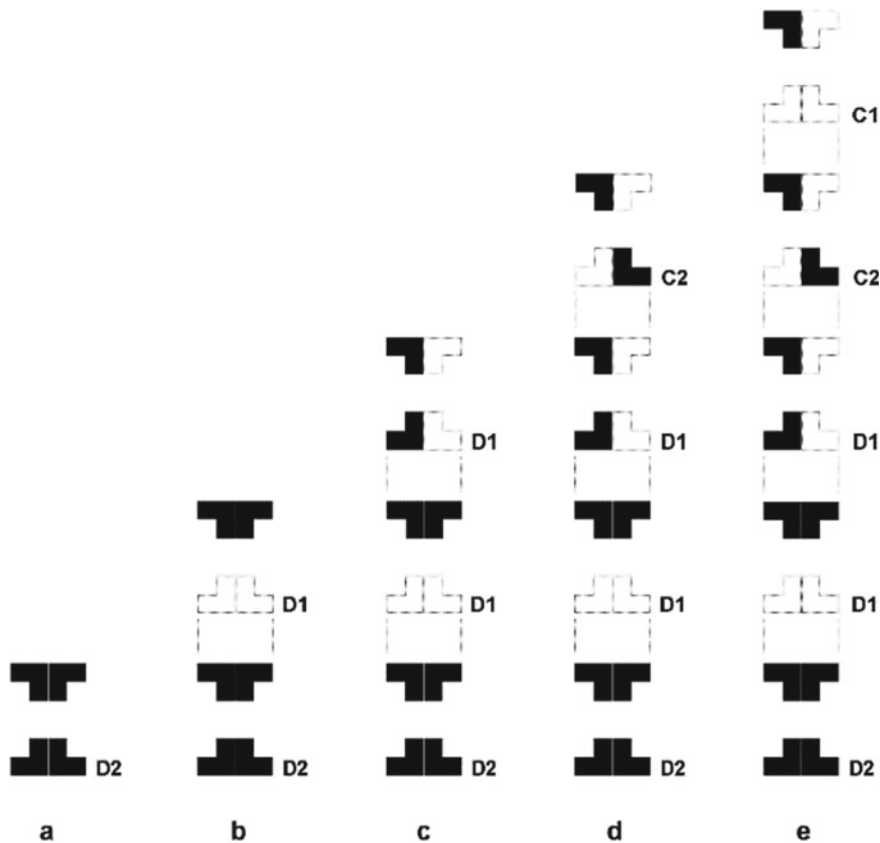


Fig. 4 All possible subgroups of symmetries of a rectangle; the dark square has the full symmetry group D_2 . The bottom row has a motif with two mirrors and rotational symmetry, which is denoted as D_2 . The two above rows consist of a motif with vertical and horizontal reflection, which is denoted as D_1 . The fourth row has a motif with a 180° rotation, which is denoted as C_2 . The top row has a motif without symmetry, which is denoted as C_1

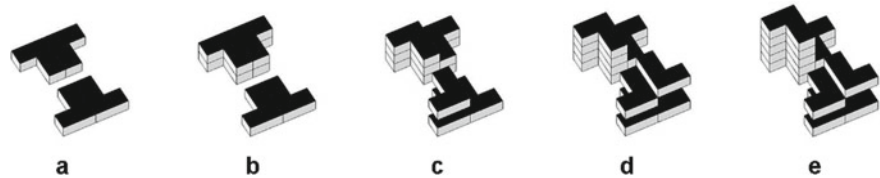


Fig. 5 A simple overlay of different subsymmetries of rectangle

The National Assembly Building appears to be a collection of various shapes of buildings, and the central area of the building is circular. Kahn used the subsymmetries of D16 in the floor plan by analyzing in terms of subsymmetry. Upon inspection, the inner circular boundary of the Assembly Chamber underlies under a 16-sided regular polygon. The octagonal National Assembly Building is clearly characterized by D8 symmetry. The symmetry is reduced to D8 with the introduction of outer walls, the parasol-like parabolic roof of the Assembly Chamber above the floor, and the bottom structural wall for the chamber. Four office blocks are diagonally placed around the assembly hall to produce D4 symmetry of the square. Stairs and elevators for the Minister's Lounge and the Dining and Recreation Room are set along two mirrors and rotational symmetry, which are the subsymmetries of D2. The Entrance Hall, the Dining and Recreation Room, the Chamber of Ministers, and the Hall of Debates are characterized by D1 symmetry. However, the Mosque oriented toward Mecca is marked by its break from the axial symmetries of the secular structure, and its placement ensures that the entire design is asymmetrical despite an approximately obsessive concern for symmetry in the parts. The analysis illustrates that no pure cyclic subsymmetries of D16 are found in Kahn's design. From the sketches of Louis Kahn, various architectural elements are dissolved into the body of the collective whole. Kahn indicated that the symmetry principle and geometric juxtaposition guide the major decisions of the formal and spatial compositions and architectural details (Fig. 6).

A frieze pattern is considered, which consists of 2D motifs repeating in one direction only. Seven distinct groups of the frieze symmetry group exist in an infinite sequence of equidistant points arranged in a linear series on the plane. Thus, every frieze pattern belongs to one of the seven mathematically possible patterns. Five types of isometries, namely, translation, half-turn (180° rotation), vertical reflection, horizontal reflection, and glide reflection, occur in the frieze groups. Different possible combinations of the above isometries form seven distinct symmetry groups together [8, 9] (Fig. 7).

Many frieze patterns are found on building facades and plans. In particular, individual row houses are arranged along a single street on each side. Houses are randomly arranged. Multiple prototypical houses can be bonded together in an orderly manner along a street. Although many examples show the means of deploying frieze symmetry, a simple but strong design example associated with the symmetry of the frieze groups on the building plan is illustrated. The Tara housing by Charles Correa in 1978 illustrates a typical instance wherein a few unit prototypes are interlocked, stacked, and arrayed in a linear pattern. Housing units have two types, namely, two bedrooms (84 m^2) and three bedrooms (130 m^2). Basically, pairs of long rectangular boxes come together side by side and are translated. A series of cubical structures comes together side by side, stacked, translated, and aligned repeatedly along an axis line. The linear pattern of the unit arrangement shows a synthetic structure of various boxes interlocked in four stacked layers of backward stepped buildings to maximize natural light and cool winds. This staggered arrangement provides each unit a large open terrace that is protected by a pergola and big overhangs. A linear public spine is formed between the two linear arrangements of the assembly. It is used

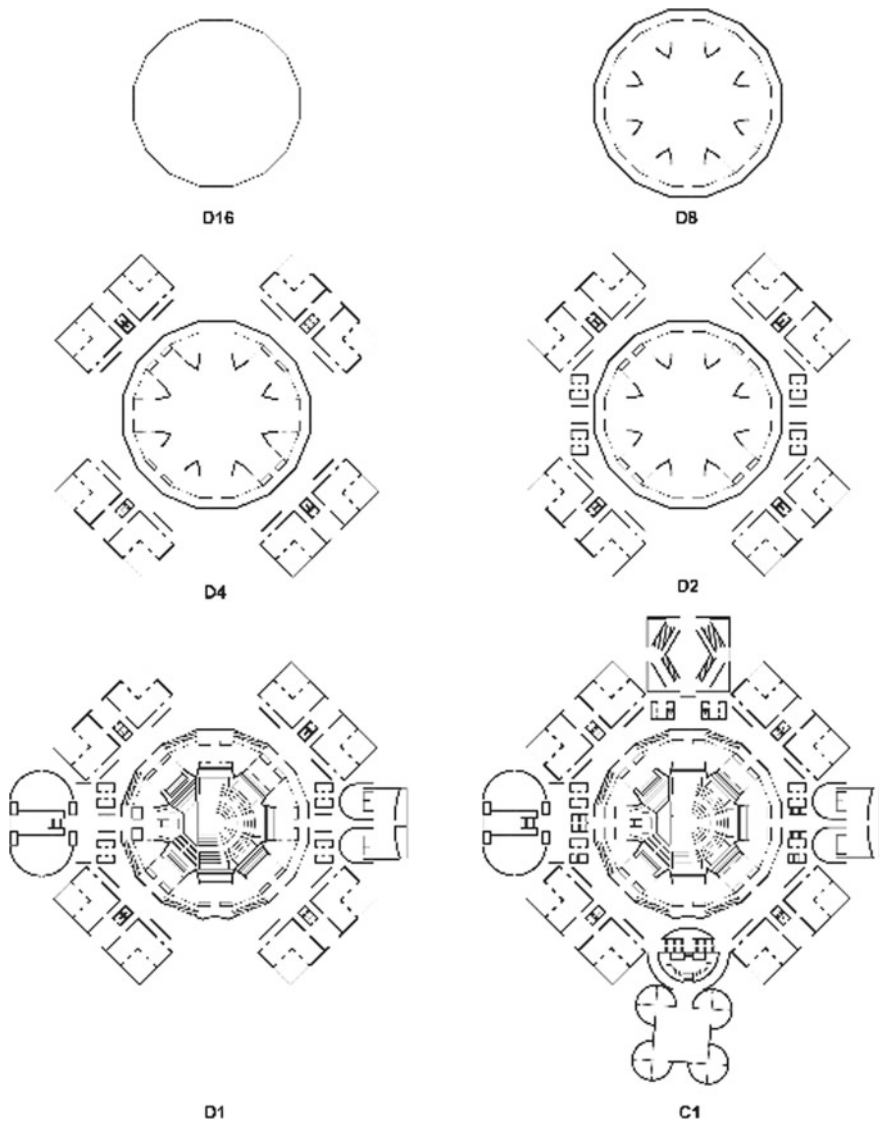


Fig. 6 Subsymmetry analysis diagram of Louis Kahn's National Assembly Building in Bangladesh

as a community open garden space. Correa's previous experiment with regard to the frieze symmetry was observed in a series of projects, such as the unbuilt Cablenagar Township designed in 1967 and the Previ Housing in Lima, Peru (Fig. 8).

A wallpaper pattern is created by repeatedly deploying a basic motif in a plane. A total of 17 distinct plane symmetry groups are classified. Classification is determined by four isometric motions of the plane, such as translations, reflections, glide

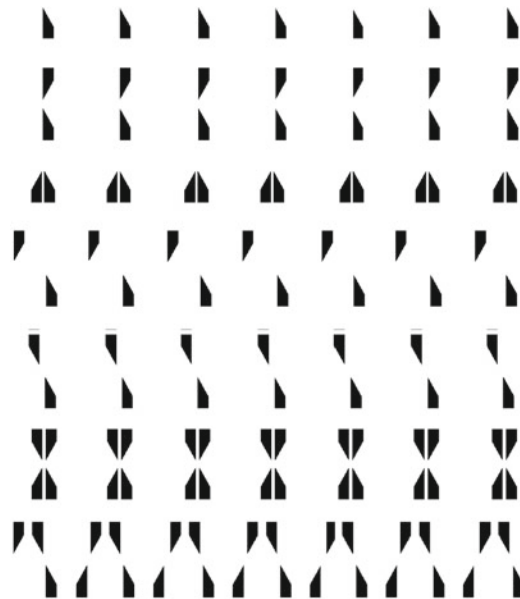


Fig. 7 Seven distinct groups of the frieze symmetry



Fig. 8 Charles Correa's Tara housing layout

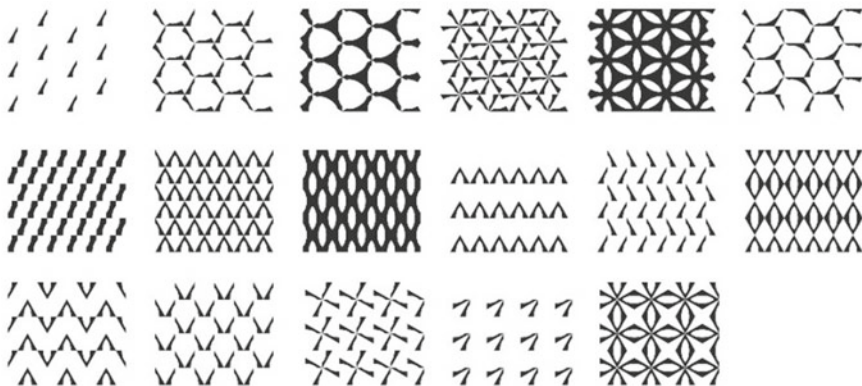


Fig. 9 17 distinct wallpaper symmetry groups

reflections, and rotations. Isometry refers to the process of moving a geometric object from one place to another without changing its size or shape. The motion is called an isometry when a geometric figure is transformed to preserve distances between any two points (Fig. 9).

Wallpaper patterns are commonly used in architecture and decorative art. Their patterns are composed of repetitions of basic motif that covers a finite plane. An interesting consequence is that the repeating patterns consist of the motif at regular intervals in two directions. In architecture, repetitive wallpaper patterns, such as ceramic tiles, textiles, carpets, and wallpapers, are found from antique to contemporary designs. Designers have exhausted all possible plane groups of symmetric designs because of the considerable time they have spent in designing and constructing ornaments. In particular, Islamic designers have developed distinct varieties of similar geometric pattern and ornamental form. Most symmetric wallpaper designs are found in Greek and Roman antiquities and buildings in Alhambra in Granada, Spain (Fig. 10).

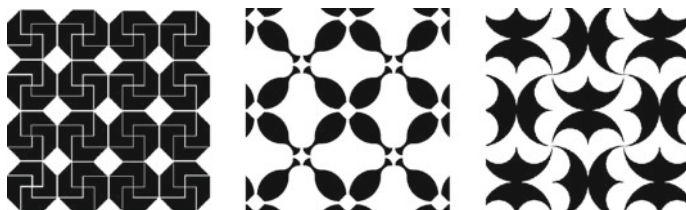


Fig. 10 Roman Mosaic patterns where the wallpaper group of symmetry appears

4 Emergent Designs with Boolean Operations

Regular patterns with the chosen motif are planned and constructed based on the system of the symmetry group. Patterns may be superimposed or computed to form new emergent patterns rather than simply arraying the motif symmetrically. Multiple patterns can move at the same juxtaposition and continuously overlap in different directions. Distinctive patterns may be arrayed and stacked together on top of one another.

Different wallpaper patterns generate a new planar pattern when they are superimposed. Despite several potential means in which patterns can be grouped together, we aim to combine numerous interlaced patterns by using the Boolean operation in this section. Only a few patterns can be computed by using the Boolean operation, thereby coalescing into a single pattern. Here, four Boolean operators are used to construct different sets of designs. An infinite number of new designs emerge depending on the order and the number of sets of rules applied.

The simple process combines shapes in different patterns. The process becomes a constructive method for producing complex geometric figures where two or more shapes interlock. The shapes and patterns can be subtracted, added, and overlapped. Boolean operations can be performed by using the following operators, such as union, subtraction, intersection, and symmetrical difference. Two or more sets of operators can be performed. Consequently, the final patterns become seemingly ambiguous overlapping layers of dynamic patterns although they are generated by rules and principles.

From a computational point of view, patterns can be combined by logically operating a set of rules rather than generating patterns in arbitrary means. Numerous new intriguing patterns can be generated when patterns are combined by using Boolean operations [11]. The operation is straightforward and easy to implement. The basic operations of Boolean algebra are described as follows:

The union of A and B (denoted by $A + B$) patterns is the pattern produced by combining the two patterns. Then, the two patterns completely join together. The intersection of A and B patterns (denoted by $A \cdot B$) is the pattern consisting of partial patterns in A and B. Hence, only the intersecting part remains. The difference of A and B patterns (denoted by $A - B$) is the pattern consisting of the pattern in A that are not patterns in B. The resultant pattern leaves only the part of A where B is subtracted. The symmetric difference of A and B patterns (denoted by $A \Delta B$) is the pattern that are in either of the patterns and not in their intersection. This pattern is the difference of union and intersection.

We can evaluate emergent patterns by computing basic patterns. We simply reduce the basic pattern to 50% in scale to make the second pattern and rotate the 50% reduced pattern to make the third pattern. We reduce the basic pattern to 25% to make the last pattern. Then, each pattern is computed by using Boolean operations and combining various patterns into a single pattern and creating a number of intricate patterns. Overall, the computational process is simple, but the output patterns appear to be unexpected from the initial patterns (Figs. 11 and 12).

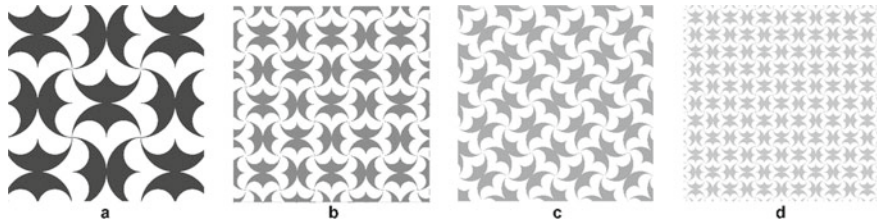


Fig. 11 Four Basic patterns: **a** basic pattern; **b** 50% reduced pattern; **c**. 45° rotated pattern; **d** another 50% reduced pattern

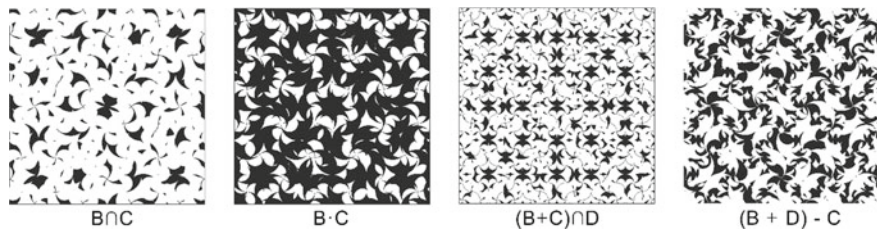


Fig. 12 Four examples of emergent patterns based on the Boolean operations

5 Summary

This article investigates the use of formal techniques as a tool for evaluating and designing the interlace of spatial compositions in architecture. The notion of the point, frieze, and wallpaper group symmetry is simply delineated with regard to their potential use in architectural designs. Wide-ranging applications can be practically addressed to arrive at various design results by using the techniques. This condition proves that symmetry is far from a tiresome notion of a classical ideal.

New designs that are difficult to predict can emerge. Some concepts may be unexpected, and no one can claim that such emergent designs are poor. Such an approach confidently contributes to the vigor of the generation of new designs.

The design process is a sequence of steps that enables architects to apply and describe every aspect of the design procedure. The entire design process is a straightforward procedure and can be explained in a logical manner. The techniques are not an ad hoc tactical decision but another type of logical process of creating designs. The potential of such techniques depends on the strategy and new design tool in the hands of contemporary architects.

References

1. Grossman I, Magnus W (1964) Groups and their graphs. Random House, New York NY

2. March L, Steadman P (1971) *The geometry of environment: an introduction to spatial organization in design*. RIBA Publications, London
3. March L (1996) The smallest interesting world. *Environ Plan* 23:133–142
4. Martin G (1982) *Transformation geometry: an introduction to symmetry*. Springer, New York
5. Oxman R (2002) The thinking eye: visual re-cognition in design emergence. *Des Stud* 23(2):135–164
6. Park J (2000) Subsymmetry analysis of architectural designs: some examples. *Environ Plan* 27(1):121–136
7. Park J (2001) Analysis and synthesis in architectural designs: a study in symmetry. *Nexus Netw J* 3(1):85–97
8. Park J (2018) Subsymmetries for the analysis and design of housing facades. *Nexus Netw J* 20(1):251–266
9. Park J (2019) Arraying prototypical houses in strip patterns: Gregory Ain's Park planned homes of 1946–1949. *Nexus Netw J* 21(3):623–639
10. Schön DA (1983) *The reflective practitioner: how professionals think in action*. Basic Books, New York
11. Stiny G (1980) Introduction to shape and shape grammars. *Environ Plan* 7(3):343–351
12. Stiny G (1982) Shapes are individuals. *Environ Plan B* 9(3):359–367
13. Tzonis A (ed) (1987) *The Louis I. Kahn archive: personal drawings: the completely illustrated catalogue of the drawings in the Louis I. Kahn collection*. University of Pennsylvania and Pennsylvania Historical and Museum Commission, Garland

Research and Development of New Spaces on the Sea for Industrial and Recreational Applications



Kok Keng Ang, Jian Dai, and Chi Zhang

1 Introduction

Singapore is a tiny island city-state with only about 710 km² of land. Besides housing, schools, shops, parks, offices, hotels and other facilities that all cities provide, Singapore also has to provide land for industry, reservoirs, ports, airports, power stations, waste treatment facilities as well as national defense, all of which are typically located in the larger metropolitan areas and beyond the limits of most cities.

Land has always been a precious resource in Singapore. Through careful planning and policies for conserving and recycling land, Singapore has been making efforts to ensure that there is enough land capacity and provided the necessary infrastructure to support the longer-term needs. However, like all cities, land remains a limited resource in the longer term and the future faces even more uncertainties and complexities.

Land reclamation is one of the many ways Singapore creates more space to meet our land use needs. However, the extent to which land can be reclaimed is limited by the need to retain enough sea space to meet shipping passage, anchorages and other maritime needs. Furthermore, land reclamation is also resource intensive, which poses a challenge.

Building very large floating structures (VLFS) is an alternative to create space for various uses in Singapore. Worldwide successful examples include the floating oil storage bases in Japan, desalination plant in Saudi Arabia, floating bridges in Japan and Norway, and floating performance stage in Singapore. Floating structures are

K. K. Ang (✉) · C. Zhang

Department of Civil and Environmental Engineering, National University of Singapore, Singapore 117576, Singapore

e-mail: ceearangkk@nus.edu.sg

J. Dai

Department of Marine Technology, Norwegian University of Science and Technology, 7491 Trondheim, Norway

immune to earthquake attacks as they are base-isolated, and they are insensitive to sea water surface elevation induced by global warming.

Towards exploring and implementing large floating structure applications, the Land and Liveability National Innovation Challenge (L2 NIC) Directorate and JTC Corporation have provided a research grant to the National University of Singapore (NUS) and SINTEF to conduct research on multi-purpose floating structures (MPFS). The objective of the MPFS research and development project is to develop design concepts, innovative and optimal structural, foundation and construction solutions for large floating structures. The project focuses on three specific applications, namely the floating hydrocarbon storage facility (FHSF), the floating bridge (FB) and the modular multi-purpose floating structure (MMFS). Besides research on very large floating structures for heavy industry and infrastructure, Singapore also invested on floating structure technology for energy production and creating floating wetlands.

This paper presents the recent research and development activities in Singapore pertaining to the use of floating structures for both industrial and recreational applications. These include the results of a research-funded study on floating hydrocarbon storage facility, floating bridge and modular multi-purpose floating structures. In addition, details of the successful development and construction of the first locally designed floating solar farm at the world's largest floating photovoltaics testbed in a reservoir as well as soon to be constructed commercial floating solar farm in coastal marine water and floating wetlands in Singapore are presented.

2 Floating Hydrocarbon Storage Facility (FHSF)

2.1 Design Concept

The study on the FHSF focuses on the research and development of a design concept for a floating facility that can accommodate the storage and trading of 300,000 m³ stockpile of hydrocarbon products at a chosen site. If constructed, it will be the world's first floating prestressed concrete hydrocarbon storage structure. The facility is intended for Singapore surrounding sea condition, and thus is targeted for sea depths that are considered shallow and with relatively calm sea conditions. The design shall provide spaces for PMEI system and blending/mixing equipment and has a service life of 60 years. A detailed description of the design requirements was documented by Dai et al. [1] and Ang et al. [2].

The design concept of the floating hydrocarbon storage facility (FHSF) is shown in Fig. 1. The proposed facility is self-contained with all essential services and amenities such as power generation plant, desalination plant, slop and wastewater treatment plant, control room, warehouse, pump rooms, offices and accommodation quarters for workers. It has floating berths on the sides for loading/offloading operations and bunker supply. The floating berths and barges also serve as a protection of the fuel storage modules, like floating breakwaters [3], against waves and ship collision.

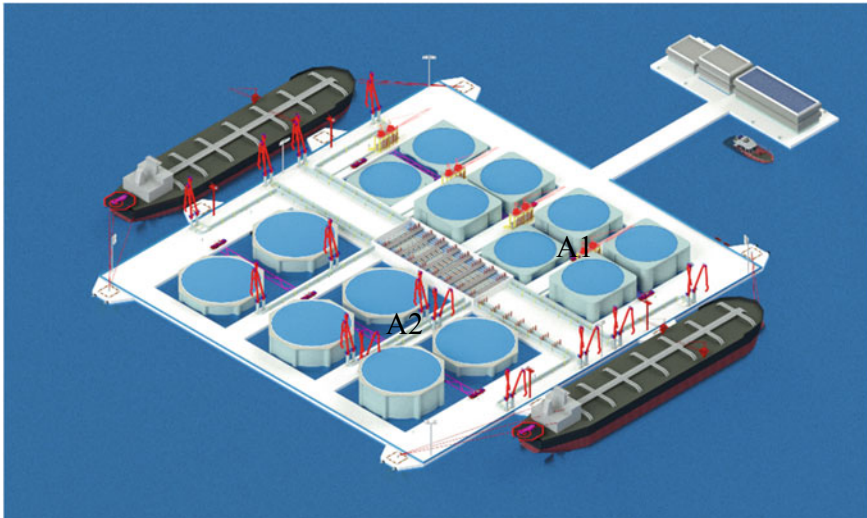


Fig. 1 Floating hydrocarbon storage and bunker facility

The FHSF stores hydrocarbon and provides bunker fuel to ships in harbors. The individual tanks are designed such that they are self-stabilizing and the maximum tilt angle under environmental loads does not exceed allowable limits. Depending on the types of product stored, the tanks are categorized into two groups, namely the small tanks and the big tanks. The small tanks (see A1 in Fig. 1) are intended for Clean Petrochemical Products (CPP). Their storage capacity ranges from 5000 to 15,000 m³. The big tanks (see A2 in Fig. 1) are for crude and fuel oil and they have a practical storage capacity ranging from 20,000 to 35,000 m³.

2.2 Stability and Motion of Floating Tanks

The stability and predicted motion of the storage tanks subject to environmental loads are important considerations in determining the feasibility of the proposed FHSF concept. The floating hydrocarbon storage tanks must be self-stabilizing and the displacements of the tank must not exceed limiting values. The latter is required so that loading and offloading processes are not disrupted during operations and the tank does not capsize or damage the surrounding structures and facilities under extreme weather conditions.

Consider a floating hydrocarbon storage tank enclosed by floating barges on the sides, as shown in Fig. 2. In view of the barges protecting the tanks from incoming waves, we shall assume that the tank is mainly subjected to wind and water current loads. The yellow region in the tank represents the stored hydrocarbon product. The wind and water current speeds are assumed to be constant in the model so that a

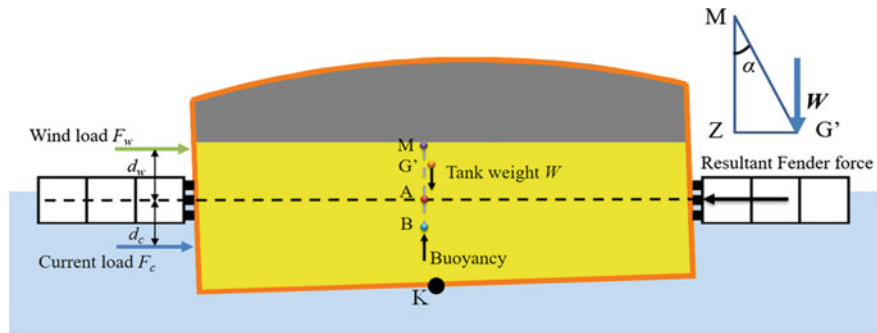


Fig. 2 Floating tank enclosed by barges subjected to wind and current loads

simple static analysis is possible. In addition, the fenders are designed to restrain the horizontal motion of storage tanks. Thus, only angular movements, i.e. tilting motion, will be examined.

With the given information on structural configuration and geometry of tank components as well as fuel loading condition, we can estimate the locations of the tank's centre of gravity (CG) and centre of buoyancy (CB) as shown in Fig. 2. The initial metacentric height GM may be calculated from

$$GM = KB + BM - KG \quad (1)$$

where M, G, B and K are the meta-centre, the centre of gravity, the centre of buoyancy and the keel, respectively. In a partially filled condition, there will be a shift in liquid surface arising from a small tilt in the structure due to the existence of free liquid surface. This is known as the Free Surface Effect (FSE) that further reduces the GM, which should be accounted for in the calculation. In addition, the wind and water current loads acting on the structure can be assumed as a uniformly distributed load on the tank wall. The wind and current pressure can be acting in two opposing directions or in the same direction. The combination of these two cases that yields the most severe destabilizing moment is used for calculations.

The tilting angle of the tank can be calculated based on moment equilibrium about point A, the intersection between resultant fender reaction and the metacentric radius (BM) as shown in Fig. 2. The formula for calculating the tilting angle α is

$$W \times GM \tan \alpha = |F_w d_w| + |F_c d_c| \quad (2)$$

where W is the weight of the tank, F_w and F_c are the resultant wind load and water current load exerted on the tank walls, d_w and d_c are the lever arms from the centre of the wind load and current load to point A, respectively.

The proposed FHSF tank has a single hull cylindrical tank with a dome roof on top, a flat slab at the bottom, and several hollow cylindrical floaters attached to the tank wall to increase buoyancy and enhance stability. This single hull design has

the benefit of nearly balanced internal and external hydrostatic pressure on the tank walls, thus significantly reducing the induced wall stresses. The tank has a diameter D and height H . The dome roof has a common rise to span ratio of $H_r/D = 1/8$. Table 1 lists the key properties of the storage tank [1]. The hourly mean wind and water current speed at the selected site in Singapore coastal water are 15.9 m/s and 24 m/s, respectively, for the 100-year return period. The corresponding magnitudes for the 1-year return period are 1.46 m/s and 1.90 m/s, respectively.

Figure 3 presents the maximum tilting angles of small CPP storage tanks of various storage capacities subject to combined wind and current loads at their 1-year and 100-year return periods. Larger tank D/H ratios lead to smaller tilting angles (and thus the tanks are more stable). Results show that tanks with $D/H = 1.7$ fulfil the stability and operational requirements on tilting motion when the storage capacity is above 12,500 m³. When tank D/H exceeds 1.8, all the tanks satisfy the design checks. Similarly, the maximum tilting angles of big oil storage tanks under combined wind and current loads are presented in Fig. 4. The study showed that a D/H ratio exceeding 2.4 is necessary to satisfy stability and tilt motion criteria.

Table 1 Storage tank properties

Parameter	Value	Parameter	Value (mm)
Concrete density	1800 kg/m ³	Outer wall thickness	450
Water density	1025 kg/m ³	Inner wall thickness	300
Fuel density	870 kg/m ³	Roof slab thickness	200
Air density	1.25 kg/m ³	Diagonal stiffener thickness	350
Bottom slab thickness	750 mm		

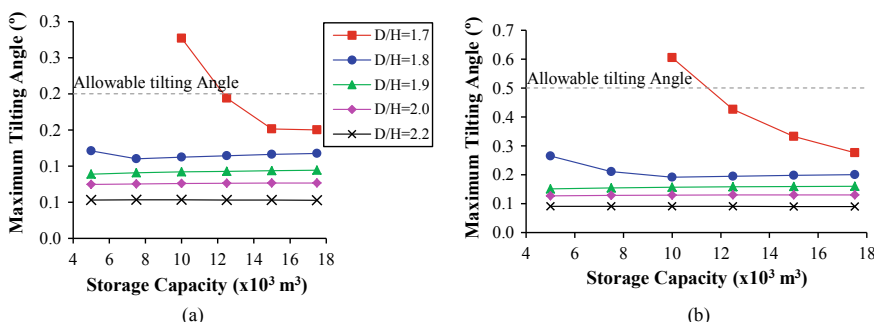


Fig. 3 Maximum tilting angle of small tanks under **a** 1-year design load and **b** 100-year design load

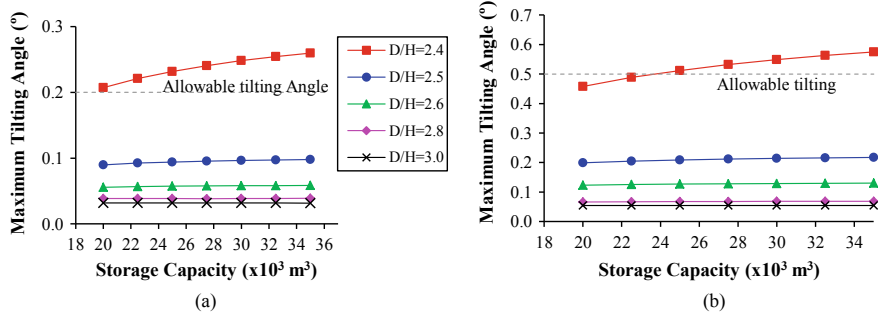


Fig. 4 Maximum tilting angle of big tanks under **a** 1-year design load and **b** 100-year design load

2.3 Hydrodynamic Performance

The hydrodynamic response of the floating hydrocarbon storage facility has been investigated comprehensively. The entire system is very complex and consists of many bodies. There exist hydrodynamic coupling, mechanical coupling and sloshing. It is thus very difficult to evaluate the conceptual design through either experimental or numerical studies. To rationally study its hydrodynamic performance, the research work has been divided into three stages. At each stage, experimental and numerical studies have been conducted in parallel. The hydrodynamic performance of the facility is also improved stage by stage.

The first stage is to investigate the hydrodynamic performance of a single hydrocarbon storage tank (Fig. 5). The tank size and shape were optimized based on the research findings. One important finding is that the pitch motion of a single storage tank (5000 m^3) is large. To reduce the pitch motion, a special design has been adopted by introducing thin heave plate to the bottom of the tank. This modification introduces damping and added mass to the single tank. It was found that the heave

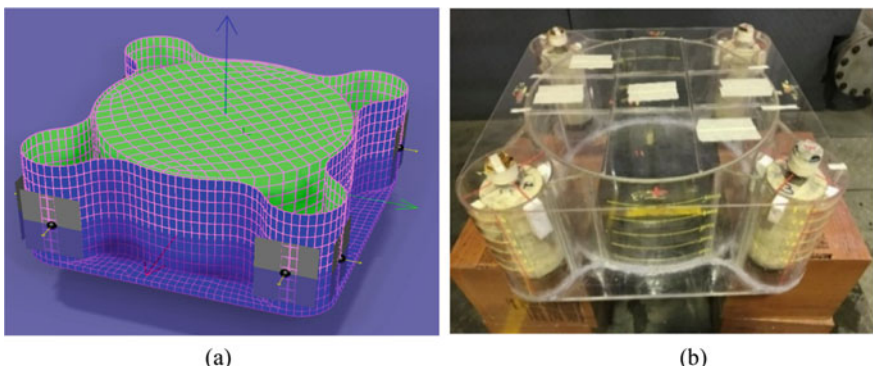


Fig. 5 Hydrocarbon storage tank for first research stage **a** numerical model and **b** experimental model

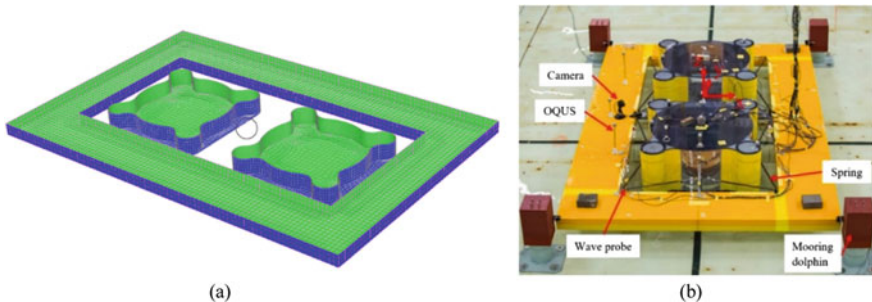


Fig. 6 Simplified hydrocarbon storage tank system for second research stage **a** numerical model and **b** experimental model

plate improves the hydrodynamic response of the storage tank significantly [4, 5]. Another finding is that the sloshing in the single tank is found to be serious. To avoid the effect of severe sloshing in the tank, a larger size storage tank ($12,500 \text{ m}^3$) is selected for both numerical and experimental study in the second stage (Fig. 6).

In the second stage, a simplified system was selected for the hydrodynamic studies [4, 5]. The simplified system consists of two storage tanks and a barge frame. This system represents the main characteristic of the entire system. At this stage, the hydrodynamic interactions and the performance of the mooring system are of main interest. The responses of the system under different incident wave, wind and current conditions have been studied. It was found that with the existence of the barge frame, the motion of the storage tank is further reduced. However, the barge frame can introduce gap resonance in the narrow gaps between tank and barge. The maximum wave elevation in the narrow gaps between the barge frame and the tank can be around 4 m/m. Green water was found on the barge frame as the barge frame's freeboard is only 2 m in the initial design (Figs. 6 and 7).

The third stage is to investigate the hydrodynamic performance of the entire floating hydrocarbon storage facility. The entire system consists of more than 30 bodies as the barge frame is constructed by connecting a number of smaller modules. The scaled model test of the entire system was conducted at the ocean basin of SINTEF Ocean [6]. The test was carried out for several cases of combined environmental conditions. Through these model tests, it was found that the performance of the proposed concept is acceptable. Under the extreme conditions with 100-year return period, the maximum pitch is found to be smaller than 5° . The surge motion is smaller than 2 m. The green water and gap resonance problems were observed to occur. However, these undesirable effects can be easily mitigated though increasing the freeboard of the barge frame. The complex numerical study of the entire floating hydrocarbon facility for the third research stage is still ongoing. It becomes very difficult for the frequency domain simulation based on potential flow and for the time domain simulation based on convolution integrals. Some efficient numerical methods have been introduced for the numerical modelling of the entire system which will be updated once it is validated. These results will subsequently be documented in another publication.

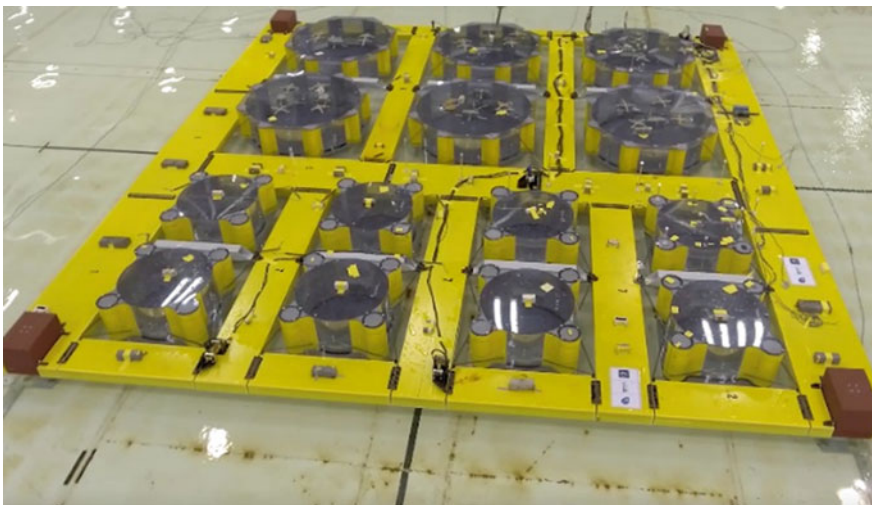


Fig. 7 Experimental model of entire hydrocarbon storage tank system for third research stage

3 Modular Multi-purpose Floating Structures

3.1 Design Concept

The objective of the research on modular multi-purpose floating structures (MMFS) is to develop innovative solutions for the creation of ‘land on sea’ of any desired size and shape for various application by connecting several standard modular units. The size and shape of the basic modular units are to be carefully investigated and determined that is optimal with respect to fulfilling several important requirements. These include constructability and ease of marine installation, as well as connectivity and flexibility in meeting the global shape and size of the intended land on sea. The basic modules are to be optimally designed considering cases of combined loadings due to dead, live and environmental loads. The potential applications of the MMFS concept include floating aggregate storage facility, floating flatted factory and floating dorms.

Different applications impose different design loads onto the floating structures. Typically, the payload for the abovementioned potential applications may be reasonably categorized into three groups, namely, category 1 for low-rise residential and recreational application (≤ 25 kPa), category 2 for low-rise industrial flatted factory (25–45 kPa) and category 3 for heavy industrial use and storage (45–80 kPa).

The MMFS is formed by connecting several basic modules to form the required size and global shape. Figure 8 shows a large floating structure formed through connecting standard rectangular modules in a staggered configuration. Standard square and so-called triangular modules are employed at the edges and corners. This concept is expected to provide a wide choice in connecting modules that gives global

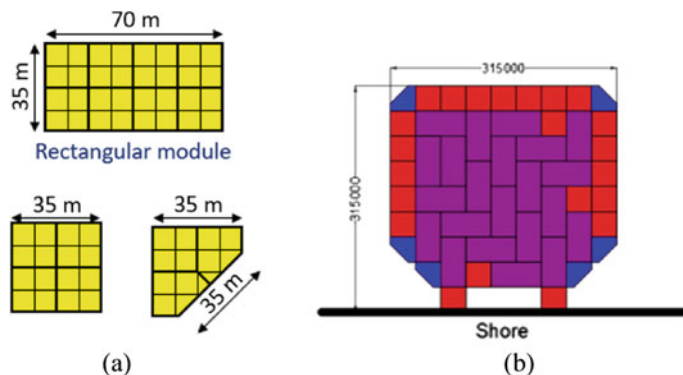


Fig. 8 Design concept of MMFS, **a** modular shape and size and **b** global arrangement

shapes with naturally straight edges for berthing purposes. The standard shapes also facilitate the fabrication process.

3.2 Feasibility Study

To evaluate the global performance of the proposed design concept, a segment of the global layout of the MMFS is selected for the investigation of the modules under various load patterns. Figure 9 shows the selected segment of the global layout under four different loading patterns. Finite element models are constructed accordingly based on plate theory with the properties evaluated from the actual 3D modular model, as shown in Fig. 10. Inter-modular connection stiffness is assumed to be

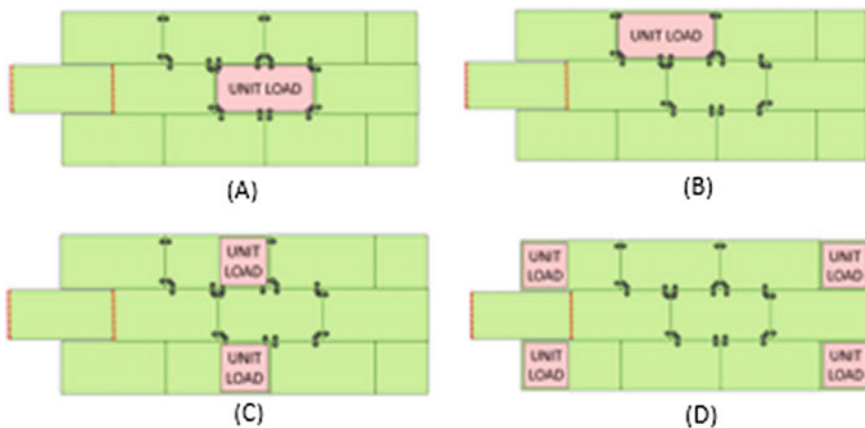


Fig. 9 Load patterns



Fig. 10 Finite element model of selected global segment

Table 2 Maximum connection load

Connection load	Value	Unit
Shear (under 25 kPa)	537	kN/m
Shear (under 80 kPa)	1.62	MN/m
Bending (under 25 kPa)	14.3	MNm/m
Bending (under 80 kPa)	45.7	MNm/m
Twisting (under 25 kPa)	8.5	MNm/m
Twisting (under 80 kPa)	20.1	MNm/m

rigid, which represents the conventional connections using prestressed tendons/bars at the top and bottom of the connected modules. The modules are suspended by area springs representing the hydrostatic pressure. Two different loading levels are considered, namely 25 and 80 kPa, which represent the loading corresponding to a floating residential application and heavy-duty aggregate storage, respectively. This part of the study aims to evaluate the shear forces and moments developed at the connectors.

It is observed that among the four loading patterns, load case (b) tends to induce the highest connection loads. Table 2 summarizes the maximum shear force, bending and twisting moments per unit length along the connection interface. Through a detailed structural modelling and analysis, it is found that the values summarized in Table 2 are within acceptable limits and appropriate inter-modular connections can be designed for.

3.3 Hydrodynamic Performance

To evaluate the hydrodynamic performance of modular floating structures under the design sea conditions, comprehensive numerical and experimental studies have been conducted. In the numerical and experimental studies, two simplified models

have been tested. One consists of 7 modules in one line. Another consists of 9 modules placed in 3 by 3 configuration. The two simplified models contain the basic hydrodynamic characteristic of the entire system. With the simplified model, the requirement on both computational resources and experimental work has been significantly reduced.

The numerical simulation was done in frequency domain using HydroStar based on potential theory and the results are imported into SIMO, a time domain simulation code [7]. Model tests were conducted in the wave basin at the National University of Singapore. The model test was performed based on a 1:50 scale. In both experimental and numerical studies, the random wave conditions in 1-year and 100-year return period have been studied. The numerical model and the physical model in the basin are shown in Figs. 11 and 12, respectively. The two sea states represent the operational and extreme sea conditions respectively. In these studies, the effect of the different outermost module design and the effect of the connection types have been studied.

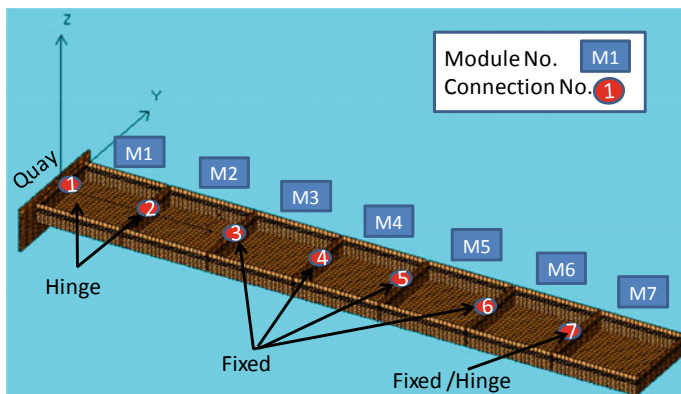


Fig. 11 Hydrodynamic model of 1-line system

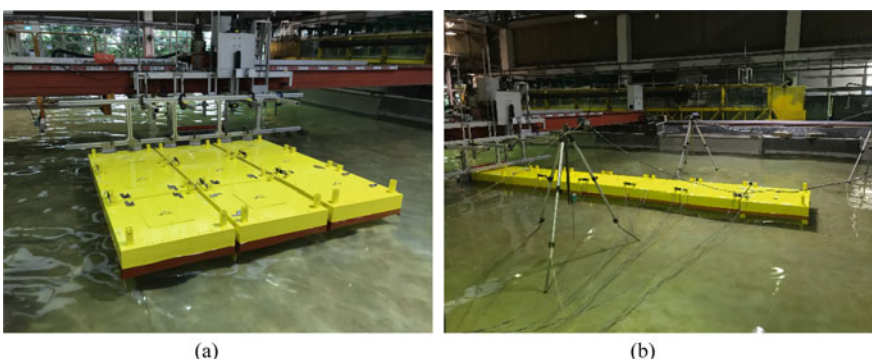


Fig. 12 Physical models of **a** 3 by 3 system and **b** 1-line system

Through the experimental and numerical studies, it is found that the hydrodynamic performance of the two systems is very promising except for the outermost module which has the largest motions if the connection is a hinge type. The remaining modules have mild motions. To reduce the motion of the outermost modules, three options have been explored. One is to introduce fixed connectors between the outermost modules. The second solution is to increase the draft of the outermost modules. The last option is to introduce heave plate on the outermost module. The heave plate is found effective in reducing the motion of floating modules. By comparing the efficiency of these solutions, it can be concluded that fixed type of connectors can reduce the motion significantly but, as to be expected, large increase in the connection force. The other two options were found to be effective in increasing the inertia of the outermost module which reduces its motions.

4 Floating Solar Farms

4.1 Project Information

Although Singapore relies heavily on hydrocarbon as the main energy source to power up the nation, looking for clean and renewable energies as replacement of hydrocarbon products is always a target set by the government. Located in a tropical region, Singapore identified that solar energy is a suitable renewable energy source. However, limited land resource poses a serious challenge for the deployment of large solar farms on land. As such, there is an impetus to find other suitable locations for large scale deployment or installation of solar panels. One of the solutions is to deploy solar panels on water bodies and surrounding sea spaces as a floating solar farm. On water, the solar panels can potentially receive maximum sunlight as these water bodies are typically free of obstruction from tall buildings, structures and vegetation. The efficiency of the solar panels can also be maximized owing to the natural cooling mechanism above the water surface. Furthermore, the deployment of floating solar farms can reduce the evaporative loss.

To promote the adoption of solar energy and to test the performance of photovoltaic (PV) panels above water surface, Singapore launched the world's largest floating PV test-bed at Tengeh reservoir. A total of 10 different designs of floating PV farms, each generating 100 kWp of power, were deployed at the test-bed. Among the 10 designs, the first locally-designed floating PV farm has the feature of having only one standardized floating module which is shown in Fig. 13 [8]. This innovative design has been patented¹ by HDB. The module can serve as a floater to support a PV panel or be used as a walkway floater which can support personnel doing maintenance work in the floating solar farm. Each floating module, made of high-density polyethylene (HDPE), is designed with a corrugated surface and a row of grooves

¹Floating Solar Module by Housing and Development Board—Singapore/patent no. PCT/SG2019/050220.

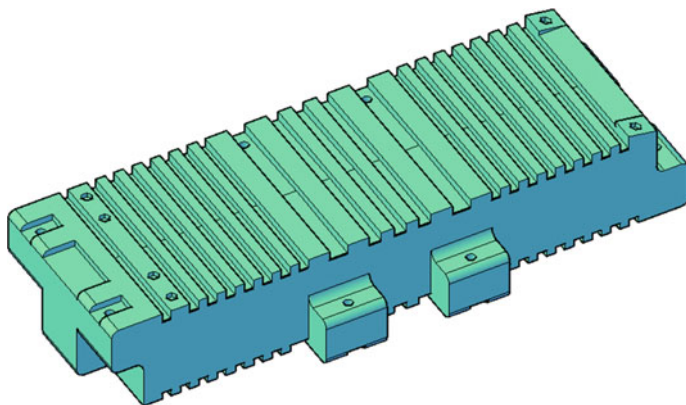


Fig. 13 Floating module

and ridges to provide rigidity and strength. Each floating module is designed with innovative male and female connector parts on the sides. The modules can therefore be easily connected to each other by inter-locking them with stainless steel pins. The interlocking inter-modular connection ensures a safe and stable maintenance walkway. With a specially designed pillow module, the floating module can be used to support solar PV panels, as shown in Fig. 14. Figure 15 shows the global layout

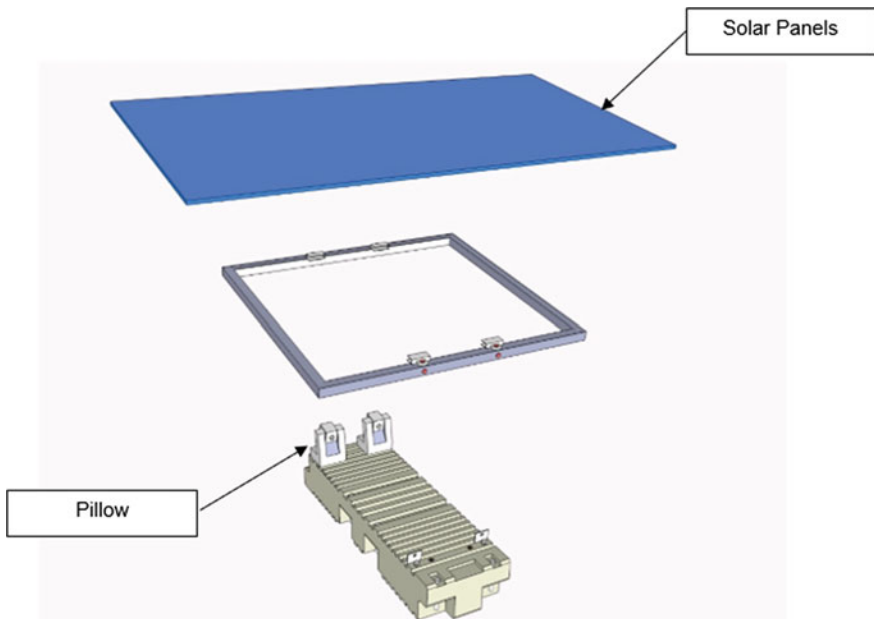


Fig. 14 Floating module used as support for PV panel

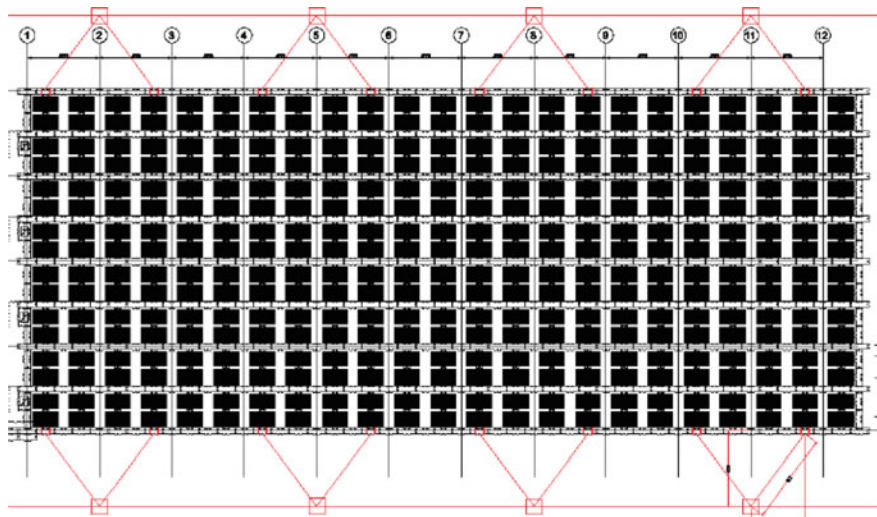


Fig. 15 Global layout of floating PV farm at Tengeh reservoir

of the 100 kWP floating solar farm. The designed farm was successfully deployed at Tengeh reservoir in mid-2018, as shown in Fig. 16.

The successful pilot implementation at Tengeh reservoir created industrial interest and a much larger-scale project was launched to construct one of the world's largest



Fig. 16 Constructed floating solar farm at Tengeh reservoir

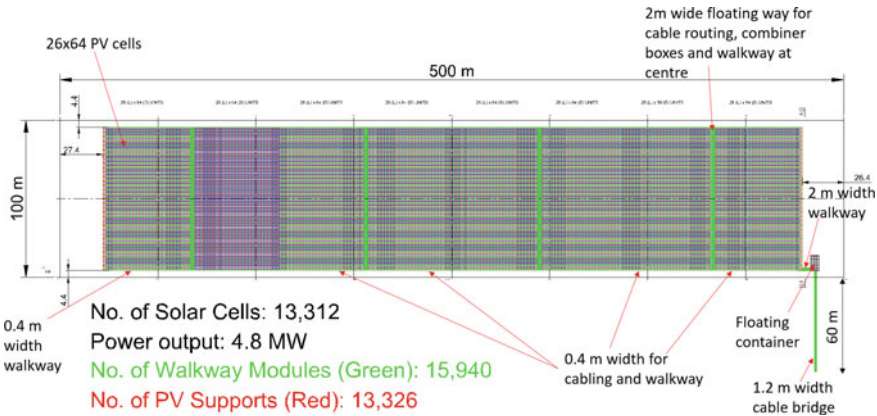


Fig. 17 Global arrangement of floating solar farm offshore Woodlands

5 MWp coastal floating solar farm offshore Woodlands, Singapore. Figure 17 shows the global layout of the designed floating solar farm. The site is within a well sheltered channel where the environmental conditions are like those at Tengeh reservoir, except that there is a higher water current speed and a larger tidal variation. Besides, the corrosive sea water brings the concern of corrosion. Furthermore, marine growth on floating modules needs to be accounted for. In view of the environmental condition, the design used for Tengeh reservoir was modified accordingly to suit the design requirements at Woodlands. The key differences include (1) different sizes are used for walkway modules and PV modules to achieve an optimal use of the given space; (2) high-strength nylon pins are used to replace stainless steel pins at the connection to avoid corrosion; and (3) marine grade aluminium brackets are used to replace pillow structures for the support of solar PV panels. The floating solar farm is expected to be deployed onsite in late 2019.

4.2 Structural Analysis

The finite element model of a typical floater module is shown in Fig. 18. The model is constructed using thin shell elements. Winkler-type linear area springs, representing the hydrostatic pressure, are applied at the bottom surface of the model. Equivalent hydrostatic pressures at the sides are also applied through the area load assignment. Note that this finite element model is a simplified representation of the module shown in Fig. 13. The major simplifications are: (1) wider rib and trough width and (2) simplified geometry of the connectors. These simplifications are justifiable in view that wider rib and trough width leads to a relatively conservative prediction of the analysis results. The geometry of the connectors is not of interest in the analysis of one single floating module. An independent detailed connection model

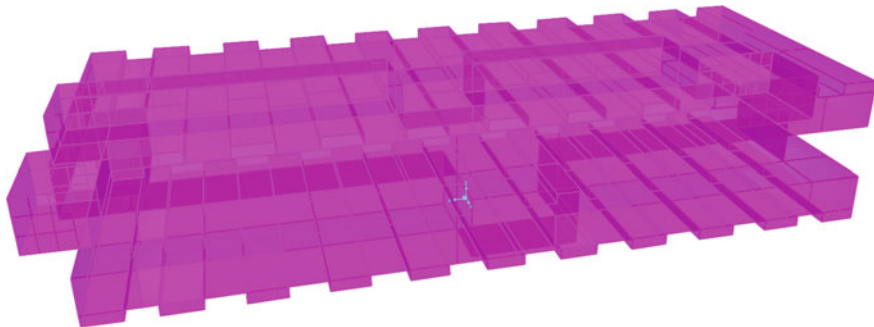


Fig. 18 Finite element model of floater module

is constructed for the analysis and design of the inter-modular shear key connection. The simplifications adopted here are for the purpose of computational efficiency by avoiding undesirable effects due to irregular geometry and irregular elements.

Figure 19 shows the total displacement contour plot of the top surface of the floating module under service condition supporting the weight of a service personnel. The 3D deformed shapes are shown in Fig. 20. Note that the total deflection includes the draft of the module. The differential deformation is found to be within acceptable range.

In addition to serviceability check, the strength adequacy of the module must also be examined. Figure 21 shows the contour plot of the von Mises stress at the top surface under ultimate limit state. As can be seen, the maximum stress of 20 MPa is smaller than the yield stress of 27 MPa of the HDPE material. The design is thus deemed satisfactory.

Figure 22 shows a local finite element model of the connection region between two floater modules. The HDPE module parts are represented by thin shell elements. The pins are modelled as frame elements with the same geometric information as

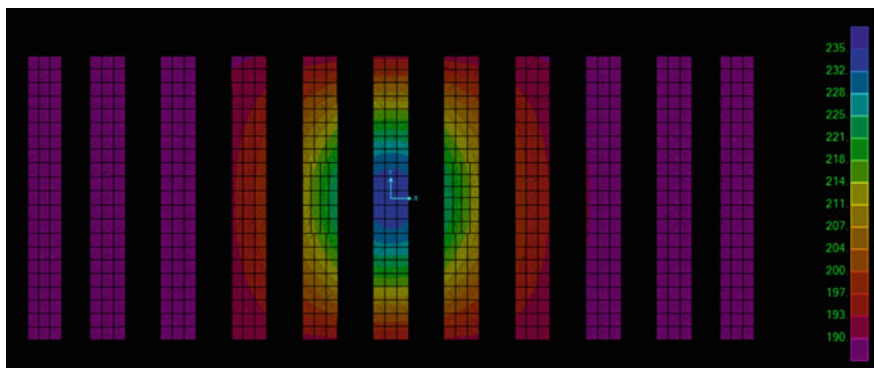


Fig. 19 Total deflection of module top surface (unit: mm)

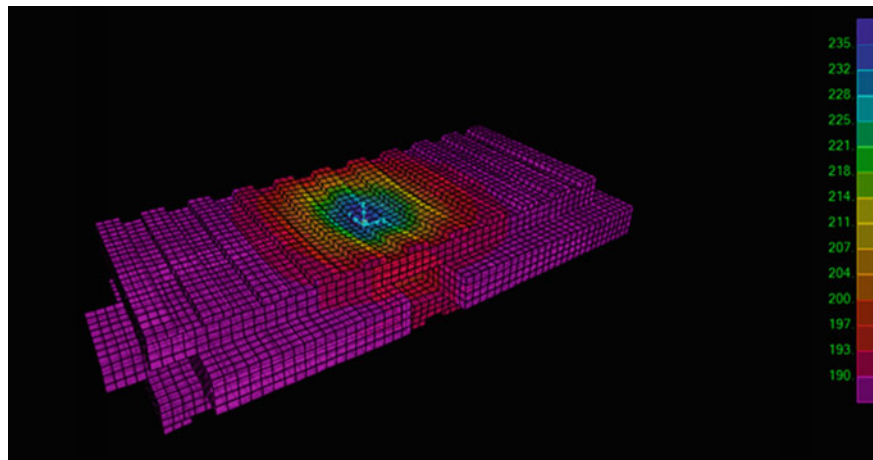


Fig. 20 Deformed module (unit: mm)

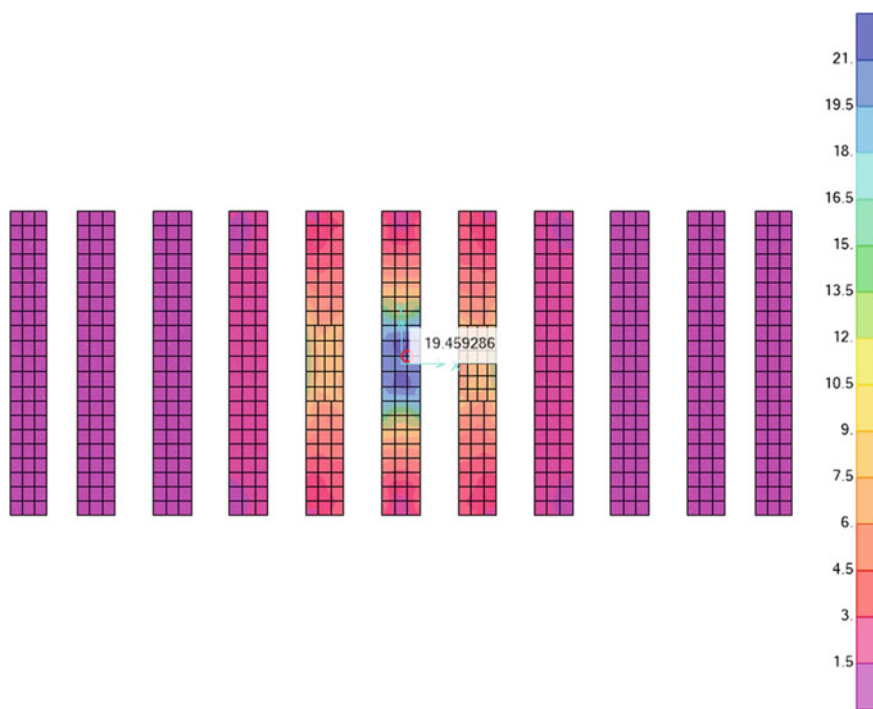


Fig. 21 von Mises stress under ultimate limit state (unit: MPa)

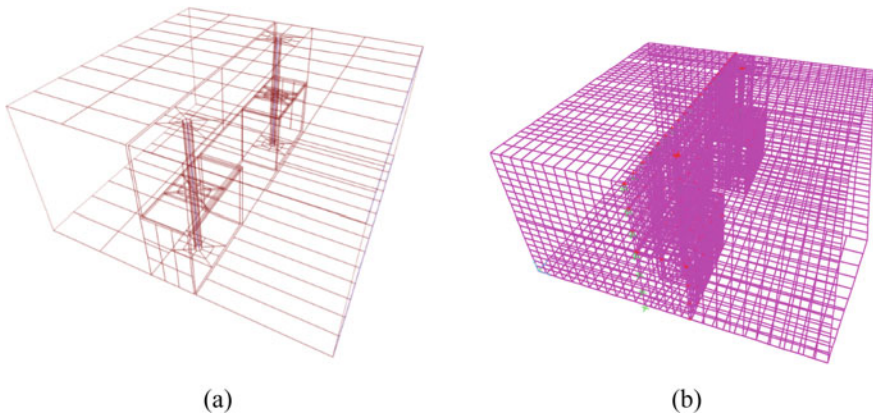


Fig. 22 Connection model: **a** model outline and **b** finite element mesh

the steel pin. Bilinear elastic springs are applied to the connection interface between the two modules. Line loads of the same magnitude but in different directions are applied to the top and bottom edges of the other module part to create a moment at the connection interface. A nonlinear finite element analysis is carried out to examine the adequacy of the connector strength and assess the stiffness of the connection.

Based on a prior global analysis, a maximum bending moment of 0.4 kNm at the connection is identified and applied to the nonlinear local connector model for strength check. Figure 23a shows the von Mises stress contour plot of the connector.

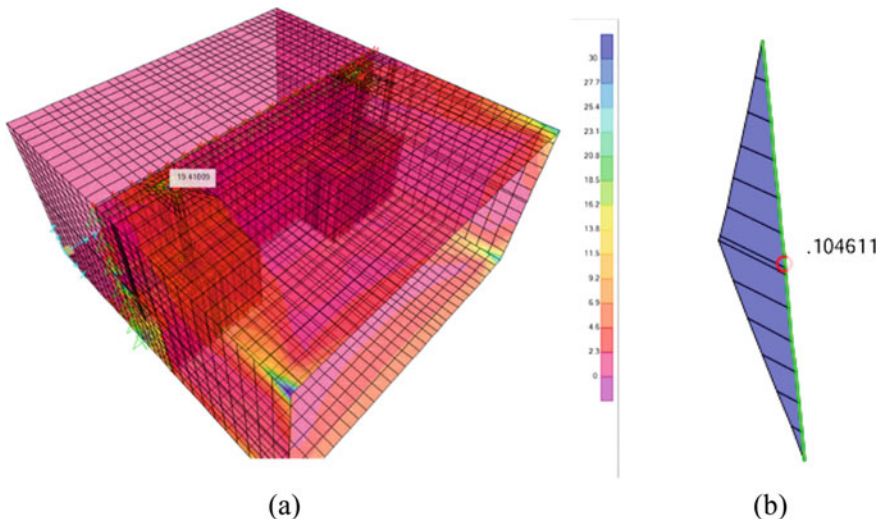


Fig. 23 Analysis of connection, **a** von Mises stress (MPa) and **b** bending moment at connection pin (kNm)

As can be seen, the stress concentration is observed near the bolt slot on the top surface of the module. The maximum stress is about 19 MPa, which is smaller than the yield stress of the HDPE material. At the inter-modular connection, the steel bolt is subjected to a bending moment of 0.1 kNm at the mid-span (see Fig. 23b). This value is smaller than the strength of a Grade 316 bolt. Thus, the current design of the inter-modular connector is satisfactory.

4.3 Hydrodynamic Test

Hydrodynamic responses of the floating structure under environmental actions is critical to safety in both daily operation and survival condition. This is especially important when the floating solar farm system is in the sea subject to marine conditions. In reservoir condition, the water is almost calm, and no large water current is expected. However, in sea condition, there can exist relatively large waves as well as current and tides. Due to the large number of modules in a typical size floating solar farm, it is not possible to conduct hydrodynamic analysis for the entire system. A simplified model is necessary to reduce the cost of computational resources and time. To reasonably represent the characteristics of the entire floating solar system, a section of the system consisting of 10 modules is selected for the hydrodynamic study for laboratory tests and numerical simulations. The sub-system is assumed to be from the outer most area of the solar farm which is subject to larger wave loads as compared to other parts of the farm.

Since a floating solar farm has never been developed for deployment under marine condition, experimental verification of the system is desired to understand its behaviour. The experimental results can also provide a means for the validation of results obtained from numerical hydrodynamic analysis. The model test was conducted in full scale in the hydraulic laboratory at the National University of Singapore. Both hydrostatic and hydrodynamic tests were carried out. The former is to examine the stability and maximum vertical load carrying capacity of the floating system. The latter is to evaluate the performance of the system under wave conditions. Figure 24 shows the coastal basin which is used for carrying out the model tests. The schematic drawing of the layout of the model test is shown in Fig. 25. The physical model of sub-system of the floating solar farm used in the tests are shown in Fig. 26.

The model tests were conducted for regular, irregular and focus wave conditions. These tests are to measure the response amplitude operators (RAOs) and the statistical responses of the model floating system. Two irregular sea conditions, namely normal sea and extreme sea have been defined based on the expected conditions at the actual site where the farm is to be built. The tested irregular wave conditions are summarized in Table 3. All these test conditions were calibrated before the model test is conducted. The motions in 6 degrees of freedom have been recorded.

Experimental laboratory test results revealed that the hydrostatic and hydrodynamic performance of the system is very good. The maximum vertical load capacity

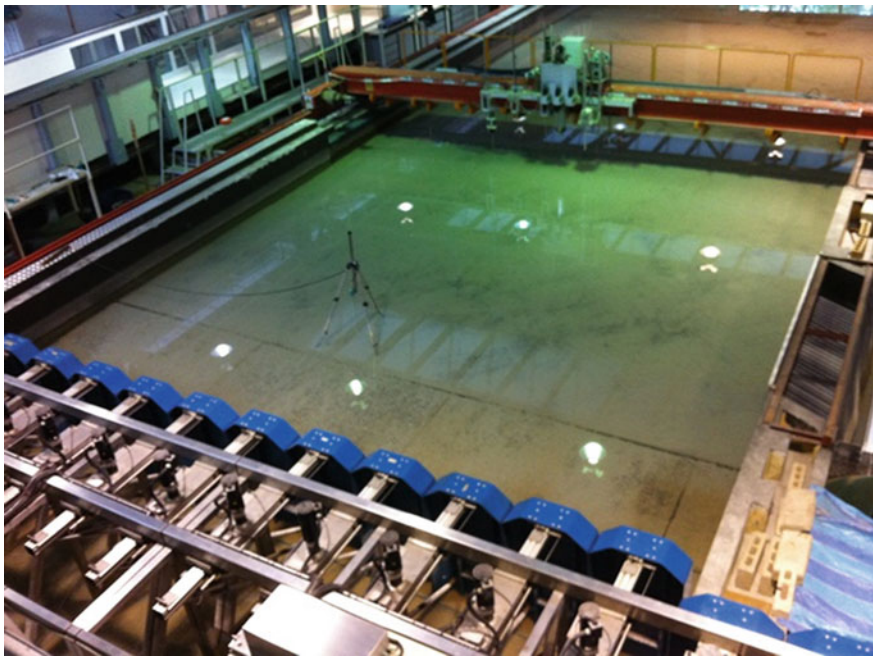


Fig. 24 Wave basin in Hydraulic lab, National University of Singapore

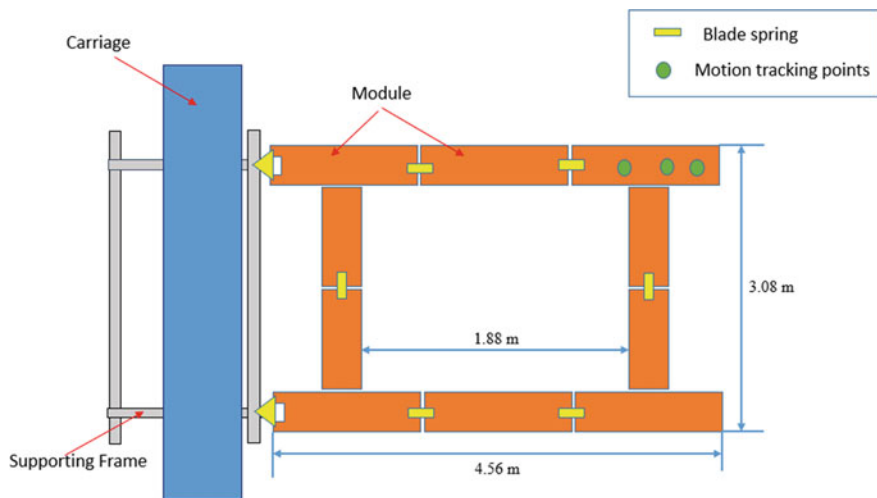


Fig. 25 Schematic drawing of layout of model test



Fig. 26 Physical model of tested sub-system of floating PV farm

Table 3 Environmental conditions simulated in the model tests

Conditions	Hs (m)	Tp (s)
Normal conditions	0.03	1.0
Extreme conditions	0.1	1.7

of the floating module is found to be around 160 kg. The maximum heave is around 0.06 m and the maximum pitch is around 3.5° in the extreme sea conditions. The motion of the system in the normal sea condition is almost negligible. Since the waves can be reflected by the outer modules, the response of the remaining modules which are in the centre area is expected to be small. Further work will be conducted to validate the numerical model so that the response of the tested system in a harsher sea state can be simulated.

5 Floating Wetlands

5.1 Project Information

Singapore is constantly making efforts to improve the water quality of ponds and reservoirs and provide a natural habitat for birds and fishes. Examples include the artificial floating wetlands already deployed at Punggol [9], as shown in Fig. 27.



Fig. 27 Floating wetland at Punggol



Fig. 28 Proposed floating wetlands at Pulau Ubin **a** site location and **b** view of Pekan Quarry. Photo credit: almostland.com

Floating wetlands not only enhance the eco-system but also bring people closer to nature for them to enjoy the scenic views. Besides Punggol, a project was launched to build several floating wetlands to enhance the site for wetland wildlife at Pulau Ubin, an island situated in the north east of Singapore. Figure 28 shows the location and image view of Pekan Quarry at Pulau Ubin where several clusters of floating wetlands are to be built. The floating wetlands are to be built through assembly of standardized modular floaters, which were used to build the floating wetlands at Punggol. The innovative modular floater has been patented² by HDB. These modules

²Floating Wetlands Module by Housing and Development Board—Singapore/patent no. PCT/2014013866, Malaysia/patent no. PCT/ PI 2015700120, People's Republic of China/patent no. PCT/ZL201380042813.0, Hong Kong/patent no. PCT/HK1207040.

are hexagonal in shape with male and female parts to facilitate easy inter-connection between modules. The modules are made of HDPE material and in-filled with PU foam so that they are unsinkable and buoyant. There are two different sizes of the standardized modules, one with a height of 250 mm and the other 410 mm. The planar shape and dimensions of the module are shown in Fig. 29. Details of the inter-connection of modules are shown in Fig. 30. Structures, mimicking trees with branches suitable for housing nests, are to be built using aluminum poles of various lengths on one of the floating wetlands for the purpose of attracting herons to nest, mate and build colonies in these artificial trees.

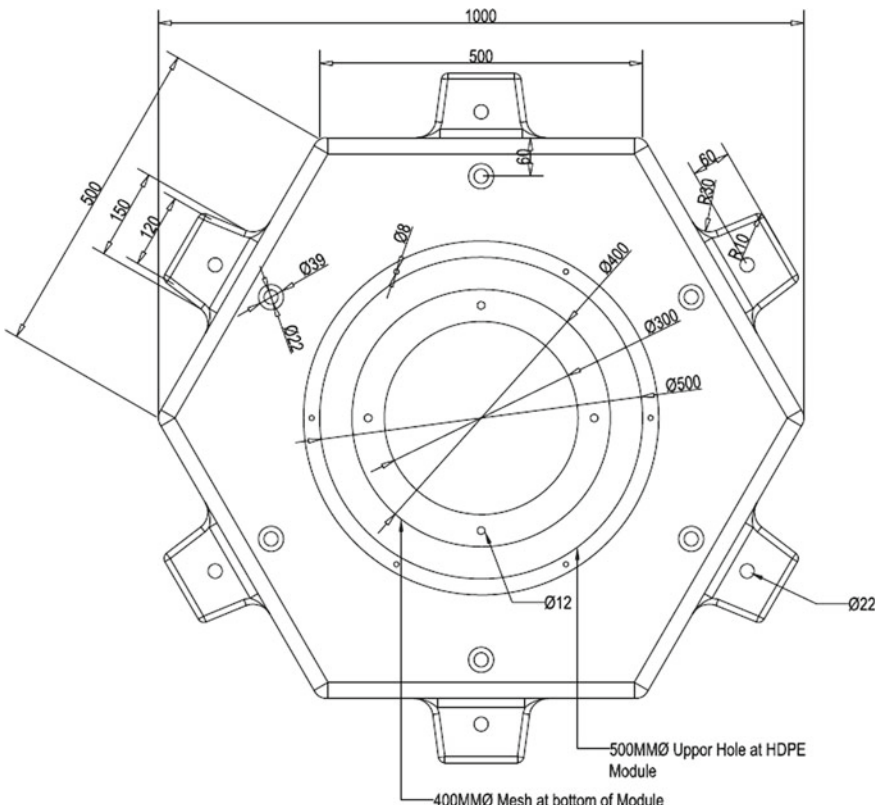


Fig. 29 Plan view of floater module



Fig. 30 Elevation view of connected modules

5.2 Analysis of Floating Wetlands

The proposed floating wetland system at Pekan Quarry, Pulau Ubin is to be designed for reservoir condition. For such a condition, the wave driven by wind is expected to be negligible. Hence, there is no need to consider the dynamic response of the floating wetlands. The main environmental actions are from the surface current and wind. As these environmental actions are mainly horizontal, these loads are to be resisted by the mooring system. So, the analysis of the floating wetlands is driven by the hydrostatic requirements. The balance between buoyancy and the vertical loads have been checked carefully. The vertical load includes the self-weight of the floating modules, the weight of plants and the weight of the nesting structures. The weight of plants is assumed evenly distributed on the floating wetlands. The weights of nesting structures are placed at their desired locations. It was found that under these vertical loads, the average draft of the floating wetlands is around 70 mm. Considering the depth of the floating module is 250 mm, it may be concluded that there exists enough reserve buoyancy.

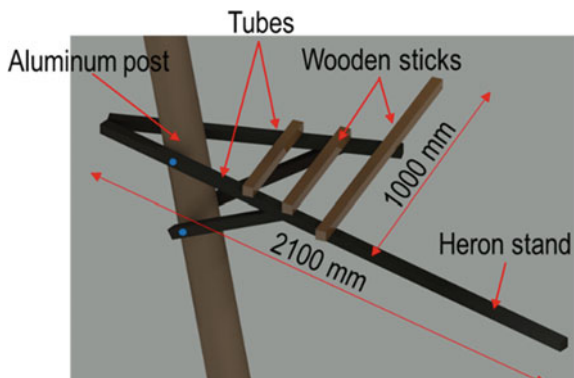
The static stability of the floating wetlands is also critical to the safety of the system. The metacentric height (GM) is a measurement of the initial static stability of a floating body. The value of GM for a single floating wetland is computed to be larger than 100 m. As this is much larger than 0.15 m, the minimum requirement on GM for a vessel from IMO [10], it can be concluded that the design of floating wetlands can fulfil the requirements on hydrostatics, both buoyancy and stability.

5.3 Analysis of Nesting Structures

Pekan Quarry at Pulau Ubin is a roosting habitat for the Grey Heron. They nest primarily in flooded timber zones/wetlands. When foraging, they are usually solitary, standing motionless in shallow water, stabbing at its prey with its long, sharp, dagger-like bill. When nesting, they are sociable birds, invariably nesting in trees and establishing heronries. To sensitively enhance the habitat for herons at Pekan Quarry, artificial nesting structures are to be designed and erected on the proposed floating wetlands. The design of the nesting structures must mimic nature as much as possible and be appealing to herons. Their living and nesting habits must be well addressed in the design concept.

Through a comprehensive literature review of the requirements for an artificial heron nesting and detailed consultancy with bird expert, an innovative design concept is proposed. Figure 31 shows the conceptual design of a nesting platform attached to a vertical post mounted onto the HDPE floaters. The main post is made of aluminium circular hollow section, powder coated brown to mimic a natural tree. The post is welded on and braced by metallic members, which are mounted onto the HDPE floaters through bolt connection to the metallic members. Several posts of various heights, the maximum of which is proposed to be 9 m, are to be built on the floating

Fig. 31 Conceptual design of nesting structure



wetland. Up to four nesting platforms are to be mounted onto these posts with the requirement that the lowest nesting platform is elevated 2.5 m from the floaters top surface to avoid potential attacks from lizard's or other wetland ground-based animals. Each two adjacent nesting platforms are to be spaced sufficiently apart with different orientations to avoid conflicts between families of herons, as illustrated in Fig. 32 which shows several posts and the layout of nesting platforms on the posts. The lowest two platforms are to be orientated in the opposite direction and the same applies to the top two nesting platforms. This special arrangement has the advantage of bending moment reduction along the aluminium post.



Fig. 32 Possible load patterns. Photo credit: Linda Tanner

Comprehensive structural analyses were carried out by accounting for various possible load patterns as shown in Fig. 32. Detailed finite element analyses and design checks were conducted as per EC9. Optimization of structural members were also carried out to achieve a reliable and cost-effective design.

6 Conclusions

This paper presents the recent research and development activities as well as completed and ongoing projects pertaining to the use of floating structures for both industrial and recreational applications in Singapore. In particular, the theoretical and experimental studies on floating hydrocarbon storage tanks and modular floating structures are presented. The project background, design considerations as well as structural and hydrodynamic analyses of floating solar farms and proposed floating wetlands are also discussed. Owing to the merits of floating structures, they serve as an approach for land creation from water bodies for various applications. The concepts and designs presented here may be applied in other parts of the world with appropriate modifications to cater for the local design requirements.

Acknowledgements This research is supported in part by the Singapore Ministry of National Development and the National Research Foundation, Prime Minister's Office under the Land and Liveability National Innovation Challenge (L2 NIC) Research Programme (L2 NIC Award No L2 NICTDF1-2015-2). Any opinions, findings, and conclusions or recommendations expressed in this material are those of the author(s) and do not reflect the views of the Singapore Ministry of National Development and National Research Foundation, Prime Minister's Office, Singapore. We thank the JTC and MND for their support.

The floating solar farm project at Tengeh reservoir is funded in part by the Housing and Development Board (HDB) and Economic Development Board (EDB), and M/S Million Lighting Co Pte Ltd. B. Part of the space in Tengeh Reservoir was allocated by Public Utilities Board (PUB) of Singapore for floating solar PV test bedding.

The floating solar farm project offshore Woodlands is funded in part by SUNSEAP and ISOTEAM.

The floating wetlands project at Pekan Quarry, Pulau Ubin, is funded in part by NParks, HOCKLIM Engineering and ISOTEAM.

References

1. Dai J, Ang KK, Jin J, Wang CM, Hellan Ø, Watn A (2019) Large floating structure with free-floating, self-stabilizing tanks for hydrocarbon storage. *Energies* 12:3487
2. Ang KK, Dai J, Hellan O, Watn A, Si MBI (2020) Design and potential applications of floating structures in Singapore. In: Wang C, Lim S, Tay Z (eds) WCFS2019. lecture notes in civil engineering, vol 41. Springer, Singapore
3. Dai J, Wang CM, Utsunomiya T, Duan W (2018) Review of recent research and developments on floating breakwaters. *Ocean Eng* 158:132–151

4. Zhang C, Wan L, Magee AR, Han M, Jin J, Ang KK, Hellan Ø (2019) Experimental and numerical study on the hydrodynamic loads on a single floating hydrocarbon storage tank and its dynamic responses. *Ocean Eng* 183:437–452
5. Zhang C, Magee AR, Fonseca N, Hellan Ø, Ang KK (2019) Hydrodynamic responses and loads of a model floating hydrocarbon storage tank system for concept validation and numerical verification. In: WCFS2019. Springer, Singapore, pp 155–171
6. Fonseca N, Zhang C, Rodrigues J, Ren N, Hellan Ø, Magee AR (2019) Hydrodynamic model tests with a large floating hydrocarbon storage facility. In: OMAE2019, Glasgow, UK
7. Ren N, Zhang C, Magee AR, Hellan Ø, Dai J, Ang KK (2019) Hydrodynamic analysis of a modular multi-purpose floating structure system with different outermost connector types. *Ocean Eng* 176:158–168
8. Dai J, Zhang C, Lim HV, Ang KK, Qian X, Wong JLH, Tan ST, Wang CL (2020) Design and construction of floating modular photovoltaic system for water reservoirs. *Energy* 191:116549
9. Wong LH, Tan HS, Wang CL, Lim H, Ho HC, Wang CM, Tay ZY, Gao RP (2013) Floating wetlands at Punggol. *IES J. Part A: Civ Struct Eng* 6(4):249–257
10. IMO (International Maritime Organization) (2009) International code on intact stability, 2008

Analytical Methods for Dynamic Interaction Between Strip Foundations and Poroelastic Soils



Teerapong Senjuntichai and Suraparb Keawsawasvong

1 Introduction

The study of dynamic interaction between foundations and soils has a rich history in geomechanics. Analytical methods based on linear elasticity have been employed by many researchers to investigate the dynamic response of foundations. When the length of a foundation is much greater than its width, the foundation is usually as a strip foundation, and the plane strain condition is adopted for the study of its dynamic responses. Dynamic interaction problems between a rigid strip and an isotropic elastic half-plane were analytically investigated in the past, e.g. the works by Karasudhi et al. [10], Oien [16] and Luco and Westmann [15]. The dynamic response of a group of flexible strip foundations under vertical loading resting on an isotropic elastic half-plane was studied by Wang et al. [22]. It is well known that natural soils and rocks exhibit some degrees of anisotropy, and a simplified model, called transversely isotropic, is widely adopted for the analysis of dynamic interaction between foundations and anisotropic soils. The dynamic interaction between a rigid strip and transversely isotropic elastic media was studied by Gazetas [8, 9]. In addition, Lin et al. [14] and Ai and Zhang [1] investigated the dynamic response of a rigid strip on a multi-layered transversely isotropic elastic half-plane.

Geo-materials are often two-phase materials with a solid skeleton and pores, which are saturated with water. Such materials are commonly known as poroelastic materials, and a salient feature of their responses is the generation and dissipation of pore pressure under applied loading. The theory of elastic wave propagations in an isotropic poroelastic material was established by Biot [4]. Subsequently, Kassir

T. Senjuntichai (✉) · S. Keawsawasvong

Applied Mechanics and Structures Research Unit, Department of Civil Engineering, Faculty of Engineering, Chulalongkorn University, Bangkok 10330, Thailand
e-mail: Teerapong.S@chula.ac.th

S. Keawsawasvong

Department of Civil Engineering, Thammasat School of Engineering, Thammasat University, Pathumthani 12120, Thailand

and Xu [11] and Bougacha et al. [6] employed Biot's poroelastodynamics theory to study the dynamic responses of a rigid strip on homogeneous poroelastic half-plane and poroelastic layer respectively. Senjuntichai and Rajapakse [19] presented dynamic interaction between a rigid strip and a multilayered poroelastic half-plane by employing an exact stiffness matrix method [18]. Vertical vibrations of multiple flexible strips resting on a multi-layered poroelastic half-plane was also investigated by Senjuntichai and Kaewjuea [20].

By incorporating his anisotropic material parameters [3, 5] presented the theory of elastic wave propagations in an anisotropic porous elastic material. Cheng [7] later reformulated Biot's parameters [3] with material parameters that are easily identifiable with laboratory measurement. The dynamic interaction between a rigid strip and a transversely isotropic poroelastic half-plane was recently studied by Keawsawasvong and Senjuntichai [12] who showed that the anisotropic properties have a significant influence on the dynamic response of the rigid strip. In addition, Keawsawasvong and Senjuntichai [13] presented the dynamic response of a system of rigid strips on a homogeneous transversely isotropic poroelastic layer.

This paper reviews the applications of Biot's theory of poroelasticity to study the dynamic interaction between a strip foundation and a poroelastic half-plane as shown in Fig. 1. Biot's equations of poroelastodynamics under a plane strain condition are briefly reviewed for both isotropic and transversely isotropic poroelastic materials. The analytical general solutions for poroelastic materials are then presented. An exact stiffness matrix scheme for the analysis of a multi-layered half-plane is also outlined. The dynamic interaction problem is analyzed by employing a semi-analytical discretization technique based on the influence functions corresponding to the surface displacements of a poroelastic half-plane. Selected numerical results are illustrated to investigate the influence of various parameters such as the degree of anisotropy and the frequency of excitation on the strip response.

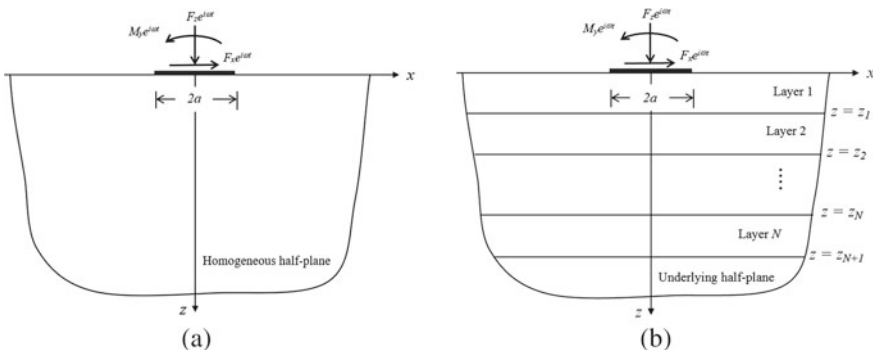


Fig. 1 A rigid strip foundation under time-harmonic loading bonded to: **a** a homogeneous poroelastic half-plane; **b** a multi-layered poroelastic half-plane

2 Basic Equations and General Solutions for Poroelastic Half-Plane

2.1 Isotropic Poroelastic Medium

Consider a homogeneous isotropic poroelastic half-space with a Cartesian coordinate system (x, y, z) defined such that the z -axis is perpendicular to the free surface of the half-space. It is assumed that the deformations of the half-space are plane strain in the xz -plane, i.e. $\varepsilon_{xy} = \varepsilon_{yy} = \varepsilon_{yz} = 0$. According to Biot's theory of poroelasticity [2], the constitutive relations for a homogeneous isotropic poroelastic half-plane can be expressed by using the standard indicial notation as,

$$\sigma_{ij} = 2\mu\varepsilon_{ij} + (\lambda\varepsilon_{kk} - \alpha p)\delta_{ij}, \quad i, j = x, z \quad (1a)$$

$$p = -(\alpha M\varepsilon_{kk} + Mw_{i,i}) \quad (1b)$$

In the above equations, σ_{xx} , σ_{zz} and σ_{xz} are the total stress components of the bulk material; ε_{xx} , ε_{zz} and ε_{xz} are the strain components of the solid matrix that are related to the displacement u_i ($i = x, z$) as in the theory of linear elasticity; μ and λ are Lame' constants of the bulk material; δ_{ij} is the Kronecker delta; p is the excess pore fluid pressure (suction is considered negative); and w_i ($i = x, z$) is the fluid displacement relative to the solid matrix in the i -direction. In addition, α and M are Biot's parameters accounting for compressibility of the two-phased material.

The equations of motions of the poroelastic half-plane, in the absence of body forces and a fluid source, are written in the terms of displacement u_i and w_i as [5],

$$\mu u_{i,jj} + (\lambda + \alpha^2 M + \mu)u_{j,ji} + \alpha M w_{j,ji} = \rho \ddot{u}_i + \rho_f \ddot{w}_i \quad (2a)$$

$$\alpha M u_{j,ji} + M w_{j,ji} = \rho_f \ddot{u}_i + m \ddot{w}_i + b \dot{w}_i \quad (2b)$$

where the superposed dot denotes the derivative with respect to time; ρ and ρ_f are the mass densities of the bulk material and the pore fluid respectively; m is a density-like parameter that depends on ρ_f and the geometry of the pores; and b is the parameter accounting for the internal friction due to the relative motion between the solid matrix and the pore fluid, and it is defined as the ratio between the viscosity of the pore fluid and the intrinsic permeability. If the internal friction is neglected, then $b \approx 0$. In addition, the motion under consideration is assumed to be time-harmonic of the form $e^{i\omega t}$, where ω is the frequency of the motion, and i is the imaginary number. The term $e^{i\omega t}$ is hereafter omitted.

The Fourier integral transform with respect to the x -coordinate and its inverse relationship can be expressed as [21],

$$\bar{f}(\xi, z) = \frac{1}{\sqrt{2\pi}} \int_{-\infty}^{\infty} f(x, z) e^{-ix\xi} dx \quad (3a)$$

$$f(x, z) = \frac{1}{\sqrt{2\pi}} \int_{-\infty}^{\infty} \bar{f}(\xi, z) e^{ix\xi} d\xi \quad (3b)$$

By using Helmholtz representation for a vector field together with applying the above Fourier integral transform to Eq. (2), the following general solutions can be expressed in the frequency-wave number domain by Senjuntichai and Rajapakse [18] as,

$$\bar{u}_x = i\xi(A_1 e^{\gamma_1 z} + B_1 e^{-\gamma_1 z} + A_2 e^{\gamma_2 z} + B_2 e^{-\gamma_2 z}) + \gamma_3(A_3 e^{\gamma_3 z} - B_3 e^{-\gamma_3 z}) \quad (4a)$$

$$\bar{u}_z = \gamma_1(A_1 e^{\gamma_1 z} - B_1 e^{-\gamma_1 z}) + \gamma_2(A_2 e^{\gamma_2 z} - B_2 e^{-\gamma_2 z}) - i\xi(A_3 e^{\gamma_3 z} + B_3 e^{-\gamma_3 z}) \quad (4b)$$

$$\bar{w}_z = \gamma_1 \chi_1(A_1 e^{\gamma_1 z} - B_1 e^{-\gamma_1 z}) + \gamma_2 \chi_2(A_2 e^{\gamma_2 z} - B_2 e^{-\gamma_2 z}) - i\xi \chi_3(A_3 e^{\gamma_3 z} + B_3 e^{-\gamma_3 z}) \quad (4c)$$

$$\bar{\sigma}_{xz} = 2i\xi \gamma_1(A_1 e^{\gamma_1 z} - B_1 e^{-\gamma_1 z}) + 2i\xi \gamma_2(A_2 e^{\gamma_2 z} - B_2 e^{-\gamma_2 z}) + b_3(A_3 e^{\gamma_3 z} + B_3 e^{-\gamma_3 z}) \quad (4d)$$

$$\bar{\sigma}_{zz} = c_1(A_1 e^{\gamma_1 z} + B_1 e^{-\gamma_1 z}) + c_2(A_2 e^{\gamma_2 z} + B_2 e^{-\gamma_2 z}) - 2i\xi \gamma_3(A_3 e^{\gamma_3 z} - B_3 e^{-\gamma_3 z}) \quad (4e)$$

$$\bar{p} = a_1(A_1 e^{\gamma_1 z} + B_1 e^{-\gamma_1 z}) + a_2(A_2 e^{\gamma_2 z} + B_2 e^{-\gamma_2 z}) \quad (4f)$$

in which A_1 – A_3 and B_1 – B_3 denote the arbitrary functions to be determined by employing appropriate boundary conditions. In addition, all parameters appeared in Eq. (4) are given elsewhere [18].

2.2 Transversely Isotropic Poroelastic Medium

For a homogeneous transversely isotropic poroelastic half-plane, the constitutive relations can be expressed according to Biot [3] and Cheng [7] as,

$$\sigma_{xx} = c_{11} \frac{\partial u_x}{\partial x} + c_{13} \frac{\partial u_z}{\partial z} - \alpha_h p \quad (5a)$$

$$\sigma_{yy} = c_{12} \frac{\partial u_x}{\partial x} + c_{13} \frac{\partial u_z}{\partial z} - \alpha_h p \quad (5b)$$

$$\sigma_{zz} = c_{13} \frac{\partial u_x}{\partial x} + c_{33} \frac{\partial u_z}{\partial z} - \alpha_v p \quad (5c)$$

$$\sigma_{xz} = c_{44} \left(\frac{\partial u_x}{\partial z} + \frac{\partial u_z}{\partial x} \right) \quad (5d)$$

$$p = -M \left(\alpha_h \frac{\partial u_x}{\partial x} + \alpha_v \frac{\partial u_z}{\partial z} + \frac{\partial w_x}{\partial x} + \frac{\partial w_z}{\partial z} \right) \quad (5e)$$

where c_{11} , c_{12} , c_{13} , c_{33} and c_{44} are elastic moduli of the bulk material. The equations of motions of the half-plane, in the absence of body forces and a fluid source, are given by,

$$c_{11} \frac{\partial^2 u_x}{\partial x^2} + c_{44} \frac{\partial^2 u_x}{\partial z^2} + (c_{13} + c_{44}) \frac{\partial^2 u_z}{\partial x \partial z} - \alpha_h \frac{\partial p}{\partial x} = \rho \frac{\partial^2 u_x}{\partial t^2} + \rho_f \frac{\partial^2 w_x}{\partial t^2} \quad (6a)$$

$$c_{44} \frac{\partial^2 u_z}{\partial x^2} + c_{33} \frac{\partial^2 u_z}{\partial z^2} + (c_{13} + c_{44}) \frac{\partial^2 u_x}{\partial x \partial z} - \alpha_v \frac{\partial p}{\partial z} = \rho \frac{\partial^2 u_z}{\partial t^2} + \rho_f \frac{\partial^2 w_z}{\partial t^2} \quad (6b)$$

$$-\frac{\partial p}{\partial x} = \rho_f \frac{\partial^2 u_x}{\partial t^2} + m_h \frac{\partial^2 w_x}{\partial t^2} + b_h \frac{\partial w_x}{\partial t} \quad (6c)$$

$$-\frac{\partial p}{\partial z} = \rho_f \frac{\partial^2 u_z}{\partial t^2} + m_v \frac{\partial^2 w_z}{\partial t^2} + b_v \frac{\partial w_z}{\partial t} \quad (6d)$$

In Eq. (6), the parameters h and v are used in the subscript of material parameters to define their properties either in the plane of isotropy ($i = h$) or in the perpendicular direction to the isotropic plane ($i = v$). It can be shown that [12] the following general solutions are given in the frequency-wave number domain as,

$$\bar{u}_x = \chi_j A_j e^{\lambda_j z} - \chi_j B_j e^{-\lambda_j z} \quad (7a)$$

$$\bar{u}_z = \psi_j A_j e^{\lambda_j z} + \psi_j B_j e^{-\lambda_j z} \quad (7b)$$

$$\bar{p} = \xi_j A_j e^{\lambda_j z} - \xi_j B_j e^{-\lambda_j z} \quad (7c)$$

$$\bar{w}_z = \varpi_j A_j e^{\lambda_j z} + \varpi_j B_j e^{-\lambda_j z} \quad (7d)$$

$$\bar{\sigma}_{xz} = \varphi_j A_j e^{\lambda_j z} + \varphi_j B_j e^{-\lambda_j z} \quad (7e)$$

$$\bar{\sigma}_{zz} = \eta_j A_j e^{\lambda_j z} - \eta_j B_j e^{-\lambda_j z} \quad (7f)$$

where A_1-A_3 and B_1-B_3 are once again the arbitrary, and all parameters appeared in Eq. (7) are given explicitly by Keawsawasvong and Senjuntichai [12].

3 Influence Functions

3.1 Homogeneous Poroelastic Half-Plane

The analysis of the dynamic interaction problems between a strip foundation and poroelastic soils as shown in Fig. 1 by using the proposed discretization technique requires the implementation of appropriate influence functions. Those influence functions are the fundamental solutions of boundary-value problems corresponding to uniform strip loading of unit intensity and a width ‘ l ’ applied on the surface of supporting poroelastic soils. Consider the case of a homogeneous isotropic poroelastic half-plane subjected to vertical and horizontal strip loads applied on its surface. The general solutions given by Eq. (4) are employed in the analysis of this boundary-value problem with $A_j \equiv 0$ to ensure the regularity of the solutions at infinity. The boundary conditions corresponding to a homogeneous isotropic poroelastic half-plane subjected to the two surface loads in the Fourier transform domain are given by,

$$\bar{\sigma}_{xz}(\xi, 0) = -\bar{f}_x(\xi) \quad (8a)$$

$$\bar{\sigma}_{zz}(\xi, 0) = -\bar{f}_z(\xi) \quad (8b)$$

$$\bar{p}(\xi, 0) = 0 \quad (8c)$$

and

$$\bar{f}_n(\xi) = \sqrt{\frac{2}{\pi}} \frac{\sin(\xi l)}{\xi}; \quad (n = z, x) \quad (8d)$$

where $\bar{f}_n(\xi)$ denotes the Fourier transforms of uniform strip loading of unit intensity and a width ‘ l ’ applied in the vertical ($n = z$) and horizontal ($n = x$) directions. It is convenient to solve the boundary value problem corresponding to the vertical and horizontal loads separately. Substitution of the solutions for the arbitrary functions B_1 , B_2 and B_3 corresponding to the two loading cases to Eq. (4) yields the required influence functions for the analysis of dynamic interaction problems as shown in Fig. 1a.

The above procedure is also applicable for the case of a homogeneous transversely isotropic poroelastic half-plane except that the general solutions given by Eq. (7) are employed in the derivation of the required influence functions.

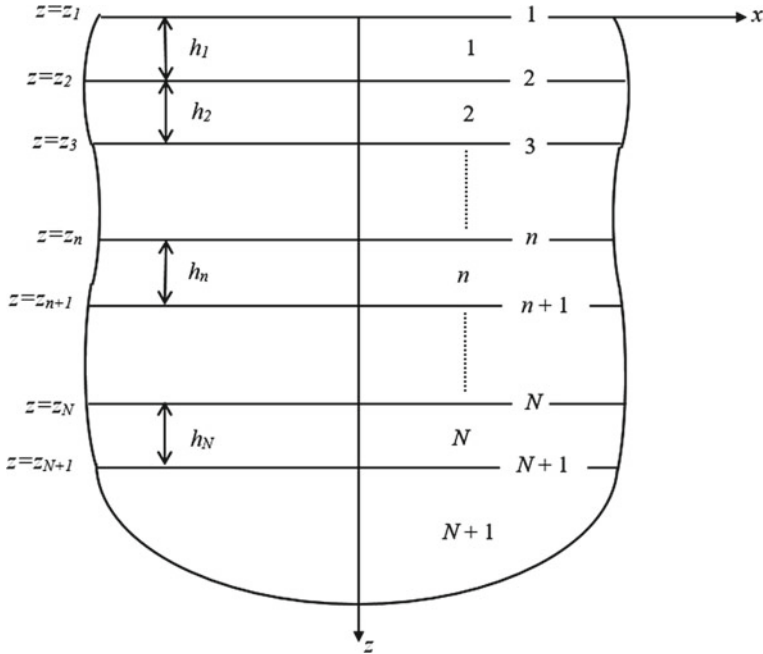


Fig. 2 Geometry of multi-layered half-plane under consideration

3.2 Multi-layered Poroelastic Half-Plane

Consider a multi-layered isotropic poroelastic medium consisting of N poroelastic layers overlying a homogeneous poroelastic half-plane. Layers and interfaces are numbered as shown in Fig. 2 where the superscript n denotes quantities associated with an n th layer ($n = 1, 2, \dots, N$). The general solutions given by Eq. (4) can be expressed in the following matrix form:

$$\mathbf{u}(\xi, z) = \mathbf{R}(\xi, z) \mathbf{C}(\xi) \text{ and } \mathbf{f}(\xi, z) = \mathbf{S}(\xi, z) \mathbf{C}(\xi) \quad (9a)$$

where

$$\mathbf{u}(\xi, z) = [\bar{u}_x \bar{u}_z \bar{p}]^T \text{ and } \mathbf{f}(\xi, z) = [\bar{\sigma}_{xz} \bar{\sigma}_{zz} \bar{w}_z]^T \quad (9b)$$

In Eq. (9), the superscript T denotes the transpose of a matrix and $\mathbf{C}(\xi) = [A_1 \ B_1 \ A_2 \ B_2 \ A_3 \ B_3]^T$.

For the n th layer, the following relationships can be established by using Eq. (9a):

$$\mathbf{U}^{(n)} = \begin{bmatrix} \mathbf{R}^{(n)}(\xi, z_n) \\ \dots \\ \mathbf{R}^{(n)}(\xi, z_{n+1}) \end{bmatrix} \mathbf{C}^{(n)} \quad (10a)$$

$$\mathbf{F}^{(n)} = \begin{bmatrix} -\mathbf{S}^{(n)}(\xi, z_n) \\ \dots \\ \mathbf{S}^{(n)}(\xi, z_{n+1}) \end{bmatrix} \mathbf{C}^{(n)} \quad (10b)$$

where

$$\mathbf{U}^{(n)} = [\mathbf{u}^{(n)}(\xi, z_n) \ \mathbf{u}^{(n)}(\xi, z_{n+1})]^T \text{ and } \mathbf{F}^{(n)} = [-\mathbf{f}^{(n)}(\xi, z_n) \ \mathbf{f}^{(n)}(\xi, z_{n+1})]^T \quad (11)$$

In Eq. (10), $\mathbf{U}^{(n)}$ denotes a column vector of generalized displacements for the n th layer whose elements are the Fourier transforms of displacements and pore pressure of the top and bottom surfaces of the n th layer, and $\mathbf{F}^{(n)}$ denotes a generalized force vector whose elements are the Fourier transforms of tractions and fluid displacements of the top and bottom surfaces of the n th layer. The matrices $\mathbf{R}^{(n)}$ and $\mathbf{S}^{(n)}$ in Eq. (10) can be obtained from Eq. (9a) by substituting the relevant material properties of the n th layer with $z = z_n$ or $z = z_{n+1}$. In addition, the vector $\mathbf{C}^{(n)}$ is the arbitrary coefficient vector corresponding to the n th layer.

In view of Eq. (10), the following relationship can be established for the n th layer

$$\mathbf{F}^{(n)} = \mathbf{K}^{(n)} \mathbf{U}^{(n)}; \quad n = 1, 2, \dots, N \quad (12)$$

where $\mathbf{K}^{(n)}$ is an exact stiffness matrix for the n th layer describing the relationship between the generalized displacement vector $\mathbf{U}^{(n)}$ and the generalized force vector $\mathbf{F}^{(n)}$. Similarly, the stiffness matrix for the underlying half-plane $\mathbf{K}^{(N+1)}$ can be obtained by establishing a relationship between the generalized displacement vector $\mathbf{U}^{(N+1)}$ and the force vector $\mathbf{F}^{(N+1)}$.

The global stiffness matrix of a multi-layered half-plane is assembled by using the layer and half-plane stiffness matrices together with the continuity condition of traction and fluid flow at the layer interfaces. The final equation system can be written as,

$$\mathbf{K}^* \mathbf{U}^* = \mathbf{F}^* \quad (13)$$

where \mathbf{K}^* is the global stiffness matrix and \mathbf{U}^* is the global vector of generalized displacements. In addition, \mathbf{F}^* is the global force vector. To obtain the required influence functions for the dynamic interaction problems shown in Fig. 1, \mathbf{F}^* is given by,

$$\mathbf{F}^* = [-i\bar{f}_x(\xi) \ -\bar{f}_z(\xi) \ 0 \ 0 \ \dots \ 0]^T \quad (14)$$

and $\bar{f}_n(\xi)$ ($n = x, z$) is defined in Eq. (8d).

4 Formulation of Interaction Problem

Consider a strip foundation, with a width of $2a$, subjected to time-harmonic vertical, horizontal and moment loads, as shown in Fig. 1. The strip is assumed to be rigid, massless, and undergoing time-harmonic translational and rotational displacements. In addition, it is assumed to be perfectly bonded to the underlying poroelastic half-plane with fully permeable contact surface. The horizontal and vertical displacements of an arbitrary point on the contact surface under the strip are given by,

$$u_x(x, 0) = \Delta_x, \quad -a \leq x \leq a \quad (15a)$$

$$u_z(x, 0) = \Delta_z + x\phi, \quad -a \leq x \leq a \quad (15b)$$

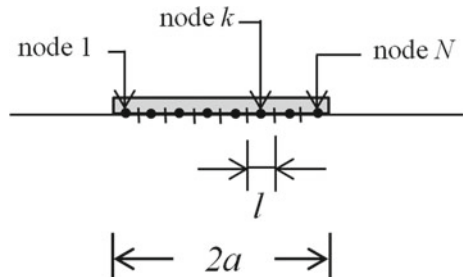
where Δ_j ($j = x, z$) represents the displacement amplitude in the j -direction at the center of the strip; and ϕ denotes the amplitude of the rotation about the y -axis of the strip. Let define the unknown traction in the j -direction generated at the contact surface between the rigid strip and the underlying half-plane as T_j ($j = x, z$). To determine the unknowns T_x and T_z , the contact surface under the strip is discretized into N equally spaced nodes with the tributary length of $l = 2a/N$ as shown in Fig. 3. It is assumed that T_x and T_z are uniformly distributed over each discretized element. The displacements at the node k , with the coordinate $(x_k, 0)$ on the contact surface under the strip footing, can be expressed as,

$$u_x(x_k, 0) = \sum_{l=1}^N U_{xx}(x_k; x_l) T_{xl}(x_l) + \sum_{l=1}^N U_{xz}(x_k; x_l) T_{zl}(x_l) \quad (16a)$$

$$u_z(x_k, 0) = \sum_{l=1}^N U_{zx}(x_k; x_l) T_{xl}(x_l) + \sum_{l=1}^N U_{zz}(x_k; x_l) T_{zl}(x_l) \quad (16b)$$

where $U_{mn}(x_k; x_l)$ denotes the influence function, which is the horizontal ($m = x$)

Fig. 3 Discretization of the contact surface under rigid strip



or vertical ($m = z$) displacement at the nodal location ($x_k; 0$) at the contact surface due to a uniform horizontal ($n = x$) or vertical ($n = z$) strip load of unit intensity applied at the nodal location ($x_l; 0$) at the contact surface. In addition, T_{xl} and T_{zl} ($l = 1, 2, \dots, N$) denote the shear and normal contact traction at the node l of the strip, which are assumed to be uniformly distributed over the tributary length of the node. Note that the influence function $U_{mn}(x_k; x_l)$ is obtained from Sects. 3.1 and 3.2 for homogeneous and multi-layered half-planes respectively.

The equilibrium equations of applied forces on the rigid strip can then be expressed as,

$$F_x = - \sum_{l=1}^N T_{xl} t \quad (17a)$$

$$F_z = - \sum_{l=1}^N T_{zl} t \quad (17b)$$

$$M_y = - \sum_{l=1}^N T_{zl} t (-x_l) \quad (17c)$$

Finally, the relationship between the applied forces and the displacement amplitudes of the rigid strip, can be expressed in the following matrix form:

$$\begin{Bmatrix} F_z \\ F_x \\ M \end{Bmatrix} = \begin{bmatrix} K_V & 0 & 0 \\ 0 & K_H & K_C \\ 0 & K_C & K_M \end{bmatrix} \begin{Bmatrix} \Delta_z \\ \Delta_x \\ x\phi \end{Bmatrix} \quad (18)$$

where K_V , K_H , K_M and K_C represent vertical, horizontal, rocking, and coupling impedances of the strip respectively.

5 Numerical Results

An accurate numerical quadrature scheme [17] is employed to determine the required influence functions appearing in the terms of infinite integrals given by Eq. (5b). This scheme subdivides the interval of the integrand and employs a 21-point Gauss–Kronrod rule to evaluate the integral over each interval. In the numerical study, the following material parameters are employed: E_h and E_v are drained Young's modulus in the plane of isotropy (xy -plane) and in the plane normal to the plane of isotropy (vertical direction) respectively; G is the shear modulus; ν_h is the drained Poisson's ratio characterizing the transverse strain reduction in the plane of isotropy due to a tensile stress in the same plane; ν_{vh} is the drained Poisson's ratio corresponding to the transverse strain reduction in the plane of isotropy due to a tensile stress normal

to it. The relationship between these parameters and the elastic moduli, c_{11} , c_{22} , c_{33} and c_{44} was given by Cheng [7]. In addition, a non-dimensional frequency, defined as $\delta = \omega a \sqrt{\rho^{(1)}/G^{(1)}}$, is used in all numerical results presented in this paper; and other normalized material parameters are defined as: $E_i^* = E_i/G^{(1)}$; $M^* = M/G^{(1)}$; $\rho_f^* = \rho_f/\rho^{(1)}$; $m_i^* = m_i/\rho^{(1)}$ and $b_i^* = b_i a / \sqrt{\rho^{(1)} G^{(1)}}$, where $i = h$ and v and $G^{(1)}$ and $\rho^{(1)}$ are the material properties of the first layer. In addition, non-dimensional dynamic compliances of a rigid strip foundation are defined as:

$$K_V^* = \pi F_z / G^{(1)} a \Delta_z \quad (19a)$$

$$K_M^* = \pi M_y / G^{(1)} a^3 \phi \quad (19b)$$

$$K_H^* = \pi F_x / G^{(1)} a \Delta_x \quad (19c)$$

$$K_C^* = \pi M_y / G^{(1)} a^2 \Delta_z \quad (19d)$$

Figure 4a shows the comparison of non-dimensional vertical compliance ($C_V^* = 1/K_V^*$) for a rigid strip bonded to an isotropic elastic half-plane with the Poisson's ratio of 0.25 between the present solution and the existing solutions given by Luco and Westmann [15]. Figure 4b shows the comparison between the present solution and the solutions by Ai and Zhang [1] for C_V^* of a rigid strip on a multi-layered transversely isotropic elastic half-plane, consisting of the first and second layers, with the thicknesses of $4a$ and $3a$ respectively, overlying a homogeneous half-plane. The normalized parameters are $E_h^* = 8$ and $E_v^* = 4$ for the first layer;

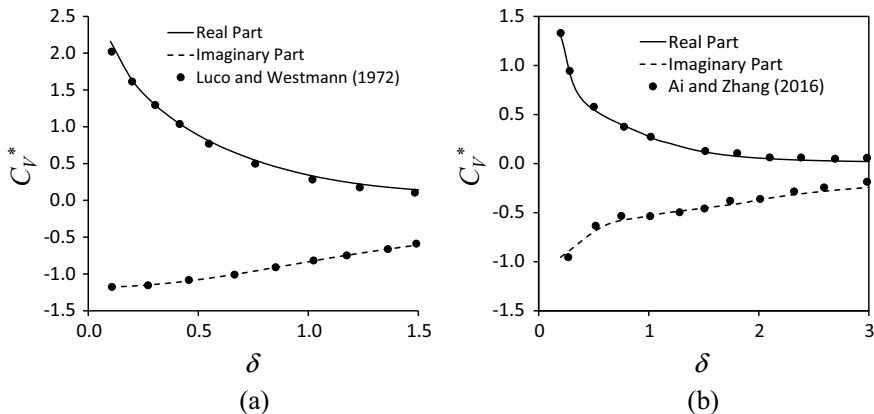


Fig. 4 Comparison of vertical compliances of a rigid strip on: **a** an isotropic elastic half-plane; **b** a multi-layered transversely isotropic elastic half-plane

$E_h^* = 6$ and $E_V^* = 3$ for the second layer; $E_h^* = 4$ and $E_V^* = 2$ for the half-plane. In addition, ν_h and ν_{vh} are equal to 0.25 and G^* is equal to 1 for all layers, whereas other poroelastic parameters are set to be negligibly small. It is evident from Fig. 4 that the present solutions with $N = 32$ are in very good agreement with both existing solutions.

The dynamic impedances of a rigid strip footings bonded to a homogeneous transversely isotropic poroelastic half-plane are first studied. The material properties are given as follows: $E_h^* = 3$, $\nu_h = \nu_v = 0.3$, $\alpha_h = \alpha_v = 0.95$, $\rho_f^* = 0.5$, $m_h^* = m_v^* = 1$, $M^* = 12.5$, and $b_h^* = b_v^* = 2$. Note that the ratio $n = E_v^*/E_h^*$ is varied to portray the influence of Young's moduli on dynamic impedances of the footing, and the case $n = 1$ then corresponds to a homogeneous isotropic poroelastic half-plane. Non-dimensional dynamic impedances of rigid strip footing resting on a transversely isotropic poroelastic half-plane are presented in Fig. 5a–d for vertical, rocking, horizontal and couple impedances respectively for different values of n over the frequency range $0.2 \leq \delta \leq 3$. Numerical results presented in Fig. 5a–d indicate that all impedances vary smoothly with the frequency for both real and imaginary parts. It is evident that both real and imaginary parts of the vertical, rocking and coupling impedances depend significantly on the parameter n . A larger value of n results in the half-plane being less stiff under vertical and moment loading as shown in Fig. 5a, b. On the other hand, a lower value of n yields an increase of coupling impedances as shown in Fig. 5d. In addition, numerical results presented in Fig. 5c indicate that the influence of the parameter n on the horizontal compliances is almost negligible due to the fact that variation of the parameter n represents the variation of anisotropic properties in the vertical direction ($n = E_v^*/E_h^*$).

Next, the dynamic impedances of a multi-layered transversely isotropic poroelastic half-plane, consisting of two layers with a thickness a overlying a homogeneous half-plane, are presented in Fig. 6 over the range of $\delta = 0\text{--}3$. The properties of the multi-layered half-plane are given in Table 1. Another system considered in Fig. 6 is a multi-layered isotropic poroelastic half-plane, with the properties identical to those given in Table 1 except that the properties in the direction normal to the isotropic plane ($i = v$) are set to be equal to those in the plane of isotropy ($i = h$), in the two layers and the underlying half-plane. It is evident from Fig. 6 that non-dimensional impedances corresponding to a multi-layered half-plane display more oscillatory variations with frequency when compared to the case of homogeneous half-plane shown in Fig. 5. Once again, non-dimensional vertical, rocking and coupling impedances show a significantly dependence on the anisotropic effects, whereas for the horizontal impedance, the influence of anisotropy is virtually negligible. Thus, the variations of the parameter E_h^* should be considered to investigate the influence of anisotropic properties on horizontal vibrations of rigid strip.

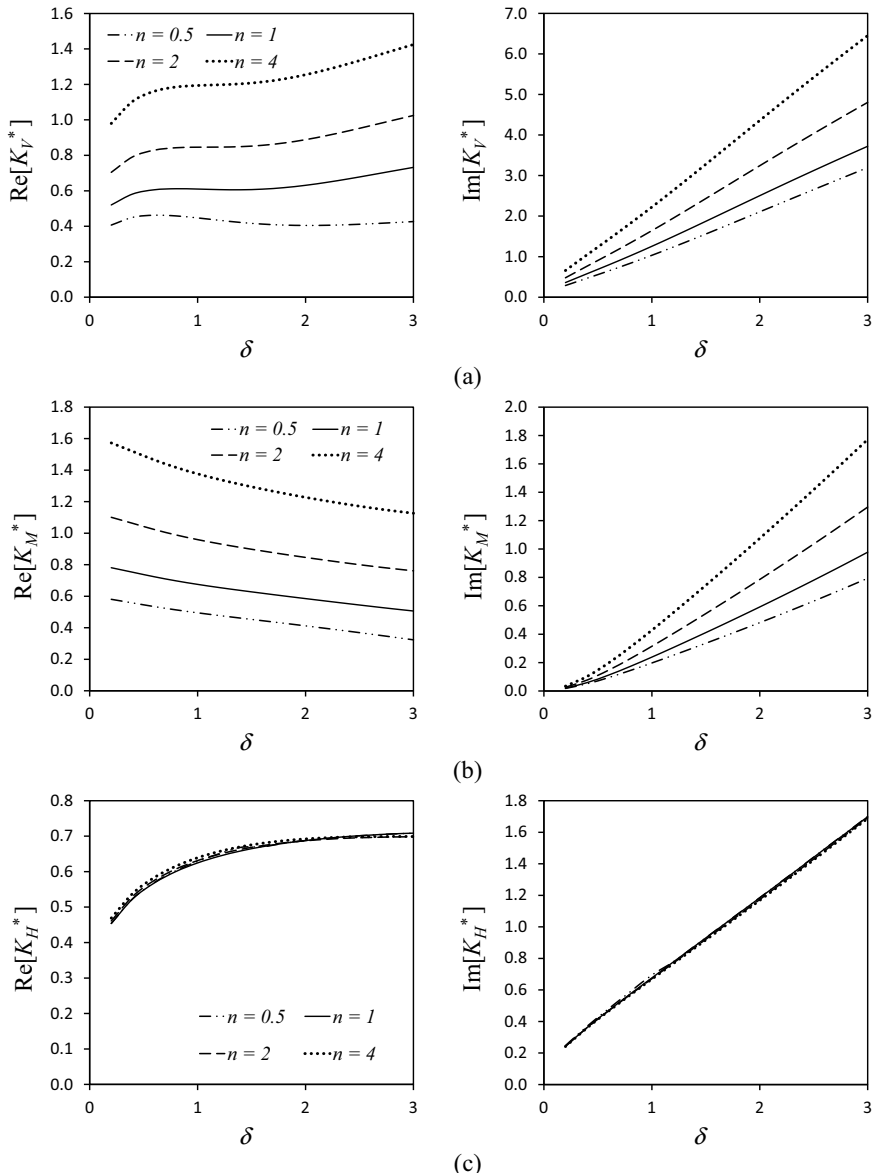


Fig. 5 Non-dimensional dynamic impedances of a rigid strip on a homogeneous transversely isotropic poroelastic half-plane: **a** vertical; **b** rocking; **c** horizontal; and **d** coupling

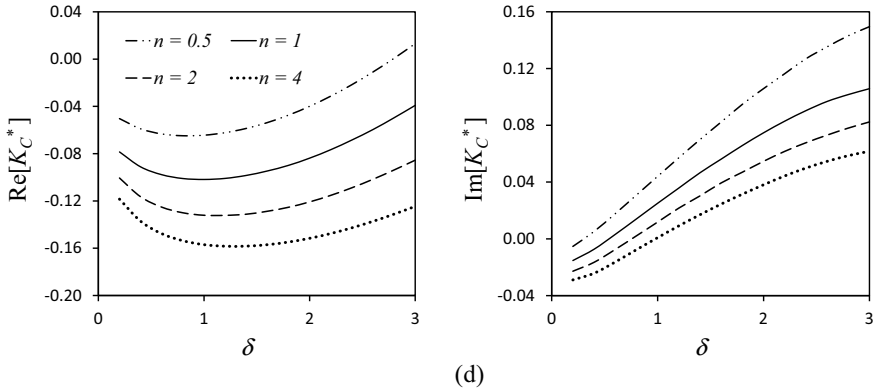


Fig. 5 (continued)

6 Conclusions

In this paper, Biot's theory of poroelastodynamics is reviewed for application in the analysis of dynamic interaction between strip foundations and poroelastic soils. Vertical, horizontal, rocking, and coupling impedances of a rigid strip on homogeneous and multi-layered poroelastic half-planes are obtained, for both isotropic and transversely isotropic materials, by employing a discretization technique with the use of displacement influence functions. Numerical results show that non-dimensional impedances vary significantly with the frequency of excitation and the degree of anisotropy. In addition, the variations of impedances with frequency is smooth for a homogeneous half-plane but shows oscillatory behaviour for a layered medium. The present solution scheme can be extended to investigate other soil-structure interaction problems involving anisotropic saturated soils such as embedded footings, impermeable footings, and a system of multiple footings.

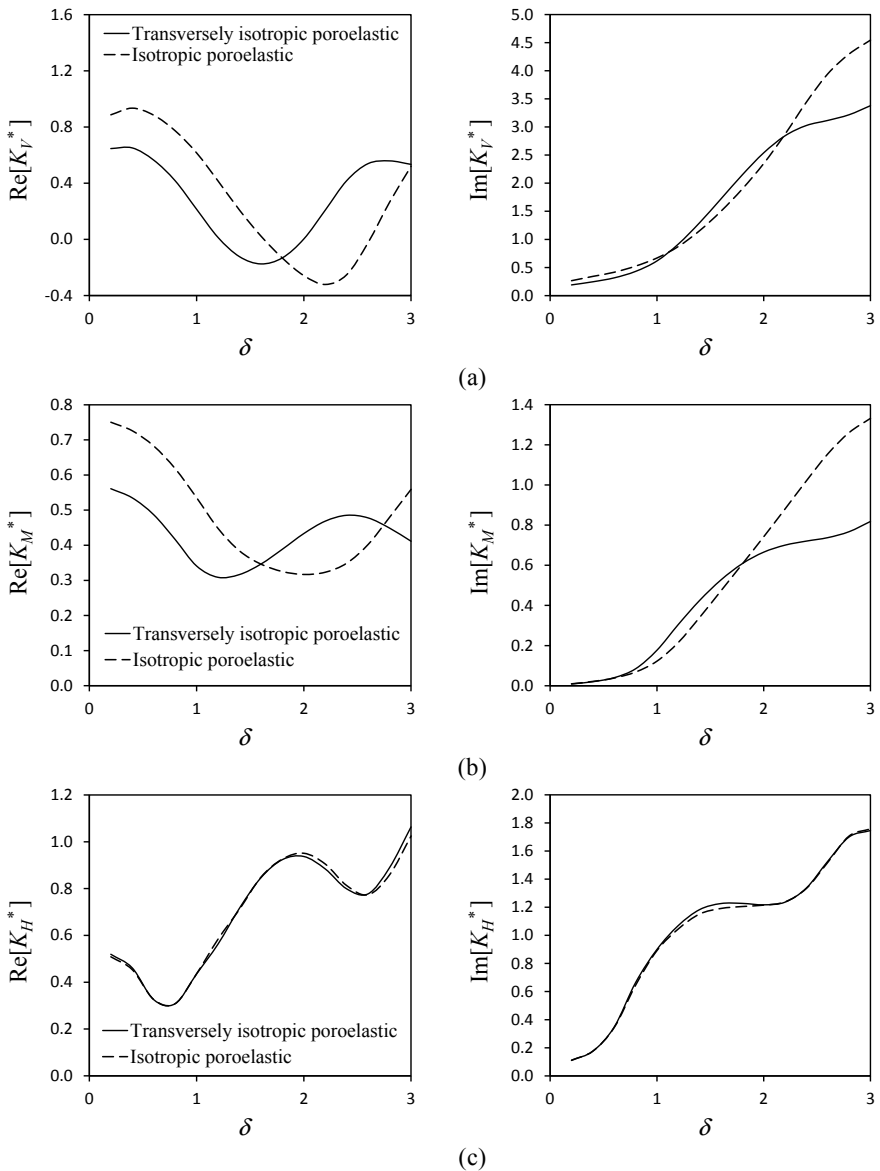
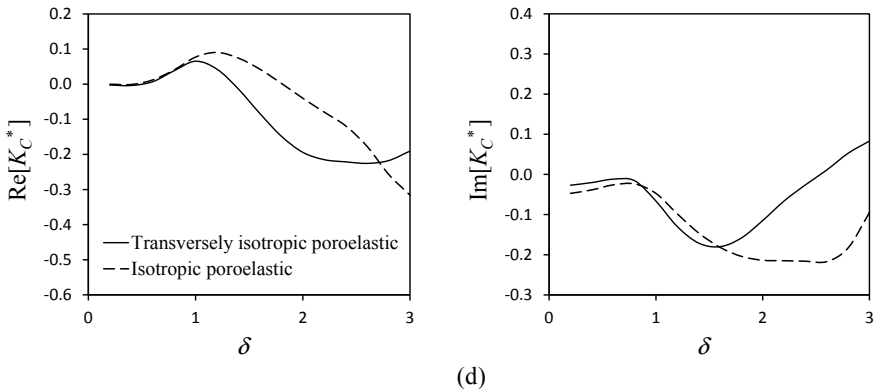


Fig. 6 Non-dimensional dynamic impedances of a rigid strip bonded to a multi-layered poroelastic half-plane: **a** vertical; **b** rocking; **c** horizontal and **d** coupling

**Fig. 6** (continued)**Table 1** Material properties of multi-layered transversely isotropic half-plane considered in Fig. 6

	E_h^*	E_v^*	v_h^*	v_{vh}^*	G^*	α_h^*	α_v^*
First layer	3	1.5	0.3	0.3	1	0.95	0.5
Second layer	2.5	1.25	0.3	0.3	0.5	0.98	0.98
Half-plane	10	5	0.25	0.25	4	0.9	0.9
	ρ^*	ρ_f^*	m_h^*	m_v^*	b_h^*	b_v^*	M^*
First layer	1	0.5	1	1	2	3	12.5
Second layer	0.8	0.5	0.9	0.9	1.5	1.5	7.5
Half-plane	1.2	0.5	2.4	2.4	6	6	8

References

1. Ai ZY, Zhang YF (2016) Vertical vibration of a rigid strip footing on a transversely isotropic multilayered half-plane. *Appl Math Model* 40:23–24
2. Biot MA (1941) General theory of three-dimensional consolidation. *J Appl Phys* 12:155–164
3. Biot MA (1955) Theory of elasticity and consolidation for a porous anisotropic solid. *J Appl Phys* 26:182–185
4. Biot MA (1956) Theory of propagation of elastic waves in a fluid-saturated porous solid. I. Low-frequency range. *J Acoust Soc Am* 28:168–178
5. Biot MA (1962) Mechanics of deformation and acoustic propagation in porous media. *J Appl Phys* 33:1482–1498
6. Bougacha S, Roesset JM, Tassoulas JL (1993) Dynamic stiffness of foundations on fluid-filled poroelastic stratum. *J Eng Mech* 119(8):1649–1662
7. Cheng AHD (1997) Material coefficients of anisotropic poroelasticity. *Int J Rock Mech Min* 34(2):199–205
8. Gazetas G (1981) Dynamic compliance matrix of rigid strip footing bonded to a viscoelastic cross anisotropic halfspace. *Int J Mech Sci* 23(9):547–559
9. Gazetas G (1981) Strip foundations on a cross-anisotropic soil layer subjected to dynamic loading. *Geotechnique* 31(2):161–179
10. Karasudhi P, Keep LM, Lee SL (1968) Vibratory motion of a body on an elastic half plane. *J Appl Mech* 35:697–705

11. Kassir MK, Xu J (1988) Interaction functions of a rigid strip bonded to saturated elastic half-space. *Int J Solid Struct* 24:915–936
12. Keawsawasvong S, Senjuntichai T (2019) Poroelastodynamic fundamental solutions of transversely isotropic half-plane. *Comput Geotech* 106:52–67
13. Keawsawasvong S, Senjuntichai T (2019) Dynamic interaction between multiple rigid strips and transversely isotropic poroelastic layer. *Comput Geotech* 114:103144
14. Lin G, Han Z, Zhong H, Li J (2013) A precise integration approach for dynamic impedance of rigid strip footing on arbitrary anisotropic layered half-space. *Soil Dyn Earthq Eng* 49:96–108
15. Luco JE, Westmann RA (1972) Dynamic response of rigid footing bonded to an elastic half space. *J Appl Mech* 39:527–534
16. Oien MA (1971) Steady motion of a rigid strip bonded to an elastic half space. *J Appl Mech* 38(2):328–334
17. Piessens R, Doncker-Kapenga E, Uberhuber CW, Kahaner DK (1983) QUADPACK, A subroutine package for automatic integration. Springer, Berlin
18. Rajapakse RKND, Senjuntichai T (1995) Dynamic response of a multi-layered poroelastic medium. *Earthq Eng Struct Dyn* 24:703–722
19. Senjuntichai T, Rajapakse RKND (1996) Dynamics of a rigid strip bonded to a multilayered poroelastic half-plane. In: Selvadurai APS (ed) Mechanics of poroelastic media. Kluwer Dordrecht, Netherlands
20. Senjuntichai T, Kaewjuea W (2008) Dynamic response of multiple flexible strips on a multilayered poroelastic half-plane. *J Mech Mater Struct* 3(10):1885–1901
21. Sneddon IN (1951) Fourier transform. McGraw-Hill, New York
22. Wang Y, Rajapakse RKND, Shah AH (1991) Dynamic interaction between flexible strip foundations. *Earthq Eng Struct Dyn* 20(5):441–454

Floating Offshore Wind Turbines in Goto Islands, Nagasaki, Japan



Tomoaki Utsunomiya, Iku Sato, and Takashi Shiraishi

1 Introduction

In order to mitigate greenhouse gas emission, it is necessary to increase renewable energy production. In Japan, the production of renewable energy is still very limited. However, offshore wind energy resources in the Japanese EEZ (Exclusive Economic Zone) are now considered to be huge. In particular, the offshore wind energy resource in deeper waters (where the water depth is greater than 50 m) is remarkable. For developing deep water wind energy, the use of floating-type foundations is considered to be more economical than the use of bottom-fixed foundations [2]. However, there existed only one multi-megawatt floating wind turbine in 2010; that was the Norway's Hywind, built and installed in September 2009 [1]. The second multi-megawatt floating wind turbine, WindFloat—a semisubmersible-type floating wind turbine, was installed in Portugal in October 2011 [6]. Since then, Japan's Ministry of the Environment kicked-off a demonstration project on floating offshore wind turbine (FOWT). The project took six years; beginning from September 2010 to March 2016. In this project, two floating offshore wind turbines have been installed and tested. Some details are given in Utsunomiya et al. [12, 15], Utsunomiya [13]. This paper summarizes the demonstration project and states current situations.

T. Utsunomiya (✉)

Department of Marine Systems Engineering, Kyushu University, Fukuoka, Japan
e-mail: utsunomiya@nams.kyushu-u.ac.jp

I. Sato

Energy Division, Toda Corporation, Tokyo, Japan

T. Shiraishi

Power Production Management Division, Power Business Unit, Hitachi Ltd., Hitachi, Japan

2 Outline of the Demonstration Project

The ultimate objective of the demonstration project is to reduce the greenhouse gas emission through commercialization of FOWT in the Japanese EEZ. Towards the commercialization of FOWT, a mandatory and important step is to demonstrate its technical feasibility. In particular, a demonstration of installation and operation of a multi-megawatt floating offshore wind turbine at sea is the primary objective of the project. Although the installation/operation of a multi-megawatt FOWT is the main target of the demonstration project, a step-by-step approach is generally preferred, in order to reduce possible risks. Also, social acceptance may be gained by such a step-by-step approach. Thus, the half-scale model, of which its length scale is almost half of the full-scale model, was planned to be installed before the installation of the full-scale model.

Figure 1 shows the location of the at-sea demonstration site. The site is about 1 km offshore of Kabashima Island, Goto city, Nagasaki prefecture, Japan. The mean water depth is 97.2 m (at mean sea level; MSL). The site is surrounded by the island on the north-western side, but it is open in the south-eastern side. The marine cable has been installed for the grid-connection. The distance to the shore from the FOWT along the marine cable is about 1.8 km.

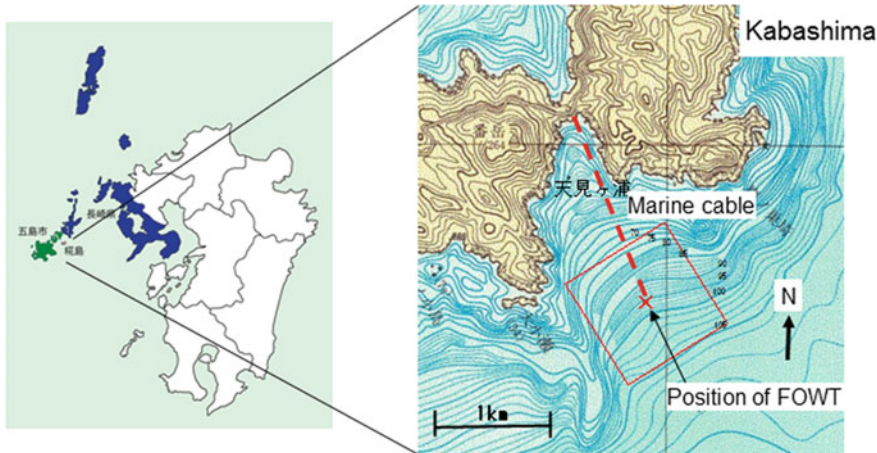


Fig. 1 Demonstration site: Kabashima, Goto city, Nagasaki prefecture

3 Half-Scale Model

3.1 Description

Figure 2 shows the outline and main dimensions of the half-scale model. Figure 3 shows the general view with an access boat used for maintenance. The floating foundation has a slender cylindrical shape (spar), with a draft of 37.05 m, an outer diameter of 3.8 m at the bottom and an outer diameter of 2.375 m at the sea level. The bottom half of the floating foundation is made of precast PC (pre-stressed concrete) segments whereas the upper half is made of ring-stiffened steel. In order to mitigate the yaw motion, four straight fins are attached along the PC part. Conventional catenary chain system is used as the mooring system. Three stud-link chains (JIS Grade 3) with a nominal diameter of 56 mm are used. For the anchors, two concrete sinkers (each weight in air is 200 tf) and one Danforth-type anchor (weight in air is 10 tf) were selected after considering the sea-bed condition.

The wind turbine (SUBARU 22/100) has a rated output of 100 kW. However, during the demonstration test, the maximum power was limited to 40 kW so as to increase the possibility of occurrence of wind speed above rated wind speed, where pitch control of blades is made. The wind turbine was modified to a down-wind type from the original up-wind type design. The down-wind type turbine is considered

Fig. 2 Dimensions of half-scale model (in m)

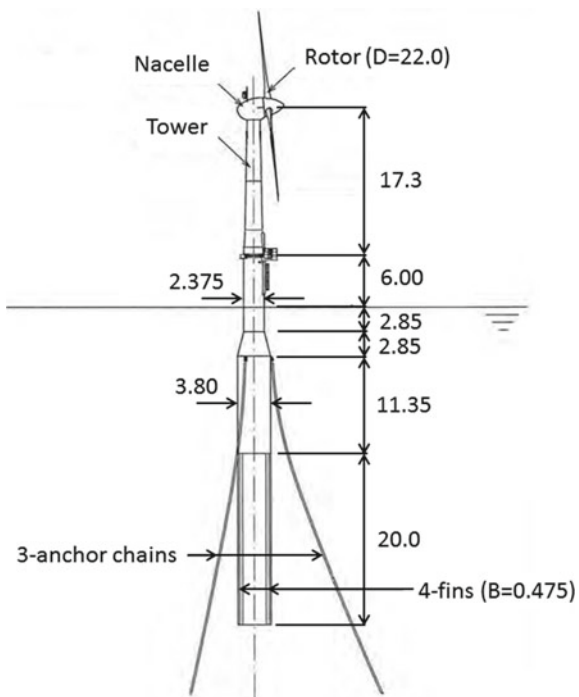


Fig. 3 General view of the half-scale model with an access boat



to have advantages such as weather-vane effect in yaw direction and the rotor axis being horizontal when the tower is tilted due to wind action.

The structural design of the floating wind turbine was made by relying on the time-domain numerical simulations. Some details of the numerical simulations and the experiments used for validation are presented in Utsunomiya et al. [10] and Kokubun et al. [4].

3.2 Response During Typhoon Attack

During the demonstrative experiment of the half-scale model, the FOWT was attacked by two separate severe typhoons, that is, by Bolaven (international designation: 1215) and Sanba (international designation: 1216). Sanba (1216) was a record-making typhoon event. It was closest to the at-sea experiment site at around 5:00 am on 17 September 2012. At that time, the central atmospheric pressure of the typhoon was 940 hPa. During the typhoon, several data were obtained, that include the wind speed, wave height, motion of the floating body, strains of the tower and the floating body, tension of a mooring line. The details of the measurement can be found in Ishida et al. [3]. In the following, some details during the typhoon attack are presented (for details, see [8]).

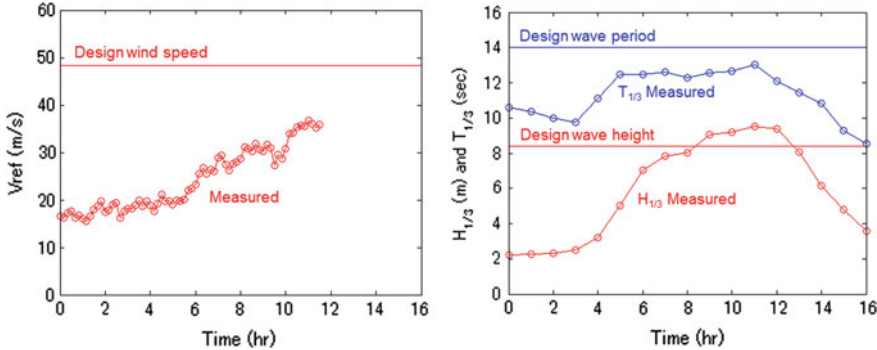


Fig. 4 (left) 10 min average wind speed measured on top of nacelle. Time 0 h corresponds to data for 18:00–18:10 on 16 September, and 11 h to 05:00–05:10 on 17 September. (right) Significant wave height and significant wave period. Time 0 h corresponds to data for 18:00–19:00 on 16 September, and 11 h to 05:00–06:00 on 17 September

Figure 4 (left) shows the 10 min average wind speed measured at the top of the nacelle by the cup-type anemometer. The maximum 10 min average wind speed was 36.8 m/s taken during 05:00–05:10 am on 17 September 2012. The design wind speed corresponding to the return period of 50 years as the 10 min average wind speed for the FOWT is 48.3 m/s at the hub-height (23.3 m above sea level). Thus, the maximum wind speed during the typhoon event was 24% lower than the design wind speed. Figure 4 (right) shows the significant wave height and the significant wave period measured by the wave measuring buoy. The maximum significant wave height was 9.5 m taken during 05:00–06:00 am on 17 September 2012, and the maximum significant wave period was 13.0 s taken also at the same time. The maximum significant wave height of 9.5 m exceeded the design wave height of 8.4 m (for 1 h reference period), but the maximum significant wave period was below the design value of 14.0 s.

In order to validate the numerical simulation method, the dynamic responses have been re-produced by using the measured wind and wave time series data. Figure 5 shows the minimum and maximum values of the platform motion in pitch. The reference point of the motion is at 6 m above the sea level (at the tower base). Basically, good agreement can be seen between the experimental (Exp) and simulation results (Cases 1–3). It should be emphasized that although the significant wave height of 9.5 m exceeded the design wave height of 8.4 m that corresponds to the return periods of 50 years, the FOWT experienced no damage by the typhoon attack.

3.3 Response During Power Production

The dynamic response of the FOWT at power generation is presented below. Nielsen et al. [5] reported that for a spar-type FOWT, a conventional wind turbine control

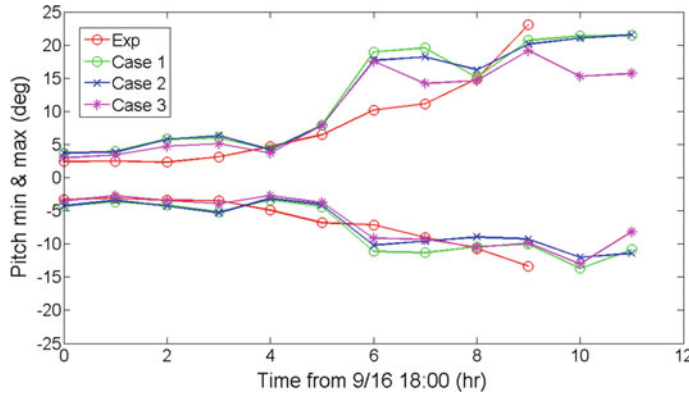


Fig. 5 Minimum and maximum values of platform motion in pitch

scheme may induce a magnification of the pitch motion. The effect may be referred to as “negative damping effect”. The wind turbine control scheme for the FOWT at Kabashima was modified to suit a floating wind turbine so as to avoid the negative damping effect. In order to confirm the effectiveness of the control scheme, the field measurement at power generation has been made, and the results are presented below (for details, see [9]).

Figure 6 shows the turbulence intensities of the wind data used for comparison herein. Figure 7 shows the mean values of the pitch response. A fairly good agreement between the simulation results and the measured values is observed. The effect of turbulence intensities is insignificant for the mean values. Figure 8 shows the standard deviations of the pitch response (pitch SD). As it can be seen in Fig. 8, the numerical simulation results show that the turbulence intensities affect the pitch SD considerably. Thus, a large scatter of the pitch SD in the measured values is due to the large scatter of the turbulence intensities themselves (see Fig. 6). The simulation results of pitch SD predict fairly well the upper bound of the measured data for the corresponding turbulence intensity class (IEC category A).

Fig. 6 Turbulence intensities (T.I.) (solid line: IEC category A, broken line: IEC category C, +: T.I. above IEC category A, circle: T.I. between IEC category A and C, triangle: T.I. below IEC category C)

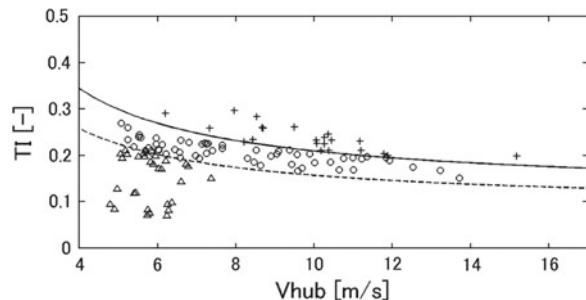


Fig. 7 Mean values of pitch response

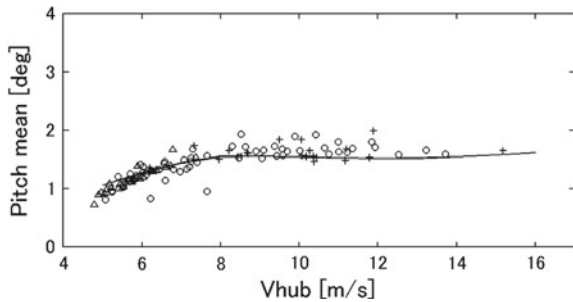
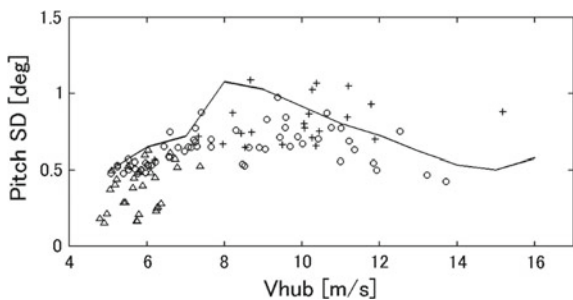


Fig. 8 Standard deviations (S.D.) of pitch response



4 Full-Scale Model

4.1 Design, Construction and Installation

The half-scale model was removed from the demonstration site as scheduled. Subsequently, the full-scale model was installed at the same site. Figure 9 shows the main dimensions of the full-scale model. Basically, the design concept of the spar platform is the same as the half-scale model except for the scaling up to about twice in the length dimensions. Some details of the design procedure, construction and installation can be found in Utsunomiya et al. [11].

The installation procedure can be summarized as follows (Fig. 10).

- The PC parts and the steel part were connected at a quay yard in the horizontal position.
- The completed floater (hybrid spar) was towed to the northern part of the Kabashima Island by using a barge (dry tow).
- The floater was then upended by using a large floating crane. The procedure is basically the same as the half-scale model.
- The tower (in two pieces), the nacelle, and the rotor were assembled to the floating body.
- After completion of the floating wind turbine, it was towed to the southern part of Kabashima Island.

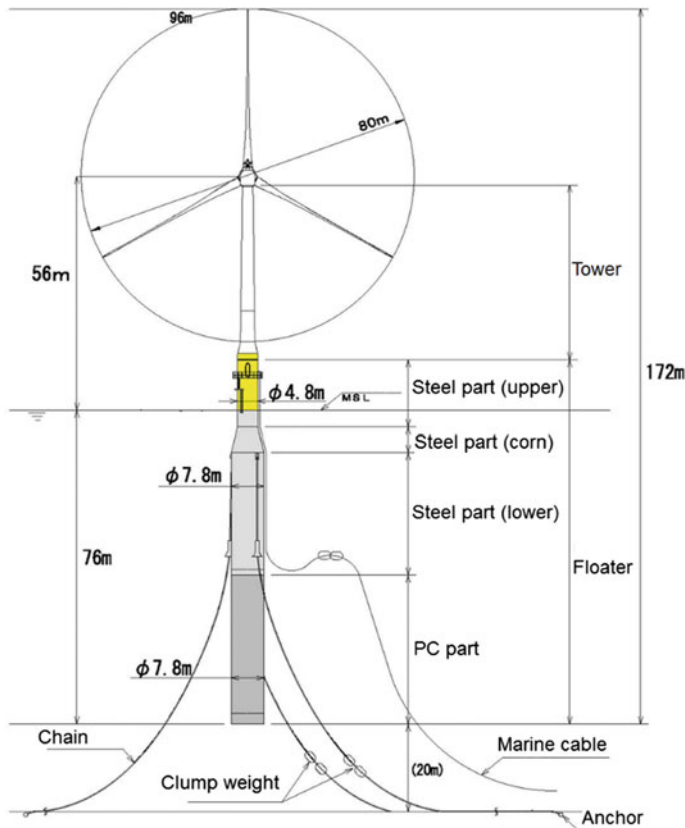


Fig. 9 Main dimensions of the full-scale model

- (f) Finally, the anchor chains were hooked-up to the floating body. Here, the anchor chains had been pre-laid. The final hook-up was completed on 18 October 2013.
- (g) After the electric marine cable hook-up and the grid-connection, the opening ceremony, as the first multi-megawatt floating wind turbine in Japan, was held on 28 October 2013.

4.2 Operation and Relocation

The full-scale model was operated and tested at the Kabashima demonstration site for more than 1 year. During the test, several measurement was made, and they were checked against the numerical simulations. Some details can be found in Utsunomiya et al. [14].

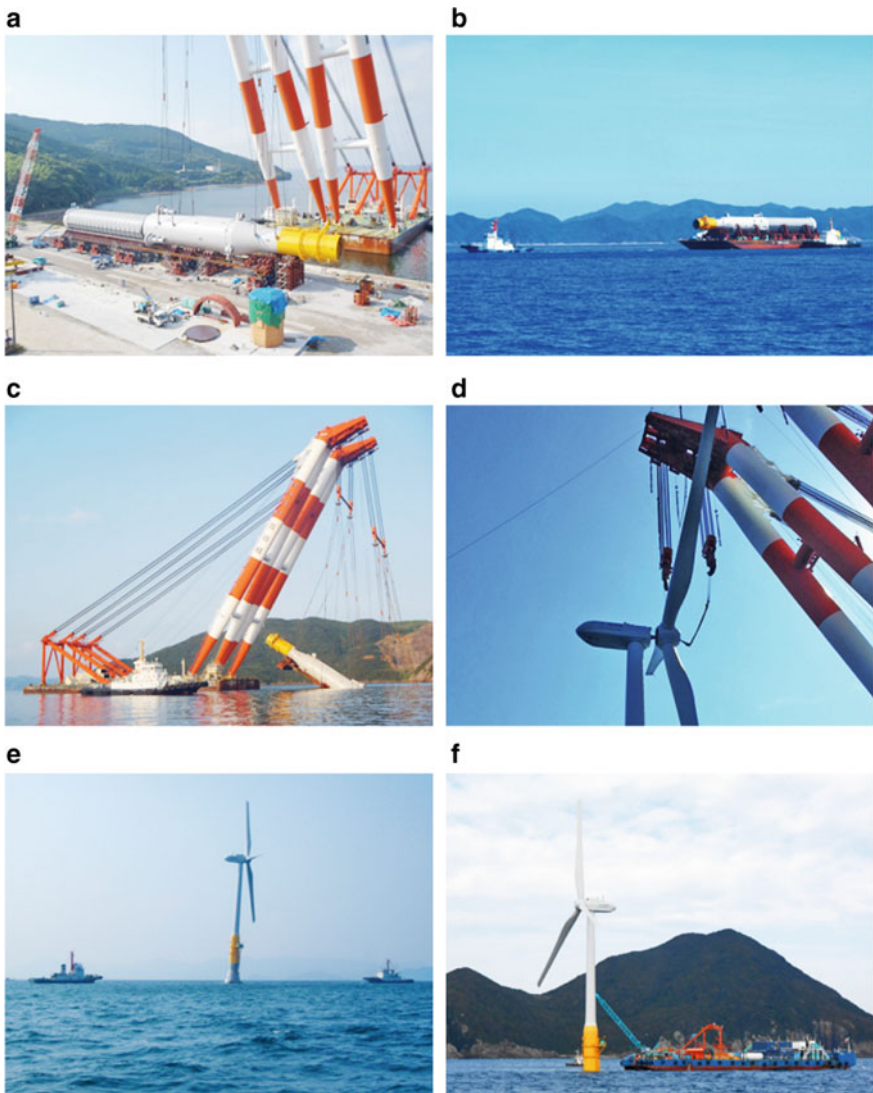


Fig. 10 Installation procedure of the full-scale model (from top left to bottom right; **a** connection between PC part and steel part, **b** towing of the floater, **c** upending of the floater, **d** assembly of the rotor, **e** towing to the demonstration site, **f** hook-up of anchor chains)

The demonstration project completed successfully in March 2016 as scheduled. In order to utilize the full-scale model for further demonstration toward commercialization, it was removed from the site, and relocated to 5 km offshore of Fukue Island. There, a full 2 MW power generation is possible, and future expansion to a floating offshore wind farm is expected. Figure 11 shows the general view of the full-scale



Fig. 11 General view of the full-scale model during power production

model at the relocated site during power production. Due to the thrust force acting on the rotor, steady inclination and elastic deformation of the blades can be observed. Currently, the full-scale model is used as a commercial wind turbine, selling its product with FIT-based revenues. Also, the full scale model was hit by severe typhoons several times but it had not been damaged. Comparison of the measured responses during the typhoons with simulations can be found in Tanaka et al. [7].

5 Concluding Remarks

This paper introduced the demonstration project on floating offshore wind turbine held at Kabashima Island, Goto city, Nagasaki prefecture. The half-scale model was attacked by a very severe typhoon, but it survived with no damage. Comparison of the measured data during the typhoon event and the power production with the simulation results confirmed the validity of the simulation tool and the design method.

The full-scale model has also been installed with a great success. It also demonstrates the feasibility of the spar-type FOWT in Japan. The success of the hybrid spar combining lower PC precast segments and upper steel part has opened up the realization of a low-cost floating wind turbine system in near future.

Acknowledgements This work is a part of the floating offshore wind turbine demonstration project funded by the Ministry of the Environment of Japan.

References

1. Byklum E, Atcheson M (2016) State-of-the-Art. 2 Hywind. In: Cruz J, Atcheson M (eds) Floating offshore wind energy—the next generation of wind energy. Springer, Switzerland
2. EWEA (2013) Deep water—the next step for offshore wind energy [Online] July 2013. Available at: <https://windeurope.org/about-wind/reports/deep-water/>. Accessed 27 Aug 2019
3. Ishida S, Kokubun K, Nimura T, Utsunomiya T, Sato I, Yoshida S (2013) At-sea experiment of a hybrid SPAR type offshore wind turbine. In: Proceedings of the 32nd international conference on ocean, offshore and arctic engineering, Nantes, France, 9–14 June 2013. OMAE2013-10655
4. Kokubun K, Ishida S, Nimura T, Chujo T, Yoshida S, Utsunomiya T (2012) Model experiment of a SPAR type offshore wind turbine in storm condition. In: Proceedings of the 31st international conference on ocean, offshore and arctic engineering. Rio de Janeiro, Brazil, 1–6 July 2012. OMAE2012-83993
5. Nielsen FG, Hanson TD, Skaare B (2006) Integrated dynamic analysis of floating offshore wind turbines. In: Proceedings of the 25th international conference on ocean, offshore and arctic engineering. Hamburg, Germany, 4–9 June 2006. OMAE2006-92291
6. Roddier D, Cermelli C, Weinstein J (2016) State-of-the-Art. 1 WindFloat. In: Cruz J, Atcheson M (eds) Floating offshore wind energy—the next generation of wind energy. Springer, Switzerland
7. Tanaka K, Sato I, Utsunomiya T, Kakuya H (2019) Comparison of dynamic response in a 2 MW floating offshore wind turbine during typhoon approaches. In: Proceedings of the 38th international conference on ocean, offshore and arctic engineering. Glasgow, Scotland, June 9–14, 2019. OMAE2019-95889
8. Utsunomiya T, Sato I, Yoshida S, Ookubo H, Ishida S (2013) Dynamic response analysis of a floating offshore wind turbine during severe typhoon event. In: Proceedings of the 32nd international conference on ocean, offshore and arctic engineering. Nantes, France, 9–14 June 2013. OMAE2013-10618
9. Utsunomiya T, Yoshida S, Kiyoki S, Sato I, Ishida S (2014a) Dynamic response of a spar-type floating wind turbine at power generation. In: Proceedings of the 33rd international conference on ocean, offshore and arctic engineering. San Francisco, California, USA, 8–13 June 2014. OMAE2014-24693
10. Utsunomiya T, Yoshida S, Ookubo H, Sato I, Ishida S (2014) Dynamic analysis of a floating offshore wind turbine under extreme environmental conditions. *J Offshore Mech Arct Eng* 136(2):020904
11. Utsunomiya T, Sato I, Kobayashi O, Shiraishi T, Harada T (2015a) Design and installation of a hybrid-spar floating wind turbine platform. In: Proceedings of the 34th international conference on ocean, offshore and arctic engineering. St. John's, Newfoundland, Canada, May 31–June 5, 2015. OMAE2015-41544
12. Utsunomiya T, Sato I, Shiraishi T, Inui E, Ishida S (2015b) Floating offshore wind turbine, Nagasaki, Japan. In: Wang CM, Wang BT (eds) Large floating structures—technological advances. Springer, Singapore
13. Utsunomiya T (2016) State-of-the-Art. 3 Goto Island Project. In: Cruz J, Atcheson M (eds) Floating offshore wind energy—the next generation of wind energy. Springer, Switzerland
14. Utsunomiya T, Sato I, Kobayashi O, Shiraishi T, Harada T (2019) Numerical modelling and analysis of a hybrid-spar floating wind turbine. *J Offshore Mech Arct Eng* 141(3):031903
15. Utsunomiya T, Sato I, Shiraishi T (2019b) Floating offshore wind turbines in Goto Islands, Nagasaki, Japan. In: Wang CM et al (eds) WCFS2019, lecture notes in civil engineering, vol 41. Springer, Singapore

Architecture Session

Adaptive and Variable Building Envelopes: Formal Methods and Robotic Fabrication



Su Jung Ji, Jin-Ho Park, Se Jung Jeong, and Yang Sook Jeon

1 Introduction

Building skin functions as a key element that covers the façade of a building. It is in direct contact with the outer climate, thus playing a significant role in sustainable techniques for energy saving. Under extreme climate conditions of Middle Eastern areas, Mashrabiya breaks direct sunlight while allowing natural light to enter the interior. The climate requires utilizing passive architectural solutions with local materials and techniques to mitigate the harsh weather in buildings. The façade structure is an inevitable part of the external glass wall where it combines attributes of visual appearance and environmental performance. A well-designed façade can efficiently regulate physical environmental factors, such as wind, heat and light, while improving the occupant's comfort within a building. Recently, Mashrabiya has been reintroduced through different forms of designs to keep up with modern technologies. Here, reviewing the device of the traditional Mashrabiya used in Middle Eastern countries, presenting its components and techniques, and reviewing the potential usages in the contemporary context of the architecture are necessary.

The aim of this research is to conduct on the one hand, a systematic study on the generation of a variety of building facades using the symmetry method, investigating the visual effect and its design potentials, and on the other hand, a pilot study to fabricate a mock-up façade model with a robotic arm.

S. J. Ji · J.-H. Park (✉) · S. J. Jeong · Y. S. Jeon
Department of Architecture, Inha University, Incheon, Korea
e-mail: jinhpark@inha.ac.kr

2 Traditional Screen Techniques

The principal function of Mashrabiya is to break direct sunlight and allow natural ventilation while preserving privacy for Middle Eastern people. It is typically composed of a projecting window made of wooden latticework. It is attached to the exterior wall mainly on the second story or higher of the building. It allows natural daylight and ventilation to the inner rooms. It also offers an overlooking view of the street or the inner courtyard. A Mashrabiya is covered by finely turned wood pieces in a lattice pattern. These fine woods are assembled in different geometrical patterns, plant ornaments, and some other Arabic patterns. The complex arrangement of the Islamic patterns seems to have infinite shapes that expand without a start or an end. It is designed to fit within a frame that surrounded the patterns. Mashrabiya not only covers openings but also saves occupants from the harsh surrounding environment. It provides shade inside a room without closing the windows, thus ensuring airflow to pass through openings and mitigate high temperature (Fig. 1).

It controlled air flow and light through the different size of openings in its lower and upper parts. The lower part had small openings to break sunlight and to get constant airflow, as that part was at the eye level, while it provided privacy for the occupants. The upper part had the bigger openings to ensure the flow of cool air and light which is away from and above eye level to avoid blurring in vision. Through the wooden balusters and lattices, direct sunlight was broken to avoid blurry vision.

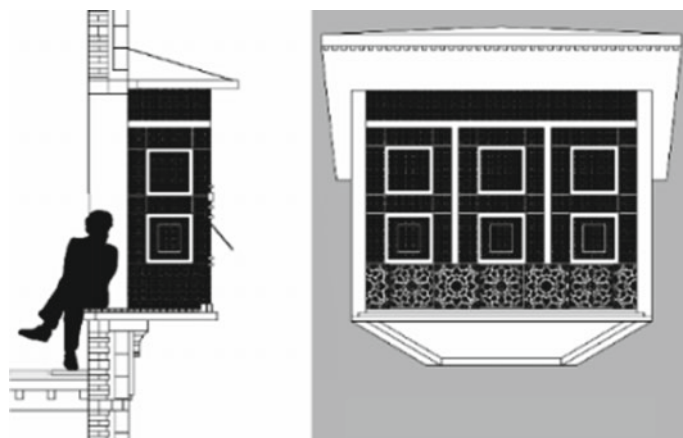


Fig. 1 Section and exterior view of a traditional Mashrabiya, Bayt Al-Suhaymi, Egypt, 1648

3 Modern Applications

Several architects have faced challenges in reinterpreting the concept of Mashrabiya, which characterizes the local identity into a modern architectural language. These architects have intended to apply Mashrabiya to high-rise towers using Islamic-inspired geometrical patterns. Two contemporary façade designs inspired by the traditional Mashrabiya are introduced, that is, the designs of the Doha Tower and the Louvre Abu Dhabi. Both designs by Arch. Jean Nouvel share the same geometric aesthetics and functional purposes [1].

3.1 Doha Tower Façade

The system for the Doha tower is a fixed four-layered aluminium screen that simply covers the entire façade. Four layers of the same design but with different scaled patterns are superimposed together. A unit motif of the pattern appears to have a triangular shape. The basic pattern shows a rotated, reflected, and translated motif, which forms the wallpaper group of symmetry. The same pattern is then reduced consecutively and superimposed in two, three, or four layers. Each design is selected as a double-layer screen in response to the orientation of the sun and direct light intensity throughout the year. Considering that Doha is known for its hot weather and high sun glare, the screen functions as a protection from heat and direct sunlight and provides interior shading (Fig. 2).

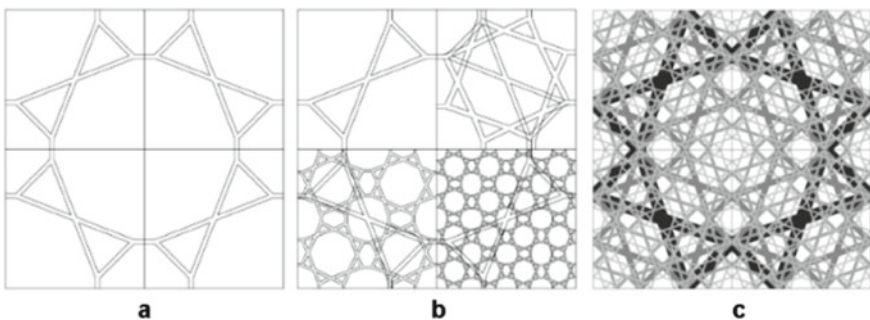


Fig. 2 The façade system for the Doha Tower: **a** Basic pattern of the screen; **b** reduced patterns; **c** superimposed patterns

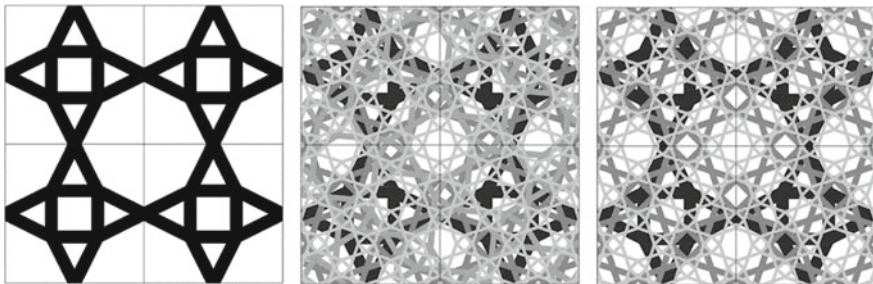


Fig. 3 Basic pattern as well as various scaled patterns overlapped for the Louvre Abu Dhabi roof dome

3.2 *Louvre Abu Dhabi Dome*

The warm weather in Abu Dhabi prevails throughout the year with the occasional rainfall in winter. The dome for the group of buildings acts as a shading canopy to protect the exterior plaza and the buildings below from the daylight. This structure provides a comfortable working area for visitors around the galleries, open plaza, and other facilities. The structure for the dome is composed of double layers. The top outer and bottom inner parts of the dome are each overlapped with four levels of aluminium designs of different sizes with geometric patterns. Nevertheless, its fundamental design is simply formed with wallpaper patterns. The dome design with perforated openings filters light but still allows the sea breeze into the complex. At first look, the design of the dome looks randomly weaved. However, a closer look reveals that the dome's complex pattern is the result of a meticulously studied geometric design (Fig. 3).

4 New Synthetic Designs

We focus our attention on the geometric designs and fabrication of the façade screen. The symmetry principle is used to test the design possibilities of generating different window screens by arraying a simple motif in accordance with the principle and overlaying various symmetries of the wallpaper group.

4.1 *Formal Method*

The geometric patterns of the building facades are created by repeating geometric motifs in accordance with the symmetry of the wallpaper groups [2]. Planar symmetry has two types, namely, the finite and infinite groups. The former is called the point

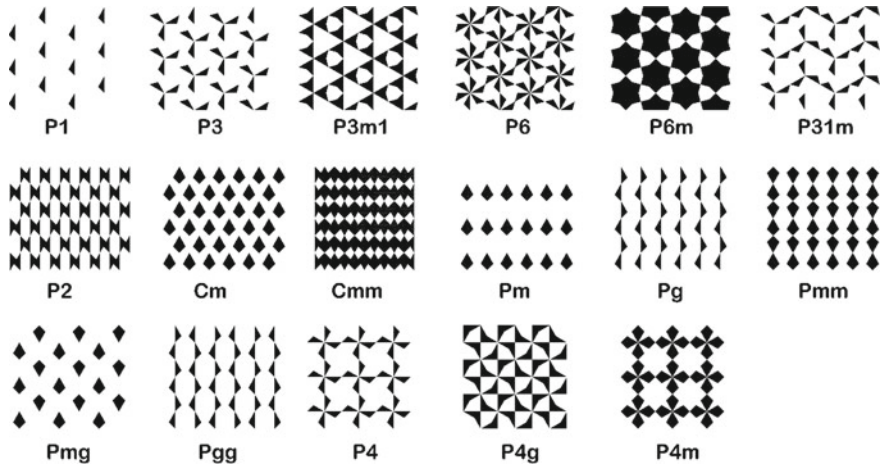


Fig. 4 Examples of 17 wallpaper patterns based on a simple triangular unit motif

group whose isometric transformations occur in a fixed point or line. In the latter, isometric transformations occur under unidirectional translations called the frieze group; the two-directional translations are called the wallpaper group [3, 4]. Here, only the wallpaper group is considered.

There are 17 distinct wallpaper groups in the plane. Each is classified with respect to four spatial transformations including translations, reflections, glide reflections, and rotations, as well as five basic lattices such as square, hexagonal, rectangular, rhombic, and parallelogram. Basically, a unit motif is recursively transformed and placed within the lattice frame. Whereas each wallpaper group contains a distinct combination of the above transformations and lattices, it is characterized by a unique pattern that periodically repeats [5] (Fig. 4).

4.2 Constructing Potential Designs for Façade Screens

Infinite numbers of the geometric screen designs can be created with respect to the symmetry of the wallpaper group. The overlay of different subsymmetries in various layers are methodically expanded to inspire diverse screen ideas. Suppose that a black-and-white simple motif is selected. The selected motif is repeatedly arranged as a pattern in accordance with the symmetry of the wallpaper groups. Initially, the subsymmetry of the wallpaper groups can be strictly applied to generate distinct window screens, where each screen corresponds to a specific plan symmetry group. After arranging each motif in accordance with the principles of symmetry, architects can then manipulate and transform the motifs in accordance with their functional and aesthetic requirements. Different ways of overlapping and binding the symmetries of the wallpaper groups in a single screen design can be used. Several

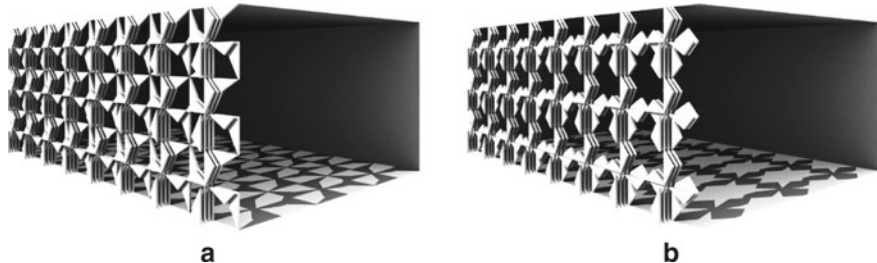


Fig. 5 Several window screens during the winter: **a** p4g-p4-p2-p1 are superimposed; **b** p4m-p4-p2-p1 are superimposed

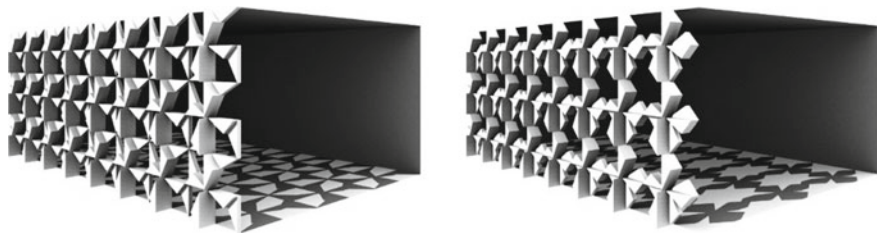


Fig. 6 Morphed screens of the subsymmetries of wallpaper patterns with the square lattice

screens illustrate the symmetry principle that is applied in a pattern, whereas other screens are visually compelling but are slightly connected to their flat representations of symmetry (Fig. 5).

The superimposed layers can be morphed together to form a single structural entity. The aggregated layers are placed in ordered positions with some distance apart. Contemporary computer technology can generate a multitude of morphed designs. One layer of patterns mutates into another. Each layer can be set and morphed in a single axis [6] (Fig. 6).

4.3 Test Fabrication with Industrial Robot Arm

With advanced computer technologies, various designs have tested its technical details and construction by fabricating the designs offhandedly. Recently, changes in architectural fabrication systems, such as laser cutters, CNC (Computer Numerical Control) milling machines, 3D printers, and robotic arms, allow us to produce prototypes economically and easily. In this project, complex free-formed designs are fabricated using a robotically controlled wire to cut from the Expanded Polystyrene (EPS) foam. This process involves computing tool paths and rapidly prototyping potential forms. These processes are efficient devices for creating mock-up models of computer-generated designs. Most industrial robots work in car assembly lines or



Fig. 7 Component unit cutting with the hot wire

heavy-duty works. Recently, industrial robots have been implemented to increasingly creative works because they can operate more efficiently than humans considering their accuracy. Given that the morphed structure of various layers is an assembly of the modular unit, we fabricate and assemble the unit while it is applied in a real building (Fig. 7).

Based on potential designs for facades designs, a full-scale mock-up model of the building envelope is fabricated with the industrial robot arm. The fabrication of a full-scale mock-up model of the building envelope aims at verifying and testing the performance of the design and the suitability of the structure. With the help of such technology, concept designs can be offhand examined into physical reality so that the designs can be progressively enriched as well by the reciprocal process. The process may change our working environment, as the computer has replaced the drawing tools of the past. It forecasts the change to working environment in which design as well as fabrication process will be gradually integrated so that both eventually occurs in one place (Fig. 8).

5 Summary

Mashrabiya with repeated geometric patterns has been revived in contemporary architecture and further utilized as an integral part of practices for the development of sustainable architecture. The symmetry of the wallpaper groups was briefly introduced and then applied to test synthetic window screens. The symmetry principle may serve as a tool for unlimited creativity for screen designs in the hands of architects, thereby allowing the design of various façade structures. Here, the notion of wallpaper group symmetry was used to generate different screen patterns. In addition, methods for overlaying different patterns of screens were tested to generate various depths of the screens. Therefore, a simple technique has numerous potentials for generating a diverse range of designs and applying them to sustainable screen



Fig. 8 Modular unit screen fabricated using a robotic arm where various subsymmetries are superimposed

designs of architecture. A mock-up model was fabricated with the industrial robotic arm for demonstration, design evaluation, and constructability.

Acknowledgements This research is funded by NRF(NRF-2018R1D1A1B07048986) of Korea. The authors thank to all D-Lab staffs for the project fabrication and installation in the Department of Architecture at Inha University.

References

1. Abdelkader R, Park J (2018) Sustainable building facades: modern usages of the traditional mashirabiya. *Open House Int* 43(2):69–76
2. March L, Steadman P (1971) The geometry of environment. The MIT Press, Cambridge
3. Park J (2000) Subsymmetries analysis of architectural designs: some examples. *Environ Plan* 27(1):121–136
4. Park J (2001) Analysis and synthesis in architectural designs: a study in symmetry. *Nexus Netw J* 3(1):85–97
5. Martin G (1982) Transformation geometry: an introduction to symmetry. Springer, New York
6. Park J (2005) Early Shape morphing: the metamorphosis of polygons in Antoni Gaudi's Sagrada Familia Cathedral and Le Corbusier's Firminy Church. *J Asian Archit Build Eng* 4(1):25–30

An Analysis of Green Building Certification Systems in Vietnam



Le Thi Hong Na and Dang Nguyen Hong Anh

1 Introduction

Over the past decades, Vietnam has witnessed negative impacts on the country's development and economy from global warming and climate change. The government, organizations, stakeholders and citizens have all joined hands in the mitigation of this problem. In 2015, the United Nations General Assembly established the 2030 Sustainable Agenda with 17 global goals set to end poverty, protect the planet, and ensure prosperity for all. In that context, Vietnam has adopted various national strategies for sustainable development, specifically 115 detailed targets, compared to 169 set in the Sustainable Development Agenda 2030 [1]. Of this, the construction industry is placed at a high priority as it exerts great influence on the natural environment, resource consumption and human health. As a result, the importance of sustainability in the construction industry has been recognized and promoted both globally and locally. In response to the demand for more sustainable buildings, Vietnam has experienced a significant increase in the number of GBs. This makes GB an emerging crucial element in the process of reducing the detrimental impacts of the construction industry.

A GB is a building, of which, its design, construction and operation minimize its negative impacts on human health and natural environment while preserving precious natural resources and improving the quality of life. GB plays an important role in delivering environmental, social and economic benefits to the construction industry, which contributes to the world's sustainable development. In Vietnam, GB is becoming increasingly associated with different rating systems, which confuses stakeholders in the promotion of their GB. These include LEED (Leadership in Energy and Environmental Design), LOTUS, EDGE (Excellence in Design for Greater Efficiencies), DGNB (Deutsche Gesellschaft für Nachhaltiges Bauen), GO-AIT VN (Green

L. T. H. Na (✉) · D. N. H. Anh
Ho Chi Minh City University of Technology,
VNU-HCM, Ho Chi Minh City 740128, Vietnam
e-mail: na.bmkt@hcmut.edu.vn

Office of Asian Institute of Technology in Vietnam), HQE (Haute Qualité Environnementale), BCA Green Mark, Green Star, WELL and FITWEL. Therefore, to easily and accurately decide on GB investment, it is of great essence for stakeholders to differentiate between the main features of different GB rating systems.

In spite of the growing adoption of GB rating tools, there is no study to review all the certification systems used in Vietnam. Thus, the purpose of this paper is to systematize, analyze and identify the outstanding features of each certification system which would assist stakeholders in having a better understanding of these different GB rating systems in order to make appropriate choices in GB investment.

2 The Development of GB Movement in Vietnam

In 1993, the first United State Green Building Council (USGBC) was founded—creating a global movement to encourage sustainable adoption in the construction industry to achieve sustainable development. The GB movement began to attract more and more attention from green leaders and developers from countries around the world and Vietnam was not an exception. As a result, to bring together a group of people with the same views towards GB, the World Green Building Council was founded in 1999. In the upcoming decades, GB activity should continue to increase across the globe. In Asia, Singapore and China are ranked as the top performers in developing GB. Whereas, Vietnam achieved a relatively modest number of certified GBs at about 100 at the beginning of 2019, compared to 197, 154, 3269 and more than 1000 GBs in Thailand, Taiwan, China and Singapore respectively [2]. However, according to the 2018 report of World Green Building Trend, in recent years, Vietnam saw considerable growth in the level of green activity, and this is predicted to increase significantly in the next few years [3]. The expected percentage of respondents participating in more than 60% of green projects will nearly double from 13 to 24% in 2021. It can be concluded that Vietnam is a potential market for GB development. The GB movement in Vietnam has just taken the first steps. There has not been a real action and been interested by community, although the GB movement in the world has been for 25 years [4].

To recognize a work as a GB, various GB rating systems, which comply with the combination of sustainability-based factors, have been launched. Currently, there are 10 different GB certification systems being applied in Vietnam as shown in Table 1. LEED, which is established by USGBC in 2010, is appropriate for projects seeking global brand recognition. EDGE, developed by the World Bank Group's International Finance Corporation (IFC), focuses on minimizing the usage of natural resources including energy, water, and materials. Meanwhile, FITWELL and WELL, both created by the U.S., emphasizes more on human wellbeing and the occupants' comfort. As an indispensable trend, Vietnam Green Building Council (VGBC) has created its own domestic GB standard called LOTUS, with its aim to comply with Vietnam's construction practices, regulations, and climate. HQE and Green Mark are a national typical certification of France and Singapore, in which the GB movement is

Table 1 Basic information of 10 GB certification systems presented in Vietnam

Year	Country	Certification system	Organization	Target markets
1998	US	LEED	U.S. Green Building Council	U.S./International
2002	France	HQE	Alliance HQE-GBC (France) and Cerway (award HQE worldwide)	Europe and developing countries in Africa
2003	Australia	Green Star	Green Building Council of Australia	only Australia
2005	Singapore	Green Mark	Building and Construction Authority (Singapore)	Singapore and Asia
2009	Germany	DGNB	German Sustainable Building Council	Developing countries
2010	Viet Nam	LOTUS	Vietnam Green Building Council	Viet Nam
2013	Switzerland	EDGE	IFC – World Bank Group	Developing countries
2014	US	WELL	International WELL Building Institute	U.S./International
2017	US	FITWEL	U.S. Department of Health and Human Services	U.S.
2017	Viet Nam	GO - AIT VN (Green Office)	Asian Institute of Technology in Vietnam (AIT VN)	Viet Nam

Source Authors

strongly developing with the significant quantity of projects. GO-AIT is a certification for offices and companies which had finished the training course. As there is only a single project with DGNB certification by German investor, it is not popular in Vietnam. There is a building in Vietnam which was designed in accordance with Green Star standard. However, as Australia GB Council only provides Green Star certification for domestic projects, this building was not certified. The most popular certifications used to evaluate GB in Vietnam are LEED and LOTUS certification systems. Some GB developers have started to consider to apply FITWELL for their project [5].

Over the past 5 years, more and more GB rating tools have been applied in Vietnam, followed by a significant surge in the number of certified GB especially in the period from 2016 to 2018. The total figure for certified GB in Vietnam as of early 2019 is 106 certified buildings under LEED, LOTUS, Green Mark, EDGE, HQE, DGNB and WELL standards (Chart 1). LEED experienced remarkable growth in the number of certified GB from 2 projects in 2010 to 54 in 2019, which makes it the most commonly used GB rating tool in Vietnam. Meanwhile, LOTUS is applied the



Chart 1 Number of certified projects in Vietnam. *Source* Authors

second most common for GB certification with 23 certified buildings as of 2019. The number of projects achieving Green Mark certification gradually rise year by year and has reached the number of 7 in 2019. Despite being lately applied, EDGE certified buildings witnessed a climb up to 18 buildings in 2019, passing the number of those certified by Green Mark. EDGE certification monitors the building's emission rate through the EDGE App, which is an easy-to-use tool for designers and operators for buildings.

There are various factors driving this trend upwards. The most significant of which to the growth of GB in Vietnam comes from the market demands for more valuable buildings. This indicates the important role of owners' involvement in green in pushing this market. However, there are numerous obstacles interfering with the development of GB. The lack of well-trained green experts and political support/incentives are the biggest barriers to the growth of the green market in Vietnam. In addition, concerns about higher first costs and lack of public awareness should also be considered as barriers.

3 Remarkable Aspects of GB Movement in Vietnam

The GB certification system provides a recognized third-party verification. It makes the design, construction and operation of buildings more environmentally responsible. On the other hand, human comfort and health, being affected by GB's measures, plays a significant role in the productivity of buildings [6]. GB's categories depend on national legal and construction laws so that their criteria are extra requirement to make high-performance buildings. Different GB rating systems based on sustainability-based criteria vary from energy consumption, water efficiency, waste management, indoor air quality, technology, community to innovation application.

Based on the analysis and synthesis of categories of all GB certification systems presented in Vietnam, there are 2 groups of criteria including environmental concern

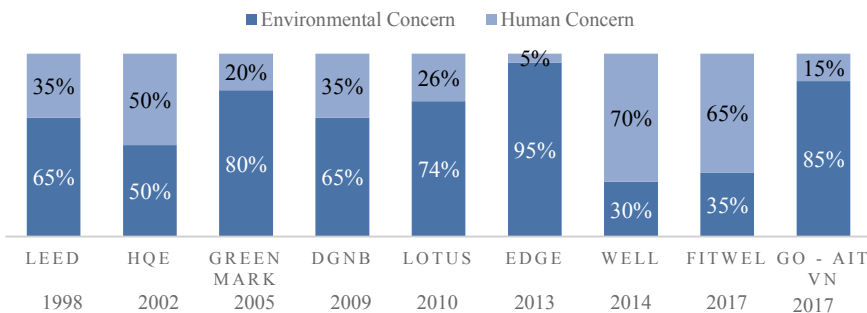


Chart 2 Proportion of 2 orientational criteria in GB certification systems in Vietnam. *Source* Authors

and human concern. These are considered as 2 main destinations that all criteria are heading to. However, that aspect is the majority differs from each GB rating tools. Of which, the environment-related criteria are points about energy, environment elements, waste, and pollution; while human-related criteria focus on human health and well-being [7]. The level of concern for each GB certification system is as shown in Chart 2. Among them, LEED, LOTUS, EDGE, Green Mark, DGNB and GO-AIT concern more about environmental aspects in minimizing the usage of energy, natural resources, reducing waste and pollution. Meanwhile, FITWEL, WELL and HQE seem to care more about health comfort factors by focusing on improving the quality of living conditions. Accordingly, the cognizance of the dominant aspect of each GB certification system could assist stakeholders in adopting the appropriate GB activity in accordance with their prior objectives.

The systematic review of all GB rating systems in Vietnam demonstrates a prosperous development of GB and readiness to adopt advanced technology to keep up with the sustainable development trend of the world. According to Table 2, the statistic shows all GB certification tools can be applied for most types of building. However, not all of them are available in the Vietnam construction market.

It is noticeable that industrial projects account for the highest percentage of certified GB in Vietnam. Industrial works is a major sector of the GB market due to factory construction laws on energy, environment and health quality that are regulated by going through the documentation and certification process. In addition, some industrial constructions, which is administered by international corporations or complied with import and export enforcement, must be applied for GB certification by foreign investment law. These buildings are mostly verified by the LEED certification system, a long-standing, widely-used global standard.

The next most-rated building types are office and residential buildings. The number of these categories has been increasing rapidly for the last 3 years due to 4 main causes. First, following the requirements of construction market about improving sustainable quality, most new buildings are racing against time to receive GB certification. Higher building-value is also considered as the primary cause. Also, with all certified categories from GB organizations, these buildings are all able to provide

Table 2 Building types in accordance with GB certification systems in Vietnam

BUILDING TYPES	LEED	LOTUS	EDGE	DGNB	HQE	Green Mark	WELL	Total
1 Commercial/ Office building	13	1	2	1		1	1	19
2 Office Interior/ Workplace	1	1						2
3 Education	1	3	1		1			6
4 Healthcare								0
5 Hospitality			1		1			2
6 Single/ Multi Residential		6	1			5		12
7 Neighbourhood/Urban								0
8 Industrial	37	6	1			1		45
9 Retail	2	6						8
	Available in systems				Not available in systems			
	Available in Vietnam				1 Number of projects			

Source Authors

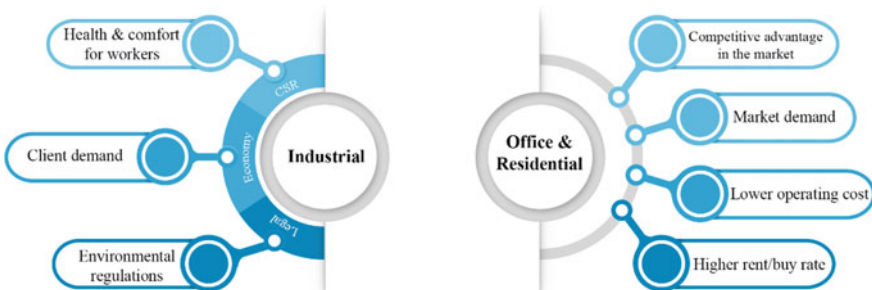


Fig. 1 The main causes of development of 2 typology projects in Vietnam. Source Authors

higher living quality and improve user health. Last but not least, the operating cost of a GB is lower than that of a normal building, which faster recovers invested capital [5]. The main causes of development of 2 typology projects in Vietnam is as shown in Fig. 1.

4 Case Studies

To clarify the status of green buildings in Vietnam, three domestic buildings, recently built and certified as GB, were chosen to be analyzed in Table 3. The results show that they all apply basic environment-friendly design techniques and technologies

Table 3 Case studies of lately GB projects in Vietnam

Project	ATAD factory office	Haus Neo	Genesis school
Image			
Address	Lot F, Long Khanh Industrial Zone, Dong Nai	District 9, Ho Chi Minh City	West of Ho Tay New Urban, Hanoi City
Type of building	Office	Residential	School
GFA	6,963 m ²	43,467 m ²	6,128 m ²
Year	2017	2018	2019
Certification	LEED Platinum (83/110 points)	EDGEE	LOTUS Gold (72/118 points)
Green features	<p>Energy</p> <ul style="list-style-type: none"> • 48% improvement on baseline building performance rating • 13% on-site renewable energy <p>Water</p> <ul style="list-style-type: none"> • 100% reduction in potable landscape water • 50% reduction in wastewater • 40% reduction in baseline indoor water use 	<ul style="list-style-type: none"> • 29% energy savings <p>Water</p> <ul style="list-style-type: none"> • 32% water savings 	<ul style="list-style-type: none"> • 5.74% renewable energy • 60.9% energy using reductions <p>Water</p> <ul style="list-style-type: none"> • Rainwater is used for irrigation • 11.45% water consumption • 47.9% water savings through fixtures
Materials	<ul style="list-style-type: none"> • 20% recycled materials • 20% local and regional materials • 75% diversion of construction and demolition debris 	<ul style="list-style-type: none"> • 47% less embodied energy in materials • Cored bricks with plaster for external and internal walls 	<ul style="list-style-type: none"> • All products, coatings and floorings are low-VOC
Greenery	<ul style="list-style-type: none"> • 90% of occupied space has quality views 	<ul style="list-style-type: none"> • 80% of bedrooms have access to a logia • Total CO₂ savings: 339.5 tCO₂ per year 	<ul style="list-style-type: none"> • 39.2% of the site area is vegetated • 835 m² green roof area • 94% of occupied areas have quality views

Source Authors

to reduce the usage of natural resources and mitigate negative impacts on the environment. In particular, apartment Haus Neo, a Bauhaus architecture, which applied advanced technologies not only achieved but also exceeded the standard assessment of 20% by IFC with figures of 29, 32, 47% on energy savings, water saving and less-embodied energy in materials respectively. Meanwhile, Genesis School, a kindergarten and primary school, obtained LOTUS Gold Certification in May 2019 with its various green features. It reduces energy use to only 60.9% thanks to the use of effective housing shell, AC systems and solar panels. In addition, 94% of occupied areas have quality views to the outside with vegetation all around the building. In terms of LEED-certified GB, ATAD Dong Nai was selected as it is the first LEED factory in Asia invested and built entirely on Vietnamese resources. Despite limitations in knowledge and experience, this project is a factory designed, constructed and consulted in accordance with LEED by the Vietnamese people. It suggests that the Vietnamese construction market holds potential for future development in GB activities.

5 Conclusion

GB is not just a temporarily superficial trend of Vietnam's construction industry but also is an inevitable campaign for sustainable development. GB adoption should be considered as a compelling measure to cope with the increasing challenges of the Vietnamese construction sector, for example, over-population and urbanization, natural resources consumption, waste and pollution management and detrimental impacts of climate change. In the rates of future levels of green activity in Southeast Asia, Vietnam accounts for a high percentage, which makes it a potential market for GB in the next 5 years. The number of verified GB have been increasing consistently over the past 3 years and is projected to witness a dramatic rise in the future.

On the way to further the sustainable revolution by doing GB movement, there is a wide range of obstacles facing the Vietnam construction market. Besides raising public awareness related to GB among inhabitants and stakeholders, the government also plays an important role in promoting GB by adopting the appropriate political strategies, regulations, and intensives.

References

1. UN (2015) United Nations "The Sustainable Development Agenda"
2. Green Building Information Gateway—USGBC (2019). Available from: <http://www.gbig.org/places/>
3. DODGE Data and Analytics (2018) World green building trends 2018, South East Asia. Smart Market Report
4. Pham DN (2017) Development of sustainable architecture—green architecture in Vietnam. Knowledge Publisher

5. Na LTH, Quang DHN (2018) Green building in Vietnam, workshop on the First Vietnam—Korea on the Future of Construction Engineering, HCMUT
6. Yudelson J (2007) Green building A to Z, understanding the language of green building
7. France Green Building Council (2015) International environmental certifications for the design and construction of non-residential buildings, The positioning of HQE certification relative to BREEAM and LEED

Design Exploration and Fabrication Using Industrial Robotic Arm



Seung Beom Park, Jin-Ho Park, You Jin Park, and Tuan Anh Nguyen Vu

1 Introduction

Advanced technologies allow architectural design exploration far beyond traditional ways. However, marginal parts are in the design practice, mainly in the fabrication toward more complex parametric designs. In architecture, industrial robots have been frequently used to explore geometrically complex designs with the property of materials. In construction, robots are used to resolve and construct complex designs. Robots have slowly become creative tools for architectural explorations [1]. Nevertheless, although the number of industrial robots employed has increased during the past years, the use of robots in architecture is still far limited compared with tasks in industrial mass production, such as in the automobile industry. The wide range use of robots involves difficulties or challenges. The use of industrial robots in architecture should be incorporated with other fields, such as controlling and modeling in the software industry and different custom-made end effectors in the mechanical industry [2]. Many professional architects are not aware of any of these advantages because they do not commonly use such techniques in their daily practice.

Advanced technology has changed the ways architects work in the office and in the construction jobsite. Architects can design complex imaginary forms with utmost precision using computer technologies. By working with a computer and robotic arm, architects can conceive, design, fabricate, and assemble all building components. The design data are provided to manufacturing, where components are made with suitable materials and assembled offhand. This procedure is known as the design process of recursion that oscillates between design and fabrication. Overall, this technology is expected to cause a big ripple effect in the design process and construction sites.

S. B. Park · J.-H. Park (✉) · Y. J. Park · T. A. N. Vu
Department of Architecture, Inha University, Incheon 22212, Korea
e-mail: jinhopark@inha.ac.kr

2 Project Description and Concept Design

The project intends to add a new design to an existing internal corridor in an architectural school building. The corridor is relatively long, yet a skylight is built in the middle. The corridor serves as a cooperative space for a variety of student daily activities. At times, students exhibit their works on the corridor wall or students and faculty interact along the hallway.

Nevertheless, the current corridor looks desolate and noises tends to destroy speech intelligibility. The use of the corridor seems to expedite circulation or just to allow movement of people. Direct and reflected sunlight during daytime strikes the corridor between classrooms and studios. The sunlight reflected off a corridor wall causes discomfort, strain, and fatigue. Moreover, the reflection of light can lead to glaring problems.

Accordingly, a symbolic notion of the execution of the project design is conceptualized. A human heart is the initial reference point for the design such that the final design is reminiscent of a heart. To live a healthy life, the circulatory system must optimally work to support a healthy heart. Likewise, the building hall, vestibule, and corridor play a significant part in the internal perspective of buildings. The building corridor is not just a passage way but a public area, which engages users of the building. Furthermore, the corridor represents user identity to showcase the image of the building program. The corridor should not be thought of as a bare passage but should be treated in a variety of ways to assist the peace of mind of the people in the building.

The heart shape is taken as an image motif and interpret it into a part of the corridor design (Fig. 1). The heart's blood vessels allow the controlled admission of natural light and direct sunlight and facilitate ventilation. The present corridor area that was selected as a project site was designed where natural light can be interpenetrated into the corridor and noises can be absorbed as though blood is circulating through a system of blood vessels. With the installation, the corridor will be transformed with

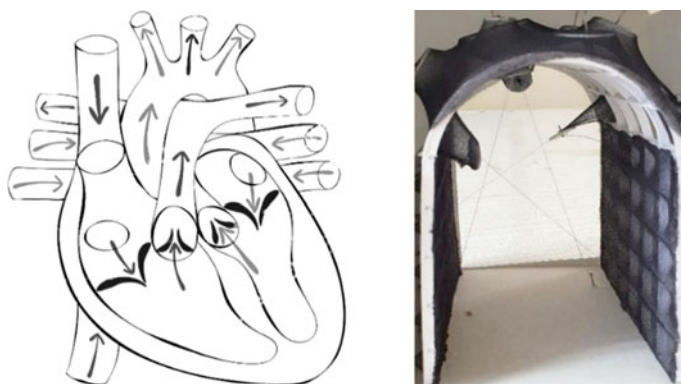


Fig. 1 Concept image of human heart (left) and concept model (right)

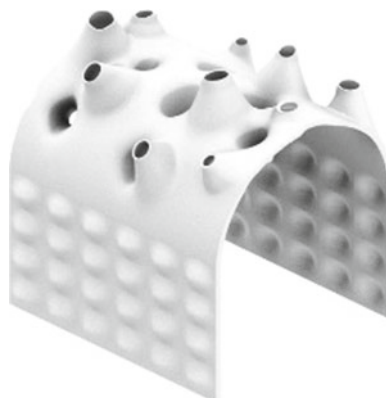
a new inspirational design that will infuse new vitality into the corridor and create new activities.

The audio and visual qualities of the corridor are closely related to the dynamics of the space [3]. While working along the corridor, mixed sounds, noises, lights, and other visual elements surround the passers-by. The various noises reflecting on the sidewalls of the corridor are additional design inspirations. Minimizing noise levels deserves design consideration. Adding a new design will improve the corridor visually and acoustically. After designing the initial shape, the amount of accumulated light exposure that fell on the corridor through the new design and permitted angular adjustments of light emitted by the light inlet tube is tested, as depicted in Fig. 2. Then, the effective areas of the average cumulative sun-exposure conditions during different seasons are simulated to observe the effect of sun exposure on the corridor, and thereafter, the design is finalized (Fig. 3).



Fig. 2 Simulations of the light effect of the corridor during spring, summer and winter

Fig. 3 Final design of the skylight corridor



3 Tools: Hot Wire Cutter with Robotic Arm

In this exercise, the design from layers of foam that were sliced with the hot wire attached to the robotic arm is fabricated and then assembled together to form the intended object. The hot wire heated with electric current allows precise cut-ruled surfaces of the chosen material. Here, the expanded polystyrene (EPS) foam is used. The hot wire technique was used because the equipment is readily available and relatively easy to install and to use. In addition, it is widely accepted for architects as the most commonly technique for modelling making.

A rigid and hollow frame to properly hold the wire cutter is manufactured. The frame acts as a base for the 2-axis positioning devices. Cables for powering the hot wire need to be neatly inserted in the hollow frame to control hazards. A cutting force acting perpendicular to the wire may bend readily, and thus, the wire needs to be pulled tightly under high tension provided by a spring that is capable to adopt the wire current extension. When using a hot temperature, the wire may expand, which requires the spring to tighten up the loose wire. At the other end of the frame, a hot protection sleeve for mirror screw is installed to hold the wire. The frame has to be light enough for the robot's 10 kg maximum payload, where the weight the robotic arm can be lifted. The frame is a custom-made frame with C-shaped hollow aluminum rectangle tubes due to its high strength-to-weight ratio (Fig. 4).

Then, the wire diameter and current strength are considered because of the kerf left after the cutting. Relying on the strength of the current and the diameter of the wire, the kerf width influences the loss of the material and thus needs to be minimized. Adjusting the settings on the power supply and wire cutter takes time. Cutting different foams are subsequently experiment with because different material properties have various resistance levels when the wire is pulled through the foam.

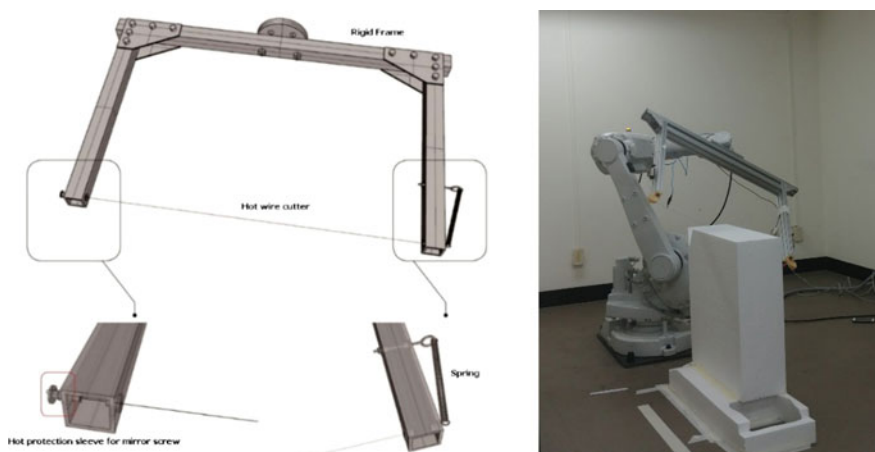


Fig. 4 Hot wire cutter components attached to the robot arm in the beginning of the experiment

In addition, different current temperatures and cutting speeds need to be considered. Cutting occurs below the melting point of the material. And it requires the application of force in the direction of cutting to increase the heat input. Any change in the feed rate affects the kerf width and cut surface. The wire must move smoothly at a constant speed. Holding the hot wire stationary for a few seconds will generate a round hole in the material. If the hot wire stays longer, then the hole will become bigger.

After experimenting with the test cuts with different temperatures and speeds, the appropriate results to be applied for the fabrication are come up with. The length of the wire is 90 cm and the thickness of the wire is 0.5 mm. A typical material for the wire is stainless steel or Nichrome. A Nichrome wire is used, which is fixed at the end of the two points of the aluminum frame. The wire can be exchanged by unfastening the nuts and bolts holding them together. The current heats the wire and the operational voltage ranges from 20 to 40 V in the width and length of the wire. Slidacs is used to convert input to output voltage and allows continuously adjusting the input AC voltage output target.

4 Cutting Test

The final design is developed in Rhino's Grasshopper, and the robotic arm is programmed using HAL, which is a Grasshopper plugin for the simulation and control of ABB industrial robots. The plugin allows the creation of toolpaths to enable the wire cutter to move in a predefined velocity and direction. After developing 3D models in Rhino, an appropriate size of parts for the final cut can be determined. In accordance with the sizes of the wire cutter and robotic arm, the ruled surfaces are subdivided and further dissected into segments for precise cutting (Fig. 5).

The dataset of the dissected parts is linked to the Grasshopper. From the ruled surface of the parts to be cut, two curves are extracted. Then, the points along the curve are divided and lines between these points are drawn. As such, the surface is discretized into several segments by nodes, and the segments are connected and calibrated to form the smooth path curves. The consecutive lines between the curves are the areas where the hot wire will pass through (Fig. 6).

The device trims the object using the ABB Teach Pendant. The wire cutter moves perpendicular to the surface such that the toolpaths are smoothly controlled. The appropriate cutting speed and strength of the current regulating the wire temperature that will create a smooth and consistent cut need to be tested. Speed and wire temperature are tested for the different sizes of the material. To control the curvature of the wire in the cutting process, several ways to get it worked are tested.

Fig. 5 16 pieces of the design was sliced according to the appropriate sizes to be cut

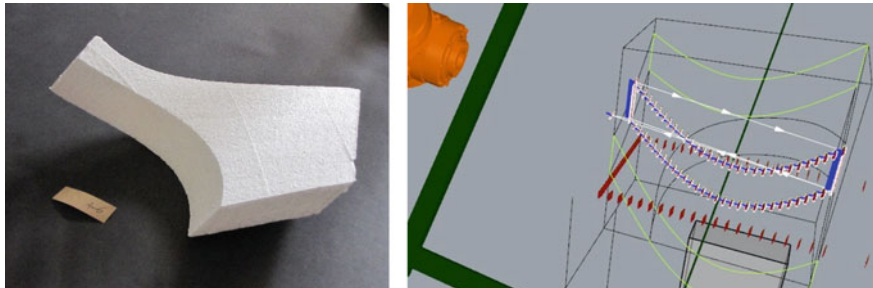
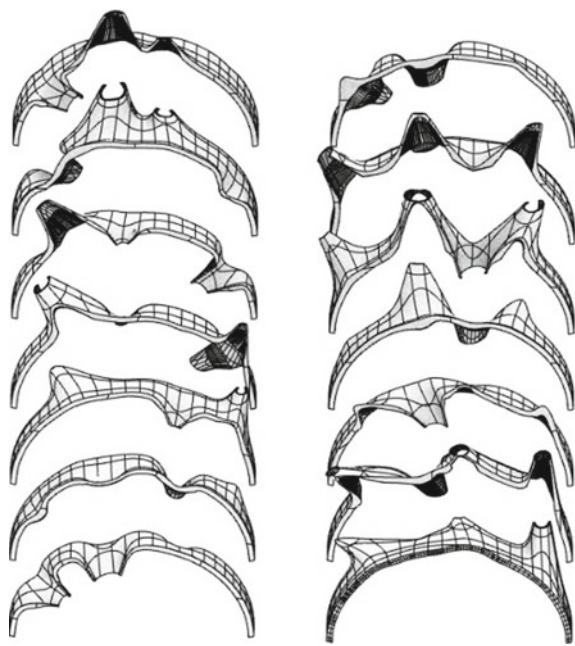


Fig. 6 Tool path and a component tested to be cut

5 Assembling and Installation

After cutting the components of the model, the pieces are assembled together (Fig. 7). The locations and specific sizes of all the pieces can vary, and thus, each unit is numbered after cutting. The assembled unit components are placed by hand in order. Although the pieces are cut and unit components are assembled in accordance with the drawings, discrepancies and mistakes were present during the cutting and assembling processes. Several parts of the unit components needed to be slightly adjusted



Fig. 7 Examples of components and their test assembly

or re-trimmed. It is assumed that the wire cutter with robotic arm did not reach sufficient cutting accuracy. Nevertheless, the wire cutter demonstrates a wide range of capabilities for the cutting of refined rule surfaces.

After custom-made plastic screws and foam bond are used to assemble the trimmed pieces together. After waiting for the final assembled design to harden, the design is smoothed along the common joining faces until they are both finer and planer. The pieces are then assembled together and installed into the job site. The final design is manufactured and assembled out of the EPS foam.

Despite earlier inaccuracies, the pieces fit exactly as the way they are created. The surfaces lack smoothness at times. The preferred method for surface finishing involves a thin cementitious polymer mortar or an elastic acrylic-based protective coating sprayed on the surface. The sprayer for coating the assembled EPS foam is tested. Finally, by using a piston-type airbrush and compressor, white paint is sprayed in several layers on the previous primed surfaces. The dried paint will form the homogenous coating of extraordinary strength and resistance.

6 Summary

This design, fabrication, and installation project is still an ongoing research. The project is expected to be finished in the next few months and possibly presented in a conference. At this stage of the research, geometric and fabrication discrepancies between the simulated form and the trimmed output have been experienced. However, these issues have yet to be fully described in full detail. Further tests and explorations, such as detailed analysis of the model for the purpose of optimizing and calibrating the digital simulation and fabrication, will be a topic for continuing research. Additional tests on the loss of materials and efficient ways to cut components need further investigation.

By switching its end effectors, the device can cope with a great degree of task variability. In this project, the potential of the hot wire cutter is only used. A variety of

other end effectors may be tested with different materials, such as grippers, welders, and lasers. The use of robots may open up new possibilities of design and fabrication of fairly complex spatial forms. Despite the potential of robotic fabrication, the method has been rarely integrated in architectural practice until now. Most of the applications are at the level of experimentations for small-scale projects.

One of the major challenges in the design process is the direct integration of the design software, hardware, and programming ideas with fabrication tools in the project. To make effective use of the overall process, architects should be fully equipped with the knowledge of software programming and hardware for the development of custom-made end effectors and tools for robots. Each end effector should be custom-made to meet the particular needs and demands of the design construction. Relying on the different needs for particular projects, switching its custom-made end effectors for the specific tasks of the fabrication system is needed.

Acknowledgements This research is funded by NRF (NRF-2018R1D1A1B07048986) of Korea. The authors thank to all D-Lab staffs for the project fabrication and installation in the Department of Architecture at Inha University.

References

1. McGee W, de Leon M (eds) (2014) Robotic fabrication in architecture, art and design. Springer, Berlin
2. Willmann H et al (eds) (2018) Robotic fabrication in architecture, art and design. Springer, Berlin
3. Park J-H (2013) Graft in architecture: recreating spaces. Images Publishing

Assessment of Roof Architecture of Street Houses in Some Central Districts of Ho Chi Minh City



Le Thi Hong Na and Nguyen Dang Hoang Nhat Truong

1 Introduction

The population is increasingly concentrated in urban areas, and it is forecasted that by 2050, 49.4% of the population will live in urban areas [1]. That is the reason why SH developed strongly to meet residential and business needs due to high population density. The uncontrolled development of such dwelling has created various challenges, especially with the top part of the houses. People tend to pay more attention to the facade of the house while the roof, which is also an important part of the house, is the last part to be built, is normally reconstructed and renovated for different purposes such as room expansion or be used as technical space. Thus, the roof is cluttered with different sizes and shapes of technical equipment such as AC outdoor unit, water tank, solar water heater, etc. Besides, the building envelope, especially the roof system with large contact area against the sun, remarkably affects the air quality inside and outside of the house in terms of thermal comfort and glare. On a large scale, the roof is considered the “fifth face” of the building, which can be seen from above [2]. Correlation of roof proportions, colors and materials will greatly affect the overall aesthetic of not only the building but also its surroundings. Moreover, the surface material of the roof is the major factor of heat island effect which influence on global warming.

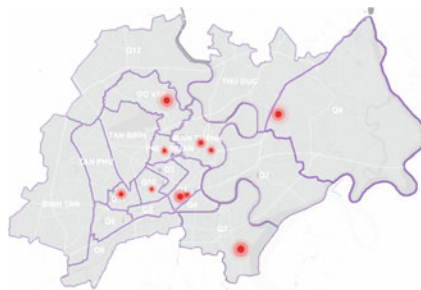
In the world, this issue has been concerned and studied many years ago. In the Environmental Science and Technology magazine on October 1st, 2009, Kristin L. Getter’s article “Sequestration Potential of Extensive Green Roofs” analyzed the current status of the roof and assessed the ability of green roofs in the area. Midwestern United States—problems and solutions for the region. World Green Infrastructure

L. T. H. Na (✉)

Ho Chi Minh City University of Technology, VNU-HCM, Ho Chi Minh City 740128, Vietnam
e-mail: na.bmkt@hcmut.edu.vn

N. D. H. N. Truong

ARDOR Company, Ho Chi Minh City 740128, Vietnam



No.	Address	District	Photo taken	Lighting Measure	Temperature Measure
1	449/57 Su Van Hanh St., ward 9	10	x		
2	Lot 37A, Bac Rach Chiec resident area	9	x	x	x
3	157/13/10 D2 St., ward 25	Binh Thanh	x	x	x
4	135/7, Tran Hou Trang St., ward 10	Phu Nhuan	x		
5	357 Quang Trung St., ward 10	Gò Vấp	x	x	x
6	511/31 Tran Hung Dao St	1	x	x	x
8	0236/12/03 Dien Bien Phu St., ward 22	Binh Thanh	x	x	x
9	Lac Long Quan Apartment, ward 3	11	x		
10	137/14c Nguyen Cu Trinh St.	1	x		

Fig. 1 Surveyed house location map. *Source Authors*

Congress 2018 with the theme “Rethinking Sustainability with Green Walls, Green Roofs and Greening the City” held in Bengaluru, India represents a worldwide concern for roofing issues in general and the benefits of green roofs in sustainable practice in particular. Nevertheless, in Vietnam, although there are initial steps in developing standards and regulations for SH architecture, studies of the current situation on typical parts like roofs to provide appropriate solutions are limited. Little attention has been paid to the need of reanalyzing the characteristics and assessing the impacts of the roof on buildings and urban areas.

Thus, this study is aimed to evaluate the current condition of the SH’s roof in terms of architecture and building physics for the purpose of proposing solutions for a better living condition that meets future demands. This study also helps researchers, planners and policy-makers in realizing the potential for developing rooftop space and accomplishing the standards for construction and urban management.

In order to analyse the status of SH’s roof, houses from different districts and vary in style, dimensions and typology were selected. In particular, 120 houses in 10 different locations have been surveyed by direct observation from an elevated point. Then, five out of such locations are chosen to be measured the physical configuration including surface temperature and glare. The recorded information is intended to synthesize and identify the main features of rooftop architecture. Following this, it is to analyse the correlation between material, colour and the effect of heat and light radiation to inside and outside of the house. A brief description of these houses is given below in Fig. 1.

2 Overview of SH and SH’ Roof in HCMC

In the Vietnamese language, this housing type is called by various ways such as “Nhà lô” (lit., block house), “Nhà ‘ông” (lit., tube house) according to physical and typological layout. Whereas, “Nhà phố” (lit., street house) is the most popular name as it emphasizes a street front position in a busy, commercial area [3]. This is a typical type of housing in Vietnam primarily with a “tube form layout” and a “narrow frontal

facade” that can be accessed directly from a street or an alley [4]. It was built mainly in big neighborhoods and urban areas that meets the demands of residential and commercial spaces.

Roof covers the top of a building, however, it not only just protect the building from the effects of weather, but also makes a great contribution to creating the architectural appearance of each individual house on overall urban area. The roof plays an important part in forming the shape and style of the building through the correlation of material, color and the ratio of architectural components. In urban area, the viewpoint is not only limited to the ground, but it can also be captured from nearby buildings, skyscrapers at an elevated point or even from airplane. With a diverse position of view, we can easily observe the roofs of SH and somehow recognize the urban characteristics and living standards of an area. This proves the significant impact of the fifth facade of a building on urban image. In HCMC, from those high points of observation, people can see the **clutter, unevenness and inconsistency in shape, material and color** of the roof (Fig. 2). This not only affects the aesthetics and appearance of a whole area but also the comfort of the people living around.

The roof is directly in contact with natural conditions such as sunlight and rain, which makes it a shell to prevent the building against harmful agents. Thus, it is **easily affected by external factors such as weather, temperature and time**. As HCMC has a tropical climate with a hot and humid weather all year round, it is a



Fig. 2 Roof of SH in HCMC from different elevated points. *Source Authors*

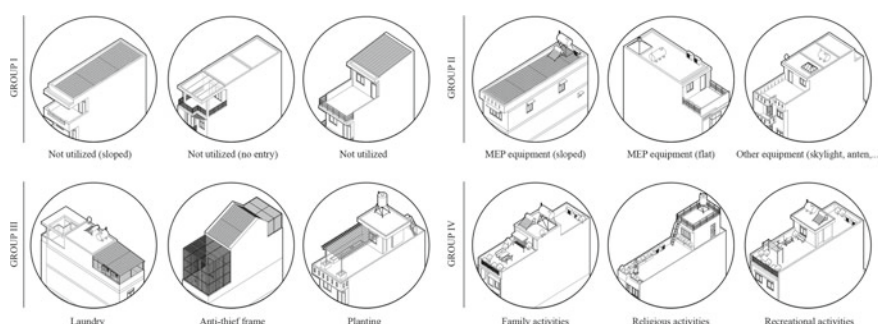


Fig. 3 Functional categories of the SH's roof. *Source Authors*

favorable condition for the development of moss, mold on the surfaces of the building, especially the roof. Therefore, the design and selection of shape and material should also be considered accordingly.

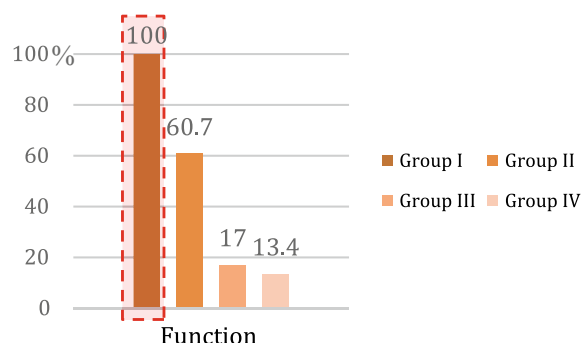
3 Architectural Identification of SH' Roof in HCMC

The usage of space upon the roof of a street house in HCMC is diverse and depends mainly on the needs of the owner. The roof is mostly used as a covering layer of a building and a space to put technical equipment such as water tanks, solar water heaters, AC outdoor units, etc. (Chart 1). These are basic functions appearing in most houses in the surveyed area. Besides, the roof also serves some essential needs of homeowners such as laundry, gardening to exploit the narrow living space in the city. Meanwhile, a few families have taken advantage of the space above the roof as a relaxing place, family activities or place of worship to improve the quality of life and increase the aesthetics of the house. However, this function only accounts for a small percentage of the survey results. Those functions can be classified into four specific groups, which are temporarily named as I, II, III, IV groups as described in the Fig. 3.

- Group I: only cover for the building, protect the building from natural conditions such as heat, rain cover, security, etc.
- Group II: space for arranging technical equipment for family activities.
- Group III: offer necessary functions in daily life, activities to serve daily needs such as laundry, storing, planting trees and so on.
- Group IV: functions that require the most artistic needs, selective activities, users have the right to choose or not to satisfy religious activities, relaxation and entertainment, improve the quality of life.

The observed results witness the potential of the roof for future vertical expansion. Based on resident's specific require, new activities can be added to create more rooms for entertainment, social interaction and even commercial purposes. In the context

Chart 1 The percentage of roof usage for 4 function groups. *Source Authors*



of intense density of over-urbanization, the rooftop space indicates a robust potential that need to be exploited in the near future.

According to statistics, there are numerous components presented on the roof. In which, the most used technical component on the roof of a SH is the water tank (about 45%) (Chart 2). At the same time, it was found that the materials used in the architecture of the SH's roof in HCMC are varied: corrugated metal sheet, concrete, brick, glass, mica, poly sheet, terracotta tiles... The survey showed that a large proportion of materials is corrugated metal sheet (Chart 3), but most of them are quite old, rusted and uneven colours. Consequently, technical utilization without proper shielding method as well as difference in using roofing materials have made a cluttered and chaotic perspective of a whole neighbourhood, which greatly affects the urban appearance. In addition, most of the urban districts in HCMC have no specific regulations to control the colours, materials and the arrangement of technical equipment for newly built and existing SH, thus creating the consistency and harmony for the space at the rooftop level is absolutely challenging. Urban planning and

Chart 2 The number components presented on the surveyed roof. *Source* Authors

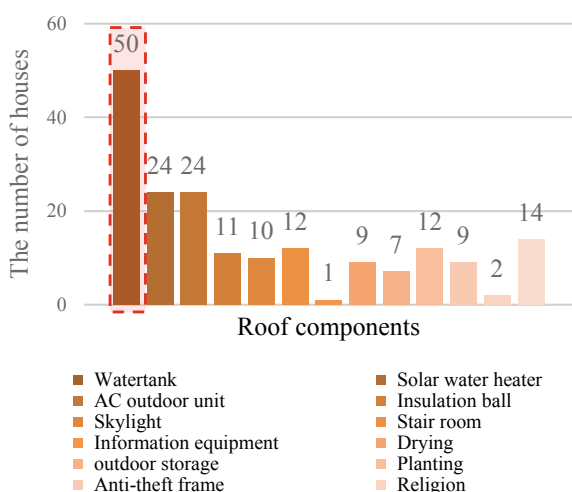
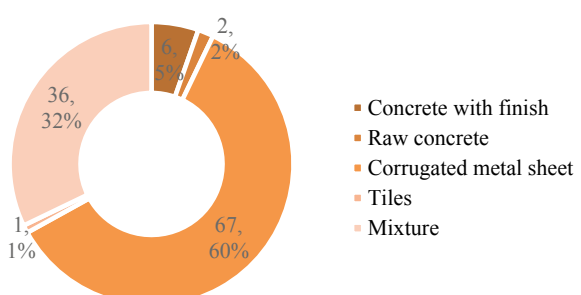


Chart 3 The percentage of roofing materials. *Source* Authors



development should focus on overcoming these issues to improve the urban image and enhance the quality of human life.

4 Thermal and Visual Comfort Assessment

The results (Table 1) recorded a disparity between different roof surface and outside ambient temperature at the same time of measurement. Different types of materials varied in surface temperature. In specific, the glass surface temperature in the skylight areas is quite high (40°C), which increases the indoor temperature (house no. 1). The results show the temperature difference on terracotta tile surface between house no. 3 and house no. 4 (8.5°C). It can be observed that the shade from a flower pergola of house no. 4 reduces the roof surface temperature while the roof of house no. 3 exposes directly to the sun. Besides, the surface temperature of the cold corrugated roofing sheet is lower than that of the rough concrete surface (house no. 2), which shows the effectiveness of this heat-resistant solution. In term of glare, the glow from stainless steel water tank area is quite dazzling, the luminance recorded is $18,000\text{ cd/m}^2$.

These data indicate that the usage of different materials directly affects the temperature of the roof surface and inside of a building. Also, materials of technical equipment impact on visual comfort of resident living around. Thus, the consideration of using appropriate covering and insulation solutions could contribute to enhance the indoor and outdoor environmental quality.

5 Proposal Solutions

In order to improve the resident living quality and urban appearance of HCMC area, some solutions are proposed based on natural, cultural and social condition of a tropical city (Table 2). The following measures are synthesized from the actual situation including the control of roofing color and material, technical equipment arrangement and green roof adoption.

First, color and roofing material management in an area is of great important to create a consistency and harmonious urban image from above. It is well-known that roof color impacts on the ability to reflect sunlight. As darker colors tend to absorb more heat radiation from the sun, the roof with a high reflectivity (light-colored materials) should be used to decrease the temperature of the air inside the building. It is to reduce the cost of electricity for air conditioning in rooms. Likewise, materials used for the roof also should be synchronously controlled, which not only creates the tidiness but also can characterize the city image. Local materials with economic and environmental benefits are highly recommended such as unburned tile and cold rolled roofing sheet. In addition, limiting the use of concrete for the roof helps to lower the urban air temperature and mitigate the heat island effect. Roof color and material management has been implemented by many countries around the world.

Table 1 Measured results of surface temperature and glare on the roof of SH

House	No. 1	No. 2	No. 3	No. 4
Address	Lot 37 A, Bac Rach Chiec Residential Area, District 9	511/31 Tran Hung Dao, Cau Kho Ward, District 1	0236/12/03 Dien Bien Phu, Binh Thanh District	135/7 Tran Huu Trang, Ward 10, Phu Nhuan District
Roofing surface temperature	<ul style="list-style-type: none"> Concrete (T1): 45 °C Card tiles (T2): 35 °C Glass (T3): 40 °C Mica (T4): 33 °C 	<ul style="list-style-type: none"> Corrugated metal sheet (T1): 36 °C Ceramic tiles (T2): 39 °C Concrete (T3): 40 °C Mica (T4): 33 °C 	<ul style="list-style-type: none"> Ceramic tiles (T1): 39 °C Glass (T2): 35 °C 	<ul style="list-style-type: none"> Terracotta tiles (T1): 30.5 °C Mica (T2): 30.5 °C Concrete (T3): 36 °C Corrugated metal sheet (T4): 43 °C

Roof sketch:

1. Sky light
2. Water tank
3. Solar water heater
4. Stair
5. Atrium
6. Corrugated metal sheet
7. AC outdoor unit
8. Vegetation

L: Luminance from water tank

Source Authors

Table 2 Proposal solutions for rooftop architecture and management

Material and color	Technical layout and arrangement	Green roof
<ul style="list-style-type: none"> - Use roof with lighter color to reduce heat absorption - Color and roofing materials should be strictly managed to create a harmonious image of urban from above 	<ul style="list-style-type: none"> - <i>Newly built house</i>: Space for technical equipment should be considered at the design stage - <i>Existing house</i>: Using shielding solutions to control the glare of stainless steel. Encouraging materials having low glare and light color to reduce heat radiation 	<ul style="list-style-type: none"> - Intensive green roof - Extensive green roof - Roof farming: hydroponics, geponics or container gardens

Source Authors

For HCMC in particular and Vietnam in general, it is necessary to strictly manage the architectural regulations for newly built SH.

Second, shielding solutions for technical equipment especially water tank need to be applied to control the glare of stainless steel to surrounding environment and cover the clutter of such items. In addition, alternative material is proposed to replace stainless steel currently being used, which encourages materials having low glare and light color to reduce heat radiation. Furthermore, space and arrangement for technical equipment should be considered in advance at the design stage.

At present, green roof has been applied by some SH, however small and uncommon. Despite higher first cost, green roof serves various purposes for a building [5]. Green roof not only provides a more aesthetically enjoyable landscape, but also help to improve the microclimatic condition inside and outside of the building as it filter rainwater and treat air. Furthermore, roof farming, such as hydroponics, geponics or air-dynaponics systems or container gardens, may provide food, temperature control, recreational activities and even ecological benefit. It is recommended that the government should have more supportive policies or incentives to promote adopting green roof widely over the city.

In recent years, the outstanding development of science and technology with new materials, new structures, and modern construction techniques has created various new forms of roofs applied in construction in different scales. While glass roof is used to exploit light and enhance interior space, green roof is a growing trend with a spirit towards nature, environmental protection and energy saving, however, lacks of uniformity. As the growing desire of residents to have a better living environment and affordability of new technology in the future as well as stricter management of the government, there are vast potentials for wide applicability of such proposal solutions [6].

6 Conclusion

The research results show that the current aesthetic status of SH's rooftop architecture in HCM City is seriously degrading. With such problems and potential that it could bring, the roof of SH deserves more concern in the context of over-urbanization and increasing demand for buildings in Vietnam. This presented study should be considered as a starting point in SH's roof research and analysis. More detailed review and investigation is needed for future proofing of this paper's findings and further conclusion. Despite limitations, this paper would contribute to provide stakeholders a "large image" of current SH's roof condition in HCMC urban area and widen their understanding about the potential for future urban adjustment at the rooftop level. The proposal solutions also makes this study helpful for the completion of regulations on architecture and construction of SH in particular and on urban management in general.

Acknowledgements This paper uses the results of the scientific research project of the group of students from HCMC University of Technology in 2018, including Nguyen Dang Hoang Nhat Truong (project leader), La Thi Xuan Vy and Le Quang Hoai, under the guidance of PhD. Le Thi Hong Na.

References

1. Truong NDHN, Vy LTX, Hoai LQ (2018) Assessment on roof architecture of street house in Ho Chi Minh City. General report on scientific research topics. HCMUT
2. Na LTH, Thang DD (2017) An analysis on architecture of street house in HCMC. Min Construct J 4(2017):117–120
3. Kien To (2008) Tube house and neo-tube house in Hanoi City. J Asian Architect Build Eng 262:255–262
4. Na LTH, Park J-H, Cho M (2013) Lessons from Vietnamese urban street houses for contemporary high-rise housing. Open House Int 38(2)
5. Haibo F, Kasun NH (2018) Benefits and costs of green roofs
6. Kristin LG, Bradley Rowe D, Philip Robertson G, Bert MC, Jeffrey AA (2009) Sequestration potential of extensive green roofs. Environ Sci Technol 43(19):7564–7570

Hanoi Old Quarter with Its Historic Tube House Transition in the Vietnam Context



Minh Hung Ngo

1 The Environmental Changes of the Heritage

Hanoi Old Quarter has been considered as “National historical relic” since 2004 (at decision No. 14/2004/QĐ-BVTT of the Ministry of Information and Culture, dated 5 April 2004) and controlled by the recent regulation on Urban Planning and Architecture (Decision No. 6398/QĐ-UBND, dated 24 Oct 2013).

Over last 20 years ago, new and modern buildings, upgrading infrastructure projects, massive destruction and renovation have made negative changes to the Quarter. Moreover, paving 11 streets, categorized into 2 groups (first commercial streets—from Hang Ngang to Hang Dao and Hang Duong; Dong Xuan to Hang Giay; second food-fair streets—from Hang Buom to Ma May, then Luong Ngoc Quyen; Hang Giay to Dao Duy Tu), is being considered and proposed by Hanoi Old Quarter Management Board [1]. From what has been gathered, it showed that top-down approach for current preservation has raised caused more pressure on local economy, quality of life and facilities than preservation of the significance and authenticity of the heritage, physically.

The area is described by William [2] as “a living tradition”, Nguyen [3] as “a living heritage” or “cultural place” [4] reflecting vernacular lifestyle, architecture and local culture. There are 79 streets and 83 residential blocks within 10 wards’ boundary (Fig. 1), which consists of tube-houses built in various periods. There are about 553 valuable buildings, which include 205 special and 348 common values [5]. Physically, there are a number of valued shop-houses required conservation and restoration urgently. The HOQ still contains five architectural styles that are Vietnamese traditional architecture (before 1900), Chinese style (before 1930), and three European forms (period 1900–1930 and 1931–1945) as considerably as the remaining physical heritage. In 2013, about 120 historical, religious and cultural relics were officially

M. H. Ngo (✉)

Van Lang University, Ho Chi Minh City, Vietnam

e-mail: Hungnm_vn@yahoo.com

Fig. 1 The boundary of HOQ (free scale, 2013)



recognized and listed [5], there is regulatory basis towards sustainable development of residential blocks that have shaped a charming and harmonious HOQ.

In fact, the attraction of economic growth and need of upgrading buildings for better life and place for tourists are happened within the HOQ. Recent observation figures out that the modern buildings are illegal, and influencing ancient ones, which are badly managed in poor quality. These new houses built with modern architectural styles (aluminium windows, doors and tinted glass curtain wall) contrasts with the traditional forms of surrounding old buildings. Furthermore, the functional units with air conditioners negatively changed the elegance and traditional architecture of the Ancient Quarter. Importantly, contemporary architectural design is unavoidable in the environment of city core, but those should be paid more attention to details of housing façade, scale and dimensions, etc.

From the findings, it shows that the blocks have been structured by typological variety of the Ancient Quarter streets. Each block contains its own features and history with diversified tube-houses as considerably as its basic cell. There are three summarized forms expressing the enlargement of the block: *firstly*, four outside directions towards the core of square street blocks; *secondly*, triple side-direction and; *thirdly*, a single direction (Fig. 2).

Meanwhile, the blocks gradually took shape with tube-houses' typologies, which expanded to the block core. Thus, these block structures reflect the history of the urban settings and tube-houses of Hanoian. With 36 old streets were established spontaneously, it existed unsuitable land-use ratio because of the land-value and parcels, which were built by private constructions in the block. Consequently, physical space for public and social activities, kindergartens, primary schools and health care facilities; dry and wet courtyards and private kitchen in one original tube-house, for instance, in the history seems to be very limited.

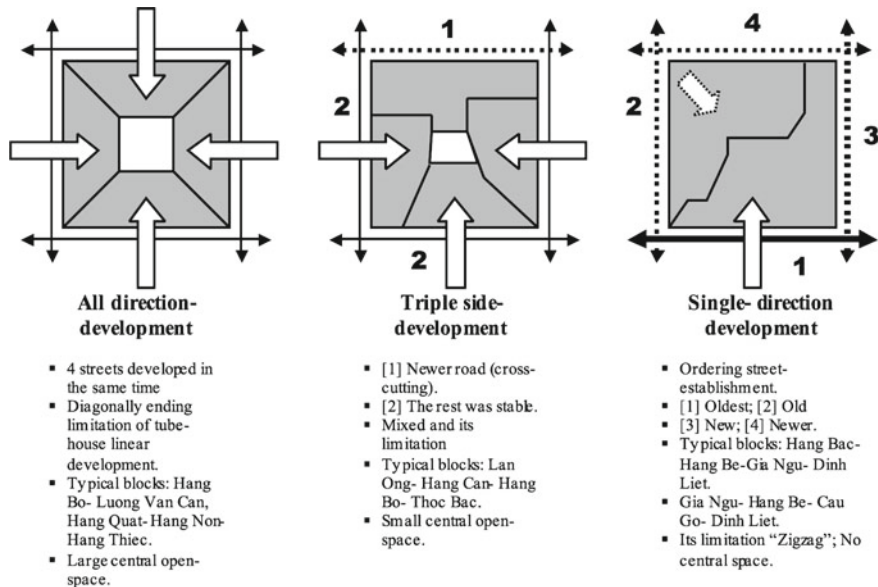


Fig. 2 Conceptual enlargement of blocks in the Old Quarter [8]

2 The Tube-House Transition in the History

Most of the tube-houses have facades from 2 to 4 m in width and depths changing from 50 to 60 m. These have been characterized as “two-access” or “one-access” tube-houses [6]. Because of its typical façade and section, the tube-house was also classified as “Chồng diêm” (heaped-up match box) style [7] in pre-1900 to 1930. This urban type is usually one or two storey in height.

Tube-house developed from early prototypes over a century ago. Its extraordinary narrow typology can be traced back to the traditional rural house, which is one room only in depth with a wide front comprising of three rooms (three-span garden house). A yard in front of the house also contains a “kitchen-house” and the toilet; a pond, forming the “heart” of the house, is located in the back. The transformation of the city from agricultural production to commercial activities was gradual. This initial step towards urbanization of the area resulted in the re-functionalizing of the house fronts as market stalls, taking advantage of the street. Subsequently, the kitchens and the toilets were relocated to the back, closer to the pond. In addition, during the pre-colonial rule (1802–1883), it was prohibited to build a house higher than the palace of the emperor. In the colonial period, the French accelerated the growth of the city by introducing two-storey buildings in the Old Quarter. The ponds were quickly filled up, while the kitchens and toilets were moved further to the rear of the land plot, producing the characteristic narrow “tube-like” effect, explaining for the nick name “tube-house”.

The tube-house, as with other forms of vernacular constructions, contains many variations. From the beginning, the tube-house was often intended for one family, generally the owner of the shop-in the front. This space was linked to the living spaces with a courtyard, followed by a “wet” courtyard consisting of a kitchen and toilets at the end. The issue of “ownership” was the primary factor in the layout-pattern. Currently, in the state-owned tube-houses, the living spaces are shared by several families. The principle of maximizing the utilization of space has exerted great pressure on the desire for privacy, inside and outside each family cluster. In the privately-owned tube-houses, the living quarters are used by families, which extended over. In both instances, the layout of the tube-houses follows a common pattern. Previously, the different parts, from the front to the back of each house, were formatted as follow: (1) shop, courtyard, altar, living room, courtyard, kitchen, toilet (or); (2) shop, living room, courtyard, room for rent, bedroom, room for eldest son or a teacher, courtyard, kitchen, toilet respectively.

As described above, the transition of the heritage environments of Hanoi city went beyond the vestiges of layering heritage objects that partially demonstrated the cultural identity of not only the native inhabitants but also of Vietnamese migrants. In addition, gentrifying the built heritage elements at the block is, sooner or later, unavoidable, more specifically, in the areas of conservation grades.

Besides, the Hanoians’ perceptions about significant functional properties of the built heritages are perhaps not as optimistic as in the previous periods. They are currently facing difficulties in their everyday lives because of the degradation of the physical settings of the sub-environments, leading to a “shifting-out” of HOQ. On the contrary, the presence of a series of buildings that are unused and kept empty and in poor conditions while new apartment building projects are no longer giving attention to the heritage users (mainly non-businessmen). Moreover, there is a layering stratification in the residential blocks: *First*, degraded block core phenomenon (after the “first layer”, which refers to space from street front to the first yard of traditional tube-houses); *Second*: increase of renovated constructions along the street front and commercial locations due to pressure from the front on second layer of the blocks and due to people’s demand in housing expansion for the sake of economic growth.

3 Concluding Remark

The built space of the Old Quarter has been changed gradually. This environmental transformation figures out cultural behaviour of the local people for architectural elements and the surfaces of such physical settings to be featured. Actually, this provides local people and community with a chance of better perception for designing partial surroundings that are more appropriate to socio-cultural and communicative activities in comparison with designed physical settings designed completely. In conclusion, the lifestyle of Hanoian made use of functional space and structures within the blocks and HOQ to develop business society, maximize the level of activity and produce traditional goods, which were arranged on each locality’s layouts.

Consequently, the built surfaces, such as facade, pavement, yards and architectural elements were able to be suitably utilized to establish functions fitting such layers of every block. In addition, multi-functional development because of accommodation limitation (transformed from cooperative ownership houses, privately-owned houses to multi-family houses) shaped various physical setting and space as which were considerable to belong “collective ownership” in many cases.

Due to these changes, the spatial structures and elements of the Old Quarter will probably be misused to cause uncontrollable influence to the heritage authenticity of Hanoi City. Lastly, understanding local community’s behaviour is a key factor to managing future change towards local built heritage and enhancing sustainable development of HOQ in the Vietnam context as well.

References

1. Trinh N (2015) Vấn nghiên cứu thực hiện lát đá phố cổ ở Hà Nội. TNO. <http://www.thanhnien.com.vn/kinh-te/van-nghien-cuu-thuc-hien-lat-da-pho-co-o-ha-noi-597985.html>
2. William SL (2005) Ancient Quarter Hanoi—a living tradition. In: Asian Ethical Urbanism—a radical postmodern perspective. World Scientific Publishing, Singapore, pp 91–102
3. Nguyen BD (2005) Bảo tồn, tôn tạo các hình thức [U+1EBF]n trúc Nhà ở - Cửa hàng trong khu di tích Quốc gia - Phố cổ Hà nội v [U+1EDB] i s nâng cao điều kiện sống cho người dân. In: International conference on “restoration of Asian and European Historic city centers: a forum for the preservation and highlighting of our heritage. 30 Nov–02 Dec 2005, Hanoi, Vietnam
4. Quynh Chi L, Thanh Tu N (2018) Street in Hanoi Ancient Quarter as cultural place: a case study of Hang Buom street. J Sci Technol Civ Eng NUCE 2018 12(3):102–112
5. HPC (2013) Decision No. 6398/QĐ-UBND about regulation on urban planning and architecture of Hanoi Old Quarter, dated 24 Oct 2013, Hanoi, Vietnam
6. Hoang HP, Yukio N (1990) The historical environment and housing conditions in the “36 old streets” quarter of Hanoi. Asian Institute of Technology, Thailand, pp 35–80
7. AusAID (1995) HPC: The old quarter local structure plan, Hanoi, Vietnam
8. Hung NM (2009) Affordances of heritage environment: a conservation approach to Hanoi Ancient Quarter in Vietnam. Ph.D. dissertation, National University of Singapore, Singapore, pp 55–87

Identifying and Assessing the Attractiveness of Public Spaces for the Youth as a Key Factor to Help Establish Social Sustainability—Case Studies from Hanoi



Quang Minh Nguyen, The Trung Doan, Quynh Hoa Ta, Manh Tri Nguyen,
Tien Hau Phan, Ngoc Huyen Chu, and Thi Thanh Hien Pham

1 Introduction

1.1 Current Situation

Just like many other cities in Vietnam and in the developing countries (also known as the Global South), Hanoi is facing a crisis of public space for all, due to the rapid urbanisation and population explosion. In fact, new and upgraded/redeveloped public spaces are planned, built and brought into use every year, but they do not keep up with the demographic growth rate and therefore fail to meet the increasing demand of the city residents. In some districts and wards, local people are happy about the well-designed and well-equipped parks and/or community gardens offered to them, yet those places are always crowded. In some other district and wards, there are many public spaces, but not frequently used, as they are rather poor and/or not very safe. In several living quarters, the inhabitants complain about both the quality and the quantity of public spaces, especially in social housing projects.

Public space plays a very important role in making a city work. Walking down the street, talking face-to-face with neighbours, meeting friends in cafés or beer gardens, playing sports together, etc., which generally take place in public spaces, are all basic daily life needs. In a post-industrial society, people tend to be busier with their work calendars, study courses and family affairs. They work harder in the offices, travel more extensively on the roads, stay longer at homes and spend more time surfing numerous websites, but they also need to go out at least a few times a week and do some outdoor activities in order to be healthier and regain the balance.

Q. M. Nguyen (✉) · T. T. Doan · Q. H. Ta · M. T. Nguyen · T. H. Phan · N. H. Chu
Faculty of Architecture and Planning, National University of Civil Engineering, Hanoi, Vietnam
e-mail: minhnq@nuce.edu.vn

T. T. H. Pham
Department of Urban Studies and Tourism, University of Québec at Montreal, Montreal, Canada

A number of research projects conducted by both Vietnamese experts and international scholars in recent years have reflected various aspects of public spaces in Hanoi and shown some problems to solve as follows:

- Lack of water bodies: As an essential component of public spaces in Hanoi water surface decreased quickly while public gardens and parks increased considerably [1].
- Accessibility: All the public areas should be planned within a short walk from homes, with 53% of the respondents choosing to walk and 13% of them preferring to go by bike [1].
- Poor facilities: The number of interviewees who rated the quality of facilities “average” and “poor” would be 32% and 21%, respectively [1].
- Low level of liveliness: 18% of the residents asked said that it was low, 50% judged it to be “average” and only 32% regarded it as “good”. Nearly 55% of the interviewees go to public places to participate in physical activities, about 32% wanted to relax and the rest (13%) for other purposes. An in-depth interview was carried out on 60 volunteers and one third of them did not go there very often (once a week or every two weeks), one fourth of them went alone while one third was accompanied by small groups of friends. In most cases, they stayed there less than three hours [1].
- Gender imbalance among users: Young women are sometimes absent, because of gender-related issues in using public spaces [1].
- Illegal occupation of public spaces: This can be seen in both old and new living quarters, in the city centre as well as in the suburbs. Children and teenagers have almost no playgrounds [2].
- Incompetent management: The top-down management of street space is often too rigid to respond to the changing needs of citizens, and they have to act “creatively” in using public spaces that should belong to them, but somehow they are not allowed to do so [3].

Consequently, many settlements are not liveable. Thus, it is imperative to undertake more investigations into public spaces in Hanoi and other major cities in Vietnam, in terms of quantity and especially quality.

1.2 *Literature Review*

Public space has been quite comprehensively investigated worldwide over the past 20 years. Architect Jan Gehl, in his famous book “Life between Buildings”, classified outdoor activities into three types: necessary, optional and social activities. Social activities are activities that depend on the presence of others in public spaces, such as children at plays, greetings and conversations, communal activities of various kinds and finally seeing and hearing other people. Social activities occur in many places throughout a living quarter as well as the city and are called “resultant” activities, as they evolve from the other two categories. Social activities come mostly from optional

activities and happen spontaneously as a direct consequence of people moving about and staying in the same spaces, and are indirectly supported whenever necessary and optional activities are given better conditions in public spaces. In addition, social activities are a self-reinforcing process, and social distance of 1.3–3.75 m should be noted in design. In public spaces, people can assemble or disperse, integrate or segregate, be invited or repelled, open up or close in, depending on the quality of design as well as activities organised [4].

Helen Willey took a closer look at public space and analysed the four benefits that a public space with active recreational activities can bring: (1) Social benefits (with focus on community life and culture); (2) Health benefits (both physical and mental health); (3) Environmental benefits (including climate, ecosystem and wildlife) and (4) Economic benefits (job opportunities and income). In her opinion, public spaces should be open to all and make a major contribution to social equity through various kinds of communication and cooperation [5].

Matthew Carmona emphasised “a sense of place” when he talked about public spaces. At first, people must understand a place through its history and culture, form and image. Then they will feel a sense of belonging and be emotionally attached to that place. The human activity refers to diversity and vitality on a basis of events, culture and local traditions [6]. Public spaces can have a positive impact on property prices, trade, land value and investment as well as regional economic performance. If planned into a system, they help boost social contact by providing more learning opportunities for children and juveniles through creative plays, nurturing their social and cognitive skills, reducing incidents of crimes and anti-social behaviour, promoting neighbourliness and social cohesion, offering a venue for social events and interchanges, and finally supporting the local community life. In order to ensure the quality, public space must be well-designed and well-managed [7].

The UN Habitat published a Toolkit for Public Space as part of the Global Agenda towards Sustainable Urban Development, in which public space is interpreted as the banner of urban civility, promoter of equity, our commons towards urban prosperity, driving force of great cities, ideal opportunities for citizen involvement, producer of environmental sustainability, generator of income, investment and wealth creation. The main idea is that cities become great when they develop great public space systems with attractiveness of public space as a key point. In this global review, public space is upgraded to a Charter (Charter of Public Space) and redefined/reconfirmed as “all places publicly owned or of public use, accessible and enjoyable by all for free and without a motive for profit”. The essence of public space includes accessibility, no-cost policy, improvement of the quality of urban life and an integral part of urban architecture as well as landscape along with a determinant role in shaping the overall image of a city. There are 16 types of public space: (1) Avenues, boulevards and streets; (2) Bicycle paths; (3) Squares; (4) Pavements/sidewalks; (5) Passages; (6) Highways and highway corridors; (7) Riverbanks and waterfronts; (8) Parks; (9) Gardens; (10) Playgrounds; (11) Sports fields and facilities; (12) Beaches; (13) Museums and galleries; (14) Public libraries; (15) Civic centres and (16) Municipal markets [8]. Public space offers the following 12 services: (1) Protection against traffic accidents; (2) Protection against crime and violence; (3) Protection against unpleasant

sense/experience; (4) Possibilities for walking; (5) Possibilities for standing; (6) Possibilities for sitting; (7) Possibilities for seeing; (8) Possibilities for hearing/talking; (9) Possibilities for playing; (10) High-quality social services; (11) Comfortable climate and (12) Positive experience [9].

Alessandro Rigolon argued that socio-economic-status (SES) review and urban green space (UGS) index should be used to assess the quality of public space in the Global South cities, because both SES and UGS are fundamental elements of sustainable, healthy and liveable cities in those countries where development goals are often largely affected by economic difficulties and social issues as the direct consequences. Analysing equity in the provision of UGS in the Global South cities matters for at least three reasons: first, rapidly growing cities might not be adequately planned for green spaces, thus leaving a majority of the population underserved; second, informal settlement that are common in many regions generally lack urban green spaces and other basic public services; and third, people in many developing countries have relatively shorter life expectancy than those in the Global North. This fact can however be improved by increasing access to health-promoting environment, such as green spaces. Proximity is described as part of quality of public/green space. The findings suggest that by enhancing proximity, quantity and quality of green space, it would be possible to ensure health benefit for the public in the Global South cities, if all SES groups had equal access to it [10]. Equity as an aspect of public space is also advocated and supported, no matter where it may happen, in the Global South or in the Global North. The quality of public space contributes immensely to the city's liveability and international competitiveness. Public space works best when it does not offer intended uses, but rather provides equal opportunities for different groups of people to make use of it in a way that suits them, which can be seen in the motto "place for everyone". This principle shall be applied first to high-density urban areas where a hybrid style for inclusivity, efficiency, cost effectiveness and liveability needs to be incorporated in all development and redevelopment programmes. The six types of main public space (main streets, promenade routes, districts with some special features and identity, transportation hubs, city open markets and central city parks) could be chosen as case studies for the reconceptualisation and revitalisation of public space [11].

1.3 Research Objectives

Public spaces in Vietnam's major cities, particularly in Hanoi, should be more intensively investigated with specific case studies with particular factors and conditions, rather than in general. With these in mind, the research team aims to:

- Understand how a public space works and interacts with different groups of users, especially the youth (aged from 16 to 30) in reality;

- Find out what attracts the youth the most or what they expect from a public space, and recommend that these factors of attractiveness should be integrated in urban design;
- Improve the quality of a public space in terms of re-designing the space and re-organising the activities;
- Help consolidate social contacts/relations and achieve social sustainability in each living quarter as a basic unit of urban studies.

1.4 Research Methods

In order to reach these objectives, the following research methods have been used in Phase One of the group's research project:

- Site survey and observation;
- Data analysis;
- Case studies;
- Mapping.

2 Public Space in Hanoi—A Review from Five Case-Study Wards

As stated above, public space in view of spatial design and activity should be examined (practically considered) case by case—in a comparative study among several living quarters, rather than just theoretically analysed, in order to find out similarities as well as common problems, and to highlight differences simultaneously. Attractiveness of the local public spaces in the opinion of the youth—as a very important factor—is emphasised. In this regard, five wards have been selected as case studies (Table 1).

In total, 94 sites have been systematically surveyed on one weekday and two weekend days. The five wards selected are presented in chronological order and quite typical for the urban development in Hanoi over the past five decades. Truong Dinh ward is characterised with an early socialist housing programme by the state based on 2.0 industrialisation as a driving force in the blueprint of the French urban planning while Chuong Duong ward is noted for spontaneous urban development with self-built family houses shortly before and after the Economic Reform came out (in late 1986). My Dinh 1 is an outstanding example of project-based housing development plan closely connected with large-scale urban public buildings (National Sports Centre). The other two wards (Thuy Phuong and Sai Dong) are adjacent to

Table 1 Data of five case-study wards (Hanoi Statistical Yearbook 2017, 2018)

Ward	Truong Dinh	Chuong Duong	My Dinh 1	Thuy Phuong	Sai Dong
Land area (ha)	39	103	228	287	91
Population (2017)	23,000	22,000	26,000	15,000	16,000
Population density (residents/ha)	590	214	114	52	176
Location	Inner city	Inner city	Periphery	Periphery	Outlying
Major urban development period	In the 1970s	In the 1980s	In the 1990s	In the 2000s	In the 2010s
Original status	Mixed urban residential area	Mixed urban residential area	Village	Village	Village
Level of urbanisation	Very high	Very high	High	Medium	Medium
The number of public spaces surveyed	26	20	18	18	12

new industrial zones in the 3.0 era and becoming more and more populous with thousands of migrant workers either settling in dormitory buildings or renting villagers' houses (Table 2).

In general, as the statistics have shown, the number of groups of residents using public spaces on each of the three different days of the week did not change (in My Dinh 1 ward) or did not change so much (in the other four wards). In all the five wards investigated in the survey, there is a vast difference between the two groups of young public space users (local and migrant), except for migrant students in two wards (Truong Dinh and My Dinh 1), because migrant students have more free time, especially in the evening and at the weekend. They are active to share the public spaces available with the local inhabitants. Other migrant groups, on the contrary, work from 7 am to 8 pm or 9 pm, and have therefore almost no time nor in the mood to go to public spaces. They tend to spend the evening on their own, with their roommates or within a closed group of their country fellows. On Sunday, they cook together or to go back to their home towns/villages within 50–60 km and visit their family members there. Although the public spaces in these five wards vary in size, density, frequency of use, etc., they have two things in common: (1) Spontaneous development if privately organised or delivered and (2) Uneven distribution as a consequence of lacking a long-term planning vision [12] (Table 3; Fig. 1).

In Truong Dinh ward, thousands of boarding students from the National University of Economics and the National University of Civil Engineering form a majority of

Table 2 Characteristics of public spaces in five case-study wards [12]

Ward	Truong Dinh	Chuong Duong	My Dinh 1	Thuy Phuong	Sai Dong
<i>Type of public space</i>					
A. Streets with pavements	21	13	05	06	02
B. Official public spaces (public parks and gardens, playgrounds)	–	03	04	04	06
C. Yards within religious buildings (temples, pagodas)	–	01	03	02	–
D. Vacant land plots for other purposes temporarily used as public spaces	–	–	01	–	–
E. Sports fields (football, volleyball, tennis, etc.)	04	02	04	02	–
F. Others (school yards, office yards used after 6 pm as additional public spaces)	01	01	01	04	04
Total	26	20	18	18	12
<i>Groups of users (weekday)</i>					
Used by youth only	12	04	00	01	00
Shared by youth and others	02	07	11	11	06
Not used by youth	12	09	07	06	06
Total	26	20	18	18	12
<i>Groups of users (Saturday)</i>					
Used by youth only	12	01	00	00	00
Shared by youth and others	03	09	11	07	05

(continued)

Table 2 (continued)

Ward	Truong Dinh	Chuong Duong	My Dinh 1	Thuy Phuong	Sai Dong
Not used by youth	11	10	07	11	07
Total	26	20	18	18	12
<i>Groups of users (Sunday)</i>					
Used by youth only	15	02	00	01	00
Shared by youth and others	02	08	11	07	04
Not used by youth	09	10	07	10	08
Total	26	20	18	18	12

Table 3 Characteristics of public spaces in five case-study wards [12]

Ward	Truong Dinh	Chuong Duong	My Dinh 1	Thuy Phuong	Sai Dong
<i>Youth (aged 16–30)</i>					
Local young people	x	x	x	x	x
Migrant students	x		x		
Migrant workers				x	x
Migrant manual labourers	x	x			
Migrant street vendors	x	x			

public space users. Their most favourite public spaces include street restaurants and pavement iced teashops near their dormitory buildings. They also share two nicely designed open-air cafés and two out of three sports facilities in the area (except the tennis court) with local young residents after 6 pm on five weekdays, early in the morning and after 4 pm on two weekend days. The most outstanding purposes of public space use are drinking, eating and sports training. The precincts of two religious buildings in this area (one church and one pagoda) are not opened for public use.

In Chuong Duong ward, there are many migrant manual labourers and street vendors. As aforementioned, most of them have to earn their living all day and just return to their homes/rental houses very late, even on two weekend days. Therefore, they do not participate often in the local communal activities. Public spaces here are narrow streets and pavements with many small shops or some yards within old residential blocks mostly used by young permanent residents along with middle-aged

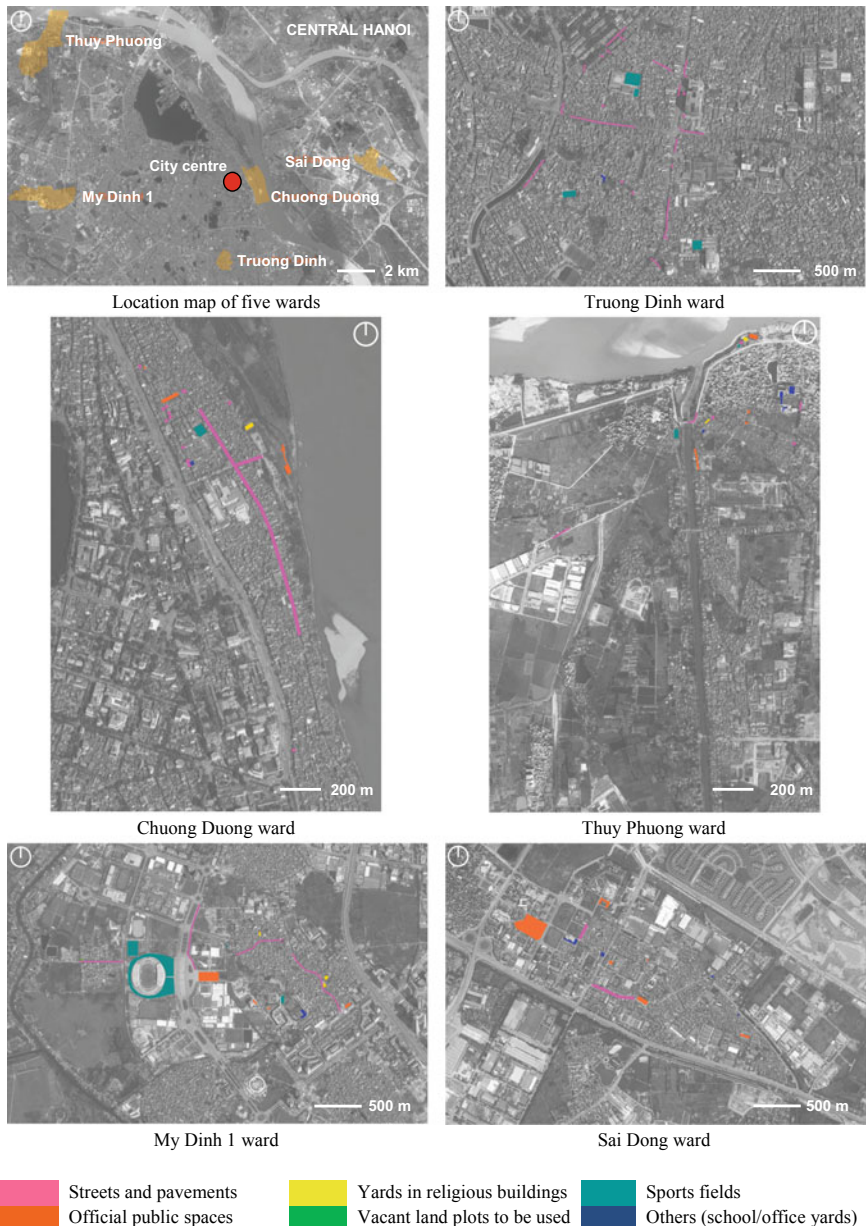


Fig. 1 Types of public spaces in five wards and their distribution [12]

and senior people. The most exceptional public space in this ward is a large open land area located on the riverbank overlooking the Red river used as an ideal playground for children and juveniles, as well as a favourite meeting point for the youth who love farming and photography.

In My Dinh 1 ward, just like in Truong Dinh ward, the public spaces are shared between young permanent inhabitants and migrant students of Vietnam National University and the University of Social Sciences and Humanities. Young people living here, especially migrant students, enjoy a very large square around and a well-designed park in front of the National Stadium. They can also make use of many small shops in several streets nearby. The most important activities here are walking, sitting and chatting, relaxing, eating and drinking.

In Thuy Phuong ward, most of the public spaces available are rather small. However, they are quite diverse, since this is a newly urbanised village, with one temple yard, one communal house front yard, four public parks, one football field, one playground for children jointly invested by the local authority and community, three school yards which are opened after 6 pm for local children to play football and even for some adults to play badminton. But only a few migrant workers go there. Many pavement shops can be found here like elsewhere.

In Sai Dong ward, similarly, there is a community of migrant workers living next to villagers. Some of them are living in rental houses provided by local residents. These migrant workers just go out for a walk in the evening around their houses. In the meantime, those living in dormitory buildings offered at reasonable prices by the industrial zone management unit enjoy relaxing and communicating with one another in open spaces and small flower gardens in the middle of their residential blocks as the first meeting point. A few more options, such as office yard, police station yard and schoolyard, are primarily used by local permanent residents.

Activities	Ward				
	Truong Dinh (26)	Chuong Duong (20)	My Dinh 1 (18)	Thuy Phuong (18)	Sai Dong (12)
0: None	0	0	0	0	0
1: Very few	1–5	1–4	1–3	1–3	1–2
2: Some	6–9	5–7	4–6	4–6	3–4
3: Quite many	10–15	8–12	7–10	7–10	5–8
4: So many	16–26	13–20	11–18	11–18	9–12

In all five wards, talking/chatting is the most popular activity, taking place throughout the day in public spaces. This kind of activity does not require so much space or any special context, even a small street corner or a narrow pavement with a few square metre iced tea shop can be just enough for a few people to meet and have conversations. Such an “informal” space is ubiquitous in the city, except in some compounds. The second most popular activity is drinking/eating, most notably in Truong Dinh, Chuong Duong and My Dinh 1, even in the other two wards—Thuy Phuong and Sai Dong, where many residents are migrant workers with low income, thus preferring to cook at home instead of eating out. It is apparent in most cases that there is no big difference (three grades) in the number of activities in each category (from No. 1 to No. 9 in Table 4) between one weekday and two weekend days.

Table 4 The use of public spaces for different purposes in five wards among site studies [12]

Interestingly, Thuy Phuong tops the list in the number of sitting/relaxing activities (category No. 2), thanks to the beautiful waterfront landscape, four public parks, one pagoda and one traditional community house with a large yard and so many shade trees. In terms of sports training (category No. 3) and special activities (category No. 9), My Dinh 1 outperforms, because many sports facilities are open to the public. Moreover, a well-planned public space system invites people to take part in various special activities, such as pop/rock music concerts, propaganda campaigns and action programmes for the environment, etc. which often attract a large number of students and youngsters.

Note: In consideration of the quantity of public spaces in each ward, the level of use per space for grading the frequency of activities should be adjusted to ensure equivalence as follows:

3 Quality Will Definitely Become an Essential Issue

Apart from quantity, quality of public space has always been a great concern to the community. People decide whether or not they should go to a public space in consideration of the quality it offers. In terms of quality, a wide range of factors will be taken into account. Based on the observation of the most frequently visited public spaces in the five selected wards, a good public space must be well-designed and well-equipped (Table 5).

Table 5 Physical aspects of a good public space [12]

Design	Equipment/facilities
Hard and soft ground cover (permeable for rainwater)	Park benches and other kinds of seats
Decorative lighting at night and on special occasions	Trash bins
Water surfaces	Lighting systems
Walk ways	Watering systems
Shade trees and ornamental plants	Other technical systems (parking, firefighting, etc.)
Artworks (sculptures, mosaic wall pictures, etc.)	Sports facilities (for adults)
Kiosks and pavilions	Play facilities (for children: swings, see-saws, etc.)

4 Attractiveness Should Be Regarded as Another Crucial Issue in Organising Public Spaces

In addition to the above-listed components of quality, people as users, especially the youth, pay attention to the following nine factors: safety, accessibility, diversity, flexibility, convenience, comfort, friendliness, inclusive services and interactive/creative atmosphere. Each factor contributes to the overall concept—attractiveness (Table 6; Fig. 2).

For young migrant people in five wards, a no-entrance-fee and no-fence public space policy, particularly adopted and/or supported by private developers, is an

Table 6 Attractiveness of a public space from five study cases [12]

Component of attractiveness	Interpretation
Safety	No injury or accident happening, including security (no threat/violence)
Accessibility	Easy to access for all people. Centrally located and/or evenly distributed
Diversity	Many mini-spaces are combined. Many different activities are organised
Flexibility	One space can be suitable for many people and activities
Convenience	Easy to use all the equipment/facilities available
Comfort	Pleasant feelings. Protected from excessive sunlight, rain, hot/cold winds
Friendliness	Easy and happy to make contact and communicate with people
Inclusive services	Meeting the demands of the public (playing, drinking, relaxing, etc.)
Interactive and creative atmosphere	Ready to exchange and share with other people. Encouraging arts/talents



Fig. 2 Informal but preferred public space in Hanoi, where attractiveness means crowded, chaotic and happy to many migrant young people and even local permanent residents. Taken by NUCE students, 2019

important feature of an attractive public space. They tend to choose “informal” public spaces with “popular” services, primarily pavements with tea and vermicelli stalls, street cafés and mini-parks, where they sometimes just need a place underneath a shade tree to sit and relax for hours. Another option is vacant land temporarily used by the local communities as a playground or a sports field. In their opinions, “attractive” means “crowded and happy” in short, even when it goes without basic facilities for public use [12].

Among these nine factors of attractiveness, diversity and flexibility should be understood in both spatial design and organising activities. A small public space will look nicer with several design concepts for the foreground and background, corners and sides. It is advised to combine water surfaces and green areas in semi-public and public places in view of creating better landscape and maximising the cooling effect against the urban heat island effect in a densely constructed city like Hanoi. Simple facilities, such as trash bins or park benches, also require new designs rather than *déjà-vu* patterns, if urban designers really think about users first. Similarly, a variety of activity scenarios can be developed for each case study, so that different groups of users can share the space at the same time and all of them would like to go there several times a week. Each time, they will find something new and interesting in the activities organised. Creating an interactive and creative atmosphere is a new idea, enhancing the attractiveness of a public space, especially when the creativity is emphasised as a key factor. Then, not only professional but also amateur artists in the community will have the opportunities to contribute their talents to the spatial design with their installation artworks which can change over time and intensify the interactions between artworks and users, as well as among users. In fact, this has been successfully applied in many countries worldwide, as seen in the Top 20 liveable cities like Vienna, Melbourne, Copenhagen, Toronto and Tokyo, and also penetrated into Vietnam in recent years, promising to be a future development trend. The Creative City project in Hanoi has already demonstrated this potential.

5 Conclusions

In five wards investigated in the survey conducted by NUCE academic staff and students, it is noted that even the best public spaces to date have not yet been able satisfy the urban design and social planning requirements, as far as living quality and social sustainability are concerned. Key factors to attractiveness of public spaces, such as safety, accessibility, diversity, flexibility, convenience, comfort, friendliness, inclusive services and interactive/creative atmosphere, will soon be regarded as fundamental criteria and incorporated into rating systems. The quality should be offered to people from all walks of life and also targeted at migrant young people, because they have made major contributions to the socio-economic development and socio-cultural diversity of a city, and thus they have the right to use well-designed and well-organised public spaces with all the services available to improve their spiritual

lives and succeeded in integrating into the local communities. Hereby it is possible to establish and achieve social sustainability as an ultimate goal of urban development.

Acknowledgements This academic paper has been written as a summary of Phase One (2018–2019) within the framework of a large research project called TRYSPACES with four participating cities over three continents: Montreal and Mexico City (North America), Paris (Europe) and Hanoi (Asia). The National University of Civil Engineering (NUCE) is a member institution based in Hanoi (Vietnam). The authors would like to thank the National Institute of Scientific Research of Canada and Canadian Research Council in Social Science for the generous support, not just financially. Our special thanks also go to the NUCE students as well as other collaborators for the site surveys and data collection in Phase One of the project.

References

1. Boudreau JA, Labbé D, Geertman S, Charton L, Pham TTH, Dang NA (2005) Hanoi youth public space. In: Social Sciences and Humanities Research Council of Canada (SSHRC), pp 15–17
2. Tran THG (2015) Old villages and new streets—stories about public space: public space system in Trung Hoa—Nhan Chinh new town. *J Constr* 74:52–53 (Ministry of Construction, Hanoi)
3. Ta AD, Manfredini M (2016) The production of plural evolutionary spatialities: conclusions and complicity between public and private space in the streets of Hanoi, Vietnam. In: Proceedings of CDUD16 international conference on planning cities, the past and the future, Istanbul. <https://www.researchgate.net/project/The-production-of-plural-evolutionary-spatialities-Collusions-and-complicities-between-public-and-private-in-the-streets-of-Hanoi-Vietnam>
4. Gehl J (2001) Life between buildings. Danish Architectural Press, pp 11–14, 17, 71–75, 83–123
5. Willey H (2005) Urban open space and active recreation. Taylor and Francis, London, pp 12–74
6. Carmona M, Heath T, Oc T (2003) Public places urban spaces. Architectural Press, London, pp 96–99
7. Carmona M, de Magalhaes C, Hammond L (2008) Public space (the management dimensions). Routledge, pp 2, 6–9
8. Martinez-Bäckström N, Petrella L, Garau P (2014) Public space in the Global Agenda for sustainable urban development—The Global Public Space Toolkit. UN Habitat report, pp 17–25, 29–31, 39, 48
9. Gehl J (2010) Cities for people. Island Press, Washington DC, p 239
10. Rigolon A, Browning B, Lee K, Shin S (2018) Access to urban green space in cities of the Global South. *Urban Sci* 2:67. <https://doi.org/10.3390/urbansci12030067>
11. To K, Nakaseko A (2017) Public space as a key drive towards liveable cities for all. In: Proceedings of 2017 international conference of Asian Pacific planning societies. https://www.academia.edu/37631446/Public_Space_as_a_Key_Drive_towards_Liveable_Cities_for_All
12. Nguyen QM, Doan TT, Ta QH, Nguyen MT, Tran MT (2019) Survey of five wards (Truong Dinh, Chuong Duong, My Dinh 1, Thuy Phuong and Sai Dong)

Public Park Behavior Relationship in Danang: An Impact of Physical Environment on User's Behaviors



Duy Thinh Do and Thi Vy Phuong Vo

1 Introduction

1.1 Background

Endeavors in improving quality of life in urban area have obtained certain achievements in terms of theory and practical results. An assessment framework with more informed, coherent and transparent evaluation method has been proposed with the aim of measuring different parameters involving multiple disciplines. The disciplines include health and safety, happiness, transportation and services, environment and surrounding spaces and biodiversity, and so on [4]. Other quantitative approaches, urban indicators (e.g. green landscape, urban sprawl, fragmentation, spatiotemporal) and density are also considered in identifying urban problems[5]. Therefore, developing, improving environment should consider taking account into environment-behavior objective, psychological, scientific and comprehensive manner that contributes an opportunity to develop a cumulative body of knowledge for evidence-based design [10]. Urban public space is a key factor in achieving the quality of life in urban areas with high densities of buildings and population [6]. Urban open space has been studied as to its uses, purposes and perceptions of citizens that can be a fundamental basic for sustainable city-developing. In Asia, research on relationships

D. T. Do (✉)

Architecture Faculty, Mien Tay Construction University (MTU), Vinh Long, Vietnam
e-mail: doduythinh@mtu.edu.vn

T. V. P. Vo

Civil Engineering Department, University of Technology and Education – The University of Da Nang, Da Nang, Vietnam

between physical factors in spatial environment and users' behaviors is of interest to scholars as well. Notably, Neto et al. [8] discovered impacts of physical factors on users' impression about public space and proposed the prediction model of desire to stay and rest in public spaces [8]. Zeng (2018) investigated relationships between children's behaviors and residential landscape elements [13]. Do (2018) studied physical elements set up along the street space that drew the attention of pedestrians [3]. The government attempts public space planning solutions to increase the area of urban open space such as upgrading the existing parks, streets and pseudo-public space. Indeed, there are not many parks in urban areas, most of which are district parks and serve daily activities of the people. Currently, the already proposed solution for district park is simply arranging benches, providing children's playgrounds, lawns, putting up such artistic statues as carved stones, huts or fitness equipment to attract people's access. There is a question about the efficiency of these plans that remain unclear as too much public open space has yet to be used and fully exploited [7]. While Vietnam is located in Asia, it has the different society, cultures and economy; thus, it is difficult to develop a standard development model for all Asian countries. The understanding of problems and feedback mechanism to environment use still depends on each country for its development [11]. In Vietnam, studies on such relationships have yet to be well known, and most scholars just pay attention to research on theories about space landscape planning in a large scale [7]. The gap between theory and practice are still vague, there are no established, technical standards or specific instructions on methodology as the basis for planning and design in practice. Almost no research on the interaction between user's behaviors and environment, especially public open space, is conducted. Indeed, given approaches to the development and improvement of open space, especially places that have been recently upgraded, have yet to be evaluated and examined in practice. Hence, this research attempts to fill the knowledge gap for the development of urban open space in Vietnam. More specifically, this study aims to discover physical setting characteristics of a district park and the users' behaviors. Analysis is made to provide the correlative evidence for relationships between environmental factors and behaviors in this space by providing a prediction model of physical elements that affect user's satisfaction. This study contributes towards the understanding of user-environment interaction mechanisms in the park. This understanding helps urban designers/planners develop evidence-based designs and minimize the difference between practical effectiveness and expectation for Vietnam.

2 Materials and Methods

2.1 Object of Study

Da Nang is the third largest city in Vietnam. With the high potential growth of economy, Da Nang population is predicted to double to approximately two million

in 2030. The authors chose 29-3 Park located in Da Nang as a large open space for study. This district park is located in Thanh Khe district with the area of over 20 hectares and established after 1975. It is the largest and oldest public open space in Da Nang; the park has various distinct sections for recreational, cultural and sporting activities. This space has been historically upgraded and renovated several times, most recently in 2014–2015. Generally, among all existing green, open space in Da Nang, 29-3 Park is a useful to, and accessed by, residents across the district whom undertake a wide range of activities; and also a local gathering place for nearby residents (Fig. 1a). 29-3 Park plays an important role as a pilot model for other development projects. It is with the usage characteristics mentioned above, the place is considered a suitable case for this research.

2.2 *Outline of Investigation*

The observation was conducted within 29-3 Park from October 14th to November 11th, 2018, with the aim to understanding all the park's users in term of their behaviors and surrounding environments. Observers were assigned and recorded all activities on paper-based map by using the place-centered behavior mapping method [12]. In addition, all physical elements of the park were also investigated and measured based on the encounter survey method and remote sensing technology in measure greenery cover by using satellite image (Two Landsat 8OLI) [2, 9]. The survey was undertaken at four different times: (1) Morning (6:00 a.m.–10:00 a.m.), (2) Noon (10:00 a.m.–2:00 p.m.), (3) Afternoon (2:00 p.m.–6:00 p.m.) and (4) Evening (6:00 p.m.–8:00 p.m.). Survey data of two weekdays and two weekend days were collected to check the objectivity of the survey. Owing to complex features of the space and its boundary, user's behaviors can be affected by various environment factors. The behavior setting can be defined by the boundary of space characteristics and space functions. A total of 19 sections were included and specified in Fig. 1b; (1) First zone was split into seven sections, (2) second zone with seven sections, (3) Third zone with two sections, and (4) Fourth zone with three sections based on characteristics of initial environmental characteristics such as functional, topographical area within each zone. In addition, other information of each section was captured (Fig. 1b). Although there is a different use pattern in various events in this park, people mainly use the park for their daily activities. Therefore, this study focuses on understanding relationship between users' daily activities and physical environments in the district park. The research frame work is illustrated in Fig. 2 identifying the connections between the procedures in the research.

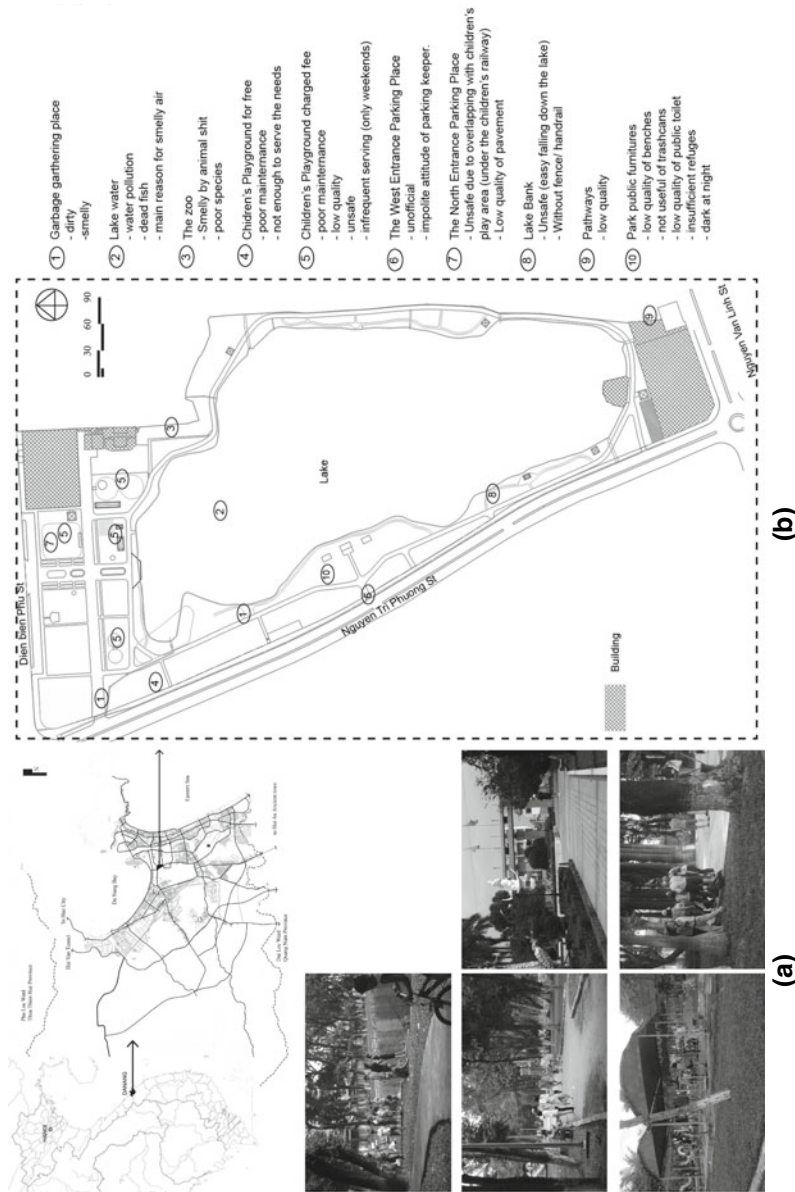


Fig. 1 Investigation profile of 29-3 Park: a location and overview; b section division of landscape and information

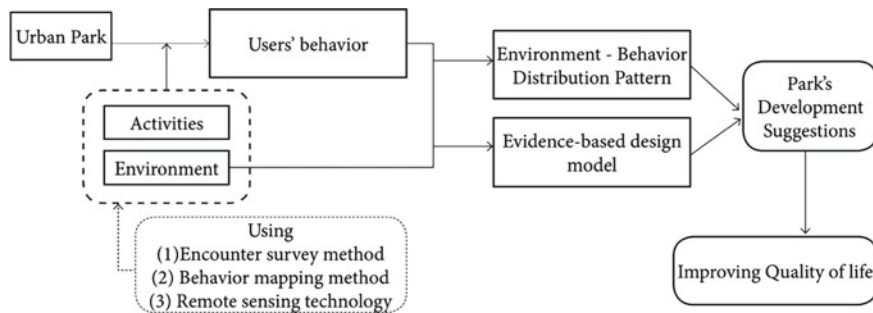


Fig. 2 The research framework diagram

3 Results and Discussion

3.1 Behavior Characteristics of Users

All user's behaviors were collected and classified into main and sub categories as listed in Table 1.

As the main focus of the study involving user's behaviors and surroundings, the maintenance/service activities carried out by staffs such as taking care of plants, cleaning, selling food or beverage, and guarding the park are considered out of the study scope. The results showed that most of the user's activities in the park were for (1) relaxation (e.g. Fishing, Strolling, and Idling), (2) health-related (e.g. Doing exercise, and jogging) and (3) social interaction (e.g. Children playing, Chatting, and Couple Dating). This finding identified the significant role of this open space to daily activities, especially recreational ones, of local residents. Although various previous studies of other countries involving urban parks indicated that the district park are more related to weekend and holiday activities (e.g. picnicking) compared to small parks next to residential, this finding shows that, in context of Vietnamese city, most people tend to participate in this district park for their daily activities and relaxation due to the lack of residential parks in surrounding residential areas. There are obvious differences between behavior categories and their frequency recorded in various sections that was explained the next part of this paper.

Table 1 Categories of user behaviour found in the park

Health-related	Social interaction	Recreation	Service
Doing exercise	Children playing	Walking baby	Maintenance
Jogging	Couple dating	Watching animals	Selling
Doing Taichi	Camping/picnic	Idling	
	Chatting	Strolling	
		Fishing	
		Resting	

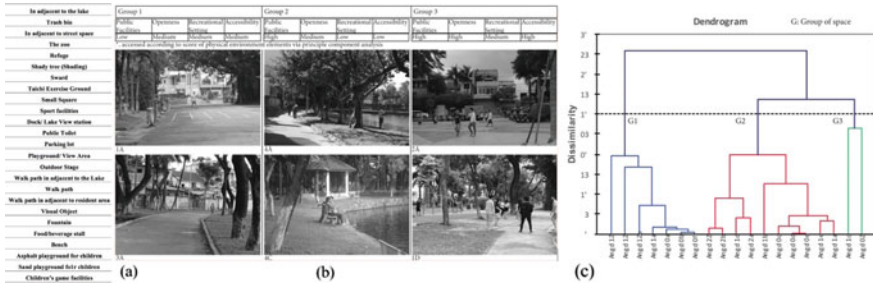


Fig. 3 Physical environment characteristics analysis: **a** park physical elements; **b** characteristics of three space groups based on score of physical elements analysis; **c** three kinds of space deriving from CA

3.2 Spatial Environment Analysis Based on Physical Setting Characteristics

Physical Environment features such as amenities, interface, the relative boundary of the space, functional physical elements, shady trees, lawns or pavement were counted and tabulated (Fig. 3a). The data of those characteristics of this space were analyzed by Principal Component Analysis; accordingly, the cumulative contribution rate shows that the hefty 83% means if the data are represented from the 1st to the 4th column. The cluster analysis results indicated three kinds of space within the park and visually illustrated each space feature in Fig. 3b, c.

3.3 Physical Environment-Behavior Relationship

The environmental behaviors relationship pattern of this park could be classified into three types, as shown in Fig. 4. In Group 1, most activities often take place in some lake-adjacent space that has public facilities such as bench, trash bin, vegetation and

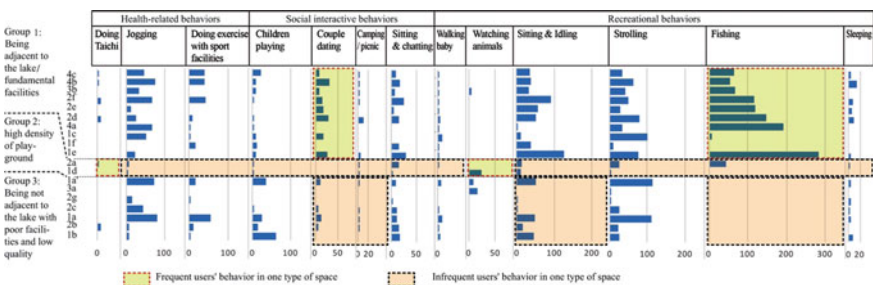


Fig. 4 Distribution of users' behaviors

visual objects, or has the medium level of openness, which has a high frequency of couples dating and people fishing. However, this space has the low accessibility level and no recreational setting such as game facilities for fee, and fitness equipment. As can be seen, despite the low quality of public functions and the low level of accessibility, most activities still take place in this space. In addition, for contributing private activities like couple dating, the openness factor in the space also needs to be considered in developing public space process. Natural or artificial water bodies are prerequisites in the design of open space for human activities as water is a compelling factor as it reflects their ego [1]. Group 2 attracts almost no activities. That is, although these spaces in the group are equipped with amenities of open space such as square, huts, flower garden, and good quality pavement, the high level of openness and accessibility deters user's activities. Park users appear to want some privacy. Also, the accessibility to this researched place is seen as a buffer zone to allow outsiders' access using motorbikes, bikes or going by foot. As a buffer zone for park entry, users tend to find other spaces for their activities instead of using the entry space. However, as small squares or common playgrounds well paved are inevitably open space, some activities like doing Taichi/exercises which require the ground, have the highest frequency, concurrently some activities that require lengthy line of sight such as watching animals, or birds, often takes place in this space. In Group 3, minimal activities take place as the space is neither adjacent to the water nor of good quality. This space is simply a vacant place or lawn without public facilities. Some recreational amenities as game facilities for fee and fitness equipment are set up here, but almost no one uses them very often. More importantly, such space has very limited use for activities like sitting and idling or couples dating. Figure 5 depicts the distribution of users' activities within each type of space.



Fig. 5 The user's behavior distribution on each spatial type of 29-3 Park: **a** Group 1—the sections are adjacent to the water surface or provided fundamental facilities; **b** Group 2—the sections prevailed by play-ground areas; **c** Group 3—the sections are not adjacent to water surface or low quality/lack of facilities

The current situation of open space in 29-3 Park revealed that apart from improving quality of such amenities set up for public space as bench, trash bin, vegetation and well paved paths, the development or renovation of open space needs to take openness and privacy into consideration; the entrance zone/gate also needs to separate such accessible space as parking lots from buffer zone between streets and inside space. The maximal development of water-adjacent space opens more avenues for people to get closer to the water. Also, research findings identified that whether the removal of the boundary between the inner part of the park and surrounding street space is necessary as the current spatial border of 29-3 Park is formed by the high degree of disparity between inside and outside spaces that leads to no activities in the street-adjacent space. Thus, the increased interaction between open space and street space would encourage much more activities, to exploit unused spaces.

3.4 User's Behavior and Physical Environment Density Analysis

Physical Environment features indicated in Fig. 3a were measured by their density on each sub-section. The density of physical environments was defined as open space's area or perimeter occupied by physical elements. A correlation test for physical elements and behaviors would be applied, any behavior that did not correlate well with physical environment element was omitted (the correlation index <0.5). There were 11 behaviors out of 13 that had the good correlation with 13 physical environments of the total 25. When it comes to the integration of environment behaviors, except for fixed relationships like watching animals, visiting the zoo, doing Taichi, or doing exercises and sports, other notable relationships may help to predict the number of users' behaviors accordingly. Analysis results of the user behaviors and physical environment density provided a calculation model for evidence-based designs. The positive correlation between activities in the space and physical environment density plays a role as a reference value for input data of the design and renovation process.

4 Conclusions and Implications

Although the Vietnamese government is seeking to increase urban open space area and to attract more users in various ways. The optimal way to improve or create an open space that can attract human activities remaining an unanswered question. In this paper, the relationship between physical environment and user's behavior is explained systematically, contributing a theoretical basis for creating a successful and user-friendly park. The design and development of urban park should consider three main functions serving recreational purposes, health-related activities and social interaction. For thoroughly exploiting and making the park more attractive, it is

required to (1) improve quality and quantity of public amenities; (2) separate accessible space/buffer zone from used space near entrance zone/gate inside the park; ensure privacy in the space; (3) provide walk path to approach the water surface; and (4) remove obstacles (e.g. walls around the park) to give a clear view from the inside park to streets outside and vice versa. The calculation model for evidence-based designs provides input data for reorganization of public space/park is suggests in accordance with area density of corresponding physical environment to human activities. In addition, the frequency of users' behaviors can be adjusted based on the ratio of physical environment in each section, which helps designers, planners, and authorities to improve or design open space in the near future. The findings provide information for the design and renovation, although with limitations. The survey time should be extended to a whole day to discover all activities in this space, including negative activities at night. Activities need to be surveyed in different seasons and events to explore the change in activities. Moreover, this investigation does not account for the contextual aspects of the park such as location in the city, transportation models, and other surrounding social factors that influence on the behavior pattern of the park. Future studies should consider the mentioned recommendations and compare the relationship between behaviors and the environment in different climates, cultures, user profiles and affordability. Behavior mapping method needs improvement by using Google-based GPS to minimize errors when data are collected. Measurement of indicators as to green trees, lawn and other objects through Google and Landsat images with low resolution was carried out, so it wasted much more time to collect data. IKONOS (1 m) images with higher resolution will facilitate the data collection for the faster and more precise calculation of the density of physical settings. In addition further improvements can be made by collection of feedback from professionals, experts, administrators and users. This can help to prepare input data for subsequent studies in the future. Such research can deeply explore the environmental quality of open space to users' impression.

Acknowledgements The first author would like to express the sincere gratitude for SEU scholarship for aiding their research financially. The authors would like to thank Phan Quang Minh and his students from Duy Tan University who supported the authors for a part of this investigation. Finally, the first author extends his gratitude towards his brother-in-law, Jason Muirhead, for proofreading the paper

References

1. Alexander C (1977) A pattern language: towns, buildings, construction. Oxford University Press
2. Campbell HW, Christman SP (1982) Field techniques for herpetofaunal community analysis. In: Herpetological communities, pp 193–200
3. Do TD, Mori S, Nomura R (2018) Passenger's attention behaviors along street space: a case study of Da Nang City. J Civ Eng Archit (4)
4. Faria PA, Ferreira FA, Jalali MS, Bento P, António NJ (2018) Combining cognitive mapping and MCDA for improving quality of life in urban areas. Cities 78:116–127

5. Garcia-Ayllon S (2018) Urban transformations as indicators of economic change in post-communist Eastern Europe: territorial diagnosis through five case studies. *Habitat Int* 71:29–37
6. Jim CY, Chen SS (2003) Comprehensive greenspace planning based on landscape ecology principles in compact Nanjing city, China. *Landscape Urban Plann* 65(3):95–116. [https://doi.org/10.1016/s0169-2046\(02\)00244-x](https://doi.org/10.1016/s0169-2046(02)00244-x)
7. Loan PT (2016) *Không gian công cộng trong đô thị – Từ lý luận đến thiết kế* (Urban space - From theory to design). Vietnam Association of Architects
8. Neto OA, Jeong S, Munakata J, Yoshida Y, Ogawa T, Yamamura S (2016) Physical element effects in public space attendance. *J Asian Archit Build Eng* 15(3):479–485
9. Ran L, Zhang Y, Wei W, Zhang Q (2017) A hyperspectral image classification framework with spatial pixel pair features. *Sensors* 17(10):2421
10. Rapoport A (2008) Environment-behavior studies: past, present, and future. *J Archit Plann Res* 276–281
11. Syamwil IB (2012) Social construction view in environment behaviour studies: the potential for asian context in environment behaviour knowledge in architecture and urban design. *Procedia Soc Behav Sci* 42:27–33
12. Whyte H (2000) How to turn a place around. Projects for Public Space Inc, p 52
13. Zeng R, Li Z (2018) Analysis of the relationship between landscape and children's behaviour in chinese residential quarters. *J Asian Archit Build Eng* 17(1):47–54

Studies on Household Water Consumption and Water-Saving Solutions for Four Cities in the Red River Delta (Hanoi, Hai Phong, Hai Duong and Nam Dinh)



Quang Minh Nguyen

1 Introduction

Water efficiency forms an integral part of all green building criteria and rating systems worldwide. For example, in LEED rating system developed by the United States Green Building Council (USGBC) as the world's most popular and influential green building work tool, water efficiency in home design is given 12 points out of 110 points in total. Vietnam Green Building Council (VGBC) has established its own criteria called LOTUS. Water efficiency in the LOTUS scorecard for residential buildings makes up 13 points out of the maximum 108 points (Table 1).

Table 1 Water efficiency in LEED and LOTUS systems for home design (comparative study)

International (LEED rating system) [7]		National (LOTUS rating system) [9]	
Category	Points	Points	Category (equivalent)
Integrative process	2	8	Management
Location and transportation	15	20	Site and environment
Sustainable sites	7		
Energy efficiency	37	32	Energy efficiency
Water efficiency	12	13	Water efficiency
Materials and resources	9	13	Materials and resources
Indoor environmental quality	18	14	Health and comfort
Additional score (innovation and priority)	10	8	Exceptional performance
Total score	110	108	Total

Q. M. Nguyen (✉)

Faculty of Architecture and Planning, National University of Civil Engineering, Hanoi, Vietnam
e-mail: minhqn@nuce.edu.vn

In LEED system, water efficiency is divided into three sub-categories, namely Water metering (required—no score), Indoor water use (eight points) and Outdoor water use (four points) [7] while in LOTUS system water efficiency consists of four criteria: Water-efficient fixture (five points), Water-efficient landscaping (two points), Water monitoring (one point) and Sustainable water solutions (five points) [9].

Water efficiency ranks fourth in terms of importance in both systems, but its share in LOTUS total score is slightly higher than in LEED (12.04% compared to 10.91%). Household water consumption, probably due to this “modest” marking, has not yet been systematically or comprehensively investigated in Vietnam’s major cities. Most of the research projects ever undertaken and outcomes related to green building in Vietnam nationally/internationally published so far have focused on energy efficiency, indoor air quality/bio-climatic comfort and materials/resources as key indicators No. 1, No. 2 and No. 3 respectively. Water issues, such as clean water supply capacity, water resource management and protection, water quality and sanitation, wastewater treatment process and technology, water landscaping, reduction of flooding in cities, etc. are mentioned in various reports annually/periodically published by either international organisations (World Bank—WB, Asian Development Bank—ADB, Japanese International Cooperation Agency—JICA, etc.) or state agencies (Ministry of Construction, Ministry of Natural Resources and Environment, etc.). One water supply problem in major cities, apart from input water contamination with arsenic compounds or heavy metals in some regions, is a high rate of non-revenue water: 23% in Hanoi and 32% in Ho Chi Minh City [6]. Another problem to solve in urban areas across the country is wastewater, when only 15% of a total daily wastewater amount of 750,000 m³ could be properly treated [3]. It is apparent that these water issues are considered and analysed at urban planning level. At building level, very few research projects have ever chosen to go into household water consumption along with the possibility of substituting (and hereby saving) tap water in daily use. An individual study conducted in 2014 on 56 households in central Hanoi from March to July that year with a water meter attached to every household water-consuming fixture. The average water consumption was 85.9 litres/person/day (l/p/d) for four purposes from most to least: pre-cooking, cooking, drinking and dish-washing (31.2 l/p/d), toilet flushing (21.7 l/p/d), clothes washing (18.9 l/p/d) and showering (14.1 l/p/d), [8]. The data in this study were precise and detailed as the measurement was both technically and financially supported, but collected within four months only and thus did not represent the water consumption in a whole year. The types of households in that survey were not given either. In reality, the demand can be higher, as other purposes of use, for example plant watering, floor cleaning, etc., should be taken into account. Another independent survey undertaken based on household monthly water bills in 2009 collected from 75 families in Hanoi revealed that tap water consumption ranged between 130 l/p/d (apartments and row-houses) and 200 l/p/d (villas and some shop-houses) [5].

In the context of on-going climate change, vigorous city development, increasing air temperature and greater urban heat island effect, city residents tend to consume more water while underground water has been depleted as a consequence of over-exploitation. Surface water continues to be polluted by solid as well as liquid waste

from industrial zones and residential areas. In this circumstance, water resource protection and water saving have become urgent matters and it is necessary to carry out more research on water issues in cities, especially household water consumption and wastewater reuse as an important part of ensuring water sustainability.

The study primarily aims to better understand how city residents in different cities and different housing types use water in daily life, what they often do to economise on clean water and how they are aware of the importance of water sustainability in particular from a broad spectrum of sustainable urban development.

In order to fulfil this objective, the author used the following research methods in this academic paper:

- Survey: In total, data on water consumption and several water-related issues from 198 households in four cities in the Red River delta (Hanoi, Hai Phong, Hai Duong and Nam Dinh) were collected;
- Data analysis: Data were categorised, analysed and compared with one another, where appropriate;
- In-depth interview: In-depth interviews were conducted to gain more information that helps explain why the results are similar or different, if necessary;
- Case studies: Ten case studies (from No. 1 to No. 10) out of 198 households with special or typical needs were selected.

2 Household Water Consumption

Households selected for research should be as diverse in patterns and widely distributed as possible. In total, 198 households in four main cities in the Red River delta were located as follows in Table 2.

In Hanoi as the most intensive case study, 152 households are surveyed and distributed by district as follows in Table 3.

Statistics shows that household water consumption per capita in 2018 varied immensely, from 51.1 l/p/d (the lowest) to 365.5 l/p/d (the highest) and can be divided into three levels:

Table 2 Distribution and types of households surveyed [4]

City	Type 1: villa/garden house	Type 2: row-house	Type 3: apartment	Total
Hanoi	14	82	56	152
Hai Phong	03	20	02	25
Hai Duong	03	08	00	11
Nam Dinh	02	08	00	10
Total	22	118	58	198

Table 3 Distribution of number of households surveyed in Hanoi by district [4]

No.	District	Number of households
01	Thanh Xuan	34
02	Hai Ba Trung	33
03	Dong Da	21
04	Hoang Mai	12
05	Long Bien	10
06	Cau Giay	09
07	Ha Dong	08
08	Hoan Kiem	07
09	Ba Dinh	06
10	Thanh Tri	04
11	Tay Ho	03
12	South Tu Liem	02
13	Hoai Duc	02
14	Me Linh	01
	Total	152

- High level of water consumption: more than 200 l/p/d with 34 households (Group A—17.2%);
- Medium level of water consumption: from 100 l/p/d to 200 l/p/d with 105 households (Group B—53.0%);
- Low level of water consumption: less than 100 l/p/d with 59 households (Group C—29.8%).

In Group A with 34 households, the main reasons for a considerably higher amount of tap water are given below:

- Private swimming pools and/or large gardens with many trees and plants to be watered every day: five villas and 18 row-houses;
- Water-consuming services (restaurant, hair salon and laundry, beauty parlour): three shop-houses;
- Office for rent with over 20 staff: one row-house;
- Special needs: seven high-end apartments.

In most cases (157 out of 198 households—79.3%), the monthly demand for water from May to September 2018 as five hottest months of the year was 20% higher than the average consumption, because the demands for showering, clothes washing, toilet flushing, floor cleaning and plant watering all increased in this period. Among the rest, 24 out of 41 families had monthly water consumption levels that stayed almost the same (as the difference between the highest and lowest monthly amount of water consumption did not exceed 03 m³, or 20–25 l/p/d). There were 17 families which had considerably lower water consumption in those summer months,

since they went on business or holiday for several time, each time for two or three weeks [4] (Table 4).

There are two criteria used to choose three typical case studies: (1) Reaching the upper baseline of daily water consumption per capita (All three groups) and (2) Having a specific water-consuming activity (Groups A and B) (Fig. 1).

The water consumption levels stood above the average line in February, April, May, June, July and August (Case study No. 1 from Group A), in February, May, June, July, August and September (Case study No. 2 from Group B), and in May, June and July only (Case study No. 3 from Group C). In group A and group B case studies, the water consumption levels in February were equally high to a summer month, because Vietnamese traditional New Year's Festival took place in mid February 2018, and many households consumed a larger amount of water than usual for cooking special meals. This fact could be found in further 93 households [4].

The breakdown of household water consumption could be obtained with assistance of a collaborator and her family (three adults and one child) living in one 110 m² apartment with one kitchen, three toilets/bathrooms and two loggias. Water was 100% provided from the pipeline. No rainwater was used. On three consecutive days in May 2019, this family helped calculate the input/output amount of water for every water-consuming fixture and need with one stick note, one 1.5 l-jug and one 10-l bucket. The results are summarised in Table 5 (Fig. 2).

3 Water-Saving Scenarios for Households

Just like energy efficiency, water efficiency is an essential requirement and a key indicator in a green building. Water saving can be achieved by installing water-saving washing machines, dishwashers and shower heads at home which can economise on water by 10–25% subject to product types [1]. In addition, using rainwater instead of tap water in categories No. 6, 7 and 8 from Table 5 is another good option, because super clean water is not really needed for toilet flushing, plant watering and floor cleaning. Before grey water can be treated on-site which requires an initial investment in technology/equipment and then reused, the collection of rainwater should be considered and applied wherever appropriate. In four cities Hanoi, Hai Phong, Hai Duong and Nam Dinh in the Red River delta, the annual rainfalls are reported to be abundant: 1600 mm; 1700 mm; 1500 mm and 1750 mm, respectively [10]. Therefore, collecting rainwater for daily use would be highly recommended. However, in fact, using rainwater has not yet been popular in Vietnam's major cities, especially in central districts. Out of 198 households surveyed, only 21 households (seven villas and 14 row-houses/shop-houses, mostly located 5 km or further from city centres) used rainwater to a certain extent with one 500-l plastic tank in 16 cases and one 1000-l inox tank in five others. The most common locations for such a rainwater tank are in the garden, in the front/back yard and on the top terrace [4]. Rainwater is used for the following purposes in Table 6.

Table 4 Monthly household water consumption ($l/p/d$)—case studies No. 1 (A), 2 (B) and 3 (C) [4]

Type	Ave	Jan	Feb	Mar	Apr	May	Jun	Jul	Aug	Sep	Oct	Nov	Dec
A	343.9	322.6	375.0	282.3	358.3	387.1	416.7	411.3	387.1	341.7	258.1	291.7	298.4
B	181.8	169.4	192.9	154.8	140.0	193.6	206.7	206.5	225.8	200.0	174.2	160.0	148.4
C	68.5	56.5	62.5	64.5	66.7	80.6	91.7	88.7	64.5	66.7	56.5	58.3	64.5

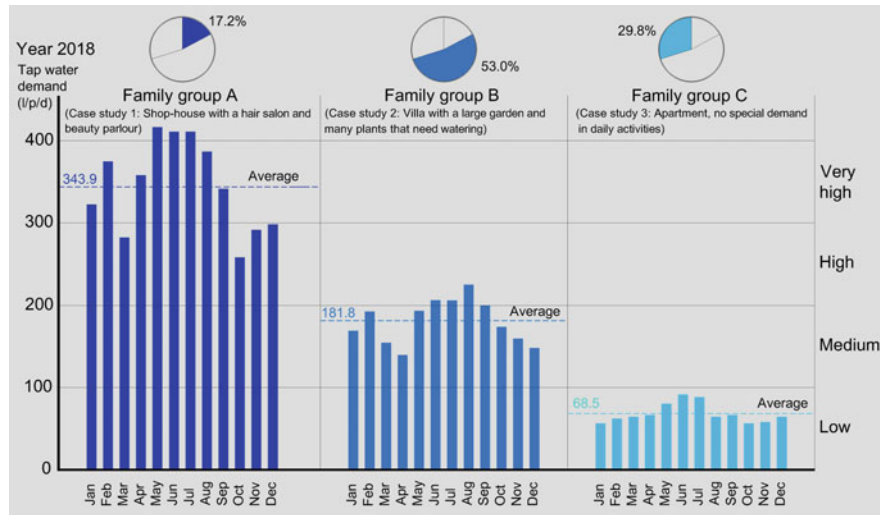


Fig. 1 Monthly water consumption (l/p/d) in three typical households from groups A, B and C [4]

Table 5 Specific data on daily household water consumption—case study No. 4 [4]

No.	Purpose of use (three adults and one child)	Friday, May 10th 2019		Saturday, May 11th 2019		Sunday, May 12th 2019	
		Amount (l)	Percentage (%)	Amount (l)	Percentage (%)	Amount (l)	Percentage (%)
01	Cooking	36	6.3	42	5.6	45	6.3
02	Drinking	10	1.8	12	1.6	11	1.5
03	Dish washing	36	6.3	45	6.0	45	6.3
04	Showering	320	56.0	350	46.3	340	47.2
05	Clothes washing	95	16.6	190	25.2	190	26.4
06	Toilet flushing	60	10.5	72	9.5	75	10.4
07	Plant watering	14	2.5	14	1.8	14	1.9
08	Floor cleaning	0	0.0	30	4.0	0	0.0
	Total amount (l)	571	100.0	755	100.0	720	100.0
	Per capita (l/p)	≈143		≈189		180	

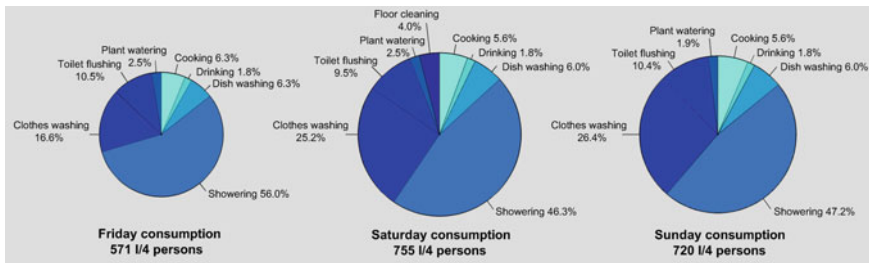


Fig. 2 Specific data on daily household water consumption in May 2019—case study No. 4. The top three purposes of tap water use are showering, clothes washing and toilet flushing [4]

Table 6 Purposes of rainwater use among 21 households surveyed [4]

Purpose(s) of use	Quantity	Purpose(s) of use	Quantity	Purpose(s) of use	Quantity
Plant watering only	04	Cooking, hand washing	03	Towel washing only	01
Floor cleaning only	04	Cooking, tea making	03	Fish raising only	01
Cooking only	04	Dish washing only	01	Total	21

It is surprising that rainwater is not used for toilet flushing, although a simple pipe system connecting two or three toilets to one 1000-l plastic rainwater tank with some auxiliary appliances does not cost so much, less than 300 USD per full set in the market [4]. Rainwater is often collected from roofs and stored in tanks that require a certain floor or ground area. In high-rise residential buildings, it is difficult to install a rainwater tank within an apartment. Furthermore, one unit of roof area from 70 to 100 m² (equal to a floor area of a typical apartment) is shared by 20 or more households, thus insufficient for use either. In this regard, it is advised to apply a water-saving strategy first to low-rise housing. In a villa or a row-house as well as a shop-house, the roof area is large enough for one family to collect rainwater. The amount of rainwater collected from the roof depends on roof type and roof material, apart from roof area, and can be calculated as follows:

$$V_{\text{rain water}} = \varphi \times r \times S \quad (1)$$

in which φ is run-off co-efficient (including splashing, evaporation and surface wetness grade) of water on the roof, depending on material (0.9 for metal roofs, 0.8 for tiled roofs and 0.5 for green roofs) and also on slope;

r is annual rainfall (m) falling on 1 m² roof area;

S is total roof area of the building to be investigated (m²) [2].

Table 7 Household tap water using and saving possibility through rainwater—case study No. 5 [4]

Location	Hoang Mai district (Hanoi)	Roof area	70 m ²
Function	For living only	Roofing material	Metal
Type of housing	Row-house	Using rainwater	Yes
Business/service	No	Main purpose of use	Plant watering
Number of persons	06 (04 adults + 02 children)	Other purpose of use	None
Number of people staying at home	Morning (06–12 h)	Afternoon (12–18 h)	Evening and night (18–06 h)
Monday to Friday	02	02	06
Saturday	06	06	06
Sunday	06	06	06
Defecation (total)	42 times (within one week)	Urination (total)	174 times (within one week)
Toilet flushing for defecation	252 l (06 l/time)	Toilet flushing for urination	522 l (03 l/time)
Total flushing	774 l (within one week)	Total plant watering	35 l (within one week)
Total demand for rainwater	809 l (within one week)	Amount of collected rainwater [Formula (1)]	100,800 l (within one year) 1938 l (within one week)
Level of meeting the demand for rainwater	239.5% (toilet flushing and plant watering)		
Weekly surplus amount	1129 l		

The possibility of tap water saving (by means of using rainwater) can be illustrated and demonstrated with further six case studies in Hanoi (from No. 5 to No. 10) (Tables 7, 8, 9, 10, 11 and 12).

Table 8 Household tap water using and saving possibility through rainwater—case study No. 6 [4]

Location	Long Bien district (Hanoi)	Roof area	62 m ²
Function	For living only	Roofing material	Tiled roof
Type of housing	Row-house	Using rainwater	Yes
Business/service	None	Main purpose of use	Plant watering
Number of persons	03 (02 adults + 01 child)	Other purpose of use	Fish raising (one aquarium), 01 m ³ (1000 l) per week
Number of people staying at home	Morning (06–12 h)	Afternoon (12–18 h)	Evening and night (18–06 h)
Monday to Friday	01	00	03
Saturday	02	03	03
Sunday	03	03	03
Defecation (total)	21 times (within one week)	Urination (total)	95 times (within one week)
Toilet flushing for defecation	126 l (06 l/time)	Toilet flushing for urination	285 l (03 l/time)
Total flushing	411 l (within one week)	Total plant watering	70 l (within one week)
Total demand for rainwater	1481 l (within one week)	Amount of collected rainwater [Formula (1)]	79,360 l (within one year) 1526 l (within one week)
Level of meeting the demand for rainwater	100% (toilet flushing and plant watering)		
	104.5% (fish raising)		
Weekly surplus amount	45 l		

Table 9 Household tap water using and saving possibility through rainwater—case study No. 7 [4]

Location	Hai Ba Trung district (Hanoi)	Roof area	40 m ²
Function	For living and service	Roofing material	Metal
Type of housing	Row-house	Using rainwater	Yes
Business/service	Shop for rent (mobile phones)	Main purpose of use	Plant watering
Number of persons	08 (04 adults + 02 children as family members and 02 staff employed from 08 am to 06 pm, Monday to Saturday)	Other purpose of use	None
Number of people staying at home	Morning (06–12 h)	Afternoon (12–18 h)	Evening and night (18–06 h)
Monday to Friday	04	04	06
Saturday	06	08	06
Sunday	06	06	06
Defecation (total)	48 times (within one week)	Urination (total)	258 times (within one week)
Toilet flushing for defecation	288 l (06 l/time)	Toilet flushing for urination	774 l (03 l/time)
Total flushing	1062 l (within one week)	Total plant watering	35 l (within one week)
Total demand for rainwater	1097 l (within one week)	Amount of collected rainwater [Formula (1)]	57,600 l (within one year) 1107 l (within one week)
Level of meeting the demand for rainwater	100.1% (toilet flushing and plant watering)		
Weekly surplus amount	10 l		

Table 10 Household tap water using and saving possibility through rainwater—case study No. 8 [4]

Location	Thanh Xuan district (Hanoi)	Roof area	54 m ²
Function	For living and service	Roofing material	Metal (30 m ²), tiled (24 m ²)
Type of housing	Row-house	Using rainwater	Yes
Business/service	Hair salon and beauty parlour	Main purpose of use	Plant watering
Number of persons	06 (04 adults + 02 children) Service: 30 customers per day on average	Other purpose of use	Towel washing: 04 m ³ per month—01 m ³ or 1000 l per week
Number of people staying at home	Morning (06–12 h)	Afternoon (12–18 h)	Evening and night (18–06 h)
Monday to Friday	03	02	06
Saturday	03	03	03
Sunday	04	04	04
Defecation (total)	37 times (within one week)	Urination (total)	189 times (within one week)
Toilet flushing for defecation	222 l (06 l/time)	Toilet flushing for urination	567 l (03 l/time)
Total flushing	789 l (within one week)	Total plant watering	70 l (within one week)
Total demand for rainwater	1859 l (within one week)	Amount of collected rainwater [Formula (1)]	73,920 l (within one year) 1421 l (within one week)
Level of meeting the demand for rainwater	100% (toilet flushing and plant watering)		
	56.2% (tower washing)		
Weekly surplus amount of rainwater	0 l		
Weekly amount of rainwater to be supplied more	438 l		

Table 11 Household tap water using and saving possibility through rainwater—case study No. 9 [4]

Location	Thanh Xuan district (Hanoi)	Roof area	120 m ²
Function	For living only	Roofing material	Tiled roof
Type of housing	Villa	Using rainwater	Yes
Business/service	None	Main purpose of use	Plant watering (for back-side garden)
Number of persons	04 (03 adults + 01 adolescent)	Other purpose of use	Front yard cleaning, twice a week, 150 l each
Number of people staying at home	Morning (06–12 h)	Afternoon (12–18 h)	Evening and night (18–06 h)
Monday to Friday	04	01	04
Saturday	04	02	04
Sunday	04	04	04
Defecation (total)	28 times (within one week)	Urination (total)	162 times (within one week)
Toilet flushing for defecation	168 l (06 l/time)	Toilet flushing for urination	486 l (03 l/time)
Total flushing	654 l (within one week)	Total plant watering	350 l (within one week)
Total demand for rainwater	1304 l (within one week)	Amount of collected rainwater [Formula (1)]	153,600 l (within one year) 2954 l (within one week)
Level of meeting the demand for rainwater	226.5% (toilet flushing and plant watering)		
Weekly surplus amount	1650 l		

Table 12 Household tap water using and saving possibility through rainwater—case study No. 10 [4]

Location	Hoan Kiem district (Hanoi)	Roof area	60 m ²
Function	For living only	Roofing material	Tiled roof
Type of housing	Villa	Using rainwater	Currently no
Business/service	None	Main purpose of use	Currently no
Number of persons	04 (02 adults + 02 children)	Other purpose of use	Currently no
Number of people staying at home	Morning (06–12 h)	Afternoon (12–18 h)	Evening and night (18–06 h)
Monday to Friday	02	00	04
Saturday	04	04	04
Sunday	04	04	04
Defecation (total)	28 times (within one week)	Urination (total)	136 times (within one week)
Toilet flushing for defecation	168 l (06 l/time)	Toilet flushing for urination	408 l (03 l/time)
Total flushing	576 l (within one week)	Total plant watering	70 l (within one week)
Total demand for rainwater	646 l (within one week)	Amount of collected rainwater [Formula (1)]	76,800 l (within one year) 1477 l (within one week)
Level of meeting the demand for rainwater	228.6% (toilet flushing and plant watering)		
Weekly surplus amount	831 l		

Using rainwater in a city saves tap water. In each of the six case studies from No. 5 to No. 10, the amount of rainwater collected from the roof can cover 100% of the demand for toilet flushing and plant watering. The remaining amount of rainwater in five out of six case studies Nos. 5, 6, 7, 9 and 10 (**1129 l—45 l—10 l—1650 l—831 l**, respectively) can be used for other meaningful purposes, or to provide some neighbouring families where the amount of rainwater collected is not sufficient due to a special need (for service), such as in case study No. 8.

4 Conclusions

Water indeed plays a very important role in shaping a city and making every building much greener for a more sustainable future. It is therefore necessary to emphasise and facilitate water efficiency, not only by giving bonus points in green building certificates or encouraging people to buy household water-saving washing machines

and/or dishwashers, but also by changing the public behaviour and persuading them into instantly using rainwater instead of tap water in some categories of use for various good reasons, and later by on-site recycling and reusing grey water, when innovative environmental engineering is transferred and applied in Vietnam's major cities.

The data collected and analysed in this study are quite diverse (with different housing types and various purposes of rainwater use), typical (as case studies could be easily selected) and reliable (directly taken from monthly water bills and measured with water containers when water meters were not available), proving that there is a high potential of using rainwater in cities, even in a densely constructed city like Hanoi. However, more case studies from other cities/districts should be added to the database to ensure the equivalence between groups of sites and objects of research, and probably to find out more interesting or special case studies. For further investigations into household tap water consumption and rainwater utilisation, the author will broaden the scope of research and hopes to consolidate the database as well as to make a more significant contribution to sustainable urban development in view of water issues.

Acknowledgements This research paper has been completed with generous support from the author's family members as well as from colleagues, friends, collaborators and students at the National University of Civil Engineering in collecting input data for analysis.

References

1. Australian Government (2018) Water rating. Home page <https://www.waterrating.gov.au/>
2. Glücklich D (2005) Ökologisches Bauen - Von Grundlagen zu Gesamtkonzepten. DVA Verlag, München, p 109
3. Netherlands Ministry of Foreign Affairs (2018) Water in Vietnam. Annual report, p 3
4. Nguyen QM (2019) Study results of household water consumption of families in Hanoi, Hai Phong, Hai Duong and Nam Dinh
5. Nguyen QM (2010) Ein Konzept für ökologischen Siedlungsbau in Hanoi und seiner Umgebung am Beispiel der Siedlung Phung Khoang. Ph.D. dissertation, Bauhaus Universität Weimar, p 79
6. UK Department for International Trade (2018) Vietnam water sector briefing 2017:6
7. United States Green Building Council (2018) LEED criteria and rating system. <https://new.usgbc.org/leed-v41>
8. Vietnam Environment Group (2014) How to estimate household water consumption. <https://moitruong.com.vn/tai-lieu/phuong-phap-xac-dinh-luong-nuoc-tieu-thu-ho-gia-dinh-18397.htm>
9. Vietnam Green Building Council (2016) LOTUS criteria and rating system. <https://vgbc.vn/en/resources/>
10. Vietnam Ministry of Construction and Institute of Building Science and Technology (2009) Climate data of cities and province. National Building Code, Hanoi, pp 188–189

The Inter-relationships Between LST, NDVI, NDBI in Remote Sensing to Achieve Drought Resilience in Ninh Thuan, Vietnam



Nguyen Quoc Vinh, Nguyen Trong Khanh, and Pham Thi Anh

1 Introduction

Due to the Industrial Revolution, the rapid industrialisation and population growth in urban regions have become a global problem and a huge challenge. More than half (54%) of the world's population live in cities and is expected to increase. While the cities occupy only 2% of the planet's surface, their population consumes 75% of the total amount of energy generated and is responsible for 80% of the greenhouse effect. The impacts of CC on the earth systems include melting ice, altered hydrological systems, shifting species, migrating patterns, and so on. Additionally, global warming has led to the fact that extreme weather events: heat waves, drought, extreme precipitation, inland and coastal floods, landslides, cyclones, etc., occur more and more frequently [1]. The natural hazards are more severe in riverine, coastal and even urban areas across the world and particularly in Asian countries. In vulnerable areas of Ninh Thuan province, current findings show high pressures of drought, particularly in Phan Rang-Thap Cham city, the worst area in the province. Drought intensity is often accompanied with above-normal temperatures, and would increase due to a large part of the recent surface warming attributed to human-induced GHG increases [2]. Increasing land surface temperature is ecologically and socially considered as a main part of drought.

With such increase in environmental stress on urban regions, scholars started to focus on urban sustainability and resilience. These concepts are ecology-based, where a city is basically considered as a complex of Social-Ecological Systems (SES) [3]. Urban information has become increasingly complex by that trend. To

N. Q. Vinh (✉) · N. T. Khanh

Faculty of Civil Engineering, Ho Chi Minh City University of Technology,
VNU-HCM, Ho Chi Minh City 740128, Vietnam
e-mail: vinh.bmkt@hcmut.edu.vn

P. T. Anh

Institute for Environmental and Transport Studies, Ho Chi Minh City University of Transport, Ho Chi Minh City, Vietnam

© Springer Nature Singapore Pte Ltd. 2020

J. N. Reddy et al. (eds.), *ICSCSEA 2019*, Lecture Notes in Civil Engineering 80,
https://doi.org/10.1007/978-981-15-5144-4_15

help understand the complexity of the SES, RS and GIS are the most effective tools and methods to make a more appropriate approach to the planning and design of cities, particularly in geo-spatial database [4].

As LST was considered the main part of drought, other relevant factors such as NDVI and NDBI will be extracted from RS images for analysing their inter-relationships. The results will show that LST is raised by NDBI and in contrast, is reduced by NDVI. Therefore, green spaces and their structure will play a large role in spatial planning to achieve drought resilience.

2 The Notions of Resilience and Study Methodology

2.1 *Resilience Spatial Planning*

The notion of resilience first appeared in 1973, when the author referred to systems and their ability to cope with external shocks and disturbance while former structures and functions remain [5, 6]. Later, various scholars considered it in terms of the adaptive cycle [7, 8], which focuses on the dynamics of systems that do not have a stable or equilibrium condition but repeatedly pass through four phases: growth and exploitation; conservation; collapse or release; renewal and reorganisation.

The concept got attention of urban planners much later in the 1990s. It considered a city as “SES”, which is supported by natural services, including: (i) provision of food and water, (ii) regulation of floods, drought, and disease, (iii) supporting soil formation and nutrient cycling, and (iv) culture such as recreational, spiritual, religious and other nonmaterial benefits [9]. Among many definitions, Sendai Framework defined resilience as the ability of a city exposed to hazards to resist, absorb, accommodate to and recover from the effects of a hazard [10]. S. Meerow described urban resilience as the ability to maintain or rapidly return to desired functions, to adapt to change and to transform systems that limit current or future adaptive capacity [11].

With regard to urban planning, a number of studies acknowledge that spatial planning plays an important role in promoting urban resilience [12–14]. In a research showing a proper urban structure which can mitigate multi-hazards, authors introduced several indicators for the assessment of the resilience in spatial planning [13]. Among them, keeping areas free of development, such as green open space, as the form of ecological diversity in the city, is part of the strategies for resilience through “nurturing conditions for recovery and renewal after disturbance” [15]. Moreover, enhancing green spaces in urban areas was identified as an appropriate mitigation approach of UHI [16], and increasing biodiversity and vegetated land cover will increase resilience to drought risk [17].

In Vietnam, these emerging concepts have so far only been introduced in seminars and policies. Resilience oriented spatial planning to mitigate urban heat is a necessary step moving toward drought resilience in Ninh Thuan.

2.2 Study Methodology

The most relevant factors related to drought conditions and the key urban components that help increasing capacity of an urban environment to deal with the risk of CC and disaster are how urban green open space, and built-up areas spatially structured [15]. These factors will be examined for Phan Rang-Thap Cham city from the year of 1990 when urbanization started up till 2019. Final outcomes help analyse their inter-relationships, transformations and define the main ways to reduce LST and achieve drought resilience through spatial planning.

However, traditional approaches and techniques designed for cities may prove to be inadequate to meet the challenges of rapid urban development. They require timely and reliable information [18], that lacks in Vietnam. RS and GIS technologies could very much help.

RS and GIS in urban planning Robust results of LULC could be extracted from RS. Satellite RS with repetitive and synoptic viewing capabilities, as well as multispectral capabilities, is a powerful tool for mapping and monitoring the ecological changes in land use. It may help to reduce unplanned urban sprawl and the associated loss of natural surrounding and biodiversity.

RS and GIS for studying ecological services Spatially explicit ecosystem service values are important for its management. RS provides images covering the Earth surface, which can be useful for quantitative assessment of ecosystem services [19]. Several important categories of information can be directly extracted from RS data as water, barren land, vegetation, built-up areas, etc. The spatial and temporal information, which is one of the key elements in ecosystem management [20], is stored in a geospatial database and used in GIS.

RS and GIS for studying LULC, LST, NDVI and NDBI in Phan Rang-Thap Cham City LULC maps of Phan Rang-Thap Cham city in three years (1990, 1997 and 2019) is firstly examined through RS images to explore the overall land covers. Based on that, LST, NDVI and NDBI maps are extracted from which we obtained key figures of heat, green spaces, and built-up areas, respectively, transformed through years.

LULC The multispectral Landsat satellite images of the following table were used (Table 1). The Landsat images were registered to Universal Transverse Mercator projection, zone 49 N, WGS84 Datum, spatial grid of 30 m resolution. The dates of

Table 1 Detailed characteristics of the Landsat Satellite images used in the study

Path/row	Acq. date	Dataset	Producer	Attribute	Type
123,052	26/03/1990	TM	USGS	Ortho, GLS2000	Geotiff
123,052	29/03/1997	TM	USGS	Ortho, GLS2000	Geotiff
123,052	11/04/2019	OLI-TIRS	USGS	Ortho, GLS2000	Geotiff

the Landsat images were chosen to be as close as possible to the same vegetation season. The methodology used includes the following stages: image pre-processing, the design of classification scheme, image classification, accuracy assessment and analysis of the LULC changes.

- Image pre-processing: including cloud masking, layer stacking, sub-setting by administrative boundary;
- Classification scheme: utilising four classes (Urban—Built Up, Water, Barren soil, Vegetation);
- Image classification: training data was used for Maximum Likelihood Classification (MLC) and accuracy assessment. In this research, colour composites; ratio images (MNDWI, NDBI, NDVI); Google Earth, topographical map was used to generate training data.
- Accuracy assessment: such assessment was performed for the classified maps of all three steps. Error matrices were used to assess classification accuracy using two measures: overall and Kappa statistics.

NDVI NDVI is used to quantify vegetation by measuring difference of near-infrared (vegetation reflects) and red light (vegetation absorbs) [21]. The NDVI algorithm subtracts the red reflectance values from the near-infrared and divides it by the sum of near-infrared and red bands.

$$NDVI = \frac{(NIR - Red)}{(NIR + Red)}$$

The NDVI values are represented as a ratio ranging from -1 to $+1$, negative values represent water, around zero is bare soil, built-up areas, from 0.2 to 0.5 is for shrubs, grassland, and over 0.6 is dense green vegetation.

LST The temperature at the interface of the earth's surface up to the height of $2\text{--}3$ m of the air can be measured. The steps to calculate the final LST are as followed:

- Converting the Satellite Digital Number (DN) to Radiance value;
- Conversion of Radiance to At Sensor Temperature;
- Conversion of Satellite Brightness Temperature into LST.

NDBI Among land cover surfaces, built-up areas have higher reflectance in middle infrared wavelength than near infrared. Thus, NDBI is useful to extract urban built-up areas and calculated with the following formula:

$$NDBI = \frac{(MIR - NIR)}{(MIR + NIR)}$$

The NDBI algorithm subtracts the NIR reflectance values from the MIR and divides it by their sum. NDBI value lies from -1 to $+1$. Negative values are water bodies, the higher is built-up areas, and the lower is vegetation.

3 Results and Discussions

3.1 Natural Conditions of Ninh Thuan Province and Phan Rang-Thap Cham Capital City

Ninh Thuan is the coastal province in the Southern central part of Vietnam, located at the co-ordinates: $11^{\circ} 18' 14''$ to $12^{\circ} 09' 15''$ Northern latitude, $108^{\circ} 09' 08''$ to $109^{\circ} 14' 25''$ Eastern longitude.

Hydrology: total area of rivers basin is 3092 km^2 , including 46 rivers, main streams and four main aquifers, of which the Dinh river basin covers the majority of the area 3000 km^2 , and others - 92 km^2

Meteorology: dry (75–77%), hot (26–27 °C) and strong wind (2.3–5 m/s, the strongest is of 25 m/s) and high rate of vapourisation.

Extreme weather events: the climate alternates from drought to floods. However, floods are reduced thanks to many reservoirs, dams and dikes.

Three climate sub-regions can be distinguished. The coastal area (III) has the worst droughts with an average rainfall of around 500–700 mm/year, here the studied site of Phan Rang-Thap Cham city is located. The plain area (II) also suffers from drought with rainfall from 750 to 1200 mm/year, here Phuoc Dan and Tan Son cities are located. The mountainous area (I) has a rainfall of 1000–1700 mm/year (Fig. 1).

3.2 The Mutual Relationships of LST, NDBI, NDVI

Results of RS images—LST, NDVI, NDBI maps To quantify the research, three key drought relevant factors (LST, NDVI, NDBI) of the Phan Rang-Thap Cham will be extracted from LULC (Figs. 2 and 3), as the methods described above.

The mutual relationships All data collected from above RS images related to LST, NDVI and NDBI is then generally analyzed in pairs on the following correlation graphs.

LST versus NDBI As seen at the Fig. 4, the maximum LST is found in built-up areas, showing values higher than zero. They generate much surface temperature variations and are the key contributor to UHI. The lower values represent vegetation areas, where LST is reduced enormously. A strong positive correlation existed in LST-NDBI with $R^2 = 0.9619, 0.9529, 0.9879$ in each of the three years 1990, 1997 and 2019, respectively.

LST versus NDVI The correlation is strongly negative, particularly in 4/2019, with $R^2 = 0.9621, 0.957, 0.981$ in three years 1990, 1997 and 2019 respectively. It means that low LST is found in dense greenery (>0.6) (Fig. 5).

NDBI versus NDVI The relationship is extremely negative, with $R^2 = 0.9982, 0.9999, 0.9982$ in the three years 1990, 1997 and 2019 respectively (Fig. 6). It is proven that

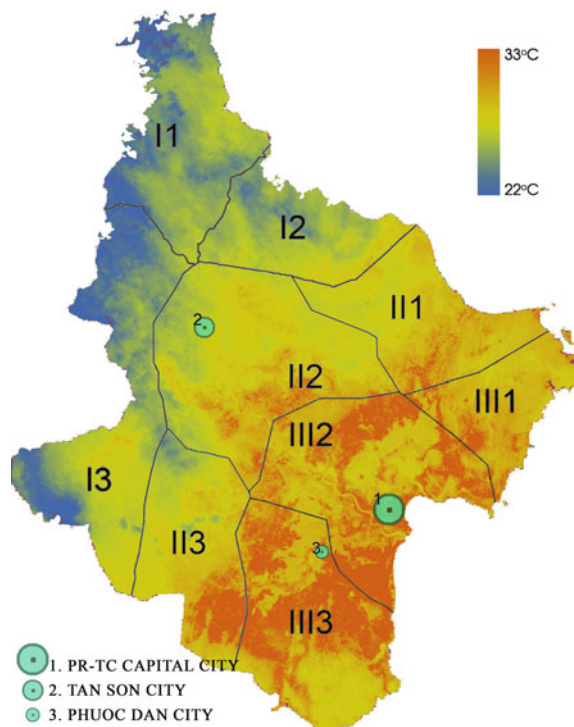


Fig. 1 Three climatic sub-regions of Ninh Thuan. *Source Authors*

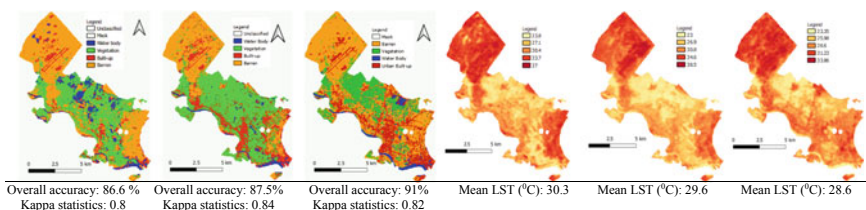


Fig. 2 LULC and LST maps of Phan Rang-Thap Cham in 1990, 1997 and 1999, respectively. *Source Authors*

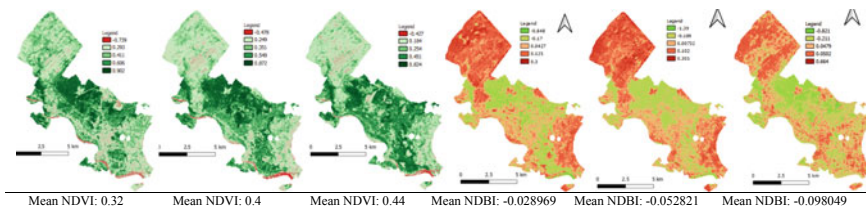


Fig. 3 NDVI and NDBI maps of Phan Rang-Thap Cham in 1990, 1997 and 2019, respectively. *Source Authors*

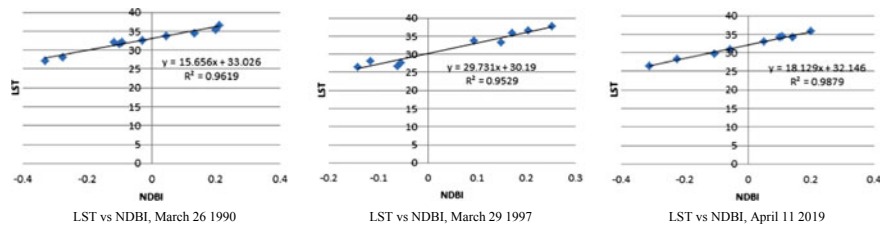


Fig. 4 Relationships between LST and NDBI in Phan Rang-Thap Cham in 1990, 1997 and 2019.
Source Authors

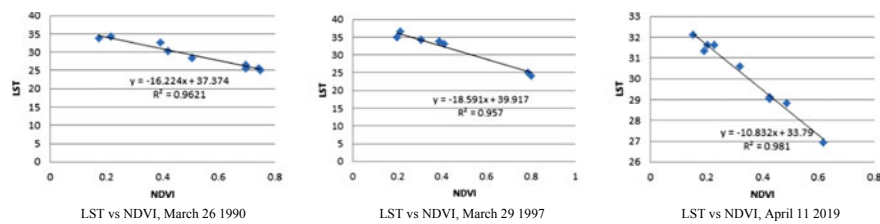


Fig. 5 Relationships between urban LST and NDVI of Phan Rang-Thap Cham in 1990, 1997 and 2019.
Source Authors

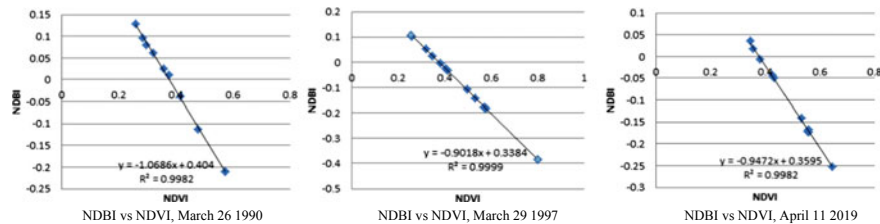


Fig. 6 Relationships between NDBI and NDVI of Phan Rang-Thap Cham in 1990, 1997 and 2019.
Source Authors

vegetation plays a very important role in cooling LST.

Relationships among LST, NDBI, NDVI

From the results above (Table 2), the three main factors relevant to UHI and drought conditions, such as LST, NDVI, NDBI, are mutually intertwined. Comparing the figures in the three years, slightly increased NDVI has reduced LST remarkably. In

Table 2 The relationships between LST, NDBI, NDVI of Phan Rang-Thap Cham City in 1990, 1997 and 2019

	LST	NDBI	NDVI
Built-up in 1990	30.613073	0.047276	0.188402
Built-up in 1997	30.499507	0.034283	0.266400
Built-up in 2019	29.662003	0.048447	0.234729

Source Authors

1990, NDVI (values < 0.2) demonstrated that the land cover was mostly bare soil; LST was quite high accordingly (30.6). In 1997 and 2019, when NDVI were higher (>2), LST started to decrease. Logically, built-up areas are the main factor generating UHI, but green spaces in a city are the key driver in reducing land surface temperature, particularly in dense vegetation (>0.6). As a result, how green spaces and vegetated land covers are spatially planned and structured would be an appropriate mitigation approach of UHI to increase resilience to drought risk [17] for Phan Rang-Thap Cham capital city.

4 Conclusions

City—‘SES’ as a complex adaptive system, is not only dynamic but also self-organising and actively adjusting to cope with all predictable and unforeseeable shocks. With spatial planning, a city can be ecologically and socially managed. Besides traditional approaches, this paper introduces an ecological point of view where spatial planning for drought resilience of Ninh Thuan with RS techniques and GIS should be effectively utilised. The geo-spatial database of three drought relevant factors at the city of Phan Rang-Thap Cham scale: LST, NDVI, NDBI extracted from RS images prove that they are interrelated. LST is increased by increasing NDBI but is reduced by enhancing NDVI. It proves that vegetated areas in urban areas could remarkably reduce urban heat. Urban extension seems to be a never-ending process, how citizens experience heat and drought will very much depend on how its green open areas are organised and structured. Spatial planning focusing on urban greenspace structure plays a key role for achieving drought resilience.

Acknowledgements The authors wish to acknowledge the assistance and encouragement from the colleagues at the Department of Architecture, Department of Geomatics Engineering, Faculty of Civil Engineering, HCMC University of Technology, VNU-HCM, Ho Chi Minh City, and from HCMC University of Transport, as well as the support from the Construction Department of Ninh Thuan province.

References

1. IPCC (2014) Climate change, adaptation, and vulnerability. *Organ Environ* 1–44
2. Dai A (2011) Drought under global warming: a review, pp 55–57
3. Pickett STA, Cadenasso ML, McGrath BM (2013) Ecology of the city as a Bridge to urban design. In: Resilience in ecology and urban design, pp 7–28
4. Jhawar M, Tyagi N, Dasgupta V (2012) Urban planning using remote sensing, pp 42–57
5. Eraydin A, Taşan-kok T, Stead D, Taşan T, Lu P, Dias LF, ... Henriksson A (2013) Resilience thinking in urban planning, pp 39–51
6. Holling CS (1973) Resilience and stability of ecological systems. *Annu Rev Ecol Syst* 4:1–23
7. Folke C (2006) Resilience: the emergence of a perspective for social-ecological systems analyses, pp 253–267

8. Holling CS, Gunderson LH (2002) Resilience and adaptive cycles. Understanding Transformations in Human and Natural Systems, Panarchy, pp 25–62
9. Millennium Ecosystem Assessment (2005) Millennium Ecosystem Assessment: ecosystems and human well-being
10. Sendai Framework for Disaster Risk Reduction (2015) Sendai framework for disaster risk reduction 2015–2030, pp 1–25
11. Meerow S, Newell JP, Stults M (2016) Defining urban resilience: a review. *Landscape Urban Plann* 147:38–49
12. Davoudi S, Strange I (2009) Space and place in the twentieth century planning: an analytical framework and an historical review, pp 7–42
13. Fleischhauer M (2008) The role of spatial planning in strengthening urban resilience, pp 273–298
14. Hoa NT, Vinh NQ (2018) The notions of resilience in spatial planning for drought—flood coexistence (DFC) at regional scale, pp 14–16
15. Ni'mah NM, Lenonb S (2017) Urban greenspace for resilient city in the future: case study of Yogyakarta City, vol 70, pp 0–8
16. Dissanayake D, Morimoto T, Ranagalage M, Murayama Y (2019) Land-use/land-cover changes and their impact on surface urban heat islands: case study of Kandy City, Sri Lanka, p 99
17. Crossman ND (2018) Drought resilience, adaptation and management policy (DRAMP) framework, p 17
18. Singh VK (2017) The applicability of night time remote sensing data in Indian context to analyze urban dynamics, pp 29–30
19. Feng X, Fu B, Yang X, Lü Y (2010) Remote sensing of ecosystem services: an opportunity for spatially explicit assessment, p 2
20. Lachowski HM, Johnson VC (2001) Remote sensing applied to ecosystem management, pp 135–136
21. Rouse W, Haas RH, Deering DW (1974) Monitoring vegetation systems in the Great Plains with ERTS, NASA SP-351. In: Third ERTS-1 symposium, vol 1

Urban Appearance in the Industry 4.0—In Case of Ho Chi Minh City



Le Thi Bao Thu

Abbreviations

AI	Artificial Intelligence
CBD	Centre Business District
HCM	Ho Chi Minh City
IoT	Internet of Things

1 Introduction

Industry is the determinant of urban appearance, caused by its role as growth pole in consuming of resources, energy, labour, invention and finance.

Along with society evolving and science/technology advancing so far, Industry has developed over four periods, which have prompted urban formation by each's characteristics, that reflecting the correlation of Industry with social context (Fig. 1).

One impact from industry to urban structure is the way that man/stuff/materials move to and from in production and consumption.

The era of AI's role in operating, moving in industry certainly change and then in turn, the urban appearance under impact of Industry 4.0 should change.

Ho Chi Minh City is the key industry region in Vietnam. This city has resources enough to develop IoT/AI, and the trend moving to industry 4.0 is inevitable. In that trend, above arguments need to be discussed to contribute to policy maker, urban planner.

L. T. B. Thu (✉)

Faculty of Civil Engineering, Ho Chi Minh City University of Technology, VNU-HCM, HCM City, Ho Chi Minh City, Vietnam

e-mail: thu.bmkt@hcmut.edu.vn

INDUSTRY 1.0	INDUSTRY 2.0	INDUSTRY 3.0	INDUSTRY 4.0
100 years - in 18th century (1750-1850)	50 years - in 19th century (1870-1920)	30 years - in 20th Century (1960-1990)	Today - 21st Cen.
Mechanization	Assembly Line	Automation	Cyber physical system
Steam Power	Electric engine	Computer	Internet
Weaving Loom	Automobile Vehicle	Electronics	Iots, Big Data, AI
Manchester of Great Britain	Detroit-USA	Asian New Industrial Countries	Global wide
Transferred from rural to urban with immigration for labor in workshops	Highway system developed	Industrial belt on surroundings of city	Suggestion: cyber space with AI control

Fig. 1 Four periods of Industry development. Re.: Authors

2 Research

2.1 Overview

Industry has affected to form the city along routes to circulate its massive load of resources for production and distribution. Achievement in transportation from requirement of Industry decided structure of urban. Those were railway and waterway in I.1.0; federal highway in I.2.0; ring road and multi-level traffic in I.30.

- a. *Industry 1.0*: consumption of coal for steam engines lead to invention of train. System of railway and canal were the main axis to locate urban functional zones in Manchester—where so call workshop of the world (Fig. 2).
- b. *Industry 2.0*: high-speed road in traffic—based on the invention fossil fuel engines vehicles—had played role in expansion of urban scale. Detroit—the thriving industrial metropolis of USA was an example (Fig. 3).
- c. *Industry 3.0*: in the latter half of twentieth century, achievement in Information Technology has triggered global trend, FDI in manufacturing flew to Asia that



Fig. 2 a Canals, rivers, and the industrial city: Manchester's industrial waterfront, 1790–1850. <https://www.jstor.org/stable/23271699>. b Manchester City Google map 2019



Fig. 3 Map of Detroit-USA Re: <https://www.wsupress.wayne.edu/books/detail/mapping-detroit>

led to requirement of vast plots for industrial use. In Ho Chi Minh City, key economic zone of Viet Nam, more than 20 Industrial Parks appearing in 10 years (1996–2006). Those have clung to outskirt of the city, promoting to upgrade surrounding traffic system, then form the spatial structure of the city (Fig. 4).

In 3 initial periods of Industry time, massive load for producing has been the main reason for government to build and develop traffic system. Those traffics have formed main frame for buildings grow up, then, sketching the urban appearance.

Industry 4.0 may have some difference, base on Conclusions of UNIDO as below:

Industry 4.0, as part of smart city initiatives, will make cities and human settlements more inclusive, safe, resilient, and sustainable, and will help address global challenges.

(in Conference of BRI 2017—UNIDO) [6, 7]

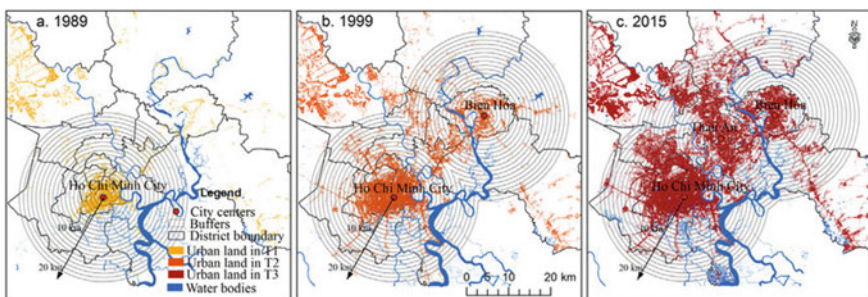


Fig. 4 Urbanization in HCMC in Industry 3.0. Re: Understanding urban expansion combining macro patterns and micro dynamics in Southeast Asian megacities from 1990 to 2014: Bangkok, Ho Chi Minh City, and Manila (2019). Gang Xu, Limin Jiao, Jiafeng Liu, Zhongkui Shi

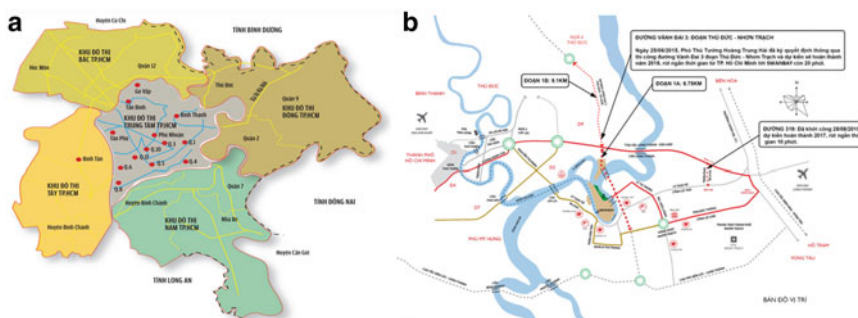


Fig. 5 **a** Urban functional structure. **b** Eastward city in traffic system of HCMC. Re: www.planic.org.vn

2.2 Research

2.2.1 Experience of Industrialization in Ho Chi Minh City

Within 10 years (1996–2006), there are 3 Export Processing Zones, 16 Industrial Parks, 1 Hi-Tech Park, initially locate in the outskirt rural area of HCMC. With massive load of moving to and from, each industrial park become node that connected together to form centric ring roads. Along those roads, buildings for other use grew up and that draw urban appearance.

In the global trend of IoTs and AI, bases on ability of relevant resources from National University and Hi-Tech park, HCMC Authorities plan to develop I.4.0 in the next period of development.

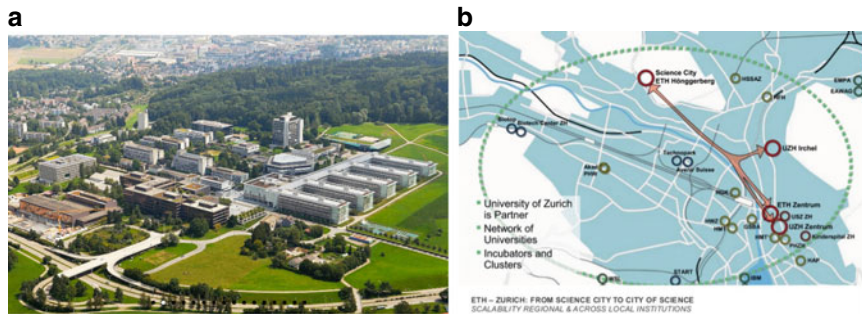
The government plan to develop eastward city as Creative city on existing resources:

- Social resources: National University; Hi-Tech Park and new urban areas in District 9; District 2
 - Infrastructure: Hanoi highway road, metro, SaiGon river waterway and Cat Lai port (Fig. 5).

2.2.2 Case Study

a. Life Science Center Schlieren-Zurich, Switzerland

The Swiss Federal Institute of Technology Zurich (ETH) and the University of Zurich are building up a number of spin-off establishments in the Life Sciences. The top-class proximity academic base on modern facility in convenient location will be the essential asset for high scientific research (Fig. 6).



32 ha masterplan with 450.000 sqm for education and research, congress centre, library, commercial facilities, housing and leisure as extension of the campus capacity

Fig. 6 ETH and regional relationship with institutes. Re: https://www.kcap.eu/en/projects/v/science_city_eth/

With space of 55.000 m², Center provides tailored infrastructure solution for more than 40 companies and some academic institutions, to support and promote the exchanges about life science among organizations located on the premises [2].

b. Pennsylvania Advances Plans for Innovation and Research Park

Considering research as a new power of economy, the University of Pennsylvania has developing an asset of 23 acre, located along the Schuylkill River in the Grays Ferry section of Philadelphia for their plan of a research park. From this park, research and innovation can be commercialized into new products or services [5] (Fig. 7).

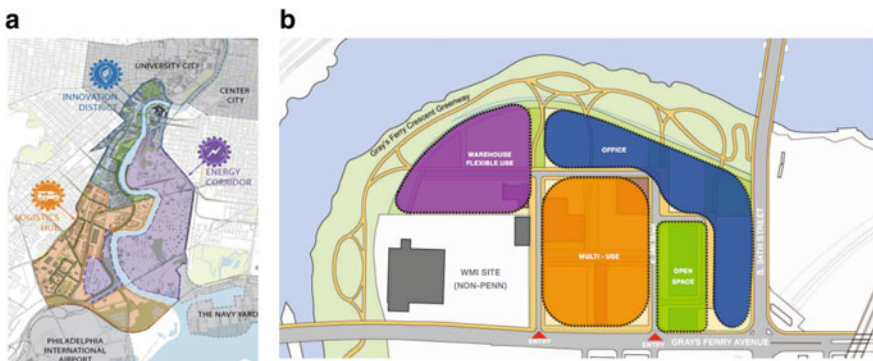


Fig. 7 a Location map. b Preliminary land use concepts. Re: <https://www.pennconnects.upenn.edu>

3 Analysis

3.1 Situation of HCMC

3.1.1 Population

HCMC's population reach 10 millions in 2018 survey with 60% in age of labor. That means HCMC need to continue with Industry 3.0 that can absorb massive labor. Existing Industrial premises supply 3.2 million jobs and creative 3 times in secondary fields (GSO).

3.1.2 Infrastructure

Industrial park is a growth pole that absorbed labor and service and finance as initial elements to change from rural to urban status in its region. In fact, Industrial park is well developed based on its owner's plan; but all the outside of its fence hadn't been. Many slums appeared quickly to provide temporary settlement and related services for workers. The traffic are always in vulnerable situation, that can be stuck by any reason.

In this existing condition, it's difficult for HCMC to move all its Industry to Industry 4.0, because I.4.0 need the infrastructure of logistic 4.0, based on AI's control.

3.2 Potential for I.4.0 in HCMC

While Industry 1.0, 2.0, 3.0 had based on invention of tool, engine and advanced technology, Industry 4.0 has been defined on achievement of AI and IoT devices. It has expected to reach an ideal result: controlled processes under algorithm bring more efficiency, less waste.

Companion of Industry 4.0 is Logistic 4.0. When processing are optimized in smart factories, stream of goods can be flown in an optimal way with smart infrastructure. In the scenario of 4.0, containers, vehicles, ... just move when they know their goods and the route from-to are ready with the help of AI on data from traffic camera, report of port/railway station, ... and report of processing result of factory [1]. In the scenario, it seems warehouse can replaced by smart vehicles. Then, the urban appearance can be changed [3].

In this case, the 2nd phase of Hi-Tech Park, or "Creative Science Park"—an asset of 195 ha, seems a potential key to set-up a project like ETH-Switzerland or SouthBank project of Pennsylvania-USA. The problem is, which scenario be right for HCMC ambition of I.4.0.

4 Discussion

4.1 Legal Issue

On June 3rd, 2019, Ho Chi Minh City People's Committee submitted a report to the Prime Minister on the policy of adjustment. HCMC general construction planning project to 2025 according to the Decision No. 24/QĐ-TTg of the Prime Minister, proposed to the Prime Minister to approve the adjustment of 194.84 ha land use planning in Long Phuoc Ward, District 9 from the function of tourism land, monuments and landscapes into the function of science and technology parks.

4.2 Feasible Scenarios

a. Expansion of Hi-Tech park phase 1

In this scenario, the main obstacle is the legal standard for Industry park, that prohibits all kind of civil buildings such as residence, entertainment, ... located inside boundary of the premises. Meanwhile, labor in Industry 4.0 need a comfortable and convenient space to work.

b. Satellite of National university

In this scenario, the premise play the role of workshop or Lab of National University, with multi-fields approach to cover. With no key field to focus, the scenario seem not to align to aim of the government.

In case study of ETH or Penn. University, they choose the key field to develop, i.e. Life Science of ETH. To follow the paradigm of case study, HCMC authorities need to decide which field to be fundamental strength.

c. Paradigm of smart city

Smart cities requires integrated interventions in planning, investment, and the uptake of new technologies. AI can help to enhance urban transportation, to manage waste or water supply, to allot energy through smart grids efficiently.

In the scenario of smart city, creative science park of HCMC has some important advantages to develop. Here is a non-vacant plots so far, it seems still in natural condition with river, lawn, damp environment with some wild animal. It seems now the right time to study of design the masterplan for the smart city in context of HCM megacity.

Four principles guide designers, planners, and policy makers in creating the sustainable cities of the future, as reference for authorities: (1) *Restore Natural Systems*; (2) *Densify Urban Districts*; (3) *Diversify Land Uses*; (4) *Connect Communities* [4].

5 Conclusion

1. Industry 4.0 should not put its footprint on urban appearance widely as former Industry. Industry 4.0 in case of Ho Chi Minh City should be found at the Creative Science Park.
2. To identify the urban appearance in Industry 4.0 can help avoiding disarranged belt surrounding Industrial premise as existing.
3. Industry 4.0 technology and its related services enhance city to smart governed. In partially, logistics 4.0 defines urban spatial structure with 2 main route of transport. One route for Industry use with constant situations, operated automatically by AI, and one route for Civil use with random situation.
 - Two route are planned separated to avoid congestion with different fundamentals such as vehicles, speed, stops,
 - In the structure of 2 systems of traffic infrastructure; the city may exist 2 types of moving: one of AI controlled with programmed moving, one of nature controlled with seasonal moving.

References

1. Barreto L, Amaral A, Pereira T (2017) Industry 4.0 implications in logistics: an overview
2. IAU (2010) Science cities: science campuses and clusters in 21st century metropolises science city in the Zurich ‘Wissenshub’
3. I-Scoop (2018) Logistics 4.0 and smart supply chain management in Industry 4.0
4. Kindel PJ (2019) Biomorphic urbanism: a guide for sustainable cities
5. Sasaki (2006) Penn connects: a vision for the future
6. UNIDO (2017a) Industry 4.0 opportunities and challenges of the new industrial revolution for developing countries and economies
7. UNIDO (2017b) The belt and road initiative: Industry 4.0 in sustainable and smart cities. Summary of BRI session on urban industrial solution

Concrete and Steel Sessions

A Study on Strain Contour Plots and Crack Development for Reinforcement Concrete Beams Based on the Application of DIC Technique



Anh Thang Le, H. T. Tai Nguyen, N. T. Hung, and Quy Duc Le

1 Introduction

Due to the increasing dramatically of steel slag in Vietnam, there are several researchers attempting to apply these industrial wastes as material in concrete. Steel slag is usually studied to replace for the natural materials in asphalt or cement concrete. However, the question is whether replacing materials would change the performance of the concrete. In this study, steel slag replacing for the natural stone is used in the concrete mixture. The Digital image correlation (DIC) method is selected for the exploration of crack development. It is selected because DIC is a cheap, exact and powerful approach.

Digital image correlation (DIC) is an image-processing method capturing displacement and deformation of an object bearing load. DIC needs the digital images of an object at different loadings using digital imaging devices. Differentiation analysis is approached to quantitatively extract full-field displacement and strain responses of materials [8]. The colorful image of an object's surface is transformed to the grey image. The DIC method will use the grey scale distribution characteristics to compare the deformed and un-deformed images in order to obtain relative positions. These variations of points on image at difference load levels are utilized to infer the normal strains, shear strain and Von-Mises strain field [9].

For concrete, strain localization and crack sizes are two key parameters needed to estimate the permeability, strength and durability of structural concrete components [2]. A direct observation of surface deformation or a crack development process is

A. T. Le (✉) · H. T. Tai Nguyen · N. T. Hung
Faculty of Civil Engineering, Ho Chi Minh City University of Technology and Education,
HCM-UTE, Ho Chi Minh City, Vietnam
e-mail: thangla@hcmute.edu.vn

Q. D. Le
Gia Lai road & bridge repair management and construction joint stock company, Pleiku, Vietnam

difficult because of the small values of them. The DIC approach could overcome the issue. The method gives high-resolution measurements of a displacement field [4].

Chu et al. [5] reported the application of digital-image-correlation techniques to experimental mechanics. The huge number of studies and its application marked the historical developments of DIC techniques over the past 35 years. Huang and Xu [6] proposed a method of cracking inspection, and detection applied for pavement. Yamaguchi et al. [11] introduced an image-based approach to detect cracks in concrete surfaces. Valen  a et al. [10] studied on the properties of concrete cracks during experimental tests using image processing. Kozicki et al. [7] conducted a study to apply digital image correlation techniques to measure displacement on the concrete surfaces. In the same year, Shih and Sung [9] conducted an applied study of the digital image correlation method in the analysis of cracks changing in reinforcement concrete beams. Adhikari et al. [1] proposed a method to determine the properties of cracks to detect and quantify cracks in concrete based on image processing techniques.

For the study, there are two types of concrete grades denoted by B22.5 and B15. The B22.5 have the minimum strength of 30 MPa, while the B15 has the minimum strength of 20 MPa after 28-day construction. Besides, there are two differences types of aggregate in the concrete mixture, including the natural stone aggregate and steel slag. Thus, three groups of reinforcement concrete beams were produced. They are the beams of B22.5 with and without steel slag, and the other group is the beams of B15 with the natural stone. The beam bending test is the three-points bending test. Canon EOS 7D digital camera takes photos for the DIC method. The observed analysis results for discussion are strain contour plots at the crack tip and the crack mouth opening displacement.

2 Experiment

2.1 Experimental Material

Materials used for the concrete mixture include aggregate, sand, Portland cement and water. The natural aggregate used for casting specimens is the stone obtained in the Dong-Nai province. Aggregate is cleared, dried, and sieved before they are composited according to the TCVN 7570:2006. The average aggregate size is of 20×10 mm; uniform particles size. Steel slag replacing for natural stone is collected by a factory in Phu-My-1. They are categorized and screened before being sold to the market. The steel slag properties are similar to the steel slag utilized in concrete in the world. They are used in many studies in southern of Vietnam. Sand is river sand. They were cleared, dried, screened to obtain the size of sand particles in accordance with TCVN 6227:1996. The sand composition and the cleanness of sand satisfy the TCVN 7570:2006. Water of the concrete mixture is domestic water ensured good

quality, does not affect the curing time of the concrete. Portland cement (PC40) was used meeting the specification of TCVN 2682:2009.

2.2 Experimental Equipments

Strain gauge, Fig. 1a, was used to measure deformation of the structural surface. In this experiment, the strain gauge was placed in the middle of span of the beam and at 100 mm from the upper edge of the reinforcement concrete beam. Strain gauge was located near the top edge of the beams so that the crack development due to the bending does not damage strain gauge. On the other hands, strain gauge was placed at a certain distance from the top of the beam so that the directly bending force on the concrete beam does not destroy the strain gauge.

The steel bending frame, shown in Fig. 1c, has the ability bending force up to 50 tons. The piston is placed at mid-span of the beam controlling the load following vertical direction. During testing process, data logger collects automatically the synchronization values of strain from the strain gauge, the bending load, and displacement at mid-span of the reinforcement concrete beams. Linear Variable Displacement Transducer (LVDT) is used to measure the beam deflection.

The cannon EOS 7D digital camera was used to take images for the DIC analysis. The images with the resolution of 5184×3456 were captured in the room lighting. The camera was placed on a fixed tripod, perpendicular to the beam, and located at a meter from the reinforcement concrete beams. Images were collected at different load levels. The taken image was synchronized with the testing data obtained from the data logger by time. The time was matched based on the time recorded on the image and the counter clock of data logger.

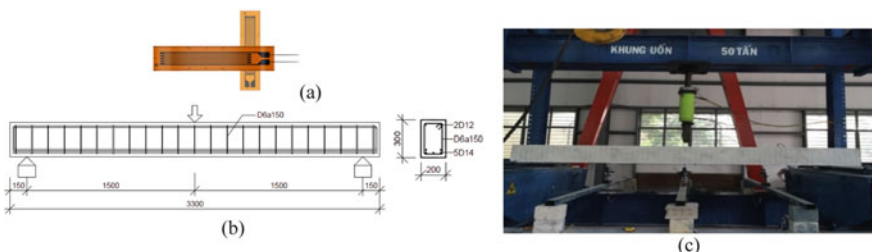


Fig. 1 Experimental equipments: **a** Strain gauge, **b** experimental reinforcement concrete beams, and **c** the bending frame

2.3 Experimental Reinforcement Concrete Beams

Figure 1b presents the geometry of a reinforcement concrete beam and the location of steel bars. The beams had the size of $3300 \times 200 \times 300$ (mm). The basic concrete properties were tested by the Vietnamese standard. The longitudinal steel reinforcement was the steel AII grade, $f_y = 280$ MPa. As a reinforcement, steel bars of the diameter 12 mm and 14 mm were used. The experimental investigation was performed on the beams in which the reinforcement was of $5\phi 14$ at the tensile part of beam and $2\phi 12$ at the compressive part of the beam. The stirrup bars of $\phi 6$, the steel grade of AI with $f_y = 225$ MPa, were arranged along the length of the beam at the distance of 150 mm.

3 Strain Contour Plots

3.1 Comparison of Strain Values Obtained by Strain Gauge and the DIC Method

The photograph, which obtained from the camera of Canon EOS 7D, may need to be processed before of the applying DIC analysis. The IMAGEJ software was used for cropping photos so that the images were uniform in size, and the studying object was in the right position to be processed. The NCORR, an open-source program running on Matlab environment [3], was selected to perform DIC analysis.

At first, the sub-images extracted from the photograph capturing the side of a beam was selected at the time before loading. The position of the sub-image is also the position of the strain Gauge. This image is called as the original image. Next, the sub-images in the same position at different load levels were selected for comparative analysis of the pixel's position changing. Based on the changing of pixel's position in the sub-image compared to the original sub-image, the strain on the beam surface within the sub-image could be calculated corresponding to the certain load level.

Figure 2 shows the deformation results on the surface of the reinforcement concrete beam with the same load-level based on two different methods. The strain value showing in the left-hand side figure is determined by the DIC method at the position of strain gauge. The right-hand side figure is the deformation directly measured by strain gauge and recorded by the data logger. DIC gives a result of $-207.61 \mu\epsilon$, shown in Fig. 2a.

Figure 2b shows the value obtained from the screen of data logger. The observed value is $-206.72 \mu\epsilon$. The negative value indicates the strain determined in the compressive concrete area. This value was approximately equal to that estimated by the DIC method, because the strain gauge was attached to the same position of strain evaluated by DIC. The error was less than 1%.

If it were assumed that the strain value measured by the strain gauge is the real value, then the error of the DIC method compared to the actual result is negligible.

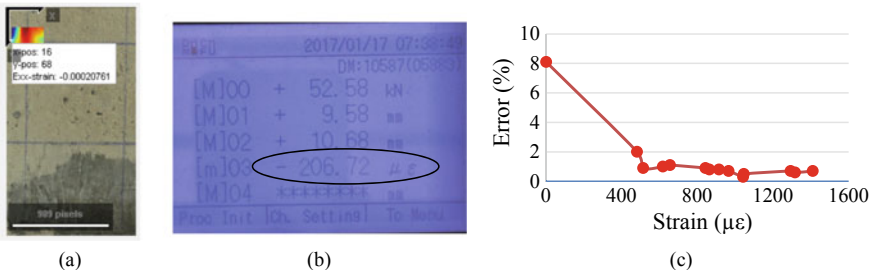


Fig. 2 Deformation on the beam surface estimated by the different methods: **a** DIC, **b** Strain gauge, **c** errors of DIC method at various strain values

Besides, the small error of DIC method indicates that all input parameters required for DIC analysis, including the parameters of a photograph such as the resolution, the brightness, the size of sub-image, etc. could be used for the next analysis steps.

3.2 Exploration the Sensitive of Error

Table 1 summarizes the comparison of strain induced by different load levels. During the beam testing of B22.5, fourteen images were taken for the reinforcement concrete beams with the aggregate. The beam was failed at loading level of 94.64 KN. Table 1 also shows the error of estimate deformations by DIC method varying following the value of strain. The DIC method could measure the small deformation at low loading level to the larger deformation at the loading level corresponding to the destruction of the reinforcement concrete beams sample. The deformation, that DIC can accurately determine, is about 500 $\mu\epsilon$. DIC still gives good results as the strain greater than

Table 1 Comparison of beam's deformation at different load levels

RC beam of B22.5				RC beam of B22.5			
Load (KN)	Strain gauge ($\mu\epsilon$)	DIC ($\mu\epsilon$)	Error (%)	Load (KN)	Strain gauge ($\mu\epsilon$)	DIC ($\mu\epsilon$)	Error (%)
6.19	-1.93	-2.10	8.1	86.84	-915.77	-922.70	0.8
54.93	-482.03	-491.90	2.0	87.22	-966.00	-972.40	0.7
58.02	-514.88	-519.80	0.9	89.94	-1043.28	-1046.60	0.3
60.15	-619.21	-625.50	1.0	90.31	-1047.14	-1052.90	0.5
69.65	-655.97	-663.20	1.1	92.78	-1294.44	-1304.50	0.7
83.63	-844.28	-852.10	0.9	93.28	-1317.62	-1325.40	0.6
84.88	-864.57	-871.80	0.8	94.64	-1411.33	-1421.50	0.7

$1400 \mu\epsilon$. The errors of the DIC method corresponding to fourteen load levels of the B22.5 beams are shown in Fig. 2c. In the initial, the value of strain is very small resulting in large errors due to noise.

3.3 Strain Contour Plots

The strain contour plots were explored for the various beams of B22.5, B15, and B22.5 with steel slag. The photos captured the cracks located at mid-span of the beams and developed bottom-up due to the three-points bending test. The strain contours were plotted at the crack tip areas corresponding to different value of loading. The chosen loading levels were the load levels as the beam failure. For the reinforcement concrete beam of B22.5, the strain contours of crack was captured at the load of 93.28 KN (Fig. 3a). Besides, the strain contour was plotted at the crack tip as the load reaching to 77.81 KN for the reinforcement concrete beam of B15 (Fig. 3c). The load of 101.81 KN was selected to explore strain contours at the crack tip for the reinforcement concrete beam of steel slag (Fig. 3b).

Based on the strain contour plots, the plastic zone near the crack tip might be observed. For the concrete grade of B22.5, the plastic zone in front of a crack tip could be observed clearly such as Fig. 3a, b. They are the light color areas locating at the head to the crack tip. However, that zone could not be observed clearly in case of the concrete grade of B15 (Fig. 3c). It indicates that the area of plastic zones in front of a crack tip were strongly depended on the concrete grade rather than the source of aggregate. The plastic zones in front of a crack tip are related to the crack development. The crack development will be considered in the next sections.

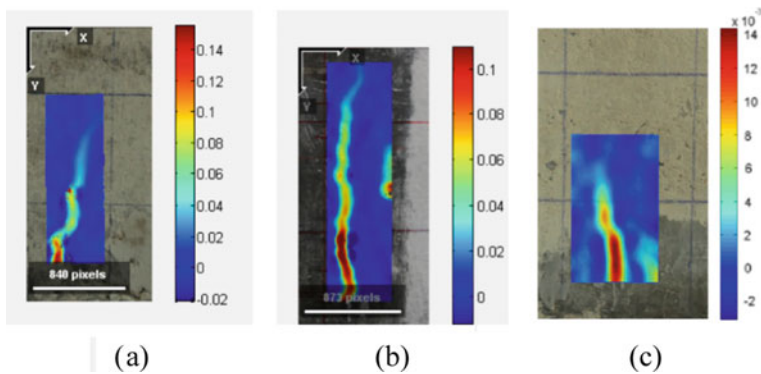


Fig. 3 The strain contour plots at the crack tip: **a** the reinforcement concrete beam of B22.5, **b** the reinforcement concrete beam of steel slag and **c** the reinforcement concrete beam of B15

4 Crack Development of Concrete Beams

Figure 4 shows the crack mouth opening displacement (CMOD) varying with the bending load of beams. CMOD is measured at the position of the outer layer of the tension steel bars. CMOD might be effected by steel reinforcements. With the layout of the steel bar reinforcements as in Fig. 1b, the CMOD was estimated at the 30 mm from the bottom of the beams.

For the beam of B22.5 (Fig. 4a), CMOD was observed through the image-processing results. When the load P was less than 60 KN, there had not been cracking seen on the beam. At this loading level, the beam still worked in the elastic phase. As the loading over 70 KN, the lower part of the beam started to appear cracks. The initial CMOD could be observed as 0.102 mm. The CMOD did increase gradually with the increasing of the load. At the load of 94.64 KN, the ultimate loading of the beam, the CMOD was 1,085 mm. For the beam of B15 (Fig. 4c), the beam still worked in the elastic phase as the load P was less than 38 KN. As the loading level over 38 KN, the initial CMOD could be observed as 0.113 mm. The CMOD also did increase gradually with the increasing of the load. At the ultimate load of 77.81 KN, the largest CMOD was 0.185 mm.

There is the comparing of the crack development in the reinforcement concrete beams with the same steel reinforcements and difference concrete grades. The development crack in the B15 beam appeared earlier than that of the B22.5 beam. The initial observed CMOD of both beams was the same, $CMOD = 0.1$ mm. Besides, the CMOD corresponding to the ultimate load of the B15 beam is ten times smaller than that of the B22.5 beam. It indicates that the grade of concrete in a reinforcement concrete beam effects to the initial development and the width of crack, although the crack might be control by the steel reinforcements.

For the beam of steel slag (Fig. 4b), the beams still worked in the elastic phase as the load P was less than 70 KN. As the loading level over 70 KN, the initial CMOD could be observed as 0.119 mm. The CMOD kept the increase with the increasing of the load. However, there was a jump of CMOD as the load reached up to 94.89 kN. At the ultimate load of 101.81 KN, the largest CMOD was 1.922 mm. The aggregate affected the bending load capacity of a beam. The steel slag beam had the loading capacity higher than that of the B22.5 beam.

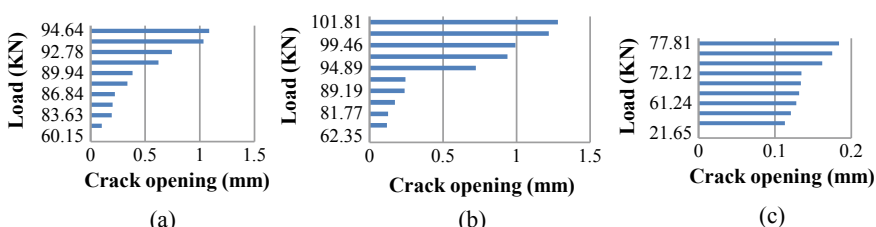


Fig. 4 The CMOD: **a** the reinforcement concrete beam of B22.5, **b** the reinforcement concrete beam of steel slag, and **c** the reinforcement concrete beam of B15

The crack development might depend on the stone aggregate. As comparing beams having the same concrete grade with and without steel slag, the initial CMOD was the similar, but the process of crack development of the beam containing steel slag was a little different from the conventional beams. With the steel slag beam, the CMOD corresponding to the ultimate loading was increased 77% comparing to that of the natural aggregate beams with the same concrete grade. The crack development speed accompanying the increasing of load was also increased. On the other words, the steel slag aggregate did affect in the crack development of the reinforcement concrete beams.

5 Conclusions

The three-point bending test was performed on the reinforcement concrete beams with dimensions of $3300 \times 200 \times 300$. This test was for exploration the strain contour plots at the crack tip and crack development of beam structure with and without steel slag replacing natural stone aggregate. Besides, the beams with difference concrete grades were tested for the comparison. DIC method was chosen for analyses the deformation of the reinforced concrete beams. At first, the method was calibrated and verified by the comparison between the deformation determined by DIC and that measured from strain gauge. The following conclusions could give as:

- The areas of plastic zones in front of a crack tip were strongly depended on the concrete grade instead of the aggregate. The lower the concrete grade we have, the smaller the area of the plastic zone at a crack tip could be observed.
- The crack development in a reinforcement concrete beam might not depend on the stone aggregate; it depends on the concrete grade. CMOD corresponding to the ultimate load in case of B15 is smaller than the CMOD in case of concrete grade of B22.5.
- The steel slag aggregate did effect to the crack development of the reinforcement concrete beams.

Acknowledgements The authors are grateful for the financial support as well as the experimental equipment of the HCM University of Technology and Education.

References

1. Adhikari RS, Moselhi O, Bagchi A (2014) Image-based retrieval of concrete crack properties for bridge inspection. *Autom Constr* 39:180–194
2. Bazant ZP (1998) Fracture and size effect in concrete and other quasi-brittle materials. CRC Press LLC, Boca Raton
3. Blaber J, Adair B, Antoniou A (2015) Ncorr: open-source 2D digital image correlation matlab software. *Exp Mech* 55(6):1105–1122

4. Bornert M, Brémand F, Doumalin P, Dupré JC, Fazzini M, Grédiac M, Hild F, Mistou S, Molimard J, Orteu JJ, Robert L (2009) Assessment of digital image correlation measurement errors: methodology and results. *Exp Mech* 49:353–370
5. Chu TC, Ranson WF, Sutton MA (1985) Application of digital-image-correlation techniques to experimental mechanics. *Exp Mech* 25(3):232–244
6. Huang Y, Xu B (2006) Automatic inspection of pavement cracking distress. *J Electron Imaging* 15(1):013017
7. Kozicki J, Tejchman J (2013) Application of DIC technique to concrete—study on objectivity of measured surface displacements. *Experimental Mechanics* 53(9): 1545–1559
8. Pan B (2018) Digital image correlation for surface deformation measurement: historical developments, recent advances and future goals. *Meas Sci Technol* 29(8):082001
9. Shih MH, Sung WP (2013) Application of digital image correlation method for analysing crack variation of reinforced concrete beams. *Sadhana* 38(4):723–741
10. Valença J, Dias-da-Costa D, Júlio ENBS (2012) Characterisation of concrete cracking during laboratorial tests using image processing. *Constr Build Mater* 28(1):607–615
11. Yamaguchi T, Nakamura S, Saegusa R, Hashimoto S (2008) Image-based crack detection for real concrete surfaces. *IEEJ Trans Electr Electron Eng* 3(1):128–135

Application of Modified D-Value Method Considering Plastic Strain Hardening Effect to Prediction of Structural Mechanics of Steel Moment Resisting Frames with New Column Support System



Naoki Tamura, Sachi Furukawa, and Yoshihiro Kimura

1 Introduction

As a connection type of column bases of steel moment-resisting frames to reinforced concrete base beams, embedded type column base is commonly adopted in Japan. With embedded type column base, or fixed column base, column bases of the first story columns for frames designed following current design codes may yield, because it cannot be avoided that the bending moment become substantially large at the base. Kimura et al. [2, 3] has proposed the concept to realize beam yielding mechanism of a steel moment-resisting frame by applying a pin-support column base system to midpoints of the first story columns. With this system, or mid-story pin column system, moment at the top and base of the first story columns are adjusted to be uniform. Therefore, the first story columns are designed to be remained in elastic until the maximum story drift of the frame exceeds 0.03 rad. In practice, structural design requires multiple trials to optimize selection of structural components whether their combinations meet designated seismic demands on a frame. The D-value method [5] is a design method based on fundamental structural mechanics to predict story drift distribution of a moment-resisting frame under designated lateral force distribution. The D-value method has advantage to predict structural performance directly with respect to structural properties of members.

This paper evaluates seismic performance, especially flexural demand on columns for a moment-resisting steel frame adopting a mid-story pin column base to maintain them elastic until a frame reaches the ultimate limit state. Because the original D-value method is only applicable to a frame with linear structural behavior and to that

N. Tamura (✉) · S. Furukawa · Y. Kimura
Graduate School of Engineering, Tohoku University, Sendai, Japan
e-mail: naoki.tamura.s7@dc.tohoku.ac.jp

with a conventional column base, it is extended to predict elasto-plastic behavior of frames [5]. In addition, this paper furtherly develop the modified D-value method, originally developed by Ando et al. [1], to consider strain hardening effect of beams on seismic structural mechanics.

2 Prediction of Elasto-plastic Mechanical Behavior of a Steel Moment-Resisting Frame with Mid-story Pin Column Base by Modified D-Value Method

2.1 Bending Moment Distribution Prediction

In calculation of bending moment distribution of elastic stories, the original D-value method is adopted by Muto [5], i.e., calculating them by determining the height ratio of inflection points of all stories (Fig. 1). In the D-value method, the height ratio of inflection points y_i is estimated considering mechanical characteristics of the frame: distribution of lateral load, P_{fi} (y_{0i} in Eq. 1), distribution of beam-to-column stiffness ratios (y_{1i}), story height of all stories (y_{2i} and y_{3i}), and restrained condition of the column base at the first story (y_{4i}). The last term of y_{4i} is newly introduced to consider a change of a column base system from a conventional, to which the original D-Values method is applicable, to a mid-story pin column base. Each term is determined in terms of a column-to-beam flexural stiffness ratio.

$$y_i = y_{0i} + y_{1i} + y_{2i} + y_{3i} + y_{4i} \quad (1)$$

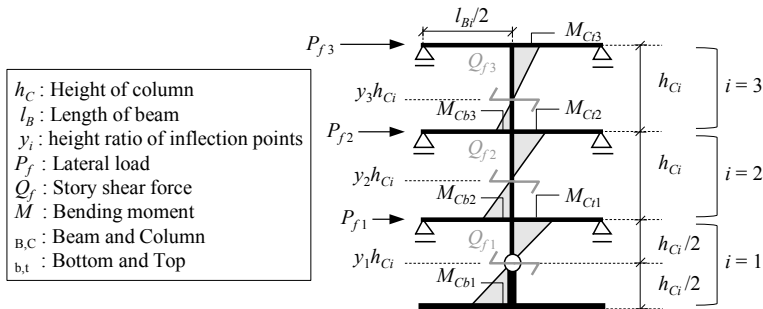


Fig. 1 Definition of stress distribution of moment-resisting frame with mid-story column base

2.2 Story Drifts Prediction

Because the original D-value method is only applicable to a frame with linear structural behavior and with a conventional column base, it is extended to predict elasto-plastic behavior of a moment-resisting frame with mid-story pin column base. In the modified D-value method, increments of stress and deformation of a post-yield frame are calculated every after additional beams are yielded as lateral forces increases. Here, beams are assumed to be yielded sequentially from the bottom to the top stories, while columns are assumed to remain in elastic. In some calculational step, a frame mechanical model is divided into two groups, as shown Fig. 3: One is the ‘post-yield’ lower stories where beams have been already yielded, and the other is the ‘pre-yield’ upper stories where beams are remained in elastic. The former lower stories are defined as ‘a plastic story,’ and the later as ‘elastic stories,’ hereinafter. The m th-story in Fig. 2 represents the top story of a plastic story, where beams are going to be plastic in the current incremental calculation step.

(i) Elastic stories

A Story drift of elastic stories are estimated by following the original D-value method [5].

(ii) Plastic story

To predict bending moment and story drift distributions, a plastic frame is modeled as a story with a long continuous column extending multiple stories and with elastic beams on the top, after removing all yielding beams (Fig. 2). Where perfect elasto-plastic flexural behaviour is adopted for beams. Bending moment, story drifts of a plastic story and rotational angle of yielded beam ends are calculated by applying a virtual work theory. Lateral deformation of the continuous column at the i th story ΔD_i is assumed to be given by the summation of the cantilever bending deformation of the column ΔD_{Fi} and the sway deformation restrained by a rotational spring at the top whose notational stiffness is provided by elastic beams ΔD_{Ri} (Eq. 2). The

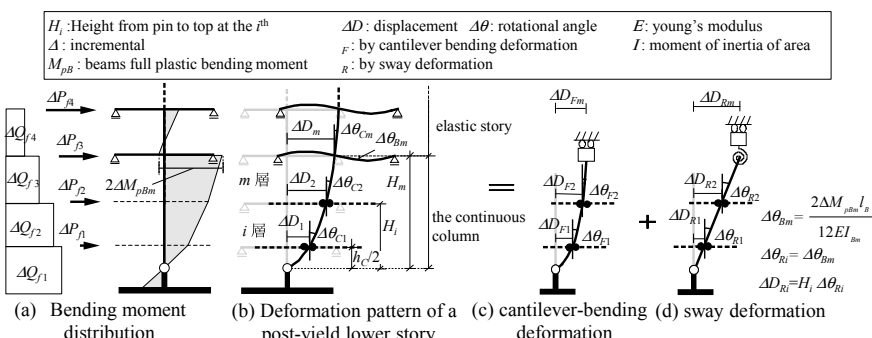


Fig. 2 Lateral deformation of a post-yield frame (in the case of $m = 3$)

rotational angle of beam end $\Delta\theta_{Bi}$ is assumed to be equal to that of the column $\Delta\theta_{Ci}$ at the i th story, which is also obtained by the summation of the cantilever bending deformation of the column $\Delta\theta_{Fi}$ and the sway deformation $\Delta\theta_{Ri}$ (Eq. 3).

$$\Delta D_i = \Delta D_{Fi} + \Delta D_{Ri} \quad (2)$$

$$\Delta\theta_{Ci} = \Delta\theta_{Fi} + \Delta\theta_{Ri} \quad (3)$$

3 Prediction of Elasto-plastic Mechanical Behavior of a Steel Moment-Resisting Frame with Mid-story Pin Column Base by Modified D-Value Method Considering Plastic Strain Hardening Effect of Beams

3.1 Bending Moment Distribution Predicted

Redistribution of bending moment of a frame due to plastic strain hardening of beams is additionally considered in the formulation of the modified D-Value method.

Figure 4 shows column moment distribution with and without considering strain hardening effects of beams (Fig. 3a, b respectively). As shown in Fig. 4, The incremental column moment distribution (Fig. 3b) at a some frame plastic condition is assumingly obtained as the summation of incremental column moment distribution (Fig. 3b), calculated for a perfect elasto-plastic frame model described in Sect. 2, and redistributed column moment $\Delta M'_{Ci}$ (Fig. 3c) due to strain hardening of beams.

(i) Increment of beam moment due to strain hardening of beams

Giving the skeleton curve of beam's plastic moment with respect to a rotational angle of a beam end, the increments of beam moment due to strain hardening (Fig. 3c) can be determined if a frame's flexural deformation is determined. Here, flexural

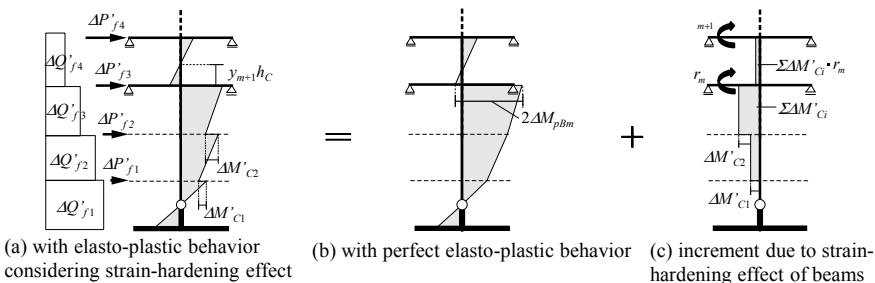
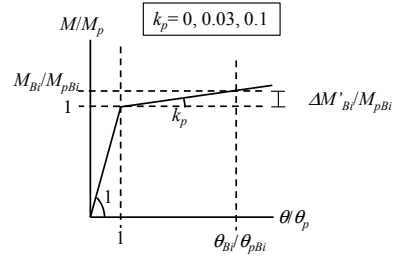


Fig. 3 Column moment distribution of moment-resisting frame (in the case of $m = 3$)

Fig. 4 Moment—plastic rotation relationship



deformation of a frame, including rotational angles of beam ends, is assumed to be equal to that of a frame, whose beams have perfect elasto-plastic behaviour. Therefore, the incremental rotational angle of beams $\Delta\theta_{Bi}$ can be calculated by Eq. 4.

The rotational angle θ_{Bi} of the i th-story beam end is calculated by Eq. 4. Where θ_{pBi} is the rotational angle of the i th story's beam-to-column connection when the beams reach their full plastic bending moment M_{pBi} .

$$\theta_{Bi} = \Delta\theta_{Bi} + \theta_{pBi}, \quad \theta_{pBi} = \frac{M_{pBi}l_B}{12EI_{Bi}} \quad (4)$$

Assuming a bilinear mechanical behaviour of a beam, as shown in Fig. 4, the increment of the i th story beam moment due to strain hardening of the beam is given as follow:

$$\Delta M'_{Bi} = M_{Bi} - M_{pBi}, \quad M_{Bi} = M_{pBi} \left\{ \left(\frac{\theta_{Bi}}{\theta_{pBi}} - 1 \right) \cdot k_p + 1 \right\} \quad (5)$$

(ii) Column bending moment distribution in i th story beams become plastic

Redistributed column moment due to strain hardening, $\Delta M'_{Ci}$ ($=2\Delta M'_{Bi}$) obtained from Eq. 4, acts on the i th story's beam-to-column connection of the continuous column as concentrated moment (Fig. 3c). The moment at the top of the continuous column of a plastic story is calculated as the summation of $\Delta M'_{Ci}$ for $i = 1$ to $m - 1$. The moment that propagates to the upper elastic stories are calculated by considering a carryover factor r_i . Where a carryover factor r_i is a coefficient of transmitting ratio of redistributed moment from the i th story to the adjacent stories proposed in [5]. Here, r_i is determined considering change in height of the lower story, or a plastic story, comparing with elastic stories, following [5].

3.2 Prediction of Bending Moment Distribution of Fishbone-Shaped Frame

The lateral displacement ΔD_i of the i th story considering the strain hardening effect of beams is obtained based on Eq. 2. Where the lateral displacement induced by $\Delta M' C_i$ is additionally included in the cantilever bending deformation of the column in the i th story ΔD_i in Eq. 2.

4 Analytical Model: Static Analysis of a Six-Story Steel Frame

Figure 5 shows the analytical models for a six-story fishbone-shaped steel frame model with mid-story pin column base. Beams and columns are modelled by beam element based on Bernoulli-Euler theory. ABAQUS version 6.13 is adopted for analytical simulation. The frame model is designed following the current Japanese design standards. Lateral force distribution is determined following Ai distribution, i.e., design shear distribution designated in the Japanese design code. Element sections with a beam-to-column stiffness ratio of 1.8 are assigned. However, columns are set to be elastic in analysis until frame mechanism is formed to clarify the maximum flexural moment demand on the columns. Young's modulus E_s and yield stress σ_y of steel are 205,800 (N/mm²) and 235 (N/mm²), respectively. Young's modulus E_c of concrete is 27,300 (N/mm²). As shown in Fig. 4, 0, 0.03 and 0.1 is given as a parameter of the secondary stiffness of yielding beam members due to strain hardening k_p . $k_p = 0$ means perfect elasto-plasticity, while $k_p = 0.03$ is considered as standard secondary stiffness of H-shaped steel beams [4].

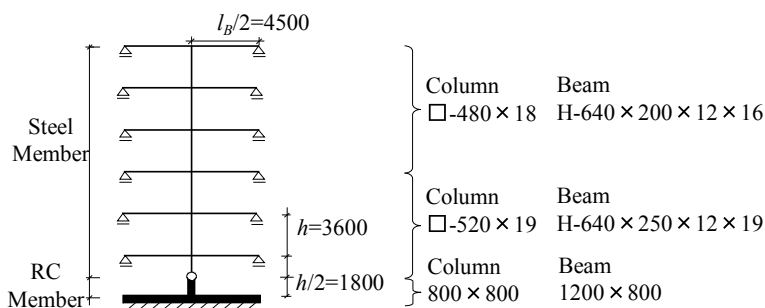


Fig. 5 Model of 6th-story frame

5 Results of Static Analyses: Verification of D-Value Method and Strain-Hardening Effects on Frame Behavior

Figure 6 shows the increments of column moment when the 4th-story beams starts to yield, comparing the results of the modified D-value method and those of the numerical analysis. The parameter is the secondary stiffness of yielding beam members k_p . The vertical axis shows the story number and the lateral axis shows the increments of column moment. The modified D-value method successfully predicts the results obtained by numerical analysis.

Figure 7 shows The changing the required value due to changes in k_p . Figure 7a shows the relationship between k_p and the maximum story drift, and Fig. 7b shows the relationship between k_p and the maximum column moment normalized the full plastic moment of beams M_C/M_{pB} at initial yielding of each story beams. Figure 7b shows the flexural strength demand on columns in order to keep them elastic. The results obtained by the modified D-value method are shown by lines, and the results of numerical analysis are shown by plots. The modified D-value method successfully predicts the results obtained by numerical analysis. Figure 7(a) shows that the maximum story drift decreases as k_p increases. This is because yielded beams keep resisting further deformation by strain hardening effect, and the deformation of the frame becomes smaller. On the other hand, M_C/M_{pB} in Fig. 7b does not change regardless of k_p .

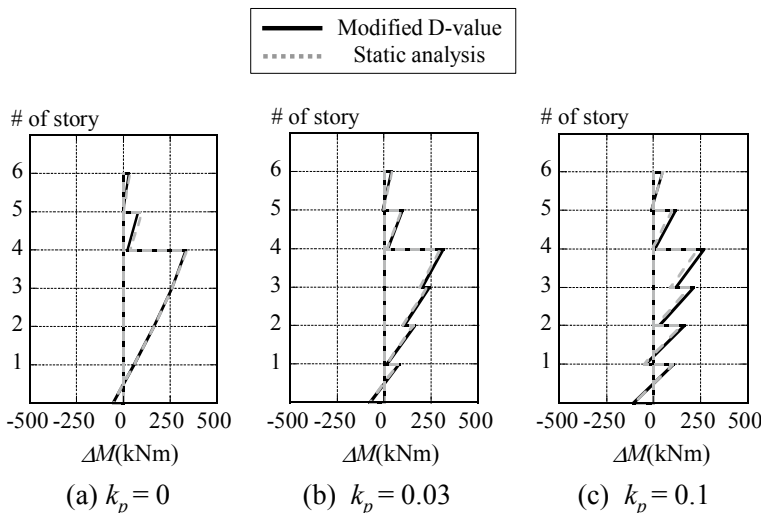


Fig. 6 Increment of column moment (in the case of $m = 4$)

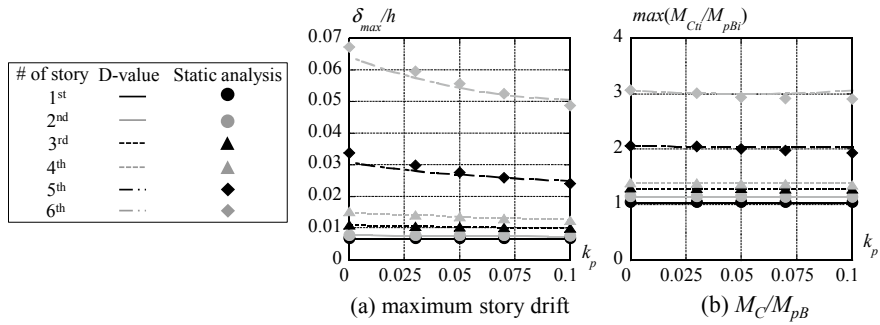


Fig. 7 Effect of k_p on mechanical characteristics of frames at initiation of beam yielding of i -th story

Figure 8 shows the comparison of column moment at initial yielding of the second, 4th and 6th story for different k_p . As k_p increases, the moment of the first- and second-story columns increase, while larger column moment of the top side of the 3rd to 6th stories scarcely change. This results shows that strain hardening effect of beams do not cause further increase in the moment of the upper stories' columns.

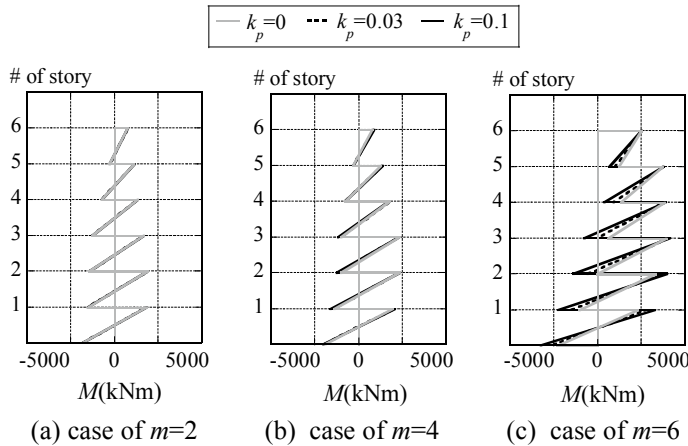


Fig. 8 Comparison of column moments for different k_p

6 Conclusions

- (1) Based on A modified D-value method proposed by Ando et al. [1], a method was proposed to predict bending moment and story drift distributions of a steel moment-resisting frame with a mid-story pin column base when considering strain hardening effect of beams.
- (2) Considering strain hardening effect of beams, the maximum story drift decreases because plastic beams resist further deformation every after they are yielded.
- (3) Strain hardening effect of beams do not cause increase in the moment of the upper stories' columns.

Acknowledgements This works is supported by JST Program on Open Innovation Platform with Enterprises, Research Institute and Academia.

References

1. Ando M, Kimura Y, Furukawa S (2017) Proposal of modified D-value method to seismic performance of steel moment resisting frames with new column support system. Proc Constr Steel 25:627–630 (in Japanese)
2. Kaneda K, Kimura Y, Miyahara N, Wada A (2011) Ultimate seismic capacity of multi-story steel moment resisting frames having new column support system. J AJJ 76:649–658 (in Japanese)
3. Kaneda K, Kimura Y, Mutsukura K, Kadoya H, Watanabe T, Takahashi K (2011) Cyclic loading test for partial frames with new column support system for multi-story steel moment resisting structures to perform beam yielding mechanism. J AJJ 76:1357–1366 (in Japanese)
4. Kato B, Akiyama H, Obi Y (1977) Deformation characteristics of H-shaped steel members influenced by local buckling. J AJJ 76:1357–1366 (in Japanese)
5. Muto K (1963) Seismic design method (in Japanese)

Calibrating the K&C Material Model for Fiber Reinforced Concrete Structures



Duc-Kien Thai and Duy-Duan Nguyen

1 Introduction

Fiber reinforced concrete (FRC) has been widely used in construction. A number of studies concerning about structural behavior of FRC have been carried out. For numerical analysis approach, the problem comes from the fact that, while there have been numerous material models for conventional concrete, none of the model has been developed specifically for FRC structures. Actually, the need to simulate FRC structures is increasing. This requires the improvement of material models relevant to structural behavior of FRC under both static and dynamic load conditions, which is very urgent.

The commercial software, LS-DYNA, provides several material models for concrete such as Karagozian & Case Concrete (K&C) model (MAT#072r3), Winfrith Concrete (MAT#084), and Continuous Surface Cap (CSC) model (MAT#159). Among them, K&C model, which was initially proposed by Malvar et al. [7], has been widely chosen by researchers for simulation of FRC structures subjected to both static and dynamic loading conditions. Since the structural behavior of FRC is quite different from the conventional concrete, it is required to calibrate the input parameters using test data. Lin and his colleagues [4, 5] calibrated this material model for high performance and ultra-high performance fiber reinforced concrete. However, the most significant limitation in these works is lacking of tri-axial test data, which directly support the calibration of the input parameters of the K&C model. Moreover, none of the given calibration provided calibrated input parameters that are capable to modeling of FRC. This fact gives a strong motivation to conduct this study.

This paper presents the calibration of K&C model for simulating the structural behavior of FRC structures under different loading conditions. For this purpose, various experimental data on tension, compression, and high-rate behaviors of FRC

D.-K. Thai (✉) · D.-D. Nguyen

Department of Civil and Environmental Engineering, Sejong University, Seoul 05006, Korea
e-mail: thaiduckien@sejong.ac.kr

material using axial and tri-axial tests are used to calibrate the input parameters. Numerical simulations of single tests on compression and bending subjected to static loading and of a FRC beam under blast loading are carried out to illustrate the performance of the calibrated material model. It is shown that results induced by the calibrated material model proposed in this study are in good agreement with the experimental data.

2 Calibration of Material Model

2.1 Three Failure Surfaces

The K&C material model [7] is a three-invariant model, in which the three independent shear surfaces are the functions of the hydrostatic pressure, as shown in Fig. 1. These three failure surfaces are determined based on three specific points yield (Pt. 1), maximum (Pt. 2), and residual (Pt. 3) strengths on the typical stress-strain relationship of compression test of concrete, as presented in Fig. 2.

The yield strength surface $\Delta\sigma_y$, maximum strength surface $\Delta\sigma_m$, and residual strength surface $\Delta\sigma_r$, are expressed as the function of pressure as

$$\Delta\sigma_y = a_{0y} + \frac{p}{a_{1y} + a_{2y}p}; \Delta\sigma_m = a_0 + \frac{p}{a_1 + a_2p}; \text{ and } \Delta\sigma_r = \frac{p}{a_{1f} + a_{2f}p} \quad (1)$$

Fig. 1 Three failure surfaces in K&C model

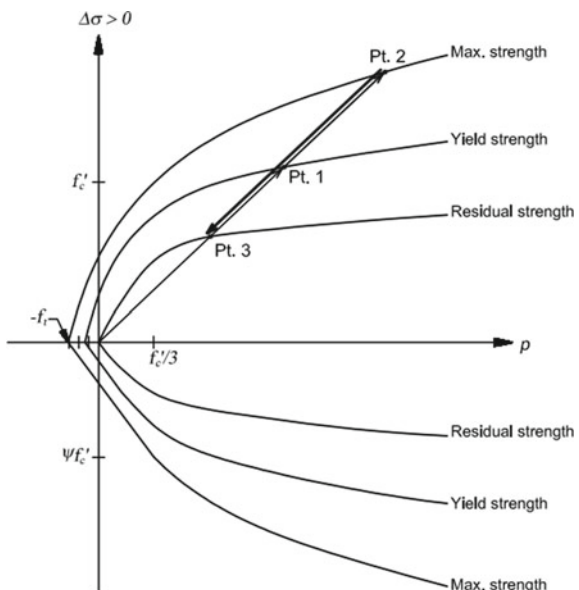
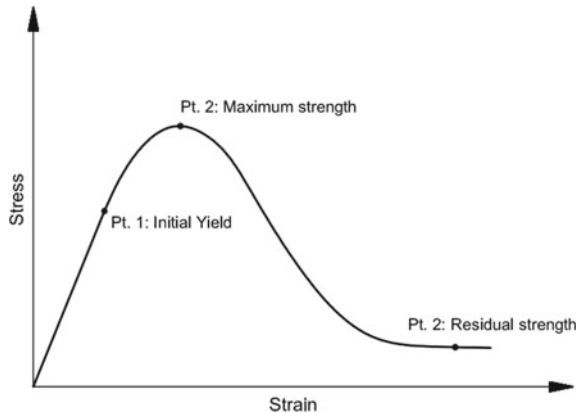


Fig. 2 Typical stress-strain curve of concrete



where $p = -(\sigma_1 + \sigma_2 + \sigma_3)/3$ is the pressure and a_{ij} are defined failure surfaces parameters, which are determined based on the tri-axial compression test data. The current stress limited by the deviatoric stresses is determined by mean of linear interpolation between the two surfaces, governed by the user-defined curve (η, λ) .

The modified effective plastic strain is defined by the damage functions as

$$\lambda = \begin{cases} \int_0^{\bar{\varepsilon}^p} \frac{d\bar{\varepsilon}^p}{r_f(1+p/r_f f_t)^{b_1}} & \text{for } p \geq 0, \\ \int_0^{\bar{\varepsilon}^p} \frac{d\bar{\varepsilon}^p}{r_f(1+p/r_f f_t)^{b_2}} & \text{for } p < 0. \end{cases} \quad (2)$$

where $d\bar{\varepsilon}^p$ is the increment of effective plastic strain; r_f is the strain rate enhancement factor; f_t is the tensile strength of concrete; and b_1 and b_2 are the damage scaling parameters for the case of compression and tension, respectively.

To control the volumetric damage in tri-axial tension, a volumetric damage increment is added to the deviatoric damage whenever the stress path is close to the tri-axial tensile path. A ratio of $|\sqrt{3J_2}/p|$ is measured to be closeness to this path. The incremental damage now is multiplied by a factor f_d , given by

$$f_d = \begin{cases} 1 - \frac{|\sqrt{3J_2}/p|}{0.1}, & 0 \leq |\sqrt{3J_2}/p| < 0.1, \\ 0, & |\sqrt{3J_2}/p| \geq 0.1. \end{cases} \quad (3)$$

The modified effective plastic strain is incremented by

$$\Delta\lambda = b_3 f_d k_d (\varepsilon_v - \varepsilon_{v,yield}) \quad (4)$$

where b_3 is a damage parameter; k_d is the internal scalar multiplier; ε_v and $\varepsilon_{v,yield}$ are the volumetric strains at current and at yield, respectively.

The volumetric behaviour of this material model is governed by a pressure—volumetric strain curve, described by a tabulated compaction equation of state (EOS) function, expressed as

$$p = C(\varepsilon_v) + \gamma T(\varepsilon_v)E \quad (5)$$

where p is the current pressure; ε_v is the volumetric strain; $C(\varepsilon_v)$ is the tabulated pressure evaluated along the isotherm at 0.0 K; $T(\varepsilon_v)$ is the tabulated temperature-related parameter; γ is the specific heat ratio; and E is the internal energy.

2.2 Calibration of K&C Material Model

K&C model has total of 49 input parameters, which are defined by the user [6]. This section presents the calibration of input parameter for FRC based on the test data. The parameters on (1) failure surfaces, (2) damage function, (3) equation of state function, and (4) damage evolution are determined.

A series of compressive tests of FRC under active confining pressure, conducted by Gholampour and Ozbakkaloglu [1], is used. They provided the test data of axial stress-strain relationship with different levels of confining pressures of 0, 5, 10, 15, and 25 MPa. Two FRC mixes C50-1 and C100-1, corresponding to compressive strengths of 50 and 100 MPa, containing hooked fiber at a volume ratio of 1%, are selected for the purpose of this study.

A calibration procedure presented in Markovich et al. [8] is adopted in this process. Based on the stress-strain curves from the test data, the yield strengths, maximum strengths, and residual strengths are defined. Figure 3 shows the fitting curves for three independent strength surfaces. While, the calculated failure surface parameters for two different FRC mixes are summarized in Table 1.

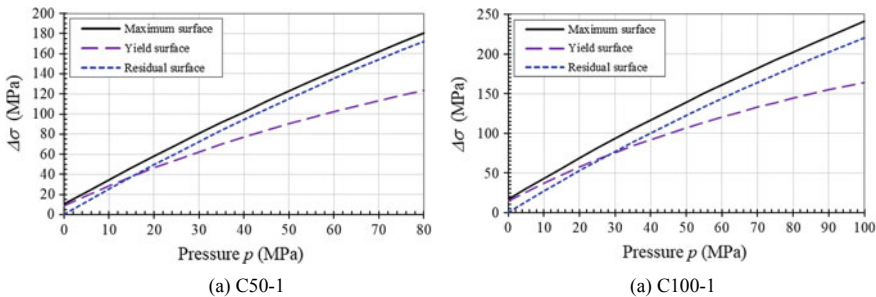


Fig. 3 Three independent strength surfaces

Table 1 Calculated failure surface parameters for FRC mixes

FRC mix	Failure surfaces parameters ^a							
	a_0	a_I	a_2	a_{0y}	a_{Iy}	a_{2y}	a_{If}	a_{2f}
C50-1	10.32	0.40,181	0.00085	8.46	0.47128	0.00281	0.38268	0.00102
C100-1	16.68	0.37027	0.00076	14.26	0.41249	0.00254	0.36272	0.00091

^aThe unit used for strength of FRC is MPa

Table 2 Defined rate enhancement factors

Strain rate	DIF	Strain rate	DIF
-1000	3.60	0	1.00
-500	3.09	0.00001	1.04
-100	1.90	0.0001	1.08
-53	1.33	0.001	1.12
-30	1.32	0.01	1.16
-20	1.31	0.1	1.21
-10	1.29	1	1.25
-1	1.25	10	1.30
-0.1	1.20	20	1.32
-0.01	1.15	30	1.60
-0.001	1.10	50	1.94
-0.0001	1.05	100	2.53
-0.00005	1.03	500	4.66
0	1.00	1000	6.07

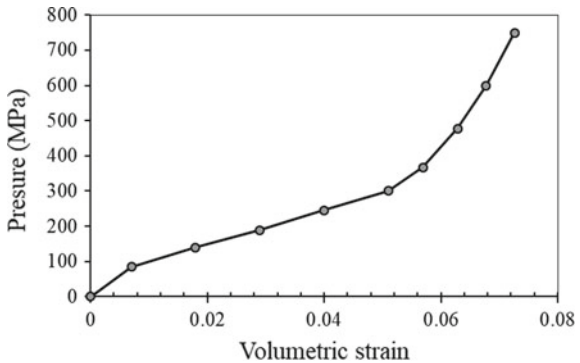
The effect of strain-rate is taken into account by inputting the dynamic increment factor (DIF). In this study, the model of Sun et al. [10] is chosen for compression, whereas the model of Park et al. [9] is employed for tension. The input data for strain-rate enhancement factors are summarized in Table 2.

The damage function $\eta(\lambda)$ is a user-define function inputted as a series of 13 (η , λ) pairs. In this study, based on fitting with the test data, the calibrated input series of 13 (η , λ) pairs is presented in Table 3.

Table 3 Input parameters of damage function

Fair no.	λ	η	Fair no.	λ	η	Fair no.	λ	η
1	0	0.000	6	7.0e-4	0.920	11	5.0e-3	0.099
2	5.0e-6	0.200	7	8.0e-4	0.780	12	1.0e-0	0.001
3	1.0e-5	0.250	8	1.2e-3	0.520	13	1.0e-10	0.000
4	1.0e-4	0.660	9	1.8e-3	0.350			
5	6.0e-4	1.000	10	3.0e-3	0.180			

Fig. 4 Modified pressure versus volumetric strain curve for EOS



In LS-DYNA [6], the EOS used for MAT072r3 material model is the tabulated compaction equation of state, or EOS 8. Ten pairs of data points are required for input to define the equation of state function. Due to lack of test data on volumetric strain versus pressure of FRC, a modified curve from Unosson [11] is adopted in this study, as shown in Fig. 4.

3 Results and Discussion

3.1 Static Compression

To evaluate the performance of the calibrated model, a compression test conducted by Lee et al. [3] is selected and analyzed. The cylindrical specimen has diameter of 150 mm and length of 300 mm. The hooked fibers with aspect ratio of 63.6 and fiber content of 1% are used. The design compressive strength of the matrix is set to 50 MPa.

The solid element is used for FRC specimen model. The mesh size used in this study is 10 mm. Relevant boundary condition is applied to the specimen. This analysis uses the static option. Figure 5 shows the stress-strain curves of FEA and test results. Different values of damage parameter b_1 are varied to control the softening behavior of the compressive stress-strain curves. It is shown that the FEA curve fits well with the test curve at the damage parameter $b_1 = 0.53$. The comparison also emphasizes that the calibrated material model induces the compression behavior of FRC specimen accurately.

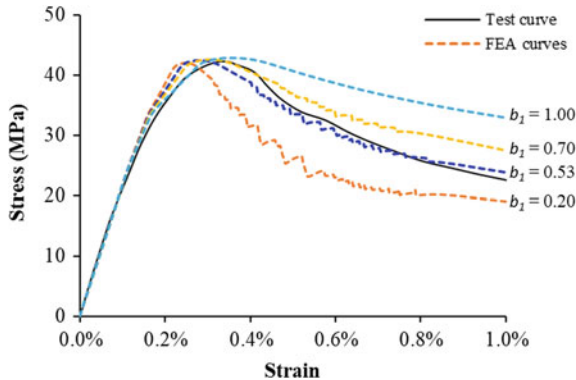


Fig. 5 Comparison of stress-strain curves

3.2 Blast Loading on FRC Beam

The dynamic performance of the calibrated model is also evaluated by simulating the FRC beam subjected to blast loading conducted by Lee et al. [2]. The specimen has section dimensions of 125 mm \times 250 mm, and the length of 2438 mm, as shown in Fig. 6. Two longitudinal bars with diameter of 19.1 mm are installed in the tension face of the beam. Hooked fibers with content of 1% and aspect ratio of 60 were used in the test. Other detailed information of the test can be seen in Lee et al. [2]. A blast-like loading, which was generated using the shock tube system installed in the University of Ottawa, is adopted in this numerical analysis in terms of pressure-time history.

Solid elements are used for modelling of the FRC beam, whereas beam elements are utilized for modelling of the rebars. The mesh size of the finite element model is approximate 10 mm. Relevant boundary conditions are applied to the specimen to describe the realistic reaction of the support system. The dynamic analysis solver is used in this case.

Table 4 compares the maximum mid-span displacement between the test and FEA results. The comparison shows that the FEA result agrees well with the test datum

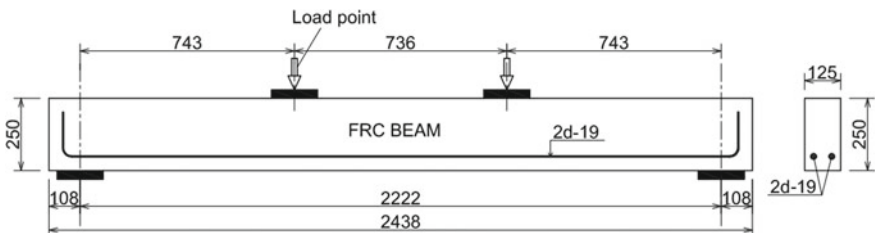


Fig. 6 Detail of specimen

Table 4 Comparison of maximum mid-span displacement

Method	Load	Max. mid-span displacement
Test	Blast No. 1	7.67
FEA	Blast No. 1	7.04
<i>Difference</i>	—	8.2%

since the difference of the maximum mid-span displacement is only 8.2%. It can be concluded that the FE modelling using the calibrated material model described in Sect. 2 can predict the dynamic behaviour of FRC beam under blast loading accurately.

4 Conclusion

A calibration of a material model implemented in LS-DYNA for analysing the static and dynamic behaviour of fiber reinforced concrete is presented in this paper. FE analyses of a FRC single specimen under static compressive loading and a FRC beam under blast-like loading are carried out to illustrate the performance of the calibration model. The results reveal that the FE analyses using the calibrated material model predict the structural behaviour of FRC components under both static and dynamic loading accurately. Thus, this calibrated material model can be used for further analyses of FRC structures under a wide range of loading rate.

Acknowledgements This work was supported by the National Research Foundation of Korea (NRF) grant funded by the Korea government (MSIT) (No. 2018R1C1B5086385).

References

1. Gholampour A, Ozbakkaloglu T (2018) Fiber-reinforced concrete containing ultra high-strength micro steel fiber under active confinement. *Constr Build Mater* 187:299–306
2. Lee JY, Shin HO, Yoo DY, Yoon YS (2018) Structural response of steel-fiber-reinforced concrete beams under various loading rates. *Eng Struct* 156:271–283
3. Lee SC, Oh JH, Cho JY (2015) Compressive behavior of fiber-reinforced concrete with end-hooked steel fibers. *Materials* 8:1442–1458
4. Lin X (2018) Numerical simulation of blast responses of ultra-high performance fibre reinforced concrete panels with strain-rate effect. *Constr Build Mater* 176:371–382
5. Lin X, Gravina RJ (2017) An effective numerical model for reinforced concrete beams strengthened with high performance fibre reinforced cementitious composites. *Mater Struct* 50(212):1–13
6. Livermore (2007) LS-DYNA keyword user's manual, version 971. California
7. Malvar LJ, Crawford JE, Wesevich JW, Simons D (1997) A plasticity concrete material model for DYNA3d. *Int J Impact Eng* 19(9):847–873
8. Markovich N, Kochavi E, Ben-Dor G (2011) An improved calibration of the concrete damage model. *Finite Elem Anal Des* 47:1280–1290

9. Park JK, Kim SW, Kim DJ (2017) Matrix-strength-dependent strain-rate sensitivity of strain-hardening fiber-reinforced cementitious composites under tensile impact. Compos Struct 162:313–324
10. Sun X, Zhao K, Li Y, Huang R, Ye Z, Zhang Y, Ma J (2018) A study of strain-rate effect and fiber reinforcement effect on dynamic behavior of steel fiber-reinforced concrete. Constr Build Mater 158:657–669
11. Unosson M (2000) Numerical simulations of penetration and perforation of high performance concrete with 75 mm steel projectile. In: FOA-R-00-01634-311-SE (ed.) Virginia

Cyclic Loading Tests of Steel Pile Filled with Concrete at Pile Top Subjected to Tensile Axial Force



Tomoya Saito, Toshiharu Hirose, and Yoshihiro Kimura

1 Introduction

In Japan, for real structures with the steel pile foundation, the steel pile top is filled with concrete in order to connect it to the RC footing beam rigidly [1]. At the pile top, slip stoppers are usually attached to the inside of the steel pile to help stress transmission between concrete infill and the steel pile. However, there is a risk that tensile axial force by overturning moment of structures acts upon steel piles during earthquake. Then, steel piles may have huge damage, which is caused by the pile's fracture or the infilled concrete's crack at the pile top.

In previous papers, the structural capacity of steel piles filled with concrete at the pile top subjected to compressive axial force was clarified [2].

In this paper, cyclic loading tests of steel piles filled with concrete at the pile top subjected to tensile axial force are carried out, and this paper clarifies the ultimate flexural strength and stress transfer mechanism between steel pile with the internal ring and the concrete infill.

2 Outline of Experiment

Experimental equipment is shown in Fig. 1. Test specimens are placed so that pile top is vertically downward.

T. Saito (✉)

Graduate School of Engineering, Tohoku University, Sendai, Japan
e-mail: tomoya.saito.p2@dc.tohoku.ac.jp

T. Hirose

Japanese Technical Association for Steel Pipe Piles and Sheet Piles, Tokyo, Japan

Y. Kimura

Professor Graduate School of Engineering, Tohoku University, Sendai, Japan

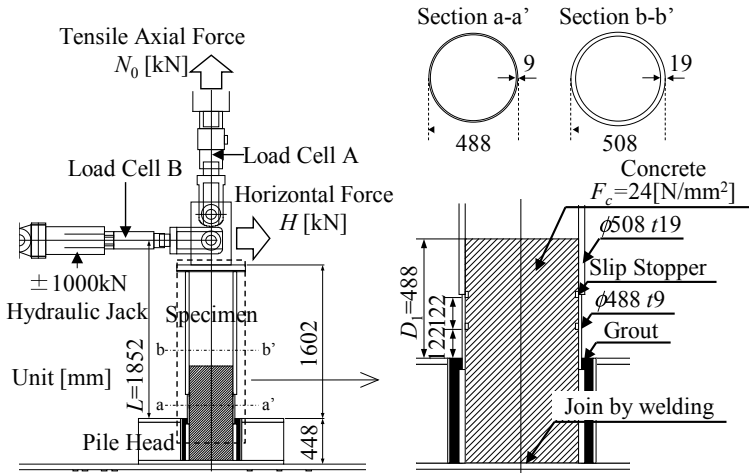


Fig. 1 Experimental equipment and specimen

A test specimen consists of a steel pipe with different cross-section and a concrete member at the pile top.

For the steel pipe, the outside diameter and thickness of a-a' section are 488 and 9 mm, and those of b-b' section are 508 mm and 19 mm respectively. Concrete is filled at the pile top up to 488 mm height same as the diameter of a-a' section.

In this paper, thickness of a-a' section is thicker than that of b-b' section to clarify the local buckling behavior at the pile top filled with concrete. In addition, slip stoppers are attached on the inside of the steel pile at 122 and 244 mm height. The distance from the pile top to the loading point is 1852 mm. As described in this paper, it is assumed that the point of contrary flexure occurs at quadruple height of the pile's diameter from the pile head subjected to the horizontal force.

Strain gauges are placed as described in Fig. 2.

Fig. 2 Strain Gage's point

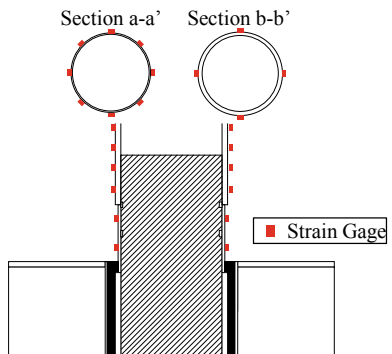
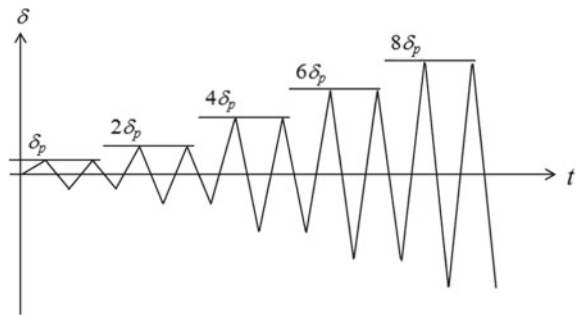


Fig. 3 Loading protocol of horizontal force



The horizontal load and axial load are applied by ± 1000 kN and 2000 kN hydraulic jack, respectively. The horizontal load is controlled with normalized horizontal displacement $\delta/\delta_p = 1, 2, 4, 6, 8, \dots$ regardless the magnitude of axial force.

Where, δ_p denotes the nominal full-plastic displacement of the specimen as described in Fig. 3. The loading is given until the load decrease to 80% of the ultimate strength after maximum load.

Table 1 presents the specimen specifications. Where, N_y represents the yield strength and N_0 stands for the initial axial force.

For the tests, there are 3 specimens with different initial axial forces of 0, 500 and 1000 kN. However, Case0 is a test specimen tested in reference 1). Each specimen has same length and pile thickness.

Material properties are tabulated in Table 2. Here, E_s : the steel elastic modulus, σ_y : the steel yield stress, ε_y : the steel yield strain, E_c : the concrete elastic modulus, σ_B : the concrete ultimate compressive stress.

Table 1 List of specimens

Specimens	Specimens length L_0 (mm)	Pile thickness t (mm)	Axial force ratio N_0/N_y	Axial force N_0 (kN)
Case 0	1852	9 (a-a' section) 19 (b-b' section)	0.0	0
Case 1			0.13	500
Case 2			0.26	1000

Table 2 Material properties

	Steel	E_s (N/mm ²)	σ_y (N/mm ²)	ε_y (%)
		2.11×10^5	287.9	0.136
Concrete	E_c (N/mm ²)	σ_B (N/mm ²)	-	
		2.76×10^4	27.3	-

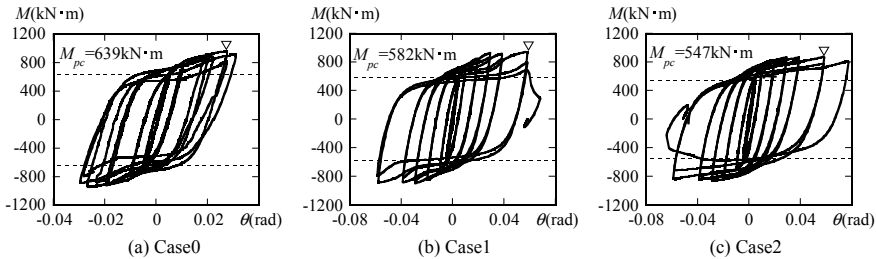


Fig. 4 Hysteresis curves of specimens

3 The Experimental Result

3.1 Hysteresis Curve and Fracture Characteristics of Specimens

Figure 4a, b, c show the hysteresis curve of specimens with axial force of 0, 500 and 1000 kN.

Figure 4a portrays the result of Case 0 specimen without axial force ($N_0 = 0\text{ kN}$), and Fig. 4b, c represent those of Case 1 under $N_0 = 500\text{ kN}$ and Case 2 under $N_0 = 1000\text{ kN}$, respectively.

Here, M : the bending moment with P - δ effects, M_{max} : the ultimate strength, M_{pc} : the full-plastic strength considering axial force, θ : the deflection angle. As shown in Fig. 4, the white triangle symbol indicates the ultimate strength.

The ultimate strength of Case 0 specimen has 960.5 kNm at $\theta = 0.0286\text{ rad}$, those of Case 1 and Case 2 reaches 942.2 kNm at $\theta = 0.0576\text{ rad}$ and 870.6 kNm at $\theta = 0.0579\text{ rad}$, respectively. The ultimate strength of Case1 and Case2 is about 1.6 times that of M_{pc} .

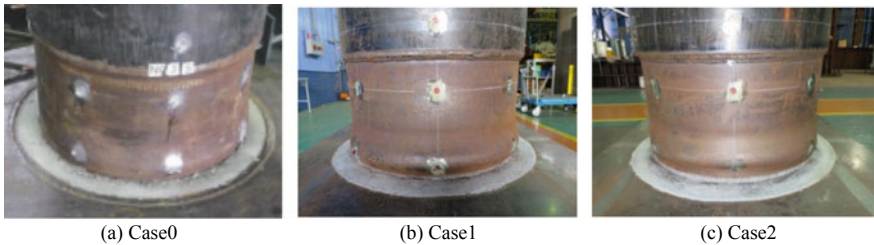
3.2 Fracture Properties of the Specimen

Photos 1a, b, c display local buckling of the specimens around the pile top after the loading test.

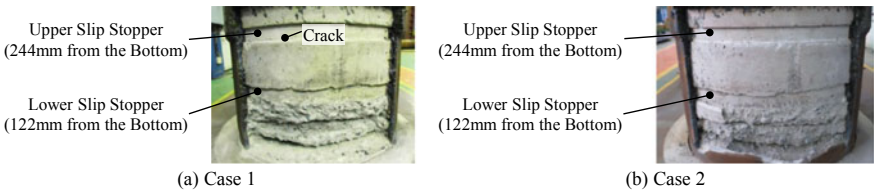
Regardless of the magnitude of the axial forces N_0 , local buckling occurs in the region below the lower slip stopper located at 122 mm from the base plate. The fracture of steel pipe occurred in both of Case 1 and Case 2 when the displacement reached $\delta/\delta_p = 16$.

Photos 2 shows the damage of filled concrete after loading.

From the Photos 2, the damage of the concrete between upper and lower slip stopper is small, but the damage between fixed end and lower slip stopper is large. This crack extended to the inside of the concrete issued from bending moment. The



Photos 1 Local buckling of the specimens



Photos 2 Damage of filled concrete

crack is also caused by the tensile force of the contact region surface of the upper slip stopper.

Figure 5 shows the axial strain distribution when the axial force carried. In this figure, white triangle symbols indicate the height of slip stoppers and the black triangle symbol shows the concrete filling height, and the gray line indicates the strain distribution of hollow steel pipe under the axial force action, which is calculated from the elasticity theory.

As described in Fig. 5a, stain gauges are placed at the points of A–E. The cross-section at the points of E and F is same to b-b' section of the steel pipe only. On

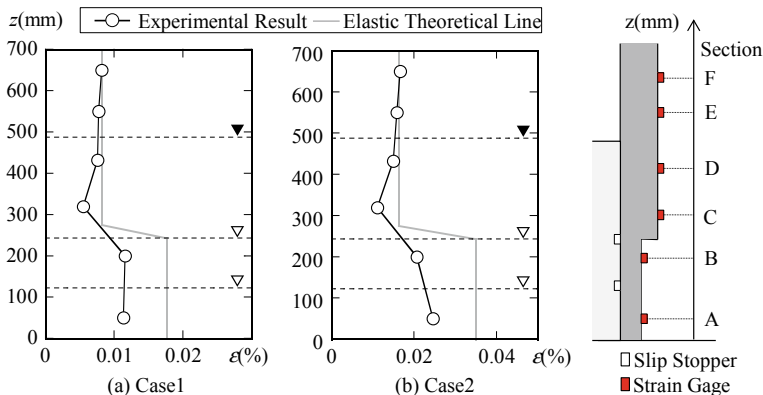


Fig. 5 Axial strain distribution at the completion of axial force introduction

the other hand, the cross-section at A–D is composed of the steel pipe and the filled concrete. The cross-section of the steel pipe at C and D is b-b' section, and that of the steel pipe at A and B is a-a' section. The strain of the experimental result is smaller than the theoretical line at the A and B cross sections, and the strain is almost constant from the B cross section to the A cross section. Therefore, it is considered that the tensile axial force is mainly transmitted to the filled concrete through the upper slip stopper.

4 The Ultimate Strength and the Deformation Capacity

Figures 6 and 7 show the ultimate strength and deformation performance of each test specimen. Then, the test specimen of $N_0/N_y = -0.3$ and -0.6 is the test specimen of reference 2).

$cftM_u$ is the ultimate flexural strength calculated as Concrete Filled Tube (CFT) member [3]. δ_p , $cft\delta_u$ are lateral displacements of the loading point at M_p and $cftM_u$, when the test specimen is assumed to be a hollow steel pipe having the same section as the a-a' section.

As shown in Fig. 6, the $M_{max}/cftM_u$ is larger when the tensile force is subjected. M_{max} is maximum in the non-axial force, and the value tends to decrease as the axial force increases. It is considered that the concrete carries no stress in the case of under the tensile axial force, so that $cftM_u$ is lower than that under no axial force. However, in the specimens of this experiment, it is considered that the strength was increased because the concrete carried the stress in the case of under the tensile axial force. As a result, the ratio of $M_{max}/cftM_u$ increased under the tensile axial force, even though $cftM_u$ is lower than that under no axial force.

Fig. 6 Ultimate strength of specimen

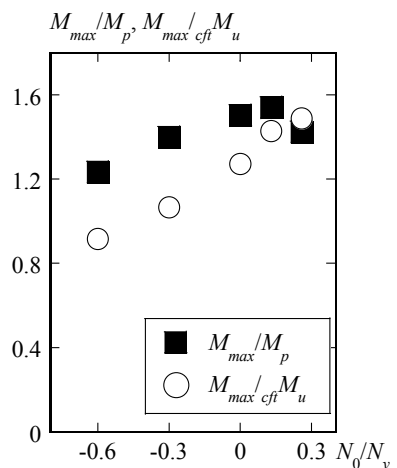
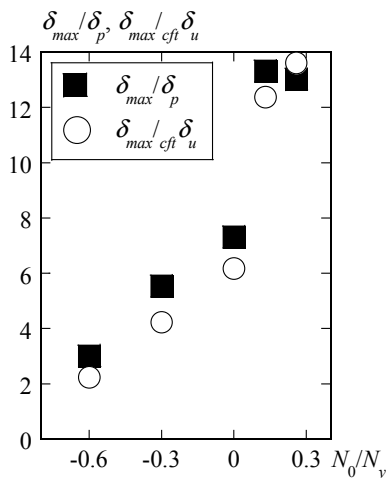


Fig. 7 Deformation performance of specimen



As shown in Fig. 7, the deformation capacity is higher than others regardless of the dimensionless value when the tensile axial force is acting. It is considered to be due to delay of the generation of the local buckling by the action of the tensile axial force.

5 Conclusion

This paper carries out the cyclic loading test of steel pile filled with concrete at pile top in which tensile axial force and bending act.

The ultimate strength is due to the fracture of steel pipe after the occurrence of local buckling, and is higher than the full-plastic strength of steel pipe.

It was clarified that the deformation capacity becomes the largest when the tensile axial force is acting.

Acknowledgements This work was supported by JSPS Grant-in-Aid for Scientific Research (A). The cyclic loading tests are funded by Japanese Technical Association for Steel Pipe Piles and Sheet.

References

1. Recommendations for Design and Building Foundations, Oct 2001 (in Japanese)
2. Kimura Y, Hirose T, Matoba M, Sato M (2017) Structural capacity of steel piles with concrete filled at pile top. *Jpn Soc Steel Constr J Constr Steel* 25:614–618 (in Japan)
3. Recommendations for Design and Construction of Concrete Filled Tubular Structures, Jan 2008 (in Japanese)

Effect of Indentation Strain Rate on Plastic Properties in SS400 Steel Weld Zone



Thai-Hoan Pham and Ngoc-Vinh Nguyen

1 Introduction

The excellent weldability and machinability of structural steel, which caused by its high strength, stiffness, toughness, and ductility, have led to the common usage of this material in many construction fields including buildings, bridges, tunnels and in the manufacture of machinery parts and equipment [13]. Welding is considered as the preferred method to form the strong and continuous joints between the steel members, where the structural steel is used. However, the welding joints are also considered as the weakest parts of structures [15]. The heating or cooling stages influence the microstructures in the weld zone, including the weld metal (WM) region, the heat-affected zone (HAZ), and base metal (BM) region near the weld due to the transformation of solid-state phases, leading to the change of material properties in the weld zone [2, 12]. Thus, the properties in the local regions of weld joints need to be evaluated, especially plastic properties that are important for design of structures. It has also been pointed out that the plastic properties of structural steel are governed by the metallurgical aspects and strongly dependent on the conditions of strain rate [5, 6].

Indentation has been known as an efficient method in extracting properties of materials at both the macro- and nano-scales [16]. For characterization of the mechanical properties under different strain rate levels, it has also proved to be reliable and efficient since this approach can not only provide accurate results [4, 7, 8] but also overcome the uneconomical and time-consuming dynamic tensile tests.

This work aims to evaluate the strain rate influences on the plastic properties in the weld zone of SS400 steel using indentation tests. Two types of indentation test were

T.-H. Pham (✉)

Department of Concrete Structures, National University of Civil Engineering, Ha Noi, Vietnam
e-mail: hoanpt@nuce.edu.vn

N.-V. Nguyen

Department of Civil and Environmental Engineering, Sejong University, Seoul, South Korea

performed at a number of strain rate values from 0.03 to 0.2 s⁻¹ in the WM, HAZ, and BM regions of the weld zone. The plastic properties including σ_y , n , and α values in WM, HAZ, and BM were then determined from the combination of Berkovich and spherical load-depth curves by utilizing a proposed method. The indentation strain rate effects on plastic properties in all regions of the weld zone were then evaluated.

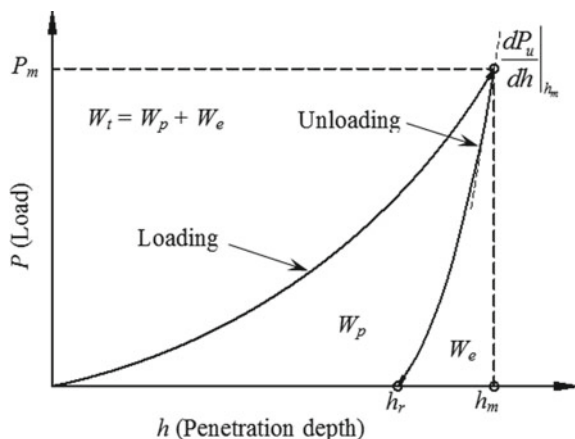
2 Method

The load-depth (P - h) curves of indentation provides an opportunity to access the elastic-plastic properties of materials by correlating these properties with the parameters obtained from the curves, which can be typically illustrated in Fig. 1. As is seen in this figure, the maximum load (P_m), the maximum depth (h_m), the residual depth (h_r), the residual plastic work (W_p), the elastic work (W_e), and the total work (W_t) can be directly measured from the P - h curve, whereas some necessary other parameters such as the initial unloading slope (S) and the projected area of contact (A_c) can only be computed based on the characteristics of unloading and loading portions of the curve.

By correlating the material properties with the aforementioned parameters, several methods have been developed for the extraction of both elastic and plastic properties of indented materials from indentation curves [10, 11, 14]. For the extraction of elastic property (i.e. elastic modulus E) of materials, the Oliver and Pharr's method [10] has been considered the most popular one for both Berkovich and spherical indentations. In this method, the following relations allow extracting E :

$$E_r = \frac{\sqrt{\pi}}{2\beta} \frac{S}{\sqrt{A_c}} \quad (1)$$

Fig. 1 Illustration of indentation load-depth (P - h) curve



$$E_r = \left[\frac{1 - \nu^2}{E} + \frac{1 - \nu_i^2}{E_i} \right]^{-1} \quad (2)$$

In Eqs. 1 and 2, E_r is the reduced modulus owing to the effects of elastic deformation of the indenter. E , ν , E_i , and ν_i are the elastic modulus and Poisson's ratio of the material and indenter, respectively. $S = dP/dh|_{h=h_m} = mB(h_m - h_r)^{m-1}$ where $B(h_m - h_r)^m$ is the fitting power-law function of the unloading portion of $P-h$ curve, β is a factor related to indenter shape, and the projected contact area A_c can be computed from the contact depth h_c . According to Oliver and Pharr method [10], $A_c = 24.5h_c^2$ where $h_c = h_m - \varepsilon^* P_m/S$ and $\varepsilon^* = 0.75$ for sharp indenters, whereas $A_c = \pi(2Rh_c - h_c^2)$ where R is the radius of spherical indenter and $h_c = (h_m + h_r)/2$ for spherical indenter.

Considering E as a known property of materials, numerous studies have proposed method to determine the material plastic properties from indentation [11, 14] including method for the extraction of σ_y , n , and α values of structural steels. This kind of steels shows the plastic plateau in their stress-strain curve and α value is defined as the ratio between the strain at beginning-point of strain hardening and the yield strain [11]. The details of true stress-strain behavior of structural steel can be found in previous works [11, 14]. Recently, a method [9] that allows to extract not only strain hardening exponent, yield strength, and α value of structural steels but also these properties at different strain rate levels has been proposed by combining the relationships between strain rate level, elastic-plastic properties of materials, and indentation parameters from both Berkovich and spherical indentation curves. In present study, this method was used to evaluate the plastic properties in SS400 weld zone with respect to different strain rate levels.

3 Experiment

The indentation specimen consists of SS400 steel weld zone was first cut out from the welded plate, which was formed from two 12 mm-thickness plates of SS400 steel by metal arc method with suitable weld material. The specimen was then mounted in epoxy and polished in seven stages by silicon carbide papers, poly diamond particles, and colloidal silica with the fineness of the last stage about 40 nm to obtain a flat and smooth surface.

Indentation testing was carried out using a Nano Hardness Tester at room temperature conforming to standard [1]. Two types of indentation test with Berkovich and spherical indenter tips were undertaken in three regions, WM, HAZ, and BM of the weld zone by using the displacement control mode without a holding time at a number of strain rate values from 0.03 to 0.2 s⁻¹. For each type of indentation, 5 indenting points were performed at each strain rate value of 0.03 s⁻¹, 0.06 s⁻¹, 0.1 s⁻¹, and 0.2 s⁻¹ for individual region of the weld, leading to the total of 40 and 120 indenting points in individual region and in all regions of the weld, respectively. Both

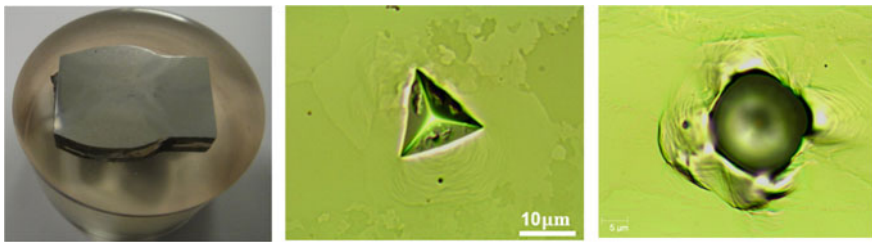


Fig. 2 Indentation specimen and images of Berkovich and spherical indentation

Berkovich and spherical indenter tips are made of diamond with elastic modulus of $E_i = 1141$ GPa and Poisson ratio of $\nu = 0.07$. All Berkovich indentations were carried out with a maximum applied depth of 2000 nm, whereas spherical indentations were conducted with a maximum applied depth of $0.3R$ (R is the radius of spherical indenter tip, $R = 5$ μm). Figure 2 shows the specimen surface after polishing, on which the weld regions can be clearly observed, and the optical microscope images of Berkovich and spherical indentation.

4 Results and Discussion

Figure 3 shows the representative P - h curves at different levels of strain rate obtained from indentation tests in BM. For both indentation types, the loading curvature tends to be reduced with the decreasing strain rate, leading to the higher maximum load with the higher strain rate level due to the constant maximum displacement in all the tests. The same trend was observed from the curves of both indentation types in

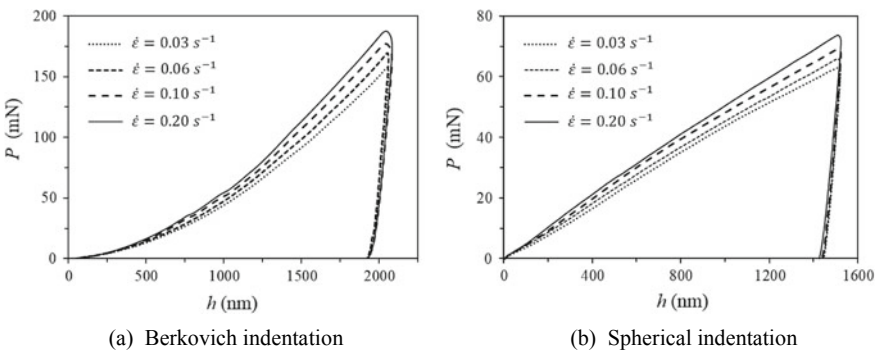


Fig. 3 Representative P - h curves in BM of weld zone

HAZ and WM regions of the weld zone but they are not presented in the text due to the limit of space. This effect of strain rate levels on the indentation P - h curve is consistent with the change of plastic properties in the weld zone, which will be discussed below.

Based on the necessary parameters measured and calculated from the P - h curves, the elastic modulus E in individual region of weld zone can be easily extracted by using Eqs. 1 and 2. The calculated results of E exhibit that Berkovich and spherical indentations provide similar value of E in individual region of the weld zone and indentation strain rate does not have effect on the elastic modulus of material in the weld zone. This observation is also a well-known knowledge, which has been reported in literature [10]. Due to the fact that elastic modulus of individual region of weld zone is not governed by neither indentation types nor strain rate level, the mean value of all obtained E values from all strain rate levels and indentation types (i.e. from 40 indentation tests) in individual region is considered the representative elastic modulus, which is 216.3 GPa, 211.5 GPa, and 205.8 GPa for WM, HAZ, and BM region, respectively. Once the elastic modulus is known, the proposed method [9] was applied for the determination of strain hardening exponent, yield strength, and α value at different strain rate levels in the weld zone.

Figures 4 present the determined results of yield strength (σ_y), strain hardening exponent (n), and α values in the weld zone in such the way to show the change of σ_y , n , and α values with respect to different strain rate levels in all regions of the

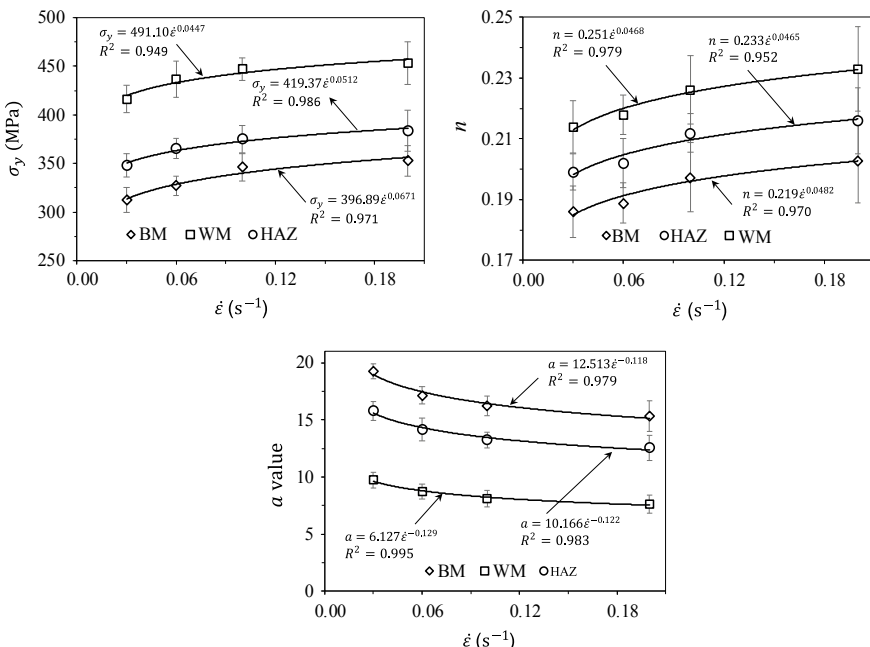


Fig. 4 Strain rate effect on plastic properties in the weld zone

weld as well as the distinguishable σ_y , n , and α values in the three regions. In this figure, each presented σ_y , n , and α value is the mean of 25 corresponding σ_y , n , and α values obtained from 25 combinations of 5 Berkovich and 5 spherical indentation tests in individual region, together with the corresponding error bar of ± 1 standard deviation. The best fit curve of the changing trend of σ_y , n , and α values in each region is also accompanied. From Fig. 4, the effect of strain rate on σ_y , n , and α values in individual region of weld zone are clearly observed. For σ_y and n , the same trend is that higher strain rate level leads to the higher σ_y and n values for all regions WM, HAZ and BM of the weld zone. This trend is recognized that the σ_y and n values quite rapidly increase as strain rate level increases from 0.03 to 0.1 s^{-1} and the increment of σ_y and n values reduce when strain rate levels change from 0.1 to 0.2 s^{-1} . It is interesting to observe that the change of σ_y and n values in individual region with respect to different strain rate levels seem to be obeyed power-law functions. It is also noted that the σ_y and n in BM are lower than the corresponding ones in HAZ at a certain strain rate level, while the corresponding σ_y or n in WM are highest in the weld zone. Contrary to σ_y and n values, the higher strain rate level leads to the lower α value for all regions BM, HAZ and WM of the weld zone. The reducing speed of α values when strain rate value changes from 0.03 to 0.1 s^{-1} is greater than the corresponding one of α values when strain rate value changes from 0.1 to 0.2 s^{-1} . Similar to σ_y and n , the change of α value in individual region with respect to different strain rate levels seem to be obeyed a power-law function. Considering the correlation between the α values in each region, the α value in BM is highest in the weld zone, while the α value in HAZ at a certain strain rate level is higher than the corresponding one in WM. These obtained results are consistent with the reported trend for weld zone of other structural steels [3, 13].

Since the necessary properties to construct the true stress-strain curves of materials in the weld zone at different strain rate levels are determined, these stress-strain curves are established and presented in Fig. 5. From this figure, an overview of the effect of strain rate on the plastic properties in individual region of SS400 steel weld zone are clearly exhibited.

In order to demonstrate the reliability and accuracy of the present results, the obtained yield strength, strain hardening exponent, and α value at a certain strain rate of 0.03 s^{-1} were compared with the corresponding values in the same weld zone, which are available in the literature [3], as listed in Table 1. It is obvious that the obtained results in this work are acceptable and reliable.

5 Conclusion

In this study, the influences of strain rate on the plastic properties in SS400 steel weld zone was investigated using indentation. The following conclusions can be withdrawn:

Strain rate level has strong effect on the plastic properties for all regions in the weld zone. The σ_y and n values quite rapidly increase as strain rate level increases

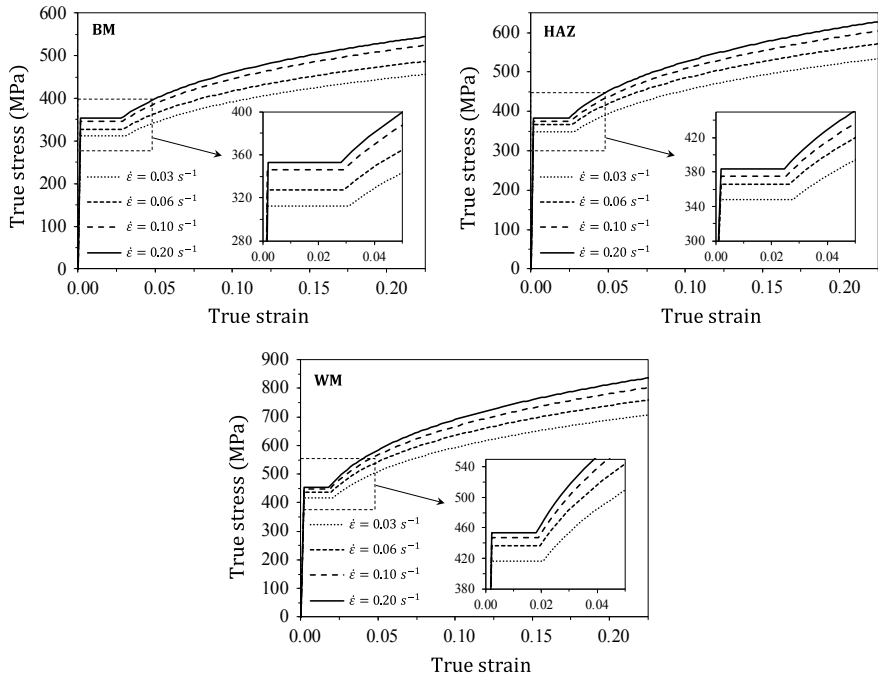


Fig. 5 Strain rate effect on true stress-strain behaviour of materials in the weld zone

from 0.03 to 0.1 s^{-1} and the increment of σ_y and n values reduces when strain rate levels change from 0.1 to 0.2 s^{-1} .

The higher strain rate level leads to the lower α value for all regions BM, HAZ and WM of the weld zone. The reducing speed of α values when strain rate value changes from 0.03 to 0.1 s^{-1} is greater than the corresponding one of α values when strain rate value changes from 0.1 to 0.2 s^{-1} .

In conclusion, the plastic properties in the investigated SS400 steel weld zone are influenced by strain rate and the relationships between these properties with strain rate obtained in present study provide an assessment of plastic properties in the weld zone at a specific strain rate level without conducting any additional tests.

Table 1 Plastic properties at strain rate of 0.03 s^{-1} between present and previous works [3]

	σ_y (MPa)				n	α value
	Present work	Previous work	Error %	Present work	Previous work	Error %
BM	312.50	302.70	3.24	0.186	0.191	-2.62
HAZ	348.10	331.40	5.04	0.199	0.195	2.05
WM	416.30	403.50	3.17	0.214	0.203	5.42

Acknowledgements This research is funded by Vietnam National Foundation for Science and Technology Development (NAFOSTED) under grant number 107.01-2018.22.

References

1. ASTM E2546-07 (2007) Standard practice for instrumented indentation testing. West Conshohocken, PA
2. Boumerzoug Z, Derfouf C, Baudin T (2010) Effect of welding on microstructure and mechanical properties of an industrial low carbon steel. *Engineering* 02:502–506
3. Kim JJ, Pham TH, Kim SE (2015) Instrumented indentation testing and FE analysis for investigation of mechanical properties in structural steel weld zone. *Int J Mech Sci* 103:265–274
4. Lu YC, Tandon GP, Putthanarat S, Schoeppner GA (2009) Nanoindentation strain rate sensitivity of thermo-oxidized PMR-15 polyimide. *J Materials Sci* 44:2119–2127
5. Luecke WE et al (2005) Mechanical properties of structural steels. NIST NCSTAR 1-3D
6. Nagarajara, N, Lohrmann M, Tall L (1966) Effect of strain rate on the yield stress of structural steel. *ASTM J Mater* 1 (1), Publication No. 293
7. Nguyen NV, Pham TH, Kim SE (2018) Characterization of strain rate effects on the plastic properties of structural steel using nanoindentation. *Constr Build Mater* 163:305–314
8. Nguyen NV, Pham TH, Kim SE (2019) Microstructure and strain rate sensitivity behavior of SM490 structural steel weld zone investigated using indentation. *Constr Build Mater* 206:410–418
9. Nguyen NV, Kim JJ, Kim SE (2019) Methodology to extract constitutive equation at a strain rate level from indentation curves. *Int J Mech Sci* 152:363–377
10. Oliver WC, Pharr GM (1992) An improved technique for determining hardness and elastic-modulus using load and displacement sensing indentation experiments. *J Mater Res Camb Core* 7:1564–1583
11. Pham TH, Kim JJ, Kim SE (2015) Estimating constitutive equation of structural steel using indentation. *Int J Mech Sci* 90:151–161
12. Pham TH, Kim SE (2016) Microstructure evolution and properties changes in the weld zone of a structural steel during low-cycle fatigue studied using indentation testing. *Int J Mech Sci* 114:141–156
13. Pham TH, Kim SE (2017) Characteristics of microstructural phases relevant to the mechanical properties in structural steel weld zone studied by using indentation. *Constr Build Mater* 155:176–186
14. Pham TH, Phan QM, Kim SE (2018) Identification of the plastic properties of structural steel using spherical indentation. *Mater Sci Eng, A* 711:44–61
15. Tamboli AR (1999) Handbook of structural steel connection design and details. MacGraw-Hill, NY, USA
16. Wei Q (2007) Strain rate effects in the ultrafine grain and nanocrystalline regimes-influence on some constitutive responses. *J Mater Sci (Springer)* 42:1709–1727

Elastic Buckling Load of Continuous Braced H-Shaped Beams with Fork Restraint



Yui Sato and Yoshihiro Kimura

1 Introduction

In Japanese design code [1], the boundary condition of beams against lateral buckling is provided as simple support. Meanwhile, beams are often jointed to box sectional columns with high torsional rigidity as shown in Fig. 1. Therefore, beam ends have fork restraint by high torsional rigidity of column on lateral buckling of beams, which is considered the rotational effect between warping and fully fixed supports [7]. Our previous paper [6] elucidated the lateral buckling behavior for H-shaped beam with fork restraint.

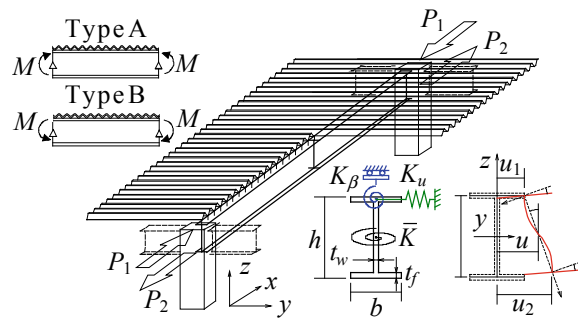
On the other hand, long span main beams may not possess the full plastic strength due to lateral buckling, so that many lateral braces should be set up along the beams to prevent the lateral buckling deformation [2]. When non-structural members such as folded-roof plate are directly jointed to beams, these may be used as the continuous braces. Our previous paper [4] clarified the lateral buckling behavior for H-shaped beam with continuous braces when the boundary condition of beam is simple support.

In this paper, the effect of fork restraint on elastic lateral buckling load for H-shaped beams with continuous braces is clarified. Firstly, this paper develops the equations of elastic lateral buckling load for H-shaped beams with warping and fully fixed supports under uniform flexural moment by the energy method. Secondly, this paper derives the equation of elastic lateral buckling load for beams with fork restraint by using ratio of fork restraint, which has effect between warping and fully fixed supports. Finally, this paper elucidates the relation between fork restraint and elastic lateral buckling load by comparing the equations with the numerical analyses results.

Y. Sato (✉)
Graduate School of Engineering, Tohoku University, Sendai, Japan

Y. Kimura
Graduate School, Tohoku University, Sendai, Japan

Fig. 1 H-shaped beam with continuous braces and beam-to-column joints

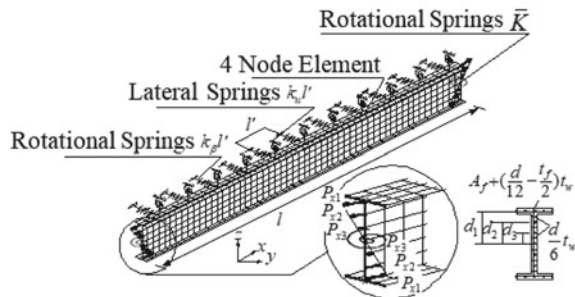


2 Numerical Analysis Model

Figure 2 presents the numerical analysis model for H-shaped beams with continuous braces on upper flange. ABAQUS with version 6.14 is used as numerical analysis program. H-shaped beam is consisted of four node shell elements. The continuous braces are replaced by the lateral and rotational springs along the beam's axis and fork restraint of the beam ends are replaced by the rotational springs. Fixing the rotation between upper and lower flanges at the end of the beam is corresponding to warping fixed support. The uniform flexural moment is replaced by the axial loads distributed to each node of the beam ends as shown Fig. 2. In this paper, it is assumed that non-structural members are rigidly jointed to H-shaped beam.

Considering combinations of H-shaped beam and folded-roof plate regarded as continuous braces in real space structures, our previous paper [4] clarified lateral and rotational rigidities of the folded-roof plate distribute as follows: $K_\beta/(GK_f/d) < 0.1$ and $K_u/(EI_f/l^3) < 3$ [4]. In this paper, λ_1 is adopted as lateral slenderness ratio [5] and the range from 160 to 280 is selected. The area which carries the compressive force represents the accumulative area, A_1 . Where, l is the length of beam, i_1 is secondary radius of cross section, I_f is the sectional secondary moment of frange, A_f and A_t are cross section of frange and web.

Fig. 2 Numerical analysis model



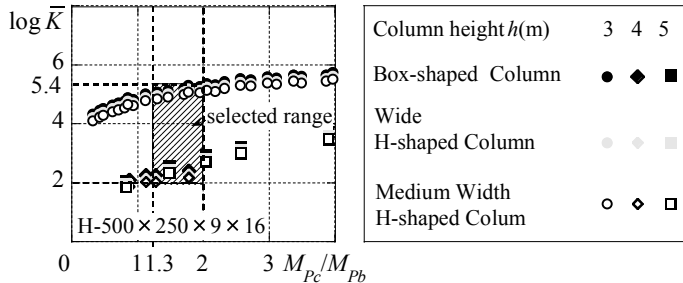


Fig. 3 Relationship between column-to-beam's strength ratio and rotational rigidity

$$\lambda_1 = \frac{l}{i_1}, i_1 = \sqrt{\frac{I_f}{A_1}}, A_1 = A_f + \frac{A_w}{6} \quad (1)$$

Figure 3 describes the relation between rotational rigidity of beam ends, \bar{K} and Column-to-beam's strength ratio, M_{pc}/M_{pb} using actual column and beam dimensions [3]. Column-to-beam's strength ratio approximately ranges from 1.3 to 2.0 for the real steel moment resisting frames. This is because the beams under uniform flexural moment reach the full plastic moment earlier than columns when structures receive seismic forces in the seismic design. Then, the plots distribute from 10^2 to $10^{5.4}$ (kN mm/rad) as shown in Fig. 3.

3 Elastic Lateral Buckling Load for Continuous Braced H-Shaped Beam with Warping and Fully Fixed Supports

In this chapter, the equations of elastic lateral buckling load of H-shaped beams with continuous braces under the uniform flexural moment are developed by the energy method. The braces are assumed to be set up at upper flange and uniform flexural moment are replaced by the axial forces of both flanges, P_1 and P_2 as shown in Fig. 1. When H-shaped beam is subjected to the uniform flexural moment as shown in Fig. 1, two types of loading conditions are considered. One of the loading conditions, which is called as Type A, is the case that the upper flange carries the compressive load, and another, which is called as Type B, is that the under flange carries the tensile load.

Accordingly, the equations of lateral buckling load for beams with warping and fully fixed supports are developed by the energy methods, and then the potential energy, U of beam with continuous braces is expressed as the following [4]. Where, EI_y is the flexural rigidity of H-shaped beam, $E\Gamma$ is the flexural torsional rigidity, GK is the torsional rigidity, k_u and k_β are the lateral and rotational rigidity of the continuous brace and \bar{K} is the fork rigidity as shown in Fig. 1. M is the uniform flexural moment at beam ends.

$$U = \frac{1}{2} \int_0^l \{ EI_y u_i''^2 + E \Gamma \beta''^2 + GK \beta'^2 + Mu_i'^2 + k_\beta \beta^2 + k_u u_0^2 \} dx \quad (2)$$

Lateral deformation, u and torsional angle, β are expressed as trigonometric functions approximately. Where, u and β are calculated with the lateral deformation of upper and lower flanges, u_{uf} and u_{lf} as follows. When the boundary condition of beam is warping fixed support, lateral and rotational deformations are expressed as u_1, β_1 in Eqs. (4a), (5a). On the other hands, when the boundary condition of beam is fully fixed support and the first lateral buckling mode, $n = 1$, they are expressed as u_2, β_2 in Eqs. (4b), (5a). As more than the second lateral buckling mode, $n \geq 2$, considering the boundary condition, they are expressed as u_3, β_3 in Eqs. (4c), (5b).

$$u = \frac{u_{uf} + u_{lf}}{2}, \quad (3a)$$

$$\beta = \frac{u_{uf} - u_{lf}}{d} \quad (3b)$$

$$u_1 = a \sin \frac{n\pi}{l} x, \quad (4a)$$

$$u_2 = a \begin{cases} \sin^2 \frac{n\pi}{l} x \left(0 \leq x \leq \frac{l}{2n} \right) \\ \sin \frac{n\pi}{l} x \left(\frac{l}{2n} < x \leq \frac{2n-1}{2n} l \right), \\ \pm \sin^2 \frac{n\pi}{l} x \left(\frac{2n-1}{2n} l < x \leq l \right) \end{cases} \quad (4b)$$

$$u_3 = a \begin{cases} \sin^2 \left(\frac{10n\pi}{13l} \right) x & \left(0 \leq x < \frac{13l}{20n} \right) \\ \sin \left(-\frac{10n\pi}{7l} x + \frac{10\pi}{7} \right) & \left(\frac{13l}{20n} \leq x < \frac{l}{n} \right) \\ (-1)^n \sin \left(\frac{n\pi}{l} x - n\pi \right) & \left(\frac{l}{n} \leq x < \frac{(n-1)l}{n} \right) \\ (-1)^{n-1} \sin \left(\frac{10n\pi}{7l} x - \frac{10\pi}{7} \right) & \left(\frac{(n-1)l}{n} \leq x < \frac{(20n-13)l}{20n} \right) \\ (-1)^{n-1} \sin^2 \left(-\frac{10n\pi}{13l} x + \frac{10n\pi}{13} \right) & \left(\frac{(20n-13)l}{20n} \leq x \leq l \right) \end{cases} \quad (4c)$$

$$\beta_1 = b \begin{cases} \sin^2 \frac{n\pi}{l} x & \left(0 \leq x \leq \frac{l}{2n}\right) \\ \sin \frac{n\pi}{l} x & \left(\frac{l}{2n} < x \leq \frac{2n-1}{2n}l\right), \\ (-1)^{n-1} \sin^2 \frac{n\pi}{l} x & \left(\frac{2n-1}{2n}l < x \leq l\right) \end{cases} \quad (5a)$$

$$\beta_2 = b \begin{cases} \sin^2 \left(\frac{10n\pi}{13l} \right) x & \left(0 \leq x < \frac{13l}{20n}\right) \\ \sin \left(-\frac{10n\pi}{7l} x + \frac{10\pi}{7} \right) & \left(\frac{13l}{20n} \leq x < \frac{l}{n}\right) \\ (-1)^n \sin \left(\frac{n\pi}{l} x - n\pi \right) & \left(\frac{l}{n} \leq x < \frac{(n-1)l}{n}\right) \\ (-1)^{n-1} \sin \left(\frac{10n\pi}{7l} x - \frac{10\pi}{7} \right) & \left(\frac{(n-1)l}{n} \leq x < \frac{(20n-13)l}{20n}\right) \\ (-1)^{n-1} \sin^2 \left(-\frac{10n\pi}{13l} x + \frac{10n\pi}{13} \right) & \left(\frac{(20n-13)l}{20n} \leq x \leq l\right) \end{cases} \quad (5b)$$

Substituting Eqs. 4 and 5 into Eq. 2 and performing partial differentiation, the elastic lateral buckling loads, ${}_nP_k$ are obtained as the followings. Where, $k = 1$ and 2 express warping and fully fixed supports.

$$\begin{aligned}
n P_1 &= \pm \frac{k_u}{2} \left(\frac{l}{n\pi} \right)^2 + \sqrt{\left\{ \frac{k_u}{2} \left(\frac{l}{n\pi} \right)^2 \right\}^2 + \frac{2(n^2 - 5n + 15)}{5} \left[EI_f \left(\frac{n\pi}{l} \right)^2 + \frac{GK_w}{d^2} + \frac{GK_f}{d^2} (\tau_1 + \tau_2) \right.} \\
&\quad \left. - \frac{(n-5)}{2} EI_f \left(\frac{n\pi}{l} \right)^2 \right\] + \frac{2(n^2 - 5n + 15)}{5} \left[EI_f \left(\frac{n\pi}{l} \right)^2 + \frac{GK_w}{d^2} + \frac{GK_f}{d^2} (\tau_1 + \tau_2) \right.} \\
&\quad \left. - \frac{n-6}{5} k_u \left(\frac{l}{n\pi} \right)^2 + \frac{n+6}{10} \frac{k\beta}{d^2} \left(\frac{l}{n\pi} \right)^2 \tau_1 \right\} + \frac{k_u}{4} \left(\frac{l}{n\pi} \right)^2 \left\{ \frac{GK_w}{d^2} + \frac{GK_f}{d^2} \left(\frac{l}{n\pi} \right)^2 \tau_1 + \frac{n+5}{500} k_u \left(\frac{l}{n\pi} \right)^2 \right\} \right] \quad (6) \\
{}_1 P_2 &= \pm \frac{3}{8} k_u \left(\frac{l}{\pi} \right)^2 \\
&\quad + \sqrt{\left(\frac{3}{8} k_u \left(\frac{l}{\pi} \right)^2 \right)^2 + 8EI_f \left(\frac{\pi}{l} \right)^2 \left\{ 2EI_f \left(\frac{\pi}{l} \right)^2 + \frac{GK_w}{d^2} + \frac{GK_f}{d^2} (\tau_1 + \tau_2) + \frac{3}{4} \frac{k\beta}{d^2} \left(\frac{\pi}{l} \right)^2 \tau_1 + \frac{3}{8} k_u \left(\frac{l}{\pi} \right)^2 \right\} + \frac{3}{4} k_u \left(\frac{l}{\pi} \right)^2 \left\{ \frac{GK_w}{d^2} + \frac{GK_f}{d^2} (\tau_1 + \tau_2) + \frac{3}{4} \frac{k\beta}{d^2} \left(\frac{\pi}{l} \right)^2 \tau_1 \right\}} \quad (7) \\
n P_2 &= \pm \frac{B}{4} k_u \left(\frac{l}{n\pi} \right)^2 \\
&\quad + \sqrt{\left\{ \frac{B}{4} k_u \left(\frac{l}{n\pi} \right)^2 \right\}^2 + 2A \frac{EI_f}{2} \left(\frac{n\pi}{l} \right)^2 \left\{ \frac{A}{2} EI_f \left(\frac{n\pi}{l} \right)^2 + \frac{GK_w}{d^2} + \frac{GK_f}{d^2} (\tau_1 + \tau_2) + B \frac{k\beta}{d^2} \left(\frac{l}{n\pi} \right)^2 \tau_1 + \frac{k_u}{2} \left(\frac{l}{n\pi} \right)^2 \right\} + B k_u \left(\frac{l}{n\pi} \right)^2 \left\{ \frac{GK_w}{d^2} + \frac{GK_f}{d^2} (\tau_1 + \tau_2) + B \frac{k\beta}{d^2} \left(\frac{l}{n\pi} \right)^2 \tau_1 \right\}} \quad (8) \\
&\quad ; \because A = -0.36n + 2.9, \quad B = 0.07n + 0.6
\end{aligned}$$

Fig. 4 Relationship between elastic lateral buckling stress and lateral slenderness ratio

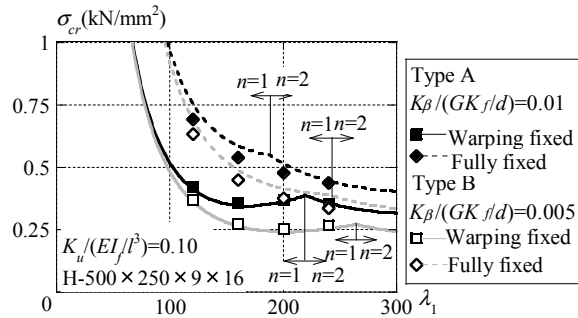


Figure 4 presents the relation between the elastic lateral buckling stress, σ_{cr} ($= nP_k/A_1$) and lateral slenderness ratio, λ_1 for H-shaped beams with continuous braces. H-500 × 250 × 9 × 16 as a narrow cross-sectional beam is selected. The boundary conditions are warping and fully fixed supports. The black and grey curves express the lateral buckling stress for Type A and Type B calculated from Eqs. 6–8, respectively. The symbols show the eigenvalue analyses results. The arrows are the points to change from $n = 1$ to $n = 2$ and from $n = 2$ to $n = 3$.

The equations can be applied to estimate the elastic lateral buckling stress of H-shaped beams with warping and fully fixed supports under uniform flexural moment as the lateral buckling curves agree with the symbols of the eigenvalue analyses results.

4 Effect of Fork Restraint on Elastic Lateral Buckling Load

Considering fork restraint by torsional rigidity of column, the elastic lateral buckling load of H-shaped beam with continuous braces, P_{cr} is expressed as the loads between warping and fully fixed supports in the followings [6]. Where, $j = 1$ and 2 express Type A, and Type B.

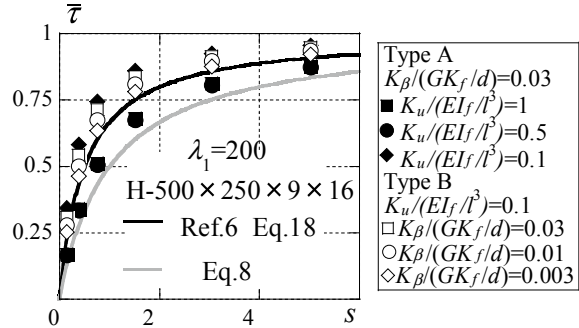
$$P_{cr} = (nP_{2j} - nP_{1j})\bar{\tau} + nP_{1j} \quad (9)$$

$\bar{\tau}$ is defined as the ratio of fork restraint of beam ends and its value ranges from 0 to 1. The value of τ changes from 1 to 4, and then $\tau = 1$ and 4 is corresponding to warping and fully fixed supports, respectively. s is the ratio of fork rigidity for beam ends to flexural rigidity for compressed flange.

$$\bar{\tau} = \frac{\tau - 1}{3}, \quad (10a)$$

$$\tau = 4 - \frac{3}{1 + 2s}, \quad (10b)$$

Fig. 5 Relationship between ratios of fork restraint and fork rigidity to flexural rigidity for compressive flange



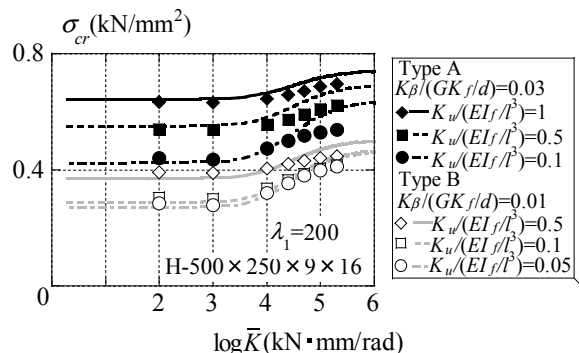
$$s = \frac{\bar{K}}{l} \sqrt{\left(\frac{\pi}{l}\right)^2 EI_f} \quad (10c)$$

Figure 5 presents the relation between ratio of fork restraint, $\bar{\tau}$ and ratio of fork rigidity for beam ends to flexural rigidity for compressive flange, s . For Type A and Type B, H-shaped beam with $H-500 \times 250 \times 9 \times 16$ as a narrow cross-sectional shape and $\lambda_1 = 200$ is selected. The curve is drawn from Eq. (10a). The symbols indicate the eigenvalue analyses results with different lateral rigidities, k_u , rotational rigidities, k_β , and fork rigidities, \bar{K} . Where, $\bar{\tau} = 0$ and 1 involve warping and fully fixed supports, respectively. The curve of Eq. (10a) converges to 1 as s increases. It is shown that some symbols below Eq. (10a). Then, Eq. 11 is created for reference to Eq. (10a) so that all symbols get higher than the curve. Grey curve is drawn from Eq. 11.

$$\tau = 4 - \frac{3}{1+s} \quad (11)$$

Figure 6 describes the relation between the elastic lateral bucking stress, σ_{cr} of H-shaped beam with fork rigidity, \bar{K} . The symbols in Fig. 6 indicate the eigenvalue

Fig. 6 Relationship between elastic lateral bucking stress for H-shaped beams with fork restraint and fork rigidity



analyses results. They use different lateral rigidity ratio, $K_u/(EI_f/l^3)$. H-500 × 250 × 9×16 as a narrow cross-sectional shape and $\lambda_1 = 200$ are selected. The black and grey curves express the elastic lateral buckling stress for Type A and Type B obtained by Eq. 9, respectively. The lateral buckling stress become large as lateral rigidity, k_u or fork rigidity, \bar{K} increases. The same phenomenon such as k_β increasing is also observed. The lateral buckling curves in Eq. 9 agree with the symbols of the eigenvalue analyses results, so that Eq. 9 is available to estimate the elastic lateral buckling stress of H-shaped beams with fork restraint under the uniform flexural moment.

5 Conclusion

This paper evaluates the effect of fork restraint on elastic lateral buckling load for H-shaped beams with continuous braces. Results show the following.

1. The elastic lateral buckling loads with warping and fully fixed supports under uniform flexural moment are developed by energy method, and can be estimated with Eqs. 6–8.
2. Effect of fork restraint is expressed as $\bar{\tau}$, which complements between warping and fully fixed supports. The lateral buckling load with fork restraint can be calculated by Eq. 9.
3. It is shown that the lateral buckling stress becomes larger, as lateral rigidities, k_u , rotational rigidities, k_β or fork rigidity, \bar{K} increases.

Acknowledgements This work was supported by JST Program on Open Innovation Platform with Enterprises, Research Institute and Academia.

References

1. Architectural Institute of Japan, AIJ (2005) Design standard for steel structures. (in Japanese)
2. Architectural Institute of Japan, AIJ (2010) Recommendation for limit state design of steel structures (in Japanese)
3. Japan Steel Corporation (2007) Material handbook for buildings
4. Kimura Y, Yoshino Y, Ogawa J (2013) Effect of lateral-rotational restraint and strength of continuously braces on lateral buckling load for H-shaped beams. J AIJ 683:193–201 (in Japanese)
5. Kimura Y, Miya M, Liao W (2018) Effect of restraint for continuous braces on lateral buckling load for H-shaped beams to column joint. J Struct Constr Eng (Trans AIJ) 83(751):1353–1363 (in Japanese)
6. Suzuki T, Kimura Y (1999) Buckling length of H-shaped beams in steel rigid frame. J AIJ 521:127–132 (in Japanese)
7. Suzuki T, Kimura Y (2000) Lateral buckling of H-shaped beams with warping restraint of beam-to column joints. J AIJ 537:115–120 (in Japanese)

Experimental Study of Reinforced Concrete Beams Strengthened by High-Strength Fiber Reinforced Concrete



T. Hung Nguyen, Anh Thang Le, G. Phat Kha, and C. V. Duc Phan

1 Introduction

Recently, the precast concrete elements of which the steel fiber reinforced concrete (SFRC) having the role of the formworks are the topic studying in Vietnam. The efficiency of existing reinforced concrete structures strengthening with SFRC have been studied by many authors [1, 3, 6, 8]. High cost of SFRC causes many limits to carry out the application and experiment, especially in the developing countries.

In contrast to concrete, the tensile strength of SFRC could be enhanced with the existing of steel fiber. It depends on a number of factors as mixing components, the amount of steel fibers, mixing equipment and procedure. Steel fiber keeps the concrete maintains the loading capacity after load reaching to the peak of load. The tensile test could be found in various literatures [2, 11].

The reinforcement concrete beams strengthened by a SFRC layer at the bottom of beams can exhibit the better the structural performance [1, 3, 5, 6, 8, 9]. Besides, it is also reported that SFRC enhances flexural behavior of the beam, increased stiffness, and reduced crack widths. SFRC could serve as protection function for reinforcement due to its low-water permeability [5]. There were experiments carried out by other researches in order to measure the bonding strength between the ordinary concrete and SFRC [4, 7, 10].

T. H. Nguyen · A. T. Le (✉)

Faculty of Civil Engineering, Ho Chi Minh City University of Technology
and Education, Ho Chi Minh City, Vietnam

e-mail: thangla@hcmute.edu.vn

G. P. Kha

MSc student, Ho Chi Minh City University of Technology
and Education, Ho Chi Minh City, Vietnam

C. V. D. Phan

Student Faculty of High Quality, Ho Chi Minh City University of Technology and Education, Ho Chi Minh City, Vietnam

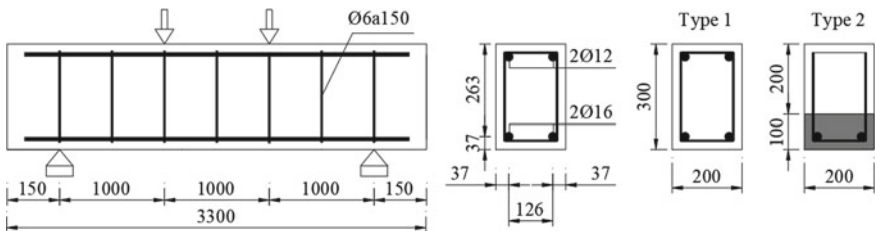


Fig. 1 Detailing of the RC beams and the concrete-SFRC composite beams

The article is a study of the behavior and performance of reinforcement concrete beams strengthened by an SFRC layer in the beam's tension zone. Several conventional concrete grades combined with the same type of SFRC and steel reinforcement in a beam were tested in the laboratory. The bending strength and performance of the beam were observed and discussed in the paper.

2 Experimental Investigations

2.1 Test Program

Experiments were carried out for exploring the flexural behavior of the composite beams having SFRC. The characterizations of concrete, SFRC and steel reinforcement were considered before the bending test. The beams bending were performed on four groups of the intermediate-scale beams by the 4-point bending tests (Fig. 1).

2.2 Mixtures and Material Properties

All beams were reinforced with the same manner. Longitudinal reinforcement of Ø16 mm placing in the lower part, reinforcement of Ø12 mm placing in the upper part. The rebar stirrups of Ø6 mm were arranged at equally distances along the beam as shown in Fig. 1. Average yielding strength of steel rebar (f_{sy}) is 300 MPa and modulus of elasticity (E_s) is 200 GPa. In the study, steel fibers (1.6% by volume) with the tensile strength ($f_{fb,u}$) of 135 MPa were used for the SFRC mixture. Fiber length (l_f) is 35 mm; diameter (d_f) is 0.55 mm, and the ratio (l_f/d_f) is 64. The elastic modulus of steel fiber ($E_{fb,s}$) is 200 GPa (Fig. 2a). The composition in the concrete is presented in Table 1. M20, M25 and M30 are the abbreviation of concrete grade corresponding to the strength class of 20, 25 and 30 MPa, respectively. M80-Fibers is the abbreviation of the concrete with the steel fibers having the strength class of 80 MPa.

The material composition used in SFRC is shown in Fig. 2. In which silica fume (Fig. 2e) and plasticizer (Fig. 2f) are additive for enhancing strengthen and workability of the concrete mixture. The compressive strengths of conventional concrete



Fig. 2 SFRC materials: **a** Steel fibers, **b** Aggregate, **c** Fine sand from Binh-Dinh province, **d** Fly ash, **e** Silica fume, **f** Plasticizer

Table 1 Compositions of conventional concrete and SFRC

Materials	Quantity (kg/m ³)			
	M20	M25	M30	M80—Fibers (SFRC layer)
Cement	297.0	346.0	378.0	690.0
Aggregate 5 × 10				1050.0
Aggregate 10 × 20	1164.8	1150.8	1142.4	
Sand	522.0	501.0	477.0	310.0
Water	195.0	195.0	195.0	195.0
Fly ash				35.0
Silica fume				80.0
Plasticizer				16.5
Steel fibers—Dramix 3D				40.0
Compressive strength (MPa)	22.4	29.2	33.4	87.0

and SFRC were tested at the age of 28 days. Average values of compressive strength are presented in Table 1. In generally, the compressive strengths were satisfied the strength requirements of the corresponding concrete grade.

Table 2 The concrete grades of beams

Beam type	Beam description	Concrete normal	HPFRC
Type 1	B1-CC20	M20	
Type 2	B2-20	M20	M80—Fibers
Type 2	B3-25	M25	M80—Fibers
Type 2	B4-30	M30	M80—Fibers

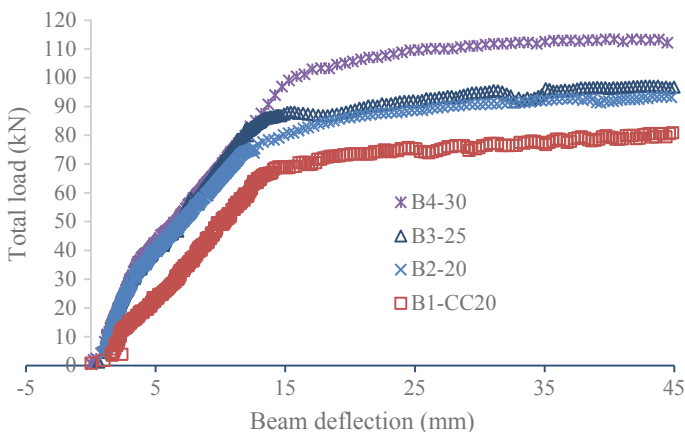
2.3 Preparing Specimens

SFRC was placed in the tension zone of beams. The concrete grades of beams are summarized in Table 2. Each type of cross section had two beams. The conventional RC beams and the composite beams of SFRC were cast in the laboratory as shown in Fig. 1. There were two types of the beam section with and without 10 cm thickness of SFRC layer (Fig. 1). The concrete grades of the beams are summarized in Table 2. In the composite beams, SFRC was placed in the tension zone. Each type of cross section had at least two beams.

3 Experimental Results

3.1 Deflection

Figure 3 shows the curves of the relationship between load and deflection at mid-span of the beams. It can be seen that there is a difference in mid-span displacement of

**Fig. 3** Load and deflection at the mid-span of a beam

the beams with and without SFRC. The elastic modulus of reinforcement concrete beams having SFRC is the same and higher than the elastic modulus of conventional reinforcement concrete beams. As increasing the grade of the concrete in the beam's upper part from 20 MPa, 25 MPa, and 30 MPa, the bending load capacity of the beam increases 17.7%, 20.0% and 40.2%, respectively, comparing to the conventional reinforcement concrete beam. The difference between the beams of B2-20 and B1-CC20, the same concrete grades, is 17.7%. It indicates that the bearing capacity of the reinforced concrete beam increases significantly with the strengthening of SFRC.

3.2 Crack Patterns

As the crack occurring, there is the difference in the crack pattern of beams with and without SFRC. As shown in Fig. 4, it could be said that the SFRC had a significant effect upon the crack propagation. The distances between cracks of beams with SFRC are closer than that of beams without SFRC. There is the phenomenal that the steel fiber was pulled out the concrete matrix.

In the Fig. 4, B4-30 shows fewer cracks than beams of B2-20, and B3-25 in the lower part of conventional concrete layer. This indicates that the bonding of the various concrete grades with the SFRC layer may cause the difference in the crack pattern.

On the other hand, it could be seen that there are more cracks in the SFRC layer. The phenomenon of sliding between the two layers of concrete that may cause the number of cracks in the SFRC part is more than the number of cracks in the normal concrete. Besides, there is the phenomenal of restart crack in the conventional concrete layer. The crack does not go through the contact face. The crack in the conventional concrete layer starts at a distance away from the crack in the SFRC layer.

Figure 4 also shows that B1-CC20, B2-20, B-25 and B4-30 have the number of cracks of 16, 15, 16 and 14, respectively. The maximum crack widths measured on the specimens of B2-20, B-25 and B4-30 are 9.6 mm, 8.7 mm, and 6.5 mm, respectively. This indicates that the higher the grade of concrete combined with SFRC, the more the decreasing crack width of a reinforcement concrete beam.

3.3 Curvature and Ductile of Beams

At the working load values (under 70 KN), Fig. 3 shows that all curves of B2-20, B3-25 and B4-30 beams are above that of B1-CC20. The curvature of strengthen SFRC beams might less than that of the conventional beam. It could be explained that the beams strengthened with SFRC are stiffer than the beam of traditional concrete due to the higher elastic modulus of the SFRC layer. The effect of SFRC could be seen easy in Fig. 3.

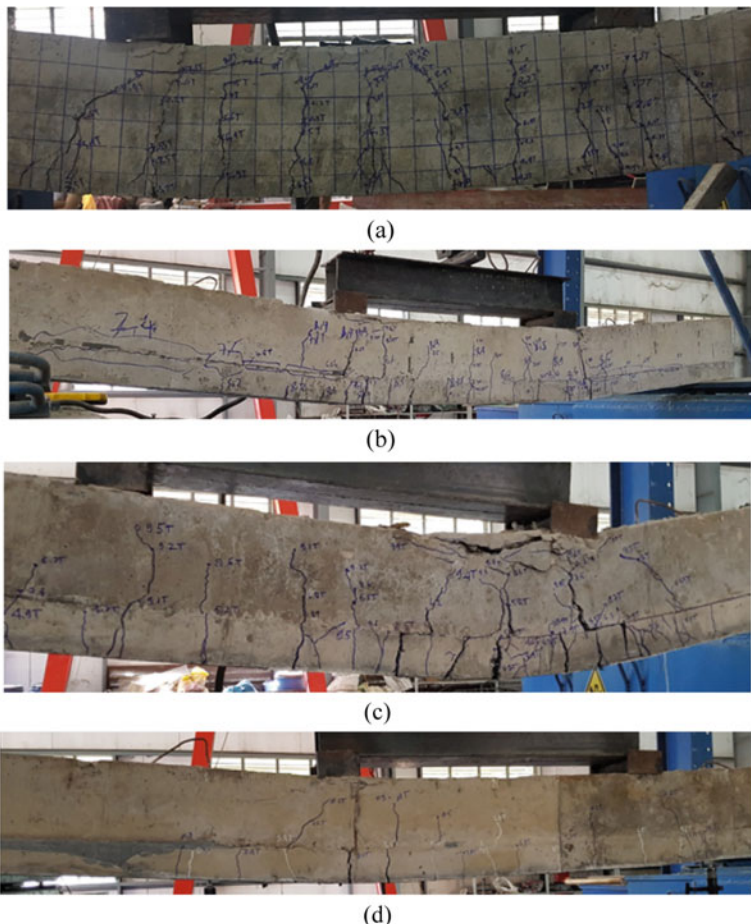


Fig. 4 Cracking patterns of different type of tested beams at failure load: **a** B1-CC20, **b** B2-20, **c** B3-25 and **d** B4-30

At the ultimate load level, the curvatures of the reinforcement concrete beams with SFRC are higher than that of conventional reinforcement concrete beams. The beams with SFRC at the tension zone could maintain the load carrying capacity and increasing vertical deformation due to the ductile ability of the SFRC. This led the curvature of the composite beams with SFRC is higher than that of the normal concrete beam.

Due to the limit of LVDT of 50 mm, the displacement of the beams cannot be measured up to 50 mm. The relationship curve of load and displacement went down as shown in Fig. 3. B1-CC20 cannot maintain the bearing load after the displacement above 45 mm. On the other hands, the reinforcement concrete beams with SFRC can maintain the bearing load up to the vertical displacement of 150 mm (Fig. 5). Thus, the curvatures of beams with SFRC are higher than the curvature of conventional

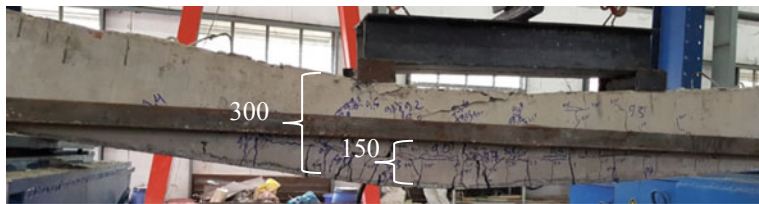


Fig. 5 The curvature of B2-20

beams without SFRC. It could be said that the ductility of the beam increases as the beam is strengthened by an SFRC layer.

3.4 Layer Separation

The phenomenon of slippage at the contact face between conventional concrete and SFRC could be observed easily (Fig. 4). The gap between two concrete layers of the beams of B2-20, B3-25 and B4-30 are 4.1 mm, 3.9 mm and 3.5 mm, respectively. Those gaps are measured at the mid-span of the beam. The beams have the higher the load-bearing capacity leading the smaller the gap between two concrete layers of the beam. Gaps may be caused by difference in the stiffness of various layers. The stiffness of SFRC layer is higher than that of conventional concrete layer.

4 Conclusions

The experimental results show the efficiency in loading capacity of the composite beams between the conventional concrete and SFRC. Besides, there are some conclusions related to the behavior and performance of beams:

- The performance of beams having the SFRC layer could also be enhanced as bending. The composite beams have the increased stiffness, and the crack widths reduced. SFRC layer could help the reinforcement concrete beams increasing both the curvature at the ultimate load level and the ductile.
- The behavior of the beam is affected significantly by concrete's grade working with SFRC. The performance of B4-30 is better than the performance of B2-20 and B3-25. Thus, the closer the grade of conventional concrete to the concrete grade of SFRC, the better performance of the bending beams could be observed.
- The phenomenon of slippage at the contact face between conventional concrete and SFRC could be observed easily in every case of beams having the SFRC layer.

Acknowledgements The authors are grateful for the financial support as well as the experimental equipment of the HCM University of Technology and Education, and the unconditional help of the faculty of construction so that we can complete this research.

References

1. Brühwiler E, Denarié E (2013) Rehabilitation and strengthening of concrete structures using ultra-high performance fibre reinforced concrete. *Struct Eng Int* 23(4):450–457
2. Graybeal B (2014) Tensile mechanical response of ultra-high-performance concrete. *Adv Civ Eng Mater* 4(2):62–74
3. Habel K, Denarié E, Brühwiler E (2006) Structural response of elements combining ultrahigh-performance fiber-reinforced concretes and reinforced concrete. *J Struct Eng* 132(11):1793–1800
4. Harris D, Muñoz M, Ghetasi A, Ahlborn T, Rush S (2015) The challenges related to interface bond characterization of ultra-high-performance concrete with implications for bridge rehabilitation practices. *Adv Civ Eng Mater* 4(2):1–27
5. Hussein L (2015) Structural behaviour of ultra high performance fibre reinforced concrete composite members. Ph.D. thesis, Department of Civil Engineering, Ryerson University, Toronto, Canada
6. Lampropoulos A, Paschalidis S, Tsoulou O, Dritsos S (2016) Strengthening of reinforced concrete beams using ultra high performance fibre reinforced concrete (UHPFRC). *Eng Struct* 106:370–384
7. Muñoz C, Harris D, Ahlborn T, Froster D (2014) Bond performance between ultrahigh-performance concrete and normal-strength concrete. *J Mater Civ Eng* 26(8):04014031
8. Noshiravani T, Brühwiler E (2013) Experimental investigation on reinforced ultra-high-performance fibre reinforced concrete composite beams subjected to combined bending and shear. *ACI Struct J* 110(2):251–261
9. Noshiravani T, Brühwiler E (2014) Analytical model for predicting response and flexure-shear resistance of composite beams combining reinforced ultrahigh performance fiber-reinforced concrete and reinforced concrete. *J Struct Eng* 140(6):04014012-1–04014012-10
10. Tayeh B, Bakar B, Johari M (2013) Characterization of the interfacial bond between old concrete substrate and ultra high performance fiber concrete repair composite. *Mater Struct* 46(5):743–753
11. Wille K, El-Tawil S, Naaman A (2014) Properties of strain hardening ultra high performance fiber reinforced concrete (UHP-FRC) under direct tensile loading. *Cement Concr Compos* 48:56–66

Investigating the Crack Velocity in Ultra-High-Performance Fiber-Reinforced Concrete at High Strain Rates



Tri Thuong Ngo, Duy Liem Nguyen, and Ngoc Thanh Tran

1 Introduction

Ultra-high-performance fiber-reinforced concretes (UHPFRCs) have demonstrated superior mechanical properties, in comparison with normal concrete (NC) and high-performance fiber-reinforced concrete (HPFRCs), including very high compressive strengths, tensile strengths, shear strength, tensile strain capacities, energy absorption capacities, and strain-rate dependent [7, 14, 15]. These properties favor the enhancement of the resistance of civil infrastructure, buildings, especially military structures to extreme loads, such as seismic, impact, and blast loads [4, 5, 12, 13]. However, the initiation and propagation of crack in UHPFRCs, which is a key and complex mechanism leading to failure of structures, is still very little information both at static and high strain rates.

Several researchers have been investigated the cracking process in plain concrete as well as FRC using several methods such as high-speed camera [3], acoustic emission [1], digital image correlation [17], and a strain gauge or crack gauge [17]. However, it is still very little information about the crack velocity in UHPFRCs, in comparison with plain concrete and fiber reinforced concrete [10]. Mindess [3] using a high-speed camera system measured the crack velocity in plain concrete under a drop-weight impact loading. [1] reported that the formation and growth of cracks in plain concrete could be detected by the acoustic emission technique. The

T. T. Ngo (✉)

Faculty of Civil Engineering, Thuylo University, 175 Tay Son, Dong Da, Ha Noi City, Vietnam
e-mail: trithuon@tlu.edu.vn

D. L. Nguyen

Faculty of Civil Engineering, Ho Chi Minh City University of Technology and Education,
01 Vo van Ngan St, Thu Duc District, Ho Chi Minh City, Vietnam

N. T. Tran

Department of Structural Engineering, Faculty of Civil Engineering,
HCMC University of Transport, Ho Chi Minh City, Viet Nam

crack velocity in fiber reinforced concrete (FRC) under different loading rates was measured by the bonded strain gauges technique by Zhang et al. [17]. Pyo et al. [10] measured the crack speed in UHPFRCs reinforced 0.0, 0.5, and 1.0 vol.-% short smooth fibers by using the DIC technique.

The aim of this study is to propose method to investigate crack velocity and the effect of fiber reinforcement and applied strain rates to the crack velocity in UHPFRCs.

2 Experimental Program

2.1 Material and Specimen Preparation

The composition of matrix mixture and compressive strength of the ultra-high-performance concrete (UHPC) matrix was shown in Table 1. The fiber reinforcement is 2.0 vol.-% smooth steel fiber with the diameter is 0.2 mm and the length is 19 mm.

The mixing and curing procedure of UHPFRCs specimens can be found in [4, 8]. In their experiment, the average compressive strength of 50 mm cubic UHPC specimens was 184 MPa [4]. The cement, silica fume, silica powder, and silica sand were dry-mixed for 10 min. Water was then added to the dry mixture at intervals of 2–3 min. The water and superplasticizer then were gradually poured into the mixture and continuously mixed before steel fibers were added into the mixture by hand. The specimens were then stored in a laboratory at room temperature during 48 h prior to demolding and were cured in a hot water tank at $90 \pm 2^\circ\text{C}$ for 3 days. Two layers of polyurethane were sprayed on the surfaces of dry specimens for crack detection. All specimens were tested in a dry condition at the age of 28 days.

Twenty-four prism specimens were cast and tested as shown in Fig. 1. The size of specimen is $50 \times 50 \times 210 \text{ mm}^3$. Before testing, a notch with 10 mm in depth and 2 mm in width was made at the bottom of specimen. Stone powder was sprayed on the surface of specimen at static test, while the random speckle patterns were used for those at high strain rates tests, respectively.

Table 1 The composition of UHPC matrix by weight ratio

Cement (Type I)	Silica fume	Silica sand	Silica powder	Super-plasticizer	Water	Compressive strength (MPa)
1	0.25	1.10	0.30	0.067	0.2	184

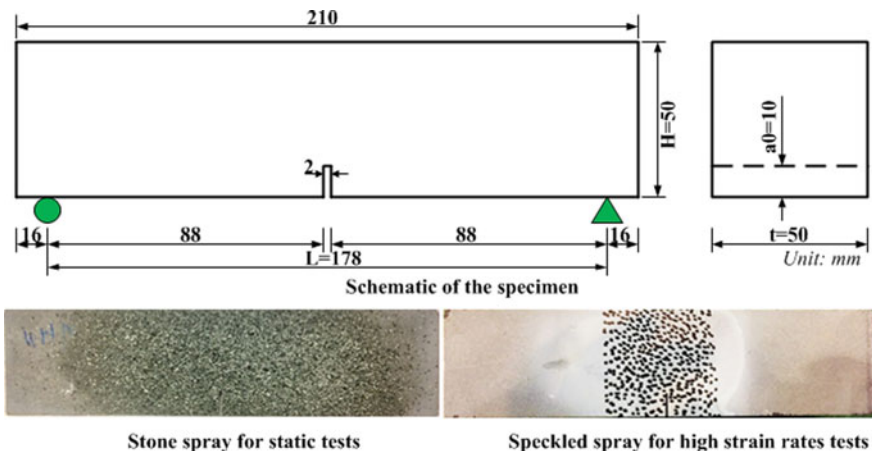


Fig. 1 Schematic of the specimen

2.2 Test Setup and Procedure

Three-point bending specimen was installed in the Universal Test Machine (UTM) and the Improve—Strain Energy Frame Impact Machine (I-SEFIM) to investigate the crack velocity in UHPFRC specimens at different strain rates. The displacement speed of the UTM was 1 mm/min and the applied forced was measured by a load cell placed inside the machine as shown in Fig. 2.

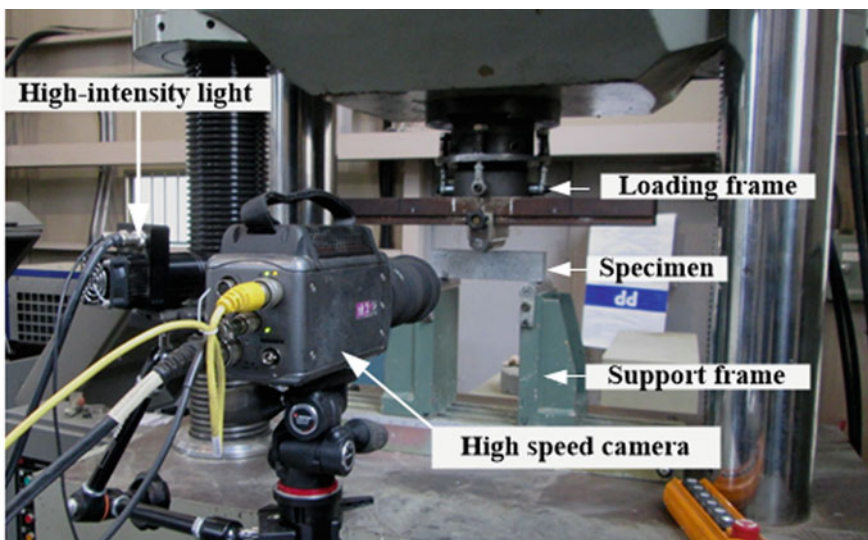


Fig. 2 Three-point bending test at static rates

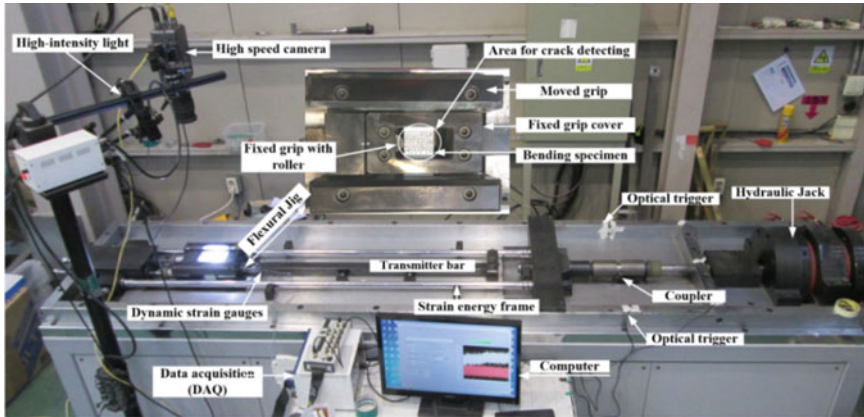


Fig. 3 Three-point bending test at high strain rates

A three-bending test setup was installed into the I-SEFIM to do the test at high strain rates as shown in Fig. 3. The applied load speed into the specimen could be changed by using difference coupler and energy frame. A combination of 800 kN coupler and high strength steel energy frame, which could generate an estimated theoretical impact velocity of 13.83 m/s [9] was used in this study. Two dynamic strain gauges were glued on the transmitter bar and connected to a Data Acquisition (DAQ) system to measure the applied load, while a high-speed camera system was used to measure the displacement of UHPFRC specimens. The detail of I-SEFIM can be founded in [9].

2.3 Measuring the Crack Velocity in UHPFRCs

The frequency of the high-speed camera was set to at 2.500 frames per second and a resolution of 128×88 pixels to capture images of the specimen during static tests, while those of high strain rate tests were 100,000 frames per second and the resolution of 160×80 , respectively. The images captures by the camera were analyze using the EDAs and the DIC technique to obtain the initiation and propagation of crack in UHPFRCs.

The DIC is an optical and non-contact technique in measuring the displacement of an object of interest. The fundamental algorithm of the DIC technique is comparing two digital images, capture by the high-speed camera before and after deformation. The underlying theory of DIC technique can be referred in [11].

The crack velocity using the DIC technique can be calculated according to Eq. (1).

$$\text{Crack velocity} = \frac{\sum_1^n \frac{y_{GL_i} - y_{GL_{i-1}}}{t_i - t_{i-1}}}{n - 1} \quad (1)$$

Where y_{GL_i} is the coordination in the y-axis of a strain gauge i (GL_i); t_i is the time of strain increase continuously at strain gauge GL_i ; n is the number of gauges.

The cracking velocity in UHPFRCs was also calculated by using the EDAs technique as can see in Fig. 5. The underlying theory of EDAs could be found in [2]. Two EDAs (Canny and Prewit algorithms) in an image processing program (MATLAB) were used in this study. The images are firstly post-processed to detect the boundary and tip of the crack. The length of crack in each image was measured by an image reading technique in MATLAB. Then, the crack velocity was calculated

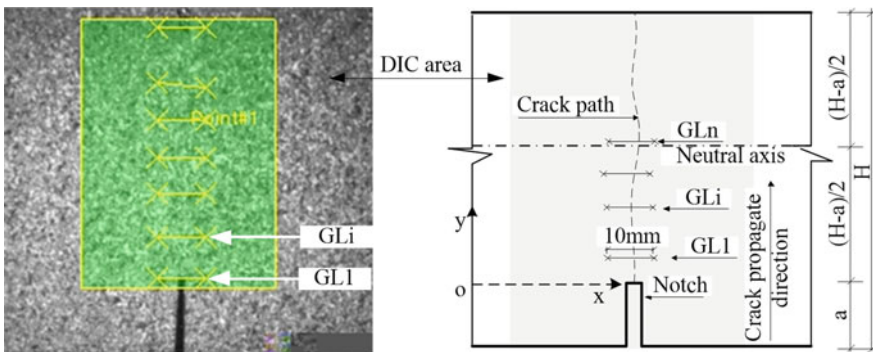


Fig. 4 Calculating the crack speed using DIC technique

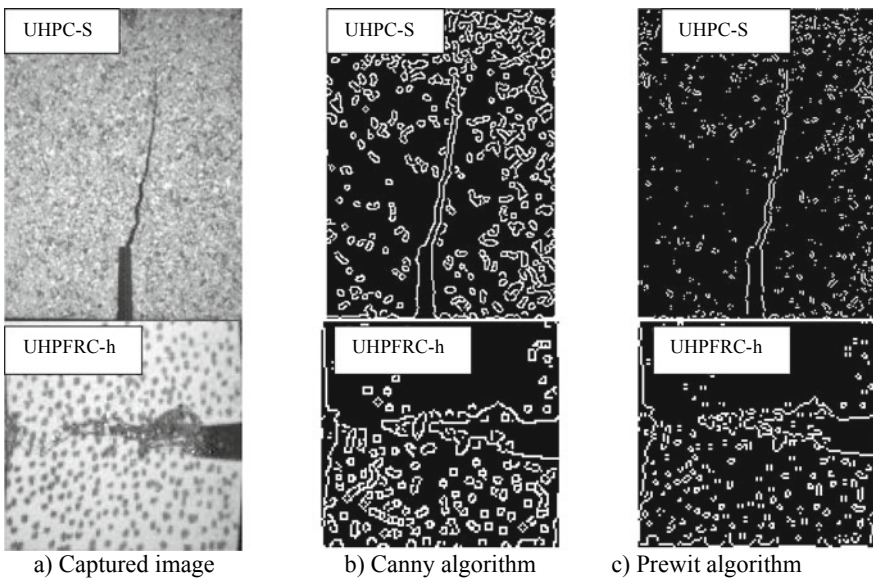


Fig. 5 Calculating the crack speed using the different EDAs

by dividing the difference between the crack lengths of two continuous images with the increment time between them.

3 Results and Discussions

The crack velocity (v) in UHPFRCs calculated according to the DIC and EDA methods are listed in Table 2. Whereas the number in parentheses is the standard deviation values (SD). Generally, the value of v measured by the EDAs technique was smaller than those by the DIC technique, owing to the difficulty in detecting a very fine crack boundary at the tip of the crack. As can see in Table 2, the v according to the DIC techniques of UHPC and UHPFRC at static rate is 5.64 and 0.0019 m/s increased to 738.82 and 496.91 m/s at high strain rates. Whereas, those value of the EDA technique is 4.56 and 0.0017 m/s at static rate and 554.12 and 496.91 m/s at high strain rates.

The effect of fiber reinforcement and applied loading speed on the crack velocity in UHPFRC is showed in Fig. 6. The crack velocity increased as the applied loading speed increased in both UHPC and UHPFRCs. The crack velocity of UHPC specimens increased from 5.46 to 738.82 m/s as the loading speed increased from 1.67×10^{-5} to 13.83 m/s. Those of UHPCs are 0.0019 and 552.12 m/s, respectively. The increase of cracking velocity as the applied loading speed increased has been reported by several researchers [6, 10]. In addition, the fiber reinforcement significantly slowed down the crack velocity in the UHPFRCs at both static and high strain rates. The crack velocity decreased from 5.64 to 0.0019 as the fiber reinforcement was 2 vol.-% smooth steel fiber at static and from 738.82 to 552.12 m/s at high strain rates. This decrease velocity in UHPFRCs can be attributed to the interfacial bond stress between fiber and matrix, which delayed the formation and propagation of cracks [16].

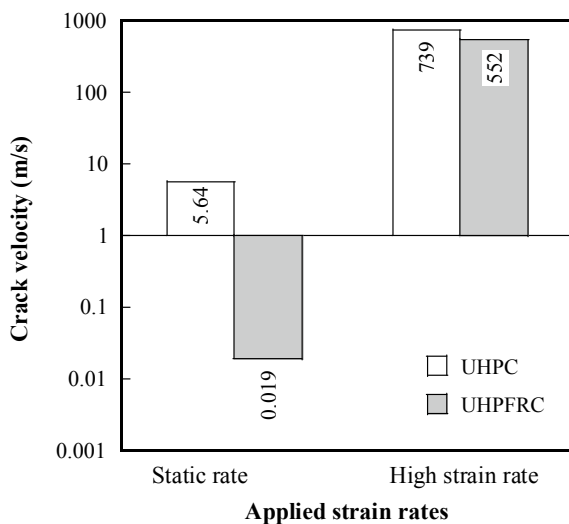
Table 2 Crack velocity according to DIC and EDA methods

Series	Loading speed	Crack velocity, v , (DIC)	Crack velocity, v , (EDA)
	m/s	m/s	m/s
UHPC-S	1.67×10^{-5}	5.64 (2.8 ^a)	4.56 (0.22)
UHPC-h	13.83 ^b	738.82 (80.3)	554.12 (26.7)
UHPFRC-S	1.67×10^{-5}	0.0019 (0.00081)	0.0017 (0.00069)
UHPFRC-h	13.83 ^b	552.12 (51.3)	496.91 (45.2)

^aThe number in parentheses stand for Standard Deviation (SD)

^bTheoretical speed [9]

Fig. 6 Effect of fiber reinforcement and applied loading speed on crack velocity in UHPFRCs



4 Conclusions

The effect of fiber reinforcement and applied strain rates on the crack velocity in UHPFRCs was experimentally investigated. Based on the results of this study, the following conclusions can be drawn:

- The cracking velocity in UHPFRC can be measured by using the high-speed camera system combination of the DIC and EDA techniques, even though the DIC technique showed better results.
- The applied strain rates made strong influences on the crack velocity in the UHPFRCs: the crack velocity increased as the applied strain rate increased.
- The fiber reinforcement significantly slowed down the crack velocity in the UHPFRCs at both static rates and high strain rates.

Acknowledgements This research is funded by Vietnam National Foundation for Science and Technology Development (NAFOSTED) under grant number 107.01-2019.03.

References

1. Goszczyńska B (2014) Analysis of the process of crack initiation and evolution in concrete with acoustic emission testing. *Arch Civ Mech Eng* 14(1):134–143
2. Maini R, Aggarwal H (2009) Study and comparison of various image edge detection techniques. *Int J Image Process* 3(1):1–11
3. Mindess S (1995) Crack velocity in concrete subjected to impact loading. *Can J Phys* 73:310–314

4. Ngo TT, Kim D-J (2018) Synergy in shear response of ultra-high-performance hybrid-fiber-reinforced concrete at high strain rates. *Compos Struct* 195:276–287
5. Ngo TT, Kim DJ (2017) Shear stress versus strain responses of ultra-high-performance fiber-reinforced concretes at high strain rates. *Int J Impact Eng* 1–23
6. Ngo TT, Park JK, Kim DJ (2019) Loading rate effect on crack velocity in ultra-high-performance fiber-reinforced concrete. *Constr Build Mater* 197:548–558. <https://doi.org/10.1016/j.conbuildmat.2018.11.241>
7. Ngo TT, Park JK, Pyo S, Kim DJ (2017) Shear resistance of ultra-high-performance fiber-reinforced concrete. *Constr Build Mater* 151:246–257
8. Park JJ, Kang ST, Koh KT, Kim SW (2008) Influence of the ingredients on the compressive strength of UHPC as a fundamental study to optimize the mixing proportion. In: Proceeding of the second international symposium on ultra high performance concrete, Kassel, Germany, pp 105–102
9. Park SH, Kim DJ, Kim SW (2016) Investigating the impact resistance of ultra-high-performance fiber-reinforced concrete using an improved strain energy impact test machine. *Constr Build Mater* 125:145–159. <https://doi.org/10.1016/j.conbuildmat.2016.08.027>
10. Pyo S, Alkaysi M, El-Tawil S (2016) Crack propagation speed in ultra high performance concrete (UHPC). *Constr Build Mater* 114:109–118
11. Shah SG, Chandra Kishen JM (2011) Fracture properties of concrete-concrete interfaces using digital image correlation. *Exp Mech* 51(3):303–313. <https://doi.org/10.1007/s11340-010-9358-y>
12. Tran NT, Tran TK, Jeon JK, Park JK, Kim DJ (2016) Fracture energy of ultra-high-performance fiber-reinforced concrete at high strain rates. *Cem Concr Res* 79:169–184
13. Tran TK, Kim DJ (2014) High strain rate effects on direct tensile behavior of high performance fiber reinforced cementitious composites. *Cement Concr Compos* 45:186–200
14. Wille K, Kim DJ, Naaman AE (2011) Strain-hardening UHP-FRC with low fiber contents. *Mater Struct* 44(3):583–598
15. Wille K, Naman AE, Parra-Montesinos GJ (2011) Ultra—high performance concrete with compressive strength exceeding 150 MPa (22ksi): a simpler way. *ACI Mater J* 108(1):46–53
16. Wu Z, Shi C, He W, Linmei W (2016) Effects of steel fiber content and shape on mechanical properties of ultra high performance concrete. *Constr Build Mater* 103:8–14
17. Zhang XX, Yu RC, Ruiz G, Tarifa M, Camara MA (2010) Effect of loading rate on crack velocities in HSC. *Int J Impact Eng* 37(4):359–370

Modeling of Reinforced Concrete Beam Retrofitted with Fiber Reinforced Polymer Composite by Using ANSYS Software



Trong Toan Khong, Quoc Tinh Tran, and Van Trinh Do

1 Introduction

Reinforced concrete (RC) structures damaged due to various reasons and in most of the cases damage occurred in the form of cracks, concrete crushing, and large deflection, etc. Some various factors which are causes of these deteriorations, such as high load, corrosion of reinforcement, earthquake, environmental effects and accidental impacts on the structure. Therefore, repairing and improvement have become an important challenge for the reinforced concrete structures in recent years. It's very necessary to have techniques that can have low costs and fast processing time. Externally bonded fiber reinforced polymers (FRP) is a common technology which highly need for repair and strengthening of reinforced concrete structures. The FRP can be used to increase the shear and flexural capacities, provide confinement and ductility to compression structural members. The most popular type of FRP in industry is made with carbon, aramid or glass fibres. The major advantage of the retrofitting is to strengthen the structures for life safety and protection of the structures. Therefore, the existing structures be retrofitted to improve their performance in any condition and to avoid large scale damage to life and property.

Currently, FRP materials have been widely used to increase the flexural and shear capacity of RCC members. The main advantages of FRP sheet over steel plate are its low weight, high strength and noncorrosive property. In the light of above discussion, the only analytical tool which done the retrofitting modelling and able to calculate

T. T. Khong (✉) · Q. T. Tran · V. T. Do

Faculty of Civil Engineering, Ho Chi Minh City University of Technology (HUTECH), Ho Chi Minh, Vietnam

e-mail: kt.toan@hutech.edu.vn

Q. T. Tran

e-mail: tq.tinh@hutech.edu.vn

V. T. Do

e-mail: dv.trinh@hutech.edu.vn

Fig. 1 Typical beam dimensions

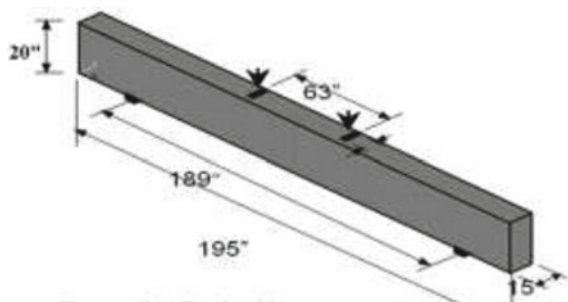
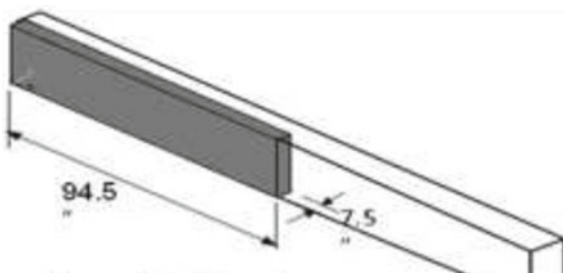


Fig. 2 Quarter beam for model



the nonlinear behaviour of the structural members and also free from all the above flaws is Finite element method.

This study focuses on analysing the behaviour of RC beams retrofitted with different FRP by using ANSYS program.

2 FRP Retrofetting

FRP sheets can be used for strengthening of RC members in flexure, shear and confinement. And there are some different warping types of externally bonded FRP are used to improve the strength of RC beams as details: (a) bonding FRP sheet on side of the beam; (b) bonding FRP on both sides and the tension face of the beam and (c) bonding FRP to the bottom of the beam. In the direction of fibres FRP has maximum strength, so they can be oriented with different angles with respect to the axis of beam in order to prevent the formation and propagation of shear cracks.

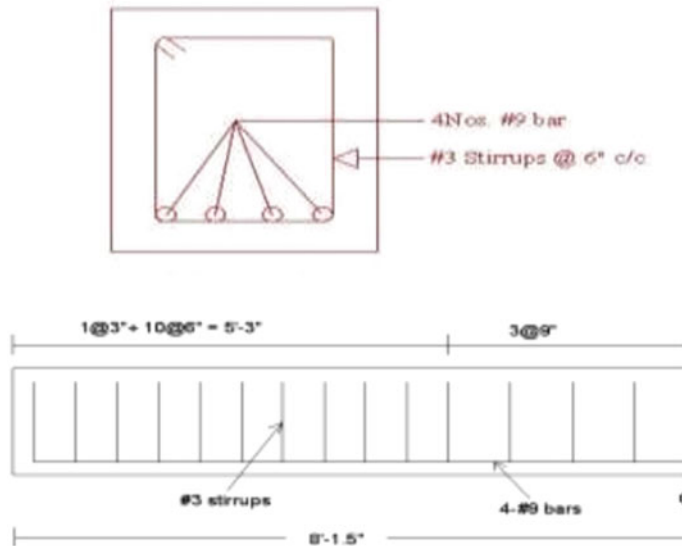


Fig. 3 Details of position of the steel reinforcements

3 Geometry

The geometry of the beam was proposed by Saifullah et al. [1] will be used in this research and are shown in Figs. 1, 2 and 3. A quarter of the beam was used for modelling because of the symmetry of the beam and saving computer resource.

4 Finite Element Modelling in ANSYS

ANSYS Work Bench version 15 was used to model and analysis. Solid 65 elements were represented for the concrete and Link 8 element was used to model for all the steel reinforcement. In another hand, no need to be analyzed, so all the steel plates at the support and under the load will be modeled by Solid45 elements. Furthermore, FRP sheet was modeled by Solid45 elements (Fig. 4). Table 1 was the list of elements were used on this modelling.

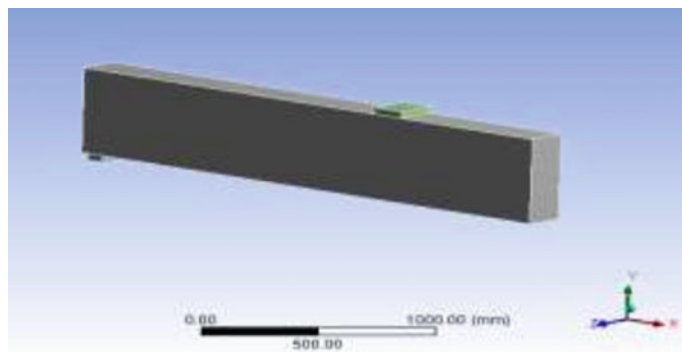


Fig. 4 Working model in ANSYS

Table 1 Element types for each materials

Material	Element types
Reinforced concrete	Solid65
Plate and support	Solid45
Steel reinforcement	Link8
FRP	Solid45

5 Material Properties

5.1 Concrete

All the input data for material properties of concrete which must to import into ANSYS as: Young modulus (E_c), Ultimate uniaxial compressive strength (f'_c), Ultimate uniaxial tensile strength (f_{cr}), Poisson's ratio (μ), Shear transfer coefficient (β_t), Compressive uniaxial stress-strain relationship for concrete (Table 2).

Table 2 Material properties of the RC concrete

Young modulus, E_c	26,457.52 MPa
Poisson ratio, μ	0.25
Shear transfer coefficients for an open crack, C1.	0.3
Shear transfer coefficients for a closed crack, C2	1
Uniaxial tensile cracking stress, C3	3.7
Uniaxial crushing stress (positive), C4	22.4

Table 3 Material properties of the Steel reinforcement

<i>Linear isotropic</i>	
Young modulus, E_c	200,000 MPa
Poisson ratio, μ	0.30
<i>Bilinear isotropic</i>	
Yield strength	410 MPa
Tangent modulus	20 MPa

5.2 Steel Reinforcement

The steel reinforcing bars grade 60 were used for this working model. Elastic modulus and yield strength of the steel reinforcement were given in Table 3.

Aiming to avoid the stress distribution and convergence easier; in the finite element models, steel plates were added at support locations and loading points. An elastic modulus equal to 200,000 MPa and Poisson's ratio of 0.3 were used for the plates.

5.3 FRP Sheet

About the FRP composites, it was very important in the finite element models and effected on the results. So many input data must to be import into ANSYS as follows: Number of layers, Thickness of each layer, Orientation of the fiber, Elastic modulus in three directions (E_x , E_y and E_z), Shear modulus for three planes (G_{xy} , G_{yz} and G_{xz}) and Poisson's ratio for three planes (ν_{xy} , ν_{yz} and ν_{xz}).

Table 4 shows the material properties assigned for the FRP materials—AFRP, CFRP and GFRP laminates used for the study.

Table 4 Material properties of the FRP sheet

Properties	CFRP	GFRP
E_x (MPa)	165,000	21,000
E_y (MPa)	9650	7000
E_z (MPa)	9650	7000
G_{xy} (MPa)	5200	1520
G_{yz} (MPa)	5200	2650
G_{zx} (MPa)	3400	1520
μ_{xy}	0.3	0.26
μ_{yz}	0.3	0.3
μ_{zx}	0.45	0.26

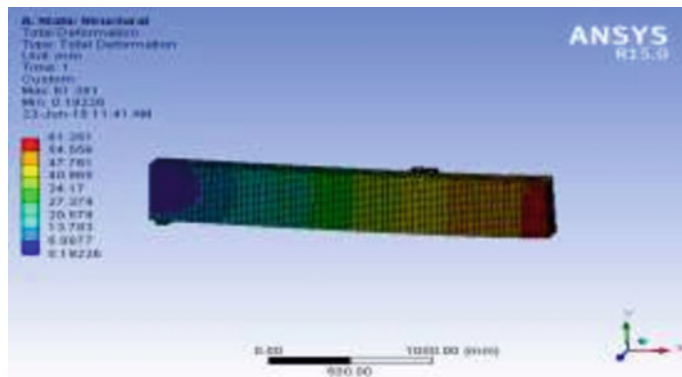


Fig. 5 Deformation shape of control beam

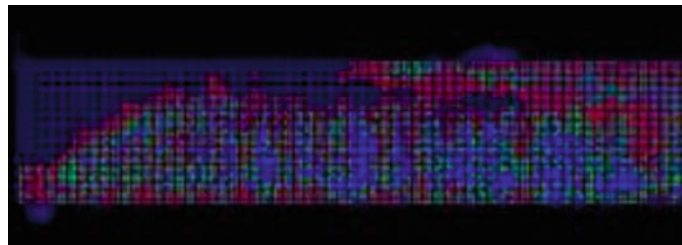


Fig. 6 Cracking development of control beam

6 ANSYS Solution

Two-point loading and supports are assigned to the beam then the deformation shape and crack pattern for the beams (control to FRP retrofitted) are obtained from ANSYS Work Bench as follows (Figs. 5, 6, 7, 8, 9, 10, 11, 12, 13, 14, 15, 16, 17, 18, 19, 20, 21, 22, 23, 24 and 25).

7 Results

Table 5 shows load and deflection at failure of control beam and beams with different combinations of FRP.

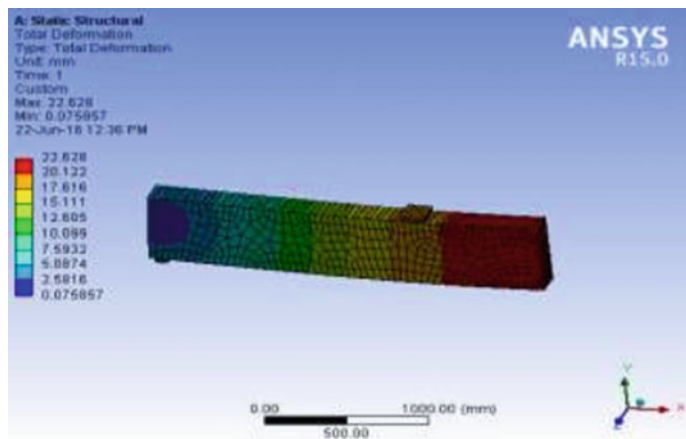


Fig. 7 Deformation shape of CFRP (sides and bottom)

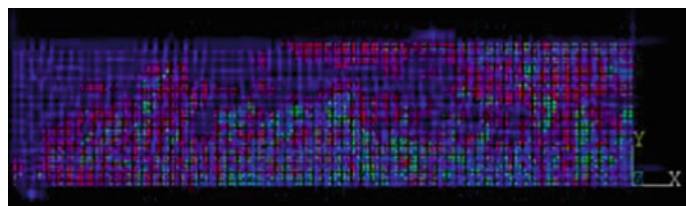


Fig. 8 Crack pattern of CFRP (sides and bottom)

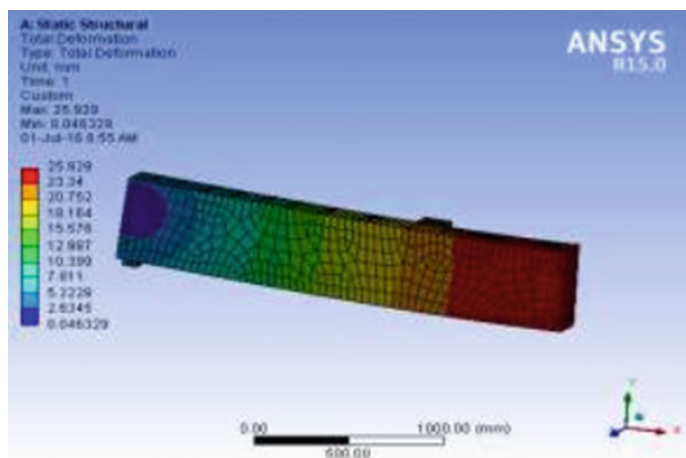


Fig. 9 Deformation shape of CFRP (parallel sides)

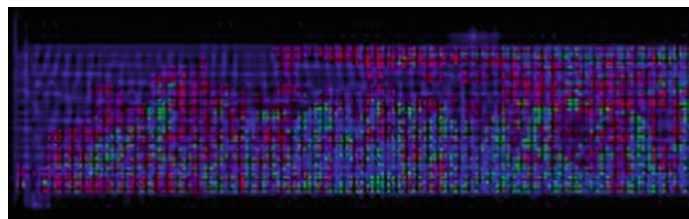


Fig. 10 Crack pattern of CFRP (parallel sides)

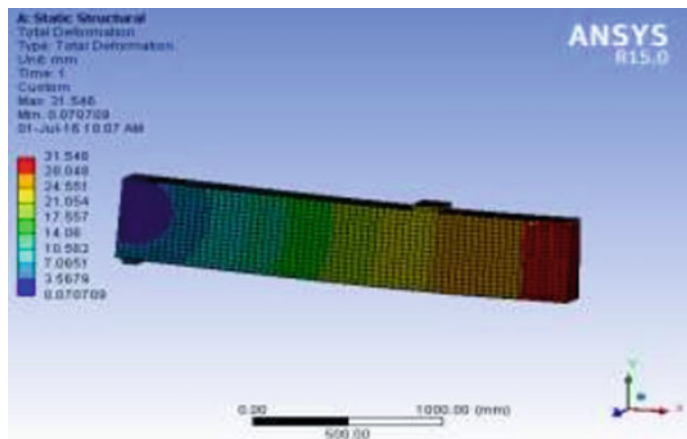


Fig. 11 Deformation shape of CFRP (bottom)

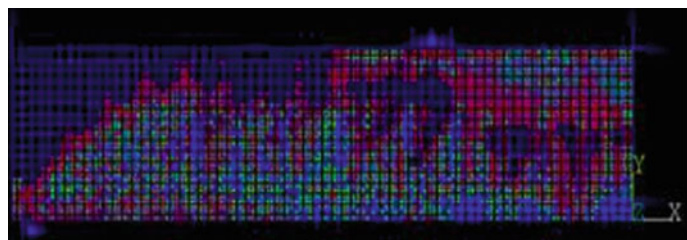


Fig. 12 Crack pattern of GFRP (bottom)

8 Results

Load-Deflection Curve is linear with a sharp slope up to 40–50 kN. The graph changes its nature after first cracking *i.e.* its slope is changed continuously. The location of initiation of the diagonal tension cracking of concrete in curves is in between the 1st

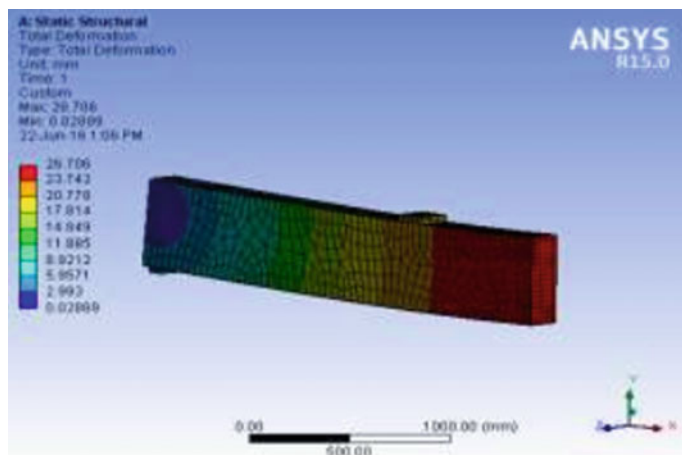


Fig. 13 Deformation shape of GFRP (sides and bottom)

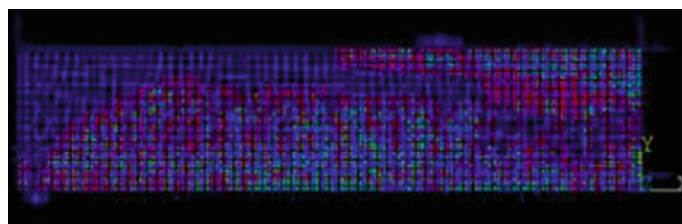


Fig. 14 Crack Pattern of GFRP (sides and bottom)

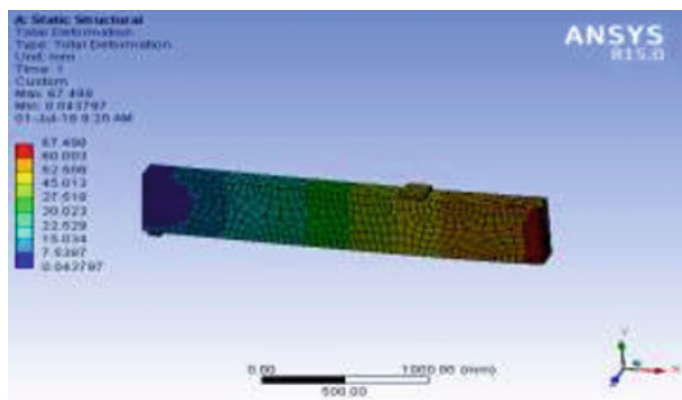


Fig. 15 Deformation shape of GFRP (parallel sides)

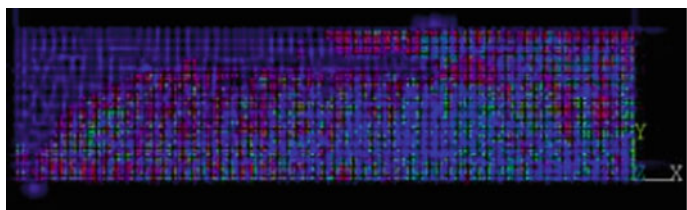


Fig. 16 Crack pattern of GFRP (parallel sides)

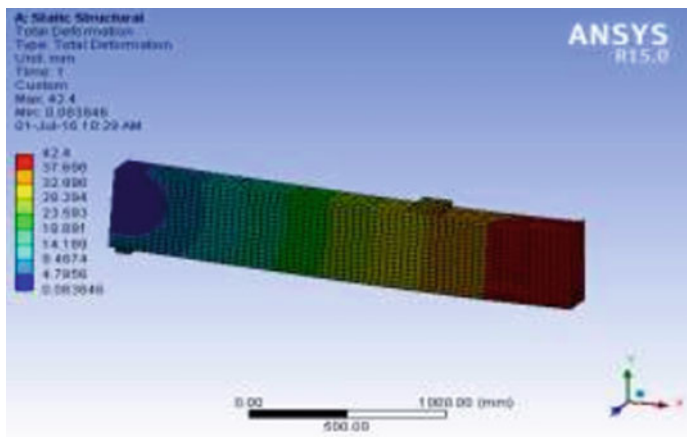


Fig. 17 Deformation shape of GFRP (bottom)

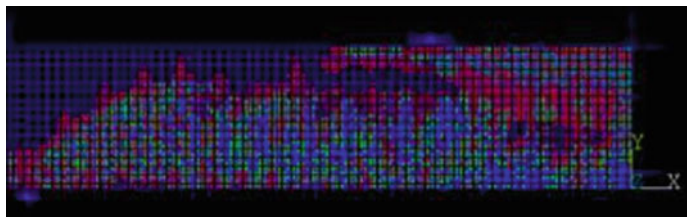


Fig. 18 Crack pattern of GFRP (bottom)

cracking loads and steel yielding loads. This crack is observed from concrete cracks and crushing plots which is within 80–110 kN.

The load-deflection graphs for the beams from control to FRP retrofitted are plotted as follows (Figs. 19, 20, 21, 22, 23, 24 and 25).

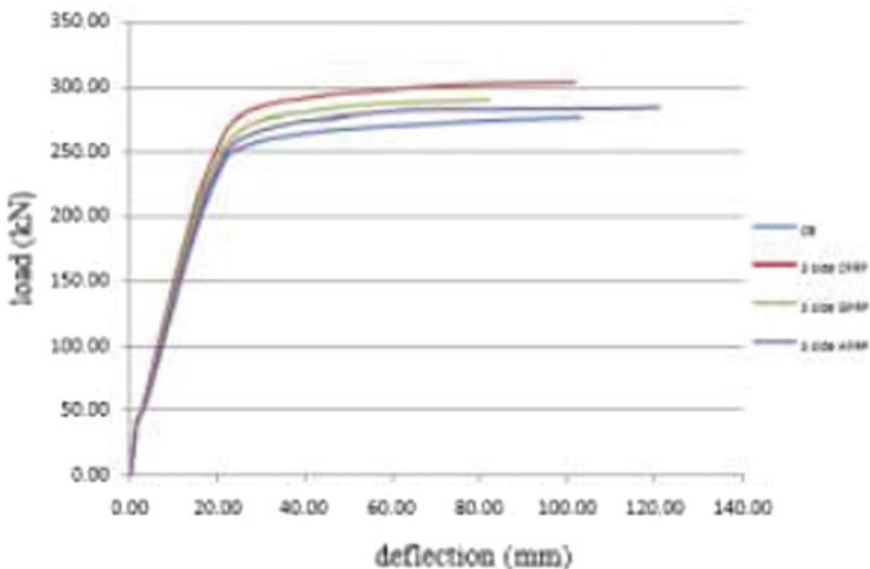


Fig. 19 Load deflection graph comparing CFRP, GFRP

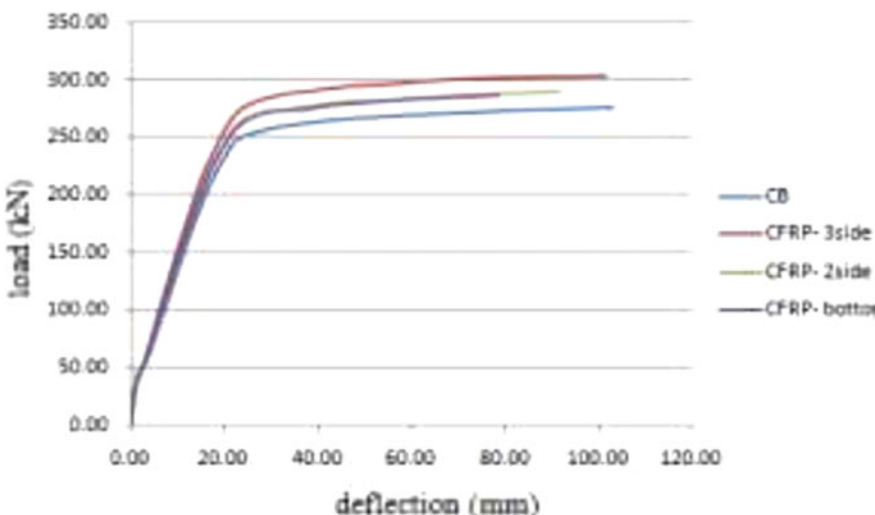


Fig. 20 Load deflection graph comparing CFRP bonded along bottom and sides, parallel sides and bottom

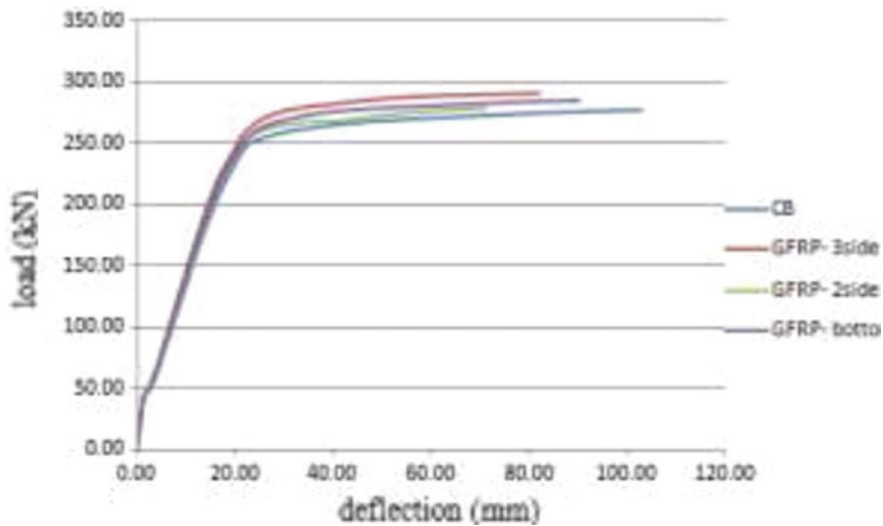


Fig. 21 Load deflection graph comparing GFRP bonded along bottom and sides, parallel sides and bottom only

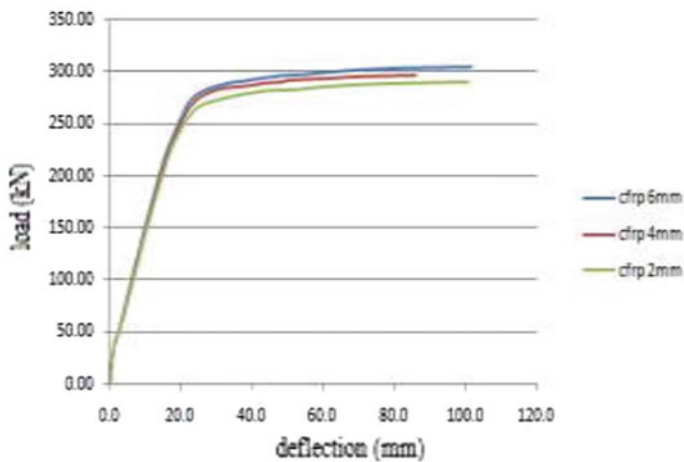


Fig. 22 Load deflection graph comparing CFRP layer of 6, 4 and 2 mm

9 Conclusions

The main objective of the project is to study the effect of CFRP and GFRP on retrofitting and to find out the best wrapping technique among the nine models of each FRP. Also, to study the effect of thickness of FRP sheet and to study the performance

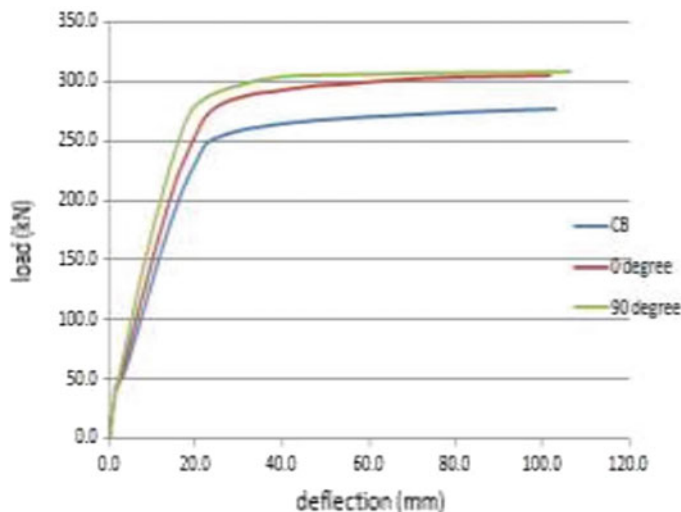


Fig. 23 Load deflection graph comparing CFRP layer with 0° and 90° fibre orientation

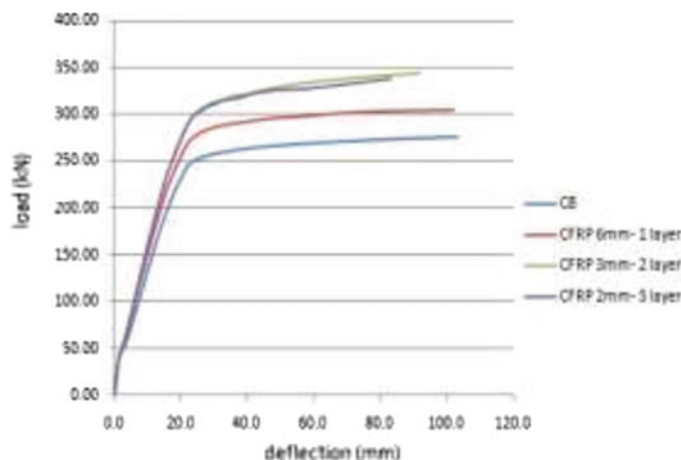


Fig. 24 Load deflection graph comparing CFRP with different layers

of the beam when FRP provide in layers. Also to check the combination of CFRP and GFRP over a single beam.

From the results of the present study, the following conclusions were made:

- RC beam retrofitted with FRP has more load carrying capacity than control beam.
- When RC beam is wrapped with carbon fiber reinforced polymer (CFRP), load carrying capacity is increased by 10%.
- When warped with GFRP load carrying capacity is increased by 5%.

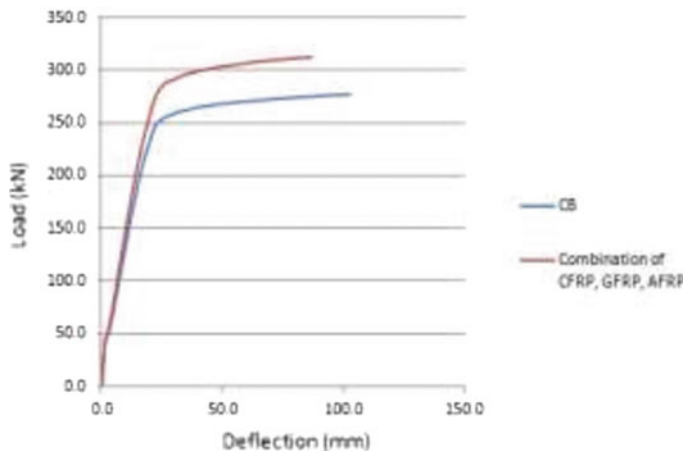


Fig. 25 Load deflection graph showing combination of CFRP and GFRP

Table 5 Results

Specimen	FRP layer thickness (mm)	Angle of fiber orientation ($^{\circ}$)	Load at failure (kN)	Deflection at failure (mm)
Control beam	6	0	276.46	102.97
CFRP (sides and bottom)	6	0	304.10	101.73
CFRP (parallel sides)	6	0	290.44	91.72
CFRP (bottom)	6	0	286.24	78.71
GFRP (sides and bottom)	6	0	290.44	82.17
GFRP (parallel sides)	6	0	278.88	71.30
GFRP (bottom)	6	0	284.12	90.10
CFRP (sides and bottom)	4	0	296.76	85.95
CFRP (sides and bottom)	2	0	290.42	100.83
CFRP (sides and bottom)	6	90	308.36	106.55
CFRP (sides and bottom)	2 layers of 3 mm	0	343.90	91.96
CFRP (sides and bottom)	3 layers of 2 mm	0	338.54	82.86
CFRP, GFRP (sides and bottom)	3 layers of 2 mm	0	312.52	86.67

- CFRP with 6 mm thickness takes maximum load.
- FRP layer with 90° fibre orientation is more superior. Its load carrying capacity is increase by 11.54%.
- If the overall thickness of FRP provided in different layers, the load carrying capacity can be increased by about 22–25%.
- The combination of CFRP and GFRP warped along a beam increases the load carrying capacity by 13% but it is less than the increment when CFRP provided in layers.
- Crack width and crack propagation get reduced for strengthen beam.
- It can be concluded that the strength of the RC beam is increased by retrofitting with fiber reinforced polymers.

Reference

1. Saifullah I (2011) Nonlinear analysis of RC beam for different shear reinforcement patterns by finite element analysis. Int J Civ Environ Eng IJCEE-IJENS 11(01)

Nonlinear Inelastic Analysis for Steel Frames



**Phu-Cuong Nguyen, Tran-Trung Nguyen, Qui X. Lieu, Thanh-Tuan Tran,
Phong Thanh Nguyen, and Trong-Nghia Nguyen**

1 Introduction

In the steel framed structural analysis, there are two common methods: plastic hinge (PH) and distributed plasticity (DP). For the PH method [7, 10–12], two plastic hinges are assumed to be appeared only at two ends of beam-column members when the yielding criteria obtains. This method is simple and efficient in the computational time but in some cases the accuracy is not satisfy. Otherwise, the distributed plasticity [1, 3, 5, 6, 8, 9] can be obtained the higher accuracy depending on beam-column methods, shell element methods, or solid element methods. This method can consider directly initial residual stresses and yielding along the member length. An advanced analysis at least must consider geometric nonlinearity and yielding of materials, besides residual stresses, geometric imperfections, panel zones, etc., should be taken into accounting. Nowadays, the powerful development of computer technology and science permits that big data problems can be solved in a short time so that the safety of buildings is more concerned by structural design engineers.

In this work, the authors employ SF established on the beam-column finite element method for developing two plastic hinge and plastic fiber methods for nonlinear analysis of 3D frames. This paper presents briefly the procedures and algorithms

P.-C. Nguyen (✉) · P. T. Nguyen · T.-N. Nguyen
Faculty of Civil Engineering, Ho Chi Minh City Open University, Ho Chi Minh City, Vietnam
e-mail: cuong.pn@ou.edu.vn; henycuong@gmail.com

T.-T. Nguyen
Faculty of Architecture, Van Lang University, Ho Chi Minh City, Vietnam

Q. X. Lieu
Faculty of Civil Engineering, Ho Chi Minh City University of Technology, Vietnam National University Ho Chi Minh City (VNU-HCM), Ho Chi Minh City, Vietnam

T.-T. Tran
Department of Civil Engineering, Kunsan National University, Gunsan, Republic of Korea
Faculty of Technology and Technique, Quy Nhon University, Qui Nhon, Vietnam

developed successfully by Nguyen et al. [5, 7, 8, 11]. A nonlinear analysis package is created for estimating strength and behavior of 3-D steel structural frames under static loadings and seismic excitations. The software might be utilized in practical engineering analysis and design problems in Vietnam and all over the world. This software is suitable for solving framed structures in more efficiency than commercial software such as ABAQUS, ANSYS, etc.

2 Nonlinear Inelastic Beam-Column Formula

2.1 Plastic Hinge Approach (PHA)

For capturing the effects of axial force on bending moments, SFs are utilized aim to optimize models and analysis time [4, 7]. One element is only utilized for tracing the $P - \delta$ phenomena correctly.

It is assumed that the plastic hinges only appear at element ends. The gradual plasticity of plastic hinges due to bending effects and residual stress is defined to be the material nonlinearity. The plasticity since residual stress is considered by adopting the CRC tangent elastic modulus and the gradually yielding due to bending is captured by a curve function [7, 10]. For more information, the readers should read the cited sources. In several problems, the plastic hinge method can capture accurately the static and dynamic behaviour of steel frames. However, when the axial force is large, yielding along members occurs, the plastic hinge approach do not predict accurately more. In these cases, we should use the plastic fiber approach.

2.2 Plastic Fiber Approach (PFA)

For monitoring distributed plasticity on the beam-column member length, a fibre approach is developed from Nguyen's work [5, 8]. Fibre beam-column members are meshed into several watched sub-sections through some integration monitoring points along the length. Watching sub-sections are divided into several small fibres as shown in Fig. 1. Using hot-rolled structural steel, initially residual stress value is assigned to steel fibers as pre-stresses. To get more knowledge, researchers should read cited sources.

3 Static and Dynamic Nonlinear Solutions

For static problems, the GDC algorithm invented by Yang and Shieh [13] prove to be the best effective and robust algorithm for solving nonlinear equations considering

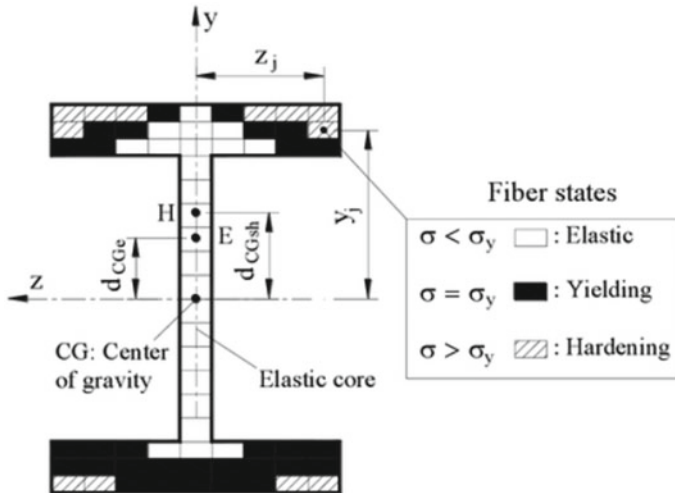


Fig. 1 Meshing of element cross-section and fiber states

static problems of framed structures with multiple snap-back and snap-through points because of the method's efficiency and numerical stability. In this software, the GDC algorithm is developed for solving static problems of steel framed structures.

For dynamic problems, an algorithm using combination of the Newmark method [2] and the Newton-Raphson balance scheme is employed aim for solving equilibrium equations of steel framed structures [4, 10] because the Newmark method family possesses second-order accuracy and unconditional numerical stability.

4 Verification

Based on the proposed formulations and algorithms, a second-order inelastic analysis software is developed. The pre- and post-procedures are developed using language C++, while the solver is written in FORTRAN language. Procedure of the proposed package includes three stage as shown in Fig. 2: pre-procedure, solver and post-procedure. The proposed software can simulate both nonlinear static and dynamic behavior of 3D steel frames by using one element per member.

The Orbison six-story 3D steel frame with rigid connecting joints was firstly analyzed by Orbison [12] as illustrated in Fig. 3. Shear modulus G , Poisson's ratio, elastic modulus E , and yield stress of steel member are 79,293 MPa, 0.3, 206,850 MPa, and 250 MPa, respectively. Uniform distributed loads on floor (9.6 kN/m^2) is transferred into forces put at column top nodes. Wind loads (53.376 kN) are put at every column tops in the Y-direction. For the PFA, one framed element using ten integration points on the beam-column element is employed to analyze the 3D steel frame. The cross-sections of all beam and column members are divided into 86 fibres (30 fibres

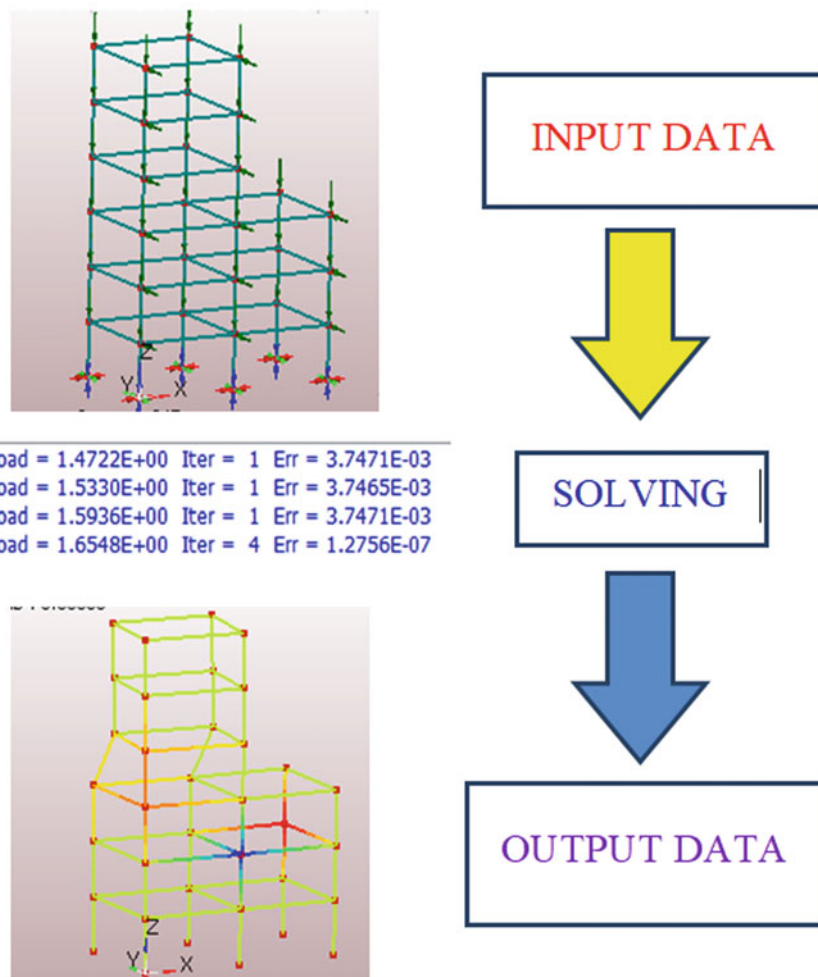


Fig. 2 Analysis procedures of developing software

at two flanges, 26 fibres at the web). Figure 4 presents the load–displacement curve at Y-direction A-node of the frame traced by the proposed procedure using both the PHA and the PFA, and comparing with Chiorean’s result [1] employing a distributed approach. The structural ultimate strength predicted using the plastic hinge approach is larger than the one using the plastic fiber approach, however, it is nearly identical to Chiorean’s result. In this study, the plastic hinge method is enough to predict correctly the ultimate load of the structures. Figure 4 presents form of plastic hinges when the frame is collapsed using the PHA. Plastic hinges appear mainly at the ends of columns. In addition, using the computer configuration including Core i7-7500U @ 2.70 GHz (4 CPUs) and 16 Gb Ram, the computational time using the PHA is

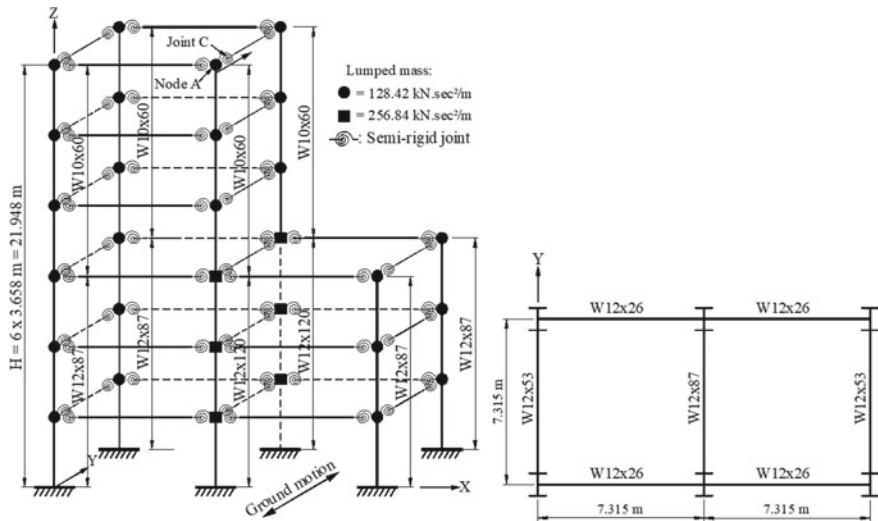


Fig. 3 Orbison six-story 3D steel frame

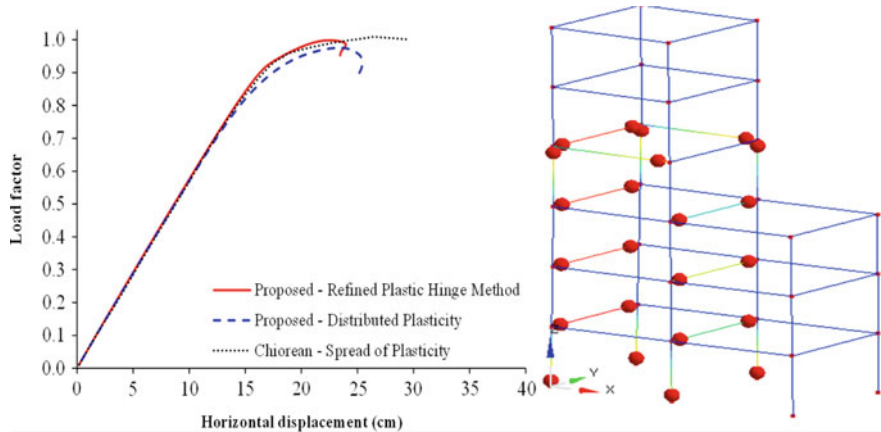


Fig. 4 Force–displacement relationship at Y-direction A-node and formation of plastic hinges when the frame is collapsed

1.86 s while using the PFA is 165.46 s. It can be concluded that the PHA is more computational effective than the PFA in engineering design.

The above-mentioned steel 3D frame using flexible connection joints from beam to column is drawn in Fig. 3. This example investigates second-order inelastic dynamic behavior for structural members under the San Fernando earthquake, its earthquake data can be found in [7, 8]. Some parameters of the Kishi-Chen curve for beam-to-column flexible connections estimated by [1] can be found in [7, 8]. Lumped masses ($128.42, 256.84 \text{ kN sec}^2/\text{m}$) are assigned at the top of columns due to floor

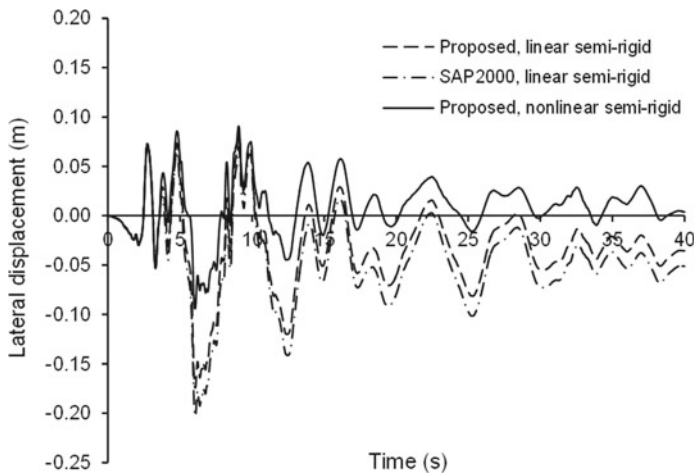


Fig. 5 Second-order inelastic displacement curves of the frame under San Fernando earthquake

loads, and they are put at the frame joints as shown in Fig. 3. Considering dynamic analysis, Rayleigh damping using a damping ratio (0.05) is adopted. Figure 5 shows the displacement curves at the A-node position utilizing the linear and nonlinear flexible joints. The proposed software uses the plastic fiber approach considering effects of initial ECCS residual stress [3, 6, 9], while SAP2000 uses the lumped plasticity approach. The developing software is better than SAP2000 software because this may predict the behaviour for steel framed structures under plasticity, residual stresses, and flexible joints are considered simultaneously. Finally, the developing software is correct and reliable in estimating the nonlinear behaviour of flexible-joint steel frames.

5 Conclusion

The objective of the manuscript shows briefly inelastic analysis procedures for space steel frames under static and seismic forces. A nonlinear analysis software utilizing the proposed procedures is developed for steel framed structural analysis and design. As a result, the proposed study proves the accuracy and the computational efficiency of the present software in estimating the second-order inelastic static and dynamic behaviour for steel framed structures. We can concluded that the present study prove that this software is reliable and valuable for designing of steel frames. In the future, this advanced analysis software will be developed for steel-concrete structures and truss structures.

Acknowledgements The authors gratefully acknowledge the financial support granted by the Scientific Research Fund of the Ministry of Education and Training (MOET), Vietnam. (No. B2019–MBS–01). The authors would also like to thank colleagues at Ho Chi Minh City Open University for supporting this project.

References

1. Chiorean CG (2009) A computer method for nonlinear inelastic analysis of 3D semi-rigid steel frameworks. *Eng Struct* 31(12):3016–3033
2. Newmark NM (1959) A method of computation for structural dynamic. *J Eng Mech Div-ASCE* 85(7):67–94
3. Nguyen P-C, Doan NTN, Kim S-E (2014) Nonlinear inelastic response history analysis of steel frame structures using plastic-zone method. *Thin-Walled Struct* 85:220–233
4. Nguyen P-C, Kim S-E (2013) Nonlinear elastic dynamic analysis of space steel frames with semi-rigid connections. *J Constr Steel Res* 84:72–81
5. Nguyen P-C, Kim S-E (2014) An advanced analysis method for three-dimensional steel frames with semi-rigid connections. *Finite Elem Anal Des* 80:23–32
6. Nguyen P-C, Kim S-E (2014) Distributed plasticity approach for time-history analysis of steel frames including nonlinear connections. *J Constr Steel Res* 100:36–49
7. Nguyen P-C, Kim S-E (2014) Nonlinear inelastic time-history analysis of three-dimensional semi-rigid steel frames. *J Constr Steel Res* 101:192–206
8. Nguyen P-C, Kim S-E (2015) Second-order spread-of-plasticity approach for nonlinear time-history analysis of space semi-rigid steel frames. *Finite Elem Anal Des* 105:1–15
9. Nguyen P-C, Kim S-E (2016) Advanced analysis for planar steel frames with semi-rigid connections using plastic-zone method. *Steel Compos Struct* 21(5):1121–1144
10. Nguyen P-C, Kim S-E (2017) Investigating effects of various base restraints on the nonlinear inelastic static and seismic responses of steel frames. *Int J Non-Linear Mech* 89:151–167
11. Nguyen P-C, Kim S-E (2018) A new improved fiber plastic hinge method accounting for lateral-torsional buckling of 3D steel frames. *Thin-Walled Struct* 127:666–675
12. Orbison JG (1982) Nonlinear static analysis of three-dimensional steel frames. Retrieved from Report No. 82-6. Department of Structural Engineering
13. Yang Y-B, Shieh M-S (1990) Solution method for nonlinear problems with multiple critical points. *AIAA J* 28(12):2110–2116

Optimization of Steel Panel Damper Design for Seismic Moment Frames

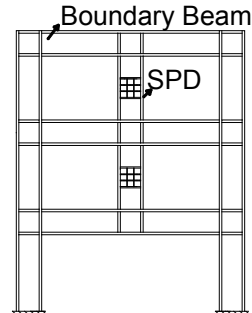


Keh-Chyuan Tsai and Chu-Hung Chang

1 Introduction

The stiffness and strength of a steel moment resisting frame (MRF) can be enhanced by incorporating steel panel dampers (SPD) into the structural design. Figure 1 schematically shows the example of an SPD-MRF. The proposed SPDs include three segments using two different steel wide-flange sections [6]. During service-level earthquakes (SLE), the entire SPD should remain elastic. Under a design-basis earthquake (DBE) or maximum considered earthquake (MCE), the top and bottom two segments, which use the same cross-sectional properties are designed to remain elastic while the middle segment can undergo large inelastic deformations. In this study, the middle segment is defined as an inelastic core (IC), while the top and bottom segments are called the elastic joints (EJ). In order to sustain a large deformation and delay shear buckling of the IC web, properly detailed stiffeners must be attached to the web and flanges of the IC. Recently, the tests of full scale SPDs,

Fig. 1 Schematic of the SPD-MRF



K.-C. Tsai (✉) · C.-H. Chang

Civil Engineering, National Taiwan University, Taipei, Taiwan

e-mail: kctsai@ntu.edu.tw

capacity design method (CDM) of the SPDs and the boundary beams, and the analysis procedures of the SPD-MRF were investigated [6]. The seismic performance of the proposed SPDs has also been tested using substructure pseudo-dynamic testing procedures [7]. Test results confirmed the effectiveness of the recommendations on the IC stiffeners made by others [3]. The analytical procedures for constructing an equivalent one-element model to substitute for the SPD's three-element model were also established. The proposed method for constructing the equivalent element model was confirmed effective.

The stiffness and strength of the proposed SPD can be decoupled. It was demonstrated that both the elastic and inelastic stiffness of the proposed SPD can be significantly enhanced by reducing the IC height or increasing the EJ web thickness without altering the SPD yield strength or the boundary beam strength requirements. The designer could apply the above method to increase the overall SPD-MRF elastic and post-elastic stiffness after the MRF member sizes and the design strength of the SPDs are determined. After the boundary beams are determined and meeting the proposed capacity design requirements, the flexural strength and the inherent stiffness of the selected boundary beams should be viewed as the minima. The SPD's strength can be determined by the shear area and the shear yield stress of the IC web. Thus, the SPD-MRF elastic stiffness can be enhanced by a number of approaches without an obvious change of the SPD strength. These include increasing the boundary beam stiffness, or the SPD flange thickness, or the EJ web thickness or height. In this study, the efficient design procedures and results of maximizing the combined SPD and boundary beam stiffness, while minimizing the total steel weight and meeting all the seismic design requirements are investigated [8] (Fig. 2).

Considering that SPDs may not be accepted into every span of a typical MRF, only the deformation characteristics of the cruciform subassembly (CS) as shown in Fig. 3 is critically analyzed using the theory of structures and finite element models. The

Fig. 2 Schematic of the steel panel damper (SPD)

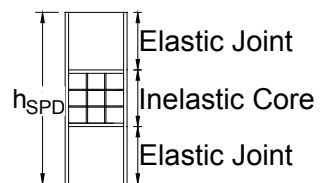
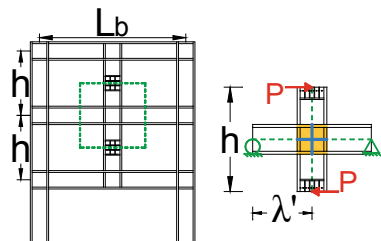


Fig. 3 Schematic of the SPDs and boundary beam cruciform subassembly (CS)



determinations of the locations and the total number of SPDs, the designs of typical beams and columns in the SPD-MRF are not the scope of this study. A typical CS can be determined from the SPD-MRF at the inflection points in the two neighboring SPDs and the common boundary beam. It is assumed that the two neighboring SPDs are identical. Given a specified SPD shear strength, the analysis methods and the efficient proportions of the SPDs, the IC stiffeners, the panel zone and the boundary beam to meet the requirements of capacity design, less weight and high stiffness are investigated in this study.

2 Three-Segment Steel Panel Dampers (SPDs)

2.1 *SPD Design, Construction and Properties*

As shown Figs. 1 and 2, the proposed three-segment SPD consists of one middle IC and two end EJs using wide flange sections. The two flanges of the proposed three-segment SPD are continuous throughout the full height. The web of the IC is either thinner or weaker than that of the EJ. The top and bottom EJs are to be welded to the top and bottom boundary beams' flanges. The entire SPD is designed to remain elastic for SLEs. During DBEs and MCEs, the IC in the SPD is expected to sustain moderate to very large inelastic shear deformations while the two EJs are proportioned to remain essentially elastic. This suggests that the strength and stiffness of an SPD could be decoupled. The lateral strength would be limited by the shear strength of the IC section while the lateral stiffness of the entire SPD could be enhanced by properly stiffening the EJ sections or reducing the IC's height. Nevertheless, the web buckling-delaying stiffeners (Fig. 4) must be detailed for the IC, and the capacity design principle must be applied for the EJ sections and the boundary beams, in order to achieve the aforementioned design objectives. Assuming the axial load in the SPD is insignificant, the nominal lateral strength of the SPD can be determined from the shear area, $A_{v,IC}$, and shear yield stress τ_y of the IC web given below:

$$V_y = A_{v,IC} \tau_y = 0.6 F_y d_{SPD} t_{w,IC} \quad (1)$$

where F_y is nominal tensile yield stress of IC web, d_{SPD} is the SPD depth, $t_{w,IC}$ is the IC web thickness. The maximum shear V_{max} that may develop in the IC considers

Fig. 4 Stiffeners in the inelastic core

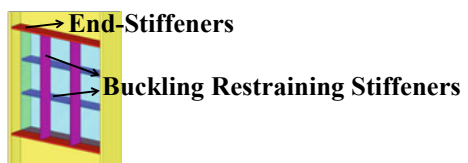
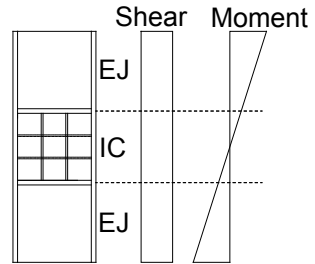


Fig. 5 Forces in the SPD

the material over-strength (R_y), and the strain-hardening factor (ω) of the IC web steel given below:

$$V_{\max} = \omega R_y V_y \quad (2)$$

Thus, based on Figs. 2 and 5, the lateral effective stiffness [6] of the SPD includes the bending and shear effects expressed in the equivalent one-element model is:

$$K_{eff} = \frac{1}{\frac{h_{SPD}}{GA_{v,eff}} + \frac{h_{SPD}^3}{12EI_{eff}}} = \frac{1}{\frac{h_{SPD}}{GQ_v A_{v,IC}} + \frac{h_{SPD}^3}{12EQ_m I_{IC}}} \quad (3)$$

where $A_{v,IC}$, $A_{v,EJ}$, and $A_{v,eff}$ are the shear areas of the IC, the EJ, and the equivalent element, respectively, and h_{SPD} is the full height of the SPD. The I_{IC} , I_{EJ} , and I_{eff} are the moments of inertia of the IC, the EJ, and the equivalent element, respectively. Effective factors, Q_v and Q_m , depend on the IC-to-SPD height ratio α and the EJ-to-IC cross-sectional property ratios.

2.2 Cruciform Subassembly of the SPDs, Boundary Beam and the Panel Zone

As noted above, the deformation characteristics of the cruciform subassembly (CS) as shown in Fig. 3 must be critically analysed in order to achieve the cost effectiveness of the SPD and the boundary beam pairs. A typical CS is determined from the SPD-MRF using the inflection points in the two neighboring SPDs and the shared boundary beam as shown in Figs. 3, 6 and 7. The CS is supported by a hinge and a roller as illustrated in Figs. 3 and 7. Assuming the two neighboring SPDs are identical and applying the SPD shears as shown on Fig. 7, the elastic deformation contributions of the SPDs, the panel zone and the boundary beam are evaluated separately before adding together [8]. Thus, under a specified SPD shear strength, optimizations on the proportions of the SPDs and the boundary beam to meet all capacity or stability design requirements, and to achieve a high stiffness of the CS can be performed.

Fig. 6 Moment diagram in the boundary beam

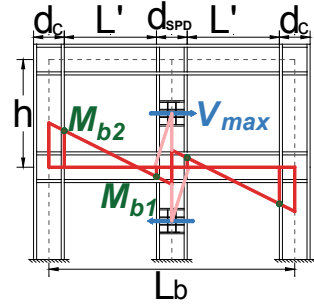


Fig. 7 Schematic of deformation components in the cruciform subassembly

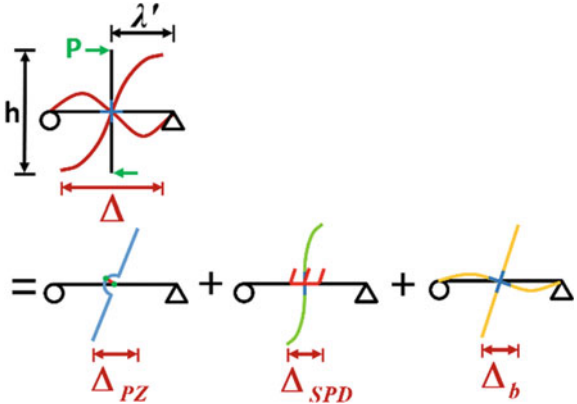


Figure 6 shows the boundary beam moment diagram with the gravity load neglected and the SPDs develop the peak shear strength. As shown in Figs. 3 and 7, the distance between each of the two beam inflection points to the center of panel zone is λ' . The L' is the distance between the SPD and column faces, h is the story height, M_{b1} and M_{b2} are the beam moments at a section at the SPD and column faces, respectively. It is assumed that flexural hinges formed at the boundary beam to column connections and the strain hardening of the SPD and the boundary beam has started but not fully developed yet by using a strain hardening factor $\omega = 1.1$.

As shown in Fig. 7, the total elastic lateral displacement under the SPD shear forces P at the mid-height of the top and bottom SPDs in the CS is contributed from the panel zone, the SPDs and the shared beam, three components as given below:

$$\Delta_t = \Delta_{PZ} + \Delta_{SPD} + \Delta_b \\ = P \left\{ \frac{h \left[(h - d_b) - \frac{d_{SPD} h}{2\lambda'} \right]}{d_b d_{SPD} t_{PZ} G} + \left[\frac{(h - d_b)^3}{12 E I_{eff}} + \frac{(h - d_b)}{G A_{v,eff}} \right] + \left[\frac{h^2 (\lambda' - \frac{d_{SPD}}{2})^3}{6 E I_b \lambda'^2} + \frac{h^2 (\lambda' - \frac{d_{SPD}}{2})}{2 G A_{v,b} \lambda'^2} \right] \right\} \quad (4)$$

where t_{PZ} is panel zone thickness including all web doubler plates, d_b is the boundary beam depth, h is the story height or the distance between the center of the top and

bottom SPDs. 1. Using the Abaqus shell-element model analyses, the accuracy of using Eq. 4 to estimate the lateral displacements of the SPDs-to-beam cruciform-subassembly is found very satisfactory [8].

3 Efficient Design of the SPDs and the Boundary Beam

3.1 Seismic Performance and Cost-Effectiveness

Under the combined load effects including the seismic forces, the shear in the SPD should be no greater than 90% of the nominal shear yield strength defined in Eq. 1 when the LRFD [1, 2] procedures are followed for the SPD-MRF design. In fact, under the aforementioned load effects, the closer of SPD demand-capacity ratio (DCR) to 1.0, the better the economy of the SPD-MRF design. This is because the boundary beams supporting the SPDs must be designed considering the possible maximum strength of the SPDs. Clearly, following the capacity design principle, over-conservatively design the SPDs in terms of strength will increase the strength requirements of the boundary beams and the columns connected to these beams. Opportunely, the strength and the stiffness of the proposed three-segment SPD can be decoupled. That is, given a specified SPD strength, the lateral stiffness of the SPD can be increased by shortening the IC length ratio, increasing the flange or the EJ web thickness [6]. Naturally, proportioning the boundary beams or the boundary beam-to-SPD panel zone doubler plates stronger than those only meeting the capacity design requirements is likely to enhance the lateral stiffness of the SPD-MRF and promote the energy dissipation in the SPDs during strong earthquakes. Therefore, there must be a balanced proportioning among the SPDs, the shared boundary beams and the panel zones in order to achieve an efficient and cost-effective design. The target SPD-MRF design must meet all the capacity and stability design requirements. The target should also achieve a minimized weight and a maximized lateral stiffness. The capacity design procedures of the SPD, the panel zone and the boundary beams have been documented [6]. The determinations of the locations and the total number of SPDs, the designs of typical beams and columns in the SPD-MRF are not the scope of this study. Instead, this study investigates the procedures and the results of optimizing the proportions among the two identical SPDs of a specific strength, the shared boundary beam and the panel zone as illustrated in the CS given in Fig. 3.

3.2 Design Variables, Objective Functions, Constraints and Algorithms in the Optimization Models

In addition to the strength requirements, the detailed dimensions of the SPD, the IC stiffeners, and the boundary beam must meet the stability requirements to prevent

local or lateral torsional buckling suggested in the model steel building codes [1, 2]. The design variables include the thickness, height, width or depth of the IC web, stiffeners and flange, and of the EJ web in the SPD, the sectional dimensions of the shared beam, the thickness of the doubler plate of the panel zone. In the optimization models, the objective function is the minimum total weight, including the weights of the two one-half SPDs with all stiffeners, the entire clear span of the shared beam, the panel zone doubler plates and the four continuity plates in the mid-span aligning the SPD flanges.

The constraints in the optimization models include the strength requirements of the EJs in the SPDs, the shared beam and the panel zone to prevent yielding occurred except in the two beam-to-column moment connections when the V_{max} defined in Eq. 2 is developed. The stability requirements consider various width-to-thickness ratio limits on the IC's stiffeners and the EJs' and on the shared beam's flange and web. The boundary beam out-of-plane lateral support is assumed at the SPD location. Additional lateral supports are spaced about 2–3 m as those in the practical building design, following the model seismic provisions for special MRF (AISC 341-16). The unbraced length limits are applied on both the SPD and the boundary beam as the required constraints. In order to avoid an excessive deformational demand on the IC of the SPD, the minimum IC height-to-SPD height ratio α is constrained to no less than 0.3. The SPD flange width must be no greater than the shared beam flange width for constructability. The width of the stiffeners at the ends of the IC is assumed no smaller than one-half of the SPD flange width.

The optimization models in the MATLAB Toolbox [5] are utilized so that all the fifteen variables can be conveniently incorporated into the evaluations of the weight. The MATLAB optimization toolbox combining the simulated annealing algorithm [4] with the gradient-descent method was adopted to find the minimum steel weight design.

4 Design Examples

In this study, it is assumed that the typical story height $h = 3.6$ m, the SPD shear yield strengths range from 600 to 1500 kN, beam spans range from 8 to 12 m. All steel is assumed SN490B except the IC web is SN400B. A total of 95 cases are investigated [8]. Considering the minimum weight as the objective function and all the aforementioned constraints, the resulting design for each case is identified as the Basic design. The lateral deflection (Eq. 4), or the elastic lateral stiffness of the associated cruciform-subassembly (CS) of the Basic design is then evaluated as the two SPDs reach the yield strength V_y . This study further apply an additional constraint of increasing the aforementioned elastic stiffness of the Basic design, by 50% as the example. The resulting minimum weight design for such stiffness-enhanced design is identified as $1.5 \times K$ design. All the tasks described above were performed using the MATLAB in a desktop PC with a CPU of Intel Core i7-2600 (3.4 GHz) and

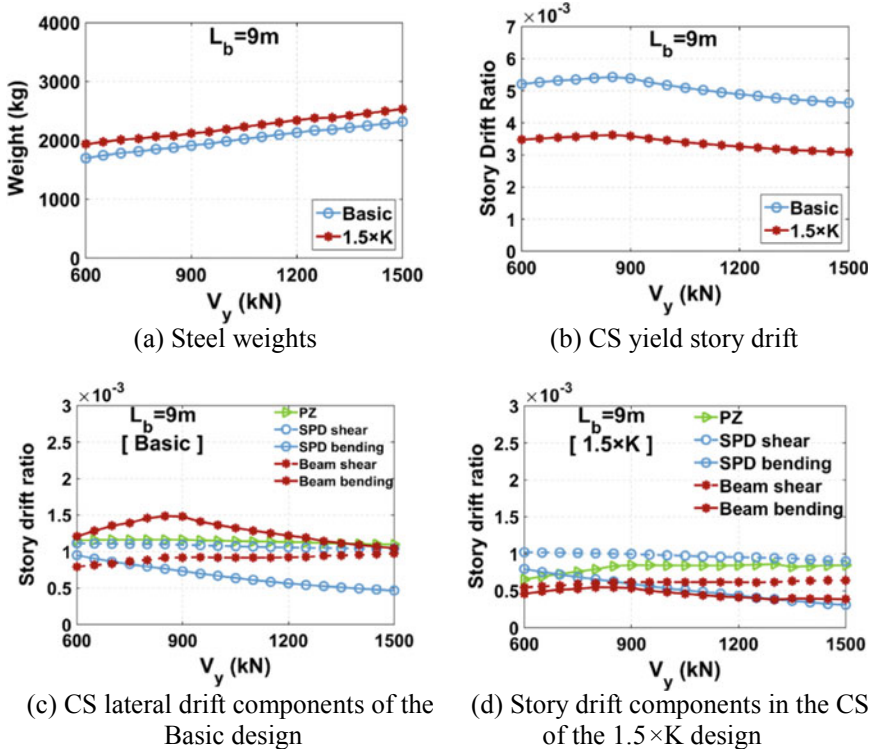


Fig. 8 The optimized design results for the case of 9 m beam span

20 GB of RAM. It took about 60 s to finish each Basic or $1.5 \times K$ design. Some typical results from using the 9 m beam span case are given in Fig. 8.

Figure 8a clearly shows that the total steel weight increase is only about 20% for the SPD strength to increase by 150% from 600 to 1500 kN. Figure 8a also shows that the penalty on the weight to go from the Basic to the $1.5 \times K$ designs is not significant at all for all the listed SPDs of different yield strengths. Figure 8b confirms that the story drifts among the Basic and the $1.5 \times K$ designs are 50% more. Figure 8c shows the contributions of the two SPDs and the panel zone on the CS deformations are similar for various SPD strengths. Figure 8a, d indicate that the $1.5 \times K$ designs of the CSs can be cost-effectively achieved by bringing down the beam shear and bending deformations.

While the $1.5 \times K$ designs only increase the total weight slightly, it is found that the boundary beam depth and the corresponding flexural strength would increase significantly. These could reduce the architectural functions and violate the strong column weak beam design requirements in the SMRF. Results of applying additional constraints to limit the beam depth and flexural strength growth have been documented [8].

5 Conclusions

1. Applying the proposed optimization procedures and the constraints, the minimum weight designs can be effectively achieved for the SPDs and boundary beam pairs meeting the capacity and stability design requirements.
2. Considering five different beam spans, nineteen different SPD yield strengths, results of a total of ninety five optimized SPD and boundary beam designs are provided. The methods and the results can be conveniently adopted in the preliminary designs of the SPDs and boundary beams in the SPD-MRF.
3. While complying with all constraints, the steel weight is increased only by about 9% to achieve a 50% more stiffened design. The stiffness of the subassemblies is found enhanced most effectively by increasing the boundary beam depths and web thicknesses.

Acknowledgements The grant from Taiwan Ministry of Science and Technology (MOST 107-2625-M-002-017-MY3) and National Taiwan University (Grant No. 107L892510) are gratefully acknowledged.

References

1. AISC 341-16, American Institute of Steel Construction (2016) Seismic provisions for structural buildings
2. AISC 360-16, American Institute of Steel Construction (2016) Specification for structural steel buildings
3. Chen Z, Ge H, Usami T (2006) Hysteretic model of stiffened shear panel dampers. *J Struct Eng ASCE* 132:478–483
4. Kirkpatrick S, Gelatt CD Jr, Vecchi MP (1983) Optimization by Simulated Annealing. *Science* 220(4598):671–680
5. Mathworks (2014) MathWorks announces release 2014a of the MATLAB and Simulink product families
6. Tsai KC, Hsu CH, Li CH, Chin PY (2018) Experimental and analytical investigations of steel panel dampers for seismic applications in steel moment frames. *Earthquake Eng Struct Dyn* 47(6):1416–1439. <https://doi.org/10.1002/eqe.3023>
7. Wang KJ, Chuang MC, Tsai KC, Li CH, Chin PY, Chueh SY (2018) Hybrid testing with model updating on steel panel damper substructures using a multi-axial testing system. *Earthquake Eng Struct Dyn* 48:347–365. <https://doi.org/10.1002/eqe.3139>
8. Tsai KC, Chang CH (2019) Seismic design of steel panel dampers and boundary beams to achieve performance and cost-effectiveness. *Earthquake Eng Struct Dyn* (in review)

Relationship Between the Intensity and Young's Module of Concrete Over Time



Phuc Binh An Nguyen, Quang Thai Bui, and Thanh Dung Ho

1 Introduction

In order to determine the deformation of reinforced concrete structures (RC), post-tensioned structures or design measures for construction work beams, the value of the Young's module E is the necessary parameters to be determined. The Young's phase analysis of the structure system will be done accurately by selecting an appropriate value E, through parameter E can help determine the intensity or displacement of the structure system to be analyzed.

There are many approaches to value the Young's module E of concrete. However, at present, most of them still rely on the determination of Young's module E according to the table of reference from TCVN standard or testing formulas of foreign standards. However, in general, the threshold of the defined value lies in the fairly great deviation from the margin, along with the determination of the Young's module E over development duration of concrete can be found in very few documents and standards.

In this study, Using determining the Young's module E method according to ASTM C 469-02: "Testing method for determining static Young's module", (details of testing method determining Young's module E according to ASTM C 469-02 will be presented in detail in the next section). To determine the value of Young's module E and concrete intensity of more than 336 samples. Eliminating of the error samples according to the theory of statistical method, the remaining samples will be used to evaluate for the development of E Young's module of concrete over time (E-T relationship) from 1 to 7 days old and from 7 to 28 days old.

The approach to find the testing formula for determining the E-module over time will be established based on the correlation between the module E and the average

P. B. A. Nguyen · Q. T. Bui · T. D. Ho (✉)
Ricons Construction Investment JSC, Ho Chi Minh City, Vietnam
e-mail: dung.hothanh@ricons.vn

concrete compressive intensity according to the development time (relationship of E-f'c according to the age of concrete development. Establishing an testing relationship is essential for the practicality of the research content.

2 Testing Tools and Methods

The testing of Young's module E will be determined with each sample set of 4 sheets corresponding to each type of age date. In which 1 sheet is for destructive compression to determine the force threshold for the other samples to be still in Young's working. Based on that, the remaining 3 samples are compressed to determine the E Young's module.

Prepare a sample set of 4 prism concrete samples with the same intensity of concrete, diameter of 150 mm and height of 300 mm. Use 1 sample to compress for the intensity test and the remaining 3 samples to determine the Young's module. The modeling, casting, curing of concrete, concrete model cutting and drilling, and concrete size selection to test prism intensity and Young's module are carried out according to TCVN 3105-1993. The upper and lower surfaces of the cylinder sample shall be perpendicular to the sample axis with a tolerant $\pm 0.5^\circ$; roughness not exceeding 0.05 mm. Accurately measure the diameter and length of cylindrical samples with caliper.

Compressor: Use 3000 KN hydraulic compressor from Matest—Italia to determine intensity compression resistance of concrete according to ASTM C 469-02 (Fig. 1).

Deformation meter: using tranducer-type deformation meter to measure vertical displacement and horizontal displacement with an accuracy of 0.001 mm (Fig. 2).

Data measuring set: Using data recorder to automatically read vertical displacement and horizontal displacement geodatalog (8 channels) and a computer connecting to concrete compressors to record data continuously and accuracy.

3 Steps of Testing

1. Select the appropriate load capacity of the meter so that when compressing the maximum load value is expected to be in the range of 20–80% of the maximum load capacity.
2. Determination of prism intensity (f_{LT}): Measure the size of the compression cross section and destructive superimposed load of each sample sheet such as testing the compressive intensity of concrete before determining the Young's module.
3. Determine the Young's module (E):

Install vertical deformation and horizontal deformation meters in accordance with the standard around the cylinder (Fig. 3).



Fig. 1 Deformation frame and meter



Fig. 2 Deformation meter

Fig. 3 Distortion frame and meters



Place each sheet into the main sample center board of the compressor. Increase the load on sample at $241 \pm 34 \text{ kPa/s}$ until the test stress is reached by about 40% of the prism intensity value defined in Article 2 at least 2 cycles (the first cycle does not record data). Stress strain-deformation data is automatically recorded by the machine continuously.

Determine the compressive stress (S_1) corresponding to a relative vertical strain of 0.000050; determine the vertical deformation corresponding to the load when reaching 40% of the sample destructive load. Relative vertical deformation is determined by taking the total deformation divided by the distance between the measurement points.

4 Report Testing Results

Calculation:

1. Prism intensity (f_{LT}) of each concrete sample is calculated in daN/cm^2 , according to the formula:

$$f_{LT} = \frac{P}{F} \quad (1)$$

where as:

P—Destructive load, daN;

f—Area of compression cross section, cm².

2. Prism intensity of concrete is determined from the intensity values of the sheets in the sample set.
3. The Young's module in static compression (E) of each sample sheet is calculated in psi units according to the formula:

$$E = (S_2 - S_1) / (\varepsilon_2 - 0.000050) \quad (2)$$

where as:

S_1 —stress corresponding to 40% of ultimate load;

S_2 —stress corresponding to a longitudinal strain, '1, of 50 millionths, MPa;

ε_2 : longitudinal strain produced by stress S_2 .

Young's module of static compression of concrete is calculated from the value of the members in the sample.

5 Analysis of Testing Results

5.1 Summary Table of Testing Results

See Table 1.

5.2 Compare Testing Results with Design

Based on the comparison table that can be seen at the durability level B25, there are 5-day samples $E_{B25} = 27,126$ which have achieved nearly 90% of the design $E_{B25} = 30,000$ MPa at 28 days, and 14 days to achieve 100% compared with design. With B30 durability level, the sample of minimum 5 days $E_{B30} = 29,427$ MPa has reached 91% of the design value $E_{B30} = 32,500$ MPa and a maximum of 21 days can achieve 100% of the design. Similar to durable level B35 with $E_{B35} = 30,832$ MPa at 7 days has also reached 91% of the design $E_{B350} = 34,000$, a maximum of 28 days, the sample has reached 100% of the design.

For concrete intensity $f'c$ in durable grade B25, a minimum of 5 days it can reach 90% and up to 14 days can reach the design intensity. Similarly, B30 and B35 durable statues with a minimum of 5 days and a maximum of 28 days achieve design intensity. Thus, the Young's module E and concrete intensity $f'c$ always grow faster than the design.

Table 1 Summary table of testing results

	1,5 day			3 day			5 day			7 day		
	s1	s2	s3	s5	s6	s7	s9	s10	s11	s13	s14	s15
B25	E (MPa)	22,108	24,243	23,971	26,337	26,921	26,862	30,363	31,079	30,008	32,059	32,281
	f'c (MPa)	15.99		23.99			25.29				30.66	31,845
	E (MPa)	21,982	19,295	19,933	21,942	22,019	22,036	26,042	26,192	26,217	26,977	26,823
	f'c (MPa)	10.22		14.17			22.99				23.54	26,399
	E (MPa)	17,578	17,383	17,964	20,851	20,517	21,316	21,245	21,393	21,681	22,210	22,002
	f'c (MPa)	11.12		17.05			18.43				23.59	22,832
	E (MPa)	26,193	27,103	26,469	28,354	28,939	28,193	30,909	30,321	30,057	31,779	31,028
	f'c (MPa)	16.25		27.2			30.74				32.39	31,361
B30	E (MPa)	25,772	25,770	25,870	30,438	30,250	30,282	31,008	31,454	31,617	32,341	31,956
	f'c (MPa)	17.9		31.65			32.19				32.31	32,506
	E (MPa)	23,389	23,906	23,114	26,696	27,332	27,281	27,756	27,471	27,806	28,127	28,367
	f'c (MPa)	11.61		16.16			17.7				24.62	28,296
	E (MPa)	19,344	19,675	19,886	22,858	22,263	22,533	24,454	25,641	25,028	25,647	26,078
	f'c (MPa)	14.78		19.94			25.51				25.68	25,338
	E (MPa)	27,497	27,976	27,676	31,884	31,153	31,608	33,560	33,416	33,910	33,928	34,543
	f'c (MPa)	24.88		26.93			33.5				39.84	34,123
B35	E (MPa)	28,036	28,028	27,900	32,203	32,115	31,565	32,432	32,398	32,535	33,478	32,637
	f'c (MPa)	26.87		33.05			35.29				36.9	32,739
	E (MPa)	25,804	25,177	25,976	27,993	27,758	27,483	29,274	30,049	29,997	31,126	31,763
	f'c (MPa)	18.39		24.06			32.13				34.45	30,778

(continued)

Table 1 (continued)

	1,5 day				3 day				5 day				7 day			
	s1	s2	s3	s5	s6	s7	s9	s10	s11	s13	s14	s15				
B25	E (MPa)	23,768	22,641	23,161	26,291	26,692	26,002	26,792	26,065	26,325	27,100	27,296	28,698			
	f'c (MPa)	18.43			23.86			28.56			30.63					
	E (MPa)	25,269	25,391	25,204	27,348	27,908	28,182	29,573	28,915	29,012	31,095	31,590	31,681			
	f'c (MPa)	18.17			23.71			29.46			32.42					
	14 day				21 day				28 day							
	s17	s18	s19	s21	s22	s23	s25	s26	s27							
B30	E (MPa)	32,935	33,112	33,301	33,409	33,203	33,637	33,907	34,022	34,223						
	f'c (MPa)	30.91			33.16				34.73							
	E (MPa)	29,232	28,720	29,258	30,161	29,975	30,441	30,212	30,585	31,006						
	f'c (MPa)	30.19			30.45				30.98							
	E (MPa)	23,023	23,359	23,176	23,928	24,068	23,781	26,552	26,243	25,958						
	f'c (MPa)	26.51			26.51				27.98							
	E (MPa)	32,174	32,555	31,884	32,825	33,142	33,451	33,829	34,012	33,438						
	f'c (MPa)	32.88			33.83				36.78							
	E (MPa)	33,698	33,198	32,996	34,229	34,415	34,085	34,704	34,441	34,135						
	f'c (MPa)	37.12			39.32				38.97							
	E (MPa)	29,060	29,262	29,567	31,033	31,668	31,934	31,936	32,500	32,305						
	f'c (MPa)	25.78			25.84				29.99							
	E (MPa)	27,987	29,028	28,459	29,366	28,893	29,108	29,512	29,883	30,161						

(continued)

Table 1 (continued)

	14 day			21 day			28 day		
	s 17	s18	s19	s21	s22	s23	s25	s 26	s27
	f'c (MPa)	29.26		29.51			30.44		
	E (MPa)	34,348	34,741	34,461	34,513	34,741	34,811	35,028	35,393
	f'c (MPa)	40.76		39.84			42.7		35,817
B35	E (MPa)	34,110	33,941	34,272	34,631	34,736	34,294	34,942	35,154
	f'c (MPa)	37.81		38.97			40.76		35,053
	E (MPa)	32,438	32,351	32,158	33,882	34,142	34,035	34,415	33,869
	f'c (MPa)	37.97		44.68			43.15		34,797
	E (MPa)	28,698	29,136	29,916	30,709	30,468	29,564	31,526	32,809
	f'c (MPa)	35.21		33.5			36.26		31,885
	E (MPa)	32,648	33,054	33,588	34,143	34,743	33,866	34,799	34,627
	f'c (MPa)	38.58		40.02			40.02		34,107

5.3 Evaluate the Relationship Between Young's Module and Concrete Intensity

From the results of Table 1 we construct diagrams that show the relationship between E and $f'c$ according to different levels of durability and collectively for all three durable levels to find the general trend line and reliability of the testing results (Figs. 4, 5 and 6).

The testing analysis chart shows the relationship between E and $f'c$ of the three stable levels B25, B30 and B35 both linearly in a straight line. Equation of trend line $y = 555.7x + 13,188$ (B25), $y = 425.27x + 17,417$ (B30), $y = 416.27x + 16,960$ (B35) corresponding to values $R^2 = 0.7891$, $R^2 = 0.7984$, $R^2 = 0.8836$ has high reliability in this testing result. All the chart analyzing testing results are highly

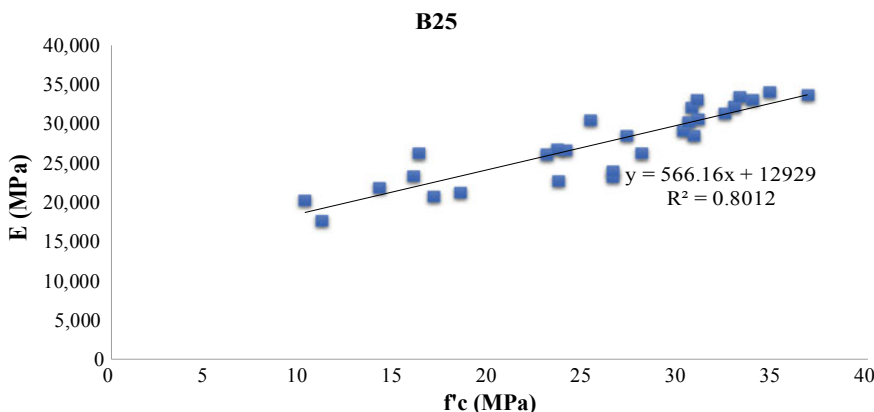


Fig. 4 Relationship between E- $f'c$ (B25)

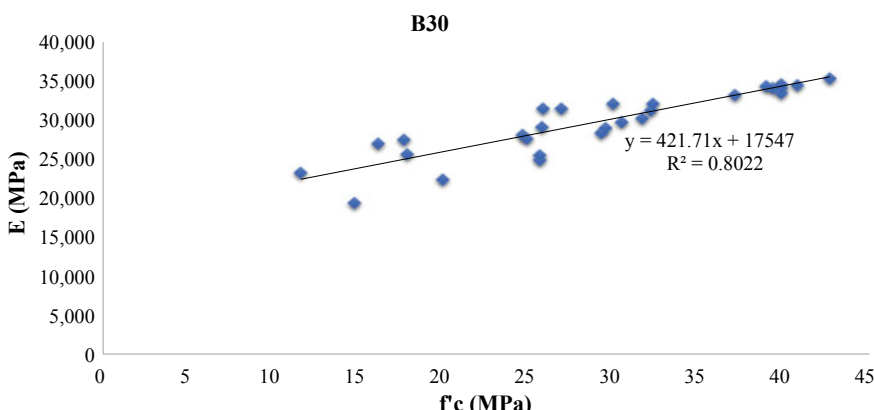


Fig. 5 The relationship between E- $f'c$ (B30)

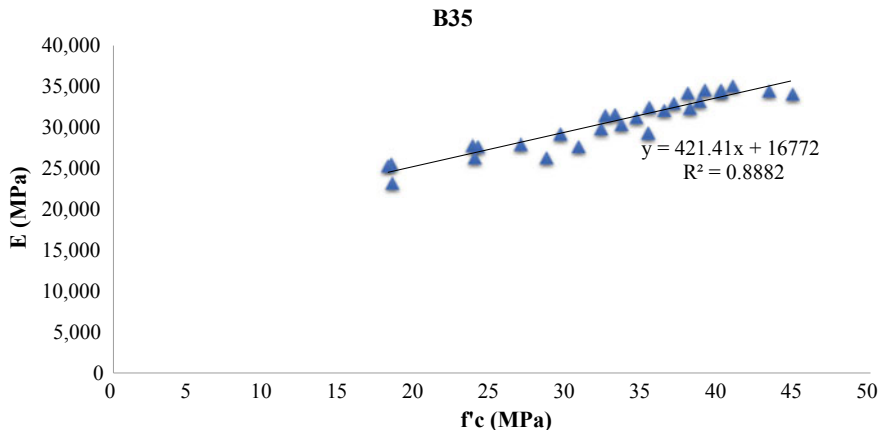


Fig. 6 The relationship between $E-f'c$ (B35)

reliable, based on the relationship E and $f'c$ we can use it to convert Young's module according to intensity $f'c$ for the concrete of intensity development over time.

The relationship between E and $f'c$ with 3 levels of stability on the same chart (Fig. 7), over time the Young's module E and $f'c$ both increase. However, the growth rate of intensity $f'c$ is faster than that of module E . During the 28-day period, E increases by 1.75 times (approximately from 20,000 MPa to 35,000 MPa) and $f'c$ increases 4 times (approximately from 10 to 40 MPa). Thus with $R^2 = 0.814$ it is possible to see highly reliable testing results to build the relationship between E and $f'c$ over time. Correlating behavior from 1.5 days to 28 days is similar and follows a defined function.

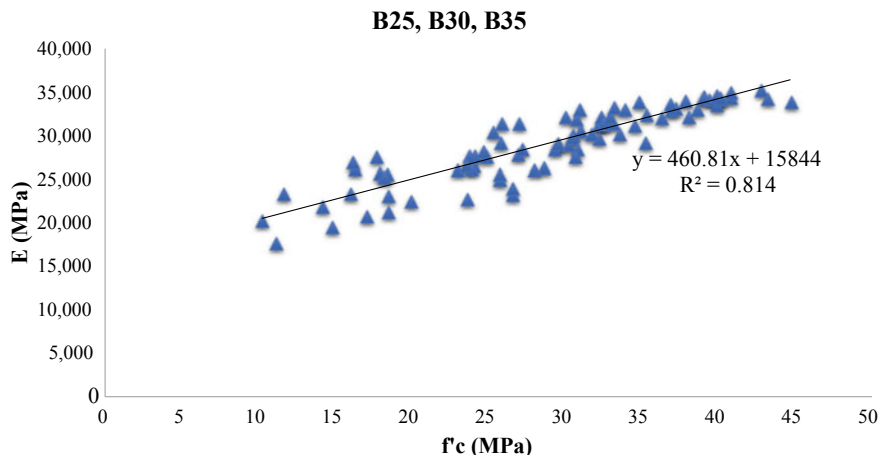


Fig. 7 The relationship between $E-f'c$

5.4 Change of Young's Module and Compressive Intensity Over Time with Respect to Each Level of Durability

Remark: For the durability level B25, B30 and B35, the Young's module (E) and compressive intensity ($f'c$) tend to increase over time. At the same time, this value increases sharply in the period from 1.5 days to 7 days, then it increases slowly and went into stable values. The curves: $E(t)$ and $f'c(t)$ all have the same logarithmic form. So between E and $f'c$ there is a certain correlation from 1.5 days to 28 days, so the formula $E = K \sqrt{f'_c}$ (ACI 318-08) can be used to reverse the rest of the timelines (Fig. 8, 9 and 10).

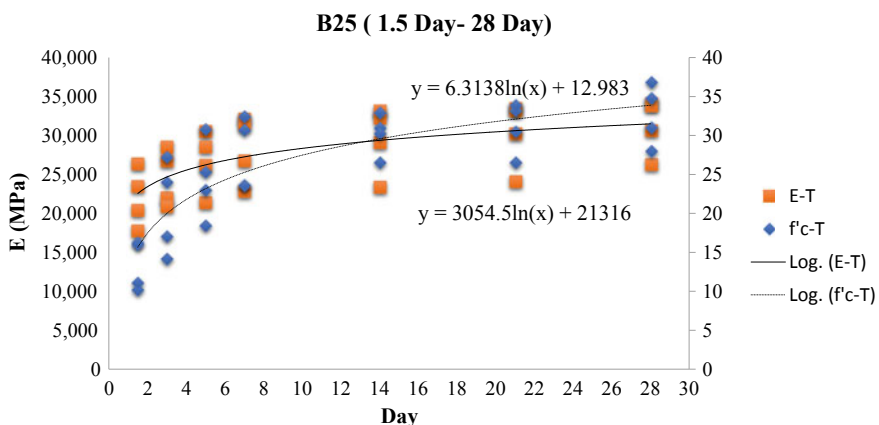


Fig. 8 Relationship E-f'c over time B25

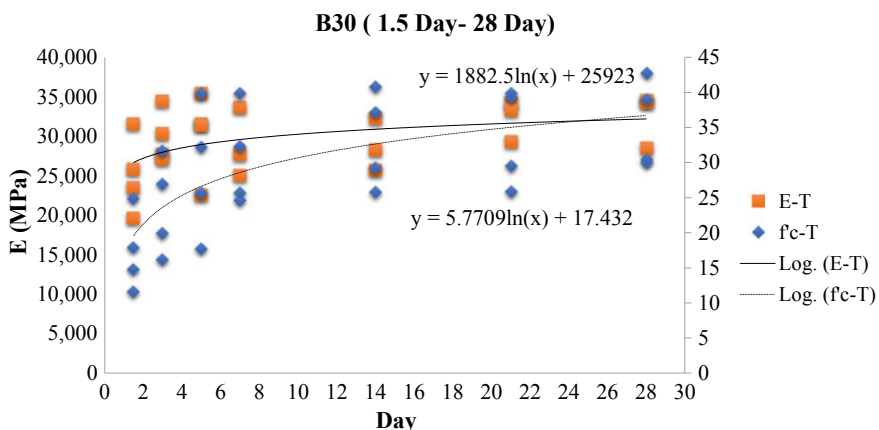


Fig. 9 Relationship E-f'c over time B30

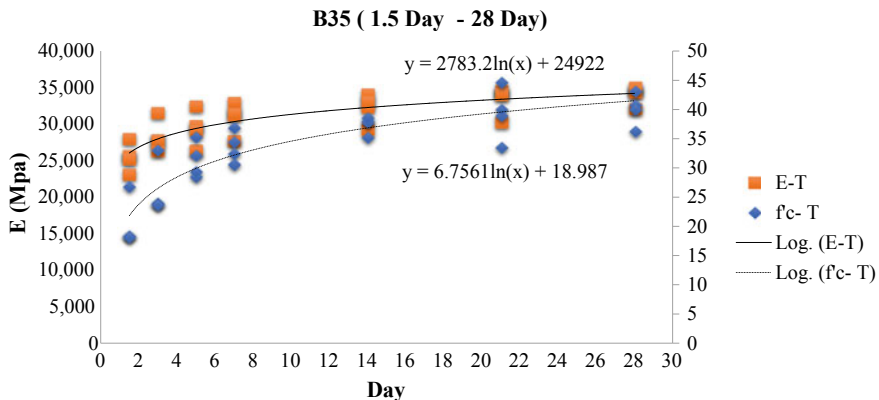


Fig. 10 Relationship E-f'c over time B35

From the results of chart analysis it is possible to construct a correlation function between E and f'c according to a certain formula at 7 time frames (1.5 days, 3 days, 5 days, 7 days, 14 days, 21 days and 28 days).

with K as an testing constant it is possible to take the mean K average = 6033 for 1.5 days for the durable level B25, K average = 5913 with B30 and K average = 5679 for B35. Similar to developing K for the remaining time frame of 3 days, 5 days, 7 days, 14 days, 21 days and 28 days.

From the summary table, build an testing formula $E = K\sqrt{f'_c}$ to use for the conversion from E to f'c and vice versa based on K in Table 4.

6 Conclusions and Recommendations

From the research results, E and f'c always grow faster than the design according to Tables 2 and 3. At the same time, the correlation between E and f'c is similar and develops rapidly in the period from 1 to 7 days, with E and f'c in 5 days has reached 90% of the design, and 14 days to 21 days has reached 100% of the design.

Testing results to build testing formula $E = K\sqrt{f'_c}$ according to Table 4 in 3 levels of durability B25, B30, B35. Based on the coefficient K to calculate the determination of E or f'c of concrete over time.

K_M is the average value of the test pieces of the durable grades B25, B30, B35 corresponding to the number of days of age of concrete tested. The number of more than 336 samples of the research team suggested the next study to increase the number of samples and additionally apply to other concrete levels with a larger number of samples for higher reliability results.

Table 2 Summary of testing results compared with E designed of 28 days

		1.5 days	3 days	5 days	7 days	14 days	21 days	28 days
B25	E (MPa)	22,019	24,524	27,126	28,178	29,391	30,169	31,163
	% Design	73%	82%	90%	94%	98%	101%	104%
	number of samples	10	12	10	10	10	10	12
B30	E (MPa)	24,156	27,890	29,427	30,104	31,400	32,400	32,984
	% Design	74%	86%	91%	93%	97%	100%	101%
	number of samples	12	12	12	12	12	12	12
B35	E (MPa)	25,530	28,456	29,447	30,832	32,193	33,268	33,999
	% Design	75%	84%	87%	91%	95%	98%	100%
	number of samples	12	12	12	12	12	12	12

Table 3 Summary of testing results compared to f'c designed of 28 days

		1.5 days	3 days	5 days	7 days	14 days	21 days	28 days
B25	f'c (MPa)	13.40	20.60	24.36	27.55	30.12	30.99	32.62
	% Design	54%	82%	97%	110%	120%	124%	130%
	number of samples	4	4	4	4	4	4	4
B30	f'c (MPa)	17.29	23.67	27.23	30.61	33.23	33.63	35.53
	% Design	58%	79%	91%	102%	111%	112%	118%
	number of samples	4	4	4	4	4	4	4
B35	f'c (MPa)	20.47	26.17	31.36	33.60	37.39	39.29	40.05
	% Design	58%	75%	90%	96%	107%	112%	114%
	number of samples	4	4	4	4	4	4	4

With the ever-growing concrete technology, the developing relationship between E-f'c over time (day) will better serve the construction design for construction works. In-depth studies in this direction will hopefully solve the practical problem better and more accurately.

Table 4 The relationship $E = K\sqrt{f'_c}$

		1.5 Day	3 Day	5 Day	7 Day	14 Day	21 Day	28 Day
B25	k1	5862	5453	6062	5790	5956	5803	5778
	k2	6382	5844	5454	5510	5291	5471	5498
	k3	5290	5060	4994	4601	4503	4647	4963
	k4	6596	5464	5488	5515	5616	5698	5567
	K _M	6033	5455	5499	5354	5342	5405	5451
B30	k1	6099	5390	5527	5677	5465	5461	5515
	k2	6888	6742	6579	5696	5770	6206	5411
	k3	5107	5050	4958	5069	5267	5361	5411
	k4	5557	6079	5810	5418	5406	5496	5419
	K _M	5913	5815	5719	5465	5477	5631	5439
B35	k1	5399	5559	5463	5425	5547	5535	5490
	k2	5982	5656	5253	5319	5244	5089	5231
	k3	5402	5390	4939	5005	4929	5226	5326
	k4	5932	5712	5374	5524	5328	5414	5537
	K _M	5679	5579	5257	5318	5262	5316	5396
Ngày (t)		1.5	3	5	7	14	21	28
K _t		5875	5617	5492	5379	5360	5451	5429

References

- ASTM C469-02, Standard test method for static module of Young'sity and Poisson's ratio of concrete in compression
- ACI 318-08 Building code requirements for structural concrete (ACI 318-08) and commentary

Shear Resistance Behaviours of a Newly Puzzle Shape of Crest Bond Rib Shear Connector: A FEM Modelling Study to Compare with the Previous Experimental



Trong Toan Khong, Quoc Tinh Tran, and Van Trinh Do

1 Introduction

The construction of composite highway bridges includes the implementation of several categories of steel concrete composite deck systems. Nowadays, the headed shear stud has still used in the civil structure the most popular, among the several different types of shear connectors. However, the stud might cause spatial obstacles during erection, and some fatigue problems of headed studs during service life have been reported [1].

Back in 1987, a German consulting engineering firm introduced the “*perfobond*” rib shear connector for composite beams to overcome the fatigue problem of the studs under live load [1, 2]. The potential advantages of the perfobond rib shear connectors are: they are easy to customize and fabricate and a perfobond rib could replace a number of headed studs. See Fig. 1

In the last decades many research and analytical studies were performed to investigate the structural behaviour of the perfobond connectors, and several attempts were made to facilitate the design process of such systems [1, 2].

T. T. Khong · Q. T. Tran · V. T. Do (✉)

Faculty of Civil Engineering, Ho Chi Minh City University of Technology (HUTECH), Ho Chi Minh City, Vietnam

e-mail: dv.trinh@hutech.edu.vn

T. T. Khong

e-mail: kt.toan@hutech.edu.vn

Q. T. Tran

e-mail: tq.tinh@hutech.edu.vn

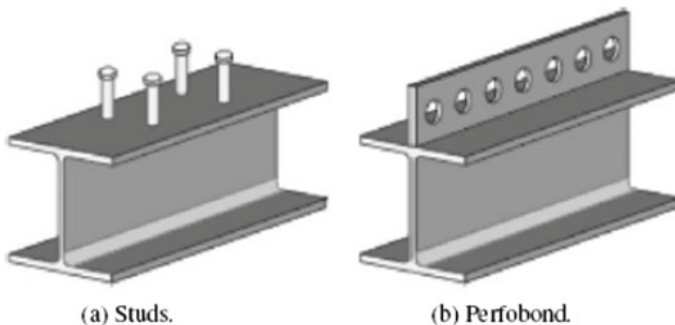


Fig. 1 **a** Traditional stud connectors, **b** perfobond connectors [2]

2 Objectives

In this study, an attempt is made to understand the influence of several parameters on the structural behaviour and strength of perfobond shear composite system. This is done by investigating how altering each of the parameters under consideration will eventually increase or decrease the strength of the whole system. These parameters include the perfobond connector dimensions, number and size of openings, as well as other parameters pertaining to the reinforced concrete slab, like the compressive strength of concrete and amount of steel reinforcement.

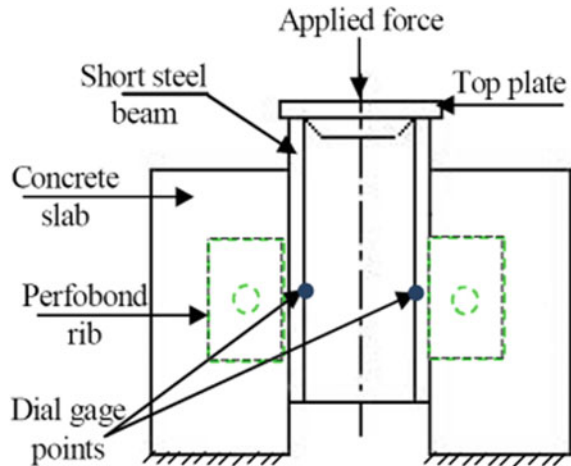
3 The Push Out Test

In the push out test (see Fig. 2), two perfobond ribs are welded to both flanges of the steel girder, while the perfobond connectors are embedded in the concrete slab. The load is then applied on the top of the steel beam, and the two slabs are supported at the bottom. The push out test is a standard evaluation of the strength of this composite system [1–4].

4 Material Modeling

4.1 Concrete

There are many stress-strain models proposed by various researchers; but in one of FEM modeling, it is difficult to check its accuracy. There is a need for a well-developed stress-strain model that can not only be used computationally, but can also

Fig. 2 Push out tests [3]

be easily adapted for hand analysis to enable rapid design checks to be performed [6].

In the present work; the stress-strain equations proposed by Kent and Park in 1971 were used as follows [5, 6]:

$$f_c = f'_c \left[\frac{2\varepsilon_c}{\varepsilon_{co}} - \left(\frac{\varepsilon_c}{\varepsilon_{co}} \right)^2 \right] \quad \text{for } 0 \leq \varepsilon_c \leq \varepsilon_{co} \quad (1)$$

$$f_c = f'_c \quad \text{for } \varepsilon_c > \varepsilon_{co} \quad (2)$$

$$\varepsilon_{co} = 2f'_c/E_c \quad (3)$$

where:

f_c : Stress at any strain ε_c (MPa)

ε_{co} : Strain at the ultimate compressive strength f'_c

E_c : The Young modulus of concrete (MPa)

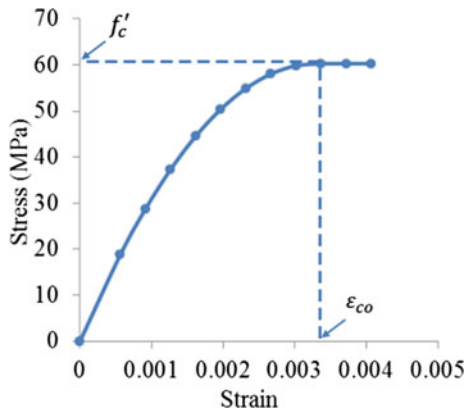
The Young modulus and modulus of rupture (f_r) for concrete, are both calculated as illustrated in the ACI 318-08 code [7]:

$$E_c = 4700\sqrt{f'_c} \text{ (MPa)} \quad (4)$$

$$f_r = 0.62\sqrt{f'_c} \text{ (MPa)} \quad (5)$$

Figure 3 below illustrates the stress-strain relationship adopted in the present research, for the concrete used in Sect. 6, which has a compressive strength of 60.3 MPa, and ultimate strain (ε_{co}) of 0.0033. These stress-strain equations are usable for other values of compressive strength as well.

Fig. 3 Concrete stress-strain curve used in the present work

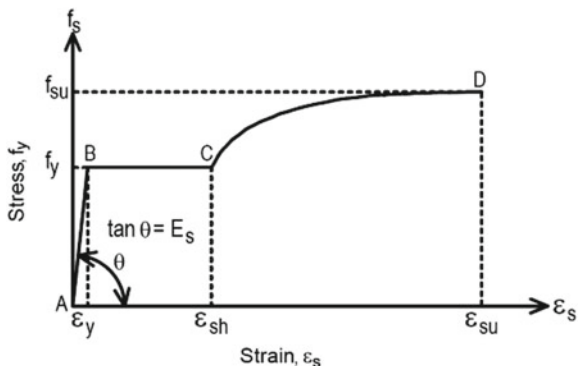


The modulus of rupture is entered separately while creating the concrete material modelling in ANSYS 12.1. The value of Poisson ratio for concrete is 0.2, and 0.3 for steel [5, 8].

4.2 Steel Bars and Steel Girder

The model proposed by Park and Paulay in 1975 [8], is used in the present study for modeling both the reinforcement steel and the steel girder. In this model, the stress-strain curve is divided into 3 regions: AB, BC, and CD, as shown in Fig. 4.

Fig. 4 Stress-strain relationship for steel proposed by park and paulay [8]



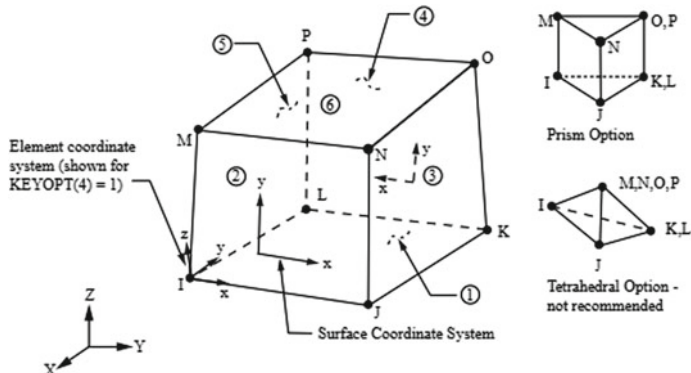


Fig. 5 Solid45 element used to model steel girder [9]

5 Finite Element Modeling

5.1 Steel Girder and Perfobond Connectors

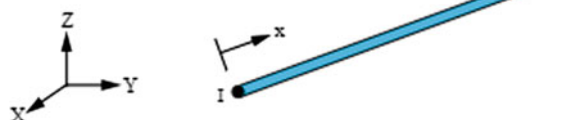
For the purpose of finite element modeling of the steel beam and perfobond connectors, the Solid45 element is used. This element has eight nodes and three degrees of freedom at each node: translations in the nodal x, y, and z directions. See Fig. 5.

In the other hand, this element has some especially characteristic liked plasticity, creep, swelling, stress stiffening, large deflection, and large strain capabilities [9].

5.2 Steel Reinforcement

The element Link180, as shown in Fig. 6, is used in the present study for modeling the reinforcement bars in the concrete slab. This element is a spar which may be used in a variety of engineering applications. Depending upon the application, the element may be thought of as a truss element, a cable element, a link element, a spring element, etc. Plasticity, creep, swelling, stress stiffening, and large deflection capabilities are included [9].

Fig. 6 Link180 element model [9]



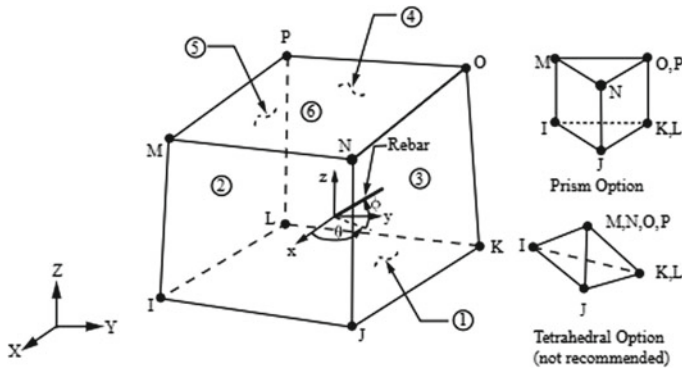


Fig. 7 Solid65 element model [9]

5.3 Concrete

The three dimensional solid concrete element “Solid65” is used in the present work for the modeling of the concrete. This element is used for the 3-D modeling of solids with or without reinforcing bars (rebar) and used to model of cracking in tension and crushing in compression. This element has eight nodes and three degrees of freedom at each node: translations in the nodal x, y, and z directions, as shown in Fig. 7. In this study; the discrete approach is used to model the reinforcement, in which reinforcing bars will be attached to concrete nodes at the conjunction points.

The most important aspect of this element is the treatment of nonlinear material properties. The concrete is capable of cracking (in three orthogonal directions), crushing, plastic deformation, and creep [9].

6 Experimental Data

The standard push out test for specimen CP1.1 tested by Valente M., I, B. [10] will be used in this study to confirm the validity of the ANSYS 12.1. The Perfobond connectors used in this specimen has the dimensions and configuration shown in Fig. 8. The entire dimensions are in (mm).

Two ribs are welded to both flanged of HEB260 girder. The geometry of this section is illustrated in Fig. 9. All the symbols represent the dimensions of this section in (mm), except G which is the weight of unit length of the girder (kg/m).

Figure 10 shows the geometry of the CP1.1 specimen. Letters b, d and e represent the dial gauges that measure the relative movement (slip) between the concrete slab and steel beam. During the preparation of the specimen; special consideration was taken to prevent attaching the concrete surface to the steel beam flanges, to transfer the entire applied load to the perfobond shear connector. Figure 11 shows a top view

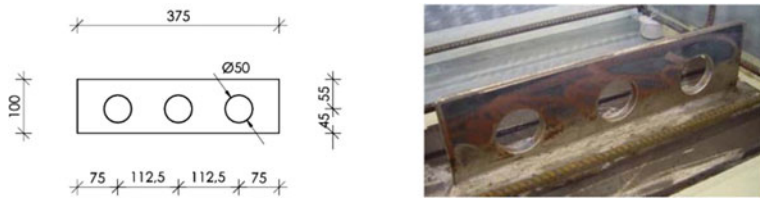


Fig. 8 Perfobond rib configuration and dimensions [10]

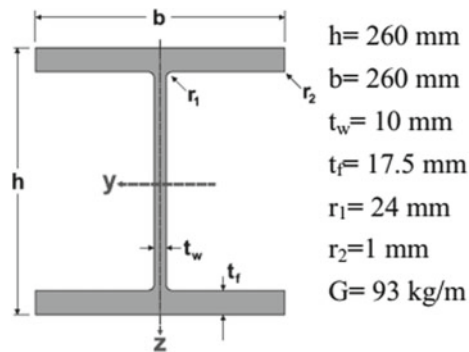


Fig. 9 Geometry of the HEB260 section

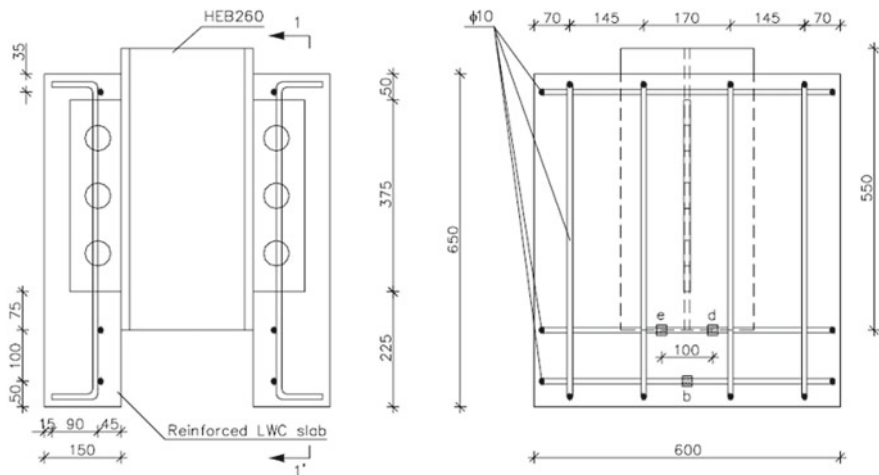


Fig. 10 The geometry of the CP1.1 specimen [10]

Fig. 11 Top view of the specimen CP1.1 [10]

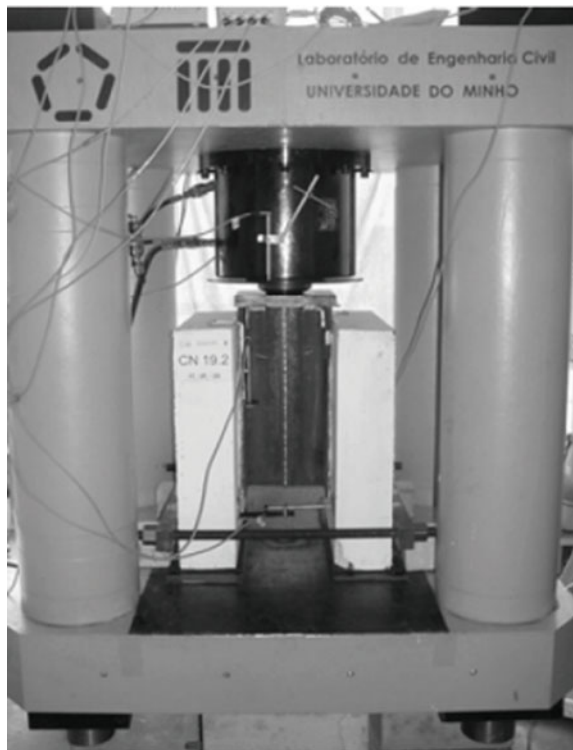


of this specimen before pouring the concrete, while Fig. 12 shows specimen during testing.

The material properties used in this test are as follows [10]:

Concrete: compressive strength $f'_c = 60.3$ MPa,

Fig. 12 Testing machine [10]



Steel bar: yield strength $f_y = 576$ MPa, ultimate strength $f_{su} = 675$ MPa,

Perfobond rib and steel girder: $f_y = 415$ MPa, ultimate stress $f_{su} = 550$ MPa.

Only one quarter of the composite system is considered in the ANSYS 12.1 model due to symmetry, as illustrated in Fig. 13. The cracked concrete slab and the deformed perfobond connector after completing the test are shown in Fig. 14, while Fig. 15 shows the experimental vs. finite element results obtained by the present ANSYS 12.1 model. The curves show good agreement, with a difference percentage of 20%. Figure 16 shows the strain contour in concrete at failure, the darker the color, the higher the absolute value of strain. The total number of elements used to obtain these results is 4810, and it was found out that increasing the number of elements above that number will have insignificant effect on the results, as shown in Fig. 17. The Mises yield criterion is the default for most of the plasticity models in ANSYS (and is used in the present study).

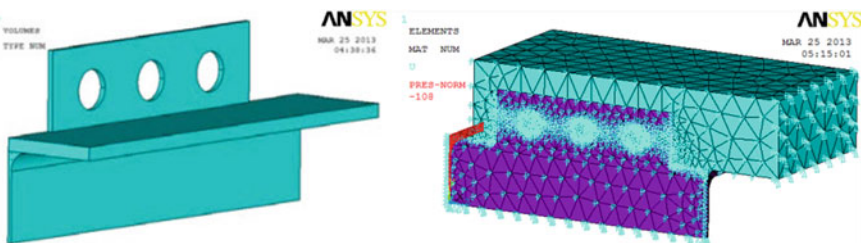


Fig. 13 One quarter of the composite system model in ANSYS 12.1



Fig. 14 Cracked slab and deformed perfobond rib at failure

Fig. 15 Experimental versus FEM model

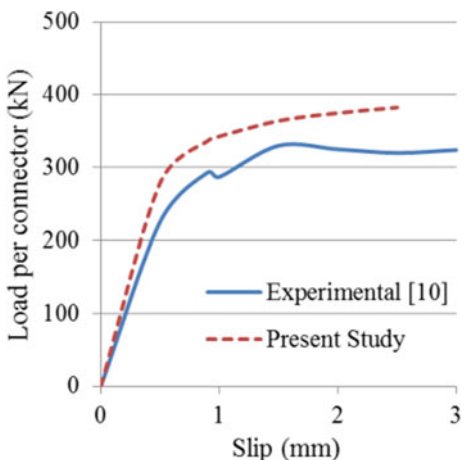


Fig. 16 Strain contour at failure for quarter of the composite system

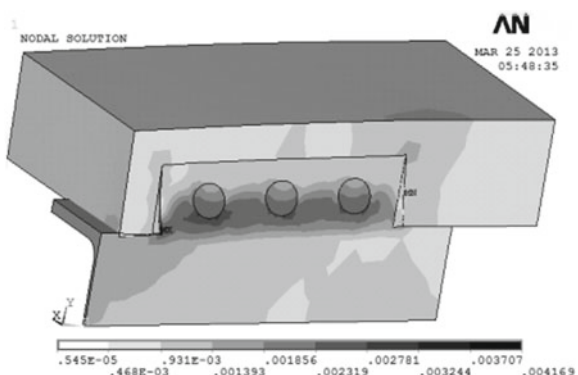
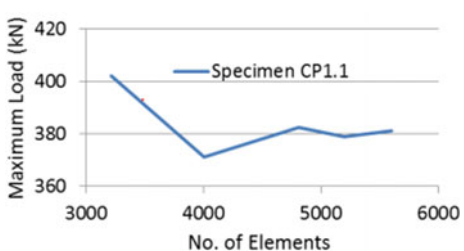


Fig. 17 Maximum load per connector versus No. of element for specimen Cp1.1



7 Results

The effects of several parameters on the strength of the perfobond connector-concrete slab composite system are studied using the ANSYS 12.1. Three cases are considered each time, which perfobond rib with three openings, two openings and single opening.

For example; Fig. 18 shows the finite element mesh and strain contour for the same specimen (CP1.1) but when reducing the number of openings in the perfobond rib to 2 openings and keeping all the other parameters fixed, and Fig. 19 shows similar visualization for the single opening case.

By investigating the strain contours in Figs. 16, 18 and 19; there are two apparent points: the first is that the strains (and therefore stresses) are intense at the conjunction between the concrete and the lower edges of the openings. The second is that the strains in the three opening case are more uniformly distributed, than strains in the two or single opening case. Figure 20 illustrates the effect of changing the perfobond rib thickness (t) on the structural strength of the composite system. Figure 21 shows the effect of changing the perfobond connector height (h_r) on the strength of specimen Cp1.1. It is clear from Fig. 19 that increasing the connector thickness has much more influence on the overall strength of the system than increasing the number of openings. Using three openings instead of one increased the strength by about 25%, while increasing the connector thickness by 80% (from 10 mm to 18 mm) resulted in increasing the strength by about 100%.

In Fig. 22 the effect of the compressive strength of the concrete slab is considered,

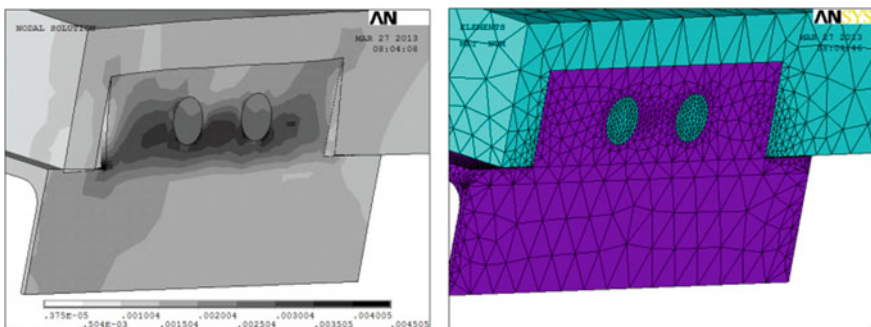


Fig. 18 Meshing and strain contour for the single opening case

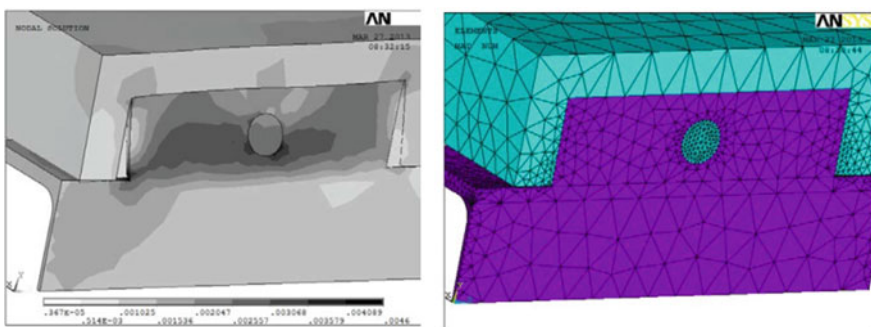


Fig. 19 Meshing and strain contour for the single opening case

Fig. 20 Strength versus rib thickness (t)

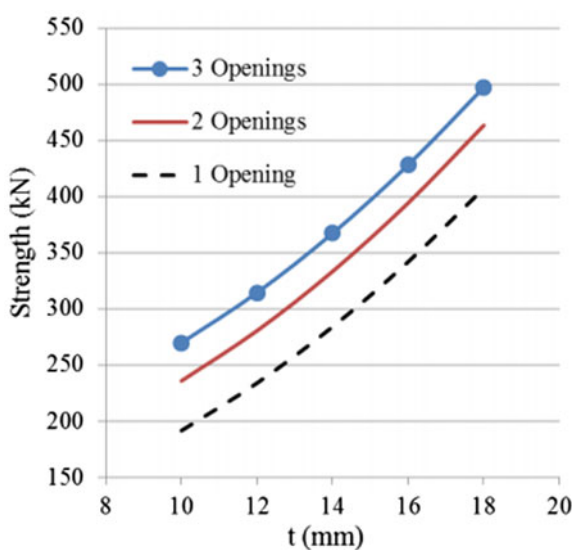
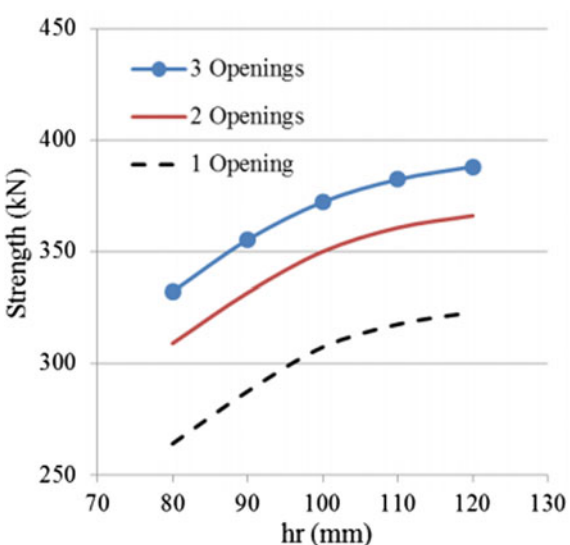


Fig. 21 Strength versus rib height (h_r)



while Fig. 23 illustrates the sensitivity of the composite system to changes in the yield stress of the reinforcement steel bars embedded in the concrete slabs of the specimen CP1.1, while keeping the remaining parameters unchanged. Figure 24 shows the effect of changing the area of transverse steel bars on the structural strength of the composite system. In this case, all the dimensions and material properties of the specimen CP1.1 considered in the present research are kept fixed, except the number of $\varnothing 10$ bars placed in the transverse direction (originally three bars with area $A_{tr} =$

Fig. 22 Strength versus concrete slab compressive strength (f'_c)

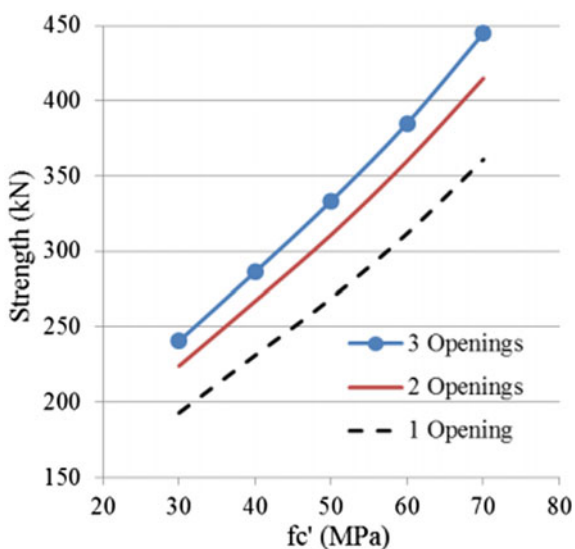
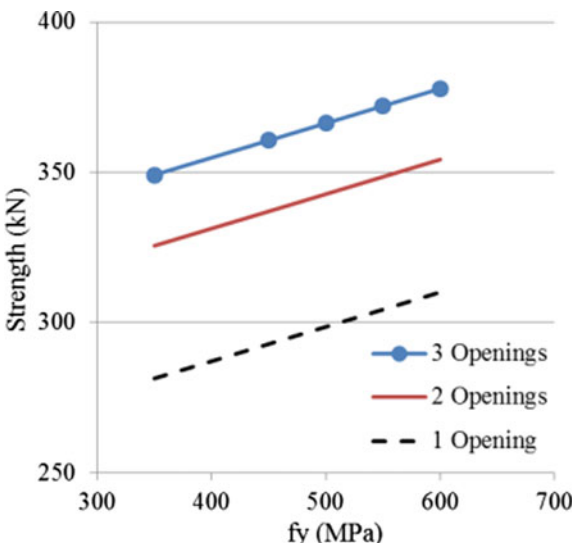


Fig. 23 Strength versus transverse steel bars yield stress



237 mm²). Figure 25 shows the effect of changing the perfobond connector opening diameter (d) on the strength of specimen CP1.1.

By studying Figs. 20 through 25, it is noticeable that the most influential parameter that affects the strength of this composite system is the connector thickness. The other two important parameters are the compressive strength of the concrete slab and the amount of the transverse reinforcement.

Fig. 24 The relative strength and area of transverse steel bars (A_{tr})

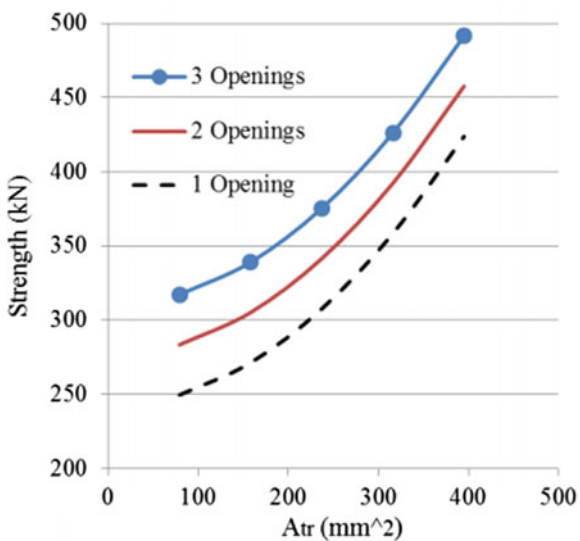
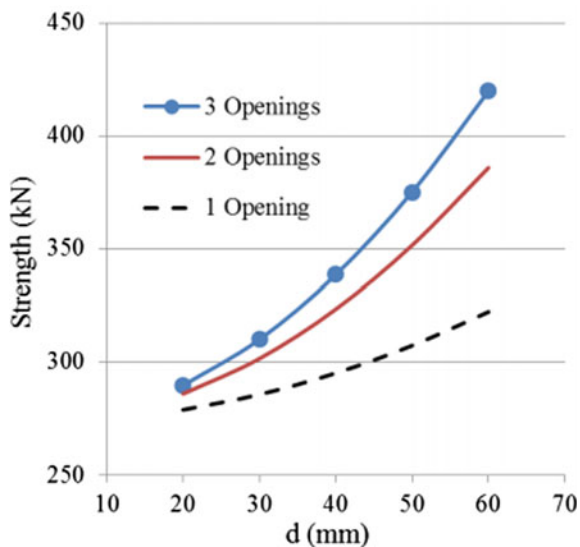


Fig. 25 The relative strength and diameter of the opening (d)



8 Conclusions

It was noticed in the present study that the failure of the perfobond connector-concrete slab composite system, occurs in the concrete slab, while the stress and strain in the steel perfobond rib remain far below the ultimate values. Hence, the material properties of the steel used in manufacturing the perfobond rib will have minor

effects on the strength of the system. By increasing the rib thickness from 10 mm to 18 mm the strength almost doubled, and increasing the compressive strength of the reinforced concrete slab from 30 to 70 MPa increased the strength of the system by about 80%. The number of transvers steel bars is also an important factor in determining the structural behavior of the system. By increasing the number of Ø 10 bars from one bar to five bars; the strength increased by about 53%. The yield stress of these bars has less effect on the strength of the system. It is also noticed that using a perfobond rib with a single large opening will produce nearly the same strength of a rib with three small openings, if the total area of these three opening is made equivalent to the single one. Finally, the ANSYS 12.1 model implemented in the present research was proved to be successful in handling the nonlinear analysis of this composite system, with a difference of about 18% from the experimental data.

References

1. Kim HY, Jeong YJ (2005) Experimental investigation on behavior of steel-concrete composite bridge decks with perfobond ribs, iraqi virtual science library (www.ivsl.org). *J Constr Steel Res* 62:463–471
2. da Vianna JC, Andrade SAL, da Velasco PCGS, Costa-Neves LF (2013) Experimental study of perfobond shear connectors in composite construction, iraqi virtual science library (www.ivsl.org). *J Constr Steel Res* 81:62–75
3. Al-Darzi SYK, Chen AR, Liu YQ (2007) Finite element simulation and parametric studies of perfobond rib connector, iraqi virtual science library (www.ivsl.org). *Am J Appl Sci* 4:122–127
4. Shariati M, Sulong NHR, Arabnejad KH, Mahoutian M (2011) Shear resistance of channel shear connectors in plain reinforced and lightweight concrete. *Sci Res Essays* 6(4):977–983
5. Kachlaklev D, Miller T, Yim S, Chansawat K, Potisuk T (2001) Finite element modeling of reinforced concrete structures strengthened with FRP laminates. Final report SPR 316, oregon department of transportation & federal highway administration, USA
6. Reddiar MKM (2009) Stress-strain model of unconfined and confined concrete and stress-block parameters. M.Sc thesis, Department of Civil Engineering, Texas A&M University, USA. Available at www.xa.yimg.com
7. ACI 318-08 (2008) American concrete institute, building code requirements for reinforced concrete. American Concrete Institute, Farmington Hills, Michigan
8. Tavio T, Tata A (2009) Predicting nonlinear behavior and stress-strain relationship of rectangular confined reinforced concrete columns with ANSYS. *Civil Eng Dimension* J 11(1):23–31
9. ANSYS (2012) ANSYS user's manual revision 12.1, ANSYS, Inc., Canonsburg, Pennsylvania
10. Valente M, Isabel B (2007) Experimental studies on shear connection systems in steel and lightweight concrete composite bridges. Ph.D. thesis, Civil Engineering Department—School of Engineering, University of Minho, Portugal. Available at www.repository.sdu.m.uminho.pt

Simulation of Concrete-Filled Steel Box Columns



Duc-Duy Pham, Phu-Cuong Nguyen, Duy-Liem Nguyen, and Hoang-An Le

1 Introduction

In recent years, CFSTCs are studied widely due to its high ductility. Furthermore, with advances in technology and material science, high strength concrete is utilized more popular. The effects of confinement help improving capacity of axial compression of the CFSTCS. However, in some cases, the ultimate strength of rectangular CFST columns is significantly reduces due to axial compression by considering imperfection and residual stress of steel tubes.

There are many previous researches investigating CFST columns using high strength materials such as: Han et al. [6], Liu [9], Liu and Gho [10], Liu et al. [11], Uy [18], and Sakino et al. [14]. Uy's research [18] carried out experimental tests and behavior analysis on high strength materials for steel and normal strength concrete. Pham and Nguyen [13] propose successfully a new formulation for finite element modelling of concrete-filled columns with outer steel circular tubes subjected to axial loadings. The strength of materials used for concrete cores is from 28 to 32 MPa and steel tubes are close to 817 MPa. The limit strength specified in EC4 standards is $f'_c \leq 60$ MPa and $f_y \leq 460$ MPa respectively. The results obtained have been compared with the Eurocode 4 standard, however it's exposed that EC4 overvalued axial compression resistance of CFST columns. Furthermore, Han et al. [6], Liu [9], Liu and Gho [10], Liu et al. [11], and Sakino et al. [14] use high-strength materials

D.-D. Pham · P.-C. Nguyen (✉)

Faculty of Civil Engineering, Ho Chi Minh City Open University, Ho Chi Minh City, Vietnam

e-mail: cuong.pn@ou.edu.vn; henycuong@gmail.com

D.-L. Nguyen

Faculty of Civil Engineering, Ho Chi Minh City University of Technology and Education, Ho Chi Minh City, Vietnam

H.-A. Le

Nguyen Tat Thanh Institute of Hi-Technology, Nguyen Tat Thanh University, Ho Chi Minh City, Vietnam

of concrete and steel with f'_c from 25 MPa to 85 and f_y from 262 MPa to 834 MPa, respectively. The empirical results were used to compare with the calculation formula from Eurocode 4 standard. The prediction of ultimate strength from EC4 gives approximate results for high strength steel, but for normal strength steel, the result from EC4 gives lower results than experimental one. Initially geometric imperfection and residual stress distribution in steel tubes are often the least considered in previous studies.

Predicting strength and behavior of CFSTCs for high strength materials is the main objective of this paper. The applied calculation for predicting the confining pressure on concrete is suggested based on experimental data of CFSTCs. The other objective is to investigate and extend the application of EC4 standard for CFSTCs using high strength materials, through parametric studies based on databases.

2 Finite Element Modeling

As shown in Fig. 1a, CFSBC simulation is using the S4R element type for steel tubes and the C3D8R element type for concrete core. The selection of element size affects on the convergence in the simulation problem, so a parameter study was conducted whereby the element size should choose $B_{eq}/15$. In addition, to increase the model convergence and reducing the computation time, boundary conditions of symmetry are also set shown in Fig. 1b, because of the symmetry of specimens. Surface at top and bottom of the model in ABAQUS is tied to the referent point at the center of the surface through rigid body constraints. The surface loading is assigned through the reference point. The surface-to-surface contact is utilized to describe interacting between concrete and steel box during axial compression. The friction coefficient (0.25) is utilized for the contact between steel and concrete. Initial imperfections and residual stress are simulated by using *IMPERFECTION and *INITIAL CONDITION options available in ABAQUS.

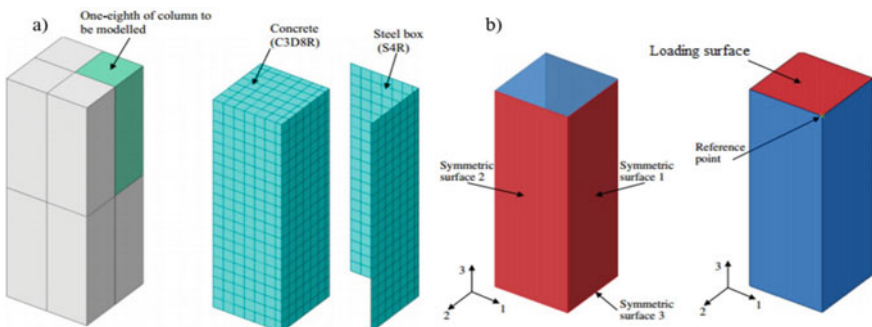


Fig. 1 **a** Simulation of CFSBCs, **b** symmetrical boundary conditions and loading surface

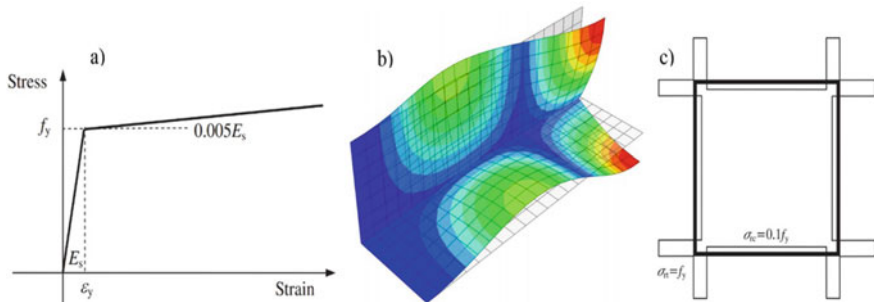


Fig. 2 a Constitutive modeling for steel, b first buckling mode shape, c residual stresses [17]

2.1 Constitutive Model of Steel

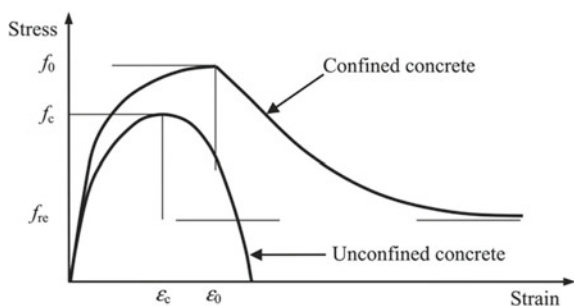
A bilinear model is applied for simulating steel material as shown in Fig. 2a. If Young's modulus (E_s) value is not declared for this paper, it should be equal to 200 GPa. After the elastic stage of steel, the strain hardening modulus ($0.005E_s$) is used. Poisson's ratio (0.3) is also used.

Based on previous research carried out by Degée et al. [3] on welded steel tubes, a local imperfection of $B_{eq}/1000$ of the cross-section width is employed as in Fig. 2b. Residual stress distribution of steel tubes is shown in Fig. 2c by Uy [17].

2.2 Constitutive Model of Confined Concrete

An improved new formula contents two-stages as illustrated in Fig. 3. An ascending branch represents the strain-hardening rule. For accuracy verification of the concrete behaviour in the ascending stage, this study uses the model proposed by Mander et al. [12] as follows:

Fig. 3 Stress-strain model for concrete



$$\frac{f}{f_o} = \frac{(\varepsilon/\varepsilon_0) \times r}{r - 1 + (\varepsilon/\varepsilon_0)^r}; \quad r = \frac{E_c}{E_c - (f_0/\varepsilon_0)} \quad (1)$$

With $E_c = 4700\sqrt{f'_c}$ MPa, is the concrete elastic modulus. In addition, for unconfined concrete, the peak stress and conforming strain are f'_c and ε_c respectively. Furthermore, for confined concrete is ε_0, f_0 two parameters that need to be determined concrete material model. ε_c is calculated as Eq. 2 proposed by Tasdemir et al. [16]. The peak stress f_0 and ε_0 for confined concrete are calculated as Eqs. 3 and 4 proposed by Xiao et al. [19].

$$\varepsilon_c = \left(-0.067 \times (f'_c)^2 + 29.9 \times f'_c + 1053 \right) \times 10^{-6} \quad (2)$$

$$\frac{f_0}{f'_c} = 1 + 3.25 \times \left(\frac{f_r}{f'_c} \right)^{0.8} \quad (3)$$

$$\frac{\varepsilon_0}{\varepsilon} = 1 + 17.4 \times \left(\frac{f_r}{f'_c} \right)^{1.06} \quad (4)$$

In the elastic stage of material, the influence of confining stress is negligible or not on the CFST columns, but later confining stress develops very rapidly when the yielding of the steel. Based on regression analysis of 64 specimens, the confining stress f_r is obtained as

$$f_r = \frac{0.0645 + 0.11 \times f_y}{(f'_c)^{0.4}} \times \exp \left(-0.07 \times \frac{B_{eq}}{t} \right) \quad (5)$$

with the equivalent width of $B_{eq} = \sqrt{\frac{B^2 + D^2}{2}}$. On the other hand, Eq. 6 is representing the branch descending in concrete models proposed by Binici [1]. With the residual stress for confined concrete f_{re} and the curve of the softening branch, based on α and β are proposed by Tao et al. [15]

$$f = f_{re} + (f_0 - f_{re}) \times \exp \left[- \left(\frac{\varepsilon - \varepsilon_0}{\alpha} \right)^\beta \right] \quad (6)$$

The CDPM (ABAQUS) is used for concrete with parameters such as: the ratio of the second stress invariant on the tensile meridian to on the compressive meridian (K_c), dilation angle (ψ), flow potential eccentricity (e), ratio of the compressive strength under biaxial loading to uniaxial compressive strength (f_{bo}/f'_c). Parameters are determined based on Tao's [15] research.

Table 1 Test specimen parameters of CFSBCs

Source	<i>N</i>	<i>B</i> (mm)	<i>H</i> (mm)	<i>t</i> (mm)	<i>f_y</i> (MPa)	<i>f'_c</i> (MPa)
[11]	5	98.2–181.2	100.3–182	4.18	550	56.6–65.7
[10]	10	100–130	120–180	4.0–5.8	300–495	56–92
[6]	2	60	60	1.87	282	81*
[2]	7	100.3–100.7	100.3–100.7	2.07–7.6	306.7–371.6	59–130.8
[8]	13	150	150	8–12.5	446–846	54–62**
[20]	13	150	150	8–12.5	446–779	142.08–164.1
[9]	10	108–140	108–160	4	495	58.40–77.60
[7]	1	109.6	109.6	4.93	762	100
[5]	2	100–120	120–180	5.70–7.69	423.20–514.53	55.3
[4]	1	150	152	8.28	488.38	55.3

* The uniaxial compression tests on cylinder specimens of 100 mm × 200 mm

** The uniaxial compression tests on cube specimens of 150 x 150 x 150 mm

The remaining specimens in Table 1 are used the uniaxial compression tests on cylinder specimens of 100 mm × 300 mm

3 Verification

The predicted precision of the FE modelling comparing with the test data is summarized in Table 1. The parameter ranges for CFST columns specimens are: $f_y = 282–779$ (MPa), $f'_c = 55.3–157.54$ (MPa), $H = 60–250$ mm, $H/B = 1–1.8$, $H/t = 12–49.46$, $L/B = 2.98–4.54$. Figure 4 is comparing the prediction of the present numerical model with experimental tests. The ultimate strength (N_{uc}) predicted by the proposed FE model, Tao et al.'s one [15] is aligned with experiments collected from sixty four specimens listed in Table 1 (N_{ue}) as shown in Fig. 5. Table 2 presents results of this proposed model, Tao et al. model, and the EC4 standard through the mean value and standard deviation (SD) of the ratio N_{ue}/N_{uc} . The mean values of N_{ue}/N_{uc} are 1.005, 1.057 and 1.104, respectively, for the proposed model, Tao et al.'s model, standard EC4. Consequently, results acquired from the proposed FE model is reasonable accuracy to Tao et al. [15] model and standard EC4 in predicting the ultimate strength.

4 Conclusion

In general, the proposed FE model gives reasonably accurate predictions, and it is appropriate to be used for rectangular with high strength material columns and large B/t ratio. Geometric imperfections and residual stress distribution causing local buckling effects for steel boxes that were considered in this current study, thereby recognizing the effect of confinement effectiveness of CFSBCs. The study has expanded

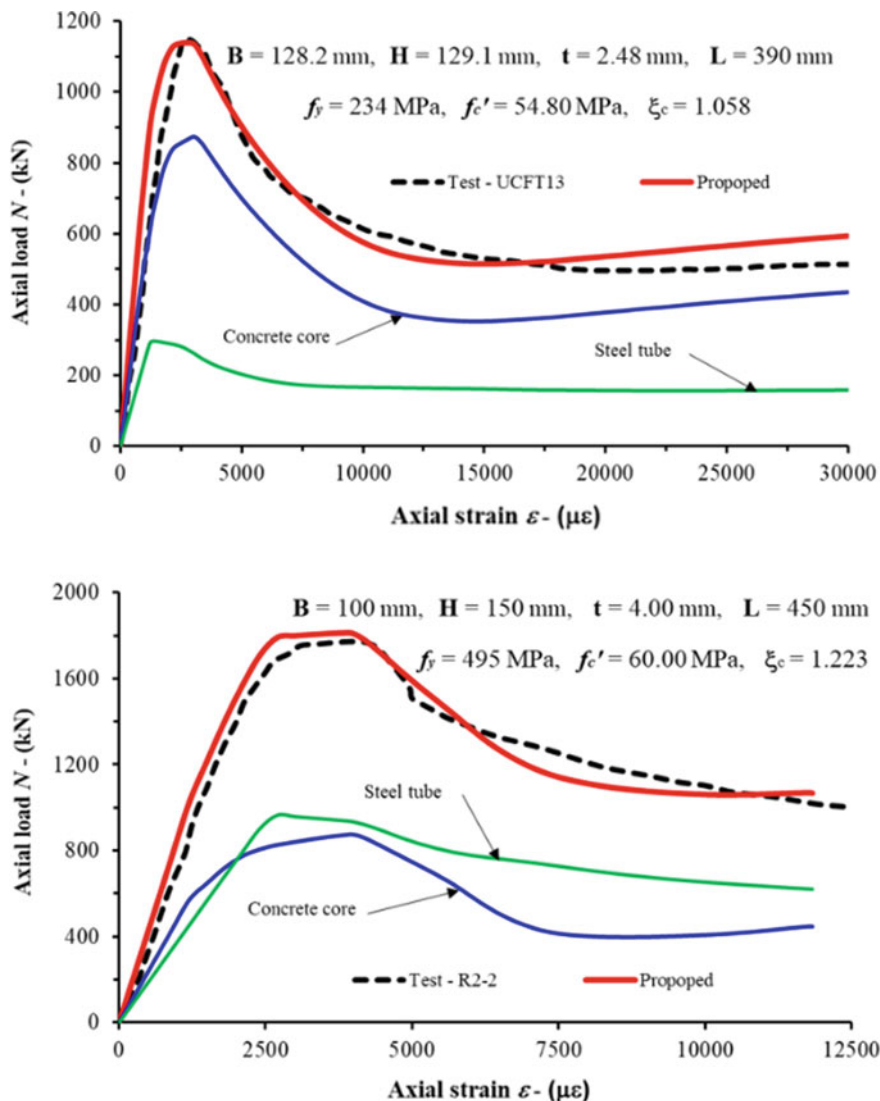


Fig. 4 Comparison between experimental data and numerical simulation

to accurately predict the ultimate strength and behaviour through comparisons are made with experimental specimen tests and other researchers all over the world. The EC4 standard approach for the ultimate strength predictions lower than the test and too safe with high-strength CFSBCs. In the future, circular steel tubes will be studied for CFSTCs by our research group.

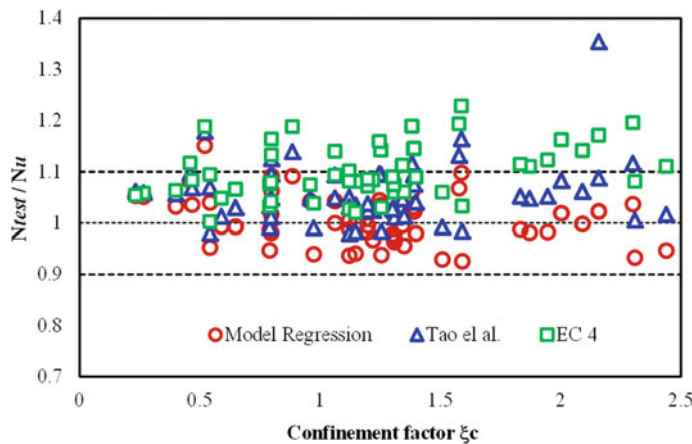


Fig. 5 Comparison between standard EC4 and FE models

Table 2 Comparison of the ultimate loads

FE model	SD	Mean
Proposed	0.045	1.005
Tao et al. [15]	0.057	1.057
EC4	0.050	1.104

Acknowledgements The authors also gratefully acknowledge the financial support granted by the Scientific Research Fund of the Ministry of Education and Training (MOET), Vietnam (No. B2019-MBS-01). The authors would also like to thank colleagues at Ho Chi Minh City Open University for supporting this project.

References

1. Binici B (2005) An analytical model for stress-strain behavior of confined concrete. Eng Struct 27(7):1040–1051
2. Chen S, Zhang R, Jia L-J, Wang J-Y, Gu P (2018) Structural behavior of UHPC filled steel tube columns under axial loading. Thin-Walled Struct 130:550–563
3. Degée H, Detzel A, Kuhlmann U (2008) Interaction of global and local buckling in welded RHS compression members. J Constr Steel Res 64(7–8):755–765
4. Du Y, Chen Z, Xiong M-X (2016) Experimental behavior and design method of rectangular concrete-filled tubular columns using Q460 high-strength steel. Constr Build Mater 125:856–872
5. Du Y, Chen Z, Yu Y (2016) Behavior of rectangular concrete-filled high-strength steel tubular columns with different aspect ratio. Thin-Walled Struct 109:304–318
6. Han L-H, Yao G-H, Zhao X-L (2005) Tests and calculations for hollow structural steel (HSS) stub columns filled with self-consolidating concrete (SCC). J Constr Steel Res 61(9):1241–1269
7. Khan M, Uy B, Tao Z, Mashiri F (2017) Behaviour and design of short high-strength steel welded box and concrete-filled tube (CFT) sections. Eng Struct 147:458–472

8. Liew JYR, Xiong M, Xiong D (2016) Design of concrete filled tubular beam-columns with high strength steel and concrete. *Structures* 8:213–226
9. Liu D (2005) Tests on high-strength rectangular concrete-filled steel hollow section stub columns. *J Constr Steel Res* 61(7):902–911
10. Liu D, Gho W-M (2005) Axial load behaviour of high-strength rectangular concrete-filled steel tubular stub columns. *Thin-Walled Struct* 43(8):1131–1142
11. Liu D, Gho W-M, Yuan J (2003) Ultimate capacity of high-strength rectangular concrete-filled steel hollow section stub columns. *J Constr Steel Res* 59(12):1499–1515
12. Mander JB, Priestley MJN, Park R (1988) Theoretical stress-strain model for confined concrete. *J Struct Eng* 114(8):1804–1826
13. Pham D-D, Nguyen P-C (2020) Finite element modelling for axially loaded concrete-filled steel circular tubes. In: CIGOS 2019, innovation for sustainable infrastructure, vol 54. Springer, Singapore, pp 75–80. https://doi.org/10.1007/978-981-15-0802-8_8
14. Sakino K, Nakahara H, Morino S, Nishiyama I (2004) Behavior of centrally loaded concrete-filled steel-tube short columns. *J Struct Eng* 130(2):180–188
15. Tao Z, Wang Z-B, Yu Q (2013) Finite element modelling of concrete-filled steel stub columns under axial compression. *J Constr Steel Res* 89:121–131
16. Tasdemir MA, Tasdemiry S, Jefferson AD, Lydon FD, Barr BIG (1998) Evaluation of strains at peak stresses in concrete: a three-phase composite model approach. *Cem Concr Res* 20:301–318
17. Uy B (1998) Local and post-local buckling of concrete filled steel welded box columns. *J Constr Steel Res* 47:47–72
18. Uy B (2001) Strength of short concrete filled high strength steel box columns. *J Constr Steel Res* 57:113–134
19. Xiao QG, Teng JG, Yu T (2010) Behavior and modeling of confined high-strength concrete. *J Compos Constr* 14:249–259
20. Xiong M-X, Xiong D-X, Liew JYR (2017) Axial performance of short concrete filled steel tubes with high- and ultra-high-strength materials. *Eng Struct* 136:494–510

Study on Two-Directional Seismic Deterioration of Tested Steel Columns



Tran Tuan Nam

1 Introduction

In 2007, a collapse experiment on a full-scale four-story steel building was conducted in Japan. In that test, various increasing scaled ground motions were applied in the building specimen until collapse by using the E-Defense—the world largest shake-table facility. The objectives of the test were to evaluate the structural and functional performance of the steel building under design-level ground motions and to determine the safety margin against collapse under exceedingly large ground motions. This test was a part of an experimental project focused on steel buildings conducted at the E-Defense [1]. Described an overview of the project, [2] and [3] reported the experimental responses of the building specimen under the weak, strong and collapse shaking levels.

With a valuable numerous data resource, the test has attracted a number of analytical studies for reasoning the building collapse. [4–6] and [7] indicated that the local buckling of columns governed the building collapse. However, most of them did not report the physical aspect of local buckling except for [8] and [9] who showed deteriorating behavior of only one selected column.

In order to provide further up-to-date investigation on the building response, this study thereby attempts to identify the different deteriorating progresses of several columns which carried the largest, moderate or smallest axial forces that are either compression or tension loads as well as correspondingly different shear forces. Moreover, the columns were subjected to a major few cycles in a particular direction and later to the largest cycle in a significantly rotated direction. Their consequent progress of two-directional deteriorations will be emphasized in this study.

T. T. Nam (✉)

Faculty of Civil Engineering, Ho Chi Minh City University of Technology (HUTECH), Ho Chi Minh City, Vietnam

e-mail: tt.nam@hutech.edu.vn

2 Full-Scale 4-Story Steel Building Collapse Test

2.1 Building Specimen and Material

The building specimen is a full-scale four-story steel moment frame whose plan dimension is 6×10 m and the height is 14.375 m (Fig. 1). SN400B and BCR295 steel were used for the beams and columns, respectively. The section shapes are given in Table 1.

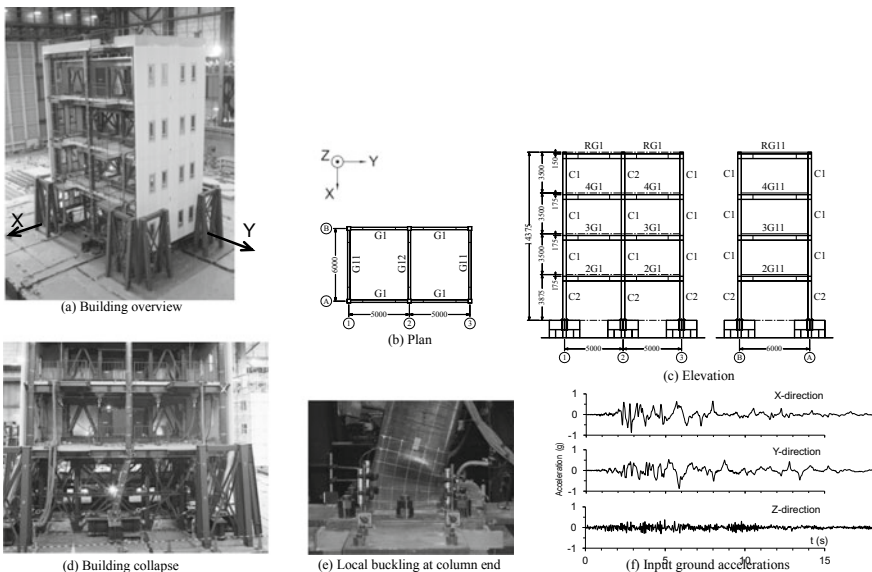


Fig. 1 Full-scale 4-story steel building specimen and input ground motion

Table 1 Sections and materials of the steel frame

		Beam (SN400B)		Column (BCR295)	
Floor	G1	G11	G12	Story	C1, C2
R	H-346 × 174 × 6×9	H-346 × 174 × 6×9	H-346 × 174 × 6×9	4	RHS-300 × 300 × 9
4	H-350 × 175 × 7×11	H-350 × 175 × 7×11	H-340 × 175 × 9×14	3	RHS-300 × 300 × 9
3	H-396 × 199 × 7×11	H-400 × 200 × 8×13	H-400 × 200 × 8×13	2	RHS-300 × 300 × 9
2	H-400 × 200 × 8×13	H-400 × 200 × 8×13	H-390 × 200 × 10 × 16	1	RHS-300 × 300 × 9

H—height × width × web thickness × flange thickness; RHS—height × width × thickness

The columns are constructed using $300 \times 300 \times 9$ cold-formed square tubes with relatively large width-to-thickness ratios ($b/t = 33$). The columns are welded to 50 mm thick baseplates (SN490C). Each baseplate is bolted using 8 anchor bolts of M36 (ABR490, 900 mm length) to fixtures attached to the shake-table. The beams are constructed using hot-rolled wide flanges.

Figure 1d shows the collapse configuration of the building with soft-story mechanism caused by deterioration of first-story columns due to local buckling at column ends (Fig. 1e).

2.2 *Input Ground Motion*

The ground acceleration histories recorded at the JR Takatori station during the 1995 Kobe earthquake (herein referred to as Takatori motion) were used as the input for the shake table experiments. The building specimen was subjected to a series of white noise motions and progressively increasing scaled Takatori motion from 5 to 100%. The EW, NS, and UD components of the ground motion were considered for the X, Y, and Z directions, respectively (Fig. 1f).

3 Accumulated Two-Directional Column Deterioration Due to Local Buckling

3.1 *Sign Convention*

Sign conventions for lateral displacement (u_X, u_Y), story drift ratio (r_X, r_Y) and moment (M_Y, M_X) are presented in Fig. 2a (right). Note that M_Y (moment about the Y axis) relates to r_X (lateral deformation along the X axis), whereas M_X (moment about the X axis) corresponds to r_Y (lateral deformation along the Y axis). Therefore in this study, positive M_X is exceptionally defined inverse to the right-hand rule, in order to present the proportionality of lateral deformation and consequent moment.

3.2 *Combined Strength Factor*

The yield capacity is governed by axial force and biaxial moments. When the column yields, its moment capacity follows the yield surface. However, if local buckling occurs, the yield surface may shrink down and consequently reduces the moment capacity. Therefore, the study utilizes the existing equation of yield capacity as an

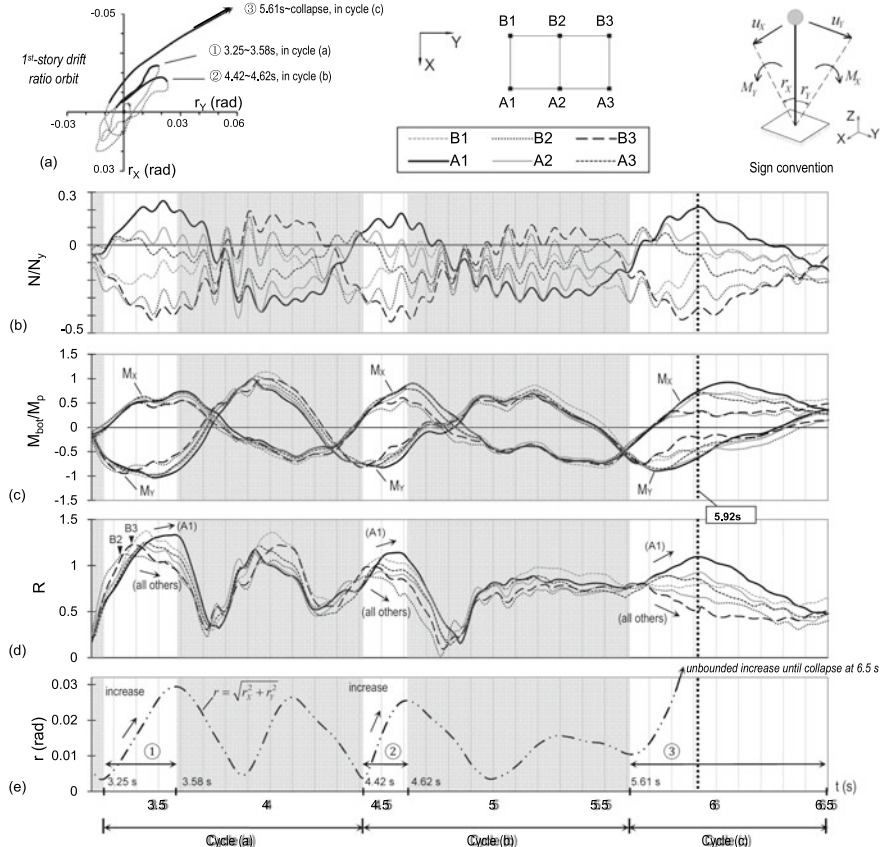


Fig. 2 a 1st-story drift ratio orbit, and time histories of b axial forces, c bottom moments, d combined strength factor R of 1st-story columns, and e 1st-story drift ratio $r = \sqrt{r_X^2 + r_Y^2}$ (100% takatori level)

indicator to detect the deterioration. Equation 1 shows the *combined strength factor* R counting for the simultaneous interaction of axial force and biaxial moments for square tube columns, i.e.,

$$R = \frac{4}{3} \left(\frac{N}{N_y} \right)^2 + \frac{\max(|M_X|, |M_Y|)}{M_p} + \frac{3}{4} \left[\frac{\min(|M_X|, |M_Y|)}{M_p} \right]^2 \quad (1)$$

where, M_p is plastic moment in case of zero axial force. According to Inoue [10], $R = 1.0$ indicates the interaction of N , M_Y , and M_X at the yield surface in the case of $|N/N_y| \leq 0.5$, corresponding to the present case where N/N_y varied from $+0.25$ to -0.44 . R in fact can be larger than 1.0 because of strain hardening effect. When yielding occurs, if N increases, then moment capacity decreases. On the other hand,

based on the relationship between the development of R and the increase of story drift ratio in the radial direction $r = \sqrt{r_X^2 + r_Y^2}$, the judgment of column deterioration due to local buckling can be made whenever R reaches peak and then declines while $\dot{r} > 0$.

3.3 Accumulated Two-Directional Column Deterioration

Figure 2 shows the (a) 1st-story drift ratio orbit, and time histories of (b) axial force including gravity load, (c) moment M_Y and M_X , (d) combined strength factor R of all six column bottom ends, and (e) 1st-story drift ratio r at 100% Takatori excitation level. Based on Fig. 2a, three main cycles are defined with durations of (a) 3.2~4.4 s, (b) 4.4~5.6 s, and (c) 5.6~6.5 s, respectively. Each cycle is defined as the period whereby u_X makes a full loop from zero to zero. The cyclic change of displacement direction was shown, where the frame tended to yield toward the Y direction with the orientation angles of nearly 53° , 38° , and 29° , respectively in the sequence of three cycles. The Y direction was also the eventual collapse direction of the building in the cycle (c).

Three segments associated with the increasing progresses of r toward the $+r_Y$ direction at 100% Takatori level, denoted by ①, ②, and ③ (Fig. 2a), are highlighted, and the other time zones are shaded. In the segment ① of cycle (a) when the r increased toward $+r_Y$ direction (Fig. 2e), the reductions of factor R (Fig. 2d) again occurred early to columns B2 and B3 at 3.33 s and 3.37 s, respectively, reflected mostly by the decrease of M_Y (Fig. 2c). The reductions of factor R occurred later to columns A2, A3 and B1, when r exceeded 0.02 rad. Column A1 was strongest during segment ① and almost did not show any deterioration, because it was under tension. A similar situation occurred in the subsequent segments ② and ③. Especially, although the magnitude of r remained almost similar after each cycle, the peak values of factor R gradually declined, indicating the cumulative deterioration caused by local buckling.

Figure 3 shows the hysteretic curves of the column B3's bottom moments M_{Y-bot} and M_{X-bot} at 100% Takatori motion level. The low-pass filtered version of column axial force (*dotted line*, in respect to secondary vertical axis) is also displayed in the plot, thereby showing the deterioration of M_{Y-bot} mainly occurring under compressive load condition when the building deformed in the negative r_X direction. Note that the axial force is low-pass filtered to eliminate the high-frequency fluctuation due to vertical acceleration, in order to provide an easily identified hysteretic curve in Fig. 3. Three points of timing when M_{Y-bot} started decreasing due to local buckling: 3.35 s (marked by Δ), 4.40 s (\square), and 5.68 s (\circ) at three cycles (a), (b), and (c), respectively are therefore selected to show; and both moments and axial forces at those instants are also indicated in Fig. 3.

Because the principal direction of biaxial bending moment in cycle (a) was close to the X direction, M_{Y-bot} early reached to peak capacity and then deteriorated due to local buckling. M_{X-bot} developed later but could not achieve high capacity as well

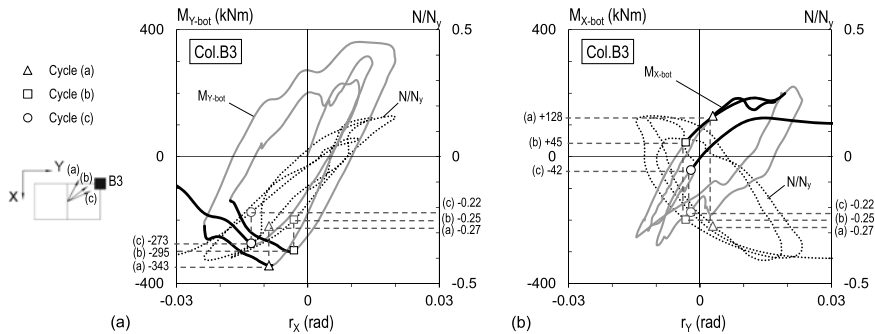


Fig. 3 Column B3's bottom moment (solid line, primary axis) and low-pass filtered axial force (dotted line, secondary axis) versus first-story drift ratio r at 100% Takatori level, and moment and axial force magnitudes at three peaks of bottom moment with compressive axial force condition: **a** $M_{Y\text{-bot}}$ versus r_x ; **b** $M_{X\text{-bot}}$ versus r_y

as linear relation with the increasing story drift r_y because of the damage by local buckling. Similar situations repeated in the subsequent cycles (b) and (c). In overall, the column was subjected to quite large compressive force of approximately $-0.25N_y$ when the local buckling and deterioration of $M_{Y\text{-bot}}$ started occurring.

The influence of compression force magnitude on the column moment deterioration is presented in the followings. Three columns having different levels of axial force variations excluding the high-frequency fluctuation: B1 (N/N_y varied from -0.2 to $+0.0$, *small compression*), B2 ($N/N_y \approx -0.3$ to $+0.1$, *moderate compression*) and B3 ($N/N_y \approx -0.4$ to $+0.2$, *large compression*) are selected to demonstrate. Figure 4 displays the accumulated moment deterioration of those columns presented in terms of skeleton curves whose plotting method is adopted from [11] and can indicate the cyclic degradation of column moment due to local buckling. The symbols showing the timing points of three cycles are also plotted in Fig. 4, indicating the earlier magnitude development of $M_{Y\text{-bot}}$ (black dash line) than $M_{X\text{-bot}}$ (black solid line) within each cycle and consequent deterioration of $M_{X\text{-bot}}$ due to the preceding degraded $M_{Y\text{-bot}}$. Note that, the grey solid and dash lines standing ahead of those black lines show the column behavior accumulated from the preceding smaller excitation levels.

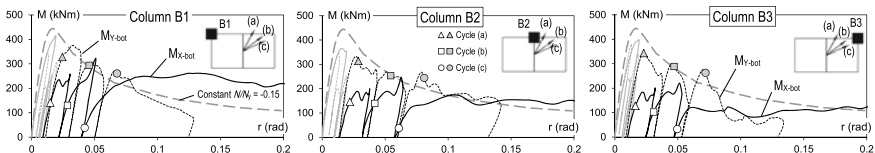


Fig. 4 Accumulated deterioration of bottom moments of three selected columns B1, B2 and B3 characterized by skeleton curves for the negative $M_{Y\text{-bot}}$ and positive $M_{X\text{-bot}}$, with symbols commonly showing both values at the times of 3.35 s, 4.43 s and 5.73 s of three cycles (a), (b) and (c), respectively

In overall, the comparison between dash and solid lines shows that the tangent stiffnesses at the early stage of $M_{X\text{-bot}}$ during each cycle were reduced to approximately 1/2~1/3 times those of $M_{Y\text{-bot}}$, confirming the two-directional correlative moment deterioration.

In addition, the skeleton curve (*grey long-dash line*) by the cyclic bending test conducted prior to the collapse experiment using the same column type under constant compression load of $-0.15N_y$ is included in Fig. 4. Based on that, the difference of moment deteriorations among the three columns is easily recognized. The level of $M_{X\text{-bot}}$ deterioration increases from columns B1, B2 to B3. This is closely related to the different compression force magnitude that developed in the columns, as indicated earlier. Larger compression forces resulted in the more significant column deterioration. Hence, the $M_{X\text{-bot}}$ skeleton curve of column B3 during cycle (c) was much lower, whereas the one of column B2 was almost similar, and the one of column B1 was much higher than the one by component test (with constant $N/N_y = -0.15$).

4 Conclusions

From the results obtained in this study, some conclusions can be drawn.

- In order to understand the experimental collapse behavior, it is necessary to study local responses and deteriorations of members subjected to biaxial bending, and relate them with different stages of the global responses including the progress and mechanism of collapse.
- Experimental results showed totally different deteriorating patterns of biaxial bending moments among all six columns because their axial force magnitudes and variations differed considerably due to the column locations.
- The column deteriorating and damaging sequence is clarified and detailed from these perspectives, in relation with the global response of base shear and story drift displacement during collapse excitation level.
- The cyclic change of displacement direction caused the two-directional accumulated deterioration of columns, reflected by the fact that earlier column damage due to local buckling in the X direction subsequently reduced the capacity in the Y direction.

Acknowledgements This study is a part of “NEES/E-Defense collaborative research program on steel structures”. The author acknowledges Prof. Kazuhiko Kasai (Tokyo Institute of Technology, Japan)-team leader for the overall program, and Dr. Bruce F. Maison (California) for their enthusiastic technical support.

References

1. Kasai K, Ooki Y, Motoyui S, Takeuchi T, Sato E (2007) E-Defense tests on full-scale steel buildings, part 1—experiments using dampers and isolators, Proc Struct Congr ASCE, Long Beach
2. Yamada S, Suita K, Tada M, Kasai K, Matsuoka Y, Shimada Y (2008) Collapse experiment on 4-story steel moment frame, part 1—outline of test results. In: 14th World conference on earthquake engineering, Beijing, China
3. Suita K, Yamada S, Tada M, Kasai K, Matsuoka Y, Shimada Y (2008) Collapse experiment on 4-story steel moment frame, part 2—detail of collapse behavior. In: 14th World Conference on Earthquake Engineering, Beijing, China
4. Isobe D, Han WS, Miyamura T (2013) Verification and validation of a seismic response analysis code for framed structures using the ASI-Gauss technique. *Earthquake Eng Struct Dynam* 42(12):1767–1784
5. Maison BF, Kasai K, Deierlein G (2009) ASCE-41 and FEMA-351 evaluation of E-defense collapse test. *Earthquake Spectra* 25(4):927–953
6. Nam TT, Kasai K (2011) Dynamic analysis of a full-scale four-story steel building experimented to collapse using strong ground motions. In: Proceedings of the international symposium on disaster simulation and structural safety in the next generation DS'11, Kobe, Japan, pp 311–318
7. Lignos GD, Hikino T, Matsuoka Y, Nakashima M (2013) Collapse assessment of steel moment frames based on E-defense full-scale shake table collapse test. *J Struct Eng* 139:120–132
8. Tada M, Tamai H, Ohgami K, Kuwahara S, Horimoto A (2008) Analytical simulation utilizing collaborative structural analysis system. In: Proceedings of the 14th world conference on earthquake engineering, Beijing
9. Yu YJ, Tsai KC, Weng YT, Lin BZ, Lin JL (2010) Analytical studies of a full-scale steel building shaken to collapse. *Eng Struct* 32:3418–3430
10. Inoue I (2003) Theory and design of steel structures (in Japanese), Kyoto University Press
11. Yamada S, Ishida T, Shimada Y, Matsunaga T (2013) Cyclic loading test on RHS columns under bi-directional horizontal forces (in Japanese). *J Struct Constr Eng, Trans AJJ* 683:203–212

Test of a Full-Scale Two-Story Steel X-BRBF: Strong-Axis Instability of Buckling Restrained Brace Associated with Out-of-Plane Bending of Gusset Connections



Dinh-Hai Pham and Chung-Che Chou

1 Introduction

A SBRB with two identical restraining members is formed by welding a steel channel to a flat plate (face plate). Unlike conventional BRBs that have a steel core embedded in the concrete-filled restraining members, the SBRB has a core plate between a pair of restraining members using high strength A490 bolts. This enables inspection after earthquakes by removing restraining members from the core plate. A SBRB is capable of sustaining stable hysteretic responses up to a core axial strain of 3% in the component and frame tests [1–5]. This work was aimed to study the stability of SBRBs with different gusset connections in a two-story steel frame.

2 X-BRBF Subassembly Test

Tests of a full-scale two-story X-BRBF with a span of 9 m and height of 7.54 m (Fig. 1a), were conducted at the National Center for Research Earthquake Engineering (NCREE), Taiwan. The entire test program consisted of two testing phases. In phase 1 test, a two-story X-BRBF subassembly that had SBRB and a dual gusset configuration with free-edge stiffeners in all gusset connections was subjected to a prescribed loading protocol from *AISC Seismic Provisions* (2016) to 1.6% second floor drift (Fig. 1b). In phase 2 test, half of free-edge stiffeners of gusset plate connections were removed from gusset configuration (Fig. 1c) and then tested using the same loading protocol to 2% second floor drift. The moment resisting frame (MRF) was tested after removing all SBRBs and gusset plates to investigate the MRF behaviour (Fig. 1d).

D.-H. Pham · C.-C. Chou (✉)

Department of Civil Engineering, National Taiwan University, Taipei, Taiwan
e-mail: cechou@ntu.edu.tw

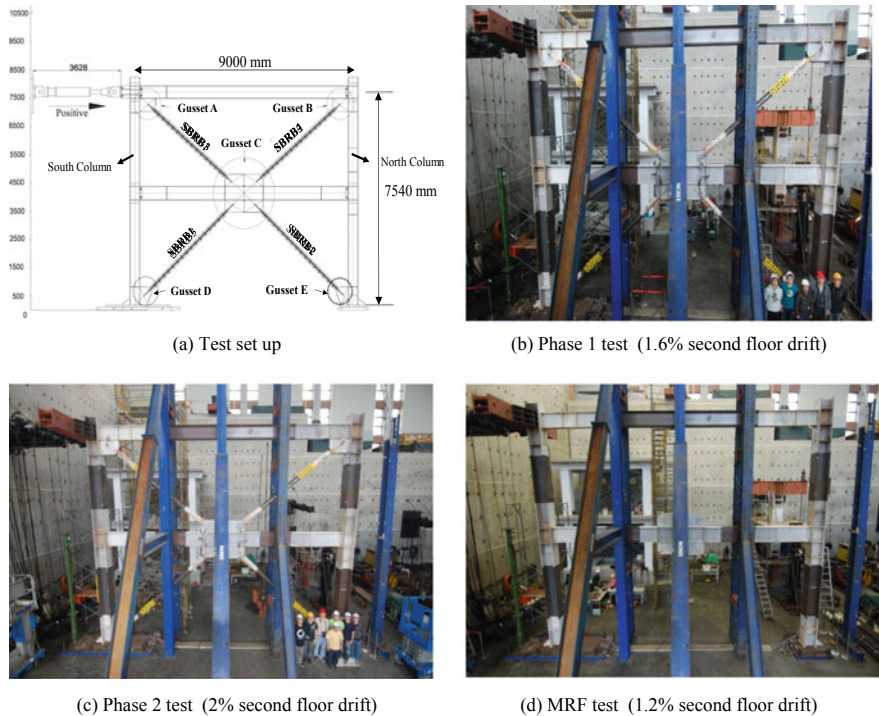


Fig. 1 Tests of a two-story X-BRBF subassembly specimen

3 Test Observation

The X-BRBF specimen performed well up to the second-floor drift of 1.6%, without buckling of SBRBs or gusset plates. By watching through the acrylic, no yielding was found on both ends of the core plate. All gusset plates with free-edge stiffeners did not show yielding in the test. The yielding of the specimen was observed only on the second-floor beam flange near the south column (Fig. 2a) and north column

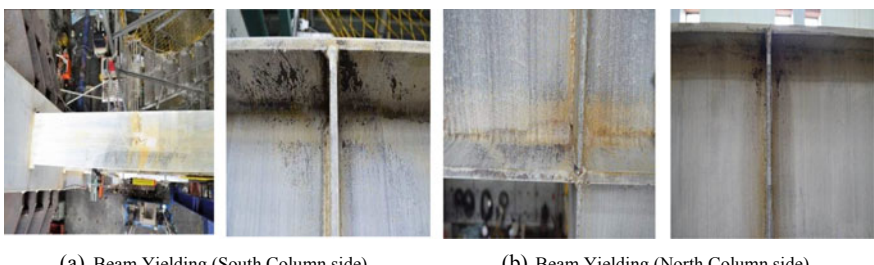


Fig. 2 Observed performance in phase 1 test (1.6% second_floor drift)

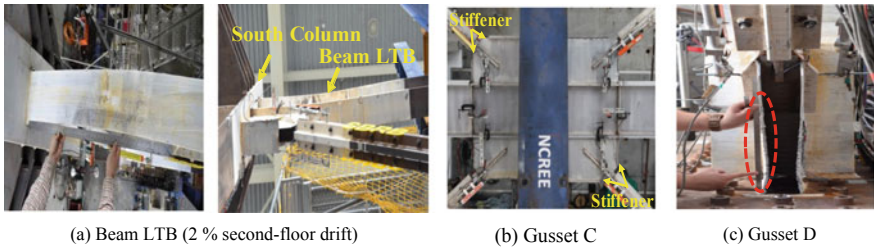


Fig. 3 Observed performance in phase 2 test

(Fig. 2b) at 1.6% second-floor drift. Although beam yielding was observed, no lateral movement or buckling of the beam was visible on the second-floor. The observation showed that the core orientation of SBRBs with the weak-axis transverse to the in-plane movement of the frame is effective to improve the sudden strength drop of BRBs with weak-axis buckling.

After completing the Phase 1 test, all free-edge stiffeners were removed from Gusset B and D, and half of the free-edge stiffeners from Gussets C (Fig. 1a) were removed. The specimen was tested again using the same loading protocol as in Phase 1 test, but up to the second-floor drift of 2%. The lateral-torsional buckling (LTB) of the second-floor beam was clearly seen between the south column and the adjacent lateral support at the second-floor drift of 2%. The out-of-plane movement of the beam top flange was 5 mm (Fig. 3a). Gusset C did not show yielding or buckling at the 2% second-floor drift (Fig. 3b), but Gusset D at the column base without free-edge stiffeners exhibited out-of-plane buckling and web crippling (Fig. 3c) when the SBRB1 was in tension, so-called the frame action buckling.

4 Test Results

Figure 4a shows the lateral force versus lateral displacement of the X-BRBF specimen in Phase 1 and Phase 2 tests. Two phase tests showed similar cyclic responses except the last cycle of 2%. The finite element analysis program ABAQUS [6] was used to correlate the response of MRF up to 2% second floor drift as shown in Fig. 4b. The beams, columns and gusset plates were modelled by the eight node solid elements (C3D8R). The mesh size of 50 mm was used for steel beams, columns and gusset plates. The column base was fixed, and the out-of-plane movement of the beam was constrained at the location of the lateral supports. Figure 4c shows MRF response from the finite element analysis is almost linearly up to 1.2% second floor drift. Figure 4d shows the axial force versus axial displacement of SBRB3 in Phase 1 and Phase 2 tests, which was obtained by subtracting the lateral force of the X-BRBF from that of the MRF. When these SBRBs buckled about the strong-axis of the core plate. Although both SBRBs showed buckling about the strong-axis of the core, the hysteretic loops were still stable with no sign of strength degradation.

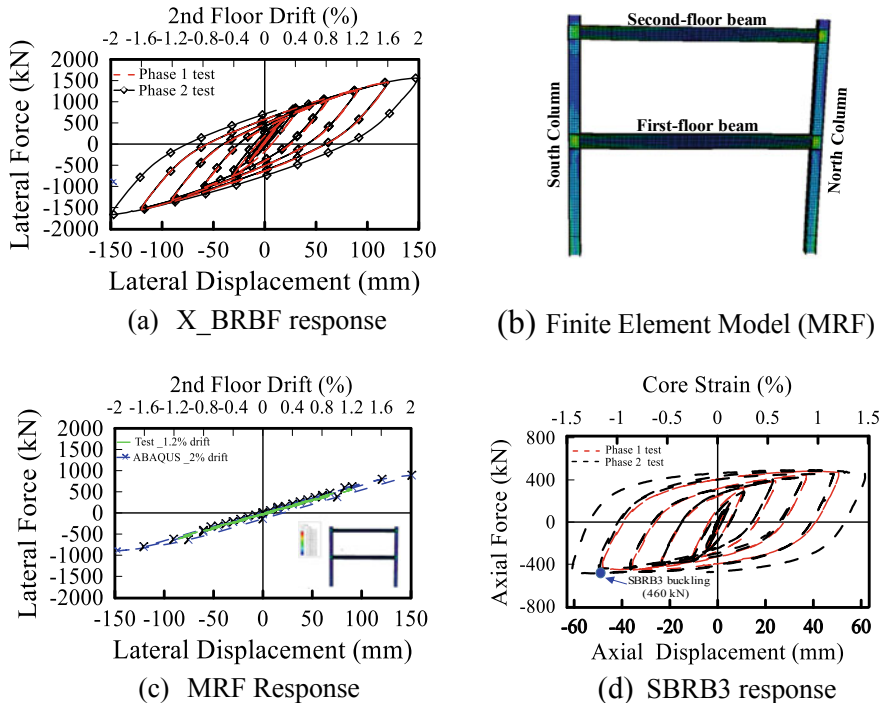


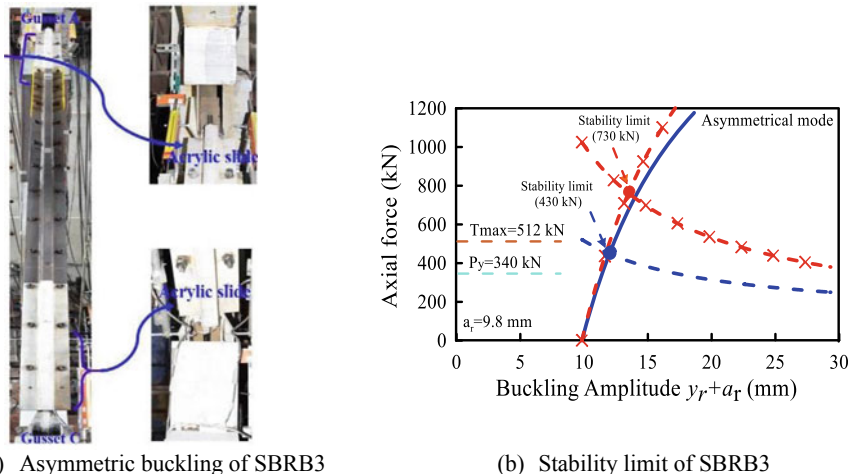
Fig. 4 Test result

5 Stability of Sandwiched Buckling-Restrained Braces

When free-edge stiffeners were removed from gusset connections of the framed specimen in Phase 2 test, the SBRB experienced buckling about the strong-axis of the core plate, which was not observed in previous component tests [1, 3, 5]. At the last peak of 1.6% drift, the Gusset C started to bend in the opposite direction to Gusset A deformation due to the beam LTB. The out-of-plane movement caused the acrylic plates, positioned on both ends of the restraining members, slide in different directions, indicating asymmetrical buckling about the strong-axis of SBRB3 (Fig. 5a). Since all gusset plates at the second floor remained elastic under frame testing at 2% second-floor drift, so that the buckling failure modes were examined by stability limit axial force from Eq. (1) in [7]:

$$N_{\lim} = \frac{(M_p^r - M_0^r)/a_r + N_{cr}^r}{(M_p^r - M_0^r)/(a_r N_{cr}^B) + 1} \quad (1)$$

Figure 5b shows that the stability limit axial force calculated based on Eq. (1). The value of N_{\lim} for the SBRB3 about the strong-axis are lower than those about the



(a) Asymmetric buckling of SBRB3

(b) Stability limit of SBRB3

Fig. 5 SBRB buckling observations

weak-axis. The stability limit for the strong axis buckling of SBRB3 ($= 430$ kN) are close to the buckling forces obtained from the Phase 2 test (Fig. 4c). Moreover, the stability limit predicted for the weak axis buckling of SBRB3 ($= 730$ kN) is much higher than that of the maximum axial load of SBRB ($T_{\max} = 512$ kN), indicating that the weak axis buckling of SBRB associated with in-plane deformation of gusset plate is not possible to occur.

6 Conclusions

The SBRB in the two-story X-BRBF subassembly presents stable hysteretic response in two test phases. At 1.6% second floor drift, the SBRB3 showed asymmetrical buckling about its strong-axis of the core due to lateral-torsional buckling (LTB) of the second-floor beam. The buckling force of SBRB could be estimated based on the stability concept of [7] together with a measured out-of-plane deformation. Not that the strength degradation of the X-BRBF subassembly or SBRB itself was not observed in the strong-axis instability of SBRBs, indicating an acceptable orientation of BRBs for eliminating typical weak-axis buckling of BRBs with sudden strength decrease.

References

1. Chou CC, Chen SY (2010) Subassemblage tests and finite element analyses of sandwiched buckling-restrained braces. Eng Struct 32(8):2108–2121

2. Chou CC, Liu JH, Pham DH (2012) Steel buckling-restrained braced frames with single and dual corner gusset connections: seismic tests and analyses. *Earthquake Eng Struct Dynam* 7(41):1137–1156
3. Chou CC, Chung PT, Cheng YT (2016) Experimental evaluation of large-scale dual-core self-centering braces and sandwiched buckling-restrained braces. *Eng Struct* 116:12–25
4. Chou CC, Hsiao CH, Chen ZB, Chung PT, Pham DH (2018) Seismic tests of Full-scale two-story steel frames with self-centering braces and buckling-restrained braces. In: 11th National conference on earthquake engineering, EERI, Los Angeles, USA
5. Chou CC, Hsiao CH, Chen ZB, Chung PT, Pham DH (2019) “Seismic loading tests of full-scale two-story steel building frames with self-centering braces and buckling-restrained braces. *Thin-Walled Struct* 140:168–181
6. ABAQUS (2003) Standard user’s manual version 6.3. Pawtucket, RI: Hibbit, Karlsson & Sorensen, Inc
7. Takeuchi T, Ozaki H, Matsui R, Sutcu F (2014) Out-of-plane stability of buckling-restrained braces including moment transfer capacity. *Earthquake Eng Struct Dynam* 43:851–856

Using Deterministic Approach to Predict Compressive Strength of High-Performance Fiber-Reinforced Concrete Under Different Sizes



Duy-Liem Nguyen, Phu-Cuong Nguyen, Ngoc-Thanh Tran,
and Tri-Thuong Ngo

1 Introduction

There has been a great and urgent demand to improve the resistance of civil and military infrastructure under serious mechanical as well as environmental loadings. High-performance fiber-reinforced concrete (HPFRC) is one of promising construction materials for the goal of improving the resistances and durability of civil and military infrastructure, since HPFRC could produce its advanced superior properties such as high strength under tension in addition to compression, large ductility and energy absorption capacity [1–3]. Beside, the work-hardening behavior accompanied by multiple tiny-cracks of HPFRC is undertaken by fiber bridging, contributes to preventing catastrophic collapse. However, like normal concrete, HPFRC were discovered to exhibit their size-dependent mechanical properties [4]. The such feature should be considered in the design work using HPFRC to aid structural designers conducting a right design. Even though the testing results of large-sized specimens or structural members would be more precise and authentic, their sizes are very numerous and their tests involves large laboratory, large testing-machines, lots of time and

D.-L. Nguyen (✉)

Faculty of Civil Engineering,

Ho Chi Minh City University of Technology and Education, Ho Chi Minh City, Vietnam

e-mail: liemnd@hcmute.edu.vn

P.-C. Nguyen

Faculty of Civil Engineering, Ho Chi Minh City Open University, Ho Chi Minh City, Vietnam

N.-T. Tran

Department of Civil Engineering, Ho Chi Minh City University of Transport, Ho Chi Minh City, Vietnam

T.-T. Ngo

Faculty of Civil Engineering, Thuyloi University, Hanoi, Vietnam

great cost. Based on the testing data of the previous report [4], the objective of this study work is to build mathematical equations using deterministic approach for the purpose of predicting compressive strength of HPFRC with large-sized specimens or structural members.

2 Deterministic Size Effect Law

Two major approaches have been used to clarify the size-dependent mechanical properties of quasibrittle material: the statistical and deterministic approaches. Weibull's law and Bažant's law have typically been demonstrative for statistical and deterministic approach, respectively. Both such laws contain material parameters representing a significance of size effect on mechanical performances [5]. Developed the law of size effect based on deterministic approach for concrete/quasibrittle materials, described in the following equation:

$$\sigma_N = Bf'_t \left(1 + \frac{D}{D_0} \right)^{-1/2} \quad (1)$$

where D_0 and B are the material parameters, D is the specimen size, f'_t and σ_N are the direct tensile strength and the other material strength, respectively. The other material strength mentioned here could be bending strength or compressive strength of the material.

Figure 1a shows a description of Bažant's size effect theory on strength of quasibrittle material using a logarithmic scale. As described in Fig. 1a, a dashed horizontal line indicates plastic behavior regarding strength criteria; a dashed inclined line with a slope of $-1/2$ indicates purely linear-elastic behavior regarding linear elastic fracture mechanics (LEFM) criteria. The σ_N of concrete and/or HPFRC regarding specimen

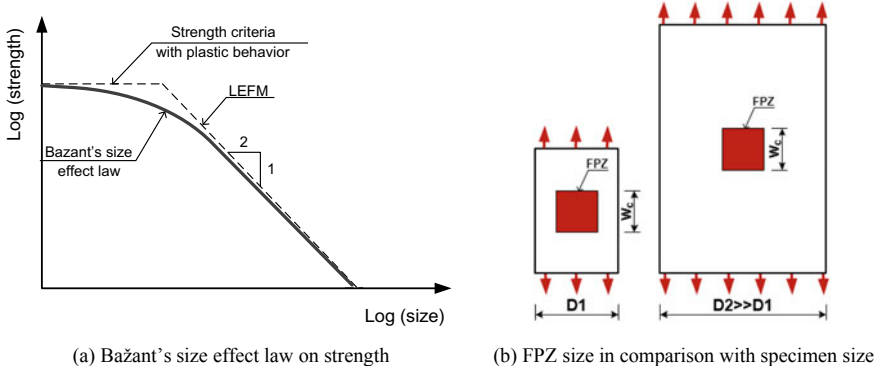


Fig. 1 Description of Bažant's size effect theory and FPZ in different-sized specimens

size is described using a solid curve in Fig. 1a, i.e., a gradual transition between two mentioned dashed line. The curve approaches the horizontal line if the specimen size is small enough and the inclined line for the member with big size.

An explanation for Fig. 1a was based on fracture process zone (FPZ) of material [6]. According to deterministic approach, there is a zone at crack tip (air hole/flaw existing in a material) having a concentration of high stress/deformation called fracture process zone (FPZ). The FPZ results stress redistribution with plastic behavior within FPZ and elastic behavior beyond FPZ. Besides, FPZ size is considered as constant material parameter that is independent on specimen or structure size. However, the FPZ size is dependent much on material type, e.g. the FPZ of normal concrete (w_c) is about 3–3.5 times the diameter of maximum particles embedded in concrete regarding [7]. With the constant value of FPZ size, the ratio of FPZ size to specimen size is different: (a) significant for small-sized specimen tending to global plasticity and negligible for large-sized specimen tending to global elasticity as shown in Fig. 1b.

Although the theory of Bažant's size effect regarding deterministic approach was initially developed for tension and flexure, it was also applied for compression [8]. This is due to compressive failure were originated from local tension or shear occurring at air hole/flaw inside specimen under loading.

3 Testing Results and Analytical Investigation

3.1 Testing Results

Three series of compressive specimens were tested with same cube shapes but different sizes as follows: side length of 70.7 mm (denoted CU070), side length of 100 mm (denoted CU100) and side length of 150 mm (denoted CU150). Each series were prepared with two forms of HPFRCs: HPFRC1 including no fiber, HPFRC2 including 1.0 vol.% macro-hooked fibers blended 0.5 vol.% micro-smooth fibers. The detail of experimental test was reported in [4]. Table 1 provides the composition of HPFRC matrix used in this study. The macro-hooked fibers used in the HPFRC2 had a aspect ratio (length/diameter) of 35 mm/0.5 mm and a tensile strength more than 1200 MPa while the micro-smooth fibers had a aspect ratio of 13 mm/0.2 mm and a tensile strength more than 2500 MPa. Figure 2 shows the photos of the hybrid fibers added in the HPFRC2. It is noticed that sand in HPFRC plays the coarse aggregates role whereas silica fume and fly-ash play the fine aggregates role due to their significantly finer particles. The finer-sized aggregate will generate smaller porosity around this

Table 1 Composition of HPFRC matrix

Cement (Insee, PC40)	Silica fume	Silica sand	Fly-ash	Superplasticizer	Water
0.80	0.07	1.00	0.20	0.04	0.26

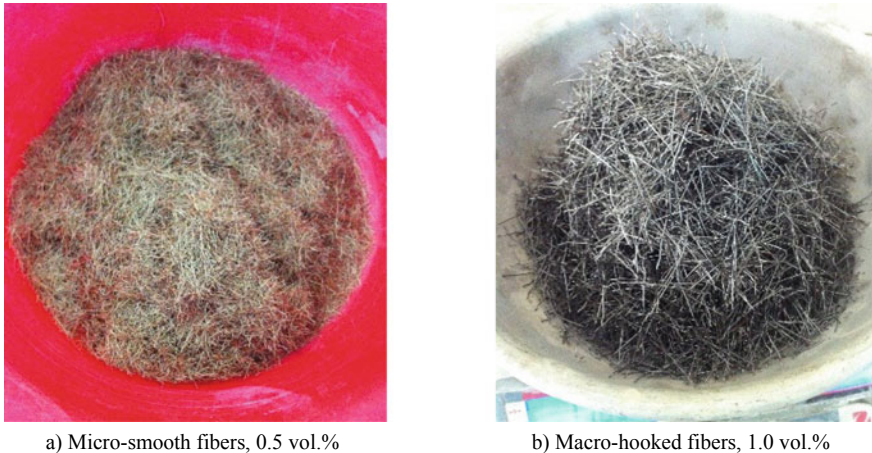


Fig. 2 Two types of steel fibers used in HPFRC2

aggregate particle owing to the lower capillary attraction of water [9]. The densified microstructure of HPFRC consequently produce its high failure strength.

Figure 3 shows the compressive behaviors of HPFRC while Fig. 4 shows their size effect on compressive strength. As described in Fig. 3, a clear size effect was observed: the compressive strength was markedly declined with increases in specimen size. Table 2 provides the compressive strengths of all tested specimens, which were used for determining parameters in Eq. (1) by analytical analysis. The testing results also revealed that HPFRC exhibited a clear size effect in compression

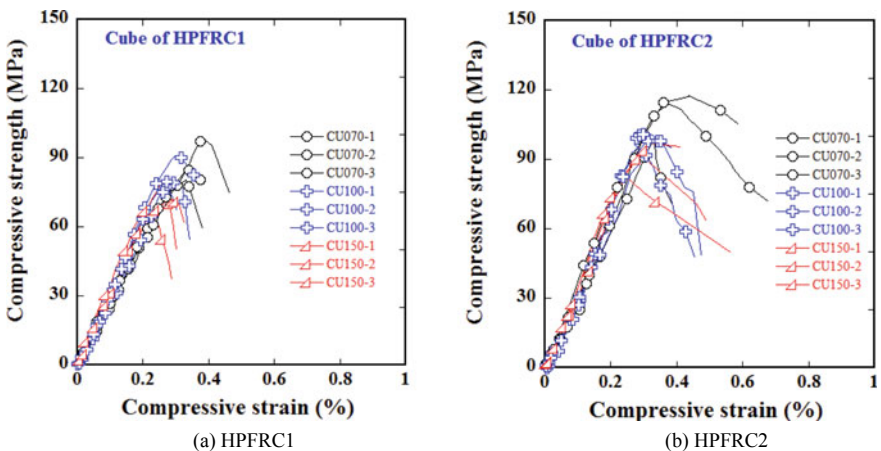


Fig. 3 Compressive behaviors of the investigated HPFRC

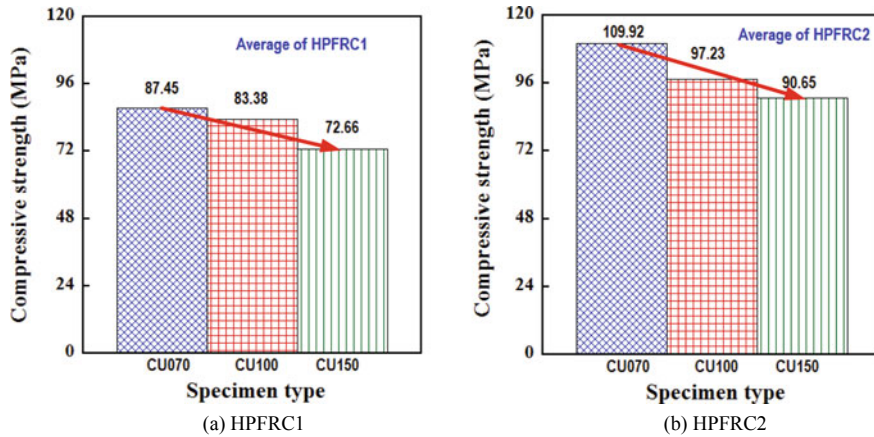


Fig. 4 Size-dependent compressive strength of the investigated HPFRC

Table 2 Compressive strength of the investigated HPFRC

Series	Compressive strength, f'_c (MPa)	
	HPFRC1	HPFRC2
70.7 × 70.7 × 70.7 (CU070)	84.49	98.07
	80.41	114.36
	97.44	117.32
	Average value	87.45
100 × 100 × 100 (CU100)	79.94	99.06
	79.40	101.01
	90.80	91.63
	Average value	83.38
150 × 150 × 150 (CU150)	78.09	97.15
	71.63	83.56
	68.26	91.23
	Average value	72.66

like normal concrete, which was recommended using conversion factors according to Vietnamese code of TCVN 8218:2009 [10] for different sizes and shapes of specimens.

3.2 Analytical Investigation on Bažant's Theory of Size Effect

To find the values of B and D_0 , Eq. (1) could be written into Eq. (2) and using testing data (σ_{Ni}, D_i) for regression analysis.

$$\left(\frac{f'_t}{\sigma_N}\right)^2 = \frac{1}{B^2 D_0} D + \frac{1}{B^2} \quad (2)$$

$$\text{or } y = ax + b \quad (3)$$

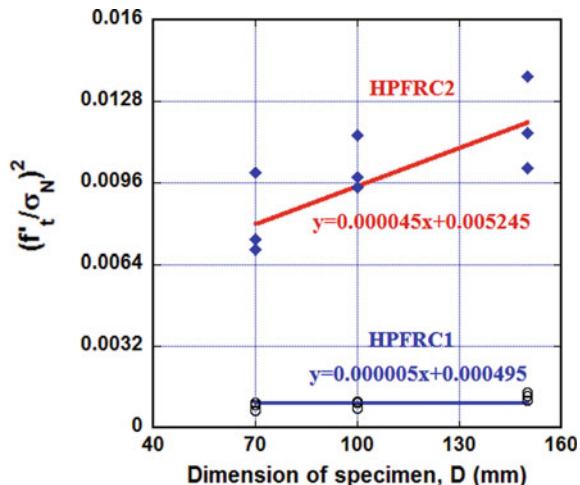
where $y = (f'_t/\sigma_N)^2$, $x = D$, $a = 1/(B^2 D_0)$, $b = 1/B^2$, σ_N in this case is the compressive strength, f'_c (MPa), using cube-shaped specimen. According to testing results of [11], the tensile strengths of HPFRC1 and HPFRC2 were 2.53 MPa and 9.81 MPa, respectively. Utilizing the least square technique and linearized regression as shown in Eq. (3), the values of a and b can be found using Eqs. (4) and (5) with the data: $y_i = (f'_t/\sigma_{Ni})^2$ and the corresponding $x_i = D_i$, the average value $y_{av} = \frac{1}{n} \sum_i y_i$ and $x_{av} = \frac{1}{n} \sum_i x_i$. Finally, the values of $B = \sqrt{1/b}$ and $D_0 = 1/(B^2 a)$ can be simply obtained.

$$a = \frac{\sum_i [(y_i - y_{av})(x_i - x_{av})]}{\sum_i (x_i - x_{av})^2} \quad (4)$$

$$b = y_{av} - a \cdot x_{av} \quad (5)$$

Figure 5 displays the least-squares method to attain the material parameters according to Bažant's theory of size effect. Each HPFRC type was analyzed from 9 cube specimens. Figure 6 shows the analysis curves of Bažant's size effect on com-

Fig. 5 Achievement of material parameters according to Bažant's theory of size effect using the least-squares method



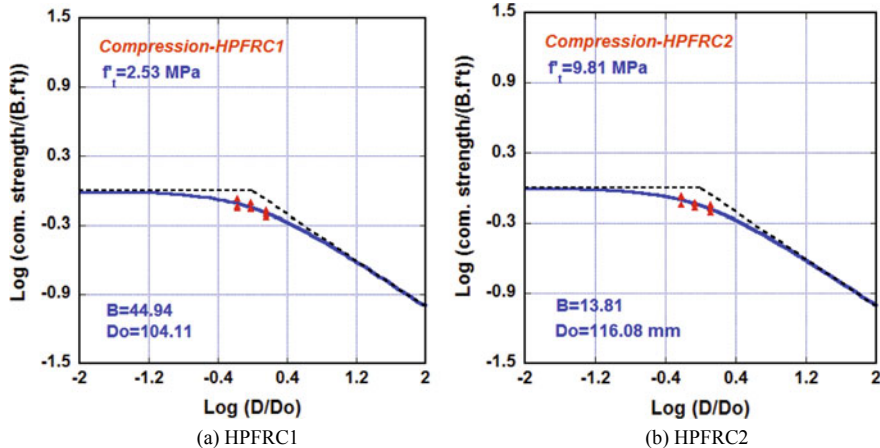


Fig. 6 Analysis curves according to Bažant's theory of size effect

pressive strength of the investigated HPFRC. As shown in Fig. 6, the testing data for two HPFRCs, including no-fiber composite (HPFRC1) and hybrid-fiber composite (HPFRC2), were in the transition zone between LEFM criterion and strength criterion. The mathematical equations for predicting compressive strength with cube shapes were given in Eqs. (6) and (7) for HPFRC1 and HPFRC2, respectively.

$$f'_c = 113.69 \left(1 + \frac{D}{104.11} \right)^{-1/2} \quad (6)$$

$$f'_c = 135.45 \left(1 + \frac{D}{116.08} \right)^{-1/2} \quad (7)$$

4 Conclusion

The drawn conclusions can be listed from this investigation as follows:

- The mathematical equations for compressive strength of the HPFRCs with different cube-sized specimens were derived using deterministic approach.
- The testing data for two investigated HPFRCs with and without fiber were in the transition zone between strength criterion and LEFM criterion.
- The derived mathematical equations were very useful in predicting compressive strength of large specimens or structural member.

Acknowledgements This research was funded by the Vietnam National Foundation for Science and Technology Development (NAFOSTED) under grant number 107.01-2017.322. The author is thankful for the support of finance.

References

1. Nguyen DL, Song J, Manathamsombat C, Kim DJ (2015) Comparative electromechanical damage-sensing behavior of six strain-hardening steel-fiber-reinforced cementitious composites under direct tension. Composites: Part B 69:159–168
2. Nguyen DL, Kim DJ, Thai DK (2019) Enhancing damage-sensing capacity of strain-hardening macro-steel fiber-reinforced concrete by adding low amount of discrete carbons. Materials 12:938. <https://doi.org/10.3390/ma12060938>
3. Song J, Nguyen DL, Manathamsombat C, Kim DJ (2015) Effect of fiber volume content on electromechanical behavior of strain-hardening steel-fiber-reinforced cementitious composites. J Compos Mater 49(29):3621–3634 (2015)
4. Nguyen DL, Thai DK, Ngo TT, Tran TK, Nguyen TT (2019) Weibull modulus from size effect of high-performance fiber-reinforced concrete under compression and flexure. Constr Build Mater 226:743–758. <https://doi.org/10.1016/j.conbuildmat.2019.07.234>
5. Bažant ZP (1984) Size effect in blunt fracture: concrete, rock, metal. J Eng Mech 110(1984):518–535
6. Fládr J, Broukalová I, Bflý P (2013) Determination of conversion factors for compressive strength of HPFRC measured on specimens of different dimensions. In: Proceedings of AFGC-ACI-fib-RILEM international symposium on ultra-high performance fibre-reinforced concrete, UHPFRC 2013, Oct 1–3, 2013, Marseille, France
7. Bažant ZP, Pijaudier-Cabot G (1989) Measurement of characteristic length of nonlocal continuum. J Eng Mech 115(4):755–767
8. Kim JK, Yi ST (2002) Application of size effect to compressive strength of concrete members. Sādhanā 27(4):467–484
9. Igashiki S, Bentur A, Mindess S (1996) The effect of processing on the bond and interfaces in steel fiber reinforced cement composites. Cement Concr Compos 18(5):313–322. [https://doi.org/10.1016/0958-9465\(96\)00022-4](https://doi.org/10.1016/0958-9465(96)00022-4)
10. TCVN 8218:2009 (2009) Hydraulic concrete—technical requirements. Vietnamese code
11. Tri-Thong N (2018) Study on manufacture and mechanical behaviors of high performance fiber reinforced concrete under normal curing condition with various sizes and shapes of specimens. Master thesis, May 2018, Ho Chi Minh City University of Technology and Education, Vietnam, 56 p

Validation of Simulated Behavior of Blast Loaded Reinforced Concrete Columns Retrofitted with Tyfo® Fibrwrap® System Through Experiments



J. Quek, C. L. Liu, J. V. P. Musngi, and P. B. Malalasekara

1 Introduction

The increasing threats from terrorist attacks over past decades have brought about the focus on protective hardening techniques to enhance the capacity of existing structures. One of the emerging protective hardening techniques is the use of Fibre Reinforced Polymer (FRP). Column protective hardening by simply ‘wrapping’ it with FRP provides additional strength and ductility in the event of blast threats [1]. Various analytical models such as SBEDS, FWrap, and CBARD have been developed to predict the response of structural elements under blast loads [2]. These models however, rely on the designer to provide peak pressure and impulse of the blast event as inputs to carry out the analysis and to obtain the response of the structural element.

The incorporation of blast prediction models such as Conventional Weapons Effect (CONWEP) model in the popular Finite Element Analysis (FEA) programs has allowed the designers to gain a holistic view of the propagation of blast waves with respect to time in addition to providing critical inputs such as peak pressure. These software, in fact, are able to predict the response of structural elements subjected to a blast load and their failure modes.

However, works has been carried out to validate the blast prediction models given in FEA software packages using CONWEP model and the reliability of using such analysis results for actual designs are far and few between. The objective of this paper is to compare the results of FEA to FRP retrofitted Reinforced Concrete (RC) columns subjected to simulated blast loads from a Shock Tube and to near contact blast load and explore its applicability in the actual engineering designs.

J. Quek (✉) · J. V. P. Musngi · P. B. Malalasekara
Fyfe Asia Pte. Ltd., 6 Clementi Loop, 129814 Singapore, Singapore
e-mail: jquek@aegion.com

C. L. Liu
K & C Protective Technologies, 125A Lorong Toa Payoh, Singapore 311125, Singapore

2 Test Programs

For this paper, two experimental programs were used to compare and validate the simulation results from a FEA analysis. The first test program was using Shock Tube to simulate the impact of blast load on columns. Tests were carried out on a control specimen and retrofitted specimens. The second test program was on retrofitted columns subjected to an actual blast impact of 20 kg equivalent TNT charge in a near contact with the column. In both cases, the columns were retrofitted with the Tyfo® Fibrwrap® System, a proprietary FRP material. The level of enhancement achieved through the retrofitting was dictated by the type of materials used and the final configuration.

2.1 Shock Tube Test

The Shock Tube test program was carried out at the Structures Laboratory of the Department of Civil Engineering at the University of Ottawa in Canada. Four column specimens were prepared at the laboratory and properties of all the constituent materials were tested to obtain the actual stress-strain parameters instead of expected or specified properties. Only two out of the four specimens were used for comparison for this paper.

Test Specimen. Each column specimen measured 150 mm (depth) × 300 mm (width) × 2440 mm long with 8 nos. of 11.3 mm diameter longitudinal bars and 6.3 mm diameter ties spaced at 150 mm center to center. One of the columns was retrofitted with FRP while the other served as a control specimen. The FRP retrofitted column was wrapped with Tyfo® SEH-51A, a Glass FRP composite material. The corners of the FRP retrofitted column was rounded to 25 mm radius of curvature, to avoid stress concentrations at the corners.

Material Properties. Tyfo® SEH-51A composite comprised of custom weaved, unidirectional glass fabric and a two-component epoxy matrix. Table 1 summarizes the composite properties of Tyfo® SEH-51A.

Each column was casted in concrete prepared in separate batches and specified to achieve a 30 MPa 28-day compressive strength. The actual tested values of compressive strength are summarized in Table 2.

Table 1 Composite properties of Tyfo® SEH-51A

Property	Value
Ultimate tensile strength in main fibre direction	575 MPa
Elongation at break	2.2%
Tensile modulus	26.1 GPa
Thickness per layer	1.3 mm

Table 2 Compressive strength of concrete

Specimen designation	Tested cylinder compressive strength, f'_c (MPa)
Control	38.5
Retrofitted	30.4

Table 3 Reinforcement steel grade

Rebar type	Yield strength, f_y (MPa)	Yield strain, ϵ_y	Ultimate strength, f_u (MPa)
Longitudinal	582	0.0028	722
Stirrups	518	0.0026	656

Fig. 1 Shock tube test set up for control column (left) and retrofitted column (right)

The reinforcement bars are from the same batch for both samples and the tested properties are summarized in Table 3.

Test Set Up. The columns were oriented to have a weak axis bending once impacted by the simulated blast load. No axial load is applied to the column to avoid a complicated test set up and eliminate uncertainty in test data during the dynamic response that arises from varying axial load [3]. The Load Transfer Device (LTD) was used to collect pressure generated from the Shock Tube and transferred the pressure as a series of point load along the length of the column. The 19 mm diameter steel rod near the ends of the columns serves as support and contact point to RC column through a tangential contact. This support configuration closely resembles simple support reactions [4].

The retrofitted column was installed with two separate layers of Tyfo® SEH-51A FRP composite. The first layer consisted of plies that were orientated longitudinally, parallel to the main axis of the column or in the vertical direction, while the second layer consisted of plies that were orientated at a right angle to the main axis of the column or in the horizontal direction.

Figure 1 illustrates the Shock Tube test set up. The pressure generated from the Shock Tube was recorded using a pressure gauge, which provided time-history details of the simulated blast condition.

2.2 Near Contact Blast Test

Test Specimen. The RC column test specimens were prepared, casted, and fabricated in Singapore and sent to the testing facility in New Mexico, U.S.A for testing. The specimens consist of 2 nos. of 1 m diameter circular RC columns with 12 nos. of 32 mm diameter main rebar and 10 mm diameter ties spaced at 250 mm c/c and casted together with the 1.3 m × 1.3 m × 450 mm thick footing reinforced with 9 nos. of 25 mm diameter rebar, top and bottom, in both directions. The total height of each RC specimens is 3.45 m (see Fig. 3). A 900 mm long, 60 × 60 × 4 mm square hollow steel section was embedded 300 mm onto the top of each columns and served as restraint to the top of the RC columns.

The cured RC column specimens were retrofitted with Tyfo® Fibrwrap® System. Each column specimens were retrofitted with 12 layers of Tyfo® SCH-11UP at full height (6 layers horizontal and 6 layers vertical) followed by 5 layers of Tyfo® SEH-51A at lower 2 m height of the column.

Material Properties. The specified strength for the reinforcing steel was 460 MPa while the tested concrete compressive strength reached was 60 MPa.

Test Set Up. An amount of explosive material (C4) that can produce a blast of 20 kg TNT equivalent was placed in between the two columns. The objective was to create a near-contact blast wave which simulates a real-world threat scenario. Figure 2 illustrates the Near Contact Blast test set up.

Fig. 2 Near contact blast test set up



3 Finite Element Simulation

Simulation for both cases is carried out using Abaqus/CAE. A 3-D finite element model was constructed representing the configuration on actual experiments set up. The RC columns and footing were modelled as 8-noded elements (C3D8R) while the rebars were modeled as 2-noded linear beam (B31). The FRP was modelled as composite layup with 4-noded thin shell elements (S4R).

3.1 Shock Tube Test

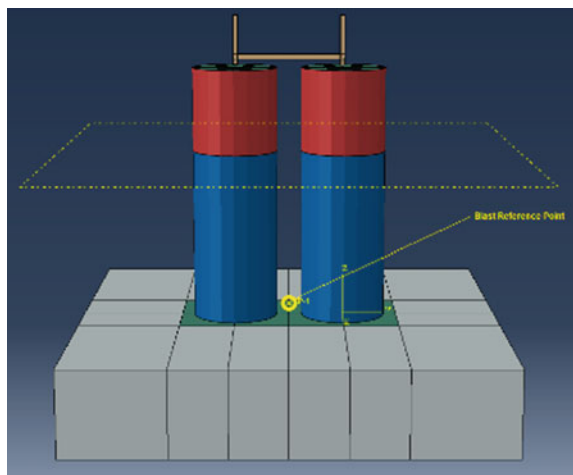
The simulation was carried out using the time-history data for pressure collected during the test as an input parameter in Abaqus/CAE. Further, the exact properties of materials measured through tests were used in the model. This allowed all the input parameters to be nearly identical as the actual test conditions.

3.2 Near Contact Blast Test

The blast load simulation was based on CONWEP model initially developed by [5]. Currently CONWEP is a built-in functionality in Abaqus which allows for modelling of an open-air blast. A reference point was assigned to represent the location of the blast (Fig. 3).

After several simulations, it was concluded to limit the duration to period of 0.06 s as the blast effects have dissipated after this point. Figure 4 shows the pressures propagated by CONWEP loading as it dissipates with time.

Fig. 3 Abaqus model with reference point for blast source



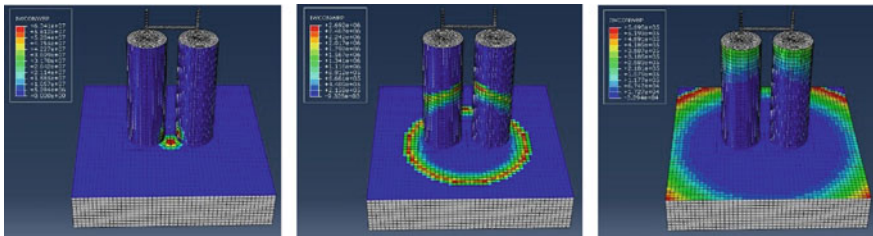


Fig. 4 Blast load propagation with time

The rebars were embedded to the concrete column and footing using the Abaqus embedded region constraints. The concrete-FRP interface is assumed to have perfect bond and modelled using Abaqus tie constraint.

4 Analysis Results and Comparison

Figure 5 shows the final state of mid span deflection in both simulation and the Shock Tube blast experiment. The recorded final mid-span deflection resulting from the experiment for the control specimen was 222 mm while the result from the simulation was 197 mm. The experiment resulted a mid-span deflection of 99 mm for the retrofitted element while the simulation provided a maximum result deflection of 136 mm.

The maximum Von Mises stress for the reinforcement bar in the control model and retrofitted model was 657 MPa and 593 MPa respectively. Figure 6 shows the von mises stresses in each of the model.

Figure 7 shows visual comparison of the final state of damages between the simulation and experimental cases for the near contact blast. The damages obtained in the

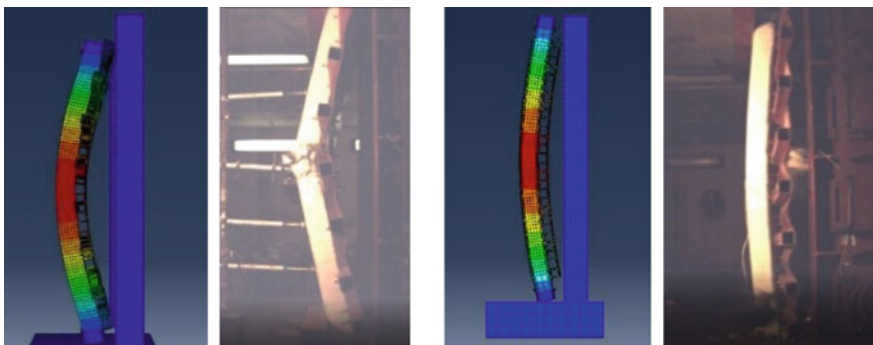


Fig. 5 Behavior of the columns after the blast for the control (left) and retrofitted specimen (right)



Fig. 6 Von Mises stress on steel reinforcement for the control (left) and retrofitted specimen (right)

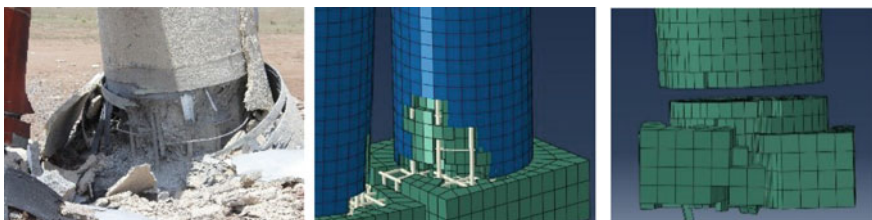


Fig. 7 Visual comparison of actual test (left) and simulation with (middle) and without retrofitting (right)

Abaqus/CAE simulation closely resembles the damages from the actual experimental results.

After the experimental blast test, the depth of the damage from the columns were measured and recorded. The average depth of the damage from the test specimen is around 132 mm while the depth of the average depth of damage from the simulation with retrofitting is 135 mm. The comparison shows agreement between the two. A separate model was created in which the column was not retrofitted. The analysis results showed that the un-retrofitted column was severely damaged leading to a complete collapse compared to the retrofitted one. This indicated the effectiveness in FRP as a protective hardening measure. The final observations made after the experimental test concluded that some of the reinforcement yielded during the blast. The locations with high stress concentrations of the reinforcement were observed in the FEA simulation which shows that the maximum Von Mises Stress is 576 MPa. Figure 8 shows the Von Mises stresses of the reinforcement steel. The locations of the highly stressed reinforcements show similarities to the test results.

The experiment results showed that the footings moved apart from each other laterally due to the weak support provided by the soil. The overall movement of the columns were consistent with the Abaqus/CAE simulation results.

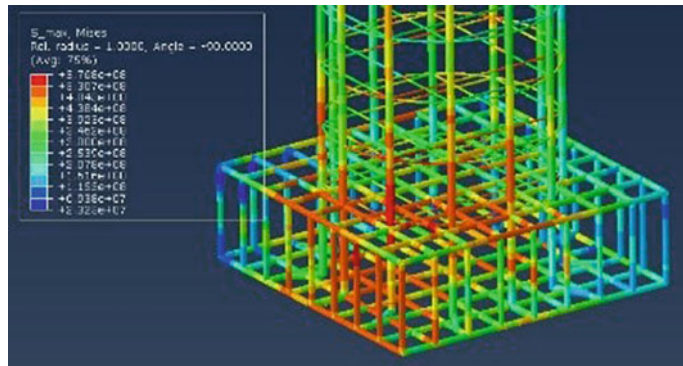


Fig. 8 Von mises stresses in the steel reinforcement

5 Conclusions

Two separate field experiments were used to validate the simulation results of blast loads using Abaqus/CAE. The first experiment used a Shock Tube to simulate a blast impact while the other was with a blast load created using a charge weight of 20 kg TNT equivalent. Table 4 shows the summary of the damage condition for near contact blast test while Table 5 shows the midspan deflection comparison for the Shock Tube test.

In both cases, the simulated behavior showed congruency with the experiment. For the Shock Tube test, retrofitting the column with FRP exhibited a significant enhancement in flexural strength which is represented by reduction in deflection of about 98% for the actual experiment and 64% for the simulation. In addition, the stresses in the steel reinforcement were significantly reduced up to 11%. The resulting values for deflection for the control specimen from both simulation and experiment was near identical with simulation resulting higher values. The simulation results for column retrofitted with FRP was 37% higher than the experimental value. For the Near Contact Blast Test simulation, retrofitting the columns demonstrated

Table 4 Comparison of concrete damage

Criteria	Experiment results	Simulation results
Depth of concrete damage (mm)	132	135

Table 5 Comparison of midspan deflection

Column	Experiment results (mm)	Simulation results (mm)
Control	197	222
Retrofitted	99	136

improvement in confined strength which is represented by the reduced depth and volume of damage compared to the un-retrofitted column.

The comparisons showed that FEA simulation provides a conservative and accurate depiction for a response of a structural element subjected to a blast load. Therefore, FEA simulation can reliably be used in actual engineering applications for design of protective hardening.

References

1. Jacques E, Lloyd A, Imbeau P, Palermo D, Quek J (2015) GFRP-retrofitted reinforced concrete columns subjected to simulated blast loading. *J Struct Eng (United States)* 141(11):1–13
2. Quek, J, Ow MC (2013) SDOF analysis of protective hardening design for reinforced concrete columns using fibre reinforced polymer wrap. In: Fourth Asia-Pacific conference on FRP in structures (APFIS 2013), pp 11–13
3. Lloyd A (2010) Performance of reinforced concrete columns under shock tube induced shock wave loading. Master's thesis, University of Ottawa, Ottawa
4. Jacques E (2011) Blast retrofit of reinforced concrete walls and slabs. Master's thesis, Department of Civil Engineering, University of Ottawa, Ottawa
5. Kingery CN, Bulmash G, (1984) U.S. Army ballistic research laboratory. Air blast parameters from TNT spherical air burst and hemispherical surface burst. Aberdeen proving ground, MD: Ballistic Research Laboratories (1984)

Vibration-Based Damage Identification of Steel Moment-Resisting Frames



Luc-Hoang-Hiep Nguyen and Duc-Duy Ho

1 Introduction

Indisputably, ensuring the undamaged condition for structures during their service life is an important target. To keep the structure safe and avoid serious casualty, timely identification of damage in structures is of paramount importance. Structural health monitoring (SHM) not only can identify structural damage but will remarkably reduce maintenance costs. In these days, many damage detection methods based on vibration characteristics have been developed and applied in a wide range of structures. In which, researches using vibration characteristics, including natural frequencies and mode shapes, to diagnose damage were conducted from 1970s [1]. Along with the rapid development of researches on SHM, damage detection methods and diagnostic formulas were introduced to reduce costs and as a replacement to destructive testing. Mathematical formulas based on frequency change of beam to detect failure positions on beams had been widely studied [6]. In addition, mode shapes are also used in many researches to diagnose structural health and achieved considerable success, one such method is the modal assurance criterion [5]. In order to determine destructive position and level by using frequencies and mode shapes, modal strain energy based-damage detection methods were introduced [7]. After proving the capability of detecting damage in the structure with minor damage, modal strain energy methods were developed by many researchers, such as a research to detect damage for beams [4].

These aforementioned methods have advantages in hybrid ways to efficiently detect damages in various structures. Currently, one of the most common retrofit

L.-H.-H. Nguyen
Simpson Strong-Tie Company Inc., Pleasanton, California, USA
e-mail: hnguyen3@strongtie.com

D.-D. Ho (✉)
Faculty of Civil Engineering, Ho Chi Minh City University of Technology (HCMUT),
VNU-HCM, Ho Chi Minh City, Vietnam
e-mail: haducduy@hcmut.edu.vn

solutions for soft-story buildings is to use steel moment-resisting frames. A special moment-resisting frame is an engineering solution that consists of structural steel comprised by steel columns, a steel beam connecting between the columns and at the beam-to-column connection the use of bolted yield-link connections. This rigid structure is strong enough to withstand tremendous shaking during an earthquake. The yield-link technology will absorb the brunt of lateral forces caused during an earthquake, the beam and columns are designed to remain essentially elastic. However, due to be designed to be damaged first, the yield-links need to be regularly monitored and determine when they should be replaced. Damage detection methods, hence, are empirically important to ensure the best working conditions for the structure.

To obtain vibration characteristics, along with using sensors which are embedded on the real structures, finite element analysis tools, such as SAP2000, ABAQUS, ANSYS, OpenSEES, etc. are also convenient and cost effective. Among these tools, OpenSEES which is a powerful software framework allowing users to create finite element applications for simulating the response of structural and geotechnical systems subjected to earthquakes is used to obtain vibration characteristics including natural frequencies and mode shapes in this research.

2 Vibration-Based Damage Detection Methods

2.1 Frequency Change-Based Damage Detection Method

The method is based on the fact that natural frequencies are sensitive indicators of structural responses. When damage happens, natural frequencies decrease, so these frequencies are used as a diagnostic parameter in structural assessment procedures. Some researches using frequency change to detect damage were conducted [1, 6]. With natural frequencies of undamaged and damaged conditions are f and f^* , respectively, the frequency change (Δf) which is not equal 0 when having any damage is evaluated by

$$\Delta f = \left(\frac{f - f^*}{f} \right) \times 100\% \quad (1)$$

2.2 Modal Assurance Criterion

The modal assurance criterion (MAC) is a statistical indicator which is often to be used to pair mode shapes derived from analytical models with those obtained experimentally [5]. For damage-detecting purpose, MAC is used to pair mode shapes

between various modes and between damaged and undamaged models. The MAC value is bounded from 0 to 1, with 1 indicating fully consistent mode shape while a value near 0 indicating that the modes are not consistent. The MAC is calculated as a normalized scalar product of the two sets of different vectors. For two models with n modes of vibration, the MAC value is expressed as

$$MAC(A, X) = \frac{\left| \sum_{j=1}^n \{\phi_A\}_j \{\phi_X\}_j \right|}{\left(\sum_{j=1}^n \{\phi_A\}_j^2 \right) \left(\sum_{j=1}^n \{\phi_X\}_j^2 \right)} \quad (2)$$

where $MAC(A, X)$ indicates the causal relationship between models A (the undamaged model) and X (the damaged model); $\{\phi_A\}_j, \{\phi_X\}_j$ is j th mode shapes of the undamaged and damaged models, respectively.

2.3 Modal Strain Energy-Based Damage Detection Method

Modal strain energy is more sensitive than other indicators, such as natural frequencies and mode shapes in damage detection. Basing on the variety in modal strain energy, a damage detection method is proposed [3]. This method uses two vibration characteristics, including frequencies and mode shapes, of two different statuses for structural damage detection.

If a beam is subdivided into N_d elements as shown in Fig. 1, in order to account for all measured modes, nm , the damage index due to stiffness reduction at j th element is expressed as

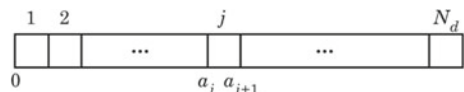
$$\beta_j = \frac{k_j}{k_j^*} = \frac{\sum_{i=1}^{nm} \gamma_{ij}^*}{\sum_{i=1}^{nm} [\gamma_i \times g_i(\lambda, \Phi) + \gamma_{ij}]} \quad (3)$$

where β_j is the damage index at j th element; k_j is the flexural stiffness at j th element of the undamaged beam; k_j^* is the flexural stiffness at j th element of the damaged beam; $\gamma_{ij}^*, \gamma_{ij}, \gamma_i, g_i(\lambda, \Phi)$ are parameters to calculate the j th element stiffness [3].

In order to obtain the damage position, a normalized damage index is introduced as

$$Z_j = \frac{\beta_j - \mu_{\beta_j}}{\sigma_{\beta_j}} \quad (4)$$

Fig. 1 A schematic illustrating a beam's N_d sub-elements



where Z_j is the normalized damage index at j th element; μ_{β_j} and σ_{β_j} represent the mean and standard deviation of the damage indices, respectively. A statistical algorithm is applied: a value, Z_o , corresponding to a degree of reliability for the results is chosen. At j th element, if $Z_j \geq Z_o$, the structure is damaged at this element. If $Z_j < Z_o$, the structure is not damaged at j th element. In this research, two values of Z_o , $Z_o = 1.5$ and $Z_o = 2$ [3], corresponding with the degrees of reliability of 93.3% and 98%, respectively, are used.

3 Numerical Verification

In order to verify the level of accuracy of three considered methods in damage detection for moment-resisting frames, an one-story, one-bay steel moment-resisting frame with yield-link connections (yielding area of 10.887E-4 m² and yielding length of 0.1524 m) from Simpson Strong-Tie company is used. In this research, OpenSEES is utilized for modal analysis to get the frame's natural frequencies and mode shapes of the first three modes which are the input data for the damage detection methods.

3.1 Model Geometry

The primary components of the yield-link connection are the links installed on the beam flanges, which are modelled using rotational springs (zero-length element with uniaxial multilinear material in OpenSEES). Elastic Timoshenko beams which are capable of taking into account shear deformation and rotational bending effect are used to model beam and columns in OpenSEES. Figure 2 shows an example of a



Fig. 2 Simpson strong-tie's moment-resisting frame (www.strongtie.com)

Simpson Strong-Tie's moment-resisting frame. Figure 3 depicts the model geometry. Table 1 shows data of the frame.

For the moment and rotation relationship of the yield-link [2] (Fig. 4), 6 points (2 points on every segment) are chosen. Note that S1S denotes the starting point of

Fig. 3 The model geometry

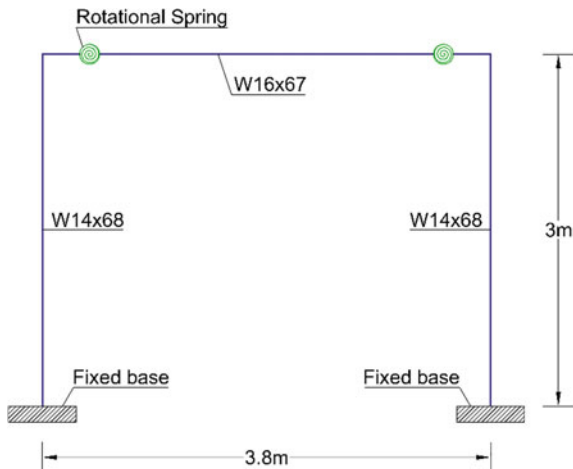
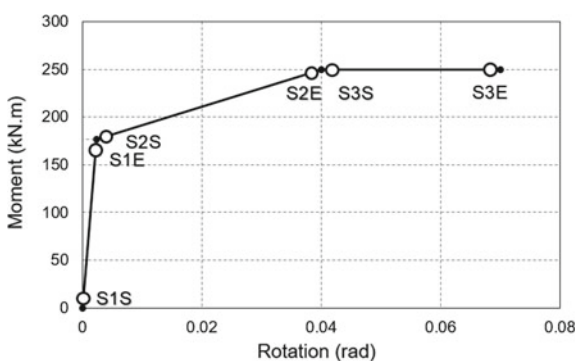


Table 1 Data of the frame

Components		Young's modulus (kN/m ²)	Shear modulus (kN/m ²)	Cross-sectional area (m ²)	Moment of inertia (m ⁴)	Shear area (m ²)
Beam	W16 × 67	199,947,980	76,903,069	12.6E-3	39.71E-5	4.15E-3
Column	W14 × 68	199,947,980	76,903,069	12.9E-3	30.05E-5	3.75E-3

Fig. 4 Moment and rotation relationship of the yield-link (ANSI/AISC 358-18 [2])



the 1st segment; S1E is the end point of the 1st segment. This is similar to S2S, S2E, S3S, S3E. From these 6 points, 21 damage scenarios (Table 2) are investigated.

3.2 Frequency Change-Based Damage Detection Method

When the yield-links are damaged, natural frequencies of moment-resisting frames decrease. Therefore, as can be seen in Fig. 5, the difference in natural frequencies between each case and the undamaged condition (case 1) gradually increases when considering higher points on moment-rotation curve except cases 1, 2, 3, 7, 8 and 12 in which links' properties is still on the elastic portion of the moment-rotation curve. Nevertheless, as described in Fig. 5, the frequency difference is different among there modes. From the chart, the frequency difference of the 1st mode is most obvious while the figures recorded for the 2nd and 3rd modes are clearly smaller. It can be explained by the fact that the positions of two yield-link connections on beam coincide with flexural points on the mode shape of the 1st mode, therefore, the results for 1st mode are higher than the other modes which having the flexural points further from the positions of the yield-link connections. Although the frequency difference is highly sensitive to damage occurring to the frame, the positions of damage on the frame can't identify by this method.

3.3 Modal Assurance Criterion

As described in Table 3, MAC values or the correlations between the mode shapes in every case and case 1 (the undamaged condition) are different. For cases 1, 2, 3, 7, 8 and 12, the MAC values are equal to 1 that means the model has no damage in these cases. However, with almost results less than 1, especially, figures for modes 2 and 3, the models in the other cases are damaged. These changes can be explained by the yield-link's properties since the 2nd and 3rd segments of the moment-rotation curve are yielding portions.

As similar to the results for every mode, the total MAC values for cases 1, 2, 3, 7, 8 and 12, are equal to 1, hence, the frame has no damage in these cases. Meanwhile, with the total MAC values being much less than 1, damage has occurred in the frames with the links' properties in the other cases. Generally, MAC indicator only gives the information whether or not the frame is damaged; it is incapable of detecting the positions of damage on the frame.

Table 2 Damage scenarios

Case	1	2	3	4	5	6	7	8	9	10	11	12	13	14	15	16	17	18	19	20	21
Left connection	S1S	S1S	S1S	S1S	S1S	S1S	S1E	S1E	S1E	S1E	S1E	S1E	S2S	S2S	S2S	S2S	S2E	S2E	S3S	S3S	S3E
Right connection	S1S	S1E	S2S	S2E	S3S	S3E	S1E	S1E	S2E	S3S	S3E	S3E	S2S	S2E	S3S	S3E	S2E	S3E	S3S	S3E	S3E

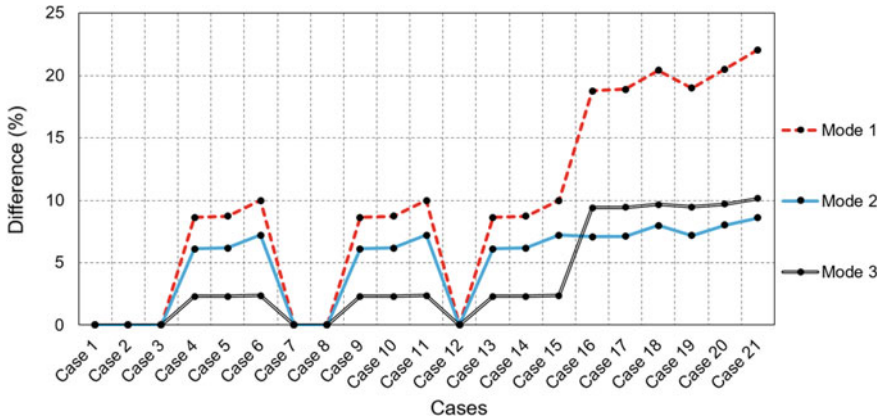


Fig. 5 The change in natural frequency

3.4 Modal Strain Energy-Based Damage Detection Method

The results of damage detection for cases 4, case 17, and case 21 using a combination of the first three modes of vibration are illustrated in Fig. 6. For comparison with the other methods, the damage indices for all of 21 cases for both yield-link connections on the beam are shown in Table 4. Additionally, the yield-link connections with changed properties belong to the beam; thus, the beam is separately considered for damage indices calculation.

From the figures described in the Table 4, the diagnostic results have a quite high level of rationality to be utilized to alert the occurrence of damage at both yield-link connections. In addition, the results from this method are similar to the others when no damage occurs in cases 1, 2, 3, 7, 8 and 12. It should be noted that the beam and columns have unchanged stiffness while the yield-links' properties are changed corresponding with all of 21 cases, hence, as shown in Fig. 6, the damage indices at both connections are remarkably higher than the other positions.

For the cases 1, 2, 3, 7, 8 and 12, the damage indices are equal to 0, hence, both yield-link connections are undamaged in these cases. It can be explained as the fact that the yield-links' properties in these cases are on the elastic segment of moment-rotation curve. Meanwhile, the damage indices are significantly high (Z_o is higher than 10) in the other cases which are on the yielding segments having the different behaviours from those 6 cases. In reality, the position of applied loads is unpredicted and there are some damaged positions which a sole mode is incapable of detection. Hence, the use of combinations of modes of vibration is necessary.

Table 3 MAC values

Case	1	2	3	4	5	6	7	8	9	10	11	12	13	14	15	16	17	18	19	20	21
U1	Mode 1	1.00	1.00	1.00	1.00	1.00	1.00	1.00	1.00	1.00	1.00	1.00	1.00	1.00	1.00	1.00	1.00	1.00	1.00	1.00	1.00
	Mode 2																				
	Mode 3																				
U2	Mode 1	1.00	1.00	0.57	0.57	0.54	1.00	1.00	0.57	0.57	0.54	1.00	0.57	0.57	0.54	0.00	0.00	0.06	0.00	0.05	0.00
	Mode 2																				
	Mode 3																				
R3	Mode 1	1.00	1.00	0.26	0.25	0.22	1.00	1.00	0.26	0.25	0.22	1.00	0.26	0.25	0.22	0.00	0.00	0.02	0.00	0.01	0.00
	Mode 2																				
	Mode 3																				

Note U1—horizontal displacement; U2—vertical displacement; R3—rotation

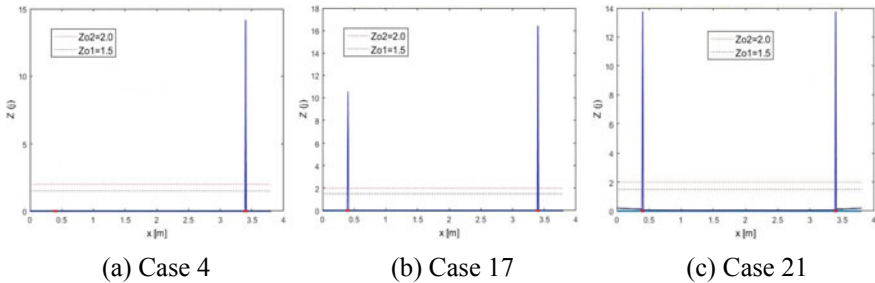


Fig. 6 Damage indices for cases 4, case 17, and case 21

4 Conclusions

In this study, three damage detection methods for yield-link connections in steel moment-resisting frames using vibration characteristics and OpenSEES are presented. All these methods showed good performance on alerting the points at which the yield-links are impaired. However, the frequency change-based damage detection method and modal assurance criterion showed limitations on damage localization. It was found that the modal strain energy-based damage detection method was more feasible to detect both the amplitude and positions of damage. Therefore, the use of modal strain energy is promising for damage detection application at link positions for moment-resisting frames since the process of checking the status of the yield-links after an earthquake event is extremely crucial. In addition, the degree of reliability of identification results depends on material properties of the yield-links inputted to OpenSEES model, the data of vibration characteristics, positions and levels of actual damage. To apply these damage detection methods in the real cases, further studies on these factors after applying an earthquake to the frame need to be conducted.

Patents

Simpson Strong-Tie® and Yield-Link® Structural Fuse are protected under one or more of the following patents and applications: US patent no. 8,001,734, US patent no. 8,375,652 B2, US patent publication no. 2015/0159362, US patent publication no. 2017/0138043, and US patent publication no. 15/935,412 and must be supplied or licensed through Simpson Strong-Tie Company Inc. Other US and international Patents Pending.

Table 4 Damage indices

	Case	1	2	3	4	5	6	7	8	9	10	11	12	13	14	15	16	17	18	19	20	21
Z	Left connection	0	0	0	0	0	0	0	0	0	0	0	0	0	0	0	0	13.7	10.5	13.3	13.7	13.3
	Right connection	0	0	0	14.2	14.2	0	0	14.2	14.2	0	14.2	14.2	0	14.2	14.2	13.7	16.4	14.2	13.7	14.3	13.7

References

1. Adams RD, Cawley P, Pye CJ, Stone BJ (1978) A vibration technique for nondestructively assessing the integrity of structures. *J Mech Eng Sci* 20:93–100
2. ANSI/AISC 358-18 prequalified connections for special and intermediate steel moment frames for seismic applications. Including supplement No. 1, Chapter 12 simpson strong-tie strong frame moment connection
3. Kim JT, Ryu YS, Cho HM, Stubbs N (2003) Damage identification in beam-type structures: frequency-based method vs mode-shape-based method. *Eng Struct* 25:57–67
4. Kim JT, Park JH, Hong DS, Park WS (2010) Hybrid health monitoring of pre-stressed concrete girder bridges by sequential vibration-impedance approaches. *Eng Struct* 32:115–128
5. Pastor M, Binda M, Harcarik T (2012) Modal assurance criterion. *SciVerse Sci Direct* 48:543–548
6. Salawu OS (1997) Detection of structural damage through changes in frequency: a review. *Eng Struct* 19(9):718–723
7. Stubbs N, Kim JT (1995) Field verification of a nondestructive damage localization and severity estimation algorithm. In: Proceedings of the 13th international modal analysis conference, pp 210–218

Construction Materials Session

Adiabatic Temperature Rise and Thermal Analysis of High-Performance Concrete Bridge Elements



Tu Anh Do, Thuan Huu Nguyen, Thanh Xuan Vu, Tuyet Thi Hoang, Tam Duc Tran, and Thanh Tien Bui

1 Introduction

Recently, the bridge construction industry has been widely using high-strength and HPC mixes so as to meet the project requirements of increased span length and accelerated construction schedules. Those concrete mixes tend to use larger cement content to surge the strength at early ages. However, hydration of a higher amount of cement leads to a greater concrete temperature and a higher temperature difference between the concrete surface and the core. As a result, thermal tensile stresses will be higher hence growing the risk of cracking [1]. Accurate characterization of the cement hydration for concrete is vital to forecast the evolution of temperature, stress field, and thermal cracking potential of the concrete element so that necessary measures can be taken to minimize cracking risk and ensure its structural integrity and durability.

To capture the thermal behavior of concrete, input hydration parameters need to be determined. There have been theoretical/mathematical models for presenting the cement hydration progress such as adiabatic curve proposed by Tanabe et al. [2]. The limitations of those theoretical models are: (1) the heat generated by reacting cement is considered uniform throughout the concrete mass and (2) the role of supplementary cementitious materials is not taken into account. Therefore, hydration parameters determined from a laboratory or field test on an actual concrete mix are more accurate [3, 4].

In this study, the ATR for a HPC mix was measured using an adiabatic calorimeter developed at the University of Transport and Communications, Vietnam. The heat

T. A. Do · T. H. Nguyen (✉) · T. T. Hoang · T. T. Bui
University of Transport and Communications, Hanoi, Vietnam
e-mail: nhthuan@utc.edu.vn

T. X. Vu
Hanoi Department of Construction, Hanoi, Vietnam

T. D. Tran
Hoa Binh Department of Transportation, Dong Tien, Hoa Binh, Vietnam

of hydration parameters [5] of the HPC mix were determined using the curve fitting method. A FE model of a bridge pier using HPC was developed using the ANSYS APDL codes. The heat of hydration parameters were then used as input parameters to the FE model in order to predict the temperature distribution in the bridge pier and footing. The temperature development of a pier using a normal concrete mix was also analyzed to compare with that of the HPC pier, then the hazard of cracking in concrete for the two cases would be discussed.

2 Experimental

2.1 ATR for HPC

Using the concept described by Gibbon et al. [6] and improved by Lin and Chen [4], an adiabatic calorimeter for measuring ATR of concrete was developed. The basic principle of adiabatic calorimetry is to keep the concrete sample temperature and the ambient temperature the same by minimizing the heat exchange. The adiabatic calorimeter, sketched in Fig. 1, automatically matches the water temperature with the concrete sample temperature in order to remain the hydration heat unchanged. There are 2 Resistance Temperature Detectors (RTD) sensors that continuously measure the concrete sample and the water temperatures at 10 Hz frequency. Two heaters will automatically turn on and off based on the difference between the water and the sample temperatures (0.1°C in this set up). The system, therefore, is very close to an adiabatic condition that can obtain ATR of the concrete sample.

The HPC mix design is presented in Table 1 whereas Table 2 lists the chemical composition of cement. After mixing, the fresh concrete was placed in the container of the adiabatic chamber before the ATR would be obtained (Fig. 2). The measured ATR over time is plotted in Fig. 3. The initial concrete temperature was 22.2°C . The rise in the sample adiabatic temperature was 54.5°C at 72 h (the peak temperature was 76.7°C).

Since the water-reducing and retarding admixture and fly ash were present in the HPC mix, the hydration reaction was delayed leading to the slow increase in the specimen temperature. After 16 h, the exothermic reaction began to accelerate. The hydration process took place very quickly within 16 and 35 h due to the low water to cement content ratio of the concrete mix [7]. The concrete temperature finally levelled off after 50 h. The ATR can be used as the input for thermal analysis of a concrete bridge structure.

Fig. 1 Schematic diagram of adiabatic calorimeter [4]

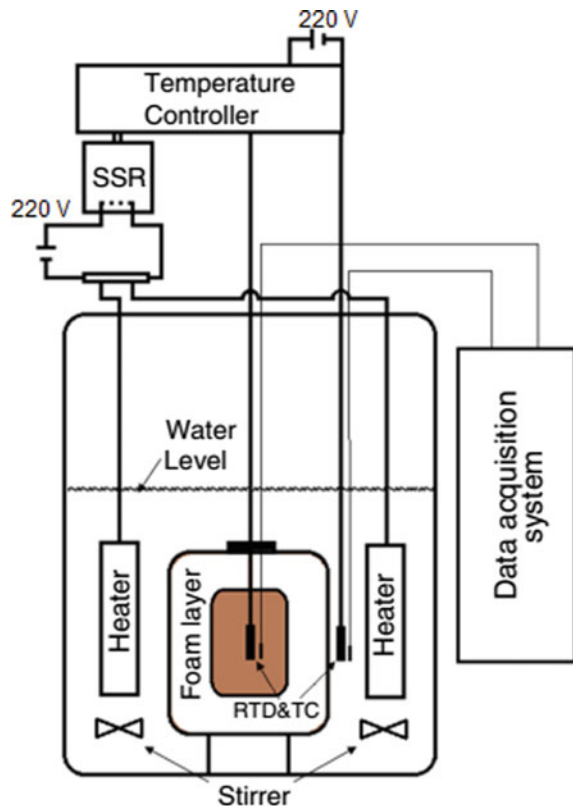


Table 1 HPC mix design (kg/m^3)

Material	w/cm	Water	Cement	Fly ash	Coarse aggregate	Fine aggregate	WRRET
Quantity	0.32	170	424	106	1050	695	7.5

WRRET = water-reducing and retarding admixture; w/cm = water-to-cementitious materials ratio

2.2 Degree of Hydration

The rate of hydration heat is a function of the hydrating concrete temperature and time. The higher the concrete temperature, the greater the rate of the exothermic reaction at an early age. The degree of hydration is proportional to the heat evolved as proposed by Van Breugel [8]:

$$\alpha(t) = \frac{H(t)}{H_u} \quad (1)$$

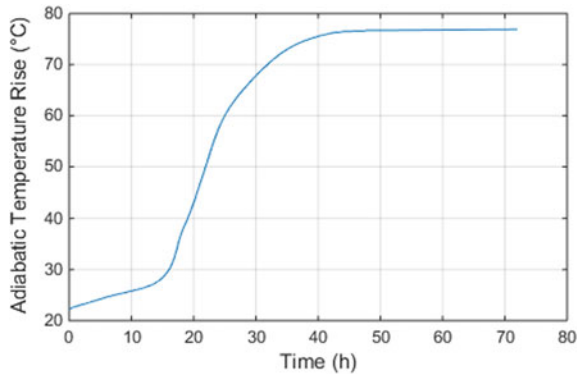
Table 2 Cement chemical composition (%)

Components	SiO ₂	Al ₂ O ₃	Fe ₂ O ₃	CaO	MgO	SO ₃	Na ₂ O	K ₂ O	Blaine (m ² /kg)
Percentages	21.49	5.40	3.49	63.56	1.40	1.65	0.15	0.70	375

Fig. 2 Placing concrete specimen in adiabatic calorimeter



Fig. 3 Measured ATR



where: $\alpha(t)$ = degree of hydration, $H(t)$ = total heat generated at time t (J/g), and H_u = ultimate heat at the end of hydration (J/g) which can be determined using Eqs. (2) and (3):

$$H_u = H_c p_{cem} + 461 p_{slag} + 1800 p_{FA} p_{FA-CaO} \quad (2)$$

$$H_c = 500p_{C_3S} + 260p_{C_2S} + 866p_{C_3A} + 420p_{C_4AF} + 624p_{SO_3} + 1186p_{FreeCa} + 850p_{MgO} \quad (3)$$

where p_{cem} = ratio of cement to cementitious materials content, and H_c = total heat evolved from pure cement hydration (J/g).

A mathematical function for degree of hydration was proposed by Hansen and Pedersen [9] as follows:

$$\alpha(t_e) = \alpha_u \exp\left[-\left(\frac{\tau_s}{t_e}\right)^\beta\right] \quad (4)$$

where τ (h) and β = hydration parameters; t_e = equivalent age of concrete (h); $\alpha_u = \frac{1.031w/c}{0.194+w/c}$ is ultimate degree of hydration [7]; and w/c = water to cementitious material content ratio.

The equivalent age of concrete is computed using Eq. (5):

$$t_e = \int_0^t \exp\left[-\frac{E_a}{R}\left(\frac{1}{273+T_c} - \frac{1}{273+T_r}\right)\right] dt \quad (5)$$

where T_r = reference temperature (20 °C or 23 °C); E_a = activation energy (J/mol); R = universal gas constant (8.314 J/mol/K); T_c = temperature of the concrete (°C); and $\Delta t_i = t_i - t_{i-1}$ is the time step used (h).

The activation energy represents “temperature sensitivity” of the exothermic reaction, and can be predicted as follows [5]:

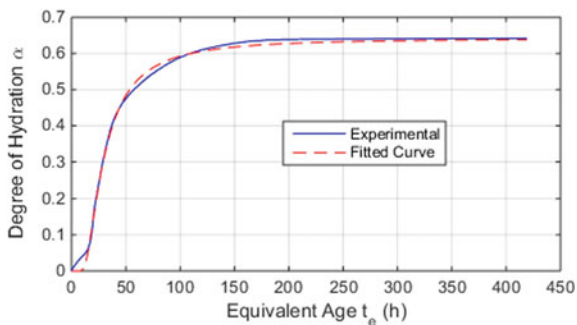
$$E_a = 41,230 + 1,416,000(p_{C_3A} + p_{C_4AF})p_{cem}p_{SO_3}p_{cem} - 347,000p_{Na_2O_{eq}} - 19.8Blaine + 29,600p_{FA}p_{FA-CaO} + 16,200p_{slag} - 51,600p_{SF} \quad (6)$$

where p_{FA} = percentage of fly ash in the cementitious material; p_{FA-CaO} = percentage of CaO in fly ash; p_{slag} = percentage of slag in the cementitious material; p_{SF} = percentage of silica fume in the cementitious material; Blaine = fineness of cement (m^2/kg); p_X = percentage of X component in the cement (cem = cement, C_3A , C_4AF , SO_3) and $p_{Na_2O_{eq}}$ = percentage of Na_2O_{eq} in cement ($0.658 \times \%K_2O + \%Na_2O$).

In this study, based on the chemical compositions of cement, the activation energy was determined to be $E_a = 34,454$ (J/mol), and $\alpha_u = 0.642$. The experimental degree of hydration versus equivalent age for the HPC mix is plotted in Fig. 4. The hydration parameters $\tau = 24.98$ h and $\beta = 1.842$ were determined using the curve fitting method from the experiment and Eq. (4) ($R^2 = 0.9949$).

In this study, based on the chemical compositions of cement, the activation energy was determined to be $E_a = 34,454$ (J/mol), and the ultimate degree of hydration $\alpha_u = 0.642$. The experimental degree of hydration versus equivalent age for the HPC

Fig. 4 Experimental and fitted degree of hydration curves



mix is plotted in Fig. 4. The hydration parameters $\tau = 24.98$ h and $\beta = 1.842$ were determined using the curve fitting method from the experiment and Eq. (4) ($R^2 = 0.9949$).

3 FE Model for Thermal Analysis of Bridge Pier

Numerical methods can be effectively used in solving the problem of heat evolution and transfer in hydrating concrete [10–15]. Following those approaches, a FE model was developed using the ANSYS Mechanical APDL codes. The structure consists of a concrete pier placed on a footing, and 1/4 of the entire structure was to be considered (Fig. 5). The concrete and the soil were modeled using an 8-node solid element (SOLID278) with a single degree of freedom at each node (temperature). The pier's dimensions are $2.0\text{ m} \times 5.0\text{ m} \times 6.0\text{ m}$ and the footing's dimensions are $12.5\text{ m} \times 8.0\text{ m} \times 2.5\text{ m}$.

Fig. 5 FE model for one-quarter pier

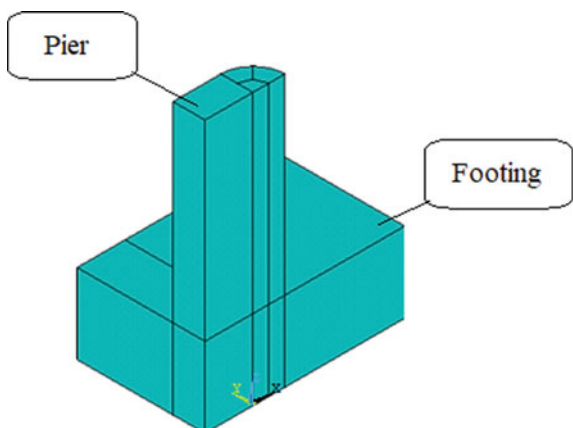


Table 3 Concrete Material Properties Used in Thermal Analysis

Mix	Thermal conductivity (J/h-m-°C)	Specific heat (J/kg-°C)	Density (kg/m ³)
HPC	6732	1049	2452
Normal concrete	7920	1043	2233

The initial and external temperatures for the model boundary conditions were assumed to be 23 and 27 °C, respectively. The surface convection coefficient for the pier was assumed to be 29,288 J/h-m² – °C [14].

The heat conduction equation in space is expressed by Eq. (7). The thermal analysis type is “transient” which considers changes of temperature and boundary conditions over time.

$$\rho c_p \frac{\partial T}{\partial t} = \frac{\partial}{\partial x} \left(k \frac{\partial T}{\partial x} \right) + \frac{\partial}{\partial y} \left(k \frac{\partial T}{\partial y} \right) + \frac{\partial}{\partial z} \left(k \frac{\partial T}{\partial z} \right) + q \quad (7)$$

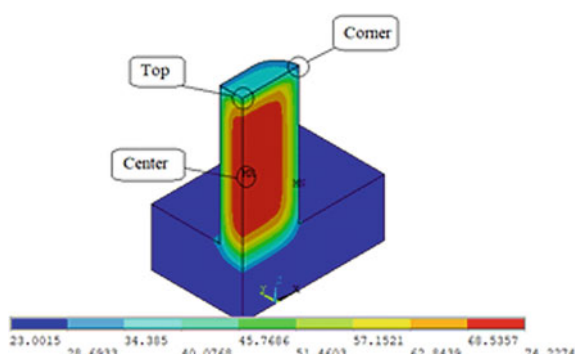
where q = rate of heat generation per unit volume (J/h-m³), ρ = concrete density (kg/m³), c_p = specific heat of concrete (J/kg- °C), k = thermal conductivity (J/h-m – °C), T = temperature (°C), and t = time (h).

In this study, a normal concrete mix properties were also adopted [16] in order to compare with the HPC mix. The material properties of the normal concrete and HPC mixes are listed in Table 3.

3.1 Discussion of Analysis Results

The predicted temperature distribution contours are presented in Fig. 6. The highest temperature was found to occur in the center of the model and decreased as it got closer to the surfaces of the pier. The pier center, top and corner temperatures are predicted and plotted in Fig. 7a. The temperature differences between the center

Fig. 6 Temperature distribution contours in HPC pier



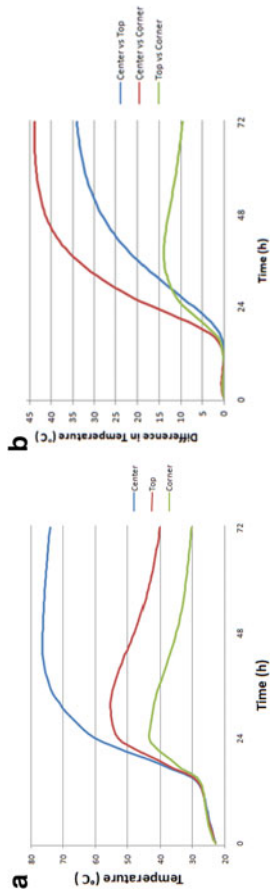


Fig. 7 Temperatures a and temperature differences b in the pier using HPC mix

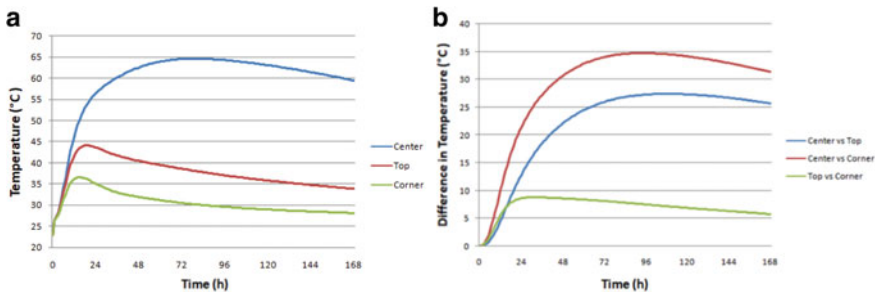


Fig. 8 Temperatures **a** and temperature differences **b** in the pier using normal mix

and other points in the pier are presented in Fig. 7b. It is noted that the maximum temperature difference (between the center and the corner) peaked at $43.7\text{ }^{\circ}\text{C}$ after 72 h that exceeds the maximum limit of $20\text{ }^{\circ}\text{C}$ suggested by ACI [17].

The temperatures and temperature differences in the pier using the normal concrete mix are also shown in Fig. 8. As can be seen, the maximum temperature difference peaked at $34.0\text{ }^{\circ}\text{C}$ in this case. From the comparison between the predicted results of the HPC and normal concrete, the pier using the HPC mix show a higher temperature difference than the normal one, thus it might have a higher thermal cracking risk. However, because the HPC has a higher tensile strength than the normal one does, the pier should be designed with smaller dimensions in order to reduce thermal cracking potential.

4 Conclusions and Recommendations

The paper presents the ATR for a HPC mix measured from an adiabatic calorimeter. The highest temperature rise in the sample was $54.5\text{ }^{\circ}\text{C}$. Through the measured ATR, hydration parameters ($\tau = 24.98\text{ h}$ and $\beta = 1.842$) were determined from the curve fitting method.

The FE model developed in ANSYS is capable to predict temperature evolution in a bridge pier. The maximum temperature difference between the core and the corner of the pier using HPC mix peaked at $43.7\text{ }^{\circ}\text{C}$ thus suggesting very high risk of early-age thermal cracking. However it further needs to conduct strength tests on the HPC mix and then perform a stress analysis on the bridge pier to fully evaluate the thermal cracking risk in the concrete.

Acknowledgements This research is funded by Vietnam National Foundation for Science and Technology Development (NAFOSTED) under grant number 107.02-2016.25.

References

1. ACI (2005) 207.1 R-05 Guide to mass concrete
2. Tanabe TA, Kawasumi M, Yamashita Y (1985) Thermal stress analysis of massive concrete. Paper presented at the finite element analysis of reinforced concrete structures
3. Do T, Chen H, Leon G, Nguyen T (2019) A combined finite difference and finite element model for temperature and stress predictions of cast-in-place cap beam on precast columns. *Constr Build Mater* 217:172–184
4. Lin Y, Chen H-L (2015) Thermal analysis and adiabatic calorimetry for early-age concrete members. *J Therm Anal Calorim* 122(2):937–945
5. Riding KA, Poole JL, Folliard KJ, Juenger MC, Schindler AK (2012) Modeling hydration of cementitious systems. *ACI Mater J* 109(2):225–234
6. Gibbon G, Ballim Y, Grieve G (1997) A low-cost, computer-controlled adiabatic calorimeter for determining the heat of hydration of concrete. *J Test Eval* 25(2):261–266
7. Mills R (1966) Factors influencing cessation of hydration in water cured cement pastes. *Highw Res Board Spec Rep* (90)
8. Van Breugel K (1993) Simulation of hydration and formation of structure in hardening cement-based materials
9. Hansen PF, Pedersen EJ (1977) Maturity computer for controlled curing and hardening of concrete
10. Do T, Lawrence A, Tia M, Bergin M (2013) Importance of insulation at the bottom of mass concrete placed on soil with high groundwater. *Transp Res Record J Transp Res Board* (2342):113–120
11. Do T, Lawrence A, Tia M, Bergin M (2014) Determination of required insulation for preventing early-age cracking in mass concrete footings. *Transp Res Record J Transp Res Board* (2441):91–97
12. Do TA (2014) Influence of footing dimensions on early-age temperature development and cracking in concrete footings. *J Bridge Eng* 20(3):06014007
13. Do TA, Lawrence AM, Tia M, Bergin MJ (2014) Effects of thermal conductivity of soil on temperature development and cracking in mass concrete footings. *J Test Eval* 43(5):1078–1090
14. Kim SG (2010) Effect of heat generation from cement hydration on mass concrete placement
15. Yikici TA, Chen HL (2015) Numerical prediction model for temperature development in mass concrete structures. *Transp Res Record J Transp Res Board* (2508):102–110
16. Tia M, Lawrence A, Do TA, Verdugo D, Han S, Almarshoud M, Ferrante B, Markandeya A (2016) Maximum heat of mass concrete-phase 2
17. ACI (2016) ACI 301-16. Specification for structure concrete

Air Permeability of Precast Concrete Box Culvert Applying Steam Curing Condition



May Huu Nguyen, Kenichiro Nakarai, and Saeko Kajita

1 Introduction

Curing plays a vital role in establishing the properties of hardened concrete with sufficient water and heat over time. It is the process of controlling the rate and extent of moisture loss from concrete to ensure an uninterrupted hydration of cement as well as ensuring to maintain an adequate temperature of concrete at its early ages [4, 12].

In order to ensure an effective curing process, various methods have been used such as steam curing at atmosphere pressure, steam curing at high pressure, electrical heating of reinforcement, imposing electrical current to concrete directly, and microwave heating [5, 23, 24]. Among these methods, steam curing at atmosphere pressure is common, especially for large precast concrete, for instance precast concrete box culvert or precast tunnel segment, in order to speed up the production efficiency [5, 19, 22].

On the other hand, the application of steam curing can contribute to several defects like enlargement of porosity, brittleness, and surface micro-crack [7, 8, 18]. Steam curing contributes to changes in pore size distribution, and hence results in the durability of concrete such as absorption, permeability, and diffusion [2]. Therein, air

M. H. Nguyen · K. Nakarai (✉) · S. Kajita

Department of Civil and Environmental Engineering, Graduate School of Engineering, Hiroshima University, 1-4-1, Kagamiyama, Higashi-Hiroshima, Hiroshima 739-527, Japan
e-mail: nakarai@hiroshima-u.ac.jp

M. H. Nguyen
e-mail: maynh@utt.edu.vn

S. Kajita
e-mail: m186051@hiroshima-u.ac.jp

M. H. Nguyen
Department of Bridge and Tunnel, Faculty of Civil Engineering, University of Transport Technology, 54 Trieu Khuc, Thanh Xuan, Hanoi 100000, Vietnam

permeability was widely used as one of the appropriate indexes that can provide useful information relating to the changes in the capillary porosity, pore system [16] as well as to verify other indexes [10, 13–15]. Therefore, monitoring the changes in air permeability in terms of applying steam curing is a significant task, providing a proper understanding the effect of the steam curing on the durability of concrete structure.

Accordingly, the goal of this study was to evaluate the cover concrete quality of a precast concrete box culvert applying a typical steam curing by monitoring the changes in air permeability. The Torrent air permeability test was employed to measure coefficient of air permeability kT for the box culvert specimen produced using steam curing, Portland cement, water-to-binder ratio of 0.485 over a period of one year.

2 Experimental Program

2.1 Materials and Mix Proportions

Table 1 illustrates the properties of the materials employed in this study. Tap water was used to mix the cement components.

The specimens were prepared by mixing the cement, aggregates, expansive agent, chemical admixture, and tap water using the proportions presented in Table 2.

Table 1 Material properties

Material	Type	Properties
Cement (C)	Ordinary Portland cement	Density: 3.16 g/cm ³ Specific surface area: 3320 cm ² /g
Expansive agent (Ex)	Ettringite type	Density: 2.95 g/cm ³ Specific surface area: 3000 cm ² /g
Fine aggregate (S)	Crushed quartz	Surface-dry density: 2.57 g/cm ³
Coarse aggregate (G)	Crushed gravel	Surface-dry density: 2.72 g/cm ³
Chemical admixture (Ad)	Superplasticizer	Polycarboxylic acid compound

Table 2 Material mix proportions of the specimens

W/B ^a	s/a ^b (vol.%)	Unit mass (kg/m ³)					
		W	C	Ex	S	G	Ad
0.485	45.0	173	307	50	801	1044	2.32

^aB: Binder includes cement (C) and expansive agent (Ex)

^ba: total volume of aggregates, s: volume of fine aggregate

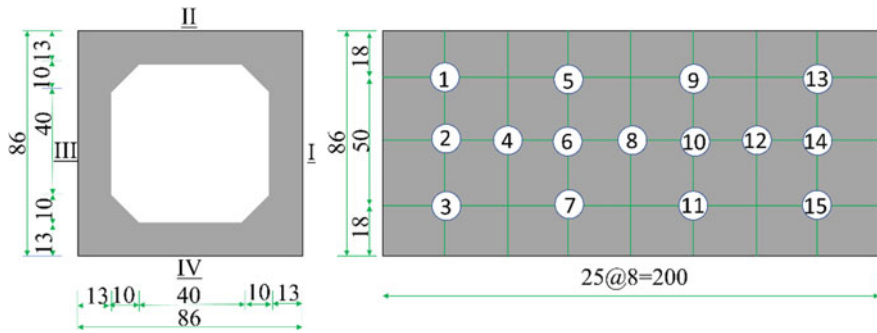


Fig. 1 Geometries of the box culvert specimen and sketch test locations (cm)

2.2 Specimen Preparation

The concrete was manufactured in a precast concrete plant. Before casting, the slump, air content and temperature of the fresh concrete were measured to determine its consistency and workability. The measured values of slump, air content, and temperature of fresh concrete were 18.5 cm, 2.2%, and 23.5 °C, respectively. A box culvert specimen was cast in horizontal direction same as cast-in-place on the site. The dimensions of the box culvert specimen were 86 × 86 × 200 cm (see Fig. 1).

Regarding curing condition, after casting, the specimen was covered with blue plastic sheeting for 3 h. The specimen was then applied a typical steam curing, which was designed by All Japan Box-Culvert Association. In details, the temperature was increased at a steady rate 20 to 60 °C/h, and it was maintained at 60 °C for 3 h before returning to the original conditions (20 °C) over an 8-h period. The specimen was thereafter exposed to a room at the age of 1 day (d). The average relative humidity (RH) and temperature were about 62% RH and 16.6 °C recording via the nearest meteorological observatories during the experiments.

2.3 Experimental Methods

As shown in Fig. 1, the specific surfaces were given, namely, I to IV. The surfaces I and II were employed as representatives to other surfaces. Fifteen test locations were then selected on the surface I and II (see Fig. 1). The selection was done to avoid the large air bubbles and cracks and minimize their effects on the experimental results. The CMEX II Concrete Encounter Moisture Meter (Tramex, Ireland) was used to determine the moisture content.

A commercially available equipment, “PermeaTORR AC” (Active Cell), a test method developed by Torrent was employed to determine the coefficient of air permeability kT [20]. The kT was automated calculated using an appropriate model

[20, 21]. The kT and moisture content were measured at the ages of 30, 60, and 365 day to evaluate the cover concrete quality according to age of the specimen.

3 Results and Discussion

The Torrent tester and moisture meter were used to measure kT and moisture content values on the selected surfaces. The variation of their average values (geometric mean for kT and arithmetic mean for moisture content) according the age of the specimen are shown in Figs. 2 and 3. The moisture content measured on the surfaces of the specimen gradually decreased over time as shown in Fig. 2. The moisture content values were significantly lower for the surface II compared to surface I. This lower can be explained by the higher porosity in the motor layer on the top of the surface II affected by casting direction [9]. Figure 3 indicates that kT on all surfaces slight reduced from age of 30 to 60 day after that increased until 365 day. The first reduction can be explained due to the increase of the gross volume of the formed cement hydrates that gradually fill part of the pore spaces originally occupied by water [6]. For the increasing in kT after 60 days, it can be associated with the increase in the open pore content caused by water evaporation [1, 3].

Additionally, in agreement with the changes in moisture content, it is obvious that kT for surface II was larger than surface I. These differences could be explained by the negative segregation on the surface II—the top surface [11, 17]. Another possible explanation associated with the higher kT on the surface II is poor curing condition since this surface was not sealed during applying steam curing. In this case, the free water subsequently evaporated, resulting in insufficient hydration. Based on kT

Fig. 2 Changes in moisture content on measured surfaces

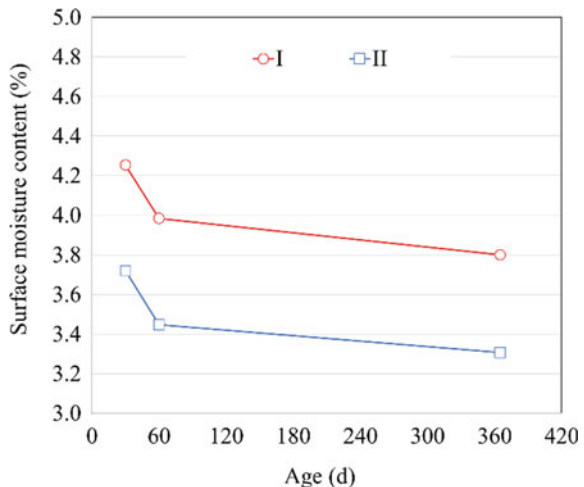
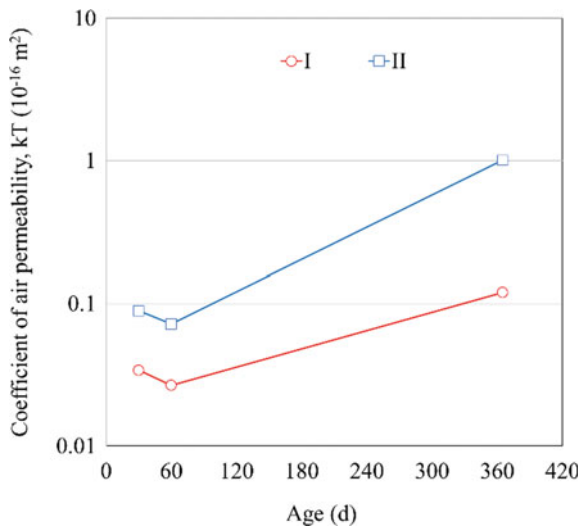


Fig. 3 Changes in kT on measured surfaces



index, it can be concluded that the measured surfaces were good quality ($kT < 0.1 \times 10^{-16} \text{ m}^2$) under applying the typical steam curing, excluding normal quality on the surface II.

4 Conclusions

This study monitored changes in moisture contents, air permeability of a precast box culvert applying a typical steam curing over a period of 365 day. Based on the obtained kT indexes, it can be concluded that the measured surfaces were good quality under applying the typical steam curing, excluding normal quality on the surface II that was influenced of segregation and sealing condition. On the basis of the findings in this study, in order to improve the cover concrete quality, all surfaces of a concrete structure should be covered to prevent the water evaporation phenomenon during applying steam curing.

Acknowledgements This study was supported by the All Japan Box-Culvert Association. The authors are grateful to Mr. Hideaki Karasawa, Mr. Yuji Tadokoro and other members of the association for assisting with the specimen preparation in experiments.

References

1. Abbas A, Carcasses M, Ollivier J-P (1999) Gas permeability of concrete in relation to its degree of saturation. *Mater Struct* 32(1):3–8
2. Ba M, Qian C, Guo X, Han X (2011) Effects of steam curing on strength and porous structure of concrete with low water/binder ratio. *Constr Build Mater* 25(1):123–128
3. Basheer PAM, Nolan E (2001) Near-surface moisture gradients and in situ permeation tests. *Constr Build Mater* 15(2–3):105–114
4. Bentz DP, Weiss WJ (2011) Internal curing: a 2010 state-of-the-art review (No. NIST IR 7765, NIST IR 7765)
5. Gonzalez-Corominas A, Etxeberria M, Poon CS (2016) Influence of steam curing on the pore structures and mechanical properties of fly-ash high performance concrete prepared with recycled aggregates. *Cem Concr Compos* 71:77–84
6. Hearn N (1998) Self-sealing, autogenous healing and continued hydration: what is the difference? *Mater Struct* 31(8):563
7. Long G, Li Y, Ma C, Xie Y, Shi Y (2018) Hydration kinetics of cement incorporating different nanoparticles at elevated temperatures. *Thermochim Acta* 664:108–117
8. Lothenbach B, Winnefeld F, Alder C, Wieland E, Lunk P (2007) Effect of temperature on the pore solution, microstructure and hydration products of Portland cement pastes. *Cem Concr Res* 37(4):483–491
9. Madandoust R, Mousavi SY (2012) Fresh and hardened properties of self-compacting concrete containing metakaolin. *Constr Build Mater* 35:752–760
10. Nakarai K, Shitama K, Nishio S, Sakai Y, Ueda H, Kishi T (2019) Long-term permeability measurements on site-cast concrete box culverts. *Constr Build Mater* 198:777–785
11. Navarrete I, Lopez M (2017) Understanding the relationship between the segregation of concrete and coarse aggregate density and size. *Constr Build Mater* 149:741–748
12. Neville AM (2011) Properties of concrete, 5th edn. Pearson, Harlow England
13. Nguyen MH, Nakarai K, Kubori Y, Nishio S (2019) Validation of simple nondestructive method for evaluation of cover concrete quality. *Constr Build Mater* 201:430–438
14. Nguyen MH, Nakarai K, Nishio S (2019) Durability index for quality classification of cover concrete based on water intentional spraying tests. *Cem Concr Compos* 104:103355
15. Nguyen MH et al (2020) Early evaluation of cover concrete quality utilizing water intentional spray tests. *Constr Build Mater* 231(20):117144
16. Pan X, Shi Z, Shi C, Ling T-C, Li N (2017) A review on surface treatment for concrete—Part 2: Performance. *Constr Build Mater* 133:81–90
17. Panesar DK, Shindman B (2012) The effect of segregation on transport and durability properties of self consolidating concrete. *Cem Concr Res* 42(2):252–264
18. Patel HH, Bland CH, Poole AB (1995) The microstructure of concrete cured at elevated temperatures. *Cem Concr Res* 25(3):485–490
19. Ramezanianpour AM, Esmaili Kh, Ghahari SA, Ramezanianpour AA (2014) Influence of initial steam curing and different types of mineral additives on mechanical and durability properties of self-compacting concrete. *Constr Build Mater* 73:187–194
20. Torrent RJ (1992) A two-chamber vacuum cell for measuring the coefficient of permeability to air of the concrete cover on site. *Mater Struct* 25(6):358–365
21. Torrent R, Fernández Luco L (2007) Nondestructive evaluation of the penetrability and thickness of the concrete cover. RILEM Report, 40
22. Türkel S, Alabas V (2005) The effect of excessive steam curing on Portland composite cement concrete. *Cem Concr Res* 35(2):405–411
23. Wu X, Dong J, Tang M (1987) Microwave curing technique in concrete manufacture. *Cem Concr Res* 17(2):205–210
24. Yang Q, Zhang S, Huang S, He Y (2000) Effect of ground quartz sand on properties of high-strength concrete in the steam-autoclaved curing. *Cem Concr Res* 30(12):1993–1998

Chloride Penetration Test of Concrete Simulating Deicing Salt Attack



Yuka Yoshizumi, Kenichiro Nakarai, May H. Nguyen, Norie Tada,
and Masayuki Yamamoto

1 Introduction

Chloride-induced corrosion is one of the main reasons of deterioration of concrete structures [1, 2]. Thus, the resistance to chloride penetration plays a vital role in the design and construction of concrete structures [3]. In order to predict the chloride penetration into existing structures, a semi-destructive procedure is widely employed to determine chloride diffusion coefficient, D_c , a robust index in predicting the chloride penetration during longer periods [4, 5].

Nevertheless, this procedure has some disadvantages such as the damage due to drilling core and long time to complete. To address the need for more practical methods, the coefficient of air permeability, kT (by Torrent method), was proposed. In laboratory test, kT and D_c has good positive correlation [6]. Furthermore, Torrent et al. [7, 8] proposed a durability design method for predicting service life of concrete structures. kT was also verified to predict permeation resistance of chloride ion in the existing structure [9].

However, for the same kT , the cause of the difference in D_c measured in salt immersion test in literatures and the existing structure in their study has not been clear. Therefore, this study aims to clarify the cause of differences in D_c measured in the salt immersion test and the existing structure by clarifying the chloride ion

Y. Yoshizumi · K. Nakarai (✉) · M. H. Nguyen

Department of Civil and Environmental Engineering, Graduate School of Engineering, Hiroshima University, Higashi-Hiroshima, Japan

e-mail: nakarai@hiroshima-u.ac.jp

M. H. Nguyen

Department of Bridge and Tunnel, Faculty of Civil Engineering, University of Transport Technology, 54 Trieu Khuc, Thanh Xuan, Hanoi 100000, Vietnam

N. Tada · M. Yamamoto

West Nippon Expressway Engineering Chugoku Co., Ltd., Hiroshima, Japan

permeation behavior focusing on the supply cycle of chloride ions. Final target will be to establish a method predicting chloride penetration into existing concrete structures using non-destructive tests.

2 Experimental Method

2.1 Specimens

Based on JIS A 1132, cylindrical specimens of 100 mm in diameter and 200 mm high were prepared by mixing ordinary Portland cement (OPC) and fine aggregate with water-to-cement ratio (W/C) of 0.55. The specimens were demolded at 1 day after sealed curing and then immersed in water for moist curing. The used 150 mm in high specimens were prepared by cutting non-used 25 mm parts from the top and bottom of the prepared specimens at 28 days. The specimens were then covered with epoxy resin excluding one circle surface using for the salt immersion test.

2.2 Salt Immersion Test

The salt immersion tests were conducted according to JSCE-G572-2003. The prepared specimens were immersed in a 10% aqueous sodium chloride solution at a temperature of 20 °C.

The specimens were then sliced every 1 cm from the surface after the immersion for six months. The chloride ion concentration was measured by potentiometric titration method (JIS-A-1154). From the relationship between each depth position and the measured total chloride ion, regression analysis was performed according to Fick's diffusion rule to calculate Dc.

2.3 Cyclic Wetting and Drying Test

For the cyclic wetting and drying tests, the cycle of supplying chloride ions with deicing salt was simulated. Specimens were placed by repeating two conditions, immersion in sodium chloride aqueous solution with concentration 10% and temperature 20 °C (wetting), and dry in temperature 20 °C and humidity 60% (drying). In order to directly compare the obtained results of this study with the exist results, it was assumed that the deicing salt spraying period in the existing structure was 3 months in wetting in 1 year. Thus, the cyclic drying-to-wetting ratio was fixed at 3 and while the length of one cycle (cycle length) was changed (Table 1). After the test, Dc was calculated in the same manner as the salt immersion test.

Table 1 The salt immersion test and the cyclic wetting and drying cycle

Cycle length (week)	The salt immersion test	1	4	12	24
Immersion period (week)	At all time	0.25	1	3	6
Dry period (week)	–	0.75	3	9	18

2.4 The Surface Air Permeability Test

In parallel with the salt immersion test, the coefficient of air permeability coefficient, k_T , was measured on cylindrical specimens (100×200 mm) using a Torrent tester [10] at the age of six months.

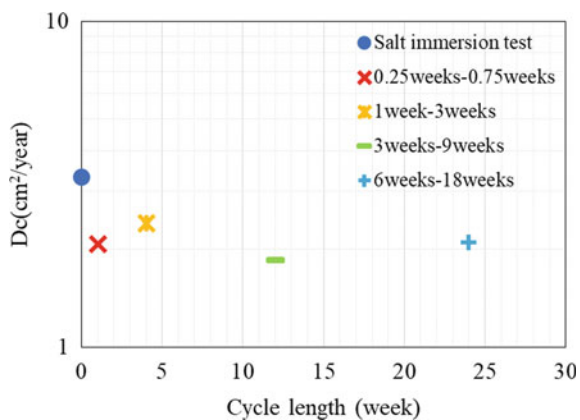
3 Results and Discussion

3.1 Changes in D_c Due to Difference in Cycle Length

The cyclic wetting and drying test was conducted on the specimens at the age of seven months to measure the chloride diffusion coefficient, D_c , as shown in Fig. 1. It can be seen from Fig. 1 that the obtained D_c was smaller in case of the cyclic wetting and drying test than that of the salt immersion test. The smaller D_c might be explained by relatively long drying periods in this study.

In addition, the difference in D_c due to the difference in cycle length was small and became almost constant implying the insignificantly influence of total cycle length on D_c . The cause of the small effect of cycle length was not clear.

Fig. 1 Relationship between cycle length and D_c (immersion time—dry time)



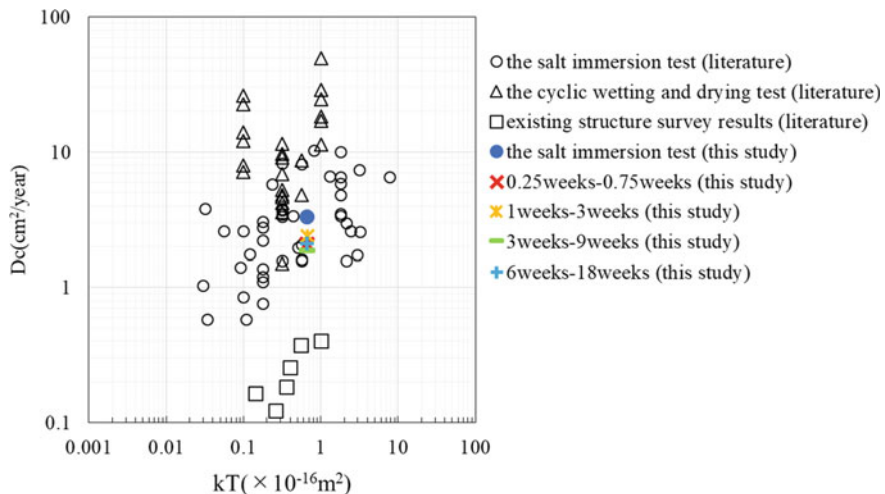


Fig. 2 Relationship between kT and D_c (immersion time—dry time)

3.2 Comparison with Existing Structure Survey Results

The obtained relationship between kT and D_c from this study is shown in Fig. 2 along with previous studies including survey results of existing structures [9]. There was a gap between the obtained D_c between the salt immersion test and the existing structure. In this study, D_c was calculated from a test in which the ratio of drying period was all tripled to simulate an existing structure. Although D_c decreased with the cyclic wetting and drying condition, the degree was small, so the cause of small D_c of the existing structure could not be explained.

3.3 Change of D_c by Difference of Ratio of Drying Period

In this study, the test was conducted under the assuming condition that the ratio of drying period was tripled, but the cause of the small D_c of the existing structure could not be explained. The changes in D_c due to the difference in the ratio of the drying period were compared with the previous literatures as shown in Fig. 3 [9, 11–13].

When the ratio of drying period is small (0.4–0.75), D_c was larger in the cyclic wetting and drying test compared to the salt immersion test [11–13]. It can be explained that concentration diffusion occurs in specimens during a short drying period and the permeation of chloride ions is promoted.

On the other hand, in the cyclic wetting and drying test, D_c decreased when the drying period became longer. The cause of the decrease in D_c is the amount of chloride ions supplied decreases when the drying period is extended. The test body is sufficiently dried and the penetration of chloride ions is stagnated. Here, D_c tends

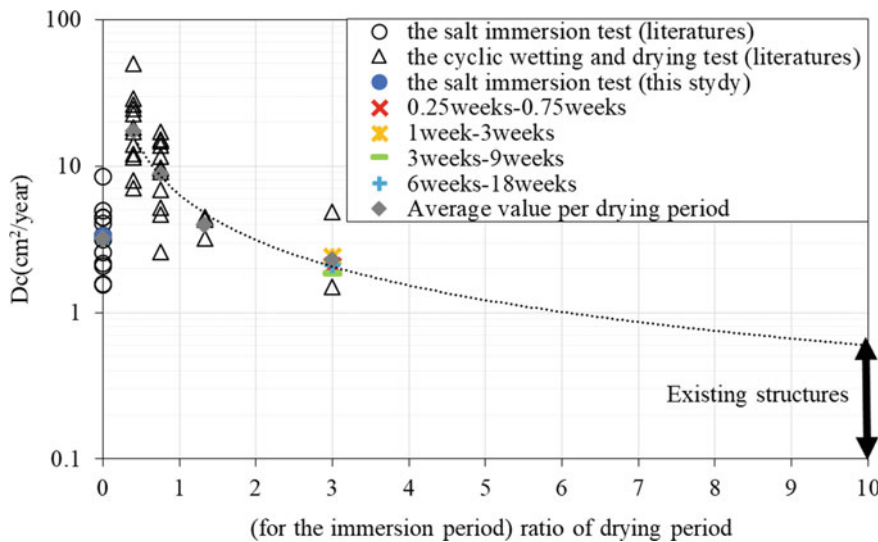


Fig. 3 Relationship between the ratio of drying period and D_c

to be smaller when the ratio of the drying period is longer. It almost agrees with the D_c in the existing structure when the approximation straight line is given and extrapolated, and when the ratio of the drying period exceeds about 10 times.

It shows the possibility to explain the permeation behavior of chloride ion. There is possibility that the ratio of the drying period in the existing structure is largely different from the originally assumption triple. It can be explained that there are no deicing salt days in winter, because depending on the location, there is a period when water leakage containing chloride ions is not supplied in existing structures.

4 Conclusions

In this study, the cyclic drying and wetting test was conducted to clarify the cause of the gap of D_c between the existing structures and the salt immersion test specimens. On the basis of the obtained results, a decrease in D_c due to the cyclic drying and wetting test was confirmed, but this did not explain the deviation from the existing structures. In addition, as a result of comparative analysis with results in existing literatures, it might be possible to clarify the cause of the decrease in D_c of the existing structure by focusing on the ratio of the drying period. In the future, we will clarify the relationship between kT and D_c by elucidating the effect of the drying ratio. The final goal will establish chloride ion permeation resistance evaluation of existing structures using the surface air permeability tests.

References

1. Francois R, Maso JC (1988) Effect of damage in reinforced concrete on carbonation or chloride penetration. *Cem Concr Res* 18(6):961–970. [https://doi.org/10.1016/0008-8846\(88\)90033-6](https://doi.org/10.1016/0008-8846(88)90033-6)
2. Neville A (1995) Chloride attack of reinforced concrete: an overview. *Mater Struct* 28(2):63–70. <https://doi.org/10.1007/BF02473172>
3. Oh BH, Jang BS (2003) Chloride diffusion analysis of concrete structures considering effects of reinforcements. *ACI Mater J* 100(2):143–149
4. Crank J, Crank EPJ (1979) The mathematics of diffusion. Clarendon Press, London
5. Tuutti K (1982) Corrosion of steel in concrete. <http://urn.kb.se/resolve?urn=urn:nbn:se:ri:diva-3051>
6. Torrent RJ et al (2007) Non-destructive methods to measure gas-permeability. Non-destructive evaluation of the penetrability and thickness of the concrete cover RILEM TC 189-NEC: state-of-the-art report, pp 41–50
7. Torrent RJ (2013) Service life prediction: theorecrete, labcrete and realcrete approaches. In: The third international conference on sustainable
8. Nguyen MH, Nakarai K, Nishio S (2019) Durability index for quality classification of cover concrete based on water intentional spraying tests. *Cem Concr Compos* 104:103355
9. Shimose C et al (2018) Evaluation of chloride penetration resistance for existing concrete structures with air permeability test. In: Proceedings of annual conference of Japan society of civil engineering Chugoku regional branch
10. Torrent RJ (1992) A two-chamber vacuum cell for measuring the coefficient of permeability to air of the concrete cover on site. *Mater Struct* 25(6):358–365
11. Kaneko T et al (2012) Effects of drying and wetting conditions on penetration and diffusion of chloride ion into concrete. Urban Disaster Mitigation (UDM) research report
12. Tsuji K et al (1984) Evaluation of penetration and diffusion of salt into concrete by the cyclic wetting and drying test. In: Proceedings of the 39th annual conference of the Japan society of civil engineers, vol 5, pp 37–38
13. Masuda Y et al (1988) Experiment on chloride penetration rate into concrete. *Proc Jpn Concr Inst* 10(2):493–498

Comparative Performances of Reinforced Beams Using Concrete Made from Crushed Sand and Fly Ash



Duy-Liem Nguyen, Van-Thuan Nguyen, Minh-Phung Tran,
and Minh-Thuan Duong

1 Introduction

Exploiting river sand in Mekong Delta zone, a traditional material for civil infrastructure, has been limited in recent years. The reason is that landslides has become a severe matter owing to overly exploiting river sand. Hence there has been a great demand to discover a new approach for not using river sand in production of concrete. In this research, we suggest using fine aggregate (also named crushed sand) for replacing river sand, some reports are available on this method [1–3]. Generally, An Giang province has many mountains containing aggregate source, it is really convenient to produce fine aggregate instead of river sand. In addition, there has been urgent demand in consuming fly ash, one of waste products in coal-fired Duyen Hai power plant at Tra Vinh province (also near An Giang province). Fly ash may help reduce cement used in concrete [4] and then may result low cost as well as minimize environmentally unfriendly impacts. In previous study [5], the main authors successfully developed the concrete using fine aggregate for fully replacing river sand and fly ash for partly replacing cement. However, there is still question about the behaviors of structural members using this type of concrete. This research is the next study to answer this question. The objective of this research is to experimentally and analytically explore bending resistance of reinforced crushed sand concrete beams. The results of research would provide useful information for practical and widely application of the crushed sand concrete in civil infrastructure.

D.-L. Nguyen (✉) · M.-T. Duong

Faculty of Civil Engineering, Ho Chi Minh City University of Technology and Education, Ho Chi Minh City, Vietnam

e-mail: liemnd@hcmute.edu.vn

V.-T. Nguyen

Faculty of Transportation Engineering, Nha Trang University, Khanh Hoa Province, Vietnam

M.-P. Tran

Faculty of Civil Engineering, Thu Dau Mot University, Binh Duong Province, Vietnam

2 Experimental Test

2.1 Materials and Preparation of Tested Beams

Eight concrete matrices are produced with their compositions and compressive strengths provided in Table 1. There are two main groups: the first is originated from matrix M1-T00 (using fine aggregate, no fly ash) having design compressive strength of 20 MPa and would be compared with matrix M200; the second is originated from matrix M1-T00 (using fine aggregate, no fly ash) having design compressive strength of 30 MPa and would be compared with matrix M300. It is noticed that matrices M200 and M300 are the traditional concretes (using river sand) having design compressive strength of 20 MPa and 30 MPa, respectively, while others are crushed sand concrete (using fine aggregate). Eight beams were prepared and named in the first column of Table 1. Table 2 provides the particle size fractions of fine aggregate while Table 3 shows the chemical compositions of fly ash.

All beams had same dimensions (depth × width × span length) $150 \times 150 \times 900 \text{ mm}^3$ (beam length 1000 mm, distance from each end of beam to its hinged support 50 mm). The experimented beams using steel reinforcement contains 2 bars with diameter of 12 mm ($A_s = 2.26 \text{ cm}^2$, $t_0 = 25 \text{ mm}$) in tension, and 2 bars with diameter of 6 mm ($A'_s = 0.57 \text{ cm}^2$, $d' = 25 \text{ mm}$) in compression, $f_y = 300 \text{ MPa}$,

Table 1 Compositions of concrete matrix

Beam name	Matrix name	Cement ^a (kG)	Fly ash ^b (kG)	Aggregate size 1 × 2 (kG)	Fine aggregate (kG)	River sand (kG)	Water (kG)	Compressive strength ^c (MPa)
D0-M200	M200	293 (1.00)	–	1355 (4.62)	–	652 (2.23)	185 (0.63)	24.63
D1-M1-T00	M1-T00	320 (1.00)	0 (0)	1150 (3.59)	715 (2.23)	–	215 (0.67)	27.19
D1-M1-T15	M1-T15	272 (0.85)	48 (0.15)	1150 (3.59)	715 (2.23)	–	215 (0.67)	36.87
D1-M1-T30	M1-T30	224 (0.70)	96 (0.30)	1150 (3.59)	715 (2.23)	–	215 (0.67)	18.17
D0-M300	M300	390 (1.00)	–	1326 (3.40)	–	598 (1.53)	185 (0.47)	37.87
D2-M2-T00	M2-T00	445 (1.00)	0 (0)	1070 (2.40)	651 (1.46)	–	234 (0.53)	34.48
D2-M2-T15	M2-T15	378 (0.85)	67 (0.15)	1070 (2.40)	651 (1.46)	–	234 (0.53)	43.13
D2-M2-T30	M2-T30	312 (0.70)	133 (0.30)	1070 (2.40)	651 (1.46)	–	234 (0.53)	30.89

Value in bracket presents corresponding ratio when total of cement and fly ash equal 1

^aCement PCB40 of An Giang ACIFA

^bProduction from coal-fired Duyen Hai power plant at Tra Vinh

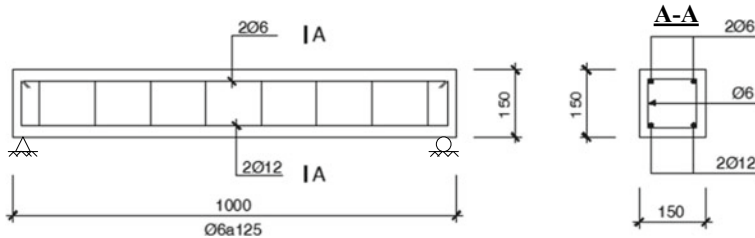
^cCubic specimen of $150 \times 150 \times 150 \text{ mm}^3$

Table 2 Particle size fractions of fine aggregate

Sieve size (mm)	Cumulation retained (g)	Percent retained on each sieve (%)	Cumulative percent retained on sieve Ai (%)
5.00	0	0	0
2.50	383.8	38.48	38.48
1.25	225.39	22.60	61.08
0.63	223.96	22.45	83.53
0.315	93.58	9.38	92.92
0.14	31.08	3.12	96.03
<0.14	39.58	3.97	100.00

Table 3 Chemical compositions of fly ash

Compound	SiO ₂	Al ₂ O ₃	Fe ₂ O ₃	CaO	MgO	MKN
Weight content (%)	54.2	24.6	9.03	1.52	1.5	6.18

**Fig. 1** Detail of geometry and reinforcement of the tested beams with span length of 900 m

$f_y' = 240$ MPa. Owing to low amount of steel reinforcement in compressive region, the experimented beams can be categorized with singly reinforced section, i.e., no compressive steel. The detail of geometry and reinforcements of the tested beam are shown in Fig. 1.

2.2 Test Setup and Procedure

A universal test machine under displacement control were used to test all 8 beams. The speed of loading was 1 mm/min. with test set up of three-point bending. During the test, the load and displacement history were measured. While the mid-span deflection of the experimented beam can be approximated as displacement of loading, the moment resistance under 3PBT is obtained using equation of $M = PL/4$, where L is

span length and P is the applied load. Then the response curves of moment–deflection of the experimented beams can be simply attained.

2.3 Testing Result and Discussion

Figure 2 shows the bending responses of the investigated beams while Table 4 shows flexural resistances of them. Generally, as the compressive strengths of matrices increase, there was an enhancement of moment resistances of beams while the deflection capacities (i.e., deflection at peak moment) and elastic stiffnesses (i.e., slope of bending response curve) of beams are not clear. Figure 3 shows the comparative moment resistances of the tested beams, the orders in term of compressive strength and moment resistance are as follows:

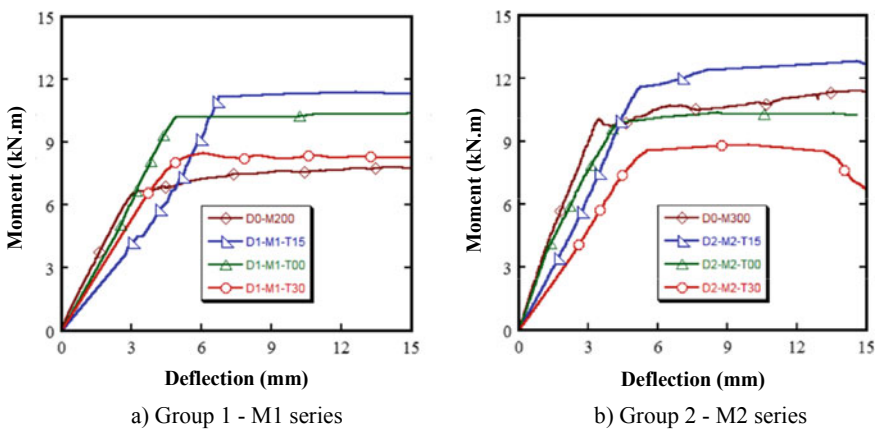


Fig. 2 Moment–deflection relationships of the experimented beams

Table 4 Flexural resistances of the tested beams

Beam name	Moment (kN m)	Deflection (mm)
D0-M200	7.781	14.543
D1-M1-T15	11.374	13.546
D1-M1-T00	10.472	18.286
D1-M1-T30	8.496	7.196
D0-M300	11.367	16.484
D2-M2-T15	12.808	14.589
D2-M2-T00	10.299	12.605
D2-M2-T30	8.84	10.712

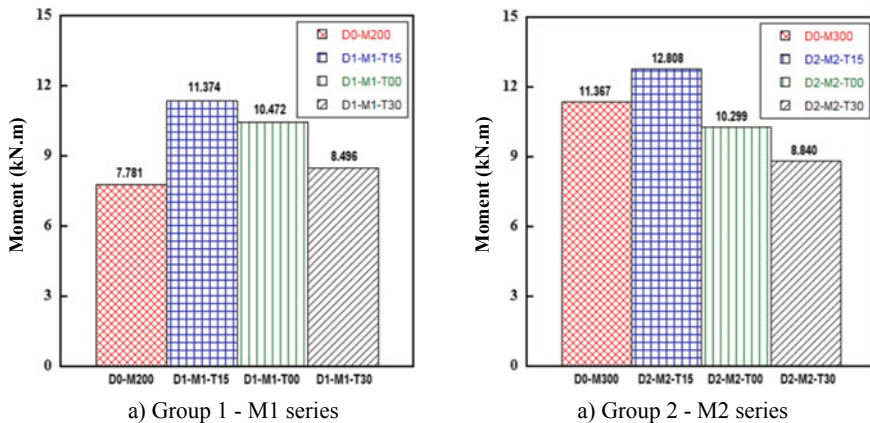


Fig. 3 Comparative moment resistances of the tested beams

- Group 1: Compressive strength: M1-T15 (36.87 MPa) > M1-T00 (27.19 MPa) > M200 (24.63 MPa) > M1-T30 (18.17 MPa) → moment resistance: D1-M1-T15 (11.374 kN m) > D1-M1-T00 (10.472 kN m) > D1-M1-T30 (8.496 kN m) > D0-M200 (7.781 kN m).
- Group 2: Compressive strength: M2-T15 (43.13 MPa) > M300 (37.87 MPa) > M2-T00 (34.38 MPa) > M2-T30 (30.39 MPa) → moment resistance: D2-M2-T15 (12.808 kN m) > D0-M300 (11.367 kN m) > D2-M2-T00 (10.299 kN m) > D2-M2-T30 (8.840 kN m).

The role of fly ash in concrete is to generate a denser mixture since the size of the air voids inside concrete are reduced, this increases strength and mechanical resistances of concrete. However, with a large amount of fly ash added to replace cement, there is not enough cement for hydration process and this decreases strength and mechanical resistances of concrete. The compressive strength of crushed sand concrete in comparison with river sand concrete was observed as follows: M1-T00 (27.19 MPa) > M200 (24.63 MPa) but M2-T00 (34.38 MPa) < M300 (37.87 MPa), i.e., the effectiveness of crushed sand is different in different grades of concrete although crushed sand is possibly replaced river sand.

3 Analytical Investigation

3.1 Moment Resistance According to Specification of TCVN 5574:2012 [6]

Figure 4 shows the distribution of stress, strain and steel force along the depth of section Moment resistance, M_{gh} , can be determined by Eq. (1), other equations are

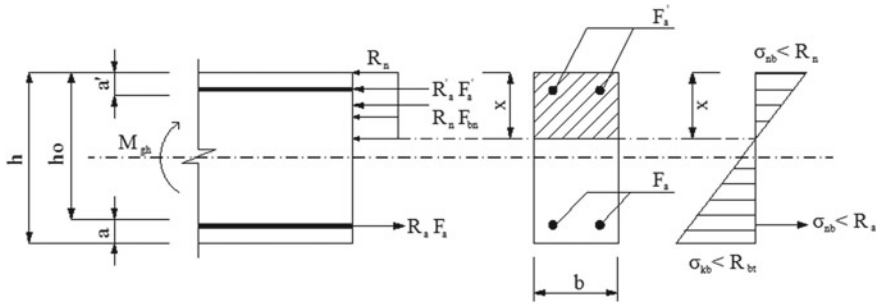


Fig. 4 Distribution of stress, strain and steel force along the depth of section according to TCVN 5574:2012

used to find the related parameters.

$$M_{gh} = \alpha_m \cdot R_n \cdot b \cdot h_o^2 + R'_a \cdot F'_a \cdot (h_o - a') \quad (1)$$

$$R_a F_a = R'_a \cdot F'_a + R_n \cdot b \cdot x \quad (2)$$

$$\zeta = \frac{x}{h_o} = \frac{R_a \cdot F_a - R'_a \cdot F'_a}{R_n \cdot b \cdot h_o} < \zeta_R \quad (3)$$

$$\alpha_m = \zeta(1 - 0.5\zeta) \quad (4)$$

where F_a, F'_a : area of tensile and compressive steel, respectively; R_a, R'_a : yield strength of tensile and compressive steel, respectively; R_{bt}, R_n : tensile and compressive strength of concrete, respectively, compressive strength using cubic specimen of 150 mm; F_{bn} : area of compressive zone of concrete; x : equivalent height of compressive zone of concrete; b, h : width and height of rectangular section, respectively; h_o : effective height of rectangular section; a, a' : distance from tensile and compressive steel to bottom and top of beam, respectively.

3.2 Moment Resistance According to Specification of ACI 318—2012

Figure 5 shows the distribution of stress, strain and steel force along the depth of section according to ACI 318:2012 [7]. The equilibriums of horizontal forces and moments at section, as provided in Eqs. (5–8).

$$0.85 f'_c (\beta_1 c) b + A'_s f_y = A_s f_y \quad (5)$$

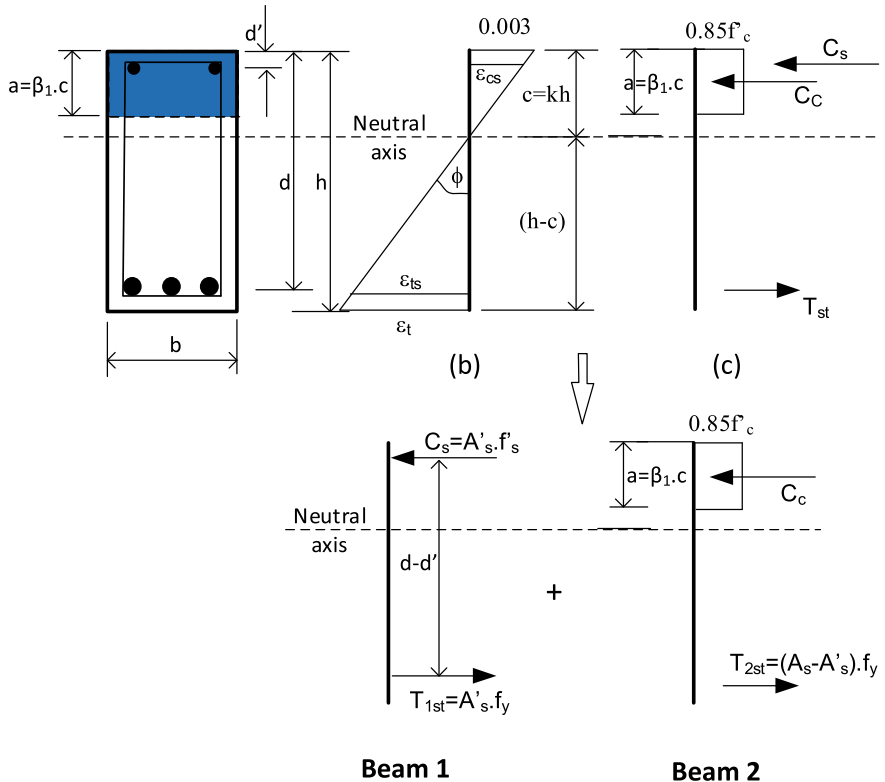


Fig. 5 Distribution of stress, strain and steel force along the depth of section according to ACI 318:2012

$$M_n = A_s f_y (d - a/2) - A'_s f_y (d' - a/2) \quad (6)$$

$$c = (A_s f_y - A'_s f_y) / (0.85 f'_c \beta_1 b) \quad (7)$$

$$a = \beta_1 c \quad (8)$$

where: A_a, A'_a : area of tensile and compressive steel, respectively; f_y, f'_y : yield strength of tensile and compressive steel, respectively; f'_c : compressive strength of concrete using cylindrical specimen of 150×300 mm, $f'_c = R_n / 1.2$.

a, b, h : equivalent height of compressive zone of concrete, width and height of rectangular section, respectively.

d, d' : effective height of rectangular section and distance from compressive steel to top of beam, respectively.

Table 5 Comparison of moment resistances derived from analytical investigation and from experimental test

Beam name	Moment (kN m)				
	Experiment (1)	TCVN 5574:2012 (2)	Difference (%) (1) and (2)	ACI 318-2012 (3)	Difference (%) (1) and (3)
D0-M200	7.781	7.737	0.6	4.765	38.8
D1-M1-T15	11.374	7.868	30.8	5.083	55.3
D1-M1-T00	10.472	7.774	25.8	5.886	43.8
D1-M1-T30	8.496	7.596	10.6	3.563	58.1
D0-M300	11.367	7.875	30.7	5.946	47.7
D2-M2-T15	12.808	7.907	38.3	5.729	55.3
D2-M2-T00	10.299	7.849	23.8	6.214	39.7
D2-M2-T30	8.84	7.818	11.6	5.449	38.4

3.3 Comparison of Moment Resistance Derived from Analytical Investigation and from Experiment

Table 5 provides the comparison result of moment resistances derived from analytical investigation and from experimental test. As shown in Table 5, the predicted moment resistances, using both TCVN 5574:2012 and ACI 318-2012, were much smaller than the experimental moment resistances, regardless of concrete matrix. The differences between experiment and TCVN 5574:2012 varied from 0.6 to 38.3% while the differences between experiment and ACI 318-2012 were observed from 38.4 to 58.1%. This means the predicted moment resistance using TCVN 5574:2012 or ACI 318-2012 is very safe.

4 Valuation on Finance Using Crushed Sand Concrete

Table 6 summarizes the comparative price including VAT tax per unit volume between crushed sand concretes and traditional concretes in An Giang province; the detail of computation can be referred to Duong [3]. The cost of crushed sand concretes are much cheaper than traditional concretes, from 25 to 80%.

Table 6 Comparative price including VAT tax per unit volume of crushed sand concretes

Compressive strength (MPa) → class of concrete	Crushed sand concrete		Traditional concrete		Ratio of price
	Matrix name	Price (VND/m ³)	Matrix name	Price (VND/m ³)	
18.17 → M150	M1-T30	666,309	M150	856,495	1.25
27.19 → M200	M1-T00	666,429	M200	931,995	1.40
30.89 → M250	M2-T30	616,683	M250	997,375	1.60
36.87 → M300	M1-T15	666,369	M300	1,064,788	1.60
43.13 → M350	M2-T15	616,765	M400	1,135,913	1.80

The unit price of concretes in An Giang province were computed at August 2018 based on current regulation

5 Conclusion

The following conclusions can be drawn from this investigation:

- Flexural behavior of reinforced beam using crushed sand concrete is similar to that using traditional concrete. Therefore, fine aggregate is possibly used as an alternative material for replacing river sand with cheaper cost.
- There is a correlation between compression strength and moment resistance of reinforced crushed sand concrete beam: the higher compression strength, the higher moment resistance.
- Both TCVN 5574:2012 and ACI 318-2012 can be used to predict moment resistance of reinforced beam with highly safe. However, we may use a factor for increasing the such predicted moments to approach the experimental results.

Acknowledgements This research was supported by Ho Chi Minh city University of Technology and Education (Vietnam).

References

1. Pham TH (2014) Experiment on using fine aggregate in production of concrete at Company VLXD 1828. Master thesis January 2014, Ho Chi Minh City University of Technology, Faculty of Materials Technology
2. Doan VC (2009) Study on using the seconds in grinding stone as fine aggregate of concrete. Southern Institute of Water Resources Research
3. Duong MT (2018) Fabrication and appraisal of the feasible approach using fine aggregate for replacing river sand in production of concrete at An Giang province, Ho Chi Minh City University of Technology and Education. Master thesis
4. Guruprasad J, Khote B, Gajarmal A, Navagare A (2018) Crushed stone waste as fine aggregate for pumped concrete. Int J Adv Res Sci Eng 7(4)

5. Nguyen DL, Duong MT (2018) Compressive resistance of environmental concrete using fly ash and fine aggregate for replacing traditional sand. In: Proceedings of the first international conference on material, machines and methods for sustainable development, MMMS 2018, 18–19 May, Da Nang, Vietnam, vol 1. Bach Khoa Publishing House, pp 79–84
6. TCVN 5574:2012 (2012) Concrete and reinforced concrete structures—design standard
7. ACI 318-12 (2012) Building code requirements for structural concrete

Effect of Fly Ash and Alkaline Solution on Rheology of Foamed Concrete



Anh Tuan Le, Thuy Ninh Nguyen, and Hyugmoon Kwon

1 Introduction

Nowadays, Vietnam is the one of countries in South of Asia which has a high coal potential. Many coal-fired power plants have been extended and constructed [3, 10]. Fly ash is known as waste materials with a large unused amount which causes a serious environmental problem. In application filed, fly ash has been used as an additive for mass concrete for dam construction or building construction such as roller compacted concrete, self-compacting concrete technology. Furthermore, fly ash is one of the most important source materials as pozzolan with contains a reasonable amount of silica and alumina. It can be improved durability of mortar and concrete [4, 8, 11].

Foamed concrete is a type of lightweight concrete that is manufactured from resource materials such as cement, sand, water, and the foam. The characteristics of foamed concrete depend on parameters such as water-binder ratio, foaming agent, and pozzolan content. This concrete is differentiated from porosity content in terms of the volume of air that is entrained. On the other hand, the porosity depends on flow and rheology of fresh mortar or concrete. The reaction of foaming agent with cement, fly ash, slag and meta-kaolin is influenced by environment [1, 6, 9, 12].

The rheological properties of mixture are important for the foamed concrete because concrete usually expand into place in construction. Moreover, rheological parameters are yield stress and viscosity. They are affected by particle sharp, surface reaction. Flow-ability of foamed concrete can be characterized by viscosity which is

A. T. Le (✉)

Ho Chi Minh City University of Technology, VNU-HCM, Ho Chi Minh City, Vietnam
e-mail: latuan@hcmut.edu.vn

T. N. Nguyen

Vietnam National University Ho Chi Minh City, Ho Chi Minh City, Vietnam

H. Kwon

Faculty of Engineering, Yeungnam University, Gyeongsan, Korea

really a concentrated suspension of fine aggregate in a viscous liquid and measured an increase in the rate of flow [2, 7, 13].

In this research, the effects of fly ash particle and alkaline solution on workability and rheology of foamed concrete are investigated. The alkaline solution is also used to activate fly ash on fresh concrete environment.

2 Experimental

2.1 Materials

Portland cement (C, type I) in accordance to ASTM C150 is used in this study and the chemical compositions are shown in Table 1.

Fly ash (FA) used in this study is low-calcium (class F) dry fly ash, according to ASTM C618. This fly ash has specific gravity is 2500 kg/m³ and total alumino-silica content is about 83.6% by weight. Chemical compositions of fly ash are shown in Table 1.

The alkaline liquid is a combination of sodium silicate and sodium hydroxide in solution. The sodium silicate solution included Na₂O and SiO₂ about 36–38% is mixed to sodium hydroxide 10 M.

In this study, river sand is used as fine aggregate. The specific gravity and bulk density of river sand are 2420 kg/m³ and 1290 kg/m³, respectively. The fineness modulus is 1.77. Sand is dried in an oven at least 24 h before mixing.

The foaming agent is used in this study, the physical properties is shown in Table 2.

Table 1 Chemical compositions of fly ash and cement

Oxide (%)	SiO ₂	Al ₂ O ₃	CaO	MgO	Fe ₂ O ₃	SO ₃	K ₂ O + Na ₂ O	LOI
Cement	21.3	5.58	61.92	1.35	4.32	1.69	—	1.17
Fly ash	51.7	31.9	1.21	0.81	3.48	0.25	1.02	9.63

LOI loss of ignition

Table 2 Properties of foaming agent

Color	Viscosity (CPS)	pH	Dosage (l/m ³)	Density (kg/m ³)
Brown	20–40	7	0.3–0.6	1200–1250

2.2 Test Method

In the mix proportion of foamed concrete, the ratio of binder and sand is 1:2 by mass. The ratio of water and binder (W/B) is mixed in range of 0.6, 0.7 and 0.8 by mass. Cement is replaced by fly ash in range from 20 to 100% by mass in binder composition. Water is replaced by alkaline liquid in water-binder ratio. Dosage of foaming agent is 0.5 l/m³. The mix proportion of foamed concrete is shown in Table 3. According to EFNARC recommendations [5], the rheological parameters are carried out on slump flow and flow time by V-funnel and mini-slump tests as shown in Fig. 1.

3 Results and Discussion

3.1 Influence of Liquid-Binder Ratio on Rheology

In this section, the influence of liquid-binder ratio on rheology of fresh foamed concrete is investigated. For LW mix proportions, the liquid is water and the alkaline solution for LL mix proportions. The test data are given in Fig. 2.

Based on Fig. 2, the spread for both LW and LL mixture increase up to 40% when liquid-binder ratio changes from 0.6 to 0.8. However, flow time in V-funnel test has contrary trend compared with the spread. The flow time value reduces with higher ratio of liquid-binder. The reduced time is about 32% in the case of LW and 40% in the case of LL. Generally, the flow diameter tends to rise up with an increase in liquid-binder ratio in mix proportions which use cement as binder. On the other hand, liquid-binder ratio seems to be significantly affected on rheology of fresh foamed concrete.

3.2 Influence of Fly Ash Content on Rheology

To evaluate the effect of fly ash on rheology of foamed concrete, the series of mixture LW1 and LL1 were conducted. The usage amount of fly ash varies from 20, 40, 60, 80 and 100% of cement by mass.

As seen in Figs. 3 and 4, both flow diameter and flow time reduce with higher amount of fly ash in binder. When the percentage of fly ash changes from 0 to 100%, the value of flow diameter decreases about 18% and 25% in the mix proportion LW and LL, respectively. With the flow time, the data decreases approximately 40% in the case of LW and 46% for LL. It can be indicated that the appearance of fly ash in mix proportion makes workability of fresh foamed concrete reduce. The main reason is that the particle size of fly ash is finer than cement and with the same amount of

Table 3 Mix proportion of foamed concrete

Mix	C	FA	W/B	D (mm)	T (s)	Mix	C	FA	L/B	D (mm)	T (s)	r (%)
LW10	100	0	0.6	190	12.3	LL10	100	0	0.6	180	10.2	26.1
LW11	80	20		185	11.3	LL11	80	20		170	8.6	28.7
LW12	60	40		175	10.5	LL12	60	40		165	7.5	29.4
LW13	40	60		170	9.3	LL13	40	60		155	6.4	35.8
LW14	20	80		170	8.2	LL14	20	80		140	5.9	36.6
LW15	0	100		165	7.3	LL15	0	100		135	5.5	38.5
LW20	100	0	0.7	240	10.2	LL20	100	0	0.7	220	7.3	28
LW21	80	20		240	8.6	LL21	80	20		210	6.7	30.7
LW22	60	40		235	7.9	LL22	60	40		195	6.1	34.7
LW23	40	60		225	7.1	LL23	40	60		180	5.4	34.4
LW24	20	80		215	6.7	LL24	20	80		170	4.8	36
LW25	0	100		210	6.5	LL25	0	100		155	4.2	38.8
LW30	100	0	0.8	265	8.4	LL30	100	0	0.8	250	6.1	30.4
LW31	80	20		255	7.8	LL31	80	20		240	5.2	33.7
LW32	60	40		250	6.9	LL32	60	40		225	4.5	33.3
LW33	40	60		240	6.4	LL33	40	60		215	3.9	36.8
LW34	20	80		235	5.8	LL34	20	80		210	3.5	41.5
LW35	0	100		220	5.1	LL35	0	100		190	3.3	44.7

C cement; FA fly ash; W/B water-binder; L/B alkaline liquid-binder; D flow diameter; T porosity; LW mixing with water; LL mixing with alkaline liquid

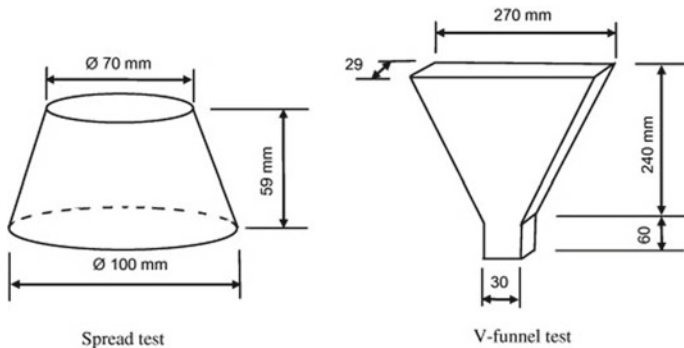


Fig. 1 Flow and flow time test [5]

liquid the mixture used fly ash can not have same workability. In the other words, with the usage of fly ash, the extra liquid should be added to maintain the same workability as before.

3.3 Influence of Alkaline Liquid on Rheology

In order to determine the influence of alkaline liquid on rheology of foamed concrete, the water content in mix portion LW is replaced by alkaline liquid in mix proportion LL. The results are shown in Figs. 5 and 6.

As seen in Figs. 5 and 6, diameter and flow time are various from 180 to 250 mm and from 10 to 6 s with alkaline-fly ash ratio in range of 0.6–0.8 with mix LL0, respectively. So, the workability and rheology are improved by high alkaline content in mix. The experiment is shown that the flow diameter reduces about 10–15% by adding fly ash. On the other hand, the flow time is strongly reduced by fly ash replacement. The time can be reduced from 20 to 40% in mix proportion LL15 and LL35, respectively. In general, viscosity of foamed concrete is significantly improved by high content of alkaline.

The physical properties can be affected by flow ability and viscosity of fresh concrete. The experiment is shown porosity increases about 5% with mix LW10, LW20 and LW30. Moreover, the porosity is clearly various by fly ash using. In Fig. 7, foamed concrete can be obtained about 40–45% in porosity by fly ash and alkaline mixing, as mix LL15, LL25 and LL35, respectively. Hence, the rheology is affected on expansion degree of foamed concrete.

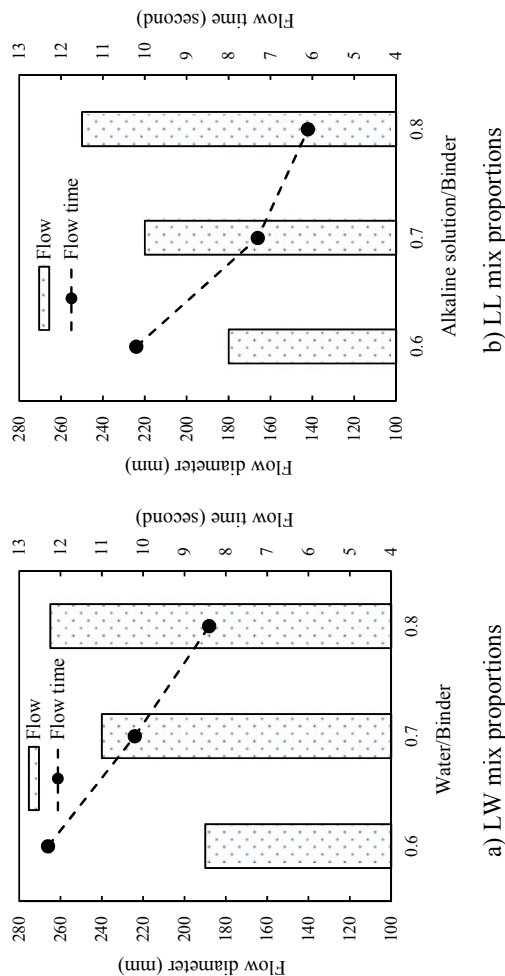


Fig. 2 Relationship between liquid-binder and rheology

Fig. 3 Effect of fly ash on flow, W/B and L/B = 0.6

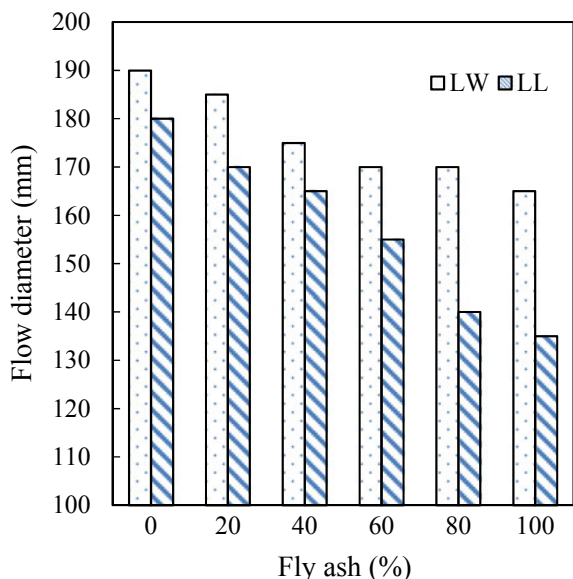


Fig. 4 Effect of fly ash on flow time, W/B and L/B = 0.6

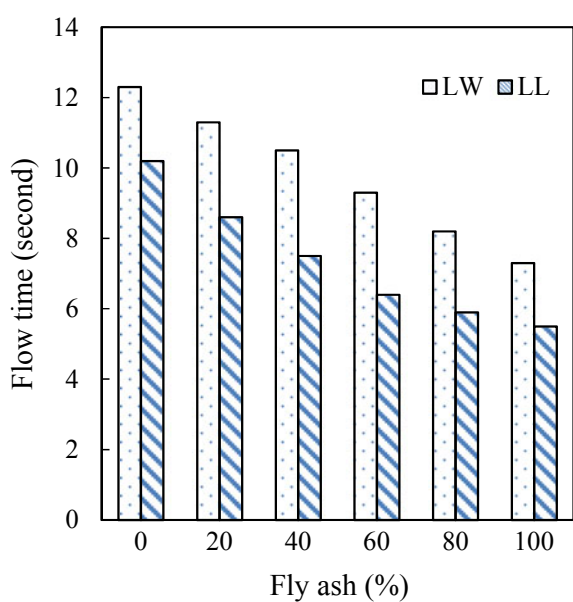


Fig. 5 Effect of fly ash and alkaline ratio on flow

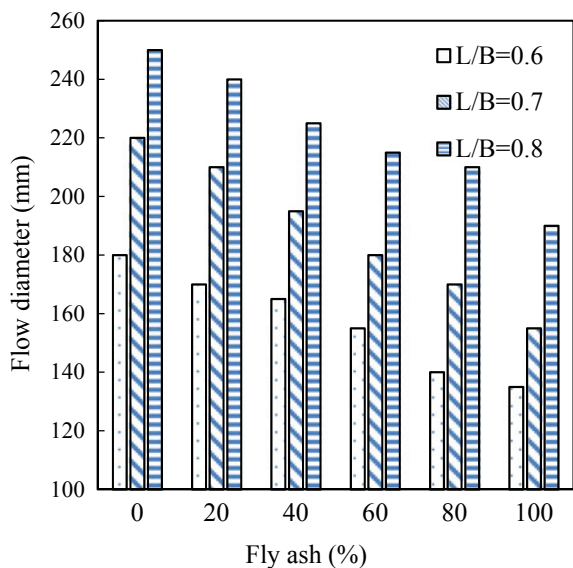


Fig. 6 Effect of fly ash and alkaline ratio on flow time

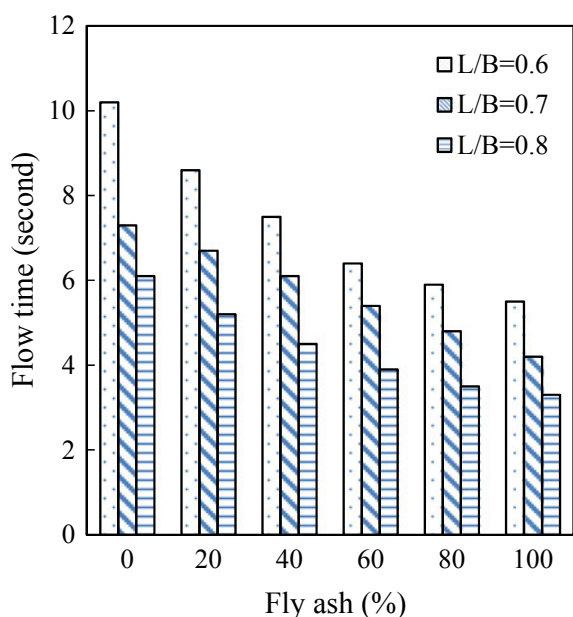
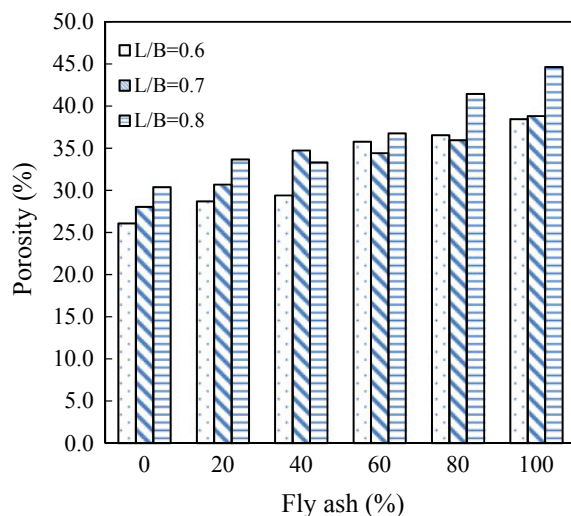


Fig. 7 Effect of fly ash on alkaline ratio on porosity



4 Conclusion

The research on the effect of fly ash on alkaline solution on foam concrete has some results as:

The flow diameter increases with high water–binder ratio and alkaline liquid–binder ratio. The flow time of concrete tends to reduce with high water and liquid content. In the case of using alkali liquid in mixture, workability reduces about 15% compared with using water in mixture. The workability and rheology of foamed concrete are affected by using fly ash and alkaline liquid. In mix proportion without cement, foamed concrete is shown higher flow diameter and less flow time about 40% compared with normal foamed concrete. Besides, the porosity of foamed concrete can be improved by using fly ash and alkaline liquid. It can be obtained 40–45% in porosity.

Acknowledgements This research is funded by Ho Chi Minh City University of Technology—VNU-HCM, under grant number T-KTXD-2018-45.

References

1. Aldridge D (2005) Introduction to foamed concrete: what, why, how? In: Proceedings of the international conference on the use of foamed concrete in construction, pp 1–14
2. Banfill PFG (1991) Rheology of fresh cement and concrete. E & FN Spon, London
3. Bui HB, Bui XN, Vu DH, Nguyen TD (2012) Characterization of a Vietnamese coal fly ash and its possible utilizations
4. Davidovits J (2011) Geopolymer chemistry and applications, 3rd edn. Institute Geopolymer, Saint-Quentin, France

5. EFNARC (2002) Specification and guidelines for self-compacting concrete. The European Federation of Specialist Construction Chemicals and Concrete Systems
6. Farzadnia N, Amran M (2015) Properties and applications of foamed concrete: a review. *Constr Build Mater* 101:990–1005
7. Ferraris CF, de Larrard F (1998) Modified slump test to measure rheological parameters of fresh concrete. *Cem Concr Aggreg* 2:241–247
8. Kearsley EP, Wainwright PJ (2001) The effect of high fly ash content on the compressive strength of foamed concrete. *Cem Concr Res* 31(1):105–112
9. Nandi S, Arnab C, Prantik S, Tanushree H (2016) Foamed concrete & its facets of application in civil engineering. *Int J Eng Res* 5(1):3–43
10. Nguyen XH, Ngo TLP (2013) Characteristics of fly ash and use ability in Vietnam. *J Agric Biol Sci* 8(12, Dem 20):785–787
11. Palomo A, Grutzeck MW, Blanco MT (1999) Alkali-activated fly ashes—a cement for the future. *Cem Concr Res* 29(8):1323–1329
12. Pan Z, Li H, Liu W (2014) Preparation and characterization of super low density foamed concrete from Portland cement and admixtures. *Constr Build Mater* 2:256–261
13. Tattersall GH (1976) The workability of concrete. A viewpoint publication. PCA

Effect of Sodium-Silicate Treatment for Recycled Concrete Aggregate on Slump and Compressive Strength of Concrete



Phuong Trinh Bui, Huynh Sang Le, Phan Phuong Uyen Nguyen,
Thanh Nam Ly, Ngoc Thanh Nguyen, Yuko Ogawa, and Kenji Kawai

1 Introduction

Concrete which is composed of cementitious materials, fine and coarse aggregates, water, and chemical admixture (if applicable) is commonly used as a construction material. With population growth and development of infrastructure and buildings, construction industry consumes a large amount of natural resources such as natural sand and natural stone, and releases a huge amount of construction and demolition (C&D) waste [5, 10, 14]. Recycling C&D waste to replace natural aggregate for concrete has been done as a promising solution to mitigate negative impacts of construction industry on environment [14] towards sustainable development. However, the use of recycled concrete aggregate (RCA) from C&D negatively influences workability and strength of concrete [7, 8]. Compressive strength of mixes with 50 and 100% RCA replacements decreased by an average of 16.6 and 26.4%, respectively [7]. This is due to adhered mortar on surface of RCA, leading to its higher water absorption, lower strength and higher crushing value than those of natural aggregate [14].

Several methods to improve the properties of RCA have been carried out in order to effectively utilize the RCA for the concrete industry. Mechanical grinding is one of methods which remove adhered mortar on surface of RCA. Nevertheless, this method could introduce micro-cracks inside RCA because of collision and grinding [9]. Chemical treatment is one of the methods which strengthen adhered mortar by using chemical solutions. Sodium-silicate solution as a chemical solution is used to treat surface of the RCA. It can be found that sodium-silicate solution significantly

P. T. Bui (✉) · H. S. Le · P. P. U. Nguyen · T. N. Ly · N. T. Nguyen
Faculty of Civil Engineering, Ho Chi Minh City University of Technology, VNU-HCM, Ho Chi
Minh City, Vietnam
e-mail: buiphuongtrinh@hcmut.edu.vn

Y. Ogawa · K. Kawai
Graduate School of Engineering, Hiroshima University, Higashi-Hiroshima City, Japan

reduced water absorption of RCA [4]. In addition, compressive strength of self-compacting concrete with RCA treated by sodium-silicate solution was higher by 11% and 8% at the ages of 28 and 90 days, respectively when compared with that of concrete with untreated RCA [4]. However, few studies on fresh and mechanical properties of normal concrete with the RCA treated by sodium silicate solution have been carried out.

Therefore, the aim of the present study was to investigate effect of sodium-silicate treatment for RCA on slump and compressive strength of concretes in order to effectively expand application of RCA to concrete production in Vietnam towards sustainable construction.

2 Experimental

2.1 Materials

Portland cement (C) supplied from Ha Tien Company conformed to TCVN 2682:2009 [13] (Portland cements—Specifications). Chemical compositions of the cement are listed in Table 1. River sand (RS) and crushed stone (CS) were used as fine and coarse aggregates, respectively. After collecting from a concrete plant, RCA was crushed into grains with a size range of 5–25 mm in order to partially replace CS for concrete production. Densities of C, RS, CS, and RCA were 3.10, 2.66, 2.70, and 2.55 g/cm³, respectively. Particle size distributions of RS, CS, and RCA are shown in Fig. 1. Water absorptions of CS and RCA were 0.20 and 5.43%, respectively. It indicates that RCA had higher water absorption and contained finer particles than CS.

RCA was divided into two groups including (1) untreated RCA and (2) treated RCA in order to investigate effect of surface treatment of RCA by sodium silicate. The RCA was treated by immersing in a solution consisting of 50% sodium silicate and 50% tap water for 1 h after drying at 105 °C in an oven. Before casting, the surface of treated RCA was dried in air. The crushing values of CS, untreated and treated RCA were 11.07, 18.58, and 14.95%, respectively. Water (W) and water-reducing agent (WRA) were also prepared in this study.

2.2 Mixture Proportion

A control mixture proportion with 0% RCA replacement was designed as per American Concrete Institute—ACI318-11 (Building Code Requirements for Structural Concrete and Commentary) [1] and ACI211.1-91 (Standard Practice for Selecting Proportions for Normal, Heavyweight, and Mass Concrete) [2]. A dosage of WRA

Table 1 Chemical compositions of cement (% by mass)

Compositions	SiO ₂	Fe ₂ O ₃	Al ₂ O ₃	CaO	MgO	K ₂ O	Na ₂ O	SO ₃	LOI
Content	21.98	2.53	4.28	62.57	1.56	0.01	0.37	1.89	2.89

LOI: loss on ignition

Fig. 1 Particle size distribution of aggregates

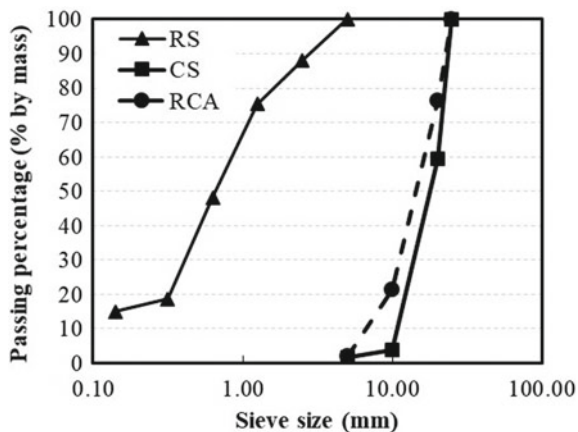


Table 2 Mixture proportion of all concretes

Mixture proportion	RCA replacement (% vol.)	W/C	Unit content (kg/m ³)					% by mass of cement	
			W	C	RS	CS	RCA	WRA	
R00	0	0.41	179	437	745	1070	0	1.0	
R25-UT	25	0.41	179	437	745	802	253	1.0	
R25-T	25	0.41	179	437	745	802	253	1.0	
R50-UT	50	0.41	179	437	745	535	505	1.2	
R50-T	50	0.41	179	437	745	535	505	1.2	

W: water; C: cement; RS: river sand; CS: crushed stone; RCA: recycled concrete aggregate; WRA: water-reducing agent; W/C: water-to-cement ratio

of 1.0% by mass of cement was employed not only to reduce partial amount of mixing water but also to make control mixture with designed slump of 120 ± 20 mm. Four mixture proportions having a constant water-to-cement ratio (W/C) of 0.41 were prepared in addition to the control mixture proportion as seen in Table 2. The replacements of CS by RCA were 0, 25, and 50% by volume. Concrete mixtures were designated the following codes: R00, R25-UT, R25-T, R50-UT, and R50-T. The numbers after R show the percentage replacements of CS by RCA (0%: R00, 25%: R25, and 50%: R50). UT and T show untreated and treated RCA, respectively.

2.3 Slump Test

After the concrete components had been mixed in a mixer, slump of fresh concrete of each mixture proportion was immediately measured as per TCVN 3106:1993 [11] (Fresh heavyweight concrete—Method for slump test).

2.4 Specimen Preparation for Compressive Strength Test

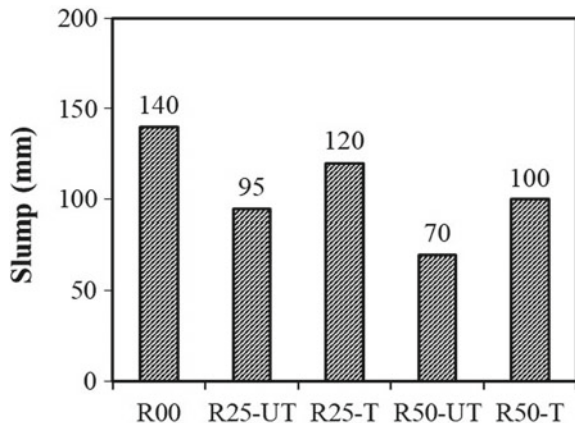
After testing slump of the fresh concrete, the concrete mixtures were cast into cubic specimens ($100 \times 100 \times 100$ mm). The placing surfaces of specimens were covered with polyethylene sheets and cured at room temperature of around 30 ± 5 °C. All specimens were demolded 24 h after casting and cured under relatively sealed condition with polyethylene sheets until the designated test ages (i.e. at the ages of 3, 7, and 30 days). Three specimens for each concrete mixture at each age were tested to determine their compressive strength as per TCVN 3118:1993 [12] (Heavyweight concrete—Method for determination of compressive strength).

3 Results and Discussion

3.1 Slump

Figure 2 shows effect of amount of untreated and treated RCA on slump of fresh concrete. It can be seen that slump of fresh concretes with RCA (R25-UT, R25-T, R50-UT, and R50-T) was lower when compared with that of control concrete without RCA (R00) regardless of sodium-silicate treatment. This is consistent with the result of a previous study [6]. Their lower slump was attributed to the physical characteristics of RCA. The RCA used in the present study was more angular and rougher than the CS due to the adhered mortar on its surface. In addition, the RCA contained finer particles and had higher water absorption than the CS as mentioned in Sect. 2.1.

Fig. 2 Effect of amount of untreated and treated RCA on slump of fresh concrete



Although the amount of WRA used in the concretes with 50% RCA replacement (R50-UT and R50-T) was higher than that in the concretes with 25% RCA replacement (R25-UT and R25-T) (see Table 2), the slump of R50-UT and R50-T was still lower than that of R25-UT and R25-T, respectively. It indicates that the higher the RCA replacement, the lower the slump of fresh concrete regardless of sodium-silicate treatment.

Figure 2 also shows that the treated RCA increased slump of fresh concrete when compared with the untreated RCA. This increase was also found in a previous study [4]. This may be due to microstructure of adhered mortar on RCA surface which was improved by sodium-silicate treatment, leading to a reduction of water absorption of RCA [4]. As a result, with the same mixing water content, the amount of excess water in fresh concrete with treated RCA was higher than that in fresh concrete with untreated RCA. The other reason could be the smooth surface of the treated RCA [4].

3.2 Compressive Strength

Figure 3a and b shows effect of amount of untreated and treated RCA on compressive strength of hardened concrete at the ages of 3 and 7 days, respectively. It can be found that the RCA reduced compressive strength of hardened concrete by 4.9–14.6% and 1.9–17.2% at the ages of 3 and 7 days when compared with that of concrete with 100% CS (R00), as seen in Fig. 3a and b, respectively. Similar results were also found in a previous study [7]. This is due to the higher crushing value of untreated and treated RCA than that of CS (18.58 and 14.95% > 11.07%). The adhered mortar on the surface of the RCA contributed to its high crushing value.

When compared with compressive strength of concrete with untreated RCA, the compressive strength of hardened concrete with treated RCA at the ages of 3 and 7 days reduced although the crushing value of sodium-silicate treated RCA was lower than that of untreated RCA (14.95% < 18.58%). This is attributed to the improvement

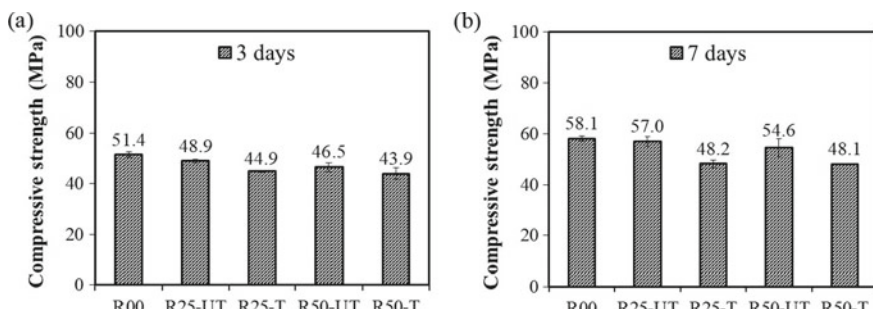
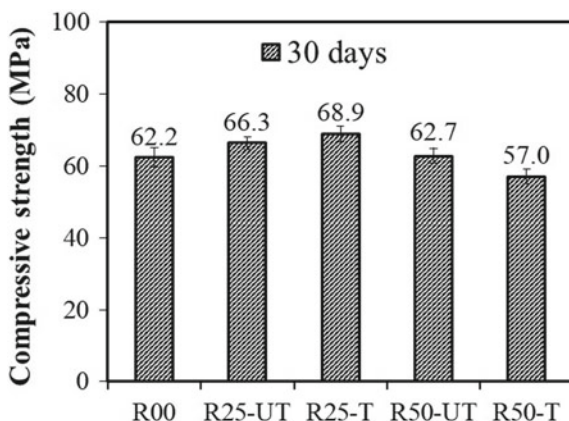


Fig. 3 Effect of amount of untreated and treated RCA on compressive strength of hardened concrete at 3 (a) and 7 (b) days

Fig. 4 Effect of amount of untreated and treated RCA on compressive strength of hardened concrete at 30 days



of water absorption of treated RCA (i.e. the water absorption of the treated RCA was different from that of the untreated RCA), resulting in the higher amount of excess water in fresh concrete with treated RCA than that in fresh concrete with untreated RCA. In addition, drying the treated RCA in air in the present study could be ineffective for sodium silicate to completely react with hydration products in adhered mortar on its surface. This may result in negative effect of sodium-silicate treatment on hydration at early ages of cement paste in the concrete despite of improving the properties of RCA.

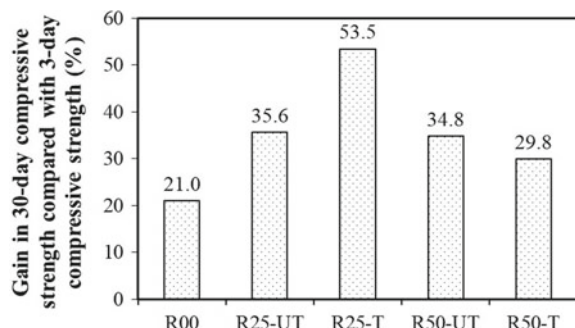
Figure 4 shows effect of amount of untreated and treated RCA on compressive strength of hardened concrete at the age of 30 days. When compared with compressive strength of concrete with 0% RCA replacement (R00), the compressive strength of hardened concrete with 25 or 50% RCA replacement was higher or nearly the same at the age of 30 days, except the concrete with 50% treated RCA replacement. The higher or nearly same compressive strength of concrete with RCA could be due to internal water released from RCA which promoted the cement hydration in the concretes. The improvement of performance of concrete with RCA as an internal curing agent was also found in a previous work [3].

Figure 5 shows gain in compressive strength at 30 days compared with the compressive strength at 3 days of all concretes. It indicates that gain in compressive strength of the concrete with RCA was more significant than that of the concrete without RCA regardless of sodium-silicate treatment. It confirms that internal water released from RCA promoted the cement hydration in the concrete at the age of 30 days.

4 Conclusion

The following conclusions can be drawn:

Fig. 5 Gain in compressive strength at 30 days compared with compressive strength at 3 days of all concretes



- The RCA reduced slump of fresh concrete because of its physical characteristics. The higher the RCA replacement, the lower the slump of fresh concrete regardless of sodium-silicate treatment.
- The RCA reduced compressive strength of hardened concrete at the ages of 3 and 7 days when compared with that of concrete with 100% CS because of its higher crushing value than that of CS regardless of sodium-silicate treatment. The higher the RCA replacement, the lower the compressive strength of hardened concrete at the ages of 3 and 7 days. However, at the age of 30 days, RCA increased the compressive strength of hardened concrete when compared with that of concrete with 100% CS because of effectiveness of internal curing with RCA.
- With the same mixing water content, the treated RCA increased the excess water content in concrete mixtures when compared with the untreated RCA and thereby leading to the higher slump and lower compressive strength of hardened concrete with treated RCA at the ages of 3 and 7 days when compared with the concrete with untreated RCA.

Consequently, the treatment of RCA by sodium-silicate solution reduced water absorption of RCA, resulting in an increase in slump of fresh concrete and a decrease in compressive strength of hardened concrete at early ages. This treatment could negatively affect cement hydration in concrete at early ages despite of improving the properties of RCA. A study of drying RCA at high temperature after immersing in sodium-silicate solution should be done in future works.

Acknowledgements The authors would like to thank Mr. Dai Thanh Le, Ha Tien 1 Cement Joint Stock Company for cement supports and undergraduate students of Department of Construction Materials, Ho Chi Minh City University of Technology, VNU-HCM for assistance in experimental work.

References

1. American Concrete Institute (2011) ACI318-11 building code requirements for structural concrete and commentary. ACI Committee, Farmington Hills, MI

2. American Concrete Institute (1991) ACI211.1-91 standard practice for selecting proportions for normal, heavyweight, and mass concrete. ACI Committee, Farmington Hills, MI
3. Dimitriou G, Savva P, Petrou MF (2018) Enhancing mechanical and durability properties of recycled aggregate concrete. *Constr Build Mater* 158:228–235
4. Guneyisi R, Gesoglu M, Algin Z, Yazici H (2014) Effect of surface treatment methods on the properties of self-compacting concrete with recycled aggregates. *Constr Build Mater* 64:172–183
5. Kisku N, Joshi H, Ansari M, Panda SK, Nayak S, Dutta SC (2017) A critical review and assessment for usage of recycled aggregate as sustainable construction material. *Constr Build Mater* 131:721–740
6. Malešev M, Radonjanin V, Marinković S (2010) Recycled concrete as aggregate for structural concrete production. *Sustainability* 2:1204–1225. <https://doi.org/10.3390/su2051204>
7. McGinnis MJ, Davis M, Rosa ADL, Weldon BD, Kurama YC (2017) Strength and stiffness of concrete with recycled concrete aggregates. *Constr Build Mater* 154:258–269
8. Safiuddin M, Alengaram UJ, Salam MA, Jumaat MZ, Jaafar FF, Saad HB (2011) Properties of high-workability concrete with recycled concrete aggregate. *Mater Res* 14(2):248–255. <https://doi.org/10.1590/S1516-14392011005000039>
9. Shi C, Li Y, Zhang J, Li W, Chong L, Xie Z (2016) Performance enhancement of recycled concrete aggregate—a review. *Clean Prod* 112:466–472
10. Tam VWY, Soomro M, Evangelista ACJ (2018) A review of recycled aggregate in concrete applications (2000–2017). *Constr Build Mater* 172:272–292
11. TCVN (1993) TCVN 3106:1993 fresh heavyweight concrete—method for slump test. Ministry of Construction, Vietnam
12. TCVN (1993) TCVN 3118:1993 heavyweight concrete—method for determination of compressive strength. Ministry of Construction, Vietnam
13. TCVN (2009) TCVN 2682:2009 Portland cements—specifications. Institute of Building Materials, Ministry of Construction, Vietnam
14. Wang L, Wang J, Qian X, Chen P, Xu Y, Guo J (2017) An environmentally friendly method to improve the quality of recycled concrete aggregates. *Constr Build Mater* 144:432–441

Effect of Water-to-Binder Ratio on Cementing Efficiency Factor of Fly Ash Regarding Compressive Strength of Concrete



Phat Tan Huynh, Phuong Trinh Bui, Yuko Ogawa, and Kenji Kawai

1 Introduction

The cementing efficiency factor (k -value) of fly ash was firstly introduced by Smith [14]. It was defined as a part of fly ash which can be considered as cement in contributing to strength development of concrete [14]. The author suggested a constant k -value of 0.25 for fly ash which was determined from compressive strengths of fly-ash concrete at 7 and 28 days by modifying a Bolomey equation [14]. Nevertheless, Bijen and Selst [3] found that the k -value of fly ash decreases with an increase in water-to-cement ratio, whereas it tends to increase with age as demonstrated by Babu and Rao [1]. Although there are many researchers [1, 3, 14] who have studied the efficiency factor of fly ash, the k -value is still suggested to be a constant value. For example, the European Standard EN 206-1 [4] broadly permits the k -value of 0.4 for fly ash without considering some conditions such as curing time, replacement ratio of fly ash, and water-to-binder ratio.

On the other hand, there are a lot of studies [2, 5, 10, 12, 13, 15] on the fly ash reaction in fly-ash cement paste. Nevertheless, the contribution of fly ash to the strength development of concrete due to the fly ash reaction have not been evaluated sufficiently and/or quantitatively. Therefore, a main purpose of this study was to investigate the effect of water-to-binder ratio on the contribution of fly ash to strength development of concrete that considers the degree of fly ash reaction in paste. In addition, calcium hydroxide (portlandite) content in paste specimens was investigated.

P. T. Huynh · Y. Ogawa · K. Kawai (✉)

Department of Civil and Environmental Engineering, Graduate School of Engineering, Hiroshima University, 1-4-1, Kagamiyama, Higashi-Hiroshima, Hiroshima 739-8527, Japan
e-mail: kkawai@hiroshima-u.ac.jp

P. T. Huynh · P. T. Bui

Faculty of Civil Engineering, Ho Chi Minh City University of Technology, VNU-HCM, 268 Ly Thuong Kiet, Ho Chi Minh City, Vietnam

To obtain above purpose, test for the compressive strength of concrete was carried out in accordance with Japanese Industrial Standard (JIS) A 1108 [6]. For paste specimens, test for the degree of fly ash reaction was done by selective dissolution method (SDM), whereas test for the portlandite content was performed by thermogravimetry and differential thermal analysis (TG-DTA).

2 Test Program

2.1 Materials

Ordinary Portland cement (OPC) and a low-calcium fly ash (FA) were used as binders. The cement (from Taiheiyo Cement Corp., Tokyo, Japan) and FA (from Chugoku Electric Power Co., Inc., Hiroshima, Japan) met JIS R 5210 [9] and JIS A 6201 [7], respectively. Table 1 shows the chemical compositions of the binder. The densities of the cement and the FA were 3.16 and 2.37 g/cm³ while their Blaine fineness were 3290 and 3530 cm²/g, respectively. Crushed sand and stone were used as fine and coarse aggregates, respectively. The fine aggregate had a fineness modulus of 2.71 while the coarse aggregate had a maximum size of 20 mm. The water absorption and the density of the fine aggregate were 1.04% and 2.61 g/cm³, whereas those of the coarse aggregate were 0.71% and 2.62 g/cm³. Besides, chemical admixtures (from Flowric Co., Ltd., Japan) including a superplasticizer or a water-reducing agent and an air-entraining agent (JIS A 6204 [8]) were used to achieve the slump of 10.0 ± 2.0 cm and air content of 5.0% ± 0.5% as the targets for all fresh concretes in the material design.

2.2 Mixture Proportions and Specimen Preparation

Concrete specimens were prepared with two water-to-binder (W/B) ratios of 0.30 and 0.50 by mass, and the FA was used to replace a part of the OPC at ratios of 0, 20, 30, and 40% by mass (i.e., FA0, FA20, FA30, and FA40) as listed in Table 2. Moreover, the control concretes with two additional W/B ratios of 0.40 and 0.60 were prepared in order that the equivalent cement-to-water ratio ($(C/W)_{eq.}$) and the k -value of FA can be evaluated experimentally.

For all mixture proportions of concrete, the masses of water and coarse aggregate were 170 and 932 kg/m³, respectively. The slump, temperature, and air content of fresh concrete were immediately measured after mixing as shown in Table 2.

Additionally, paste specimens had the same W/B ratios (0.30 and 0.50) and four replacement ratios of FA as the concrete specimens to examine the degree of FA reaction and the portlandite content in pastes. Noted that no chemical admixtures as well as no fine and coarse aggregates were employed for making paste specimens.

Table 1 Chemical compositions of binder (mass%)

Compositions	SiO ₂	Fe ₂ O ₃	Al ₂ O ₃	CaO	MgO	K ₂ O	Na ₂ O	SO ₃	LOI
OPC	20.29	2.96	4.91	65.05	1.20	0.39	0.26	1.93	2.44
FA	53.53	5.17	28.11	3.12	1.21	0.90	0.79	0.63	2.37

Table 2 Mixture proportions and properties of fresh concrete

Group	Mixture	W/B	F/(C+F) (mass%)	Unit content (kg/m ³)				Properties of fresh concrete			
				W	C	F	S	G	Temp. ^a (°C)	Slump (cm)	Air (%)
Control	30FA0	0.30	0	170	567	0	653	932	18.6	11.0	5.2
	40FA0	0.40	0	170	425	0	770	932	14.3	7.0	5.2
	50FA0	0.50	0	170	340	0	840	932	17.5	11.5	5.3
	60FA0	0.60	0	170	283	0	887	932	13.7	8.5	5.2
W/B 0.50	50FA20	0.50	20	170	272	68	821	932	21.6	11.0	4.7
	50FA30	0.50	30	170	238	102	812	932	16.9	12.5	5.4
	50FA40	0.50	40	170	204	136	802	932	16.9	13.0	4.8
	30FA20	0.30	20	170	453	113	621	932	23.6	9.5	5.1
W/B 0.30	30FA30	0.30	30	170	397	170	606	932	23.7	13.0	4.7
	30FA40	0.30	40	170	340	227	590	932	23.8	12.0	4.8

W/B is water-to-binder (cement + FA) ratio by mass, F/(C+F) is replacement ratio of FA by mass, W is water, C is cement, F is fly ash, S is fine aggregate and G is coarse aggregate

^aTemp. means temperature

All materials were prepared and stored at 20 °C. Before mixing, the moisture content of sand was examined in order to determine properly the required mixing water for each mixture proportion of concrete. Concrete was cast into cylindrical molds of 100-mm in diameter and 200-mm in height while paste was cast into 16-mL polypropylene bottles. All concrete and paste specimens were sealed at 20 °C until the ages of 3, 7, 28, 91, and 182 days.

2.3 Degree of FA Reaction and Portlandite Content in Paste

The degree of FA reaction and the portlandite (CH) content in paste specimens were measured at 3, 7, 28, 91, and 182 days by SDM and TG-DTA, respectively. At the designated ages, samples were obtained by cutting the paste specimens into the size range of 2.5–5.0 mm. In order to stop further hydration, the samples were submerged in acetone at a pressure of –0.1 MPa for at least 30 min, and this step was repeated three times with changing acetone. Samples were continually dried in a vacuum desiccator for at least 3 days. Before SDM and TG-DTA, the dried samples were ground into a powder that passed through sieve No. 100 (or 150 µm).

A method using 2-M hydrochloric acid (HCl) and 5% sodium-carbonate (Na_2CO_3) aqueous solution which was firstly proposed by Ohsawa et al. [12] was used to investigate the degree of FA reaction in paste. The degree of FA reaction, α , can be calculated as follows.

$$\alpha = 1 - \frac{X(1 - Ig')/k_2}{(1 - Ig)k_1} \quad (1)$$

where k_1 is original fraction of FA in ignited base (fraction), k_2 is extracted residue of a 1-g FA (fraction), X is extracted residue of the hydrated FA in a 1-g hydrated sample (fraction), Ig is loss on ignition of the hydrated sample (fraction), and Ig' is loss on ignition of the extracted residue (fraction).

For the TG-DTA, the temperature of a sample was raised from 30 to 1000 °C with a heating rate of 20 °C/min and kept at 100 °C for 30 min to remove free water. This measurement was conducted under N_2 environment in order to prevent carbonation and/or oxidization while monitoring the mass changes. The CH content was related to the mass loss from dehydration of CH in a paste. Equation 2 was used to calculate the CH content in the paste.

$$CH = (m_1/m_0) \times (74/18) \times 100 \quad (2)$$

where CH is the CH content in the pastes (the plain cement paste or the fly-ash cement paste) (%), m_1 is the mass loss from CH dehydration (mg), and m_0 is the initial mass of paste (mg).

2.4 Compressive Strength of Concrete and Calculation of k-Value of FA

Test for compressive strength of concrete was carried out according to JIS A 1108 [6] with the loading rate of 1.5 kN/s at 3, 7, 28, 91, and 182 days. The mean value of three tested concrete specimens was reported.

To evaluate the k -value of FA, a modified Bolomey equation which was firstly suggested by Smith [14] was used as shown in Eq. 3. As mentioned above, a relationship between the C/W and the compressive strength of the control concrete was obtained at each age. The $(C/W)_{eq.}$ was calculated by replacing the measured value of compressive strength of concrete containing FA into this relationship. The k -value of FA was calculated by using Eq. 4 which was derived from Eq. 3 [14].

$$(C/W)_{eq.} = (C + kF)/W \quad (3)$$

$$k = \left\{ \frac{(C/W)_{eq.}}{(C/W)} - 1 \right\} \times \left(\frac{1-r}{r} \right) \quad (4)$$

where $(C/W)_{eq.}$ is the equivalent cement-to-water ratio (fraction), C , F , and W are unit contents of cement, fly ash, and water, respectively (kg/m^3), k is the k -value of FA (fraction), and r is replacement ratio of FA (fraction) (i.e., $F/(C + F)$).

3 Results and Discussion

3.1 Degree of FA Reaction and CH Content in Paste

The results of degree of FA reaction and CH content relative to cement content in the pastes are shown in Fig. 1a and b, respectively. As illustrated in Fig. 1a, the degree

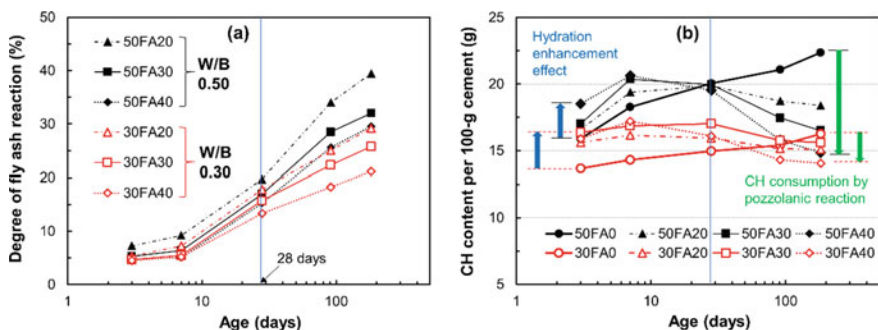


Fig. 1 a Degree of FA reaction and b CH content per 100-g cement in pastes with time

of FA reaction in the pastes increased with time but decreased with an increase in the FA replacement ratio. This result was consistent with that of Lam et al. [10]. At early ages (i.e., 3 and 7 days), the degree of FA reaction in paste was low, and there was no significant difference in the degree of FA reaction for all pastes within 28 days. After 28 days, the higher the W/B ratio, the higher the degree of FA reaction. In particular, the degree of FA reaction in paste with a high W/B ratio of 0.50 increased more significantly to 182 days compared with that in paste with a low W/B ratio of 0.30 as shown in Fig. 1a. This tendency was also confirmed in some studies [5, 10] and the reason for this response will be revealed in Fig. 1b.

Figure 1b shows the CH content per 100-g cement in pastes with time. For the paste without FA (FA0), the CH content increased with time regardless of W/B ratio. Moreover, the CH content in the FA0 increased with an increase in the W/B ratio. This can be explained due to more space and water available for cement hydration. A higher CH content might yield a higher pozzolanic reaction degree in paste containing FA. This was considered as an obvious evidence for the higher degree of FA reaction as previously mentioned. For the pastes with FA (i.e., FA20, FA30, and FA40), although the CH content per 100-g cement increased at 7 days, it decreased after 28 days because of the pozzolanic reaction of FA. Compared with the FA0, the higher CH content per 100-g cement in the FA20, FA30, and FA40 at the early ages can be attributed to an enhancement of the cement hydration by FA addition in the fly-ash cement systems as mentioned in some previous works [2, 11]. From Fig. 1b, the lower the W/B ratio was, the more the FA addition could enhance the cement hydration. Meanwhile, the CH consumption by the pozzolanic reaction of FA in the pastes with a low W/B ratio of 0.30 was very low compared with that in the pastes with a high W/B ratio of 0.50 at 182 days.

3.2 Compressive Strength of Concrete and Calculation of k-Value of FA

Compressive strengths of all concretes are presented in Fig. 2. Each value of compressive strength shown in Fig. 2 is a mean value of three tested concrete specimens, the standard deviations of which ranged from 0.1 to 2.8 N/mm² with the coefficient of variation of less than 5% for all mixtures. Figure 2a shows the results of compressive strengths of control concrete without FA as the references. The compressive strengths of the control concrete increased with time and were used to obtain a relationship between the C/W and the compressive strength of the control concrete with an extremely high correlation coefficient R² (equal to or higher than 0.995) as illustrated in Fig. 2a.

Figure 2b shows the results of compressive strength of fly-ash concrete with the relationship from the control concretes. As shown in Fig. 2b, if the compressive strength of fly-ash concrete reaches the linear relationship at corresponding age, the $(C/W)_{eq}$ and the C/W are the same. This means the k-value is equal to zero.

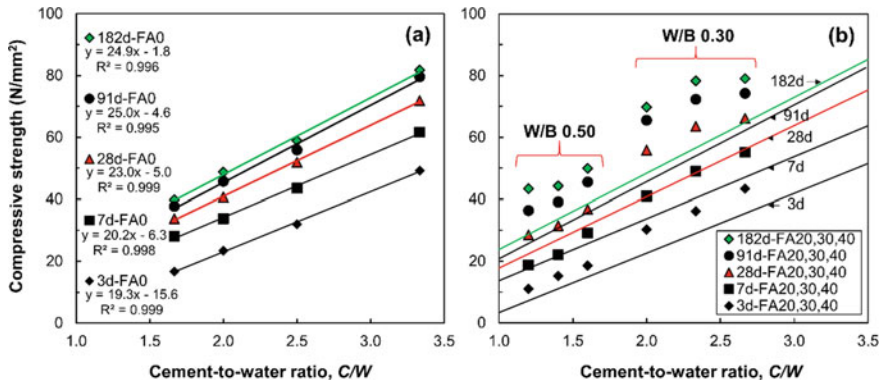


Fig. 2 **a** Relationship between C/W and compressive strength of control concrete and **b** compressive strength of fly-ash concrete

Obviously, the higher the compressive strength of fly-ash concrete compared with the relationship, the higher the k -value of FA.

The k -value with time and the relationship between the k -value and degree of FA reaction are presented in Fig. 3a and b, respectively. As shown in Fig. 3a, the k -value of FA was higher at 3 and 7 days for the mixtures with a low W/B ratio of 0.30 than that for the mixtures with a high W/B ratio of 0.50. This might be explained by the physical effect of FA resulting in improvement of cement hydration in the fly-ash cement system with a low W/B ratio. Furthermore, as demonstrated in a study of Berry et al. [2], the FA was mainly related to a formation of the ettringite at early ages. The formation of the ettringite significantly affected the space filling due to the hydration products in paste with a low W/B ratio of 0.30. This might be considered as an additional reason for the higher k -value of FA in concrete with the low W/B ratio of 0.30 at 3 and 7 days. After 28 days, the k -value of FA in mixtures with a high W/B ratio of 0.50 increased more significantly compared with that in mixtures with a low W/B ratio of 0.30. This was mainly due to the pozzolanic reaction of FA as discussed in Sect. 3.1. In detail, the k -value of FA ranged from 0.01 to 0.55 for

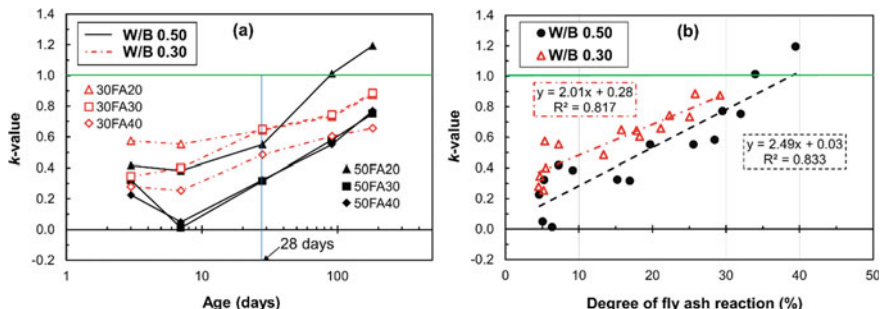


Fig. 3 **a** k -value with time and **b** relationship between k -value and degree of FA reaction

mixtures with a high W/B ratio of 0.50 while it ranged from 0.25 to 0.65 for mixtures with a low W/B ratio of 0.30 within 28 days. After 28 days, the *k*-value ranged from 0.31 to 1.19 at the high W/B ratio of 0.50 while it ranged from 0.48 to 0.88 at the low W/B ratio of 0.30 up to 182 days. The W/B ratio strongly affected the *k*-value of FA regarding strength development of concrete.

From Fig. 3b, it is confirmed that the contribution of FA to strength development of concrete with a different W/B ratio can be partly evaluated in a chemical approach by a positive correlation between the *k*-value and the degree of FA reaction. However, it cannot be said that the higher the degree of FA reaction, the higher the *k*-value in the case of different W/B ratio.

4 Conclusions

1. The effect of W/B ratio on the *k*-value of FA was significant with time. The lower the W/B ratio, the higher the *k*-value at the ages of 3 and 7 days because FA could enhance the cement hydration. Meanwhile, the *k*-value increased with an increase in the degree of FA reaction up to 182 days.
2. The *k*-value of FA ranged from 0.01 to 0.55 for mixtures with a high W/B ratio of 0.50 while it ranged from 0.25 to 0.65 for mixtures with a low W/B ratio of 0.30 within 28 days. The *k*-value ranged from 0.31 to 1.19 at the high W/B ratio of 0.50, whereas it ranged from 0.48 to 0.88 at the low W/B ratio of 0.30 after 28 up to 182 days.

References

1. Babu KG, Rao GSN (1996) Efficiency of fly ash in concrete with age. *Cem Concr Res* 26(3):465–474
2. Berry EE, Hemmings RT, Cornelius BJ (1990) Mechanisms of hydration reactions in high volume fly ash pastes and mortars. *Cem Concr Compos* 12(4):253–261
3. Bijen J, Selst RV (1993) Cement equivalence factors for fly ash. *Cem Concr Res* 23(5):1029–1039
4. EN 206-1 (2000) Concrete—Part 1: Specification, performance, production and conformity. European Committee for Standardization, Brussels
5. Hanehara S, Tomosawa F, Kobayakawa M, Hwang K (2001) Effects of water/powder ratio, mixing ratio of fly ash, and curing temperature on pozzolanic reaction of fly ash in cement paste. *Cem Concr Res* 31(1):31–39
6. JIS A 1108 (1993) Method of test for compressive strength of concrete. Japanese Standards Association, Tokyo
7. JIS A 6201 (1999) Fly ash for concrete. Japanese Standards Association, Tokyo
8. JIS A 6204 (2011) Chemical admixtures for concrete. Japanese Standards Association, Tokyo
9. JIS R 5210 (2009) Portland cement. Japanese Standards Association, Tokyo
10. Lam L, Wong YL, Poon CS (2000) Degree of hydration and gel/space ratio of high-volume fly ash/cement systems. *Cem Concr Res* 30(5):747–756

11. Moon GD, Oh S, Choi YC (2016) Effects of the physicochemical properties of fly ash on the compressive strength of high-volume fly ash mortar. *Constr Build Mater* 124:1072–1080
12. Ohsawa S, Asaga K, Goto S, Daimon M (1985) Quantitative determination of fly ash in the hydrated fly ash— $\text{CaSO}_4 \cdot 2\text{H}_2\text{O}$ — $\text{Ca}(\text{OH})_2$ system. *Cem Concr Res* 15(2):357–366
13. Sakai E, Miyahara S, Ohsawa S, Lee SH, Daimon M (2005) Hydration of fly ash cement. *Cem Concr Res* 35(6):1135–1140
14. Smith IA (1967) Design of fly ash concrete. *Proc Inst Civil Eng* 36:769–790
15. Zhang YM, Sun W, Yan HD (2000) Hydration of high-volume fly ash cement pastes. *Cem Concr Compos* 22(6):445–452

Effects of Fiber Type and Volume Fraction on Fracture Properties of Ultra-High-Performance Fiber-Reinforced Concrete



Ngoc Thanh Tran, Tri Thuong Ngo, and Duy Liem Nguyen

1 Introduction

The demand for more robust and tougher construction materials has intensively been increased to improve the resistance of infrastructure. One of the innovative construction materials for improving resistance of infrastructure is ultra-high-performance concrete (UHPC) owing to its very high compressive strength (more than 150 MPa) with optimum packing density, small aggregates size, and low water/cement ratio. However, the UHPC shows brittle fracture with poor fracture toughness under tension. Therefore, fibers have been added to achieve tensile ductility with high energy absorption capacity based on the unique strain hardening behavior after first cracking and led to new class of material known as ultra-high-performance fiber-reinforced concrete (UHP-FRC) [3, 6, 8]. Recent research on UHP-FRCs revealed that a high amount of steel fibers (usually greater than 2.0% in volume) has been required to obtain strain hardening behavior and high energy absorption capacity [1, 2]. The large amount of fiber causes the increase of cost, the reduction of workability of UHPFRC and further limits the application of this material in practical structure [5]. Thus, the amount of fiber should be minimized, while still maintaining strain hardening behavior of UHPFRC.

The performances of UHP-FRC are significantly controlled by fiber bridging capacity across a matrix crack. Due to the fracture process, the fibers have able to

N. T. Tran (✉)

Faculty of Civil Engineering, Ho Chi Minh City University of Transport, Ho Chi Minh City, Vietnam

e-mail: ngothanh.tran@ut.edu.vn

T. T. Ngo

Faculty of Civil Engineering, Thuyloi University, Ha Noi, Vietnam

D. L. Nguyen

Faculty of Civil Engineering and Applied Mechanics, Ho Chi Minh City University of Technology and Education, Ho Chi Minh City, Vietnam

arrest the growth of micro-cracks, delay the onset of crack localization and promote the formation of multiple micro-cracking as well as strain hardening behavior. Hence, the fibers play an important role in improving the material's ability to absorb energy and transfer load after cracking [4, 9]. For this reason, in order to find out an optimum fiber volume content in UHP-FRC mixture, the role of fiber properties on fracture resistance of UHP-FRC should be clearly understood. Unfortunately, very little research has focused on determining the fracture resistance of UHP-FRCs considering effects of fiber properties.

Thus, in this study, we conducted an experimental program to evaluate effects of fiber parameters including fiber type and fiber volume fraction on the fracture properties of UHP-FRCs under direct tension. The results of this study are expected to investigate UHP-FRCs with not only a high value of tensile strength but also energy absorption capacity by using low fiber volume fraction (a maximum of 2% by volume). Furthermore, they will contribute to the practical application of UHP-FRCs.

2 Experimental Program

2.1 Materials and Specimen Preparation

To investigate the fracture properties of UHP-FRC, an experimental program was designed as shown in Fig. 1. Total eight test series were tested. Two types of steel fiber including twisted fiber and smooth fiber were mixed to UHPC matrix. The dosages of fiber used were 0.5, 1.0, 1.5 and 2.0 percent by volume. One tested series included at least three specimens.

The composition of the UHPC matrix and its compressive strength are given in Table 1. The compressive strength was obtained at the age of 14 days by performing compressive test on cylinder specimens. The particle sizes of cement, silica fume, silica sand and silica powder are $0.1 \mu\text{m}$, $1 \mu\text{m}$, $500 \mu\text{m}$ and $10 \mu\text{m}$, respectively. On the other hand, fiber properties are given in Table 2 and the images of fiber are shown in Fig. 2: twisted fibers are deformed fiber while smooth fibers are straight fiber.

UHPFRCs were mixed by using A Hobart-type mixer with 20-L capacity. Firstly, the silica sand and silica fume were put into mixer and dry mixed for 5 min. After that, the cement and silica powder were put and mixed for 5 min. After dry mixing, water was divided two part and put two times and mixed for 5 min. Super-plasticizer was then added and continuously mixed for the purpose of distributing uniform fibers. When the workability and viscosity of the mixture were appropriated, steel fibers were carefully put into the mixture using hand and continuously mixed for 2 min. After mixing, a wide scoop without vibration was used to pour the fiber-containing mixture into molds. All the molds were then placed on shelves with steam at the bottom and plastic sheets at the top. After 48 h stored in at room temperature all the specimens were demolded. Then, a water tank was used to cure the specimens at a

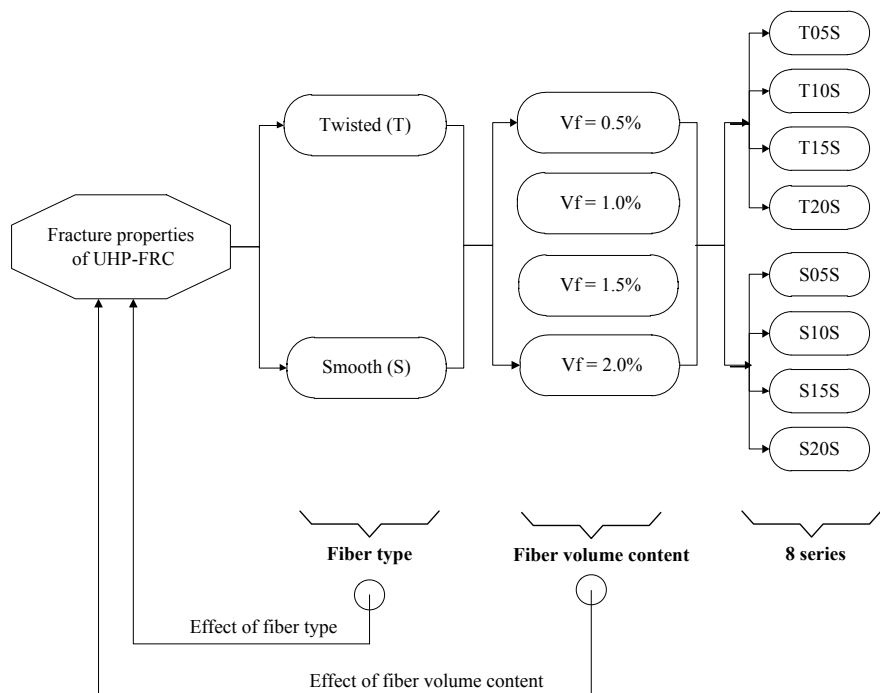


Fig. 1 Detail of experimental program

Table 1 Composition of matrix mixture by weight ratio and compressive strength

Cement (type 1)	Silica fume	Silica sand	Silica powder	Super-plasticizer	Water	Compressive strength (MPa)
1	0.25	1.10	0.30	0.067	0.2	180

Table 2 Properties of steel fibers

Fiber type	Diameter (mm)	Length (mm)	Density (g/cc)	Tensile strength (MPa)	Elastic modulus (GPa)
Twisted (T)	0.2	20	7.90	2580	200
Smooth (S)	0.2	19	7.90	2580	200

temperature of 90 °C for 3 days to accelerate hydration process of cement. Finally, the specimens were left to dry at room temperature for 11 days. All specimens were carried out to perform direct tensile test at tested the age of 14 days. A circular diamond saw was prepared to cut double notches into the edges of specimens right before testing.

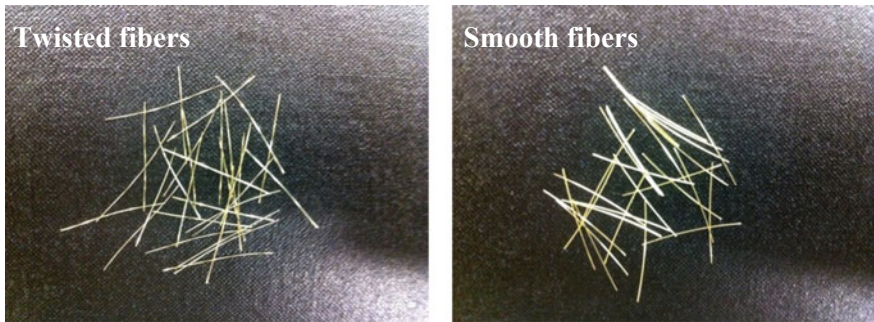


Fig. 2 Images of fibers

2.2 Test Setup and Procedure

The test set-ups are illustrated in Fig. 3. The specimen geometry is two bell-shaped ends, the cross section size was $25 \times 50 \text{ mm}^2$, the gauge length was 50 mm and the boundary condition was hinge to hinge. A universal testing machine was carried out to perform direct tensile test. The speed of actuator displacement and the data acquisition frequency were 1 mm/min and 1 Hz, respectively. The tensile stress was recorded by the load cell attached at the bottom of the cross head while two linear variable differential transformers (LVDTs) attached into the edges of specimen were used to obtain the displacement.

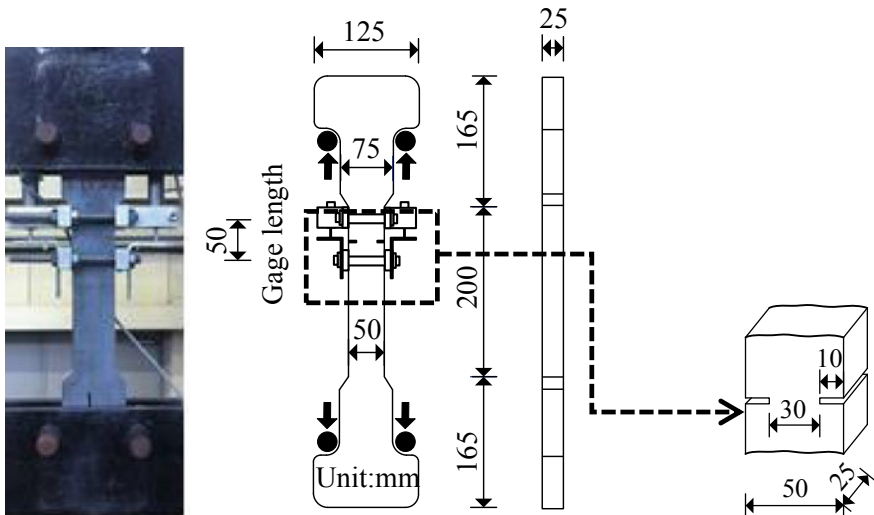


Fig. 3 Tensile test set up and specimen geometry

3 Results and Discussion

3.1 Tensile Response of UHPFRCs

Figure 4 shows the average tensile stress and displacement curves of UHP-FRCs. Most of UHP-FRCs exhibited tensile-hardening behavior under tension, except for UHP-FRCs with 0.5% smooth fibers (S05). UHP-FRCs with twisted fibers showed better performance before reaching crack localization, but faster decay in their tensile response during crack localization process than those with smooth fibers. Twisted steel fibers generated more mechanical interaction at the interface between fiber and matrix than smooth fibers before reaching crack localization owing to the additional mechanical bonding. However, the higher interfacial bond strength of twisted fibers caused them much more difficult to ensure pullout mode at large slip during crack localization process. It is clearly seen that an increase in fiber volume fraction resulted in the better performance of tensile response of UHP-FRCs.

3.2 Effect of Fiber Type and Fiber Volume Fraction on the Fracture Properties of UHP-FRCs

The fracture properties are defined as follows: the fracture strength f_t is the peak strength of the tensile stress versus displacement curve, the entire fracture energy G_f is the total area under the tensile stress versus displacement curve and the fracture toughness, also called the stress intensity factor K_{IC} , is generally calculated from:

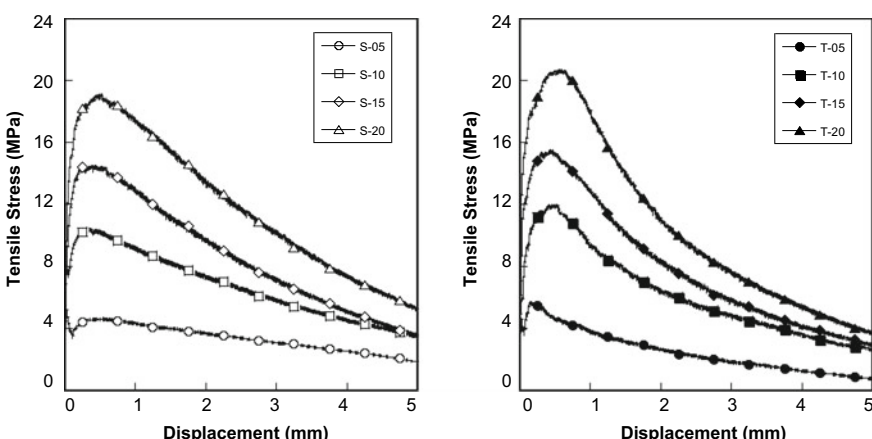


Fig. 4 Tensile stress and displacement curve of UHP-FRCs

$$K_{IC} = f_t \sqrt{\pi a} F(a/W) \quad (1)$$

where $F(a/W) = \sqrt{\frac{W}{\pi a}} \tan \frac{\pi a}{W}$ is specimen shape factor [7], a is initial crack length and W is specimen width.

The effects of fiber type and fiber volume fraction on the fracture properties are shown in Fig. 5. It is interesting that the UHPFRCs with relatively small amount of fiber (a maximum of 2% by volume) could produce fracture strength up to 20.9 MPa, fracture toughness up to 4.0 MPa $\sqrt{\text{m}}$ and fracture energy up to 59.7 kJ/m 2 . UHPFRCs with twisted fibers exhibited higher f_t and K_{IC} but lower G_f than UHPFRCs with smooth fibers. The higher f_t and K_{IC} of UHPFRCs with twisted fibers could be explained by the higher interfacial bond strength of deformed twisted fibers. However, the faster decay in tensile response during the crack localization process contributed to their lower G_f . On the other hand, increasing fiber volume fraction

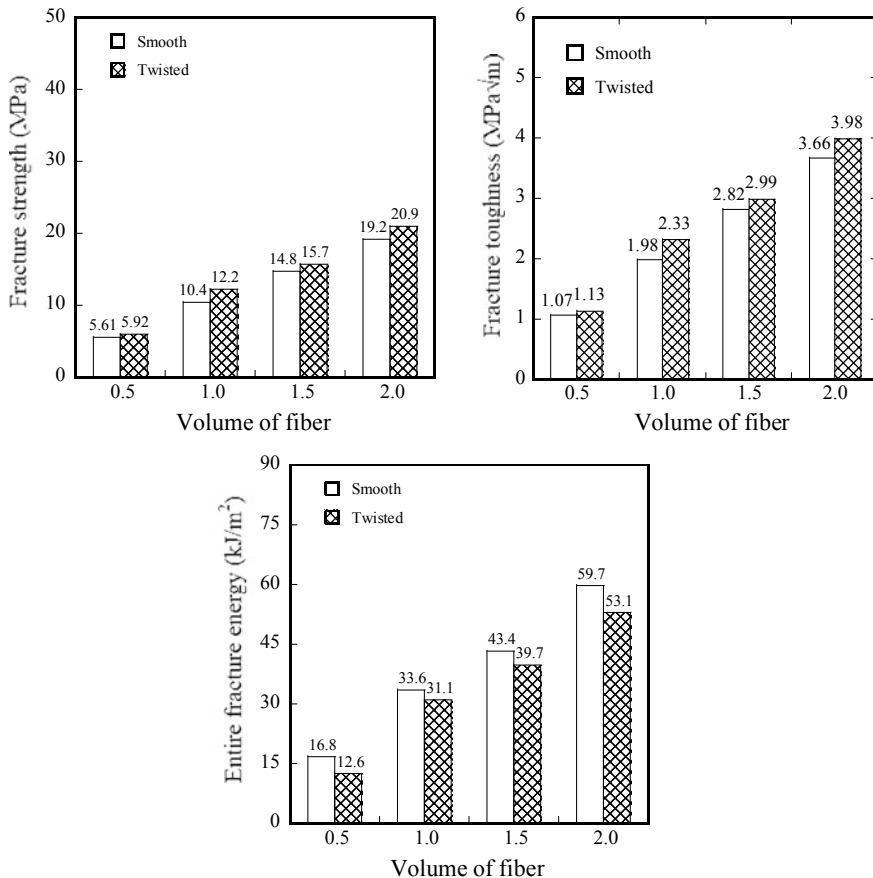


Fig. 5 Effect of fiber type and fiber volume fraction on the fracture properties of UHPFRCs

obviously increased the number of bridging fibers acrossing crack and led to an increase of all fracture properties. As the fiber volume fraction increased from 0.5 to 2%, the f_t , K_{Ic} and G_f increased up to 240%, 240%, and 250%, respectively.

4 Conclusion

This research conducted an experimental program to investigate the fracture properties of UHP-FRCs including fracture strength, fracture toughness, and entire fracture energy. The direct tensile tests were performed on UHPFRCs using two types of fiber and four different fiber volume fractions. The following conclusions can be withdrawn:

- Most of UHP-FRCs produced tensile-hardening behavior under tension, excepted for UHP-FRCs with 0.5% smooth fibers.
- UHP-FRCs using small amount of fiber (a maximum of 2% by volume) could produce fracture strength up to 20.9 MPa, fracture toughness up to $4.0 \text{ MPa}\sqrt{\text{m}}$ and fracture energy up to 59.7 kJ/m^2 .
- UHP-FRCs containing smooth fibers produced lower fracture strength and fracture toughness but higher fracture energy than UHP-FRCs containing twisted fibers. All the fracture properties enhanced as the fiber volume fraction increased from 0.5 to 2%.

Acknowledgements This research is funded by Vietnam National Foundation for Science and Technology Development (NAFOSTED) under grant number 107.01-2019.34.

References

1. Benson SDP, Karihaloo BL (2005) CARDIFRC—development and mechanical properties. Part III: Uniaxial tensile response and other mechanical properties. *Mag Concr Res* 57(8):433–443
2. Chanvillard G, Rigaud S (2003) Complete characterization of tensile properties of DUCTAL UHP-FRC according to the French recommendations. In: Proceeding of fourth international workshop on high performance fiber reinforced cement composites (HPFRCC4), Ann Arbor, MI, USA
3. Habel K, Viviani M, Denarie E, Bruehwiler E (2006) Development of the mechanical properties of an Ultra-High Performance Fiber Reinforced Concrete (UHPFRC). *Cem Concr Res* 36:1362–1370
4. Nelson PK, Li VC, Kamada T (2002) Fracture toughness of microfiber reinforced cement composites. *J Mater Civ Eng* 14:384–391
5. Park SH, Kim DJ, Ryu GS, Koh KT (2012) Tensile behavior of Ultra High Performance Hybrid Fiber Reinforced Concrete. *Cement Concr Compos* 34(2):172–184
6. Richard P, Cheyrez M (1995) Composition of reactive powder concretes. *Cem Concr Res* 25(7):1501–1511
7. Tada H, Paris PC, Irwin GR (2005) The stress analysis of cracks handbook, 2nd ed. Paris Proceedings, St. Louis

8. Wille K, El-Tawil S, Naaman AE (2014) Properties of strain hardening ultra high performance fiber reinforced concrete (UHP-FRC) under direct tensile loading. *Cem Concr Compos* 48:53–66
9. Wille K Naaman AE (2010) Fracture energy of UHPFRC under direct tensile loading. In: Jeju Oh BH (ed) Proceedings of FraMCos-7. Fracture mechanics of concrete and concrete structures, Korea, 23–28 May

Evaluate Healing Performance of Asphalt Mixture Containing Steel Slag by Using Induction and Microwave Heating



Tam Minh Phan, Dae-Wook Park, Tri Ho Minh Le, and Jun-Sang Park

1 Introduction

Based on the report from the World Steel Association, hundreds million tons of steel slag is released each year, which caused the main environmental problem. However, this by-product has some special properties such moisture stability, angular shape, ferrous material. With advantaged properties, steel slag can be used as aggregate in many applications such as hydraulic construction, production of cement and concrete, hot metal deposphorization [1]. Road construction is one of the most non-renewable resources consumption. Hence, to release the environmental problem and save the natural resources, the utilization of steel slag as a replacement for conventional aggregate in HMA is a promising key [9]. As mentioned before and literature reviews [2, 4, 6, 7] steel slag has some advantaged characteristics which can be used in HMA. The containing of steel slag helps HMA gains lower deformation with higher fatigue life compared to normal aggregate. However, the porous particles and free lime lead to higher binder consumption and volume unstable, respectively [7]. Hence, it is not recommended for 100% steel slag as replacement of conventional aggregate.

In asphalt pavement, the cracks occur throughout the services life. There are many causes of cracking such as fatigue cracking, reflection cracking, low-temperature cracking. Micro-cracks commonly occur in asphalt pavement and develop into large cracks. The preventive and maintenance of asphalt pavement not only extend the lifespan but also prevent future major damage. Due to asphalt binder viscosity is temperature dependent, it helps asphalt pavement can be healed under temperature effect. Depended on the type of mixtures, ambient temperature and resting period, the microcracks formed in asphalt pavement can be healed to a different level [3]. The

T. M. Phan · D.-W. Park (✉) · T. H. M. Le

Department of Civil Engineering, Kunsan National University, Gunsan 54150, Republic of Korea
e-mail: dpark@kunsan.ac.kr

J.-S. Park

Kumho Petro Chemical R&D Institute, Daejeon 34044, Republic of Korea

self-healing of asphalt mixture will be enhanced by applied in induction heating and microwave heating, which are two promising methods. As mentioned, steel slag has advantaged characteristics, especially, is a ferrous material, which can be affected by induction and microwave healing.

The purpose of this research is to evaluate the effect of by-product (steel slag) on the healing properties of asphalt mixture. Two healing treatments were applied, which are induction healing and microwave healing. The replacement of 30% conventional aggregate by steel slag aggregate with two different contents of SWF were considered. The healing properties of asphalt mixture were conducted by the Three-Point Bending test. Moreover, the thermal transmitting of each mixture was checked by infrared camera. Finally, the healing properties of all test samples were subjected to 8 healing-damaged cycles.

2 Material—Testing Method

2.1 Mixtures Preparation

The test samples were fabricated in the laboratory according to the Hot Mix Asphalt process. The asphalt binder PG 64-22 was used has a penetration of 71 mm/10 at 25 °C a density of 1.02 g/cm³. The conductive additive SWF has an average diameter of 70–130 µm, 4–4.5 mm in length, and density of 7.8 g/cm³. Table 1 shows the particle size distribution of normal aggregate and steel slag aggregate. The replacement of 30% coarse aggregate by steel slag was found to be the maximum dosage of by-product in this research. To exclude free-CaO in steel slag, the weathering process was applied. This process helps aggregate achieve acceptable hydration and reduce potential expansion.

According to previous researches [5, 9], two different percentages of SWF were applied to microwave and induction heating, including 2% and 6%, respectively. The mixtures were fabricated with 5.4% of asphalt binder. All asphalt mixtures were designed according to the Superpave Mix Design Method with the target air voids of $4 \pm 0.5\%$. Following the three-point bending requirement, the sample was fabricated and cut into 6 semi-circular replicates with an oversize of 100 in diameter and 30 mm in thickness.

2.2 Temperature Analysis

Under both healing treatments, the surface temperature of each sample was recorded by using an infrared camera. The testing process comprises the following steps:

Table 1 Particle size distribution of normal aggregate and steel slag (passing percent)

Sieve size (mm)	19	12.5	9.5	4.75	2.36	0.6	0.3	0.15	0.075
Normal aggregate	100	98	87	61	45	23	13	9	3
Steel slag	100	100	78	5	1	1	0	0	0

at room temperature, the temperature of test sample was recorded by infrared camera. Then, the surface temperature until they reach the desired temperature of approximately 90 °C.

2.3 Healing Performance

Two healing treatments were used unto damaged samples: the induction heating generator and microwave heating machine. The induction heater used in this study has a capacity of 50 kW and a maximum frequency of 35 kHz. The damaged sample was heated under the induction heating coil until 90 °C. Besides, the microwave oven with a maximum frequency of 2.45 MHz and a power capacity of 700 W was used to conduct microwave healing. Samples were placed in microwave oven for a period of 50 s. The specimens were placed in chamber at –18 °C for 3 h to archive the brittle condition before damaged by Three-point bending test. Then, the TPB peak load of samples was determined through initial TPB test. After damaged, the samples were let to rest at room temperature for 24 h to remove the moisture from brittle process. Based on findings [5, 8, 9] the healing level of samples, S_h , was calculated by Eq. (1)

$$S_h = \frac{F_n}{F_0} \quad (1)$$

F_0 : the peak load of sample before subjecting to damaged-healing cycle.

F_n : the peak load sample at nth damaged-healing cycle.

3 Results and Discussions

3.1 Temperature Analysis

The temperature data were extracted from infrared camera software. By using Matlab® software, a total of 200 cross-sectional average temperatures along the height of specimen were calculated. Figure 1 shows the temperature distribution of mixture with and without steel slag. As can be seen in mixture with normal aggregate, there was a gap of 50 °C between the highest and lowest temperature. However, the containing of steel slag helps asphalt mixture gains better temperature distribution. The mixtures with slag aggregate showed better temperature distribution. This can be explained by the metallic particle of steel slag gains a better heat absorption than normal aggregate.

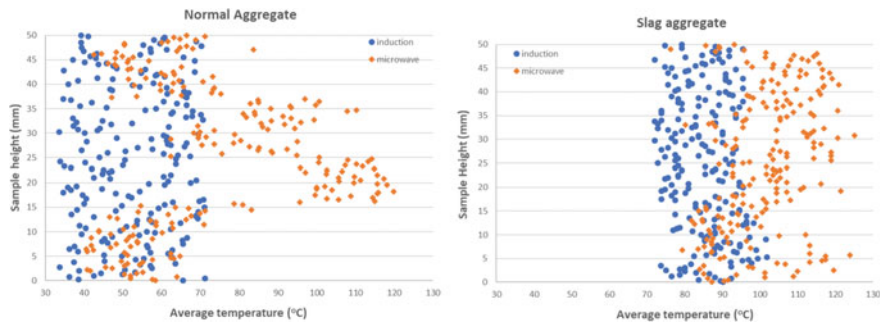


Fig. 1 Temperature distribution of mixtures with and without steel slag

3.2 Healing Level

Figure 2 shows the healing level of asphalt mixture containing steel slag aggregate. The replacement of 30% conventional aggregate by steel slag helps asphalt mixture generated a better healing level. Samples with steel slag aggregate can restore the peak load of higher 80% until the 3rd cycle. Compared to slag aggregate, mixture with conventional aggregate dropped below 80% after the 2nd cycle. Microwave healing gains the approximate 10% of healing level higher than induction healing. This may be due to the effect of microwave radiation on asphalt mixture particles, which are asphalt binder, SWF, steel slag compared to only metallic particles in induction healing.

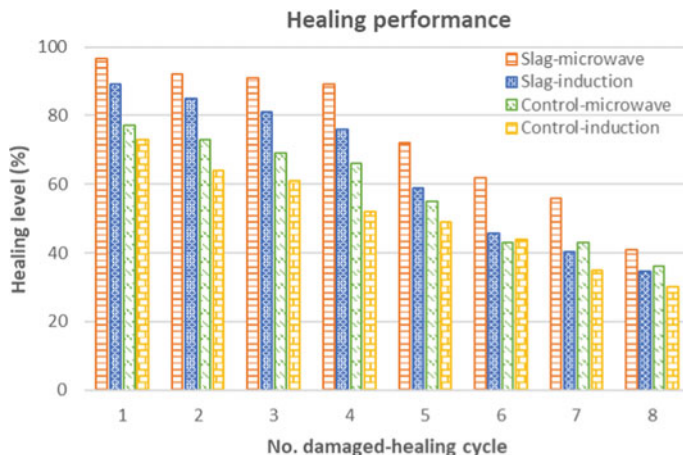


Fig. 2 Healing level of asphalt mixture with both healing treatments

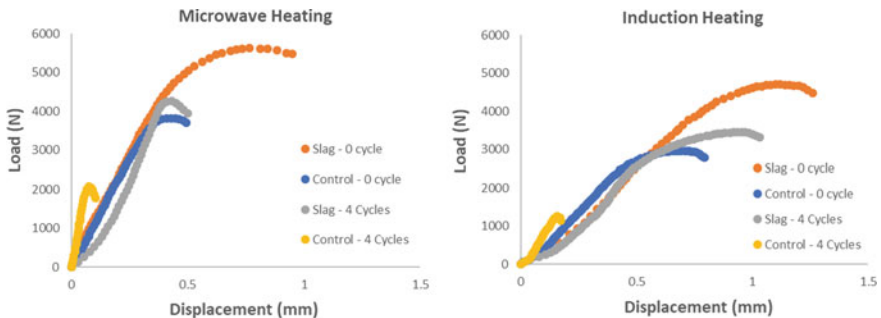


Fig. 3 Load-displacement behavior

3.3 Load-Displacement

The load-displacement relationship is shown in Fig. 3. With a replacement of 30% steel slag, which provided the higher ductile behavior for test samples compared to that of conventional aggregate mixtures (control mixtures), especially at early cycles. The improving flexibility of the whole mixture can be explained that metallic particles from steel slag, which are higher ductile compared to normal aggregate. Moreover, sample subjected to induction heating obtained higher ductile behavior than that of microwave heating. It can be explained by the induction heating only influences on metallic materials as steel slag, steel wool fiber. On the other hand, the microwave heating heat whole materials included asphalt binder. The repetition of damaged-healing cycles increases the aging of asphalt binders.

4 Conclusions

This study aims to evaluate the effect of steel slag aggregate on healing properties of Hot Mix Asphalt by using both healing treatments, which are induction and microwave healing. The results show that steel slag aggregate can be utilized for self-healing purposes. Based on the results, the following conclusion can be drawn:

- By using induction or microwave healing, it can be utilized steel slag aggregate to promote the healing properties of hot mix asphalt.
- The microwave heating gains a higher healing performance at early cycles; however, induction heating remains a better ductile behavior compared to that of microwave heating.
- The replacement 30% of conventional aggregate by steel slag gains the 80% healing level compared to 70% of the conventional mixture at 3rd damaged-healing cycle.

- The load-displacement of asphalt mixture containing steel slag aggregate was higher ductile behavior than the original aggregate due to the characteristic of steel slag aggregate.

Acknowledgements This research was supported by Basic Science Research Program through the National Research Foundation of Korea (NRF) funded by the Ministry of Education (No. NRF-2017R1D1A1B03032594).

References

1. Ahmedzade P, Sengoz B (2009) Evaluation of steel slag coarse aggregate in hot mix asphalt concrete. *J Hazard Mater* 165(1):300–305
2. Amelian S, Manian M, Abtahi SM, Goli A (2018) Moisture sensitivity and mechanical performance assessment of warm mix asphalt containing by-product steel slag. *J Clean Prod* 176:329–337
3. Bonnaure FP, Huibers A, Boonders A (1982) A laboratory investigation of the influence of rest periods on the fatigue characteristics of bituminous mixes (with discussion). *J Assoc Asphalt Paving Technol* 51:104–128
4. Chen Z, Wu S, Wen J, Zhao M, Yi M, Wan J (2015) Utilization of gneiss coarse aggregate and steel slag fine aggregate in asphalt mixture. *Constr Build Mater* 93:911–918
5. Dinh BH, Park D-W, Le THM (2018) Effect of rejuvenators on the crack healing performance of recycled asphalt pavement by induction heating. *Constr Build Mater* 164:246–254
6. Fakhri M, Ahmadi A (2017) Evaluation of fracture resistance of asphalt mixes involving steel slag and RAP: susceptibility to aging level and freeze and thaw cycles. *Constr Build Mater* 157:748–756
7. Gao J, Sha A, Wang Z, Tong Z, Liu Z (2017) Utilization of steel slag as aggregate in asphalt mixtures for microwave deicing. *J Clean Prod* 152:429–442
8. García Á (2012) Self-healing of open cracks in asphalt mastic. *Fuel* 93:264–272
9. Phan TM, Park D-W, Le THM (2018) Crack healing performance of hot mix asphalt containing steel slag by microwaves heating. *Constr Build Mater* 180:503–511

Evaluating the Effect of Steel Fibers on Some Mechanical Properties of Ultra-High Performance Concrete



Cong Thang Nguyen, Huu Hanh Pham, Van Tuan Nguyen, Sy Dong Pham, and Viet Hung Cu

1 Introduction

Over the past few decades, remarkable advances have taken place in research and application of Ultra-High Performance Concrete (UHPC), which outstanding exhibits properties including high flowability, very high compressive strength (usually greater than 150 MPa), high flexural strength (about 15–45 MPa when using steel fiber), very low porosity and excellent durability [1–6]. Therefore, UHPC has become one of the potential and economically efficient materials in specific applications such as thin shell structures, super-high-rise buildings, large span bridges and sustainable structures in marine environment, etc.

UHPC is composed by common materials such as quartz sand with the size of about 100–600 μm , cement, silica fume, water and superplasticizer. The high amount of cement in UHPC, 900–1000 kg/m³, and very high silica fume (SF) content, 150–250 kg/m³ (10–30% by weight of cement) [5] with the very low water-to-binder ratio, usually less than 0.25 by mass (Schmidt and Fehling [6, 7] will cause a high shrinkage. This phenomenon gives rise to tensile stress and can cause structural cracking, adversely affecting the properties of UHPC such as permeability, durability, etc. To improve some properties of UHPC, i.e. toughness, homogeneity to withstand the dynamic loads or to limit the crack expansion of the structures, it is necessary to add steel fibers into UHPC. Thanks to that, UHPC is possible can create the thin structures, thereby reducing dead load, increasing efficiency of space used, and

C. T. Nguyen · H. H. Pham · V. T. Nguyen (✉)

Faculty of Building Material, National University of Civil Engineering, Hanoi, Vietnam

e-mail: tuannv@nuce.edu.vn

S. D. Pham

Faculty of Building and Industrial Construction, National University of Civil Engineering, Hanoi, Vietnam

V. H. Cu

Faculty of Bridges and Roads, National University of Civil Engineering, Hanoi, Vietnam

reducing maintenance costs for projects [8–11]. However, further research is still remained in order to explore this aspect, and it is the target of this research.

This paper present experimental results to evaluate the role of the steel fibers in improving some properties of UHPC such as compressive strength, flexural strength and limiting the cracking expansion.

2 Materials and Methods

2.1 Materials

The materials used in this study are Portland cement PC40 which meets requirements of the Vietnamese standard TCVN 2682:2009; Condensed silica fume (SF) with an amorphous SiO₂ content of 92.3% and its mean particle size of 0.15 μm, reactivity index of SF in excess of 112.5%; Quartz sand with the particle size ranging from 100 to 600 μm; Steel fiber with 13 mm in length, 0.2 mm in diameter and tensile strength of 2750 MPa; Ground Granulated blast furnace slag (GBFS) with a mean particle size of 7.2 μm; and polycarboxylate superplasticizer (SP).

2.2 Methods

The compressive strength test of UHPC was determined according to ASTM C109 with sample size of 50 × 50 × 50 mm [12]. The compression test was done on a hydraulic machine with a load increase of 2.5 kN/s until the sample was damaged.

According to EN 14651, the flexural strength and the relationship between the flexural load and post-cracking behavior of the UHPC sample were carried out on the beam-shaped samples with dimensions of 100 × 100 × 400 mm.

To assess shrinkage cracking tendency in UHPC, an experiment was conducted by the restrained steel ring test according to ASTM C1581-2004. The ring UHPC test samples are 38 mm in thickness, inside diameter of 330 mm, outside diameter of 406 mm, and 152 mm in height. The UHPC mixtures were poured into the steel ring with a thickness of 12.5 mm which is able to counteract concrete shrinkage and leads arising in tensile strains. After 24 h of the casting, the UHPC samples are demolded and cured in the climate chamber ($27 \pm 2^\circ\text{C}$, $50 \pm 4\%$ RH) to measure the deformation of the steel ring with the starting time (time zero) being recorded. The upper surface of the UHPC sample is coated with silicon to ensure evaporation of water taking place along the surrounding surface of the test samples.

Table 1 Mix proportion of UHPC mixtures

No.	W/B	S/B	GBFS, %	SF, %	SP, %	Fiber, %
1	0.154	0.85	24	10	1.2	0
2	0.154	0.85	24	10	1.2	1
3	0.154	0.85	24	10	1.2	2
4	0.154	0.85	24	10	1.2	3

2.3 UHPC Compositions

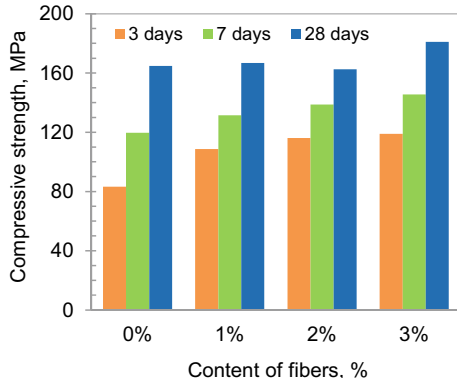
Table 1 shows UHPC mixtures which is used on all of experiments of this study to specific the compressive strength, the flexural strength and the shrinkage resistance. UHPC mixtures were designed with a sand to binder (S/B) ratio of 0.85; the water to binder (W/B) ratio of 0.154. The binder herein is a total of the cement, SF and GBFS. The SF, GBFS and SP are calculated by the weight of the binder, and the weight of steel fiber is calculated by the volume of the UHPC mixture.

3 Results and Discussion

3.1 Effect of the Steel Fiber Content on Compressive Strength of UHPC

Figure 1 shows the effect of the steel fiber content on compressive strength of UHPC. It can be seen that the compressive strength increases with increasing of the steel fiber content. The 28 day-compressive strength of the control sample without the steel

Fig. 1 Effect of the steel fiber content on compressive strength of UHPC



fibers is obtained 164 MPa. When increasing the steel fiber content to 2%, the 28 day-compressive strength of concrete is not changed significantly, i.e. 5% higher compared to that of the control sample. However, when the steel fiber content increases to 3%, the 28 day-compressive strength of concrete is increased significantly, i.e. about 10% higher than that of the control sample, and achieves the maximum value of 180 MPa. This phenomenon can be explained that when the steel fibers are added and disperses into UHPC, a very good bonding on the contact surface between the UHPC substrate and the steel fibers is created. When UHPC is affected by the load, the steel fibers will transfer stress to the UHPC substrate, thus, the formation and development of cracks are limited and the compressive strength increases.

3.2 Effect of Steel Fiber Content on Flexural Strength of UHPC

The influence of the steel fiber content on the UHPC flexural strength is shown in Fig. 2. It can be seen that when the steel fiber content increase, the flexural strength also increases. However, the addition of 1% steel fiber only increases the flexural strength of UHPC slightly, about 44% higher compared to that of the control sample without the steel fibers. When the steel fiber content increases to 2 and 3%, the flexural strength increases significantly, about 66 and 135% higher compared to that of the control sample, respectively. With incorporating 3% steel fibers, the 28 day-flexural strength can be reached the maximum value of 38.8 MPa. It was also observed that the UHPC control sample was devastated immediately after the cracks appears, while the UHPC samples with using the steel fibers were not destroyed suddenly even after UHPC samples appear cracks and the flexural strength continues to be increased.

The addition of the steel fibers not only increases the compressive strength but also limits the expansion of cracks in UHPC. It can be observed that when UHPC control sample is subjected to a load, it can be destructive in the form of brittle materials.

Fig. 2 Effect of the fiber content on flexural strength of UHPC

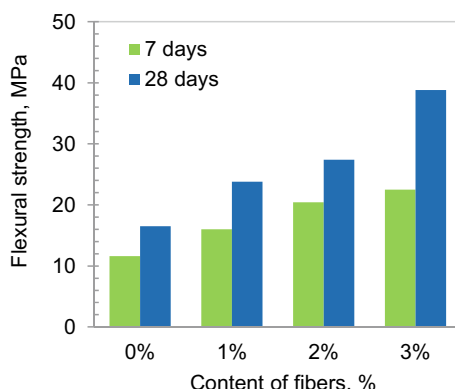
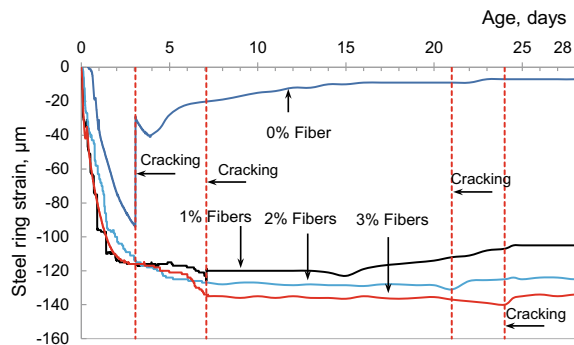


Fig. 3 Deformation of steel rings in restrained shrinkage test



However, when adding the steel fibers, the tight interface bond between these fibers and the UHPC substrate can be considered as a key factor in preventing the steel fibers from being pulled out from the substrate. The steel fibers can also effectively “bridge” between cracks, and transfer the stress to the substrate even when the UHPC sample is cracked, therefore, the flexural strength is increased and the crack formation is also limited. In fact, the improvement of the UHPC’s mechanical properties depends on the steel fiber content as well as the type of the steel fiber used.

3.3 *Effect of the Steel Fiber Content on Crack Resistance of UHPC*

In this study, some tests were also carried out using means of restrained ring test to determine the age of UHPC’s shrinkage cracking. The experimental results in Fig. 3 shows that for the control samples, the cracks appear after 3 days; but for UHPC samples using 2 and 3% of the steel fibers, the time of occurrence of cracks is 21 days and 24 days, respectively. Therefore, the addition of the steel fibers plays a key role in limiting cracking thereby slowing the process of cracking on concrete structures. When comparing the time of cracking between UHPC control samples without the steel fibers and concrete samples with M35 grade (35 MPa) in the study of Hieu [13], the experimental results showed that, the normal time cracking is 5 days for the normal concrete samples, while the cracking time of the UHPC samples is 3 days. It is important to notice that the UHPC shrinkage is larger than that of the conventional concrete, especially at the early-age. This phenomenon is caused by UHPC using a very high amount of cement and fine mineral admixture, and a very low water to binder ratio. When water in UHPC is lost due to the hydration of cement, also known as self-desiccation phenomenon in hardened cement paste, and due to evaporation of water to the surrounding environment has reduced internal relative humidity of concrete. This process creates the stress in the pores inside the concrete structure, which is considered as the total surface tension on the meniscus surface of the water in the pore system of the concrete, thereby causing shrinkage for the

concrete. It should be noted that for UHPC, the process of self-desiccation occurs more strongly at an early age and causes larger shrinkage than that of conventional concrete.

As the normal concrete shrinkage, the restrained UHPC sample through the “restrained ring test” also creates a certain pressure on the steel ring, the so-called actual residual pressure at the surface. The steel ring is considered as the required pressure causing the deformation which is equal to the deformation measured in the steel ring. This pressure is proposed by Hossain and Weiss [14] as follows:

$$P(t) = -\varepsilon_{\text{steel}}(t) \cdot E_{\text{steel}} \cdot \frac{R_{\text{os}}^2 - R_{\text{is}}^2}{2R_{\text{os}}^2} \quad (1)$$

In which:

$P(t)$ the interface pressure of the steel ring, MPa

$\varepsilon_{\text{steel}}$ the average steel strain

E_{steel} the elastic modulus of the steel

R_{os} the outer radius of the steel ring

R_{is} the inner radius of the steel ring.

Once the interface pressure is available, the pressure on the steel ring is caused by the pressure of the UHPC ring sample. Hossain and Weiss [14] also proposed the equation for calculating stress distribution in concrete as follows:

$$\sigma(r) = -\varepsilon_{\text{steel}}(t) \cdot E_{\text{steel}} \cdot \frac{R_{\text{os}}^2 - R_{\text{is}}^2}{2(R_{\text{oc}}^2 - R_{\text{os}}^2)} \cdot \left(1 + \frac{R_{\text{oc}}^2}{R_{\text{ic}}^2}\right) \quad (2)$$

where:

$\sigma(r)$ the inner pressure of the concrete ring sample, MPa

R_{oc} the outside radius of the concrete ring sample

R_{ic} the inside radius of the concrete ring sample ($R_{\text{os}} = R_{\text{ic}}$).

The concrete pressure is determined by Eqs. (1) and (2) and the relationship lines between the deformation of the steel ring and the time and is shown in Fig. 3. The relationship between the deformation of the steel ring with the concrete stress is shown in Fig. 4. It can be seen that the deformation of the steel ring increases linearly to the concrete pressure. Besides, when the concrete stress increases, the pressure in the steel ring also increases. However, at a certain point when the concrete stress continues to increase and the concrete tensile stress exceeds the tensile strength, the concrete begins to crack.

After that, the concrete stress causes the stress in the steel ring and it will be evenly distributed on the steel ring. The relationship between the steel fiber content and the concrete stress is shown in Fig. 5. From this figure, it can be seen that when increasing the steel fiber content, the concrete stress also increases, at the same time the beginning of cracking in the corresponding concrete increases and the maximum stress of the steel ring can be determined when the concrete cracks corresponding to

Fig. 4 Pressure of concrete on the steel ring

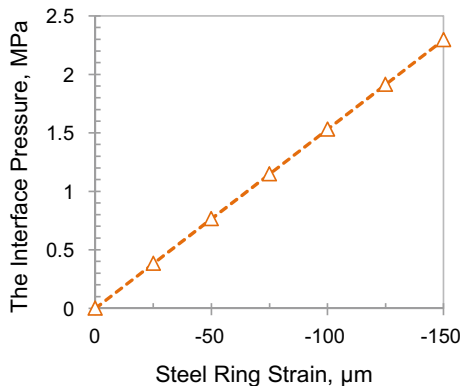
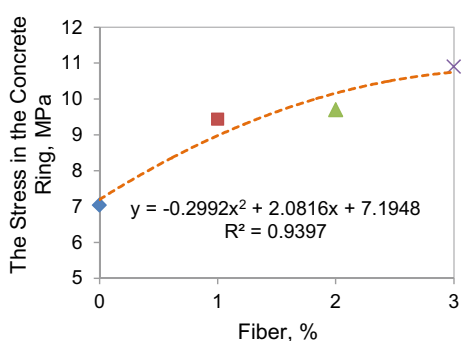


Fig. 5 Maximum stress of steel ring with the different fiber contents used



the steel fiber content used. As a result, the steel fibers have played an important role in limiting cracking and reducing the crack width development for UHPC.

Based on the relationships between the deformation of the steel ring and the time, it also can be seen that for UHPC samples, there is a great reduction of the deformation of the steel ring after cracking. Meanwhile, with UHPC samples using the steel fibers, after appearing cracks, there is no significant decrease in the deformation of the steel ring. At that time, with a tight interfacial bond between the steel fibers and the hardened cement paste, there is the process of transferring stress from the substrate to the fiber, and the bridging effect of the steel fiber through the crack when the cracks appear. Therefore, the steel fibers play a very important role in regulating the process of cracking, they slow down the development of cracks. As the concrete continues to shrink, the cracks also continue to expand, the steel fibers help to redistribute the load in the crack area thereby limiting the propagation of cracks and ensuring the continuity of the structure.

4 Conclusion

Based on the research results of this study, the following conclusions can be drawn:

- The addition of the steel fibers improves both compressive and flexural strength of UHPC, but only significantly with a high amount of steel fiber, i.e. 3%. At 28-day age, it can be achieved a compressive strength of 180 MPa, and a flexural strength of 38.8 MPa, corresponding to about 10 and 135% higher than those of the control sample.
- The addition of the steel fibers has greatly limited the cracking of UHPC due to the shrinkage. For UHPC control sample (without the steel fibers), the time to occur the cracks is 3 days, while UHPC samples using 3% of the steel fibers, this time is up to 24 days. When increasing the amount of the steel fiber, the UHPC pressure on the steel ring increases and the time of the crack appearance is correspondingly slower. Therefore, the addition of the steel fibers plays an important role in increasing tensile strength and limiting cracks thereby slowing the process of formation and development of cracks for UHPC structures.

Acknowledgements This paper is one of the results of the research project which was funded by the National University of Civil Engineering (Vietnam), grant number 210-2018/DHxD-TĐ.

References

1. Acker P, Behloul M (2004) Ductal technology: a large spectrum of properties, a wide range of applications. Ultra High Performance Concrete, Kassel, Germany, pp 13–23
2. AFGC-SETRA (2002) Ultra High Performance Fibre-Reinforced Concretes, Paris, France, Interim Recommendations
3. Buitelaar P (2004) Ultra high performance concrete: developments and applications during 25 years. In: International symposium on UHPC, Kassel, Germany
4. Collepardi M (2003) Innovative concretes for civil engineering structures: SCC, HPC and RPC
5. Richard P, Cheyrez MH (1994) Reactive powder concretes with high ductility and 200–800 MPa compressive strength. In: Mehta PK (ed). Concrete technology: past, present and future, proceedings of the V. Mohan Malhotra symposium, ACI SP 144-24, pp 507–518
6. Schimidt M, Fehling E (2005) Ultra-high-performance concrete: research, development and application in Europe. In: Seventh international symposium on the utilization of high-strength/high-performance concrete, Washington, DC, SP-228-4
7. Voort TV, Suleiman M, Sritharan S (2008) Design and performance verification of ultra-high performance concrete piles for deep foundations. Center for Transportation Research and Education, Iowa State University, pp 224
8. ASTM C1581 (2004) Standard test method for determining age at cracking and induced tensile stress characteristics of mortar and concrete under restrained shrinkage
9. Grzybowski M, Shah SP (1989) Model to predict cracking in fiber reinforced concrete due to restrained shrinkage. Mag Concr Res 41:125–135
10. Krause PD, Rogalla EA (1995) Transverse cracking in newly constructed bridge decks. NCHRP 380, Project 12.37
11. Shah SP, Karaguler ME, Sarigaphuti M (1992) Effects of shrinkage reducing admixture on restrained shrinkage cracking of concrete. ACI Mater J 89:88–90

12. ASTMC109M (2016) Standard test method for compressive strength of hydraulic cement mortars (using 2-in. or [50-mm] Cube Specimens)
13. Hieu NT, Hung NM, Dau TV (2014) Study on cracking on concrete structure due to shrinkage deformation and solution of using steel fibers to limit cracking. University level research project, No. 118-2013/TD, National University of Civil Engineering (in Vietnamese)
14. Hossain A, Weiss J (2004) Assessing residual stress development and stress relaxation in restrained concrete ring specimens. *Cem Concr Compos* 26:531–540

Evaluation of Factors of Asphalt that Influence the Dynamic Modulus of Dense Asphalt Concrete in Viet Nam



Hai Nhu Nguyen, Anh Tuan Le, Hai Viet Vo, and Hoang Minh Tran

1 Introduction

Asphalt concrete is the most widely used material for pavements in Viet Nam [1]. The failure of pavements is mainly caused by the combined effects of the repeatable load and the constant change of weather. Therefore, the study of thermomechanical properties of asphalt concrete is essential to improve the methods and components to create types of asphalt with better resistance to the above-mentioned impacts. In addition to the methods of controlling the selection of suitable aggregate and binders, or optimizing aggregate gradation used in asphalt mixtures [2], at present, the research direction is the relationship between the mechanical properties of asphalt concrete and asphalt binder. The complex shear module, G^* and phase angle, δ of asphalt are two of the most important factors in the US-based classification system. In addition, G^* and δ are two important inputs used to predict dynamic modulus values of asphalt concrete in Witczak model, modified Witczak model, and Hirsh model [3]. Studying the complex modulus and phase angle of asphalt being used in Vietnam is necessary and has scientific and practical significance. This is a target for the classification of asphalt in accordance with climate and traffic conditions in Viet Nam.

H. N. Nguyen
Hong Ha Engineering, JSC, Hanoi, Viet Nam

A. T. Le
Faculty of Civil Engineering, Ho Chi Minh City University of Technology, VNU-HCM, Ho Chi Minh City, Viet Nam

H. V. Vo (✉)
Sustainable Developments in Civil Engineering Research Group, Faculty of Civil Engineering,
Ton Duc Thang University, Ho Chi Minh City, Viet Nam
e-mail: vo viet hai@tdtu.edu.vn

H. M. Tran
Faculty of Civil Engineering, Ton Duc Thang University, Ho Chi Minh City, Viet Nam

Dynamic modulus of dense Asphalt Concrete, E^* is one of the most important input parameters is used for designing and evaluating pavement structure according to the mechanical-empirical pavement design guide [4]. Because of its importance, there has been a lot of research on predictive models of E^* as well as sensitivity analysis of input parameters that influence dynamic modulus in order to find out which one is the most influence on E^* [5]. However, the degree of affection of these input parameters on the value of E^* is quite different from one to another.

This paper is to evaluate and classify the most commonly used asphalt in Viet Nam. Sensitivity analysis of factors that influence E^* was performed to compare the effects of type of asphalt to other factors. G^* and δ were tested by Dynamic Mechanical Analyzer and predicted from the master curves constructed by 2S2P1D Model. Monte Carlo simulation was applied to perform the sensitivity analysis. Witczak Model, Modified Witczak Model, and Hirsch Model were applied to predict E^* , the degree of affection of the factors was then determined.

2 Materials and Methods

2.1 Materials

The complex shear modulus, G^* is the ratio of the maximum shear stress, τ_{max} , and the maximum shear strain, γ_{max} in the shear test. Due to the viscoelastic asphalt, there is always a time lag between the applied stresses and the deformation caused by it, this time lag is called the phase angle (δ) of the asphalt. The value of G^* can be analyzed into two components: G' -reserve module and G'' -loss module. Therefore, as the phase angle is small, the material is highly elastic and vice versa.

The prediction of dynamic modulus depends on a lot of parameters, include: Nominal maximum aggregate size, D_{max} , type of asphalt which the key property is complex shear modulus G^* or dynamic viscosity of asphalt, η passing percent No. 200 (0.075 mm), cumulative retaining percent on the sieve sizes No. 4, No. 3/8 and No. 3/4 (4.75, 9.5 and 19 mm), volumetric properties (V_a , VFA and VMA). The two types of asphalt used in the study were 60/70 asphalt and PMBIII polymer asphalt, which are the common asphalt in Viet Nam. The testing was carried out according to TCVN 7493:2005 [6] and 22TCN 319-04 [7] for 60/70 and PMBIII polymer asphalt, respectively. The rheological properties are summarized in Table 1.

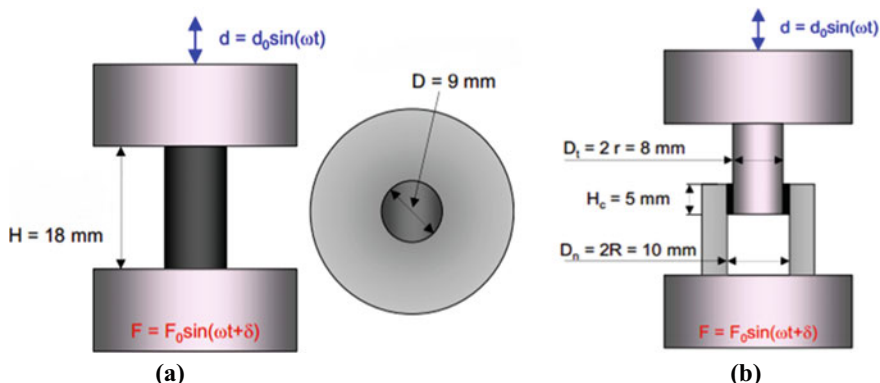
Empirical research was at the Project in Hai Phong in December 2017. Input parameters using for sensitivity analysis of the Witczak models and Hirsch model were collected from data of asphalt mixture design AC12.5 with D_{max} of 12.5, designed by Marshall method (AASHTO T245 2015). The aggregate grading and properties of AC12.5 met the requirements of Decision No. 858 [8].

Table 1 Rheological properties of 60/70 and PMBIII

No.	Asphalt	Penetration, at 25 °C (0.1 mm)	Softening point, Ring and ball method (°C)	Ductility, at 25 °C, 5 cm/min (cm)	G_b	Elasticity, at 25 °C, 10 cm (%)
1	60/70	62	49.1	>100	1.031	–
2	PMBIII	52	90.2	–	1.028	97
Standard	60–70 (60/70) 40–70 (PMBIII)	≥ 46 (60/70) ≥ 80 (PMBIII)	≥ 100	–	≥ 70	

2.2 Determination of G^* and δ

Different approaches to evaluate G^* and δ are available for different methods of testing [1]. In this study, experiments to determine the value G^* and δ of different bituminous materials were conducted at the French institute of science and technology for transport, spatial planning, development and networks (IFSTTAR) using Dynamic Mechanical Analyzer (DMA) (see Fig. 1) according to AASHTO T315-12 [9]. G^* and δ was tested at the temperatures of $-9.9, 0, 10, 15, 20, 25, 30, 40$ and 50 °C with the angular frequency of $0.1, 0.5, 1, 5, 10$ và 25 rad/s for each temperature respectively. The sample is subjected to periodic stress in one of several different modes of deformation, tension/compression (T/C) (Fig. 1a) and bending/shear (B/S) (Fig. 1b) as the temperature lower than 20 °C and higher than 20 °C, respectively. At 20 °C, the asphalt has softened so that the test T/C is considered less accurate.

**Fig. 1** Method and specimen size of the experiments **a** T/C and **b** B/S

2.3 Sensitivity Analysis

Sensitivity analysis is the technique to evaluate influence between input parameters and output results of a predicting model [10, 11]. In a global sensitivity analysis, all input parameters are varied simultaneously from their base cases and interactions among input parameters are considered. The global sensitivity analysis will evaluate which input parameter is the most influence on the output response of a model and it is more proper than Once-At-a Time method [10]. Global sensitivity analysis requires the Monte Carlo simulation which can be run by Oracle Crystal Ball software (Oracle) to carry out sensitivity analysis of input parameters for the dynamic modulus predictive models. This software can be integrated into MS Excel to perform calculation in the global sensitivity analysis. Monte Carlo simulation is a method of using random numbers or random variables received based on deterministic random numbers [12]. When randomly assigning input parameters to the predetermined distribution law, then the set of output random parameters with their distribution rule is determined. Today, simulation data are often used in the cases that resources are restricted or collecting data is costly or impractical.

3 Results and discussions

3.1 Evaluation of Asphalt Binder

There are several models that can be applied to simulate complex shear moduli and phase angles of asphalt. In this study, 2S2P1D model, developed by Bari and Witczak [13], was used to simulate the complex shear modulus of the asphalt, and construct the master curve for predicting G^* and δ based on experimental results. 2S2P1D model has 2 elastic elements, 2 viscoelastic elements, and 1 viscous element. In this model, G^* values at random frequency and temperature were determined using Eqs. (1), (2) and (3) [14].

$$G^* = G_\infty + \frac{G_o - G_\infty}{1 + \delta(i\omega\tau)^k + (i\omega\tau)^h + (i\omega\beta\tau)^l} \quad (1)$$

$$\eta = (G_o - G_\infty) \cdot \beta \cdot \tau \quad (2)$$

$$\tau = aT \cdot \tau_0 \quad (3)$$

where

i complex number;

ω frequency (Hz, or Rad/s);

k, h exponents, with $0 < k < h < 1$;

Table 2 $G^*/\sin\delta$ values at different temperatures

Type	Temperature (°C)	G^* (kPa)	δ (°)	$G^*/\sin\delta$
60/70	64	1.138	86.46	1.140
60/70	70	0.497	87.33	0.498
PMBIII	82	2.320	53.704	2.878

β, δ constants;

G_0 static modulus as $w \rightarrow 0$;

G_∞ maximum modulus as $w \rightarrow \infty$;

η Newtonian viscosity;

τ characteristic time at any temperature;

τ_0 characteristic time at the reference temperature;

aT shift factor.

Based on the master curves constructed from 2S2P1D model, predicted G^* and δ at the temperatures of 64, 70 °C with asphalt 60/70 and 82 °C with asphalt PMBIII, the $G^*/\sin\delta$ values were calculated and shown in Table 2; the results at the reference temperature of 10 °C are summarized and shown in Fig. 2 with the input parameters shown in Table 3. As seen in Table 2, it can be concluded that 60/70 and PMBIII asphalt in Viet Nam are equivalent to PG64 and PG82 asphalt, respectively according to AASHTO M320-17 [15].

As seen in Fig. 2a, both 60/70 and PMBIII asphalt have a G^* value that decreases when the temperature rises or at low frequency and vice versa. In Fig. 2b, the phase angle value of 60/70 asphalt increases as the temperature rise/frequency decreases, while with PMBIII asphalt, when the temperature rise/frequency decreases, the phase angle increases to some extent to the maximum value, then decreases (within the temperature range from -19 to 80°C). This suggests that high-temperature/low-frequency polymer modified asphalt still retains its elasticity, so using polymer modified asphalt can resist rutting and fatigue cracking.

3.2 Factors Influencing Dynamic Modulus

The dynamic modulus can be determined by experiment or prediction depending on the level of pavement structure design according to the mechanical-empirical method. E^* was estimated based on some properties of asphalt and asphalt mixture. The models,

Original Witczak Model, Modified Witczak Model, and Hirsch Model [3, 5] was applied for the prediction of E^* .

In this paper, the distribution types of the input parameters (V_a , V_{beff} , VMA, VFA, P_{200} ; P_4 ; $P_{3/8}$; $P_{3/4}$) were determined based on a database collected from actual production and construction of asphalt mixes at Hai Phong Urban Transport Development Project of the hot mix asphalt for a surface course. For dynamic modulus,

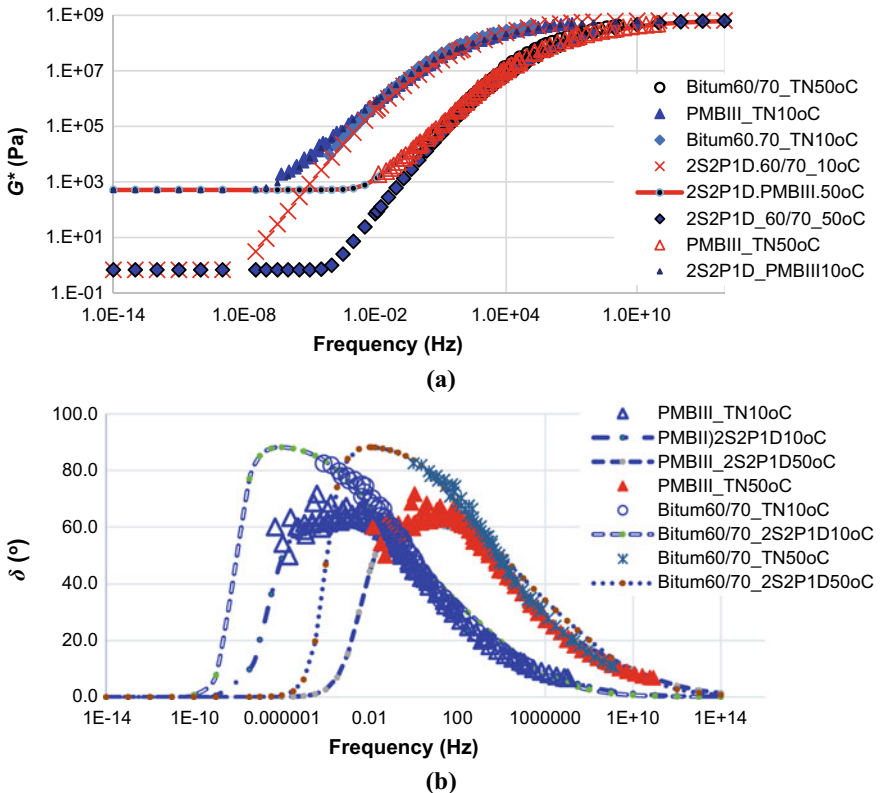


Fig. 2 Master curves of **a** G^* and **b** δ

viscosity and phase angle of asphalt (G^* , η , δ). Types of distribution are determined based on concerned data in the test of complex shear modulus of the 60/70 asphalt at IFSTTAR as mentioned above. Type of distribution of frequency influencing E^* is determined based on frequency data using for carrying out the test of E^* at the building material laboratory of University of Transport and Communications, Vietnam. The Oracle Crystal Ball software [16] was applied with the number of trial runs of 3000, confidence level of 95%.

As seen in Fig. 3, type of asphalt, G^* , η , and δ has the greatest influence on the dynamic modulus of asphalt concrete, the second one is loading frequency, f in the original Witczak Model, and then volumetric properties together with values of P_{200} , P_4 ; $P_{3/8}$; $P_{3/4}$ of the Witczak Models and Hirsch Model. Coefficients concerning the volumetric properties of asphalt mixture are smaller than coefficients of G^* , η , δ , and f , which are the properties of asphalt. Therefore, proper selection type of asphalt and the optimum asphalt content for asphalt mixture design is very important to improve the quality of asphalt pavement.

Table 3 Input parameters in 2S2P1D model

Asphalt	C_1	C_2	G_0 (Pa)	G_∞ (Pa)	k	h	δ	τ	β
60/70	15.9	115.2	6.895E-01	6.471E+08	0.30	0.620	3.80	2.295E-04	100.0
PMBIII	19.0	141.0	5.17E+02	6.47E+08	0.26	0.68	5.86	8.957E-04	2000

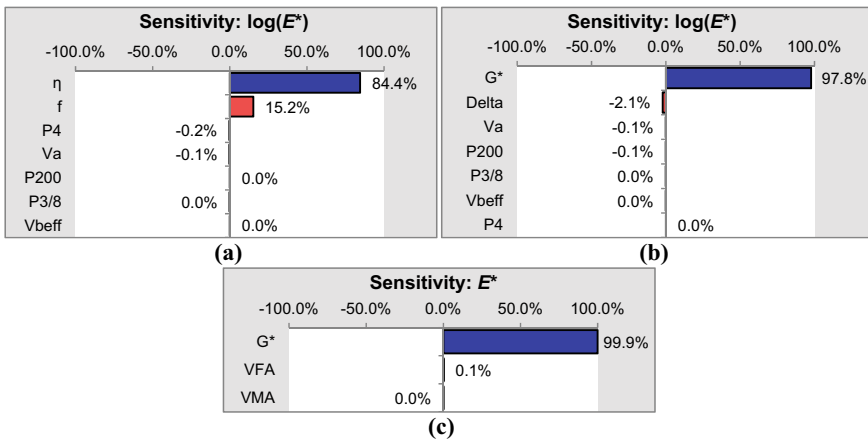


Fig. 3 Sensitivity of E^* by **a** original witczak model, **b** Modified Witczak Model, and **c** Hirsch Model

4 Conclusions

This paper is to evaluate the complex shear modulus and phase angle of the asphalt in Viet Nam and their effects on the dynamic modulus of asphalt concrete mixtures. The asphalt has been tested by the DMA and predicted using 2S2P1D model. From the experimental results, it can be assessed that 60/70 and PMBIII asphalt is equivalent to PG64 and PG82 bituminous grading based on the results of testing G^* and δ . For the two types of asphalt used in this study, the 2S2P1D model can properly predict and construct their master curves of G^* and δ . The dynamic modulus of asphalt concrete depends on many input parameters, however, type of asphalt (G^* , δ , and η) have the greatest influence, next one is the asphalt mixture design work with the selection of combined aggregate grading and optimum asphalt content that are expressed through value of air void. As the authors' consideration, it is necessary to have more experiment database to calibrate and adjust coefficients of the predictive models to ensure that they can be applied for asphalt mixes in Viet Nam.

References

1. Nguyen LM, Nguyen TQ, Hoang NTT (2015) Study on complex modulus of asphalt 60/70 used in Viet Nam by experiment on DMA machine. J Transp 11:38–41 (in Vietnamese)
2. NCHRP 673 (2011) A manual for design of hot mix asphalt with commentary. Transportation Research Board, Washington DC
3. Garcia G, Thompson M (2007) HMA dynamic modulus predictive models—a review. Report No. FHWA-ICT-07-005, pp. 8–25
4. NCHRP 1-37A (2004) Mechanistic-empirical pavement design guide of new and rehabilitated pavement structures (MEPDG). Transportation Research Board, Washington DC

5. Kim RY, Underwood B, Far MS, Jackson N, Puccinelli J (2011) LTPP computed parameter: dynamic modulus, Report No. FHWA-HRT-10-035, pp. 5–12
6. TCVN 7493:2005. Asphalt—specifications. Ministry of Science and Technology, Hanoi, Viet Nam (in Vietnamese)
7. TCN 319-04 (2004) Standard for polymer modified bitumen. Ministry of Transport, Hanoi, Viet Nam (in Vietnamese)
8. Decision No.858 (2014) Application guideline of current standards to fortify quality control of asphalt mixture design and flexible pavement construction for the road with high volume traffic. Ministry of Transport, Hanoi, Viet Nam (in Vietnamese)
9. AASHTO T315-12 Standard method of test for determination the rheological properties of asphalt binder using a dynamic shear rheometer. In: American Association of State Highway and Transportation Officials, Washington DC (2012)
10. Li R (2013) Sensitivity evaluation of mechanical-empirical pavement design guide (MEPDG) for flexible pavement performance prediction. Doctoral Dissertation, University of Maryland, College Park, MD, pp 8–16, 40–56
11. Saltelli A, Tarantola S, Campolongo F (2000) Sensitivity analysis as an Ingredient of Model. Statistical Science 15(4):377–395
12. Coddington PD (1994) Analysis of random number generators using Monte Carlo simulation. Int J Mod Phys C 5(3):547–560
13. Bari J, Witzczak MW (2007) New predictive models for viscosity and complex shear modulus of asphalt binders for use with mechanistic-empirical pavement design guide. Transp Res Rec J Transp Res Board 2001:9–19
14. Md Yusoff NI, Mounier D, Marc-Stéphane G, Rosli Hainin M, Airey GD, Di Benedetto H (2013) Modelling the rheological properties of bituminous binders using the 2S2P1D model. Constr Buil Mater 38:395–406
15. AASHTO M320-17 (2017) Standard specification for performance-graded asphalt binder. American Association of State Highway and Transportation Officials, Washington DC (2017)
16. Oracle Crystal Ball (computer software). Oracle, Santa Clara, California

Experimental Study on the Response of Ultra-High Performance Fiber Reinforced Concrete Slabs Under Contact Blast Loading



Ba Danh Le, Duy Hoa Pham, Cong Thang Nguyen, Duc Linh Ngo,
and Thi Thuy Dung Bui

1 Introductions

Nowadays, reinforced concrete is one of the most common building materials. It creates the main bearing structures of constructions. When an explosion occurs near the constructions, either on purpose or not, will leave a tremendous consequence. It destroys the materials and the structure, that may lead to a potential collapse [9]. To reduce the consequence on the works caused by blast load, it is necessary to understand the behavior of the concrete under this load, or create new high quality concrete.

Studies on the mechanical behavior of concrete under the effect of explosive loads have been carried out over the past few decades. Some studies formatted the load structure and an explosion damage to produce the same load that causes the same damage, as a basis for the first study of the theory of destructive explosions [6]. Kot et al. [5] proposed theoretical methods of concrete destruction under the effect of an explosive load, but these methods are based on some simple assumptions that affect the accuracy of calculation. In the late 1980s, a series of concrete explosion experiments were summarized by McVay [8]. Parameters affecting the destruction of concrete such as distance, explosive weight, wall thickness, strength level of concrete, concrete admixture and reinforcement content have been studied. Wang et al. [11] had conducted contact explosion experiments on square reinforced concrete sheets with

B. D. Le (✉) · D. H. Pham
Faculty of Bridge and Roads, National University of Civil Engineering, 55 Giai Phong, Hanoi,
Vietnam
e-mail: danhlb@nuce.edu.vn

C. T. Nguyen
Faculty of Building Materials, National University of Civil Engineering, 55 Giai Phong, Hanoi,
Vietnam

D. L. Ngo · T. T. D. Bui
Design Consultant and Investment of Constructions One Member Limited Liability Company,
Ministry of Defence, 21 Le Van Luong, Hanoi, Vietnam

varying amounts of explosives. The results were observed and studied, in order to verify their numerical models. Based on a large number of databases from explosion experiments on concrete slabs and walls, Marchand and Plenge [7] developed crack algorithm under the effect of explosive loads on reinforced concrete floor and wall panels.

Ultra-high quality concrete, also known as Ultra-High Performance Fiber Reinforced Concrete (UHPFRC) is a turning point in current cement concrete technology. This is a concrete with high compressive strength (≥ 120 MPa) and high fracture toughness. The flexural strength can be up to 40 MPa, with high impact resistance, high load repellency and high waterproofing; durability and long-term stability. UHPFRC's outstanding mechanical properties not only originate from the addition of high pozzolan particles, like silica fume but also from the use of steel fibers in concrete. Theoretical and experimental studies around the world have proven that UHPFRC concrete has excellent explosion-proof ability [4].

In Vietnam, research on UHPFRC materials was started in the last 10 years. The application of UHPFRC concrete have been studied, such as sea poles, civil bridges, cladding panels. The study of UHPFRC application for special projects affected by explosive load is very small. The objective of this research is to experimentally study the explosion capacity of UHPFRC materials produced by the materials available in Vietnam, thereby analyzing the advantages of UHPFRC compared to ordinary concrete (Normal Concrete—NC), serves as a basis for the research and application of this concrete for special projects in Vietnam.

In this paper, the preparation of specimens is first presented. The UHPFRC material is fabricated in laboratory using the material available in Vietnam. Then, the experimental blast testing is detailed. The tests are realized on four UHPFRC slabs with the volume fraction of micro steel fibers of 2 and 3% and two NC slabs. These slabs have the same dimension: 1000 mm of length, 800 mm of width and 120 mm of thickness. The emulsion explosive is used. The results and discussion are presented in the last section. The concrete crater and spall damage under contact blast loading are considered and compared between UHPFRC and Normal concrete.

2 Specimen Preparation

2.1 Materials

Materials used in the study including: Normal concrete (NC) used fine aggregates (yellow sand) with the fineness modulus is 2.5; coarse aggregate (broken stone) with the dimension varies from 5 to 20 mm. A UHPFRC mixture contains homogeneous silica aggregates with a particle size of 300 μm ; Portland cement PC40 (according to Vietnamese standard) with particle size of 11.4 μm ; Fly ash (FA) and silica fume (SF) used to replace cement with a density of 2400 kg/m^3 and 2200 kg/m^3 , respectively; The SiO_2 content of SF was 92.3%, the mean particle size of SF and FA were 0.15 μm .

Table 1 Concrete proportions used in the study

Sample	Sand (kg)	Broken stone (kg)	Cement (kg)	FA (kg)	SF (kg)	PS (kg)	Water (kg)	Fiber (kg)
NC	626	1210	395	–	–	–	183	–
UHPFRC-F2	1108	–	831	166	111	36.9	164	157
UHPFRC-F3	1096	–	822	164	110	36.5	162	235.5

and 5.83 μm , respectively, and the corresponding pozzolanic reactivity index were 113.5 and 104.3%; Polycarboxylate superplasticizer (PS) with a dry content of 35%; The micro steel fibers with a length of 13 mm and diameter of 0.2 mm were mixed at a volume dosage of 2 and 3%. The tensile strength of the micro steel fiber is 2750 MPa.

2.2 *Mixture Proportions*

The blast resistance capacity of NC and two types of UHPFRC using 2% (UHPFRC-F2) and 3% (UHPFRC-F3) volume fraction of micro steel fibers were experimentally evaluated. The concrete proportions used in the study is shown in Table 1.

2.3 *Mixing Process*

The test was realized on the specimens with 1000 mm of length, 800 mm of width and 120 mm of thickness (Fig. 1). Two layers of mesh reinforcements were placed in the NC and UHPFRC slab specimens. The longitudinal reinforcement rebar and stirrup rebar using 8 bars D12 and 6 bars D8 with 110 mm and 190 mm spacing, respectively (Fig. 1). Some photo of the mixing and placing processes of UHPFRC mixtures are show in Fig. 2.

2.4 *Characterization Methods*

Compressive strength of NC were determined according to Vietnamese standard TCVN 3118-1993 [10] with sample size $150 \times 150 \times 150$ mm. The compressive strength of UHPFRC was performed on 100×200 mm cylindrical specimens according to ASTM C39M [2]. Flexural strength of concrete was determined according to ASTM C1609M [1], Prismatic samples of NC and UHPFRC with a size 150×150

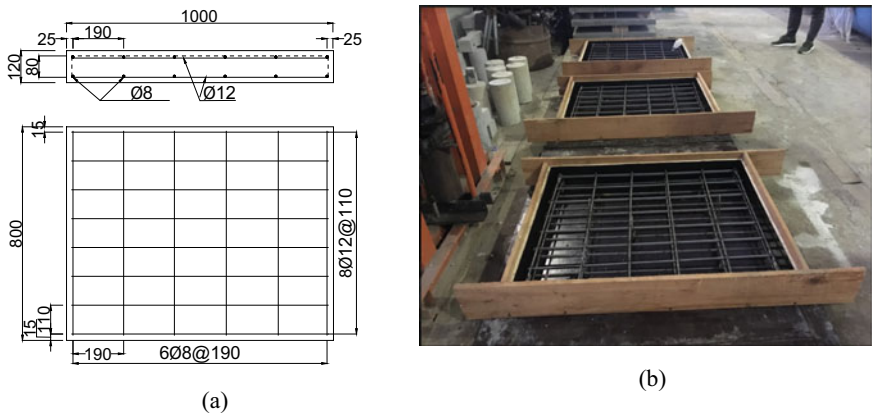


Fig. 1 **a** Arrangement of reinforcement and **b** installation of formwork



Fig. 2 **a** Mixing and **b** placing of UHPFRC mixtures

\times 600 mm and $100 \times 100 \times 400$ mm, respectively. The elastic modulus of concrete was determined according to ASTM C469M [3]. The cylinder samples of NC and UHPFRC with a size 150×300 mm and 100×200 mm, respectively. The mechanical properties of the both concrete are shown in Table 2.

Table 2 The mechanical properties of concrete

Sample	Volume fraction of micro steel fibers (%)	Compressive strength (MPa)	Flexural strength (MPa)	Elastic modulus (Gpa)
NC	–	30	3	30
UHPFRC-F2	2	120	15	48
UHPFRC-F3	3	120	16	48

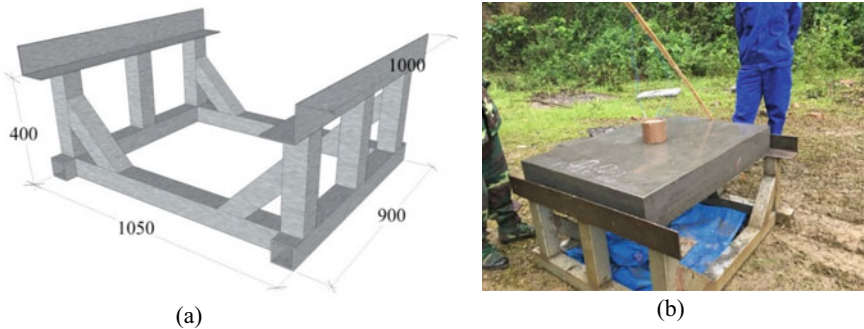


Fig. 3 **a** Steel rig configuration and **b** experimental setup



Fig. 4 Explosive block: **a** 0.5 kg and **b** 1.22 kg

3 Experimental Blast Testing

In order to perform the blast testing, the concrete UHPFRC slabs and NC slabs was placed on the steel rig using a crane (Fig. 3a). The explosive is placed directly at the center of the upper surface (Fig. 3b). The emulsion explosives is used in this study. Two cylindrical explosives blocks were used to obtain different level of damages (Fig. 4). First block has a mass of 0.5 kg, the diameter of 80 mm and the height of 86.5 mm (Fig. 4a). The last one has a mass of 1.22 kg, the diameter of 120 mm and the height of 94 mm (Fig. 4b).

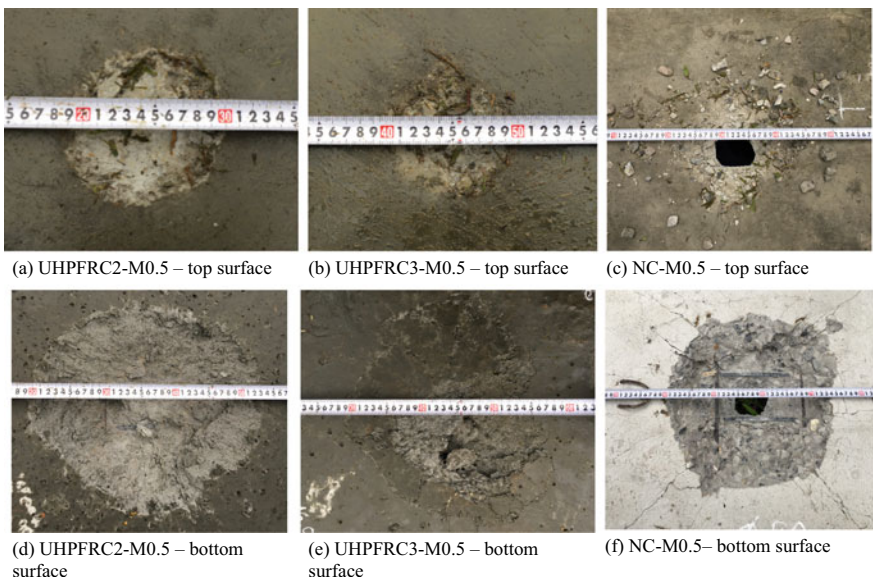
The blast testing is realized on four UHPFRC slabs and two NC slabs. The concrete crater and spall damage under contact blast loading are considered and compared between these types of specimen. The program of these tests is shown on Table 3.

4 Results and Discussion

The experimental results of four UHPFRC and NC slabs specimen correspond to 0.5 kg explosive are shown in Fig. 5. For UHPFRC2-M0.5 slab, the top surface crater

Table 3 Test program

No.	Slab material	Explosive charge weight (kg)	Slab specimen
1	UHPFRC-F2	0.5	UHPFRC2-M0.5
2	UHPFRC-F3	0.5	UHPFRC3-M0.5
3	NC	0.5	NC-M0.5
4	UHPFRC-F2	1.22	UHPFRC2-M1.22
5	UHPFRC-F3	1.22	UHPFRC3-M1.22
6	NC	1.22	NC-M1.22

**Fig. 5** The failure of slabs with 0.5 kg explosive at top and bottom surface

diameter is 10 cm (Fig. 5a), the bottom surface spall diameter is 33 cm (Fig. 5d). For UHPFRC3-M0.5 slab, the top surface crater diameter is 9 cm (Fig. 5b), the bottom surface spall diameter is 22 cm (Fig. 5e). No side concrete cracking and no reinforcement fracture was observed in both UHPFRC cases. Whereas, in UHPFRC3-M0.5, the diameters of top surface crater and bottom surface spall damage are smaller than UHPFRC2-M0.5. With NC-M0.5, a hole appears in the middle of slab, these crater and spall diameter are 26 cm and 35 cm, respectively (Fig. 5c–f). Particularly, the crack appear on both top and bottom surfaces

For 1.22 kg explosive, the top surface crater diameter and bottom surface spall diameter are 16 cm (Fig. 6a–d) and 30 cm, respectively, with UHPFRC2-M1.22. These values varies to 15 (Fig. 6b–e) and 30 cm with UHPFRC3-M1.22. However, the hole is not yet through the slab in this case. For NC-M1.22, the top surface crater

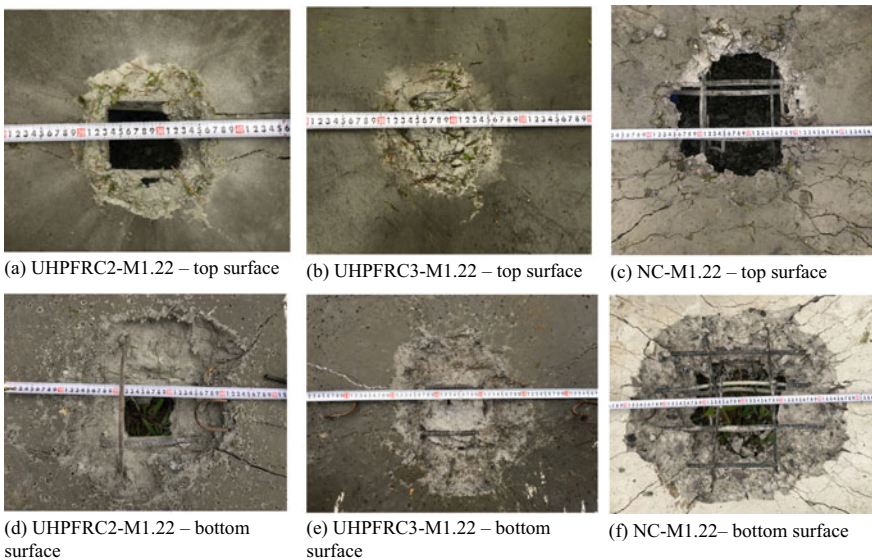


Fig. 6 The failure of slabs with 1.22 kg explosive at top and bottom surface

diameter and bottom surface spall diameter increase to 30 (Fig. 6c–f) and 58 cm. In these tests, the cracks and hole begin to appear on these UHPFRC slabs. However, the number of these cracks are limited. While, a multiple cracks and longitudinal reinforcement deformed appear on NC slab. During the blast loading, the explosion generates a compressive stress wave propagating in the structure. This stress is the cause to appear the crushing and spalling damage on the top and bottom of specimens. The shear and bending behavior is small in test because the time is too short for global structural response to develop. The experimental results demonstrate that, with the same dimension, the UHPFRC material has much higher blast resistance capacity compared to normal concrete. The cracks appear on the UHPFRC specimen less, and have a very small expansion compared to cracks in the NC specimen. This result can be explained by the role of steel fibers in UHPFRC. The steel fibers are as the bridges that connect the crack. It allows limiting the number and the opening of the crack. The blast resistance capacity of UHPFRC increases proportionally with the volume fraction of micro steel fibers. The results obtain in this study is the important basis for the future research application of this concrete for special projects in Vietnam.

5 Conclusions

Experimental studies of Ultra-High Performance Fiber Reinforced Concrete (UHPFRC) slabs and Normal slabs under contact blast loading were presented in

this paper. The UHPFRC material is fabricated in laboratory using the material available in Vietnam. These tests allow to evaluate the bearing capacity of this material against the blast loads. The experimental results demonstrate that, the UHPFRC concrete have a good resistance against this load. The steel fibers in UHPFRC plays a role as the bridges that connect the crack. It allows limiting the number and the opening of the crack appear in slabs. This study presents only the experimental results of the blast load test of UHPFRC that produces in lab. These results allow to calibrate the parameters of numerical model used to model these tests (model for explosive, model for UHPFRC) in future study. In addition, it is the important basis for the research application of this concrete for special projects against the blast load, or the impact, especially in defense projects.

References

1. ASTM C1609M (2012) Standard test method for flexural performance of fiber-reinforced concrete (using beam with third-point loading)
2. ASTM C39M (2017) Standard test method for compressive strength of cylindrical concrete specimens
3. ASTM C469M (2014) Standard test method for static modulus of elasticity and poisson's ratio of concrete in compression
4. Bibora P, Drdlová M, Prachař V, Sviták O (2017) UHPC for blast and ballistic protection, explosion testing and composition optimization. In: IOP conference series: materials science and engineering, vol 251, no 1. IOP Publishing, pp 12004
5. Kot CA, Valentin RA, McLennan DA, Turula P (1978) Effects of air blast on power plant structures and components. Argonne National Lab, Lemont, IL
6. Li J, Hao H (2011) A two-step numerical method for efficient analysis of structural response to blast load. *Int J Protect Struct* 2(1):103–126
7. Marchand KA, Plenge BT (1998) Concrete hard target spall and breach model. Air Force Research Laboratory, Munitions Directorate, Lethality, Ohio, USA
8. McVay M K (1988) Spall damage of concrete structures. ARMY Engineer Waterways Experiment Station Vicksburg MS Structures LAB
9. Ngo T, Mendis P, Gupta A, Ramsay J (2007) Blast loading and blast effects on structures—an overview. *7(S1):76–91*
10. TCVN 3118(1993) Heavyweight concrete—method for determination of compressive strength
11. Wang W, Zhang D, Lu F, Wang S, Tang F (2013) Experimental study and numerical simulation of the damage mode of a square reinforced concrete slab under close-in explosion. *Eng Fail Anal* 27:41–51

Influence of Chloride Ion in Sea Sand on Mechanical Properties of Fly Ash Concrete Exposed to Accelerated Carbonation



Quoc Viet Dang, Aoi Okada, Yuko Ogawa, and Kenji Kawai

1 Introduction

Fly ash (FA) is one of the most widely used mineral admixtures as partial ordinary Portland cement (OPC) replacement due to not only the reduction of cement usage but also the improvement in the mechanical properties of concrete [1]. However, concrete incorporating FA is vulnerable to carbonation which is a process of penetration of gaseous atmospheric carbon dioxide into cementitious materials, leading to the change in microstructure of concrete [2, 3]. Depending on the chemical composition of binder in concrete, the influence of carbonation on the mechanical properties of concrete can vary. The carbonation can remarkably increase the mechanical properties of OPC concrete because the porosity of concrete could be remarkably decreased by carbonation [4]. On the other hand, Hussain et al. [5] demonstrated that the accelerated carbonation caused the reduction of the modulus of elasticity of FA concrete compared to OPC concrete due to the reduction of portlandite content.

With the rapid growths of construction industry, the demand of concrete for the development in building and infrastructure has significantly increased. It has been predicted that the demand for concrete production will grow to approximately 18 billion tons per year by 2050 [6]. Therefore, this leads to the overexploitation of natural resources, especially river sand (RS) which is a common fine aggregate for concrete production. Under this circumstance, sea sand (SS) can be considered as one of possible materials for concrete production because it is very abundant at coastal areas. The use of SS not only takes full advantage of a local material but also has an advantage in the transportation, resulting in the reduction of construction cost. However, the presence of chloride ion in SS leads to the limitation of its use for reinforced concrete because it can cause steel bar corrosion, resulting in the serious degradation of reinforced concrete structures [7]. Normally, SS should be desalinated before

Q. V. Dang · A. Okada · Y. Ogawa · K. Kawai (✉)

Department of Civil and Environmental Engineering, Graduate School of Engineering,

Hiroshima University, Higashi-Hiroshima, Japan

e-mail: kkawai@hiroshima-u.ac.jp

using to avoid the steel bar corrosion. However, this process can be difficult at some regions where there is a lack of freshwater. Therefore, the direct use of SS without desalination is more attracting the attention of researchers. Limeira et al. [8] studied the partial replacement of crushed limestone sand with SS. The results indicated that the mechanical properties of SS concrete were similar to those of reference concrete.

In service life, concrete will be carbonated. The carbonation process affects the mechanical properties of concrete as well as the behavior of chloride ion in sea sand concrete. Many studies focused on the effect of carbonation and chloride ion ingress from external environment on the mechanical properties of concrete [9–11]. Nevertheless, based on the reviewed paper of Xiao et al. [12], there is less study related to the effect of initial chloride ion introduced by SS and carbonation on the mechanical properties of concrete, especially concrete containing FA. More studies are very necessary to clear the coupling effects of chloride ion and carbonation on the mechanical properties. Therefore, this study aims to investigate the influence of chloride ion in sea sand on mechanical properties in terms of the compressive strength and modulus of elasticity of FA concrete when FA concrete was exposed to accelerated carbonation.

2 Materials and Methods

2.1 Materials

For all mixture proportions, cementitious materials used in this study were ordinary Portland cement (OPC) and fly ash (FA) type II conforming to Japanese industrial standards JIS R 5210 and JIS A 6201, respectively. Main chemical compositions and physical properties of OPC and FA are presented in Table 1.

The maximum size of coarse aggregate (G) was 20 mm (density and water absorption are 2.62 g/cm³ and 0.67%, respectively). Fine aggregate was non-desalinated sea sand (NSS) which was exploited from the Karatsu harbor of Saga prefecture in Japan. Desalinated sea sand (DSS) obtained by removing the chloride ion from NSS was also used as fine aggregate for reference concrete. The physical properties of fine aggregates are shown in Table 2. Tap water was used for casting concrete specimens.

2.2 Mixture Proportions and Experimental Methods

Four mixture proportions were prepared with a constant water-to-cementitious material ratio of 0.50 as shown in Table 3. The FA was used to partially replace OPC with a proportion of 15% by mass. After mixing, the concrete was cast into cylindrical moulds of ϕ 100 × 200 mm for compressive strength and modulus of elasticity tests.

Table 1 Chemical compositions and physical properties of cementitious materials

Materials	Chemical compositions (% by mass)							Density (g/cm ³)			Specific surface area (cm ² /g)
	CaO	SiO ₂	Al ₂ O ₃	Fe ₂ O ₃	MgO	SO ₃	Na ₂ O	K ₂ O	Cl	LOI	
OPC	64.79	19.89	5.19	3.07	1.26	1.95	0.31	0.36	0.01	2.65	3.16
FA	1.47	59.40	29.37	5.77	0.80	—	—	1.10	—	2.90	2.24

Table 2 Physical properties of aggregates

Type of sand	Residue on each sieve size (%)					Fineness modulus <0.15 mm	Density (g/cm ³)	Water absorption (%)	Chloride content (%)
	5.0 mm	2.5 mm	1.2 mm	0.6 mm	0.3 mm				
NSS	0.0	6.2	23.7	30.3	27.9	10.6	2.83	2.60	1.33
DSS	0.3	8.3	21.8	28.7	32.8	7.1	1.0	2.60	1.31

Table 3 Mixture proportions of concretes

Mixtures	OPC–DSS	OPC–NSS	FA15–DSS	FA15–NSS
OPC (kg/m ³)	350	350	298	298
W (kg/m ³)	175	175	175	175
FA (kg/m ³)	–	–	53	53
DSS (kg/m ³)	847	–	838	–
NSS (kg/m ³)	–	847	–	838
G (kg/m ³)	966	966	956	956

After the top surface was sealed with aluminum tape to prevent water evaporation and carbonation, all specimens were placed in a controlled room at 20 ± 2 °C for 28 days.

After 28 days, half of the cylindrical specimens were continuously kept under sealed condition. The others were demoulded and put in an accelerated carbonation chamber until the age of 182 days. The CO₂ concentration in the chamber was 5%, and the temperature and relative humidity were 20 ± 2 °C and 60 ± 5%, respectively. The high concentration of CO₂ in this study would be expected to give more obvious information about the effect of carbonation on the mechanical properties of concrete.

The mechanical properties of all concrete mixtures including the compressive strength and modulus of elasticity were determined according to JIS A 1108 and JIS A 1149, respectively. A uniaxial compression test was performed on cylindrical specimens at the ages of 28, 91, and 182 days by using an automatic compression machine at a loading rate of 1.5 kN/s. The value was obtained by the average of three measurements at each age.

3 Experiment Results and Discussions

3.1 Compressive Strength

Figure 1 shows the compressive strength of all concretes under sealed and carbonation conditions. Generally, it can be seen that the compressive strength of NSS concretes was higher than that of DSS concretes regardless of ages, conditions, and FA replacement. This is attributed to the presence of chloride ion in NSS. Thomas et al. [13] revealed that chloride ion can be bound by products of cement hydration and secondary hydration, resulting in the formation of Friedel's salt. The formation of Friedel's salt can make concrete denser, leading to enhancement in the compressive strength of concrete [14].

Moreover, it is also observed that the carbonation significantly increased the compressive strength of concrete irrespective of FA replacement. The increment ratio of the compressive strength of OPC and FA concretes from 28 to 182 days under the

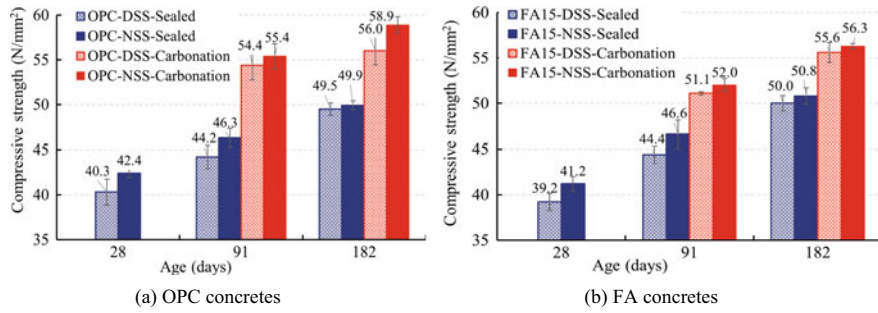


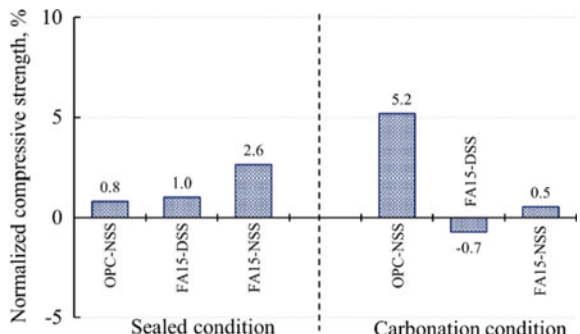
Fig. 1 Compressive strength of OPC and FA concretes under sealed and carbonation conditions

sealed condition was from 17.7% to 22.8% and from 23.3% to 27.6%, respectively. However, the compressive strength increment ratio of concrete under the carbonation condition was eventually approximately two times higher than that under the sealed condition. It is due to the carbonation of portlandite ($\text{Ca}(\text{OH})_2$, CH) which is a hydration product, resulting in the formation of calcium carbonate (CaCO_3). The precipitation of crystals CaCO_3 could partially fill pore systems, leading to the reduction in porosity. Therefore, the compressive strength of concrete was increased by carbonation [3]. Additionally, the free water which was originally combined in CH will be released by carbonation as Eq. (1). The free water from the center is transferred to the exposed surface of specimen by moisture gradient until the moisture of the surface is in equilibrium with that of the outer environment, leading to the drying process. This was confirmed by Morandeau et al. [2] and Auroy et al. [15]. As a consequence, the drying process due to carbonation might also enhance the compressive strength of concrete [16].



Figure 2 shows the percentage increase in the compressive strength of all concretes relative to the compressive strength of OPC-DSS concrete (reference concrete)

Fig. 2 Percentage increase in compressive strength of all concretes at 182 days relative to OPC-DSS concrete



under sealed and carbonation conditions at 182 days. The compressive strength of FA15-DSS concrete was 1.0% higher at 182 days under the sealed condition due to the pozzolanic reaction, whereas the percentage of increase in the compressive strength was 2.6% when FA concrete was mixed with NSS. However, under the carbonation condition, while the compressive strength of FA15-DSS concrete was 0.7% lower than that of OPC-DSS, that of FA15-NSS concrete tended to be opposite with a value of 0.5% higher compared to OPC-DSS concrete at 182 days. It implied that the chloride ion in NSS contributed to the increase in compressive strength. Additionally, due to the dilution effect as well as pozzolanic reaction, the CH content in FA concretes was lower than that in OPC concretes. Therefore, the amount of CaCO_3 due to carbonation in FA concretes was lower than that in OPC concretes [3]. In addition, concrete incorporating FA is vulnerable to carbonation shrinkage, resulting in the formation of microcracks [3]. As a consequence, FA concretes had lower compressive strength than OPC concretes.

3.2 Modulus of Elasticity

The modulus of elasticity of all concretes under sealed and carbonation conditions is shown in Fig. 3. Similar to the compressive strength, the modulus of elasticity of NSS concretes was slightly higher than that of DSS concretes irrespective of ages, conditions, and FA replacement. It indicates that the chloride ion also improved the modulus of elasticity of concrete. In addition, the gain in the modulus of elasticity of OPC concretes was approximately 5.5%, whereas that of FA concretes was approximately two times higher than that of OPC concretes under the sealed condition from 28 to 182 days. This is due to the pozzolanic reaction of FA which will contribute to a long-term gain in the modulus of elasticity of concrete [1].

On the other hand, the carbonation process significantly affected the modulus of elasticity of concrete. While the modulus of elasticity of OPC concretes was constant or slightly increased under the carbonation condition at 182 days, that of FA concretes decreased. The decrease in the modulus of elasticity of FA concretes is attributed to the formation of microcracks due to carbonation shrinkage [3]. In general, the

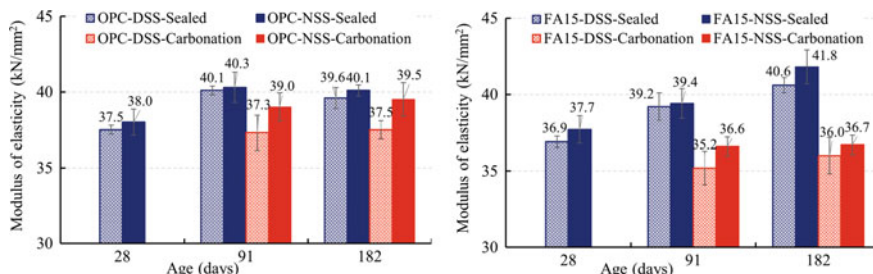
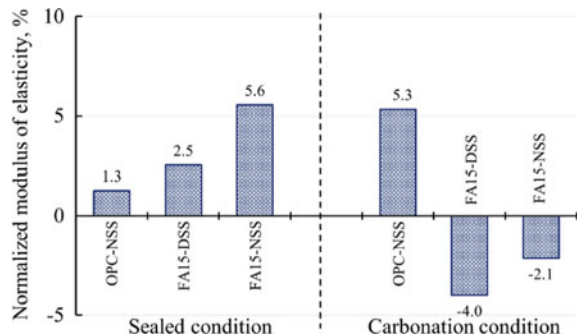


Fig. 3 Modulus of elasticity of OPC and FA concretes under sealed and carbonation conditions

Fig. 4 Percentage increase in modulus of elasticity of all concretes at 182 days relative to OPC-DSS concrete



pozzolanic reaction of FA will additionally generate calcium silicate hydrates (C–S–H) and reduce CH. The C–S–H gel formed due to pozzolanic reaction normally had a lower Ca/Si ratio than that by cement hydration [2]. Therefore, FA concretes are thought to be more susceptible to carbonation than OPC concretes because of the lower CH content and C–S–H gel with a low Ca/Si ratio [2]. The carbonation process is believed to induce the formation of microcracks [3]. Consequently, the modulus of elasticity of FA concretes was decreased under carbonation [17].

The percentage increase in the modulus of elasticity of all concretes relative to the modulus of elasticity of OPC-DSS concrete under sealed and carbonation conditions at 182 days is shown in Fig. 4. It can be observed that the modulus of elasticity of FA concrete was higher only under the sealed condition, but it was lower under carbonation than that of OPC-DSS at 182 days. Besides, the presence of chloride ion in NSS increased the modulus of elasticity of FA concrete from 2.5 to 5.6% under the sealed condition. It also recovered the percentage increase in the modulus of elasticity of FA concrete from -4.0 to -2.1% at 182 days.

4 Conclusions

- The chloride ion in NSS improved not only the compressive strength but also the modulus of elasticity of concrete under both sealed and carbonation conditions regardless of FA replacement.
- FA replacement slightly increased the compressive strength of SS concrete under the sealed condition. Meanwhile, the compressive strength of FA SS concretes was nearly the same as that of reference concrete under the carbonation condition at 182 days.
- The pozzolanic reaction increased the modulus of elasticity of FA SS concretes at 182 days under the sealed condition. However, the carbonation slightly decreased the modulus of elasticity of FA SS concretes in compared to reference concrete due to the carbonation shrinkage.

References

1. Johari MAM, Brooks JJ, Kabir K, Rivard P (2011) Influence of supplementary cementitious materials on engineering properties of high strength concrete. *Constr Build Mater* 25:2639–2648
2. Morandeau A, Thiéry M, Dangla P (2015) Impact of accelerated carbonation on OPC cement paste blended with fly ash. *Cem Concr Res* 67:226–236
3. Šavija B, Luković M (2016) Carbonation of cement paste: understanding, challenges, and opportunities. *Constr Build Mater* 117:285–301
4. Chang CF, Chen JW (2005) Strength and elastic modulus of carbonated concrete. *Mater J* 102(5):315–321
5. Hussain S, Bhunia D, Singh SB (2017) Comparative study of accelerated carbonation of plain cement and fly-ash concrete. *J Build Eng* 10:26–31
6. Mehta PK, Monteiro PJM (2014) Concrete: microstructure, properties, and materials. 4th edn
7. Angst U, Bernhard E, Larsen CK, Vennesland O (2009) Critical chloride content in reinforced concrete—a review. *Cem Concr Res* 39(12):1122–1138
8. Limeira J, Etxeberria M, Agulló L, Molina D (2011) Mechanical and durability properties of concrete made with dredged marine sand. *Constr Build Mater* 25(11):4165–4174
9. Ramezanianpour AA, Ghahari SA, Esmaeili M (2014) Effect of combined carbonation and chloride ion ingress by an accelerated test method on microscopic and mechanical properties of concrete. *Constr Build Mater* 58:138–146
10. Saillio M, Véronique BB, Fabien B (2014) Chloride binding in sound and carbonated cementitious materials with various types of binder. *Constr Build Mater* 68:82–91
11. Badar MS, Patil KK, Bernal SA, Provis JL, Allouche EN (2014) Corrosion of steel bars induced by accelerated carbonation in low and high calcium fly ash geopolymers concretes. *Constr Build Mater* 61:79–89
12. Xiao J, Qiang C, Nanni A, Zhang K (2017) Use of sea-sand and seawater in concrete construction: current status and future opportunities. *Constr Build Mater* 155:1101–1111
13. Thomas MDA, Hooton RD, Scott A, Zibara H (2012) The effect of supplementary cementitious materials on chloride binding in hardened cement paste. *Cem Concr Res* 42(1):1–7
14. Chen C, Tao J, Zhuang L, Lin X (2015) Workability, mechanical properties and affinity of artificial reef concrete. *Constr Build Mater* 98:227–236
15. Auroy M, Poyet S, Bescop PL, Torrenti JM, Charpentier T, Moskura M, Bourbon X (2015) Impact of carbonation on unsaturated water transport properties of cement-based materials. *Cem Concr Res* 74:44–58
16. Shoukry SN, William GW, Downie B, Riad MY (2011) Effect of moisture and temperature on the mechanical properties of concrete. *Constr Build Mater* 25(2):688–696
17. Nedeljković M, Šavija B, Zuo Y, Luković M, Ye G (2018) Effect of natural carbonation on the pore structure and elastic modulus of the alkali-activated fly ash and slag pastes. *Constr Build Mater* 161:687–704

Influence of Molar Concentration of Sodium Hydroxide Solution on High Temperature Resistance of Geopolymer Paste



T. Azeyanagi, A. Saludung, Y. Ogawa, and K. Kawai

1 Introduction

Geopolymers are produced from an aluminosilicate source such as fly ash (FA), which is a by-product from a thermal power plant, and ground granulated blast furnace slag (GGBS) discharged from a blast furnace of a steel mill, and with an Na-based or K-based alkali silica solution. Since geopolymer does not use cement, it is noted as a material that can greatly contribute to the reduction of CO₂ emissions. In addition, the compressive strength of geopolymer was reported to enlarge as the sum of GGBS addition increases [1]. Moreover, Budh and Warhade [2] reported that the compressive strength was improved as the molar concentration of the alkali silica solution increased. However, there are many unclear points, and the unified formulation design method has not been established yet.

On the other hand, geopolymer materials have been studied to be superior in high temperature resistance compared to cement-based materials. Hashimoto et al. [3] reported that the compressive strength after heating to 1200 °C is higher in geopolymer paste than in cement paste. However, it has also been reported that when geopolymer using GGBS is exposed to high temperature, a significant decrease in the compressive strength was observed due to the decomposition of calcium silicate hydrate (C-S-H) [4].

Although the high temperature resistance may vary depending on the composition of raw materials, there are few studies on the effect of the molarity of the alkali solution on the high temperature resistance of geopolymer. This study aims to clarify the effect of the molarity of sodium hydroxide solution on the high temperature resistance of geopolymer paste.

T. Azeyanagi · A. Saludung · Y. Ogawa · K. Kawai (✉)

Department of Civil and Environmental Engineering, Graduate School of Engineering, Hiroshima University, Higashi-Hiroshima, Japan

e-mail: kkawai@hiroshima-u.ac.jp

Table 1 Chemical constituents of ingredients

Constituents	Fly ash (mass%)	GGBS (mass%)
SiO ₂	64.44	35.45
Al ₂ O ₃	20.65	14.06
Fe ₂ O ₃	4.18	0.27
CaO	2.25	43.78
K ₂ O	1.53	0.23
TiO ₂	1.19	0.56
MgO	0.58	5.84
Na ₂ O	–	0.24
S	–	0.62
LOI	2.9	0.05

2 Experimental Outline

2.1 Materials and Specimen Preparation

Low-calcium FA (Blaine fineness = 3550 cm²/g, density = 2.24 g/cm³) which conforms to JIS A 6201 and GGBS (Blaine fineness = 4170 cm²/g, density = 2.91 g/cm³) which conforms to JIS A 6206 were got ready as forerunners. The detailed chemical constituents of both forerunners are shown in Table 1.

Samples were synthesized from 55% FA and 45% GGBS of the total binder by mass. Sodium silicate solution and sodium hydroxide (NaOH) solution were used as alkaline solutions. NaOH solution was prepared in 10, 12 and 14 M by dissolving 400, 480 and 560 g NaOH pellets in water to form a one liter solution. Both sodium silicate and sodium hydroxide solutions were prepared one day prior to mixing.

The geopolymer paste specimens were synthesized as follows: fly ash and GGBS were first dry-mixed together in a pan mixer. The sodium silicate solution and sodium hydroxide solution 10, 12 and 14 M were blended and mixed together with the solid materials expeditiously and relentlessly to create geopolymer paste. Subsequently, the fresh geopolymer paste was cast in cylindrical plastic molds with a measurement of 50 mm in diameter and 100 mm in height. After casting, the specimens were cured in a chamber at 70 °C and 70% of relative humidity (RH) for 24 h and were retained at 20 °C for the further 24 h before demolded. After demolded, the specimens were put in and cured at 20 °C and 60% RH until the ages of 3, 7 and 28 days.

2.2 Heating Test Procedures

At the age of 28 days, geopolymer paste specimens were weighed before exposure to high temperature. Subsequently, the specimens were placed in a furnace whose

temperature was raised at a heating rate of 20 °C/min to 500 and 950 °C. When the objective temperature was attained, it was kept for an additional 1 h. The furnace was then cooled down to room temperature.

2.3 Characterization and Measurements

(1) Mass loss due to high temperature exposure

The thermogravimetric analysis was conducted to study the heat stability of geopolymers from the mass loss with an increase in temperature. It was conducted using simultaneous DTA-TG apparatus DTG-60H at a heating rate of 20 °C/min from room temperature to 1000 °C. The mass of the specimen was quantified after heating and was compared to the initial mass, and then the mass loss was computed by the following equation:

$$\text{Loss in mass} = \frac{m_i - m_f}{m_i} \times 100\% \quad (\text{i})$$

where m_i is the mass of a specimen before heating and m_f is its mass after heating.

(2) X-ray diffraction test

The X-ray diffraction (XRD) test was carried out to search the phase composition of the specimens before and after disclosure to high temperature. The test was performed using a Bruker AXS D2 Phaser X-ray diffractometer in 2-theta range of 5–65° using a Cu K α X-ray source. The sample was made arrangement into powder form using a ball mill grinding machine.

(3) Compressive strength test

A compressive strength test on cylindrical geopolymer paste specimens was performed at the ages of 3, 7, and 28 days and after exposure to high temperature. A universal testing machine with a compression capacity of 250 kN was used. The loading speed was 0.2 mm/min. The test was repeated for 3 samples and an average was taken. JIS A 1108 was used for measuring compressive strength.

3 Results and Discussion

3.1 Mass Loss of Sample by Heating

Figure 1 shows the results of the thermogravimetric analysis and Fig. 2 shows the mass of the specimens quantified before and after heating in a furnace. The mass of

Fig. 1 Change in mass of geopolymers paste by thermogravimetric analysis

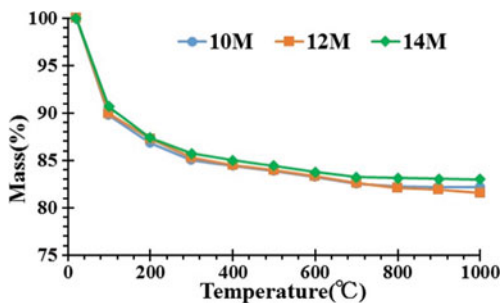
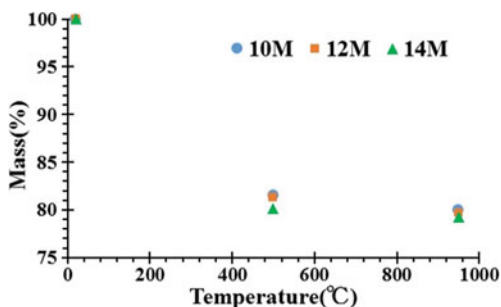


Fig. 2 Change in mass of geopolymers paste heated in furnace



the geopolymers paste decreases rapidly from room temperature to 200 °C regardless of the molar concentration of the sodium hydroxide solution. This reduction is considered to be due to the evaporation of pore water in the geopolymers paste. The gradual decrease in mass from 200 to 1000 °C may be attributed to the progress of dehydration of chemically bound water. The effect of the molarity of sodium hydroxide solution on the mass loss was insignificant.

3.2 Change in Phase Composition by Heating

Figures 3, 4 and 5 show the XRD analysis results of the specimens with different sodium hydroxide concentrations. The effect of the molarity of sodium hydroxide solution on the structure degradation of geopolymers paste at high temperature was negligible. A wide peak at 20–40° 2-theta was observed in all unexposed specimens, which confirms the amorphous characteristic of geopolymers. When the specimens were exposed to a high temperature of 500 °C, the amorphous peak was still observed; however, the crystalline C-S-H in the sample was almost decomposed while other peaks remained and no new peak was formed. On the other hand, high temperature exposure to 950 °C promoted recrystallization to secondary mineral phases such as akermanite and wollastonite.

Fig. 3 XRD patterns of geopolymers before and after heating at 500 and 950 °C (10 M)

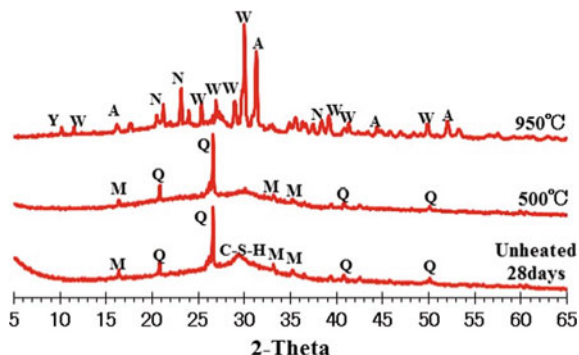


Fig. 4 XRD patterns of geopolymers before and after heating at 500 and 950 °C (12 M)

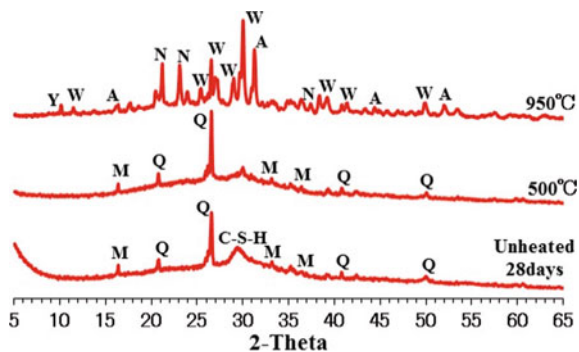
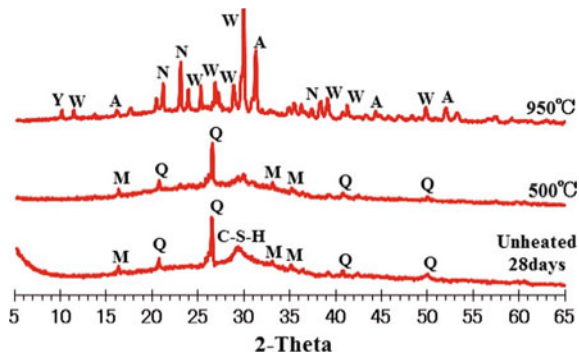


Fig. 5 XRD patterns of geopolymers before and after heating at 500 and 950 °C (14 M)



A: Akermanite ($\text{Ca}_2\text{Mg}[\text{Si}_2\text{O}_7]$)

C-S-H: Calcium silicate hydrate

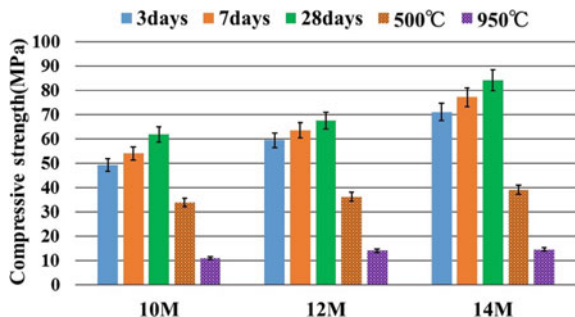
G: Grossular ($\text{Ca}_3\text{Al}_2[\text{SiO}_4]_3$)

M: Mullite ($\text{Al}_6\text{Si}_2\text{O}_{13}$)

N: Nepheline (NaAlSiO_4)

Q: Quartz (SiO_2)

Fig. 6 Compressive strength of specimens before and after heating



W: Wollastonite (CaSiO_3)

Y: Yoshiokaite ($\text{Ca}_{7.5}\text{Al}_{15}\text{SiO}_{32}$).

3.3 Compressive Strength

Figure 6 shows the compressive strength of the specimens before and after high temperature exposure. It was confirmed that the compressive strength of the unexposed specimens is improved by the increase of the molar concentration.

The high concentration of sodium hydroxide solution can promote the dissolution of aluminosilicate source in the solidification mechanism of the geopolymers, as reported in the previous research [2]. After exposure to 500 °C, the compressive strength decreased by approximately 50% in all specimens. This is considered to be because C-S-H gel which contributes to the compressive strength improvement of the specimen was decomposed. The specimens exposed to 950 °C lost approximately 80% of the compressive strength, but it became clear that the influence of the molarity of sodium hydroxide solution on this loss was insignificant, as all of specimens showed almost similar strength after exposure.

4 Conclusion

In this study, the effect of the molarity of sodium hydroxide solution (10, 12, and 14 M) on the high temperature resistance of geopolymers paste made from 55% FA and 45% GGBS was investigated. As a result, when the specimens were exposed to high temperatures up to 950 °C, the effects of the concentration of sodium hydroxide solution on the decrease in compressive strength, mineral composition change, and mass change were insignificant. Also, regardless of the concentration of sodium hydroxide solution, when the geopolymers were exposed to 500 °C, the compressive strength decreased by approximately 50% because of the decomposition of C-S-H

gel. Furthermore, when it was exposed to 950 °C, the decrease in mass proceeded slightly and the compressive strength decreased by approximately 80%.

References

1. Ganapati Naidu P, Prasad ASSN, Adiseshu S, Satyanarayama PVV (2012) A study on strength properties of geopolymer concrete with addition GGBS. *Int J Eng Res Devel* 2(4):19–28
2. Budh CD, Warhade NR (2014) Effect of molarity on compressive strength of geopolymer mortar. *Int J Civ Eng Res* 5(1):83–86. ISSN: 2278-3652
3. Hashimoto S, Kamata H, Yamazaki Y, Takeda H (2012) Application of Geopolymers to Refractory Materials 64:446–451
4. Bernal SA, Gutierrez RMD, Ruiz F, Quinones H, Provis JL (2012) High-temperature performance of mortars and concretes based on alkali-activated slag/metakaolin blends. *Mater. Constr* 62(308):471–488

Investigation of Compressive Behaviors of Geofoams Made in Vietnam



Hoang-Hung Tran-Nguyen and Vinh P. Phan

1 Introduction

EPS (Expanded Poly Styrene) Geofoam is a plastic composite, porous, and lightweight material. Density of EPS varies from 12 to 35 kg/m³, which is lighter than soils like sand or clay about 30–100 times [1, 2]. EPS have been widely applied to construct highway embankments on soft ground in Europe, the USA, and Japan. One of the key parameters of EPS Geofoams is the compressive strength. EPS compressive strength is determined by the unconfined compressive strength test (UCS) and UCS increases in increasing strain. UCS of EPS at a strain of 2% or less is from 15 to 75 kPa for EPS densities from 12 to 28 kg/m³ and at a strain of 10% is from 40 to 200 kPa [1, 3–6]. Under vertical loads, EPS have not reached the failure state at the vertical strain 70% even thought the UCS keeps increasing [1, 7]. The initial modulus of EPS increases with increasing in density and varies from 2 to 12 MPa [1–3]. The typical poisson ratio is relatedly low about 0.05–0.2 that maybe EPS having the porous structure with 2% of polystyrene grains and 98% of air [1, 2, 5, 8]. This paper aims at better understanding of compressive behaviors of EPS made in Vietnam. Compressive strength, initial and residual modulus, vertical strain, and poisson ratio were the key parameters investigated in this research. Several UCS tests of EPS types made in Vietnam were conducted in laboratory to examine the compressive behaviors. Applications of EPS to construct highway embankments on soft ground are little known, particularly EPS made in Vietnam. The results of this study are expected to be the key knowledge of EPS made in Vietnam to prepare for practical applications to build highway embankments on soft ground without soft ground improvement in Vietnam.

H.-H. Tran-Nguyen (✉) · V. P. Phan

Faculty of Civil Engineering, Ho Chi Minh City University of Technology,
VNU-HCM, Ho Chi Minh City, Vietnam

e-mail: tnhhung@hemut.edu.vn



Fig. 1 The EPS geofoam blocks provided by domestic manufacturers

Table 1 The density of the EPS geofoams made in Vietnam tested following the ASTM C303

EPS geofoam type	EPS-12	EPS-13	EPS-14	EPS-19	EPS-23	EPS-26	EPS-28
Density ρ (kg/m ³)	12.1	12.8	14.1	19.3	23.3	26.4	28.6

2 Methodology

2.1 Standards

The ASTM C303 [9], D6817 [10], and D1621 [11] standards were applied to perform the UCS tests in laboratory due to Vietnam having no standards and equivalent guidelines for testing of EPS Geofoam in laboratory for this study.

2.2 Materials

EPS Geofoam specimens were formed from the 7 types of EPS Geofoams made in Vietnam. The 5 150 mm³ specimens were made from each type of EPS Geofoams which is a EPS block having a dimensions of 0.6 × 1 × 2 m (Fig. 1). The 35 specimens were tested to determine density following the ASTM C303. The 7 types of EPS have the density ρ varying from 12.1 to 28.6 kg/m³ (Table 1).

2.3 Implementation

To investigate compressive behaviors of the EPS samples, many UCS tests were carried out following the ASTM D1621. The 35 150 mm specimens were created from the 7 types of the EPS collected from domestic manufacturers. The surfaces

of the specimens were carefully checked for smooth and even before the UCS tests performed. The all specimens were tested in room conditions such as the room temperature of $23 \pm 2^\circ\text{C}$ and the room humidity of $50 \pm 5\%$. Vertical loads were applied at a rate of 1 mm/min or smaller via an air cylinder that can generate a maximum load of 10 kN. The two vertical displacement gauges (LVDTs) were installed above the top caps to capture vertical displacements of a specimen during the test. The four LVDTs were setup at the four side of a specimens to obtain horizontal displacements during a test. Due to no actual failure of an EPS specimen happened, a maximum vertical load was applied to create a maximum vertical strain of 15%. The five cycles of loads and unloads from 0 to a maximum load of each specimen were conducted. All data of each specimen such as vertical loads, displacements, rates, room conditions, time, and date were recorded for analysis.

3 Results and Discussions

The 35 EPS specimens were tested using the UCS with the density varying from 12.1 to 28.6 kg/m³. The UCS data was obtained for analysis to comprehend the compressive behavior of the EPS Geofoams made in Vietnam. The compressive strength (q_u), initial modulus (E_i), residual modulus (E_u), vertical strain (ε), and Poisson ratio (ν) were determined for each specimen and each EPS type.

3.1 Q_u Versus Strain ε

Figure 2 displays the q_u versus ε of the EPS Geofoam types given in Table 1. q_u increases in increasing densities of the EPS Geofoams. For each type of the EPS Geofoams, q_u increases linearly at a strain of 1.14% and plastically at strain greater than 1.78%. The true linear and elastic behavior of the all tested EPS Geofoams is qualified at a strain of 1% or less [3, 7, 8, 12, 13]. For the first 4 cycles of loads and unloads, q_u increases slightly to compare with the initial loading cycle (Fig. 3). Insignificant plastic strain was obtained in these loading-unloading cycles (Figs. 2 and 3).

Figure 4 shows the compressive strength of all tested EPS Geofoams in this study. For the fifth loading-unloading, the vertical load was applied to create a strain of 15% with a rate of 1 mm/min and then unloaded. At a strain of 2–15%, q_u increases slowly and ε increases sharply. All specimens had not reached failure yet. The specimens demonstrated plastic behavior [1, 2, 7, 14]. All EPS Geofoam specimens have not failed even at a large strain of 15% or more because EPS material is a porous material containing 98% air [8, 15, 16]. q_u at a strain of 15% is higher than at a strain of 1–2%, but this strength cannot be used for practical applications due to too large plastic deformations. Therefore, the suitable q_u for applications should be used to be at a strain of 2% or less.

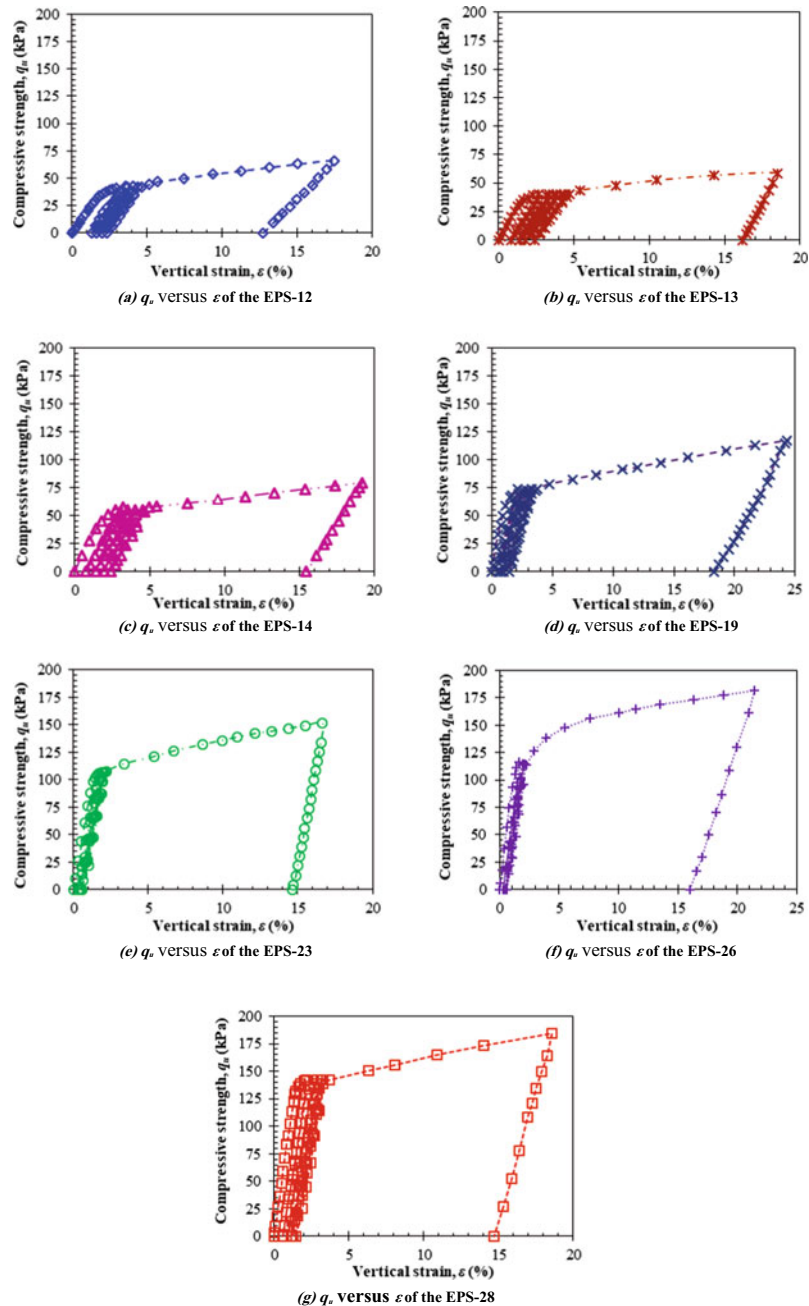


Fig. 2 q_u versus ε of the EPS specimens for the all 5 cycles

Fig. 3 q_u versus ε of the all EPS specimens for the first cycle

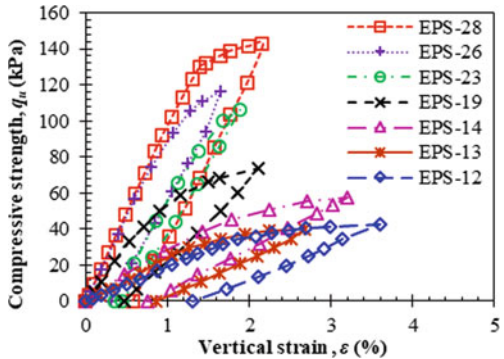
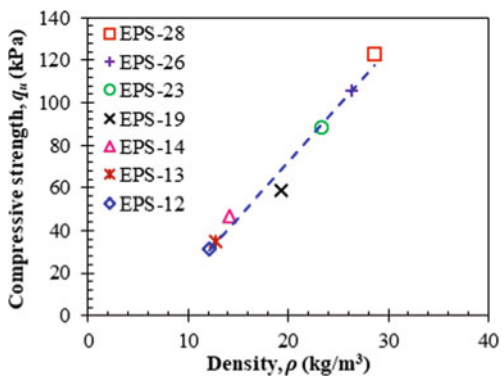


Fig. 4 q_u of the EPS at a strain of 2% or less



3.2 Initial Modulus (E_i) and Residual Modulus (E_u)

The initial modulus E_i was determined basing on the plot of q_u versus ε of the all EPS specimens obtained from the first loading-unloading cycle. E_i increases linearly with increasing in EPS density and varies around 2 to 10 MPa for from EPS-12 to EPS-28, respectively (Fig. 5). The variation of E_i obtained from the EPS made in Vietnam agrees well with E_i reported in literature [1–3, 5, 14]. E_i of this study is compared with others and shown in Fig. 6 [1, 17].

The residual modulus E_u was computed from the slope of a unloading line in a plot of q_u versus ε . E_u also increases with increasing in EPS density (Fig. 7), but was slightly lower than E_i , which varies from 1.85 to 8.51 MPa. In other word, EPS Geofoam decreases its stiffness under cycle loads.

3.3 Poisson Ratio (ν)

Poisson ratios (ν) of the EPS-12 to EPS-28 vary from 0.06 to 0.14 (Fig. 8), which are

Fig. 5 E_i versus ρ of the all tested EPS geofoam

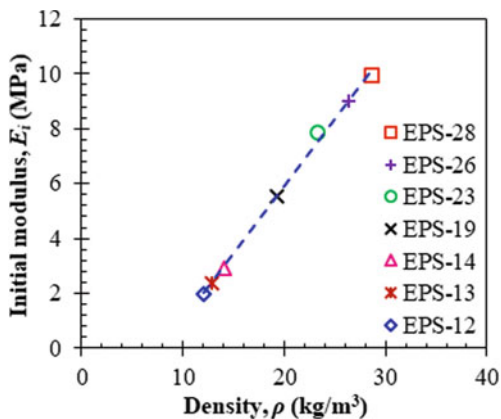


Fig. 6 Comparison of E_i of this study to the published data

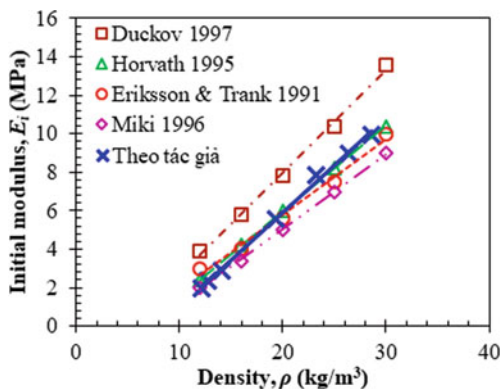


Fig. 7 E_u versus ρ of the tested EPS geofoams

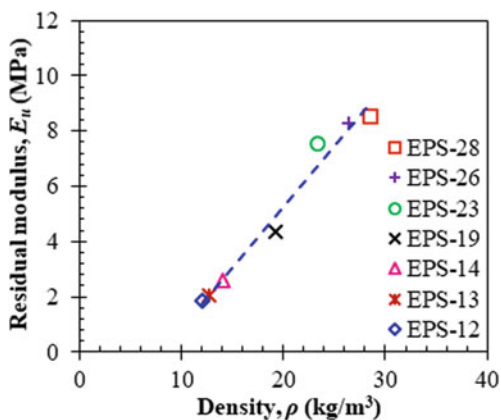
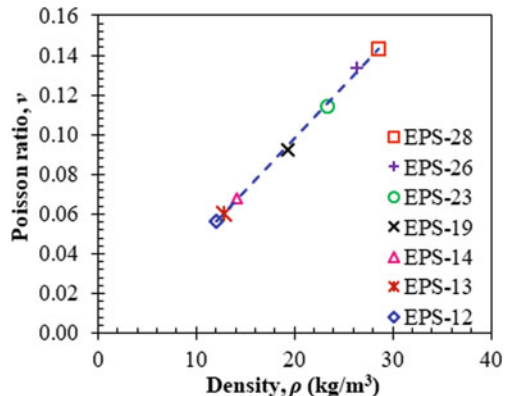


Fig. 8 Poisson ratio (ν) versus ρ of the EPS



smaller than soils and that of EPS published in literature [1, 2, 5, 6, 8, 9, 16]. Poisson ratio increases linearly in increasing the density of the tested EPS Geofoams [5, 8]. The low poisson ratio of EPS Geofoams is expected because EPS is a porous material with 98% air inside. Vertical displacements under vertical loads are mainly due to air dissipated and minimize horizontal displacements. At higher density, EPS is denser and horizontal displacements is developed greater with higher vertical displacements.

4 Conclusion

The 35 specimens were created from the 7 types of the EPS Geofoams made in Vietnam to investigate the compressive behaviors. Several unconfined compressive strength tests were conducted in the laboratory for the all EPS specimens. The all data such as vertical loads, vertical and horizontal displacements were stored for the compressive strength analysis. ρ , q_u , ε , E_i , E_u , and ν —known as the key parameters of the compressive strength—were determined basing on the all compression data of the EPS Geofoams. The relationships amongst the key parameters of the compressive strength were discussed and interpreted. The key findings are listed as the follows:

- (1) q_u increasing with EPS density increase and linear increase at a strain of 2% or less.
- (2) q_u at a strain of 2% considered a maximum strength for design. The maximum strength varys from 31.6 to 122.8 kPa respectively to the densities from 12.1 to 28.6 kg/m^3 .
- (3) A EPS Geofoam reacts repeatedly and similarly under cycle loads.
- (4) Initial modulus E_i was from 2 to 10 MPa and residual modulus E_u was from 1.85 to 8.51 MPa for the EPS density of 12.1 to 28.6 kg/m^3 , respectively.
- (5) Poisson ratio (ν) was from 0.06 to 0.14, which is relatedly low to compare in the literature and soils.

Acknowledgements This study was funded by the department of Science and Technology of Ho Chi Minh City via the contract No. 45/2018/HD-SKHCN and by Ho Chi Minh City University of Technology via the contract No. 50/HD-DHBK-KHCN&DA.

References

1. Elragi AF (2006) Selected engineering properties and applications of EPS geofoam. Softoria 39
2. Horvath JS (1994) Expanded polystyrene (EPS) geofoam: an introduction to material behavior. *Geotext Geomembr* 13:263–280
3. Duskov M (1997) Materials research on EPS-20 and EPS-15 under representative conditions in pavement structure. *Geotext Geomembr* 15:147–181
4. Horvath JS (1997) The compressible inclusion function of EPS. In: *Geotext Geomembr* 15:77–120
5. Ossa A, Romo MP (2009) Micro- and macro-mechanical study of compressive behavior of expanded polystyrene geofoam. *Geosynthetics Int* 16:327–338
6. Stark TD, Bartlett SF, Arellano D (2012) Expanded polystyrene (EPS) geofoam applications & technical data. The EPS Industry Alliance, Crofton, MD, pp 36
7. Chena W, Hao H, Hughes D, Shi Y, Cui J, Li Z (2015) Static and dynamic mechanical properties of expanded polystyrene. *Mater Des* 69:170–180
8. Mohajerani A, Ashdown M, Abdihashi L, Nazem M (2017) Expanded polystyrene geofoam in pavement construction. *Constr Build Mater* 157:438–448
9. ASTM C303 (1998) Standard specification for dimensions and density of preformed block and board—type thermal insulation. American Society for Testing and Materials, USA
10. ASTM D6817 (2007) Standard specification for rigid cellular polystyrene. American Society for Testing and Materials, USA
11. ASTM D1621 (2000) Standard test method for compressive properties of rigid cellular plastics. American Society for Testing and Materials, USA
12. Horvath JS (2001) Concepts for cellular geosynthetics standards with an example for EPS-block geofoam as lightweight fill for roads. Center for Geotechnology, USA, Research Report No. CGT-2001-4, pp 92
13. Trandafir AC, Bartlett SF, Lingwall BN (2010) Behavior of EPS geofoam in stress-controlled cyclic uniaxial tests. *Geotext Geomembr* 28:514–524
14. Ossa A, Romo MP (2012) Confining stress influence on EPS water absorption capability. *Geotext Geomem* 35:132–137
15. Horvath JS (2010a) Emerging trends in failures involving EPS-block geofoam fills. In: *J Perform Constr Facil* 24(4):8
16. Horvath JS (2010b) Lateral pressure reduction on earth-retaining structures using geofoams: correcting some misunderstandings. In: Earth retention conference 3, USA, pp 8
17. Srirajan S, Negussey D, Anasthas N (2001) Creep behavior of EPS geofoam, pp 12
18. Horvath JS (1996) The compressible inclusion function of EPS: an overview. In: Proceedings of the international symposium on EPS construction method, Japan, Tokyo, pp 71–81

Investigation of Mechanical Properties of Fly Ash/RFCC Based Geopolymer Concrete



Anh Tuan Le, Khoa Tan Nguyen, Thuy Ninh Nguyen, Eunseo Kim, and Kihak Lee

1 Introduction

In the past decades, geopolymers has been received great attention as good potential alternative cementitious materials. Many researches have revealed the advantages of geopolymer concrete, including fire and chemical resistance, low CO₂ emissions and low energy consumption [1–3]. Furthermore, these properties are based on the geopolymerization process which can be synthesized from alkali liquid and source of alumino-silicate, as fly ash [4, 5], meta kaolin, rice husk ash [6], slag [7]. On the other hand, Residue Fluid Catalytic Cracking (RFCC) is waste materials of petroleum industry, which contains Aluminium and Silicon ions. It could be used as material for fabricating concrete. With high reactivity and its chemical composition rich in Al and Si, RFCC is suitable for producing geopolymer concrete. In this research, the feasibility of producing geopolymer based on fly ash and RFCC is evaluated. The effect of the ratios of SiO₂/Al₂O₃ and Na₂O/(SiO₂ + Al₂O₃) in slump, compressive strength, and flexural strength of geopolymer concrete is assessed.

A. T. Le · T. N. Nguyen
Faculty of Civil Engineering, Ho Chi Minh City University of Technology, VNU-HCM, Ho Chi Minh City, Vietnam

K. T. Nguyen · E. Kim · K. Lee (✉)
Department of Architectural Engineering, Sejong University, Seoul 05006, South Korea
e-mail: kihakleei@sejong.ac.kr

2 Materials and Methods

2.1 Materials

In this study, fly ash type F, RFCC, and alkaline liquid were used as binder to create geopolymer concrete. Fly ash type F with the specific gravity 2500 kg/m^3 and particle sizes ranged from 10 to $300 \mu\text{m}$ was used in this study. The amount of fly ash is chosen from 300, 400 to 500 kg. RFCC is a waste material of petroleum industry with particle sizes ranged from 20 to $80 \mu\text{m}$. The percentages contents of RFCC were 20, 40, 60, 80 and 100% of fly ash by mass. The chemical compositions of RFCC and fly ash type F are shown in Table 1. Alkaline solution is a combination of sodium silicate and sodium hydroxide. The components of the sodium silicates solution were Na_2O and SiO_2 (approximately 35 to 38% by mass). The concentration of sodium hydroxide (C_M) was 10 M when the ratios of sodium silicate to sodium hydroxide solution was 1. Aggregates comprising 20 mm coarse aggregate (CA) and fine aggregates (FA) were used. The specific gravity was 2700 kg/m^3 and 2650 kg/m^3 for the coarse and fine aggregates, respectively. Details of mix proportion used for this research is shown in Table 2. In Table 2, the name of the mixtures is GRFCCab (where GRFCC = geopolymers concrete using RFCC, ab = number of series).

2.2 Mixing Process and Testing Methods

Fly ash/RFCC based geopolymer concrete included fly ash, RFCC, alkaline liquid, coarse and fine aggregate. Alkaline liquid was prepared by mixing sodium silicate and sodium hydroxide one day before. Fly ash and RFCC were mixed together after quantifying by mixer machine. Then, alkaline liquid was poured into that combination. Finally, coarse and fine aggregate were added. Before casting, fresh concrete was used to do slump test. The rest one was compacted into molds. Then, 150×300 and $100 \times 100 \times 400$ mm specimens were cured on 4 h and 60°C and tested after 7 d.

To determine mechanical properties of fly ash/RFCC based geopolymer concrete, a total of three kinds of tests such: slump, compressive strength and flexural strength were used. The slump test was based on ASTM C143. The compressive and flexural strength of specimens were evaluated based on ASTM C39 and C78, respectively.

Table 1 Chemical compositions of fluid catalytic cracking and fly ash

Compositions (%)	SiO_2	Al_2O_3	CaO	MgO	Fe_2O_3	SO_3	$\text{K}_2\text{O} + \text{Na}_2\text{O}$	LOI
RFCC	55	39	0.50	–	0.38	<1	0.21	–
Fly ash	51.7	31.9	1.21	0.81	3.48	0.25	1.02	9.63

Table 2 Mix proportions

Name	CA (kg)	FA (kg)	Fly ash (kg)	RFCC (kg)	Sodium silicate solution (kg)	Sodium hydroxide (kg)	C _M of NaOH (M)	Alkali solution/(Fly ash + RFCC)
GRFCC1	1098	810	300	0	97.5	97.5	10	0.65
GRFCC11	1098	810	240	60	97.5	97.5	10	
GRFCC12	1098	810	180	120	97.5	97.5	10	
GRFCC13	1098	810	120	180	97.5	97.5	10	
GRFCC14	1098	810	60	240	97.5	97.5	10	
GRFCC15	1098	810	0	300	97.5	97.5	10	
GRFCC2	1063	770	400	0	100	100	10	0.5
GRFCC21	1063	770	320	80	100	100	10	
GRFCC22	1063	770	240	160	100	100	10	
GRFCC23	1063	770	160	240	100	100	10	
GRFCC24	1063	770	80	320	100	100	10	
GRFCC25	1063	770	0	400	100	100	10	
GRFCC3	950	760	500	0	100	100	10	0.4
GRFCC31	950	760	400	100	100	100	10	
GRFCC32	950	760	300	200	100	100	10	
GRFCC33	950	760	200	300	100	100	10	
GRFCC34	950	760	100	400	100	100	10	
GRFCC35	950	760	0	500	100	100	10	

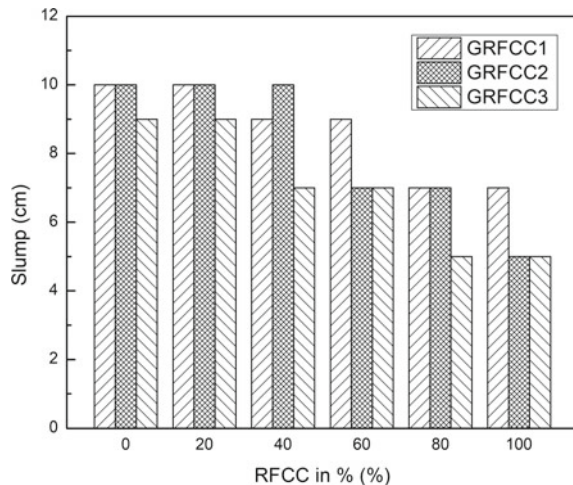
3 Results and Discussions

In this section, the test data are presented and discussed. The test results cover the effect of ratios of $\text{SiO}_2/\text{Al}_2\text{O}_3$ and $\text{Na}_2\text{O}/(\text{SiO}_2 + \text{Al}_2\text{O}_3)$ on slump, compressive strength and flexural strength of fly ash/RFCC based geopolymer concrete.

3.1 Influence of RFCC on Workability

The workability of fly ash/RFCC based geopolymer concrete is shown in Fig. 1. The slump of fly ash based geopolymer concrete GRFCC1, GRFCC2, and GRFCC3 is 10 cm, 10 cm and 9 cm, respectively. When the usage of RFCC increases to 20%, the slump of fresh concrete maintains the same value. However, the amount of RFCC is increased from 20 to 100%, the slump of geopolymer concrete decreases about 30–50%. It can be explained that the size of RFCC particles is smaller than fly ash, so the workability of fresh concrete will decrease when the amount of RFCC

Fig. 1 Relationship between usage of RFCC and slump

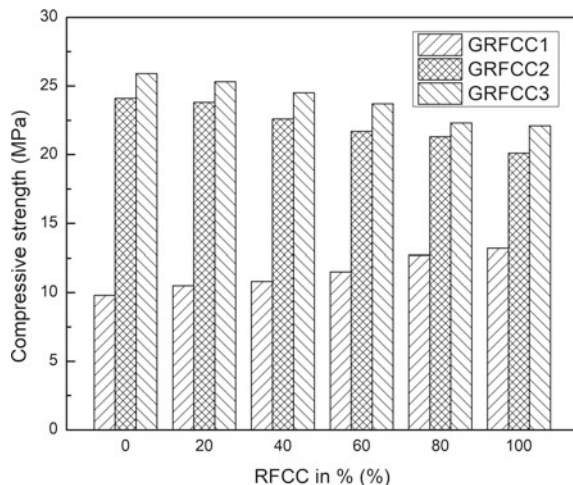


increases. To maintain same workability with mixing using only fly ash, extra water or superplasticizer should be added more into mixtures using fly ash/RFCC.

3.2 Influence of RFCC on Compressive Strength

Figure 2 shows the influence of RFCC on compressive strength of geopolymer concrete. The compressive strength of GRFCC1 increases when the usage of RFCC changes from 0 to 100%, while the compressive strength of GRFCC2 and GRFCC3 decreases about 15–20%. For GRFCC1, the ratio of alkaline liquid to fly ash and

Fig. 2 Relationship between usage of RFCC and compressive strength

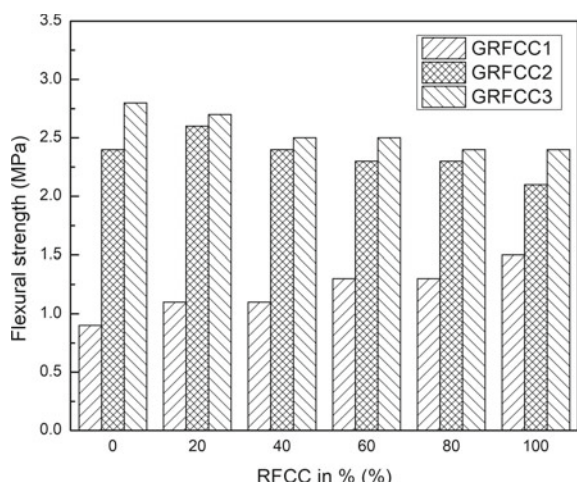


RFCC is 0.65 which is higher than 0.5 and 0.4 for GRFCC2 and GRFCC3, respectively. This higher amount of alkaline liquid might be enough for geopolymerization process creating long chain of polymer when RFCC along with rich amount of Si and Al is added. Thus, we can conclude that the compressive strength of fly ash/RFCC based geopolymer concrete is higher with higher amount of alkaline liquid and lower amount of alumino-silicate. However, with lower amount of alkaline liquid and higher amount of alumino silicate, the compressive strength is lower.

3.3 Influence of RFCC on Flexural Strength

The influence of RFCC on flexural strength of fly ash/RFCC based geopolymer concrete is shown in Fig. 3. As the influence of RFCC on compressive strength, the flexural strength of GRFCC1 increases when the usage of RFCC increases from 0 to 20%. While the flexural strength of GRFCC3 decreases when the amount of RFCC increases from 0 to 20%. Only GRFCC2 shows a little different from GRFCC1 and GRFCC3. The flexural strength of GRFCC2 increase when the usage of RFCC increases from 0 to 20%. After that when the amount of RFCC increases to 100%, the flexural strength keeps going down. It can be explained that the loss of strength of GRFCC2 and GRFCC3 is caused by RFCC. When fly ash is replaced by RFCC, the amount of alumina-silicate of mixture increases 10–15%. At that time, the ratio of $\text{SiO}_2/\text{Al}_2\text{O}_3$ and $\text{Na}_2\text{O}/(\text{SiO}_2 + \text{Al}_2\text{O}_3)$ also decreases, which makes geopolymerization happen slower than fly ash based geopolymer concrete. According to Table 2, the ratio of alkaline liquid to fly ash and RFCC for GRFCC1 is 0.65 which is higher than 0.5 and 0.4 for GRFCC2 and GRFCC3, respectively. This higher amount of alkaline liquid might impulse geopolymerization process creating long chain of polymer and higher strength.

Fig. 3 Relationship between usage of RFCC and flexural strength



4 Conclusions

In conclusion, fly ash/RFCC based geopolymer concrete requires heat curing on the oven. Furthermore, when the fly ash is replaced by RFCC, the amount of alumino-silicate increases and the ratio of $\text{SiO}_2/\text{Al}_2\text{O}_3$ and $\text{Na}_2\text{O}/(\text{SiO}_2 + \text{Al}_2\text{O}_3)$ decreases.

The slump of fly ash/RFCC based geopolymer concrete decreases 30 to % when the usage of RFCC changes from 20 to 100%. The particle size of RFCC is finer than fly ash. Thus, there is a need of extra water or superplasticizer to maintain the same workability as fly ash based geopolymer concrete.

Geopolymer concrete using RFCC needs higher amount of alkaline liquid than using fly ash to maintain the same mechanical properties.

Acknowledgements This research was supported by a grant (2019R1I1A1A01059890) from the National Research Foundation of Korea (NRF). The authors would like to express sincere gratitude for their support.

References

1. Davidovits J (2011) Geopolymer chemistry and applications. Saint-Quentin, France
2. Kong DL, Sanjayan JG, Sagoe-Crentsil K (2008) Factors affecting the performance of metakaolin geopolymers exposed to elevated temperatures. *J Mater Sci* 43:824–831
3. Temuujin J, Richard W, Lee M, van Riessen A (2011) Preparation and thermal properties of fire resistant metakaolin-based geopolymer-type coatings. *Cryt Solid* 357:1399–1404
4. Khoa TN, Namshik A, Tuan AL, Kihak L (2017) Theoretical and experimental study on mechanical properties and flexural strength of fly ash-geopolymer concrete. *Constr Build Mater* 106:65–77
5. Somna K, Jaturapitakkul C, Kajitvichyanukul P, Chindaprasirt P (2011) NaOH-activated ground fly ash geopolymer cured at ambient temperature. *Fuel* 90:2118–2124
6. Nazari A, Bagheri A, Riahi S (2011) Properties of geopolymer with seeded fly ash and rice husk bard ash. *Mater Sci Eng A* 528:3390–3397
7. Onisei S, Pontikes Y, van Gerven T, Angelopoulos GN, Velea T, Predica V, Moldovan P (2012) Synthesis of inorganic polymers using fly ash and primary lead slag. *J Hazard Mater* 205–206:101–110

Investigation of the Influence of Residue Fluid Catalytic Cracking (FCC) on Properties of Autoclaved Aerated Concrete



Anh Tuan Le, Khoa V. A. Pham, Ninh Thuy Nguyen, Chorong Lee,
and Kihak Lee

1 Introduction

Nowadays, using eco-green and friendly material in the construction industry is a necessary demand for sustainable development. In civil engineering, autoclaved aerated concrete is used widely for construction, especially high rise buildings because of its advantages such as lightweight, sound resistance, fire resistance, durability and dimension stability, as well as the ability to apply in the field. The main materials for making autoclaved concrete are cement, crushed sand, lime, calcined gypsum and aluminium powder [1]. Using new and eco-green materials for replacing cement, sand and other materials can contribute to sustainable development and reduce manufacturing cost as well as reuse industrial waste [2, 3]. In petroleum refinery manufacturing, fluid catalytic cracking (FCC) is a product of conversion process with the major component zeolite which can be used as a supplementary cementitious material. FCC could be used to replace cement in mortar, concrete and show good performance in some recent studies [4–6]. In this research, the influence of fluid catalytic cracking on the properties of autoclaved aerated concrete is evaluated by replacing totally cement and crushed sand with percentages of 25, 50, 75 and 100% and using sodium solution in geopolymmerization reaction [7]. The workability, expansion properties, strength properties are determined and compared with ordinary autoclaved aerated concrete using cement.

A. T. Le · N. T. Nguyen

Faculty of Civil Engineering, Ho Chi Minh City University of Technology, VNU-HCM, Ho Chi Minh City, Vietnam

K. V. A. Pham · C. Lee · K. Lee (✉)

Department of Architectural Engineering, Sejong University, Seoul, Republic of Korea
e-mail: kihaklee@sejong.ac.kr

Table 1 Chemical compositions of cement and fluid catalytic cracking

Compositions (%)	Al ₂ O ₃	SiO ₂	CaO	Fe ₂ O ₃	MgO	SO ₃	Na ₂ O + K ₂ O	LOI
Cement	5.58	21.30	61.92	4.32	1.35	1.69	–	1.17
FCC	39	55	0.50	0.38	–	<1	0.21	–

2 Experiment Process

2.1 Materials

The experiments were conducted by using cement, fluid catalytic cracking (FCC), crushed sand, lime, calcined gypsum, aluminium powder, and sodium solution. Cement and crushed sand were used for making a specimen without FCC and comparing with specimens using FCC. Cement PC40 was used with a compressive strength of 43 MPa, a density of 3.07 g/cm³ and a fineness of 3330 cm²/g. The composition of lime is 91.4% of CaO and MgO and the fineness is 8.4%. Sodium solution made from sodium hydroxide and sodium silicate with the composition of Na₂O and SiO₂ of 36–38% was used to activate the geopolymmerization inside the AAC structure. The main chemical composition of calcined gypsum is more than 95% of CaSO₄ and fineness at 0.08 mm is 4.8%. Aluminium powder with a specific surface area of 0.6–0.8 m²/g was mixed in these tests. Fluid catalytic cracking is a product of conversion process in petroleum refinery manufacture with particle sizes ranged from 60 to 88 μm. The chemical compositions of cement and FCC are shown in Table 1.

2.2 Testing

The experiment of autoclaved aerated concrete was shown in Table 2 with nine mix proportions CA, FA and GA. CA stood for Cement Autoclaved Aerated Concrete in which cement was the main material. FA series (Fluid Catalytic Cracking Autoclaved Aerated Concrete) including FA1, FA2, FA3 and FA4 with replacing 25, 50, 75 and 100% of crushed sand by fluid catalytic cracking. The remaining series GA represented for Geopolymer Autoclaved Aerated Concrete. GA1, GA2, GA3, GA4 was made by using the sodium solution/FCC ratio from 0.4 to 0.7. The concrete mixture was cured at 175 °C and 6–9 atm pressure in 12 h. The workability of fresh concrete was carried out according to standard ASTM C1611 by using the cone and flow table as shown in Fig. 1. Figure 2 shows the expansion test which used to obtain the expansion rate, expansion time and temperature of expansion. The expansion time was determined when the concrete mixture was poured to the measuring cylinder and the expansion finished totally. The expansion rate and expansion time were determined by the change of height and temperature of the mixture in the measuring

Table 2 Mix proportions

Mix proportion	Cement (kg)	Sand (kg)	FCC (kg)	Lime (kg)	Gypsum (kg)	Aluminum powder (kg)	Water(l)	Sodium solution (kg)	Solution/FCC ratio
CA	75	350	0	75	20	2.5	325	0	0
FA1	0	262.5	162.5	75	20	2.5	325	0	0
FA2	0	175	250	75	20	2.5	325	0	0
FA3	0	87.5	337.5	75	20	2.5	325	0	0
FA4	0	0	425	75	20	2.5	325	0	0
GA1	0	0	425	75	20	2.5	155	170	0.4
GA2	0	0	425	75	20	2.5	112.5	212.5	0.5
GA3	0	0	425	75	20	2.5	70	255	0.6
GA4	0	0	425	75	20	2.5	27.5	297.5	0.7

Fig. 1 Flow test**Fig. 2** Expansion test

cylinder. The performance of the autoclaved aerated concrete specimen was measured through the compression test, according to ASTM C1693.

3 Experimental Results and Discussions

3.1 Influence of FCC on the Workability of AAC

The performance of autoclaved aerated concrete using cement, replacing cement and crushed sand by fluid catalytic crack is shown in Table 3. The flow, expansion time, expansion rate, temperature of expansion and compressive strength of specimen CA without FCC, specimens FA1-FA4 with FCC, specimens GA1-GA4 with FCC and sodium solution were obtained from experiments.

In terms of workability, the flow of CA using cement was 34.5 cm and FA using FCC replacing for sand was 29.3–33.7 cm. As the percentage of FCC increased from 25 to 100% in the mixture, the flow decreased significantly, about 15% of the

Table 3 Performance of AAC using cement and FCC

Mix proportion	Flow (cm)	Expansion time (min)	Expansion rate (%)	Temperature of expansion (°C)	Compressive strength (N/mm ²)
CA	34.5	67	85	68	3.54
FA1	33.7	69	85	62	2.33
FA2	32.8	71	87	54	1.79
FA3	31.2	75	90	49	1.44
FA4	29.3	79	92	45	1.25
GA1	34.2	27	82	42	3.54
GA2	29.3	24	79	39	3.72
GA3	26.2	19	73	37	3.95
GA4	25.3	15	70	34	4.15

specimen using 100% FCC. Similar to FA, for GA specimens using sodium solution, the flow also decreased from 34.2 to 25.3 cm when solution/FCC ratios in a range from 0.4 to 0.7. The presence of FCC led to the decrement of workability because the various FCC particle size maintained water in the concrete mixture, compared with AAC using totally cement.

3.2 *Influence of FCC on Expansion Properties of AAC*

Expansion is an important phase in the manufacturing process of autoclaved aerated concrete. The chemical reaction of aluminium powder in the concrete mixture leads to the expansion of volume concrete by the time. The expansion time of non-FCC specimen CA was 67 min and this time was increased from 69 to 79 min with FA1-FA4 specimens using FCC as shown in Fig. 3. The presence of FCC replaced for cement and crushed sand did not make a good environment for chemical reaction happened inside the AAC structure, compared with cement. The expansion of AAC was also affected by the low quantity of CaO in FCC. However, the expansion time was shortened from 15 to 27 min because the geopolymersation happened between FCC and sodium solution at specimens GA1, GA2, GA3, and GA4.

As shown in Fig. 4, the temperature of expansion decreased along with the increase in the percentage of FCC. Compared with the temperature of the cement AAC specimen of 68 °C, the temperature of FA decreased from 62 to 45 °C and GA from 42 to 34°C. Using fluid catalytic cracking replacing for cement and crushed sand led to the decrement of the heat hydration process. In contrast to the temperature of expansion, the expansion rate of FA specimens using FCC was improved from 85 to 92% because of the good dissipation of FCC particles in the fresh mixture. However, there was a tendency in the expansion rate of geopolymers AAC from 82 to 70% when the ratio of FCC and sodium solution increased from 0.4 to 0.7.

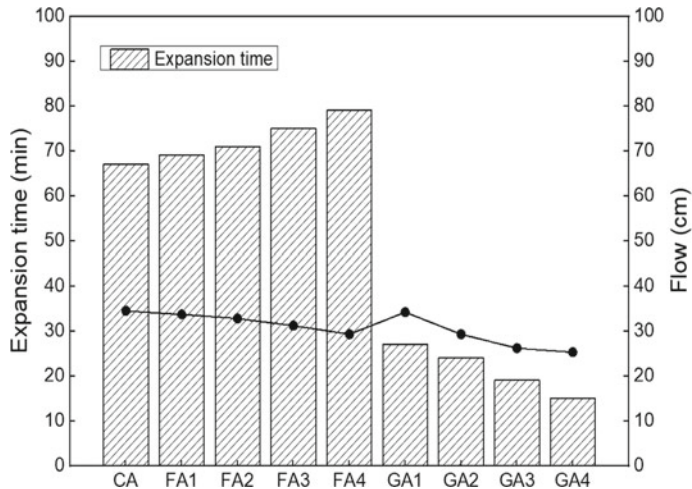


Fig. 3 Flow and expansion time

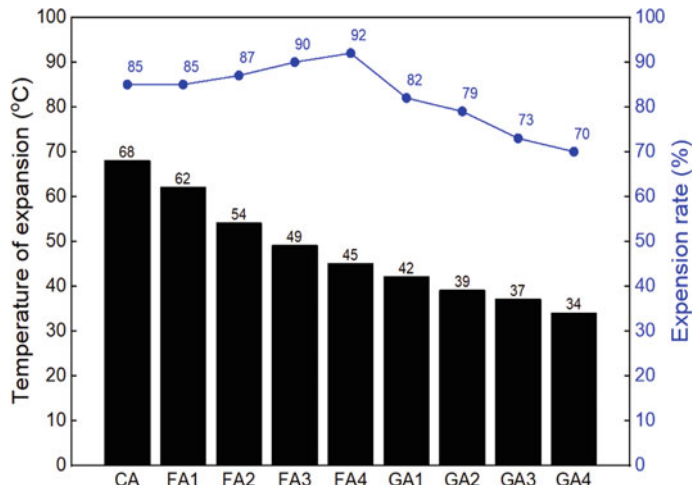


Fig. 4 Expansion properties

3.3 Influence of FCC on the Compressive Strength of AAC

Overall, there was a significant decrease in the compressive strength of autoclaved aerated concrete using fluid catalytic cracking for replacing cement and crushed sand. Compared with 3.54 N/mm^2 of cement AAC, the compressive strength of FA1 using 25% FCC decreased $30\text{--}2.33 \text{ N/mm}^2$ as shown in Fig. 5. In mix proportion FA4

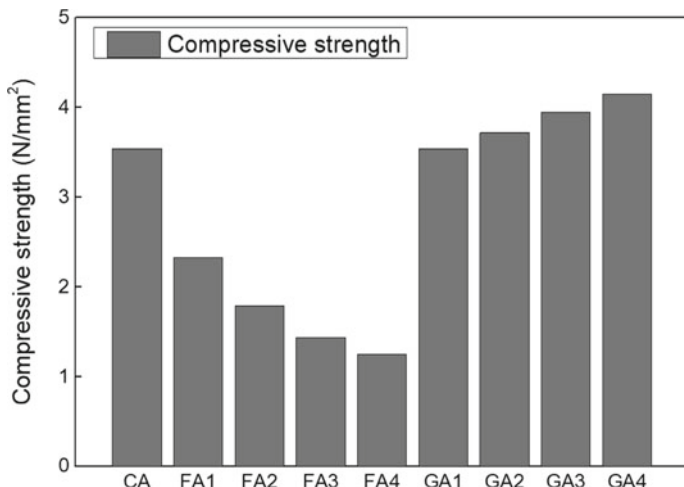


Fig. 5 Compressive strength of AAC

with 100% FCC was used, the compressive strength decreased significantly 70% at 1.25 N/mm².

In autoclaved aerated concrete, calcium silicate hydrate C-S-H and tobermorite are the most common hydration products and primarily responsible for strength performance [8]. These hydration products are created by the chemical reaction of CaO, SiO₂ in water and autoclaved environment. There is 0.5% of CaO in the composition of FCC which is much less than 61.92% in cement. As a consequence, the compressive strength of FA specimens with FCC was decreased strongly. Besides, in Fig. 6, when replacing cement and crushed sand by FCC, the void was developed

Fig. 6 Voids in AAC structure



in the concrete structure, the amount of SiO₂ was decreased and the combination of SiO₂-Al₂O₃-CaO was not as good as using cement.

In contrast to FA specimens, GA specimens performed greater behavior. When combining the FCC and sodium solution, the strength was improved 20% from 3.54 to 4.15 N/mm². Using FCC and sodium solution with ratio of 0.4, 0.5, 0.6 and 0.7, the compressive strength obtained at 3.54, 3.72, 3.95 and 4.15 N/mm², respectively. In alkaline and autoclaved environment, poly alumino-silicate was created and improved the geopolymmerization and strength of concrete [7].

4 Conclusions

The influence of fluid catalytic cracking in autoclaved aerated concrete was evaluated in this study by replacing cement and crushed sand by FCC with 25, 50, 75, 100% and combining of FCC and sodium solution with the ratio of sodium solution/FCC of 0.4–0.7. The below conclusions can be obtained from experimental results:

1. The workability and temperature of expansion of all specimens decreased to 15% compared with specimens using only cement.
2. The expansion time and expansion rate was improved significantly when using FCC and decreased when using FCC and sodium solution.
3. The usage of only FCC was not effective with the reduction of compressive strength from 30 to 70%. The geopolymmer autoclaved aerated concrete combined FCC and sodium solution performed an enhanced compressive strength of 20%.
4. Mix proportion GA1 is a suitable choice for replacing cement and crushed sand in autoclaved aerated concrete with higher compressive strength, suitable workability and expansion properties.
5. Fluid catalytic cracking is an effective material for replacing cement in autoclaved aerated concrete and contributing to sustainable development.

Acknowledgements This research was supported by a grant of the Ministry of the Interior and Safety as Earthquake Disaster Prevention Human Resource Development Project. The authors would like to express sincere gratitude for their support.

References

1. RILEM Technical Committees (1993) Autoclaved aerated concrete. Properties, testing and design (1993)
2. Krama H, Karakurt C (2009) Properties of the autoclaved aerated concrete produced from coal bottom ash. *J Mater Process Tech* 209(2):767–773
3. Walczak P, Szymanski P, Rozycza A (2015) Autoclaved aerated concrete based on fly ash in density 350 kg/m³ as an environmentally friendly material for energy-efficient construction. *Procedia Eng* 122:39–46

4. Neves R, Vicente C, Castela A, Montemor MF (2015) Durability performance of concrete incorporating spent fluid cracking catalyst. *Cem Concr Comp* 55:308–314
5. Payá J, Monzó J, Borrachero MV, Velázquez S (2013) Cement equivalence factor evaluations for fluid catalytic cracking catalyst residue. *Cem Concr Comp* 39:12–17
6. Soriano L, Payá J, Monzó J, Borrachero MV, Tashima MM (2016) High strength mortars using ordinary Portland cement-fly ash-fluid catalytic cracking catalyst residue ternary system (OPC/FA/FCC). *Constr Build Mater* 106:228–235
7. Davidovits J (2011) geopolymers chemistry and applications. Saint-Quentin, France
8. Matsui K, Kikuma J, Tsunashima M, Ishikawa T, Matsuno S, Ogawa A, Sato M (2011) In situ time-resolved X-ray diffraction of tobermorite formation in autoclaved aerated concrete: Influence of silica source reactivity and Al addition. *Cem Concr Res* 41(5):510–519

Investigation on Moisture Transfer in Mortar After Exposure to High Temperature



M. Mizoguchi, T. Kitagawa, T. Daungwilailuk, Y. Ogawa, and K. Kawai

1 Introduction

Concrete has been used in many fields, and concrete structures can be deteriorated by many factors during the service life. High temperature such as fire is one of the factors that can cause deterioration on concrete. When the temperature of cement hydrates is raised, free water will be evaporated at around 100 °C. Subsequently, the decomposition of C-S-H occurs in the range of 100–300 °C followed by the dehydration of calcium hydroxide that takes place at around 400–500 °C. From 750 to 900 °C, the decarbonation of calcium carbonate can be observed [6]. Therefore, the properties of concrete such as strength characteristics may be affected by high temperature. Even though a concrete member is exposed to high temperature (below 300 °C), it is unnecessary to be repaired when the compressive strength exceeds the standard value [2]. On the other hand, even though the mechanical properties of concrete are not affected by exposure to high temperature, its chemical properties and durability may be affected. For example, Suzuki et al. reported that the compressive strength and permeability of a mortar specimen can be continuously deteriorated when the specimen was kept outside after heating. Meanwhile, if the specimen was cured in water after heating, the compressive strength recovered up to 80% of the initial compressive strength and the permeability was also improved [8]. Although many studies have examined the influence of high temperature on the mechanical properties of concrete including strength and elastic modulus, there are few reports regarding the influence on the permeability [7]. Therefore, in this study, moisture transfer in mortar after heating was investigated using an electrical resistance method in which the electrical resistance in hardened cement paste was measured by using stainless steel rods embedded in specimens. The effect of heating methods on the moisture transfer was also investigated.

M. Mizoguchi · T. Kitagawa · T. Daungwilailuk · Y. Ogawa · K. Kawai (✉)

Department of Civil and Environmental Engineering, Graduate School of Engineering,
Hiroshima University, Higashi-Hiroshima, Japan
e-mail: kkawai@hiroshima-u.ac.jp

2 Experimental method

2.1 Specimens

Mixture Proportion Ordinary Portland cement (OPC) and fine aggregate were used to make mortar specimens in this study. The densities of OPC and fine aggregate were 3.16 and 2.62 g/cm³, respectively. The mixture proportions of mortar are shown in Table 1. Mortars were prepared with two water-to-cement ratios (W/C) of 0.35 and 0.45. Polypropylene (PP) fibers were used in mortar specimens with W/C of 0.35 at 0.34% by volume of mortar. Air entraining agent (AE) and superplasticizer (SP) were dosed to get an appropriate workability.

Specimen preparation The size of the specimen for the moisture transfer test was 40 × 40 × 160 mm as shown in Fig. 1. Stainless steel rods with a diameter of 0.9 mm were embedded in the specimens for the moisture transfer test at an interval of 15 mm, which is three times larger than the maximum size of the fine aggregate in consideration of the influence of the fine aggregate on the electrical resistance. After

Table 1 Mixture proportions

Mixture	W/C	kg/m ³				Percentage of cement by mass	
		W	C	S	PP	AE	SP
0.35	0.35	289	835	1117	–	0.001	0.5
0.35 PP	0.35	289	835	1117	3.13	0.001	0.5
0.45	0.45	289	654	1270	–	0.001	0.5

W water, C OPC, S sand

Fig. 1 Specimen of moisture transfer test

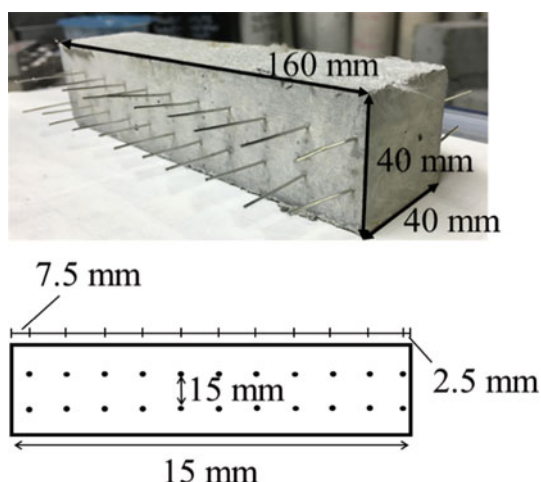
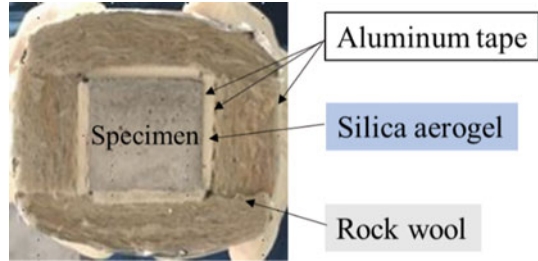


Fig. 2 Coating process

casting, the top surface of all specimens was covered with plastic wraps to prevent water evaporation and stored at 20 °C and 60% relative humidity (RH) for 24 h, then they were demolded and cured in water at 20 °C for 27 days. Subsequently, the specimens were stored at 20 °C and 60% RH for 30 days. Before heating, all the surfaces of specimens except for one surface with 40 × 40 mm were coated in five layers to avoid the temperature loss during heating, as shown in Fig. 2. Firstly, the specimens were coated with aluminum tape. Secondly, the specimens were coated with a silica aerogel heat insulating material, and it was fixed by aluminum tape. Then, the specimens were coated with a rock wool heat insulating material. Finally, it was fixed by aluminum tape. Non-heating specimens were also prepared for reference. All surfaces of non-heating specimens were coated with aluminum tape, except for one surface (40 × 40 mm).

2.2 Measurement of the Electrical Resistance

Direct current (DC) and alternating current (AC) can be used to measure small electrical resistance. However, the electrical resistance by DC cannot be measured stably because of polarization [4]. In addition, it is difficult to measure the electrical resistance in the specimen with low water content by using a small voltage. Therefore, in this study, the power supply by AC was used in the same way as the previous studies [1, 5] at 1 kHz AC and 1 V to prevent the polarization. The electrical resistance in a specimen was measured by an LCR meter (measurement range: 10–200.00 MΩ) as shown in Fig. 3a. After that, the specific resistance of the specimen was calculated by using Eq. 1 [3].

$$R = \{ \log(d/a)/(\pi \times l) \} \times \rho = Sf \times \rho \quad (1)$$

where R: electrical resistance (kΩ), d: interval of stainless-steel rods (cm), a: radius of stainless steel rods (cm), l: length of current-carrying part (cm), ρ: specific resistance (kΩ cm), and Sf: geometrical factor (In this study, it was calculated as 0.121).

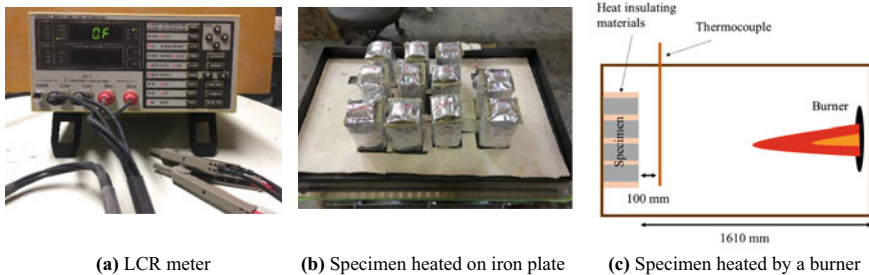


Fig. 3 Measurement apparatus

2.3 Heating Method

Iron plate heating The specimens were heated on an iron plate as shown in Fig. 3b. The iron plate was heated at a rate of 20 °C/min up to the target maximum temperature of approximately 350 °C, and then maintained for 15 min at the maximum temperature (the total heating time was 31 min from the start of heating). The temperature on the plate was controlled manually by adjusting the gas flow. The maximum temperature on the iron plate for the mixtures of 0.35 and 0.35 PP was approximately 330 °C which was slightly lower than 350 °C, whereas that for the mixture of 0.45 was slightly higher than the target temperature (approximately 360 °C).

Radiation heating The specimens 0.35 PP were heated by a burner of a refractory furnace as shown in Fig. 3c. The ambient temperature near the exposed surface of the specimen was raised to 350 °C at a rate of 20 °C/min, and then maintained at 350 °C for 15 min. The rate of temperature increase was controlled by a thermocouple which was placed at a location of 100 mm from the specimen surface.

3 Results and Discussions

3.1 Temperature History

Iron plate heating Figures 4, 5 and 6 show the temperature history on the iron plate and in the specimen for the mixtures of 0.35, 0.45, and 0.35 PP, respectively. According to Fig. 4, the maximum temperature in the specimen with W/C = 0.35 reached up to 200 °C at a depth of 2.5 mm from the exposed surface. The maximum temperature at the depths of 20, 40, and 60 mm from the exposed surface was 120 °C, 90 °C, and 70 °C, respectively. After heating, the internal temperature immediately decreased to less than 75 °C in 30 min. On the other hand, the temperature at deeper depths than 80 mm from the exposed surface increased gradually up to 50 °C and continued

Fig. 4 Temperature history in iron plate heating (mixture: 0.35)

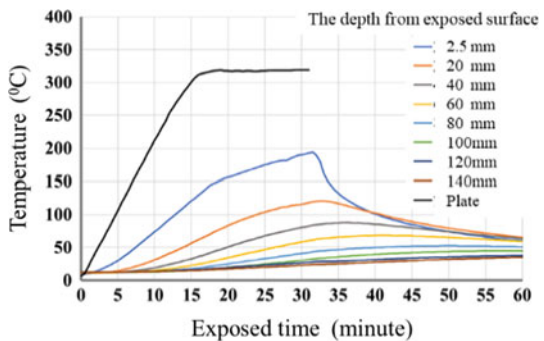


Fig. 5 Temperature history in iron plate heating (mixture: 0.45)

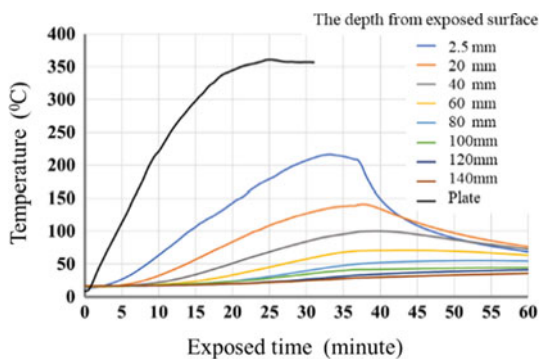
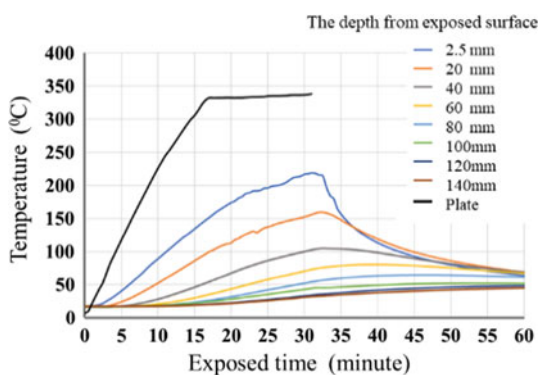


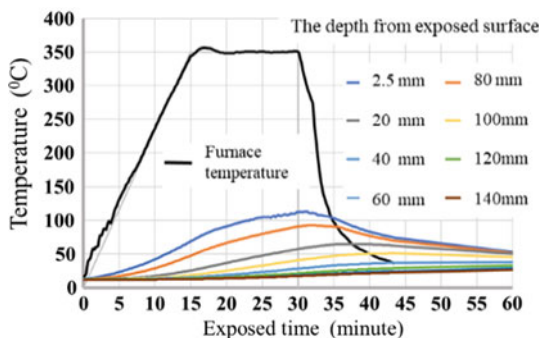
Fig. 6 Temperature history in iron plate heating (mixture: 0.35PP)



to increase slightly even after heating. Although the temperature of specimens with W/C of 0.35, 0.45, and 0.35 PP rose up in similar tendency, it should be noted that their maximum temperature were different.

Radiation heating As shown in Fig. 7, in the radiation heating, the ambient temperature history near the exposed surface of the specimens was almost the same as that on the iron plate. However, the temperature in the specimen was significantly lower

Fig. 7 Temperature history in radiation heating (mixture: 0.35 PP)



than that in the case of the iron plate heating. In the radiation heating, the maximum temperature at the depths of 2.5, 20, 40, and 60 mm from the exposed surface was 110 °C, 90 °C, 70 °C, and 50 °C, respectively. It was observed that the temperature inside the specimen during heating was totally different depending on the heating methods even when the heating curve was almost the same.

3.2 Moisture Transfer Test

Moisture transfer in specimens was evaluated using specific resistance calculated from the electrical resistance. Higher value of specific resistance indicates a lower moisture content in the specimen.

Iron plate heating Figures 8, 9 and 10 show the specific resistance in the heated specimens at different depths from the exposed surface in the iron plate heating. The specific resistance of unheated specimens was also shown with a solid line. As shown in Fig. 8, the specific resistance at the depth of 7.5 mm from the exposed surface increased significantly after heating, and then remained almost constant regardless of the elapsed time. On the other hand, the specific resistance at the depths of 22.5 mm or more decreased, and then increased gradually with time to the specific resistance of the unheated specimen. It may indicate that water in the surface layer could evaporate during heating, and additionally microcracks caused by heating can make the microstructure of the specimen more porous, thereby accelerating the water evaporation. At the depths of more than 22.5 mm, the specific resistance decreased after heating, which means that the internal relative humidity became higher.

It can be attributed to evaporation of free water and decomposition of chemically bound water by temperature rise. Moreover, moisture around the surface could move to the inside of the specimens with an increase in the surface temperature. For the mixtures 0.45 and 0.35 PP, similar tendency was observed as illustrated in Figs. 9 and 10. The increment of the specific resistance in the case of the mixture 0.35

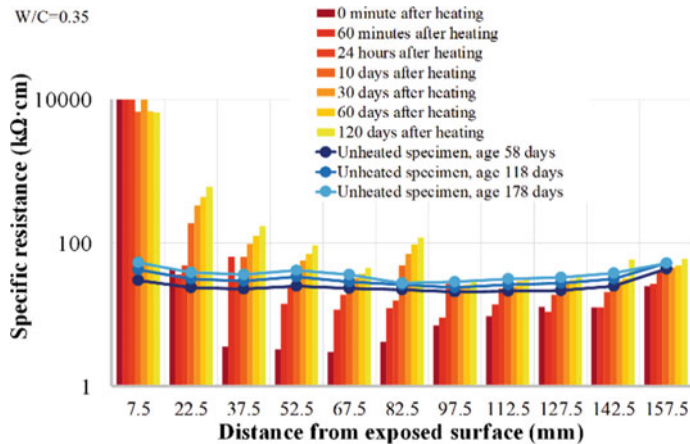


Fig. 8 Changes in specific resistance at each depth from exposed surface (mixture: 0.35)

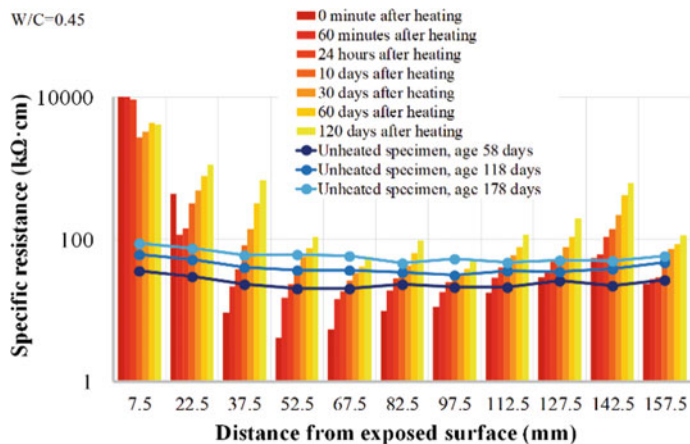


Fig. 9 Changes in specific resistance at each depth from exposed surface (mixture: 0.45)

was smaller than that of the mixture 0.45 shown in Figs. 8 and 9, probably because the denser microstructure of mortar with a lower W/C prevented water vapor from transferring during heating. Moreover, there is a possibility that the specific resistance may be affected by the difference in temperature inside the specimen. Additionally, no significant difference in the specific resistance of the mixtures 0.35 and 0.35 PP was observed in both unheated and heated specimens. It can be concluded that PP fibers have little influence on the moisture transfer within the limits of temperature in this study.

Radiation heating Figure 11 shows the specific resistance in the heated specimens at different depths from the exposed surface in the radiation heating and also the

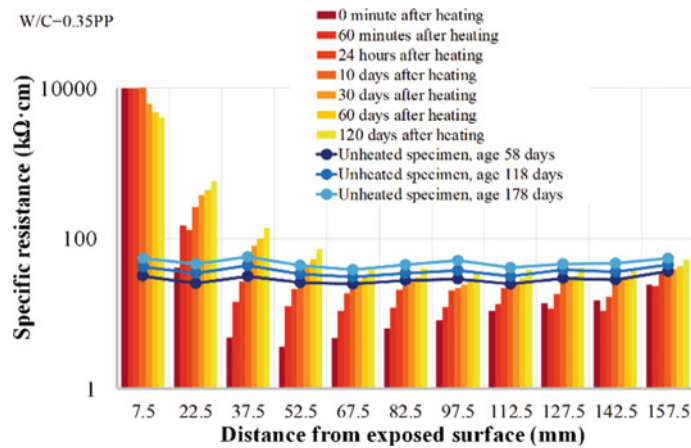


Fig. 10 Changes in specific resistance at each depth from exposed surface (mixture: 0.35 PP)

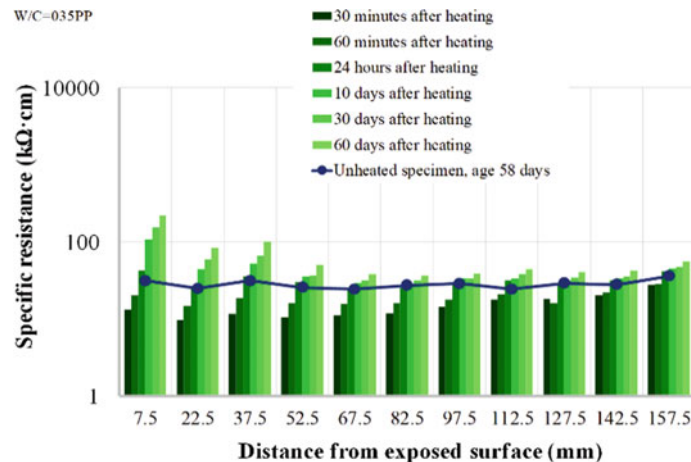


Fig. 11 Changes in specific resistance at each depth from exposed surface (mixture: 0.35 PP, radiation heating)

specific resistance in the unheated specimen at the same age as the heated specimen (i.e. at the age of 58 days). In the case of the radiation heating, the specimen was taken out approximately 13 min after heating, and then the electrical resistance was measured. Although the specific resistance at the depth of 7.5 mm from the exposed surface indicated a significantly high value after heating in the iron plate heating, the specific resistance around exposed surface in the radiation heating decreased at first before being increased gradually. It indicates that the mortar near the exposed surface was dried in the iron plate heating and the dry condition may maintain for

a long time, and the mortar in the vicinity of the exposed surface may have higher moisture content after heating in the radiation heating than in the iron plate heating.

Similarly to the inside after the iron plate heating, it can be attributed to evaporation of free water and decomposition of chemically bound water by temperature rise around the exposed surface after the radiation heating. In addition, the specific resistance of specimens at locations where the temperature was almost the same for both heating methods indicated almost the same value. However, further investigation should be needed on the effect of the exposure surface condition on the moisture transfer.

4 Conclusions

The present study aimed to investigate moisture transfer in mortar after heating and the effect of heating methods on the moisture transfer by using an electrical resistance method in which the electrical resistance in hardened cement paste was measured by using stainless steel rods embedded in specimens. The following conclusions can be drawn.

- (1) The moisture transfer in mortar due to heating can be observed by using electrical resistance method.
- (2) The temperature history in the specimens heated by radiation heating was different from that by iron plate heating even though their heating rate was almost the same. Further investigation should be needed on the effect of the exposure surface condition on the moisture transfer.
- (3) An addition of PP fibers could not have significant effect on the specific resistance.
- (4) After heating, mixture with a lower water to cement ratio of 0.35 showed the lower specific resistance than that with a higher water to cement ratio of 0.45.

References

1. Bui P, Ogawa Y, Nakai K, Kawai K (2016) Electrical resistance measurement to assess moisture transfer in cement-based mortar through water absorbing and drying processes. Proc Jpn Concr Inst 38(1):813–818
2. Concrete Society (2008) Assessment, design and repair of fire-damaged concrete structure. Technical Report, 68
3. Kamada E, Tabata M, Nakano Y (1976) The measurement of the water content in the concrete. Cement Gijutsu Nenpo 30:288–290
4. Kimata H, Ishikawa Y, Ohshita H, Tanabe T (1996) 1093 An experimental study on the water migration in nonsaturated mortar. Proc Jpn Soc Civ Eng 18(1):591–596
5. Kitagawa T, Daungwilailuk T, Bui PT, Ogawa Y, Kawai K (2017) A study on moisture transfer in hardened cement in a drying process using electrical resistance method. Proc Jpn Soc Civ Eng 472:943–944

6. Matsuzawa K, Kitsutaka Y (2015) Influence of coarse aggregate on fracture properties of concrete subjected to high temperature heating. *J Struct Constr Eng AJJ* 707(80):1–7
7. Sugino Y, Kamata R, Tanibe T, Ozawa M (2018) Influence of surface impregnation on the pore structure and permeation resistance of heated concrete. *Taiheiyo Cem Kenkyu Hokoku* 174:24–32
8. Suzuki M, Henry M, Kato Y, Katsuki F (2009) Influence of re-curing on physio-chemical properties of mortar exposed to fire. *Cem Sci Concr Technol* 63:148–154

Lead Adsorption on Cement Paste at Various pH Values Controlled by Different Methods



T. Nishiwaki, M. Yamasaki, S. J. Zhou, Y. Ogawa, and K. Kawai

1 Introduction

Recently, a large amount of carbon dioxide emission has been a serious problem in the cement and concrete industry. As a countermeasure against this problem, industrial by-products and municipal wastes are used as concrete materials and source of energy, respectively. In addition, it is estimated that more and more various industrial by-products and municipal wastes will be required to be used for concrete materials and energy source in the future in order to reduce environmental impacts furthermore. However, these wastes may contain hazardous heavy metals. As one of the problems, their influence on human and animals are concerned because heavy metals may leach out of concrete when they are used in concrete for long time. It leads to the difficulty in reusing concrete containing industrial wastes. In order to put the use of concrete containing heavy metals into practice, it is necessary to evaluate the behavior of heavy metals leaching from concrete. Previous studies showed that cement paste had the ability to fix and adsorb heavy metal ions [1]. Some previous studies also reported that lead adsorption on cement paste depends on pH value [2–4]. However, there are various causes to change pH value in actual environment. This study aims to investigate lead adsorption on cement paste at various pH values controlled by different methods. The adsorption test was carried out at various pH values controlled by three methods, including carbonation of cement paste, calcium hydroxide leaching from cement paste, and cement paste immersion in nitric acid solutions at different concentrations. The concentration of lead ions after the adsorption test was measured by using an atomic absorption spectrophotometer. In addition, X-ray diffraction test was also employed to analyse the chemical changes due to the pH value as well as lead fixation.

T. Nishiwaki · M. Yamasaki · S. J. Zhou · Y. Ogawa · K. Kawai (✉)

Department of Civil and Environmental Engineering, Graduate School of Engineering, Hiroshima University, Higashi-Hiroshima, Japan

e-mail: kkawai@hiroshima-u.ac.jp

2 Experiments

2.1 Materials and Preparation

Ordinary Portland cement and deionized water were used as cement and mixing water, respectively. Cement paste with a water-to-cement ratio of 0.40 was prepared. The cement paste was cast in a polypropylene container and cured under sealed condition at 20 °C for 28 days. After curing, it was pulverized into powders less than 150 µm in size. Before conducting the adsorption test, the content of calcium hydroxide and calcium carbonate was measured by thermogravimetry (TG) and differential thermal analysis (DTA) to investigate the change in the hydration products with time.

2.2 Adsorption Test Using Carbonated Cement Paste

The powder specimens after curing were stored at 25 °C, a relative humidity of 20% and a CO₂ concentration of 10% to accelerate the carbonation of the powder specimens. Saturated salt method was used to keep the relative humidity. Carbonation duration was set for 1, 7, 14, 30, 60, and 90 days. After each duration of carbonation, the adsorption tests were conducted. Figure 1 shows the content of calcium hydroxide and calcium carbonate in the specimen. From Fig. 1, the calcium carbonate content increased as the carbonation of the specimens progressed. However, the calcium hydroxide content did not change after 1 day, which means that calcium silicate hydrate (C-S-H) may be also carbonated. Figure 2 shows the procedure of the adsorption test. The liquid to solid ratio (L/S) in the adsorption test was set to be 20 mL/g. Firstly, 5 g of the powder sample was put into 100 mL of deionized water

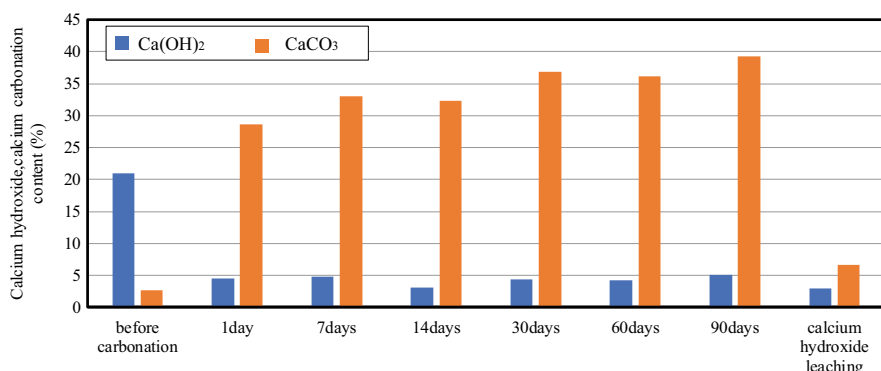


Fig. 1 Calcium hydroxide and calcium carbonate contents

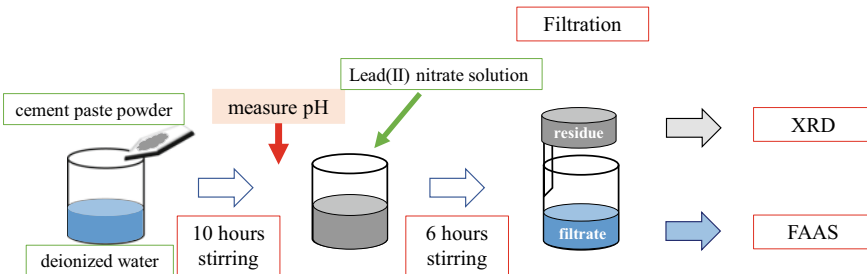


Fig. 2 The procedure of adsorption test after carbonation and calcium hydroxide leaching

and stirred for 10 h. After stirring, a pH value was measured, and 5 mL of lead (II) nitrate solution containing a certain concentration of lead ions (4000, 8000, 12000, 16000, 20000, and 25000 ppm) was put into the solution. Then, the solution was continuously stirred for 6 h. After that, the solution was filtered with a membrane-filter and the concentration of lead ions in the solution was determined with a flame atomic absorption spectrophotometer (FAAS).

2.3 Adsorption Test Using Cement Paste after Calcium Hydroxide Leaching

The powder specimens after curing was immersed and stirred in deionized water so that calcium hydroxide leached out of the specimens. After the pH value of the solution became constant, the adsorption tests were conducted in the same manner as mentioned in Sect. 2.2.

2.4 Adsorption Test under Various Nitric Acid Concentrations

The pH value in the adsorption test was adjusted by adding nitric acid solution, and two L/S (mL/g) ratios were used in this test. The detail of the test method is shown in Fig. 3. One or five grams of the powder specimen was put into deionized water and stirred for 10 h. After stirring, a certain amount of 2 mol/L nitric acid solution was added, and then stirred for further 6 h. The amount of nitric acid solution together with deionized water was determined depending on the mass of the specimen so that the total amount of the solution was 100 mL, as shown in Table 1. After stirring, 5 mL of lead (II) nitrate solution containing a certain concentration of lead ions (4000, 8000, 12000, 16000, 20000, and 25000 ppm in the case of L/S = 20, 4000, 8000, 12000, 16000, 20000, and 50000 ppm in the case of L/S = 100) was added, and then stirred for another 4 h. After stirring, the solution was filtered with a membrane-filter and the concentration of lead ions in the solution was determined with an FAAS.

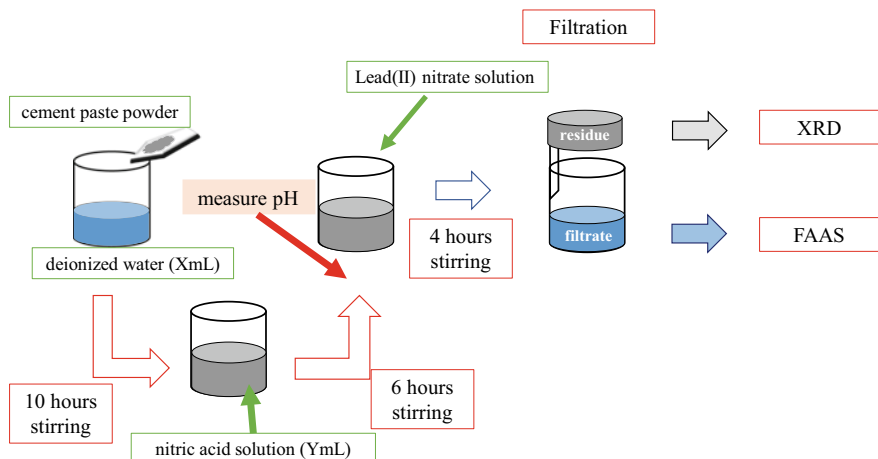


Fig. 3 The procedure of adsorption test under various nitric acid concentrations

Table 1 Experimental conditions of each sample in adsorption test under various nitric acid concentrations (see Fig. 3 for XmL and YmL)

Sample No.	L/S (mL/g)	Cement paste (g)	Deionized water (XmL)	Nitric acid solution (YmL)
1	20	5.0	100	0
2			98	2
3			94	6
4			90	10
5	100	1.0	100	0
6			98	2
7			94	6

2.5 X-ray Diffraction Test

The mineral composition of the residue samples after the adsorption tests under carbonation and various nitric acid concentrations was qualitatively analyzed using a powder X-ray diffractometer (XRD). The test was conducted at a Bragg angle (2θ) ranging 5° – 65° .

3 Results and Discussions

3.1 Adsorption Test after Carbonation and Calcium Hydroxide Leaching

Figure 4 shows the result of the adsorption test using the samples after carbonation and calcium hydroxide leaching. The average of the pH values is also shown in the figure. The adsorption isothermal curve of lead can be approximated by the Freundlich isotherm Eq. (1) for the samples before carbonation and after 1- and 7-day carbonation. It indicated that the adsorption is physical adsorption by the van der Waals force and adsorption on an inhomogeneous surface. The amount of lead adsorption increased as the value of pH in the solution was decreased. However, the change in the amount of lead adsorption was very large when samples carbonated longer than 14 days and samples after calcium hydroxide leaching were used. In other words, the change in the amount of lead adsorption was very large at a pH value lower than 12.

$$V = aP^{1/n} \quad (1)$$

where,

V amount of lead adsorption

P equilibrium concentration of lead ions

a and n constants given for adsorbate and adsorbent at a certain temperature.

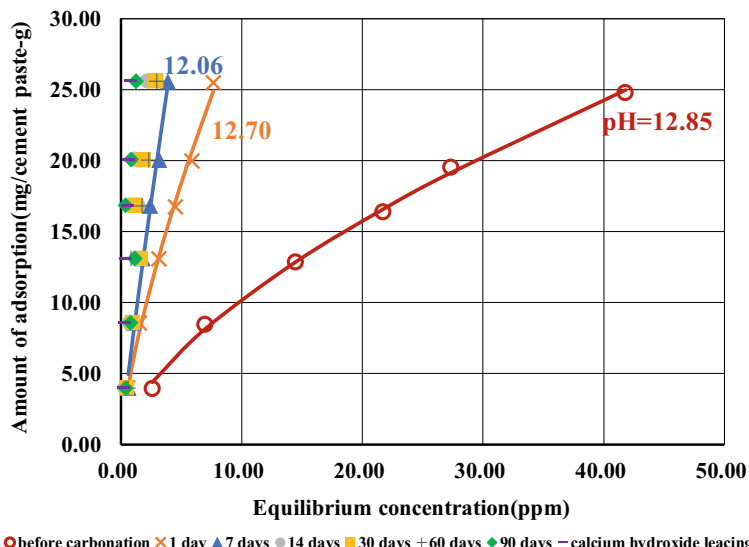


Fig. 4 The result of the adsorption test after carbonation and calcium hydroxide leaching

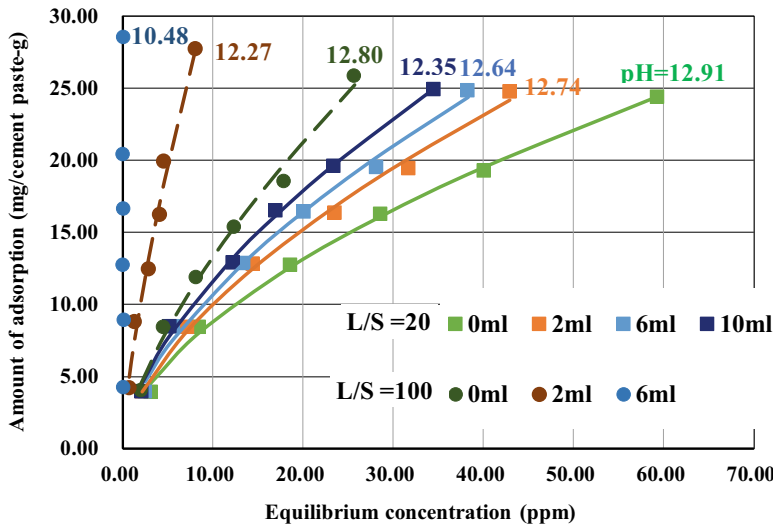


Fig. 5 The result of the adsorption test under various nitric acid concentrations

3.2 Adsorption Test under Various Nitric Acid Concentrations

Figure 5 shows the result of the adsorption test under various nitric acid concentrations. The average of the pH values is shown in the figure. The adsorption isothermal curve of lead can be approximated by the Freundlich isotherm Eq. (1) for all samples, except for the sample No. 7 in Table 1. Similar to the tendency of lead adsorption for the samples under carbonation and calcium hydroxide leaching, the amount of lead adsorption increased as the value of pH in the solution was decreased. However, the L/S ratio affects the adsorption of lead more than the pH value in this experiment.

3.3 X-ray Diffraction Test

The XRD results of the residue samples after the adsorption test under carbonation are shown in Fig. 6. From Fig. 6, it was confirmed that the peak of portlandite decreased and the peak of calcite increased after carbonation. Additionally, the amount of vaterite and aragonite continuously increased with longer carbonation.

Regarding lead compounds, the peaks of hydrocerussite were generated. That is, lead hydroxide ion may have combined with calcite, vaterite or aragonite. Figure 7 shows the XRD result of the residue sample after the adsorption test under various nitric acid concentrations. It was confirmed that the peak of portlandite decreased. However, the peak of lead compound was not detected.

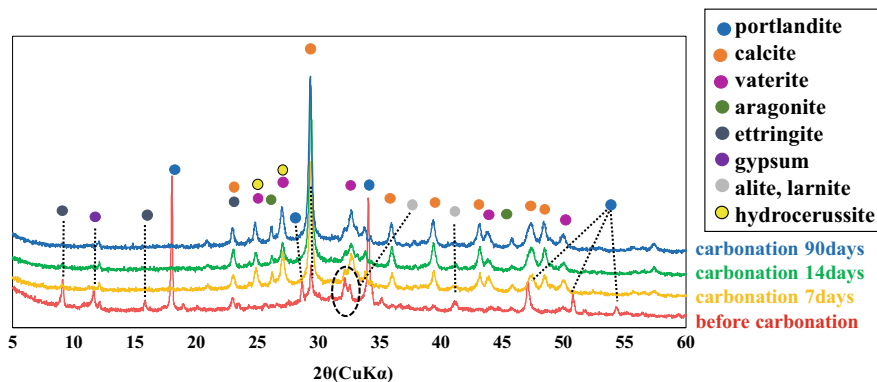


Fig. 6 The XRD result of the residue after adsorption test using the sample after carbonation

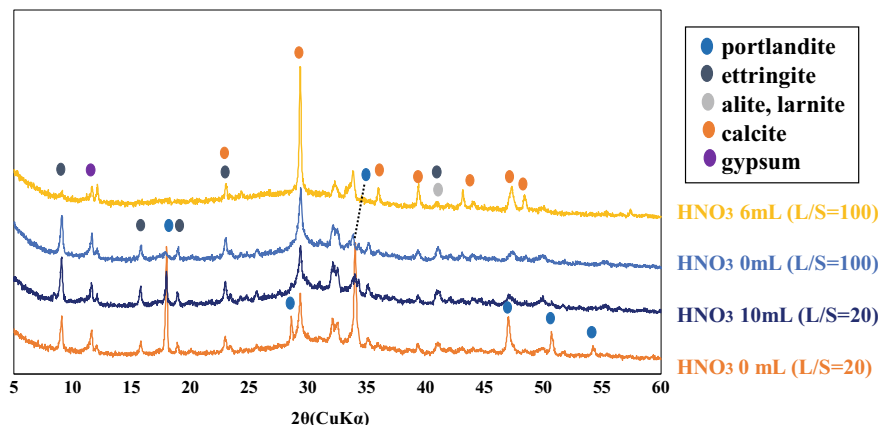


Fig. 7 The XRD result of the sample residue after adsorption test under various nitric acid concentrations

4 Conclusion

In this study, the amount of lead adsorption on cement paste was investigated at various pH values controlled by different methods. As a result, the following conclusions can be drawn within the limits of this study.

- The lead adsorption amount increased with a decrease in the pH value.
- Similar pH dependency of lead adsorption was found even though the pH values were controlled with different methods.
- The XRD result showed the formation of hydrocerussite, which suggests that lead hydroxide ions may combine with calcite, vaterite, or aragonite.

References

1. Kawai K, Hayashi A, Kikuchi H, Yokoyama S (2014) Desorption properties of heavy metals from cement hydrates in various chloride solutions. *Constr Build Mater* 67:55–60
2. Kawai K, Miyamoto Y, Sakamoto K (2007) Study of diffusion and adsorption of heavy metals in cement hydrates. *Cem Sci Concr Technol* 61:123–128
3. Li XD, Poon CS, Sun H, Lo IMC, Kirk DW (2001) Heavy metal speciation and leaching behaviors in cement based solidified/stabilized waste materials. *J Hazard Mater* 82:215–230
4. Marcello D, Teresa M, Antonio EP, Luigi P (2012) Evaluation of the leachability of heavy metals from cement-based materials. *J Hazard Mater* 227–228:1–8

Lightweight Concrete Using Lightweight Aggregates from Construction and Demolition Wastes—Production and Properties



Hung Phong Nguyen, Ngoc Lan Le, Cong Thang Nguyen, Van Tuan Nguyen, Tuan Trung Nguyen, and Xuan Hien Nguyen

1 Introduction

With the rapid development and urbanization process in Vietnam recently, the amount of construction and demolition wastes (CDW) generated, especially in huge urban areas, is increasingly high and has caused serious problems, including environmental pollution, land occupation, landscaping degradation and traffic congestion. Therefore, the recycle of CDW to make useful building materials is becoming an essential issue not only in Vietnam, but also in many countries in the world. This can also help to prevent the over-exploitation of the limited natural resources such as sand and limestone for making new building materials.

In previous research, CDW in the form of crushed concrete and brick has been used effectively as aggregates for making concrete, partially replacing natural aggregates. This research work deals with a new technology, in which, the CDW of masonry wall is made into lightweight aggregates (LWA) [1–3]. These LWA can be used as porous aggregates to make lightweight concrete (LWC) with low density and high thermal and noise insulation [4–6], which can be used as a replacement of conventional masonry brick wall. In recent research, with the facilities in Vietnam, LWA has been

H. P. Nguyen (✉)

The Graduate School, National University of Civil Engineering, Hanoi, Vietnam
e-mail: phongnh@nuce.edu.vn

N. L. Le

Academy of Managers for Construction and Cities, Hanoi, Vietnam

C. T. Nguyen · V. T. Nguyen

Faculty of Building Materials, National University of Civil Engineering, Hanoi, Vietnam

T. T. Nguyen

Faculty of Building and Industrial Construction, National University of Civil Engineering, Hanoi, Vietnam

X. H. Nguyen

Department of Science, Technology and Environment, Ministry of Construction, Hanoi, Vietnam

successfully made from mixture of brick and mortar, burned in the temperature up to 1250 °C [7].

This paper focuses on the production of LWC using two types of LWA made from CDW and the experimental tests on mechanical properties of the LWC, including compressive strength and elastic modulus.

2 The Production of Lightweight Concrete Using Lightweight Aggregates from Construction and Demolition Wastes

2.1 Materials

The materials used in the experimental work including Portland cement But Son PC40 with the properties meet the requirements of Vietnamese standard TCVN 2682-2009. The LWA used in the research including two types of LWA namely A1 and A2 with different sizes of particles, i.e. (4–8) mm and (8–16) mm, respectively. In the producing of the LWAs, the blended powers of brick and mortar, adding with expanding agent were shaped into solid spheres, dried and then burned in the rotary kiln [1–3]. The pictures of LWA and their properties are shown in Fig. 1 and Table 1. The fine aggregates used in the research is the sand from Lo River in Vietnam, whose properties satisfy the Vietnamese standard TCVN 7570:2016.

In the mix proportion of the LWC, fly ash from Pha Lai Thermal Power Plant was used. In addition, according to ACI 211.2-98, in lightweight concrete using plasticizer with air entrainment admixture will limit the segregation and increase

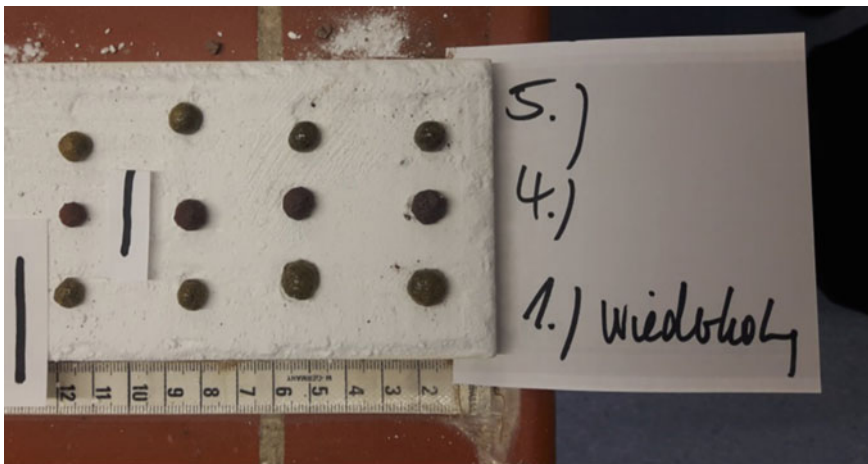


Fig. 1 LWA burned in different temperatures

Table 1 Properties of LWA from masonry CDW

Properties	Unit	LWA	
		A1	A2
Density	kg/m ³	430	369
Water absorption	%	28	32

the homogeneity for concrete mixtures. Therefore, in the study, plasticizer was used in combination with the air-entrained admixture Placc-air. Super plasticizer Placc-air followed ASTM C494 Type G was used to delay the setting time for concrete mixture with some properties such as deep brown color, suitable for all type of Portland Cement, density of 1.08 ± 0.002 g/cm³; dosage used is 0.7–1.4 litter for 100 kg of cement.

2.2 Test Method

The density of concrete was determined by Vietnamese standard TCVN 3115-1993. Compressive strength was tested using TCVN 3118-1995, using $100 \times 100 \times 100$ mm cube samples, tested at the ages of 7 days and 28 days. The samples of LWC before and after testing are shown in Fig. 2. Elastic modulus of concrete is tested following ASTM C469, with the concrete cylinder specimen of 150 mm \times 300 mm.

The testing procedure to determine elastic modulus of LWC is followed standard ASTM C469-1994, and the value can be calculated by Eq. (1).

$$E = (S_1 - S_2) / (\varepsilon_2 - 0.00005) \quad (1)$$



Fig. 2 Concrete samples for compression test

where,

- E : chord modulus of elasticity, MPa,
- S_1 : stress corresponding to a longitudinal strain, ϵ_1 , of 50 millionths, MPa, and
- S_2 : stress corresponding to 40% of ultimate load,
- ϵ_2 : longitudinal strain produced by stress S_2 .

To evaluate influence of LWA on the concrete elastic modulus, two concrete mixes were used with two types of LWA, i.e. A1 and A2 and ratio of volume of LWA to volume of concrete (V_{LWA}/V_{LWC}) is taken as 26%.

2.3 Concrete Mix Proportion

This study evaluates the influence of the volume (V_{LWA}) and the size of LWA on some properties of the concrete mix and concrete, namely the water/binder ratio (w/b) was fixed at 0.39 by weight, the sand to aggregate (V_S/V_A) ratio is fixed at 0.44 by volume, the fly ash (FA) is given as 0.26, the ratio of LWA to concrete (V_{LWA}/V_{LWC}) is taken as 0.23–0.26–0.31 and 0.34 by volume. The ratio of water, fly ash, and super plasticizer (SP) is taken by the mass of binder (b); the binder herein is a total of the cement and FA. The mix proportion of the LWC in the research is given in Table 2.

Table 2 Mix proportion of the LWC

ID	w/b	V_{LWA}/V_{LWC}	V_S/V_A	FA/binder	SP (%)	Type of aggregate
1	0.39	0.34	0.44	0.26	0.7	A1
2	0.39	0.31	0.44	0.26	0.7	A1
3	0.39	0.26	0.44	0.26	0.7	A1
4	0.39	0.23	0.44	0.26	0.7	A1
5	0.39	0.34	0.44	0.26	0.7	A2
6	0.39	0.31	0.44	0.26	0.7	A2
7	0.39	0.26	0.44	0.26	0.7	A2
8	0.39	0.23	0.44	0.26	0.7	A2

3 Experimental Study on Mechanical Properties of Lightweight Concrete from CDW

3.1 Concrete Density and Compressive Strength

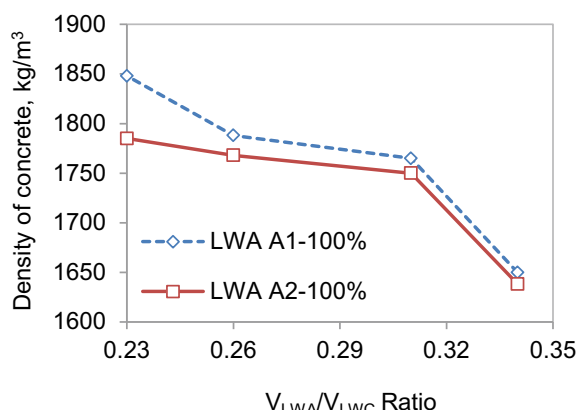
The influence of lightweight aggregates on concrete density is shown in Fig. 3. Figure 4 shows the influence of the LWA content on density and compressive strength of concrete. It is shown that with a same type of LWA used, when increasing the LWA content (by increasing $V_{\text{LWA}}/V_{\text{LWC}}$ ratio), the concrete density is decreased. With a same amount of LWA, when the aggregate size increases from 8 mm (D_{\max} of A1) to 16 mm (D_{\max} of A2), the concrete density also reduced since the density of A2 is smaller than that of A1. It should be noted that the concrete can be made with density is smaller than 1650 kg/m^3 if the aggregate content is about 34% by volume of concrete.

Regarding to the influence of the LWA content on compressive strength of concrete, with the concrete mix using A1 and A2, the compressive strength increased with time. At 7 days, the compressive strength increases rapidly, however the rising rate at 90 days is slower compared to that of 7 days. With the mix using the A1 type, the concrete strength of concrete can be achieved above 15 MPa after 7 days. Besides, with the mix using 31 and 26% LWA, the compressive strength of concrete can be achieved above 20 MPa; when reducing the LWA content to 23%, the compressive strength of concrete can be obtained above 25 MPa, and above 30 MPa after 90 days.

The concrete mix using LWA of the A2 type gives a similar trend. If the content of coarse LWA reduces, the concrete strength increases. However, when decreasing the LWA content from 26 to 23%, the compressive strength of concrete does not show a big difference.

Using A1 and A2 as LWA for concrete mixes, the tests showed that the aggregates distributed equally and no segregation can be observed. The failure mode of concrete samples was due to the cracks appeared through LWA, not cement paste (Fig. 2).

Fig. 3 Influence of LWA content on concrete density



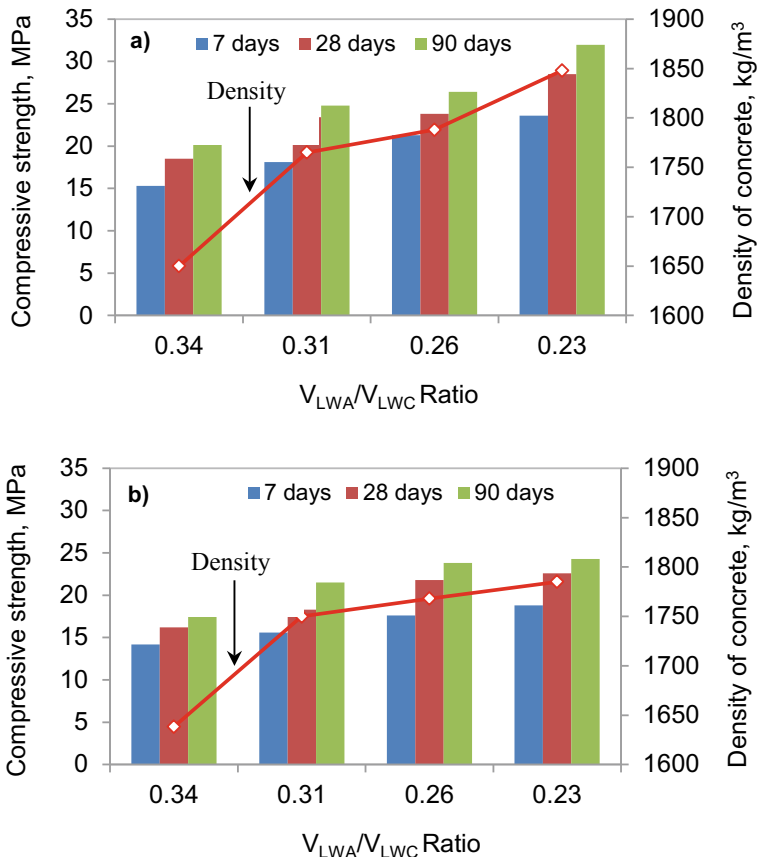


Fig. 4 Influence of LWA content on compressive strength and density of concrete. **a** LWA A1; **b** LWA A2

3.2 Elastic Modulus of LWC

The results after 7 and 28 days are shown in Table 3, Figs. 5 and 6. The stress-strain relationship at the initial stage (40% of ultimate stress) shown in Figs. 5 and 6 is a linear relationship as in the concrete theory. The difference between the elastic modulus after 7 days and after 28 days is unremarkable, showing that for the LWC the elastic modulus increases significantly after 7 days. The elastic modulus from

Table 3 Elastic modulus of LWC using LWA

Parameter	Unit	The LWA A1		The LWA A2	
		7 days	28 days	7 days	28 days
E_b	MPa	17,859	22,209	16,179	20,333

Fig. 5 Stress-strain relationship of the samples using the LWA A1

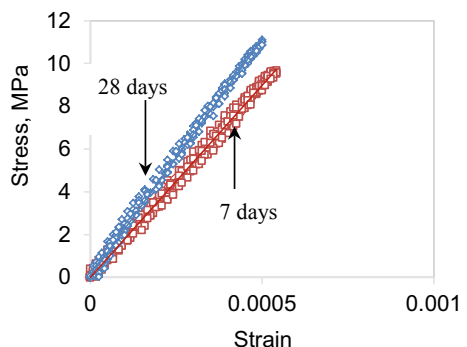
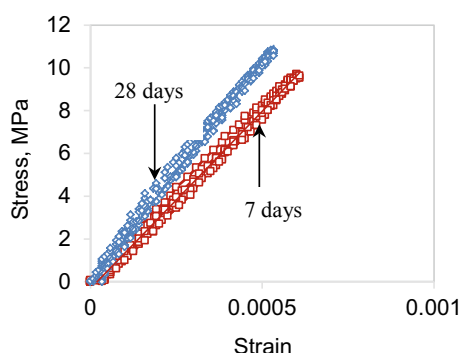


Fig. 6 Stress-strain relationship of the samples using the LWA A2



the samples using A2 is smaller than that from the samples using A1, since the A2 aggregates possess a higher porosity compared to A1.

4 Conclusions

From the experimental study to determine mechanical properties of LWC using LWA from CDW, the conclusions can be drawn as follows:

- It is possible to use lightweight aggregates recycled from construction and demolition wastes to make lightweight concrete with the density less than 1800 kg/m^3 and 28 day-compressive strength up to 25 MPa.
- The LWAs have a significant impact on the mechanical properties of concrete. As the LWA content increases, the density and compressive strength of concrete decrease as an inverse relationship. The mix using 31% and 26% LWA, the compressive strength of concrete can be achieved above 20 MPa; when reducing the LWA content to 23%, the compressive strength of concrete can be obtained above

25 MPa, and above 30 MPa after 90 days. With a same amount of LWA, as size of LWA increases, the density and compressive strength of concrete reduced.

- The compressive strength and the elastic modulus increase significantly at 7 days. At the later ages, these two values increase at a slower rate. The failure mode of concrete samples in compression test was due to the cracks appeared through the aggregates, not cement paste.

Acknowledgements The authors would like to thanks the Ministry of Science and Technology of Vietnam for sponsoring the research project NDT.21.GER/16. We would like to express our sincere thanks to Institute of Applied Construction Research—IAB Weimar—Germany for the great cooperation and support in the Project.

References

1. Mueller A, Schnell A, Ruebner K (2015) The manufacture of lightweight aggregates from recycled masonry rubble. *Constru Build Mater* 98:376–387
2. Mueller A, Sokolova SN, Vereshagin VI (2008) Characteristics of lightweight aggregates from primary and recycled raw materials. *Constru Build Mater* 22:703–712
3. Reinhold M, Muller A (2002) Lightweight aggregate produced from fine fractions of construction and demolition waste. Design for deconstruction and materials reuse. Karlsruhe, Germany, vol CIB Publication 272
4. Chandra S, Bernsson L (2003) Lightweight aggregate concrete—science, technology and applications. William Andrew Publishing, Norwich, New York
5. Hieu ND (2016) Technology for high quality lightweight concrete with porous aggregate. Construction Publish, Hanoi
6. Wilson H (1953) Lightweight aggregates for the construction industry. *Can Ceram Soc* 22(1953):44–50
7. Phong NH, Thang NC, Tuan NV, Leydolph B (2019) Production of lightweight aggregates from construction and demolition wastes in Vietnam. *J Sci Technol Civ Eng NUCE* 2019.13 (1 V):1–10

Possibility of Using High Volume Fly Ash to Produce Low Cement Ultra High Performance Concrete



Sy Dong Pham, Van Tuan Nguyen, Trung Thanh Le,
and Cong Thang Nguyen

1 Introduction

Ultra High Performance Concrete (UHPC) is a new generation of concrete which has been developed and researched in the world since the 1990s in France and Canada [2, 9] with excellent properties of flowability, compressive strength of over 120 MPa [3], ductility, durability, etc. compared with ordinary concrete and high strength concrete [1, 2, 4, 5, 10, 11]. UHPC offers new and sometimes exiting possibilities such as lighter structures, larger structures, hybrid structures, new design and new products with a potential for a better economy and resource consumption than with traditional concrete, steel and other building materials [10]. In Vietnam, so far, many studies on UHPC has been carried out since 2010 [14–16].

Some basic principles of improving properties of UHPC were suggested, i.e. the elimination of coarse aggregates, optimisation of the granular skeleton, the densification of the cementitious matrix through lowing water to binder ratio using suitable superplasticizers to reduce the porosity, and post-set heat treatment, as well as adding fibers to minimize cracks and to improve the ductility [7, 12].

In the production of UHPC, the amount of cement used is normally very high, about 800–1000 kg/m³ [10], which will greatly affect the cost and sustainable development of the product. It is known that for every tonne of Portland cement produced, approximately one tonne of CO₂ is released, which means that the Portland cement industry contributes for about 7% of the total CO₂ emissions [13]. This causes a

S. D. Pham

Faculty of Building and Industrial Construction, National University of Civil Engineering, Hanoi, Vietnam

V. T. Nguyen (✉) · C. T. Nguyen

Faculty of Building Materials, National University of Civil Engineering, Hanoi, Vietnam
e-mail: tuanv@nuce.edu.vn

T. T. Le

Vietnam Institute for Building Materials, Hanoi, Vietnam

big negative effect on the environment. Studying to use lower carbon alternatives to reduce the amount of cement used while still ensuring the properties of the concrete reduce the cost of the product, reduce the amount of waste to the environment, reuse the waste materials to achieve the goal of sustainable development. In fact, supplementary cementitious materials, such as fly ash (FA), ground granulated blast furnace slag (GGBS), rice husk ash (RHA) and silica fume (SF), are used for replacing part of cement in the effort of producing sustainable UHPC and reducing its current cement usage, among these, FA is considered as a very potential cement substitution [6]. The addition of fly ash, characterized by smooth spherical particles (average particle size in the range of 5–20 μm), will improve workability of concrete mixtures, thus reduce the amount of mixing water, increase the packing density of concrete, resulting in increasing the strength as well as the impermeability of concrete [8].

This study presents some experimental results of using fly ash (FA) from 10% to 60% in combination with combination of silica fume (SF) by mass to replace the cement to make UHPC. Besides, this study also considers the evaluation the effect of curing conditions on compressive strength of UHPC.

2 Materials and Methods

2.1 Materials

Materials used in the study including Portland cement PC50 Nghi Son with a mean particle size of 10.76 μm ; undensified SF with a mean particle size of 0.15 μm , SiO_2 content of 92.3%, the strength pozzolanic activity index with Portland cement is 111%; silica sand with a mean particle size of about 300 μm ; polycarboxylate-based superplasticizer with a condensed content of 30%. FA used with a mean particle size of 5.43 μm , the content of oxides ($\text{SiO}_2 + \text{Al}_2\text{O}_3 + \text{Fe}_2\text{O}_3$) of 85%, the pozzolanic activity index with cement was 103%.

2.2 Test Methods

The workability of mixtures was determined by means of flow table test. The flow measurements were kept between 200 and 250 mm (according to BS 4551-1:1998). Mixtures were cast into the 100 mm \times 100 mm \times 100 mm cubes for the compression test.

3 Composition of UHPC

3.1 Optimal Packing Density

Using the proposed de Larrard and Sedran method, the mixture is considered multi-constituent composed of sand and binder (cement, SF and FA). To ensure the packing density of the mixture, the sand/ binder ratio is 1 (by mass). The SF, FA contents were studied in the range of 0–30%, 0–70% by mass of binder, respectively. Besides, the use of a combination of SF and FA replaces cement was also considered in this study.

3.2 The UHPC Mix Design

Based on the results of calculated optimum packing density following the de Larrard and Sedran method, 18 concrete mixtures were used in the study with the water to binder ratio of 0.16 by mass (Table 1). The value of the superplasticizer dosage

Table 1 Proportioning of different UHPC mixtures

Mix	Binder, kg/m ³	Water to binder, by mass	Sand to binder, by mass	SF, % by mass of binder	FA, % by mass of binder	SP, % by mass of binder
1	1170	0.16	1	0	0	0.65
2	1151	0.16	1	10	0	0.58
3	1133	0.16	1	20	0	0.64
4	1116	0.16	1	30	0	0.95
5	1157	0.16	1	0	10	0.49
6	1145	0.16	1	0	20	0.47
7	1133	0.16	1	0	30	0.39
8	1121	0.16	1	0	40	0.29
9	1109	0.16	1	0	50	0.25
10	1099	0.16	1	0	60	0.20
11	1088	0.16	1	0	70	0.17
12	1139	0.16	1	10	10	0.55
13	1127	0.16	1	10	20	0.52
14	1116	0.16	1	10	30	0.49
15	1104	0.16	1	10	40	0.37
16	1093	0.16	1	10	50	0.27
17	1082	0.16	1	10	60	0.23
18	1072	0.16	1	10	70	0.19

(Table 1) was used to control the flowability of concrete mixtures in the range of 200–250 mm as mentioned above.

3.3 Test Procedures

The mixer used in the study was a 100-liter forced mixer. Mixtures were cast into the 100 mm × 100 mm × 100 mm cubes for the compression test and kept in molds under standard curing condition ($27 \pm 2^\circ\text{C}$, RH $\geq 95\%$) for 24 h. After demoulding, the samples were divided into two groups and cured in two different environments:

- (1) Standard conditions ($27 \pm 2^\circ\text{C}$, RH $\geq 95\%$) until testing.
- (2) Hot water curing ($90 \pm 5^\circ\text{C}$) for 48 h, after that, continuous curing under standard condition until testing.

Compressive strength of samples was tested at the ages of 3, 7 and 28 days.

4 Results and Discussions

4.1 Workability of Concrete Mixtures

The workability of concrete mixtures was kept in the range of 200–250 mm (BS 4551-1:1998) by adjusting the dosage of superplasticizer (Table 1; Fig. 1). The results show that in case of using SF only, the addition of SF improves the workability of concrete mixture when used in small content, i.e. with 10% cement replacement. This may be resulted from the fine spherical particles of SF, which act as miniature ball bearings,

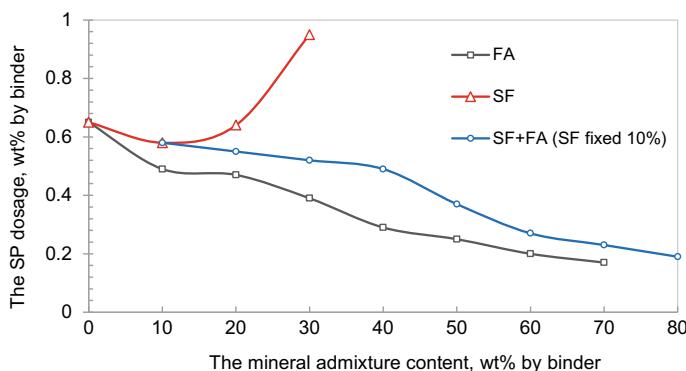


Fig. 1 The relationship between SP and the mineral admixture content, the flow measurement of concrete mixtures from 200 to 250 mm, W/B = 0.16

reducing the internal friction between cement particles thus providing a lubricant effect. Besides, ultra-fine SF particles will occupy the same amount of water that is located between the cement particles, increasing the amount of free water in the cement paste and thus improving the workability of concrete mixture.

However, when more than 20% cement is replaced by SF, the amount of superplasticizer increases dramatically to 0.64% and 0.95% for 20% and 30% SF, respectively. This can be explained by the large surface area of SF, normally about 18–20 m²/g while the specific surface area of cement is about 0.45 m²/g. Therefore, the total surface area of binder depends on the SF replacement percentage and will increase significantly with a high amount of SF used. This will require a large amount of water to wet the surface, and the ‘lubricant effect’ may not compensate the effect of its surface area when more cement is replaced by SF. This is clearly noticeable when the amount of SF increased to 30% has increased the dosage of superplasticizer significantly.

In contrast with SF admixture, the addition of FA increases the workability of the concrete mixture compared to the control (0% admixture), especially, when the FA content increases by more than 20% binder, the dosage of superplasticizer decreases sharply, which may be also explained by the smaller particle size of the spherical FA particles than cement so that increasing the free water of mixture and the lubricant effect. However the size of the FA is not too different from that of the cement as in the case of SF, so when the FA content increases, the workability of the mixture is improved (Fig. 1).

4.2 Effect of Silica Fume on Compressive Strength of UHPC

The effect of SF content on compressive strength of UHPC is shown in Fig. 2. The results of the study shows that the 28d-compressive strength of control samples without mineral admixtures can be attained above 134 MPa. When 10% SF is added, the 7d-compressive strength of concrete compression of concrete is above 120 MPa,

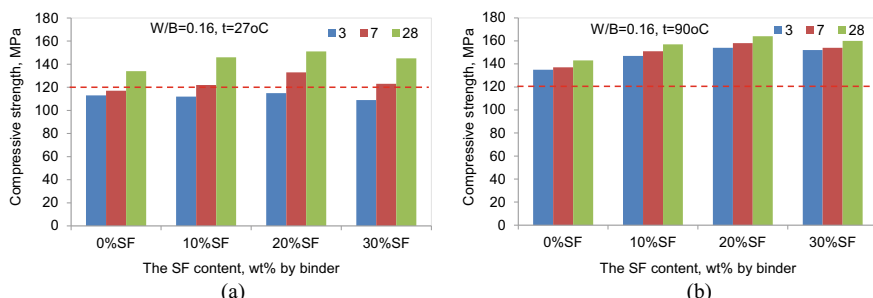


Fig. 2 Effect of the SF content on compressive strength of UHPC under different curing conditions, **a** $27 \pm 2^\circ\text{C}$, **b** $90 \pm 5^\circ\text{C}$

and the development of the compressive strength of UHPC increases sharply from 7 to 28 days, achieving 150 MPa at the age of 28 days, about 12% higher compared with that of the control sample. However, the improvement of compressive strength of concrete is not so significant with a higher SF content, i.e. 20 and 30%.

In the hot water curing condition, the compressive strength reaches over 130 MPa only after 3 days, but not increase significantly from 3 to 28 days. This may be caused by the faster rate of hydration of cement and pozzolanic reaction between SiO_2 in SF and $\text{Ca}(\text{OH})_2$ generated during the hydration of cement, resulting in a higher compressive strength. It also can be seen that the optimum amount of SF in the study is 20% to achieve the highest compressive strength, but in terms of economic aspects, the SF content is reasonable at 10% when the result of compressive strength improvement is not too different from the case of using 20% SF.

4.3 Effect of the FA Content on Compressive Strength of UHPC

Figure 3 shows the effect of FA content on the compressive strength of the UHPC. It can be observed that under standard curing condition, when the FA content increases to 30% by mass of binder, the 28d-compressive strength of concrete of over 120 MPa can be reached, but not significantly different from that of the control sample (0% FA). As the FA content increases, the compressive strength of concrete decreases, especially with a very high FA content, i.e. from 50 to 70%.

In the standard curing condition, the compressive strength of the UHPC decreases as the FA content increases. It should be noted that when 70% FA is added, the remaining 30% of cement is about 330 kg/m^3 , the 28d-compressive strength at 28 days is still attained 86 MPa. It is clearly seen that the early age compressive strength of concrete is improved with applying the hot water curing condition. The highest 28d-compressive strength is achieved 151 MPa in this study.

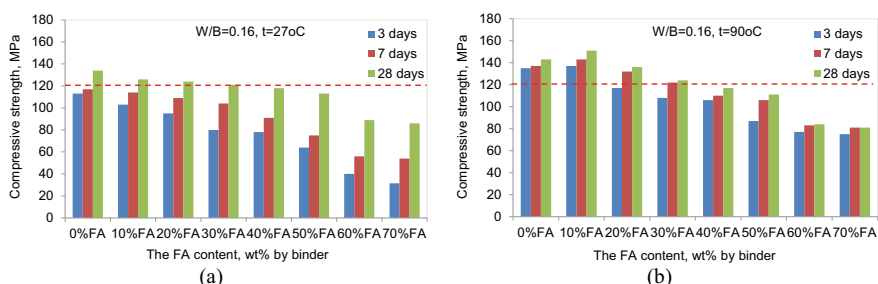


Fig. 3 Effect of FA content on compressive strength of UHPC under different curing conditions, **a** $27 \pm 2^\circ\text{C}$, **b** $90 \pm 5^\circ\text{C}$

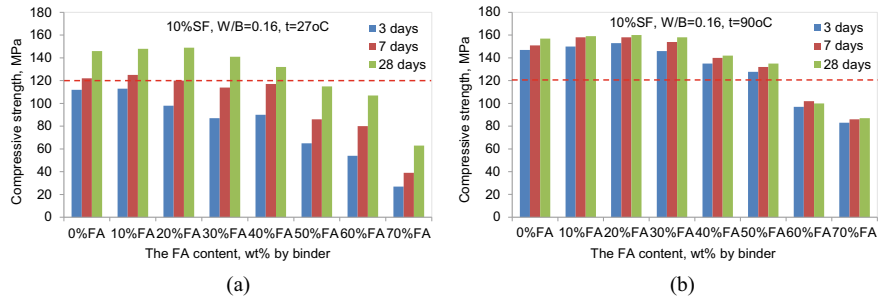


Fig. 4 Effect of the FA content on compressive strength of concrete under different curing conditions, SF fixed at 10%, **a** $27 \pm 2^\circ\text{C}$, **b** $90 \pm 5^\circ\text{C}$

4.4 The Effect of Combination of Silica Fume and Fly Ash on Compressive Strength of UHPC

As mentioned above, the reasonable amount of SF is 10% by weight of binder. Therefore, in this study, the SF content will be fixed at 10% when combined with the FA admixture.

Figure 4 shows the effect of the combination of SF and FA on the compressive strength of the UHPC. The results showed that the highest 28d-compressive strength of concrete can be achieved 149 MPa and 160 MPa with a combination of 10% SF and 20% FA corresponding to the standard curing condition and hot water curing condition. Under both curing conditions, the compressive strength of concrete reaches over 120 MPa when using up to 50% FA. It means that the total amount of mineral admixtures (SF + FA) used in this case can be up to 60% of binder, this makes great sense in the use of mineral admixture replacing cement to produce the UHPC. Therefore, it is possible to fully evaluate the use of large quantities of FA (replacing more than 50% by volume of cement [6] to produce UHPC with a compressive strength is over 120 MPa).

In addition, when using up to 80% mineral admixture (10% SF + 70% FA) to replace cement, the cement consumption is only 20% binder equivalent to about 214 kg/m^3 , the 28d-compressive strength of the sample under standard and hot water curing conditions is 63 MPa and 87 MPa. Therefore, it is possible to make high strength concrete with only about 215 kg/m^3 of cement, concrete is good for working and no separation can be observed.

It should be noted that the highest 28d-compressive strength of UHPC of 149 MPa and 160 MPa can be achieved when using 30% mineral admixture (10% SF + 20% FA) replacing the cement in both standard and hot water curing conditions, respectively, in this study.

5 Conclusion

Based on the research results, draw some conclusions as follows:

- It is possible to use fly ash with a content of more than 50% by mass of binder to product UHPC.
- The addition of SF improves the workability and compressive strength of UHPC with a small content, i.e. 10% cement replacement. The highest 28d-compressive strength of 151 MPa and 160 MPa can be achieved under standard curing condition and the hot water curing condition, respectively when using 20%SF. However, the reasonable SF content in this study is 10% when considering both the economic and technical aspects.
- The addition of FA improves the workability of UHPC mixture, and optimum FA content in the study is 10%. The 28d-compressive strength of UHPC of 126 MPa and 151 MPa can be attained under standard curing condition and the hot water curing condition, respectively.
- When using the combination of SF and FA to replace the cement, the maximum FA content can be used is 50% by mass of binder, the compressive strength of concrete reaches over 120 MPa. It means that the total amount of mineral admixtures used in this case can be up to 60% of binder.

Acknowledgements This research is funded by National University of Civil Engineering (NUCE) under grant number 220-2018/KHxD-TD.

References

1. Acker P, Behloul M (2004) Ductal technology: a large spectrum of properties, a wide range of applications. In: Proceedings of ultra high performance concrete, Kassel, Germany, pp 13–23
2. AFGC-SETRA (2002) Ultra high performance fibre-reinforced concretes. Interim Recommendations, AFGC Publication, Paris
3. ASTM C1856-2017 (2017) Standard practice for fabricating and testing specimens of ultra-high performance concrete. ASTM International, 100 Barr Harbor Drive, PO Box C700, West Conshohocken, United States
4. Buitelaar P (2004) Ultra high performance concrete: developments and applications during 25 years. In: International Symposium on UHPC, Kassel, Germany
5. Collepardi M (2003) Innovative concretes for civil engineering structures: SCC, HPC and RPC
6. Mehta PK, Malhotra V (2008) High performance, high volume fly ash concrete. ACCA
7. Mehta PK, Monteiro PJM (2011) Concrete microstructure, properties and materials. University of California
8. Ramachandra (1995) High-volume fly ash and slag concrete. Noyes 800–837
9. Richard P, Cheyrey MH (1995) Composition of reactive powder concretes. Cem Concr Res 25:1501–1511
10. Richard P, Cheyrey MH (1994) Reactive powder concretes with high ductility and 200–800 MPa compressive strength. In: Mehta PK (ed) Concrete technology: past, present and future, proceedings of the V. Mohan Malhotra symposium, ACI SP 144-24, pp 507–518

11. Schimdt & Fehling (2005) Ultra-high-performance concrete: research, development and application in Europe. In: seventh international symposium on the utilization of high-strength/high-performance concrete, Washington, D.C., USA, sp-228-4
12. Nguyen VT (2011) Rice husk ash as a mineral admixture for ultra high performance concrete. PhD thesis, Delft University of Technology
13. Wee TH, Matsunga Y, Watanabe Y, Sahai E (1995) Production and properties of high strength concrete containing various mineral admixtures. *Cem Concr Res* 25:709–714
14. Nguyen VT, Ye G, van Breugel K (2010) Effect of rice husk ash on autogenous shrinkage of ultra high performance concrete. In: Proceedings of the international RILEM conference on use of superabsorbent polymers and other new additives in concrete, RILEM (eds.), Proceedings PRO 74, Lyngby, Denmark, 15–18 Aug. 2010, pp 293–304
15. Nguyen VT, Ye G, van Breugel K (2010) Internal curing of ultra high performance concrete by using rice husk ash. In: Proceedings of the international conference on material science and 64th RILEM annual week, RILEM (eds.), Proceedings PRO 77, Aachen, Germany, 6–10 Sept. 2010, Vol. III, pp 265–274
16. Nguyen VT, Ye G, van Breugel K (2012) Mitigation of early age shrinkage of ultra high performance concrete by using Rice Husk Ash. In: Proceedings of Hipermat, the 3rd international symposium on ultra high performance concrete and nanotechnology for high performance construction materials, session 3A.7, 7–9 Mar. 2012, pp 341–348

Strength Development Properties of Core Specimens Taken from Structural Concrete Test Specimens Prepared All Over Japan



Sachie Sato, Yoshihiro Masuda, and Hiroyuki Tanano

1 Introduction

It is well known that concrete's strength development is affected by curing conditions such as temperature and moisture. In the field of building architecture in Japan, mix-proportion design and quality control protocols have long considered differences in compressive strength between structural concrete in members cast for use in real structures, and cylindrical specimens taken for quality control. Specifically, designers have assumed that a core specimen is similar in strength to a comparable specimen cured in water on site or seal-cured on site because of a similar temperature history, and therefore that its strength is the same as that of specimens cured on site. However, the wide variety of cement types, high strength requirements, and upsizing demands in recent concrete construction work means that this assumption becomes inaccurate for concrete structures made with various materials and conditions due to differences in temperature profiles and strength development as they harden.

This has prompted the adoption of a method in which the compressive strength of standard, water-cured specimens is compared with that of cylindrical, "core" samples taken from concrete specimens created to simulate structural members. The resulting data is used to guide mix-proportion designs and predict structural strength [1]. Also, derived correction factors for specific designs are given in a notification of the Ministry of Land, Infrastructure Transport and Tourism. When tasked with

S. Sato (✉)

Department of Architecture, Tokyo City University, 1-28-1 Tamazutsumi, Setagaya, Tokyo 158-0093, Japan

e-mail: s-sato@tcu.ac.jp

Y. Masuda

Utsunomiya University, Utsunomiya, Tochigi, Japan

H. Tanano

Building Research Institute, Tsukuba, Ibaraki, Japan

revising this bulletin, the authors previously proposed strength correction factors following an analysis of empirical data for structural concrete collected from many sources [2].

In this study, experimental data for concrete test members fabricated and tested at ready-mixed concrete plants all over Japan were collected and compared to examine the influence of temperature conditions and various other factors on the strength development of core specimens cut from the members.

2 Outline of Experiment

Almost all types of high-strength concrete do not conform to JIS. Therefore, before a proposed high-strength concrete can be applied in construction work, it must receive the approval of the Minister of Land, Infrastructure Transport and Tourism as a designated concrete construction material, as stipulated in Article 37-2 of the Building Standards Act.

In this study, surveyed data was collected from experiments performed to gain this approval between 2000 and 2004. Table 1 shows the survey's scope. Concretes made from three types of cement were considered—ordinary, moderate-heat, and low-heat Portland cement—all of which are standard products provided for in JIS R 5210—Portland Cement. Cements were manufactured domestically in all cases, by 10, 7, and 6 producers respectively.

Experiments followed the publication JASS 5 T-605 (Estimation procedure for structural concrete strength using core specimens). Specifically, the center of a concrete pillar is simulated by sandwiching a cubic concrete block ($\sim 1 \text{ m}^3$) between two layers of insulation foam at its top and bottom to prevent vertical heat propagation. Cylindrical “core” samples are taken from the block at designated time points. The temperature history (variation, maxima) inside the block is recorded starting immediately after the concrete is cast. For comparison, “standard-cured” cylindrical specimens are taken from the block during preparation, and undergo a standard underwater-curing procedure. Core and standard-cured specimens have their compressive strength measured and compared.

Figure 1 shows an overview of how these specimens are prepared and sampled.

In addition, specimens were classified according to the timing of their manufacture to account for seasonal variation in temperature conditions. Specifically, this framework was designed in the authors' previous work [3], based on distinct trends in the

Table 1 Survey scope

Cement type	Factories	W/C range(%) (C/W)
Ordinary	391	23–60 (4.35–1.67)
Moderate-heat	223	20–50 (5.00–2.00)
Low-heat	143	20–48.5 (5.00–2.06)

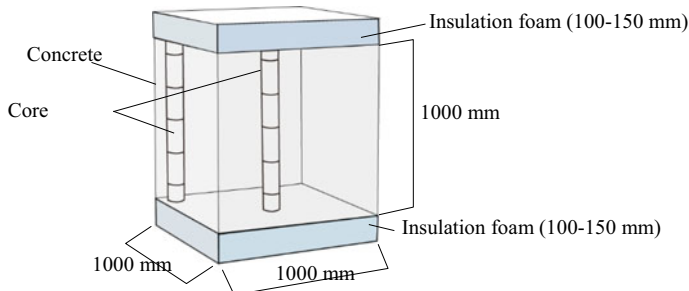


Fig. 1 Model of concrete block specimen (JASS 5T-605)

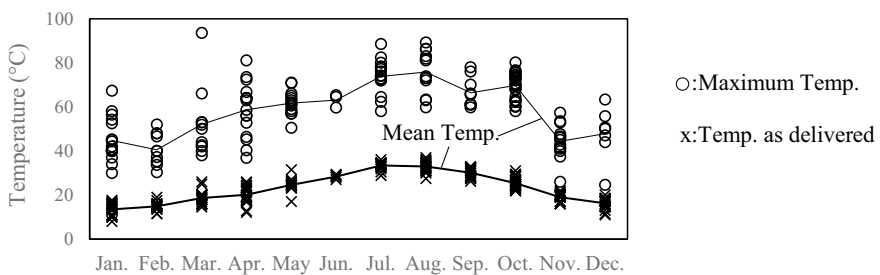


Fig. 2 Delivery and maximum temperatures of concrete block specimens [3]

delivery temperature and maximum temperature of ready-mixed concrete members at construction sites: Standard (Spring/Fall), Apr-Jun, Oct-Nov; Summer, Jul-Sep; Winter: Dec-Mar (Fig. 2).

3 Results and Discussion

3.1 Cement-to-Water Ratio and Compressive Strength

Figure 3 shows the relationships of cement-to-water ratio (C/W) and compressive strength at 28 days for standard-cured specimens of ordinary, moderate-heat, and low-heat Portland cement, along with corresponding regression equations. Figure 4 shows the relationships of cement-to-water ratio and compressive strength for respective core specimens. Table 2 details the regression equation variables (slope, intercept) and standard errors for the relationships in Figs. 3 and 4 separately for the standard, summer, and winter conditions. Figure 3 and Table 2 indicate that the same cement-to-water ratio will result in the highest compressive strength for low-heat Portland cements, followed in descending order by moderate and ordinary types. In addition, the slope of this relationship is about 5–9% smaller for core specimens than

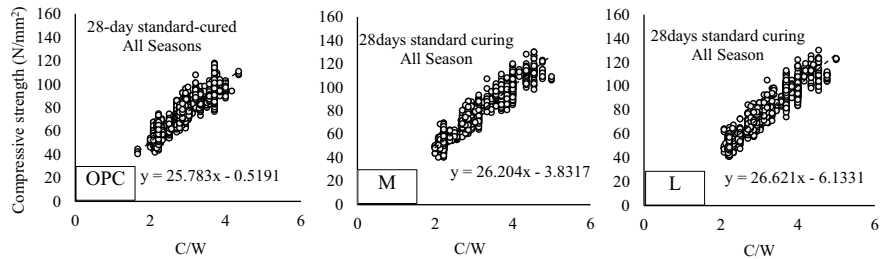


Fig. 3 Relationship of cement-to-water ratio and compressive strength (standard-cured specimens)

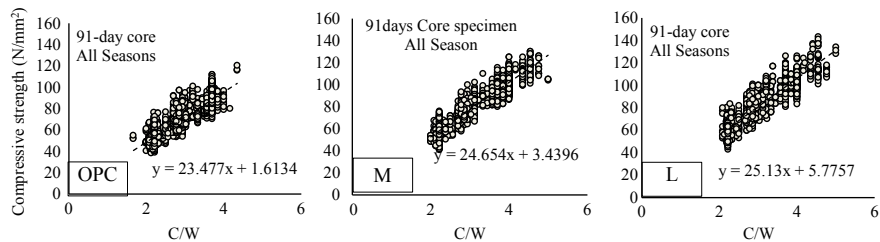


Fig. 4 Relationship of cement-to-water ratio and compressive strength (core specimens)

standard-cured specimens. Standard errors range from 5 to 8 N/mm². Thus, mixture proportions should be designed with a cement-to-water ratio no smaller than the lower confidence limit indicated by these figures, so that the resulting concrete's strength does not drop below the target value. Practically, it is thought that low-heat portland cement is used for higher strength concrete.

3.2 Relationship of Standard-Cured Strength and Core Strength

Figure 5 shows the relationships of standard-cured strength and core strength for each type of cement. Core strengths of ordinary Portland cement at 28 and 91 days were respectively ~85 and ~94% of the standard-cured strength at 28 days. For moderate-heat and low-heat Portland cement, the core strengths at 91 days were respectively ~103 and ~109% of the standard-cured strength at 28 days. These data demonstrate that the strength development of core specimens differs from that of standard-cured specimens: lower heats of hydration during the curing period result in superior strength development. Similar experimental protocols will need to be vigilant for adverse effects if a core specimen exhibits a high temperature history during curing.

Table 2 Results of regression analysis

Cement	Season	28-day standard-cured specimens				91-day core specimens			
		Slope	Intercept	SE	N	Slope	Intercept	SE	N
OPC	All	25.78	-0.52	5.05	3107	23.48	1.61	6.64	3037
	Spring/fall	25.78	-0.32	5.59	1110	23.46	2.02	6.25	1081
	Summer	25.81	-1.51	5.12	1068	23.86	-2.35	5.60	1047
	Winter	25.76	0.34	5.68	929	23.10	5.57	6.86	909
Moderate	All	26.20	-3.83	5.43	1891	24.65	3.44	6.23	1885
	Spring/fall	25.99	-3.27	5.25	621	24.36	4.34	6.20	618
	Summer	26.29	-4.72	5.28	617	24.99	2.31	5.75	614
	Winter	26.31	-3.49	5.65	653	24.61	3.66	6.68	653
Low-heat	All	26.62	-6.13	6.07	1436	25.13	5.78	7.99	1390
	Spring/fall	26.27	-6.32	6.29	475	24.91	6.61	8.03	459
	Summer	26.47	-6.42	5.56	465	24.94	6.80	7.94	452
	Winter	26.71	-5.70	6.25	496	25.50	4.08	8.02	479

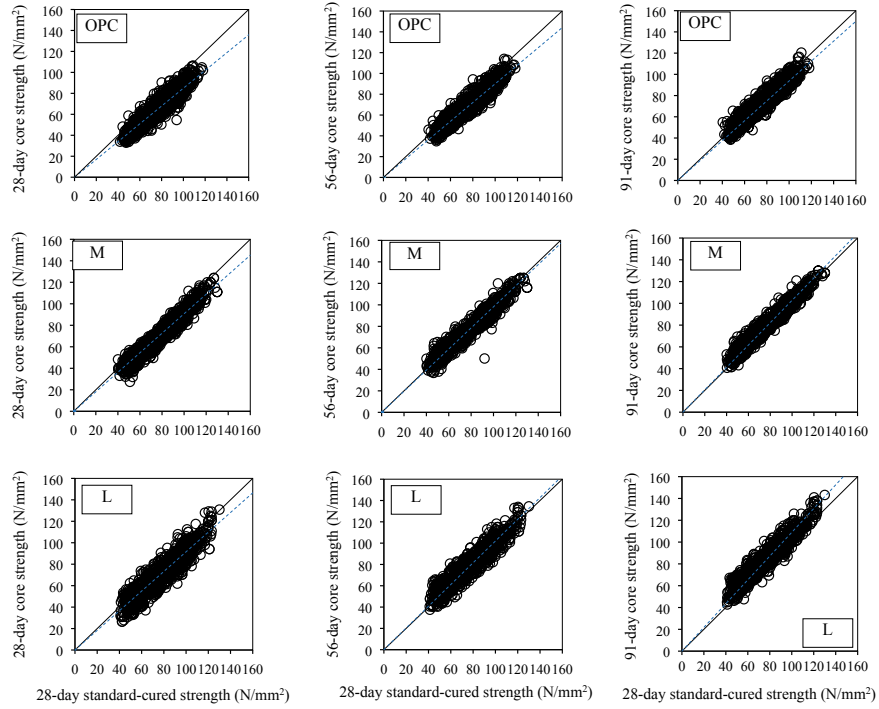


Fig. 5 Relationship of standard cured strength and core strength

3.3 Relationship of Maximum Temperature and Strength Development

Figure 6 shows the relationships of maximum temperature and strength development ratio from 28 to 91 days for core specimens. Strength ratio falls with increasing maximum temperature for all types of cement, but this effect was weakest for ordinary cement. Thus, lower heats of hydration are associated with strength development at

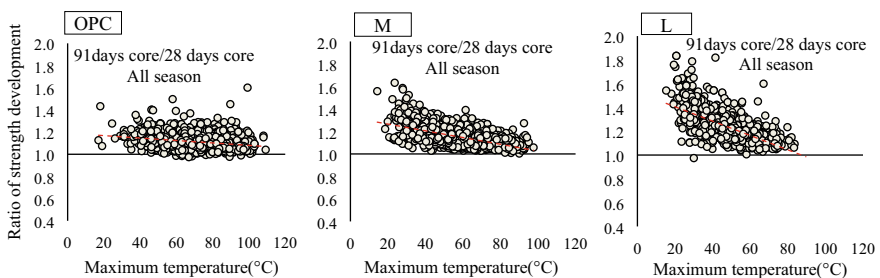


Fig. 6 Relationship of maximum temperature and strength development ratio

28 days of curing being more susceptible to internal temperature history. Generally, concrete's strength development depends on the type of cement utilized. The maximum internal temperature of a member is reached around 24 h after casting: the higher this is, the more the material's strength is enhanced early in the curing process, which results in a 'plateauing' of the subsequent long-term strength increase. In addition, the effects of maximum temperature were most striking for low-heat Portland cement.

4 Conclusion

This study looked at experimental data for concrete specimens tested since 2000, exploring the relationships between cement-to-water ratio, standard-cured and core specimen strengths, and maximum curing temperature. As the results, the difference of strength development of core specimen by cement types was shown. Also, the strength development of low-heat Portland cement concrete was most affected by maximum temperature.

Acknowledgements This work was supported by JSPS KAKENHI Grant Numbers JP16K06591, JP19K04695.

References

1. Architectural Institute of Japan (AIJ) (2018) Japanese architectural standard specifications: JASS 5 reinforced concrete work
2. Tanano H, Masuda Y, Sato S et al (2016) Examination for the control standard of concrete strength including high strength region. Building Research Data, 169, Building Research Institute, National Research and Development Agency, Japan
3. Masuda Y, Sato S, Tomosawa F (2000) Strength development of high-strength concrete in structure and proportioning strength. J Struct Constr Eng AIJ(537):13–20

Tensile Behavior of Ultra-High-Ductile Fiber-Reinforced Cementless Composites



Huy Hoang Nguyen, Jeong-II Choi, Se-Eon Park, and Bang Yeon Lee

1 Introduction

For a decade, AAS-based fiber-reinforced composites have been acknowledged as a unique construction material, combined with several features in term of greenness characteristic, self-healing ability and remarkable tensile strain capacity [11]. Notably, the tensile ductility of the material is being improved and enhanced over the years according to the advanced technology and the new modern techniques.

Lee et al. [8] investigated the strain-hardening composites based on polyvinyl alcohol (PVA) fiber-reinforced alkali-activated slag. Following that, Choi et al. [2] used polyethylene (PE) fiber to reinforce alkali-activated slag, achieving an ultra-high ductile behavior with a superior tensile strain capacity of 7.5%. Kwon et al. [7] presented the tensile behaviors and cracking patterns of slag-based composites reinforced by the synthetic fiber, i.e. polypropylene (PP), PVA and polyparaphenylene-benzobisethiazole (PBO) fiber.

Kanda and Li [5] presented the theoretical literature related to the pseudo-strain hardening (PSH) behavior on engineered cementitious composites (ECC). They demonstrated that PSH behavior was achieved when the stress performance index (SPI) or the energy performance index (EPI) were satisfied. The SPI is obtained by dividing the ultimate tensile stress (tensile strength) by the first cracking strength, and the EPI is calculated by dividing the complementary energy by crack tip toughness of the material matrix.

Although the mechanical properties of slag-based cementless composites are shown recently, the information on the activators-activated slag-based fiber-reinforced composites has been no more available. The objective of this study is to experimentally investigate effects of types of activators and age on the ultra-high-ductile behavior of cementless composites.

H. H. Nguyen · J.-I. Choi · S.-E. Park · B. Y. Lee (✉)
Chonnam National University, Gwangju, Republic of Korea
e-mail: bylee@jnu.ac.kr

2 Materials and Methodology

2.1 Mix Proportions

The mix proportion of each mixture is presented in Table 1. The binder is the combination of ground granulated blast furnace slag (GGBS) and a different type of activator. GGBS was activated by an activator, i.e. Ca(OH)_2 (calcium hydroxide), NaOH (sodium hydroxide) and Na_2SiO_3 (sodium silicate). Ca(OH)_2 and Na_2SiO_3 come from powder type to block the quick setting of the mixtures, whereas NaOH is the liquid solution made by the dissolution of NaOH flakes into water regarding a molar concentration of 8.3 M. It should be noted that the NaOH solution was prepared within one day before casting to reduce the released heat resulting in quick hardening. The amount of single activator was identical, which was 10% of binder weight. PE fiber with a high aspect ratio of 1500 (length of 18 mm and diameter of 12 μm) was applied as the reinforcing synthesis fiber for all mixtures with regard to 1.75% of the mixture volume. Table 2 indicates the physical properties of the PE fiber. Besides, polycarboxylate superplasticizer (PSP) and methylcellulose (MC) in powder form were used to adjust the workability and viscosity of the fresh mixture. An anti-foaming (AF) agent was charged to limit the air bubble formed within the mixing procedure.

2.2 Mixing Process

In the case of powder activators, the source material (GGBS) and single activator were mixed in a planetary type mixer for two minutes. Then, water was poured slowly into the mixture and was mixed for another two minutes. On the contrary, in term of the liquid solution, NaOH solution was added directly to the GGBS and was mixed for three minutes. In the next step, to achieve both good fiber distribution and proper viscosity, PSP and MC were simultaneously charged into the mixture. Besides, an AF agent was added to diminish the air bubbles. Then, PE fiber was inserted into the mixer and mixed for an additional five minutes.

The fresh mixture was cast into the dog-bone shape molds for tension tests and cube molds for compressive strength tests to quantitatively measure the mechanical properties of the composites. Three tensile specimens and three cube specimens were prepared for each mixture. Those specimens were covered by the plastic sheet to limit the evaporation of moisture and was removed after two days. It is essential to mention that the specimens were cured under a submerged environment in a water tank at a room temperature of $23 \pm 3^\circ\text{C}$ until the testing days.

Table 1 Mix proportions

Mixture ID	GGBS Binder	$\text{Ca}(\text{OH})_2$	NaOH	Na_2SiO_3	Water	PSP	MC	AF	Fiber (vol.%)
S-Ca	0.90	0.10	—	—	0.3	0.0035	0.0010	0.001	1.75
S-Na	0.90	—	0.10	—	0.3	0.0040	0.0005	0.001	1.75
S-NaS	0.90	—	—	0.10	0.3	0.0035	0.0005	0.001	1.75

Table 2 Properties of PE fiber

Tensile strength (MPa)	Density (g/cm ³)	Elastic modulus (GPa)
2700	0.97	88

2.3 Experimental Methods

The tensile specimens were loaded to obtain the tensile properties at the ages of 7 and 28 days, whereas the compressive strength was only measured at the age of 28 days. The compressive strength test was performed based on ASTM C109/C109M, and the tension test was performed according to Japan Society of Civil Engineers (JSCE) recommendation using an electronic universal testing machine [1, 4]. The test setup can be referred by the previous literature [2, 3, 6, 11, 12].

3 Results and Discussion

Figure 1 displays the representative strain-hardening behavior of the cementless composites, which is characterized by the stress and strain curves, showing the multiple-cracking behavior. Overall, all mixtures achieved the superior tensile ductility at 7 and 28 days of age. The compressive strength (f_c) and representative tensile properties, including first cracking strength (f_{cr}), tensile strength (f_{ts}), and tensile strain capacity of each mixture, were shown in Table 3.

As described in Fig. 1, the tensile behavior of all mixtures showed the strain-hardening characteristic with respect to the multiple-cracking behavior at both 7 and 28 days of age. Especially, the tensile behavior of the composites at the age of 28 days was more stable compared to the age of 7 days, which is similar to the test results reported in the previous study [10]. Generally, the tensile strength of all mixtures was increased over time. Similarly, the first cracking strength was also risen, but not significantly. Besides, the compressive strength was proportional to the first cracking strength for all mixtures. In term of tensile performance, the S–Ca mixture showed the best tensile strain capacity and tensile strength compared two other mixtures at the age of 28 days. In addition, the values of tensile strain capacity of the S–Ca and S–Na mixtures at the age of 28 days were 13.3% and 2.7% higher than those at the age of 7 days, respectively. On the contrary, the tensile strain capacity of the S–NaS mixture at the age of 28 days was 2.5% lower than that at the age of 7 days.

In this study, the authors used the stress performance index, which is shown in Fig. 2, to consider the PSH behavior of AAS-based composites. As can be seen in Table 3 and Fig. 2, the tensile strain capacity of the S–Ca and S–Na mixtures increased over time, satisfied with a rise of the SPI from 2.06 to 2.24 and 1.88 to 1.95, respectively. Otherwise, the SPI of the S–NaS dropped at the age of 28 days compared to that at the age of 7 days, implying the reduction of tensile strain capacity. It is essential to mention that the tensile strain capacity of the S–Na mixture is remarkable,

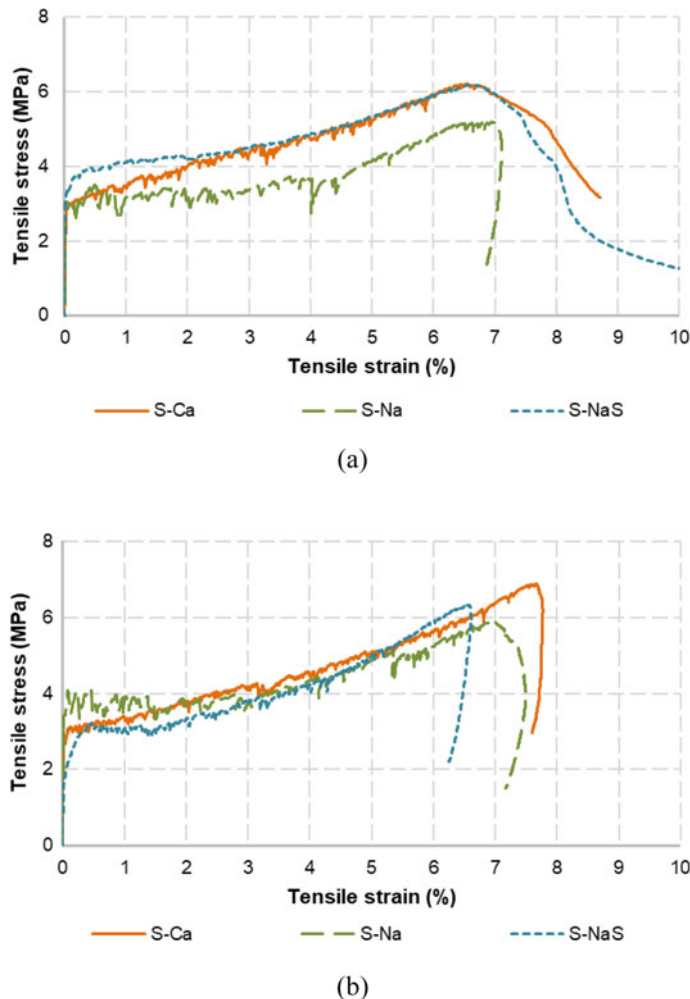


Fig. 1 Representative tensile behavior of AAS-based composites: **a** at 7 days of age and **b** at 28 days of age

Table 3 Mechanical properties

Mixture ID	Age	f_c (MPa)	f_{cr} (MPa)	f_{ts} (MPa)	Tensile strain capacity (%)
S-Ca	7 days	—	3.02	6.22	6.78
S-Na			2.75	5.16	7.01
S-NaS			3.07	6.17	6.75
S-Ca	28 days	39.8	3.07	6.87	7.68
S-Na		31.4	3.01	5.86	7.20
S-NaS		42.5	3.18	6.31	6.58

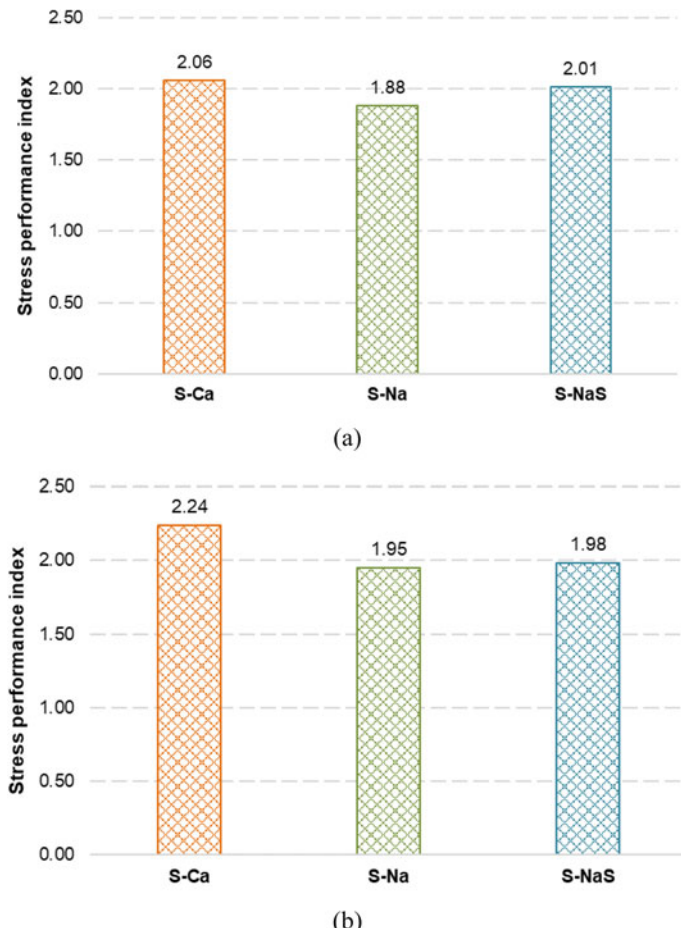


Fig. 2 SPI of AAS-based composites: **a** at 7 days of age and **b** at 28 days of age

although the SPI is somewhat lower than that of the S–Ca and S–NaS mixtures at both 7 and 28 days of age. This can be justified based on the good EPI criteria due to better complementary energy in the material matrix. Choi et al. [2] and Kwon et al. [7] reported that a higher tensile strain capacity is achievable with higher performance indices. In other words, the better complementary energy leads to an increase of the EPI (energy performance index), inducing the higher tensile strain capacity.

Table 4 shows the cracking patterns of each composite mixture at the age of 28 days. In particular, the number of cracks was counted both sides within gauge length of the tensile specimens. The average crack width was calculated by the ratio of the total deformation at maximum loading to the number of cracks, whereas dividing the gauge length by the number of cracks is the formula to obtain the crack spacing.

Table 4 Cracking patterns

Mixture ID	Crack number	Crack width (μm)	Crack spacing (mm)
S-Ca	112.0	54.7	0.71
S-Na	94.5	57.6	0.86
S-NaS	88.5	58.4	0.90

As displayed, all composite mixtures showed the saturated number of cracks at 28 days of age, which was around 100. Besides, the average crack widths were below 60 μm , leading the potential for the good durability of composite structures, demonstrated in the previous literature [9].

4 Conclusions

Mechanical properties of ultra-high-ductile cementless composites have been investigated in the paper. The mix designs achieved the superior tensile strain capacity around 7% even at an early age (7 days). The S-Ca mixtures showed the best tensile performance at 28 days of age. The first cracking strength, tensile strength, and tensile strain capacity almost increased over time for all mixtures, only a reduction found in the tensile strain capacity of the S-NaS mixture at 28 days of age. The strain-hardening behavior of cementless composites was demonstrated through theoretical criteria related to SPI. In other words, the tensile strain capacity was proportional to the SPI. Additionally, the cementless composites showed good durability performance regarding the average crack widths below 60 μm after cracking.

Acknowledgements This work was supported by the National Research Foundation of Korea (NRF) grant funded by the Korea government (MSIT) (No. 2019R1A2C4069794) and a grant (19SCIP-B103706-05) from Construction Technology Research Program funded by Ministry of Land, Infrastructure and Transport of Korean government.

References

- ASTM (2007) Standard test method for compressive strength of hydraulic cement mortars (using 50 mm [2 in.] cube specimens). American Society for Testing and Materials, ASTM C109/C109M
- Choi J-I, Lee BY, Ranade R, Li VC, Lee Y (2016) Ultra-high-ductile behavior of a polyethylene fiber-reinforced alkali-activated slag-based composite. *Cem Concr Compos* 70:153–158
- Ding Y, Yu J-t, Yu K-Q, Xu S-l (2018) Basic mechanical properties of ultra-high ductility cementitious composites: from 40 MPa to 120 MPa. *Compos Struct* 185:634–645
- JSCE, Recommendations for design and construction of high performance fiber reinforced cement composites with multiple fine cracks (HPFRCC), Japan Society of Civil Engineers, Japan (2008)

5. Kanda T, Li VC (2006) Practical design criteria for saturated pseudo strain hardening behavior in ECC. *J Adv Concr Technol* 4(1):59–72
6. Kim G-Y, Choi J-I, Park S-E, Kim H, Lee Y, Lee BY (2018) Response of UHPFRC and HDFRC under static and high-velocity projectile impact loads. *Constr Build Mater* 188:399–408
7. Kwon S-J, Choi J-I, Nguyen HH, Lee BY (2018) Tensile strain-hardening behaviors and crack patterns of slag-based fiber-reinforced composites. *Comput Concr* 21(3):231–237
8. Lee BY, Cho C-G, Lim H-J, Song J-K, Yang K-H, Li VC (2012) Strain hardening fiber reinforced alkali-activated mortar—a feasibility study. *Constr Build Mater* 37:15–20
9. Lepech MD, Li VC (2009) Water permeability of engineered cementitious composites. *Cem Concr Compos* 31(10):744–753
10. Li M, Li VC (2011) High-early-strength engineered cementitious composites for fast, durable concrete repair-material properties. *ACI Mater J* 108(1):3
11. Nguyễn HH, Choi J-I, Song K-I, Song J-K, Huh J, Lee BY (2018) Self-healing properties of cement-based and alkali-activated slag-based fiber-reinforced composites. *Constr Build Mater* 165:801–811
12. Yu K, Wang Y, Yu J, Xu S (2017) A strain-hardening cementitious composites with the tensile capacity up to 8%. *Constr Build Mater* 137:410–419

Geotechnical and Transportation Sessions

An Exploratory Test of Communicative Mobility Management for Promoting Modal Shift in Ho Chi Minh City



Hong Tan Van, Kiyohisa Terai, and Tetsuo Yai

1 Introduction

In many countries, public transportation usually faces much difficulty in competing with private modes. In Ho Chi Minh City (HCMC), Vietnam, the similar situation happen when regular bus service suffering failures. Despite receiving much investment and subsidy from the government, regular buses are still perceived as low-quality transport service in terms of travel time, reliability, and accessibility. Thus, bus passengers have reduced significantly since 2013 with an average rate of more than 10% annually [1]. The remaining potential bus-riders are possibly students or low income people who cannot afford a motorcycle (MC).

MC becomes more and more indispensable to many people in HCMC as it is generally perceived high comfort, convenience and freedom. Until end of 2018, number registered MC in the city has reached 7.5 millions. More than 85% of trips are made by MC. Consequently, excessive number of MC has impeded the moving of buses, increasing the delay of buses as well as worsening the whole road-based traffic.

Even though from the view of managing supply, such a developing city like HCMC needs to build more transportation infrastructures for the growing travel demand, it is important to manage travel demand as well. Literatures have also demonstrated many efforts by governments in US and European countries to deal with the root of

H. T. Van (✉)

Faculty of Civil Engineering,

Ho Chi Minh City University of Technology, Ho Chi Minh City, Vietnam

e-mail: vhtan@hcmut.edu.vn

K. Terai

International Research Center of Advanced Energy Systems for Sustainability,
Tokyo Institute of Technology/Toshiba Corporation, Tokyo, Japan

T. Yai

Tokyo Institute of Technology, Tokyo, Japan

the transport problem on the basis of demand management. This is the application of policies and strategies to reduce the number of vehicle using the road network, especially private modes, by shifting people into use more sustainable travel modes such as public transport. In HCMC, where there is excessive use of MC, proper measures of managing demand would be helpful in dealing with the problems of mode choices.

Demand management policies usually compose of three types: Regulatory, economic and cooperative instruments. Regulatory instruments are those standards, restrictions and administrative procedures set by local governments to hinder vehicular usage, e.g. vehicle restriction. Economic instruments use a variety of pricing mechanisms to discourage motorized vehicle ownership and usage and to encourage environmental-friendly technology through subsidies for low emission vehicles. Cooperative instruments are voluntary engagement of individuals in choosing a travel option that would best fit their personal preference and family needs. Cooperative instrument is mostly referred as Mobility Management (MM), e.g., Travel Feedback Program [6], Travel Plans [2, 3] ..., which aimed at influencing and changing travellers' attitudes and behavior.

Typical MM measures might include information giving, awareness raising and promotion of sustainable modes, education and training, travel plans.... MM measures can be applied to four target groups: students, employees, visitors and residents. Among them, students seem to be easiest for providing educational information. Examples of these MM measures are Travel Feedback Program in Japan, Travel Plans in UK which have been considered successful in reducing car use and CO₂ emission [2, 5]. MM measures were also verified effectiveness in promoting bus use in Japan [10].

The ‘expanded’ MM might combine several measures, ranging from information, advice and awareness to the supply of alternatives, incentives and restraints. Specifically, there are several types of Mobility Services which can be divided into two categories: “soft” or communicative MM measures [9] and ‘harder’ measures, including organizing sustainable transport to make using the service easier and more convenient. Incentives to promote and stimulate the use of the sustainable modes fall under this category.

A previous study which investigated psychological structure of people in HCM City showed that TPB is applicable to predict the behavioral intention of mode choice in HCM City [7]. This implied that it is possible to develop some measure of MM such as information, marketing, communication etc. to shift people to more use of bus. While the government in HCMC is still in a tangle in finding proper solution against overwhelming bike-traffic, this study implemented an exploratory test of MM initiatives by combining several types of Mobility Services to promote students to use bus for schooling as an alternative to MC.

The analyses in this paper have two objectives: (1) to find the effectiveness of communication mobility management in changing behavioral intention to shift to use bus; (2) to find out the key features that influence shifting to bus use. The findings of this study are expected to provide some insights into designing effective mobility management measures in order to increase bus passengers and to lessen high reliance

on MC use. The remaining of the paper is structured as follows. Section 2 describes outline of the pilot school MM and the survey in HCMC. The analyses and results are presented in Sect. 3, followed by conclusions in Sect. 4.

2 The Pilot MM Initiatives in HCMC

2.1 *Target Group and Characteristics*

As mentioned above, MM strategy is usually composed of a number of sub-strategies that are aimed at specific target groups to achieve the desired outcomes. In this study, university students were chosen as the target group to encourage a change of attitude and behavior towards greater use of bus. At the beginning, 87 students at HCMC university of Technology were subjected to our MM initiatives. They are 3rd and 4th year students in Civil Engineering who were openly recruited via notices on faculty email group. However, four students skipped attending the last survey, making up a final sample of 83 students. Each participant received an incentive for their time in the two surveys. For those students, 92% are male and 82% owns a MC. This gender ratio in the survey is similar with that in the Civil Engineering Faculty. Most of the participants live around 5 km away from the university, thus almost all of them are highly dependent on MC use for their school trips. Most of the students' MC trips to the university are unchained (51.8%) and single occupant (74.7%).

2.2 *Tools for Providing Information*

The tools developed for MM initiative in this study include Smart phone app and a slideshow lecture.

Smart phone app: The latest and real-time data about the bus service in HCMC, which includes more than a hundred bus routes with over 2000 bus stops, was integrated to create a smart phone app named BusMap. This app has the purpose of helping bus commuters to experience better and safer bus rides. Accordingly, BusMap provides users the most optimal ways to commute between two places, with features such as smart navigation guide in which users can easily lookup all bus routes, find bus stops in the user's area on the Google map on users' device. Furthermore, it is able to view waiting time for the next bus to arrive at the waiting bus stop based on real-time on-board GPS trackers. With those features, this app, available on Android, iOS, and Windows Phone and web, were chosen as a MM tool for easily and conveniently providing information to the users. That is, all participating students were requested to use their own smart phones to download, install and use BusMap to

lookup detailed information of available bus routes between their living places and the university.

Lecture: In addition to BusMap, the participating students received a slideshow lecture on negative externalities of private mode use and the benefits of using bus. The lecture lays emphasis on the idea that private vehicle use is the direct cause for current severe traffic congestion in HCMC and bus use could be the only viable solution that requires voluntary actions first from the students.

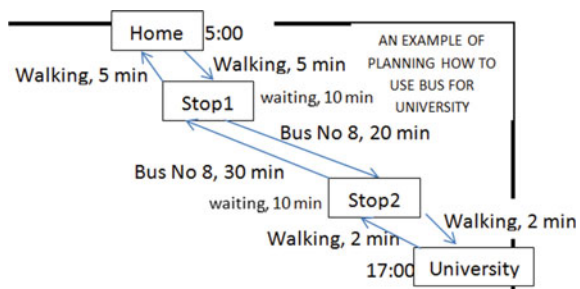
2.3 MM Procedure and Survey

Procedure for MM initiatives involves two contacts. At the first contact, after introducing about the test, we started conducting the 1st wave survey about the participants' MC trips from home to university and about whether they have intention "to try to shift to use bus for university trips". Behavioral intention was rated in a 5-point scale, ranging from "not at all" [1] to "yes, strongly" [5]. After introducing BusMap App, each student were asked to use the app to look up information on how to use bus to travel from their home to the university.

After that, we requested the participants to follow an exampled template as in Fig. 1 to draw a diagram about how to use bus for their student transport. This kind of making behavioral plan requires the students to think and estimate a time schedule for their new trip by bus rather than by MC. Importance of making behavioral plan in increasing the effect of travel behavior change has been demonstrated by Fujii and Taniguchi [6]. This is because when a person could describe a specific time, location for a behavior, his/her implementation intention could be boosted and consequently increases the likelihood of the actual behavior [8]. This study assumes that such a technique is effective in increasing behavioral intention. Finally, each participant was asked to try to use bus for their trip to university from that day on, and was reminded to take a snap shot of this planned diagram so that they can use if there is no internet connection for the BusMap app.

The second contact occurred after ten days. At this meeting, the participants reported about whether they tried to use bus for student transport and if having,

Fig. 1 The exampled diagram for making behavioral plan



how many times it was. The follow-up questionnaire includes questions regarding bus use, and again their behavioral intention “to try to shift to use bus for university trips”. Then, we gave all the participants a slideshow lecture on negative externalities of private mode use and the benefits of using bus on alleviating traffic congestion, followed by a short discussion. The respondents were asked to give their third answer about the intention to use bus instead of MC for school transport. Finally, the participants were asked to answered several stated choices regarding using bus or MC to the university.

2.4 Stated Choices and Survey Items

First, we had the respondents review all attributes of the MC and bus trips for school transport, which they had answered during the 1st wave survey, including travel times and costs, risk of accident if using MC and estimated seat availability rates if using bus. Once the respondent was fully understood about attributes of MC and bus trips, four SP scenarios in combination of various attributes of bus, MC, and presumed incentives were then presented to the respondent. He/she was asked to consider whether he/she would change to use bus for that school trip with the form of binary choice (Yes or No). Note that to compensate for longer travel time by bus than by MC as well as to promote “temporary structure change” [4], the participants were said to presumably receive an amount of point incentive each time he/she rides bus to the university.

The experiment of stated choices between MC and bus involves several steps of design and testing. First, after consulting expert opinions as well as referring to another survey by the authors, we assume that the incentive per ride, travel time and cost, seat availability rate, and travel time and cost, having priority lane for buses would be influential attributes specific to bus and risk of traffic accidents might be specific attribute to MC. More detailed explanations are as follows:

1. The *presumed incentives* were set to be about 50 and 100% of value of time difference between using bus and MC. Hence for each participant, we assigned two values of incentives, i.e. 50 and 100% in four scenarios. The values were calculated and rounded to the nearest thousand (but not smaller than 1000 VND and not larger than 8000 VND). The customized two levels of incentives ensure that they are suitable to the respondents and they do not just face only low or high levels of incentive.
2. The attributes of *having priority lane* had two levels (yes/no, i.e. buses have a priority lane, thus not being affected by traffic jam/Buses share the road with MC, still being affected by traffic jam).
3. *Seat availability rates* were supposed to have five levels for the respondents to choose: “very highly occupied” (lower than one out of three rides is seated), “highly occupied” (one out of three rides is seated), “fairly occupied” (one out

- of two rides is seated), “low occupied” (three out of four rides are seated) and “very low occupied” (higher than three out of four rides are seated).
4. While bus is supposed to be absolutely safe, *the risks of accident using MC* are rated based on either of “one out of 40/50/100/200/300 times using MC is assumed yielding accidents at certain levels”.
 5. In all scenarios, *MC parking fee* is assumed to doubly increase to 4000 VND.

Secondly, to minimize respondent confusion, important words in SP design are bold and capitalized in the questionnaire. Also, to ensure the suitability of the value of time and the SP scenarios, we implemented a simple testing survey on 20 people. Their feedbacks showed that up to four choice task with two changed plus four fixed attributes of bus and three fixed attributes of MC may not be a hard work to most of them, thus might help enhance the accuracy for the survey. Besides, the testing survey resulted in an average VOT of 100 VND/min (≈ 0.28 USD/h), which was used for the above incentive calculation.

3 Analyses and Results

3.1 Effectiveness of MM Techniques

In the study, we had three times asking the participants about their behavioral intention to shift to use more bus for school transport. One was before making behavioral plan, another was after ten days at the second wave survey and the remainder was after lecture and discussion about negative externalities of private mode use and the benefits of using bus. We examines whether the BusMap App, the behavioral plan and the lecture play roles in enhance behavioral intention to shift to use bus. To investigate this, repeated-measures t-tests were implemented on the dependent variable of *intention to try to shift to use bus for university trips*. The mean score of behavioral intention before making behavioral plan was 3.01 (SD = 0.69); the mean score afterwards was 3.51 (SD = 1.03). The t-value proves this difference to be significant, $t(82) = -5.15$, $p < 0.001$. This suggests that making behavioral plan affects behavioral intention to shift to use bus for school transport, supporting our assumption. In addition to that, there is a significant difference in the scores for behavioral intention before and after the lecture, $t(82) = -8.94$, $p < 0.001$. Specifically, the mean scores of behavioral intention after giving the lecture was 4.22 (SD = 0.91). This means that giving lecture about negative impacts of private mode use while praising good aspects of bus use could help increase the behavioral intention to use bus instead of MC.

3.2 SP Incentives and the Effects on Mode Choices

Our main purpose is to explore the effects of different factors on shifting to bus through using stated preference data. Regarding modal choice, travel time and travel cost are highly likely important constituents. Travel cost and travel time of MC and buses were computed by summed up all times and costs expended for the trip, including the presumably-increased parking cost. Furthermore, we hypothesized that the risks of accident using MC would be important in decisions about mode choice. This is because accidents involving MC use in mixed traffic has become alarming in Vietnam. With regard to bus, we hypothesized that *having priority lane* and *Seat availability rates* would be the two main dimensions of quality of service that influence mode choice. Finally, two participants ‘socioeconomic characteristics, i.e. gender, and MC ownership, and two trip attributes, i.e. the trip is chained with other trips and carrying another person, would be important in mode choice decisions.

Since the choice faced by respondents is dichotomous between MC and bus, we chose a binary logit model where disturbances ε_{in} are distributed according to logistic distributions. Besides, to understand the valuation of bus time relative to MC travel time, we used mode specific time and cost parameters. From those assumptions, the deterministic utilities are specified as the following Eqs. 1 and 2:

$$V_{Bus,n} = ASC_{Bus} + \beta_{time}^{Bus} Time_{Bus,n} + \beta_{cost}^{Bus} Cost_{Bus,n} + \beta_{seat} Seat_{Bus,n} + \beta_{lane} Lane_{Bus,n} \quad (1)$$

$$V_{MC,n} = \beta_{time}^{MC} Time_{MC,n} + \beta_{cost}^{MC} Cost_{MC,n} + \beta_{risk} Risk_{MC,n} + \beta_{gender} Gender_n \\ + \beta_{MCown} MCown_n + \beta_{carry} Carry_n + \beta_{chain} TripChain_n \quad (2)$$

where ASC is an alternative specific constant and β s are associated parameters with each explanatory variable.

Using Biogeme, the model was estimated by maximizing likelihood method (see Table 1). The resulted models were found to be statistically significant with a χ^2 equal to 185.1, exceeding the critical value of χ^2 for the 99.9% level of confidence. The high value of adjusted ρ^2 suggests that the model specification in which travel times and costs are alternative-specific improves goodness-of-fit of the model.

First, travel time and travel cost have negative significant effects on likelihood of travel mode use as expected. The negative significant coefficients of the travel time and travel cost of bus imply that the utility of the bus service and the probability that it will be chosen decreases as the travel time or travel cost of bus increases. For MC, though travel time and cost have a negative significance on MC use, such impacts are just marginally significant ($p < 0.15$). From these four coefficients, we also found that the computed VOT students spent in MC trips (≈ 0.64 USD/h) was reasonably higher than in bus trips (≈ 0.07 USD/h) due to the lower marginal utility of travel time savings on bus. However, these VOT are much lower than the GDP of HCMC (≈ 2.0 USD/h), which is consistent with student income. This implies that a minute of travel time by bus has very low marginal disutility to bus users. Besides,

Table 1 Estimation results of binary logit model for mode choice (N = 332)

Exogenous variables [alternatives] (definition)	Parameter	t-values	p-values
ASC (Bus)	-1.73	-1.48	0.14
Time [MC] (in minute)	-0.0236	-1.58	0.11
Cost [MC] (in VND)	-0.0001	-1.45	0.15
Carry [MC] (1: Carry others, 0: otherwise)	0.304	0.79	0.43
TripChain [MC] (1: Trip is chained, 0: otherwise)	-0.161	-0.51	0.61
Risk [MC] (risk of MC use)	-67.6	-2.49	0.01
Gender [MC] (1: male, 0: female)	0.456	0.65	0.52
MCown [MC] (1: having, 0: otherwise)	0.147	0.34	0.73
Time [Bus] (in minute)	-0.0125	-2.29	0.02
Cost [Bus] (in VND)	-0.0005	-5.92	0.00
Seat [Bus] (Bus seat availability rate)	0.241	0.34	0.74
Lane [Bus] (1: having priority lane, 0: otherwise)	2.75	7.84	0.00
Initial log likelihood	-230.1	χ^2	185.1
Final log likelihood	-137.6	ρ^2	0.350

we found that there were two highly significant alternative specific factors, i.e. *Lane* and *Risk*. The significant coefficient of *Lane* indicates that students are more likely to choose bus service if buses have a priority lane, not being affected by the traffic jam. Meanwhile, the risks of accident using MC is an important factor that significantly disutilize MC use. This indicates that MC users might tend to shift to use bus if they perceive higher risk of being involved in traffic accidents when using MC. Of the personal attributes, the main effects of MC ownership and gender are not statistically significant, but the results demonstrate that males and those having a MC are more inclined to travel by MC for school transport. The resulted negative constant also implies that when all else is equal the probability of choosing MC is higher than that of bus. Lastly, regarding trip characteristics the results show that chained trips and trips carrying an additional person have no significant effects on students' mode choice.

4 Conclusions

In this paper, we examines whether communicative MM measures play the roles in enhance behavioral intention to shift to use bus. Repeated measures tests show significant increase of behavioral intention if using BusMap App and requesting to make behavioral plans are jointly used. Additionally, giving the lecture could also be an effective persuasive technique. This indicates that disseminating talks about social (dis)benefits of private modes vs. bus could be an effective method of MM in HCMC,

at least to the students for modal shift from MC to bus. Moreover, a combination of those communicative MM techniques would amplify such effects.

Besides, we employed SP data to investigate the question as to how various factors affect mode choice by students between MC and bus. Results of binary logit model have confirmed that together with travel times, and costs, two mode specific factors, i.e. priority lane for bus, and the risk of traffic accident for MC are significant determinants of mode choice. Incentives to reduce bus cost could be used as a supplemental instrument for MM in promoting modal shift to bus. These results could have important implications for planning for bus service as well as for dissemination campaign.

Acknowledgements This research is funded by Vietnam National University HoChiMinh City (VNU-HCM) under grant number C2019-20-38. The authors thank Toshiba Corporation for cooperative support in the study.

References

1. Dau AP (2016) Summarizing the public transportation operation in HCMC. A report at the workshop on summarizing PT operation and bus subsidy in HCMC in the period of 2002–2015
2. Department for Transport (DOT UK) (2004) Smarter Choices: Changing the Way We Travel. London, UK
3. Department for Transport (DOT UK) (2004) Personalised travel planning demonstration programme. Presented at Personalised Travel Planning: End of Programme Conference, Bristol, UK
4. Fujii S, Gärling T (2005) Temporary structural change: a strategy to break car-use habit and promote public transport. *Traffic Transp Psychol* 585–592
5. Fujii S, Taniguchi A (2006) Determinants of the effectiveness of travel feedback programs—a review of communicative MM measures for changing travel behaviour in Japan. *Transp Policy* 13:339–348
6. Fujii S, Taniguchi A (2005) Reducing family car use by providing travel advice or requesting behavioral plans: an experimental analysis of travel feedback programs. *Transp Res D* 10(5):385–393
7. Fujii S, Van HT (2009) Psychological determinants of the intention to use the bus in Ho Chi Minh City. *J Pub Transp* 12(1):97–110
8. Gollwitzer PM, Brandstätter V (1997) Implementation intentions and effective goal pursuit. *J Pers Soc Psychol* 73:186–199
9. Jones P (2003) Encouraging behavioural change through marketing and management: what can be achieved? In: Presented at the 10th international conference on travel behaviour research, Lucerne, Switzerland
10. Taniguchi A, Fujii S, Hara F (2005) Promotion of a public transport by MM and verification of its quantitative effect: a case study for community bus in Obihiro city. *Proc EASTS* 5:316–324

Analyze Shear Strain of Inhomogeneous Soil Considering Interaction Between SFRC Foundation and Soil



Tran-Trung Nguyen, Phu-Cuong Nguyen, Trong-Nghia Nguyen,
Ngoc-Tuan Tran, Minh-Hoang Le, and Phong Thanh Nguyen

1 Introduction

In construction, the foundation is an essential part, because it receives the load directly from upper-structures and transmits it to the ground through the foundation structure system. Soil will gradually be compressed or consolidated, and then normal stresses and shear stresses are generated. The shear stress occurs due to volume change, and the failure surface will form when shear stress values arrive at critical values, also known as the limiting shear stress strength, as illustrated in Fig. 1.

In practice, the stress state is very complex, and according to some fundamental theories [8], in general, there are two special cases as follows: (i) Triaxial (axial symmetry) with parameters used for analysis such as deviator stress, shear strain, normal stress, volumetrical strain, and specific volume; (ii) Simple or direct shear using parameters such as shear stress, shear strain, normal stress, volumetrical (normal) strain and void ratio. Moreover, in the direct case, draw a Mohr circle is impossible for a shear test unless stresses on vertical planes are measured. The strength of the soil is the ability under the maximum shear stress (τ_f) or the shear stresses are achieved when the failure surface appears, and there are three distinct strengths: peak, ultimate, and residual stages that they are shown in Fig. 2, the relationship between τ_f and σ' .

So, how is the shear strain effect in the interaction problem of foundation and soil? Previous studies are about the interaction between foundation and soil subjected to axial compression load such as [9, 14, 15]. In those studies, authors were used FEM methods by ANSYS APDL simulation software to solve the above interaction problem with the obtained results compared with the experimental test [14]. The

T.-T. Nguyen

Faculty of Architecture, Van Lang University, Ho Chi Minh City, Vietnam

P.-C. Nguyen (✉) · T.-N. Nguyen · N.-T. Tran · M.-H. Le · P. T. Nguyen

Faculty of Civil Engineering, Ho Chi Minh Open University, Ho Chi Minh City, Vietnam

e-mail: cuong.pn@ou.edu.vn; henycuong@gmail.com

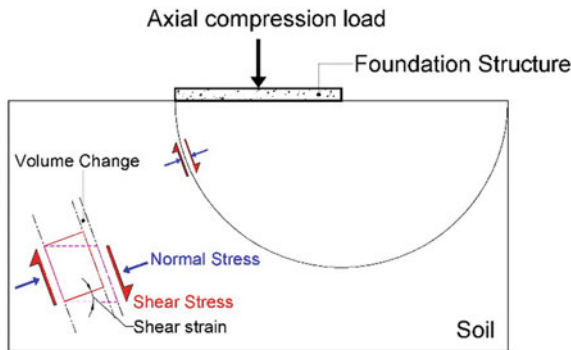


Fig. 1 A soil element is subjected to normal stress and shear stress

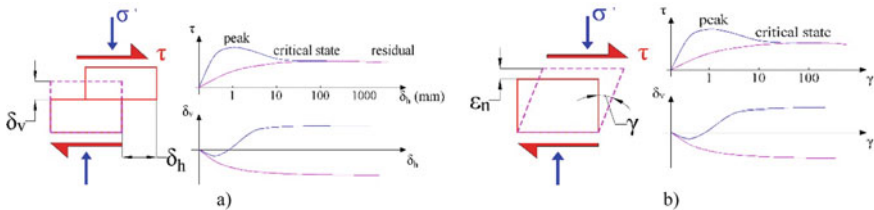


Fig. 2 The τ_f and σ' relationship: **a** Drained direct shear method. **b** Drained simple shear method

foundation structure was made by Steel Fiber Reinforced Concrete (SFRC), and the Soil was assigned by Subsoil or Inhomogeneous Soil (IS). The characteristics and theories for subsoil are described in detail in the documentation [7]. In the simulation, element types used for SFRC foundation and Subsoil were SOLID65 and SOLID45 elements, respectively. Furthermore, the material models are the most important for corresponding element types; authors define nine specific parameters of SOLID65 concrete and parameters using in the MCFC for the soil are also mentioned. Moreover, the parameters of SOLID65 concrete used in the above previous studies established from experimental tests, and this problem will be difficult for other similar studies to refer.

In this study, the authors based on the study [14] but using ANSYS Workbench software to solve the interaction problem of SFRC foundation and IS, so use only one element type is a SOLID186 element for both foundation and soil structures. Additionally, the material model for SFRC is established based on the proposed formulation of Barros and Figueiras mentioned in studies [1, 2]. The obtained results prove the strong influence of the type of element and material models in the simulation problem, and they will be discussed in the below sections.

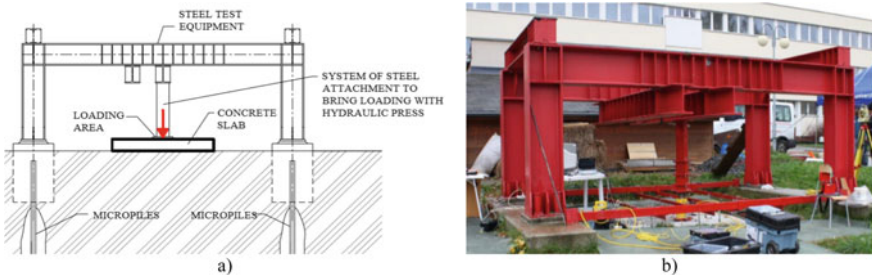


Fig. 3 Test equipment: **a** Scheme. **b** Actuality [3]

2 Experimental Test

The actual results used in earlier studies that have been mentioned, as well as for the results of this study, are from real experiments that conducted at the Technical University of Ostrava, Czech Republic [3, 4], shown in Fig. 3. The compression load levels used in the experiment are 75 (kN), 150 (kN), 300 (kN) and 450 (kN) to suit the comparison with the previous study [14].

3 Material Models Using in Simulation

3.1 SFRC Model

The SFRC material used for the shallow foundation in practical experiments and previous researches is modelled by nine specific parameters of the SOLID65 concrete element. The formulation of the above parameters will be transformed in the SSRC, which is proposed from the formula of [1]. the SSRC is capture through Eqs. 1 to 4 as follows:

$$\sigma = f_{cf} \frac{\frac{\varepsilon}{\varepsilon_{pf}}}{(1 - p - q) + q \left(\frac{\varepsilon}{\varepsilon_{pf}} \right) + p \left(\frac{\varepsilon}{\varepsilon_{pf}} \right)^{(1-q)/p}} \quad (1)$$

$$q = 1 - p - \frac{E_{pf}}{E_c} \quad (2)$$

$$p + q \in [0, 1] \text{ and } \frac{1 - q}{p} > 0 \quad (3)$$

$$E_{pf} = \frac{f_{cf}}{\varepsilon_{pf}} \text{ and } E_c = 21,500 \sqrt[3]{\frac{f_{cf}}{10}} \quad (4)$$

where f_{cf} is the average compressive strength. Using the least squares method for 3D DRAMIX 65/60B6-25 kg m⁻³ steel hooked-end fibers with $L_f = 60$ (mm), $D_f = 0.9$ (mm), $L_f/D_f = 65$

$$\varepsilon_{pf} = \varepsilon_{co} + 0.00022W_f \quad (5)$$

$$p = 1 - 0.853e^{-0.311W_f} \quad (6)$$

where $\varepsilon_{co} = 0.0022$ is the value of the deformation at the stress peak of the concrete without considering steel reinforcement and W_f is the percentage of steel fiber weight present in the concrete mix. Authors propose $W_f = 0.86\%$ and determine the values of C25/30 concrete is $f_{cf} = 33$ (MPa) according to the study of [14].

3.2 Soil Model

The soil model in this study is IS with two basic parameters is Poisson's ratio μ and Elastic modulus E_{def} for linear analysis. In which, E_{def} has the increased value gradually with the depth of the soil layer and is calculated corresponding to the thickness of each layer according to the proposed formula in the research [14] and [7], as follows:

$$E_{def} = E_o \left(\frac{z}{z_o} \right)^m \text{ where } m = \frac{1}{\mu} - 2 \quad (7)$$

with E_o is the elastic modulus at the surface determined from the experiment, z is coordinated in-depth, z_o is a unit length, sometimes replaced by the width B or the diameter D of the foundation; m is the coefficient depending on Poisson's ratio μ ; E_{def} is the elastic modulus of layers with a thickness of 0.75 m. In nonlinear analysis, soil model was considered using MCFC with parameters of yield surface such as Inner Friction Angle ϕ and Cohesion c .

4 Numerical Analysis

In this study, the ANSYS Workbench software package is used for simulating the foundation and soil interaction that differs from previous studies. Moreover, it offers more accuracy post-processing results and powerful optimization tools, such as Design Exploration, Topology Optimization, and other specialized tools, correctly, Application Customization Toolkit (ACT). A SOLID186 element is used for SFRC foundation and Homogeneous Soil with sizes of dimension of 2.00 × 2.00 × 0.15

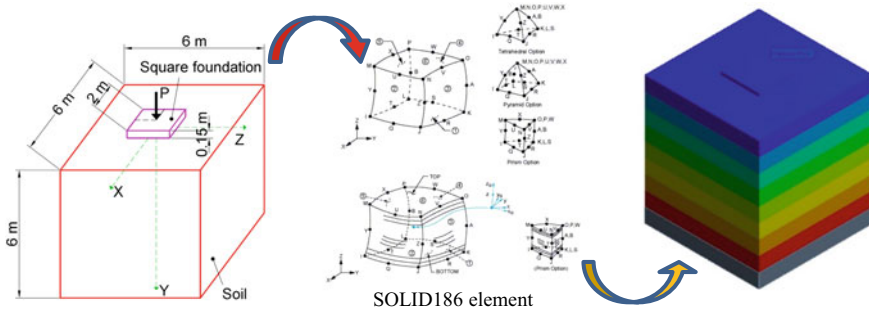


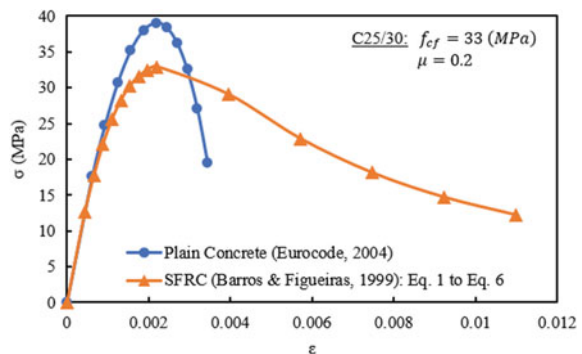
Fig. 4 Structural models in simulation

(m) and $6.00 \times 6.00 \times 6.00$ (m), respectively. Besides, IS model will be divided into several layers with layer thickness of 0.75 (m), shown in Fig. 4.

The material models that used for the concrete foundation structure in this study, including two models: Plain concrete model that is established according to [6] and SFRC model that proposed by [1]. Both models are described by a SSRC described in Sect. 3.1 and shown in Fig. 5. Characteristics of homogeneous or IS are made of clay with consistency class F4, and its thickness is about 6 m [14]. The soil model is homogeneous and heterogeneous that there is two primary parameters, E_{def} and μ for linear analysis, while MCFC is applied for nonlinear behavior analysis. Moreover, E_{def} of IS is calculated by Eq. 7 with $E_0 = 12.5$ MPa [14] and is gradually increased in-depth as shown in Fig. 6.

All boundary and contact conditions are shown in Fig. 7. The selection of the boundary conditions is consistent with the previous study [14] because of its result of displacement of SFRC foundation is the basis for verifying the results of the proposed material model in this study.

Fig. 5 Concrete models



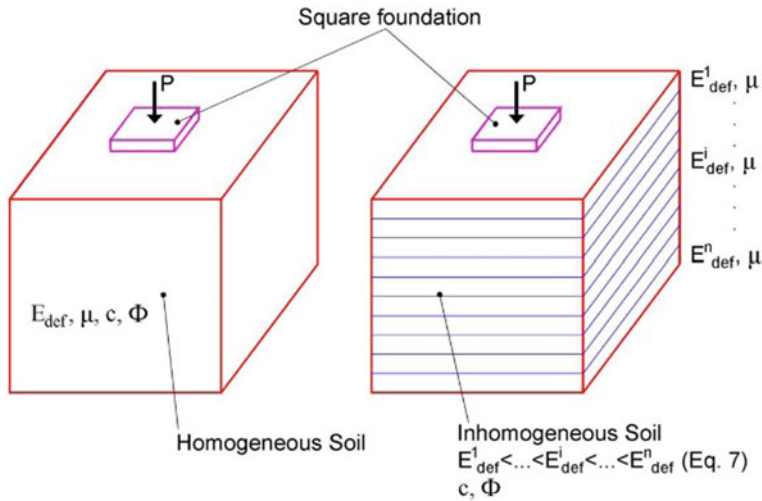


Fig. 6 Homogeneous and IS models

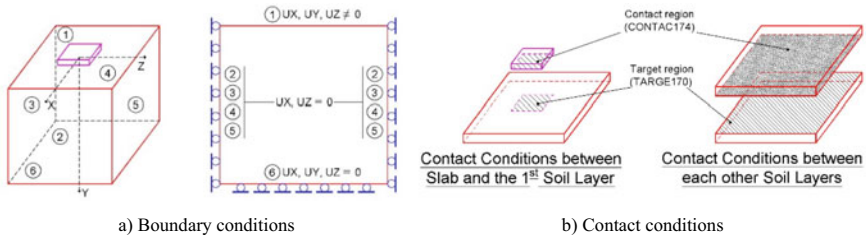


Fig. 7 Constraint conditions for interaction problem

5 Result and Discussion

The results of the displacement of the SFRC foundation are shown in Fig. 8, it is demonstrating that the SFRC material model is proposed by the SSRC set from Eqs. 1 to 6, giving more accurate results than the previous research [14] as compared with the results of experiments.

After the evaluation step, the proposed model achieved the accepted accuracy. The authors analyze the effect of the model on shear deformation. As shown in Fig. 9, the normal stress and shear stress relationship visually shows values within the safety limit. Moreover, SFRC Foundation and IS model in this study has more values outside the failure surface with native soil considering as perfect consolidation soil. The question for this research to be continued developing is: If the land is no less than saturated or partially saturated, will the proposed model be better? With these questions, the authors continue to contact previous studies to find out answers to at least be saturated or unsaturated soil. It was unexpected when the studies of

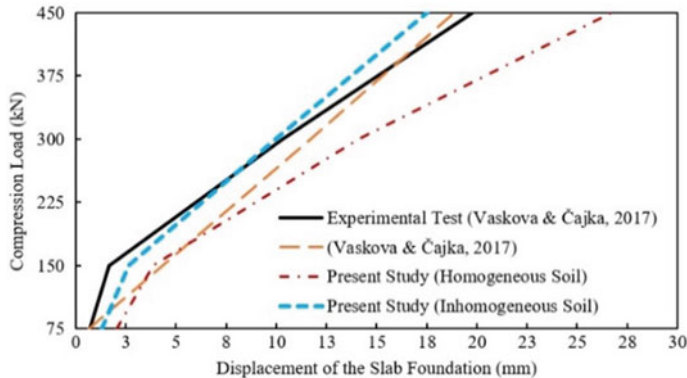


Fig. 8 The results of the displacement of the foundation slab

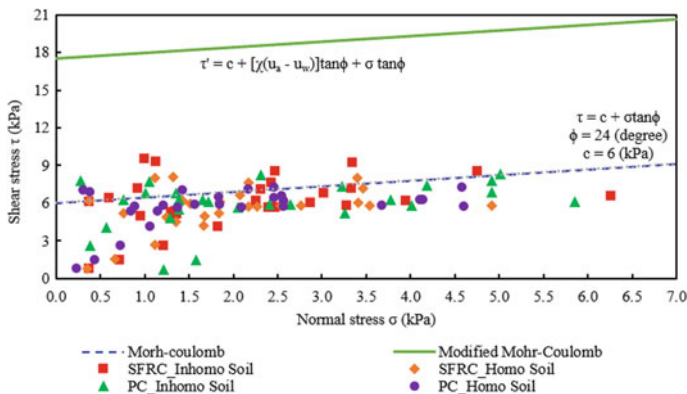


Fig. 9 The shear stress and normal stress relationship

[5, 10, 12, 13] showed a failure surface change when performed according to Mohr-Coulomb criteria. The soil is assumed in the present study to be in consolidation and fully saturated state, $\chi = 1$ is the effective stress parameter, matric suction ($u_a - u_w$) will be referred from chart of soil-water characteristic curves [11] with a degree of saturation $S = 24$, and shear strength may be described by incorporating the modified effective stress expression into the classical Mohr-Coulomb failure criterion [10] as shown in Fig. 9.

6 Conclusion

This study demonstrates reliable obtained results in the problem of interaction between foundation and soil using simulation software, ANSYS Workbench, compared with an experimental test. In the numerical analysis, SOLID186 element is assigned for both SFRC foundation, and IS. Nonlinear behavior of above two structural types is considered under the effects of axial compression loads. Moreover, the behavior analysis procedure of the foundation in the interaction problem considers large deformation with the SSRC of the SFRC material given a faster convergence result. Also, it shows the necessity in building material models with mathematical models based on essential parameters of material characteristics that are necessary and also capable of developing better models in future research.

Acknowledgements The authors gratefully acknowledge the financial support granted by the Scientific Research Fund of the Ministry of Education and Training (MOET), Vietnam. (No. B2019–MBS–01). The authors would also like to thank colleagues at Ho Chi Minh City Open University for supporting this project.

References

1. Barros JA, Figueiras JA (1999) Flexural behavior of SFRC: testing and modeling. *J Mater Civ Eng* 11(4):331–339
2. Bencardino F, Rizzuti L, Spadea G, Swamy RN (2008) Stress-strain behavior of steel fiber-reinforced concrete in compression. *J Mater Civ Eng* 20(3):255–263
3. Buchta V, Janulikova M, Fojtik R (2015) Experimental tests of reinforced concrete foundation slab. *Procedia Eng* 114:530–537
4. Čajka R, Křivý V, Sekanina D (2011) Design and development of a testing device for experimental measurements of foundation slabs on the subsoil. *Trans VŠB Tech Univ Ostrava Civ Eng Ser* 11(1):1–5
5. Chen P, Wei C, Liu J, Ma T (2013) Strength theory model of unsaturated soils with suction stress concept. *J Appl Math*. <https://doi.org/10.1155/2013/756854>
6. Eurocode C (2004) 2: design of concrete structures—part 1-1: general rules and rules for buildings (EN 1992-1-1: 2004). Comité Eur de Normalisation, Brussels
7. Feda J (2013) Stress in subsoil and methods of final settlement calculation. Elsevier, vol 18
8. Kaniraj SR (1988) Design aids in soil mechanics and foundation engineering. Tata McGraw-Hill
9. Labudková J, Čajka R (2017) 3D numerical model in nonlinear analysis of the interaction between subsoil and SFCR slab
10. Lu N, Likos WJ (2006) Suction stress characteristic curve for unsaturated soil. *J Geotech Geoenviron Eng* 132(2):131–142
11. Rahardjo H, Fredlund DG (1995) Experimental verification of the theory of consolidation for unsaturated soils. *Can Geotech J* 32(5):749–766
12. Russell A, Khalili N (2006) A unified bounding surface plasticity model for unsaturated soils. *Int J Numer Anal Meth Geomech* 30(3):181–212
13. Vanapalli S, Salinas L, Avila D, Karube D (2004) Suction and storage characteristics of unsaturated soils. Paper presented at the unsaturated soils: proceedings of the third international conference on unsaturated soils, UNSAT 2002, 10–13 March 2002, Recife, Brazil

14. Vaskova J, Čajka R (2017) 3D numerical model of the subsoil-structure interaction and comparison of the results with experimentally measured values. Paper presented at the key engineering materials
15. Vašková J, Čajka R (2018) Interaction of nonlinear numerical model of SFRC slab and nonlinear numerical subsoil model. Int J GEOMATE 15(47):103–110

Application of Bailey Method in Determining Aggregate Gradation in Dense Graded Asphalt Concrete in Vietnam



Manh Tuan Nguyen

1 Introduction

Permanent deformation or rutting is the most distress in flexible pavement of heavy traffic roads in Vietnam these days such as National Highway No. 1, No. 3, and No. 5. From many researchers, the factors caused rutting are as follows:

- The increased traffic volume especially heavy truck;
- The high temperature;
- Pavement design is not appropriate;
- Quality material including asphalt binder, aggregate, and filler; and
- Construction technology, especially compaction method.

From above causes, the studies and solutions to overcome the rutting distress are becoming urgent and necessary. In developing countries such as United States, England, Germany, Japan, or Korea, the asphalt binder used in asphalt concrete is polymer modified asphalt (PMA) to improve the quality of asphalt concrete i.e. increasing the adhesive between aggregate and binder, improving the performance of material under hot and/or cold weather, and resistance to rutting [1]. In Vietnam, there are the specifications and construction method of asphalt concrete used PMA binder. However, the asphalt concrete used PMA is not applied widely in Vietnam because the cost of construction and material is much more expensive than conventional asphalt concrete. As a result, the solution without increasing the cost of construction, which is the role of aggregate gradation, is one of requirement solution in Vietnam.

The Bailey method was developed by Robert D. Bailey of the Illinois Department of Transportation in the early 1980s. The Bailey method gives a good method for mix design and a supplement to adjust at the plant in order to improve air voids,

M. T. Nguyen (✉)

Faculty of Civil Engineering, Ho Chi Minh City University of Technology, VNU-HCM, Ho Chi Minh City, Vietnam

e-mail: nmanhtuan@hcmut.edu.vn

VMA and overall workability of the mix when using Marshall or Superpave method [11]. The concentration of Bailey method is the aggregate packing that includes coarse aggregate structure and the particles fit into the voids within that structure. The aggregate gradations based Bailey method were used around the world and had high efficiency in United Arab Emirates, France, Canada and many states in United States [9, 10].

In Vietnam, there are not many studies based Bailey method. In 2015, Nguyen and Nguyen [8] introduced Bailey method for designing a gradation of dense graded asphalt concrete in a Vietnam paper. In 2016, Tran DH and Tran TKD applied Bailey method for gradation design of asphalt treated base which nominal maximum size is 25 mm used in the base of flexible pavement although the Bailey method is used for asphalt concrete.

This paper shows principles of Bailey method, simple steps for aggregate gradation design, and the evaluation of five aggregate gradations in which two of them are from Bailey method. The paper also focuses on mechanical properties of five gradations including Marshall stability, indirect tensile strength, resilient modulus based Vietnam specification, as well as wheel tracking test.

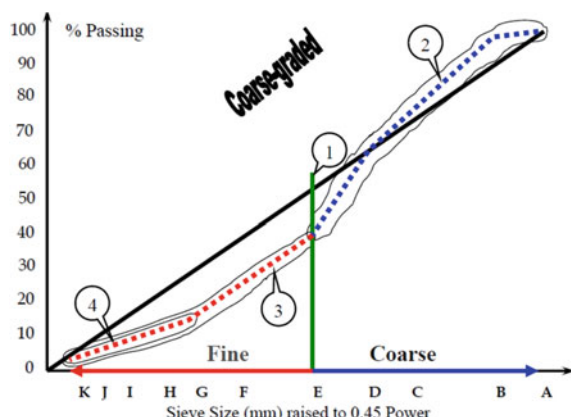
2 Mix Design Based Bailey Method

2.1 Bailey Method

There are four principles to consider from the Bailey method:

- Determine the coarse and fine and which one is in control of the aggregate structure (No. 1 and 2 in Fig. 1);
- The packing of coarse portion in coarse aggregate;

Fig. 1 The four Bailey method principles



- The coarse portion of fine aggregate relates to the packing of the overall fine fraction in the combined blend (No. 3 in Fig. 1);
- The fine portion of fine aggregate relates to the packing of the fine portion of the gradation in the blend (No. 4 in Fig. 1).

According to Circular number E-C044 [9], the Bailey method design calculation for hot-mix asphalt mixture gradation could be showed from 13 steps in Fig. 2. The Bailey ratios or aggregate ratios are CA ratio, FAc ratio, and FAf ratio presented in Table 1.

$$\text{CA ratio} = \% \text{ Passing Half Sieve} - \% \text{ Passing PCS}/(100 - \% \text{ Passing Half Sieve}) \quad (1)$$

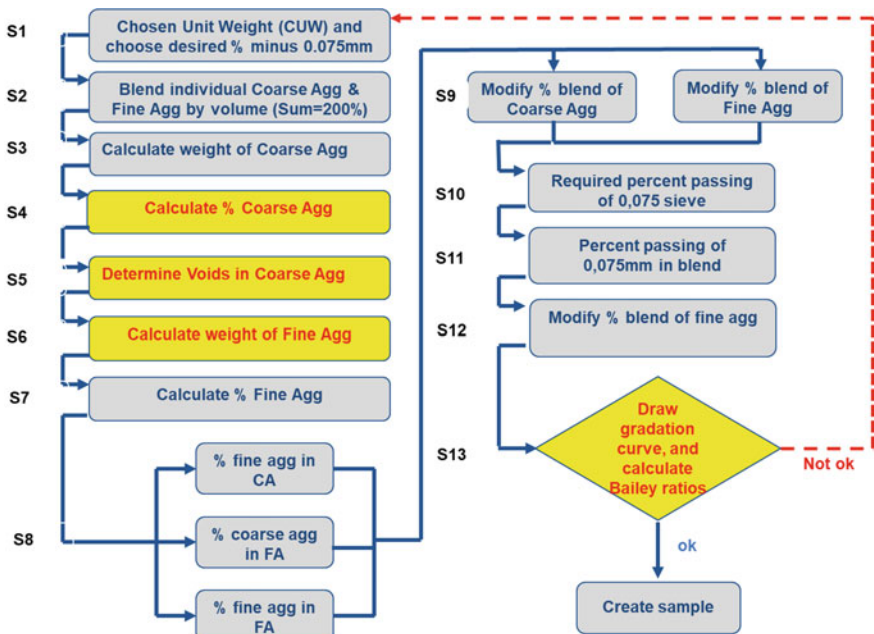


Fig. 2 Steps from Bailey method

Table 1 Recommended aggregate ratios [9]

Nominal maximum aggregate size (mm)	19.0	12.5	9.5
CA ratio	0.60–0.75	0.50–0.65	0.40–0.55
FAC ratio	0.35–0.50	0.35–0.50	0.35–0.50
FAf ratio	0.35–0.50	0.35–0.50	0.35–0.50

Note CA coarse aggregate; FAC coarse portion in fine aggregate; FAf fine portion in fine aggregate

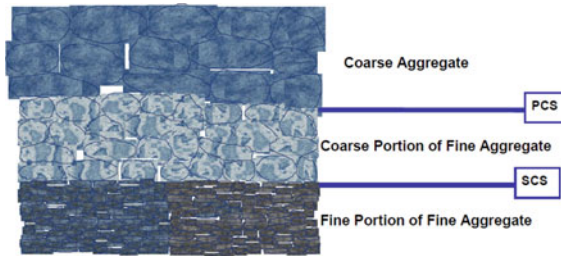


Fig. 3 The divisions in a continuous gradation [9]

$$\text{FAc ratio} = (\% \text{ Passing SCS}) / (\% \text{ Passing PCS}) \quad (2)$$

$$\text{FAf ratio} = (\% \text{ Passing TCS}) / (\% \text{ Passing SCS}) \quad (3)$$

where: PCS = Primary control sieve; SCS = Secondary control sieve; TCS = Tertiary control sieve as shown in Fig. 3.

2.2 Grading Design

There are five gradations, as shown in Fig. 4, which nominal maximum particle size of 12.5 mm are chosen in this study and two of them are from Bailey method to have the aggregate gradation. The gradation 3, 5, 4 are near the top limit, the bottom limit, and middle between bottom and top limit, respectively. The gradation 1 has the feature that the small size is near the bottom limit and the big size is near the

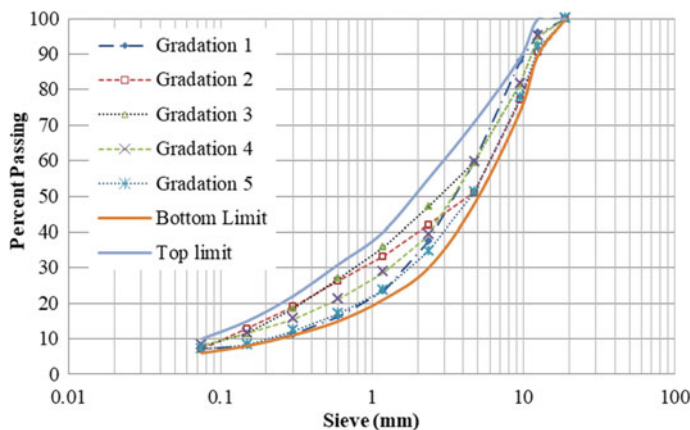


Fig. 4 Aggregate gradations in this study (bottom and top limit based on TCVN 8819:2011 [3])

Table 2 Aggregate ratios

Type	CUW (%)	Aggregate ratios		
		CA	FAc	FAf
Gradation 2	95	0.54	0.43	0.49
Gradation 5	103	0.61	0.489	0.485

top limit. In contrast with gradation 1, the gradation 2 has the small size near the top limit and the big size near the bottom limit. For gradation design from Bailey method, two mixes, which are gradation 2 and 5, prepared based 95% and 103% of CUW (chosen unit weight) which are compaction behaviour. Their aggregate ratios are conducted and presented in Table 2.

3 Gradation Evaluation

3.1 Material

In this study, the asphalt binder, which penetration grade is 60/70 from Petrolimex Corporation in Vietnam, is used. The mechanical properties of asphalt binder are presented as follows (Table 3).

The aggregate is from Tan Dong Hiep, Binh Duong Province, Vietnam. The gradations are used shown in Fig. 4. The mix design is conducted based Marshall method or TCVN 8820:2011 [4] specification published by Vietnam MOT. The final goal of mix design is the optimum asphalt content of gradation 1, 2, 3, 4, 5 that are 5.43%, 4.97, 5.74, 5.65, 5.71% by total weight of asphalt concrete, respectively. The air void of five mixtures is about 4%.

Table 3 Asphalt binder properties

No	Characteristic	Result	Requirement from TCVN 7493-2005 [2]
1	Penetration at 25 °C, 0.1 mm	64	60–70
2	Softening point from ring and ball test, °C	49.5	46
3	Flash point, °C	>300	Min 232
4	Ductility at 25 °C, cm	>110	Min 100
5	Adhesion with aggregate	Level 3	Min level 3
6	Specific gravity, g/cm ³	1.03	1–1.05



Fig. 5 Set-up for Marshall stability, indirect tensile strength, resilient modulus, and wheel tracking test (from left to right)

3.2 Test Results and Discussion

Marshall stability, indirect tensile strength at 25 °C, resilient modulus at 30 °C, are conducted for evaluating of five mixtures; three replicates for each mixtures were made at 4% air void and conducted tests. The wheel tracking test is used to evaluate three mixtures which are 1st, 2nd, and 3rd gradation because of the limit of fund and time; one replicate for each mixture was made at 7% air void.

Marshall stability was obtained according to TCVN 8820:2011 specification [4]. Before testing, all specimens were kept in water at 60 °C for 40 min and then loaded with a constant compression rate of 50 mm/min as shown in first picture in Fig. 5. The maximum load applied to the specimen is the Marshall stability.

The indirect tensile strength (IDT) was obtained by a compressive load based on TCVN 8862-2011 [5]. The compressive load increased continuously and evenly with displacement rate (50 mm/min) regulations until the specimen is damage. The tensile strength of the material is calculated from load which created the damage of specimen (P) as follows:

$$R = 2P/\pi HD \quad (4)$$

where D and H are the specimen diameter and height, respectively (mm).

Before the resilient test, all specimens were prepared based 22TCN 211-06 [7] and put in the chamber at 30 °C. The resilient modulus tests were conducted by using the 0.5 MPa of loading pressure (p) into asphalt concrete specimens. The resilient modulus (E) of asphalt concrete is determined from resilient displacement (L) as follows:

$$E = pH/L \quad (5)$$

where H is also the specimen height (mm).

According to 1617/QD-BGTVT [6], the specimen dimensions of wheel tracking test are 300, 300, and 50 mm. The specimens were created by using roller compaction and put in the air about 1 days before testing. The test is conducted in water at 50 °C by using steel wheel as shown in the last picture of Fig. 5. The frequency of wheel over the specimen is 25 ± 5 cycles per minute.

The results of four types of evaluated test are shown in Fig. 6.

Figure 6 shows that the gradations which affect to the mechanical properties. The gradation 2 and 5 are from Bailey method but they are different in chosen CUW; as a result, the gradation 2 give the best based mechanical properties. Besides, the Fig. 7 shows that there are good relationships between VMA (voids in mineral aggregate) from gradation and Marshall stability, indirect tensile strength, and resilient modulus because the coefficient of determination (R^2) are rather good, bigger than 0.7. The results from Fig. 7 shows that the mixture which has the smallest VMA could have the best mechanical properties.

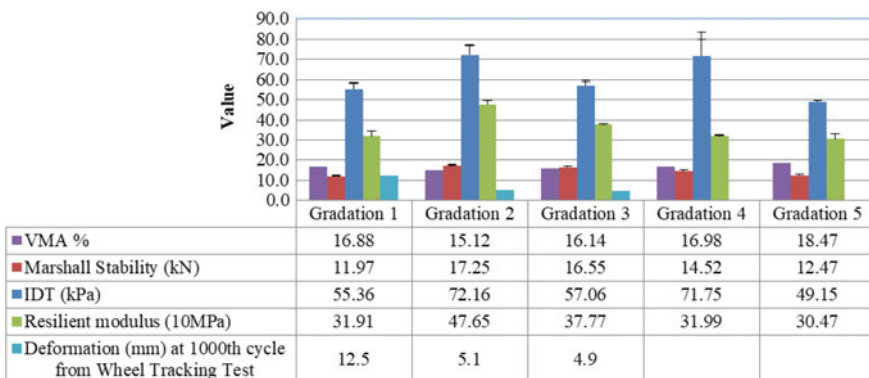
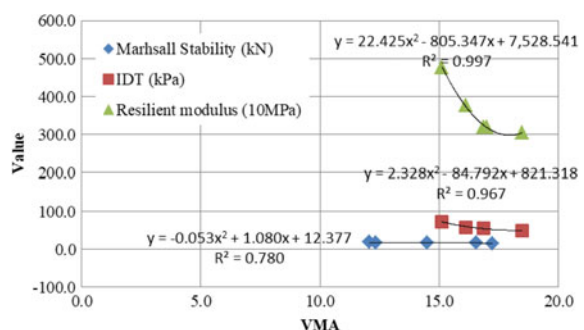


Fig. 6 Results of VMA, Marshall stability, indirect tensile strength, resilient modulus, and tracking test

Fig. 7 Relationship between VMA and Marshall stability, indirect tensile strength, and resilient modulus



Mixture based gradation 1, 2, and 3 were conducted the wheel tracking test and the asphalt concrete mixture from gradation 2 and 3 gives the better rutting performance than gradation 1. Maybe the mixture that has smallest VMA also give the best resistance in terms of rutting performance.

4 Conclusion

In this paper, the principles and design step of Bailey method are presented. Two gradations were applied the Bailey Method beside other three gradations. Five mixtures based five gradations were designed based on Marshall method and evaluated from Marshall stability, indirect tensile strength and resilient modulus. Three mixtures are conducted by using wheel tracking test. The following conclusions are from the obtained results:

- The optimum asphalt content of mixture which has gradation 1, 2, 3, 4, 5 is 5.43%, 4.97, 5.74, 5.65, 5.71% by total weight of asphalt concrete, respectively;
- The mixture which has 95% of CUW or gradation 2 is better than the mixture which has 103% of CUW in terms of Marshall stability, indirect tensile strength, resilient modulus value;
- There are good correlations between voids in mineral aggregate and Marshall stability, indirect tensile strength, as well as resilient modulus. The smaller VMA give better performance.

References

1. Kim TW, Baek J, Lee HJ, Choi JY (2013) Fatigue performance evaluation of SBS modified mastic asphalt mixtures. *J Constr Build Mater* 48:908–916
2. Ministry of Science and Technology, Bitumen—specifications, TCVN 7493-2005, Vietnam (2005)
3. Ministry of Science and Technology, specification for construction of hot mix asphalt concrete pavement and acceptance, TCVN 8819:2011, Vietnam (2011)
4. Ministry of Science and Technology: standard practice for asphalt concrete mix design using Marshall Method, TCVN 8820:2011, Vietnam (2011)
5. Ministry of Science and Technology: standard test method for splitting tensile strength of aggregate material bonded by adhesive binders, TCVN 8862:2011, Vietnam (2011)
6. Ministry of Transportation: decision on technical guide of determining rutting susceptibility of asphalt paving mixtures using the wheel tracking, 1617/QD-BGTVT, Vietnam (2014)
7. Ministry of Transportation: flexible pavement—requirements and design guide, 22TCN 211-06, Vietnam (2006)
8. Nguyen MT, Nguyen HV (2015) Thiết kế sự phân bố cốt liệu cho hỗn hợp bê tông nhựa bằng phương pháp Bailey (Design of aggregate gradation in asphalt concrete by using Bailey method). *Vietnam J Transp* 11(51):42–44
9. Vavrik WR, Huber G, Pine WJ, Carpenter SH, Bailey R (2002) Bailey method for gradation selection in hot-mix asphalt mixture design. *Transportation Research Board Circular No.E-C044*, Natl Res Counc, Washington DC

10. Vavrik WR, Pine WJ, Huber G, Carpenter SH (2001) The Bailey method of gradation evaluation: the influence of aggregate gradation and packing characteristic on voids in the mineral aggregate. *J Assoc Asphalt Paving Technol* 70
11. Vince A, Pine WJ, Lum P (2009) The Bailey method—achieving volumetric and HMA compatibility. Course Materials and Handouts (2009)

Application of EPS in the Road Construction on Soft Grounds



Hirahara Naoyuki, Le Ba Vinh, Satoshi Kobayashi, and To Le Huong

1 Introduction

In the road construction practice, there are two common types of geofoam as Expanded Polystyrene (EPS) and Extruded Polystyrene (XPS). Because EPS has a density that is less than 1% of typical soil fills, this lightweight material is used to reduce vertical stresses beneath embankments, or to reduce lateral stresses on retaining walls, abutments or foundations. Especially, using EPS fills for the soft ground condition can save time and construction costs as compared to other solutions of soft ground improvement or reinforcement. EPS has been used in highway construction in Norway since 1972 [2], and after that was used in other countries. The remarkable effect of subsidence mitigation was confirmed after using EPS for the soft ground condition. In Japan, the cumulative amount of EPS has been gradually increased up to 8,000,000 m³ since 1985. Figure 1 shows a typical road construction using EPS in Japan. Based on the case studies, the applicability of EPS solution for the soft ground conditions, especially in Vietnam, is analysed in this paper.

H. Naoyuki · S. Kobayashi
Okasan Livic Co. Ltd., Tokyo, Japan

L. B. Vinh (✉) · T. L. Huong
Faculty of Civil Engineering, Ho Chi Minh City University of Technology, VNU-HCM, Ho Chi Minh City, Vietnam
e-mail: lebavinh@hcmut.edu.vn



Fig. 1 Road construction using EPS in Japan [3]

2 Physical and Mechanical Characteristics of EPS General Paper Style

2.1 Physical Characteristics of EPS

A typical EPS block and XPS block measuring (2.0 m × 1.0 m × 0.5 m) and 2.0 m × 1.0 m × (0.1–0.5 m), respectively. Common types of EPS, XPS, and its unit weights are shown in Table 1.

* Uniformity Test of EPS Block

In the case of non-uniform material, stress concentrates on the spot with low density, causing local deformation. Therefore, several uniformity tests have been carried out to ensure EPS's quality. Firstly, Japanese and Taiwanese blocks are cut into small elements to measure its density. Then, these values are compared with the specification of 20 kg/m³ (+1.5/-1.0). Test results of Japanese blocks showed a rate of 0.5% out of specification, meanwhile this rate is 51.6% for Taiwanese blocks as shown in Figs. 2, 3, and 4, 10 pieces were smaller than the standard value, and the variation in density was very large. Generally, Japanese EPS block is specially manufactured for civil engineering; specific strength, uniformity and flame retardancy are ensured. In manufacturing process, some technical know-how such as choosing raw material and molding control is necessary.

Table 1 Types of EPS, XPS, and its physical properties

Type	Expanded polystyren (EPS)			Extruded polystyren (XPS)		
	D-30	D-25	D-20	DX-35	DX-29	DX-24H
Unit weight (kN/m ³)			+0.015			
	0.30	0.25	0.20	0.35	0.29	0.24
	±0.02	±0.015	-0.01	±0.03	±0.03	±0.03
Allowable compressive stress (kN/m ²)	90	70	50	200	140	100

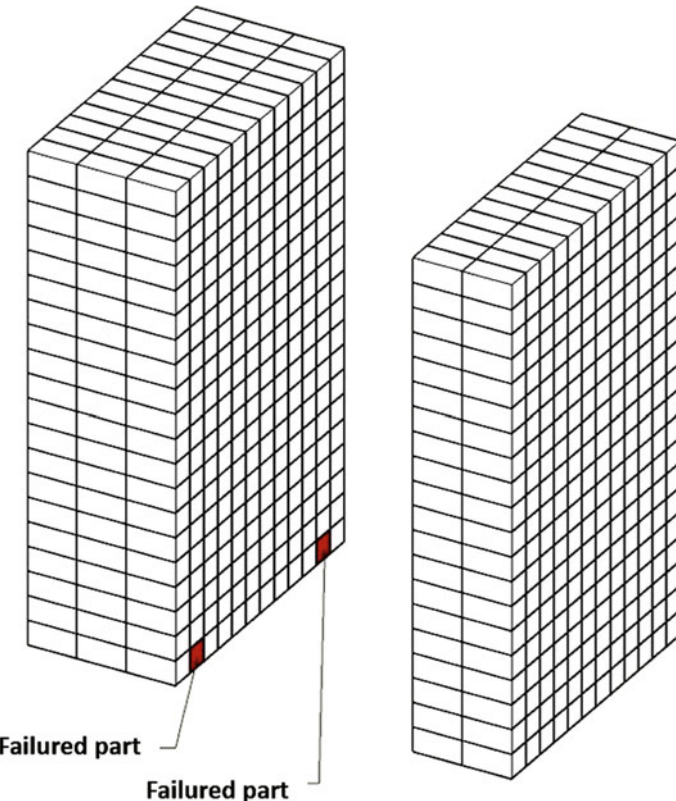


Fig. 2 Japanese D-20 (1) locations of failure

2.2 *Compression Property*

In Japanese standard, the strength at 10% strain is defined as the maximum compressive stress. The elastic limit is about half of the maximum strength, which is approximately equivalent to the strength at 1% strain. We need to adopt an appropriate block to withstand the assumed loads. The allowable compressive stress of various EPS is shown in Fig. 5 and Table 1.

2.3 *Flammability and Durability of EPS Block*

Flammability: Flame retardant is added in the raw material and it extinguishes the fire within 3 s if the fire source is kept away. EPS blocks can be normally used in a temperature condition which is lower than 80 °C.

Weatherability: EPS block can be discolored by the ultraviolet radiations.

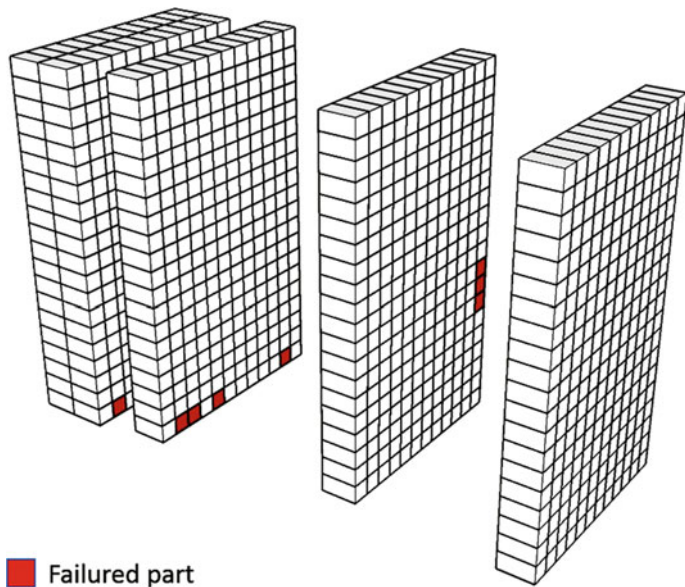


Fig. 3 Japanese D-20 (2) locations of failure

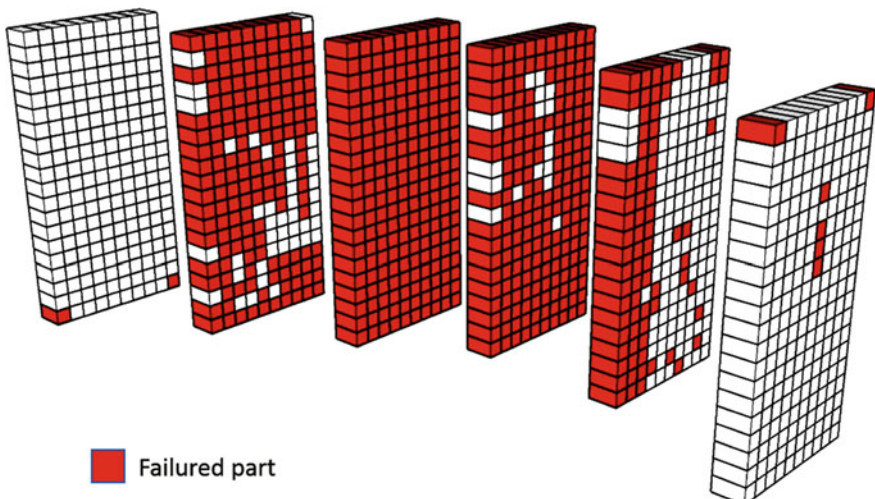
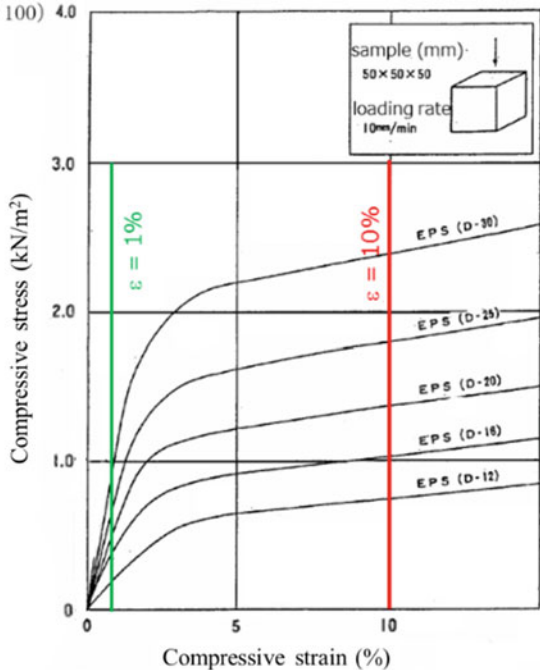


Fig. 4 Taiwanese D-20 locations of failure

Fig. 5 Relationship between stress-strain of EPS



Chemical resistance: EPS block can be dissolved in gasoline, asphalt, and oil paint, however it is stable against cement, sea water, water-based paint. Therefore, EPS blocks should be covered by soil, facing material and concrete.

3 Design Aspects of the Application of EPS in the Road Constructions [1]

EPS solution comes from the idea that when building a road base with light materials on soft ground, it will cause a small settlement or not cause subsidence. Therefore, using EPS fills for the soft ground condition can save time and construction costs as compared to other solutions of soft ground improvement or reinforcement.

Excavation depth is determined in principle which there is no increment of the load on soft ground after the embankment construction as shown in Fig. 6. Based on a stress distribution inside the EPS ground as shown in Fig. 7, types of EPS material are calculated to ensure its strength. In case the groundwater level is high, it is necessary to consider the effect of buoyancy force on EPS blocks. A safety factor of buoyancy which is larger than 1.3 can be achieved by designing EPS blocks for buoyancy as shown in Fig. 8. These special EPS blocks have a large void ratio of 0.6, so the buoyancy force can be 0.4 times reduced.

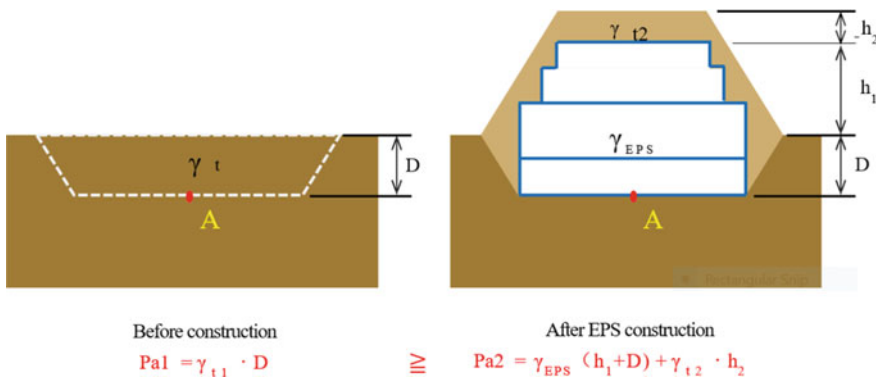


Fig. 6 Design principle of EPS—embankment on soft grounds

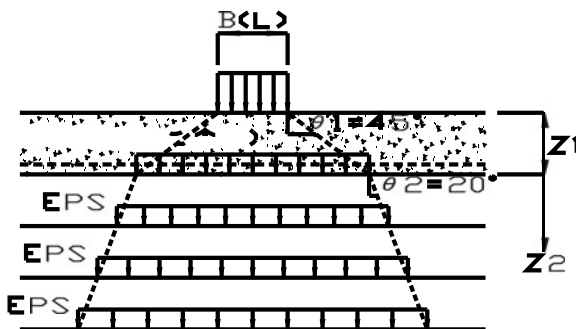


Fig. 7 Stress distribution inside the EPS ground

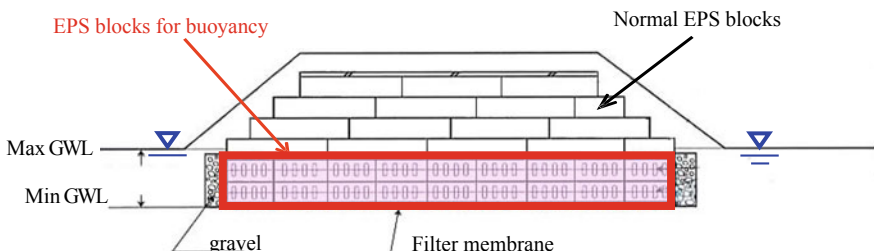


Fig. 8 Design of EPS blocks for buoyancy

4 Case Studies of Application of EPS in the Road Constructions

4.1 Damage Investigation of Sanriku Expressway, Japan

Yamato-Ishinomaki road is an embankment section of Sanriku Expressway as shown in Fig. 9. In 2011, the Great East Japan Earthquake occurred with Japanese seismic scale 6+ in this section and damaged several roads. The total length of this expressway is 26.5 km and there were two lanes at the time of the earthquake. EPS was used at 11 bridges of Yamato-Ishinomaki road as shown in Fig. 10. EPS Construction Method Development Organization of Japan, EDO, conducted a visual observation on the back of the abutment of the remaining 7 bridges. According to the Ministry of Land, Infrastructure and Transport report, the whole ground of Ishinomaki City subsided about 30 cm. At the abutments where the most serious damage occurred, EPS embankment followed the ground settlement which is approximately 8–27 cm. Most of the settlement of EPS was likely to be attributed to the settlement of the ground under EPS as shown in Fig. 11. At the other abutments which used EPS,

Fig. 9 Arial view of Sanriku expressway



Fig. 10 Using EPS at the connection between the access embankment and the abutment

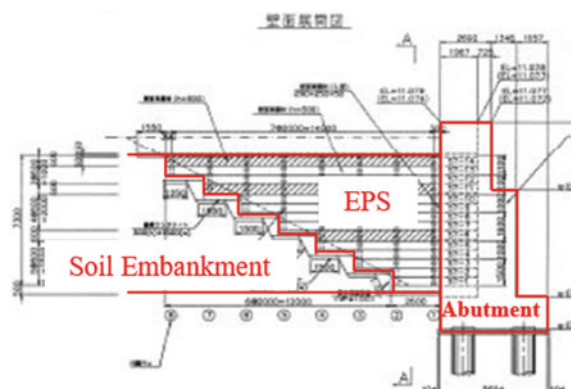


Fig. 11 Settlement of the access embankment, Fukumura-Bridge A1

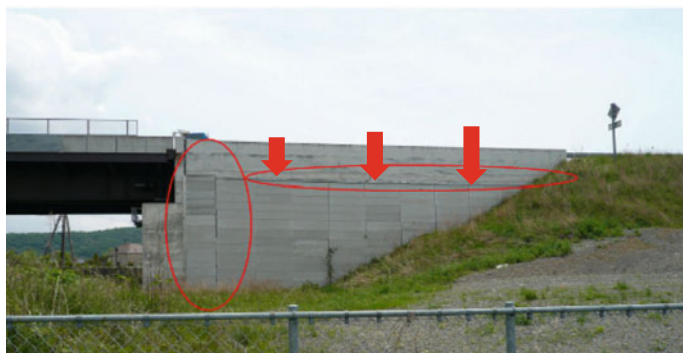


Fig. 12 Deformation of the facing panel, Sobanokami-Bridge A1

settlement caused small deformation on the facing panel and the protective panel at the edge, but not severe as shown in Fig. 12; and the whole embankment was kept its stability. Despite the destructive earthquake as Japanese seismic scale 6+, the road resumed its service in only 3 days as an emergency road. These results showed that EPS had sufficient functions against large earthquakes.

4.2 A Pilot Test of Embankment Construction in Phu My, Viet Nam

In Vietnam, there is often a differential settlement at the position between the bridge abutment and the backfill soil which seriously affects the traffic condition. The heavy-weight of the high embankment and thick layers of soft soil results in the large settlement. However, the lightweight material as EPS is quite new and has not been widely used in Vietnam. Therefore, a pilot test of EPS construction has been planned to consider the effectiveness of this solution in Vietnam condition.

Tables 2 and 3 shows the geotechnical design parameters for each soil layer and embankment's material, respectively. According to the design plan, three cases of embankment construction are considered and shown in Figs. 13, 14 and 15. Case 1 uses the filling soils for the conventional embankment construction. In case 2, EPS material is used to replace most of the filling soils in case 1. Similarity, in the last case, EPS material is also used to replace most of the filling soils and a surface layer in case 1. Calculation results of the consolidation settlement of each case are shown in Fig. 16. At the degree of consolidation of 90%, there is a remarkable amount of the consolidation settlement of 0.284 m for case 1. This settlement is larger than the consolidation settlement of 0.071 m in case 2, meanwhile there is no consolidation settlement in case 3. The additional simulation of case 1 by PLAXIS 3D [4] as shown in Figs. 17, 18 and 19 also results in small difference with the analytical settlement.

Table 2 Geotechnical design parameters for each soil layer

Layer	H (m)	γ (kN/m ³)	e_0	C _C	C _S	P _C (kPa)
Silt	3	15.4	1.848	0.750	0.123	46.4
Clay	5	19.8	0.667	0.137	0.045	216.0

Table 3 Design parameters for embankment's material

Layer	Earth fill	Soil	Concrete	EPS (DX-24)	EPS (D-20)	Sand
H (m)	3.5	0.65	0.15	0.5	2.1	0.1
γ (kN/m ³)	19.0	19.0	23.0	0.24	0.20	19.0

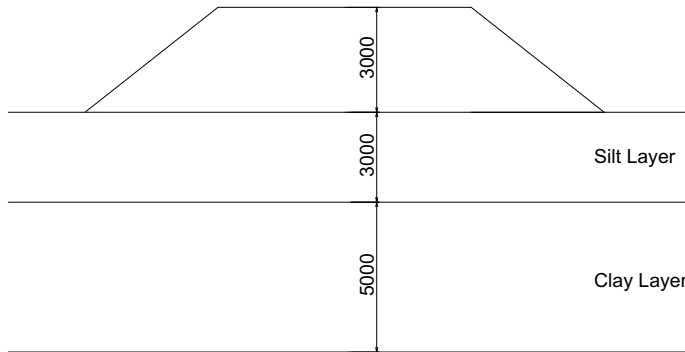


Fig. 13 Embankment construction using earth fill, case 1

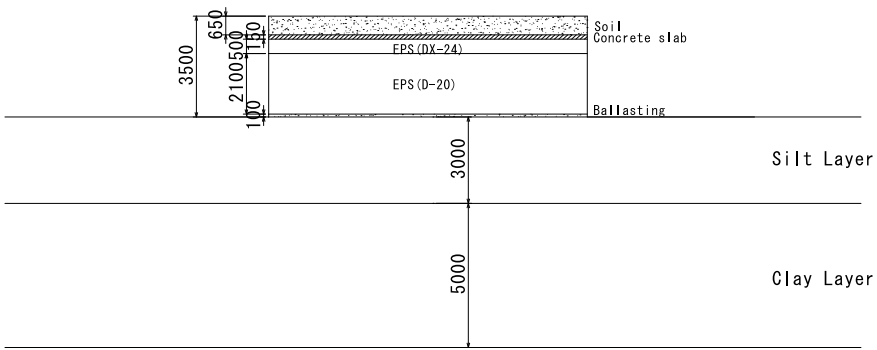


Fig. 14 Embankment construction using EPS fill, case 2

Fig. 15 Embankment construction using EPS fill, case 3

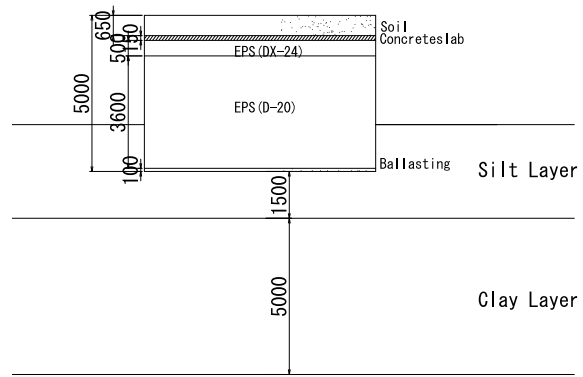
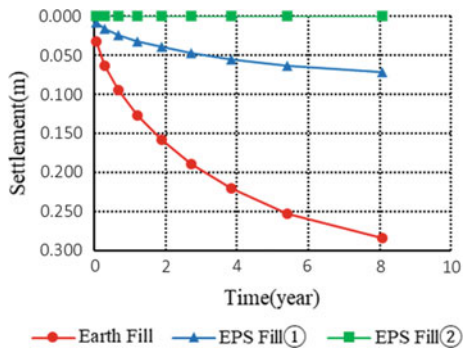


Fig. 16 Change of the consolidation settlement with time



5 Conclusions

Because of its lightweight and independence, EPS is a unique construction method which can be used for repairing the road damaged by disaster. The past observation

Fig. 17 3D mesh of embankment model in PLAXIS

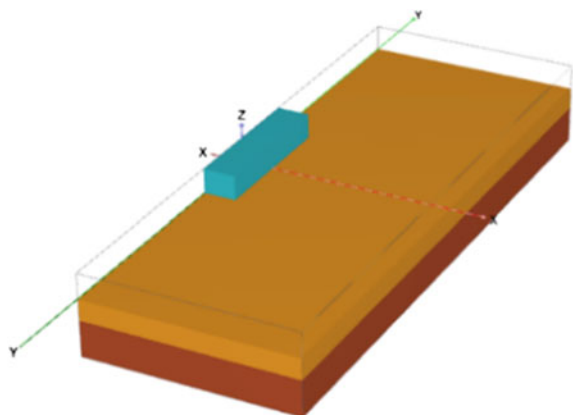
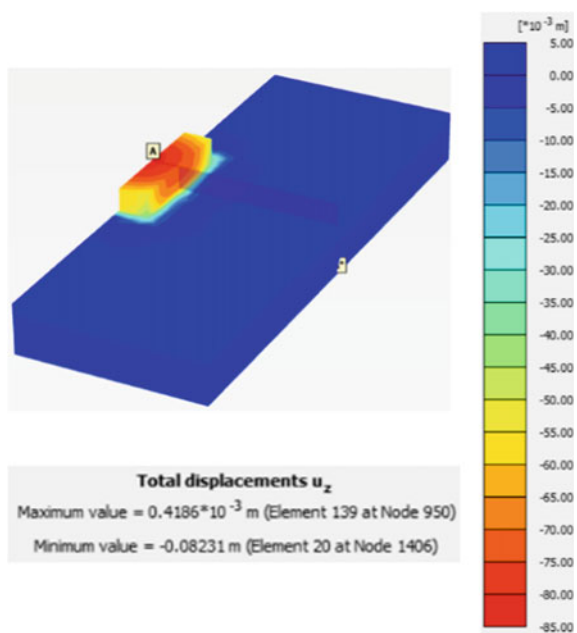
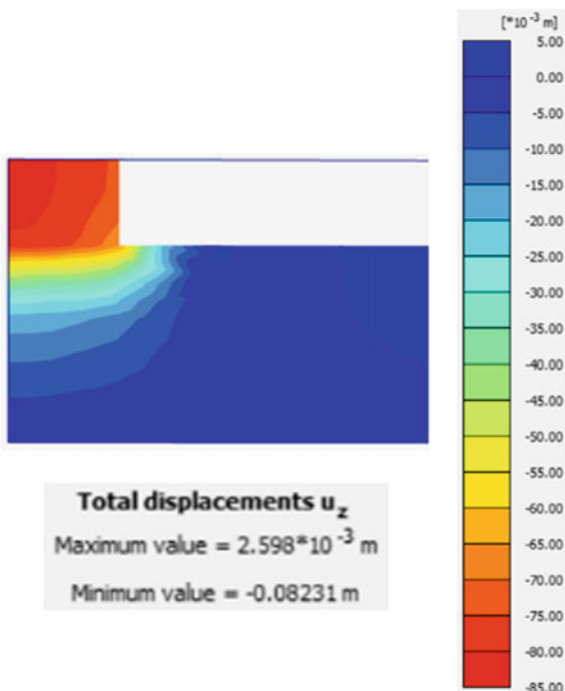


Fig. 18 3D displacement of embankment model in PLAXIS



results of several EPS embankments in Japan showed that EPS had sufficient functions against large earthquakes. EPS fills for the soft ground condition can save time and construction costs as compared to other solutions of soft ground improvement or reinforcement. EPS fills on the soft ground of Vietnam may result in an allowable amount of settlement or no consolidation settlement. Because EPS solution is quite new and has not been widely used in Vietnam, it is necessary to develop the Vietnamese standards to promote the EPS construction method in Vietnam.

Fig. 19 Vertical displacement of embankment model in PLAXIS



References

1. EDO (EPS Development Organization: JAPAN) (2007) EDO-EPS method designing/application code (in Japanese)
2. Frydenlund TE, Aaboe R (2001 December) Long term performance and durability of EPS as a lightweight filling material. In: Proceedings of EPS Geofoam 2001, 3rd international conference, Salt Lake City, pp 1–14
3. Miki G (1996) EPS construction method in Japan. In: Proceedings of international symposium on EPS (expanded poly-styrol) construction method, (EPS-Tokyo'96), Japan, pp 2–7
4. Plaxis (2017) Plaxis 3D reference manual

Back Analysis on Deep Excavation in the Thick Sand Layer by Hardening Soil Small Model



Quoc Thien Huynh, Van Qui Lai, Viet Thai Tran, and Minh Tam Nguyen

1 Introduction

Analysing the behaviour of Diaphragm wall (D-wall) by FEM with HS model was successfully implemented in many researches [1, 2]. However, using the HHS model, which was the modification of HS model with advanced parameters, can give better results than those ones from HS model in some cases [3, 4]. Applying the HSS model in predicting the response of D-wall is still limited in Viet Nam and Ho Chi Minh City (HCMC). Besides, choosing the suitable parameters of soil sand model from investigated tests was still limited because it takes time and cost to get the well sample in sand layers. It is better if the parameter can be selected from empirical formulas or back-analysis. Therefore, this paper presented back analyses for 3 deep-basement projects in the thick layer of sand in HCMC. The main parameters of HSS model such as E_{50} , P_{ref} , G_0 , $\gamma_{0.7}$ were varied by the correlation between N(SPT) and depth z to get a well agreement between the results from predictions and measurements. Besides, the small comparisons between the calculated results from HS model and HSS model were also implemented.

Q. T. Huynh · V. Q. Lai (✉) · M. T. Nguyen

Faculty of Civil Engineering, Ho Chi Minh City University of Technology, VNU-HCM, Ho Chi Minh City, Vietnam

e-mail: lvqui@hcmut.edu.vn

V. T. Tran

Hoa Binh Construction Group Joint Stock Company, Ho Chi Minh City, Vietnam

2 Project Descriptions

The 3 studied projects including Madison project (Case A), Hai Quan project (Case B) and Saigon Center project (Case C), located at District 1, HCMC, as shown in Fig. 1a. Stratigraphic condition at the area could be divided into five layers, as described in Fig. 1b. In that, the third layer, loose to dense sand with stratum depth varied from top level -5 m to bottom level -40 m, was the most influence on the behaviour of the excavation, because excavating work of all stages was operated in this layer. For the analysis purposes, the correlation between the N(SPT) value and depth (z), which was synthesized from 20 investigated boreholes of the three projects, was proposed and shown in Eq. (1) and Fig. 1c.

$$N(SPT) = -0.0008z^3 - 0.0504z^2 - 1.3116z + 1.3549 \quad (1)$$

Three projects had excavation depths ranging from 15.5 to 28.5 m, and the number of basement floors ranged from three to five. The excavations were operated by different construction methods such as bottom-up, semi-top-down and top-down method. Diaphragm walls with the thickness ranging from 800 to 1000 mm and the depth from 37 to 60 m were used as the earth retaining structure. The cross sections and excavation sequences were described as Fig. 2. The inclinometers in the diaphragm walls were also installed to measure lateral displacements during construction phases.

3 The Parameter of Soil Models

Hardening Soil model (HS) is an advanced model based on isotropic hardening, and has some basic characteristics following: stress dependent stiffness according to the power law, plastic straining both due to primary deviatoric loading (shear hardening) and primary compression (compression hardening, cap yield), elastic un/reloading, dilatancy effect and failure criteria according to the Morh-Coulomb failure criterion. The response of soil model was described much more accurately by using different input stiffnesses: the triaxial loading stiffness E_{50} , the triaxial unloading stiffness E_{ur} , and the oedometer loading stiffness E_{oed} .

The Hardening Soil model with small strain stiffness (HSS), based on the research of Benz [5], is a modification of the HS model considering the increasing stiffness behaviour of soils at small strains. At small and very small strain levels, most soils show a higher stiffness than that at large strain levels. To describe the behavior of soil at small strain which is less than 10^{-3} , two additional parameters including the initial shear modulus G_0 and the shear strain $\gamma_{0.7}$ are defined in HSS, as shown in Fig. 3. The parameter $\gamma_{0.7}$ is the strain when the secant shear modulus is reduced to about 70% of G_0 . The initial stiffness E_0 can be derived from the relationship of

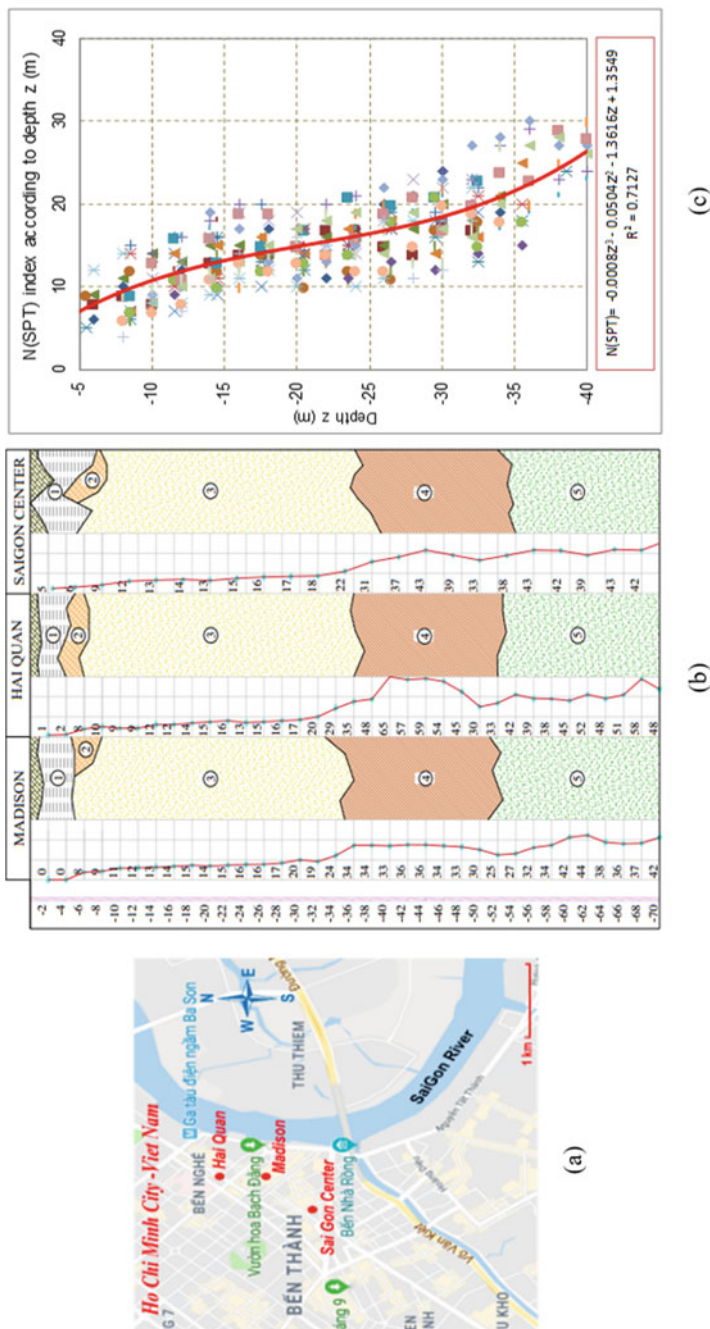


Fig. 1 **a** Location of the projects, **b** The soil profiles in this area, and **c** N(SPT) index according to depth z in thick sand layer

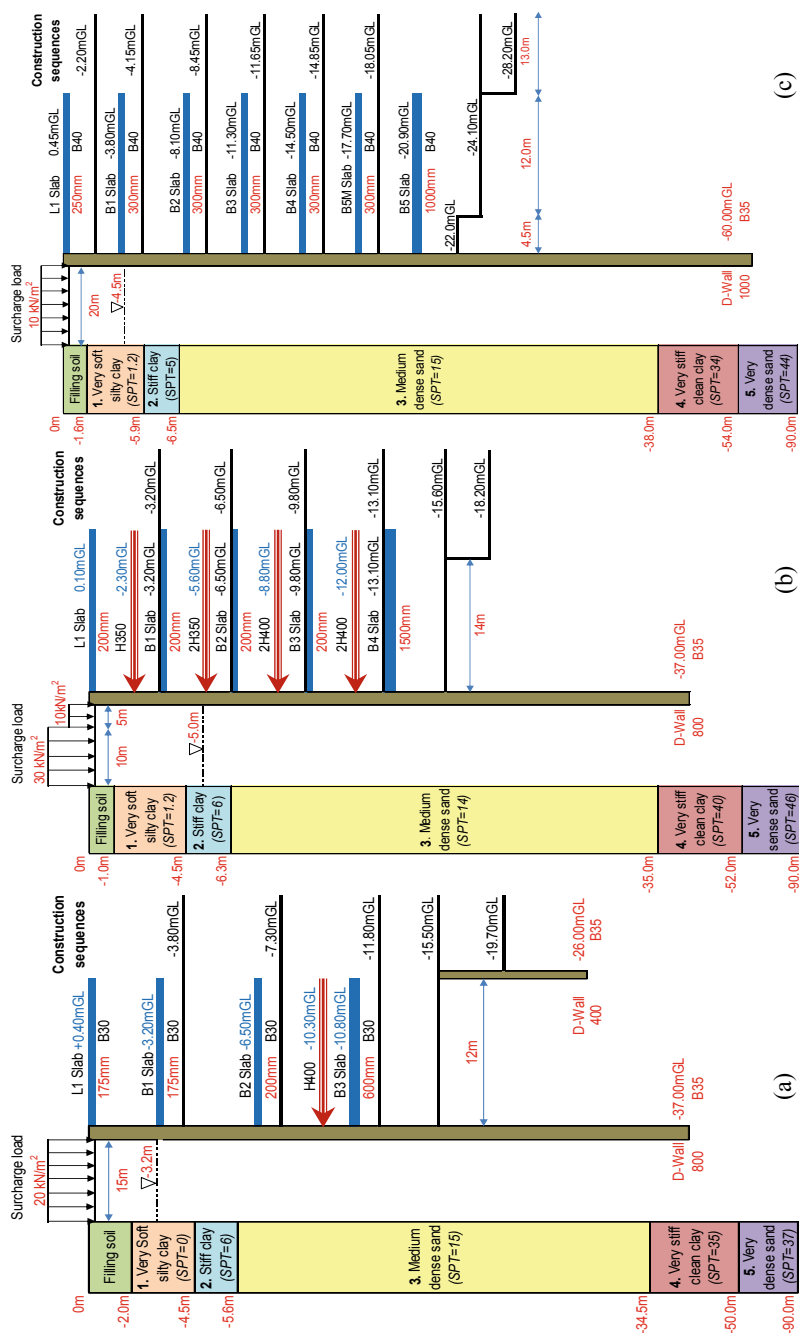


Fig. 2 Construction section of **a** Madison project, **b** Hai Quan project, **c** Sai Gon Center project

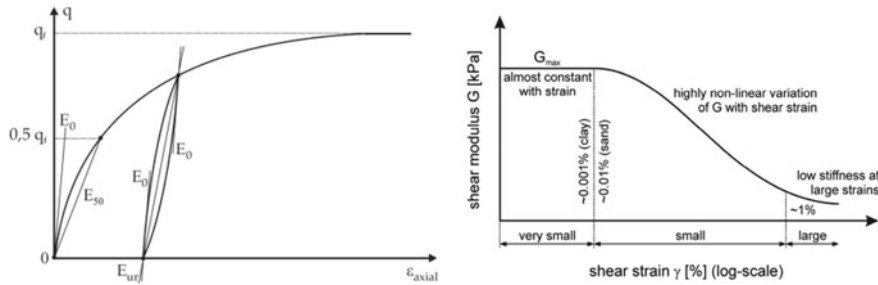


Fig. 3 Hardening soil small model and shear modulus variation

initial shear modulus G_0 and Poisson's ratio ν . Furthermore, The HSS is still based on the Mohr-Coulomb failure criterion.

Almost soil parameters in HS and HSS are commonly defined from the CD test and OED test. However, for sand, it is understood that to get good quality sampling for determining the soil properties are comparatively difficult. Thus, the N(SPT) value is commonly used for engineering practice. Shear strength parameters and young's modulus can be estimated from the empirical formulas obey to the correlation with the index N. In that, the max shear modulus G_0 at very small strains, Eq. 2, can be determined from the shear wave velocity.

$$G_0 = \rho V_s^2 (\text{kPa}) \quad (2)$$

where: ρ is total density of soil; V_s is shear wave velocity.

For determining the V_s , there were many different correlation formulas between the shear wave velocity (V_s) and the N(SPT) index formed for sand soils in various places around the world. All of these equations were established by the regression method, and in a power-law relationship $V_s = AN^B$, where A and B are regression parameters. A correlation between V_s and N value, which was developed from 60 global correlations by Marto et al. [6] shown in Eq. 3, was used for back analysis because its coefficient of determination is quite high, $R^2 = 0.876$.

$$V_s = 77.13 N^{0.377} \quad (3)$$

The values of $\gamma_{0.7}$ were very scattered for various types of soil. According to previous researches of Benz [5], Lim et al. [1], Likitlersueng et al. [2], $\gamma_{0.7}$ was in range 0.0001–0.0002 for sand soils and $\gamma_{0.7}$ was in range 0.00005–0.0001 for clay soils.

For determination the stiffness parameters such as E_{50} , E_{ur} , E_{oed} , it was suggested that $E_{ur} = 3E_{50}$, $E_{oed} = E_{50}$. And the E_{50} are depended on the stress σ_3 according to the power law and can be determined by Eq. (4)

$$E_{50} = E_{50}^{\text{ref}} \left(\frac{c' \cos \varphi' + \sigma_3 \sin \varphi'}{c' \cos \varphi' + P_{\text{ref}} \sin \varphi} \right)^m \quad (4)$$

where E_{50}^{ref} is secant stiffness at a reference stress level p_{ref} . The value of p_{ref} and m usually take as 100 kPa and 0.5 (for sand soils) respectively.

In term of clay soils, when the total stress undrained analysis with undrained internal friction angle ($\varphi = \varphi_u = 0$) and undrained shear strength ($c = S_u$) were used, E_{50} is equal to E_{50}^{ref} from Eq. 4. Moreover, E_{50} could be computed by $300S_u$ for soft soil and $500S_u$ for stiff clay. It is noted that, the S_u value could be defined from vane shear test (VST) or direct shear (DS) test. In case of sandy soils, $c \approx 0$ $\varphi = \varphi'$, the determination of E_{50} used Eq. (4) with $p_{\text{ref}} = 100$ kPa is not suitable for thick sand layer. So that, to obtain E_{50} which approximately equals E_{50}^{ref} from Eq. (4), the authors suggested that the P_{ref} value should be varied with the depth by dividing the thick sand layer into several small layers. And the P_{ref} value of each small layer was equal to σ_3 at the middle of its respective layer. It is noted that the suggested thickness of the small layer was smaller than 5 m. Besides that, the value of E_{50}^{ref} was calculated from the correlation with N(SPT) value by many previous researches [3, 7].

Based on the above concept to select the parameters for HS model and HSS model, Table 1 summarized the soil parameters of the three studied projects for analysing purposes.

4 Back Analysis

By using the parameters mentioned in Table 1, the authors made investigations by changing of stiffness-related parameters of HSS model to get acceptable outcome with the monitoring wall deflection. Based on the results as shown in Fig. 4, it is suggested that E_{50} is equal to 2500 N. Besides, the small comparisons between the results of HS and HSS model was also implemented in Fig. 4. It can be seen that the results from HS and HSS model gave the good agreement with results from measurement. However, the results from HSS model was better than those ones from HS model when they were compared to measured data. This thing showed the advantage of HSS model considering the shear modulus G_0 and the shear strain $\gamma_{0.7}$ at very small strains.

Furthermore, the value of the shear strain $\gamma_{0.7}$ was also varied in the mentioned range to see their influence on results of HSS model. As shown in Fig. 5, the best-fit between predicted and measured wall deflection will be get if the shear strain $\gamma_{0.7}$ equals 0.0002.

By using the back-analysis soil parameters such as secant stiffness E_{50} , shear modulus G_0 and shear strain $\gamma_{0.7}$, the predicted wall displacement perfectly shows good agreement with measured results in each excavation stage of all the case studies, presented in Fig. 6. This shows that the selected soil parameters for HSS are completely suitable for analysing the deep excavation behaviour in the thick sand layer.

Table 1 Input parameter for soil layers

Soil layer	Depth (m)	N (value)	ϕ' (deg)	c' (kPa)	S_u (kPa)	E_{50}^{ref} (kPa)	G_{50}^{ref} (kPa)	$\gamma_{0.7}$	P_{ref} (kPa)	m
1. Soft silt clay	1–4	0–1	–	–	17–23	300 S_u	–	–	–	1
2. Stiff clay	4–6	6–9	–	–	34–47	500 S_u	–	–	–	0.8
3. 1–3.6 Medium dense sand	6–40	8–25	26–28	5–8	–	2000 N–2500 N	6000 $\rho N^{0.75}$	0.0001–0.0002	50–200	0.5
4. Very stiff clay	40–55	30–60	–	–	170–270	500 S_u	–	–	–	0.7
5. Very dense sand	55–90	25–52	31–33	5–10	–	2000 N–2500 N	6000 $\rho N^{0.75}$	0.0001–0.0002	250	0.5

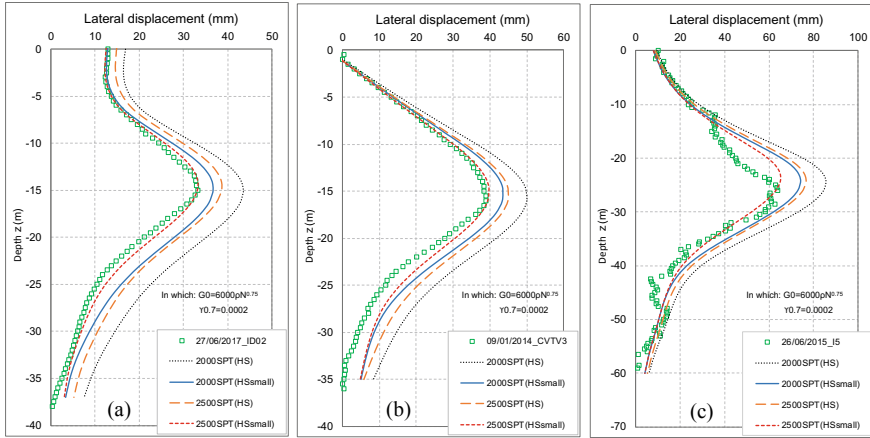


Fig. 4 Predicted displacement various secant stiffness E_{50} of **a** Madison, **b** Hai Quan, **c** SaiGon center

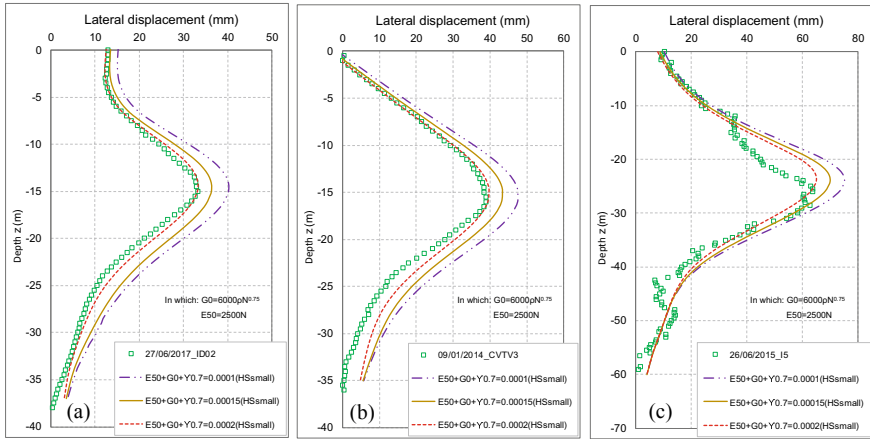


Fig. 5 Predicted displacement at various shear strain $\gamma_{0.7}$ of **a** Madison, **b** Hai Quan, **c** SaiGon center

5 Conclusions

The paper presents the back-analysis using FEM to predict the behaviour of D-wall in deep excavation. Three case study in the thick layers of sand in Ho Chi Minh City was selected to model and analyse. The first case is Madison (Case A), second case is Hai Quan (Case B) and final case is Saigon Center (Case C). Several conclusions are summarized:

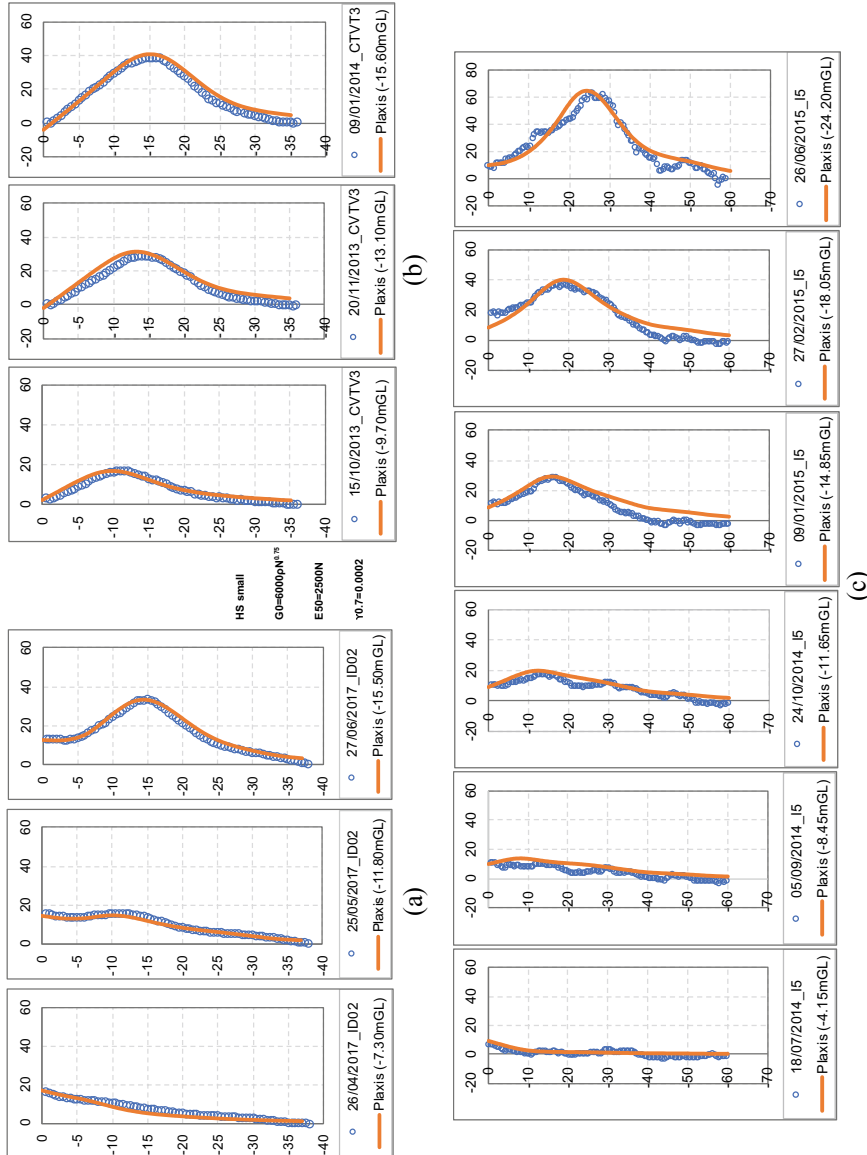


Fig. 6 Predicted value and field data at various phases of **a** Madison, **b** Hai Quan, **c** Saigon center

1. Using Hardening Soil Small model is given the better results than by the Hardening Soil model in predicting the behaviour D-wall displacement in deep excavation.
2. The N(SPT) value of the thick layer of sand in HCMC can be determined from the correlation with depth z: $N(SPT) = -0.0008z^3 - 0.0504z^2 - 1.3116z + 1.3549$ with $R^2 = 0.7127$.
3. Using secant stiffness parameters E_{50} determined from undrained shear strength (S_u) and N(SPT), would give the acceptable outcome compared to observation results. In term of cohesive soil, E_{50} is suggested equaling $300S_u$ for soft soil and $500S_u$ for stiff clay. In term of cohesionless, E_{50} could be determined by using the values of reference E_{50}^{ref} equal to 2500 N, power law with m equal to 0.5 and the reference pressures p_{ref} equals σ_3 at the middle of layer soil. Besides, it should be divided the thick sand layer into several small layers.
4. Using Hardening Soil Small model with the shear modulus at very small strains G_0 equal to $6000 \mu\text{N}^{0.75}$ (unit in kPa) and shear strain $\gamma_{0.7}$ equal to 0.0002 for the thick layer of sand in HCMC are given a very well agreement between results of prediction and measurement.

References

1. Lim A, Ou CY, Hsieh PG (2010) Evaluation of Clay constitutive models for analysis of deep excavation under undrained conditions. *J Geo Eng TGS* 5(1):9–20
2. Likitlersuang S, Surarak C, Wanatowski D, Oh E, Balasubramaniam A (2013) Finite element analysis of a deep excavation a case study from the Bangkok. *Soils Found* 53(5):756–773
3. Xuan F, Xia XH, Wang JH (2009) The application of a small strain model in excavations. *J Shanghai Jiaotong Univ (Sci)* 14(4):418–422
4. Schweiger HF (2009) Influence of constitutive model and EC7 design approach in FEM analysis of deep excavations. In: Proceeding of ISSMGE international seminar on deep excavations and retaining structures, Budapest, pp 99–114
5. Benz T (2007) Small-strain stiffness of soils and its numerical consequence. In: PHD thesis, Institute of Geotechnical Engineering, University of Stuttgart, Germany (2007)
6. Marto A, Soon TC, Kasim F (2013) A correlation of shear wave velocity and standard penetration resistance. *Electron J Geotech Eng* 18:463–471
7. Hsiung BCB, Yang KH, Aila W, Ge L (2018) Evaluation of the wall deflections of a deep excavation in Central Jakarta using three-dimensional modeling. *Tunn Undergr Space Technol* 72:84–96

Consolidation Behavior of Soft Soil with Different Sample Sizes—A Case Study of Preloading Without PVD in Ho Chi Minh City



Nhat-Truyen Phu and Ba-Vinh Le

1 Introduction

In order to calculate the consolidation process and long-term settlement of soft ground under embankments, it is necessary to determine several important parameters about consolidation properties of soil, such as coefficient of volume compressibility, pre-consolidation pressure, compression index, swelling index, the coefficient of consolidation, the coefficient of secondary compression of soils. According to ASTM D2435 [1], there are many requirements for the soil sample dimensions such as: The minimum specimen diameter shall be 50 mm (2 in), the minimum initial specimen height shall be 12 mm (0.5 in), the minimum specimen diameter to height ratio shall be 2.5. Nowadays, there are many type of consolidation test equipment with different sizes of sample. For example, Chinese devices have dimensions of 61.8 mm in diameter \times 20 mm in height and 80 mm in diameter \times 20mm in height, the devices of Controls Corporation (Italia) has dimensions of 50.8 mm in diameter \times 20 mm in height.

In the past, there were many studies related to this problem. For example: O'Kelly [2] developed a new consolidation apparatus with drained length is very long (250 mm), his result shown that to cause the similar deformation on soil sample, the consolidation pressure in the new apparatus is smaller than the classical apparatus (with drained length is 25 mm). Chew and Bharati [3] conducted the consolidation test on two kind of soil dimension, one has 150 mm in diameter and another is 70 mm, the result shown that the compression index of large sample is higher than the smaller one. In Vietnam, Man [4] carried out several oedometer tests

N.-T. Phu (✉)

Faculty of Geology and Petroleum Engineering, Ho Chi Minh City University of Technology, VNU-HCM, Ho Chi Minh City, Vietnam
e-mail: pntruyen@hcmut.edu.vn

B.-V. Le

Faculty of Civil Engineering, Ho Chi Minh City University of Technology, VNU-HCM, Ho Chi Minh City, Vietnam

on the Mekong delta soils by two kind of apparatus: one of them is from Chinese and another is from Japan and the result of this experiment is the variation of the consolidation properties of soil.

This paper mainly studies on the consolidation behavior of soil samples of different sizes by conducted the consolidation test on five kinds of soil sample dimension. After that, the experiment results will be used as input data to calculated final settlements of the embankment by using one-dimension consolidation theory and finite element method. And then, them will be compared with the final settlement from field monitoring data using Asaoka's method. Base on this comparison, the best apparatus and best dimensions will be proposing.

2 Analysis the Consolidation Behaviour of Soil with Different Samples Sizes

2.1 Soil Descriptions

Soil samples were taken from the “Riviera Point” project at district 7, Ho Chi Minh city, Viet Nam. The geotechnical profile includes three main soil layer: first layer is fat clay, blackish greenish gray, very soft, the thickness is varying from 20.3 to 23.2 m; next layer is the fat clay, reddish brown-yellowish brown-bluish gray, very stiff-stiff, the thickness is varying from 7.5 to 7.7 m; and last layer is poorly graded fine to medium sand, whitish gray-yellowish brown, medium dense, the bottom of the borehole with depth 45 m is stop at this layer. The soil properties are shown in Table 1.

Table 1 Soil parameters

Layer	1	2	3
% Sand	6	9	82
% Silt	37	42	14
% Clay	57	49	4
N-SPT	0–3	9–28	14–35
Water content (%)	95.3	30.8	22.4
Unit weight (kN/m ³)	14.67	18.62	19.38
Density	2.620	2.706	2.671
Void ratio	2.488	0.898	0.686
Liquid limit (%)	71.2	49.8	NP
Plastic limit (%)	35.4	24.6	NP

2.2 Test Results of Soil Samples of Different Size

In order to study the effects of size of sample on consolidation characteristic of soils, the oedometer tests were carried out on several samples of different cross sections and thickness, three times for each different cross section and thickness, as shown in Table 2. Consolidation tests on the undisturbed specimens were carried out by different consolidation pressures of 12.5, 25, 50, 100, 200, and 400 kPa to determine the consolidation properties of soil. Based on the experimental results as shown in Fig. 1, it can be seen that increasing of sample's diameter from 5.05 cm to 7.98 cm results in the remarks as follows:

Table 2 Sample's dimensions used in the soil tests

No.	1	2	3	4	5
Diameter (cm)	5.05	6.18	7.98	7.98	7.98
Cross section area (cm^2)	20	30	50	50	50
Thickness (cm)	2	2	2	3	4

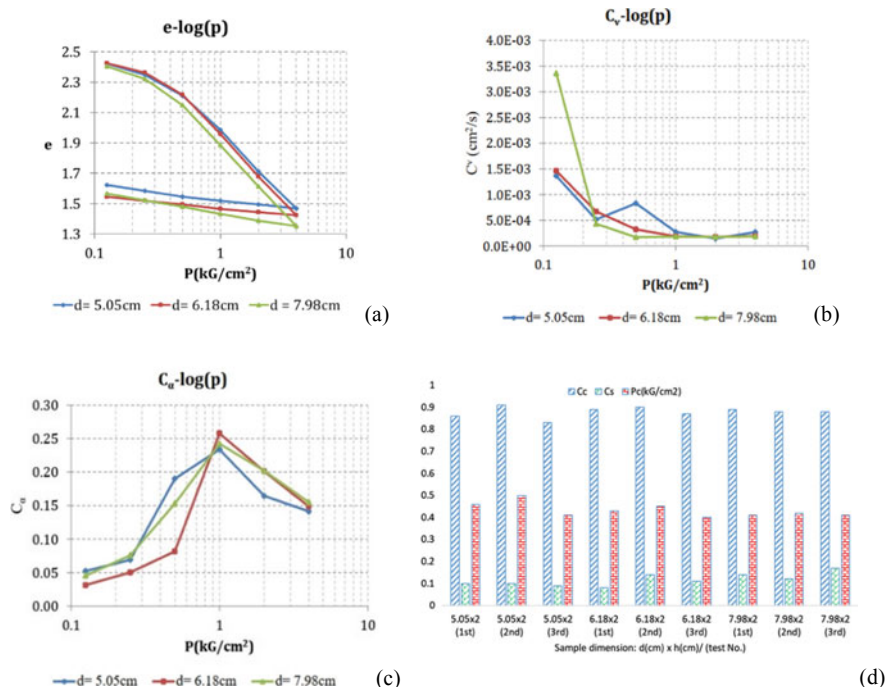


Fig. 1 Test result of samples of various cross section areas: **a** Consolidation curves, **b** Change of coefficient of consolidation with consolidation pressure, **c** Relationship between C_a and consolidation pressure, **d** Variation of P_c , C_c and C_s as increasing sample's diameter

The conclusions about the variation of consolidation properties of soil when increase the sample diameter: Using the result of the sample with the smallest diameter ($d = 5.05$ cm) as the reference, when the consolidation pressure is smaller than the pre-consolidation pressure, the consolidation properties of soil have high variation: the coefficient of volumetric compressibility increase from 10 to 107.5% and the coefficient of consolidation varied from -79 to 256.9% . When the consolidation pressure is greater than the pre-consolidation pressure, the opposite result is obtained: the coefficient of volumetric compressibility increase from 2.2 to 21.1%, the coefficient of consolidation has a smaller variation, from -43.4 to 46.9% . The coefficient of secondary compression is irregularly changed from -120 to 57% . The reason for this fluctuation is that the inside diameter of the sampling tube in this paper is 8.7 cm, so that the small diameter sample will be less affected by the disturbance than the large diameter sample.

Several tests of 7.98 cm—diameter samples have been carried out to study on the effects of increasing sample's thickness on some consolidation characteristic of soils. Based on the experimental results as shown in Fig. 2, it can be seen that increasing of sample's thickness from 2 to 4 cm results in the remarks as follows: Depending on the consolidation pressure, the coefficient of volumetric compressibility tends to

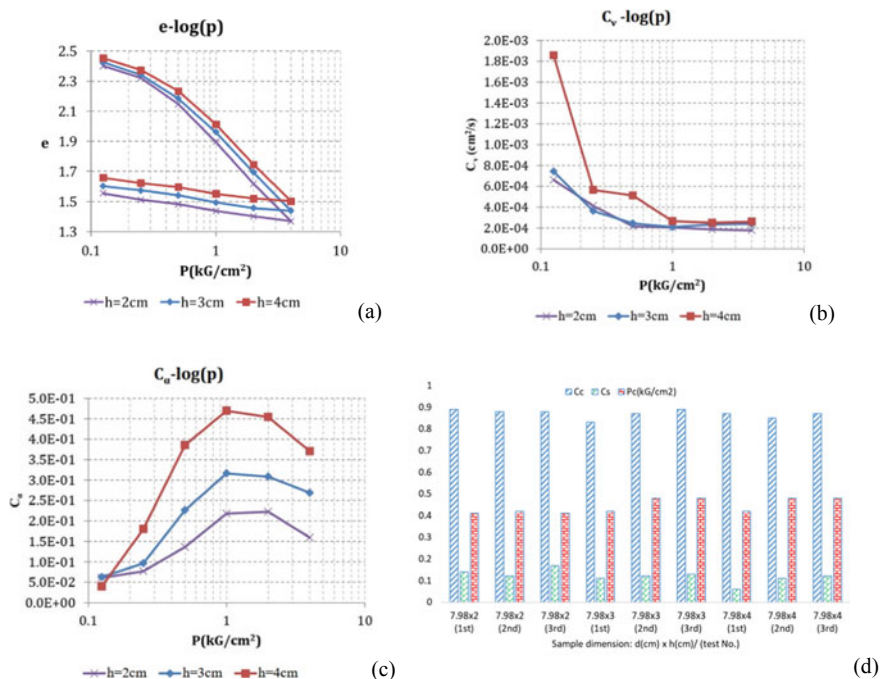


Fig. 2 Test result of samples of various thickness: **a** Consolidation curves, **b** Change of coefficient of consolidation with consolidation pressure, **c** Relationship between C_α and consolidation pressure, **d** The variation of C_c , C_s and P_c in the experiments

decrease from -1.2 to -58.7% as the consolidation pressure is smaller than the pre-consolidation pressure. If the pressure is greater than the pre-consolidation pressure, the change is not large, from -12.75 to 2.86% . As the consolidation pressure is smaller than the pre-consolidation pressure, the coefficient of consolidation has a large variation, ranging from -77.7 to 301.1% . As the consolidation pressure is greater than the pre-consolidation pressure, less variation occurs, from 1.8 to 81.1% . The coefficient of secondary compression is tending increase from 3.44 to 183% . The cause of this fluctuation is due to the increase in thickness of the sample, the longer the time required for the specimen to fully consolidation. But in this paper the consolidation time for a given load is 24 h.

3 Predicted Settlement of an Embankment Without PVD in Ho Chi Minh City

All the experiment results mentioned above will be used as the input data to predict the final settlement of the above soft ground under embankment without PVDs by two methods: one of them is using consolidation theory and another one is using finite element method (PLAXIS 2D software). After that, the predicted final settlements are compared with the field measurements to conclude the most suitable sample's size for the Oedometer test.

3.1 The Calculation and Simulation of Settlements

In order to predict the consolidation settlement of soft ground, the finite element method via Plaxis software is applied with the 2D-model as shown in Fig. 3. There are 5 PLAXIS model with the input soil parameter as shown in Table 3, and the layer 1st consolidation parameter ($\lambda, \kappa, k_x, k_y$) will be the average value of three result from three time of experiments of each kinds of sample dimensions. In addition, the analytical calculations of the settlement are carried out by using the test result of

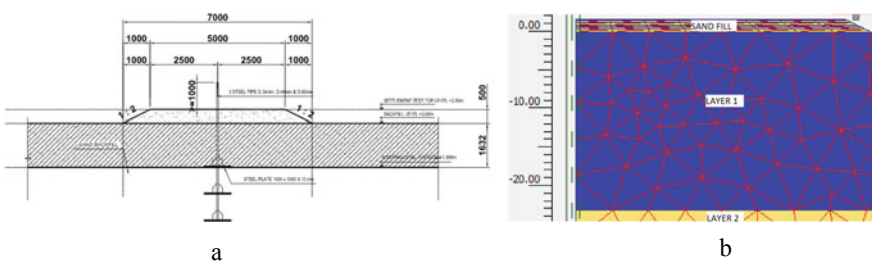


Fig. 3 Cross section of the embankment (a) and Finite element mesh in PLAXIS 2D (b)

Table 3 Input soil parameters in PLAXIS 2D

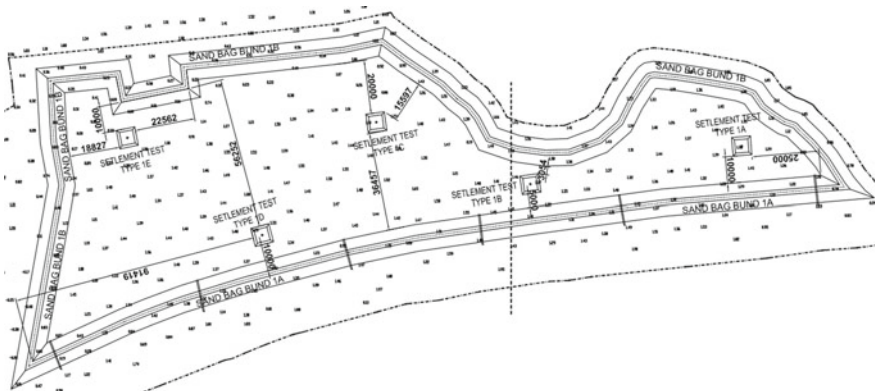
Layer	Filling soil	1	2	3
Model	M-C	S-S	M-C	M-C
Type	Drained	UnDrained	UnDrained	Drained
γ_{unsat}	18	14.76	18.62	19.09
γ_{sat}	19	14.88	18.99	19.48
k_x	1	X	8.81E-3	1
k_y	1	X	8.11E-3	1
E_{ref}	30,000	X	46,982	88,634
E_{oed}	48,148	X	65,121	106,360
v	0.350	0.331	0.310	0.25
C'	1	14.7	25.30	7.8
ϕ'	30	15.73	19.85	25.77

samples of different dimensions mentioned above. Finally, the settlements predicted by Plaxis, the analytical calculations, and the monitored data are compared.

3.2 The Field Monitoring of Settlements

As shown in Fig. 4, there are 5 settlement observation points with the duration of monitoring is 12 months include 28 monitoring cycles based on the following schedule: The first stage of 2 months: 1 times/week (in total: 8 times/2 months), the second stage of 10 remaining months: 1 times/2 weeks (total: 20 times).

After observing the results, the final settlement is evaluated by the method of Asaoka as shown in Fig. 5. The final settlement at different positions is different, one

**Fig. 4** Location plan of field monitoring of settlements

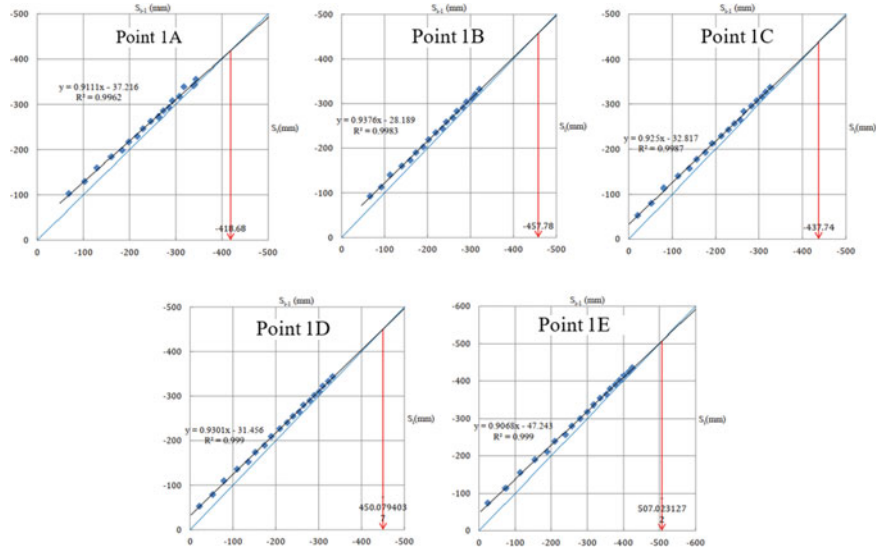


Fig. 5 Asaoka analysis of field monitoring of settlements at different positions

of the reasons of this phenomenon is due to the heterogeneous geology condition at the monitoring positions.

As shown in Fig. 6, because of the variation of input parameter of layer 1st (depend on the sample dimensions), the final settlement is also varied. The final settlements of hand calculated method is settlements at centre of embankment while the settlement observation points are located at border of embankment, so that to compare accurate with the observation settlement, the final settlements from PLAXIS 2D is settlement at border of embankments. The comparison shown that with the input data from

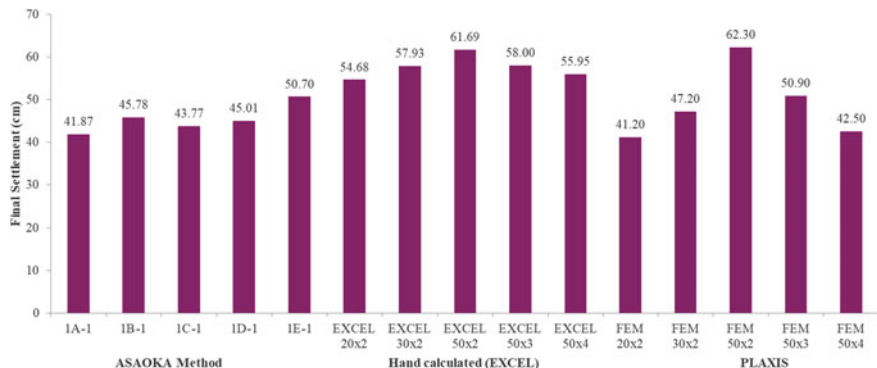


Fig. 6 Comparison between the settlements predicted by Plaxis, analytical calculations, and the field data

sample dimension ($20 \text{ cm}^2 * 2 \text{ cm}$). The settlement from PLAXIS 2D is similar with the observation settlement.

4 Conclusion

The analyses of experimental and numerical results mentioned above lead to the conclusions as follows:

- The reason for the variation of consolidation properties of soil when increase sample diameter is: the small diameter sample will be less affected by the disturbance than the large diameter sample. In this paper the inner diameter of the sampling tube is 8.7 cm while the sample sizes are 5.05, 6.18 and 7.98 cm. Therefore, the soil in the large diameter sample will be most disturbed due to the sampling and opening process.
- In case increase sample thickness, the variation of consolidation properties occurs because the consolidation time for a given load in this study is 24 h but the time request for fully consolidation process belong to the drained length (the sample thickness) resulting in a change in the secondary compression ratio, which in turn leads to a change in other parameters.
- In predicting the final settlement of soft grounds under embankments, the difference between the analytical results and monitored results is smallest in case the test result of samples of dimension $d \times h = 5.05 \text{ cm} \times 2 \text{ cm}$ is used.

References

1. ASTM (2011) Standard test methods for one-dimensional consolidation properties of soils using incremental loading. ASTM D2435, West Conshohocken, PA
2. O'Kelly BC (2009) Development of a large consolidometer apparatus for testing peat and other highly organic soils. SUO - Mires and Peat 60(1–2):23–36
3. Chew SH, Bharati SK (2011) Effect of large diameter sample testing for offshore site investigation. In: The 14th Pan-American Conference on Soil Mechanics and Geotechnical Engineering, Geo-Innovation Addressing Global Challenges, October 2–6, 2011, Toronto, Ont., Canada, pp 1–6
4. Man BT (2001) The errors of the oedometer test caused by the inaccuracy of the commercial-purpose oedometer mold. In: Proceedings of conference on science and technology, Ho Chi Minh City University of Technology

Determination of Unloading—Reloading Modulus and Exponent Parameters (m) for Hardening Soil Model of Soft Soil in Ho Chi Minh City



Trung Ngo Duc, Phan Vo, and Thanh Tran Thi

1 Introduction

In Ho Chi Minh City (HCMC) in recent years, the calculation of geotechnical works often uses finite element method with constitutive models. The biggest problem for design engineers is to properly analyze the behavior of the soil by selecting the right constitutive model and input parameters.

The Hardening Soil (HS) model is based on the Dun-can Chang model showing more advances than the Mohr-Coulomb (MC) model. Similar to the MC model, stress states of stress are expressed by the friction angle φ , the cohesion force c , the dilatation angle ψ , but the stiffness of the soil is expressed with greater precision by using 3 different input modulus variables: secant modulus; unloading-reloading stiffness and tangent oedometric modulus.

The HS model also explains the dependence of the stiffness on stress. The level of dependence of stress is below given by the exponent m . In order to simulate stress dependence according to the logarithmic law, Schanz et al. [4] investigated soft soils, the chosen exponent is $m = 1$. According to Janbu [2], the value of m is about 0.5 for sand and clay in Norway. Whereas von Soos (1980) has a m value of $0.5 < m < 1$ [7]. Usmani [6] proposed that $m = 0.67$ in stress-strain analysis of Delhi clay sand.

Thus, the choice of the m -parameter makes it difficult for engineers to correlate the empirical expressions, since the amplitude is still relatively wide and results in large discrepancies.

T. Ngo Duc (✉)

Faculty of Architecture, Civil Engineering and Applied Arts, Nguyen Tat Thanh University, Ho Chi Minh City, Vietnam

e-mail: ngoductrung@gmail.com

P. Vo

Faculty of Civil Engineering, University of Technology, VNU-HCM, Ho Chi Minh City, Vietnam

T. Tran Thi

Faculty of Civil Engineering, University of Industry, Ho Chi Minh City, Vietnam

This paper will identify the m parameter for soft soil Ho Chi Minh City on the basis of drained triaxial compression test as defined in the HS model.

2 Overview of Soft Soil in HCMC

HCMC belongs to the Saigon River delta, the stratigraphic structure of this area belongs to the Quaternary period—Cenozoic Era and the Neogene period accumulates which form a total of 6 layers of natural soil. Layer 1 and layer 2 consist of slurry and thick soils with a depth of 20 \div 30 m, high organic content, high water content of 85–104%, void ratio $e = [1.5 \div 2.5]$ soft soil is very compact, high liquid IL index, reaching 1.85 [3] (Fig. 1).

Soft soil of HCMC is located in: Binh Thanh District, Can Gio District, District 6, District 7, District 4 and Binh Chanh District. Soft soils are highly compressive, with very low load capacity. One or more of the physical properties, durability and deformation of the soil are within the following range: Void ratio $e = [1.5 \div 2.5]$; Water content $W \geq 65\%$; Water unit weight $\gamma_w = [14 \div 16] \text{ kN/m}^3$; undrained shear strength $S_u < 50 \text{ kPa}$; standard penetration test $N_{30} < 4$; cohesion intercept $c < 10 \text{ kPa}$; Settlement ratio $a_{1-2} > 5 \text{ m}^2/\text{kN}$; Deformation modulus $E < 5000 \text{ kPa}$.

This study was conducted on two soft clays of HCMC: very soft clay and soft clay with a depth of 4 to 30 m below groundwater, which often affects the stability and deformation of underground structures.

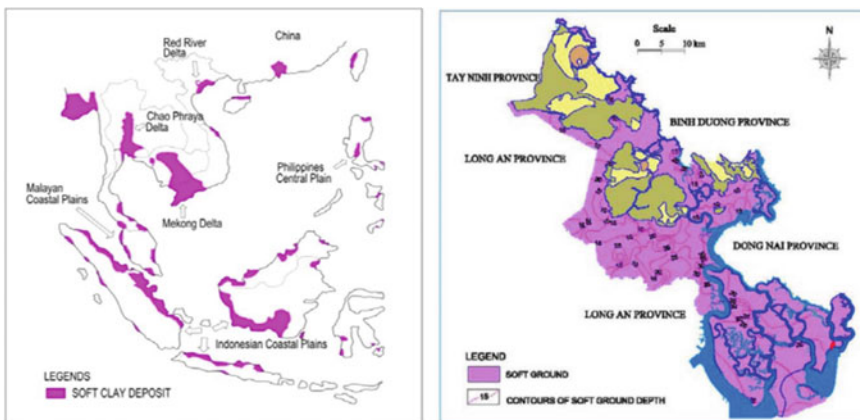


Fig. 1 Distribution of soft clay in Southeast Asia region and in HCMC [3]

3 Overview of Hardening Soil Model

The HS model developed by Schanz et al. [4] is based on the classical elastic-plastic theory to simulate the resilient and flexible behavior of the soil. Its elasticity uses two stiffness modules, are the secant modulus E_{50} and unloading-reloading stiffness E_{ur} . Plasticizers follow the nonlinear flow rule and the directional re-orientation standard, to describe the relationship between stress and strain of the soil in a hyperbolic curve (Figs. 2 and 3).

Yield surface:

$$f_1 = \frac{q_a}{E_{50}} \frac{(\sigma_1 - \sigma_2)}{q_a - (\sigma_1 - \sigma_2)} - \frac{2(\sigma_1 + \sigma_2)}{E_{ur}} - \gamma_p \quad (1)$$

$$f_2 = \frac{q_a}{E_{50}} \frac{(\sigma_1 - \sigma_3)}{q_a - (\sigma_1 - \sigma_3)} - \frac{2(\sigma_1 - \sigma_3)}{E_{ur}} - \gamma_p \quad (2)$$

$$f_3 = \frac{q_a}{E_{50}} \frac{(\sigma_2 - \sigma_3)}{q_a - (\sigma_2 - \sigma_3)} - \frac{2(\sigma_2 - \sigma_3)}{E_{ur}} - \gamma_p \quad (3)$$

Fig. 2 Definition of E_{50} and E_{ur} in drained triaxial test [4]

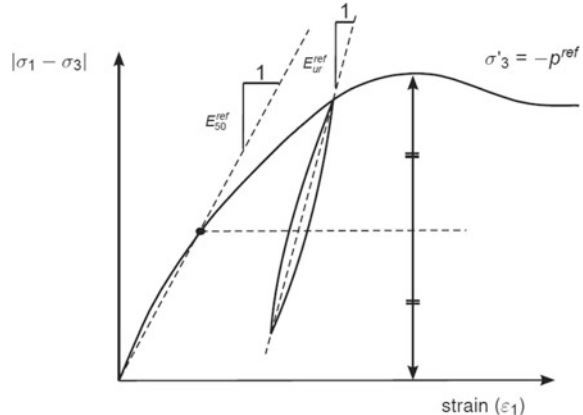
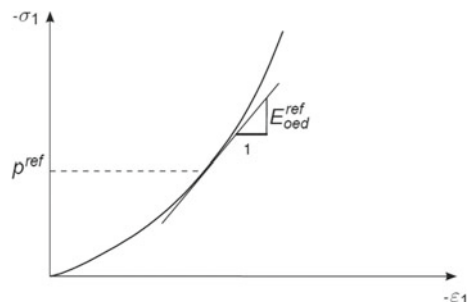


Fig. 3 Definition of E_{oed}^{ref} in oedometer test [4]



With q_a , E_{50} and E_{ur} are defined by formulas (4), (5), (6) and the notation γ_p for plastic stress.

$$E_{50} = E_{50}^{ref} \left(\frac{c \cot g\varphi - \sigma'_3}{c \cot g\varphi + p^{ref}} \right)^m \quad (4)$$

$$E_{ur} = E_{ur}^{ref} \left(\frac{c \cot g\varphi - \sigma'_3}{c \cot g\varphi + p^{ref}} \right)^m \quad (5)$$

$$q_f = (c \cot \varphi - \sigma_3) \frac{2 \sin \varphi}{1 - \sin \varphi}, q_a = \frac{q_f}{R_f} \quad (6)$$

In the un-loading and re-loading stress paths, the stress-strain relationships are still in the form of hyperbolic, and empirical studies [1] show that modulus E_{50} in the unloading and reloading experiments is larger than in the conventional triaxial compression tests many times and different from each soil type. In this study, we focused on the E_{ur}/E_{50} ratio for the soft clay in HCMC.

Equations (4), (5) defines E_{50} , E_{ur} , and E_{oed} is defined by the following equation:

$$E_{oed} = E_{oed}^{ref} \left(\frac{c \cot g\varphi - \sigma'_3}{c \cot g\varphi + p^{ref}} \right)^m \quad (7)$$

E_{oed}^{ref} is tangent oedometric modulus in oedometer test at the vertical stress $-\sigma'_1 = p^{ref}$.

The advantage of the HS model over the MC model is not only the use of hyperbolic strain curves instead of linear relations but also the control of the stiffness dependence on the stress load. When using the MC model, the user must select a fixed Young module value while the real stiffness level depends on the pressure level. It is then necessary to estimate the pressure level in the soil and use that pressure level to obtain the appropriate stiffness value. With the HS model the difficult selection of input parameters is no longer necessary. Instead, the modulus is defined by the smallest stress $\sigma_3 = p^{ref}$ as the default value in Plaxis is $p^{ref}=100$ (kN/m²).

However, defining the parameters E_{ur}^{ref} , E_{oed}^{ref} in Plaxis generally chooses the default word for all types of soil as formulas (8) often make calculations difficult [5]:

$$E_{oed}^{ref} = E_{50}^{ref}; E_{ur}^{ref} = 3E_{50}^{ref} \quad (8)$$

4 Determination of M and E_{ur}/E_{50} of the HS Model for Soft Soil in HCMC

4.1 Drained Triaxial Compression Test

To determine the parameter m , which depicts the dependence of the stiffness on the stress for soft soil in HCMC, the author carried out experiments on 12 clay samples at depths from 4 to 30 m below the groundwater, with drained triaxial tests have unloaded and reloaded at the cell pressure level σ'_3 are 50, 100, 200 and 400 kPa. The samples are located in Binh Chanh District. Results of the analysis of mechanical properties are given in Table 1.

The results of the experiment for the two clay layers are shown in Figs. 4, 5, 6, 7, 8, 9, 10 and 11.

From the stress-strain diagram (q , ε_1), we define c' , φ' and the parameters as Table 2. With $(\sigma'_{1f} - \sigma'_{3f})$ is deviator stress.

Table 1 Physical characteristics of soft soils in HCMC

Parameters	Symbol	Very soft clays	Soft clays
Water content (%)	W_n	70 \div 100	60 \div 70
Void ratio	e	2.0 \div 3.0	1.30 \div 2.0
Water unit weight (kN/m^3)	γ_n	14.0 \div 16.0	16.0 \div 17.0
Dry unit weight (kN/m^3)	γ_d	7.5 \div 8.5	8.5 \div 12.0
Liquid limit (%)	W_L	70 \div 80	45 \div 70
Plastic limit (%)	W_P	30 \div 40	20 \div 30
Saturation (%)	S	95 \div 98	99 \div 100

Fig. 4 The relationship (ε_1 – q) of sample No. 1, 2, 3

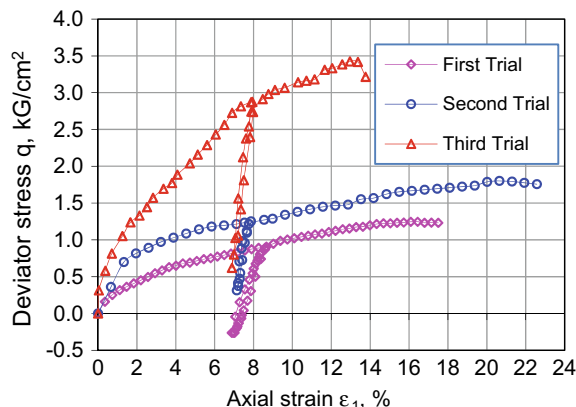


Fig. 5 The relationship ($\varepsilon_1 - \varepsilon_v$) of sample No. 1, 2, 3

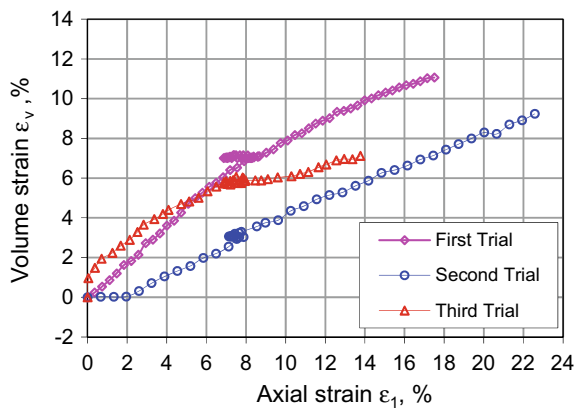


Fig. 6 The relationship ($\varepsilon_1 - q$) of sample No. 4, 5, 6

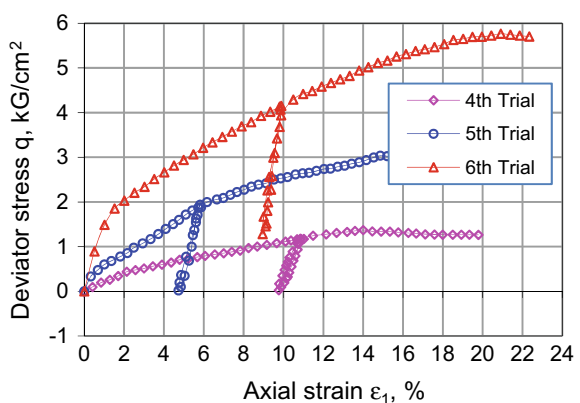


Fig. 7 The relationship ($\varepsilon_1 - \varepsilon_v$) of sample No. 4, 5, 6

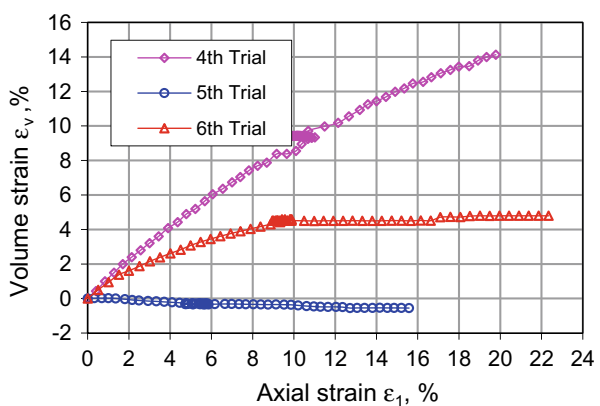


Fig. 8 The relationship ($\varepsilon_1 - q$) of sample No. 7, 8, 9

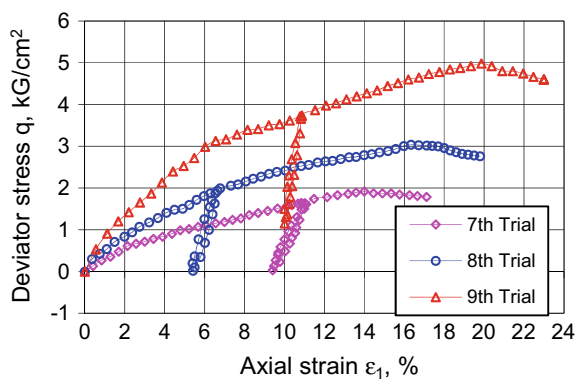


Fig. 9 The relationship ($\varepsilon_1 - \varepsilon_v$) of sample No. 7, 8, 9

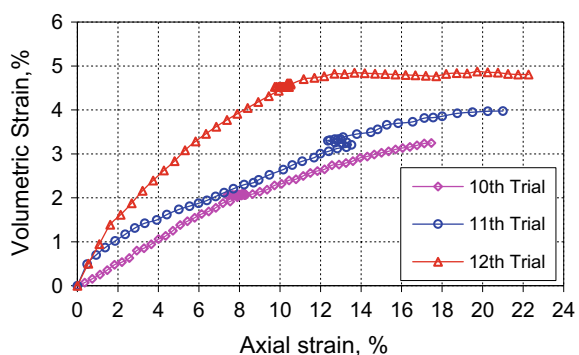


Fig. 10 The relationship ($\varepsilon_1 - q$) of sample No. 10, 11, 12

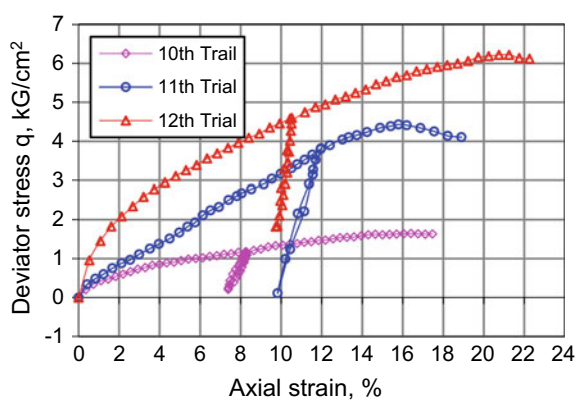


Fig. 11 The relationship ($\varepsilon_1 - \varepsilon_v$) of sample No. 10, 11, 12

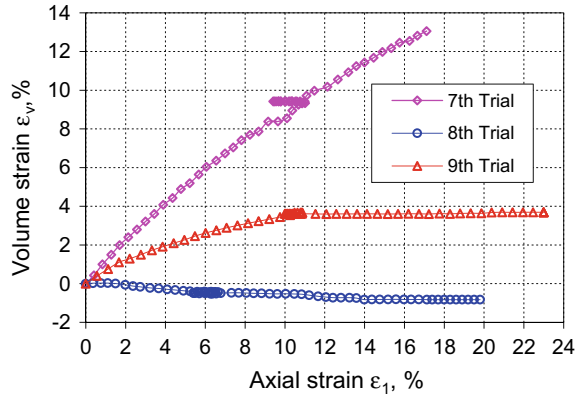


Table 2 Shear strength parameters

Depth (m)	Sample no.	C' (kG/cm ²)	φ' (°)	σ'_{1f} (kG/cm ²)	σ'_{3f} (kG/cm ²)	$\frac{\sigma_y}{p^{ref}}$
<i>Vert soft clays</i>						
4 ÷ 6	1	0.12		25.85	1.40	0.485
	2				3.05	1.074
	3				5.29	1.690
12 ÷ 14	4	0.09		26.28	2.16	0.885
	5				5.01	1.758
	6				9.48	3.300
<i>Soft clays</i>						
18 ÷ 20	7	0.10		26.02	2.17	0.88
	8				3.92	1.674
	9				8.94	3.394
24 ÷ 26	10	0.11		26.32	2.37	0.98
	11				4.02	1.747
	12				9.64	3.442

4.2 To Determine the Power M from the Drained Triaxial Compression Test

The parameter m represents the dependence of the stiffness on the stress state of the ground. In this section, the author proceeds to define the exponent m from the modulus of the distortion in the HS model according to expressions (4, 5).

On the stress-strain diagram ($q - \varepsilon_1$), draw the secant-line E_{50} as defined by the E_{50} deformation modulus of the HS model. From there, the secant modulus E_{50} can be identified as shown in Table 2.

Based on the definition of E_{50} in the HS model, formula (4), we have:

$$E_{50} = E_{50}^{ref} \left(\frac{\sigma_y}{p^{ref}} \right)^m = E_{50}^{ref} \left[\frac{c \cot \varphi' - \sigma'_3}{c \cot \varphi' + p^{ref}} \right]^m \Rightarrow m = \log \left[\frac{\sigma_y}{p^{ref}} \right] \left[\frac{E_{50}}{E_{50}^{ref}} \right] \quad (9)$$

The power m can be determined as E_{50} as shown in Table 3, with $p^{ref} = 100$ kPa (Fig. 12).

From there, the value of parameter m determined from the triaxial compression test through the secant modulus E_{50} is as follows:

Table 3 Modulus E_{50} , E_{50}^{ref} and m-parameter parameters from the triaxial compression test

Depth (m)	Sample no.	E_{50} (kG/cm ²)	E_{50}^{ref} (kG/cm ²)	$\frac{E_{50}}{E_{50}^{ref}}$	$\frac{\sigma_y}{p^{ref}}$	M (-)
<i>Very soft clay</i>						
4 ÷ 6	1	17.29	33.88	0.51	0.485	0.93
	2	33.88		1.00	1.074	–
	3	49.44		1.46	1.690	0.72
12 ÷ 14	4	21.15	21.15	1.00	0.885	–
	5	33.72		1.59	1.758	0.83
	6	60.51		2.86	3.300	0.88
<i>Soft clay</i>						
18 ÷ 20	7	20.72	20.72	1.00	0.899	–
	8	29.12		1.41	1.674	0.76
	9	52.05		2.51	3.394	0.75
24 ÷ 26	10	22.93	22.93	1.00	0.982	–
	11	30.66		1.48	1.747	0.72
	12	64.69		2.81	3.442	0.84

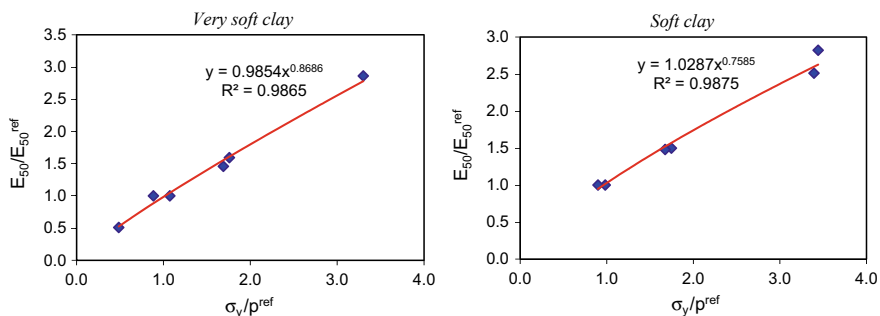


Fig. 12 The regression equation correlates between $\frac{E_{50}}{E_{50}^{ref}}$ and $\frac{\sigma_y}{p^{ref}}$

$$\text{Very soft clay: } m = [0.72 \div 0.93]; \frac{E_{50}}{E_{50}^{ref}} = 0.9854 \left(\frac{\sigma_y}{p^{ref}} \right)^{0.8686}, R^2 = 0.9865 \quad (10)$$

$$\text{Soft clay: } m = [0.72 \div 0.84]; \frac{E_{50}}{E_{50}^{ref}} = 1.0287 \left(\frac{\sigma_y}{p^{ref}} \right)^{0.7585}, R^2 = 0.9875 \quad (11)$$

This value is consistent with the experimental results of von Soos [7] that m is between $0.5 \leq m \leq 1.0$ with the lower catchment as sand and the upper margin is soft clay.

From the stress-strain diagram obtained from the experiment, draw the tangents line E_{ur} as defined by the modulus E_{ur} of the HS model to determine the loading and re-loading E_{ur} , resulting in present in Table 4.

Based on the definition of E_{ur} in the HS model, formula (5), we have:

$$E_{ur} = E_{ur}^{ref} \left(\frac{\sigma_y}{p^{ref}} \right)^m = E_{ur}^{ref} \left[\frac{c \cot \varphi' - \sigma_3'}{c \cot \varphi' + p^{ref}} \right]^m \Rightarrow m = \log \left[\frac{\sigma_y}{p^{ref}} \right] \left[\frac{E_{ur}}{E_{ur}^{ref}} \right] \quad (12)$$

From Eq. (12), the parameter m is determined according to the unloading module E_{ur} as shown in Table 4.

From the relationship between E_{ur}/E_{ur}^{ref} and σ_y/p^{ref} (formula 12), the regression line of TRENDLINE as shown in Fig. 13, we have the following results:

Table 4 E_{ur} , E_{ur}^{ref} and m from test results

Depth (m)	Sample no.	E_{ur} (kG/cm ²)	E_{ur}^{ref} (kG/cm ²)	$\frac{E_{ur}}{E_{ur}^{ref}}$	$\frac{\sigma_y}{p^{ref}}$	M (-)
<i>Very soft clay</i>						
4 ÷ 6	1	68.98	127.27	0.54	0.485	0.85
	2	127.27		1.00	1.074	–
	3	205.90		1.62	1.690	0.92
12 ÷ 14	4	106.09	106.09	1.00	0.885	–
	5	177.23		1.67	1.758	0.91
	6	284.03		2.68	3.300	0.82
<i>Soft clay</i>						
18 ÷ 20	7	99.39	99.39	1.00	0.899	–
	8	149.33		1.50	1.674	0.79
	9	276.73		2.78	3.394	0.84
24 ÷ 26	10	108.31	108.311	1.00	0.982	–
	11	173.42		1.60	1.747	0.84
	12	298.81		2.76	3.442	0.82

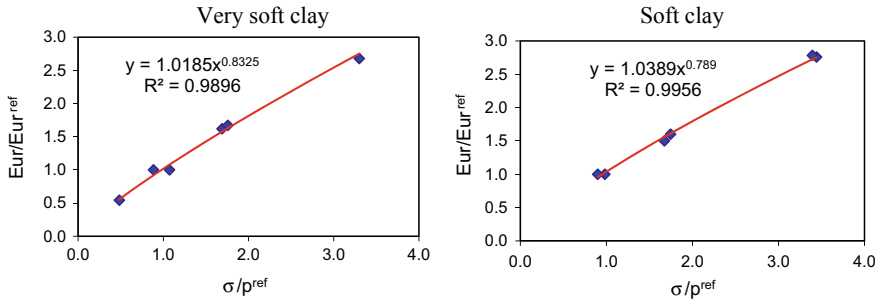


Fig. 13 The regression equation correlates between E_{ur}/E_{ur}^{ref} and σ_y/p^{ref}

Very soft clays: $m = [0.82 \div 0.92]$; $\frac{E_{ur}}{E_{ur}^{ref}} = 1.0185 \left(\frac{\sigma_y}{p^{ref}} \right)^{0.8325}$, $R^2 = 0.9896$ (13)

Soft clays: $m = [0.79 \div 0.84]$; $\frac{E_{ur}}{E_{ur}^{ref}} = 1.0389 \left(\frac{\sigma_y}{p^{ref}} \right)^{0.789}$, $R^2 = 0.9956$ (14)

4.3 Determination of Correlation Coefficient E_{ur}/E_{50} for Soft Soil in HCMC

With the default set of parameters of the HS model in Plaxis, $E_{ur}^{ref}/E_{50}^{ref} = 3$ is often chosen [4]. However, the actual ratio is very different for each soil type. From the results of experiments on soft soil in HCMC. The authors propose this coefficient as Table 5 (Fig. 14).

From there, the mean value of the correlation coefficient $E_{ur}^{ref}/E_{50}^{ref}$ for soft soil is given HCMC is:

$$\text{Very soft clay } \frac{E_{ur}^{ref}}{E_{50}^{ref}} = [3.99 \div 5.26] \quad (15)$$

$$E_{ur}^{ref} = 4.5462 E_{50}^{ref} - 2.077, R^2 = 0.9371 \quad (16)$$

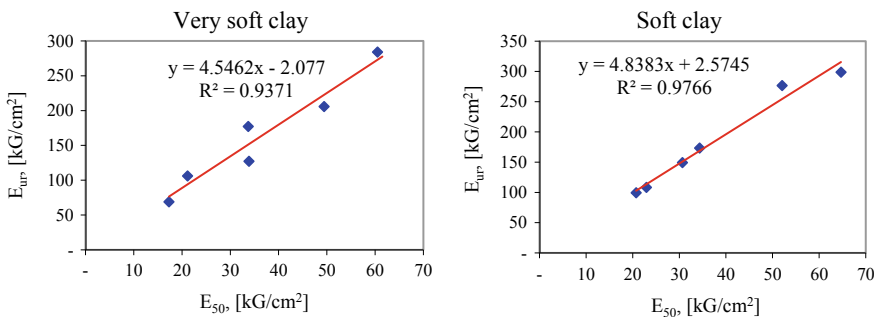
$$\text{Soft clay } \frac{E_{ur}^{ref}}{E_{50}^{ref}} = [4.62 \div 5.32] \quad (17)$$

$$E_{ur}^{ref} = 4.8383 E_{50}^{ref} + 2.5745, R^2 = 0.9766 \quad (18)$$

This coefficient differs considerably from the default value in Plaxis according to Vemeer [6] for all soil types:

Table 5 Correlation coefficient E_{ur}/E_{50} for soft soil in HCMC

Depth (m)	σ_c (kG/cm ²)	E_{50} (kG/cm ²)	E_{ur} (kG/cm ²)	$\frac{E_{ur}}{E_{50}}$
<i>Very soft clay</i>				
4 ÷ 6	0.5	17.29	68.98	3.99
	1.0	33.88	127.27	3.76
	2.0	46.97	205.90	4.16
12 ÷ 14	1.0	21.15	106.09	5.02
	2.0	33.72	177.23	5.26
	4.0	60.51	284.03	4.69
<i>Soft clay</i>				
18 ÷ 20	1.0	20.72	99.39	4.80
	2.0	29.12	149.33	4.87
	4.0	52.05	276.73	5.32
24 ÷ 26	1.0	22.93	108.31	4.72
	2.0	34.35	173.42	5.05
	4.0	64.69	298.81	4.62

**Fig. 14** The regression equation correlates $E_{ur}^{ref} - E_{50}^{ref}$ of soft soil HCMC

$$E_{ur}^{ref} \approx 3E_{50}^{ref} \quad (19)$$

5 Conclusions

- The stiffness of the soil depends on the state of stress, the dependence of the hardness on the stress state of soft soil of HCMC is in the range:
 - Determined from the drained triaxial compression test through E_{50} :

Very soft clay : $m = [0.72 \div 0.93]$; Soft clay : $m = [0.72 \div 0.84]$

– Determined from the drained triaxial compression test through E_{ur} :

Very soft clay : $m = [0.82 \div 0.92]$; Soft clay : $m = [0.79 \div 0.84]$

– Mean m value for soft soil of HCMC:

Very soft clay : $m \approx 0.86$; Soft clay : $m \approx 0.80$.

- Soil has a large modulus and non-linear in the stress path of loading and unloading, the actual stiffness of the soil is much higher than the modulus of deformation obtained from conventional test. With soft soil of HCMC ratio $E_{ur}^{ref}/E_{50}^{ref}$ as follows:

$$\text{Very soft clay : } \frac{E_{ur}^{ref}}{E_{50}^{ref}} = [3.99 \div 5.26]; \text{ Soft clay : } \frac{E_{ur}^{ref}}{E_{50}^{ref}} = [4.62 \div 5.32]$$

References

1. Brinkgreve RBJ (2005) Selection of soil models and parameters for geotechnical engineering application. J Geotech Geoenvironmental Eng, ASCE
2. Janbu N (1963) Soil compressibility as determined by oedometer and triaxial tests. In: Proceedings of european conference on soil mechanics and foundation engineering. Wiesbaden, pp 19–25
3. Long PV, Bergado DT, Nguyen LV, Balasubramaniam AS (2013) Design and performance of soft ground improvement using PVD with and without vacuum consolidation. Geotech Eng J SEAGS & AGSSEA 44(4) December 2013 ISSN 0046–5828
4. Schanz T, Vermeer PA, Bonnier PG, Brinkgreve RBJ (1999) Hardening soil model: formulation and verification, beyond 2000 in computational geotechnics. Balkema, Rotterdam, pp 281–290
5. Terzaghi K, Peck RB, Mesri G (1995) Soil mechanics in engineering practice, 3rd ed. Wiley (1995)
6. Usmani A (2007) Characterization of shear strength behavior of Delhi silt and application to boundary value problems. PhD thesis, Indian Institute of Technology Delhi, Delhi
7. Von Soos P (1980) Properties of soil and rock. In: Grundbautaschenbuch, Part 4. 4th ed. Ernst and Sohn, Berlin (in German)

Effects of SPT Numbers on Liquefaction Potential Assessment of Fine Soil



Tham Hong Duong

1 Introduction

Standard Penetration Test (SPT) has been very common in situ testing method for obtaining information about the density of non-cohesive soil. It proves to be reliable for sandy soil, especially medium dense sand or coarse-grained soil; but prior documentation recommended that the test cannot be applied to cohesive soil because of its scatter in data; the test has long time been viewed as “rather unreliable” for clays and fine soil in general (Peck 1976). For fine soils such as silty sand, very fine sand or clay, SPT data are so scattered that people can say that its correlation between values in SPT and other relevant tests is a crude approximation. Nevertheless, the fact is that this in situ test has still applied in site investigation, even for large-scale projects. Consultants still used it to infer other parameters, both in predicting soil strength, bearing capacity and compressibility of soil.

This paper firstly showed practicability of SPT data (i.e. N values) in predicting soil properties of cohesive soils_especially clayey soil_including physical properties, soil strength and compressibility. Secondly, a spreadsheet using SPT numbers was created to compute the safety factor against liquefaction for cohesive soil layer and finally, recommendation about the effects of N data on safety factor of liquefaction was pointed out.

T. H. Duong (✉)

Faculty of Civil Engineering, Saigon Technology University, Ho Chi Minh City, Vietnam
e-mail: tham.duonghong@stu.edu.vn

2 Factors to Be Considered When Using SPT

2.1 Literature Review on N Numbers and Their Correction

Standard Penetration Test has still been complied with ASTM D-1586. Energy delivered to blows of penetrating the tube 50/35 mm diameter into the soil will loss due to friction of hammer as gliding against the rod, string to pull against pulleys, machinery friction of robe around cylinder, skin friction between penetrometer and soil around it, etc. An energy ratio (ER) defined as the measured energy divided by theoretical energy as suggested by different research works. Meyerhoff (1976), Kowas (1983) and Shioi and Fukui (1985) suggested the ratio is 55%; Seed (1985) proposed the 60% percentage based on lots of technical reports in nationwide of America, meanwhile, Bowles and Aoki and De Alenca (1975) suggested a number of 70% that seemed to be fairly reasonable [1]. Effective energy that delivered to penetrometer is 60%:

$$N_{60} = \frac{ER}{60} N \quad (1)$$

where N is blow count recorded at site. For Vietnamese conditions, a percentage of 55% seems to be appropriate to use in pile bearing capacity (Hoang T. Q and Tam N. M, [1]).

2.1.1 Correction Factors

Because of the difference in energy for various depths of penetration and because of the difference in the dissipation of pore water pressure in cohesive soil as compared to that of non-cohesive soils, it is necessary to correct N numbers (hereinafter the NsPT) with respect to the depth of testing. For fine sand and silty sand below the water table, N-value will be corrected firstly due to depth of testing and then further corrected secondly to get the final corrected value N'' as below:

Bazaraa (1967) [2] proposed the following corrections to the actual count N, based on the over burden pressure

For $p_o \leq 75$ kPa

$$N' = \frac{4N}{(1 + 0.04p_o)} \quad (4)$$

For $p_o > 75$ kPa

$$N' = \frac{4N}{(3.25 + 0.01p_o)} \quad (5)$$

where, N' = corrected N value due to depth (overburden pressure); p_o = over burden pressure (kPa), equals to γD . For silty or fine sand, we have a finally corrected value of N as below:

$$N'' = 15 + \frac{1}{2}(N' - 15) \quad (6)$$

As for fine soil as clay or silty sand, correction should be considered carefully, because of the temporary increase of pore water pressure and scattered results. Therefore, in many textbooks, N_{SPT} are proposed to be rather unreliable in predicting consistency of cohesive soil as clay (Peck et al. [3]). This study will focus on the liquefaction assessment for such a kind of fine soil.

2.2 Uncertainties for Obtaining the Proper SPT Numbers

N data are used in various approaches of geotechnical engineering. The common procedure is to interpret N numbers appropriately and it is difficult to express statistically N value in terms of properties such as fine content, effective size, law of statistical distribution especially for fine cohesive and silty soil.

In terms of statistical data, the uncertainty of the overburden pressure is that unit weight varies randomly in soil layers of foundation. This random parameter has a relatively small coefficient of variation, $COV(\gamma)$, less than 10% with normal distribution [4]. Furthermore, for cohesive soil like clayey sand and sandy clay, it is difficult to determine the correction will be chosen as for a sandy soil (once to obtain N') or as for a fine-grained soil (twice to obtain N''). Because there are two kinds of correction, this indicates that correction due to the depth of the test will be more self-explanatory (N to N') than that due to soil kind (N' to N''). This implies uncertainties in getting proper value of N_{SPT} .

2.3 Prediction of Soil Properties Using SPT

Based on data obtained in many sites, SPT can predict soil properties to a high extent of confidence. For non-cohesive sandy soil, the data are reliable, but for clayey soil, corrected SPT blows are relatively reliable as follows [5].

Results obtained from abovementioned regression analysis can compare to those of previous works conducted by Abdel Naiem Mahmoud [6]. On the other hand, by using some other geotechnical properties, including physical and mechanical properties, N' values are shown as in Table 2.

3 Liquefaction Assessment

3.1 Approaches for Liquefaction Assessment in Vietnam

There are many approaches for liquefaction assessment; TCVN 9386: 2012 uses a factor of liquefaction assessment F_L providing at least three liquefiable conditions of sandy soil are met (item 4.1.4); JRA (2000) using a safety factor of liquefaction F_L relating to D_{50} and plasticity of cohesive soil; NCEER method as a deterministic approach using cyclic resistance ratio (CRR) and cyclic stress ratio (CSR) for the moment magnitude of earthquake $Mw = 7.5$ (Seed and Idriss 1971). For years, other studies focused on threshold acceleration, relating to compaction level D (%) and size distribution (Ivanov 1962), Index of liquefaction potential P_L (Iwasaki 1978) developed from research works of Seed and Idriss (1971) [7] (Fig. 1).

For N numbers, their corrected value was highly correlated to the internal friction angle of all the soil classes, including non-cohesive, cohesive soil and clayey soil, as described in Table 1. Hence, it is necessary to quantify the essential role of SPT data for liquefaction assessment. According to Gandomi et al. [8], the most significant correlated variable to SPT is the internal friction angle. The correlation matrix for

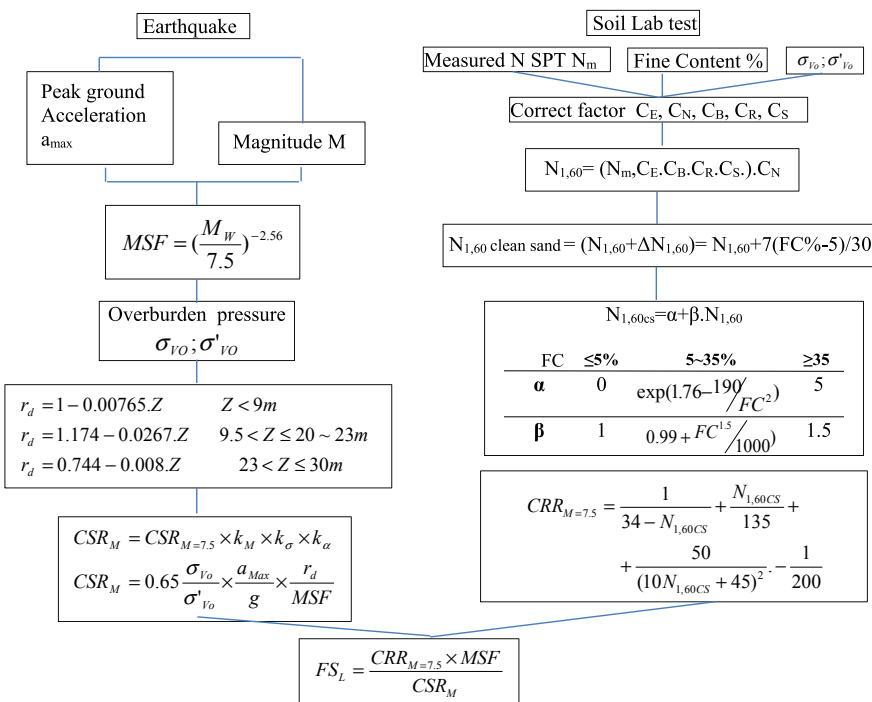


Fig. 1 Flow chart for determining safety factor of liquefaction (Seed and Idriss 1971) [7]

Table 1 Correlation between SPT number N and mechanical properties

		Confidence level	
		85%	95%
Sand	E	$E = 111.54 + 1.826 N'$	$E = 118.8 + 2.431 N'$
	φ	$\Phi = 32.6^\circ - 0.01 N'$	$\Phi = 32.93^\circ - 0.02^\circ N'$
Clay	E	$E = 52.6 + 1.7 N''$	$E = 56.7 + 1.939 N''$
	C	$C = 0.367 + 0.02 N''$	$C = 0.407 + 0.022 N''$
	φ	$\Phi = 15.89 + 0.36 N''$	$\Phi = 16.5 + 0.39 N''$
Clayey sand/sandy clay	E	$E = 57.67 + 2.38 N''$	$E = 61.63 + 2.37 N''$
	C	$C = 0.134 + 0.001 N''$	$C = 0.141 + 0.002 N''$
	φ	$\Phi = 19.81 + 0.52 N''$	$\Phi = 20.33 + 0.56 N''$

all variables and parameters participating in liquefaction assessment is described in detail of many research works.

It may come to a viewpoint that based upon internal friction angle, N_{SPT} can be inferred and applied in liquefaction assessment for comparison purposes. The benefit of using N computed from the internal friction angle is that it simplifies complicated formulas. In other words, it is possible to compute N from soil properties and others (as in Table 2) instead of correcting N numbers with so many coefficients.

3.2 Fine Content and Other Randomly Distributed Predictors

Many computations related to fine content (FC, %) and other randomly distributed variables and parameters (for instance, $N_{1,60}$ as N of clean sand, peak horizontal acceleration...etc.).

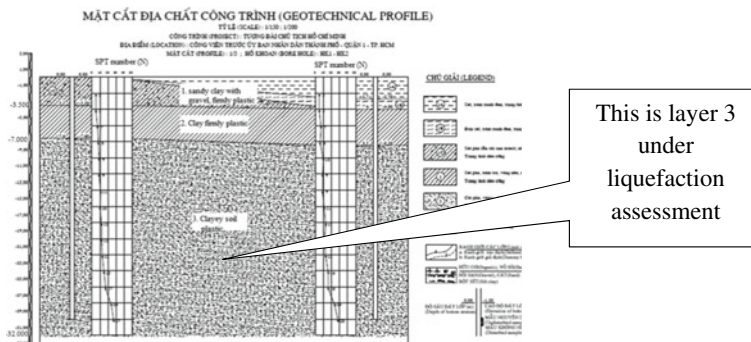
3.3 Factor of Safety Against Liquefaction

Soil data were selected from geotechnical reports of a soil foundation at a real site in central location of Ho Chi Minh City (Fig. 2). The project name is the Administration Building of People's Committee in HCMC, District 1. Layer 1 distributed from the soil surface to Elevation –3.500 and layer 2 from Elevation –3.500 to Elevation –

Table 2 Correlation between SPT number N and different geotechnical parameters [5]

Classification of soil	Number of observations	Multi-variable regression equation	Adjusted R ²	Significance F
Sand	37	$N' = 224.9 - 0.13 \times (Z) + 0.022 \times (\omega) - 7.89 \times (\gamma_d) - 139.67 \times (e) + 0.002 \times (E)$	0.456	0.005
Clayey sand/sandy clay	185	$N'' = 9.955 + 0.036 \times (Z) - 0.026 \times (\omega) + 0.813 \times (\gamma_d) + 0.098 \times (I_p) + 0.009 \times (E)$	0.341	2.07E-15
Clay	236	$N''' = 78.629 - 0.044 \times (Z) - 82.65 \times (\omega) - 2 \times (\gamma_d) + 7.31 \times (I_p) + 0.048 \times (E)$	0.171	2.99E-9

where, Z = depth of testing; ω = water content; γ_d = dried unit weight (kN/m^3); e = void ratio; E = modulus of deformation (kN/m^2); I_p = index of plasticity

**Fig. 2** Borehole and soil profile for liquefaction assessment

7.000 is respectively soft peat soil and firmly plastic clay; layer 3 from Elevation – 7.000 to Elevation – 30.000 is a thick, plastic clayey soil and highly susceptible to liquefaction. This is a dominant layer of clayey soil which will be assessed with a wide range of the fine content FC %. Below this layer 4 is a very firmly stiff clayey one, $N_{SPT} \sim 40$. A spreadsheet was created for computing the safety factor against liquefaction as in Fig. 3.

The first step is to identify the liquefiable layer as per US EPA Seismic Design Guidance [9]. Fine content (FC%) was chosen to be a random variable, and the maximum value of the coefficient of variation is $\text{COV}(\text{FC}\%) = 0.35$, average value was

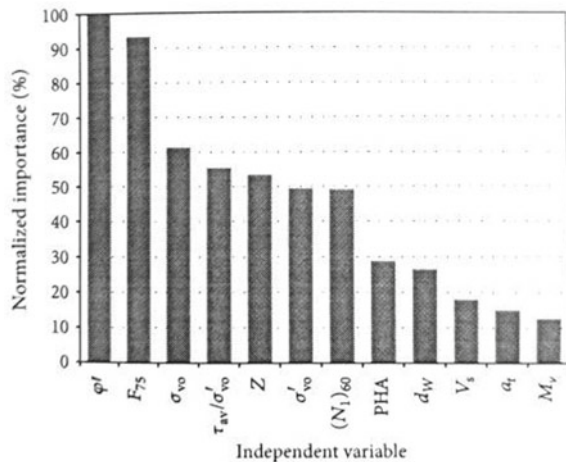
soil layer	Z(m)	FC % (cov = 5%)	FC % round up	N	N60 (round up)	$\sigma'v_0$ (kN/m ²)	σv_0 (kN/m ²)	r _d	CN	CRR	CSR 7.5	N _{1,60}	N _{1,60cs} (clean sand)	CRR with α and β	CRR at Mw	CSR	FS	FS with varied FC and N	
layer 3	10	29.82	30	11	18	166.22	246.22	0.91	0.78	0.2255	0.0950	13.9615	20.2948	20.8368	0.2261	0.1916	0.1122	2.0098	1.7077
	12	26.78	27	11	18	183.04	283.04	0.86	0.74	0.2049	0.0936	13.3045	19.4879	19.1315	0.2049	0.1736	0.1104	1.8557	1.5725
	14	33.72	34	11	18	199.86	319.86	0.81	0.71	0.2196	0.0910	12.7324	20.4990	20.3348	0.2196	0.1861	0.1074	2.0449	1.7328
	16	28.04	28	11	18	216.68	356.68	0.76	0.68	0.1945	0.0876	12.2252	18.5949	18.2351	0.1945	0.1648	0.1084	1.7940	1.5203
	18	25.32	25	11	18	233.50	393.50	0.71	0.65	0.1888	0.0835	11.7796	17.4462	17.7312	0.1888	0.1600	0.0986	1.9150	1.6227
	20	29.89	30	11	19	250.32	430.32	0.65	0.63	0.1980	0.0789	12.0090	18.8423	18.5413	0.1980	0.1678	0.0931	2.1265	1.8024
	22	30.34	30	12	19	267.14	467.14	0.60	0.61	0.1988	0.0739	11.6248	18.4581	18.6149	0.1988	0.1685	0.0872	2.2801	1.9323
	24	29.63	30	12	20	283.96	503.96	0.55	0.59	0.1975	0.0688	11.8682	18.7020	18.4972	0.1975	0.1678	0.0812	2.4318	2.0665
	26	25.69	26	12	21	300.78	540.78	0.54	0.58	0.1907	0.0677	12.1086	18.0085	17.9018	0.1896	0.1607	0.0798	2.3900	2.0138
	28	29.35	29	13	21	317.60	577.60	0.52	0.56	0.1969	0.0664	11.7885	18.3835	18.4502	0.1969	0.1669	0.0783	2.5150	2.1315
	30	33.44	33	14	24	334.42	614.42	0.50	0.55	0.2190	0.0650	13.1240	20.6573	20.2888	0.2190	0.1856	0.0767	2.8557	2.4198
	32	32.57	33	15	24	351.24	651.24	0.49	0.53	0.2172	0.0635	12.8059	20.3392	20.1466	0.2172	0.1841	0.0753	2.8850	2.4449
	34	28.55	29	17	28	368.06	688.06	0.47	0.52	0.2320	0.0619	14.5948	21.1948	21.2790	0.2320	0.1966	0.0744	3.1181	2.6425

Fig. 3 Worksheet for studying effects of N_{SPT} on the safety factor of liquefaction

set to be 25%; N numbers were taken in laboratory testing report; calculation was conducted with/without correction to investigate the sensitivity of N data on safety factor of liquefaction (FS = CRR/CSR). There were several formulas for N_{1,60}, N_{1,60cs} (N_{1,60} clean sand, COV = 0.15 – 0.45, normal distribution). Amplitude scale factor, MSF, was computed to moment magnitude of earthquake from M_w = 7.5 (Youd et al. 2001). According to TCVN 9386:2012, peak horizontal acceleration at the ground surface in Ho Chi Minh City was chosen a_{max} = 0.108 g for a conservative point of view.

- Results in the last two columns in Fig. 2 indicated that:
 - the smaller FC value is, the smaller safety factor FS is, as CSR reduced faster than CRR;
 - below a depth of 20 m, FS decreased rapidly with corrected N than that of no corrected N, and this will not occur in the upper depth;
 - N might be slightly more sensitive than FC%.
- N-SPT could be used in terms of variables as in regression equations in Table 2. By many observations of sandy soil, cohesive soil and clayey soil, significant correlation between N-SPT and other geotechnical parameters were proposed that N can be obtained alternatively by regression equations in Table 2, instead of using complicated formula according to US EPA Seismic Design Guidance in 1995.
- Another method is probabilistic approach where many different sources of uncertainties are taken into account. As N-SPT did not change much when corrected values were used, results also indicated that SPT number was not the sensitive parameter in liquefaction assessment; this point agreed with those in previous research works of Gandomi et al. [8] as illustrated in Fig. 4.

Fig. 4 Importance of 12 predictors of liquefaction assessment (*Source* Gandomi et al. [8])



4 Conclusion

SPT is a common in situ test that is useful for most specific problems of foundation engineering, though it has uncertainties in ways of interpreting its data (corrected N values) and in various working conditions in situ. Fine soil weakly correlated to N partly because of scattered data in stratum and other sources of inherent uncertainties, and corrected N values would not cover all these factors. By analyzing real data from projects in Ho Chi Minh City [10], regression equations for N in terms of properties of fine sandy soil and cohesive soil are found. They showed that the corrected number of blows N'' also significantly correlated to internal friction angle, cohesion, and modulus of deformation. Liquefaction can be assessed by several approaches recommended by different codes, in which SPT is dominant in many empirical formulas of calculation. Corrected N' for sandy soil or N'' for fine soil could be selected by using regression equations, which considered the depth of testing, plasticity, fine content, and dried unit weight (an indicator of density) and internal friction angle (clayey sand or sandy clay). This study also pointed out that the safety factor of liquefaction was small in soil having low FC percentage, and corrected N'' values gave conservative FS below 20 m of depth. This allows N'' is used to replace the other factors in liquefaction assessment of clayey soil as an alternative for comparison with other approaches.

References

1. Hoang TQ, Tam NM (2016) Predicting the bearing capacity of a pile from N-SPT and method of a numerical model, Master Thesis. University of Technology, Vietnam National University
2. CivilBlog.Org (2013) Correction applied to SPT value, post by Suryakanta at <https://civilblog.org/2013/05/13/correction-applied-to-spt-value/>
3. Peck RB, Hanson WE, Thornburn TH (1976) In: Foundation engineering, 2nd edn. John Wiley & Sons Inc, New York
4. Phoon KK, Kulhawy FW (1999) Characterisation of geotechnical variability. Can Geotech J 36:612–624
5. Truong MN (2018) Assessment of the reliability of SPT number in predicting the bearing capacity of precast pile installing into cohesive soil in district 1, HCMC. Master thesis, Open University in HCMC
6. Abdel Naiem Mahmoud MA (2013) Reliability of using standard penetration test (SPT) in predicting properties of silty clay with sand soil. Int J Civil Struct Eng 3(3). ISSN 0976-4399, <https://doi.org/10.6088/ijceser/201203013050>
7. Seed HB, Idriss IM, Arango I (1983) Evaluation of liquefaction potential using field performance data. J Geotech Eng 09(3):458–482
8. Gandomi AH, Fridline MM, Roke DA (2013) Decision tree approach for soil liquefaction assessment. Sci World J 2013, Article ID 346285, <https://doi.org/10.1155/2013/346285>
9. US EPA Seismic Design Guidance (1995) US EPA Website, <http://www.epa.gov/clhtml/pubtitle.html>
10. Soil Investigation Report for Ho Chi Minh's Statue Monument, located at the Administration Building of People Committee in HCMC, District 1. Documented by RECTIE, BachKhoa University (2013)

Evaluating the Possible Use of High Modulus Asphalt Mixtures in Flexible Pavements in Vietnam



T. Nhan Phan and H. T. Tai Nguyen

1 Introduction

In Vietnam, asphalt pavement represents more than 90% of the road transport system due to its advantages over rigid pavement, e.g. smoothness for vehicles and ease of construction and repair. Under the hot climatic conditions, most asphalt pavements in highly trafficked roads of Vietnam are eventually subjected to rutting distress, giving rise to a shortage of traffic safety.

Although many groups of solutions have been applied in the country, e.g. modification of the mixture gradation, bitumen rheology improvement and tight quality control in manufacturing and construction of AC (e.g. [1–4]), the issue is still not thoroughly resolved. HMAC has long-time been found good material for preventing rutting distress and improving the fatigue life of asphalt pavement and is well recognised by its high stiffness, which is 1–2 times higher than that of conventional AC. HMAC can be produced by using hard bitumen or by adding polymer additives to increase its stiffness. As a result, HMAC shows very high resistance to deformation including the permanent one. In theory, it is possibly a good material for the issue of rutting in Vietnam. However, there is little research on the possibility of applying HMAC in the conditions of Vietnam which characterizes by the small thickness of asphalt layers, ranging from 12–15 cm, and hot climatic conditions [5, 6]. For that reason, there is still concerns about the fatigue cracking of flexible pavement structures comprised of HMAC in the country. In effect, the current national standard for

T. Nhan Phan

Faculty of Architecture, Thu Dau Mot University, Binh Duong, Vietnam

e-mail: nhanpt@tdmu.edu.vn

H. T. Tai Nguyen (✉)

Faculty of Civil Engineering, Ho Chi Minh City University of Technology and Education, Ho Chi Minh City, Vietnam

e-mail: tainht@hcmute.edu.vn

R&D Department, BMT Construction Investment J.S.C., Ho Chi Minh City, Vietnam



Fig. 1 Typical rutting profile of flexible pavements in Vietnam. Photos taken by BMT J.S.C. in May 2014 at National Highway 1A, located between An Suong and An Lac intersections

designing flexible pavement [7] does not give a guideline for checking the resistance to fatigue and rutting of asphalt pavements while the use of other standards, e.g. [8], is not a straightforward work since model parameters should be correlated to fit the conditions in Vietnam. For that reason, experiences with HMAC pavements in Europe and other countries cannot be directly applied. Therefore, the service life relating to rutting and fatigue cracking of flexible pavements using HMAC should be examined.

Since the resistance to rutting of HMAC is better than that of conventional AC, the use of HMAC in the wearing course or (and) in the binder course will obviously increase the resistance to rutting of flexible pavements. However, according to our observations in the field, the rutting distress occurs primarily in the wearing course as shown in Fig. 1 due to the high temperature at the surface and high stress caused by overloaded vehicles. Consequently, HMAC should be used in wearing course or in both two courses to maximize its contribution to the resistance to rutting of the whole flexible pavement structure.

In this study, the resistance to fatigue cracking of different combinations of AC and HMAC layers in flexible pavement structures will be examined and ranked from the lowest to the highest value so as to select the most effective use of HMAC (relating to fatigue cracking) in flexible pavements in the conditions of Vietnam. To achieve this goal, two following specific objectives are defined: (i) analysing the stress and strain in thin asphalt pavement structures (12-cm in thickness of asphalt layers) comprised of one or two HMAC layers with an assumption of perfect bond condition between layers and (ii) conducting experimental studies on the fatigue behaviour of AC and HMAC using the cyclic four-point bending test to determine the characteristic fatigue lines. The bottom-up fatigue life of flexible pavement structures was predicted by using the semi-analytical approach as proposed in [9].

2 Composition and Finite Element Modelling of Flexible Pavement Structures

The flexible pavement structure in Vietnam typically comprises 4 layers: AC of surface, AC of base, graded aggregate and road base as shown in Fig. 2. The thickness of asphalt layers is very small, normally varying from 12 to 15 cm. The pavement structures studied in this work comprised one or two layers of HMAC (PS-1, PS-2 and PS-3) while the reference pavement structure (PS-Ref) is a very commonly used one consisting of 2 layers of conventional AC. In all pavement structures, the thickness of the wearing course is 5 cm, that of the binder course is 7 cm and that of the base course is 40 cm.

Let σ be the Cauchy stress tensor, ϵ be the strain tensor in the structure. The behaviour of the base course and the road base is modelled by Hooke elastic law

$$\boldsymbol{\sigma} = 2\mu\boldsymbol{\epsilon} + \lambda tr(\boldsymbol{\epsilon}).\mathbf{I} \quad (1)$$

where \mathbf{I} is second order tensor of unity, μ is shear modulus, λ is Lamé constant, and trace of a tensor is defined as $tr(\boldsymbol{\varepsilon}) = \varepsilon_{ii}$. The asphalt concrete has viscoelastic behaviour which depends on the loading frequency and temperature. In an approximate way, we can consider its behaviour as quasi-elastic at a fixed value of loading frequency and temperature. We will analyse the behaviour of pavement structures only at loading frequency of 10 Hz and temperature of 25 °C as suggested by Tran et al. [10]. The elastic modulus of conventional AC and HMAC is respectively 5 GPa and 15 GPa and the Poisson ratio of both AC and HMAC is equal to 0.35. The equivalent elastic modulus of the aggregate layer and the road base is assumed to be equal to 160 MPa and the Poisson ratio is 0.3.

The wheel loading applied to the pavement is standardised in the national standard (22 TCN [7]), in which the tyre-print is assumed to be a circle having 36-cm diameter and the standard wheel pressure is 0.6 MPa resulted from a half of 12-ton axle load. The pavement structures can be considered working in axisymmetric conditions and the structures can therefore be modelled in 2 dimensions to reduce the computing time (Fig. 3).

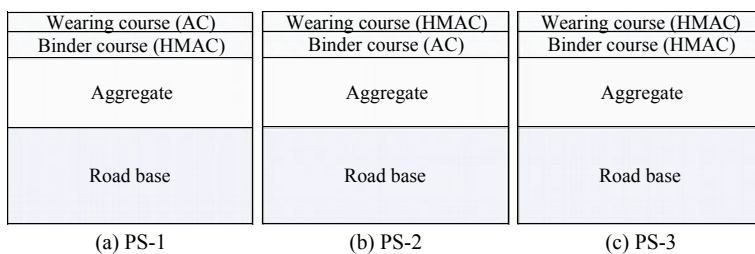
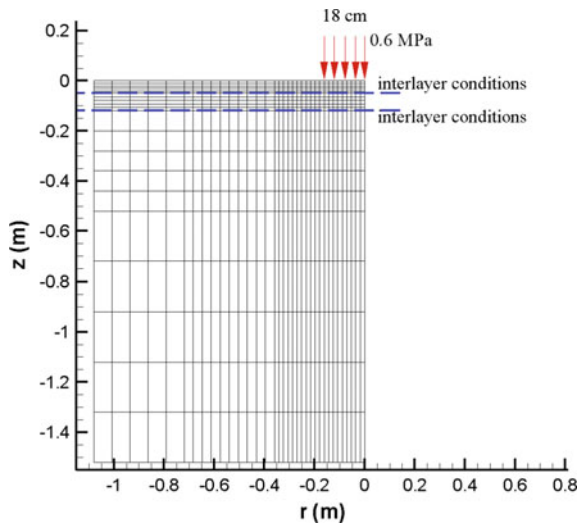


Fig. 2 Typical composition of pavement structures in Vietnam

Fig. 3 Finite element discretisation of pavement structures using 8-node planar elements



The structures were discretised by 700 8-node planar element. The total nodes of the problem are 2133. The interactions between the wearing course and the binder course and between the binder course and the aggregate layer were treated with a frictional contact and bond conditions such that there is not slipping and debonding. It was assumed that the friction coefficient between layers is 0.5, the tangential bond strength is 0.5 MPa at 25 °C and the normal bond strength is small enough, 0.1 MPa, to not create debonding. In order to determine these parameters, the sample preparation and testing methods presented in [11] can be applied.

The boundary conditions of the problem are as follow: the nodes at the leftmost and rightmost surfaces are fixed for horizontal displacement while all the nodes at the bottom surface are fixed for all displacements. The analysis was performed using a homemade FEM programme and the obtained results will be reported and discussed in the following Section.

3 Analysis Results

The distributions of tensile stress (σ_{rr}) in pavement structures PS-1, PS-2, PS-3 and PS-Ref at 25 °C are presented in Figs. 4 and 5 and the profiles of tensile stress with depth of pavement structures at $r = 0$ m are shown in Fig. 6. It can be observed that the maximal tensile stress is located at the bottom of binder courses ($z = -0.12$ m) because of full bond conditions between layers. The PS-1 has highest tensile stress at bottom of binder course (3.41 MPa), followed by PS-3 (2.87 MPa), PS-Ref (1.93 MPa) and the PS-2 has smallest tensile stress (1.75 MPa). For comparison purposes, the stresses were also determined by using the approximated formula

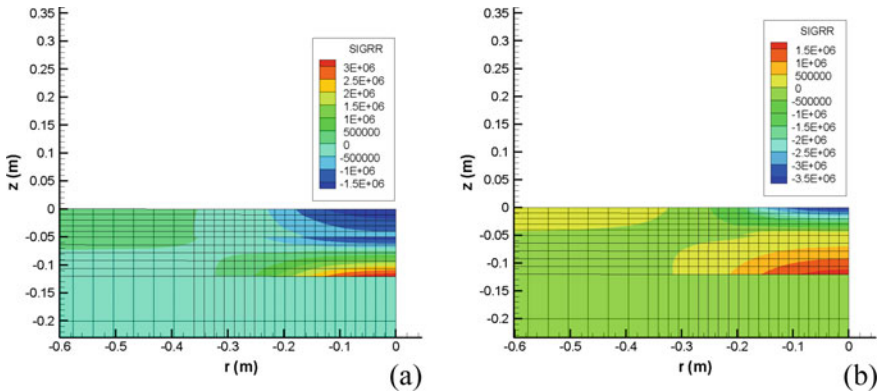


Fig. 4 Stress in asphalt layers at 25 °C. **a** PS-1. **b** PS-2

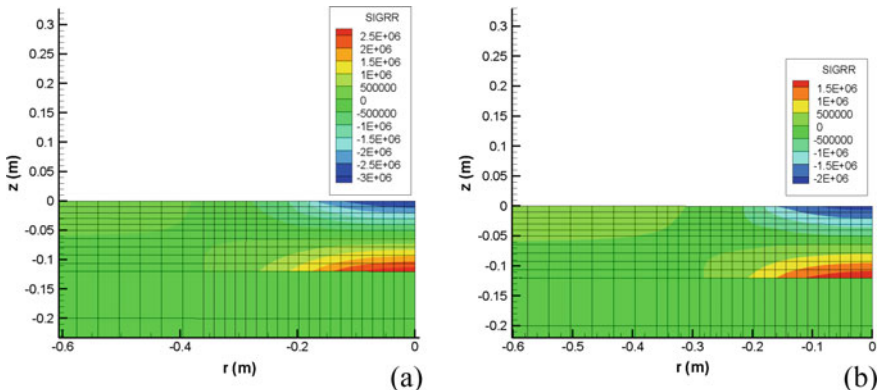
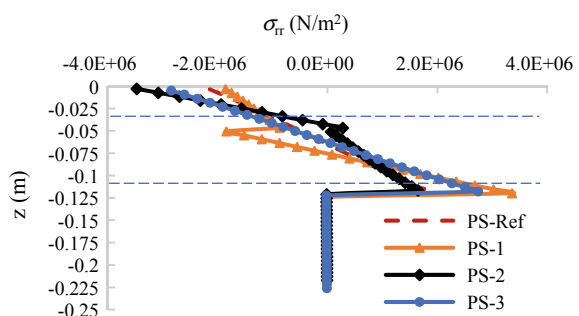


Fig. 5 Stress in asphalt layers at 25 °C. **a** PS-3. **b** PS-Ref

Fig. 6 Profiles of maximal tensile stress in the pavement at $r = 0$ m



(Eq. F-4) provided in 22 TCN-11 (2006). The obtained maximal bottom-up tensile stresses are as follows: $\sigma_{rr} = 2.49, 1.49, 2.19$ and 1.8 MPa for PS-1, PS-2, PS-3 and PS-Ref, respectively. Because the errors between these stresses are relatively large varying from 7% in cases of conventional AC pavement to 37.3% in cases of HMAC pavement, the stresses were compared again to those obtained based on Burmister multi-layered elastic theory. It can be shown that the stresses obtained with FEM and multi-layered elastic theory are in good agreement. The errors are less than 9.5%—namely, $\sigma_{rr} = 3.17, 1.60, 2.69$ and 1.80 MPa for PS-1, PS-2, PS-3 and PS-Ref, respectively. Since the tensile strengths of AC and HMAC are different, the ratio of tensile stress with respect to tensile strength ($\sigma/R_{tensile}$) should be determined. We have characterised the indirect tensile strength of AC and HMAC at 25°C , 1.1 MPa for AC and 2.1 MPa for HMAC. The calculation shows that the stress/strength ratio of PS-3 is smallest (0.91) followed by that of PS-2 (1.59), PS-1 (1.62) and PS-Ref (1.75). Therefore, PS-3 seems to have the best resistance to fatigue, followed by PS-2, PS-1 and PS-Ref.

In order to verify the ranking obtained from previous analysis based on the stress/strength ratio, the resistance to fatigue of asphalt mixtures was characterised using the cyclic four-point bending test at 25°C and 10 Hz. In additions, the strain in the pavement structures were also extracted and presented in Fig. 7. The values of ε_{rr}^{\max} are $150, 236, 126$ and $264 \mu\varepsilon$ for PS-1, PS-2, PS-3 and PS-Ref, respectively. Based on experimental results, the characteristic fatigue lines of both AC and HMAC are presented in Eq. (2) [5]:

$$N_f^{AC} = 7.86 \times 10^{16} \left(\frac{1}{\varepsilon} \right)^{4.53}; N_f^{HMAC} = 7.35 \times 10^{13} \left(\frac{1}{\varepsilon} \right)^{3.73} \quad (2)$$

By substituting the values of maximal tensile strain at the bottom of the binder course for the variable ε in Eq. (2), the predicted fatigue lives of pavement structures are obtained and ranked in ascending order as follows: 5.62×10^5 cycles for PS-1; 8.42×10^5 cycles for PS-Ref; 1.08×10^6 cycles for PS-3 and 1.4×10^6 cycles for PS-2. Therefore, the use of HMAC in the wearing course in PS-2 gives the highest fatigue life while the use of HMAC in the binder course in PS-1 gives the lowest one. It should be noted that Eq. (2) is used only for comparison of fatigue lives of different pavement structures. The fatigue life in reality of pavement structures is much higher than that obtained from these equations because many other influencing factors are not considered yet in the prediction, e.g. wheel wander effect, self-healing of asphalt mixtures during resting periods (no loading), hot temperature periods and other effects that increase the reduction of stiffness during fatigue testing [12–14].

Based on the previous results, both PS-1 and PS-Ref have lower resistance to fatigue than PS-2 and PS-3 does. In terms of economic aspect, using one layer of HMAC is less costly than using two layers of HMAC. Therefore, the use of HMAC in the wearing course of the pavement structure will be a twofold application: (i) preventing rutting distress due to its highly rutting resistant property and (ii) reducing the tensile stress and strain at the bottom of the binder course, giving rise to better

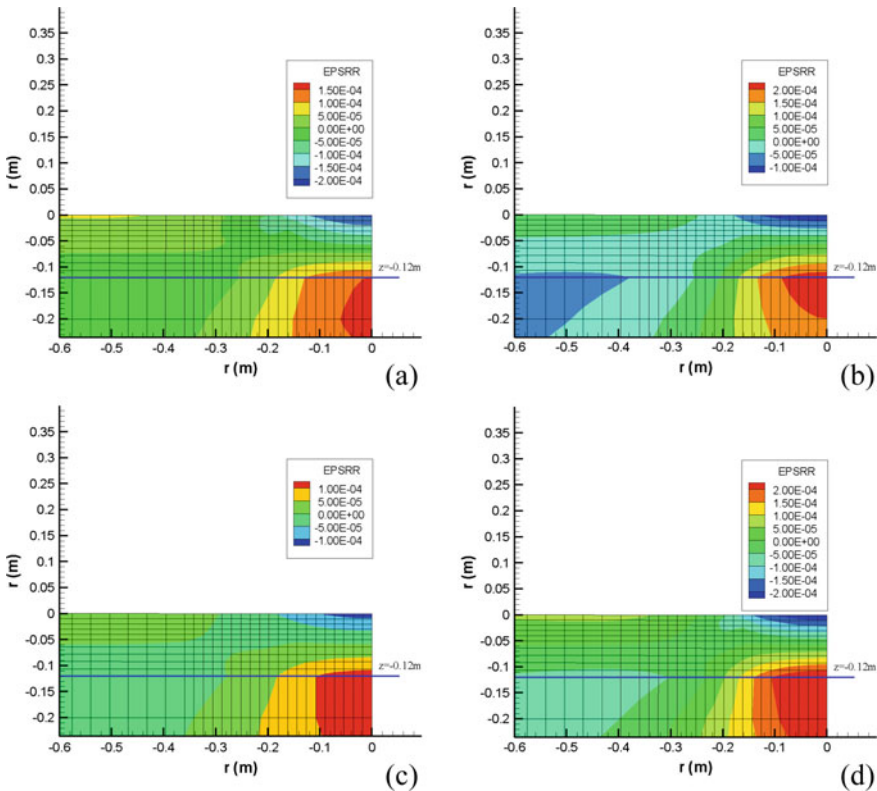


Fig. 7 Strain in asphalt layers at 25 °C. **a** P-1. **b** P-2. **c** P-3. **d** P-Ref

fatigue life of pavement structures. It should be highlighted again that the above-obtained results are only valid if the layer-to-layer bond is always ensured. The verification of layer-to-layer bond has been reported in a previous study [15] and will not be presented in this study.

4 Conclusions

The possible use of high modulus asphalt mixtures in thin flexible pavements like those in Vietnam has been successfully examined. When HMAC is properly used in flexible pavements, the resistance to fatigue of the pavement does not decrease as concerned yet increases. For maximize the contribution of HMAC to the resistance to rutting of flexible pavement structures, HMAC must be used in the wearing course or in both the wearing and binder courses. The fatigue lives of the flexible pavements in these compositions are the largest ones. In considering the economic aspects, using only one HMAC layer for the wearing course is the best solution because the HMAC

layer in wearing course will increase the resistance to rutting of the pavement while it will reduce the tensile stress and strain at the bottom of the underneath AC layer, increasing the resistance to bottom-up cracking of the pavement.

Acknowledgements The authors would like to acknowledge the scientific research program of Ho Chi Minh City University of Technology and Education for funding this study.

References

1. Decision 858-MOT (2014) Applying current technical standards to strengthen the quality of management of design and construction of hot mix asphalt pavement of high traffic roadway. MOT, Hanoi
2. Nguyen HTT, Tran TN (2017) Laboratory study for the use of stone mastic asphalt in Vietnam (in Vietnamese). *Sci J Thu Dau Mot Uni* 1(32):57–62
3. Nguyen HTT, Tran TN (2018) Effects of crumb rubber content and curing time on the properties of asphalt concrete and stone mastic asphalt using dry process. *IJPRT* 13(3):238–244
4. Tran TN, Nguyen HTT, Nguyen KS, Nguyen NTH (2018) Semi-flexible material: the sustainable alternative for the use of conventional road materials in heavy-duty pavement. In: *Congrès International de Géotechnique—Ouvrages—Structures*, pp 17–24. Springer, Singapore (2018)
5. Nguyen HTT, Tran TN (2016) Fatigue characterisation of high modulus asphalt mixture for evaluating its possible use in Vietnam (Technical report). BMT Construction-Investment J.S.C.
6. Tran DH (2018) Research on high modulus asphalt mixture using for flexible pavements of high-class road in Vietnam. Ph.D. thesis. University of Transport and Communications, Hanoi
7. TCN 211-06 (2006) Flexible pavement—requirements and specifications for design. MOT, Hanoi
8. MEPDG (2008) Mechanistic–empirical pavement design guide—a manual of practice. American Association of State Highway and Transportation Officials
9. Setra—LCPC (1994) Conception et dimensionnement de structures de chaussée—Guide technique, Service d'études techniques des routes et autoroutes. Laboratoire central des ponts et chaussées, Paris
10. Tran TL, La VC, Nguyen XD (2015) Experimental study on the resistance to fatigue of asphalt concrete used for pavement surface in Vietnam (in Vietnamese). *J Trans* 4
11. Nguyen HTT et al (2017) Evaluating the bonding between asphalt and cement concrete layers. *J Civil Eng (Vietnam)*, 8
12. Di Benedetto H, Nguyen QT, Sauzéat C (2011) Nonlinearity, heating, fatigue and thixotropy during cyclic loading of asphalt mixtures. *Road Mater Pavement Des* 12(1):129–158
13. Huang YH (2004) Pavement analysis and design, 2nd edn. Person Prentice Hall, Upper Saddle River
14. Nguyen HTT, Nguyen NH (2018) Using a non-local elastic damage model to predict the fatigue life of asphalt pavement structure. In: Proceedings of the international conference on advances in computational mechanics 2017. Springer, Singapore
15. Nguyen HTT, Tran VT (2019) Analysing the interlayer shear stress of asphalt pavement composed of conventional and high modulus asphalt. *J Sci Technol Civil Eng* 13(5V):85–92

Experimental Studies on the Improvement of Soft Soils by Cement in Vinh Long City



Quang Vinh Pham, Nhat Truyen Phu, Ba Vinh Le, and Dinh Uy Vo

1 Introduction

During the last decades, cement deep mixing (CDM) method, normally forming soil-cement columns in the ground, is widely used to improve soft clayey subsoils for highway constructions. At the present time, there are many kinds of CDM technology, such as: dry mixing, wet mixing, jet grouting.... Depend on the geotechnical profile and required technical design, engineer shall choose the suitable technic. The soil-cement column is not a new technology in the context of Vietnam, it was introduced since 2000s and so far has been employed widely in various area in Ho Chi Minh City [1]. Most studies of soil cement piles only perform unconfined compression test [1–5], even Vietnam standard TCVN 9403:2012 [6], it merely requires unconfined compression strength parameter (UCS) on dry soil cement samples. However, in fact, the soil cement columns are always in saturated condition in situ, which means that UCS parameter on dry samples may contain some error. In order to clarify this difference, we conducted several unconfined compression test (UCT) on both dry and saturated samples. In addition, we also carried out the unconsolidated-undrained triaxial test (UU) in saturated samples to examine the effect of confining stress on the values of peak strength and Young's modulus.

Q. V. Pham

Faculty of Civil Engineering, Mien Tay Construction University, Vinh Long City, Vietnam

N. T. Phu (✉) · D. U. Vo

Faculty of Geology and Petroleum Engineering, Ho Chi Minh City University of Technology,
VNU-HCM, Ho Chi Minh City, Vietnam

e-mail: pntruyen@hcmut.edu.vn

B. V. Le

Faculty of Civil Engineering, Ho Chi Minh City University of Technology, VNU-HCM, Ho Chi
Minh City, Vietnam

Moreover, soil-cement columns are usually designed as not only reduce settlements of soil under high-way and embankment but also retaining wall for deep excavation projects in which the parameters of hydraulic conductivity and shear strength of soil-cement samples are necessary. Thus, in this study, we conducted several permeability and direct shear test that is beneficial for future research in understanding behavior of CDM by simulation on PLAXIS software. This study could be considered as precedent for studies of CDM method and its related issues in the area in the future.

2 Samples Preparation

The study site is located in Vinh Long city, the capital of Vinh Long Province in Vietnam's Mekong Delta, where is known to have a thick layer of soft soil; still, CDM technique remains little applied. The geotechnical profile consists a thick layer of peaty clay alternated with thin layers of fine sand.

Soft clay samples at depths from 0 to 20 m were taken and mixed with cement in various content, namely 100, 150, 200, 250 kg/m³. Mixer features a 5-liter stainless steel bowl and stirrer wing, and a two-speed motor, which runs at either 140 ± 5 rpm or 285 ± 10 rpm. After mixing and molding, the stabilized soil was cured for 14 and 28 days. The molding of specimens was done in such a way that a constant unit weight for each cement content was obtained. The specimens are cured in a foam container with a moisture content of 90–100% and a temperature of 25 °C. In terms of saturated specimens, they were soaked in water and vacuumed 1 day before the experiment (Figs. 1, 2 and 3; Tables 1 and 2).

3 Results and Discussion

3.1 Result of Direct Shear Test

The soft clay samples were intimately mixed with cement at a content of 100–250 kg/m³ of wet soil. After mixing and molding, the stabilized soil was cured for 14 and 28 days. At least three specimens for each cement content were molded for each curing period. The molding of the specimens was done in such a way that a constant unit weight for each cement content was obtained. The specimens are cured in a foam container with a moisture content of 90–100% and a temperature of 25 °C. After that, direct shear test is carried out in order to determine shear strength parameters of the specimens for each curing. The results are show in Table 3 and Fig. 4.



Fig. 1 Study area and Soil sampling (ward 3 and ward 9—Vinh Long City) [Google map]

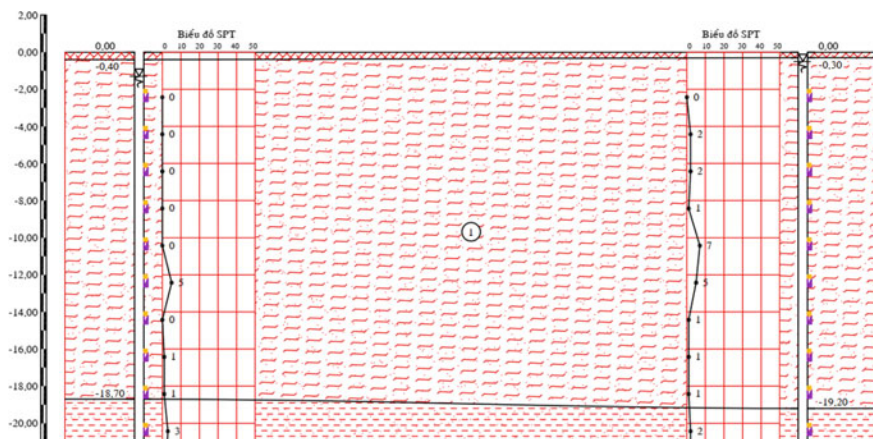


Fig. 2 The geotechnical cross section at study area [7]

3.2 Result of Permeability Test

The hydraulic conductivity of the specimens for each cement content was determined by the falling head test. As shown in Table 4, the hydraulic conductivity of the soil decreased significantly when increasing the cement content.



Fig. 3 Sample preparation

Table 1 Soil profile [7]

Parameters	Symbol	Unit	Value
Unit weight	γ_w	(kN/m ³)	16.4
Internal friction	φ	(degree)	4°01'
Cohesion	C	(kPa)	6.0
Water content	W	(%)	55.49
Liquid limit	W _L	(%)	51.8
Plastic limit	W _P	(%)	31.5
Plastic index	I _p	(%)	20.3
Specific gravity	G _s	—	2.68
Void ratio	e	—	1.524
Compression ratio	a ₁₋₂	(m ² /kN 10 ⁻²)	0.152
Percent clay	—	(%)	35.2
Percent silt	—	(%)	39.5
Percent sand	—	(%)	25.3
Percent gravel	—	(%)	—

3.3 Result of Unconfined Compression Test (UCT)

Like the direct shear test, the unconfined compression test was conducted in samples with cement content of 100–250 kg/m³ wet soil, which was cured for 14 and 28 days. As being shown in Fig. 5, the deviator stress and Young's modulus of UCT from dry sample have a linear relationship with cement content (Table 5).

Moreover, the UCT was conducted in saturated sample, which was soaked in water and vacuumed 1 day before. The results were compared with those of dry samples. The results are shown in Table 4 and Fig. 5. The deviator stress and Young's modulus of UCT from saturated samples are smaller than those parameters of dry samples. The deviator stress decreases from 15 to 37% and the Young's modulus decreases from 55 to 65% depending on cement content (Fig. 6; Table 6).

Table 2 The number samples were prepared

Cement content (kg/m ³)	Test types						Unconsolidated—undrained triaxial test	
	Direct Shear Test		Unconfined compression test			Permeability test		
	Dry sample	Dry sample	Saturated sample					
Curing time								
14 Days	28 Days	14 Days	28 Days	28 Days	28 Days		28 Days	
Dimension (cm)								
d × h = 6.18 × 2		d × h = 4 × 8				d × h = 6.18 × 4		
100	9	9	3	3	3	9	3	
150	9	9	3	3	3	9	3	
200	9	9	3	3	3	9	3	
250	9	9	3	3	3	9	3	

Table 3 Result of direct shear test

Cement content (kg/m ³)	Curing time: 14 days		Curing time: 28 days	
	Internal friction φ (°)	Cohesion c (kPa)	Internal friction φ (°)	Cohesion c (kPa)
100	27.3	173.3	31.4	190.8
150	48.7	133.4	48.0	237.0
200	40.1	322.8	41.8	391.5
250	35.6	414.7	49.6	437.7

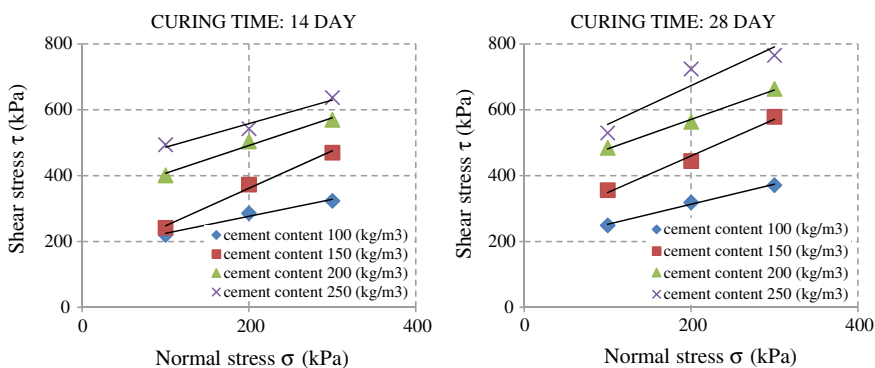
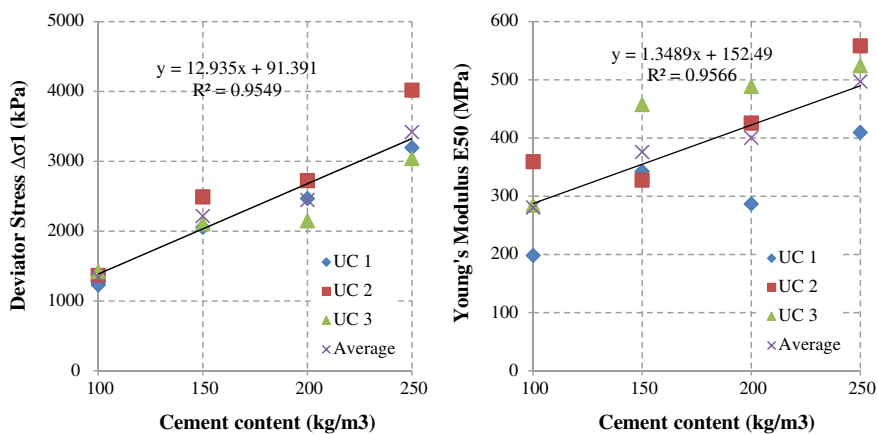
**Fig. 4** Result of Direct shear test

Table 4 The result of permeability test

Cement content (kg/m ³)	Hydraulic conductivity K (cm/s)	Decrease (%)
Natural	7.60E-07	
100	9.15E-08	731
150	2.91E-08	2512
200	1.56E-08	4772
250	1.28E-08	5838

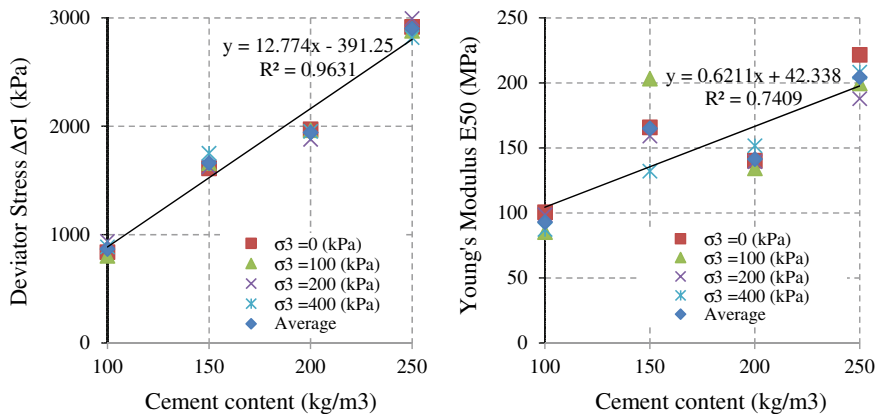
**Fig. 5** UC test results**Table 5** The result of unconfined compression test

Curing time	Deviator stress	Young's modulus
14 day	$\Delta\sigma_1 = 12.188x - 250.97$	$E_{50} = 1.2829x + 26.94$
28 day	$\Delta\sigma_1 = 12.935x + 91.391$	$E_{50} = 1.3489x + 152.487$

where x is Cement content (kg/m³)

3.4 Result of Unconsolidated—Undrained Triaxial Test (UU)

The unconsolidated—undrained tri-axial test was conducted on the saturated specimens, which were cured for 28 days, under confining pressure of 0, 100, 200, 400 (kPa). As being shown in Fig. 6, when we increase confining pressure from 0 to 400 (kPa), the deviator stress $\Delta\sigma_1$ changes very slightly for all cement content whereas the deviator stress and Young's modulus of UU have a linear relationship with cement content (Table 7).

**Fig. 6** UU test results**Table 6** The average shear stress increase from 14 to 28 day depend on cement content

Cement content (kg/m ³)	Deviator Stress $\Delta\sigma_1$ (kPa)			Young's modulus E_{50} (MPa)		
	Dry sample	Saturated sample	Decrease (%)	Dry sample	Saturated sample	Decrease (%)
HL100	1339	839	37	281	101	64
HL150	2217	1613	27	376	166	56
HL200	2446	1973	19	400	140	65
HL250	3418	2917	15	497	222	55

Table 7 The result of unconsolidated—undrained triaxial test

Curing time	Deviator stress	Young's modulus
28 day	$\Delta\sigma_1 = 12.774x - 391.25$	$E_{50} = 0.6211x + 42.338$

With x: Cement content

4 Conclusion

In this paper, we performed diverse experiments (namely, direct shear test, permeability test, unconfined compression test and unconsolidated—undrained tri-axial compression test) on soil cement samples on both dry and saturated condition. The results are as follows:

1. In the direct shear test, the internal friction is range from 31.4° to 49.6°, the cohesion increases when increase cement content.
2. When increasing the cement content, deviator stress and young modulus from UCT and UU also increases linearly with a very high correlation coefficient.

3. Hydraulic conductivity of soil after mix cement decrease depend on cement content.
4. Deviator stress and young modulus from UCT of dry sample are higher than saturated one.
5. Deviator stress and young modulus at different confining pressure levels (0, 100, 200 and 400 kPa) vary negligibly.

Acknowledgements The authors acknowledge the support provided by Faculty of Civil Engineering, Mien Tay Construction University, Vinh Long City, Vietnam for conduct this research (following scientific research contract No. GV.01.17.04).

References

1. Tran-Nguyen HH, Tho T, Ly TH (2014) A field trial study on jet grouting to improve the subsoil in Ho Chi Minh City, Vietnam. *J Teknologi* 69(3)
2. Lambert S, Spéciales KF, Rocher-Lacoste F, SETRA S, Le Kouby A (2012) Soil-cement columns, an alternative soil improvement method. In: ISSMGE-TC 211 international symposium on ground improvement, vol 3, pp 179–188
3. Jaritngam S, Swasti S, Tonnayopas D, Thongchim P (2008) Improvement for subsoil by cement column—a case study in Thailand. In: Proceedings of the 13th international conference of Hong Kong society for transportation
4. Bergado DT, Ruenkrairergsa T, Taesiri Y, Balasubramaniam AS (1999) Deep soil mixing used to reduce embankment settlement. *Proceed Inst Civil Eng-Ground Improv* 3(4):145–162
5. Hashim R, Islam MS (2008) Properties of stabilized peat by soil-cement column method. *Electron J Geotech Eng* 13:1–9
6. TCVN 9403:2012, Stabilization of soft soil- The soil cement column method
7. Geotechnical report of Vinh Long Provincial Party Committee Building Project

Finite Element Analysis of a Deep Excavation Adjacent to the Ben Thanh—Suoi Tien Metro Tunnels



Le Ba Vinh, Ngoc Trieu Hoang, Hoang The Thao, and Hoang Long Hai

1 Introduction

Recently, in Ho Chi Minh City, due to rapid developments and limited urban area, more and more deep basements were constructed for high-rise buildings as car parks and shopping areas. In some cases these basements were constructed adjacent to existing metro tunnels, so it is important to check potential effects of constructing deep excavations on adjacent metro tunnels in design stage. Total displacement of tunnels are one of the important criteria to ensure the Metro tunnels operates normally. Moreover, the impact of excavations on surrounding structures is also an important part of design process when excavating in a limited urban area. In this study both finite element method is carried out to predict these potential effects during the performance of this excavations. However, there is a difference in the results between 3D and 2D finite analyses because 2D model depends on plane strain simulation and does not accurately describe the actual excavations as 3D models. Whereas, in 3D models the whole size excavation is modelled, so the “three-dimensional effect” or the “corner effect” is considered and it results in a reduction of ground movement near the corners of the excavation due to the stiffening effects of the corners. By comparing the ground movement assessment and the total displacement of tunnels in 3D and 2D finite analyses, this paper concentrate on demonstrating the benefit of adopting 3D finite element analysis for potential economical engineering design.

L. B. Vinh · N. T. Hoang (✉) · H. T. Thao · H. L. Hai

Faculty of Civil Engineering, Ho Chi Minh City University of Technology, VNU-HCM, Ho Chi Minh City, Vietnam

e-mail: trieuhn@hcmut.edu.vn

Fig. 1 The location of the high-rise building



2 Project Background

The high-rise buildings is located in the central area of Ho Chi Minh City on Ton Duc Thang Street and overlooking Sai Gon River. The location of the high-rise building is shown in Fig. 1. The deep excavation is only roughly about 4.2 m away from the existing bored tunnel segments of Ho Chi Minh City Urban Railway Construction Project, from Opera House Station to Ba Son Station at chainage point: $\text{km}^1 + 300 \div \text{km}^1 + 400$. There will be many problems are anticipated during the construction of this deep basement, especially the total displacements and differential movement of bored tunnel segment.

3 Deformation Analysis During Excavation by Finite Element Method Analysis

3.1 Soil Profile

The high-rise building and underground tunnel of the first line from Ben Thanh Market to Suoi Tien Park are located in District 1, with the sub soil profile to a dept of 100 m can be described by 8 sata:

- (F) Fill soil, Clayey sand mixed with construction debris (brick, concrete, etc.) mostly 0.5–1 m thick.
- (1a) Soft to very soft clay with organic matter, the stratum thickness varies from 1.4 to 4 m. The SPT value (N30) is mostly 1–3.
- (2) Medium dense silty sand, the stratum thickness varies from 26.8 to 31.6 m. The SPT value is approximately 10 on average.
- (3) Very stiff clay with occasional fine laterite gravel, the stratum thickness varies 7.5 to 12.2 m. The SPT value is approximately 34 on average.

Table 1 Adopted geotechnical design parameters for each strata layer

Layer	F. Fill soil	1a. Soft Clay	2. Silty sand	3. Stiff clay	3a. Stiff sandy clay	4. Clayey sand	5. Stiff clay	6. Dense silty sand
Type	HSM drained	HSM undrained	HSM drained	HSM undrained	HSM undrained	HSM drained	HSM undrained	HSM drained
γ_{unsat} (kN/m ³)	18	15.50	21.20	20.90	21.70	21.10	21.10	21.30
γ_{sat} (kN/m ³)	18.5	15.71	21.40	20.99	21.92	21.44	21.30	21.67
E_{50}^{ref} (kN/m ²)	10,000	3500	16,000	74,000	50,000	75,000	60,500	93,000
$E_{\text{oed}}^{\text{ref}}$ (kN/m ²)	10,000	3500	16,000	74,000	50,000	75,000	60,500	93,000
$E_{\text{ur}}^{\text{ref}}$ (kN/m ²)	30,000	10,500	48,000	222,000	150,000	225,000	181,500	279,000
c' (kN/m ²)	5	12.70	5.10	21.90	15.60	4.30	46.30	4.30
ϕ' (°)	25.00	20.88	27.82	29.35	28.62	28.97	19.75	29.27

- (3a) Very stiff sandy clay, the stratum thickness range from 3 to 6.5 m. The SPT value is approximately 46 on average.
- (4) Medium dense clayey sand, the stratum thickness ranges from 20 to 36 m. The SPT value is approximately 38 on average.
- (5) Very stiff lean clay with sand, the stratum thickness ranges 0.5 to 3 m. The SPT value is approximately 28 on average.
- (6) Dense to very dense silty sand with occasional sandstone cobble, the stratum thickness is higher than 10 m. The SPT values are between 34 and higher than 50.

3.2 Geotechnical Parameters

In this study both 3D and 2D finite element analyses are carried out by using PLAXIS program [1, 2]. Hardening Soil Model (HSM) in PLAXIS program was used to simulate the behaviour of the soils in all layers and all the soil parameters in HSM are described in Table 1.

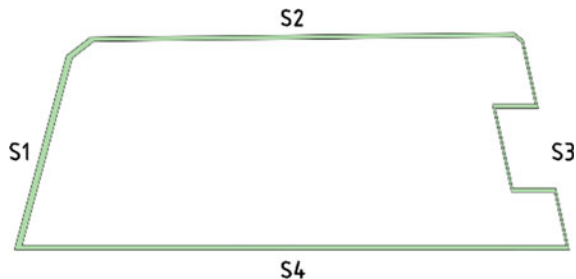
3.3 Structural Material Properties

a. Tunnel

Table 2 Adopted Properties for Tunnel Segment

Outside diameter (mm)	Inside diameter (mm)	Width (mm)	Concrete grade
6650	6050	1200	C48

Fig. 2 Layout of diagram wall



Concrete grade C48 will be used for tunnel segment. The properties of tunnel segment are described in Table 2.

b. Diagram wall (DW)

Diagram wall (DW) using Grade C35/45 concrete material including 2 dimension types: 1500 mm type for diagram wall adjacent to Metro line (S1) and 1000 mm type for the others (S2, S3, S4), which are described in Fig. 2.

c. Basement slab

Basement slabs, with large horizontal stiffness, act as bracing systems in the Semi-Top down construction method during excavation. Basement slab using Grade C30/37 concrete material including 5 basement BM, B1, B2, B3 300 mm thick and B4 floor thickness 1000 mm.

3.4 2D Finite Element Method

The 2D model was developed in two sections as being described in Fig. 3. The soil parameters, material properties and drainage types in 2D models are presented in Sect. 3 and the diaphragm wall as well as the precast concrete segments of tunnel were modeled as “plates” [1].

Based on the PLAXIS 2D analysis result, settlement increases as construction stages increases. The maximum ground settlement occurred at the final stage when excavating to the bottom of STP (sewage treatment plant) tank and foundation is approximately 75 mm, Figs. 4 and 5, and the total displacement of the tunnel is about 33.7 mm, Fig. 12. The total displacement results of the tunnels from the PLAXIS 2D analysis far exceeded the design limit of 15 mm.

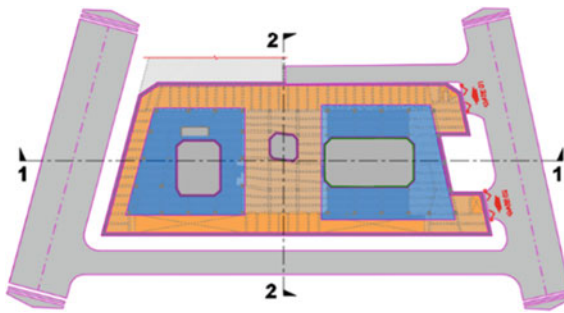


Fig. 3 General view of 2D model

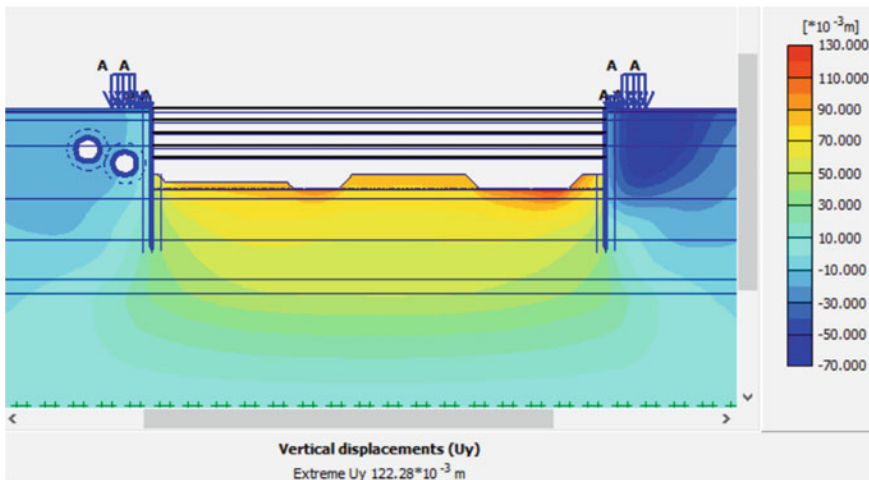


Fig. 4 PLAXIS 2D Result—Settlement due to excavation to the bottom of STP for section 1-1

3.5 3D Finite Element Method

The 3D model was developed in a $300\text{ m long} \times 200\text{ m wide} \times 100\text{ m deep}$ rectangular block, representing a $130\text{ m long} \times 50\text{ m wide} \times 22\text{ m deep}$ basement that constructed based on Semi-Topdown method. Two existing Metro tunnels are also simulated in the 3D model that is located about 4.2 m away from S1 diaphragm wall. A general view of the 3D model is presented in Figs. 6 and 7. The soil parameters, material properties and drainage types in the 3D model remain the same from 2D models. In PLAXIS 3D model, the diaphragm wall and the tunnel's precast concrete segments were modeled as "plates" [2]; the walings were modeled as "beams" [2]. Groundwater and groundwater boundary condition in 3D model remain the same from 2D model. Construction sequence in 3D model kept the same as the 2D model.

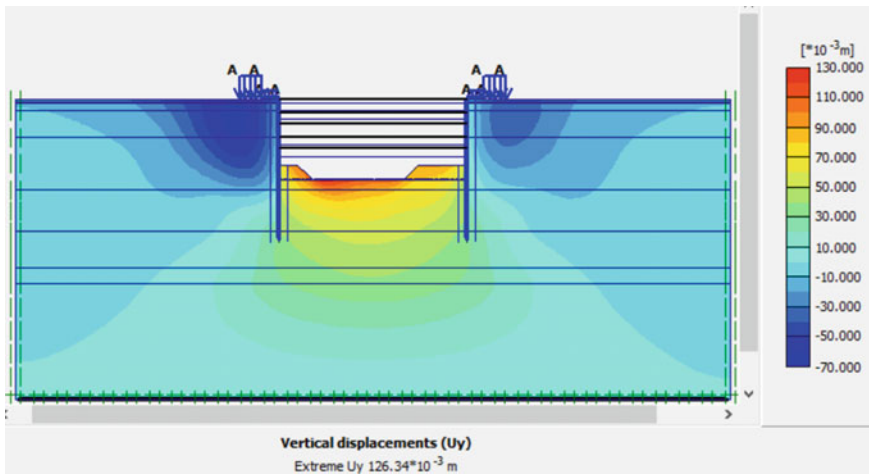


Fig. 5 PLAXIS 2D Result—settlement due to excavation to the bottom of STP for section 2-2

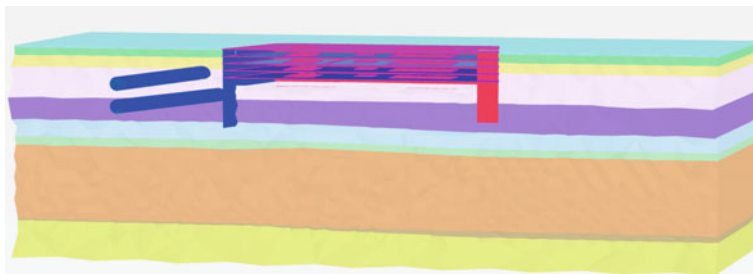


Fig. 6 General view of 3D model

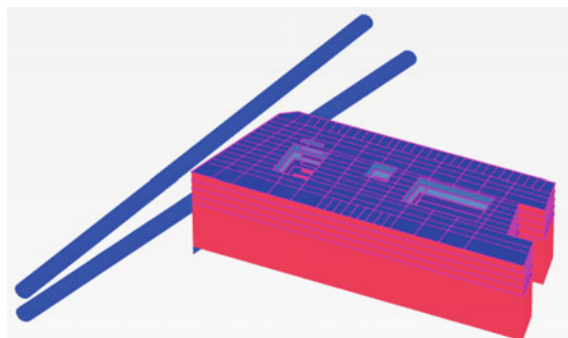


Fig. 7 General view of 3D model structural elements

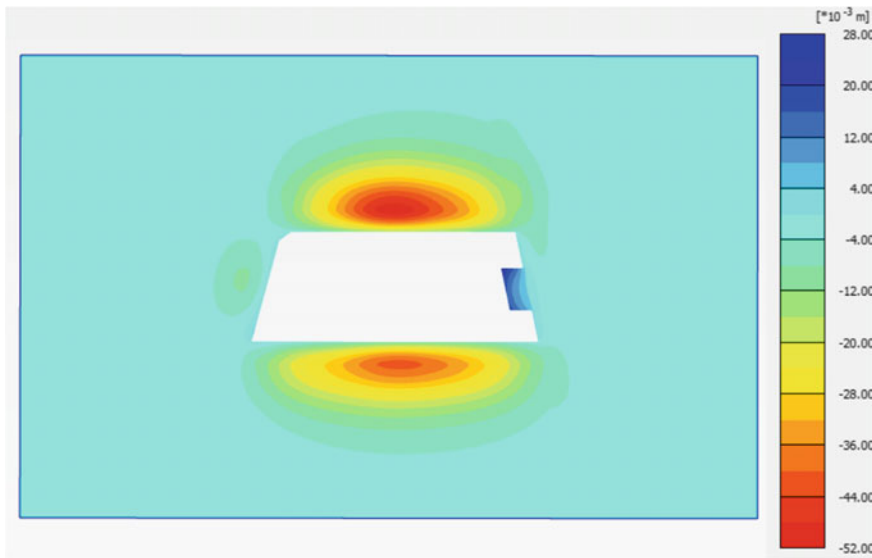


Fig. 8 PLAXIS 3D Result—Settlement due to excavation to the bottom of STP (Plan view)

The result of the PLAXIS 3D analysis showed the maximum ground settlement at the final stage excavating to the bottom of STP tank and foundation is about 50.55 mm. According to Figs. 8 and 9, the calculated ground movement near the corners from PLAXIS 3D are generally smaller than those near the center.

3.6 Deformation Results Compared Between Two Types of Finite Element Analysis and Discussion

The results of ground settlements from PLAXIS 2D and PLAXIS 3D have a big difference, the calculated ground movements from PLAXIS 3D are generally smaller than those in PLAXIS 2D for all four diaphragm walls. The diaphragm wall S1 has a distance between two edges is about 50 m, according to Figs. 10a and 11a, the corner effect has affected the results of ground settlement and wall deflection in 3D model. As can be seen from the Fig. 10a, the maximum ground movement in 2D model when excavating to the bottom of STP tank and foundation is approximately 19 mm, which is nearly two times higher than those in 3D model, with 8.3 mm. Especially, the S3 diaphragm wall has a fractured shape so the distance between edges are very small with about 20 m and the corner effect has a great influence on the ground settlement and horizontal displacement of diaphragm wall. The Fig. 10c show that the maximum ground movement in 2D model is about 60.1 mm, while the figure for 3D model is considerably low with approximately 2.0 mm due to the proximity of two corners. In terms of wall deformation, there is a big different

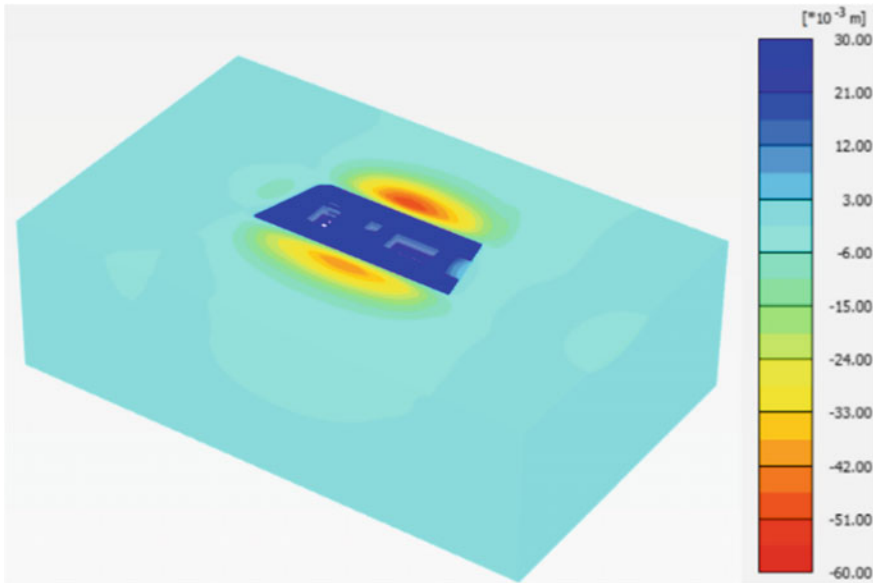


Fig. 9 PLAXIS 3D Result—Settlement due to excavation to the bottom of STP (3D view)

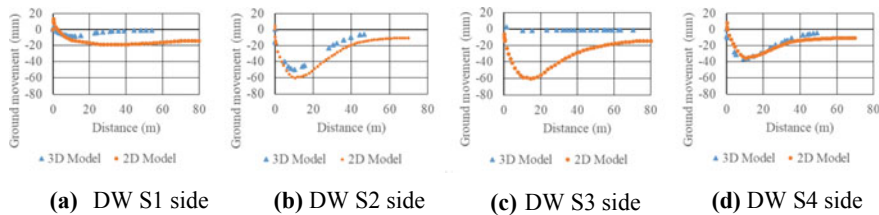


Fig. 10 Comparison of ground settlement between 3D model and 2D model

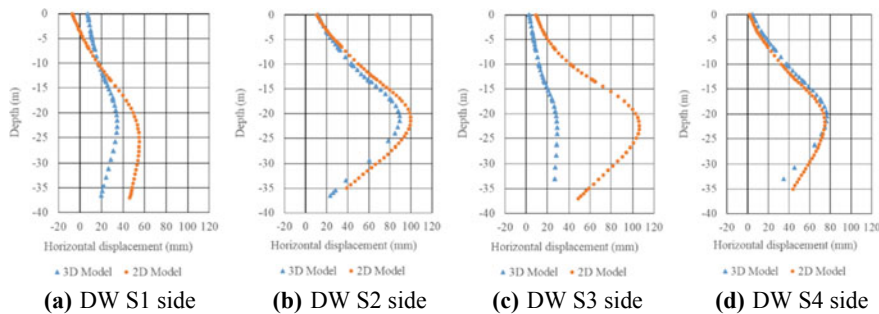


Fig. 11 Comparison of horizontal displacement between 3D model and 2D model

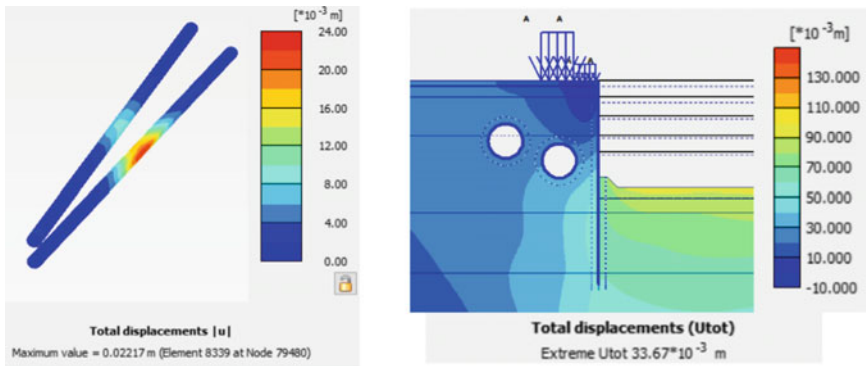


Fig. 12 Comparison of metro tunnel's total displacement between 3D model and 2D model

between diaphragm wall's horizontal displacement from 2D analysis and 3D analysis results with 106.5 mm and 28.9 mm respectively. The S2 and S4 diaphragm walls have a quite large distance between corners so the corner effect does not seem to affect this results very much, Figs. 10b, d and 11b, d.

In addition, the Metro tunnels is built on the S1 diaphragm side with about 4.2 m away from the S1 wall. Due to the close distance, the total displacement of Metro tunnels are related to the ground settlement and the horizontal displacement of diaphragm wall. Based on comparing the total displacement of Metro tunnels from 2D model and 3D model in Fig. 12, the corner effect also seem to cause the Metro tunnel's total displacement less than 2D model, with 22.2 mm and 33.7 mm respectively.

4 Displacement Control of Metro Tunnels

It is clear that the deep excavation is carried out closely adjacent to Metro tunnels, so there are various issues to invest in detail before the construction. The following design criteria for controlling deformation of Metro tunnels were determined: the total displacement of the tunnels were controlled within 15.0 mm and the deferential movement in any plane was less than 1/1000.

4.1 Diaphragm Wall T-Shape Type

One of the solutions to reduce total displacement of Metro tunnels is using T-Shape type for diaphragm wall S1, which is adjacent to Metro tunnels. As is shown in Fig. 13, there are 6 T-Shape diaphragm wall type spaced equally with thickness 1000 mm. This T-Shape diaphragm wall is given to increase the bending resistance



Fig. 13 General view of T-shape diaphragm wall

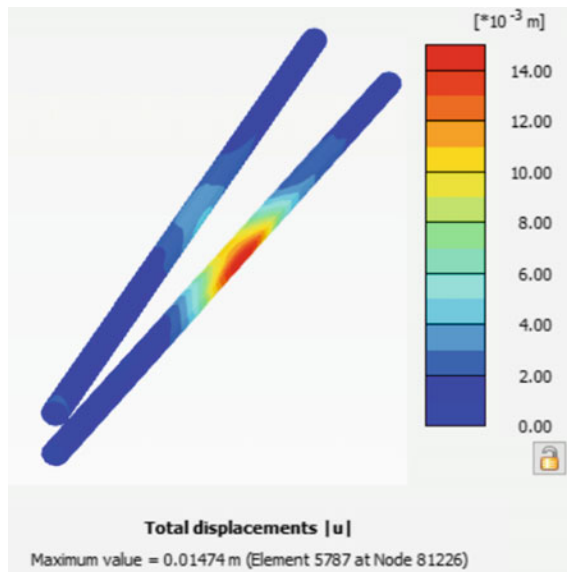


Fig. 14 The total displacement of metro tunnels

and reduce the total displacement of Metro tunnels to 14.74 mm which is less than 15.0 mm, Fig. 14.

4.2 Cement Deep Mixing Method (CDM)

The second solution to reduce the total displacement of Metro tunnels is using Cement Deep Mixing Method (CDM) in order to reduce deformation of diaphragm wall S1 as well as the horizontal displacement of tunnels. As shown in Fig. 15, CDM is located beside diaphragm wall S1 from the same level of Metro tunnels to the depth of 10 m and after excavating to the bottom of STP the highest total displacement of tunnels is 15.6 mm, Fig. 16, which nearly ensure the design criteria for controlling deformation of Metro tunnels.

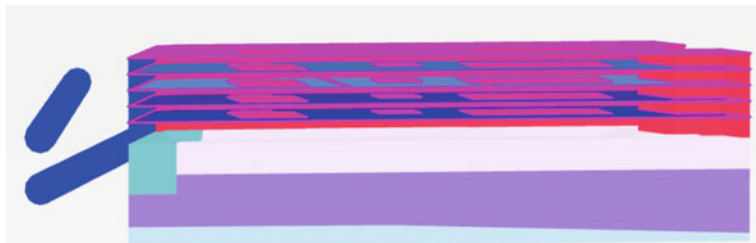


Fig. 15 General view of CDM method

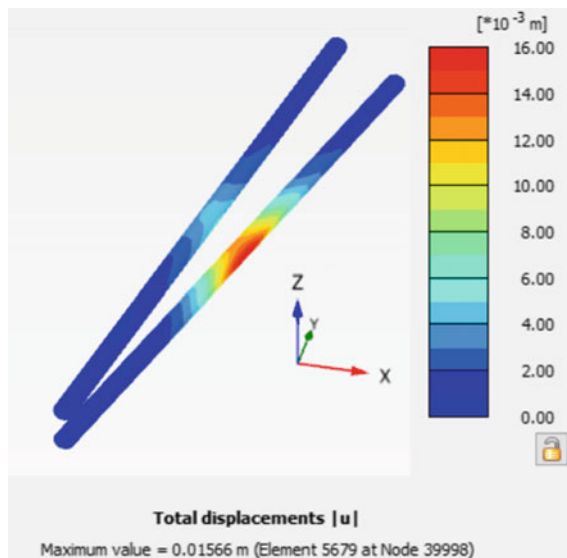


Fig. 16 The total displacement of metro tunnels

5 Conclusion

Two—Dimensional (2D) finite element analysis, which assumes plane strain condition is commonly taken to evaluate the possible deformations as well as estimate ground movements. However, in practice excavations have different boundary conditions and ground movement near the corners of the excavation is considerably smaller than those near the center. In this paper, both 3D and 2D finite element analyses was used and the results between these two finite element analysis types were compared to each other. The distance between two edges of boundary conditions or “corner effect” has affected the results of ground settlement as well as wall deflection in 3D method. In addition, due to this “three-dimensional effect” the total displacement of Metro tunnels from 3D analysis seem to be one and a haft times smaller than

that of 2D analysis, with 22.2 mm and 33.7 mm respectively. From this study the benefits of the 3D analysis is proved and engineers can adopt an economical solution in engineering design. Furthermore, this research also presents two effective measures to control deformation of closely adjacent Metro tunnels within design criteria (15.0 mm): T-Shape Diaphragm wall and Cement Deep Mixing Method.

References

1. PLAXIS 2D Version 8, Reference manual
2. PLAXIS 3D 2017, Reference manual

Generating a 3D Point Cloud of a Small Steel Bridge Model Structure Using a Hokuyo UTM 30LX Laser Scanner



Ngoc Thi Huynh and Anh Thu Thi Phan

1 Introduction

Due to the increase in infrastructure development, many construction projects of various scope have recently been built. During the construction and operation period, many tasks must be performed to ensure all safety requirements. The inspection of the situation, and health of under-building or existing construction, is necessary to minimize accidents that may cause danger to the existing construction, or to human life.

Many methods are utilized to determine the status and health of construction projects, including direct and indirect methods. Specifically, for direct methods, or the contact method, technicians must carry out a direct survey, or use the contact sensor for data collection [1]. The accuracy of the results depends on the professional level of the technicians, and the methods they use for the evaluation. Moreover, the direct survey collects local information, and does not cover the whole scope of construction. In some cases, direct contact to the target objects is very difficult. Achieving accurate data sources takes a great deal of time, labor and effort. In addition, some indirect methods, or non-contact methods, have been applied [2]. Scientists also use sensors, or image quantitative methods, to determine the status of the construction [3, 4].

Today, laser-scanning techniques can collect data regarding surface information of target objects with a dense, high-precision point cloud in a short period of time [5]. This technique has been popular in construction restoration, architecture, surveying and mapping [6–8]. With an accuracy of several millimeters, and the ability to receive up to a million scanned points in a second, laser scanning devices are an effective tool in many areas. However, collecting data with an airborne laser scanner, or a terrestrial laser scanner, is costly because of the expensive LiDAR sensor each requires; therefore, these devices are not economical. In order to reduce equipment costs, a

N. T. Huynh · A. T. T. Phan (✉)

Faculty of Civil Engineering, Ho Chi Minh City University of Technology, VNU-HCM, Ho Chi Minh City, Vietnam

e-mail: ptathu@hcmut.edu.vn

cheaper, 2D laser-scanning device is recommended. The 2D laser scanners are a non-survey grade laser scanner and they are not used for survey purposes. However, observing an object at close range can accurately capture the target object's surface.

In this study, the surface information of the small steel bridge is collected by a 2D laser scanner. Specifically, the Hokuyo UTM 30 LX laser scanner. As a result, the scanned images and point clouds of the bridge are generated. From these point clouds, the characteristics of the bridge structure are preliminarily recognized and evaluated directly from the monitor.

2 Equipment Setup and Data Acquisition

The selected device for this study is the Hokuyo UTM 30LX. This is a small and lightweight device with a maximum scanning range of 30 m, 0.25° of angular resolution and 905 nm of wavelength (Table 1). In order to develop the scanning system, the scanner is mounted on a rack and hung on a rail bar that is fixed on the frame (Fig. 1). Thanks to the movement of the motor, the scanner is able to move and receive images from the surface of the target objects located below it. The data-acquisition mechanism is similar to that of the airborne laser scanner. In laboratory-level research, the scanner can only move at a distance of 1.2 m, from a height of 0.5 m above the floor. A small steel bridge model is selected; its size in length, width and height are: 120 cm, 70 cm and 21 cm, respectively (Fig. 1). The ability to capture the images of objects with complex shapes and many details using the Hokuyo UTM 30LX laser scanner is evaluated in this study.

Before conducting data collection on September 15th, 2019, several reflective markers were placed, for correcting and aligning the point clouds. They were arranged on 2 rows and separated by a space of 80 cm. The markers on each row were 40 cm apart. Then the system to record images of reflective stickers was started. From the scanned results, the movement speed of the device was checked based on the position of the marker. We assumed that during the data-acquisition process, the movement speed of the scanner would be stable, without variation. After that, a steel-bridge

Table 1 The Hokuyo UTM 30LX scanner and its specifications

	Weight	370 g
	Range	From 0.1 to 30 m
	Compact size	60 × 60 × 87 mm
	Wavelength	905 nm
	Field of view	270°
	Angular resolution	0.25°
	Scan speed	25 ms
	Accuracy	±30 mm (<10 m)

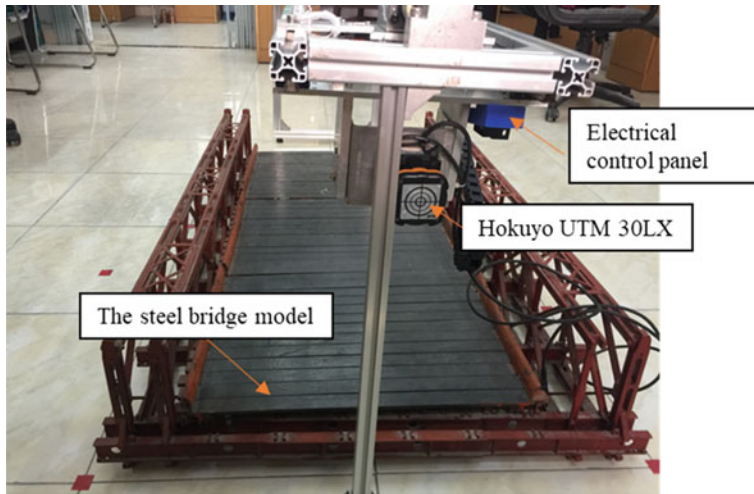


Fig. 1 The laser scanner moves along the rail to collect the surface information of the steel bridge model

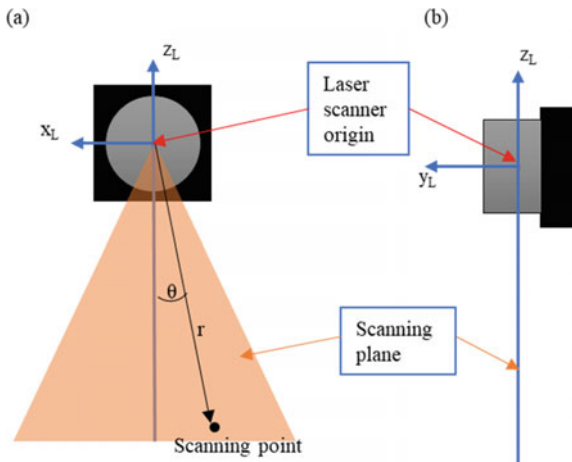
model was arranged under the scanner to conduct data collection. The setting field of view was $\pm 65^\circ$ and the laser scanner moved along the rail wall under motor power at a speed of 2 cm/s. Simultaneously with scanner movement, the intensity and distance values of the scanning points were recorded by UrgBenriPlus software.

3 Data Processing

As mentioned above, the data recorded by the Hokuyo UTM 30 LX laser scanner included the range and reflectance values corresponding to each scanning position. After obtaining the raw data, all range and intensity data was separated into a text-format file by a developed source code in R language. Then, the 3D coordinates of the scanning points were computed in an assumed-coordinate system and stored as point clouds. The coordinate system of the laser scanner was defined as, “The Righthand 3D Orthogonal Coordinate System.” In this case, the origin corresponded to the origin of the LiDAR sensor at the starting point. The Y axis was matched with the rotation mirror axis, and the positive direction of the Z axis corresponded to the zenith. The scan angle was positive in the counter-clockwise direction around the Y axis (Fig. 2). The scan angle at zero degrees was matched with the nadir.

For one scanning line, the coordinates of any point in the scanner-coordinate system were determined from the range value (r), with the assumption that the scanning speed of the scanner was constant during the data-acquisition process by applying the Eq. (1). Then the point cloud was generated by considering the movement speed of the scanner. However, during the movement, many causes, such as miscalculated speed,

Fig. 2 The position of the scanning point in the laser coordinate system. **a** x-z plane and **b** y-z plane



or the vibrating scanner movement, resulted in a deformed-object image. Therefore, the point-cloud correction was indispensable. Specifically, the coordinates of the reflective markers were manually determined on the point cloud generated by the R source code. Then, their actual coordinates were measured and used as reference coordinates to correct the point cloud using affine transformation and the least-square method. After applying the correction method, the point cloud displayed the actual size of the sample objects (Fig. 3).

$$\begin{pmatrix} x_L \\ y_L \\ z_L \end{pmatrix} = \begin{pmatrix} -r \cdot \sin \theta \\ 0 \\ -r \cdot \cos \theta \end{pmatrix} \quad (1)$$

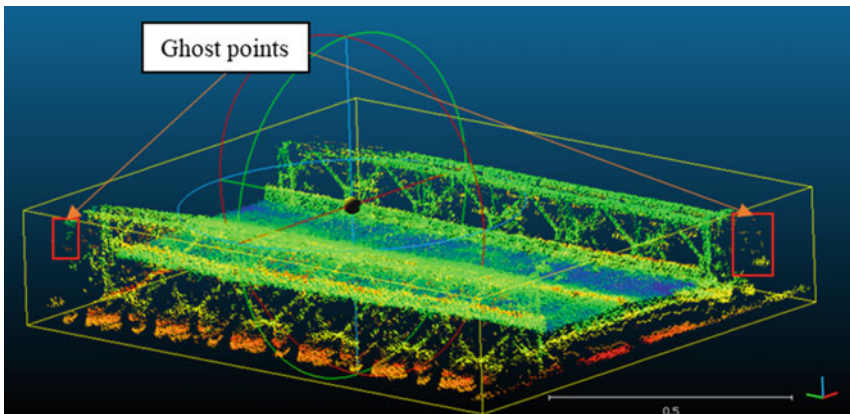


Fig. 3 Generated point cloud from the first scan. There are many ghost points, and the image of the steel handrail is not clear

4 Results

In this study, a small steel-bridge model is observed by a 2D laser scanner at close range. The scans have been performed to capture the point clouds of sample objects generated from raw data using the developed R source code. The intensity value of the objects made up of different materials varies. Before conducting the point cloud correction, the image of the objects is lightly deformed. After conducting the correction, the geometric deformation is removed significantly. By applying Affine transformations, geometric distortions are eliminated, and we can capture the object image and recover the original shape and size of the object. To evaluate the accuracy of the point cloud, the 3-dimensional size of the steel-bridge model is measured directly on the point clouds. The measured result in length, width and height are: 116.4 cm, 69.5 cm and 20.5 cm, respectively. As a result of the comparison, the difference in size between the model and true object is several millimeters. The Hokuyo UTM 30 LX is a non-surface grade laser scanner; therefore, the achieved results are acceptable. Moreover, the rough surface of the object can also be detected from observing the point clouds from the computer screen (Fig. 4).

Due to the characteristics of a single-beam scanner derived from a scanning origin, the image of the object is often obscured in the area near the bottom of target object. According to the results, even the images of small objects, such as the steel handrail in the bridge model, are also shown. At the movement speed of 2 cm/s, the point density is very dense. However, there are many ghost points which appear in the steel handrail (Fig. 3). These noisy points are difficult to remove from the combined point cloud (Fig. 5).

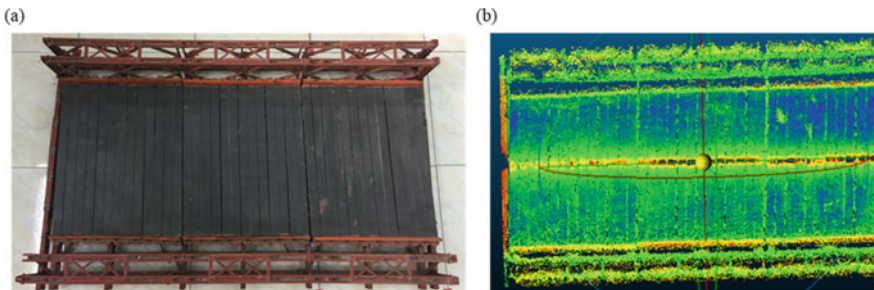


Fig. 4 The rough surface of the object can also be detected from observing the image of the point clouds from the computer screen. **a** The photo of steel bridge model and **b** the image of steel bridge visualized from a point cloud

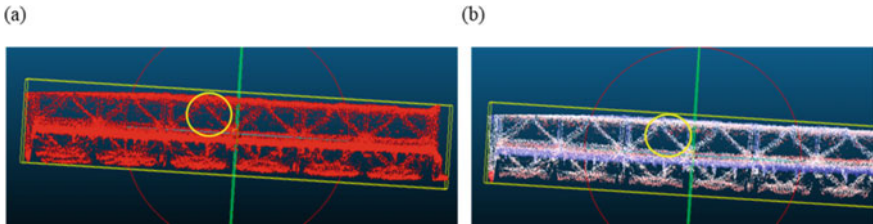


Fig. 5 The image of a point cloud **a** before and **b** after applying the noisy filter. The noisy points inside the yellow circle cannot be removed completely

5 Discussion and Conclusion

In this study, the point cloud which modifies the shape of the steel-bridge model is generated from data recorded by the Hokuyo UTM 30 LX laser scanner at the moving speech of 2 cm/s. According to the results, the shape of the steel bridge is slightly restored. By applying the affine transformation and least-square method, the corrected point clouds show the actual size of all samples. Moreover, the full image of the steel bridge model is generated by combining several point clouds. As a result, the rough surface of the object can also be detected by observing the image of the point clouds from a computer screen. Combined with intensity data, we can detect some unusual features on the object surface, such as surface indentations. With close-range observation, the image of objects with small size, such as the steel handrail in the bridge model, is also clearly shown. The results show that at the level of laboratory research, the 2D scanner Hokuyo UTM 30LX is capable of collecting the surface information of small-sized target objects. If the movement range of the laser scanner is expanded, we can capture images of actual objects with larger sizes in close observational range.

In addition, during the data-acquisition process, we assumed that the velocity of laser-scanner movement would be constant, and that the scanner would move in a straight line. Therefore, in order to be able to apply this to the observation of real works, the scanner should be allowed to move more flexibly. In order to ensure the accuracy of generating 3D coordinates of the point clouds, it is necessary utilize an ultra-small motion logger to record the variation in the speed of the sensor in 3 directions, and a GPS receiver to determine the location of the scanner. Moreover, ghost points will affect to the quality of the point cloud; therefore, in the next study, they should be eliminated for better results. For a complex object with many details, its correct image cannot be captured by one scan. Therefore, many point clouds should be combined to visualize the full image of the object.

Acknowledgements Our sincere thanks also go to Mr. Matthew Jerome Weerts for helping us correct English grammar of this paper.

References

1. Garbacz A, Piotrowski T, Courard L, Kwasniewski L (2017) On the evaluation of interface quality in concrete repair system by means of impact-echo signal analysis. *Constr Build Mater* 134:311–323. <https://doi.org/10.1016/j.conbuildmat.2016.12.064>
2. Hoła J, Schabowicz K (2010) State-of-the-art non-destructive methods for diagnostic testing of building structures—anticipated development trends. *Arch Civ Mech Eng* 10:5–18. [https://doi.org/10.1016/s1644-9665\(12\)60133-2](https://doi.org/10.1016/s1644-9665(12)60133-2)
3. Chan BYM, Saul JJ, Pettigrew TJ, Anstice DJ (2017) Photogrammetric modelling for bridge inspection and remediation, 8th Australian small bridges conference. https://www.eiseverywhere.com/file_uploads/7039a6c034d18105f8bc6fcf29d2f314_Photogrammetric_Modelling_forBridge_Inspection_and_Remediation_GHD_Brody_Chan.pdf
4. Memon ZA, Majid MZA (2006) The use of photogrammetry techniques to evaluate the construction project progress, *J Teknologi* 44(B):1–15
5. Arayici Y, Hamilton A, Gamito P (2006) Modelling 3D scanned data to visualise and analyse the built environment for regeneration 17
6. Fowles PS, Larson JH, Dean C, Solajic M (2003) The laser recording and virtual restoration of a wooden sculpture of Buddha. *J Cult Heritage* 4:367–371
7. Baltsavias EP (1999) A comparison between photogrammetry and laser scanning. Elsevier *ISPRS J Photogrammetry Remote Sens* 54(2–3):83–94
8. Petzold B, Reiss P, Stössel W (1999) Laser scanning—surveying and mapping agencies are using a new technique for the derivation of digital terrain models. *ISPRS J Photogrammetry Remote Sens* (2–3):95–104

Optimal Design for Rutting Resistance of Asphalt Concrete Pavements by Experimental Testing and Finite Element Modelling



**Chau Phuong Ngo, Van Bac Nguyen, Ngoc Bay Pham,
Thanh Phong Nguyen, Van Phuc Le, and Van Hung Nguyen**

1 Introduction

Rutting is one of the most serious distresses in asphalt pavements affecting the pavement service life. In the last three decades, there have been a lot of studies focused on prediction of rutting resistance of asphalt pavements. A wide number of numerical studies with more realistic constitutive models have been conducted that included more practical models in different FE programs [1–4]. In these studies, the visco-elastic-plastic (creep) model used was in the ‘time hardening’ form and moving loads were treated as a static load. However, as this model was only developed for the constant load, it might not be applicable for the moving load situation [5]. Recently, there has been a significant amount of studies on different FE modelling techniques and material constitutive models on predicting rutting in asphalt pavements [6]. However, there has been limited investigations on optimal design of asphalt pavement mixes, considering the effects of varying material parameters on the mixes’ rutting resistances.

In this paper, 3D Finite Element models using ANSYS (version 18.1, 2018) to simulate the laboratory testing of asphalt mixes in triaxial compression and HWTD tests were developed. The triaxial repeated load creep and creep recovery test results have been used to obtain the associated creep parameters for asphalt concrete mixes. A creep model of the ‘strain hardening’ form was employed to represent the time-, stress- and temperature-dependent behavior of asphalt pavement materials. An optimization process using the Design Of Experiments using a response surface was undertaken to examine the influence of material parameters on rutting and to propose an optimal designed asphalt mixes for rutting resistance.

C. P. Ngo · N. B. Pham · T. P. Nguyen · V. P. Le (✉) · V. H. Nguyen
University of Transport and Communications, Ha Noi, Vietnam
e-mail: lvphuc@utc2.edu.vn

V. B. Nguyen
University of Derby, Derby, UK

2 Methods

2.1 Experimental Testing

Experimental testing data of a previous study [2] was used in this study. Three different asphalt mixes with target air-void of 4% included HL3 with asphalt content of 5.3% for AC mixture: conventional dense graded Marshall surface course mix; SMA L with asphalt content of 5.7% for AC mixture and SMA G with asphalt content of 5.7% for AC mixture: two Stone Mastic Asphalt 12.5 mm surface course mixes.

The triaxial repeated load creep testing was carried out in cylindrical samples 100 mm diameter \times 150 mm height. The testing was carried out at a constant temperature of 50 °C. The test results to investigate the creep behavior of the asphalt mixes and to develop the material parameters used in the FE modelling. Air-voids content in triaxial repeated load creep testing specimens is 6.3%, 6.9%, and 5.8% for HL3, SMA L, and SMA G, respectively

The Hamburg Wheel Tracking Device (HWTD) testing general view and diagram are shown in Fig. 1. The wheels are solid rubber (50 mm wide), and the load applied to the wheels is 710 N. The test path is 230 mm long and the average speed of each wheel is approximately 1.1 km/h. The number of wheel passes being used was typically 20,000. Air-voids content in HWRT specimens is 6.5%, 6.8%, and 6.2% for HL3, SMA L, and SMA G, respectively.

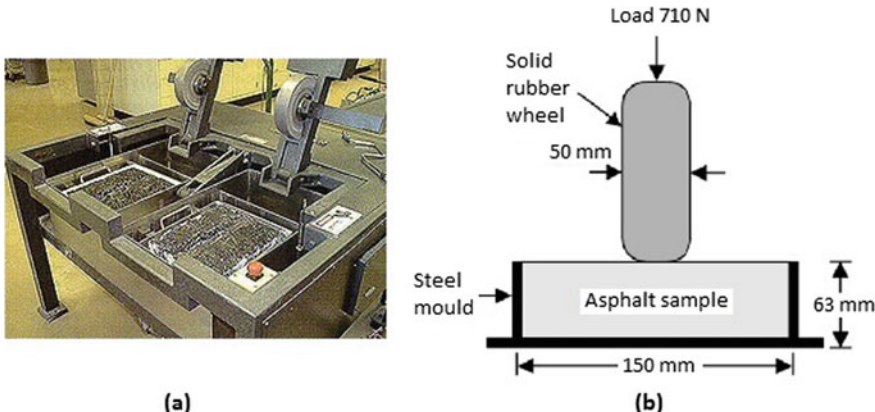


Fig. 1 General view (a) and testing diagram (b) of the HWTD

Table 1 Material parameters of asphalt mixes [2]

Mix	Material parameter				
	Elastic		Creep		
	E_{ac} (kPa)	μ_{ac}	C_1	C_2	C_3
HL3	950,000	0.41	2.691×10^{-5}	4	-1.703
SMA L	800,000	0.42	2.837×10^{-8}	4.727	-3.545
SMA G	800,000	0.42	2.284×10^{-7}	6.238	-3.762

2.2 Material Characterization

Visco-elasto-plastic model in the form of ‘strain hardening’ was used in this research and it can be written in the form of creep strain rate which is expressed as a function of stress, strain and temperature [2]

$$\dot{\varepsilon}_{cr} = C_1 \sigma^{C_2} \varepsilon_{cr}^{C_3} \quad (1)$$

where $\dot{\varepsilon}_{cr}$ is the creep strain rate, σ is the equivalent stress, ε_{cr} is the creep strain at the time t. C_1 , C_2 , C_3 are the obtained material-related parameters as shown in Table 1.

2.3 Numerical Modelling

The FE model setup for the wheel track test HWTD is shown in Fig. 2 which also shows the mesh. The bottom and the four surrounding vertical boundaries were set to be confined with restricting displacement in all directions. For the load of 710 N applied in this area, it was equivalent to a uniform loading pressure of 0.5 MPa.

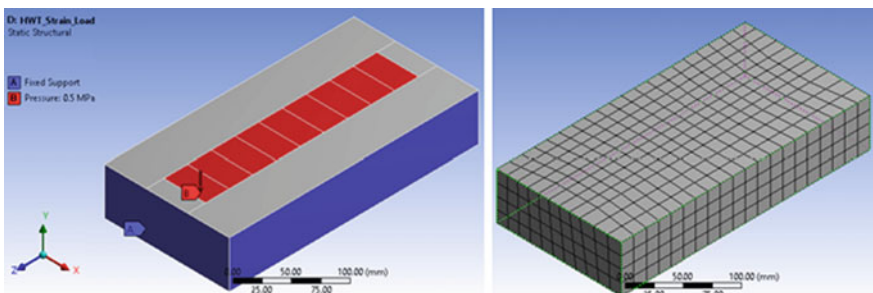


Fig. 2 FE model setup of the triaxial compression testing which shows loading, boundary conditions and mesh

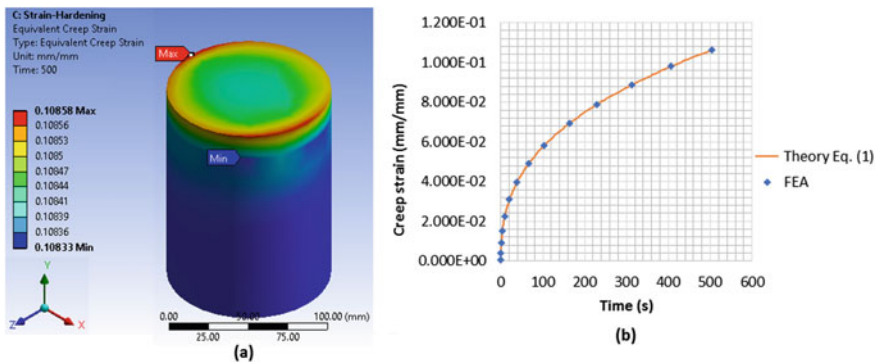


Fig. 3 FE creep results for axial compression loading (a) and comparison with theoretical axial compression creep model as presented in Eq. (1), demonstrating HL 3

2.4 Optimization

The optimal asphalt pavement mix design and finite element simulations were carried out in three stages: (1) Developing new asphalt pavement mixes by varying parameters C_1 , C_2 , C_3 against the target performance of the mixes, (2) Planning the Design Of Experiments (DOE) using a response surface model, running multiple simulations and determining C_1 , C_2 , C_3 values that give the target minimum rutting, and (3) Simulating the HWTD of new optimal mixes and validation.

3 Results

3.1 The Triaxial Repeated Load Creep Testing

The FE modelling was first verified by comparing the results obtained from the triaxial repeated load creep testing model with the theoretical axial compression creep model as presented in Eq. (1), which shows the FE model predicted accurately the axial compression and creep behavior of the asphalt mix under axial constant loading (Fig. 3).

3.2 The Hamburg Wheel Tracking Device Testing

The FE and measured rut depths versus time for all mixes at any time of loading up to about 4500 s are shown in the Fig. 4. The difference are as high as 4–16% (Fig. 5).

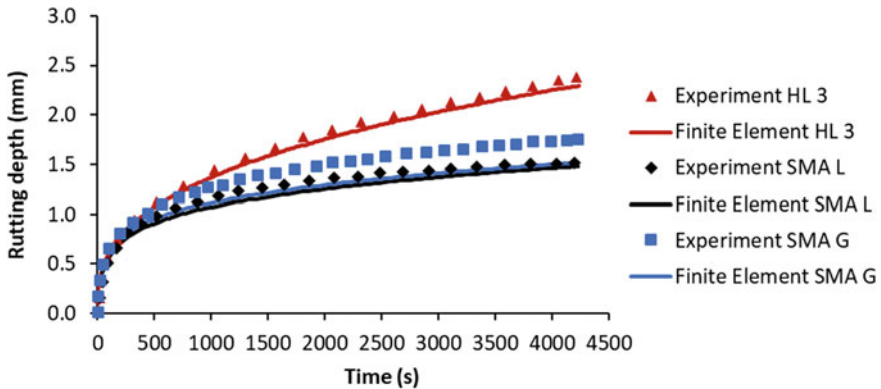


Fig. 4 Comparison between rutting depths predicted by FE and measurements in HWTD tests

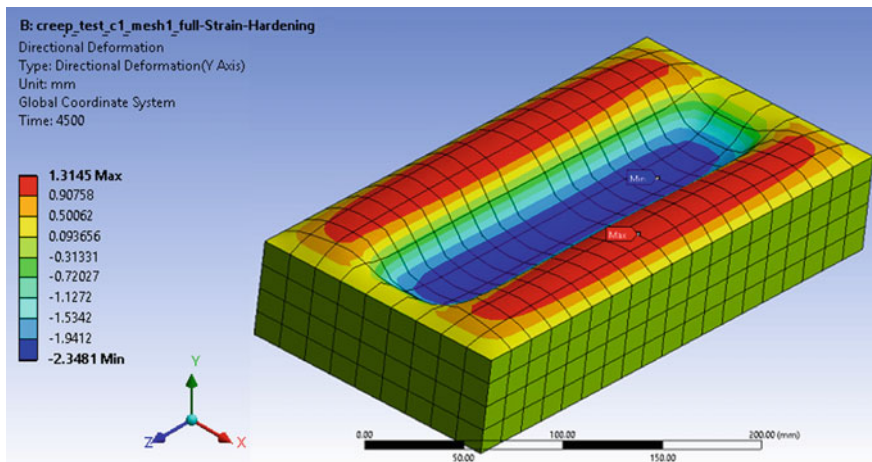


Fig. 5 FE predicted deformation shape of the HL 3 mix after 20,000 passes (the rutting depth is not in a correct scale)

3.3 Optimisation Techniques

Mathematically, the objective function of parameters $\vec{X} = [x_1, x_2, x_3, \dots, x_n] \in D^n$ for the α^{th} application can be expressed as $f_{k\alpha}(\vec{X} \in D^n)$ with $k = 1, 2, 3, \dots, L_\alpha$ and $\alpha = 1, 2, 3, \dots, A$. The best feasible solution for one single objective can be found by $\text{Min } f_{k\alpha}(\vec{X} \in D^n)$ with the constraint $g_{j\alpha,\min} \leq f_{k\alpha}(\vec{X} \in D^n) \leq g_{j\alpha,\max}$, $j = 1, 2, 3, \dots, m_\alpha$. In which, n is the total number of design parameters, L_α is the total number of objective functions, m_α is the total number of parameters. Details

of the response surface's mathematical forms can be found in ANSYS Documentations (version 18.1, 2018). A numerical procedure of straightforward direct search is employed to optimize multiple objective functions. The whole design space is first represented by discrete points that are evenly spaced in each dimension. The objective functions and state variables are then mapped to the points, forming the response surface. A graphic method is thus used and described as follows: all regions of optimum solutions are plotted together on a matrix of 2-D plots with all possible combinations of two design parameters out of n design parameters. In this study, design parameters are C_1 , C_2 , C_3 and objective function is the rutting depth.

The validated FE model (of HL 3 mix) was then extended for modelling and developing new asphalt pavement mixes. The rutting performance of the new mixes was examined by changing creep parameters including: $C_1 = [2.837 \times 10^{-8} \div 2.691 \times 10^{-5}]$, $C_2 = [4 \div 6.238]$, $C_3 = [-3.762 \div -1.703]$. Each parameter was assigned 5 different values in the range from min to max value. The target responses selected in this study were the rutting depths. Results are illustrated in Fig. 6.

The rutting depth was very sensitive with C_1 and C_2 , and increased with increasing with C_1 and C_3 values. That could be due to C_1 and C_3 were directly related to the amount of asphalt content. The DOE results determined that the asphalt pavement mix with $C_1 = 2.8 \times 10^{-6}$, $C_2 = 6.029$, and $C_3 = -1.895$ could be the optimal mix for rutting resistance.

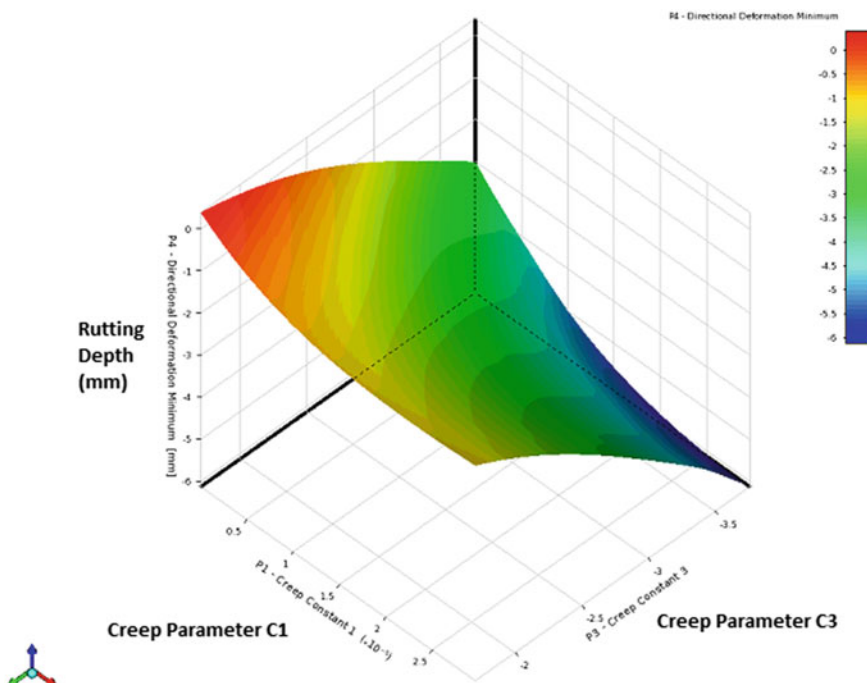


Fig. 6 Response surface for the effects of creep parameters on the rutting depth

4 Conclusions

In this paper, the Finite Element models were developed to simulate the laboratory testing of asphalt mixes in triaxial compression and HWTd tests. The associated creep material parameters for asphalt concrete mixes were obtained from the triaxial repeated load creep and creep recovery test results. The FE models employed the characterized creep parameters associated with 'strain hardening' creep models were first verified against the theoretical creep model for the axial compression loading on asphalt cylinder sample. The characterized material properties determined in this manner were employed in the Finite Element models and validated against the HWTd test results for three different asphalt mixes. Very good agreement was found between the FE predicted and HWTd measured rutting depths.

This paper has also presented the design and development of new asphalt pavement mixes by using a combined approach of the finite element analysis and optimization using DOE method to simulate the HWTd rutting responses and obtain the optimum design for the mixes. The creep parameters of the asphalt pavement were defined as input parameters in FE modelling and assigned a range of values so that a wide range of FE results was obtained. A response surface model was then used for the results to determine parameter values that achieve the rutting resistance as the target optimized performance. The optimization study conducted using the FE models gained more understanding on the influences of creep parameters to the rutting resistance of asphalt mixes. It can be concluded that the Finite Element simulations can be used to effectively evaluate and optimize the rutting resistance of asphalt concrete pavements.

Acknowledgements This study is part of the FIRST project 'The development of numerical simulation and optimization technologies for optimal performance of concrete asphalt pavements considering the traffic and climate conditions of Vietnam' (35/FIRST/1a/UTC). We acknowledge FIRST Project, Ministry of Science and Technology, Vietnam, for sponsoring this project.

References

1. Zaghloul SM, White TD (1993) Use of three-dimensional Finite Element program for flexible pavement. *Trans Res Record* **1388**:60–69, TRB
2. Uzarowski L (2006) The development of asphalt mix creep parameters and finite element modelling of asphalt rutting. PhD thesis, University of Waterloo (2006)
3. Darabi MK, Abu Al-Rub RK, Masad EA, Huang CW, Little DN (2011) A thermo-viscoelastic-viscoplastic-viscodamage constitutive model for asphaltic materials. *Int J Solids Struct* (48):191–207
4. Nahi MH, Kamaruddin I, Ismail A, Al-Mansob RA (2014) Finite element model for rutting prediction in asphalt mixes in various air void contents. *J Appl Sci* (14):2730–2737
5. Betten J (2005) Creep mechanics. 2nd ed. Springer, Germany
6. Abu Al-Rub RK, Darabi MK, Huang CW, Masad EA, Little DN (2012) Comparing finite element and constitutive modelling techniques for predicting rutting of asphalt pavements. *Int J Pavement Eng* (13):322–338

Performance Analysis of a Combination Between D-Wall and Secant Pile Wall in Upgrading the Depth of Basement by Plaxis 2D: A Case Study in Ho Chi Minh City



Van Qui Lai, Minh Nhan Le, Quoc Thien Huynh, and Thanh Hai Do

1 Introduction

In recent year, together with the development of economics in Viet Nam, the number of sky-building has been rapidly increasing in Ho Chi Minh City, which is the biggest City in Viet Nam. This increasing made the demand of using the underground space become more and more necessary. The number of basement and excavation works, thus, were carefully designed to service for the demand of sky-building in initial stage. However, in some special cases, the number or the depth of basements must be changed. Those things lead to some replacement in retaining structure as well as the statement method of excavation.

The Alpha City project located in the District 1 of Ho Chi Minh City was an example, Fig. 1. In the initial design, the project which comprised 35-storey and 3 basements, and the average depth of excavation was 14.85 m from ground surface. The D-wall and Semi top-down method were designed for excavation works. The project was constructed in 2010 and D-wall was installed in 10/2011. However, the project was sold for another investor by unknown reasons. The result was that the number of storey was increased from 35-storey to 50-storey. And the average depth of excavation was increased from 14.85 m to 17.85 m. To make excavation work was still safety with increasing the excavation depth, the secant pile wall (SP-wall) was chosen to installed next to the original D-wall.

For design the retaining wall structure, there are many approaches including FEM, BEM, Experiment method [1]. In that, the commercial FEM software, Plaxis, is more commonly for deep excavation design [2, 3]. However, using the Plaxis 2D

V. Q. Lai (✉) · Q. T. Huynh · T. H. Do

Faculty of Civil Engineering, Ho Chi Minh City University of Technology, VNU-HCM, Ho Chi Minh City 740128, Vietnam

e-mail: lvqui@hcmut.edu.vn

M. N. Le

Faculty of Civil Engineering, Ho Chi Minh City University of Transport, Ho Chi Minh City 740128, Vietnam



Fig. 1 Project location in HCM city

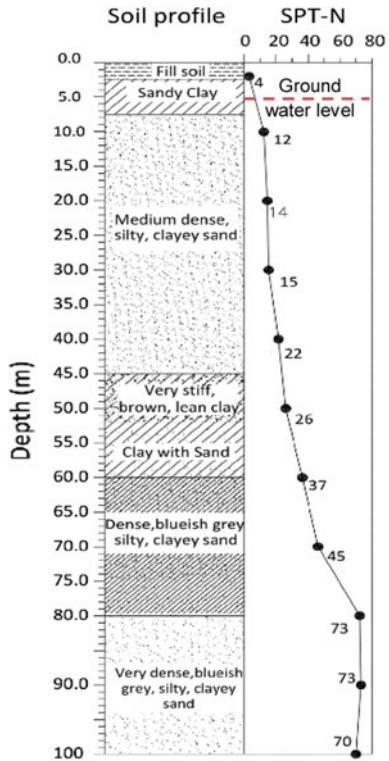
for analysis the response of combination system of D-wall and SP-wall in upgrading the excavation depth is still rarely. Thus, in this study, the authors applied the Plaxis 2D for analyzing the behavior of combination wall. The results of analysis were compared with field observation. Based on the comparison, some recommendation was given for future research and design works.

2 Project Information

The Alpha City project is aim at to be the Central Business Building of Ho Chi Minh City. It is located next to the main business street Tran Hung Dao of Ho Chi Minh City. The soil profile under building was showed in Fig. 2. This soil profile is the common soil profile of District 1, Ho Chi Minh City with main layer is sand located from -7 to -45 m. And, almost the bottom basements of high buildings in this area are placed in this sand layer.

In the beginning stages, the project was originally intended to be 35-storey tall and 3 basement levels. The pile foundation system was designed. The average excavation depth was around 14.85 m. Besides, in some places, the deeper excavation depth was up to 18.0 m at the lift areas having pit foundations depths of 4.0 m. To protect the excavation, the D-wall with 0.8 m of thickness and 30.0 m of depth combined with Semi top- down excavation method was designed.

However, after the D-wall was installed, the project was sold for another investor. The tower height and number of basements were decided to increase to 50-storey and

Fig. 2 Soil profile

4 basement levels respectively. This thing made the average excavation depth was increased to 17.85 m and the deepest excavation depth was 21.0 m. This issue created the challenges for designer in making certain that the proposed structural systems and excavation methods were safety and did not adversely affect the surrounding adjacent properties.

To solve the issue, the SP-wall with thickness of 0.9 m was installed next to the original D-wall, as shown in Fig. 3. For more detail about the combination of retaining wall system, the cross section of excavation area was shown in Fig. 4. It can be seen that, the distance between two kind of wall was 0.4 m. The top and bottom depth level of secant pile wall was 9.15 and 35.15 m. Comparing to the top and bottom depth level of original D-wall, the retaining wall system was 9.15 lower and 5.15 m deeper than original D-wall. The overlap between D-wall and SP-wall was 20.85 m. Besides, the thickness of combine wall at overlap areas was increased to 2.1 m compare to 0.8 m of D-wall.

The deep excavation was carried out according to the Semi Top-down method including 2 main stages: construction of retaining wall and construction of base-memt structure. Table 1 presented the detailed construction sequences clearly. To survey the behaviour of D-wall, SP- wall and surface ground, the monitored equipment was installed such as inclinometer measurement (ICL, INC), ground settlement

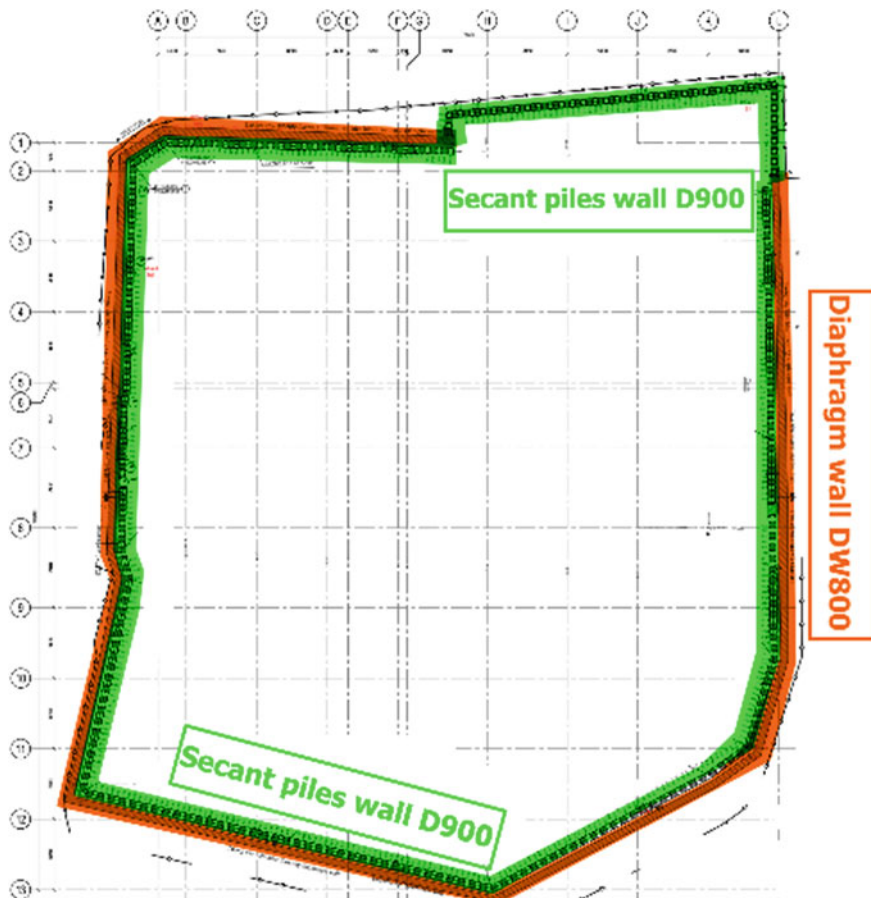


Fig. 3 Layout of combination retaining walls system

measurement (GSM). Figure 5 was showed the arrangement of monitored points in construction site.

3 Numerical Analyses

In this study, the commercial software PLAXIS 2D was used as useful tool to simulate the behaviour of soil layers and the response of the retained structures. The Hardening Soil model (HSM) is an advanced soil model having suitable characteristics for the soil's behaviour in excavation analyses. HSM is based on isotropic hardening, able to generate more realistic soil response in terms of non-linearity, stress dependant stiffness according to the power law, plastic straining both due to primary deviatoric

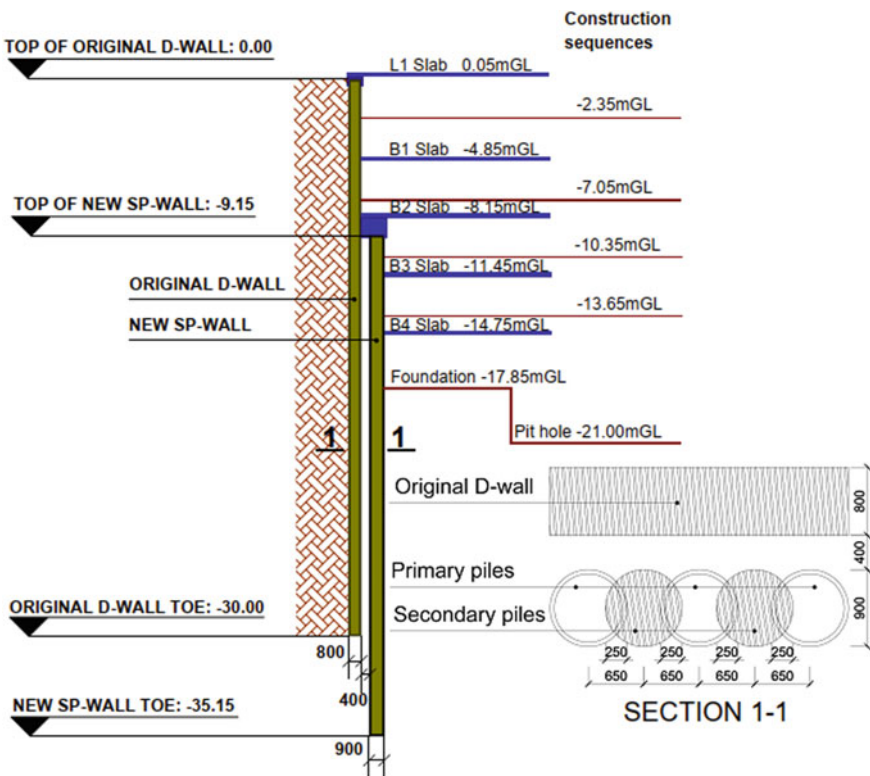


Fig. 4 Basement section of project and combined wall

loading and primary compression, elastic un/reloading, dilatancy effect and failure according to the Mohr-Coulomb criterion. Most of the soil parameters in HSM are commonly defined from consolidated drained triaxial compression test (CD) and consolidation test (OED). In the absence of OED test, the oedometer loading stiffness $E_{\text{oed}}^{\text{ref}}$ can be set equal to the triaxial loading stiffness E_{50}^{ref} . If the unloading-reloading cycle is not conducted in the CD test, the triaxial unloading stiffness $E_{\text{ur}}^{\text{ref}}$ can be determined by 3 times of E_{50}^{ref} according to the default. However, the main excavating work was operated in the thick layer of sand ranging from -7 to -45 m in depth. It is understood that to get good quality sampling for determining the soil properties are comparatively difficult. So, the CD and OED tests were not carefully carried out in this project. For analysis, soil parameters were determined based on empirical formulas from the results of direct shear test, SPT.

For sand, the secant modulus could be estimated from some empirical equations proposed by many previous researchers such as: [4–6]. E_{50}^{ref} is equal to 2000 N. For the shear strength parameters, it could be determined from direct shear test or according to the correlation with the N index because the internal friction angle of sand (ϕ') is independent with stress states. As above mentioned, the behaviour of combining wall

Table 1 Construction sequences

Construction sequences	Finishing date
<i>Stage 1: Construction of the retaining walls</i>	
Package 1: Diaphragm wall construction & Kingpost system: D-Wall: D = 800 mm, L = 30 m	10/2011
Package 2: For upgrading the depth of basement, adding Secant piles wall D = 900 mm, L = 26 m	06/2018
<i>Stage 2: Construction of basement structure</i>	
Phase 1: Excavation console from ground level to level -2.35 m and Concrete for L1 beam slab	23/12/2018 (Cycle 57)
Phase 2: Excavation to level -7.05 m and Concrete for B1 beam slab system at level -4.85 m	21/03/2019 (Cycle 145)
Phase 3: Excavation to level -10.35 and Concrete for B2 beam slab system at level -8.15 m	15/06/2019 (Cycle 231)
Phase 4: Excavation to level -13.65 m and B3 beam slab system at level -11.45 m	11/08/2019 (Cycle 288)
Phase 5: Excavation to bottom level of foundations -17.85 m and Pit hole -21.0 m	Under construction

was significantly influence by thick layer of sand. So that, to obtain the best results, the thick layer of sand was divided into 4 fine layers with approximately thickness 10 m.

In term of clay, the total stress undrained analysis with undrained internal friction angle $\varphi_u = 0$ and undrained shear strength S_u were used $c_u = S_u$. The S_u value can be defined from direct shear test. The secant modulus for clay can be computed by the empirical equation: E_{50}^{ref} equals to $(300\text{--}500)S_u$ as suggested in previous studies of Lim et al. [1], Yong et al. [3], Hsiung et al. [2], and Tran [5] (Table 2).

To simulate earth-retaining structures including the D-wall and the SP-wall, plate element in Plaxis 2D model was employed. In case of slab struts, it was also simulated by the plate elements but the weight of these ones was zero ($w = 0 \text{ kN/m}^2/\text{m}$). The linear elastic model was adopted to model both the D-wall, the SP-wall and slab struts. This model requires three main input parameters including flexural stiffness EI ($\text{kN/m}^2/\text{m}$), axial stiffness EA (kN/m) and Poisson's ratio v . The Poisson's ratio was taken to be 0.2 for all of them. The stiffness parameters of the excavation-retaining structures were calculated and presented in Table 3.

2-dimensional cross section of deep excavation was adopted for the numerical analyses by Plaxis 2D model as presented in Fig. 6. The length of cross section was 85 m according to actual design of basement. The base of the finite element model was placed at the clayey sand layer with a depth of 80 m from the ground surface. The distance from the lateral boundary of the model to the retaining wall was 80 m. This value was appropriately three times excavation depth and two times retaining wall depth, and larger than the boundary size suggested by Plaxis. The horizontal movement was restrained for the lateral boundaries, and both the vertical and horizontal movements were restrained for the bottom boundary of the model.

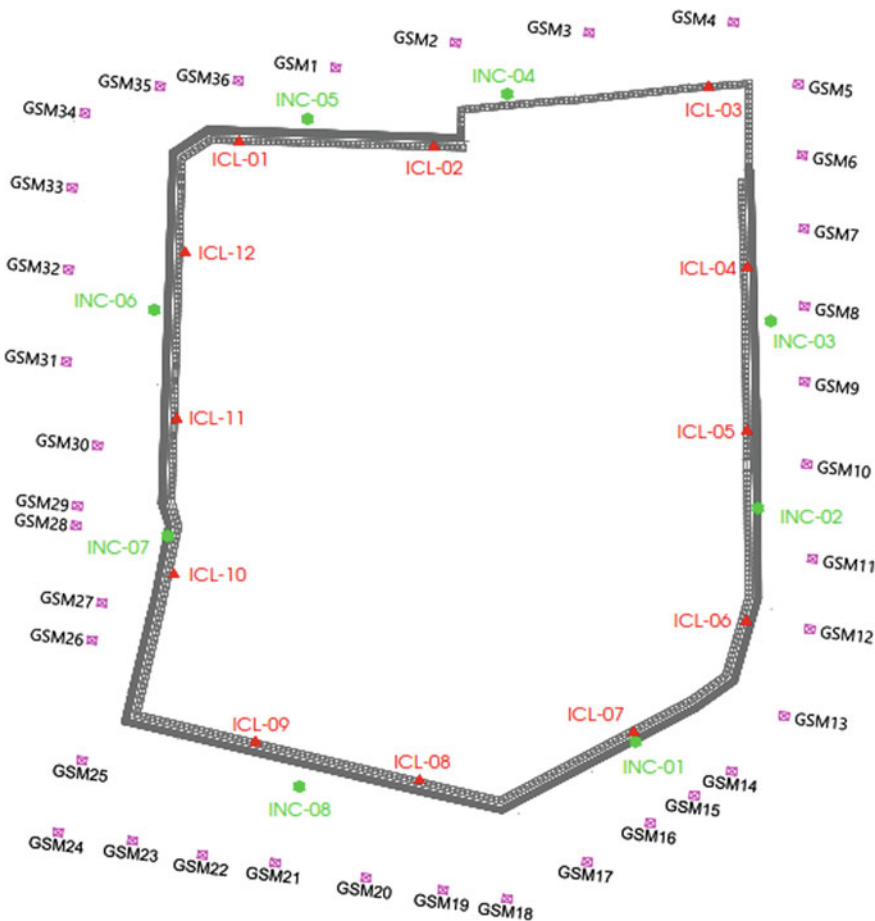


Fig. 5 The arrangement of monitored points in construction site

After analysis progress, the predicted settlement of surface ground was shown in Fig. 7. Besides, the horizontal displacement of the D-wall and the secant pile wall were showed in Fig. 8a, b. It can see in Fig. 7 that the calculated settlement of surface ground in the phase 4 was reasonably larger than the monitoring data. Some monitoring points has the best fit between settlement results of modelling and observation results such as GSM10 and SGM11 points. Furthermore, the ratio between the maximum ground surface settlement and maximum wall displacement, $\delta_{vmax}/\delta_{hmax}$ ratio, which ranges from 0.8 to 1.0. Those analysis results are close to the upper limit of the empirical value, which is $\delta_{vmax}/\delta_{hmax}$ equal to 0.5–1.0 as proposed by Ou et al. [7].

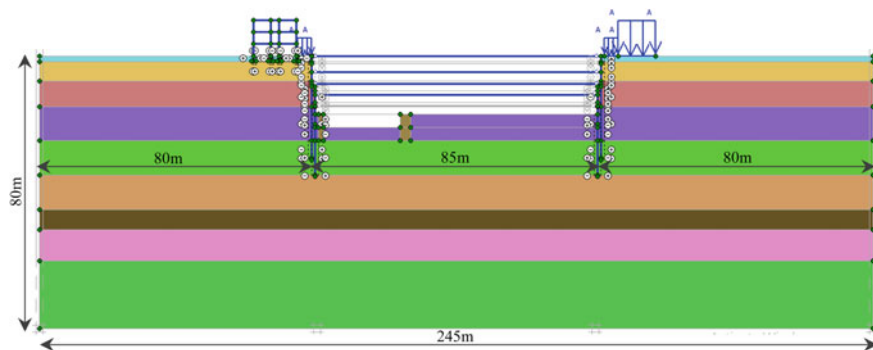
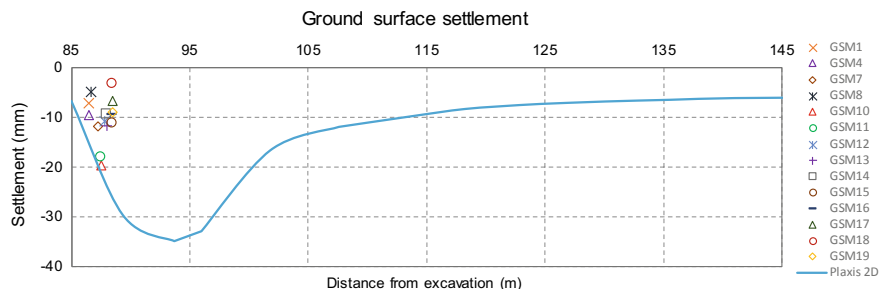
In Fig. 8, the comparisons between predicted and measured results of lateral wall displacement of retaining walls were carried out. As seen in Fig. 8a, the lateral wall displacement of D-wall was shown for discussion. Predicted results was got good

Table 2 Input parameters for soil layers

Soil layer	Depth (m)	N (value)	ϕ' ($^{\circ}$)	c' (kPa)	S_u (kPa)	E_{50}^{ref} (kPa)	E_{oed}^{ref} (kPa)	E_{oed}^{ref} (kPa)	m
1. Stiff sandy clay	1–7	8–12	—	—	3–47	500 S_u	E_{50}^{ref}	$3 E_{50}^{ref}$	1
2.1–2.4. Medium dense, clayey sand	7–45	12–25	25–27	5–8	—	2000 $^{\circ}$ N			0.8
3. Very stiff to hard, lean clay	45–52	21–32	—	—	160–180	500 S_u			0.5
4. Very stiff, clay with sand	52–60	29–37	—	—	186–210	500 S_u			0.7
5. Dense, clayey sand	60–80	32–51	26–28	7–10	—	2000 N			0.5

Table 3 Input parameter for the excavation-retaining structures

Parameters		D-wall 800 mm	SP-wall D900a1300	L1 and B1 300 mm	B2 and B3 200 mm	Unit
Axial stiffness	EA	23,200,000	17,620,000	10,350,000	6,900,000	kN/m
Flexural stiffness	EI	1,237,000	892,000	77,600	23,000	kNm ² /m
Weight	w	5.60	5.46	0	0	kN/m ² /m
Poisson's ratio	v	0.20	0.20	0.20	0.20	—

**Fig. 6** 2-dimensional analysis model by Plaxis 2D**Fig. 7** The comparisons of ground surface settlements between calculated and field data

agreement with observation results in general. The predicted displacements were little larger than those values from measurement. In another words, they were on the safety side. The largest error between prediction and measurement was focused on the top of D-wall. This thing can occur because the actual stiffness of slab struts was not ideal as modelling. They were adversely affected by extremely complex factors which wasn't totally considered in calculating lateral wall deflection such as:

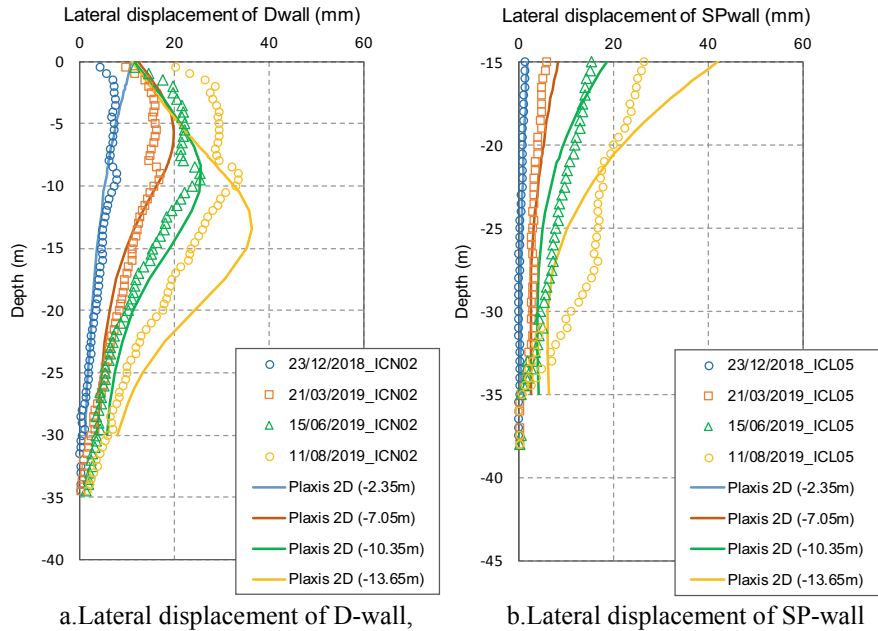


Fig. 8 The comparisons of retaining wall's lateral displacement between calculated and field data

the shrinkage of concrete slab, the development of the elastic modulus of concrete according to construction sequences time and the sudden loading. Figure 8b was prepared for discussion on the lateral wall displacement of SP-wall. In the phase 1 and 2 of excavation, the prediction was successful perform the response of SP-wall by best fit between predicted and measured results. In the phase 3, the difference was started occurred. Then, in the phase 4, the much difference was got between predicted and measured values. This can be seen that, there still have some undefined parameters to perform the lateral displacement of SP-wall in this case. It can be the new issue for studying. However, in total, the maximum lateral displacement of prediction was also larger than measurement. In another words, prediction still in safety side.

4 Conclusions

Based on the FEM—Plaxis 2D analysis results and comparisons, the combined system of D-wall and SP-wall can be successfully modelled by Plaxis 2D. Comparing to the observed results, the predicted settlements of surface ground and horizontal wall displacements were got a good agreement with those values from observation. Furthermore, the predicted values were on the safety side with little larger than those

values from observation. In the future, there should be have more research to get the best fit between predicted and measured results.

References

1. Lim A, Ou CY, Hsieh PG (2010) Evaluation of clay constitutive models for analysis of deep excavation under undrained conditions. *J Geo Eng* 5(1):9–20
2. Hsiung BCB, Dao SD (2016) Evaluation of constitutive soil models for predicting movements caused by a deep excavation in sands. *Electron J Geotech Eng* 19:17325–17344
3. Yong CC, Oh E (2016) Modelling ground response for deep excavation in soft ground. *Int J* 11(26):2633–2642
4. Hsiung BCB (2009) A case study on the behaviour of a deep excavation in sand. *Comput Geotech* 36(4):665–675
5. Tran VT, Huynh QV (2018) Back analysis on deep excavation in the new alluvial sediment layer in Ho Chi Minh City. In: Numerical analysis in geotechnics—NAG2018, Ho Chi Minh City. Vietnam (2018)
6. Tan YC, Chow CM (2008) Design of retaining wall and support systems for deep basement construction—a Malaysian experience. In: Seminar on “Deep excavation and retaining walls. Jointly organised by IEM-HKIE, Malaysia, vol. 24 (2008)
7. Ou CY, Hsieh PG, Chiou DC (1993) Characteristics of ground surface settlement during excavation. *Can Geotech J* 30(5):758–767

Performance Analysis of Axially Loaded Piles by Load Transfer Method: A Case Study in Ho Chi Minh City



Van Qui Lai, Quoc Thien Huynh, Thanh Hai Do, and Thi Gai Nguyen

1 Introduction

In recent year, pile foundation having the large diameter and super-long become more and more popular in Ho Chi Minh where number of high-rise building increases quickly. Following that, predicting the performance of pile, in particular, axially loaded pile need more accuracy. There have many exactly approach to predicting the performance of pile as FEM, BEM, Static load test.... However, choosing the suitable parameter as well as model by FEM, BEM are not simple for practical engineering. Static load test is the best approach to perform the response of axially loaded pile. But, it takes cost and time for implementing. Although it is not powerful as FEM and BEM, load transfer method is simple and can perform the response of axially loaded pile as same as static load test.

Load transfer method was firstly suggested by Seed and Reese [11] and had been refined by many researchers [1, 7, 16]. In this method, the interaction between a pile section and surrounding soil is described by the load transfer curve (which is also referred to as the t-z curves for axially loaded problems). Originally, a t-z curve was determined empirically based on measured data Seed and Reese [11]. However, the interaction between a pile and surrounding soil could also be derived in elastic theory framework. For instance, the semi-analytical method proposed by Randolph and Wroth [10].

Although, this approach was popular in predicting performance of axially loaded pile, the application for pile design in Viet Nam or Ho Chi Minh City is so limited. Thus, in this paper, the load transfer methods were quickly reviewed in firstly. Then,

V. Q. Lai (✉) · Q. T. Huynh · T. H. Do

Faculty of Civil Engineering, Ho Chi Minh City University of Technology, VNU-HCM, Ho Chi Minh City 740128, Vietnam

e-mail: lvqui@hcmut.edu.vn

T. G. Nguyen

Faculty of Civil Engineering, Ho Chi Minh City University of Transport, Ho Chi Minh City 740128, Vietnam

previous proposed load-transfer method of the author Boonyatee and Lai [1] was extended to apply for a project in Ho Chi Minh City was presented.

2 Methodology

2.1 Assumptions and Mathematical Models

In the load transfer method, a pile is divided into many segments as shown in Fig. 1. As mention in introduction part, the response between a pile section and surrounding soil, in another word, the relationship between mobilized shear stress, $\tau_{,i}$ and soil deformation, $z_{,i}$ is described by the load transfer curves or t-z curves. To simulate the nonlinear behavior of piles, physical models and mathematic equations had been proposed for load transfer curves.

For physical models, the slip and non-slip models had been suggested, as shown in Fig. 2. In non-slip model, Fig. 2c, was assumed perfect pile-soil bonding between pile-soil interface. Following that, the settlement of a pile segment i , was equal the soil deformation, $z_{,i}$. However, in the slip model, Fig. 2b, the slippage was assumed to occur in a narrow zone next to the pile shaft. The settlement of a pile segment i , $z_{,i}$, which equals the soil deformation, was divided into inelastic part (slippage), $z_{,i}^s$, and elastic part (deformation of ground), $z_{,i}^e$. As discussed by Sheil and McCabe [12], at the pile-soil interface the slippage is still likely to occur, even at low load levels [9, 14]. By considering slippage [7, 15], the influence of shaft friction is limited in a narrow zone and the settlement of surrounding ground along with the pile-soil-pile interaction can be described in a more realistic manner.

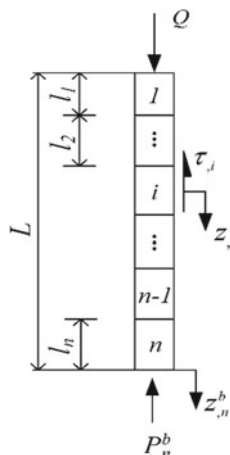


Fig. 1 The technique of load transfer methods

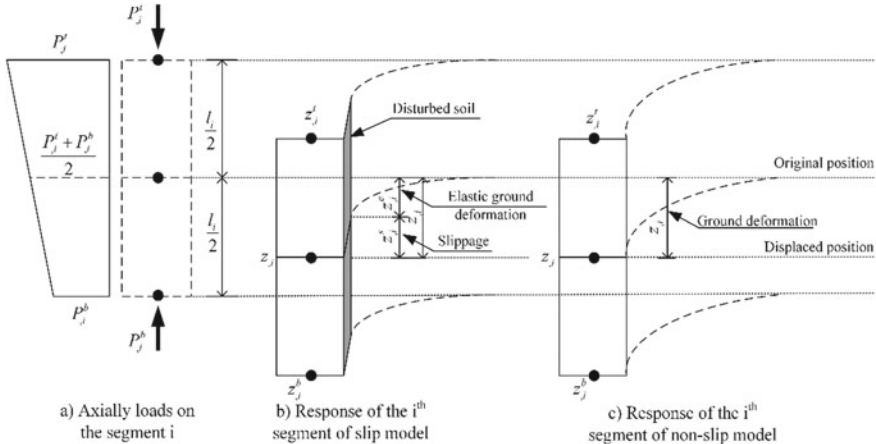


Fig. 2 The technique of load transfer methods

For mathematic equations, some equations including hyperbolic equation, ratio function, the exponential equation and 80% function, had been proposed by observed data [4]. In slip models, these equations had been used to describe the relationship between the slippage, $z_{,i}^s$, and mobilized shear stress, $\tau_{,i}$. In contrast, the non-slip models, these equations would be used to describe the relationship between the ground deformation, $z_{,i}$, and mobilized shear stress, $\tau_{,i}$.

Although, there still not have the comparison of results between using slip and non-slip model of load-transfer curve in analysis axially loaded pile, the slip model of load-transfer curve seemed to describe the pile response in more realistic manner than non-slip model. And, in this study which was the extension of previous study Boonyatee and Lai [1], used the slip model.

Following the slip-model shown in Fig. 2b expressed the response of each segment, the settlement of a pile segment i , $z_{,i}$, can be calculated by equation below:

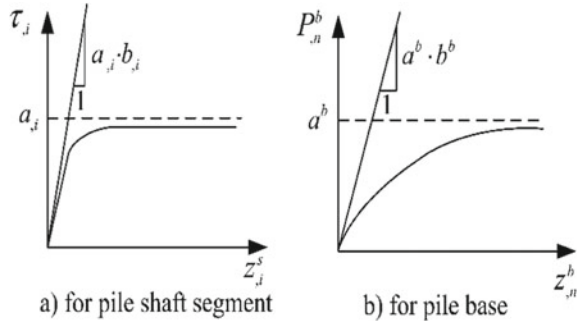
$$z_{,i} = z_{,i}^s + z_{,i}^e \quad (1)$$

In that, the exponential load-transfer curve [15], was used to simulate the model of the slippage, $z_{,i}^s$, and mobilized shear stress, $\tau_{,i}$ of pile segment i . In particular, it is described in Eq. (2) and shown in Fig. 3a.

$$\tau_{,i} = a_{,i} \left(1 - e^{-b_{,i} \cdot z_{,i}^s} \right) \quad (2)$$

Mathematically, the $a_{,i}$ parameter can be used as the asymptote of Equation. It can be determined by Eq. (3). In that, $\tau_{,i}^f$ is the maximum unit skin friction, and R is the reduction factor. The reduction factor was in range from 0.8 to 0.95 [3].

Fig. 3 The technique of load transfer methods



$$a_{,i} = \frac{\tau_{,i}^f}{R} \quad (3)$$

From the load-pile test results, the mobilized friction, $\tau_{,i}$, can be determined from distribution of the axial load with depth, Eq. (4)

$$\tau_{,i} = -\frac{1}{2\pi r_o} \frac{P_{,i}^t - P_{,i}^b}{l_i} \quad (4)$$

Although, determining the maximum unit skin friction from the pile load test is more accurate. However, it is more usual to determine them from the following empirical formulas because such information is usually unavailable in initial design.

$$\tau_{,i}^f = \begin{cases} \alpha_{,i} S u_{,i} & ; \text{for clay} \\ \beta'_{,i} v_{,i} & ; \text{for sand} \end{cases} \quad (5)$$

Normally, the α and β in Eq. (5) can be estimated from S_u and ϕ by empirical formulas developed from experiment and field load test results. These formulas were proposed by Stas and Kulhawy [13], Kerisel [6], Burland [2], Zeevaert [16] and McCarthy [8]. These relationships are described in Fig. 4. Although there are some mismatches among these formulas, they are really used in designs.

The value of $b_{,i}$ was estimated by Eq. (6) where the r_m was assumed to be $2.5L(1 - v_s)$ [10]

$$b_{,i} = \frac{G_{s,i}}{a_{,i} r_o \ln\left(\frac{r_m}{r_o}\right)} \quad (6)$$

The elastic deformation of soil, $z_{,i}^e$, was calculated by below equation [10]:

$$z_{,i}^e = \frac{r_o}{G_{s,i}} \ln\left(\frac{r_m}{r_o}\right) \tau_{,i} = C_{,i} \tau_{,i} \quad (7)$$

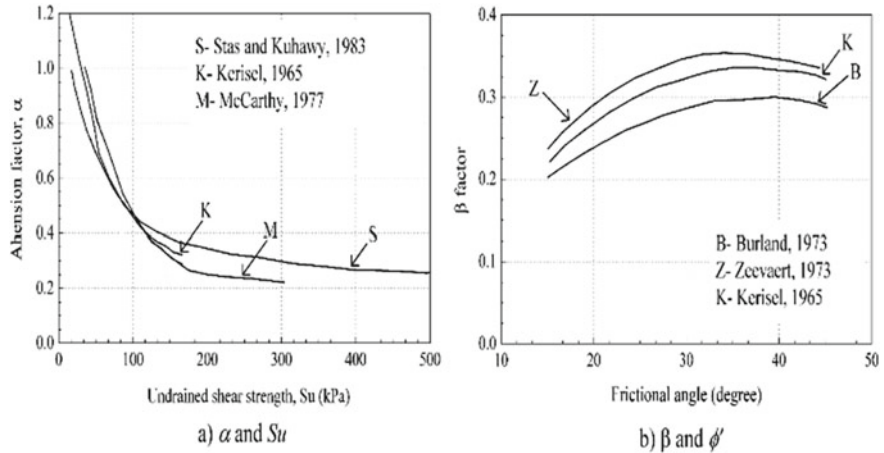


Fig. 4 The technique of load transfer methods

The shear modulus, $G_{s,i}$, was calculated from the relationship with SPT value which was estimated with different soil types [5]

$$G_{s,i} = 14.12(N_{SPT,i})^{0.68} \text{ (MPa)} \quad (8)$$

The relationship between the settlement at pile base, $z_{,n}^b$, and mobilized tip resistance, $P_{,n}^b$, was assumed by Eq. (9) and Fig. 3b.

$$P_{,n}^b = a^b \left(1 - e^{-b^b \cdot z_{,n}^b} \right) \quad (9)$$

The a^b parameter was determined by

$$a^b = \frac{P^{bf}}{R} \quad (10)$$

where

$$P^{bf} = \begin{cases} A_p \sigma'_{vb} N_q^* & ; \text{ for sand} \\ A_p (9S_u b + \sigma_{vb}) & ; \text{ for clay} \end{cases} \quad (11)$$

The value of b^b can be obtained by

$$b^b = \frac{4G_{sb}r_o}{a^b(1 - v_{sb})} \quad (12)$$

In this paper, determining the maximum unit skin friction and maximum pile base resistance by Eqs. (5) and (11), respectively, were still followed the previous

research of the author [1]. However, it is noted that in the Viet Nam condition these equations were also showed in the TVCN standard 10304-2012 for pile design. In particular, these was equations of appendix G of the standard. Although, there have some difference in coefficients but the meanings of equations were the same as Eq. (5) and (11) in this study. Thus, it totally can use the equation from TVCN standard 10304-2012 to estimate the skin friction.

2.2 Algorithm for Determining the Settlement at Pile Head

The settlement of pile top can be determined by following the algorithm shown in Fig. 5. This was the sequent calculation and including some main steps: In the beginning, from the bottommost segment, $i = n$, the settlement base pile ($z_{,i}^b$) was assumed to be z^b for calculating the mobilized tip resistance from Eq. (9). Based on the relationship between mobilized shear stress, $\tau_{,i}$ and ground deformation in Eqs. (1) and (2), the slippage deformation, $z_{,i}^s$, can obtained by implicit equation. Then the load ($P_{,i}^t$) and the settlement ($z_{,i}^t$) at the top of the base segment was determined. In the limited space of paper, this process can be reference to the original algorithm Boonyatee and Lai [1].

Since the values at the top of the bottommost segment were compatible to those at the bottom of the segment above, $z_{,i-1}^b = z_{,i}^t; P_{,i-1}^b = P_{,i}^t$ the same process at bottom segment was repeated on the above segment in sequence until reaching the topmost segment for obtaining the load and settlement at the pile top.

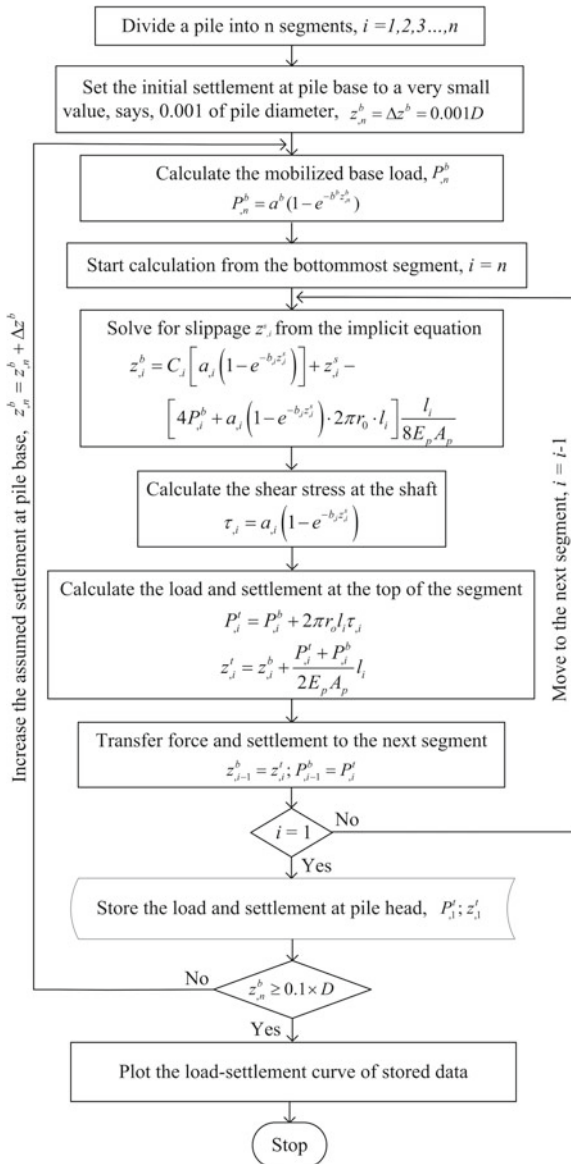
By increasing the value of $z_{,n}^b$ in steps of z^b and repeating the whole process, the relationship between load and settlement of a pile can be obtained.

3 A Case Study in Ho Chi Minh City

The Friendship Tower was a high building including 21 stories and 4 basements. It located on Le Duan Street which was the most prestigious streets in the heart of Ho Chi Minh City, Fig. 6. The soil profile at the construction site is typically characterized as alluvial deposits with alternating layer of sand and clay, as shown in Fig. 7. According to Fig. 7, the studied testing pile was simply introduced with diameter of 1.5 m, length of 80.2 m and well-instrumented with 10 strain gage level. Besides, the design capacity was 1500 tons. The maximum load test was twice time of design capacity, 3000 tons. The TCVN 9393: 2012 standard was applied for field load test process.

Following the methodology in part 2, the response of the studied bored pile was performed. The results of prediction were compared with measured results, as shown in Fig. 8. In that, Fig. 8a showed the load-settlement curve at pile head. It can be seen that, a well agreement between results of measurement and prediction was got. For

Fig. 5 The technique of load transfer methods



more detail, the prediction results were larger than measured results. In another words, prediction results were in safety side with small different with measured results. At the design capacity, the settlements of pile were 10.3 and 13.4 mm for measurement and prediction, respectively. At the twice time of design capacity, the settlements of pile were 33.0 and 40.7 mm for measurement and prediction, respectively.

Fig. 6 Project location in District 1, HCM



Furthermore, Fig. 8b showed the load-distribution with depth z . It is also the importance results to demonstrate the response of axially loaded pile and it is always showed in pile load test results. From the figure, the same behavior between measurement and prediction results were also got. It is noted that 1500-M was measurement result and 1500-P was prediction result. At design capacity, the difference between predicted and measured results was larger in middle of pile. At the maximum load test, the difference was more increasing. It seems the mobilized based load from prediction was increased more quick then reality when pile was loaded nearly ultimate. To solve this issue, it was out scope of this study and need more research to make the best fit between predicted and measured results.

4 Conclusion

The paper presented a quickly review about load-transfer method and an extension work from the previous research of the author for a case study in Ho Chi Minh City. The comparison between the predicted and measured results was implemented. Predicted results of load-settlement curve and load distribution with depth were well agreement to those results from measurement. At the design capacity, the settlements of pile were 10.3 and 13.4 mm for measurement and prediction, respectively. At the twice time of design capacity, the settlements of pile were 33.0 and 40.7 mm for measurement and prediction, respectively.

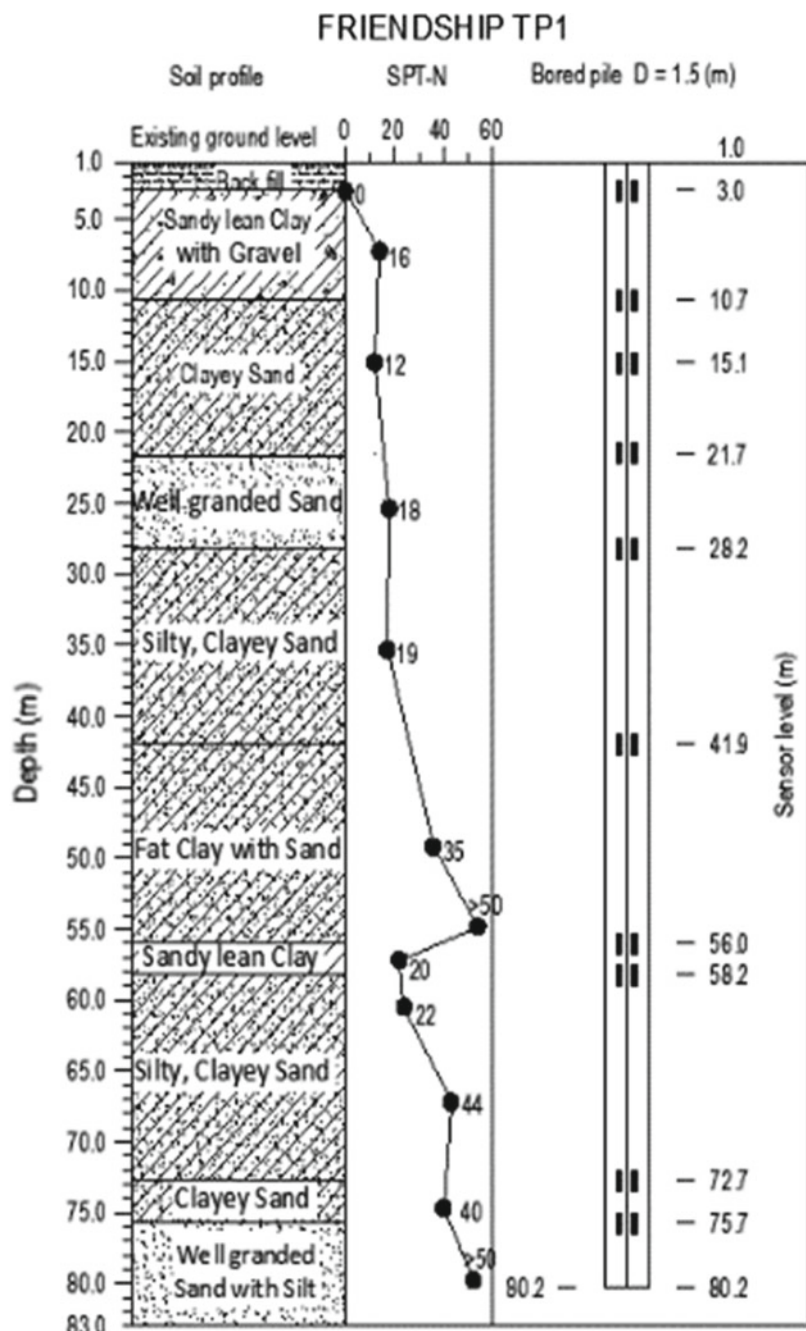


Fig. 7 The technique of load transfer methods

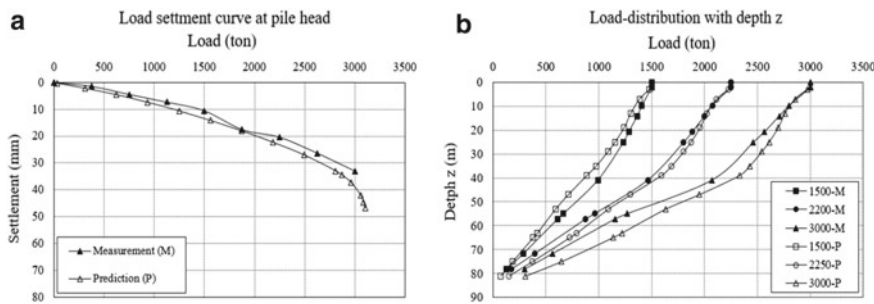


Fig. 8 Comparison between results from prediction and measurement: **a** Load-settlement curve at pile head, **b** Load distribution with depth

Acknowledgements The authors are grateful to FECON South (FCS) who have provided valuable data on instrumented piles.

References

- Boonyatee T, Lai QV (2017) A non-linear load transfer method for determining the settlement of piles under vertical loading. *Int J Geotech Eng*, 1–12
- Burland J (1973) Shaft friction of piles in clay—a simple fundamental approach. Publication of: *Ground Engineering*, UK 6(3)
- Clough GW, Duncan JM (1973) Finite element analysis of retaining wall behavior. *J Soil Mech Found Div* 99(sm 4)
- Fellenius BH (2013) Discussion of “A simplified nonlinear approach for single pile settlement analysis” 1. *Can Geotech J* 50(6):685–687
- Imai T, Tonouchi K (1982) Correlation of N-value with S-wave velocity and shear modulus. In: *Proceedings of the 2nd European symposium on penetration testing*, pp 57–72
- Kerisel J (1965) Vertical and horizontal bearing capacity of deep foundations in clay. In: *Proceeding of symposium on bearing capacity of settlement of foundations*, Duke University, Durham, NC
- Lee K, Xiao Z (2001) A simplified nonlinear approach for pile group settlement analysis in multilayered soils. *Can Geotech J* 38(5):1063–1080
- McCarthy DF (1977) *Essentials of soil mechanics and foundations*. Reston Publishing Company
- Perri JF (2007) Assessment of capacity and seismic demand on axially loaded piles in soft clayey deposits. University of California, Berkeley
- Randolph M. F. and Wroth, C. P. 1978 Analysis of deformation of vertically loaded piles. *J. Geotech. Geoenvir. Eng.* 104(ASCE 14262)
- Seed H, Reese L (1957) The action of clay Along friction piles. *J Geotech Eng* 504:92
- Sheil BB, McCabe BA (2016) An analytical approach for the prediction of single pile and pile group behaviour in clay. *Comput Geotech* 75:145–158
- Stas CV, Kulhawy FH (1984) Critical evaluation of design methods for foundations under axial uplift and compression loading. Electric Power Research Institute
- Trochanis AM, Bielak J, Christiano P (1991) Simplified model for analysis of one or two piles. *J. Geotech. Eng.* 117(3):448–466
- Wang Z, Xie X, Wang J (2012) A new nonlinear method for vertical settlement prediction of a single pile and pile groups in layered soils. *Comput Geotech* 45:118–126
- Zeevaert L (1983) Foundation engineering for difficult subsoil conditions. VNB

Practical Performance of Magnetostrictive Vibration Energy Harvester in Highway Bridge



Tuan Minh Ha, Sajji Fukada, Toshiyuki Ueno, and Duc-Duy Ho

1 Introduction

One of the challenges of health monitoring systems for actual structures is that the number of power supplies is not always enough for field operations. Over the years, vibration-based energy production technology is employed efficiently in many fields. The technology has opened up many opportunities for battery-free wireless devices and the power for the module is obtained from vibration. The self-powered sensor operation is also advantageous in structural soundness monitoring and factory to notify degradation of civil engineering works such as bridges. There, the labor cost for the battery replacement and troublesome work is no more required.

So far, many studies relating to the power harvester using iron–gallium alloy have been performed. In 2011, Ueno and Yamada [4] developed a bimorph vibration energy harvester in which two rods of the iron-gallium (Fe-Ga) alloy were tested and capable of generating 10 mW/cm^3 . The recognition of this energy harvester over conventional ones, such as those utilizing piezoelectric components, is a smaller size, higher productivity, and robustness. Four years later, the energy harvester was improved by utilizing less amount of Fe-Ga and magnet as compared to the previous version [2]. The device has a parallel beam structure consisting of cuboids of Fe-Ga and iron yoke. This transforms small force exerted by vibration to large mechanical stress to the material leading to the change of magnetic flux due to the inverse magnetostrictive effect. Recently, a different prototype of the vibration power-generating device is under investigation [3].

T. M. Ha (✉)

Ho Chi Minh City University of Technology (HUTECH), Ho Chi Minh City, Vietnam
e-mail: hm.tuan@hutech.edu.vn

S. Fukada · T. Ueno

Kanazawa University, Kanazawa, Japan

D. D. Ho

Ho Chi Minh City University of Technology (HCMUT), VNU-HCM, Ho Chi Minh City, Vietnam

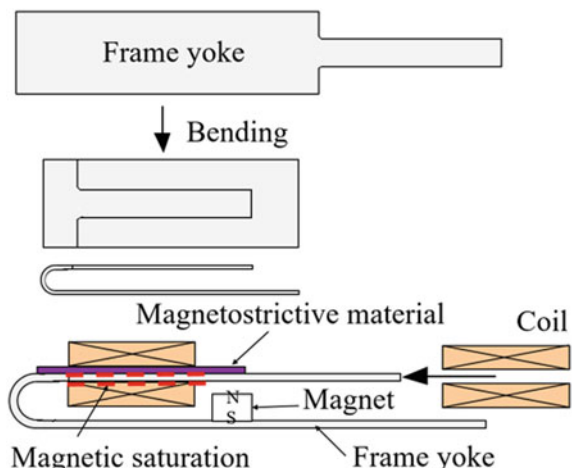
In this study, the power-generating device utilizing a Fe-Ga alloy plate proposed by Ueno [3] was tested on a highway bridge to demonstrate its practical performance. Specifically, the principle of the power generation is based on the inverse magnetostrictive behavior of the plate. The objective bridge of this study is a part of the elevated line of a highway of the Hokuriku district. First, the vibration properties of target members of the bridge, such as the frequencies, mode shapes, and damping ratios, were estimated by using the measurement data of the vibration monitoring tests along with the generated open-circuit voltage of the device during each test. Then, a parametric study was conducted on several preliminary options of the weight mounted on the tip of the U-frame to investigate the appropriate value for vibration resonance between the vibration source and the device. Finally, the device was installed at the bridge again to check the performance improvement with the calibrated mass.

2 Principle and Configuration of the Device

The configuration of the proposed energy harvester is presented in Figs. 1 and 2. The device has a plate-like Fe-Ga alloy attached to a U-shaped magnetic frame (Fig. 1 top). A coil is wound around the Fe-Ga plate. Especially, a permanent magnet is arranged in an appropriate location within the frame so that the part where the Fe-Ga plate is fixed becomes magnetically saturated by magnetic bias, while other parts remain unsaturated. When the upper frame is bent, the uniform stress occurs in the longitudinal direction of the magnetostrictive element.

The principle of the energy-generating technique is described in Fig. 3. First, the energy harvester is fastened to a vibrating object, a weight is attached to the tip of the frame. When the device is shaken, the inertial force of the weight opens and closes

Fig. 1 U-frame (top) and device structure (bottom)



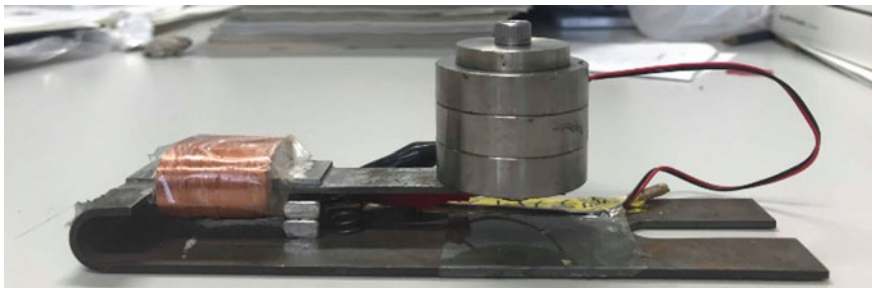
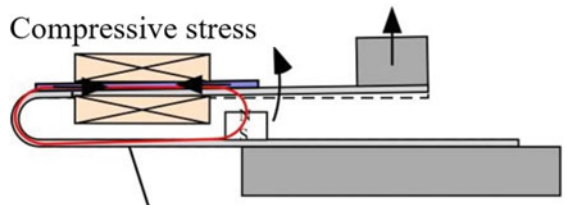
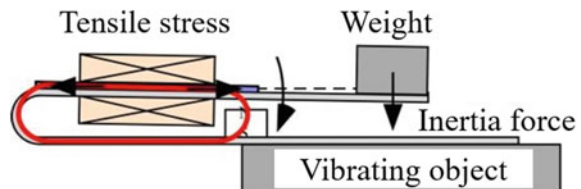


Fig. 2 A prototype vibration energy generator

Fig. 3 Principle of the energy-generating technique:
Inertial force downward
(top) and upward (bottom)



Flux variation by inverse magnetostrictive effect passes through this close loop

the opening of the U-shaped frame. Uniform tensile and compressive stresses occur longitudinally within the Fe-Ga plate. Consequently, the variation in the magnetic flux caused by the inverse magnetostrictive effect (see Fig. 4) flows in a closed magnetic circuit in sequence with the element, frame, magnet, and gap. Therefore, an electromotive force proportional to the temporary change of the magnetic flux of the element is produced in the coil. The time variations of the fluxes lead to a voltage on the coils by Faraday's law of induction. In other words, voltages are induced in the wound coils around the Fe-Ga plate due to time-varying magnetic fields and the power is harvested.

The design highlight of the proposed device is the simple shape of the steel frame, which can be easily produced from a Fe plate. The magnetostrictive member can be attached to the frame in advance and the air-core coil can be installed later. Therefore, the device is suitable for mass production. The produced energy can be modified by handling the coil thickness, while the generated voltage and the resistance can be

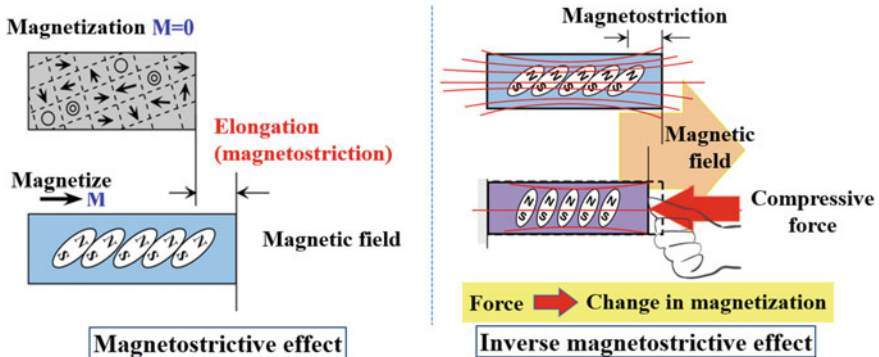


Fig. 4 Inverse magnetostrictive effect

improved by manipulating the wire diameter. Moreover, the frame is more efficiently vibrated by smooth curving compared to the conventional parallel-beam version [2], and also durable. Hence, the proposed design meets both mass production and high performance.

3 Overview of the Test Bridge

Located in the Hokuriku district, the objective bridge of this study is a part of the elevated line of a highway. As can be shown in Fig. 5, the bridge is a composite structure with a slab thickness of 220 mm and four main steel girders, namely girders G1, G2, G3, and G4. Forty years have passed since the bridge was started in 1978 as a part of the important route which has a volume of traffic of 27,000 vehicles per day and connects the East and West sides of the Kanazawa city.

4 Preliminary on-Site Investigation

With a large, complex structure of the objective bridge consisting of many components, the obstacle is finding the location to place the device to obtain the maximum voltage. To obtain free damped vibrations, the accelerometers were placed at the positions of the sway brace and lateral brace between G1 and G2 main girders, the handrail of the inspection catwalk, and the web of main girder G2. The arrangement of measurement points is summarized in Fig. 6. As can be seen in this figure, the measurement items are the vertical accelerations of the sway and lateral braces, the horizontal acceleration of the handrail and the G2 web, and the relative displacement between the deck slab and the sway brace, and the relative displacement between



Fig. 5 The test bridge of this study

the lateral brace and the inspection catwalk. During each examination, the excitations occurred alternately via ordinary vehicles running on the bridge. To follow the change in the dynamic parameters and the generated voltage, the measurement was conducted in 5 min and continuously for a day, with 60,000 data points obtained at a sampling rate of 200 Hz. The dynamic responses were extracted from the measured data using the eigensystem realization algorithm (ERA) [1].

For the preliminary study, a weight of 985 g was fixed at the tip of the frame. Figure 7 presents the frequency response results estimated by a fast Fourier transform (FFT) analyzer. When the weight was 985 g, the frequencies of the generated voltage was ~ 12 Hz. Also, the voltage waveform is shown in Fig. 7a. In particular, the time series waveform has intermittent responses due to the traffic load. The maximum voltage was measured as ~ 3.1 V. On the other hand, the predominant frequency of the lateral brace acceleration was around 19 Hz. From this, when considering the lower lateral brace as the vibrating object, the power generation device was not functioning efficiently. Therefore, it is necessary to adjust the dominant frequency by adjusting the weight attached to the tip of the frame. In addition, no significant frequency component was found from the relative displacement data.

5 Calibration at the Laboratory

This study employed a commercial electrodynamic vibration test system to reproduce the actual oscillation of the bridge at the laboratory. Specifically, the vibration data of the lateral brace between girders G1 and G2 were utilized as input and target

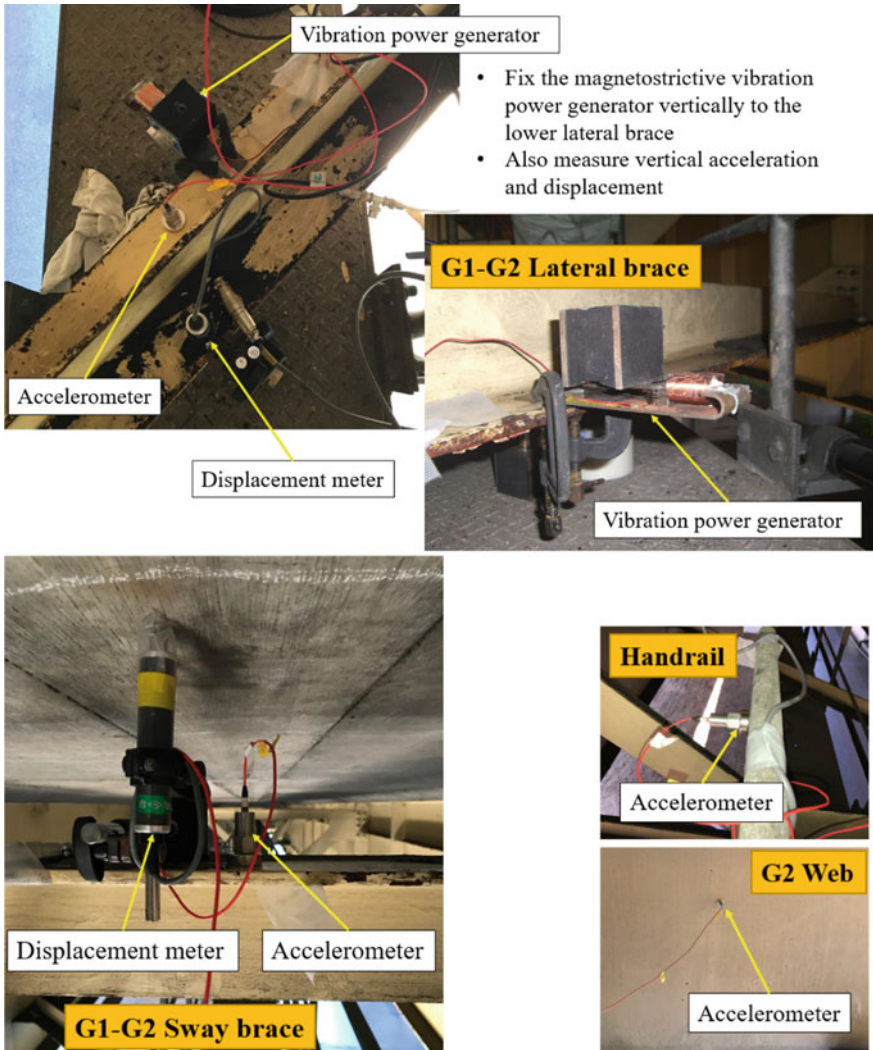


Fig. 6 Preliminary on-site investigation set-up

waveforms of the system. The experiment set-up and the frequency responses results of the reproduced voltage and lateral brace acceleration are shown in Fig. 8. The outcome demonstrates that the frequency of the generated voltage increased with the decrease in the weight mounted. Moreover, with an attached weight of 312.8 g, the frequency of the frame's oscillation matched the frequency of the vibration of the lateral brace, which was estimated to be ~19 Hz. Therefore, the energy harvester was installed at the field again to check the performance improvement with the calibrated mass.

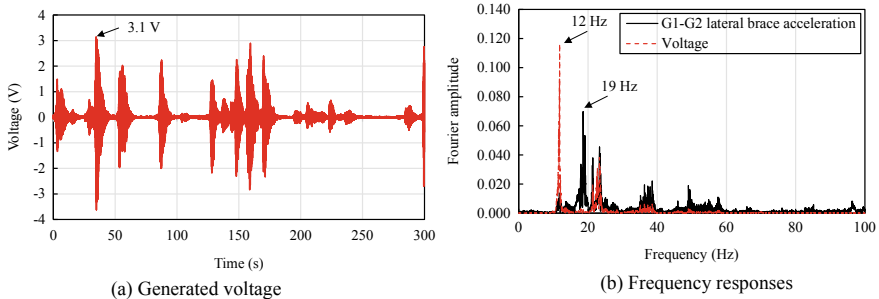


Fig. 7 Results of preliminary on-site investigation

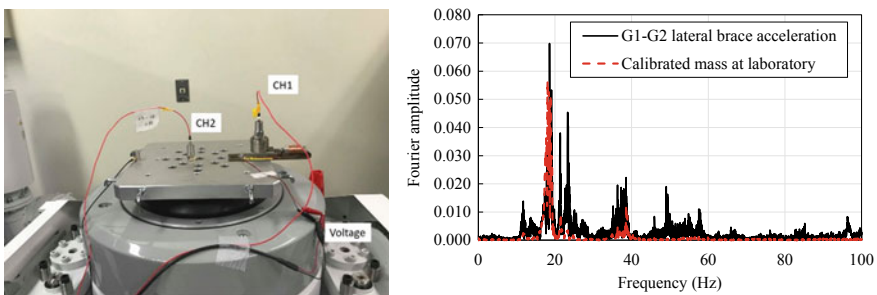


Fig. 8 Weight calibration at the laboratory

6 Performance of the Proposed Power-Generating Device

After the calibration, the measured voltage waveform is exhibited in Fig. 9. When the weight was 312.8 g, the frequencies of the generated voltage was ~19 Hz. During the monitoring period, the maximum voltage was obtained as ~7.8 V, which was significantly higher than the voltage measured at the preliminary investigation

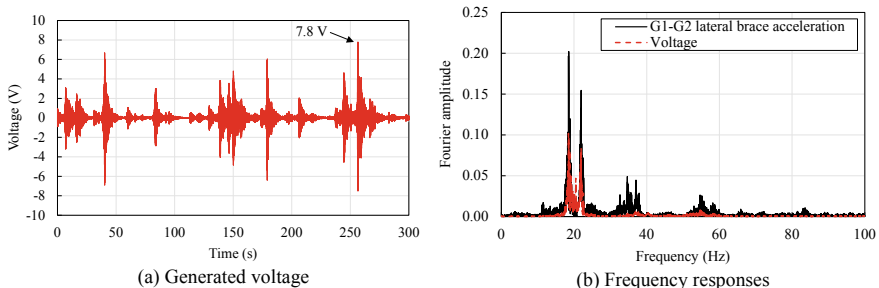


Fig. 9 Performance of the device with the calibrated weight

(~3.1 V). These outcomes demonstrate that with an attached weight of 312.8 g, the frequency of the frame's oscillation matched the frequency of the vibration of the lateral brace, which was estimated to be ~19 Hz. This caused the system to oscillate with a larger amplitude than when the other weights were applied, and thereby the resonance occurred and the open voltage could be observed at a high value.

7 Conclusions

This study proposed and tested a vibration power-generating device using a Fe-Ga alloy plate on an actual highway bridge to investigate its practical performance. The attached weight at the tip of the U-frame was modified to obtain the appropriate value for vibration resonance between the lateral brace and the device. The main outcomes drawn from this study are as follows.

- With a weight of 312.8 g utilized, an open-circuit voltage of ~7.8 V at a vibration of ~19 Hz was generated by free damped vibrations due to vehicle loads.
- It is advisable to employ resonant vibration of high frequency to produce high electrical power efficiently.

In this study, the harvester was confirmed to produce the maximum voltage of ~7.8 V at the resonance frequency of ~19 Hz. This work is a start point for a novel vibrational power-generating device using magnetostrictive material for bridge monitoring system, and further investigation is required on the topic. Regarding long-term outlooks, to obtain high electrical energy, the location of the device and the weight attached to the frame of the device should be modified and improved. Moreover, further numerical studies should be carried out to predict accurately the behavior of the proposed device in actual circumstances, and forthcoming schemes can target advancements in the designs and simulation methods. Besides, studying the environmental influences on the performance of the proposed device is also vital to adequately utilize the monitoring techniques and modifications to the design.

Acknowledgements This study was promoted by the Regional Innovation Ecosystems Program from the Ministry of education, culture, sports, science and technology, Japan. The authors wish to thank the concerned parties for their valuable collaboration, sub-consultants, and support.

References

1. Juang JN, Pappa RS (1985) An eigensystem realization algorithm for modal parameter identification and model reduction. *J Guid Control Dyn* 8:620–627
2. Ueno T (2015) Performance of improved magnetostrictive vibrational power generator, simple and high power output for practical applications. *J Appl Phys* 117:17A740

3. Ueno T (2018) Magnetostrictive low-cost high-performance vibration power generator. *J Phys: Conf Ser* 1052:12075
4. Ueno T, Yamada S (2011) Performance of energy harvester using iron-gallium alloy in free vibration. *IEEE Trans Magn* 47:2407–2409

Quality Assessment of Field Soilcrete Created by Jet Grouting in the Mekong Delta



Hoang-Hung Tran-Nguyen and Nhung H. D. Ly

1 Introduction

Jet Grouting—Soil Cement Deep Mixing technology (SCDM)—cuts and erodes the in situ soils by high pressure beams then to mix with cement slurry to create soil-cement composite material or soilcrete [2, 9]. Soilcrete has better engineering properties than those of the in situ soils. The unconfined compressive strength of soilcrete is 10–100 times higher than that of the in situ soils [9]. The permeability of soilcrete is also lower than that of the in situ soils [3, 4]. Jet Grouting has been applied for several practical applications but still has been in research in Vietnam [5–7]. Tran-Nguyen and Quach [6] attempted to apply Jet Grouting to reinforce bridge abutments in Dong Thap province, Vietnam. The two field experiments applying Jet Grouting to reinforce Tam Bang and Vam Dinh bridge abutments in Dong Thap province were conducted in 2017 basing on the primary research results of Tran-Nguyen [9]. The mechanical properties of soilcrete specimens created in the laboratory using the soil samples taken at the research site were reported by Tran-Nguyen and Quach [7]. This paper investigated the field soilcrete characteristics of the soilcrete column created by Jet Grouting at the Vam Dinh pilot test in Dong Thap province. The investigated characteristics of the pilot soilcrete column consist of the shape and dimensions, unconfined compressive strength, secant modulus of elasticity, and strain at failure. A number of field core soilcrete samples (BHs) were taken at the field to form soilcrete specimens for unconfined compressive strength tests in the laboratory (ASTM D2166) [1].

H.-H. Tran-Nguyen (✉) · N. H. D. Ly

Faculty of Civil Engineering, Ho Chi Minh City University of Technology, VNU-HCM, Ho Chi Minh City, Vietnam

e-mail: tnhhung@hcmut.edu.vn

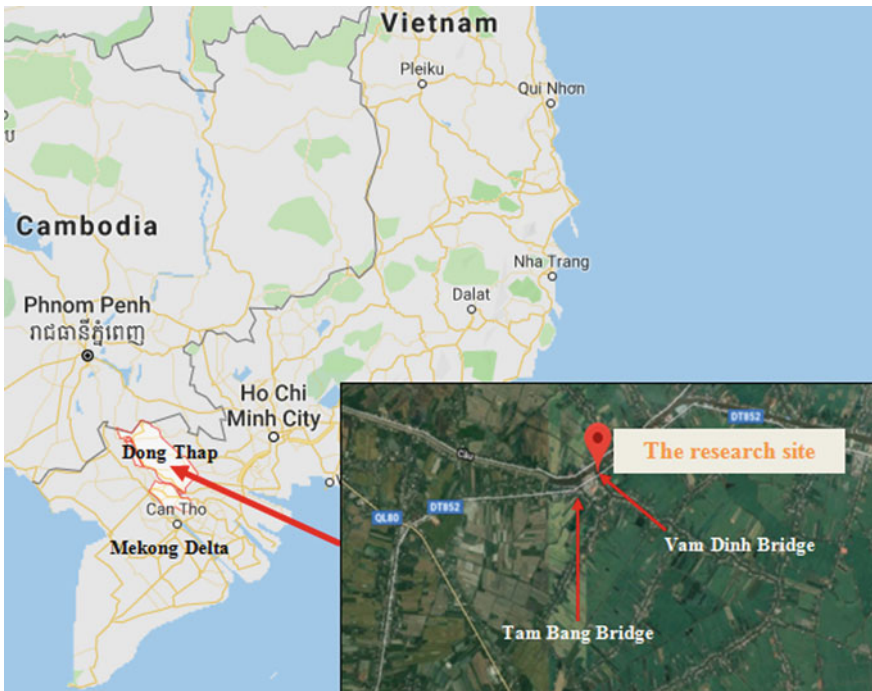


Fig. 1 The location of the research site in Dong Thap province, Vietnam (Google Maps)

2 Methods

2.1 *The Research Site*

Figure 1 shows the location of the research site in Dong Thap province which is one of the 13 provinces in the Mekong delta in Vietnam. The two boreholes were drilled for a soil investigation (Table 1).

2.2 *Materials*

The Portland blended cement, PCB40, was used for this research. The cement meets the TCVN 6260:2009. The fresh water or water in rivers was utilized to mix with dry cement. The water was tested and meet the TCVN 4506:2012. The water and cement ratio (*w:c*) was 1.5:1.

Table 1 The key in situ soil properties of the research sites

The research site	Vam Dinh bridge		Tam Bang bridge	
	Layer 1	Layer 2	Layer 1	Layer 2
Soil type	Medium clay	Soft clay	Very soft clay	Soft clay
Thickness, H (m)	3.6	13.8	10	12
Fine content (%)	92.8	94.3	96.3	84.1
Moisture, w (%)	34.1	55.8	53.1	46.7
Unit weight, γ_w (kN/m ³)	18.24	16.22	16.46	16.79
Plastic Limit, PL (%)	42.1	48.7	50.6	52.4
Plasticity Index, PI (%)	18.2	21.1	20	17.8
Modulus, E (kN/m ²)	3105	1539	1659	1852
Unconfined compressive strength, q_u (kN/m ²)	117.91	59.61	56.06	70.54
pH	-	7.78	6.81	7.55
Organic content (%)	-	5.07	6.13	3.02

2.3 Equipment

The secondhand Jet Grouting (JG) system was used in this study (Fig. 2). A YBM SI-30S (Japan) was employed to created JG columns. The SI-30S was installed with the two 2.5-diameter nozzles at the tip of the JG rod. A used high pressure pump can create a maximum pressure of 35 MPa. The mixers and a generator were also utilized.

**Fig. 2** The secondhand Jet Grouting system used for this study

Table 2 The key operating parameters of the JG to create soilcrete columns

Parameters	Pilot column at VD	Reinforced columns at VD
Depth or length (m)	10	7–9
Pump pressure (MPa)	20–25	20
Rotation of JG rod (rpm)	5–6	6
Round per step	6	1
Length per step (cm)	5	5

3 Results and Discussion

3.1 Field Experiment

Table 2 presents the field Jet Grouting experiment at Vam Dinh bridge abutment. The average reinforced depth of 10 m from the ground surface was applied for an area of 5×10 m behind the abutment of Vam Dinh (VD). The soilcrete columns were arranged in square by 2×2 m.

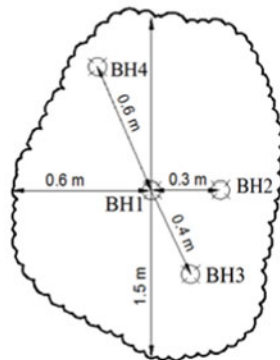
3.2 Quality Assessment for Vam Dinh Bridge Abutment

3.2.1 Visual Inspection

A pilot column was excavated for visual investigation after 21 days constructed. The top of the soilcrete column at a depth of 1.5 m from the ground surface was exhibited for observation and measurement. Stiff cross-sectional diameters varied from 1.2 to 1.5 m (Fig. 3a). The cross section of the column was not circular like expected. The top soil layer was filled by several materials such as trees, mud, aggregates, and so on. A decaying root was found at this depth and close to the column. These factors are believed to cause the non-uniform shape of the column. The 4 positions (BH1, BH2, BH3, BH4) on the cross section of the soilcrete column were marked for the continuous core samples taken along the whole depth of the column (Fig. 3b). The soilcrete specimens created from the core borehole samples have the average diameter (D) of 68 mm with 140 mm in high (H) or a H/D ratio of 2–2.5.



(a) The top of the pilot column appeared at a depth of 1.5 m



(b) The positions for the core borehole samples

Fig. 3 The cross section of the pilot soilcrete column created at the Vam Dinh bridge

3.2.2 Unconfined Compressive Strength, q_u (ASTM D2166)

The 6 qualified soilcrete specimens were made from the core soilcrete samples taken at the site. Unconfined compressive tests were carried out on the soilcrete specimens to assess the field soilcrete characteristics following the ASTM D2166 at a speed of 1 mm/min or less. Unconfined compressive strength, q_u , at a curing time of 114 days varied from 1.7 to 2.2 MPa for the medium clay layer and about 1.6 MPa for the soft clay layer (Fig. 4). q_u of the soilcrete was higher 15–20 times than that of the medium clay (0.12 MPa) and about 18 times greater than that of the soft clay (0.06 MPa). q_u of soilcrete was slightly lower than those of the field experiments in Ho Chi Minh City (HCMC) in 2012 [13–15]. The $w:c$ ratio of 1.5:1 which is higher than 1:1 in the tests in HCMC caused increasing in the water content of soilcrete. The organic content of the soft clay (Table 1) is believed to cause low q_u [3, 4, 9].

3.2.3 Secant Modulus of Elasticity, E_{50}

E_{50} was from 127.2 to 389.5 MPa and E_{50}/q_u from 57 to 231, respectively (Fig. 5). E_{50}/q_u was slightly lower than the published data [2, 3, 5, 8, 10–15], but was common for the Mekong delta soft clays [4, 5, 8–15]. E_{50} is appropriate for reinforcement to mitigate differential settlement at the Vam Dinh bridge abutment. E_{50} is higher 100–400 times than that of the in situ soft clay. E_{50} indicates that the soilcrete can improve soft ground effectively to reduce settlement.

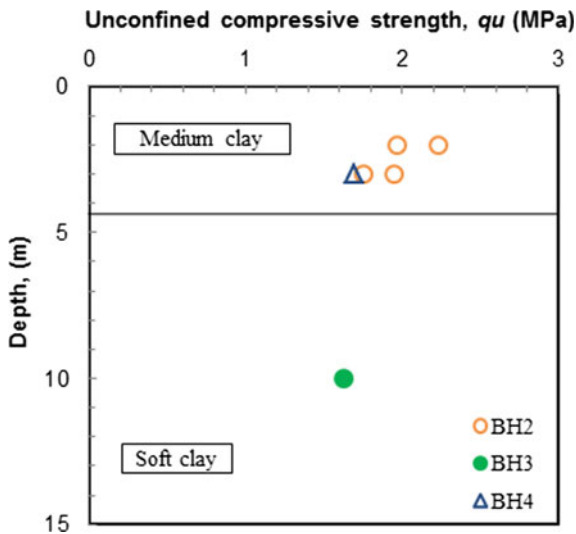
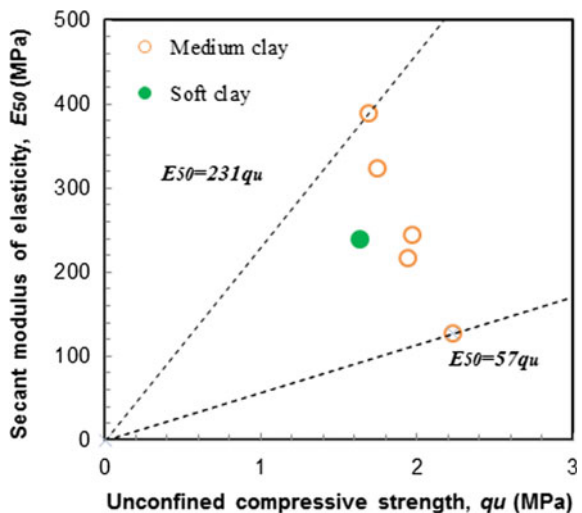


Fig. 4 Unconfined compressive strength of field soilcrete created by Jet Grouting at the VD bridge

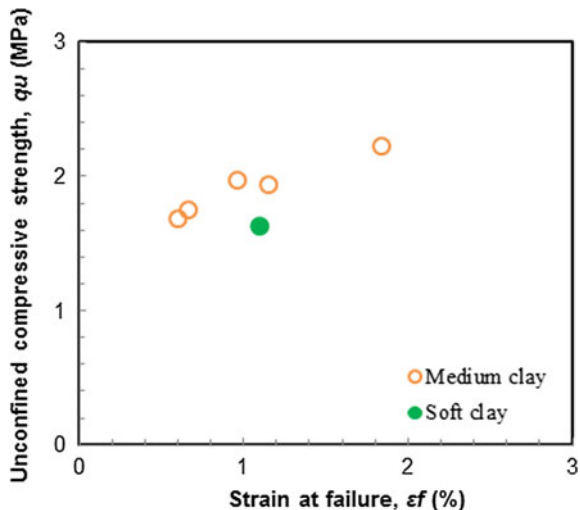
Fig. 5 Secant modulus of elasticity of field soilcrete created by Jet Grouting at the VD bridge



3.2.4 Strain at Failure, ϵ_f

Figure 6 displays the strain at failure of the soilcrete specimens varying from 0.6 to 1.8%. ϵ_f of soilcrete is relatively small which is typical about 2% or less [3, 4, 8, 10–15]. The failure patent of soilcrete is often vertical cracks and happens quickly. The soilcrete failure is similar to concrete. ϵ_f indicates that the soilcrete is a brittle material type.

Fig. 6 Strain at failure of field soilcrete created by Jet Grouting at VD bridge



4 Conclusions

The pilot soilcrete column was successfully created by Jet Grouting at the Vam Dinh bridge. The column diameter of 1.2–1.5 m was determined at the depth of 1.5 m below the ground surface. The 4 core borehole samples were taken along the depth of the column. There were only 6 good soilcrete specimens with the 68 mm diameter made at the ratio of height to diameter by 2–2.5. The unconfined compressive strength tests were performed to investigate the quality of the field soilcrete. The results indicate the following findings:

1. The diameter of the pilot soilcrete column varies from 1.2 to 1.5 m meeting the designed diameter.
2. The cross section of the column was not circular due to the non-uniform soil layers.
3. q_u from 1.6 to 2.2 MPa, which is higher than the designed strength of 0.5 MPa.
4. E_{50}/q_u from 57 to 231.
5. ε_f from 0.6 to 1.8%, which is lower than 2%—a typical strain at failure of soilcrete.

Acknowledgements This study was funded by Dong Thap province and An Binh Co. Ltd. via a research contract No. 108/2015/DT-KHCN. The authors thank HCMUT for their effective support.

References

1. ASTM (2016) ASTM D 2166 standard test method for unconfined compressive strength of cohesive soil. American Society for Testing and Materials, USA, 8 p
2. Croce P, Flora A, Modoni G (2014) Jet grouting: technology, design, and control, 278 p
3. Kitazume M, Terashi M (2013) The deep mixing method, 405 p
4. Tran-Nguyen HH (2019) Soil cement mixing technology (SCM) to improve soft ground, 547 p (in Vietnamese)
5. Tran-Nguyen HH, Le PL, Le KB, Ly TMH (2018) Field trials on soil cement mixing technology to reinforce earth levees in the Mekong delta. Vietnam ASEAN Eng J 8(1):14–26
6. Tran-Nguyen HH, Quach HC (2017a) Mechanical behaviors of soilcrete created from soils of Tam Bang and Tam Bang bridges simulating Jet Grouting technology. In: Grouting 2017, Geotechnical Special Publication No. 289. ASCE, pp 62–72
7. Tran-Nguyen HH, Quach HC (2017b) Jet Grouting mitigating settlement of bridge approaching embankments of Tam Bang and Vam Dinh bridges. In: CIGOS Vietnam 2017, Lecture notes in Civil Engineering, vol 8. Springer, pp 736–745
8. Tran-Nguyen HH, Truong DC, Truong TK (2017) Effects of operating parameters the NSV system on field soilcrete characteristics in the Mekong delta, Vietnam. In: CIGOS Vietnam 2017. Lecture notes in civil engineering, vol 8. Springer, pp 704–715
9. Tran-Nguyen HH (2016) Jet Grouting, 368 p (in Vietnamese)
10. Tran-Nguyen HH, Le KB, Le PL (2016) Behaviors of field soilcrete created by a light-weight equipment system to reinforce an earth levee in Vietnam. Malays J Civil Eng 28(1):91–107
11. Tran-Nguyen HH, Kitazume M, Tanaka H, Kobayashi T, Truong KT, Le BK, Le LP (2015) Effects of deep mixing method to reinforce earth levees in the Mekong Delta, Vietnam. In: The deep mixing 2015, pp 151–160
12. Tran-Nguyen HH, Le BK, Le LP, Do CMT, Nguyen TB, Truong CD, Mai PA (2015) Laboratory investigation of soilcrete created from the Mekong Delta's soils mixed with cement. In: The deep mixing 2015, pp 725–734
13. Tran-Nguyen HH, Le TT, Ly TH (2014) A field trial study on Jet Grouting to improve the subsoil in HCM City in Vietnam. J Teknologi Sci Eng 69:23–29
14. Tran-Nguyen HH, Kitazume M, Luong BT, Bui TT (2014) Laboratory investigation on An Giang soil mixed with dry cement. Malays J Civil Eng 26:77–88
15. Tran-Nguyen HH, Le TT, Ly TH (2013) Soilcrete characteristics created by a single Jet Grouting system in Ho Chi Minh City. In: the 2nd international conference on geotechnics for sustainable development, pp 465–474

Studies on the Effects of Raft and Piles on Behavior of Piled Raft Foundations



Le Ba Vinh, To Le Huong, Le Ba Khanh, and Hoang The Thao

1 Introduction

Piled-raft foundations are considered to be one of the most effective foundations for high-rise buildings in ensuring load bearing capacity, and settlement, permissible differential settlement. However, these behaviors heavily depend on design parameters such as the number of piles, pile length, layout type, the thickness of rafts, etc. While the upper load can be supported by the raft, the piles are included to reduce the settlement of the raft. Also, the piles can be arranged to reduce the differential settlement in the raft. The idea of central piles to reduce both differential settlement and bending moments is in the case of Cooke et al. [1]. Randolph [5] proposed the possibility of minimizing the differential settlement by installing small piles below the center of the raft. Subsequently, Horikoshi and Randolph [2] verified this concept by the centrifuge model method.

The arrangement of piles and the size of piles and rafts also significantly affect the behavior of piled raft foundation [3]. In this paper, by changing the pile layout with the total length of the piles to be constant, and changing the thickness of the raft, the authors studied their effect on the settlement and the differential settlement of piled-raft foundation.

L. B. Vinh (✉) · T. Le Huong · L. B. Khanh · H. T. Thao

Faculty of Civil Engineering, Ho Chi Minh City University of Technology, VNU-HCM, Ho Chi Minh City, Vietnam

e-mail: lebavinh@hcmut.edu.vn

T. Le Huong

e-mail: tolehuong@hcmut.edu.vn

2 Model of the Analyzed Pile-Raft Foundation

The model used in this paper is a piled-raft foundation consisting of 100 piles installed on a homogeneous clay base. Geometry and 3D modeling in PLAXIS 3D are shown in Figs. 1 and 2, respectively. Because of the symmetry of the foundation in both the

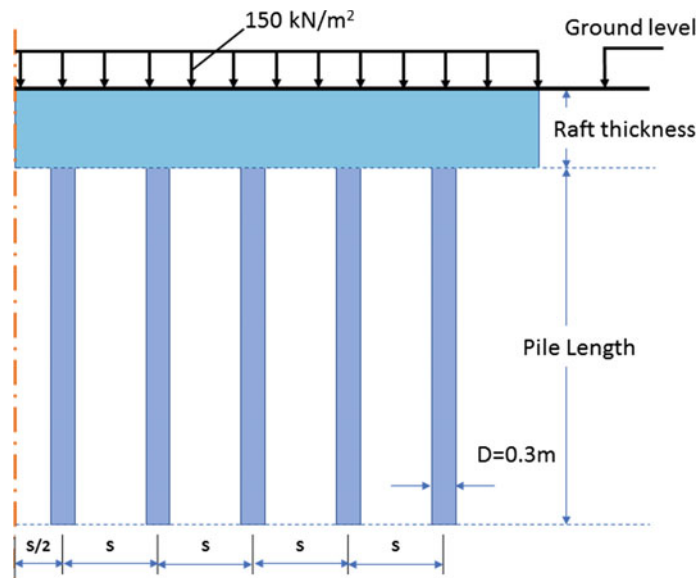


Fig. 1 Geometric model of piled-raft foundation

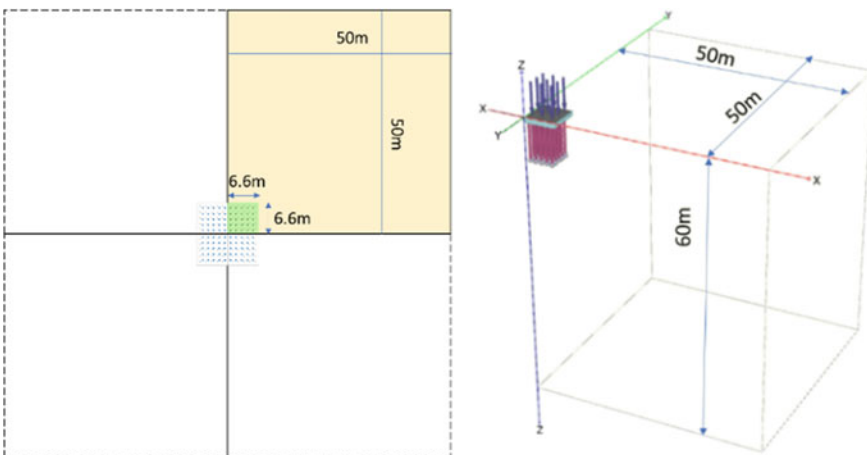


Fig. 2 3D model of the analysed pile-raft foundations in PLAXIS 3D

x and y-axes, only 1/4 of the nails are simulated. The parameters of a quarter-model are shown in Table 4.

Hardening Soil model with the parameters in Table 1 is used for clay layer according to the Plaxis 3D's Manual [4]. A 1 m-thick raft with input parameters in PLAXIS is shown in Table 2. Piles with a diameter of 0.3 m are simulated with the parameters shown in Table 3.

2.1 Effect of the Pile Layout on the Behavior of Piled-Raft Foundation

In order to assess the effect of pile placement with a total unchanged pile length, 10 cases of pile arrangement of the same total lengths are analyzed with the illustration in Figs. 1 and 3. Cross-section of each case are presented in Fig. 4. Raft width in a quarter-angle model is $6.6\text{ m} \times 6.6\text{ m}$ based on the reference design of Vietnamese Standard about spacing between piles in foundation. The purpose of this research is to test the effect of the pile layout on the settlement reduction, and also the differential settlement reduction. From case 2 to case 6, the piles are distributed in the middle of the raft with different number of piles (25, 16, 9 piles on the quadrant symmetry model) and the distance between the piles is 3D, or 4D (with D is Diameter of the pile). In addition, staggered pile layout also contributes to increasing the distance between piles in the raft compared to the normal layout, thus also affecting the pile foundation settlement. These cases are illustrated from Case 7 to Case 10. The load in 10 cases is the uniform distribution load of 150 kN/m^2 .

In general, the results in Fig. 5 show that the staggered pile layout leads to a smaller settlement than ones of the uniform distributed pile layout. When considering the same distance S between the piles in a uniform distributed pile layout, the settlement of the 9-piles model decreases by 40% as compared to the 25-piles model. However, the results in Fig. 6 show that the decrease in total settlement is not synonymous with a decrease in differential settlement. Case 1 to Case 4 gives a large total settlement, but results in the small differential settlement which is smaller than the allowed value of $(2/1000)$ of Vietnamese Standard, TCVN 10304:2014 [6], while Case 5 to Case 9 gives the lower total settlement but the differential settlement exceeds the minimum requirement. Case 10 can be the optimum pile layout which satisfies both the allowable settlement and differential settlement.

2.2 Effect of the Raft Thickness on the Behavior of Piled-Raft Foundation

When the load is transferred to the piled-raft foundation, the raft also participates in the load bearing. Therefore, to assess the effect of the raft's thickness on piled raft

Table 1 Input parameter of soil in the model

γ_{sat}	E_{50}^{ref}	E_{ur}	m	c'_{ref}	φ	ψ	ν_{ur}	p_{ref}
(kN/m ³)	(kN/m ²)	(kN/m ²)	-	(kN/m ²)	(°)	(°)	-	(kN/m ²)
20.1	20.5	6300	18,900	1	37.3	18.9	0	100

Table 2 Raft properties in PLAXIS 3D

Material type	d	γ	E	ν
-	(m)	(kN/m ³)	(kN/m ²)	-
Elastic	1.0	25	3.25E7	0.15

Table 3 Pile properties in PLAXIS 3D

Material type	Predefined beam type	Diameter	γ	E
-	-	(m)	(kN/m ³)	(kN/m ²)
Elastic	Massive circular beam	0.3	25	3.25E7

Table 4 Data of model in case studies

Case	Raft thickness (m)	n	L	ΣL	S	Note
		Number of Piles	Length of 1 pile (m)	Total Length of Piles	Space between piles (m)	
1	1	25	8.00	200	1.2	4D
2	1	25	8.00	200	0.9	3D
3	1	16	12.50	200	1.2	4D
4	1	16	12.50	200	0.9	3D
5	1	9	22.22	200	1.2	4D
6	1	9	22.22	200	0.9	3D
7	1	13	15.38	200	1.70	4D $\sqrt{2}$
8	1	13	15.38	200	1.27	3D $\sqrt{2}$
9	1	12	16.67	200	1.70	4D $\sqrt{2}$
10	1	12	16.67	200	1.27	3D $\sqrt{2}$

foundations, the thickness of rafts in Case 1 and Case 9 are changed from 1 m into 2 m, 3 m, and 5 m. The size of the piles, material parameters of the ground, raft, piles, and load on the piled raft foundations remain the same.

As shown in (Figs. 7 and 8), in both cases of uniform and staggered distribution, the settlement of piled-raft foundation increases when increasing the thickness of the raft from 1 m to 5 m. However, the change in the raft's thickness helps to reduce the differential settlement between the piles of uniform layout. In the analysed cases, the differential settlements are smaller than the allowed value of 2/1000. Moreover, increasing the raft's thickness also increases the shear forces and bending moments in rafts as shown in Figs. 9 and 10.

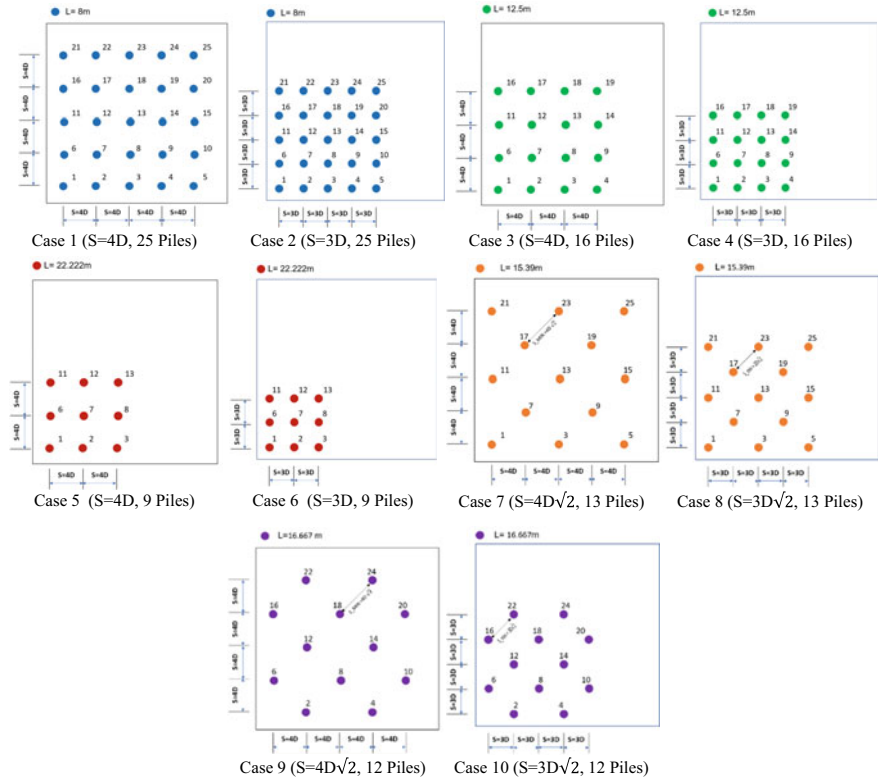


Fig. 3 Case studies of piled-raft foundations of different layouts and lengths

3 Conclusion

The analyses of different cases of pile layout and raft's thickness lead to the conclusions and recommendations as follows:

When changing the pile layout of the piled raft foundation with a constant total length of piles, the concentration of piles at the center area of the raft and increasing the length of piles will considerably reduce the settlement, and differential settlement. As shown in this study, case 10 can be the optimum pile layout which satisfies both the allowable settlement and differential settlement.

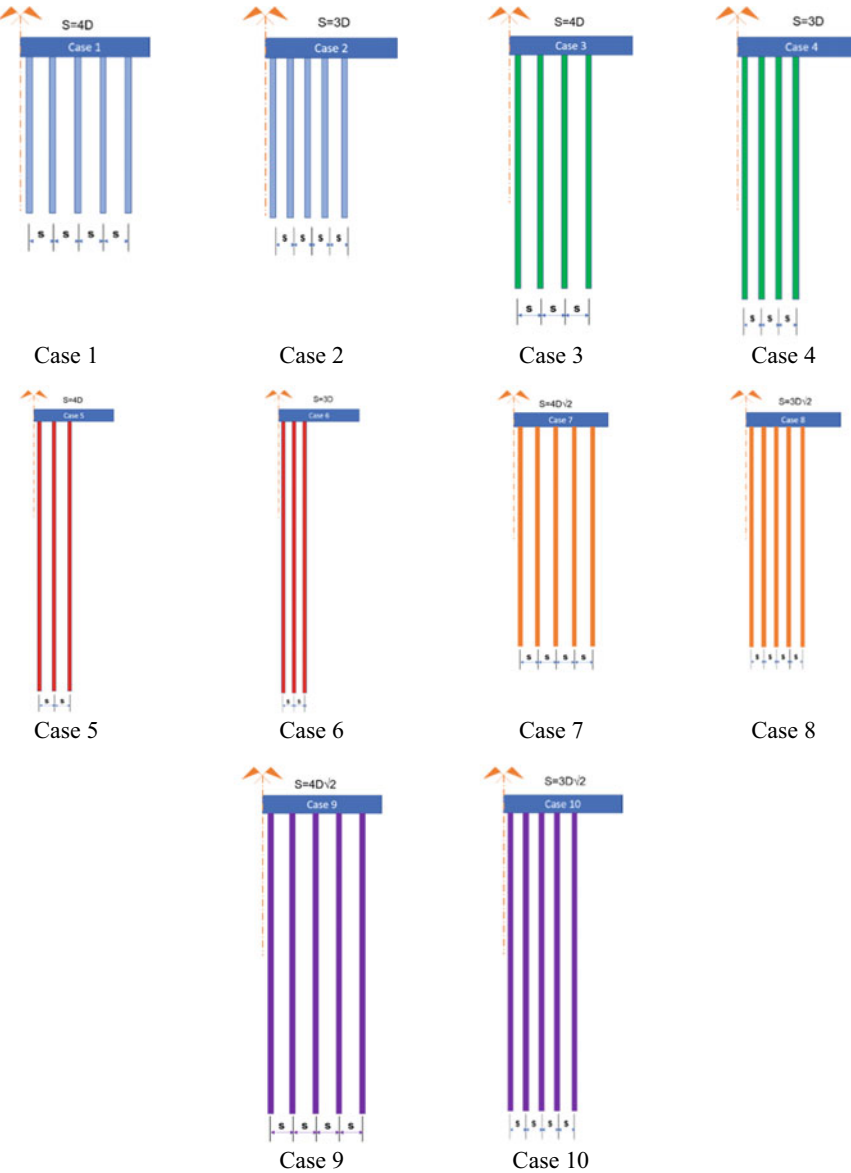


Fig. 4 Section view of the case studies on the effect of the number of piles and the length of piles in piled-raft foundation

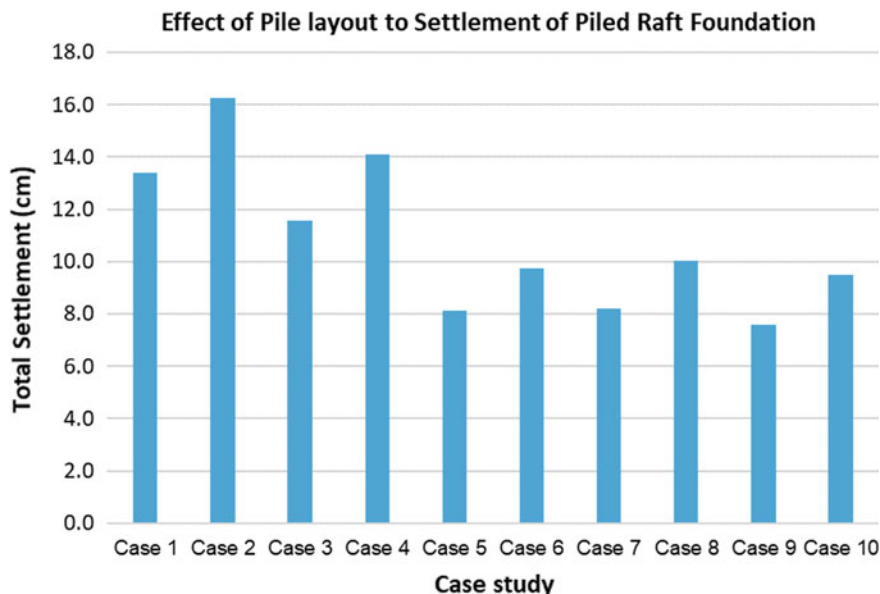


Fig. 5 Effect of the pile layout and the pile's length on the total settlement of piled raft foundation

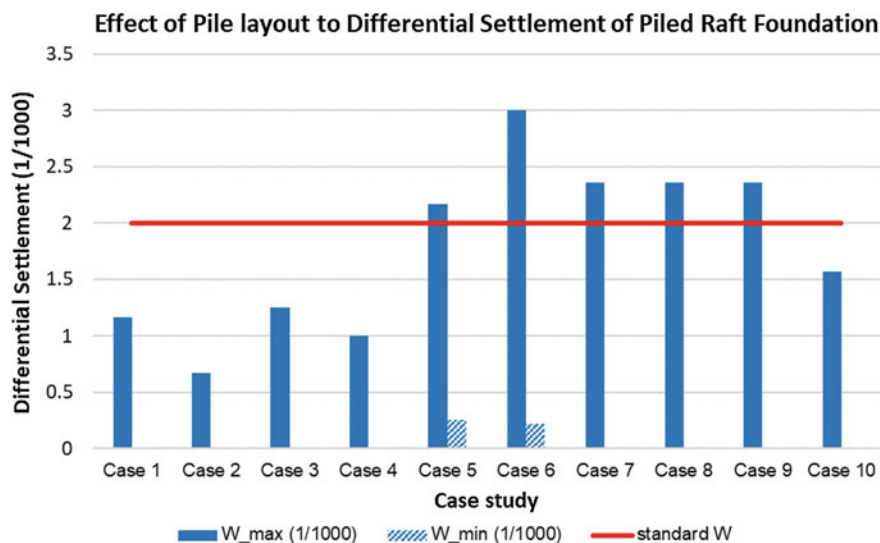


Fig. 6 Effect of the pile layout and the pile's length on the differential settlement of piled raft foundation

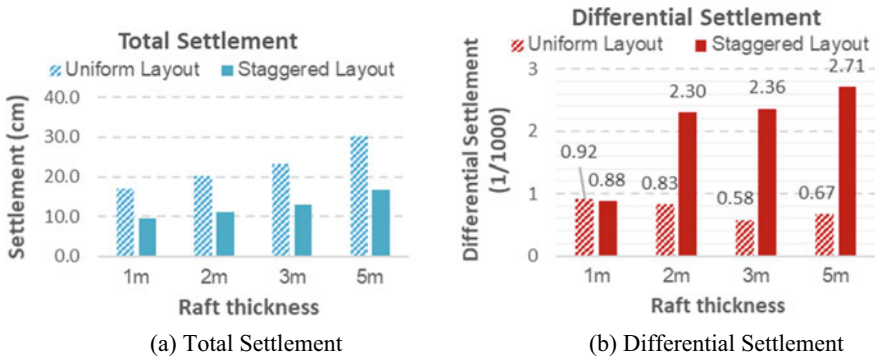


Fig. 7 Effect of raft thickness on settlement and differential settlement of piled-raft foundation

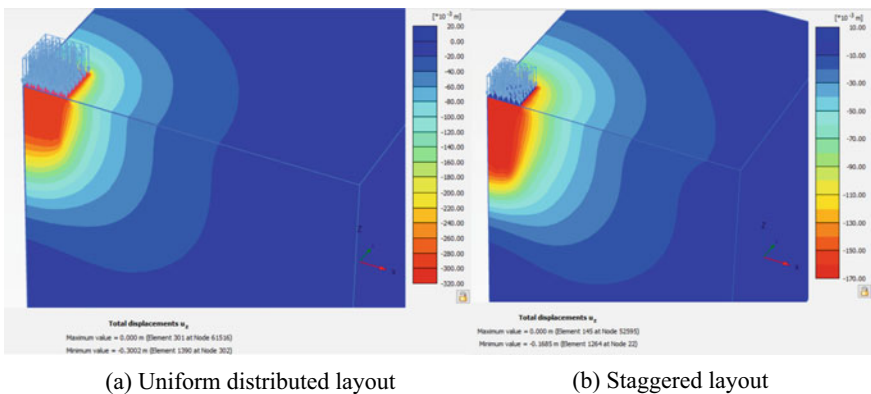


Fig. 8 Settlement of piled-raft foundation with raft thickness of 5 m

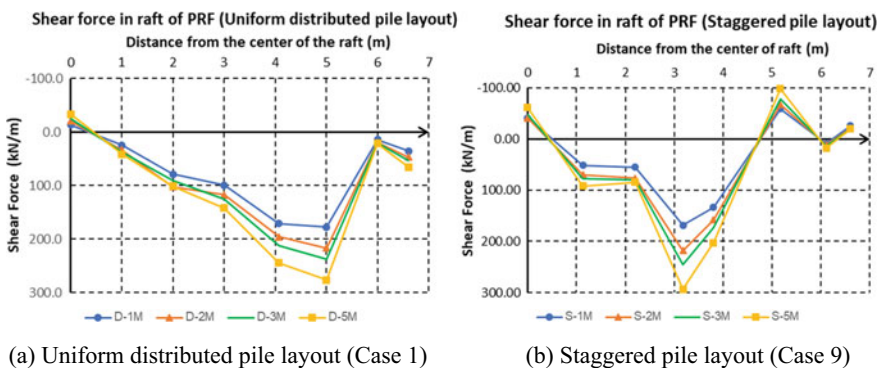


Fig. 9 Effect of the raft thickness on the shear force of raft in PRF

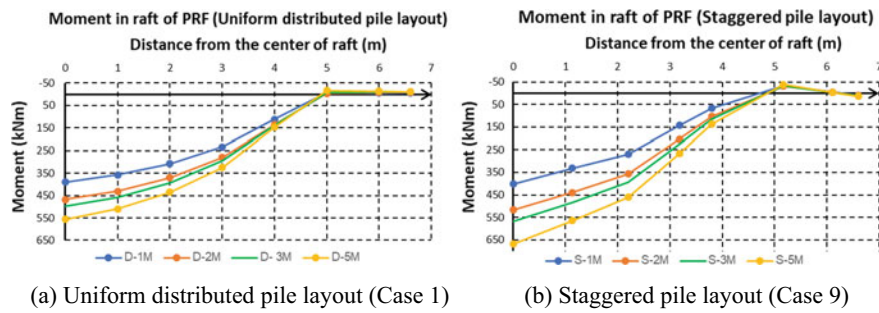


Fig. 10 Effect of the raft thickness on the moment of raft in PRF

In addition, increasing the raft's thickness may reduce the differential settlement of the piled raft foundation but the settlement, the internal forces such as the shear forces and the bending moments of raft increases. Therefore, the piled raft foundations designed with a moderate thickness of raft combined with staggered piles layout will considerably reduce the settlement, and differential settlement of piled raft foundations.

Acknowledgements This research is funded by Ho Chi Minh City University of Technology—VNU-HCM, under grant number T-KTXD-2018-110. We acknowledge the support of time and facilities from Ho Chi Minh City University of Technology (HCMUT), VNU-HCM for this study.

References

1. Cooke RW, Bryden-Smith DW, Gooch MN, Sillett DF (1981) Some observations of the foundation loading and settlement of a multi-storey building on a piled raft foundation in London clay. Proc. ICE, London 107(Part 1):433–460
2. Horikoshi K, Randolph MF (1996) Centrifuge modeling of Piled raft foundation on clay. Geotechnique 46(4):741–752
3. Kim KN, Lee SH, Kim KS, Chung CK, Kim MM, Lee HS (2001) Optimal pile arrangement for minimizing differential settlements in piled raft foundations. Comput Geotech 28(4):235–253
4. PLAXIS Material Model Manual, PLAXIS 2017
5. Randolph MF (1994) Design methods for pile groups and piled rafts. In: Proceedings XIII international conference on soil mechanics and foundation engineering, New Delhi, vol 5, pp 61–82
6. TCVN 10304:2014 Pile Foundation – Design Standard, Vietnamese Technical Standard

Uncertainties in Problem of Ground Improvement Using Prefabricated Vertical Drains (PVD) and Seeking a Cost-Effective Design Applying Monte Carlo Sampling



Tham Hong Duong and Kim Truc Do Thi

1 Introduction

Prefabricated Vertical Drains (PVD) is typical solution of soil improvement. It is simply a horizontal consolidation that its concept can be used and adjusted suitably to predict consolidation of soil-cement columns, sand drains, and stone columns, etc. It is necessary to construct a preloading over a vast area to create a required hydraulic gradient for provoking a flow in soil stratum and PVD will be used to shorten the path of drainage. Unfortunately, because PVD always is a solution applied over vast areas, so it faces diversity in soil properties and uncertainties in geotechnical conditions. The diversity of soil properties can vary to both in area and in depths of compressible layers. Hence, there is always a wide range of uncertainties in collecting and treating soil data both in aleatoric (inherent properties of natural soil) and epistemic uncertainties (relating to tester's skill and knowledge, measurement errors and analyzing models). This article aims to find a cost-effective solution of PVD design considering randomly varied parameters due to uncertainties in soil properties and soil disturbance during drain installation, and agreeing with investor's requirements about time and investment budget.

T. H. Duong (✉)

Faculty of Civil Engineering, Saigon Technology University, Ho Chi Minh City, Vietnam
e-mail: tham.duonghong@stu.edu.vn

K. T. Do Thi

Open University, Ho Chi Minh City, Vietnam

2 Theoretical Background

2.1 Degree of Consolidation of PVD

In general, Prefabricated Vertical Drains (PVD) must have relevant strength and capacity during installing into soft soil. The most important factor of PVD is discharge capacity, which should be at least 50–60 m³/year [1]. The design for the spacing of PVDs is summarized by a flow chart in Fig. 1.

In real condition, there are always uncertainties in soil properties and its spatial diversity both in vast area and depth. On the other hand, during PVD installation, if a mandrel was used, soil remoulding around a drain happened and significantly reduced the permeability. There are also uncertainties due to the soil properties and their law of distribution. Degree of horizontal consolidation is:

$$U_H = 1 - \exp\left(-\frac{8T_H}{F(n)}\right) \quad (1)$$

where $F(n) = \ln(n) - 3/4$. When smear zone during PVD installation is considered, degree of horizontal consolidation will be $U_H = 1 - \exp\left(-\frac{8T_H}{F}\right)$ in which $F = F(n) + F_s + F_r \cdot F_s$ is for considering smear zone during PVD installation and F_r for drain resistance. in which $F = F(n) + F_s + F_r \cdot F_s$ is for considering smear zone during PVD installation and F_r for drain resistance.

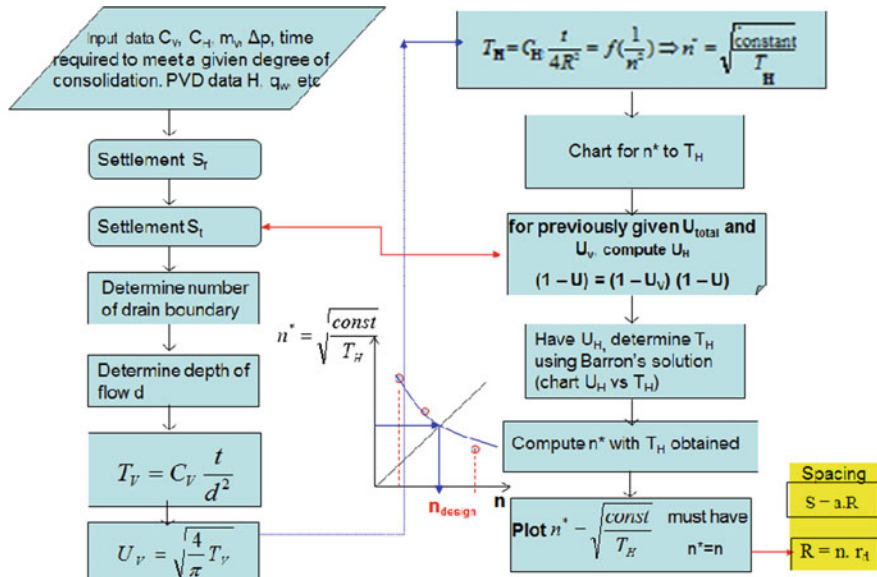


Fig. 1 Flow diagram for determining spacing of PVD

$$\begin{aligned} F(n)_{smearzone} &= F(n) + F_S + F_R \\ &= \ln(n) - \frac{3}{4} + \left[\left(\frac{k_h}{k_s} - 1 \right) \right] \ln \left(\frac{d_s}{d_w} \right) + \pi z(l-z) \frac{k_h}{q_w} \end{aligned} \quad (2)$$

where z equals to distance from the top of drain boundary to the final point of drain; l is length of PVD when the compressible layer is half-closed (l is taken half of the drain length if the compressible layer is an open layer). D_e and d_w is the diameter of horizontal drainage and PVD, respectively; $n = D_e/d_w$. Hence, F (or $F(n)_{smearzone}$ in case there is smear zone around PVDs) depends on the coefficient of horizontal filtration k_h , k_s , and discharge capacity q_w . These are random variables with normal and lognormal distribution.

2.2 Monte Carlo Sampling (MCS) Method

Steps of Monte Carlo Sampling are as follows:

- Determining law of distribution for random variables and parameters in problem. This will be determined by reviewing prior research works.
- Generating random data for variables and parameter.

With a normal distribution

$$x_i = \mu_x + z_i \cdot \sigma_x \quad (3a)$$

With a lognormal distribution (for coefficient of variation, C.O.V < 20%):

$$x_i = \mu_x \exp[z_i \cdot COV(X)] \quad (3b)$$

where μ_x is average and σ_x standard deviation for variable, sample generating value z_i is readily tabulated in statistical textbooks. Number of required trials in MCS

$$N = \left[\frac{d^2}{4(1-\varepsilon^2)} \right]^v \quad (4)$$

- V is number of variables (in this paper, v equals to 5); d is the expected standard deviation to meet a degree of confidence ε (from 0 to 100% in digital number). There are at least four groups of variables. It normally needs a standard deviation <10% (this study selects $d = 8\%$), degree of confidence equals to $\varepsilon = 0.05$ (or 5%). So according to Eq. (4), N is approximately 100,000.
- Only when the overall degree of consolidation U_{total} attains to previously assigned value (e.g. 85%), then the cost of the project and other requirements (e.g. time) from investors will be analyzed to support a decision for investment.
- According to the Monte Carlo method, probability of failure is

$$P_f = \frac{1}{N} \sum_{k=1}^N Function(D \geq 0) = \frac{n}{N} \quad (5)$$

in which n is number of failed runs in which a performance function D was defined as the difference between expected settlement and time dependent settlement has value greater than zero.

2.3 Investor's Constraints of PVD Design

Total cost included two item costs of PVD and of surcharge or preloading:

$$COST = \frac{A}{s^2} L \cdot G_{unit PVD} + A \cdot h \cdot G_{surcharge} \quad (6)$$

Constraints to be considered	Min $COST$ (total cost)
	$t \leq t_{required}$.
Such that	For engineering aspect: degree of consolidation $U \geq U_{target}$
	For performance, working condition
	For financial aspect: Budget is within limits (min, max).

After randomly sampling and run a large enough number of runs ($N = 10^5$), the next step is to estimate the cost of a designed solution as in formula (6). The cost-effective configuration of PVD solution will occur when the height of preloading is minimal, and a maximal spacing of drains.

3 Example for Illustration

3.1 Solution for PVD Design Considering Controlling Factors

Given a site with all required geotechnical data. Target is to seek a cost-effective solution of improvement using PVD and then estimate the total cost for it. The investor requires the period t for preloading and the total cost does not exceed some range of investment. A selected kind of PVD was utilized in project and constructor chose a kind of PVD that had discharge capacity q_w . Constructors have definite experiences

and skills for working on drain installation. A Monte Carlo spreadsheet was established in Excel, with a total of 32 columns with/without considering smear zone, from $N = 10^5$ trials. It is necessary to attain an overall degree of consolidation $U_{\text{total}} > 85\%$ and then compute the total cost for the most reasonable designed configuration. An illustrated spreadsheet was shown in Fig. 2. H is the thickness of the compressible layer in meters, q_w , D_e , d_w was defined as in Sect. 2.1, in meters; t is the time of consolidation in years; C_V and C_H are the coefficient of consolidation in vertical and horizontal direction respectively, m^2/year ; m_v is the coefficient of volume compressibility, m^2/kN ; E is the modulus of deformation in kPa; T_V and T_H are dimensionless time factor corresponding to vertical and horizontal consolidation, respectively. Law of distribution was assigned to variables according to Phoon and Kulhawy [2].

When both normal and lognormal distribution were considered, results were shown in Fig. 3.

Results indicated that in case normal distribution was assumed to apply to all variables and parameters [3], probability of attaining $U \geq 85\%$ was about 92.4% and when smear effects were taken into account, the probability decreased to 61%. In the case of using both normal and lognormal distribution to relevant variables

Trials	Configuration of PVD site			Preloading	Time suggested	Compressibility (temporarily $C_h = 2C_v$)						
	H (m)	D_e (m)	d_w (m)			k_v (m/s)	K_b (m/s)	k_h (m/s)	C_v (m^2/year)	C_h (m^2/year)	m_v (m^2/kN)	E (kN/m 2)
1	26.5723588	2.72870999	0.18401949	37.63242	1.06790535	6.3373E-06	1.1328E-05	5.495E-06	1.88545633	3.99420103	0.00045721	7419.7064
2	25.6349164	2.57532128	0.17814082	28.319224	1.49733548	5.8628E-06	1.1902E-05	6.325E-06	1.51961364	3.92428579	0.00045687	4954.4245
3	21.8445605	3.09002665	0.20276508	21.067172	1.48212226	6.6307E-06	6.279E-06	1.1769E-05	1.31776715	3.24571851	0.00033163	7142.6278
4	26.6535356	2.20509157	0.18537437	35.882097	1.09154839	6.0468E-06	1.1645E-05	5.952E-06	1.43552565	3.30181067	0.0005532	6741.3144
5	22.9627952	2.11357832	0.15558524	31.144443	1.05503233	5.8696E-06	1.1687E-05	4.9946E-06	1.39567929	2.92810397	0.00033802	5381.8376
6	24.0920499	2.12465345	0.22980241	36.705436	1.25879301	5.9676E-06	1.1963E-05	5.171E-06	1.51497122	3.30544001	0.00039455	4892.9696
7	23.5851187	2.61949337	0.23485222	36.348385	1.4117129	5.9826E-06	1.1471E-05	4.985E-06	1.36854052	3.79734045	0.00049741	7602.6634

Vertical discharge capacity of PVD					U(t) as in $U_{\text{total}}=1-(1-U)(1-U_h)$							Assign 1 if U exceeds target 85%
q_w (m^3/year)	z (m)	L (m)	selected value of PVD length of drainage (m)	smear zone ds (m)	T_V	U_V	Uv when >60%	T_H	U_H	$U_{\text{total}}=1-(1-U)(1-U_h)$		
91.6113078	21.7811778	22.6324358	21.7811778	0.2958800	0.00518151	0.08122379	0.08122379	1.22485265	0.994640097	0.995075449	1	
83.8843384	24.7126303	24.7126303	24.7126303	0.30393131	0.00300294	0.06183413	0.06183413	0.96594079	0.980468264	0.981675992	1	
90.4528037	21.2032552	23.7323888	21.2032552	0.40098254	0.00421752	0.07327968	0.07327968	0.60767649	0.934089613	0.938919506	1	
71.7915377	20.1587527	20.1587527	20.1587527	0.59701203	0.0053463	0.08250532	0.08250532	0.81599714	0.964555984	0.967480304	1	
53.2286271	24.4417763	27.1181723	24.4417763	0.29680896	0.002669986	0.05863078	0.05863078	0.40084073	0.765191591	0.77895859	0	
82.993216	22.347462	25.16752	22.347462	0.57768561	0.00386375	0.07013902	0.07013902	1.20869113	0.999002237	0.999072219	1	
80.8082732	24.823782	24.823782	24.823782	0.64163345	0.00354369	0.06717121	0.06717121	1.18819398	0.998764166	0.998847179	1	

U(t) as in $U_{\text{total}}=1-(1-U)(1-U_h)$				Probability exceeds 85% target primary settlement	Scenario considers smear zone, randomly varied data						
Uv when >60%	T_H	U_H	$U_{\text{total}}=1-(1-U)(1-U_h)$		Factors: $F_s + F_r$	$F(s)$ without smear	Degree of radial consolidation $U_{h,\text{smear}}$	U_{total}	Assign 1 if U exceeds target 85%	Probability exceeds 85% target primary settlement	
0.08122379	1.22485265	0.994640097	0.995075449	1	0.9242227	0.572712118	1.87400616	0.98177358	0.983254	1	0.611916425
0.06183413	0.96594079	0.980468264	0.981675992	1	0.877078315	1.96343664	0.93415598	0.93822739	1		
0.07327968	0.60767649	0.934089613	0.938919506	1	0.986800966	1.7876392	0.82661031	0.83931625	0		
0.08250532	0.81599714	0.964555984	0.967480304	1	1.709958963	1.954606071	0.83159459	0.84548893	0		
0.05863078	0.40084073	0.765191591	0.77895859	0	0.563809185	2.21038362	0.68487604	0.703535	0		
0.07013902	1.20869113	0.999002237	0.999072219	1	1.373806603	1.3993541	0.69640217	0.7154827	1		
0.06717121	1.18819398	0.998764166	0.998847179	1	1.127316462	1.41958461	0.97605996	0.97766804	1		
0.05796819	0.81061615	0.987923936	0.988629107	1	1.691391124	1.46818098	0.87158277	0.87902689	1		
0.05466769	0.40320035	0.826378051	0.835869562	0	1.486324774	1.8422804	0.62055871	0.64130189	0		
0.0670758	0.56235442	0.889779175	0.897172326	1	1.307307829	2.04003887	0.73919973	0.75669312	0		
0.06266165	1.03462722	0.993431664	0.993843247	1	0.871152279	1.64700553	0.96263174	0.9649733	1		

Fig. 2 Spreadsheet with normal distribution, applied for all variables and parameters

U(t) as in $U_{total}=1-(1-Uv)(1-Uh)$				Assign 1 if U exceeds target primary settlement	Probability exceeds 85% target primary settlement	Scenario considers smear zone, randomly varied data				
Uv when >60%	T_R	U_R	$U_{total}=1-(1-Uv)(1-Uh)$			Factors: $F_s + F_r$	$F(n)$ without smear	Degree of radial consolidation $U_h, smear$	U_{total}	Assign 1 if U exceeds target 85%
0.06224831	0.27133277	0.658960682	0.680189803	0	0.74424	0.975785441	2.01779879	0.51572617	0.5458714	0
0.05487345	1.21455948	0.997541257	0.997676177	1	(Lognormal distribution)	0.552746097	1.61722801	0.9886404	0.98926374	1
0.07719261	1.49211599	0.998732059	0.998829934	1		0.054654947	1.78954759	0.99845492	0.99857419	1
0.073707855	1.62532683	0.999831949	0.999844336	1		6.734632878	1.49605915	0.79397788	0.80916347	0
0.09629663	1.27784091	0.998107312	0.998289571	1		0.001114704	1.63048219	0.99809919	0.99828223	1
0.08179976	3.05446931	0.99999994	0.999999945	1		0.453386577	1.46910368	0.99999698	0.99999723	1
0.07833419	0.4835432	0.817836915	0.832106513	0		0.466016125	2.27168507	0.75658572	0.77565338	0

Fig. 3 Spreadsheet for consolidation attaining $U \geq 85\%$, using normal and lognormal distribution

and parameters, probability of attaining $U \geq 85\%$ decreased from 74% in case of no smear zone to approximately 64% with the smear zone. Because many possible alternatives for PVD configuration could happen, some stochastic scenarios were studied for seeking a cost-effective design [4–6].

Figure 4 is a part of the spreadsheet estimating the cost for PVD design, considering time and range of assumed budget planned by the investor. A trial scenario was studied in which the height of preloading was kept to be fixed and time of consolidation was chosen with intention (for example, 1 year), randomly varied outcomes could be found by pressing F9; results indicated that the cost—height relationship varied anomalously meanwhile cost—spacing relationship was nearly linear. Figure 5 showed the total cost in relation to spacing (in terms of D_e) and the height of preloading. Graphs in Fig. 5 indicated some local minimum costs at a specified height of preloading. In this example, the unit price for 1 m of PVD length and 1 cubic meter of preloading volume was assumed and easy to update with actual unit price.

Approval criteria:		Total cost attains as lowest as possible and less than a percentage of maximum budget					Owner's Investment (billions)	
Suggest		Range of investment budget is to be planned					Max	3
b)		Scenario considers smear zone, randomly varied data					Min	0.6
U_H	$U_{total}=1-(1-Uv)(1-Uh)$	Assign 1 if U exceeds target 85%	Probability exceeds 85% target primary settlement	Factors: $F_s + F_r$	$F(n)$ without smear	Degree of radial consolidation $U_h, smear$	Assign 1 if U exceeds target 85%	Total cost, including PVD + surcharge (\$0 for PVD, 100 for filling)
0.902553682	0.908322	1	0.7228428	0.168999622	1.67053404	0.87931055	0.886455128	1
0.626557905	0.648256	0	(Lognormal distribution)	0.577425608	1.978794322	0.53349754	0.560602458	0
0.948267177	0.952109	1		1.520194602	1.911063804	0.307857732	0.822127404	0
0.999999999	1	1		0.96999307	1.1477632	0.999985303	0.999986773	1
0.749048421	0.760361	0		0.573155118	1.724605842	0.645711835	0.661682876	0
0.943152602	0.948824	1		0.132947787	2.12431917	0.932693772	0.939408726	1
0.999932257	0.999938	1		0.677703504	1.737214309	0.998990818	0.999085496	1
0.634304987	0.65916	0		1.330864535	2.265294659	0.469380355	0.505426298	0
0.9997612	0.999791	1		0.5739850495	1.297754738	0.997053766	0.997246901	1
0.761653216	0.778961	0		1.285698698	2.251397948	0.598590737	0.627738986	0
0.999370197	0.99943	1		0.000194333	1.801282317	0.999386969	0.999429195	1

Fig. 4 Spreadsheet with constraints about time, budget for investment, and cost estimation

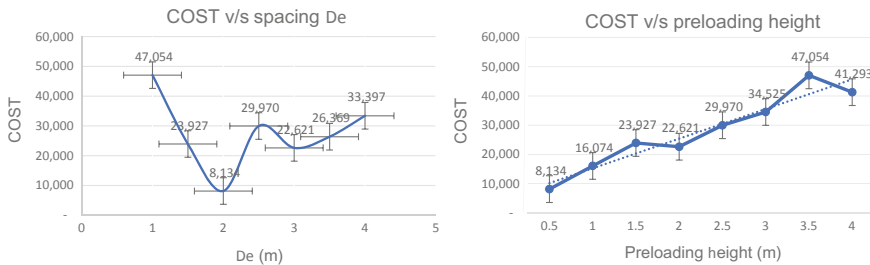


Fig. 5 Graphs for relationship between cost versus PVD spacing and cost—preloading height

4 Conclusion

In this paper, Monte Carlo Sampling was applied to seek a cost-effective solution of PVD design that many conditions were simultaneously taken into account, including uncertainties of soil properties, different laws of distribution of variables, smear zone caused by constructors, prescribed time of consolidation, and investor's budget. Uncertainties are quantified by coefficient of variation (COV) and the law of distribution (i.e. normal and lognormal distribution). The coefficient of permeability, smear zone and time of consolidation are the most sensitive variables. For variables with $\text{COV} > 20\%$, it is possible to use a statistical formula to compute the standard deviation and average. In normal cases, the heavier preloading is, the wider spacing between PVDs is, resulting in the highest cost of preloading. A spreadsheet for computing the probability of attaining a target overall degree of consolidation (e.g. $U_{\text{total}} \geq 85\%$) was established, a reasonable design can be selected in which all uncertainties and possibly happened variation of the project are considered altogether. Several stochastic scenarios for cost estimation were investigated and their results tentatively indicated that cost at various spacing was nearly linear to the height of preloading, meanwhile the cost with a specified height of preloading varied anomalously to the spacing. This requires further study about stochastic optimization, and this study would be viewed as a practicable example for a decision support system..

References

1. Indraratna B, Chu J (2005) *Ground Improvement Case Histories Book Volume 3* Elsevier, London, 1115p.
2. Phoon KK, Kulhawy FW (1999) Characterisation of geotechnical variability. *Can Geotech J* 36(1999):612–624
3. Duong HT, Do Thi KT (2019) Identifying uncertainties in problem of soil improvement using prefabricated vertical drains (PVD). In: Proceedings of national Congress on engineering mechanics, held in Institute of Mechanics, Vietnam Academy of Science and Technology, Hanoi
4. Saurer E, Marcher Th (2011) Grid space optimization of jet grouting columns. In: Proceedings of the 15th European conference on soil mechanics and geotechnical engineering. <https://doi.org/10.3233/978-1-60750-801-4-1055>

5. Mission JL, Kim H-J, Won MS (2012) Ground improvement optimization with PVD and surcharge preloading. In: The 2012 world congress on advances in civil environmental and materials research ACEM'12, Seoul
6. Bo MW, Arulrajah A, Horpibulsuk S (2015) Quality management of PVD materials in mega land reclamation projects: a case study. *J Soil Found* (Elsevier article) The Japanese Geotechnical Society. <http://dx.doi.org/10.1016/j.sandf.2015.06.019>

Remote Sensing, Construction Management and Water Resource Engineering Sessions

A Proposed Model for Predicting the Risks of Contamination Intrusion in Water Distribution System



Thi Minh Lanh Pham and Quang Truong Nguyen

1 Introduction

Including the leakage positions; crack; reservoir; water tower; and pump station, Water distribution system is not a closed system. Thus, the risks of contaminant intrusion into the system occur in case of determinate factors appearing at the same time. These factors are analyzed to determine the potential risks of contaminant intrusion into the water supply pipelines by experimental models, software-based modeling and practical data collection.

López-jiménez et al. [1] placed the water pipe with a break hole in the pipe wall in a water environment and changed inside pressure by valve control. By modeling on ©Fluent Inc software at the same time, the author concluded that although the leakage size is very small (1.5 mm), the contaminant intrusion entering the pipe still occurs. Based on the study of López-jiménez, Collins, by using the software, established the model of the contaminated flow intrusion into a water pipe. The result shows that the contaminant flow enters the water pipe when the pipe pressure is lower than -1 m .

In an empirical study of Chiara M. Fontanazza and her co-worker, it is shown that the pollutants are entering the water pipe in a period of 40 s when the negative pressure appears from 0 to -10 m [2]. According to Yang et al. [3], even though electricity is unexpectedly off for a second, and a period of valve closing at each pump is 0.1 s, the contaminant intrusion through the leakage is occurring.

The results show that during the short period of negative pressure, through a small size of the leakage, the contaminant intrusion into water pipe is possible. Therefore, estimating risks of contaminant intrusion into water pipe is considered as a key

T. M. L. Pham

Department of Urban Engineering, University of Architecture Ho Chi Minh City, Ho Chi Minh City, Vietnam

T. M. L. Pham · Q. T. Nguyen (✉)

Faculty of Civil Engineering, Ho Chi Minh City University of Technology, VNU-HCM, Ho Chi Minh City, Vietnam

e-mail: nqtruong@hcmut.edu.vn

problem of 3 input variables, such as potential pipe crack; negative pressure value; and impact level of contaminant source, and 1 output variable as a potential contaminant intrusion into the water distribution systems. In this paper, fuzzy logic theory will be used to build a model to predict the risk of contaminated water distribution systems. The proposed model will be applied to the actual water distribution system in Hai Chau district, Da Nang city.

2 Methodology

Based on the theory of Dempster-Shafer, D number or fuzzy logic, studies estimate the potential risks of contaminant intrusion into the water distribution system.

2.1 Dempster-Shafer Theory

Evaluating the potential risks of contaminant intrusion by Dempster-Shafer theory is applied by Rehan Sadiq on water pipe working with contaminated levels separately, including 4 thresholds of zero, low, medium, and high one [4]. The method is not applied to real water distribution system yet, due to a significant exclusion for the probability of the potential risks in theory. In spite of the Dempster-Shafer theory optimized and simulated by the advanced software, its results are impossible to apply in the practice [5].

2.2 D Theology

Dempster-Shafer, Gou and his co-workers issued an approach to evaluate the potential risks of contaminant intrusion into the water distribution system by D number tool [6], a present of unsure information. Three decision factors of the contaminant intrusion into water flow are intrusion way—a rate of pipe crack per year (D1), potential intrusion—exceeded pressure on water distribution system (D2) and contaminant source—estimating the distance between contaminant source and main water pipeline (D3). D number is considered for three sets including $\{P\}$; $\{NP\}$; and $\{P\}$, in which P, NP are values of intrusion or not. As a result, considering scenarios is to evaluate the high or low level of potential contaminant intrusion into the water distribution system. The method of D number provides individual coefficient for each evaluating potential factor. It is the practical research due to establishing the probability domain in each case. However, it is a restrictive result due to synthetically looking into the potential risks.

2.3 Fuzzy Logic Theology

Mansour-Rezaei used uncertain assessment technique to evaluate the potential risks of contaminant intrusion into the water distribution system [7]. Based on fuzzy logic, he computes the contaminant intrusion into the cast-iron pipe through break holes. The impacting factor is the change of water pressure through a closing valve, the author considered the possibility of low or negative pressure. However, its results are not tested on the practical water distribution system. Furthermore, the chosen triangular and trapezoidal function has irregular variability reducing the accuracy of the result.

With the advantages of fuzzy logic, this study chooses this theory to build the potential predicting model, and to improve the accuracy of predicting results with the function of Gaussian, S-Sigmoidal and Z-Sigmoidal. These functions are variable curves and symmetry with a horizontal line, the tiny variation of values on a horizontal axis is shown. The predicting model has verified the potential application on real water distribution system.

3 Research Content

3.1 Fuzzy Logic

The classical logic theory uses the probability of certain or uncertain information to evaluate the potential appearance of an event. There is much uncertain information, in which an object has more than 2 states to consider. Thus, Professor Lotfi Zadeh of California University (USA) issued fuzzy theory in 1965 and it is popularly applied in studies. The theory is used to evaluate uncertain information by fuzzy sets, membership functions, and fuzzy logic.

Fuzzy set developed from a fundamental set is defined: “Fuzzy set A is defined $A = \{\mu_A(u) | u : u \in U, \mu_A(u) \in [0, 1]\}$ with fuzzy set A in universe of information U and u element in-universe of information U. In that, membership function $\mu_A(u) : U \rightarrow [0, 1]$ is called as membership degree of u element to fuzzy set A”.

A shape of a fuzzy set depends on distinct membership functions. This research considers a membership function of Gaussian, S-Sigmoidal, and Z-Sigmoidal as shown in Fig. 1.

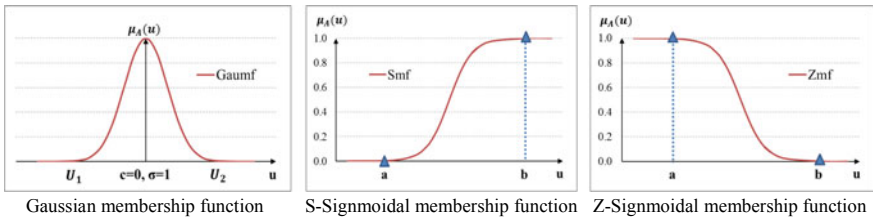


Fig. 1 Membership function of fuzzy sets

3.2 The Predicting Model for the Potential Contamination Intrusion into the Water Distribution System

Based on the fuzzy logic theory, 3 input fuzzy values to construct potential contaminant intrusion modeling are P_f —potential pipe crack, H_n —negative pressure value, S_c —a level of contaminant source. An analysis of the model is the Fuzzy Inference System (FIS). The output value is a certain value P_c —potential contaminant intrusion into the water distribution system. To combine with Fuzzy Logic Design tool (FLD) and SIMULINK, this study creates a model in MATLAB software as shown in Fig. 2.

According to the evaluation of the author, the P_c and P_f factors are assessed on 4 levels. Each level corresponds to a fuzzy set ranging from 0 to 1. However, P_c is a certain value, the fuzzy set corresponds to a certain number. Two other factors (H_n and S_c) are assessed with 3 fuzzy sets of low, medium and high level as shown in Table 1.

Certain domain value (U) agreement of the fuzzy set in Table 1 is defined based on visual assessment. Extremum of the membership function is set by dividing range equally in U domain to ensure the size of fuzzy set. Nevertheless, the fuzzy set is chosen by complementary characteristic to ensure importing values belonging to a certain fuzzy set, and not to empty set. From 4 fuzzy sets of pipe cracking factor and 3 fuzzy sets of 2 other factors, it is equal to 36 sets. The fuzzy set is a fundament to issue

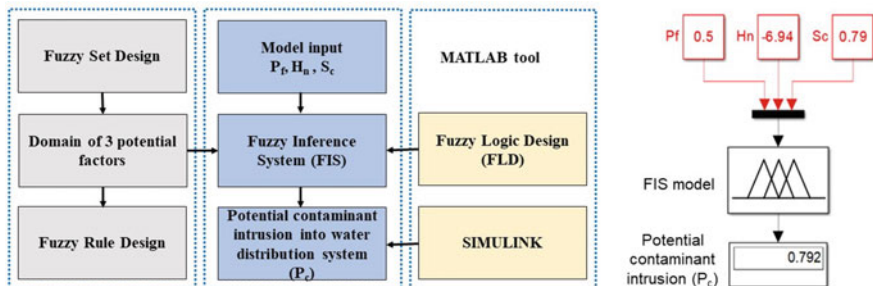


Fig. 2 Model of predicting contaminant intrusion into water distribution system

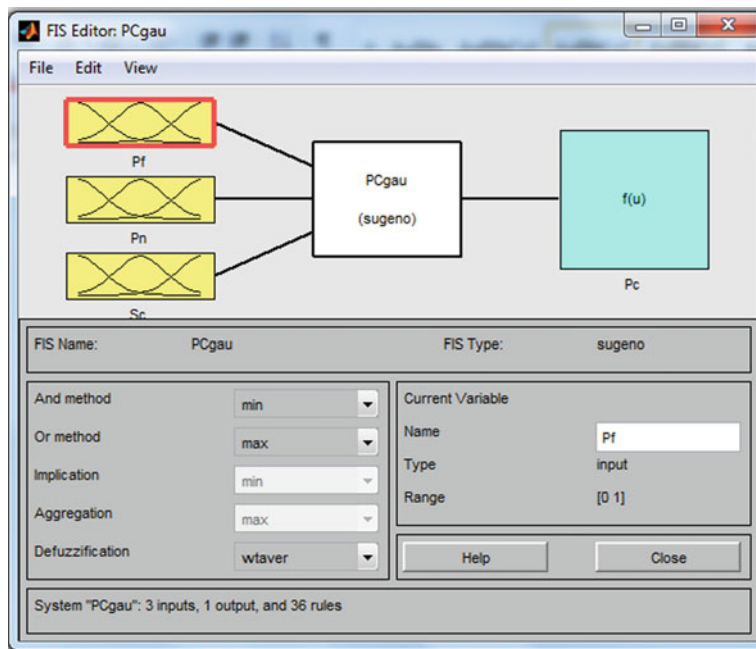


Fig. 3 Designing fuzzy logic in FLD tool

Table 1 Fuzzy logic symbols of input and output variables in FIS model

Variable	Fuzzy set A and certain domain [U]			
	Low	Medium	High	Very high
P_{fi}	$L_1[0 \ 0.4]$	$M_1[0.2 \ 0.6]$	$H_1[0.4 \ 0.8]$	$VH_1[0.6 \ 1.0]$
H_{ni}	$L_2[-5 \ 0]$	$M_2[-7.5 \ -2.5]$	$H_2[-10 \ -5]$	—
S_{ci}	$L_3[0 \ 0.5]$	$M_3[0.25 \ 0.75]$	$H_3[0.5 \ 1]$	—
P_{ci}	$L = 0.25$	$M = 0.50$	$H = 0.75$	$VH = 1$

a decision to the output of the potential intrusion into the water distribution system (P_c). The output is much more accurate with a good fuzzy set control. Reason—result statement of the fuzzy set (IF ... and ... THEN) plots 3D in MATLAB software as Fig. 4. Result statement P_c is defined, based on visual considering of designer (Fig. 3).

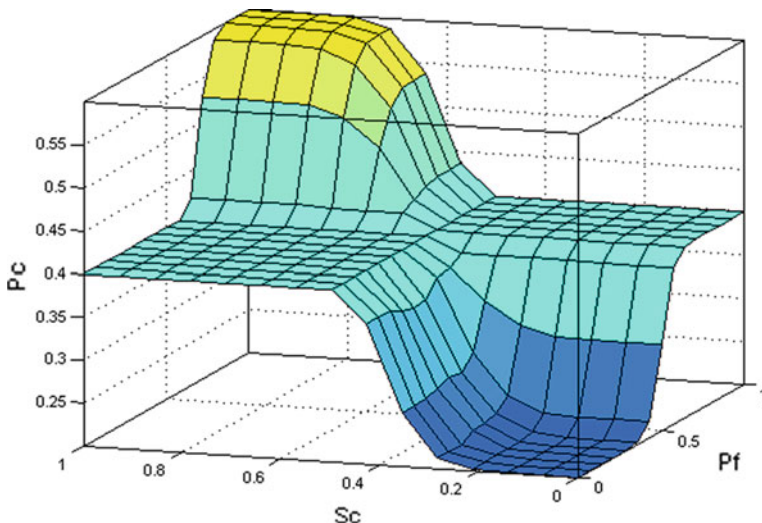


Fig. 4 Fuzzy logic in FIS model

4 Case Study: Application of the Proposed Model for the Water Distribution System in the HC05 Area of Hai Chau District, in DaNang City

The water distribution system of Hai Chau District is divided into 5 district metering areas (DMA), from HC01 to HC05. Each DMA managed by valve and water Meter has from 2 to 3 water supply resources. DMA HD05 locating near a water source of Hai Chau District is the largest water supply zone comparing with other DMA. Therefore, this DMA is chosen to predict the potential contaminant intrusion into the water distribution system (see Fig. 5).

The potential pipe crack (P_f), the potential negative pressure value on water pipe (H_n) and the potential impact of contaminant source into water pipe (S_c) showing in Table 2 are chosen from documents [8]. These values are saved in excel file, and then they are put in the predicting contaminant intrusion into the water distribution system model on MATLAB software. The results of contamination intrusion are shown in Fig. 6. Green color shows low potential contaminant intrusion into water pipe (lower than 36%). Turquoise and blue colors show a medium rate of it (from 36 to 52%). Purple color shows high potential contaminant intrusion into water pipe (from 68 to 84%). Very high potential contaminant intrusion into water pipe (from 84 to 100%) is shown in red color.

According to the domestic water quality verified document of Da Nang water supply joint stock company (DAWACO), based on Vietnam national standard 01:2009/BYT of Ministry of Public Health, collecting water sample periodically for analyzing available chlorin, *E. coli* in it is done to test domestic water quality.



Fig. 5 The water distribution system of HC05 area—Hai Chau District

Table 2 Input data for the predicting model of the potential contaminant into the water distribution system

Id	P _f (%)	H _n (m)	S _c (%)	Id	P _f (%)	H _n (m)	S _c (%)
1	33.90	-9.98	39.44	8	7.98	-9.98	59.78
2	3.20	-3.16	16.50	9	7.00	-9.98	87.84
3	37.90	-9.98	89.73	10	7.00	-9.98	5.24
4	29.50	-9.98	89.23	11	4.74	-1.39	2.32
5	1.80	-9.98	84.51	12	64.21	-9.98	20.52
6	1.80	-9.98	59.70	13	64.21	-9.98	57.77
7	4.00	-9.98	41.77

Domestic water quality control department of DAWACO takes the sample 8 times per month at 10 distinct outlets representing for individual water supply area. There are over 100 water sample each year.

Water samples collected at the water treatment plant outlet meet the national standard, but some of the water samples collected on water pipeline do not meet the national standard at all. According to given data from DAWACO, there are more than 100 water samples with low or non-available chlorine, high turbidity in the year 2014 and 2015. Water outlet collecting water sample regularly are marked in Fig. 7. In general, on the water pipes where the model estimates the potential contamination intrusion at the low degree, the sample below the quality standard is not marked in fact. Some water distribution pipes are projected with a high value of P_c because their positions are located near city sewer pipe and their risks of cracking are high. Although in-pipe water does not meet the national standard due to other reasons, applying a model of study can estimate the potential contaminant intrusion into each

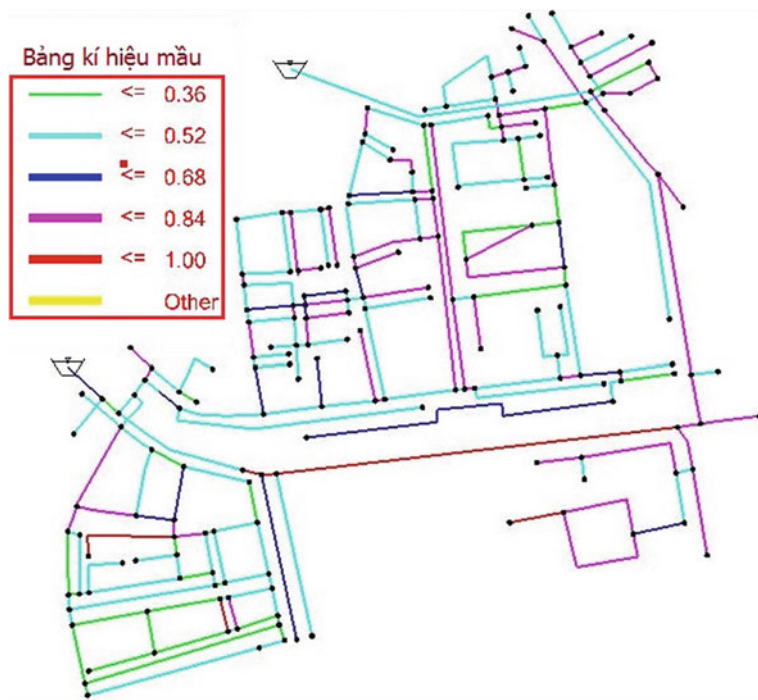


Fig. 6 Result of contamination intrusion into water pipe

water pipe. It is a foundation to supervise water quality in the water distribution system.

5 Conclusion

According to the fuzzy inference system (FIS) applying the fuzzy set of Gaussian, Sigmoidal S, and Sigmoidal Z, the research proposes the predicting model of potential contaminant intrusion into the water distribution system. The model predicted potential contaminant intrusion into individual water pipe of the water distribution system. These values correspond to the testing results of domestic water quality control on the system. Associated with SIMULINK, the predicting model got accurate results and reducing subjective errors in the fuzzy period. The result of the research is a base to evaluate contaminant intrusion into the water pipe and the vulnerable water distribution system.

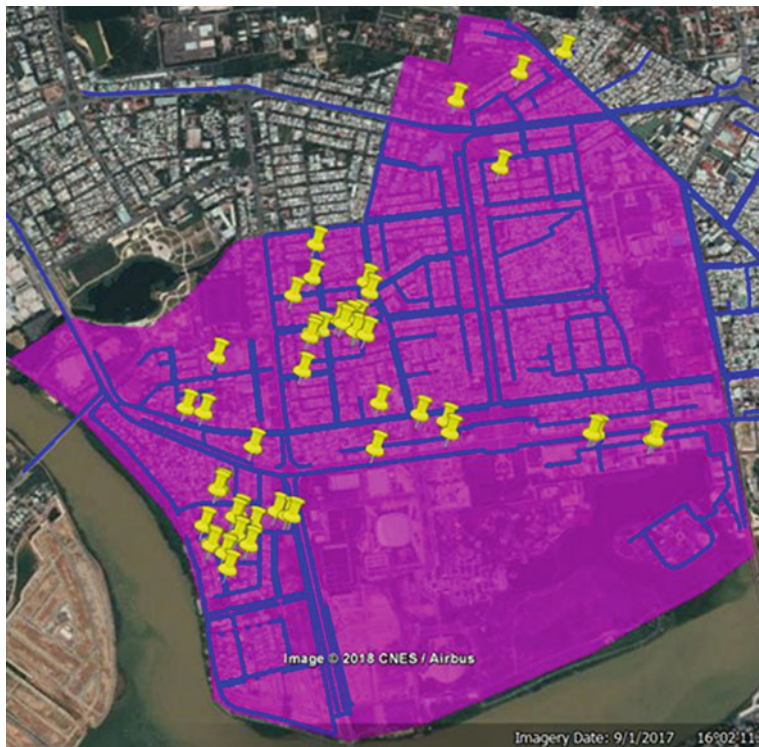


Fig. 7 Positions where the water quality is lower than the regulatory threshold

References

1. López-jiménez PA, Mora-rodríguez J (2010) 3D computational model of external intrusion in a pipe across defects. In: 2010 international congress on environmental modelling and software
2. Fontanazza CM, Notaro V, Puleo V, Nicolosi P (2015) Contaminant intrusion through leaks. Computer control for water industry. Procedia Eng 119:426–433
3. Yang J, LeChevallier MW, Teunis PFM, Xu M (2011) Managing risks from virus intrusion into water distribution systems due to pressure transients. J Water Health 9(2):291–305
4. Sadiq R, Kleiner Y, Rajani B (2006) Estimating risk of contaminant intrusion in distribution networks using fuzzy rule-based modeling, pp 318–327
5. Deng Y, Jiang W, Sadiq R (2011) Modeling contaminant intrusion in water distribution networks: a new similarity-based DST method. Expert Syst Appl 38(1):571–578
6. Gou L, Deng Y, Sadiq R, Mahadevan S (2014) Modeling contaminant intrusion in water distribution networks based on D numbers. CoRR, vol abs/1404.0
7. Mansour-Rezaei S, Naser G, Sadiq R (2014) Predicting the potential of contaminant intrusion in water distribution systems, no February, pp 105–115
8. Lành PTM (2018) Đề xuất mô hình dự báo hệ thống phân phối nước bị ô nhiễm, Thành phố Hồ Chí Minh)

Accuracy Assessment of 3D Point Clouds Collected by a Low Cost UAV-Based Laser Scanner System



Cong Bang Van Dang, Kazuyoshi Takahashi, and Anh Thu Thi Phan

1 Introduction

Airborne laser scanners (ALS) have been developed for terrain mapping and forest inventories [1, 2]. By using ALS, the surface information of the target objects can be achieved in large area, with high resolution and in real time. However, this system costs a lot of money for system cost and operation and must be controlled by a trained pilot with takeoff and landing challenges. Additionally, in some country, using of aircraft for surveying or other research purposes encourages strictly regulations from the government.

Nowadays, a growing number of Unmanned Aerial Vehicle (UAV) has been being developed with different weight, payload, endurance and range, speed, wing loading, cost, engine type and power. UAV-based systems have been developed for many purposes with various sensors such as imaging sensor [3–5], multispectral sensor [6] or LIDAR sensor [7]. Such systems inherit the advantage of manned aerial vehicle system. In some situation of studies, small UAV-based systems are more flexible and could collect multi-temporal data acquisitions with low costs [8, 9]. Because of payload limitation, the compact and light weight sensor are required for small UAV-based LiDAR systems. Although flight duration is short, a small UAV-based LiDAR system has a possibility to observe large target area with multi transects.

In precision agriculture, it is necessary to collect the crop information in each individual paddy. The transportation of heavy and bulky devices to the field is difficult. As a result, a small UAV-based LiDAR system for monitoring agricultural crops is proposed to be developed. Before applying this system for the crop growth monitoring

C. B. Van Dang · A. T. T. Phan (✉)

Faculty of Civil Engineering, Ho Chi Minh City University of Technology, VNU-HCM, Ho Chi Minh City, Vietnam

e-mail: ptathu@hcmut.edu.vn

K. Takahashi

Environmental Remote Sensing Laboratory, Nagaoka University of Technology, Kamitomioka, Nagaoka, Niigata 940-2188, Japan

purpose in the future, this study is carried out to check the accuracy of 3D point clouds collected by the developed UAV-LiDAR system. The accuracy of building 3D laser point cloud is assessed in specific situations of non-applying and applying correction method using ground control points.

2 System Description and Data Acquisition

A low-cost, compact, and light-weight UAV-based LiDAR system was developed. In detail, The DJI spreading wings S800 (DJI S800) was selected as platform [10]. The sensor, Hokuyo UTM30LX, was a compact laser scanner with 0.37 kg of weight, detection range from 0.1 to 30 m with the wide angle of 270° [11]. The light source emitted all wavelengths of 905 nm, and 0.25° of angular resolution with scan frequency of 40 Hz. A 3-axis gimbal (TAROT 5D) was used in order to maintain the horizontal attitude of the line laser scanner. Moreover, a single-frequency GPS receiver (Sensor-Com Kinematic GPS Evaluation Kit) was installed to locate the position of UAV. The line laser scanner and the GPS receiver were both controlled by a single-board PC (Raspberry Pi). Finally, the whole system was supplied the power by Pin Lithium Polymer (LiPo) for capable of flight times of about 5 min (Fig. 1a). The total cost of the developed system was approximate 9500 USD. For performing the experiment, 9 markers were arranged on a flat area in the campus of National Institute of Technology, Kumamoto College, Kumamoto prefecture in Japan on Dec. 18th, 2014 (Fig. 1b). The marker coordinated were identified in local coordinate system by a total station for validating the accuracy of 3D point cloud generation. The point clouds were collected with the setting of a 100° of field of view, and at the setting height of about 7 meters from the ground surface.

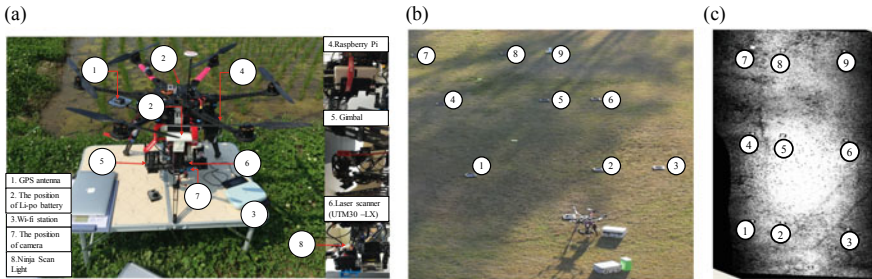


Fig. 1 System description and data acquisition. **a** The UAV- based LiDAR system, **b** experimental site, and **c** the intensity images of collected data

3 Generation of 3D Laser Point Clouds

3.1 Computation of the GPS Antenna Coordinates in Japanese Mapping Coordinate System (JMCS)

For generating the 3D point clouds from UTM30LX raw data, the position of UAV $(x_{UAV}, y_{UAV}, z_{UAV})^T$ was firstly calculating by using GPS data. The output of this procedure was the coordinates of GPS antenna in Japanese mapping coordinate system (JMCS). To achieve the expected results, the GPS antenna position was firstly located in global coordinate system. For this, the observed GPS data received by a single-frequency GPS receiver was applied post processed kinematic (PPK) method with RTKLIB version 2.4.1 to achieve the GPS antenna geographic coordinates [12]. These coordinates were converted to mapping coordinates in JMCS using Gauss-Krüger projection equations. Then, the position of UAV's GPS antenna corresponding to each scanline was computed.

3.2 Generation of the 3D Coordinates of Laser Scanning Points in LiDAR Sensor Coordinate System

The LiDAR sensor coordinate system (LSCS) was defined as right hand 3D orthogonal coordinate system (Fig. 2). The origin corresponded to the mechanical origin of the line laser scanner. The Y axis, corresponded to the rotation axis of the scanning mirror and its positive pointed to moving direction of the scanner. The positive Z pointed to the zenith. The X axis belonged to the scanning plane and its positive pointed to scanning direction. The scan angle θ was positive in the counter clockwise direction around the Y axis. The scan angle at zero degree matched with the nadir. For each scanned line, the coordinates of an observation point were calculated from observed range (Eq. 1).

$$\begin{pmatrix} x_L \\ y_L \\ z_L \end{pmatrix} = \begin{pmatrix} -r \cdot \sin \theta \\ 0 \\ -r \cdot \cos \theta \end{pmatrix} \quad (1)$$

where

- | | |
|---------------------|--|
| $(x_L, y_L, z_L)^T$ | The coordinate of scanning point in LiDAR sensor coordinate system |
| r | Observed range |
| θ | Scanning angle. |

3.3 Generation of the 3D Coordinates of Laser Scanning Points in UAV Coordinate System

As mentioned above, the position of UAV in the local coordinate system was identified by the position of GPS antenna whereas the position of a scanning point in any scanning line was identified with the origin of LiDAR sensor. Unfortunately, the origin of LIDAR sensor and the origin of the flight controller (GPS antenna) were totally different. Therefore, the relationship between the UAV coordinate system and the LiDAR sensor coordinate system should be figured out. For this, the coordinate system of UAV was set as the righthand 3D orthogonal coordinate system (Fig. 3). Its origin corresponded to GPS antenna. The Y axis matched with the nose direction of UAV and the Z axis in positive corresponds to the zenith. The translation vector between two origin of two coordinate system was measured as $(x^T, y^T, z^T)^T$. The coordinate of an scanning point in LiDAR sensor coordinate system was converting to UAV coordinate system by adjusting the translation value (Eq. 2).

$$\begin{pmatrix} x_U \\ y_U \\ z_U \end{pmatrix} = \begin{pmatrix} x_L \\ y_L \\ z_L \end{pmatrix} + \begin{pmatrix} x^T \\ y^T \\ z^T \end{pmatrix} \quad (2)$$

where

- $(x_U, y_U, z_U)^T$ The coordinate of scanning point in UAV coordinate system
- $(x_L, y_L, z_L)^T$ The coordinate of scanning point in LiDAR sensor coordinate system
- $(x^T, y^T, z^T)^T$ Translation vector between two origin of two coordinate systems.

3.4 The Coordinate of Scanned Point in Local Coordinate System

In the Japan orthogonal coordinate system, the Y axis in positive was the north direction. The angle between nose direction of UAV and the north direction was symbolled as β . The value of β was computed from the location of UAV recorded by the GPS receiver. According to the observed data, β was achieved with the value of approximate 147.52° . Then, the coordinates of all scanning points, 3D point cloud, in local coordinate system were calculated (Eq. 3) (Figs. 2 and 3).

$$\begin{pmatrix} x \\ y \\ z \end{pmatrix} = \begin{pmatrix} \cos(-\beta) & \sin(-\beta) & 0 \\ -\sin(-\beta) & \cos(-\beta) & 0 \\ 0 & 0 & 1 \end{pmatrix} \begin{pmatrix} x_U \\ y_U \\ z_U \end{pmatrix} + \begin{pmatrix} x_{UAV} \\ y_{UAV} \\ z_{UAV} \end{pmatrix} \quad (3)$$

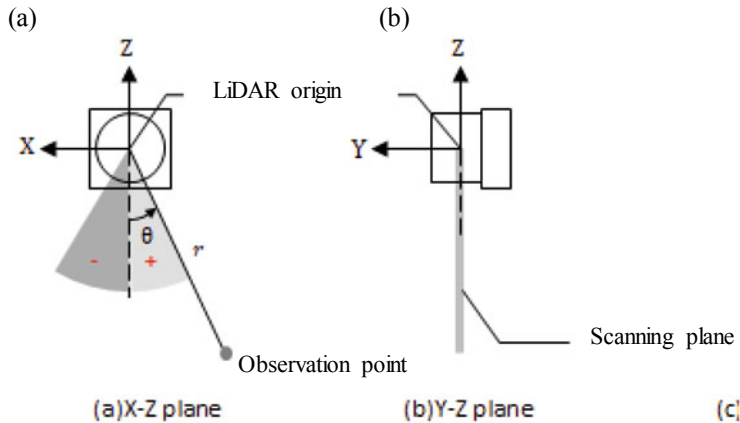


Fig. 2 The description of LiDAR sensor coordinate system in **a** X-Z plane and **b** Y-Z plane

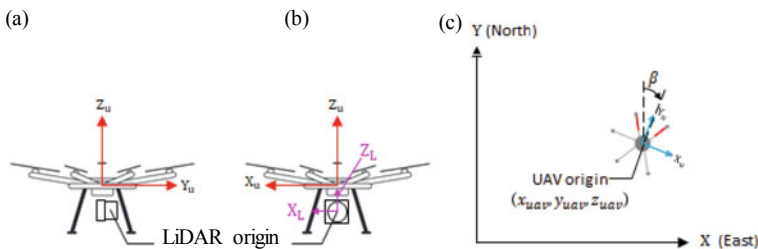


Fig. 3 The description of UAV coordinate system in **a** X-Z plane, **b** Y-Z plane, and **c** nose direction of UAV

where

$(x \ y, \ y)^T$ The coordinates of scanning point in local coordinate system.

$(x_U, y_U, z_U)^T$ The coordinates of scanning point in UAV coordinate system.

$(x_{UAV}, y_{UAV}, z_{UAV})^T$ The coordinates of GPS antenna corresponding to scanning point in local coordinate system

β The angle identifies the nose direction of UAV.

4 Point Clouds Accuracy Assessment

After generating the 3D point cloud, the locations of 9 markers were manually identified. Their coordinates were estimated from four scanning points closest to marker's

center. These coordinates were compared with the coordinated measured by the total station to validate the positioning accuracy of generated point clouds. The accuracy of building 3D laser point clouds was assessed by the mean absolute error (MAE) (Eq. 4). As a result, the 3D point cloud was achieved with the poor mapping accuracy of 3.13 m in horizontal and 1.09 m in vertical.

$$\text{MAE} = \frac{\sum_{k=1}^n |P_{\text{point cloud}}^k - P_{\text{total station}}^k|}{n} \quad (4)$$

where

MAE The mean absolute error

$P_{\text{point cloud}}^k$ The position of GCP points extracted from point cloud

$P_{\text{total station}}^k$ The position of the GCP points measured by the total station.

In case of applying the correction method, the chosen correction method was 7 parameters transformation with 4 ground control points. With the belief that the farther distance two separated points was selected, the more accurate results achieved; therefore, four points P1, P3, P7 and P9 locating at four corners of target field were chosen for identifying 7 transformation parameters including 1 scaling factor, 3 translation parameters and 3 rotation angles. Other markers became checked points for evaluating the positioning accuracy of 3D point could. As a result of calculating transformation parameters, the scaling factor was approximate 1.0, and the rotation angles around the X and Z axes were approximated 3° and 5° , respectively. The rotations around the Y axes was approximate 0° . The 3D point cloud is achieved with the mapping accuracy of meter in horizontal and several decimetres in vertical (Table 1).

5 Discussion

In this study, the 3D laser point clouds were generated with trajectory adjustment using GPS data. However, the unstable and gradually increasing of flight altitude causes the significant difference in elevation of scanning points (Fig. 2b). Without applying correction method, the achieved MAE is 3.13 m in horizontal and 1.09 m in vertical. To improve the mapping accuracy of 3D point cloud, the 7 parameters transformation was applied with 4 GCPs. As a result, the approximate 1.0 of scale factor and the small rotation angles demonstrate that translation transformation is suitable for correcting the point cloud generated from the developed system with the absolute error of 1 m in horizontal and several decimetres in vertical. In the comparison with previous studies, Sugiura et al. [5] reported the results of generating map regarding crop status using imaging sensor mounted on the helicopter with spatial error range from 0.18 to 0.29 m. Johnson [13] used an UAV-baser laser scanner system for terrain mapping and achieved the results of less than 0.5 m and

Table 1 The errors of checked points

True coordinate			Calibrated coordinate			Residual			
ID	X (m)	Y (m)	H (m)	X (m)	Y (m)	H (m)	dX (m)	dY (m)	dH (m)
MP2	-37,001.953	-58,136.244	36.110	-37,001.504	-58,136.541	36.048	0.449	-0.297	-0.061
MP4	-36,997.702	-58,128.691	36.157	-36,997.892	-58,129.705	35.565	-0.190	-1.014	-0.591
MP5	-36,996.541	-58,129.528	36.135	-36,996.672	-58,130.547	35.559	-0.131	-1.019	-0.576
MP6	-36,993.358	-58,132.066	36.174	-36,994.074	-58,132.227	35.723	-0.716	-0.162	-0.451
MP8	-36,992.083	-58,123.953	36.143	-36,991.795	-58,124.370	36.088	0.288	-0.417	-0.055

1.0 m in vertical and horizontal accuracy, respectively. Wallace et al. [7] developed a UAV-LIDAR system for forest inventory with horizontal and vertical accuracy of 0.34 m and 0.14 m. In general, the accuracy of 3D point cloud generated by the developed system is not suitable for mapping purpose. However, this result is good enough for the purpose of monitoring the crop in precision agriculture. Moreover, the approximate 0° of the rotations around the Y axes implied that trajectory adjustment with GPS data is good enough for generating the 3D point cloud in this study.

Besides the encouraging results, a number of limitations must be improved in future studies. In detail, the unstable flight altitude causes the significant difference in elevation of scanning points. Therefore, for future study, flight altitude should be maintained. Furthermore, this result of rotation angle around X and Z shows that, the horizontal status of LiDAR sensor is not balance. A small test was performed for checking the horizontal status of laser scanner with the continuously test flight including backward movement and without resetting the gimbal. As a result, in such situations, the laser altitude was not stable. To solve this problem, the backward movement should be avoided, and the gimbal is suggested to be reset before performing observational flight. For observing the wide target area with long flight endurance in the future, the horizontal attitude of laser scanner is not easy to maintained in whole flight; therefore, the rotation angles consisting of pitch, roll and yaw angle should be recorded for correcting the generated point clouds.

6 Conclusion

The developed system consists of DJI S800 platform, Hokuyo UTM30LX LiDAR sensor, a 3-axis gimbal (TAROT 5D), a single-frequency GPS receiver (Sensor-Com Kinematic GPS Evaluation Kit), an ultra-small motion logger (Ninja Scan Light) and a single-board PC (Raspberry Pi). The accuracy of 3D point cloud collected by the developed light-weight and low-cost UAV-based LiDAR system is checked. As a result, the 3D point cloud is achieved with MAE of 3.13 m in horizontal and 1.09 m in vertical in case of without applying the correction method. In case of applying 7 parameters transformation, the absolute error of 3D the point cloud generated from the developed system is improved to 1 m in horizontal and several decimeters in vertical. The achieved accuracy could be improved by using more than 4 GCPs or correcting the angles consisting of pitch, roll and yaw angle of the system. This system is simple installation, easy operation, easily removable and can be manually carried to the target fields. Although the flight endurance is limited, the developed system shows its capability of multi transects for observing target area. The data can be collected at low altitude with high resolution under cloudy condition. Moreover, such systems are cheaper, more compact, light-weight and flexible to use in the comparison with manned aerial vehicle or heavy UAV-based system. Although the accuracy of 3D point cloud is not suitable for mapping purpose but is good for the purpose of monitoring the crop in precision agriculture. The results of this study

confirm that the developed system can be applied for monitoring the rice plant in paddy level.

Acknowledgements This study was partially supported by Ho chi Minh City University of Technology-VNU-HCM under grant number T-KTXD-2018-113.

References

1. Lee AC, Lucas RM (2007) A LIDAR-derived canopy density model for tree stem and crown mapping in Australian forest. *Remote Sens Environ* 111:493–518
2. Riano D, Meier E, Allgower B, Chuvieco E, Ustin SL (2003) Modeling airborne laser scanning data for the spatial generation of critical forest parameters in fire behavior modeling. *Remote Sens Environ* 86(2):177–186
3. Hunt ER, Hively WD, Fujikawa SJ, Linden DS, Daughtry CST, McCarty GW (2010) Acquisition of NIR-green-blue digital Photographs from Unmanned aircraft for crop monitoring. *Remote Sens* 2:290–305
4. Rango A, Laliberte A, Herrick JE, Winters C, Havstad K, Steele C, Browning D (2009) Unmanned aerial vehicle-based remote sensing for rangeland assessment, monitoring, and management. *J Appl Remote Sens* 3:033542
5. Sugiura R, Noguchi N, Ishii K (2005) Remote-sensing technology for vegetation monitoring using an unmanned helicopter. *Biosys Eng* 90(4):369–379
6. Berni JA, Zarco-Tejada PJ, Suárez L, Fereres E (2009) Thermal and narrowband multispectral remote sensing for vegetation monitoring from an unmanned aerial vehicle. *IEEE Trans Geosci Remote Sens* 47(3):290–305
7. Wallace L, Lucieer A, Watson C, Turner D (2012) Development of a UAV-LiDAR system with application to forest inventory. *Remote Sens* 4:1519–1543
8. Lin Y, Hyypä J, Jaakkola A (2011) Mini-UAV-Borne LIDAR for fine-scale mapping. *IEEE Geosci Remote Sens Lett* 8(3):426–430
9. Zahawi RA, Dandois JP, Holl KD, Nadwodny D, Reid JL, Ellis EC (2015) Using lightweight unmanned aerial vehicles to monitor tropical forest recovery. *Biol Cons* 186(2015):287–295
10. DJI Innovation, Spreading Wings S800 User Manual, http://dl.djicdn.com/downloads/s800/S800_User_Manual_en.pdf. Accessed on 6 Sept 2016
11. Hokuyo Automatic Co. LTD, Communication protocol specification for SCIP2.0 standard. http://www.hokuyo-aut.jp/02sensor/07scanner/download/pdf/URG_SCIP20.pdf. Accessed on 6 Sept 2016
12. RTKLIB source program package version 2.4.1 <http://www.rtklib.com>. Accessed on 1 June 2016
13. Johnson P (2006) Unmanned aerial vehicle as the platform for lightweight laser sensing to produce sub-meter accuracy terrain maps for less than \$5/km². Mechanical Engineering Department, Columbia University, New York

Application of Information and Communication Technology in Construction Companies in Vietnam



Khoa Dang Vo, Chau Ngoc Dang, Chau Van Nguyen, Hiep Trong Hoang, An Thanh Nguyen, Quan Khac Nguyen, and Long Le-Hoai

1 Introduction

Information and communication technology (ICT), which is used to handle data, information and knowledge [14], is today seen as a vehicle to gain a competitive advantage [11]. ICT has been widely applied across many sectors to increase competitiveness and reduce costs [10]. Nowadays, ICT has a large impact on the architecture/engineering/construction (AEC) industry [14]. Many organizations have adopted new information technologies in support of their businesses to increase

K. D. Vo

Department of Construction Engineering and Management, Faculty of Civil Engineering, Ho Chi Minh City University of Technology, Vietnam National University Ho Chi Minh City (VNU-HCM), Ho Chi Minh City, Vietnam

C. N. Dang (✉)

Applied Computational Civil and Structural Engineering Research Group, Faculty of Civil Engineering, Ton Duc Thang University, Ho Chi Minh City, Vietnam
e-mail: dangngocchau@tdtu.edu.vn

C. Van Nguyen

KCon Construction & Investment Co. Ltd., Da Nang City, Vietnam

H. T. Hoang

Ho Chi Minh City University of Transport, Ho Chi Minh City, Vietnam

A. T. Nguyen

AXA Engineers Co. Ltd., Ho Chi Minh City, Vietnam

Q. K. Nguyen

Bach Khoa Saigon Construction Joint Stock Company, Ho Chi Minh City, Vietnam

L. Le-Hoai

Vietnam National University Ho Chi Minh City (VNU-HCM), Ho Chi Minh City University of Technology, Ho Chi Minh City, Vietnam

K. D. Vo

Faculty of Civil Engineering, Ho Chi Minh City Open University, Ho Chi Minh City, Vietnam

their reputation in the market. The implementation of ICT is becoming strategically important [12], because ICT facilitates communication and improves integration [5]. Through the use of ICT, collaboration and coordination can be achieved [3]. Today, many organizations could link, communicate and cooperate with each other using computers, telecommunication networks (e.g. the internet) or intranet. The EAC industry is significantly changing, especially in design and construction, due to the development of ICT [4].

In Vietnam, ICT has developed very impressively and become a common goal for many industries. In the forum of the global information technology (IT) 2009, delegates from many countries assessed the development of IT in Vietnam is noteworthy [20]. In 2012, the IT industry directly contributed about 7% to the Vietnamese Gross Domestic Product (GDP). Vietnam was ranked in the top 10 most attractive software outsourcing areas [7]. Vietnam also has a goal oriented to 2020 is to integrate information systems and establish widespread network environments. The IT industry will become the top economic-technical industry [8]. It is not so surprising that such development of the ICT industry could affect the Vietnamese EAC industry. Using raw and discrete data collected in a survey of Vo [21], this paper will systematically present the current application of ICT in construction companies, the attitude of managers with the application of ICT in information management, and the main barriers to applying ICT in information management of construction companies. Such results could be useful to improve the application of ICT in Vietnamese construction companies.

2 Literature Review

Many researches have focused on the implementation of ICT in the construction industry. Ahmad et al. [2] contended that appropriate IT investment and management's commitment and ability to provide leadership under the changed atmosphere were crucial to the successful implementation of IT in the construction industry. Studying the use of IT in the Canadian construction industry, Rivard et al. [19] identified the following issues: the electronic distribution of documents is more efficient and cheaper; the short time-line and the tight budgets make it difficult to introduce new technologies on projects; the industry is locked in one CAD system and it is difficult to introduce new ones; it is costly to maintain trained CAD and IT personnel; and companies that lag behind reduce the potential benefits of IT. Acar et al. [1] indicated that there was a relationship between the organizational size and the use of ICTs in the building construction sector in Turkey. Peansupap and Walker [16] identified 11 factors that could enable ICT diffusion and actual implementation in construction organizations, and then, grouped them into management, individual characteristics, technology and workplace environment clusters. Kasim [13] explored that the implementation of ICT in construction projects in Malaysia was at the early stage, in which Microsoft Excel Spreadsheet and handheld devices were the common

ICT tools adopted in the materials management processes. Onyegiri et al. [15] documented and analyzed ICT, its importance, obstacles and preconditions for effective use by focusing on literature and journals concerning communication in construction projects. Through a field survey of contractor firms in Turkey, Cakmak and Tas [6] determined the current use of IT, the main objectives in the use of IT, the benefits and obstacles arise from the use of IT and the impacts of IT implementations.

Furthermore, other studies have focused on the barriers for the ICT implementation. Stewart et al. [17] presented a conceptual framework for incorporating the impediments, such as operational factors, financial constraints, limited marketing and human resource management expertise, limited strategic planning and ineffective IT implementation. Then, Stewart et al. [18] explored the most effective coping strategies to overcome the impediments in an empirical investigation into the link between IT implementation barriers and coping strategies in the Australian construction industry.

The literature study indicates that in many countries, ICT plays a vital role in the EAC industry and has attracted much research. In Vietnam, little research has focused on the application of ICT in construction companies, as well as in the EAC industry. Thus, this paper will attempt to fill this gap.

3 Methodology

A qualitative study was used to explore the research objectives. Semi-structured interviews were conducted to collect data from construction organizations in the Vietnamese EAC industry. A questionnaire was formulated consisting of 17 questions. The questions focused on three following issues: the current application of ICT in construction companies, the attitude of managers with the application of ICT in information management, and the main barriers to applying ICT in information management.

Semi-structured interviews were carried out with the participation of practitioners of small-to-large organizations. In-depth interview method was selected to explore the information. The interview was started with the informal introduction of the research objectives, which lasted around 10 min. Then, practitioners were interviewed based on the study objectives and the preformatted interview process. Due to the limitation of time of practitioners, the overall interview process took around 45–60 min.

Snowball sampling technique was employed to collect data. A sample of 3 practitioners was first identified. During the interviews, two thirds of practitioners introduced more potential practitioners. A total of 17 practitioners were listed for the interviews. With snowball sampling technique, the sample size was not determined before data collection, and the data collection process was stopped when no more information was explored. After interviewing 10 practitioners, the results showed that the collected information was nearly similar. However, in order to ensure the accuracy and adequacy of the collected information, the interview process was still

performed with 7 remaining practitioners. The results of interviewing 17 practitioners showed that there appeared to be no more new information and, therefore, the interview process was stopped.

Out of 17 practitioners, 10 (59%) worked for contractors, 5 (29%) worked for project management/supervision consultants, 1 (6%) worked for design consultant, and 1 (6%) worked for owner. About working position, 4 (24%) were directors, 5 (29%) were deputy directors, 6 (35%) were project managers, 1 (6%) was an IT manager, and 1 (6%) was a senior engineer. In terms of experience, 9 (53%) had 5–10 years of experience, 2 (12%) had 11–15 years of experience, 3 (18%) had 16–20 years of experience, 2 (12%) had 21–25 years of experience, and 1 (6%) had more than 25 years of experience. It can be seen that 17 practitioners had much experience in the EAC industry and high position in their organizations. Thus, the ICT-related information that they provided was reliable.

4 Results

4.1 Current Application of ICT in Construction Companies

The current application of ICT in construction companies is assessed based on 4 levels: low = “the ICT system does not have a specific process and most activities are handled”, moderate = “the ICT system is established with a specific management process but is not automatic”, fair = “the ICT system has a clear management process but is not completely automatic”, and high = “the ICT system has a clear management process and is completely automatic”. In order to assess the level of application of ICT in the system of information management in construction organizations, the practitioners were interviewed about 4 aspects: the organization size, the forms of information exchange, the main tools, and the satisfaction of top management. The organization size is assessed based on 4 levels: very small = “less than 10 employees”, small = “10–200 employees”, medium = “200–300 employees”, and large = “more than 300 employees” [9]. The forms of information exchange are related to 4 steps in the process of information management: disseminating information, collecting information, storing information, and providing information. The main tools are the tools and software that the organization is usually applying for information management. The results of the interviews can be briefly presented as follows:

- In terms of the organization size, 7 (41%) are small companies, 6 (35%) are medium companies, and 4 (24%) are large companies.
- Regarding the forms of information exchange, a server system for exchanging the information is currently established in most construction organizations, and email and phone are preferred to be used in exchanging the information every day. However, the server system is only used within each organization with separate folders, and the server systems of construction organizations are not coordinated or linked with each other. From the server system, the internal information is

collected, disseminated, stored, and provided for the staff in the organization. Although the server system is not professional, the interviewees still appreciate the benefits brought from the server system. On the other hand, in some companies, handwork and hardcopy are still widely used. The staff must manage the files and information by themselves without any supporting tool of information management.

- Relating to the main tools applied for information exchange, the Microsoft Office software (such as Microsoft Excel and Microsoft Word) is preferred to be used in the organizations. In addition, email and phone are usually used for exchanging the information every day. According to the interviewees, using email is not considered official although many benefits can be brought from using email, such as fast, compact, time saving, and cost saving. Especially, many documents and information can be saved on emails. The staff can also make phone calls to others when they need specific information of the related works. In general, the tools applied for information exchange now is very traditional. Very few organizations use the current software of information management.
- With regard to the satisfaction of top management, 10 (59%) of interviewees feel satisfied with the current management process of ICT. Noticeably, although the level of ICT application is not high (i.e. 20% are at the low level, 70% are at the moderate level, and 10% is at the fair level), they still feel satisfied with the current management process of ICT. On the other hand, 7 (41%) of interviewees say that the current management process of ICT is not good enough to satisfy them and their organizations will invest a new higher ICT system for information management, such as a webserver or an automatic system of ICT, in the future.

In summary, the results of the interviews indicate that the interviewees have a positive attitude with the benefits of ICT in information management. However, this is not reflected in the investments of their organizations. The current application of ICT in many construction companies is only at the low-to-moderate levels. Noticeably, although the application of ICT is not so high, the interviewees still think that the benefits brought by the ICT application are large and most of them are feeling satisfied with the current process of ICT. The interviewees also confirm that now they do not invest more for the ICT system in information management and will consider investing for the ICT system in the future.

4.2 Attitude of Managers with the Application of ICT in Information Management

The attitude of managers with the application of ICT in information management were explored by interviewing the practitioners about 9 aspects: the role of ICT in information management, the benefits of ICT, the deflection of ICT in information management, the attention to new technologies, the costs used for the investment of ICT, the reason of not investing a high ICT system in information management, the

infrastructure of ICT and IT implementers, the staff, and the external factors. The results of the interviews can be briefly presented as follows:

- Regarding the role of ICT in information management, the interviewees think that ICT is only a supporting tool and does not bring a competitive advantage to the organization. Such thoughts make them not invest for ICT properly and not use the potential advantages of ICT.
- About the benefits of ICT, the interviewees suppose that ICT is fast, compact and convenient, which is reflected in the increase of labor productivity. However, they do not mention the support of ICT for making strategic decisions which can help to develop the organization.
- Relating to the defection of ICT in information management, the interviewees suppose that ICT does not have any large defects. They also think that they can overcome the defects of ICT easily if they face any defects of ICT.
- With regard to the attention to new technologies, the interviewees say that they rarely pay attention to the information about new technologies in information management. This makes them encounter a lack of information to improve the current management process and a lack of appropriateness in applying ICT at the beginning.
- About the costs used for the investment of ICT, the interviewees suppose that the costs are low and their organization can afford to invest. However, the costs are not low as they think. Inadequately quantifying the costs makes a lack of budget for the ICT investment, which can significantly affect the business cash flow and could cause a failure for the plan of improving the system of information management.
- Regarding the reason of not investing a high ICT system in information management, the interviewees say that their organizations currently do not need to apply a high level of ICT for information management because the contracts in the EAC industry now have low profit margins and the economic difficulties now do not allow them to invest much for ICT.
- Relating to the infrastructure of ICT and IT implementers, the interviewees suppose that except for the suitability and diversity of the information management software, the infrastructure of ICT is currently at the moderate-to-fair levels, and the IT engineers in their organization do not work for the aims of developing the management technologies.
- About the staff, the interviewees say that the ICT-related skills of the staff are not a problem for the investment of ICT and the staff can meet the needs of development.
- Regarding the external factors, the interviewees suppose that the development strategies of information management by using ICT depend on the competitors or investors, the spread and advertising have a small impact on the development of the organization, and the upgrading of the existing ICT system mainly depends on the development strategy of the organization.

4.3 Main Barriers for the Application of ICT in Information Management

The results of the interviews show that there are five main barriers for the application of ICT in information management: leader-related factors, current company size unsuitable for the application of high ICT, current non-professional process of information management causing difficulties in restructuring the organization, cost burden under financial crisis, and unnecessary application of high ICT for information management in the current market. The results can be briefly presented as follows:

- Leader-related factors are considered as a barrier for applying ICT in information management by 12 interviewees. According to the interviewees, lack of fully understanding the benefits of ICT, lack of development strategy for ICT, lack of commitment for implementation, absence of need for use, and limited knowledge of ICT are the leader-related factors which can prevent the effective application of ICT.
- Current company size unsuitable for the application of high ICT is assessed to be a barrier by 8 interviewees. The interviewees suppose that their organization now does not need to apply a high ICT system for information management and the use of ICT now depends on their organization's business capability.
- Current non-professional process of information management causing difficulties in restructuring the organization is mentioned by 5 interviewees. The interviewees say that the current process of ICT in their organization now is not professional, their organization encounters difficult challenges in redesigning the current process of ICT, and the information communication in their organization is not so clear.
- Cost burden under financial crisis is noticed by 4 interviewees. According to the interviewees, the high cost and the problem of payback have a negative impact on the investment of ICT.
- Unnecessary application of high ICT for information management in the current market is mentioned by 4 interviewees. Except few organizations now use a modern ICT system, e.g. Enterprise Resource Planning (ERP), the levels of ICT in information management in many organizations are similar to each other and generally not so professional.

5 Conclusions

A part of the whole picture about the application of ICT in the Vietnamese EAC industry is explored through interviewing 17 representatives from small-to-large construction companies using a semi-structured questionnaire. The results of the interviews indicate that the level of the application of ICT in Vietnamese construction

companies is not so high. However, the organizations' managers still feel satisfied with the current process of ICT and also have a positive attitude with the benefits of ICT in information management. The results of the interviews also show that there are five main barriers to applying ICT in information management: leader-related factors, current company size unsuitable for the application of high ICT, current non-professional process of information management causing difficulties in restructuring the organization, cost burden under financial crisis, and unnecessary application of high ICT for information management in the current market. The results are useful information for construction companies, which are paying attention to the application of ICT in information management.

References

1. Acar E, Kocak I, Sey Y, Arditı D (2015) Use of information and communication technologies by small and medium-sized enterprises (SMEs) in building construction. *Constr Manag Econ* 23(7):713–722
2. Ahmad IU, Russell JS, Abou-Zeid A (1995) Information technology (IT) and integration in the construction industry. *Constr Manag Econ* 13(2):163–171
3. Ahuja V, Yang J, Shankar R (2010) Perceptions affecting ICT adoption for building project management in the Indian construction industry. *Int J Constr Manag* 10(2):1–18
4. Amor R, Betts M, Coetzee G, Sexton M (2002) Information technology for construction: recent work and future directions. *J Inf Technol Constr* 7(16):245–258
5. Bjork BC (1999) Information technology in construction: domain definition and research issues. *Int J Comput Integr Des Constr* 1(1):3–16
6. Cakmak PI, Tas E (2012) The use of information technology on gaining competitive advantage in Turkish contractor firms. *World Appl Sci J* 18(2):274–285
7. CAND (2015) Information technology is one of the most important driving forces of development. Available at: http://www.ictsummit.vn/index.php?option=com_content&view=article&id=189&Itemid=172
8. Decision 1605/QĐ-TTg: Approving the national program for information technology application in the activity of state agencies in the period of 2011–2015
9. Decree 56/2009/NĐ-CP: Supporting the development of small and medium enterprises
10. Dehlin S, Olofsson T (2008) An evaluation model for ICT investments in construction projects. *J Inf Technol Constr* 13:343–361
11. Earl MJ (1993) Experiences in strategic information systems planning: editor's comment. *MIS Q* 17(1):1–24
12. Isikdag U, Underwood J, Kuruoglu M, Goulding JS, Acikalin U (2009) Construction informatics in Turkey: strategic role of ICT and future research directions. *J Inf Technol Constr* 14:412–428
13. Kasim N (2011) ICT implementation for materials management in construction projects: case studies. *J Constr Eng Project Manag* 1(1):31–36
14. Klinc R, Turk Ž, Dolenc M (2010) ICT enabled communication in construction 2.0. *Pollack Periodica* 5(1):109–120
15. Onyegiri I, Nwachukwu C, Jamike O (2011) Information and communication technology in the construction industry. *Am J Sci Ind Res* 2(3):461–468
16. Peansupap V, Walker DHT (2005) Factors enabling information and communication technology diffusion and actual implementation in construction organizations. *Electron J Inf Technol Constr* 10:193–218

17. Stewart RA, Miller C, Mohamed S, Packham G (2003) Sustainable development of construction small and medium enterprises (SMEs): IT impediments focus. CIB REPORT, 284–361
18. Stewart RA, Mohamed S, Marosszky M (2004) An empirical investigation into the link between information technology implementation barriers and coping strategies in the Australian construction industry. *Constr Innov* 4(3):155–171
19. Rivard H, Froese T, Waugh LM, El-Diraby T, Mora R, Torres H, Gill SM, O'Reilly T (2004) Case studies on the use of information technology in the Canadian construction industry. *Inf Technol Constr* 9:19–34
20. Viet Anh (2009) Vietnam ICT sector: developing as storm (Vietnamese). Available at: <http://www.baomoi.com/Nganh-cong-nghe-thong-tin-Viet-Nam-Phat-trien-vu-bao/76/3685574.epi>
21. Vo NKX (2013) Investigating the application of ICT and proposing the resolutions to improve the ICT in information management in the Vietnamese construction industry. Master Thesis (Unpublished), Ho Chi Minh City University of Technology, Vietnam

Apply System Dynamic in Resolving the Dispute of Time Delay in Viet Nam Construction Project



H. L. Pham and N. T. Le

1 Introduction

Vietnam's economy is developing strongly in the global development trend, the future of the construction industry is considered very positive, especially for developing and emerging economy like Vietnam. Catching up with the development trend of the world will help Vietnam to receive more opportunities as well as challenges to successful adaptation. The development of the construction industry also distributes increasing the number and scale of construction projects in Vietnam. Some of the obstacles of foreign investors in Vietnam are the legal barrier and the way to resolve arisen disputes which is always the prior interest of both owner and contractor. According to Arcadis [1], the trend of disputes is more costly and more complexity, which the three most common methods for resolving disputes in construction in 2017 are negotiation, mediation, arbitration. Following to statistics of the Vietnam International Arbitration Center (VIAC) in 2017, the number of disputes which this organization has resolved is increasing rapidly in recent years. In the last three years, the number of dispute cases almost equal to the total number of dispute cases in the previous six years. Moreover, in 2017, the number of construction industry disputes that this organization settled accounted for 24% of the total number of disputes. It is the second-highest compared to the rest of the industries and most disputants involved in China, the United States, and Singapore. The current trend of construction disputes in the world and Vietnam is growing the level of complexity and the number of dispute cases. So how to solve construction disputes to achieve goals as satisfying

H. L. Pham (✉)

Faculty of Civil Engineering, Ho Chi Minh City University of Technology, VNU-HCM, Ho Chi Minh City, Vietnam

e-mail: phluan@hcmut.edu.vn

N. T. Le

Ho Chi Minh City University of Technology, VNU-HCM, Ho Chi Minh City, Vietnam

e-mail: lenhotuanxdkb09@gmail.com

the parties and reducing costs, time disputes is always an urgent issue, so it is essential to find solutions in recent years.

2 Literature Review

NADRAC [2] claimed that dispute is the situation that people do not expect or have different beliefs, opposing views, disagree on issues or do not reach agreement on terms, it appears and prevents parties, harms their relationships. Garner [3], The Mavrommatis Palestine Concessions [4] pointed out that disputes are disagreements, conflicts, discrepancies about a point in law under the view of the law or the will of the parties, rising to the material of litigation. Fenn et al. [5], Kumaraswamy [6]: The dispute is the result of conflict, claims that issues related to judgment by law. Kumaraswamy [6], Ayudhya [7]: Construction disputes can originate from one or several simple reasons. Due to bad trends, these claims can be exaggerated, leading to a lot of complex—intertwined terms in contractual agreements. Dispute impedes project implementation, and results can lead to increased project completion time. This research referred on twenty previous studies about the causes of delays in construction projects, that addressed 59 causes of delay according to the responsibilities of the parties in causing delays and classified into seven groups: Causes related to the owner “1”, the contractors “2”, the consultants “3”, the design “4”, the contract “5”, the project “6”, and caused by external factors “7”.

2.1 And How to Resolve Delay Disputes?

Chong [8]—Not all disputes are resolved by the court, there are other formal or informal alternatives, one of which is the Alternative Dispute Resolution Method (ADR). The usual steps to resolve disputes in the Malaysian construction industry include non-binding solution (Grievance—Negotiation—Mediation/Conciliation) or binding solutions (Adjudication—Arbitration—Litigation). Safinia [9] point out common dispute resolution solutions in the UK including Negotiation, Arbitration, Litigation, Adjudication, Ombudsman, ADR (Conciliation, Meditation, Executive tribunal). Fenn et al. [5] divided dispute resolutions into two categories as Non-binding (Conciliation, Executive tribunal, Mediation), and binding (Adjudication, Arbitration, Expert determination, Litigation, Negotiation). Cheung and Suen [10] used five strategies to resolve disputes including negotiation, mediation, arbitration, ADR and eight critical selection factors in the decision-making model such as overall duration, relative cost, flexibility, confidentiality, preservation of relationship, binding decision, degree of control by parties, degree of control by third-party neutral. Chou [11] used six dispute resolution outcomes including no disputes occurred, negotiation, mediation, arbitration, litigation, administrative appeals in the predicting dispute solution model, which rely on dispute categories and project attributes

for Public-Private Partnership projects (PPP). This study used seven previous studies that revealed twenty-one factors affecting the decision of choosing a dispute solution.

2.2 *System Dynamic*

System dynamics was enlightened by Forrester in 1958, applied by mathematicians and scientists in many fields. Richardson and Pugh [12], Mawdesley and Al-Jibouri [13]: System dynamics is quite useful for management and simulation processes that have two characteristics: changing over time and allowing the response impact by transferring and collecting information. Coyle [14]: System dynamics helps to describe and interpret the time-dependent behavior of both qualitative and quantitative management systems. Sterman [15] expressed that large construction projects belong to complex dynamic system types, including several aspects such as extremely complex, including many interrelated elements, such dynamics, including many responding processes, nonlinear relationships, including “hard” and “soft” data.

3 The Methodology of the Study

Step 1: Ranking the top important factors in causing delays. Factors causing the delay will be asked about the frequency of occurrence and the degree of influence of those factors on the construction delay. Considering the linear correlation between the frequency of occurrence and the degree of influence by using Spearman's rank correlation coefficient with a significance level of 0.01. The results have collected from analyzing the survey, which used the severity index based on Babbie [16] to rank the severity of factors following two characteristics: the level of occurrence frequency and the degree of influence on delay. Then, the Importance Index is used to interpret the importance level of a factor causing delay by considering both the frequency of occurrence and the degree of influence of that factor.

$$\begin{aligned} \text{Importance Index (II)} &= SI(\text{frequency of occurrence}) \\ &\times SI(\text{degree of influence}). \end{aligned}$$

Step 2: Selecting the factors that affect the selection of dispute resolution methods about time completion in a construction project. Using one-way analysis variance method (abbreviated one-way ANOVA) to test the null hypothesis about the agreement between the participating groups: Owner, contractor, consultant, and designer ..., in a way to judge the impact level of the factors to the selection of dispute resolution methods with significance level at 0.01. Then, selecting the greatest impact factors by using one-sample T-test to compare the true mean value with value three. Factors were satisfied with the alternative hypothesis assuming that the true mean of

the sample is greater than the comparison value, will be chosen. The result tested at the 0.01 significance level.

Step 3: Set up the primary model to resolve delayed project completion. By combining the most important factors in causing delays with the greatest impact factors in selection dispute resolution methods that are indicated by previous analysis. Simultaneously, interviewing experts about the relationship among factors in the model and presenting a primary model.

Step 4: Test the primary model by using actual projects to simulate the delay, adding more relationships of new influence factors. Next, determining the influence weight of factors causing delays by expert interviews and data from the delayed project.

Step 5: Check the suitability of the ith model on the progress causing the delay compared to reality. If it is not satisfied, correct the new relationship and weight of the influence factors.

Step 6: If it satisfied, analyzing the behaviors of the model by comparing the forecast dispute resolution method with an actual dispute resolution method. If it is not suitable, turning back to correct the relationship of the primary model.

Step 7: If the results of the model fit the actual behaviors, so conclude and present the final model.

4 Data Collection and Analysis

This study used 93 questionnaires from engineers and managers working as owners, contractors, designers, consultants. This research focuses on the construction implement period, then it will consider the delay causes in the execution phase. Some of these causes will differ from the ones happening in the other phase of the project cycle. To develop the primary model, this research tested out the conformity in three actual delayed projects including (1) construction foundation package of the high-rise apartment building project, (2) school project, (3) office project. New factors causing delay occur in these projects will be added more to the primary model to develop the model. The results of the survey revealed that the nine most important factors causing the delay in the construction process include: (1) changing and arising work; (2) slow payment of completed work; (3) drawing errors; (4) financial difficulties of contractors; (5) lack of manpower, (6) shortage of material; (7) poor management; (8) inaccurate estimating initial plan; (9) subcontractor delay. The top eight factors affecting the choice of dispute resolution methods include (1) time for dispute resolution; (2) expenses for dispute resolution; (3) satisfaction of the parties; (4) preserving the relationship between the parties, (5) the power imbalance of the parties, (6) the involved expert judgment; (7) the capacity to presenting background information; (8) conserving reputation. These factors are used to create the primary framework for supporting choosing dispute resolution by the system dynamics approach. The supporting choosing dispute resolution model consists of two sub-models: Detecting-cause-of-dispute model and Dispute-resolution-predicting model.

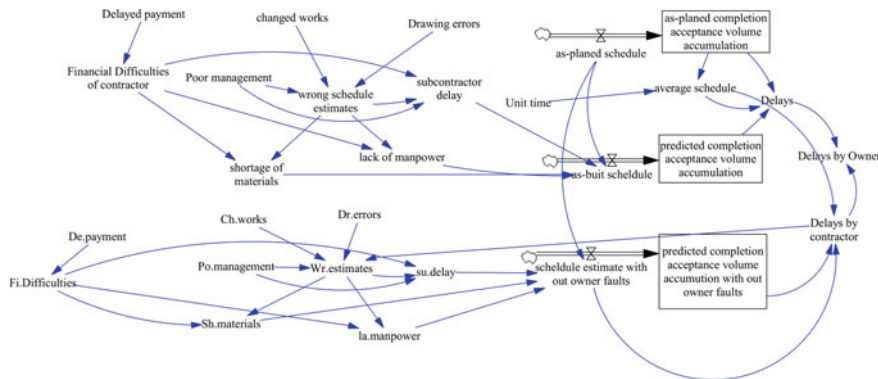


Fig. 1 Detecting-cause-of-dispute model

- The Detecting-cause-of-dispute model (Fig. 1) is a neutral tool that helps to quantify the fault of each party in causing the delay. Nine most important factors (mentioned above) causing the delay in the construction process were used to form this primary detecting-cause-of-dispute model by interviewing experts about the relationships among them. In other particular projects, new factors and relationships will be added more to the primary detecting fault model, so that it becomes suitably well-suited for the actuality. This study proposes a formula to calculate the impact level of the factors causing the delay. The effect size varies in magnitude from 0 to 1, with 0 indicating almost unaffected and 1 indicating perfect effect.

$$\text{Factor}_R(t) = A(t) \times \text{Factor}_R + [1 - A(t)] \times \text{Factor}(t)$$

where

$A(t)$ The proportion of Factor_R 's own effect in causing delay at time t .

$\text{Factor}_R = 1$ (or = 0) The weight of Factor_R occurrence.

$\text{Factor}(t)$ The proportion effect of other factors in causing Factor_R at time t .

The proportion effect pointed out in the model by interviewing construction experts who participated in the construction project.

For the long-term affecting factors causing the delay, the proportion effect = the weight influence of causing delay factor given by experts/K. Where K is the influence adjustment ratio that is corrected by basing on the actual project delay.

For affecting factors at a particular time in causing the delay, the effect range fluctuates between 0 and 1, were defined by expert assessments about its own effect in causing delay at that time, with 0 indicating almost unaffected and 1 indicating the perfect effect.

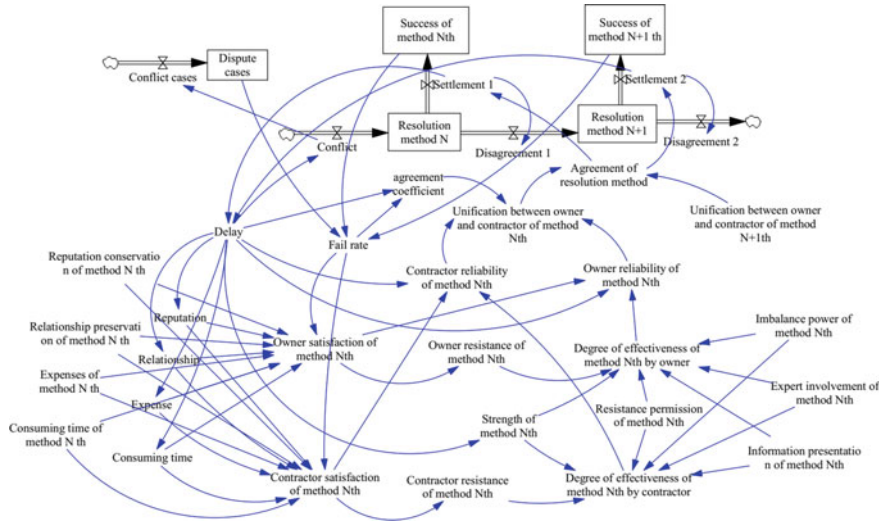


Fig. 2 Dispute-resolution-predicting model

- The Dispute-resolution-predicting model (Fig. 2) proposes five dispute resolution methods including (1) negotiation, (2) mediation, (3) adjudication, (4) arbitration, (5) litigation ($N = 0 \div 5$). All achievements of resolution methods include preserving the relationship between the parties, conserving their reputation and their damages of resolution such as consumed time for dispute resolution; expenses of dispute resolution will affect the satisfaction of the parties to the dispute. The power imbalance of the parties, the involved expert judgment; the capacity to presenting background information, will affect the effectiveness of the dispute resolution method. The resistance to the resolution method has stirred the involvement of the party's satisfaction with the proposed resolution method. The more pleasant parties get, the lesser parties resist and vice versa. The resistance influences the effectiveness of the dispute resolution method decreased by increasing it. However, each method has its strength and resistance permission, these help to reduce the impact of parties' dissatisfaction on the effectiveness of the dispute resolution method. Finally, choosing the dispute resolution method must be considered between satisfaction and the effectiveness of that method within a reasonable limit.

5 Results

A Comparison of model results with the actual data from the three projects shows that the Pearson correlation coefficient of 0.99 and Coefficient of Determination (R^2)

Squared) of 0.99 of the linear regression between the actual completion acceptance volume accumulation and the predicted completion acceptance volume accumulation. These results unveil that the model has the capacity of flexibly to simulate the delay process in construction projects (Figs. 3, 4, 5, 6, 7, 8, 9, 10, 11, 12, 13 and 14).

Project No. 1: Negotiation method is an efficient method to resolve this dispute when the negotiation success rate is highest compared to the others. At the time from 0 to 9, the negotiation success rate raised gradually to 87% and decreased to 63% at the time from 9 to 14. The prediction results of the model reflected the fact which the kind of actual dispute resolution method used successfully in this project is the negotiation method.

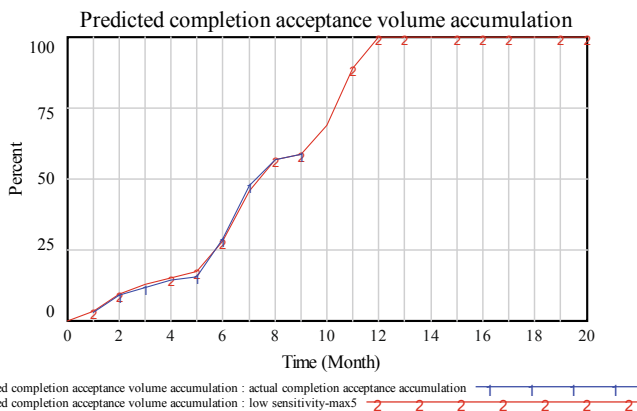


Fig. 3 Predicted and the actual completion of project 1

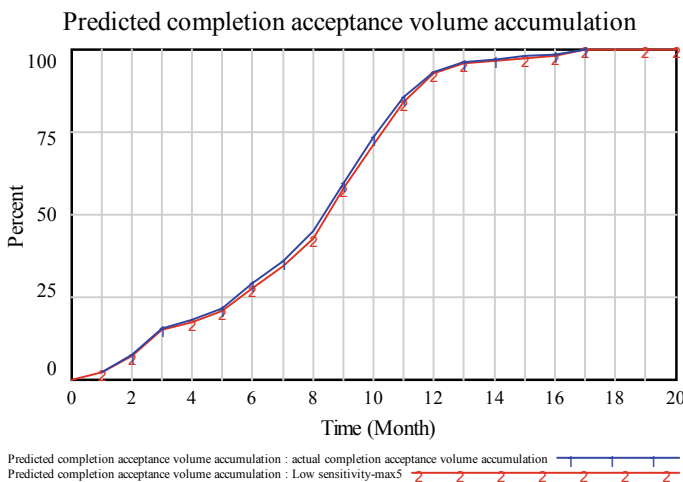


Fig. 4 Predicted and the actual completion of project 2

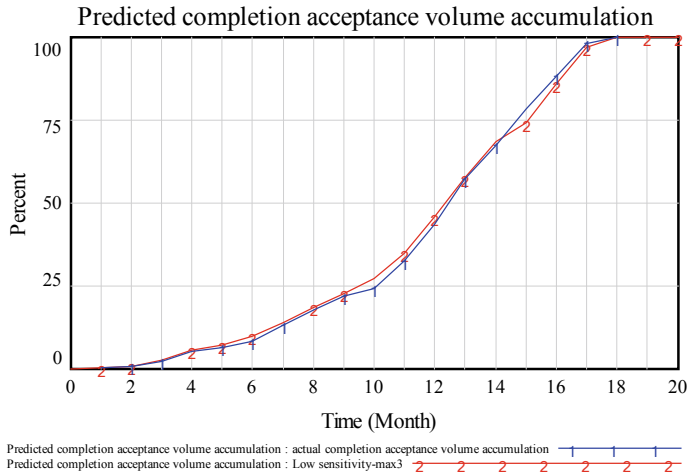


Fig. 5 Predicted and the actual completion of project 3

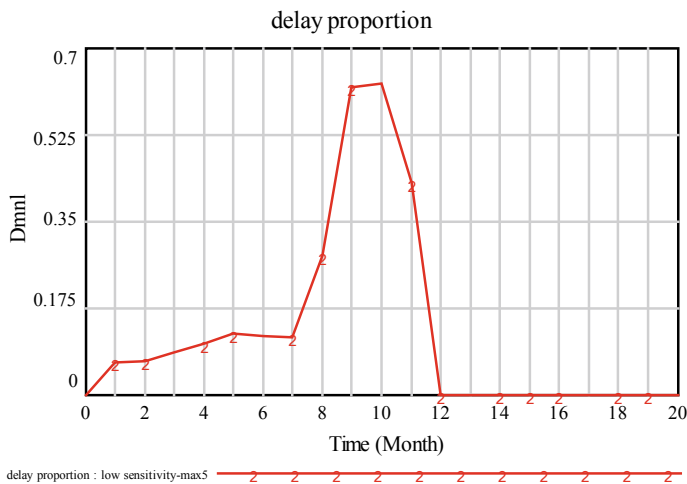


Fig. 6 Predicted delay proportion of project 1

Project No. 2 is similar to Project No. 2 as an effective resolving dispute method that model predicted is the negotiation method. From the time of 0–14, the successful negotiation rate increased gradually to 92% and decreased to 75% at the time from 14 to 17.

For Project No. 3, the negotiation method proved ineffective in resolving this dispute. At the time from 0 to 3, the negotiation success rate increased to a maximum at 50%, then decreased sequentially to 5% (Fig. 11). In contrast, the model also indicates from the time of 6–18 that the probability of success of the arbitration

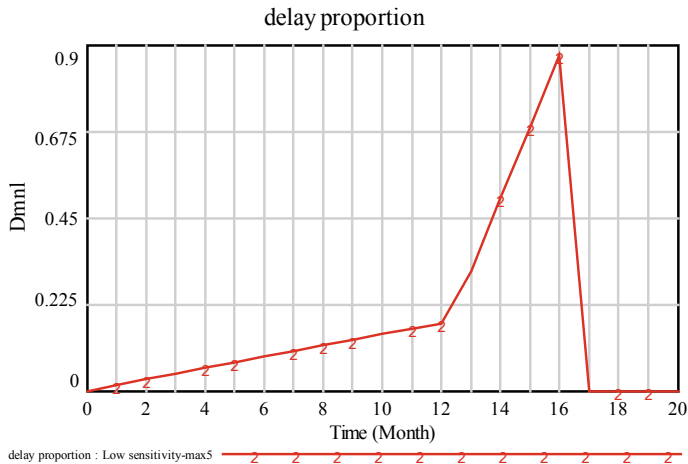


Fig. 7 Predicted delay proportion of project 2

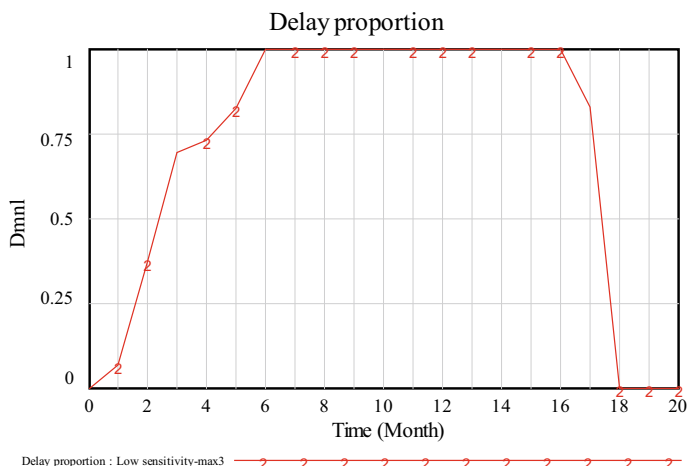


Fig. 8 Predicted delay proportion of project 3

method dominated the others while gradually enhance to 70% (Fig. 14). This results aimed that should use the dispute resolution method as arbitration.

It is suitable for the fact that the simple negotiation method doesn't seem to be effective while the tension of parties is still at a high level, and may need to choose the other dispute resolution method. Rising sensitivity means increasing bargaining times in the same period. Meanwhile, when rising the sensitivity, the numerous delay problem is fragmented into smaller problems, and parties would resolve the big problem by solving these tinier pieces. The model shows that with the more slight delay, the more bargaining will enhance the success rate of methods that help

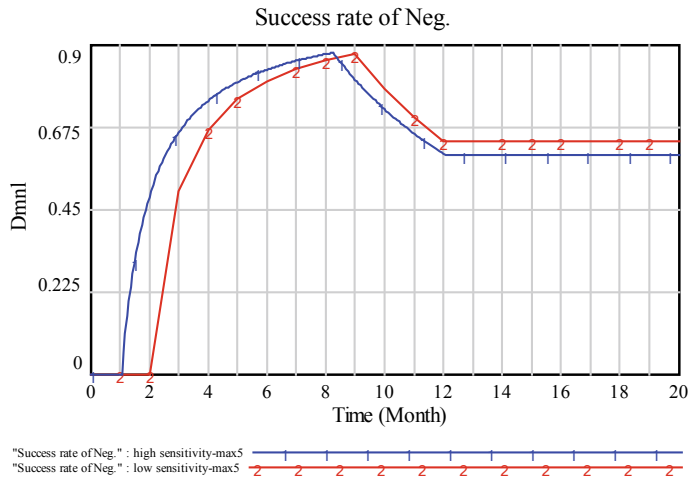


Fig. 9 Predicted success rate of negotiation for project 1

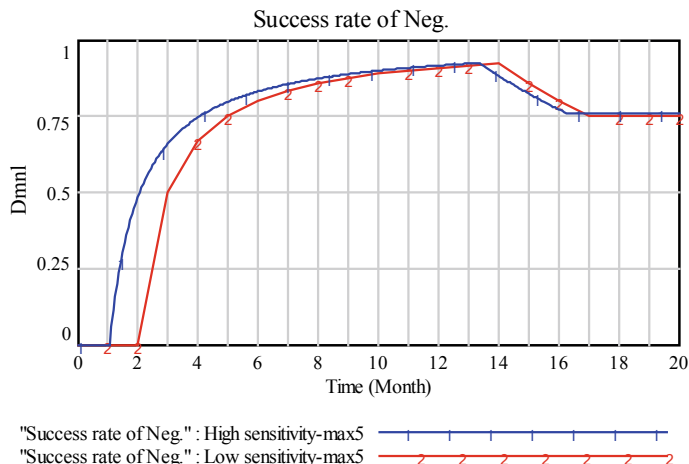


Fig. 10 Predicted success rate of negotiation for project 2

to raise the satisfaction of the parties, and vice versa for the severe delay which more bargaining amplifies the success rate method focusing on the effectiveness of the method.

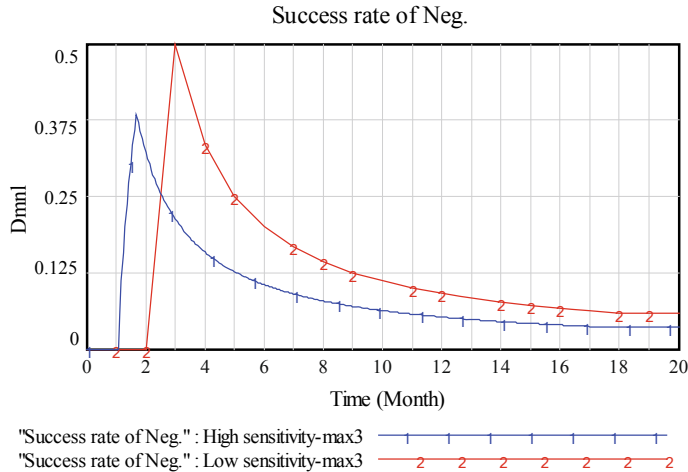


Fig. 11 Predicted success rate of negotiation for project 3

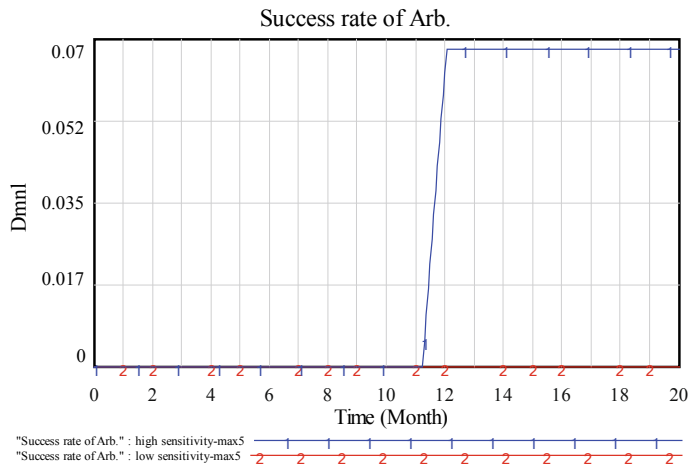


Fig. 12 Predicted success rate of arbitration for project 1

6 Conclusion

This study has proposed a framework for resolving disputes by system dynamics approach. The primary model of dispute resolution consists of two sub-models: Detecting fault model and predicting the dispute resolution model. The primary model of dispute resolution is formed based on the relationship of nine (9) causes of delay and eight (8) factors affecting the choice of dispute resolution methods, which outlined by the digging into questionnaires. The study used three (3) actual

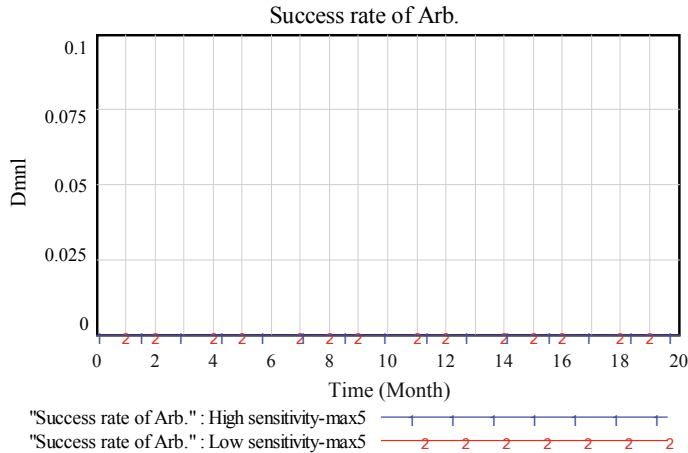


Fig. 13 Predicted success rate of arbitration for project 2

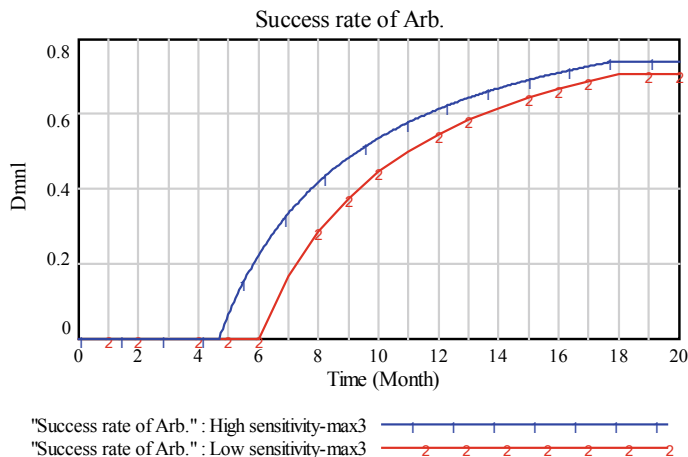


Fig. 14 Predicted success rate of arbitration for project 3

delayed project data, then combine the connection of the new causes of delay in these delayed projects to the primary model so that it becomes the final developing model. Finally, this combination helps to form the developing dispute resolution model that suitable to the actuality. The test results show that the developing model improved from the primary dispute resolution model is capable of simulating the delay process and timely flexible in predicting a dispute resolution method which is consistent with the perspective of disputants.

Acknowledgements We would like to thank Viet Nam National University-Ho Chi Minh City that supported our research under the framework of title code C2018-20-22.

References

1. Arcadis (2019) The ninth annual Arcadis Global construction disputes Report: laying the Foundation for success
2. National Alternative Dispute Resolution Advisory Council (NADRAC) (2012) Your guide to dispute resolution, Australia
3. Garner A (ed) (1999) Black's law dictionary
4. Mavrommatis Palestine Concessions (Greece v. Great Britain) (1924) Judgment of 30 August 1924, 1924 PCIJ (Ser. A) No. 2, at 11. 5
5. Fenn P et al (1997) Conflict and dispute in construction. *Constr Manag Econ* 15(6):513–518
6. Kumaraswamy MM (1997) Conflicts, claims and disputes in construction. *Eng Constr Archit Manag* 4(2):95–111
7. Ayudhya BIN (2011) Common disputes related to public work projects in Thailand. *Songklanakarin J Sci Technol* 33(5):565–573
8. Chong H-Y (2012) Selection of dispute resolution methods: factor analysis approach. *Eng Constr Archit Manag* 19(4):428–443
9. Safinia S (2014) A review on dispute resolution methods in UK construction industry. *Int J Constr Eng Manag* 3(4):105–108
10. Cheung S-O, Suen HCH (2002) A multi-attribute utility model for dispute resolution strategy selection. *Constr Manag Econ* 20(7):557–568
11. Chou J-S (2012) Comparison of multilevel classification models to forecast project dispute resolutions. *Expert Syst Appl* 39
12. Richardson GP, Pugh AL (1981) Introduction to system dynamics modelling with dynamo. MIT Press, Cambridge, MA
13. Mawdesley MJ, Al-Jibouri S (2010) Modelling construction project productivity using systems dynamics approach. *Int J Prod Perform Manag* 59(1):18–36
14. Coyle RG (1996) System dynamics modelling: a practical approach. *J Oper Res Soc* 48(5)
15. Sterman JD (1992) System dynamics model for Project Management. Massachusetts Institute of Technology
16. Babbie E (1989) The practice of social research, 5th edn. Wadsworth Publishing, Belmont, California, USA

Applying Water Footprint Model to Estimate Water Requirements of Rice Crops



Vu Hien Phan and Anh Tuan Nguyen

1 Introduction

The water footprint concept was introduced by Hoekstra as an indicator of freshwater use [8]. The water footprint of a product is the volume of freshwater used to produce the product, measured over the full supply chain. The water footprint consists of green, blue, and grey components [9]. The blue water footprint refers to consumption of water resources such as surface and groundwater, the green water footprint refers to consumption of water resources such as rainwater insofar as it does not become run-off, and the grey water footprint refers to pollution and is defined as the volume of freshwater that is required to assimilate the load of pollutants given natural background concentrations and existing ambient water quality standards. Recently most work on the water footprint has focused on agriculture and food production [14]. Mekonnen and Hoekstra [11] estimated fresh water requirements for crops including vegetable, tubers, fruits, and cereals, from 1996 to 2005, corresponding about 300 m³/ton, 400 m³/ton, 1000 m³/ton, and 1600 m³/ton, respectively. Based on the crop evapotranspiration, derived from meteorological datasets, Landsat-7 images and ASTER GDEM, Abuzar et al. [1] estimated fresh water requirements of crops in Macalister, Australia from December 2011 to March 2012. In the similar way to Abuzar, El-Shirbeny et al. [4] exploited Landsat-8 images in combination with topographic map and meteorological datasets to calculate ETC of crops in the Nile basin, Egypt, in 2013. In this paper, we have also used meteorological datasets, Landsat-8 images and ASTER GDEM to estimate fresh water requirements, following to the

V. H. Phan (✉)

Department of Physics, Ho Chi Minh City International University, VNU-HCM, Ho Chi Minh City, Vietnam

e-mail: phvu@hcmiu.edu.vn

A. T. Nguyen

Department of Land Management, Mientrung Industry and Trade College, Tuy Hoa, Phu Yen, Vietnam

e-mail: dodacmdc@gmail.com

water footprint model, for the 2016 winter-spring rice crop in Phu Yen Province, Vietnam.

2 Data and Methods

2.1 Study Area

Phu Yen is a coastal province in Southern Central Vietnam ($108^{\circ}40'40''$ E– $109^{\circ}27'47''$ E and $13^{\circ}41'28''$ N– $12^{\circ}42'36''$ N) [13]. It touches Binh Dinh Province to the north, Khanh Hoa Province to the south, Provinces of Dak Lak, Gia Lai to the west, and facing the East Sea to the East, as described in Fig. 1a. This region's terrain is slop from west to east with gradation mountains, highlands, plains and shoreline. It occupies a natural area of 5045 km^2 and the coastline is 189 km long. Phu Yen has a tropical monsoon climate with oceanic influence. Average annual temperature is 26.5°C , annual average precipitation is from 1500 to 3000 mm, average annual luminosity is 2450 h, and average relative humidity is above 80%. The province has high potential for industrial and fruit crops planting in highland areas and rice crops planting in plain areas. Additionally, Phu Yen has been long considered a rice bowl of Central Vietnam.

Annually, there are two rice crops in Phu Yen, including the winter-spring rice crop, from the end of December of the previous year to April, and the summer-autumn rice crop, from June to September. For each rice growing season, sowing to harvest ranges from 90 to 120 days, or more [10]. The length of time from establishment to harvest is known for each variety. It may vary a little depending on the growing conditions especially water availability and solar radiation. depending on variety, and solar radiation. Figure 1b shows rice growth stages, from seeding to harvest. Duration

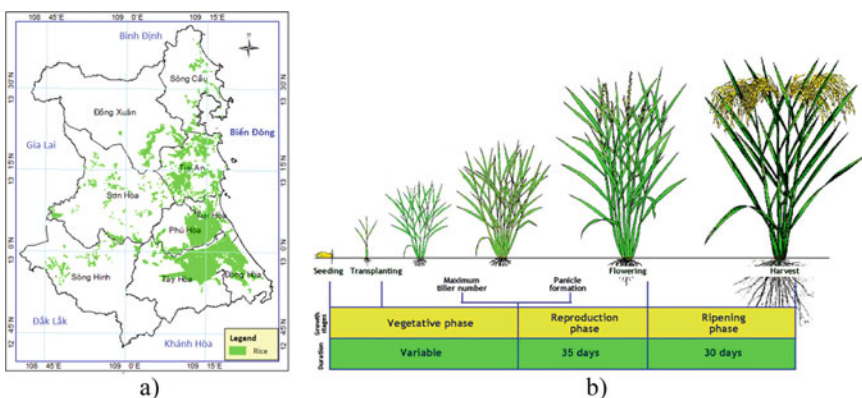


Fig. 1 a Rice mask derived from the 2016 land-use map in Phu Yen, and b Rice crop stages [10]

Table 1 The 2016 winter-spring rice crop in Phu Yen

Growth stages	Duration	2016 winter-spring crop	Landsat 8
Vegetative phase	Variable	20 Dec 2015–15 Feb 2016	LC81240512016004LGN02 LC81230512016045LGN01
Reproductive phase	~35 days	16 Feb 2016–20 Mar 2016	LC81240512016068LGN01 LC81230512016077LGN01
Ripening phase	~30 days	21 Mar 2016–30 Apr 2016	LC81230512016093LGN01 LC81240512016100LGN01 LC81230512016109LGN01 LC81240512016116LGN01

of the vegetative phase differs with variety while most varieties take 60–65 days from panicle initiation to harvest, as presented in Table 1. Additionally, sowing seeds is not the same time, for example the 2016 winter–spring rice crop in Phu Yen is from 20 Dec 2015 to 10 Jan 2016.

2.2 Water Footprint Model

The total water footprint (WF) of the process of growing crops or trees is the sum of the green, blue and grey components, following Eqs. (1), (2), (3), and (4) [9].

$$WF = WF_{Green} + WF_{Blue} + WF_{Grey} \quad (1)$$

$$WF_{Green} = \frac{CWU_{Green}}{Y} = \frac{10 \sum_{d=1}^{lg p} ET_{Green}}{Y} = \frac{10 \sum_{d=1}^{lg p} \min(P, ET_C)}{Y} \quad (2)$$

$$WF_{Blue} = \frac{CWU_{Blue}}{Y} = \frac{10 \sum_{d=1}^{lg p} ET_{Blue}}{Y} = \frac{10 \sum_{d=1}^{lg p} \max(0, ET_C - P)}{Y} \quad (3)$$

$$WF_{Grey} = \frac{(\alpha \cdot AR) / (C_{max} - C_{nat})}{Y} \quad (4)$$

where CWU_{Green} is the ‘green’ crop water use (m^3/ha), CWU_{Blue} is the ‘blue’ crop water use (m^3/ha), and Y is the crop yield (ton/ha). The crop water use depends on the stands for length of growing period (lgd , day) and the crop evapotranspiration (ET_C , mm/day) as well as the effective precipitation (P , mm/day). Additionally, α is leaching-run-off fraction, i.e. fraction of applied chemicals reaching freshwater bodies, AR is the application rate of a chemical (fertilizer or pesticide) per unit of land (kg/ha); C_{max} is the maximum acceptable concentration of a chemical in a receiving water body (kg/m^3), and C_{nat} is the natural concentration of a chemical in the receiving water body (kg/m^3).

The crop evapotranspiration (ETC) equals the crop water requirements [16], following Eq. (5). Here, k_c is the crop factor, computed from NDVI values, representative for vegetable-surface characteristics, following Eq. (6) [5], and ET_0 is the reference crop evapotranspiration (mm/day), following the Penman-Monteith Eq. (7) [16].

$$ET_C = k_c \cdot ET_0 \quad (5)$$

$$k_c = \frac{1.2(NDVI - NDVI_{min})}{(NDVI_{max} - NDVI_{min})} \quad (6)$$

$$ET_0 = \frac{0.408\Delta(R_n - G) + \gamma \frac{900}{T_{Mean} + 273} u_2(e_s - e_a)}{\Delta + \gamma(1 + 0.34u_2)} \quad (7)$$

where R_n is the net radiation at the crop surface ($MJm^{-2}day^{-1}$), G is the soil heat flux density ($MJm^{-2}day^{-1}$), T_{Mean} is the mean air temperature at 2 m height ($^{\circ}C$), u_2 is the wind speed at 2 m height (m/s), e_s and e_a are the saturation and actual vapor pressures (kPa), Δ is the slope vapor pressure curve ($kPa/^{\circ}C$), and γ is the psychrometric constant ($kPa/^{\circ}C$).

2.3 Input Data and Preprocessing

Meteorological datasets. The meteorological data are collected from four stations surrounding and inside (i) Phu Yen, as shown in Table 2 [12]. The types of measurements, or meteorological parameters, include daily minimum and maximum temperatures (T_{Min} and T_{Max}), mean humidity per day (RH_{Mean}), sunshine hours (n), wind speed at the height of 2 m above land surface (u_2) and precipitation (P). The collected measurements are from 20 Dec 2015 to 30 Apr 2016, corresponding to the winter-spring rice crop in this region, following to Department of Agriculture and Rural Development of Phu Yen. For example, Table 2 presents the meteorological

Table 2 Meteorological stations and measurements on 6 Feb 2016

Station	Lat.	Lon.	T_{Min} ($^{\circ}C$)	T_{Max} ($^{\circ}C$)	RH_{Mean} (%)	n (h)	u_2 (m/s)	P (mm)
Tuy Hoa (i)	13°05'	109°17'	21.7	25.6	88	1.9	2.5	3.3
Cung Son (i)	13°02'	108°59'	22.2	25.1	88	2.2	2.5	2.8
Madrac	12°44'	108°46'	21.5	24.1	87	8.5	3.0	3.1
Quy Nhon	13°46'	109°13'	24.7	27.7	87	2.0	3.1	2.7

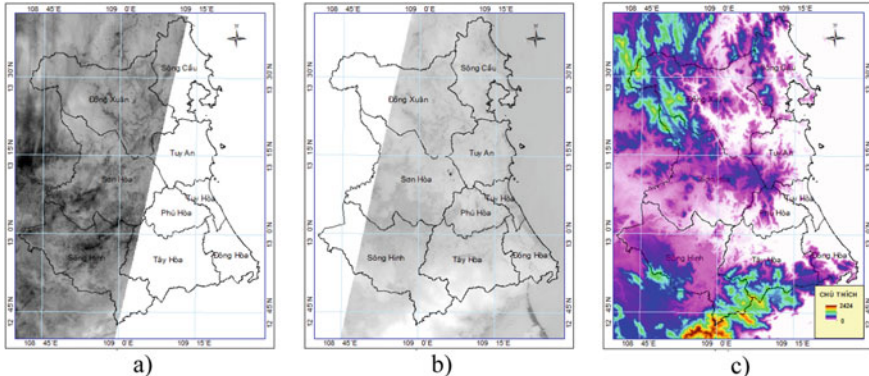


Fig. 2 Landsat 8 images captured **a** on 8 Mar 2016, **b** on 17 Mar 2016, and **c** ASTER GDEM

parameters T_{Min} , T_{Max} , RH_{Mean} , n , u_2 , and P were measured on 6 Feb 2016. From the locations of meteorological stations, a station layer is created in the ESRI shapefile-point format. For each meteorological parameter, we create a table of measurements in which each field will store daily measurements. After joining the station layer with the table, we use the ArcGIS IDW interpolation tool to create daily 30×30 m resolution grids of the meteorological parameter. Subsequently, daily measurements of the meteorological parameters at the four stations are converted to the daily 30×30 m resolution grid data.

Landsat 8 images. Table 1 shows the available Landsat-8 multi-spectral images captured during the observed period, available on the USGS Earth Explorer website [3]. To cover the whole province, two adjacent Landsat censes are needed, but they are belonging to two different paths, as illustrated in Fig. 2a, b. We assume two such adjacent images present contemporary land surface. Subsequently, they are mosaicked and clipped to the provincial boundary after radiant calibration. We use red and near-infrared band to compute NDVI vegetation index, following Eq. (8). Here, ρ_{RED} and ρ_{NIR} are red and near infrared band spectral reflectance, derived from 4 and 5 bands [15].

$$NDVI = \frac{\rho_{RED} - \rho_{NIR}}{\rho_{RED} + \rho_{NIR}} \quad (8)$$

ASTER GDEM. The ASTER GDEM data is available on the USGS Global Data Explorer website [7], providing the digital elevation model of the study area, as shown in Fig. 2c.

Land-use map. The 2015 land-use map in Phu Yen is given by Department of Natural Resource and Environment of the Phu Yen Province [2], providing the state of paddy fields in Phu Yen in 2015, as presented in Fig. 1a.

Then, the rice map is used to clip all 30×30 m grids of daily meteorological parameters, NDVI indices, and elevations. So, the data processing is performed at

locations of rice growing. Note that all geospatial data are converted to be referenced to the VN2000 coordinate system.

2.4 Data Processing

We design tools using the ArcGIS Model Builder extension, following steps.

Step 1. Compute the daily reference crop evapotranspiration ET_0 , following Eq. (7). The parameters R_n , G , T_{Mean} , e_s , e_a , Δ and γ are computed, following equations described in details in the FAO 56 method [16], based on daily minimum and maximum air temperatures, mean humidity, elevation above sea level, latitude of the study area, and Julian days of the observed period.

Step 2. Compute the crop factor k_C , following Eq. (6), corresponding to the periods of rice growth, as described in Table 1.

Step 3. Compute the crop evapotranspiration ETC, following Eq. (5). We assume the crop factors will present the characteristics of rice growth.

Step 4. Compute the water footprints WF_{Green} , WF_{Blue} , and WF_{Grey} , following Eqs. (1), (2), and (3), respectively. Here, the crop yield Y of the 2016 winter-spring rice crop is collected from Department of Agriculture and Rural Development of Phu Yen, as shown in Table 3.

For the WF_{Grey} computation, dominant three chemical sources reaching fresh water from rice growing in Phu Yen include nitrogen, phosphorus, and pesticides. Following to Department of Agriculture and Rural Development of Phu Yen, the application rate of a chemical (fertilizer or pesticide) per unit of land AR (ton/ha) is an average of 0.09, 0.06, and 0.0005, respectively. Following Franke et al. [6], the

Table 3 Water footprints (m^3/ton) for the 2016 winter-spring rice crop in Phu Yen

District name	Y (ton/ha)	WF _{Green} (m^3/ton)	WF _{Blue} (m^3/ton)	WF _{Grey} (m^3/ton)	WF (m^3/ton)
Tuy An	6.6	60.17	334.68	20.75	415.60
Dong Xuan	6.0	65.54	334.46	22.82	422.82
Son Hoa	6.3	56.73	295.21	21.73	373.67
Tay Hoa	7.8	50.28	310.47	17.56	378.31
Dong Hoa	7.2	55.32	354.40	19.01	428.73
Phu Hoa	7.8	49.24	311.34	17.56	378.14
Song Hin	6.2	55.85	299.14	22.08	377.07
Song Cau	6.4	65.21	290.47	21.39	377.07
Tuy Hoa	7.7	48.83	339.67	17.78	406.28
Average	6.9	56.35	318.87	20.07	395.29
Percentage (%)		14.25	80.67	5.08	100

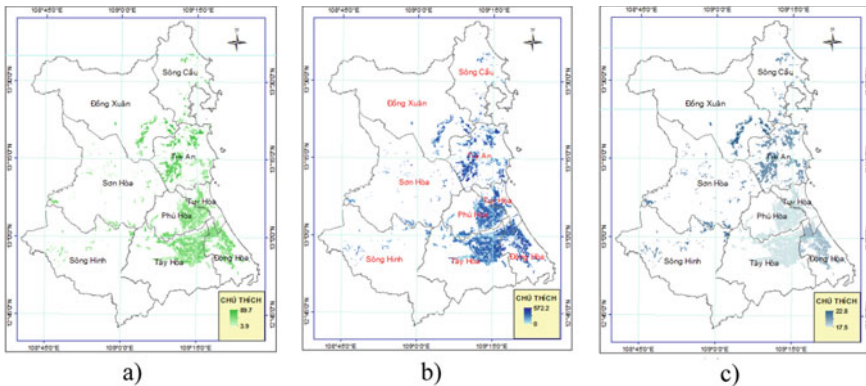


Fig. 3 The components of water footprint **a** WF_{Green}, **b** WF_{Blue}, and **c** WF_{Grey} for the 2016 winter-spring rice crop in Phu Yen

leaching-run-off fraction α is 1%, 0.01%, and 0.01%; the natural concentration of a chemical C_{nat} (mg/l) is 0.1, 0.01, and 0; and the maximum acceptable concentration of a chemical C_{max} (mg/l) is 13, 0.1, and 0.0001, respectively.

3 Results and Discussions

Applying the data processing, the water footprints WF_{Green}, WF_{Blue}, and WF_{Grey} are computed, representative for fresh water requirements of the winter-spring rice crop in 2016 in Phu Yen, as presented in Fig. 3. The results are determined at a geospatial resolution of 30×30 m and located at rice growing. Additionally, a summary of water footprints by districts of the Phu Yen Province is performed and shown in Table 3. Subsequently, the total fresh water volume for a ton of rice equals 395.29 m^3 , in which the components of green, blue, and grey water requirement are 14.25%, 80.67%, and 5.08%, respectively. Thus, under the climate condition in Phu Yen, surface and ground water sources are dominant of the total fresh water requirement for the 2016 winter-spring rice crop.

4 Conclusions

The results indicate that fresh water requirements of the winter-spring rice crop in 2016 in Phu Yen differ in different areas of rice growing. The water footprints are computed based on the crop evapotranspiration, derived from daily in situ measurements of air temperature, humidity, wind speed, hours of solar radiation and precipitation from meteorological stations, Landsat-8 images, and ASTER GDEM during

the observed period. The tools designed by the ArcGIS Model Builder are used to estimate the components of the total water footprint. For yielding one ton of rice, the total water use requires an average of 395,69 m³ on the whole province, in which the green, blue, and grey water footprints are 14.25%, 80.67%, and 5.08%, respectively. The results are expected as a reference water requirement for the sustainable water resource planning in Phu Yen, Vietnam.

References

1. Abuzar M, McAllister A, Whitfield D, Sheffield K (2012) Remote sensing analysis of crop water use in the Macalister irrigation district. Geospatial Sciences, RMIT
2. DONRE-PY, Department of Natural Resources and Environment, Phu Yen. URL <http://sotnmt.phuyen.gov.vn/>. Last access on 13 May 2018
3. EE. Earth Explorer—USGS. URL: <https://earthexplorer.usgs.gov/>. Last access on 13 May 2018
4. El-Shirbeny MA, Ali AM, Saleh NH (2013) Crop water requirements in Egypt using remote sensing techniques. National Authority for Remote Sensing and Space Sciences, Egypt
5. El-Shirbeny MA, Abdellatif B, Ali AM, Saleh NH (2016) Evaluation of Hargreaves based on remote Sensing method to estimate potential crop evapotranspiration. Int J Geomate 11(23):2143–2149
6. Franke NA, Boyacioglu H, Hoekstra AY (2013) Grey water footprint accounting: Tier 1 supporting guidelines. Value of Water Research Report Series No. 65, UNESCO-IHE, Delft, The Netherlands
7. GDEx. Global Data Explorer—USGS. URL: <https://gdex.cr.usgs.gov/gdex/>. Last access on 13 May 2018
8. Hoekstra AY, Hung PQ (2002) Virtual water trade: a quantification of virtual water flows between nations in relation to international crop trade. Value of Water Research Report Series No. 11; UNESCO-IHE: Delft, The Netherlands
9. Hoekstra AY, Chapagain AK, Aldaya MM, Mekonnen MM (2011) The water footprint assessment manual, setting the global standard. Earthscan, London, UK, 228 p
10. IRRI. The International Rice Research Institute. URL <https://www.irri.org/>. Last access on 6 July 2018
11. Mekonnen MM, Hoekstra AY (2011) The green, blue and grey water footprint of crops and derived crop products. Hydrol Earth Syst Sci 15:1577–1600
12. NCHMF. National Centre for Hydro-Meteorological Forecasting. URL: <http://www.nchmf.gov.vn/Web/en-US/43/Default.aspx>. Last access on 6 July 2018
13. PHUYEN. Phu Yen Portal. URL <http://www.phuyen.gov.vn/wps/portal>. Last access on 6 July 2018
14. Silva V, Oliveira S, Braga CC, Brito JI, Sousa F, Holanda R, Campos J, Souza EP, Braga AC, Almeida R (2016) Virtual water and water self-sufficiency in agricultural and livestock products in Brazil. J Environ Manag 184:465–472
15. USGS. Landsat 8 User Guide Handbook. URL: <https://www.usgs.gov/media/files/landsat-8-data-users-handbook>. Last access on 13 May 2018
16. Zotarelli L, Dukes MD, Romero CC, Migliaccio KW, Morgan KT (1998) Step By step calculation of the Penman-Monteith evapotranspiration (FAO 56 Method). Agricultural and Biological Engineering Department, University of Florida

Cost and Environmental Benefit Analysis of Solar—Panel Installation on Glass Surfaces to Reduce the Energy Consumption in High Rise Buildings



Trung Quang Nguyen, Duc Long Luong, Anh-Duc Pham,
and Quynh Chau Truong

1 Introduction

Global climate change is becoming more serious. The negative manifestations of global warming can be seen through rising sea levels, backward glaciers, tropical waves, storms, floods, drought, disaster, economic depression, loss of biodiversity and ecosystem destruction [6]. According to previous studies on global climate change, the utilization of fossil materials in the production area and human life plays an important role for those issues because energy is the most important factor for the economic development of any country. According to Sarkar et al. (2019), energy directly impacts the main risks that the world has to face such as poverty, environmental issues, and food safety. In International Energy Report (2009), a technical description of the US Ministry of Energy mentioned that the total energy consumption is forecasted to increase by 44% in the period of 2006–2030 (International Energy Outlook 2009).

Currently, reducing energy demand (energy efficiency) and using renewable energy attract the attention of almost countries to minimize the harmful effects of the greenhouse. In order to reduce energy consumption of building, some studies utilized double-skin façades [4, 11, 15], blinds cover [14], optimal window rate on the wall (WWR—Window to Wall Ratio) [5, 10], smart curtains [9] or some innovation research about building envelopes that focus on glass election [1, 3]. Additionally, a solar panel that is the optimal solution of investors is utilized their designs to lessen energy consumption in buildings [7, 8, 12].

T. Q. Nguyen (✉) · D. L. Luong

Faculty of Civil Engineering, Ho Chi Minh City University of Technology, VNU-HCM, Ho Chi Minh City, Vietnam

e-mail: nqtrung.sdh16@hcmut.edu.vn

T. Q. Nguyen · A.-D. Pham · Q. C. Truong

Faculty of Project Management, University of Science and Technology, the University of Danang, Danang, Vietnam

Although there are a lot of studies that mention about the glass faceplate optimization, there are not any studies that combine faceplate and solar panel at the same time to install solar panels on the faceplates to absorb solar. Therefore, this paper proposes the approach to either analyze and determine the building surface glass or optimize the installation area of solar panels on the faceplates to reduce energy demand in the operation stage of the building based on the analysis of the project life cycle.

2 Model Setup

This study that bases on previous research and principle of conservation of energy is described in Fig. 1.

2.1 *Running Energy Simulation of the Building in Each Kind of Glass*

2.1.1 Model Setup

The building simulation 3D model is initialized by Revit (Fig. 2), outer space of the building is not impacted by neighboring buildings according to the following features:

- The 1st-floor heights 4.00 m, the remaining floors are 3.60 m high. The 1st floor is designed with bricklaying and paving stone meanwhile glass wall is installed from the 2nd floor to the 10th floor
- Building size: 20 × 30 m
- The building is located in the East-West direction
- Location: Danang city, Vietnam.

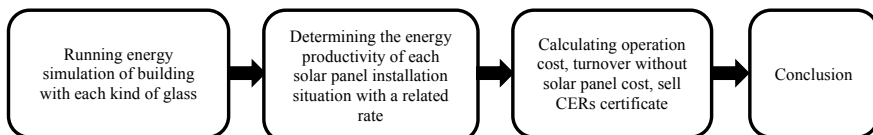


Fig. 1 Research model

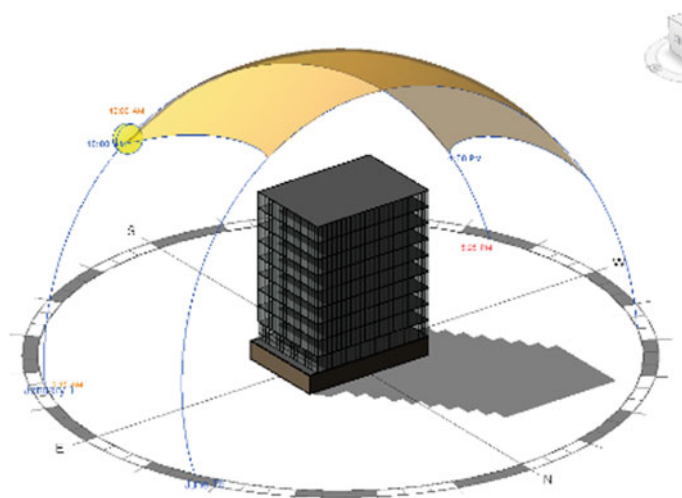


Fig. 2 Simulation model for building energy

2.1.2 Running Energy Simulation in Each Case of Glass Cover (N_e)

This research considers only three types of popular glass on the market with the primary function of light extraction, heat-insulating, force-resistant ability (Table 1).

Running the simulation model by applying energy simulation function in the model established by Revit-BIM. The building simulation is covered by three types of glass, including Tempered glass, solar control Green, and Low-E in a year. The result is highlighted in Table 2.

Table 1 The main parameters of three types of glass

Type of glass	Light transmission coefficient (%)	Heat transfer coefficient	The coefficient of solar heat absorption	Shading coefficient
Tempered glass	88	5.7 W/m ² K	0.82	0.94
Solar control Green	51	3.9 W/m ² K	0.49	0.56
Low-E	32	1.4 W/m ² K	0.27	0.31

Table 2 The total energy consumption in the building simulation in a year

Type of glass	Unit	Total
Tempered glass (A)	kWh	1,513,451
Solar control Green	kWh	1,319,102
Low-E (C)	kWh	1,187,638

Table 3 Produced energy in each case of a solar installation (kWh/year)

Direction	Area	20%	40%	60%	80%
East	648 m ²	16,981	33,961	50,942	67,922
West	648 m ²	17,138	34,277	51,415	68,554
South	972 m ²	20,870	41,739	62,609	83,478
North	972 m ²	13,746	27,492	41,239	54,985
Total produced energy in a year (kWh/year)		68,735	137,469	206,205	274,939

The energy consumption in the building is different from each type of utilized glass. Then, it can be seen that glass selection significantly impacts on energy consumption in the building.

2.2 Determining the Produced Energy Lever in Each Case of Solar Panel Installation (N_S)

According to previous studies [2] as well as the guarantee of light transmission ability in the building, this research proposes solar panel installation area in the building sides with four situations 20, 40, 60 and 80% of façades area. Running energy simulation with specialized software of Bach Khoa Solar Investment and Development JSC. The result is obtained in Table 3.

2.3 Economic Analysis

To evaluate the effectiveness of the plan, this study bases on the result of energy analysis and produced energy generated from solar panels. The initial investment cost and operation cost are calculated with the consideration of the time value of money to build annual cumulative cash flow by the following formula [1]:

$$C_G(t) = C_i + \sum_{i=1}^t \frac{C_{a,i}}{(1+r)^i} \quad (1)$$

C_i : initial investment costs (including the cost of glass installation and solar panel);

$C_{a,i}$: annual operation costs, including: electricity cost; maintenance cost. Revenue from renewable electricity and sell CERs certificate are included.

t : calculation period (year); r : real interest rate (%).

Three types of analysis cases:

- Case 1: Tempered glass (A) + the cases of solar panel area
- Case 2: Solar control Green glass (B) + the cases of solar panel area
- Case 3: Low-E (C) glass.

2.3.1 Initial Investment Costs (C_i)

Initial investment costs C_i of the project is determined base on the total new investment costs and solar panel installation cost

$$C_i = C_{k,i} + C_{SP,i} \quad (2)$$

C_k, i : installation cost of each case of glass
 C_{SP}, I : solar panel installation cost of each case.

2.3.2 Yearly Running Cost ($C_{a,I}$)

$$C_{a,i} = C_{1,i} + C_{2,i} - C_{3,i} - C_{4,i} \quad (3)$$

a. Annual electricity cost for the energy needed in the building($C_{1,i}$)

$$C_{1,i} = P_1 * N_{e,i} \quad (4)$$

$C_{1,i}$: the annual electricity cost (USD),
 P_1 : the unit cost of electricity (averaged by market unit price: 0.07 USD/kWh),
 $N_{e,i}$: Total electricity use (kWh).

The total electricity use in a year N_e , i is determined based on the principle of energy conservation law. During operation, solar batteries generate energy and create renewable electricity. This renewable electricity is the lost absorbed energy of the simulation building after installing the battery system. The actual energy used for the building is equal to the difference between the total energy in the simulation model with solar battery energy. The use of solar cells has reduced the consumption of a significant amount of electricity during the operation of the building

$$N_{e,i} = N_e - N_s \quad (5)$$

b. The maintenance cost of the solar battery ($C_{2,i}$)

The maintenance cost is mainly about the cost of cleaning glass. The unit price is assumed of 0.5 USD/m² of glass, and this activity is conducted twice a year. It is merely a clean-up activity to clean the glass to facilitate operation at the highest capacity (Tables 4 and 5).

Table 4 The costs of glasses and solar panels

Parameters	Signs	Values
Unit cost for installing tempered glass (USD/m ²)	A	12
Unit cost for installing Solar control Green glass (USD/m ²)	B	26
Unit cost for installing Low-E glass (USD/m ²)	C	53
Unit cost for installing solar panel (USD/m ²)		150

Table 5 The electricity energy used in one year after applying the solution of solar panels (kWh/year)

Situation	20%	40%	60%	80%
Situation 1	1,244,716	1,175,982	1,107,246	1,038,512
Situation 2	1,050,367	981,633	912,897	844,163
Situation 3	987,638	987,638	987,638	987,638

The total maintenance cost of solar batteries throughout the project life cycle

$$C_{2,i} = 2 * P_2 * S \quad (6)$$

P_2 : Unit cost of cleaning, maintenance solar batteries (the market price on average: 0.5 USD/m²)

S : Total area of solar batteries (m²).

c. Revenue by using energy generated from a solar battery ($C_{3,i}$)

The amount of solar energy entering the building will be absorbed by solar panels; the rest will be absorbed by the glass surface and pass through the building. The energy absorbed by the solar cell is also the renewable energy used for the building, so the first revenue is the electricity generated from the solar battery system. The electricity bill will be reduced because the use of electricity decreases equivalent to the amount of energy absorbed by the solar battery. Therefore, revenue is derived from the research model:

$$C_{3,i} = Q_{tt,i} * P_3 \quad (7)$$

P_3 : Unit price of electricity (USD/kWh) (market price on average: 0.07 USD/kWh)

$Q_{tt,i}$: Total renewable electric energy each year (kWh).

d. Revenue by selling certificate CERs of greenhouse gas emission

CERs certification is a greenhouse gas emission certificate (CERs), which is certified emission reductions granted by Clean Development Mechanism (CDM) for CDM projects and 1 CER unit determined by one ton of CO₂. In this study, the research team calculated the CO₂ emission reduction because of the use of renewable energy. The amount of CO₂ reduction after that will be converted into revenue due to the

sale of CERs certificates. According to a recent study by the US Government [13], the estimated values from 2010 to 2050, with SCC (Social Cost of Carbon) for 2010 is 24.75 USD/T CO₂ and 39 USD/T CO₂. In this study, the authors cost an average of 30 USD/T CO₂ during the calculated life cycle.

Profit from selling CERs certificates throughout the project life cycle:

$$C_{4,i} = P_4 * k * Q_{tt,I} \quad (8)$$

P₄: Unit price of converted CO₂ from electricity (USD/ton of CO₂)

Q_{tt,I}: Total renewable electric energy each year (kWh), k: Coefficient of conversion of CO₂ (k = 0.6612 kgCO₂/kWh).

3 Results

In order to help investors to evaluate the economical aspect of this solution comprehensively, the authors have calculated with the assumption that the solar panel's depreciation period is 50 years for all the above-mentioned costs. The results are shown in each case in the following charts:

The life cycle costing assessment for each type of glass and different rates of solar panels glued on the surface has recorded a significant change in total project costs for each situation. In the case of installing solar panels on 20 and 40% of the façade area, there is no change in total cost at the end of the project between situations 2 and 3. It means that the life cycle costing of using Solar control green glass and solar batteries compared to Low-E glass is nearly equal. Therefore, in this case, it is recommended to use Low-E glass because of the lower initial investment cost (Fig. 3).

However, in the case of using 60 and 80% solar panels, the results are quite different. It can be seen that although the combination of Solar control green glass and energy battery has the largest investment cost, the total cost at each stage has a significant change compared to the cost of two remaining cases. As shown in Figs. 5

Fig. 3 Life cycle costing—20% battery on façade area

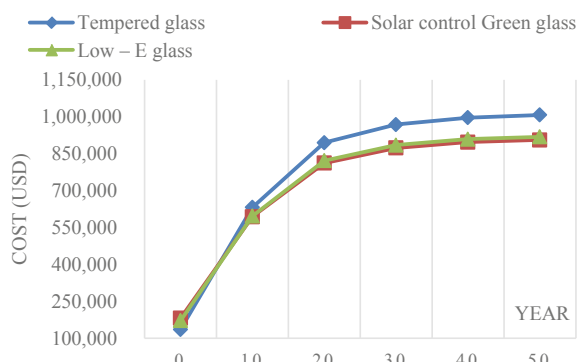
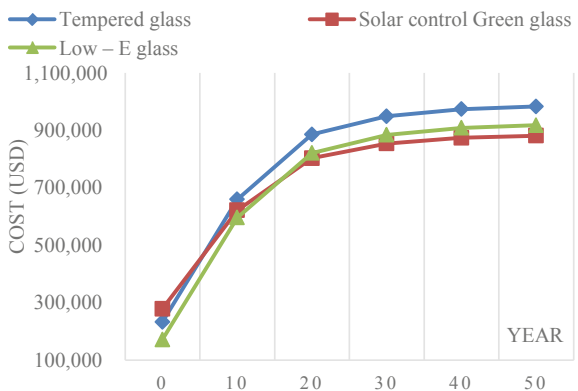


Fig. 4 Life cycle costing—40% battery on façade area



and 6, if the project is operated for more than 20 years old, the solution of combining the Solar control green glass and solar panels is more effective than the other two types of glass.

Fig. 5 Life cycle costing—60% battery on façade area

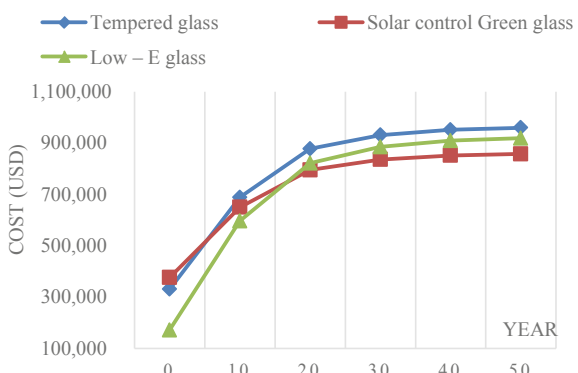
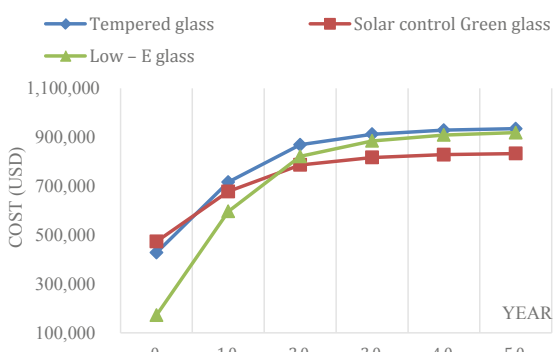


Fig. 6 Life cycle costing—80% battery on façade area



4 Conclusion

It can be said that buildings use more than 40% of global energy and about 30% of energy-related GHG emissions. Therefore, the implementation of new methods and technologies for energy saving is a way to reduce operational costs and increase user comfort. In particular, the combination of solar panels on glass surfaces in buildings is a viable option to meet sustainable goals of energy.

This paper examines the effect of each type of glass and analyses the ratio of solar cells that are glued to glass surfaces to reduce energy use in the building. The research team calculates the life cycle cost of the project with 3 specific cases. This assessment is to use the results of energy consumption analysis by Revit software and calculate the renewable energy created from solar panels by the software of BK Solar. Overall, the study has demonstrated the impact of using solar panels on the building's glazing façades in reducing energy consumption. The study proposes different cases of analysis between the rate of solar cells and the type of glass to optimize the energy use and to save operational costs. Accordingly, the authors have proposed some solutions to increase the overall energy efficiency for office buildings:

- The use of solar panels on buildings' glass surfaces is a good solution to reduce energy consumption. Besides, the building faceplate has a large area (not limited to the roof part), so it is possible to increase the area of energy battery used in the building. This is significant in enhancing solar energy use in Vietnam.
- The use of solar panels is only economically effective when using a ratio of 60% of the glazing surface area or more. In case, for some objective reasons, this use is less than 60%, it is economically ineffective.

However, this study has some limitations, such as not considering the location of surrounding buildings that will create a shadow on the surface to reduce the performance of the battery. Besides, the study has not mentioned light transmissions when using energy panels on the surface, which may affect the productivity of the people working in the building. This shows that there will be promising studies to address these limitations in the future.

Acknowledgements This work was supported by The University of Danang, University of Science and Technology, code number of Project T2019-02-59 and this research was supported technically by Bach Khoa Joint Stock Company of Investment and development of solar energy.

References

1. Allen K, Connelly K, Rutherford P, Wu Y (2017) Smart windows—dynamic control of building energy performance. Energy Build 139:535–546
2. Aste N, Buzzetti M, Del Pero C, Leonforte F (2018) Glazing's techno-economic performance: a comparison of window features in office buildings in different climates. Energy Build 159:123–135

3. Cao S, Zhang S, Zhang T, Yao Q, Lee JY (2019) A visible light-near-infrared dual-band smart window with internal energy storage. Joule 3:1152–1162
4. Fallahi A, Haghigat F, Elsadi H (2010) Energy performance assessment of double-skin façade with thermal mass. Energy Build 42:1499–1509
5. Goia F (2016) Search for the optimal window-to-wall ratio in office buildings in different European climates and the implications on total energy saving potential. Sol Energy 132:467–492
6. Hennon GMM, Williamson OM, Hernández Limón MD, Haley ST, Dyhrman ST (2019) Non-linear physiology and gene expression responses of harmful Alga *Heterosigma akashiwo* to rising CO₂. Protist 170:38–51
7. Karlsen L, Heiselberg P, Bryn I, Johra H (2016) Solar shading control strategy for office buildings in cold climate. Energy Build 118:316–328
8. Khan J, Arsalan MH (2016) Solar power technologies for sustainable electricity generation—a review. Renew Sustain Energy Rev 55:414–425
9. Leeladhar PR, Singh JP (2018) Sunlight-driven eco-friendly smart curtain based on infrared responsive graphene oxide-polymer photoactuators. Sci Rep 8:3687
10. Ma P, Wang L-S, Guo N (2015) Maximum window-to-wall ratio of a thermally autonomous building as a function of envelope U-value and ambient temperature amplitude. Appl Energy 146:84–91
11. Pomponi F, Piroozfar PAE, Southall R, Ashton P, Farr ERP (2016) Energy performance of double-skin façades in temperate climates: a systematic review and meta-analysis. Renew Sustain Energy Rev 54:1525–1536
12. Sadeghi S (2018) Study using the flow battery in combination with solar panels and solid oxide fuel cell for power generation. Sol Energy 170:732–740
13. Technical Support Document: Technical Update of the Social Cost of Carbon for Regulatory Impact Analysis Under Executive Order 12866. In: United States Government (2016)
14. Zeng Z, Li X, Li C, Zhu Y (2012) Modeling ventilation in naturally ventilated double-skin façade with a venetian blind. Build Environ 57:1–6
15. Zhou J, Chen Y (2010) A review on applying ventilated double-skin facade to buildings in hot-summer and cold-winter zone in China. Renew Sustain Energy Rev 14:1321–1328

Decision Scaling Approach to Assess Climate Change Impacts on Water Shortage Situation in the Ba River Basin—Vietnam



V. T. V. Anh, T. Thuc, N. Thong, and P. T. T. Duong

1 Introduction

Adaptive solutions to climate change related water resources in river basins often require long-term with large capital investment, therefore thorough and careful designing and planning process is necessary. Traditional top-down approach is admitted bringing effective information on potential impacts of climate change on hydrologic systems in an intended future socio-economic or emission scenarios. However, it poses difficulties for decision makers, including: (1) it only assesses impacts of climate change in several certain socio-economic or emission scenarios, so it is impossible to consider all likelihood of future climate; (2) this approach is heavily reliant on GCM projections which have deep uncertainties deriving from different sources, such as human knowledge imperfection of the climate system function, variability of climate factors in research systems, or future socio-economic and emission scenarios [1, 9].

The Ba river basin (BRB) is the largest river basins in Central Vietnam. With total natural area of 13,417 km², most of the basin is in territory of 2 central highland Gia Lai and Dak Lak provinces and a south-central Phu Yen province. With only 1,700 mm of annual rainfall and 25.72 l/s km² of average annual flow module, the river flow regimes are distributed unevenly in space and time, only 25–30% of flow concentrated in 8–9 months of dry season, leading to droughts, river flow pollution

V. T. V. Anh (✉) · N. Thong

Faculty of Civil Engineering, Ho Chi Minh City University of Technology, VNU-HCM, Ho Chi Minh City, Vietnam

e-mail: vvanh@hcmunre.edu.vn

V. T. V. Anh · P. T. T. Duong

Faculty of Hydrology, Meteorology and Climate Change, Ho Chi Minh University of Natural Resources and Environment, Ho Chi Minh City, Vietnam

T. Thuc

Vietnam Institute of Meteorology, Hydrology and Climate Change, Hanoi, Vietnam

and salinity intrusion in many places in the basin [6]. In climate change context, it is projected that the river flow in dry season is getting to decline remarkably in future [5, 6], therefore these above hazards are supposed to be more serious, threatening water delivery safety in the basin. Previous researches on assessment of impacts of climate change on the BRB system, such as [5, 6], is according to top-down approach. As analyzed above, these researches have limited assistance for policy makers at different levels in proposing optimal adaptive measures.

This paper adopts Decision Scaling (DS) approach, which uses a combination of bottom-up and top-down approaches, to assess climate change impacts on water shortage in the BRB, in order to overcome the limitations of the previous researches and to assist better for decision makers at the basin.

2 Methodology

The research adopts Decision Scaling approach to assess climate change impacts on the BRB. Figure 1 presents workflow of the research which consists of the following steps:

2.1 *Method for Determining Performance Threshold of the Ba River Basin*

To assess impacts of climate change on water shortage in the BRB system, reliability of water delivery (R) is chosen as performance indicator of the system. Reliability is originally defined as “the probability that a system performs its mission within specified limits for a given period of time in a specified environment” [7]. In this research, reliability of the BRB water delivery (%) refers to the percentage of time

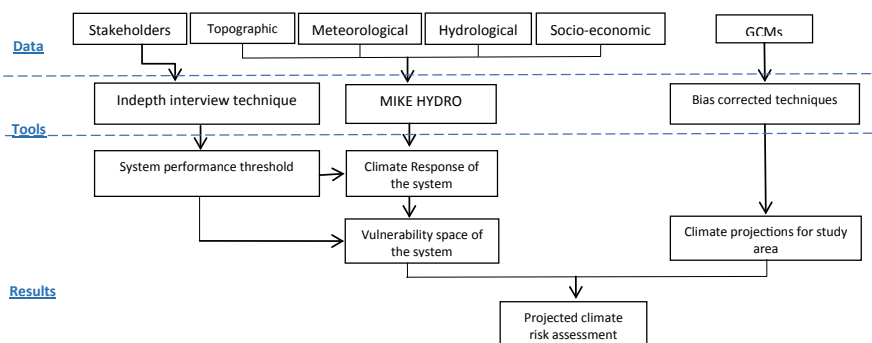


Fig. 1 Workflow of the research

that the BRB system meets water sectors' demand. Hence, performance threshold is the minimum acceptable percentage of time that the system meets water sectors' demand.

Determination of performance threshold mainly bases on analyzing past climate hazards effects in the study area [4, 9, 10]. In this research, the BRB stretches in 3 different climate zones (the Eastern Truong Son, the Western Truong Son and the middle), where climate and natural characteristics, river flow regimes are very different. Therefore, performance threshold is determined by choosing a typical drought year happened in the past in which damages are acceptable by water sectors. Totally 12 participants including water managers at different levels and representative water exploitation units in the basin are interviewed to find out this year. After that, system models are applied to simulate river flow, water demand and calculating water balance of the hydrologic system. Corresponding to each climate zone, the lowest reliability among different types of water demand nodes in the chosen typical drought year is considered as performance threshold of the system (R_{th}).

2.2 System Model Establishment

2.2.1 River Flow Simulation

River flow on different tributaries of the BRB is simulated by rainfall-runoff MIKE NAM model.

Input data:

- Observed daily precipitation and evaporation data at 16 gauges across the basin (Meteorological and rain gauges network is shown in Fig. 2).
- Observed daily flow data at 4 hydrological stations: An Khe, Song Hinh, PoMeRe and Cung Son for calibration and validation process of MIKE NAM models.

Model calibration and validation process:

Mike Nam model is calibrated and validated for 3 stations representing 3 climate zones: Po Me Re gauge (on the Ayun River) representing for the Western Truong Son, An Khe gauge (upstream of the Ba River) representing for the Middle and Song Hinh gauge (on the Hinh river) representing for the Eastern Truong Son. All results are at good level (Nash Sutcliffe from 0.68–0.81 for calibration and 0.69–0.77 for validation—(Table 1). These model parameters at these 3 gauges are used to simulate river flows for other tributaries in the basin according to 3 climate zones.

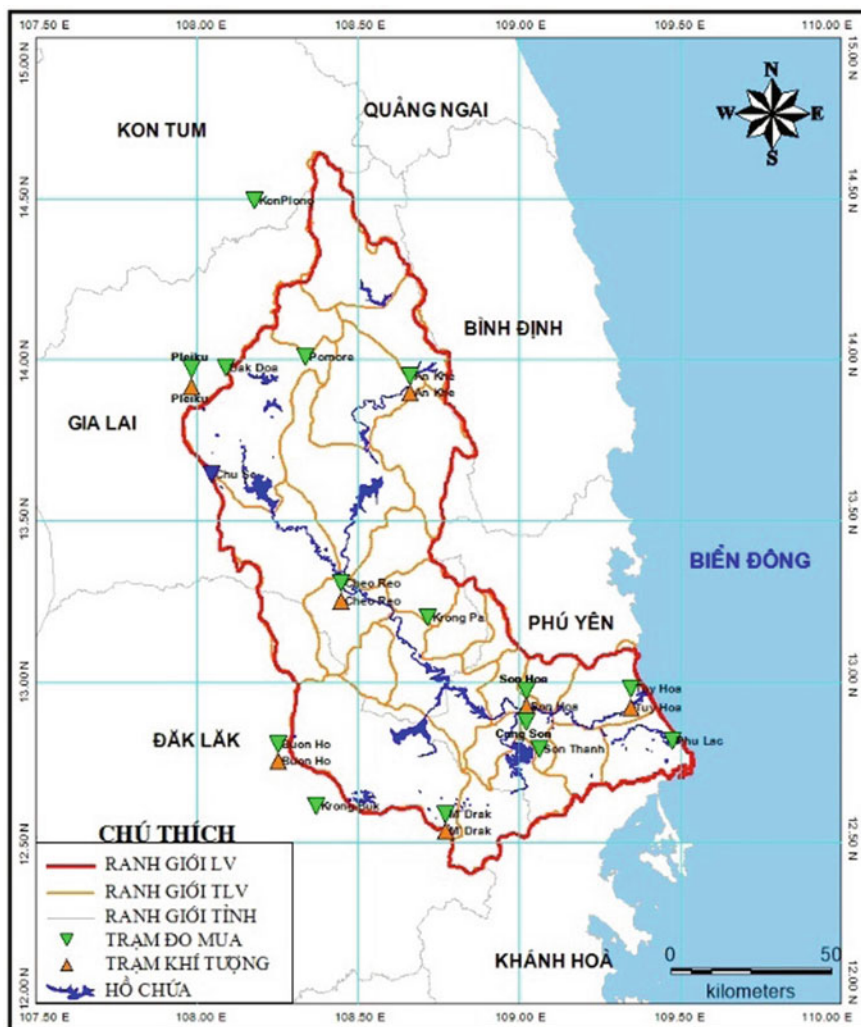


Fig. 2 Meteorological and hydrological gauges used in the research

Table 1 Calibration and validation results for 3 hydrologic gauges in the BRB

Gauges	Time period		Nash-Sutcliffe	
	Calibration	Validation	Calibration	Validation
An Khê	1980–1989	1990–1999	0.74	0.72
Sông Hình	1980–1989	1990–1995	0.68	0.77
Pô Mô Rê	2005	2006	0.81	0.69

2.2.2 Water Demand Calculation

Input data:

- Observed daily meteorological data at 7 meteorological gauges across the basin;
- Actual cultivated area data from Statistical Yearbook of the 3 provinces in 2016;
- Actual scale of water sectors from Statistical Yearbook of the 3 provinces in 2016.

Calculation process:

Water demand for water balance calculation is the actual water demand of irrigation and other sectors (domestic, industrial, livestock, aquaculture...) in the basin in 2016.

2.2.3 Water Balance Calculation

Diagram of the BRB water balance calculation is presented in Fig. 3, including 12 water reservoirs and Dong Cam dam, 45 irrigation nodes (which are in symbol IRR) and 8 water supply nodes (which are in symbol WSP) (53 nodes in total). Time step for water balance calculation is daily period. The version 2014 of model Mike Hydro is applied to:

- Calculating water balance in typical drought year to determine threshold of the system;
- Calculating water balance in changing climate conditions in order to identify climate response of the system.

2.3 Method for Identification of Climate Response and Vulnerability Space of the BRB System

Identification of climate response of the BRB bases on 2 assumptions: (1) only 2 climate variables of temperature and precipitation are changed, while other variables such as humidity, wind speed are unchanged in future; (2) Changing magnitude of future temperature and precipitation is the same in entire the BRB and in entire calculation periods.

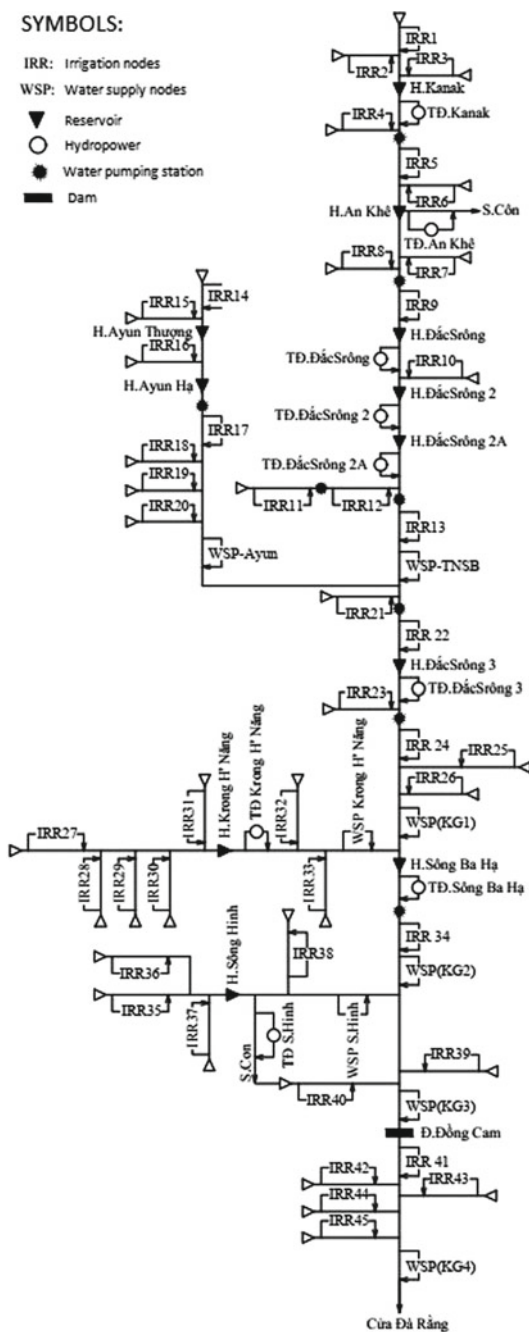
The process is implemented by parametrically varied temperature and precipitation. The system models which are already established are used to calculate reliability of water demand nodes corresponding to different inputs of climate variables. Since then, climate response of each water demand node is built.

$$\mathbf{R}_i = \mathbf{f}_i(\mathbf{T}, \mathbf{P}) \quad (1)$$

Fig. 3 Diagram of the BRB water balance calculation

SYMBOLS:

- IRR: Irrigation nodes
- WSP: Water supply nodes
- ▼ Reservoir
- Hydropower
- Water pumping station
- Dam



where: R_i : Reliability of node i

T, P: Magnitudes of temperature and precipitation changing compared to the baseline.

2.3.2 Identification of Vulnerability Space of the BRB System

After determining the climate response of each water demand nodes $R_i = f_i(T, P)$, combined with the pre-determined performance threshold (R_{th}), the climate change space is divided into different states which favors different optimal decisions. If the decisions can be made for water delivery system in the BRB are Action and No Action, the climate state which is under the threshold corresponds to Action decision is called problematic condition. In other words, in that climate state, performance of the hydrologic system is unacceptable, and it is necessary to apply adaptive measures. In the rest climate state, performance of the system is changed, but under acceptable condition, so it is not necessary to apply any actions.

2.4 Climate Projection for the BRB System

Daily projected temperature and precipitation from total 43 members of 21 GCMs with different AR5 scenarios (RCP2.6, RCP4.5, RCP6.0, RCP8.5) of Intergovernmental Panel on Climate Change (IPCC) are exploited from website of Program for Climate Model Diagnosis & Intercomparison (<http://cmip-pcmdi.llnl.gov/cmip5/>) on 15th March 2018 for 3 future periods: (1) Near future 2016–2035; (2) Mid-century 2046–2065; (3) End-century 2080–2099. These outputs are interpolated from grid points onto the coordinates of the above 7 temperature and 16 precipitation gauges by bilinear interpolation method and then systematic error adjusted by quantile mapping procedure [2].

Climate projections according to Scenarios of Climate change and Sea level rise of the Ministry of Natural Resources and Environment (SCS-MONRE) [8] in RCP 4.5 and RCP 8.5 are also exploited for the BRB.

All these projected temperature and precipitation are drawn into the climate response surface of the water demand node.

2.5 Projected Climate Risk Assessment for the BRB

In the final step, a climate risk of the BRB system is estimated. Risk is constituted by likelihood of a certain intensity of a hazardous event and consequences that the hazardous event causes on the research system [3].

Table 2 Reliability thresholds of water sectors in 3 climate zones (%)

Water sectors	Eastern zone	Western zone	Middle zone
Irrigation (Cultivation)	80	80	70
Water supply	80	80	90

$$R = \int_0^{\infty} C(x) f(x) dx \quad (2)$$

where: $f(x)$ is the probability density function (pdf) of the event
 $C(x)$ is the consequences associated with the event on the system.

In this research, in assessment of projected climate risk of each water demand node, consequences refer to the scale of water sectors in the interest node, i.e. area of crops or industrial park, population living in the area, number of cattle and poultries using water from the river system... Likelihood of a certain intensity of a hazardous event refers to the probability of the problematic condition of that water demand node, i.e. the climate states that make water delivery in that node get failed.

3 Results and Discussions

3.1 Performance Threshold of the Ba River Basin

According to the Delphi process, in order to determine performance thresholds for the BRB system, 2012, 2014, 2015 are chosen for typical drought years of the Western, the Eastern and the Middle zone in the basin, respectively. The hydrological model MIKE NAM and system model MIKE HYDRO are used to simulate river flow and calculate water balance of the river basin in these years. The lowest reliability among different types of water demand nodes in the aforementioned typical year corresponding to each climate zone is considered as threshold for that water demand node (Table 2).

3.2 Climate Response and Vulnerability Space of the Ba River Basin System

The analysis of 43 GCM outputs shows that, annual precipitation in the BRB is predicted to change from -7.1% to $+55.8\%$, while temperature is varied from $+0.52$ to $+5.63$ $^{\circ}\text{C}$. Totally 87 model runs are performed with ensembles of changed temperature from 0 to $+3.5$ $^{\circ}\text{C}$ and changed precipitation from -15% to $+35\%$ compared to

the baseline (1986–2005) in order to determine the corresponding reliability of the 53 water demand nodes. The climate response surfaces of different water demand nodes are thus determined. These climate response surfaces are expanded to different values of temperature and precipitation changes by interpolation procedure.

The climate response surfaces of different water demand nodes are combined with the thresholds defined above to determine vulnerability space of the system. The results show that, in the range of changed temperature and precipitation analyzed, out of 53 water demand nodes in the entire of the BRB, there is not any water supply node under the threshold. For irrigation nodes, there are totally 27 irrigation nodes which are above the threshold in every changing condition of climate state, including IRR3, IRR4, IRR5, IRR6, IRR7, IRR8, IRR9, IRR10, IRR11, IRR12, IRR13, IRR14, IRR15, IRR17, IRR18, IRR22, IRR24, IRR31, IRR32, IRR33, IRR34, IRR35, IRR36, IRR37, IRR39, IRR40, IRR41, which are equivalent to 27,558.14 ha of crops. That means these areas of crops are not necessary to apply adaptive measures in any condition of future climate.

Out of 18 vulnerable irrigation nodes, there are 5 irrigation nodes having reliability under the threshold in every condition. They are IRR2, IRR16, IRR23, IRR42, IRR43, equivalent to 3674.65 ha of crops. The rest 13 irrigation nodes have reliabilities under the thresholds in a certain condition, and above the thresholds in the other condition. They include IRR1, IRR19, IRR20, IRR21, IRR25, IRR26, IRR27, IRR28, IRR29, IRR30, IRR38, IRR44, IRR45, which are equivalent to 13,596.03 ha of crops. An example for this circumstance is Fig. 4, in which response function and vulnerability space of IRR21 is presented. It can be seen that, reliability of IRR21 is moderately sensitive with changes in temperature, but considerably sensitive with changes in precipitation. About 10% increase in precipitation compensates for reliability reduction when temperature increases by 3 °C. In the baseline (P change = 0

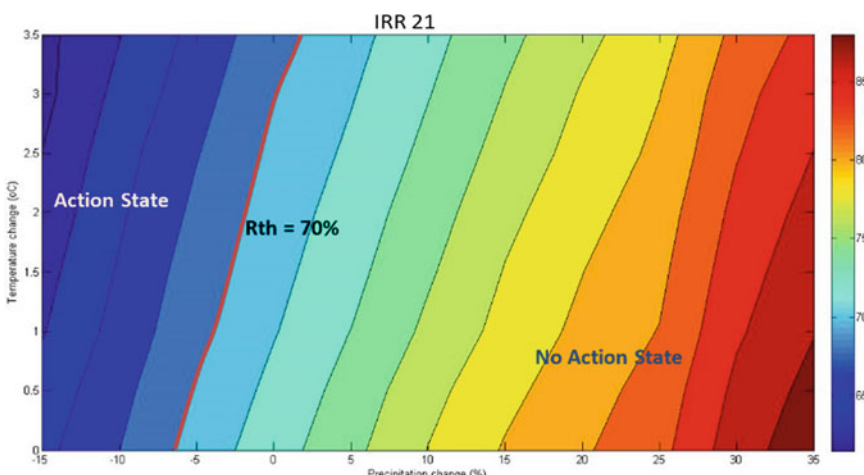


Fig. 4 Response function and vulnerability space of IRR21

and T change = 0), reliability of IRR21 is above the threshold. In future, if temperature is unchanged and precipitation decreases by more than 6.5%, this node would become failed and need adaptive action plans. However, if temperature increases by 1.5 °C, only 2.5% decrease of precipitation would make this node become failed.

Table 3 shows areas of crops corresponding to number of irrigation nodes in entire of the BRB faced with water shortage when average temperature and annual precipitation varies. In the unchanged temperature and precipitation compared with the baseline period, there are 6,642.85 ha of crops damaged. In the worst case, when average temperature increases by more than 2°C and annual precipitation decreases by 15%, this crop areas can be up to 17,270.68 ha. In the best case, when annual precipitation increases by more than 25%, the damaged crop areas can be narrowed to 3,674.65 ha.

3.3 Climate Projections for the Ba River Basin

In future, most of GCM outputs show an increase of both average temperature and precipitation in the BRB, with higher uncertainties in the far future. For average temperature, the largest number of GCMs show increased average temperature by 0.7, 1.2 and 1.8 °C in the near future, mid-century and end-century, respectively. These increases of precipitation are 10%, 17% and 17%, respectively.

3.4 Projected Climate Risk Assessment of the BRB

Adding scatter plots of 43 GCM outputs and SCS-MONRE for RCP4.5 and RCP8.5 into climate response surface of each water demand node, it can be seen the dispersion of plausible future climate conditions between 2 climate states. Figure 5 is an example for IRR30, in which most of GCM outputs concentrate in the Action State in the near future period. However, in mid-century and end-century periods, the situation of this node may get better when more GCM outputs come into the No Action State.

The projection for IRR30 by SCS-MONRE in both RCP4.5 and RCP8.5 are under the threshold. However, it can be seen that there are many other possibilities of future climate states, including which are under and above the threshold that SCS-MONRE do not mention in their results.

Out of 18 vulnerable irrigation nodes, there are 4 nodes which all GCM outputs come into the No Action state. Relative probabilities of the Action State and No action State of the rest vulnerable 14 irrigation nodes, including IRR19, IRR20, IRR21, IRR26, IRR27, IRR29, IRR30, IRR38, IRR44, IRR2, IRR16, IRR23, IRR42, IRR43, are quantified in Fig. 6. Back to the above example, likelihood of Action state of IRR30 to occur in the near future, mid-century and end-century are 97.8%; 90.7% and 88.4%, respectively.

Table 3 Areas of crops faced with water shortage in changing precipitation and temperature condition (ha)

T change (°C)	P change (%)	-15	-10	-5	0	+5	+10	+15	+20	+25	+35	+60
0	16,325.05	16,195.05	10,038.75	6,642.85	6,642.85	5,670.75	4,309.62	4,309.62	3,674.65	3,674.65	3,674.65	3,674.65
+0.5	16,325.05	16,195.05	10,038.75	10,038.75	6,642.85	5,670.75	4,926.68	4,309.62	3,674.65	3,674.65	3,674.65	3,674.65
+1	16,325.05	16,195.05	12,055.75	10,038.75	6,642.85	6,642.85	4,926.68	4,309.62	4,309.62	3,674.65	3,674.65	3,674.65
+1.5	16,325.05	16,195.05	13,957.05	10,038.75	6,642.85	6,642.85	4,926.68	4,309.62	4,309.62	3,674.65	3,674.65	3,674.65
+2	17,270.68	16,195.05	16,195.05	10,038.75	6,642.85	6,642.85	5,670.75	4,926.68	4,309.62	3,674.65	3,674.65	3,674.65
+2.5	17,270.68	16,325.05	16,195.05	12,020.75	10,038.75	6,642.85	5,670.75	4,926.68	4,309.62	3,674.65	3,674.65	3,674.65
+3	17,270.68	16,325.05	16,195.05	13,957.05	10,038.75	6,642.85	6,642.85	4,926.68	4,309.62	3,674.65	3,674.65	3,674.65
+3.5	17,270.68	16,325.05	16,195.05	16,039.05	10,038.75	6,642.85	6,642.85	4,926.68	4,309.62	3,674.65	3,674.65	3,674.65

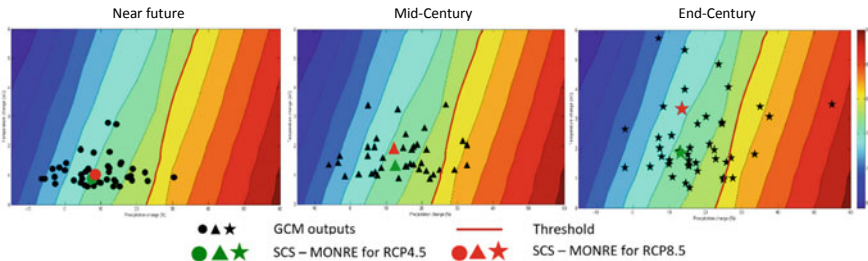


Fig. 5 Scatter plot of projected mean temperature and precipitation change over 3 periods adding into climate response surface of IRR30

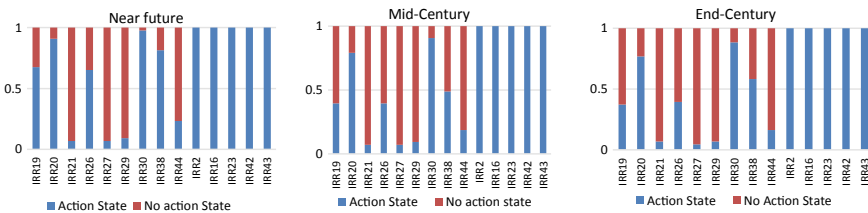


Fig. 6 Relative probability of different climate states which favor different decision options

Figure 6 also indicates number of irrigation nodes, which are equivalent to corresponding areas of crops, facing with failure situation of water delivery in a certain of likelihood of occurrence. These numbers are illustrated in Table 4. With the climate state which have 25% of likelihood, there are 10 irrigation nodes, which are equivalent to 6,642.75 ha of crops, getting failed and need adaptive measures in all future periods. In other words, with 25% of climate probability, the BRB is at risk of 6,642.75 ha of damaged crops in future. With 50% of climate probability, the crop areas at risk are 6,642.75 ha in near future; 4,926.62 ha in Mid-century and 5,670.75 ha in End-century. With 75% of climate probability, these numbers are 5,670.75 ha; 4,926.62 ha and 4,926.62 ha in near future, mid-century and end-century, respectively.

Table 4 Areas of crops damaged corresponding to different probabilities of climate states

Probability (%)	Near future		Mid-Century		End-Century	
	Number of nodes failed	Area of crops damaged (ha)	Number of nodes failed	Area of crops damaged (ha)	Number of nodes failed	Area of crops damaged (ha)
25	10	6,642.75	10	6,642.75	10	6,642.75
50	10	6,642.75	7	4,926.62	8	5,670.75
75	8	5,670.75	7	4,926.62	7	4,926.62

It can be seen that, in the traditional top-down approach, the questions posing are “What is future climate state? What are consequences of that state to the interest system?”. With the results obtained in this research, the Decision scaling approach answers two questions at once “For a specific system, what is the likelihood of the climate state which favors a certain decision in future? For the entire of the basin, with different likelihoods of future climate state, what are the corresponding consequences to the interest system?”. Such an approach will have many benefits, including: (1) this approach uses a large number of GCMs, thus considering the many possibilities of future climate in the basin; (2) the result is estimating the likelihood of different climate states, instead of focusing only on certain socio-economic scenarios or certain greenhouse gas emissions scenarios, thus it is more reliable; and (3) the defined climate states are directly linked to decision making, hence this result well supports policy makers to propose adaptive measures for the system.

4 Conclusion

This paper adopts Decision Scaling approach to assess impacts of climate change on water shortage in the BRB. Performance thresholds of the 3 climate zones are identified by participatory method. System models including rainfall-runoff Mike Nam model, water balance Mike Hydro model and water demand calculation tool are established. Entire of the BRB is divided into 45 irrigation and 8 water supply nodes. Temperature and precipitation are parametrically varied to determine system climate response function and climate vulnerability space of water shortage in the basin. Total 43 GCM outputs are used in very last step of assessment to estimate relative probability of successful and failed situations of different water demand nodes in 3 future periods. The results show:

- All 8 water supply nodes and 27 irrigation nodes are over the threshold with every climate change condition.
- There are 5 nodes that every GCM outputs come into the successful space.
- The rest 13 irrigation nodes are vulnerable to climate change in a certain number of GCM outputs.

Relative likelihood of the 2 climate states, including Action state and No Action state, of each water demand node is determined. In addition, the research also calculates areas of damaged crops in the entire BRB corresponding to different likelihood of future climate condition.

References

1. Amengual A, Homar V, Romer R, Alonso S, Ramis C (2012) A statistical adjustment of regional climate model outputs to local scales: application to Platja de Palma, Spain. *J Clim* 25(3):939–957

2. Brekke LD, Kiang JE, Olsen JR, Pulwarty RS, Raff DA, Turnipseed DP, Webb RS, White KD (2009) Climate change and water resources management—a federal perspective. US Geol Surv Circular 1331:65
3. Brown C, William W, Wendy L, David F (2011) A decision-analytic approach to managing climate risks: application to the upper great lakes. *J Am Water Resour Assoc (JAWRA)* 47(3):524–534. <https://doi.org/10.1111/j.1752-1688.2011.00552>
4. Brown C, Ghile Y, Laverty M, Li K (2012) Decision scaling: Linking bottom-up vulnerability analysis with climate projections in the water sector. *Water Resour Res* 48(9):1–12
5. Huynh TLH (2013) Impacts of climate change on Ba River flow. *J Water Resour Sci Technol* 13:71–79 (In Vietnamese)
6. IWARP (2018) Project synthesis report: adjusting irrigation planning of the Ba River Basin and vicinity area until 2025 and vision until 2035
7. Mays LW (1987) Review of advances in risk and reliability analysis for hydraulic structures. Application of frequency and risk in water resources, V. P. Singh, Dordrecht edited. Springer Netherlands, pp 227–262
8. MONRE (2016) Climate change, sea level rise scenarios for Vietnam
9. Tra TV, Thinh NX, Greiving S (2018) Combined top-down and bottom-up climate change impact assessment for the hydrological system in the Vu Gia-Thu Bon River Basin. *Sci Total Environ* 630:718–727
10. Whateley S, Steinschneider S, Brown C (2014) A climate change range-based method for estimating robustness for water resources supply. *Water Resour Res* 50:8944–8961

Development of Africa Wild Dog Optimization Algorithm for Optimize Freight Coordination for Decreasing Greenhouse Gases



Pham Vu Hong Son and Tran Trong Khoi

1 Introduction

With the strong development of society, the demand for movement and transportation is increasing. The use of transportation means leads to an increase in emission concentration, which directly affects human health and the living environment. In addition, the current means of transportation, mostly using fossil fuels, reduce the amount of limited resources. With many negative impacts on the environment and human health, the use of transport means to move, and delivery does not show signs of diminishing, but increases gradually according to the increasing social needs of people.

Currently, many countries are researching and replacing fossil fuel transportation vehicles with electric vehicles, using biofuel, etc. These are positive signs, but there are still many limitations when applied to practice and need a long time to change. This study sets out the goal of reducing the movement and transport needs of vehicles by optimizing their use. It helps vehicles reduce the use of fossil fuels, reduce emissions to the environment and increase productivity at work. The initiative is to create a new optimal algorithm called the Africa Wild Dogs (Wild Dogs), which is inspired by an organized hunting specialist. The study of this breed of dogs created WDO algorithm based on their hunting. The algorithm helps to make the most optimal travel plan for vehicles in the optimal mode of time and distance.

P. V. H. Son · T. T. Khoi (✉)

Faculty of Civil Engineering, Ho Chi Minh City University of Technology, VNU-HCM, Ho Chi Minh City, Vietnam

e-mail: trongkhoi.st@gmail.com

2 Research Overview

Optimization algorithms were created quite early, especially with many achievements in the field of herd optimization algorithm research. Many optimization algorithms developed from herding behavior have recently been invented [4, 7–10]. These new algorithms quickly gain the attention of the scientific community around the world and are applied to solve many practical problems related to local optimization and global optimization. One of the practical applications of the optimal algorithm is to optimize the transport process, one of the most studied topics in the last 10 years [5, 6, 14]. A lot of research has been done to solve the optimal problem of time, the cost of the transport process and almost apply most existing optimization algorithms to solve this problem [3, 12, 15].

However, previous studies still have many unsolved problems such as the running time of the program too long, the assumptions are not close to reality, the working environment is almost perfect, the lack of tight binding conditions [1, 2], although there have been marked improvements in the approach to the problem and the introduction of new, more effective solutions [11, 13]. This study refers to the use of the African wild dog optimization algorithm in combination with event simulation, with updated density and mobility calculation parameters to plan traffic coordination so that the multi-goal optimization is both distance and travel time. In the process of algorithm development, the computational results have become more and more optimal, thanks to the experience, inheritance and development to solve the problems of the previous algorithm, from which the results are superior. Therefore, this research proposes a new algorithm, takes advantage of the previous optimization algorithms and develops more modern algorithms to overcome remaining shortcomings, and is verified to solve specific transport cases.

3 Methodology

3.1 *African Wild Dog Algorithm*

Inspiration of algorithm development

African Wild Dog is a dangerous and agile hunting specialist. They hunt with swarms and high determination. A swarm of dogs with a population of 5–20 are usually ruled by a pair of leaders who are responsible for breeding and managing operations. As shown in Fig. 1, it is the organized and well-planned hunting activities that turn the African wild dogs into the best hunters on the planet. In the structure of dogs, there is usually a pair of leaders consisting of Husband (H) and Wife (W), which are responsible for managing the whole flock of dogs, making decisions, controlling, hunting, and resting, etc. When observing activities of dogs, scientists recognize democratic behaviors in the organization. In addition to the two individuals (H) and (W), the wild dogs also have spies experts called Search (Sa) and (Sb). They together

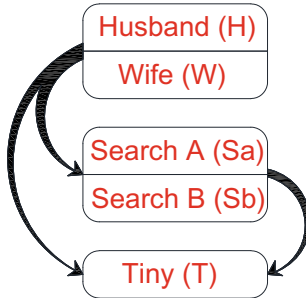


Fig. 1 Organizing chart of African wild dogs



Fig. 2 Simulation of prey surrounding activity (Photo: NATGEO WILD)

with Husband and Wife are responsible for finding their prey, assessing their potential and coordinating the control of the dogs to attack. (Sa) and (Sb) are pairs of dogs that have experienced in hunting, they are candidates to replace the pair of leaders or become leaders when separating. Except for offspring's that cannot go hunting, the remaining individuals in the flock, if not Husband, Wife or Search, are called Tiny (T) individuals (see Fig. 2).

Depending on the type of prey, size and terrain, the dogs have many different tactics such as surrounding, snaring, and raiding. In particular, there are the following main activities: (1) Find and approach prey; (2) Review and vote for attacks; (3) Follow, surround the prey until it stops moving; (4) Harass the prey until it stops moving; (5) Attack the prey.

Algorithm mathematical model

In this section, the mathematical models of the social hierarchy, tracking, surrounding and attacking preys are provided. Then the WDO algorithm is sketched. The object-oriented algorithm searches, approaches, encapsulates the optimal plan and ultimately attacks.

Social hierarchy: When mathematically modeling the social hierarchy of wild dogs during designing WDO. I consider the best solution is (H). Therefore, the second, third and fourth best solutions are named (W), (Sa) and (Sb), respectively. The rest of the candidate solutions are assumed to be (T). In the WDO algorithm,

hunting (optimization) is done mainly by (T) under the instructions of (H), (W), (Sa) and (Sb).

Surrounding the prey: In order to be able to use it in mathematical simulations, we describe behavior based on the equations below, with variable t showing the repetition of the algorithm during the search of the object.

$$\vec{A} = \left| \vec{D}(t) - \vec{B} \cdot \vec{D}_p(t) \right| \quad (1)$$

$$\vec{D}(t+1) = \vec{D}_p(t) - \vec{A} \cdot \vec{K} \quad (2)$$

In which, vector \vec{A} is a search-oriented vector, created based on vectors \vec{B} representing prey position \vec{D}_p and vector \vec{D} showing wild dog position. The vectors \vec{K} and \vec{B} are searched through the following equations:

$$\vec{K} = \vec{r}_1 - 2\vec{a}\vec{r}_2 \quad (3)$$

$$\vec{B} = 2 \cdot \vec{r}_3 \quad (4)$$

During iteration, vector \vec{a} is reduced linearly from 1 to 0 and $\vec{r}_1, \vec{r}_2, \vec{r}_3$ are random vectors, these vectors ensure randomness in the algorithm. For example, we consider a 2-dimensional vector matrix as shown in Fig. 3a, which describes the wild dogs' surrounding activity. Wild dogs (T) with coordinates in positions (X, Y) will update the new position according to the position of their prey (X^*, Y^*) .

To adjust the location of wild dogs, we use vectors \vec{K} and \vec{B} . These vectors have a random element, which allows the wild dogs to attack their prey or go away, meaning that they support updating the position of wild dogs (T) in the flock. *Hunting (searching):* During the surrounds, wild dogs (T) are guided by wild dogs (H), (W), (Sa), (Sb). To mathematically simulate the hunting behavior of wild dogs, we look at the four best options that represent the four best individuals to guide changes in other alternatives. Therefore, we keep the first four best solutions obtained so far and

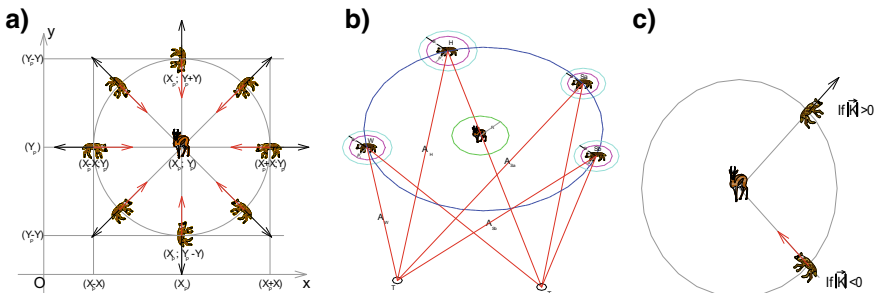


Fig. 3 **a** Surrounding model; **b** Hunting model and **c** Selecting attack or skip the prey

force search (T) agents to update their locations according to the best search agents' locations. The following formulas are proposed on this issue.

$$\vec{A}_H = \left| \vec{D} - \vec{B}_1 \cdot \vec{D}_H \right|, \vec{A}_W = \left| \vec{D} - \vec{B}_2 \cdot \vec{D}_W \right|, \vec{A}_{Sa} = \left| \vec{D} - \vec{B}_3 \cdot \vec{D}_{Sa} \right|, \vec{A}_{Sb} = \left| \vec{D} - \vec{B}_4 \cdot \vec{D}_{Sb} \right| \quad (5)$$

$$\begin{aligned} \vec{D}_1 &= \left| \vec{D}_H - (\vec{A}_H) \cdot (\vec{K}_1) \right|, \vec{D}_2 = \left| \vec{D}_W - (\vec{A}_W) \cdot (\vec{K}_2) \right| \\ \vec{D}_3 &= \left| \vec{D}_{Sa} - (\vec{A}_{Sa}) \cdot (\vec{K}_3) \right|, \vec{D}_4 = \left| \vec{D}_{Sb} - (\vec{A}_{Sb}) \cdot (\vec{K}_4) \right| \end{aligned} \quad (6)$$

$$\vec{D}_{(t+1)} = \frac{\vec{D}_1 + \vec{D}_2 + \vec{D}_3 + \vec{D}_4}{4} \quad (7)$$

Figure 3b. simulates the hunting process of elite individuals. Based on experience, elite individuals can form a good area to surround the prey and guide the remaining individuals. When conducting mathematical simulations, new alternatives are randomly generated within the potential that the four best options orient.

Searching the prey (finding): A component of the WDO that supports searching is \vec{B} . As can be seen in the Eq. 4, vector \vec{B} contain random values in $[0, 2]$. This component provides random weight for the prey to randomly emphasize ($|\vec{B}| > 1$) or when ($|\vec{B}| < 1$) the effect of prey in determining the distance in the expression (refer to Eq. 1). This supports WDOs displaying a more random behavior throughout optimization, favoring exploration and avoiding local optimization. It is worth mentioning here that there is \vec{B} no linear reduction as opposed to \vec{K} . We intentionally ask for \vec{B} random values at all times to emphasize exploration not only in the initial iteration but also in the last iteration. This component is very useful in case of local optimization delays, especially in the last iteration.

Voting attack: In fact, before a flock of wild dogs strikes their prey, Husband will usually hold a vote by “sneezing.” It is a unique feature that represents the community of wild dogs. It makes Husband's decision-making safer and more supportive. So, once a prey has been surrounded, there is still a possibility that the attack plan is canceled (diverging from the prey) probably because the attack may endanger the dogs.

Attacking the prey (exploiting): As mentioned above, dogs end the hunt by attacking the prey when it stops moving. In order for the mathematical model to approach the prey we reduce the value of \vec{a} . Note that the oscillation range of \vec{K} also reduces. Figure 3c shows that $|\vec{K}| < 0$ forces the dogs to attack the prey. With the proposed options to date, the WDO algorithm allows searchers to update their location based on the position of H, W, Sa, Sb and attack the prey. In summary, the search process begins by creating a random population of wild dogs (candidate solution) in the WDO algorithm. During repetition, the dogs H, W, Sa and Sb estimate the possible position of the prey. Each candidate solution updates its distance with prey. Parameter a has been reduced from 2 to 0 to emphasize searching and attacking accordingly.

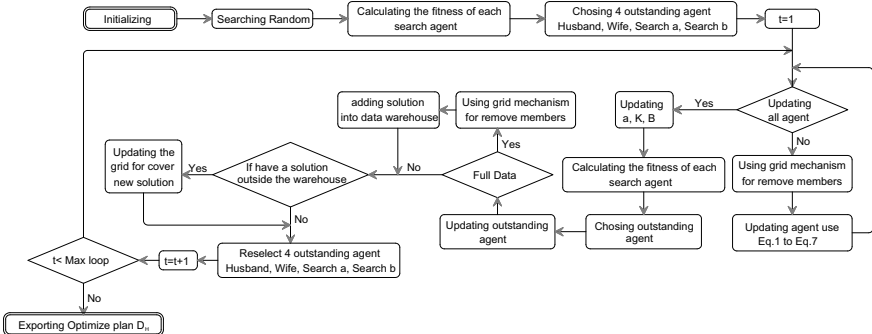


Fig. 4 WDO Wild Dog algorithm chart

Candidate solutions tend to separate from prey when $|\vec{K}| > 1$ and converge towards prey when $|\vec{K}| < 1$. Finally, the WDO algorithm is terminated by the satisfaction of one final criterion.

The proposed social hierarchy assists WDO to store the best solutions obtained so far in the iteration process as shown in Fig. 4. The proposed enclosure mechanism defines a circular neighborhood around solutions that can be extended more dimensionally as a sphere. The proposed hunting method allows candidate solutions to determine the probable location of the prey. Searching and exploration are ensured by the adaptive values of a and K . The adaptive values of the parameters a and K allow WDO to switch smoothly between searching and exploration. WDO has two main parameters to be adjusted (K and B). It is able to integrate mutants and other evolutionary operators to mimic the entire life cycle of wild dogs.

4 Application of Wild Dog Algorithm to Solve the Problem of Concrete Transportation

Nowadays, many companies selling commercial concrete tend to rely on the coordinators with a lot of experience to make concrete vehicle distribution plans to customers manually, this will make the vehicle distribution schedule to the construction site not really optimal, the workload is not being optimized leading to waste of time and, in particular, the cost of investing in vehicles when available resources are not fully utilized. The study of a concrete station distributing goods to many construction sites has been tested on a number of different algorithms, here, the study will compare the African wild dog algorithm with the multi-purpose artificial bee algorithm MOABC. Comparison chart is assessed through the following common problem (see Table 1).

Vehicle speed when going: 40 km/h; Vehicle speed when returning: 50 km/h; Vehicle capacity: 6 m³; Number of vehicles at the mixing plant: 20 vehicles; Time

Table 1 Table of data used to compare two different algorithms

No.	Commencement time of the construction site (SCT)	Amount of concrete ordered	Detail of concrete ordered by the construction site (PT)	Distance from the mixing plant to the construction site (DJ-Km)	Maximum waiting time for vehicles	Maximum waiting time for construction sites
1	8:00	18	Floor	10	45	45
2	8:15	24	Beam	8	45	45
3	8:30	24	Column	15	45	45
4	8:00	30	Floor	10	45	45
5	8:20	12	Beam	9	45	45
6	8:30	12	Column	8	45	45
7	9:00	30	Floor	10	45	45
8	8:00	30	Beam	6	45	45
9	8:30	18	Column	9	45	45
10	9:10	36	Floor	12	45	45
11	8:40	30	Beam	13	45	45
12	8:30	18	Column	7	45	45

to inject concrete into the vehicle: 1 (minutes/m³); The artificial bee algorithm is set with the following parameters: (1) Number of tests: 30; (2) Initial number of bees: 50; (3) Number of generations for each iteration: 10 generations; (4) Number of repetitions: 300 times. Details of the search results are shown in Fig. 5 and Table 2.

Through the results of the experiment, it is easy to recognize that the African Wild Dog algorithm brings very competitive results compared to previous algorithms even

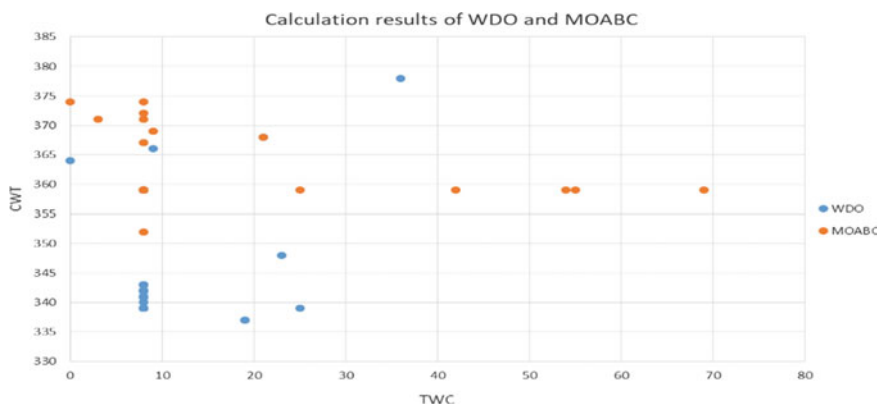
**Fig. 5** Comparison of the found results between the two algorithms MOABC & WDO

Table 2 Distribution chain value for 2 outstanding values between the two found criteria CWT and TWC via the WDO algorithm

Result	Distribution chain	TWC (min)	CWT (min)
No1	[b84aac9718a997a27b8a8355c4c2b4428342ba7667b3131]	19	337
No2	[44391c834b775aab4217793a3a42216bc298a6a88bb85c5]	0	343

(a denotes work 10, b denotes work 11, c denotes work 12)

TWC (Truck wait construction): The total time the truck waits for construction site

CWT (Construction wait truck): The total time the construction site waits for the truck

The simulation result in the table has been demonstrated that WDO is much superior to MOABC in which the total waiting time of construction is just 337 minutes in case No.1 and total waiting time of truck is zero in case No.2. The significance of bold in the table is represented for the best optimal results where CWT and TWC have reached to the smallest value

some of the superior results. The use of SI search mechanism compared with EA search mechanism of artificial bee algorithm (MOABC) has helped the ability to search results faster and less time because the search process always retains results of previous generations.

5 Conclusions and Recommendations

The proposed algorithm has demonstrated it's preeminent compare to previous study. In the search of the optimal agents with reassessment, considering the possibility of changing the direction of the search to avoid local optimization. In addition, this model can suggest many other researches works in fields of life. It is suitable for finding a solution to a problem, especially problems with a huge selection of options that people cannot assess in all cases.

In this research, there are still some limitations that could be improved in the future. The matrix showing the vehicle density in this study is proposed to be derived from satellite data. However, the extraction of data from satellites is less accurate and delayed. In the future, when the streets are fully equipped with surveillance cameras, we can use the cameras to provide fast and accurate traffic data, forming part of the smart city.

References

1. Afrapoli AM et al (2019) A multiple objective transportation problem approach to dynamic truck dispatching in surface mines. *Eur J Oper Res* 276(1):331–342
2. Anson M et al (2019) Analytical models towards explaining the difficulty in efficiently matching site concrete supply resources with placing crew needs. In: Engineering, construction and architectural management

3. Cheng M-Y, Tran D-H (2015) Integrating chaotic initialized opposition multiple-objective differential evolution and stochastic simulation to optimize ready-mixed concrete truck dispatch schedule. *J Manage Eng* 32(1):04015034
4. Faris H et al (2018) An efficient binary salp swarm algorithm with crossover scheme for feature selection problems. *Knowl-Based Syst* 154:43–67
5. Hsiao W-T et al (2011) A hybrid optimization mechanism used to generate truck fleet to perform earthmoving operations. In: *Road materials and new innovations in pavement engineering*, pp 151–159
6. Mayteekrieangkrai N, Wongthatsanekorn W (2015) Optimized ready mixed concrete truck scheduling for uncertain factors using bee algorithm. *Songklanakarin J Sci Technol* 37(2):221–230
7. Mirjalili S (2015) The ant lion optimizer. *Adv Eng Softw* 83:80–98
8. Mirjalili S, Lewis A (2016) The whale optimization algorithm. *Adv Eng Softw* 95:51–67
9. Mirjalili S et al (2014) Grey wolf optimizer. *Adv Eng Softw* 69:46–61
10. Mirjalili SZ et al (2018) Grasshopper optimization algorithm for multi-objective optimization problems. *Appl Intell* 48(4):805–820
11. Sarkar D et al (2019) Optimization of ready mixed concrete delivery for commercial batching plants of Ahmedabad, India. *Int J Constr Manage* 1–20
12. Subtil RF et al (2011) A practical approach to truck dispatch for open pit mines. In: *35th APCOM symposium*
13. Thanos E et al (2019) Dispatch and conflict-free routing of capacitated vehicles with storage stack allocation. *J Oper Res Soc* 1–14
14. Yan S et al (2011) Optimal schedule adjustments for supplying ready mixed concrete following incidents. *Autom Constr* 20(8):1041–1050
15. Zhang X et al (2019) Optimization of truck appointments in container terminals. *Maritime Econ Logistics* 21(1):125–145

Estimating Values of the Can Gio Mangrove Ecosystem Services Using Remote Sensing



Nguyen Hoang Yen and Dao Nguyen Khoi

1 Introduction

Thanks to the efforts to restore the forested area of HCM City after a long period of war destruction, the Can Gio mangrove forest was recognized by UNESCO as “Can Gio Mangrove Biosphere Reserve” on January 21, 2000. Can Gio mangrove ecosystem contribute significant value to the development of socio-economic through the benefits such as timber, fish, tourism opportunities as well as environmental services (e.g., coastal protection, carbon sequestration, water regulating) [3]. Mangrove ecosystem also plays a key role in the local economy of the majority of people living in a coastal area that depend on mangrove for their livelihoods and main source of incomes. Studies from across the world indicate that the relative contribution of mangrove-related fish species to total fisheries’ catch estimates in the range of 10–32 percent [1].

However, because of the benefit of the ecosystem services bring, the mangrove ecosystem is known to be over-extracted by the local users [10]. The services provided by mangrove ecosystem, such as converting forest area into a shrimp pond, extensive fish catching, and caused the imbalance in biodiversity through tourism activity [3]. The negative impacts can result in the loss of area, loss of habitat, reduce its ability to protect the shoreline. Because of the interaction between the mangrove ecosystem services and socio-economic development, the estimation of the monetary value of ecosystem services of Can Gio mangrove forest is necessary for the conservation of biodiversity and ecosystem services in this region.

N. H. Yen

Faculty of Environment and Natural Resources, Ho Chi Minh City University of Technology,
VNU-HCM, Ho Chi Minh City, Vietnam

D. N. Khoi (✉)

Faculty of Environment, University of Science, VNU-HCM, Ho Chi Minh City, Vietnam
e-mail: dnkhoi@hcmus.edu.vn

The objective of the study was to estimate the monetary values of ecosystem services in the Can Gio mangrove forest by using a combination of land-use area data retrieved from the classification of Landsat 8 in 2017 and data collected from household surveys to quantify the direct use values of ecosystem (comprising firewood, aquaculture product, fishery-related, salt and tourism) and indirect use value, namely, carbon sequestration using the market price and benefit transfer. The obtained results are expected to provide useful information for local policy-makers for sustainable management of the Can Gio mangrove forest.

2 Methods

The framework of this study is designed to determine the service values of Can Gio mangrove ecosystem based on data retrieved from remote sensing and household survey methods as presented in Fig. 1.

The Can Gio area, including six communes and one town, is considered for the present study. Based on the literature review and observation, the values of ecosystem services, including direct use value (e.g. aquaculture, fish catch, salt product,

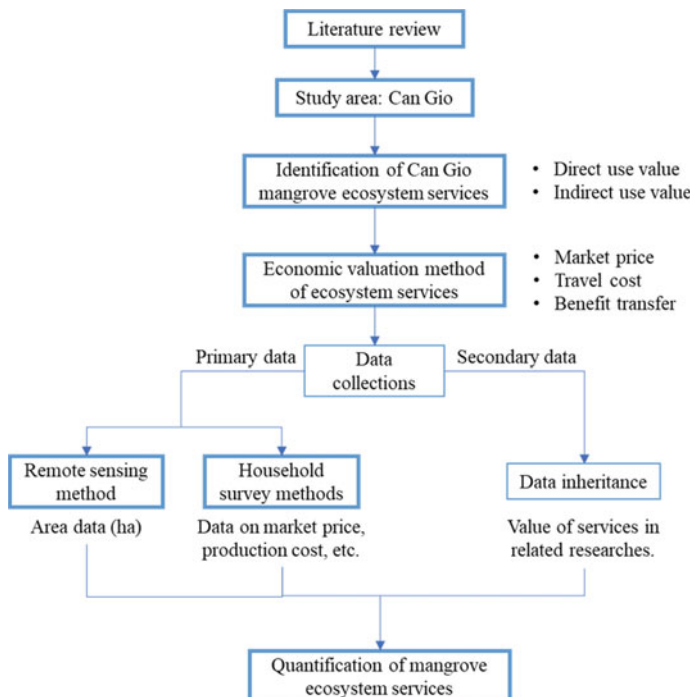


Fig. 1 The flow chart of research methodology

and firewoods/construction woods) and indirect use value (carbon sequestration and tourism) were identified. With the different services, different valuation methods, such as market price, benefits transfer, and travel cost have been applied based on the available data and literature review.

In this study, some ecosystem services (i.e., aquaculture, salt, and carbon sequestration) requires area data obtained from remote sensing as a basic input to determine the economic value. Other services not directly depend on the mangrove forest area, can be estimated using the product price value from local people activities, e.g. aquaculture farmers, salt farmers, which obtain from field survey or secondary sources.

According to Kuenzer et al. [5] provided an overview table of the methods used for the assessment of mangrove ecosystems during the past 20 years, it is shown that visual interpretation, NDVI, and pixel-based classification are the most commonly used research methods. An important mangrove-mapping method consists of visual-interpretation analysis with detailed ground information as reference input and digital classification by using pixel-based classification method. This study based on the method review of Kuenzer et al. [5] used Landsat 8 image as data, NDVI as a pre-classification step to separate mangrove from non-mangrove and pixel-based method to classify land-use type of Can Gio, and in pixel-based classification, the application of supervised Maximum Likelihoods Classifier is the most effective and robust method for classifying mangroves based on traditional satellite remote sensing data.

Two Landsat 8 images, took in 06/01/2016 and 14/02/2017 with the resolution of 30×30 m, are used for the whole study area. Using Supervised classification based on the mangrove classification result of NDVI and visual interpretation (via ROIs chosen from field observation and Google Earth) to generate the up-to-date land use map of Can Gio area, classified into seven main classes including aquacultural pond, settlement, salt farming, surface water, Avicennia, Rhizophora, and mixed trees.

The household survey includes two stages. The first stage was the development and pre-testing of a questionnaire to ensure that relevant questions were included and captured the most robust data. Based on the literature review and field survey, to identify the ecosystem services in Can Gio mangrove forest to question (e.g. aquacultural, salt farming). The survey used a semi-structured questionnaire with over 20 questions on different aspects of mangrove ecosystem services to interview the local residents which focus on aquaculture, fish catching, salt farming activities. The questionnaire includes the information on product types, production cost (include investment on pond rent, shrimp/fish seeds, foods, aerator pump, and repairing cost), as well as quantity of product per year. These are values that can be converted into money using the market price method with the following formula based on Kuenzer and Tuan [4]:

$$A = \sum (P_i Q_i - I_i)$$

In which: $A = \text{Net benefit (VND/ha/year)}$; $P_i = \text{Price of products}$; $Q_i = \text{Quantity of products}$; $I_i = \text{Investment of products}$; $i = \text{Product}$

After conducted the pre-test and revisioned the questionnaire survey, the second stage is to conduct the detailed survey of randomly 30 households in five communities, which was eventually reduced to 24 due to the lack of data provided

3 Results

The use of NDVI method is to classify the vegetation cover to non-vegetation, made it a reference to classify the mangrove types. The first result of NDVI is in binary, however, to make it easier to observe the layer of vegetation, the forest area is assigned color green (tone by the value of NDVI) and area without forest is white. The results of the NDVI classification is presented in Fig. 2 show that the vegetation index on the map has a value of 0.2–0.73, which concentration in the center of Can Gio.

In this study, the Can Gio mangrove forest was classified into three main types: Avicennia, Rhizophora, and mixed tree (including agricultural plant). Refer to the NDVI results of Nguyen et al. [7], Rhizophora has the highest NDVI value followed by Avicennia and finally the mixed tree. Using the image interpretation from Google Earth and mangrove classification map reference in IUCN [3], the study can classified mangrove forest types based on three ranges of the NDVI value, including 0.55–0.73 for Rhizophora, 0.4–0.55 for Avicennia, and 0.2–0.41 for mixed tree, respectively.

From the result of NDVI for three mangrove forest types combined with the regions of interest (ROIs) chosen by field survey data and image interpretation, the study applied Maximum Likelihoods Classified to classified the land use of Can Gio into seven classes: surface water, aquacultural pond, salt farming, settlement, Rhizophora, Avicennia, and mixed trees. The result is shown in Fig. 3. It must be mentioned here that remote sensing derived image classification is never 100% accurate, but the accuracy of this classification map is well above 98.3% and Kappa coefficient is equal 0.98 (compared to $K = 1$) as tested based on ground truth ROIs. From the classification result, the total area of mangrove is 41,430 ha (32,673 ha if not including the mixed tree), aquacultural pond (5876 ha), salt farming (2501 ha).

Results of household survey

The social-economic survey was conducted in Can Gio in April 2019 with the subjects of aquaculture households, salt farmers, etc. in order to collect input data for quantification.the economic value of mangrove ecosystems. 24 interviews were conducted during a 4-day field trip. The number of households interviewed was random, scattered in districts (Thanh An, Can Thanh, Tam Thon Hiep) of Can Gio. Accordingly, interviewing a total of 7 oyster farmers in Thanh An commune, sweet snail and clam concentrated in Can Thanh commune with 4 households, 8 households raising shrimp and tiger shrimp in Tam Thon Hiep commune.

Among interviewees, according to observations, farmers of this type usually concentrate in Can Thanh and Long Hoa. with a market price of 260,000/kg (150 sweet

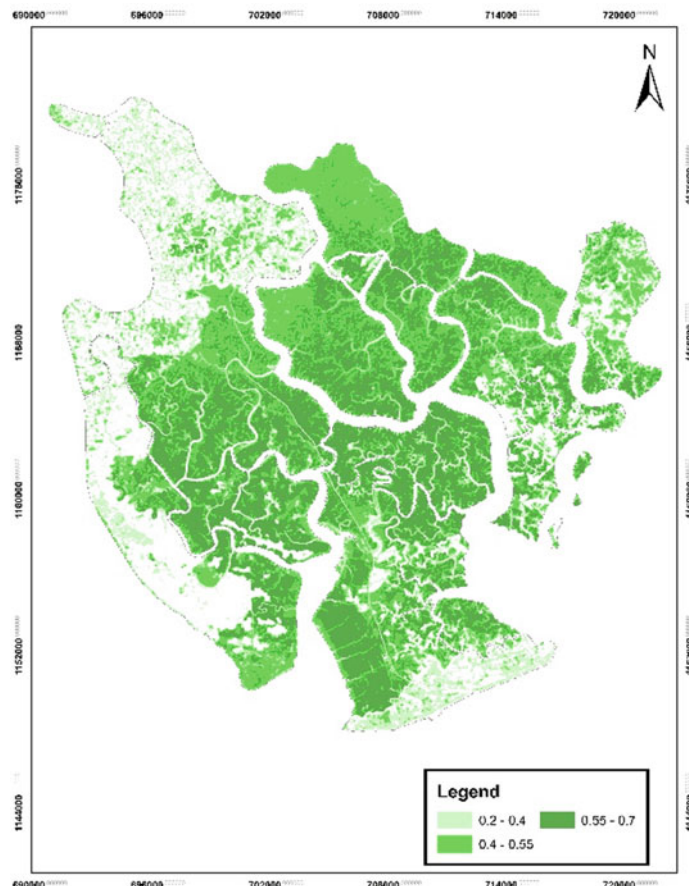


Fig. 2 NDVI map of Can Gio

snails) and 21,000/kg (63 claims). The production cost for sweet snail farming is about 450 million, with a yield of over 7-8 tons for 6 ponds (700 ha/pond), the profit is about 1.6–3 billion depending on the scale. Among aquaculture households in the District, shrimp farming is the majority, mainly tiger shrimp and white-leg shrimp. The average income of shrimp farming using semi-extensive method is between 20 and 100 million per year (if harvested full 2 crops) and 1–6 billions per year for industrial method.

Estimate the ecosystem value

- Aquacultural value

According to the data collected from the household survey in the communes in the 2019 and the current price, reference is provided by the Can Gio People's Committee, the aquaculture value of oysters, claim, sweet snails, shrimps are calculated as follow:

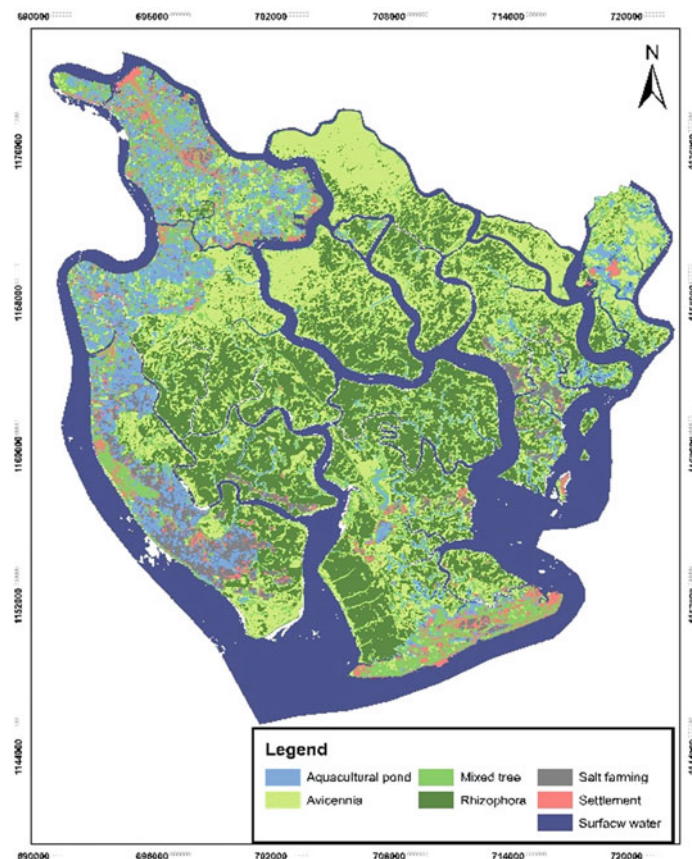


Fig. 3 Land use classification map of Can Gio in 2017

the average price of aquaculture product is 119 million VND/tons, production cost is 274 million VND/year, with the productivity per hectare is 8.58 tons, so the total net benefit is 282 million VND/ha/year. The total aquaculture pond (as calculated in remote sensing results) is 6033 ha, therefore, the total value of this goods is 1704 million VND (74 USD).

- Fish catch value

According to the report on the operation situation in 2018 [8], the fishing industry is relatively stable. Marine fish catching has 3 main types: coastal exploitation, offshore exploitation and by hand fishing. The output of each type is divided into details according to each type of fishing equipment. The study uses the income of each type of fishing equipment as the value of the services. The average income per year of each equipment (e.g. double rakes, fishing boat, single rakes, bottom trap, and by hand) is 227, 916 million VND [8]. There is the possibility that mangrove forests

provide marine fish in another way such as inshore directly catch in the mangrove area, indirect benefits as breeding places for marine fish production. De Graaf and Xuan (1998) quoted in Kuenzer and Tuan [4] that one hectare of mangroves support 450 kg/year of marine fish and shrimp catch (in 1998). With an average product price of 137,000 VND/kg with mangrove area retrieved from remote sensing of 41,430 ha (or 32,673 excluding mixed trees) resulted in the potential fish catch value per year of Can Gio mangrove area in 2018 range between 2014–2554 billions VND per year, combined with the directly fish catch value, the total fisheries-related catch value is 2,242,207 million VND/year (97 million USD/year) to 2,782,080 million VND/year (121 million USD/year), average value is 2,512,140 million VND/year (109 million USD/year).

- Salt product

The salt production value (household survey) with the average in three salt farmer household productivity in 1 ha produce 29 tons of salt per year, production cost with the support from government is around 7 million to 10 million VND. The total value of the salt product is 59,420 million/year (2.583 million USD/year).

- Firewood and construction

Currently, people do not have the right to arbitrarily enter the forest to collect firewood and timber as before and they no longer use firewood and wood as cooking fuel, so it is difficult to determine the value. However, Kuenzer and Tuan [4] from the survey in Can Gio 2011, if local people could not be retrieved from the forest construction would have to be bought at the market then the value of wood supply and firewood supply by mangroves averages 1457 USD per year (around 33,511,000 VND/year as current USD value in 2019). Knowing the population of Can Gio district is 75,330 people, assumed an average of four people/household, the district has a total of about 18,833 households. Assumed, 50% of households need to use firewood, wood for cooking, fishing tools or building houses, then the total value of firewood/construction woods per year is around 315,573 million VND/year (14 million USD/year).

- Carbon sequestration

The carbon sequestration rate (tCO_2/ha) can be retrieved from secondary sources include Nguyen et al. [7] and McNally et al. (2010) quoted in Kuenzer and Tuan [4]. The average carbon sequestration rates from both of the studies are 413.50 and 25.85 tCO_2/ha respectively. The price per tCO_2 is taken from the report of World Bank and Ecofys [11], using two prices of Asian Development Bank (ADB) and European Investment Bank (EIB) (US\$ 36.3/ tCO_2e – US\$47/ tCO_2e). Calculate with the area of mangrove forest, the total carbon sequestration value per year range between 6,875,692 million VND/year (299 million USD/year) for the smaller area (32,673 ha) to 8,718,512 million VND/year (379 million USD/year) for a larger area (41,430 ha). The average value for carbon sequestration is 7,797,102 million VND/year (339 million USD/year).

- Tourism value

The number of visitors from 2011 to 2016 to Can Gio is provided by Lap et al. [6]. In 2016 the total number of visitor is 1,116,000, with the domestic visitor is 1,031,184. Based on the tourism report, the number of visitors increased by 54% in 2017 compared to 2016 [9], and increased by 27.6% in 2018 compared to the same period in 2017, thus, the visitors in 2018 is estimated about 2,192,985 at the end of the year.

According to the General Statistic Office of Vietnam [2], the proportion of foreign visitors to Vietnam are respectively Asia (79%) and Non-Asia (21%). Assumed the same rate also applied for visitors to Can Gio. Because of the close distance and convenience of vacation in weekend assumed visitors from Ho Chi Minh City (HCMC) accounts for 85% of the domestic visitor. The transportation cost is calculated by the two-way flight cost to Tan Son Nhat airport from other provinces (Ha Noi, Nha Trang, Da Nang) and countries (Asia and Non-Asia) and the transport vehicle (bus, motorbike) to Can Gio from HCMC. Assumed all visitors took a 2-days trip, 3 meals per day and 2 night in the hotel, spent tickets for visiting site (e.g. Van Sat park), excluding any extra activities, the travel cost value can be calculated as follows:

$$\text{Travel cost value (TCV)} = \text{Total transportation cost} + \text{Accommodation} + \text{Foods} + \text{Ticket price}$$

$$\text{TCV}_{\text{asia}} = (5,326,000 + 500,000 + 330,000 + 35,000) * 0.8 * 166,667 = 825,467 \text{ million VND}$$

$$\text{TCV}_{\text{non-asia}} = (13,066,200 + 500,000 + 330,000 + 35,000) * 0.2 * 166,667 = 464,367 \text{ million VND}$$

$$\text{TCV}_{\text{HCMC}} = (25,000 + 500,000 + 330,000 * 1,972,139 = 1,532,909 \text{ million VND.}$$

$$\text{TCV}_{\text{other provinces}} = (2,549,000 + 500,000 + 330,000 + 35,000) * 348,025 = 1,037,677 \text{ million VND.}$$

Average each visitors spending range between 890,000 VND to 13,931,200 VND depend on transportation cost. The total tourism value that mangrove forest bring is 3,860,421 million VND/year (168 million USD/year).

4 Conclusion

The ecosystem services of Can Gio mangrove identified in this study includes provisioning services (aquacultural, fisheries-related, fuelwood, salt), cultural services (tourism), and regulatory services (carbon sequestration). The total economic value of all three ecosystem services of Can Gio mangrove is between 13,293,895 million VND/year (578 million USD/year) and 15,676,584 million VND/year (682 million USD/year). Overall of the total value of Can Gio mangrove ecosystem is nearly 14,485,239 million VND per year (630 million USD/year), in it the regulatory services (carbon sequestration) has generated highest value almost 7,797,102 million VND/year (339 million USD/year) accounted for 48.12% of total value, followed

by cultural services (tourism) 23.82% about 3,860,421 million VND/year (168 million USD/year) and provisioning services (aquacultural, fisheries, firewood, and salt) which total around 2,827,716 million VND/year (123 million USD/year).

Based on the land use area data obtained from remote sensing results, the percentage of each type per commune is calculated, with only focus on an area of mangrove (include mixed trees), the aquacultural and salt pond. In which, mangrove area in Long Hoa, Tam Thon Hiep, and An Thoi Dong communes accounted for more than of 50% per total area in Can Gio province, mangrove area of three communes area 8801–8045–7405 ha respectively.

From the ecosystem value results, it is possible to calculate the value per one unit of area based on the services depended on, e.g. carbon sequestration on mangrove forest, and the percentage of each service accounted for. Although the tourism value is based on visitors, however, most of the visit location is in a mangrove forest, so its value can be divided equally for the area. From there, it is possible to calculate in one unit of mangrove forest area, ecosystem services account for how many percentages: carbon sequestration (54%), firewood (2%), tourism (27%), fish-catching (17%). The ecosystem services value map per commune in Can Gio and the percentage is presented in Fig. 4, in which Long Hoa is the commune with the most economic values almost 3 billion VND/year and then An Thoi Dong, Ly Nhon with 2.6 and 2.2 billion VND/year.

5 Discussion

According to the total ecosystem value result of Can Gio in Kuenzer C. (2013), with the overall value is between 622.63 million USD to 676.10 million USD (for an area of 38,293 ha and 35,265 ha respectively), in which the tourism value generated the highest value (approximately 176 million USD). Compared these value with the result in this study for 2019 show the result value is quite different, between 578 million USD to 682 million USD and carbon sequestration services are the highest value account for more than 48% the total value in Can Gio. The different between both result, excluding the choice of services, is the up-to-date and specific information regarding to the services e.g. the price of fisheries product is increased in 2019, for example, the price of CO₂ in 2011 is assumed to be 20 USD/tCO₂ while in 2018–2019 it increase to 36.3–47 USD/tCO₂, which rapidly increase the value of carbon sequestration. But also, because of the different perspective, e.g. while estimate the tourism services, not counting the number of visitors, the different assumptions in the ratio of foreign and domestic visitors can lead to a different results (176 million USD in 2011 for ratio 0.85: 0.15 and 168 million USD in 2019 for ratio 0.8: 0.2).

Currently, as mentioned above, activities for economic development such as shrimp farming and salt production all have a negative impact on the ecosystem. However, when looking at the valuation results, it can be seen that the value of contributing over 50% of the district's total economic value is carbon sequestration and tourism. When understanding the importance of mangroves, managers can come

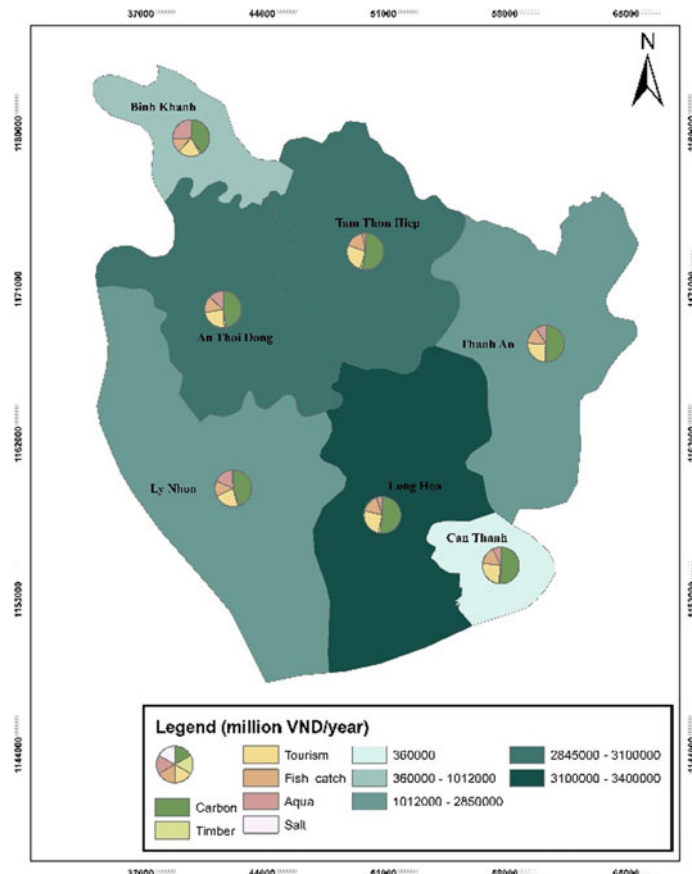


Fig. 4 Ecosystem service value in million VND/year/ha and percentage of each services in 7 communes of Can Gio

up with reasonable policies for sustainable development. If the Can Gio mangrove ecosystem is developed in a sustainable way, the total economic value of the region will increase as the natural resources exploited within the limit will continue to produce larger biomass, creating higher productivity to serve better and better human benefits

Acknowledgement The study was supported by The Youth Incubator for Science and Technology Programme, managed by Youth Development Science and Technology Center - Ho Chi Minh Communist Youth Union and Department of Science and Technology of Ho Chi Minh City, the contract number is “31/2019/HĐ-KHCN-VU”.

References

1. Anneboina LR, Kavi KS (2017) Economic analysis of mangrove and marine fishery linkages in India. *Ecosystem Services* 24:114–123. <http://dx.doi.org/10.1016/j.ecoser.2017.02.004>
2. General Statistic Office of Vietnam (2019) International visitors to Viet Nam in December and 12 months of 2018. Viewed 3 May 2019. Retrieved from: <http://vietnamtourism.gov.vn/english/index.php/items/13551>
3. IUCN (2014) Livelihood development for households participating in mangrove forest protection and management in Can Gio Biosphere Reserve. Can Gio District, Ho Chi Minh City
4. Kuenzer C, Tuan VT (2013) Assessing the ecosystem services value of Can Gio Mangrove Biosphere Reserve: combining earth-observation- and household-survey-based analyses. *Appl Geogr* 45:167–184
5. Kuenzer C, Bluemel A, Gebhardt S, Quoc TV, Dech S (2011) Remote sensing of mangrove ecosystems: a review. *Remote Sens* 3(5):878–928. <https://doi.org/10.3390/rs3050878>
6. Lap VN, Ta TKO, Pham CL, Nguyen TML, Ta DT, Nguyen HN, Vo THQ (2010) Ecotourism potential of the southeast coastal area of Ho Chi Minh City, Vietnam—Can Gio mangrove forest. *J Bio Env Sci* 12(6):1–10
7. Nguyen THD, Pham KD, Vu HT (2016) Evaluation of the use of three types of images with average and low resolution in determining the distribution and estimate biomass in four different types of mangrove forest in the Dat Mui commune, Ngoc Hien district, Ca Mau province. *Sci J Can Tho Univ* 45a:66–73
8. People's Committee of Can Gio (2018a) Current status in 2018 and tasks and solutions for 2019. Department of Economic. Can Gio. Vietnamese, 47
9. People's committee of Can Gio (2018) Identify the right direction to focus on tourism development (online), viewed May 20, 2019. Retrieved from: <http://www.cangio.hochiminhcity.gov.vn/dulichcangio/lists/posts/post.aspx?Source=/dulichcangio&Category=Ti%e1%bb%81m+n%c4%83ng+v%c3%a0+ph%c3%a1t+tri%e1%bb%83n&ItemID=78&Mode=1>
10. Ward RD, Friess DA, Day RH, MacKenzie RA (2016) Impacts of climate change on mangrove ecosystems: a region by region overview. *Ecosystem Health Sustain* 2(4):e01211. <https://doi.org/10.1002/ehs2.121>
11. World Bank and Ecofys (2018) State and trends of carbon pricing 2018. Retrieved from <https://openknowledge.worldbank.org/handle/10986/29687>

Evaluation of Spatial Planning Solutions in Terms of Urban Water Management Using the Multi-criteria Method



Ngoc Tu Tong

1 Introduction

The operations of territorial planning are carried out in an uncertain context for urban development because the project of urban and suburban planning involve several uncertain parameters within which risks related to urban water management are important. A planning project can use multiple logic of planning.

- Logic of natural drainage in which the actors respect the axis of natural drainage such as: channel, retention basins (lakes, ponds, ...), green spaces.
- Logic of drainage by drain in which the actors modify largely the natural drainage using both the drainage system by drain and different techniques with lower impact for water management such as: Basin retention, pavement tank structure, ditches and trenches for draining water.

This context poses a matter for decision makers: *What is the best spatial planning solution respecting the integrated water management?*

The objective of our research is to create an approach of decision configurable which shall facilitate the stakeholder in making decision for the territorial planning project presenting different solution (logic) which deals with planning problems related to urban water management. This is a process including the following steps:

- Risk definition of urban rain water management;
- Analysis/characterization of these risks and definition of the key-variables;
- Construction of a multi-criteria tool at the base of the key-variables;
- Verification of the effectiveness of the tool through a case study.

N. T. Tong (✉)

Faculty of Architecture and Planning, National University of Civil Engineering, NUCE, Hanoi, Vietnam

e-mail: tutn@nuce.edu.vn

2 Definition of Risks Related to Urban Rain Water Management

The approach is always based on risk analysis. Before defining the risks, we pose a question: What is the issue related to integrated urban water management that needs to be considered in a spatial planning solution?

The answer to this question leads to the analysis of the water cycle in a watershed [1]. Indeed, this process consists of two types of water management (quantitative management against flood and qualitative management against pollution), directly related to surface streaming, after to the sanitation and drainage system [2–4]. There are two options as follows:

- If the sewerage and drainage system capacity, Q^* , is greater than the total amount of water, Q , then the network is sufficient, which implies a situation of non-flood and non-pollution.
- If $Q^* < Q$: the residual flooding and pollution risks (including biodiversity), resulting storm water, are present, which can lead to a situation of human and material non-negligible losses.

A sociological survey [5] was achieved with stakeholders of a planning project for the purpose of consider multidimensional views of actors mobilized and concerned by the project. Evaluation of hydrological risks by stakeholders allowed us to check and confirm the issues identified in water management. In fact, the parameters from the survey coincide with the issues mentioned in the Fig. 1:

So, the risks to urban water management in operations of spatial/territorial planning are indicated as below:

- Risk of flood;
- Risk related to streaming—storm water drain system;
- Risk of pollution;
- Risk of cost (cost of spatial planning solutions).

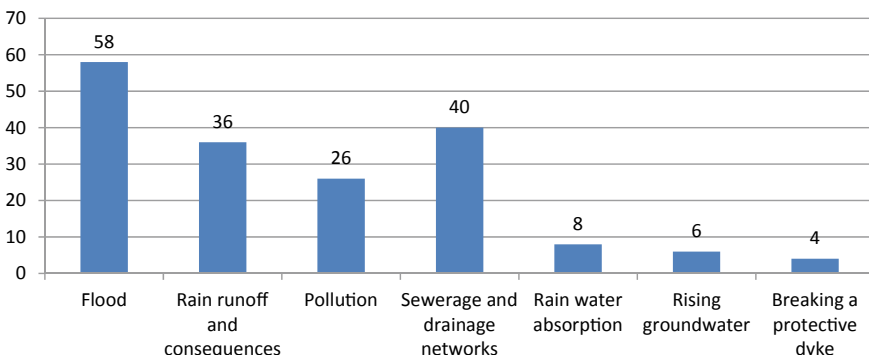


Fig. 1 Analysis of survey responses to identify risks associated with water management [5]

There are four key variables of urban rain water management in spatial planning solutions which are confirmed by hydrological experts [1, 6, 7].

3 Construction of Multi-criteria Tool at the Base of Urban Rain Water Risks

3.1 Comparison of Multi-criteria Methods

Among the multi-criteria methods, there are two dominant schools in the world: the French school (general classification) and the American school (general score) with its own strengths and weaknesses.

Roy and Bouyssou [8] illustrate the transitivity between these two school in the choice of a site on the Pacific Northwest coast to install a nuclear power plant. In this example, 9 admissible solutions (possible actions) are evaluated by two approaches: French school using the “ELimination Et Choix Traduisant la REalité” method (ELimination and Choice Expressing REality) (ELECTRE—model S) and American school using the multi-attribute utility theory (MAUT—model U). This last method proved to be much more efficient and simple than ELECTRE in a choice situation presenting several solutions, because the evaluation in the MAUT method is more transitive and coherent (see the graph below), while the first method allow to aggregate the criteria but could not treat the risks at the same time (intransitivity) (Fig. 2):

Given that the decision-making situations related to the urban planning and development will often take place in an uncertain future with different possible solutions and several evaluation criteria, we propose to use the American approach to solve this problem of decision, in terms of urban water management.

3.2 MAUT—Multi-attribute Utility Theory [9]

The approach of American school is currently widely used in the case of assistance to choose between various potential actions, compared with another approach as French school [8, 10, 11]. Among the methods of multi-criteria analysis of aid decision based on the American school, the multi-attribute utility theory (MAUT) [9], is currently the reference theory most used in the United States because it is the most sophisticated.

The MAUT does not treat the risks separately but as a coherent management framework that takes into account the diversity of risks and their interdependencies. Based on an approach “from top to down”, it prioritizes the objectives of the decision maker, from the global objective broken down into identifiable sub-goals by an index or a scale that is called “attribute”. Preferences of the decision maker relative are integrated by a multi-criteria utility function aggregating all the attributes, and then

a “global score”, called “expected utility” is measured from this function. So, the MAUT allows the “rebuilding” of the rationality of a complex organization in order to clarify and classify the spatial planning solution, to recommend finally the best decisions (solutions) for actors.

In this theory, each criterion g_i is as a utility expectation involving a utility function u_i related an attribute x_i . For each action “a”, this attribute is characterized by its probability distribution, which may, if necessary, reflect the certainty [12, 13]. This criterion synthesis g of action “a” takes the follow multiplicative form [9]:

$$g(a) = \left\{ \prod_{i=1}^n [1 + Kk_i g_i(a)] - 1 \right\} / K \text{ (with } k_i > 0, \sum_{i=1}^n k_i \neq 1, K > -1, K \neq 0) \quad (1)$$

where k_i is called a « scaling constant » and K being the only non-zero real solution and above—1 in the equation

$$\prod_{i=1}^n [1 + Kk_i] = 1 + K \quad (2)$$

It should be noted that the function g is normalized by two extreme actions: $g_i(a_*) = 0$ et $g_i(a^*) = 1$ for $i = 1 \dots n$ (a_* : worst action and a^* : best action). When the choice is made for each criterion, the theory states that there is a well-defined value for each action, for example two actions “a” and “b”, which guarantees:

$$g(a) > g(b) \Leftrightarrow aPb, \forall a, b \in A$$

By applying the theory MAUT in our research to make the decision aid tool, the following sets need to be defined: The set of the key variables defined by risk analysis; The set of possible consequences associated with variables; The set of the probabilities associated with each variable’s consequences.

3.3 Definition of Key Variables

The multi-attribute utility theory allows pooling all attributes in a multi-attribute utility function. The key variables below and their consequences should be determined:

- The first variable: **Treatment of the flood** (variable x_1), with which we offer also the associated consequences: grave flood, current flood and non-flood.
- The second variable: **Treatment of rain water runoff** (variable x_2) for which we determine three consequences: the best treatment, current treatment and the worst treatment of runoff.

- The third variable: **Treatment of pollution**” (variable x3) with theirs ordered consequences: grave, current and non-pollution.
- The fourth variable: **Treatment of cost**” (variable x4) with three consequences: the more expensive cost, current cost and cheapest cost.

3.4 Definition of Consequences

The next step of the MAUT is to define consequences related to variables. We propose, consistently for four variables, three ordered qualitative consequences according to the normalizing utilities consequences as follow:

- The worst consequences such as {grave flooding, the worst treatment of runoff, grave pollution, the more expensive cost}: utility of these consequences equal to zero.
- The best consequences such as {non-flood, the best treatment of runoff, non-pollution, cheapest cost}: utility of these consequences equal to 1.
- The current consequences such as {current flood, current treatment of runoff, current pollution, and current cost}: utility of these consequences is normally encoded by a computer program for estimating the preferences of the decision maker/stakeholders.

3.5 Multi-criteria Evaluation Tool and Signification

Based on the key variables, the set of consequences and probabilities, we construct the multi-criteria decision aid tool as follows (Fig. 3):

In this solution, we need only to elicit the current consequences in normalizing the extreme consequences: $u(\text{worst}) = 0$; $u(\text{best}) = 1$. This theoretical tool is established for the purpose of measuring the global score or global utility which is developed for four variables from Eq. 1:

$$E[U(x)] = \prod_1^4 \{1 + K * k_i * E[u(x_i)]\} * \frac{1}{K} - \frac{1}{K} \quad (3)$$

$u(x_i)$: partial utility function; $U(x)$: global utility function

$E[u(x_i)]$: partial expected utility; p_{ij} : probability distribution, $E[u(x_i)] = \sum p_{ij} u_j$
 $E[U(x)]$: global expected utility (global score)

Indeed, the global utility is a unique, quantitative, synthesis quantity that allows us to measure the performance (effectiveness, feasibility) of urban planning solutions (eliminate planning solutions with the lowest scores; and select only solutions

with scores among the highest). So, the multi-criteria method allows facilitating the decision making in a rapid, global, rational, and logical manner.

3.6 Elicitation of Partial Utilities and Scaling Constants

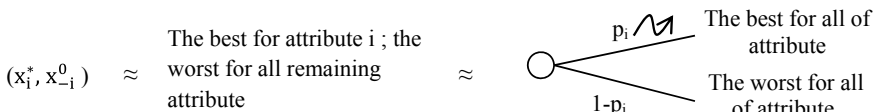
To elicit the utilities of current consequences, a technique called “lottery equivalent method” is used [9, 14]. This is a technique in which we ask the preferences of the decision maker to face risky situations that are simulated by the two binary lotteries probabilized in which the one includes extreme consequences with variable probability P and the other includes current consequence with fixed probability Q that we want to measure:



By varying the probability P according to the choice of the decision-maker until the convergence value ensuring equivalence between the two lotteries, which we will call here P^* , then applying equivalence of expected utility:

$$\begin{aligned} & Q \times u(\text{current conse.}) + (1 - Q) \times u(\text{worst conse.}) \\ &= P^* \times u(\text{best conse.}) + (1 - P^*) \times u(\text{worst conse.}) \\ &\rightarrow u(\text{current consequence}) \\ &= P^*/Q \end{aligned}$$

To elicit the scaling constants, we use the equivalent lottery method [9, 15]. The principle of this method is to propose to the expert two situations with extreme consequences, one consists of the worst consequences for all attributes to the expert, but the attribute that we want to estimate and other consists of the best consequences with probability p_i , the worst consequences with probability $1-p_i$:



By the same procedure, the probability p_i changes in terms of the choice of the expert until finding the equal probability. It is a probability making the expert indifference between the two lotteries.

$$\text{So, } U(x_i^*, x_{-i}^0) = k_i = p_i U(X^*) + (1 - p_i) U(X_*) = p_i$$

4 Case Study: The Possible Decision Aid

4.1 Description of Alternatives and the Associated Probability Distribution

An experiment was carried out in a surveyor expert office that has so much experience in the implementation of territorial planning projects. We present the application of our decision aid tool in the case study of a planning project having three solutions for which the decision maker cannot make a decision to choose the most advantageous logic. The main difference between the three solutions in terms of urban rain water management:

- Solution 1: By rearranging no effort to adapt with the existing topography, solution 1 makes a complete leveling operation of the site. All the natural vegetation has been removed, which obviously affects the hydrology. The dense drainage and sanitation by conduit everywhere was replaced with the natural drainage which was widely modified. The high rate of urbanization involves the increase of impermeability cover in this solution. The cost of investment in this solution is the greatest.
- Solution 2: In respect of the natural drainage axis, this approach preserves in this case a significant part of areas in their natural state (retention basins, natural ditches, ...) and organizes the streets taking into account the natural topography. This means that the natural characteristics of the site are preserved; only the surrounding buildings are leveled in this solution. The sewerage drainage system by ditches (without conduit) is installed along streets that are narrower than the solution 1. Urbanization is less than the first solution reducing the waterproof surface and the cost of construction.
- Solution 3: It is a mixed and intermediate solution between the two solutions described above. This solution makes a leveling part of the site and preserves the natural hydrological drainage axis in other part. The water storm drainage system is also mixed which uses both the conduit in the leveled site and the ditches in the natural protected site. The investment cost of this approach is also medium compared with two solutions 1 and 2.

4.2 Evaluation of Spatial Planning Solutions in Terms of Hydrological Water Drainage

Based on these arguments evaluations of each solution and the professional experiences, the expert estimated the probability distributions of the consequences of each planning solution that are expressed in the Table 1:

Table 1 The probability distribution of each solution in terms of consequences

Variables	Consequences	Probability distribution			The probability interval (%)
		Solution 1 (%)	Solution 2 (%)	Solution 3 (%)	
Risk related to flood	Grave flood	5	5	5	5
	Current flood	40	20	35	20–50
	Non-flood	55	75	60	45–75
Risk related to runoff	The worst treatment	5	5	5	5
	Current treatment	20	30	25	15–35
	The best treatment	75	65	70	60–80
Risk related to pollution	Grave pollution	5	15	10	5–15
	Current pollution	15	30	20	15–35
	Non-pollution	80	55	70	50–80
Risk related to cost	The most expensive	30	5	15	5–30
	Current cost	65	90	80	60–90
	Cheapest cost	5	5	5	05–10

Depending on the answers during the experiment carried out with urban planner, the results of this elicitation are synthesized in Tables 2 and 3 as follow.

The presented results in the figure below, under the form of a decision tree, allow us to have a comprehensive and comparative overview of the three planning solutions (Fig. 4).

Based on the multi-criteria method, the urban planning solutions by concrete numbers can be measured. This quantification of qualitative assessment criteria in terms of urban water management helps the planner to have an intuitive vision about

Table 2 Summary of results

Current consequences	Current flood	Current runoff	Current pollution	Current cost
Utility	0.733	0.525	0.783	0.843

Table 3 The results of variable scaling constant

Variables	Flood	Runoff	Pollution	Cost
Partial constants, k_i	0.61	0.51	0.80	0.70
Global constant, K	$K = -0.987166$			

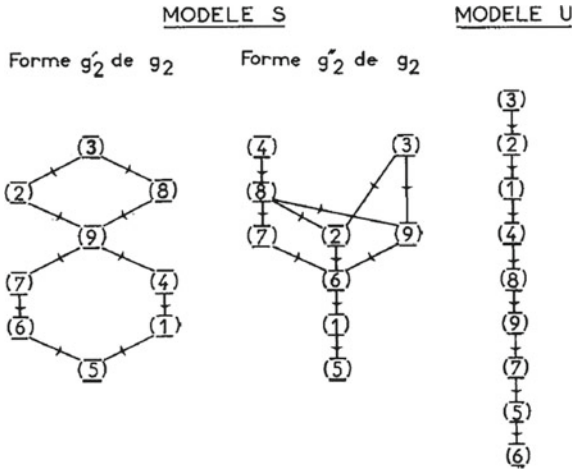


Fig. 2 The transitivity in the two methods, for the choice of a site to install a nuclear power plant [8]

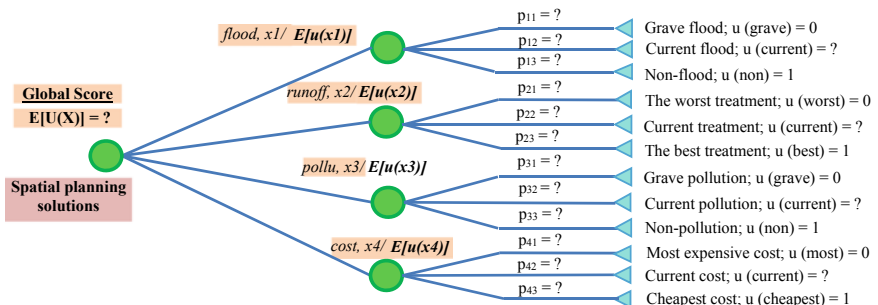


Fig. 3 Illustration of configurable theoretical tool (author)

the solutions, then facilities the decision making. According to the results in Fig. 4, it is possible to advise decision makers to hold solution 3 because of having the highest score (considered as the best solution in respecting the urban water management) and ignore the two solutions 1 and 2 as a result of having lower scores.

5 Conclusion

The multi-criteria method MAUT allows facilitating decision making in a simple and fast way. The elicitation process, original step of the recent developments on MAUT, allows quantifying the risk factors and qualitative criteria under the form of data number (global utility or global score) using an experimental psychological approach

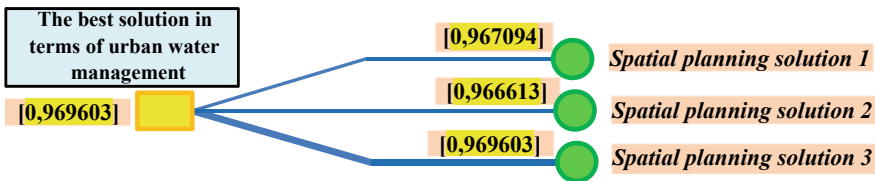


Fig. 4 Global scores of each option and the recommendation of the best spatial planning solution (author)

for translates the experience of the decision maker. The MAUT helps manager to choose the most efficient solution of urban planning project in accordance with the rules of urban hydrological water management. The application MAUT in the field of urban water management gives the perspective studies into other domains of territorial planning (management of transport, environment or housing).

Acknowledgements This research was financially supported by National University of Civil Engineering (NUCE). We thank our colleagues from Department of Science and Technology and Department of Architecture and Planning (NUCE) who provided insight and expertise that greatly assisted the research and created favorable conditions for me to focus on writing and completing this article. I would also like to show our gratitude to the professor Munier (University of Paris 1—French) and professor Bennabi (Special University of road works, Civil engineering, Industry - French) for methodology assistance, valuable comments that greatly improved the manuscript. I am immensely grateful to the 4 “anonymous” reviewers for their so-called insights, for their comments on the manuscript, although they may not agree with all of the interpretations/conclusions of this paper.

References

1. CETE East (2003) CERTU: the city and sanitation, principles, methods, tools for better integration in the water cycle, Lyon
2. Ministry of Municipal Affairs, Regions and Land Occupancy: sustainable management of rainwater, good practice guide on territorial planning and sustainable development (2010) Québec, pp 6–10 and pp 33–65
3. Ministry of Sustainable Development, Environment and Parks: Guide to Stormwater Management Chapter 1–5, 86p, Québec
4. Ministry of Culture and Environment, Ministry of Infrastructure and Planning, Ministry of Agriculture, Ministry of Health and Social Security: Technical instruction related to sewerage drainage systems of conglomerations. INT 77 284 (1977) Paris, 62p
5. Tong NT, Munier B, Bennabi A (2011) Survey report: water management in the territorial urban planning. ESTP, 20p
6. French Association for Standardization (AFNOR) (1997) European standard NF-EN 752: sewerage drainage systems in the outdoors, Paris
7. Chocat B, Bertrand-Krajewski J-L et al (1997) Encyclopedia of urban hydrology and sanitation: technical and documentation. Lavoisier, Paris
8. Roy B, Bouyssou D (1993) Decision multicriteria aid: methods and case (Chapter 9: Comparison of two decision aid studies about a case of locating a nuclear power center). Economica, Paris, pp 543–599

9. Keeney R, Raiffa H (1976) Decisions with multiple objectives: preferences and value trade-offs, Chapter 5 and 6: multiattribute preferences under uncertainty: the two (multi)-attribute case, New York, pp 219–281
10. Roy B (1968) Decision aid multicriteria methodology. *Economica*, Paris
11. Roy B (1968) Ranking and selection in the presence of multiple points of view (the ELECTRE method). *French Rev Oper Res* 2(8):57–75
12. Munier B (1989) New solution of decision under uncertainty, an interpretative essay. *Eur J Oper Res* 38(3):307–317 (Février)
13. Munier B (1998) Multiattribute utility theory: toward a more general framework. decision analysis and its applications in safety and reliability. In: Proceedings of the 12th ESReDA Seminar, Espoo, Finland, pp 1–14
14. Munier B (2008) Subjective expected utility. *Encyclopedia Quantitative Risk Assessment Anal* 4:1719–1724
15. Picand S (2010) Supporting risk in development projects of an innovative nature, proposition an implement tool in the engineering industry (PhD thesis). GRID-ENSAM, 332p

Investigating Partnering Performance in the Vietnamese Construction Industry



Khoa Dang Vo, Sy Tien Do, Thu Anh Nguyen, Chau Ngoc Dang,
Thanh Huy Tran, and Long Le-Hoai

1 Introduction

With the global integration and economic boom in recent decades, the Vietnamese construction industry has faced many new challenges, such as increased competition from foreign firms, more exacting quality standards, rapid development of new technologies, increased risks of globalization, and development of information technology. The adversarial relationships between project parties from the traditional contract arrangements have caused many difficulties. The new contract arrangement will help construction enterprises to improve their competencies and competitive advantages. Partnering concept, as a key for the study, could be considered to be useful in the Vietnamese context.

Partnering could not only reduce the principal constraints between traditional contract parties [23], but also promote cooperation and improve the competitiveness of construction parties. It is an innovative concept in construction firms [11]. Due to the multidisciplinary knowledge and skills of parties participating in a construction

K. D. Vo · S. T. Do · T. A. Nguyen

Department of Construction Engineering and Management, Faculty of Civil Engineering, Ho Chi Minh City University of Technology, Vietnam National University Ho Chi Minh City (VNU-HCM), Ho Chi Minh City, Vietnam

C. N. Dang (✉)

Applied Computational Civil and Structural Engineering Research Group, Faculty of Civil Engineering, Ton Duc Thang University, Ho Chi Minh City, Vietnam
e-mail: dangngocchau@tdtu.edu.vn

T. H. Tran

Uscons Construction Investment Corporation, Ho Chi Minh City, Vietnam

L. Le-Hoai

Vietnam National University Ho Chi Minh City (VNU-HCM), Ho Chi Minh City University of Technology, Ho Chi Minh City, Vietnam

project, partnering evolves as a cooperative strategy that could supplement and modify the traditional boundaries between independent organizations in a competitive market [14].

Although the partnering concept has been widely applied in construction from the late 1990s and early 2000s, it has not been understood and widely used by parties in the Vietnamese construction industry. Evidence for the adoption of this new arrangement has been limited to anecdotes. Thus, it is necessary to conduct an in-depth study to encourage the use of partnering in construction projects.

The main aim of this paper is to develop a model that practitioners can easily employ to evaluate the level of partnership success. The model, developed using logistic regression technique, converts the qualitative performance of success factors (SFs) into the quantitative value of the chance of partnering success in a specific context. It can also serve as a tool to help practitioners in developing, adjusting and improving their strategies to enhance partnering performance.

2 Success Factor for Partnering in Construction

Rockart [25] defined critical SFs as “*those few key areas of activity, in which favorable results are absolutely necessary for a particular manager to reach his/her goals*”. Boynton and Zmud [3] defined critical SFs as “*those few things that must go well to ensure success for a manager and an organization*”, and accordingly, they represented managerial or organizational areas which should be given special and continual attention to ensure high performance.

Since the partnering concept became popular, researches about SFs in implementing this procurement type have been intensive. Crane et al. [13] proposed a partnering process model that consisted of five phases and various SFs were identified to ensure successful partnering in each phase. Larson [20] surveyed 291 construction projects and suggested that a comprehensive approach should be applied to partnering in construction projects and that top management support for teamwork across organizations is critical to success. Cheng et al. [8] proposed a partnering framework and identified critical SFs based on a review of partnering literature. Several aspects of research about SFs were presented in Cheng and Li [9] and Cheng et al. [10, 11] to facilitate the implementation of partnering through a proposed model. SFs were investigated for a certain stage, of which four common SFs were top management support, open communication, effective coordination, and mutual trust. Black et al. [2], using a UK-wide postal questionnaire survey, indicated that partnering can and does work, but all project participants must rethink their attitudes and work to make projects more efficient, successful and free from conflict. Also based on research in the UK construction industry, Beach et al. [1] presented a conceptual framework of SFs. They reviewed the context of four categories of key elements in the literature (i.e. commitment, processes, tools, and outcomes) appeared to fit into the outcome category. Three new aspects of successful partnering were identified: best value, service, and dependency. In the Taiwanese context, Chen and Chen [6] and Chen et al.

[7] identified and assessed critical factors as certain requirements that must be met for partnering to be successful. Chan et al. [5] based on the case study of six selected projects and developed a best practice partnering framework for the Hong Kong context. Focusing on mainland China, Tang et al. [28] presented the finding from a study that was conducted to develop and test a partnering model, which revealed the relationships between critical SFs of partnering and demonstrated their importance to construction.

Most of the completed work has been context-specific. Moreover, research about the application of the partnering concept in Vietnam has not received much attention, either from the international research community in general or from the local researchers in particular. Only one study has attempted to fill the gap. Le-Hoai [21] identified twenty-eight SFs for partnering in the Vietnamese construction industry through a questionnaire survey. These SFs will be used in this paper to develop a prediction model.

3 Level of Partnering Success

Many studies (e.g., [8, 12, 13, 26]) have been conducted to measure the success of partnering in construction. The studies have identified many criteria for measuring partnering success. Cheng et al. [8] proposed that performance measures could be subjective or objective and these measures should help to set useful monitoring, control, evaluation, and correction of variations and improvements. The frequently-used measures were related to cost, schedule, quality, safety, litigation, profit, stakeholders, and community. Accordingly, collecting various measures to estimate the level of partnering success seems to encounter many difficulties, such as reliability of answers of respondents about the measures due to the sensitivity of data, limited time of respondents due to tight working schedule, and inertia of practitioners against scientific researches. The surveyed scale must be easy for respondents to respond with acceptable accuracy for the research purpose.

Several researches used a qualitative scale to estimate the measures of success and, then, estimate the success level in management. Handa and Adas [17] built a model to predict organizational effectiveness, and Han et al. [16] used a seven-point scale to predict profit performance when selecting candidate international construction projects. Success or lack of success in performance was likely to be subjectively estimated based on respondents' perceptions. Menches and Hanna [24] asked respondents to rate the performance of projects on a two-point scale: successful and less-than-successful. Chan et al. [4] requested respondents to rate their perceptions of partnering success on a five-point Likert scale (1 = "strongly disagree" and 5 = "strongly agree").

In order to overcome the difficulties and guarantee the acceptable accuracy, a ten-point scale was employed whereby respondents assigned the ratings of 1 for "completely unsuccessful" to 10 for "completely successful". Iyer and Jha [18] have

adopted a ten-point scale to subjectively estimate schedule performance of construction projects in India. Koksal and Ardit [19] also used a ten-point scale to rate the overall condition of construction company in a research on company decline.

4 Methodology

4.1 Questionnaire Survey

An empirical survey was conducted to investigate SFs for partnering application in the Vietnamese construction industry. Respondents were requested to rate the contribution of the factors to the partnering success according to a five-point Likert scale from 1 (not significant) to 5 (extremely significant). With the level of partnering success, respondents were asked to rate on a ten-point scale from 1 (completely unsuccessful) to 10 (completely successful). Data were collected through answers based on project information that respondents participated. Practitioners in the sample were identified through construction companies' web-pages and charters, project case analyses, professional fora, and personal relationships.

The questionnaires were hand-delivered, posted or sent through e-mails. The primary participants in this study were from clients, consultants and contractors working in the Vietnamese construction industry. More than 300 questionnaires were distributed. As a result, 79 valid questionnaires were received with a response rate of approximately 24%. The collected data were analyzed using SPSS statistical software. Cronbach's alpha coefficient of internal consistency yielded a value of $0.887 > 0.70$, which is considered to be reliable.

The data set includes 79 observations. In particular, 20.3%, 59.5% and 20.3% of the data sample are from clients, contractors and consultants, respectively. Thus, over 50% of respondents were from contracting firms. In terms of job position, 12.7% of respondents were senior managers, 49.4% were functional managers, 32.9% were project team members, and 5.1% were partnering facilitators. There were four experience-related groups: less than 5 years with 15.2%, 5–10 years with 36.7%, 10–15 years with 40.5%, and more than 15 years of experience with 7.6%. Regarding the origin of organizations, foreign companies accounted for 32.9% (26 responses), and the rest (53 answers or 67.1%) were from Vietnamese companies.

The ratings given to partnering success by respondents were all above 5, with a median value of 8 and a mean value of 7.66. All of these values seem to suggest that partnering has been successfully applied in the Vietnamese context.

4.2 Model Development Process

The data set of twenty-eight SFs for partnering in the Vietnamese construction industry and the level of partnering success, collected from the questionnaire survey, was used to develop a prediction model. The tests of Kendall's coefficients of concordance were all significant at 0.000. It confirms a response consensus within each respondent group. The p-values from Spearman rank correlation tests are all less than 0.05. Thus, they lead to the conclusion that there was a significant agreement between pairs of respondent groups on the ranking of SFs. Analysis of variance (ANOVA) tests between respondent groups on the level of partnering success showed insignificant differences at the 0.1 level. Since there was a good statistical agreement between respondent groups, all data could be aggregated for further analysis. Factor analysis was performed to reduce the number of variables. The extracted components were used as the independent variables in the logistic regression model. Component scores represented the components in the regression analysis.

Validation is a very important step in the application of logistic regression technique. A new model should be tested with the cases that are independent from the cases used in its development [19]. Therefore, the data set was randomly divided into two sets: building and testing sets corresponding to a ratio of 90/10 (71 cases used for building and 8 cases used for testing).

5 Factor Analysis

Factor analysis was employed to analyze the latent relationships between a large number of SFs [22]. All twenty-eight SFs were appropriate for factor analysis because their communalities were higher than 0.5. The result of Bartlett's test of sphericity tests the hypothesis that the correlation matrix is an identity matrix. The hypothesis was rejected with the significance level at 0.000 with a Chi-square value of 1258.335 [15]. Kaiser-Meyer-Olkin measure of sampling adequacy was satisfactory with the value of 0.685 [27]. Therefore, the factor analysis method was approached for the data. Principal component analysis was used to extract components.

Latent root criterion (eigenvalue greater than 1) and varimax orthogonal rotation technique were adopted. Eight components were extracted after rotation. Figure 1 shows the scree plot of the analyzed factors. With eight extracted components, 71.5% of variance can be explained. Table 1 shows the rotated component matrix which contains the loadings of SFs on each component.

Loading is the correlation of a variable on a component and indicates the degree of correspondence between the variable and the component. The patterns of extracted components were characterized by the factors which have high loadings (>0.5) on the components. The first component, consisted of early implementation of the partnering process (0.507), commitment to continuous improvement (0.673), acting consistently with objectives (0.734), dedicated team (0.556), flexibility to change (0.732),

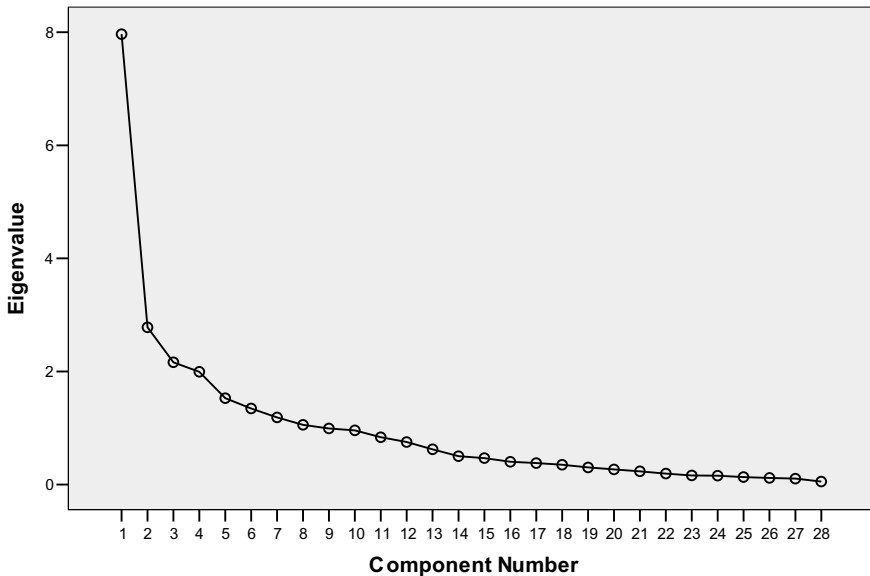


Fig. 1 Scree plot

total cost perspective (0.576), and creativity of the partnering team (0.752), could be named “dedication”. The second component was named “readiness” because it consisted of mutual trust between parties (0.528), effective communication (0.544), good cultural fit (0.618), company wide acceptance about the partnering (0.847), and technical expertise (0.699). The third and fourth components were named “coordination” and “teamwork”, respectively. The third component comprised questioning attitude about assumptions (0.637), educated and trained personnel for partnering (0.637), and effective coordination (0.715), while the fourth component included mutual trust between parties (0.524), partnering experience (0.735), and joint problem solving (0.814). Similarly, “sufficiency” and “leading” were the names given to the fifth and sixth components, respectively. The fifth component comprised adequate resources (0.753) and effective conflict resolution process (0.750), while the sixth component comprised long-term commitment (0.510), commitment from top management (0.650), financial security (0.658), and equity (0.581). “Balance” component consisted of commitment to quality (0.645), empowerment of stakeholders (0.574), and adequate partnering team building (0.806). The last component had only one factor, i.e. clear understanding about scope and objectives (0.844), and was thus named “clarity”.

Component scores have been used to represent the components in the following analysis. The weight of a factor on a component indicates the unique contribution of the factor to the score of this component. The coefficients in Table 2 are the weights of the factors used to calculate the component scores.

Table 1 Rotated component matrix

Success factors	Component							
	1	2	3	4	5	6	7	8
Mutual trust between parties	-0.053	0.528	-0.121	0.524	-0.013	0.343	0.131	-0.193
Effective communication	0.068	0.544	0.194	-0.105	0.440	0.406	-0.034	-0.024
Adequate resources	0.203	-0.006	0.232	0.078	0.753	0.314	-0.192	0.164
Long-term commitment	0.207	0.408	0.279	0.154	-0.110	0.510	-0.116	0.431
Commitment from top management	0.035	-0.122	0.181	0.124	0.340	0.650	0.004	0.066
Clear understanding of scope and objectives	0.147	-0.066	0.138	-0.033	0.189	0.001	0.058	0.844
Early implementation of the partnering process	0.507	0.464	-0.068	0.349	0.074	-0.019	0.316	0.266
Commitment to continuous improvement	0.673	-0.008	-0.007	0.283	0.286	0.006	0.069	0.039
Acting consistently with objectives	0.734	-0.135	0.466	-0.014	0.012	0.211	-0.034	-0.199
Dedicated team	0.556	0.068	0.248	-0.061	0.453	0.031	0.066	0.154
Flexibility to change	0.732	0.092	0.045	0.075	0.051	0.074	0.192	0.016
Commitment to quality	0.464	0.211	0.154	0.098	0.069	-0.036	0.645	0.218
Total cost perspective	0.576	0.202	0.253	-0.128	-0.097	0.057	0.132	0.209
Good cultural fit	0.485	0.618	0.297	0.266	-0.063	-0.087	-0.075	-0.127
Company wide acceptance about the partnering	0.152	0.847	0.049	0.125	-0.001	0.148	0.031	-0.092
Technical expertise	0.086	0.699	0.142	-0.224	0.246	-0.075	-0.012	0.377
Financial security	0.066	0.191	-0.137	-0.112	0.183	0.658	0.014	-0.167

(continued)

Table 1 (continued)

Success factors	Component							
	1	2	3	4	5	6	7	8
Questioning attitude about assumptions	0.219	0.175	0.637	0.095	-0.026	0.139	0.292	0.226
Empowerment of stakeholders	0.394	0.009	0.252	-0.065	-0.253	0.182	0.574	0.103
Creativity of partnering team	0.752	0.281	0.157	-0.079	0.226	-0.062	0.244	0.173
Equity	0.014	0.138	0.182	0.231	-0.010	0.581	0.306	0.415
Mutual vision, goals/objectives	-0.078	0.412	0.211	0.415	0.329	0.344	0.151	0.052
Effective conflict resolution process	0.137	0.150	-0.039	0.020	0.750	0.144	0.180	0.050
Educated and trained personnel for partnering	0.147	0.356	0.637	0.210	0.109	0.066	0.248	0.030
Effective coordination	0.313	-0.004	0.715	0.019	0.252	0.004	0.168	0.149
Adequate partnering team building	0.149	-0.095	0.297	0.178	0.191	0.014	0.806	-0.102
Partnering experience	0.158	-0.083	-0.086	0.735	-0.068	0.137	0.305	0.085
Joint problem solving	-0.019	0.161	0.209	0.814	0.076	0.015	-0.043	-0.131

Extraction method: Principal Component Analysis

Rotation method: Varimax with Kaiser Normalization

Bold values: Factor loadings are larger than 0.5

6 Logistic Regression

6.1 Model Development

Logistic regression is a conditional probability approach, while multinomial logistic regression is an extension of binomial logistic regression. The chances of occurrence of a particular value of the response variable are compared with the chances of occurrence of the reference value of the response variable. In this study, the reference value was level 10 of the scale of success. Forward entry stepwise method was used to identify the significant variables. The logistic regression model was developed with the success level as the dependent variable and all eight extracted components

Table 2 Component score matrix

Success factors	Component							
	1	2	3	4	5	6	7	8
Mutual trust between parties	-0.032	0.184	-0.090	0.269	-0.039	0.172	0.159	-0.154
Effective communication	-0.060	0.144	0.049	-0.078	0.157	0.097	-0.029	-0.093
Adequate resources	0.020	-0.090	0.054	0.020	0.328	0.053	-0.169	0.035
Long-term commitment	0.045	0.064	0.052	0.059	-0.241	0.262	-0.219	0.257
Commitment from top management	-0.005	-0.149	0.031	0.027	0.067	0.337	-0.043	-0.013
Clear understanding about scope and objectives	-0.022	-0.069	-0.031	-0.029	0.037	-0.054	-0.048	0.554
Early implementation of the partnering process	0.119	0.145	-0.258	0.148	-0.008	-0.073	0.090	0.135
Commitment to continuous improvement	0.256	-0.066	-0.179	0.124	0.102	-0.015	-0.076	-0.026
Acting consistently with objectives	0.276	-0.162	0.209	-0.053	-0.112	0.153	-0.193	-0.225
Dedicated team	0.135	-0.049	0.023	-0.065	0.188	-0.065	-0.053	0.016
Flexibility to change	0.272	-0.036	-0.147	0.008	-0.045	0.056	-0.008	-0.049
Commitment to quality	0.028	0.038	-0.090	-0.023	0.019	-0.082	0.320	0.060
Total cost perspective	0.172	0.010	0.036	-0.097	-0.144	0.032	-0.050	0.082
Good cultural fit	0.124	0.208	0.105	0.116	-0.098	-0.116	-0.180	-0.143
Company wide acceptance about the partnering	-0.006	0.310	-0.053	0.053	-0.057	-0.008	-0.019	-0.100
Technical expertise	-0.089	0.261	0.021	-0.117	0.102	-0.188	-0.024	0.214
Financial security	0.068	-0.002	-0.168	-0.066	0.001	0.376	0.021	-0.142

(continued)

Table 2 (continued)

Success factors	Component							
	1	2	3	4	5	6	7	8
Questioning attitude about assumptions	-0.086	-0.001	0.329	-0.030	-0.097	0.001	0.056	0.053
Empowerment of stakeholders	0.059	-0.059	0.033	-0.107	-0.198	0.132	0.264	-0.004
Creativity of partnering team	0.205	0.041	-0.088	-0.079	0.064	-0.095	0.032	0.031
Equity	-0.076	-0.033	-0.031	0.063	-0.135	0.299	0.107	0.232
Mutual vision, goals/objectives	-0.150	0.113	0.039	0.166	0.120	0.062	0.061	-0.032
Effective conflict resolution process	-0.040	0.016	-0.144	-0.017	0.411	-0.060	0.145	-0.039
Educated and trained personnel for partnering	-0.135	0.089	0.350	0.031	0.007	-0.089	0.056	-0.088
Effective coordination	-0.054	-0.074	0.402	-0.065	0.079	-0.103	-0.014	-0.017
Adequate partnering team building	-0.133	-0.067	0.086	-0.013	0.143	-0.069	0.489	-0.180
Partnering experience	0.044	-0.055	-0.194	0.339	-0.067	0.093	0.104	0.048
Joint problem solving	-0.061	0.058	0.097	0.389	0.023	-0.059	-0.108	-0.113

as the potential independent variables. The seventy-one projects in the building set were used to develop the multinomial logistic regression model.

Table 3 presents the model fitting information. Both the Akaike information criterion (AIC) and the Bayesian information criterion (BIC) indicated that the final model achieved a better fit than the intercept-only model. Furthermore, the likelihood ratio test, significant at the 0.05 level, implied that the final model was significantly different from the model with the constant only or that the null hypothesis that all the predictor effects were zero could be rejected.

Table 3 Model fitting information

Model	Model fitting criteria			Likelihood ratio tests		
	AIC	BIC	-2 Log Likelihood	Chi-Square	df	Sig.
Intercept only	258.572	269.886	248.572			
Final	159.486	216.053	109.486	139.087	20	0.000

The goodness of fit test measures the fitness of the data collected for the model being proposed [19]. The Pearson and deviance tests were included. The finding of non-significance favors the conclusion that the model adequately fitted the data. The pseudo R² values are not goodness-of-fit tests, but rather attempt to measure the strength of association of the independent variables and the dependent variable. Cox-Snell and Nagelkerke are the two common relevant values to report. Based on the produced results, the model accounted for between 85.9 and 88.6% of variability in the dependent variable.

Another way to investigate whether the model fits with data or not is the classification table. The classification table (see Table 4) presents the observed and predicted groups. The overall correct rate of the model was 63.4%. The lowest prediction rate was at level 6 with the correct percentage of 37.5. The next was at level 8 with the correct percent of 46.2. The highest correct percentage was for level 5 and the second was level 10. Level 7 ranked third with 68.8% correct. A possible explanation is that it was not really hard for participants to rate levels 5, 7, and 10 because these values represented poor, average and very excellent performance outcomes, respectively. It was more difficult to rate intermediate values like 6 and 8. Level 9 represents very good performance but it still needs a little more effort to reach the level of excellence. Thus, rating level 9 is likely to be easier than level 8. Focusing on the distribution of the predicted groups against the observed groups, the predicted level outputs were distributed around the observed level with the deviation value of ± 1 level. This has possibly resulted from the difficulty in deciding a specific score for a subjective performance level. In general, it can be concluded that the final model achieves an acceptable fit with the data.

The parameters related to the model's coefficients are tabulated in Table 5. The Wald test results show that only "dedication" is significant at success levels from 5 to 8 (reference level is 10) at 0.05. At the 0.1 level, "balance" is significant at success level 7. "Teamwork" and "sufficiency" are significant at success level 9 at 0.05. For an exploratory purpose, the selected level of significance is 0.1.

The negative coefficients for "dedication" indicate that an increase in the variable value for this component decreases the likelihood of success of partnering being at

Table 4 Classification table

Observed level	Predicted level						Percent Correct
	5	6	7	8	9	10	
5	7	1	0	0	0	0	87.5
6	2	3	3	0	0	0	37.5
7	0	1	11	4	0	0	68.8
8	0	0	2	6	5	0	46.2
9	0	0	0	3	10	3	62.5
10	0	0	0	0	2	8	80.0
Overall percentage	12.7	7.0	22.5	18.3	23.9	15.5	63.4

Table 5 Parameter estimate

Partnering success level	Effect	B	Std. Error	Wald	df	Sig.	Exp(B)
5	Intercept	-1.171	2.283	0.263	1	0.608	
	Dedication	-10.312	2.749	14.074	1	0	0
6	Intercept	0.849	1.741	0.238	1	0.626	
	Dedication	-9.997	2.643	14.302	1	0	0
7	Intercept	3.062	1.399	4.788	1	0.029	
	Dedication	-7.114	2.245	10.04	1	0.002	0.001
	Balance	1.777	1.068	2.766	1	0.096	5.911
8	Intercept	3.057	1.35	5.126	1	0.024	
	Dedication	-3.445	1.703	4.094	1	0.043	0.032
9	Intercept	0.827	1.321	0.392	1	0.531	
	Teamwork	1.455	0.661	4.847	1	0.028	4.285
	Sufficiency	2.193	1.001	4.799	1	0.028	8.96

Note The reference category is 10

the current level. This implies that, by contrast, the likelihood of achieving partnering success at level 10 increases. The opposite is the case for “balance”, “teamwork”, and “sufficiency”, i.e. any increase in the values of the variables decreases the likelihood of achieving a higher level of partnering success. The large values for the coefficients of “dedication” (-10.31; -9.99; -7.11; -3.44) indicate a strong effect of the component on the success of partnering. From the results in this research, any improvement in the performance of dedication will improve partnering performance.

At level 9, “teamwork” and “sufficiency” are significant in the stepwise logistic regression model. It is surprising that at this level, an increase in the component value will diminish the chances of improving partnering performance. Perfect performance is very difficult despite a laudable goal to reach, in which level 9 is a very satisfactory and healthy degree of achievement for any partnership. Thus, at this level, devoting an effort to maintaining the current state is a wiser decision than trying to improve to a higher state. At the near perfection, all aspects in a partnership should be considered together. Focusing on any particular feature could lead to deterioration in the outcome of the partnering.

6.2 Model Validation

The developed model should be tested with the cases independent from the cases used in building the model. Eight testing cases were employed in this section. Using the highest probability as the cut-off criterion to classify the testing cases, the results of classification are displayed in Table 6. The observed and predicted categories

Table 6 Model validation

Testing case	Probability of predicted level	Success level		Correct?
		Observed	Predicted	
1	0.458	8	7	No
2	0.629	9	9	Yes
3	0.584	6	5	No
4	0.470	7	8	No
5	0.408	7	7	Yes
6	0.420	8	8	Yes
7	0.690	7	7	Yes
8	0.817	7	7	Yes
Correct percentage				5/8 = 62.8%

Note Highest probability is the cut-off criterion

were presented in the table. The computed probability of each predicted level was also included. There were five correctly-classified cases, which corresponds to the correct prediction rate of 62.8% over the testing sample. Only three cases, out of eight cases, were misclassified. However, the misclassification is not serious because the deviations are only 1-level distance. Again, a possible explanation for the results is the difficulty in deciding a specific score for the subjective performance level ratings.

6.3 Discussions of Modeling Results

The results from logistic regression analysis suggest that only four components have a significant contribution to the performance of partnering in the current Vietnamese context. The four components are dedication, teamwork, sufficiency, and balance.

Dedication is vital for nearly all levels of performance in the Vietnamese context. Uniting thoughts, actions and effort to achieve successful partnering is essential. The role of dedication is very important, especially when there is a chance to improve the level of performance. Dedication in the Vietnamese context comprises various essential factors, such as creativity, cultural fit, flexibility, and commitment. These factors are clearly important for new and less-experienced participants toward the partnering concept, who have achieved low success levels and are hoping for improvement. By way of contrast, with perfect or nearly perfect partnership arrangement, all factors have contributed very well to success. As such, no factor plays a dominant role in the partnering process.

Surprisingly at level 7, focusing more on balance in a partnership offers less chance to achieve better performance. The balance component relates to team building and empowerment in the partnership. A possible explanation is that, at the intermediate level, it is necessary to focus on other problems rather than the balance of partnership.

In the current Vietnamese context, to improve the performance from the average level, partners should concentrate on dedication to their partnership rather than pay attention to building a team with equal/fair empowerment.

Another surprising result is that teamwork and sufficiency have a negative impact on the effort to improve at level 9. A possible explanation is that level 9 is a nearly perfect level of performance. As such, participants have good experience with the concept and the mechanism being applied has run well. Any change will disturb the equilibrium of the mechanism under the current conditions.

7 Recommendations

Based on data collected from partnering projects in Vietnam, the effect of SFs on the level of success was modeled using multinomial logistic regression. The schematic diagram for the improvement of partnering performance in the Vietnamese construction industry is presented in Fig. 2. Recommendations can be extracted as below.

In the current context in Vietnam, with partnering projects achieving low and average performance (from 5th to 8th grades), the most important factors needing attention are related to dedication. Improving the dedication of partners will increase the probability of achieving better performance.

At average performance (level 7), focusing on the improvement of balance in the partnership (team building, empowerment) could decrease the probability of achieving better performance. It is best to equally improve all aspects of partnering, especially dedication.

At very good performance (level 9), focusing on the improvement of teamwork and sufficiency will diminish the chance of further performance improvement. At this level, all factors must work very well, and thus, for the current situation in Vietnam, efforts should be devoted to maintaining the current level rather than trying to achieve an absolutely perfect level of performance (level 10).

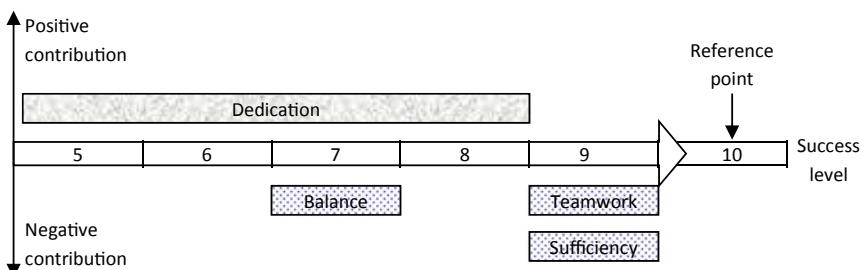


Fig. 2 Scheme diagram of partnering in the Vietnamese construction industry

Furthermore, using the logistic regression model proposed in the study, it could calculate the probability of achieving each success level. Practitioners can make decisions regarding which success level could be performed in their partnership. The maximum probability can be used as the cut-off criterion. It implies that the achieved success level is the level which has the highest chance of occurrence.

Participants can also use the procedure of the proposed logistic regression model to improve their partnering process by evaluating the impact of each factor on the probability of success level. The evaluation will allow participants to decide to devote more attention to, or put greater effort on, managing the significant factors in order to increase the chance of achieving better performance outcomes.

8 Conclusions

The results from this study show that partnering has been successfully applied in the Vietnamese construction industry. The rating given to partnering success by respondents in the survey (i.e. professionals involved in partnering projects) has a median value of 8/10 (mean value of 7.66). Emerging from this is the utility of partnering a viable procurement option in Vietnam.

Twenty-eight SFs associated with partnering performance in the Vietnamese construction industry were employed to construct a model to predict the level of partnering success. Using factor analysis, twenty-eight SFs were grouped into eight components: dedication, readiness, coordination, teamwork, sufficiency, leading, balance, and clarity. These eight components were used as independent variables for the logistic regression model.

The regression model, which included four components, namely dedication, teamwork, sufficiency, and balance, had a significant influence on the partnering performance level. The potency of each significant component varied with the level of success. It has been demonstrated that the final model is applicable in practice. The logistic regression model can be used by practitioners to convert qualitative performance data on related SFs into quantitative values of the chance of partnering success in a specific context. The model can also be used to measure the performance of partnering and enhance the performance of partnering by identifying the impact of significant factors on the performance of partnering.

References

1. Beach R, Webster M, Campell KM (2005) An evaluation of partnership development in the construction industry. *Int J Proj Manag* 23:611–621
2. Black C, Akintoye A, Fitzgerald E (2000) An analysis of success factors and benefits of partnering in construction. *Int J Proj Manag* 18:423–434
3. Boynton AC, Zmud W (1984) An assessment of critical success factors. *MIT Sloan Manag Rev* 25(4):17–27

4. Chan APC, Chan DWM, Chiang YH, Tang BS, Chan EHW, Ho KSK (2004) Exploring critical success factors for partnering in construction projects. *J Constr Eng Manag* 130(2):188–198
5. Chan APC, Chan DWM, Fan LCN, Lam PTI, Yeung JFY (2006) Partnering for construction excellence—a reality or myth? *Build Environ* 41:1924–1933
6. Chen WT, Chen TT (2007) Critical success factors for construction partnering in Taiwan. *Int J Proj Manag* 25:475–484
7. Chen WT, Huang YH, Lin CL, Mortis L (2008) A framework of critical factors for construction partnerships in Taiwan. In: *ICC 2008 Proceedings*, IEEE Communication Society, pp 5553–5557
8. Cheng EWL, Li H, Love PED (2000) Establishment of critical success factors for construction partnering. *J Manag Eng* 16(2):84–92
9. Cheng EWL, Li H (2001) Development of a conceptual model of construction partnering. *Eng Constr Archit Manag* 8(4):292–303
10. Cheng EWL, Li H, Love PED (2002) Construction partnering process and associated critical success factors: quantitative investigation. *J Manag Eng* 18(4):194–202
11. Cheng EWL, Li H, Love PED, Irani Z (2004) Strategic alliances: a model for establishing long-term commitment to inter-organisational relations in construction. *Build Environ* 39:459–468
12. Cheung SO, Suen HCH, Cheung KKW (2003) An automated partnering monitoring system—partnering temperature index. *Autom Constr* 12:331–345
13. Crane TG, Felder JP, Thompson PJ, Thompson MG, Sanders SR (1997) Partnering process model. *J Manag Eng* 13(3):57–63
14. Crowley LG, Karim MA (1995) Conceptual model of partnering. *J Manag Eng* 11(5):33–39
15. Hair JF, Black WC, Babin BJ, Anderson RE (2009) Multivariate data analysis, 7th edn. Prentice Hall
16. Han SH, Kim DY, Kim HK (2007) Predicting profit performance for selecting candidate international construction projects. *J Constr Eng Manag* 133(6):425–436
17. Handa V, Adas A (1996) Predicting the level of organizational effectiveness: a methodology for the construction firm. *Constr Manag Econ* 14:341–352
18. Iyer KC, Jha KN (2006) Critical factors affecting schedule performance: evidence from Indian construction projects. *J Constr Eng Manag* 132(8):871–881
19. Koksal A, Arditı D (2004) Predicting construction company decline. *J Constr Eng Manag* 130(6):799–807
20. Larson E (1997) Partnering on construction projects: a study of the relationship between partnering activities and project success. *IEEE Trans Eng Manag* 44(2):188–195
21. Le-Hoai L (2009) Partnering in construction: the views and experiences of foreign and local participants in Vietnamese market. Unpublished PhD Thesis, Pukyong National University, Busan, South Korea
22. Le-Hoai L, Lee YD, Lee JY (2008) Delay and cost overruns in Vietnam large construction projects: a comparison with other selected countries. *KSCE J Civil Eng* 12(6):367–377
23. Loraine RK (1994) Project specific partnering. *Eng Constr Archit Manag* 1(1):5–16
24. Menches CL, Hanna AS (2006) Quantitative measurement of successful performance from the project manager's perspective. *J Constr Eng Manag* 132(12):1284–1293
25. Rockart JF (1979) Chief executives define their own data needs. *Harv Bus Rev*, March–April, pp 81–92
26. Rowlinson S, Cheung FYK, Simons R, Rafferty A (2006) Alliancing in Australia—no-litigation contracts: a tautology? *J Prof Iss Eng Educ Pract* 132(1):77–81
27. Sharma S (1996) Applied multivariate techniques. John Wiley & Sons Inc
28. Tang W, Duffield CF, Young DM (2006) Partnering mechanism in construction: an empirical study on the Chinese construction industry. *J Constr Eng Manag* 132(3):217–229

Management of Buildings with Semantic and 3D Spatial Properties by S_EUDM Data Model



T. V. Phan, G. T. Anh Nguyen, and Trung Tran Do Quoc

1 Introduction

According to the Ministry of Construction forecasts, the urbanization rate of Vietnam in 2020 will be about 40%, 2050 about 50% (Table 1) [1]. The state target for an average area is 100 m²/person. If this rate is reached, Vietnam needs 450,000 ha of urban land. With this accelerated development, Vietnam will face more and more management issues arising from the process of urbanization.

Urbanization is the expansion of the city, calculated as a percentage of the urban population or the urban area of the total population or area of a region or region. It can be calculated according to the increase rate of the two elements according to the time axis. If calculated in the first way, called the level of urbanization; in the second way, called the speed of urbanization.

Therefore, the research on construction and development of projects Managing buildings will contribute to the management, planning and orientation of the development of the current cities.

In order to build a building management application, the key to the success of the job depends on the stage of building a 3D geographic information system (GIS) model.

T. V. Phan · G. T. Anh Nguyen (✉)

Faculty of Information & Engineering Science, University of Information Technology, Vietnam National University HoChiMinh City, Hochiminh City, Vietnam

e-mail: anhngt@uit.edu.vn

T. V. Phan

e-mail: vuphanthanh23@gmail.com

T. T. Do Quoc

Faculty of Civil Engineering, University of Technology, Vietnam National University HoChiMinh City, Hochiminh City, Vietnam

e-mail: 1870107@hcmut.edu.vn

Table 1 Name of relations and bytes in S_EUDM

Seq	Relations name	Bytes
1	ALLUSER	121
2	BLUNTED_CONE	26
3	BODY	83
4	BODY_COMP	20
5	BODY_LOD	20
6	BUILDING	54
7	BUILDING_OWNER	20
8	CERTIFICATE	224
9	CONE	26
10	CYLINDER	26
11	F_POLYGON	20
12	F_TRIANGLE	40
13	FACE	12
14	HISTORY	61
15	L_EQUATION	19
16	L_EQUATION_NODE	20
17	L_SEG_CIRCLE	40
18	L_STRAIGHT	20
19	LAND	30
20	LINE	47
21	LINE_LOD	20
22	LOD	15
23	NODE	28
24	OWNER	106
25	POINT	30
26	POINT_LOD	20
27	PRISM	24
28	PYRAMID	30
29	S_CIRCLE	23
30	S_CURVE	20
31	S_POLYGON	20
32	SIGNER	55
33	SURFACE	47
34	SURFACE_LOD	20
35	TRUNCATED_PYRAMID	30
TOTAL		1417

GIS 3D is a system that can model, represent, manage, manipulate, analyze and support decisions based on information related to 3D phenomena [2–4]. Application of GIS 3D is large and diverse: Ecological research, 3-dimensional maps, environmental monitoring, landscape planning, geological analysis, civil construction, mineral exploration and exploitation real estate, urban management ... [2, 4]. These applications have many benefits when represented in GIS 3D because they reflect truthfully about the real world. 3D GIS data model is a data model used in the analysis and design of 3D GIS applications.

There are many proposed 3D data models (Fig. 1), they are classified by four main forms [5]:

- Representing 3D objects by its boundaries (B-REP), including models: 3D-FDS, TEN, OO, SSM, UDM, OO3D, CITYGML, EUDM.
- Representing 3D objects by voxel elements, including models: 3D ARRAY, OCTREE.
- Representing 3D objects by combining basic 3D blocks (CGS).

Model	Set 1				Set 2		Set 3		
	Topology		Attribute Query		Topological Rel. Query	Position Query	Curve Surface	History	Semantics
	Measurement	Direction	Spatial Structure				LOD		
3DFDS	V	Y	N	Y	N	Y	Y	1	N
TEN	V	N	Y	N	N	Y	N	1	Y
SSM	V	N	N	Y	N	Y	Y	1	N
OO	V	Y	N	N	N	Y	N	1	Y
SOMAS	V	Y	N	N	N	Y	N	1	N
UDM	V	Y	Y	N	N	Y	N	1	Y
OO3D	V	N	N	N	N	Y	N	1	Y
CityGML	V	N	N	N	Y	Y	N	4	Y
EUDM	V	N	Y	N	N	Y	N	1	Y
LUDM	V	N	Y	N	N	Y	N	A	Y
I1-CityGML	V	N	N	N	Y	Y	N	16	Y
I2-CityGML	V	N	N	N	Y	Y	N	A	Y
3DArray	R	N	Y	N	N	N	N	1	Y
Octree	R	N	Y	N	N	N	N	1	Y
CSG	V	N	Y	N	N	Y	N	1	Y
BREP+CSG	V	N	Y	N	Y	Y	N	1	Y
V-3D	VR	N	N	N	N	Y	N	1	N

Fig. 1 Models comparision

- Representing 3D objects by combining the above 3 methods. For example, a combination of B-REP and CGS.

Most 3D data models in GIS serve applications related to urban management problems, especially models that have an approach to B-REP. Some of the remaining models serve geological applications [5]. Models with the following proposed time are often developed from the available models in the past by adding, subtracting objects, or changing approaches or mixing several approaches.

2 Data Model for Buildings Management

2.1 *Spatial Objects Need to Be Managed*

The objects to be managed for the whole application include: Building, Land, Certificate of Building ownership, Owner, Signer, Tree. Building is a 3D block, defined as a set of Blocks, which can contain cubes of the following form: complex form (Complex), Pyramid, Truncated Pyramid, Cone, Blunted Cone, Prism, Cylinder.

In addition to the Block object, the Building can also contain other special geometry objects: straight lines (e.g: straight borders, stratified dividers ...), in which Road is divided into 3 type: Road with equation (L_Equation), Straight Line (L_Straight) and Circular Supply Line (L_Seg_Circle); face (Surface) (e.g plate between 2 floors), in which the face is divided into 3 forms: Curved Face (S_Curve), Circle (S_Circle) and simply described by polygon (S_Polygon); Point. The curved face is described in many simple shapes (Face), usually a set of triangles. A building has many different levels of representation called the levels of detail (LOD).

2.2 *Semantic Objects Need to Be Managed*

Building consists of attributes: house number, house number, house level, number of floors, construction area, floor area, structure.

Owner: includes the attributes: Owner's number, identity card number, first and last name, gender.

Home ownership certificate: Certificate code; ward name, street name, district name, city name; day; Barcode; coordinates the space points of the Building that it manages.

Land: land code, area, type of land, number of sheets.

The person who signs the certificate: The signer code, the full name and position.

2.3 Select and Propose an Improved Spatial Data Model

B_{REP}-type models are advantageous in selecting building management applications [6], from UDM model, we choose EUDM model [5, 7] (Fig. 1), to specialize in geometric forms basic. The three advantages of the EUDM model are: the amount of effective data storage; time to display fast blocks; easy for displaying LOD [3] buildings.

2.4 Data Model Integrated Spatial and Semantic Components

The model in Fig. 2 only describes the spatial properties of a 3D object. An object in GIS, usually beside on spatial attributes, it also has semantic properties, even time

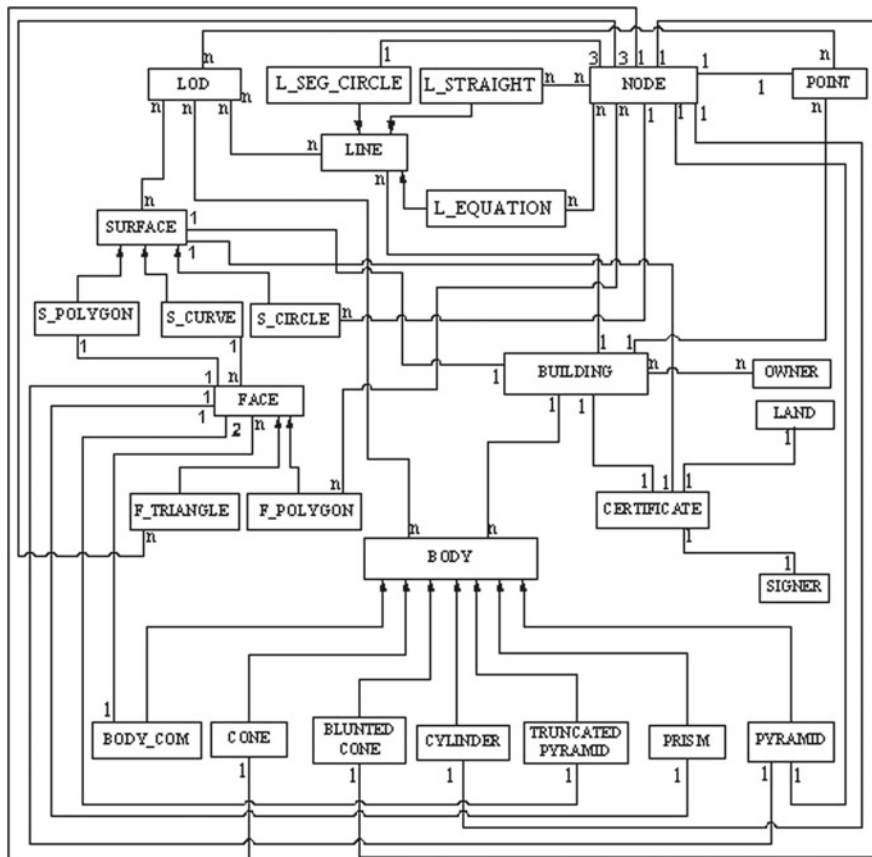


Fig. 2 Model S_EUDM

attributes. Within the limits of the paper, we do not integrate time attributes. Building objects with semantic attributes include: House, Owner, Land, Person signing certificate, Certificate of house ownership. The data model incorporates two spatial and semantic attributes as shown in Fig. 2, named S_EUDM (Semantic_EUDM). Table 1 summarizes the relationship of S_EUDM and indicates the size of a data row.

3 Experiments

Experiments include 2 parts: 1. Comparing data size and display time of 2 models of UDM and EUDM. 2. Forms to add, search, update data for buildings. We take a sample of 150 buildings (Fig. 3), each with the form as shown in Fig. 3. After calculating, we have a volume of 150 buildings according to EUDM is (25,020 bytes), and UDM is 82,350 bytes. The storage volume of UDM model is about 3.2 times that of 150 buildings.

Other forms of 3D blocks, the superiority of EUDM compared to UDM in terms of storage volume proved in [4]. Table 2 is the comparison of the display time of 150 buildings with 10 trials. So, the average UDM display time is about 2.9 times larger than EUDM.

Fig. 3 A building sample in experiment

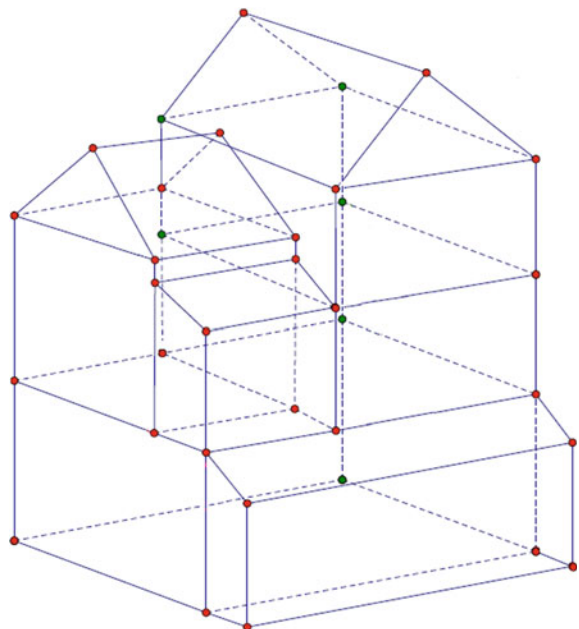


Table 2 Compare display time of UDM and EUDM

Seq	150 Buildings (Display time cost); unit: ms	
	UDM	EUDM
1	3856	1251
2	3701	1261
3	3846	1276
4	3781	1266
5	3701	1301
6	3701	1266
7	3856	1276
8	3781	1251
9	3781	1266
10	3701	1291

Some typical forms and reports of the experiment are illustrated in Sect. 3, including 4 forms. These forms are made by C # language and Oracle database administration system. Especially the data section, we use the spatial data type that Oracle has supported. This data type makes the display time of the building faster. Each form is described by two parameters: input and output.

Form 1: Search for a house by building code (Fig. 4)

Input: Building code

Output: Information of the corresponding building

Form 2: Update data for a building (Fig. 5)

Input: Semantic values and space for a newly formed building

Output: Data is saved to the database

Form 3: Search for buildings according to many criteria (Fig. 6)

Input: Building search criteria

The screenshot shows a Windows application window titled "Building Management". At the top left is a text input field labeled "Building ID" containing "BU00000001". To its right is a blue button labeled "3D Data Entry". Below this is a navigation bar with tabs: "House & Land" (selected), "Owners", and "House Ownership Papers".

The main area is divided into two sections: "House" and "Land".

House Section:

- "Number of Floors": Input field with value "4".
- "Floor Area(m²)": Input field with value "100".
- "Address": Text input field containing "202A, Trung Chính, Ward 10, Tân Bình District, HCMC".
- A small icon of a red house is displayed.

Land Section:

- "Land ID": Input field with value "LA00000001".
- "Number of Lands": Input field with value "2".
- "Land Type": Input field with value "Agricultural land".
- "Land Paper No.": Input field with value "1".
- "Area (m²)": Input field with value "150".
- A small icon of a green landscape with trees and a house is displayed.

At the bottom of the form are four buttons: "Add", "Edit", "Delete", and "Reset".

Fig. 4 Searching form for a building by building code

Building Data Entry

Building ID	BU00000013										
	Prism	Surface	Cylinder	Cone	Blunted Cone	Pyramid	Blunted Pyramid	Line	Point	Complex Block	
Prism ID	PR00000049										
Height	100				Prism type						
				<input checked="" type="radio"/> Vertical		<input type="radio"/> Horizontal					
Is the bottom surface exist?											
<input checked="" type="radio"/> Yes		<input type="radio"/> No		Bottom surface		SU00000061	Select	Level of details			
									<input type="checkbox"/> Level 1	<input type="checkbox"/> Level 2	<input type="checkbox"/> Level 3
<input type="button" value="Add"/> <input type="button" value="Edit"/> <input type="button" value="Delete"/> <input type="button" value="Reset"/>											
Prism ID	Bottom Surface ID				Prism type						
PR00000049	SU00000061				Vertical						
PR00000050	SU00000062				Horizontal						
PR00000051	SU00000063				Vertical						

Fig. 5 Updating form for a building

Search building data

Category	Owner		Category Keywords		Identity No.		Search	
Full name			from date		to date			
Birthday								
Gender	<input type="radio"/> Male <input checked="" type="radio"/> Female		Street		Ward			
					1			
District			City					
<input type="button" value="Full Data"/> <input type="button" value="3D Viewer"/>								
IDBU	IDO	Identity No.	Full name	Gender	Street	Ward	District	City
BU000000001	OW000000002	231848992	Tran Van Nam	Male	Nguyen Tri Phuong	1	10	Ho Chi Minh
BU000000002	OW000000003	125441672	Nguyen Thi Thanh	Female	Nguyen Du	1	1	Ho Chi Minh
BU000000004	OW000000009	937266332	Le Hao Anh	Male	Le Binh	1	Tan Binh	Ho Chi Minh
<input type="button" value="Exit"/>								

Fig. 6 Searching form for buildings by many criteria

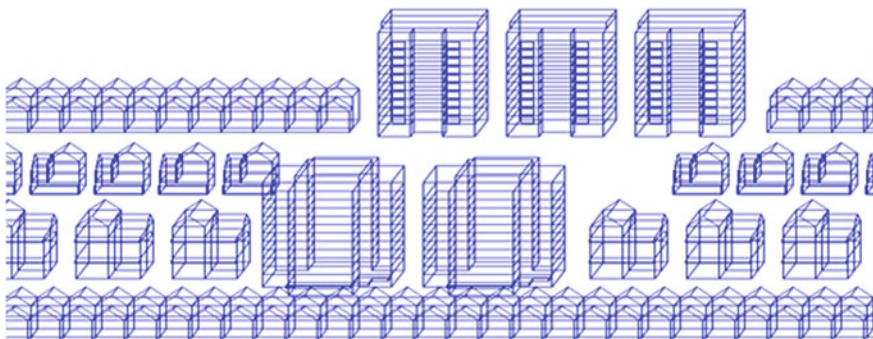


Fig. 7 Display form the space of buildings in a residential area

Output: Buildings meet criteria

Form 4: Display the space of buildings (Fig. 7)

Input: Building codes

Output: Displays the space of buildings in a residential area.

4 Conclusion

The paper presented steps: selecting, improving, designing database models and successfully installing software to manage buildings in urban areas. The main functions of the application are detailed in Sect. 4. Applications undergo steps in the process of building a software: survey, analysis, design, installation and testing.

The article also inherited and improved the UDM model with the S_EUDM new model. The new model demonstrates some advantages over the old model in terms of: storage, display time, semantic attributes and ease of displaying the level of detail on loved objects. user demand.

Acknowledgements This research is funded by University of Information Technology-Vietnam National University HoChiMinh City under grant numberD1-2019-17.

References

1. El Garouani A, Alobeid A, El Garouani S (2014) Digital surface model based on aerial image stereo pairs for 3D building. *Int J Sustain Built Environ* 3(1):119–126 (Elsevier)
2. Anh NGT, Vu PT, Tran SA, Vinh PT, Dang PV (2011) Representing multiple levels for objects in three-dimensional GIS model. In: The 13th International Conference on Information Integration and Web-based Applications & Service (iiWAS2011). ACM Press ISBN, Ho Chi Minh City, Vietnam, pp 495–499

3. Anh NGT, Dao SM, Mai-Van C (2017) A comparative survey of 3D GIS models. In: (NAFOSTED) Conference on Information and Computer Science (NICS), IEEE, pp 126–131
4. Dinh TD, Anh NGT (2014) Display, query, delete time cost for the 3D GIS objects in two database systems with oracle. In: Second international conference on emerging research in computing, information, communication and applications, vol 2, pp 55–59
5. Anh NGT, Tran PV, Khac DH (2013) Overview of three and four-dimensional GIS data models. *Multimedia Ubiquitous Eng Lect Notes Electr Eng* 240:1013–1020
6. Rahman AA (2008) Spatial data modeling for 3D GIS. Springer, Heidelberg
7. Anh NGT (2011) Innovating urban data model for new urban area management. *J Sci*, 5–18. ISSN 1859-1388

Monitoring the Spatio-Temporal Changes of Can Gio Mangrove Forest Using Google Earth Engine



Vu Hoang Dinh Phuc and Dao Nguyen Khoi

1 Introduction

Mangrove forests take the important role in coastal protection by collecting sediment from rivers and streams and slowing down the flow of water, provide protection and shelter against extreme weather events such as storm winds, floods, tsunamis, and protect human communities farther inland from natural disasters [2]. The ecosystem of mangrove forests is one of the most biologically diverse characteristics that provide the home for wide varieties of fauna and flora species, including shrimp, prawns, crabs, shellfish, snails, etc.

The Can Gio mangrove forest has many valuable ecosystem services such as construction wood, firewood, fish catch, crab catch, clam and oyster harvest. Additionally, this area has been considered as the Ho Chi Minh City's "green lung", contributing to minimizing the impacts of climate change including coastal stabilization, and protection against coastal erosion, oil spills and storm surges. To efficiently manage the mangrove forest, monitoring spatiotemporal changes of mangrove forests in the region over a long period is important to provide with valuable information for local managers and policy-makers.

Main approaches for mangrove monitoring consist of field survey and remote sensing technology [1]. Compared to field survey, remote sensing can provide mangrove forest data with detailed spatio-temporal coverage, which can help managers having more information in decision-making. The applications of remote sensing in classifying and monitor mangrove forest in Vietnam have been listed in the literature (i.e., [3, 4]).

V. H. D. Phuc

Faculty of Civil Engineering, Ho Chi Minh City University of Technology, VNU-HCM, Ho Chi Minh City, Vietnam

D. N. Khoi (✉)

Faculty of Environment, University of Science, VNU-HCM, Ho Chi Minh City, Vietnam
e-mail: dnkhoi@hcmus.edu.vn

Recently, the Google Earth Engine (GEE) platform provides cloud-computing capabilities, which can allow free access to vast and fast earth observation data. The objective of this study was to assess the spatiotemporal change of Can Gio mangrove forest by using remote sensing data and GEE cloud-computing platform. The obtained results of this study are likely to be useful for the sustainable management of Can Gio mangrove forests.

2 Methodology

2.1 Study Area

In the year 2000, the Can Gio mangrove forest was recognized as the first Mangrove Biosphere Reserve in Vietnam. This area lies between latitudes $10^{\circ}22'14''$ to $10^{\circ}40'09''$ N and longitudes $106^{\circ}46'12''$ to $107^{\circ}00'59''$ E. It is located in Can Gio district, one of 24 districts of Ho Chi Minh City (HCMC) in Vietnam. Can Gio is a coastal district with 35 km in length and 30 km in width. Covering more than 72,000 ha in area and located about 50 km southeast of HCMC and it's a deltaic confluence of the rivers of Saigon, Dong Nai and Vam Co, which drain into East Sea. Can Gio district is contributed by six communes included Binh Khanh, An Thoi Dong, Ly Nhon, Tam Thon Hiep, Long Hoa and Thanh An. Consisting of 159 species (36 true mangroves, 33 salt-tolerant and 90 associates), the mangrove has contributed an importance role in the coastal zone economic and environmental. The mangrove provides not only valuable products from mangrove forests for almost population living in these areas including timber, firewood, charcoal, tannin, food, medicinal, also the breeding ground for many species of marine organisms like shrimp, crab, fish, water and migratory birds as well as other economically terrestrial species of monkey, wild boars, boas etc. Although the research area has different types of mangrove species, this research focus on Rhizophora apiculata and Avicennia alba as described the dominant species.

2.2 Image Data

In this research, Landsat 5, 7 and 8 collections are used with resolution of 30 m and archived from Earth Engine server. For analyzing the spatiotemporal changes of landcover in 31 years from 1988 to 2018, 31 Landsat images has been extracted from 3 collections which is 14 images from Landsat 5 collections, 11 images from Landsat 7 collection and 6 images from Landsat 8 collections. Detail information of 3 Landsat collection are described in Table 1.

Image interpretation is based on the combination of satellite data and field survey results to provide the most accurate data set, contributing to improved image

Table 1 Detail information of Landsat collections

Name	Data availability	Archive period	Provider	Image collection ID
Landsat 8 Collection 1 Tier 1 Raw Scenes	Apr 11, 2013–May 4, 2019	2013–2018	USGS	LANDSAT/LC08/C01/T1
Landsat 7 Collection 1 Tier 1 Raw Scenes	Jan 1, 1999–Apr 21, 2019	2002–2012	USGS	LANDSAT/LE07/C01/T1
Landsat 5 TM Collection 1 Tier 1 Raw Scenes	Jan 1, 1984–May 5, 2012	1988–2001	USGS	LANDSAT/LT05/C01/T1

classification results. The field survey had collected 30 sample points throughout 6 communes of Can Gio, divided into 5 different types of land covers are Water, Urban and Soil, Mix species, Avicenna and Rhizophora. Sample points are represented for an area of each classification type and each point also go with pictures to provided better accurate on interpretation. Field survey data use mostly for calibrate the training data set created by image interpretation from google earth satellite layer integrated on GEE.

2.3 Training Data

The number of sample points are not similar throughout 5 groups of images, shown in Table 2, reason for differences are the application of training data set can have noise problem with classification in non-base images. The distribution of objects represented for each class can be changed by time, that mean the sample points can

Table 2 Number of samples and indicators of each class in 5 groups of images

Class	2018–2013	2006–2012	2002–2005	1993–2001	1988–1992	Indicator
Water	56	56	56	56	41	
Urban	31	31	31	13	13	
Mix species	18	19	20	13	13	
Avicenna	21	9	17	11	9	
Rhizophora	31	9	18	34	19	

be right on the base images but incorrect on other images. With many sample points representing for will may creating more noises and cannot get higher accuracy in classification. The training data set was calibrated with google earth images in the right year of capture base Landsat images, specific as 1992, 2001, 2005, 2009, 2018. Field survey data also had a contribution for correcting the training data set, especially in 2018 image. Using geometry tool integrated in GEE for creating training feature values and adding feature point collections. In all 5 groups of images, the landcover feature values setting for 5 class are Water = 0, Urban and Soil = 1, Mix species = 2, Avicenna = 3 and Rhizophora = 4.

3 Methodology

The topic includes the main stages of identifying topics, collecting data; data processing analysis, interpretation; Establish mangrove forest classified maps from 1988 to 2018 and mangrove forest area change in the period of 1988–2018, summarize, statistics and evaluate the results. Data collected from the main sources are remote sensing data (Landsat images) and GIS data (Can Gio administrative data).

3.1 *Normal Difference Vegetation Index—NDVI*

NDVI is an alternative to plant numbers and living conditions. This index is represented the characteristics of vegetation cover such as biomass and plant cover percentage, suitable for the research objective is focus on the spatiotemporal change of mangrove forest. Calculations of NDVI for a given pixel always result in a number that ranges from minus one (-1) to plus one ($+1$); however, no green leaves give a value close to zero. A zero means no vegetation and close to $+1$ (0.8–0.9) indicates the highest possible density of green leaves. NDVI are calculated for each Landsat image then applied with Random forest algorithm to supervised classify the mangrove forest cover. The Landsat 8 image group and Landsat 5 image groups are different in NDVI calculating step. Band 5 and band 4 are using for calculating NDVI in Landsat 8 collection; band 4 and band 3 for calculating NDVI in Landsat 5 and 7 collection.

3.2 *Image Pre-processing*

Import Can Gio boundary shapefile as a feature collection to GEE named as “StudyArea” shapefile, play an important role in classification processing as to fit collections into research scope and to calculate the total area of Can Gio. Landsat 7 image groups have gap problems that make those groups need to apply gap filling in the

collection loading step. The USGS Landsat 7 Collection 1 Tier 1 TOA Reflectance were loaded with the 5% cloud cover filter. For Landsat 8 and 5 image collections, USGS Landsat 8 Collection 1 Tier 1 Raw Scenes and USGS Landsat 5 TM Collection 1 Tier 1 Raw Scenes were loaded. Using a date filter, the collections are divided into small collections by years. Those small collections then again be filter and combined into Landsat TOA images that fit the study area boundary by using Landsat simple composite algorithm. For creating simple cloud-free Landsat composites, Earth Engine provides the ee.Algorithms.Landsat.simpleComposite() method.

3.3 Supervised Classification

Train the Landsat images based on the created training data set using classifier.train(). Classify an Image or FeatureCollection using classify() code. Random Forest algorithm (randomForest) classifier to predict forest and non-forest areas with default parameter. Classify the image with the 'NDVI' band used for training. The accuracy of classification results then assessed by calculating the training overall accuracy with accuracy() and Kappa coefficient with kappa() algorithms using the confusion matrix on the training data of based image from classifier.confusionMatrix(). Calculating area of each classes used PixelArea algorithms with the unit of Meter square. Print the area results in form of bar charts on console window. The GEE allow user to download the result inform of CSV file, very convenient for working statistic with Microsoft Excel.

4 Results and Discussion

Training data set, Kappa coefficient and Training Overall Accuracy calculating are based on 1 represent image of each group. In overall, Kappa coefficients of all based image higher than 81% and training overall accuracies higher than 86%. The Kappa coefficient and Training overall accuracy results of each based image are show in Table 3.

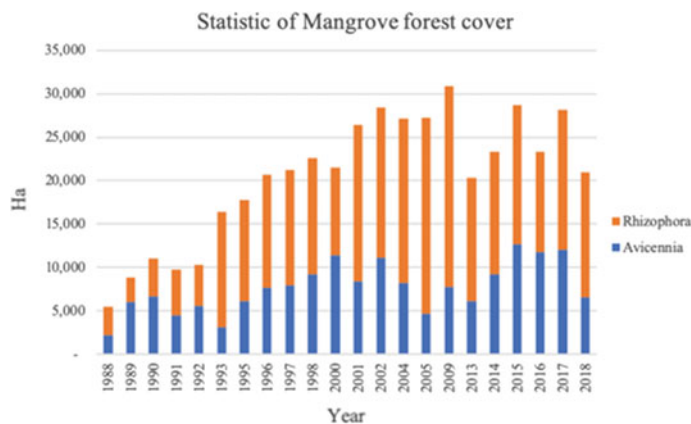
The statistic results of forest cover from 1988 to 2018 are described as bar chart in Fig. 1 and the statistic results of Mangrove forest cover from 1988 to 2018 are described as bar chart in Fig. 2.

4.1 Accuracy Assessment

The Training overall accuracy and Kappa coefficient of results are in relative level by compare with other researches that also use Landsat image for classification mangrove forest. Vo Minh Hoan (2017) has established maps of mangrove forest in

Table 3 Kappa coefficient and Training overall accuracy results

Group name	Base image	Kappa coefficient	Training overall accuracy
Landsat 8 2013–2018	2018	0.86	0.89
Landsat 7 2006–2012	2009	0.83	0.88
Landsat 7 2002–2005	2005	0.81	0.86
Landsat 5 1993–2001	2001	0.90	0.93
Landsat 5 1988–1992	1992	0.84	0.88

**Fig. 1** Statistic of Mangrove forest cover

Can Gio district using Landsat 8 images with accuracy of 83%. Pham Tien Dat and Kunihiko Yoshino (2015) was mapping the locations of mangrove and to analyze their change in Hai Phong, Vietnam from 1989 to 2013 using different Landsat sensors with overall accuracy of satellite imagery processing for the year 2013 was 83%. Nguyen Thanh Son (2016) and his partners had been developed Can Gio mangrove forest maps in 4 different periods of time: 1989–1996, 1996–2003, 2003–2009, and 2009–2014 with overall accuracies were generally higher than 90%. In international, Tran Thanh Dan (2016) has using the Landsat data to implemented mangrove forest maps in Sundarbans, West and Central Africa in 1988, 2001 and 2014. The classification get accuracy in West and Central Africa is 84.1%, in Sundarbans is 83.0%. In overall, the classified maps still can be used for analyzing the distribution of mangrove forest.

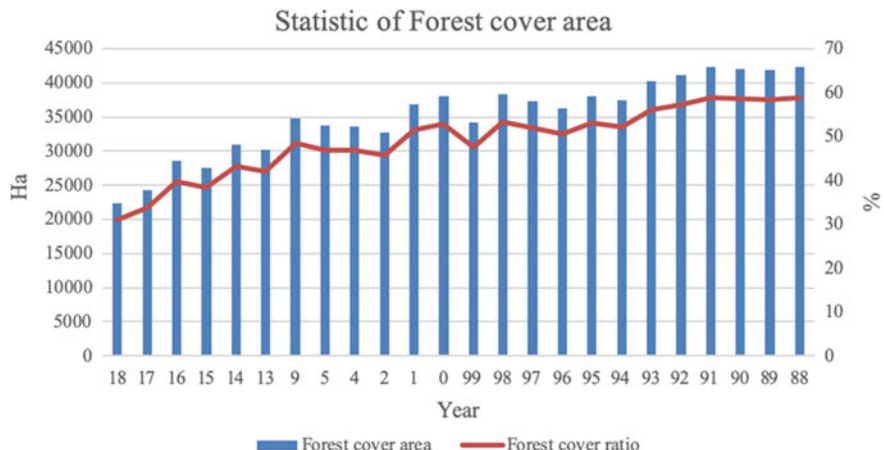


Fig. 2 Statistic of Can Gio forest cover area

4.2 Classification Assessment

The Mangrove forest classification results are used to compare with results of Son et al. [4] to assess the reliability of mangrove forest classification results. Also using multi-temporal Landsat image to monitoring Mangrove change in Can Gio Biosphere Reserve, Son et al. [4] had shown a series of Mangrove forest cover statistic results in 1989, 1996, 2003, 2009 and 2014 which is 26,447 ha; 30,437 ha; 30,679 ha; 33,083 ha and 31,283 ha respectively. At the same time, in this research shows the Mangrove forest cover statistic results in follow: 8857 ha in 1989; 20,639 ha in 1996; 27,134 ha in 2004; 30,872 ha in 2009 and 23,286 ha in 2004. The difference between 2 research's classification results are significant in 1989 which having approximately 17,000 ha difference in mangrove forest cover. In another time, this research shows less Mangrove forest cover than the research of Son et al. [4] but the growth trend of Mangrove forest between researches are similar when the Mangrove forest cover increased form 1989 until 2009 and the plumb down in 2014. The cause of difference between 2 classification results can be form in the process of classify Rhizophora, Avicenna and Mix species in this research.

In comparison with Tran Vu Khanh Linh et al. (2018), the analyzed results between 2 researches are relatively similar when the forest cover trend are increasing by the time of study. Their results in 1988, 1998, 2008, 2018 are 24,035; 29,564; 32,505; 36,651 ha respectively and for this results in 1988, 1998, 2009, 2018 are 22,311; 36,905; 37,410; 42,296 ha respectively. Unfortunately, the classified result in 2008 is unusable so for the comparation will use result in 2009 in substitution. The difference between 2 set of results are significant in 1998 with 21% but the in other year the difference are below 14%, specific as 7.7% in 1988, 11.9% in 2008 and 2009, 13.3% in 2018. The level of accuracy of classification was acceptable but it still relatively

not high when having minimum of 81%, it can due to the low resolution of the image, also can be influenced by the training data set so it could be error in classification.

4.3 Spatiotemporal Change Assessment

Figure 3 show the classification results in 2018, for the full classification results can be found in GEE as weblink on Reference. Based on the results from the construction of mangrove forest classified maps, it can be seen that the less variation areas are core zone. The areas of high variation are the areas that go deeper into the mainland, the cause of the fluctuation is the spread of urban areas and the people's production activities into shrimp, salt farming and inadequate exploitation, leading to the distribution of mangroves. Rhizophora exist mainly in core zone and buffer zone. Avicenna can mostly be live in buffer zone, contribute almost in riverside and fell in transition zone. Compare with 1988 when the forest cover in Can Gio was less and Avicenna was very rare to found, the Avicenna in present have outstanding position in Can Gio MBR, which can be found almost in any riverside. Avicenna also can be

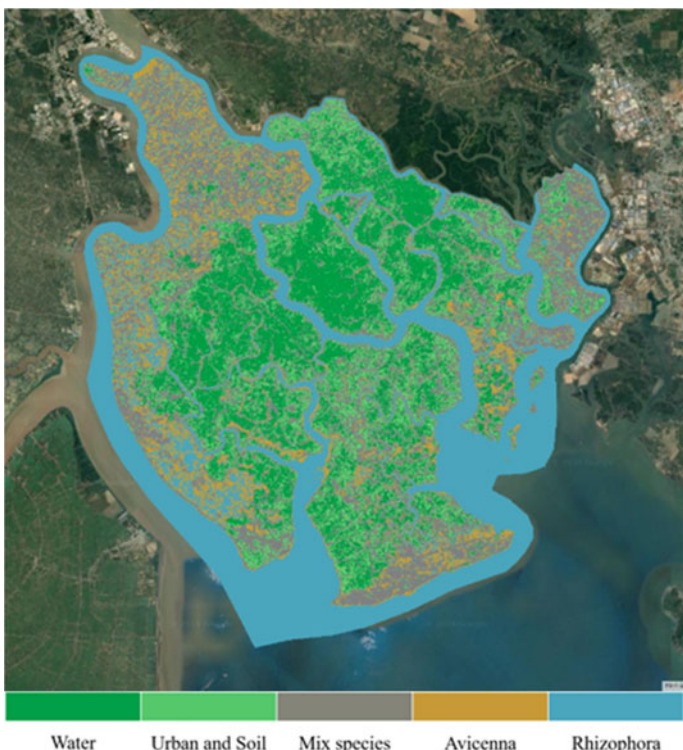


Fig. 3 Classification results in 2018

found some place in urban, especially near the riverside or the beach. Can Thanh, Tam Thon Hiep and An Thoi Dong communes are some urban place that can found Avicenna. Rhizophora and Avicenna growth strongly after 1996, expand their areas wider in buffer zone. Mix species can be any kind of trees that are not Rhizophora and Avicenna, but based on the field survey, water coconut is the most accordant to represent this class. Mix species distribute mainly in urban area because many household growths and selling water coconut for business. Some mix species can be found in buffer zone, the kind of trees are cannot be identify on google earth by eyes and too deep in forest for field survey. Mix species had high contribution in forest cover before 1997 when Rhizophora and Avicenna was still rehabilitated after the war. Then after 1997, Rhizophora and Avicenna take over place of mix species and now there are fell of mix species can be found in buffer zone and core zone.

4.4 Research Limitation

The research has some limitation in image classification process. The images from 2010 to 2012 and 2008 still have gap issues after applying Gap filling algorithm, that make the result in 2010-2012 and 2008 are significantly differenced to Can Gio total area. Besides that, in other results, there are some error between Avicenna and Rhizophora or between Mix species and Urban. In case of 2018 and 2017, the distribution of Avicenna and Rhizophora are significantly differenced. The distribution of Avicenna in 2017 is higher than 2018 and this phenomenon cannot be change in 1 year. Also, in compare of 2013 and 2014, the distribution of Mix species is differenced when in 2013 the Mix species can be found a lot in urban area and only scattered in 2014. This error mostly come from the application of training data set. Another limitation this research is that classification results cannot be show as a Geographic map, there are some problems when finding how to export the series of data in form of Geographic map. The classification results in this research is just a screenshot of GEE workplace, if it can be fully access to export function on GEE, the results can be show better.

5 Conclusion

Monitoring the spatiotemporal change of Can Gio mangrove forest had shown that the mangrove forest cover is expand in period of 1988 to 2018 which mostly contributed by Rhizophora and is a high standard evidence for the outstanding results of mangrove replant campaign provide by Can Gio district. In the period of 1988–2018, the distribution of Avicenna and Rhizophora were strongly developed, growing trend is increasing by time when mostly contributed in core zone and then in buffer zone and some in transition zone. The recovery of mangrove ecosystem will support stability of Can Gio and Ho Chi Minh City in dealing with climate change, especially

for protect coastal area from sea level rise caused by global warming. With average Training accuracy and Kappa coefficient higher than 0.8, application of remote sensing for monitoring the spatiotemporal change of Can Gio mangrove forest show that the output results have a high accuracy. The results have described the distribution of mangrove forest in consecutively year, easier for tracking the growth of mangrove forest species like Avicenna and Rhizophora also more detail in monitoring the trend of forest cover change, by that can describe the results of growing and protecting mangrove forest in Can Gio. This research has shows that GEE is a spectacular geometry tool. Only need a Wi-Fi connection to work, GEE is a most convenient tool for any researcher to work on any device. Based on the performance of GEE in the research, it can be seen that the potential of GEE in geometry science is extremely high and a perfect tool to monitoring the spatiotemporal change of landcover in over the world.

Acknowledgement The study was supported by Ho Chi Minh City Department of Science and Technology (HCMC-DOST) under the contract number “143/2017/HĐ-SKHCN”.

References

1. Adam E, Mutanga O, Rugege D (2010) Multispectral and hyperspectral remote sensing for identification and mapping of wetland vegetation: a review. *Wetland Ecol Manage* 18:281–296
2. Giri C, Long J, Tieszen L (2011) Mapping and monitoring Louisiana’s mangroves in the aftermath of the 2010 Gulf of Mexico oil spill. *J Coastal Res* 27(6):1059–1064
3. Hauser LT, Vu GN, Nguyen BA, Dade E, Nguyen HM, Nguyen TTQ, Le TQ, Vu LH, Tong ATH, Pham HV (2017) Uncovering the spatio-temporal dynamics of land cover change and fragmentation of mangroves in the Ca Mau peninsula, Vietnam using multi-temporal SPOT satellite imagery (2004–2013). *Appl Geogr* 86:197–207
4. Son NT, Thanh BX, Da CT (2016) Monitoring mangrove forest changes from multi-temporal Landsat data in Can Gio biosphere reserve, Vietnam. *Wetlands* 36(3):565–576

Progress Report on the Present Conditions and Technical Cooperation Related to Bridge Maintenance Management in Kingdom of Bhutan



T. Kameda, S. Nii, K. Takahashi, K. Wakabayashi, and K. Konno

1 Introduction

The paper introduces a technical cooperation project on bridge maintenance management in Bhutan. The project is performed under the “Technical Cooperation” program funded by JICA. As there is no railway system in Bhutan, road is an essential transport system, and there are more than 300 road bridges in the country. As Bhutan is located in the middle of steep mountain, bridges crossing rivers are one of the most important road structures to sustain the road system and support daily activities of Bhutan citizens (Fig. 1).

The central Bhutan is categorized as the “Semi Tropical Monsoon Climate”, and monthly rainfall in the monsoon season exceeds 200–300 mm resulting landslides and flash floods in steep slopes or valleys and causing damages of road bridges every year (Fig. 2).

The road system in Bhutan is currently operated and maintained by Department of Road, DoR hereafter. The data management on the bridge condition, however, is highly dependent on the individuals of DoR, and the update of the bridge conditions have not been shared among the stakeholders in a consistent manner. As the DoR officials frequently transfer to other branches or departments, loss of the latest bridge data is highly concerned. The data contents of the database are also other concern in terms of quantity and quality due to the lack of common procedure for data collection in the field (Fig. 3).

T. Kameda (✉)
Asano Taiseikiso Engineering Co., Ltd., Tokyo, Japan
e-mail: kameda@atk-eng.jp

S. Nii
Nippon Koei Co., Ltd., Tokyo, Japan

K. Takahashi · K. Wakabayashi
Japan International Cooperation Agency, Tokyo, Japan

K. Konno
Japan Overseas Consultants Co., Ltd., Tokyo, Japan



Fig. 1 Road network in Bhutan



Fig. 2 Fallen bridge due to scouring

The objectives of this project are to establish a feasible and sustainable “Data Management System” on the road bridges, to complete a “Technical Manual” for the field data collection with Bhutanese officials and to develop their technical capacity for the road maintenance and management (Fig. 4).

2 Current Condition of Road Bridges in Bhutan

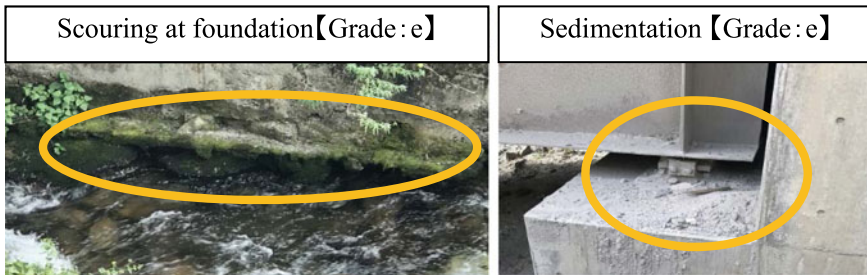
2.1 General Information of the Road Bridges

Target bridges in this project are 317 bridges all over the country as of April 2019, which are mainly crossing rivers and valleys. 295 out of 317 is “Single-span bridge”

Bridge Ledger				
		Update of Record	29/11/2016	
Bridge Name		Khusadrapchu Zam	Bridge Number	Th-1
Geographic Data	Road Name	Khusadrapchu/Benjina SNH		
	Dzongkhag	Thimphu		
	Division/Agency	Regional Office,Dol, Thimphu.		
	Location(km)	0' point		
	Coordinate (Latitude)	27°2'23.06"N		
	Coordinate (Longitude)	89°35'13.59"E		
Bridge Data	Type of Bridge	RCC T Girder		
	Number of Span	1		
	Bridge Span Length [m]	(1)	20.7	
		(2)	-	
		(3)	-	
	Bridge Length[m]	20.7		
	Effective Width[m]	3.6		
	Total Width[m]	4.25		
	Height of Abutment(L/B0)[m]	8.2		
	Height of Abutment(U/U0)[m]	8.2		
	Height of Pier[m]	(1)	-	
		(2)	-	
	Type of Deck	RCC Slab		
	Type of Pavement	Asphalt		
	Type of Wheel guard	RCC		
Type of Abutment	CRM			
Type of Pier	-			
Lading Capacity	24.00 mt			
Year of Construction	N/A			
Record of Repair	N/A			
Traffic volume (Heavy Vehicle)	-			
(Light Vehicle)	-			
(Others)	-			
(Total)	-			
Comments				

Photograph

No.1	From the right	No.2	From the left
			
No.3	From the right downstream	No.4	From the left downstream
			
No.5	From the right upstream	No.6	From the left upstream
			
No.7	From the center to downstream	No.8	From the center to upstream
			

Fig. 3 Sample of bridge data sheet**Fig. 4** Photo example for grade of damage degree

and the rest is “Multiple-span bridge”. Mostly half, 46%, of the superstructure is “Bailey Type”, commonly used as a temporal bridges in other countries but used permanently in Bhutan. 29% and 11% are RC type and Steel type respectively. Commonly recognized damages of the superstructure are crack of the concrete, water leakage from deck slab and exposure of reinforcement bar. The main cause of the damage is their poor quality in the construction phases.

72% of the substructure is RC type and 23% is Masonry type. As the bridges are usually built with shallow foundation, bridge collapses are frequently occurred by scouring due to heavy rain.

Aside from the monsoon season, as the monthly rainfall is less than 100 mm, weathered process due to water intrusion is likely to be slow.

2.2 Collection of Bridge Inventory Data

Initial bridge data, such as location, specification, photograph and repair histories from construction, etc. were collected for all 317 bridges in the first phase of the project with local DoR engineers and headquarter officials. The bridge specification includes the type of bridge, bridge length, span length, total width, effective width, height of abutment & pier, type of deck, pavement, wheel guard, loading capacity and picture of bridge from formatted eight angles. The collected data is recorded on “Bridge Inventory Sheet” in the database system. This field survey helped local engineers and officials to build up their skills and knowledge on bridge structures and their condition. Technical workshops were also held at the regional office of DoR under the instruction of Japanese experts.

2.3 Bridge Inspection Manual

Periodical inspection on the target bridges is planned to perform by local DoR engineers and headquarter officials even after the end of this project to take a corrective action in the case that unsafe condition is identified. “Technical Manual on Bridge Inspection/Diagnosis” was developed to help them to conduct the inspection in a consistent procedure and to develop a reasonable maintenance or repairment plan. Japanese Bridge Inspection manual [1] was referenced to develop the Bhutan version. Some of the items in the manual were simplified and modified to comply with the local condition. Field inspection is divided into three types, “Routine Inspection”, “Periodical Inspection” and annual “Post Monsoon Inspection”. The routine inspection is conducted in the weekly patrol through visual observation from the inside of vehicle by local engineers. In general, the periodical inspection is performed by local DoR engineers through detailed visual observation. The frequency of the periodical inspection is varied from 2 years to 10 years based on the accessibility. The bridge which is possible to conduct “close-eye inspection” allowed that its frequency is set longer. In the post monsoon inspection, scouring of the substructure is the most focused observation in Bhutan (Tables 1, 2 and 3).

Table 1 Bridge type in Bhutan

	Single-span	Multiple-span	Total
	295 (93%)	22 (7%)	317 bridges

Table 2 Type of superstructure

RC	Steel	Bailey	Others
93 (29%)	36 (11%)	148 (47%)	40 (13%)

Table 3 Type of substructure

RC	Masonry	Others
229 (72%)	73 (23%)	15 (5%)

Bridge structural parts is mainly divided into the following four parts in inspection sheet, “Whole Bridge”, “Super Structure”, “Sub Structure” and “Attachment”. Attachment includes deck surface, bearing, railing, expansion joint and drainage facility.

Standard items of the inspections are shown in the Table 4. Each part is evaluated by “Damage Degree” defined in the technical manual. As the inspection is based on the visual observation by different engineers, the damage degree for the inspected items is explained with photo samples to be objective. Thus, the damage degree is assessed between grade “a” to “e” objectively (Table 5).

Table 4 Grade of damage degree

Assessment parts	Damage degree				
	Fine—Condition—Poor				
Whole bridge	a	—	(c)	—	e
Super/Sub structure	a	b	c	d	e
Attachment	a	—	(c)	—	e

Table 5 Assessment items

Items	Subject items	
Whole bridge		Abnormal bending
		Settlement/Movement/Inclination
		Scouring
		Sedimentation
Super structure	Steel	Corrosion
		Crack
		Loosen/fallen bolt
		Fracture
		Deterioration of paint
Super/Sub Structure	Concrete	Crack
		Peeling/Exposure of Rebar
		Water leakage/Free Lime
		Poor casted concrete
Attachment		Malfunction
		Sedimentation

In the future of this project, more detailed inspection methodologies, such as a field hammer measurement for compressed strength, mechanism elucidation for water leakage and crack on concrete, will be instructed by Japanese experts in the field workshop.

3 Conclusions

Bridge inspection methodology was developed to improve the data collection procedure and data management system for the road bridges in Bhutan. Technical manual for the bridge inspection was completed to perform feasible and objective inspections by different DoR engineers and officials. The knowledge and skill on the field inspection and maintenance was also improved through the several activities in the project.

Reference

1. Guideline for periodical bridge inspection, Ministry of Land, Infrastructure and Tourism, Japan (2015)

Quantitative Structuring for the Strategy Map of Coastal Urban Projects Using a Hybrid Approach of Fuzzy Logic and DEMATEL



Truc Thi Minh Huynh, Duc-Hoc Tran, Anh-Duc Pham, and Long Le-Hoai

1 Introduction

While climate change strongly influences business decisions, strategic management is critical to organizational success in the long-term. Indeed, strategic planning becomes important when the environment becomes more vulnerable [29]. The design and implementation of a consistent and oriented plan is the first of four key management activities that help to differentiate the good from successful and unsuccessful companies [12]. For new investors or even experienced investors, the ambiguity and disorientation in the early stages of the project are likely to occur highly, especially for large-scale urban development projects. In addition to the environmental risks of climate change today, they also face the risks arising from the complexity of the coastal urban projects. Therefore, it is necessary to develop a strategic management framework for public or private organizations to enhance the likelihood of success in coastal urban development projects.

The strategic management model basically has four main elements: research of the organization's environment, formulating strategies, implementing strategies, evaluating and monitoring strategies [29]. The key aspects of strategic management in the construction industry are considered in a comprehensive way [24]. Price and Newson [24] highlight some of the main paradoxes in developing organizations' strategy and emphasize the importance of selecting tools to develop strategies for

T. T. M. Huynh (✉) · D.-H. Tran · L. Le-Hoai

Faculty of Civil Engineering, Ho Chi Minh City University of Technology, VNU-HCM, Ho Chi Minh City, Vietnam

e-mail: htmtruc.sdh16@hcmut.edu.vn

T. T. M. Huynh · A.-D. Pham

Faculty of Project Management, The University of Danang—University of Science and Technology, Danang City, Vietnam

successful planning. There have been a number of studies on the use and implementation of strategic management frameworks for the construction industry [10, 23, 29]. However, as yet there has been no focus on developing comprehensive strategies to support the investments in “vulnerable” areas like coastal zones.

In strategic planning approaches, the Balanced Scorecard (BSC) is the most common method for construction companies [18]. Through implementing a BSC system, companies aim to translate their vision into strategic objectives, communicate their vision and relate it to personal performance, business planning, and input, and then change the correct strategy [16]. The BSC approach provides leaders with the resources they need to achieve sustainable competitive success from a strategic point of view. Indeed, BSC can be seen as a way of promoting effective strategic management decision-making, helping to enhance the satisfaction of strategic objectives. It should be noted that BSC helps managers focus on strategic issues and management of strategic implementation. At the same time, providing a more comprehensive view of the business can be the best application tool, thus helping companies to behave in their best interests in the long-term [22].

According to the BSC method, the strategic goals are outlined for each strategic aspect and must be in line with the organization’s mission. Identifying strategic objectives in this way would ensure that metrics assess the success of the company. Mapping strategy is the most significant change in constructing a BSC system [17]. As shown by [17], the strategy maps provide a visual depiction of organizational goals and the important relationships that promote companies’ performance between them. The organization’s administration board, as a decision-making group, starts by combining their knowledge and experience with consensus and building a rational relationship between strategic goals. However, the actual use literature of the BSC on explaining how to determine causality is quite limited, especially for coastal construction projects.

This study applies the hybrid approach of Decision making trial and evaluation laboratory (DEMATEL) [8] and Fuzzy logic [34] to evaluate causal relations between strategic goals in the strategy map of coastal urban projects. DEMATEL has been known as the useful method in Multi-Criteria Decision Making (MCDM) methods for identifying causes and effects of a complicated system. Whereas, Fuzzy sets are famous for effective dealing with the subjectivity, ambiguity, and uncertainty of human judgment. There are several studies on the cooperation of DEMATEL and Fuzzy logic in structuring relationships. For instance, Kuo [19] applied DEMATEL, Fuzzy logic and another Fuzzy MCDM method to develop an appropriate assessment structure among criteria and propose a half breed strategy for ideal area determination for a universal conveyance focus. Altuntas et al. [2] proposed a fuzzy DEMATEL approach to the issue of installation format. Altuntas and Yilmaz [3] studied on the causal relations of marketing resources using the fuzzy DEMATEL. Malviya and Kant [21] combined Fuzzy DEMATEL and Fuzzy MCDM to develop a framework that could help to forecast and assess the success/failure of the implementation of Green Supply Chain.

The highlighted contribution of this study is the exploitation of the Fuzzy DEMATEL approach into the field of coastal urban project management which still not received adequate research attention in a coastal nation like Vietnam. The DEMATEL method will help create a total influence matrix (direct and indirect relationships) based on the experts' judgment on the impact of strategic objectives. To reduce the subjectivity and vagueness of expert judgments, the fuzzy triangle numbers are applied to convert linguistic feedback to a numerical score. Based on the total relation matrix, important causal relationships are identified and the Impact Relation Map (IRM) is developed. This is the basis for structuring the strategic map of coastal urban projects in this study. For the case study, data of Da Nang Premier Village Resort project in Danang city, Vietnam is collected to develop and structure the strategy map using the BSC method and the proposed combination of Fuzzy DEMATEL. The developed strategy map is a useful tool for the sustainable success of the coastal urban project in the context of climate change today.

2 Developing the Strategy Map for Coastal Urban Project Using the BSC Method

Balanced Scorecard method was first introduced by Kaplan and Norton in 1992. In the original BSC version, Kaplan and Norton [15] explained financial performance measures and operational performances (non-financial) grouped into three perspectives: innovation and learning, internal business processes, and customer satisfaction. Then, in the 1996 BSC version, the internal business aspect was retitled the internal business processes, whereas the innovation & learning aspect was given new name as the learning & growth [16].

There are several studies about the application of BSC in the construction industry. For instance, Kagioglou et al. [13] proposed a BSC based conceptual framework to measure construction company performances. Yu et al. [33] compared the performance of 34 Korean construction companies regarding four conventional BSC perspectives. Luu et al. [20] tried to develop a integration of SWOT and BSC to compare construction company performances in Vietnam. However, the general lack of earlier studies on the implication of BSC in the construction field is that this method has not been yet focused on successful project planning and strategic project management.

For adapting to various research purposes, the BSC approach allows organization managers to edit into different forms as well as add new aspects regarding the organizational interest [6, 7]. Many studies highly recommended adding new dimensions in terms of sustainability (such as environmental or social performance) into the traditional BSC to meet new challenges of the sustainable development [5, 6, 9, 14, 26, 27]. To develop a BSC model for construction projects in general and coastal urban projects in particular, this study proposes adding the dimension of social and environmental perspective (i.e. sustainability) into four existing traditional BSC dimensions,

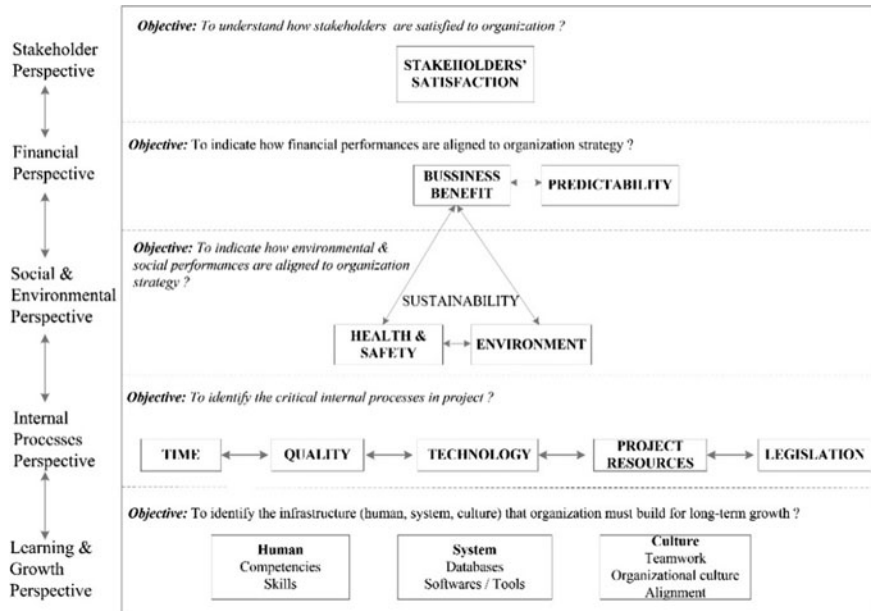


Fig. 1 The conceptual strategy map for coastal urban projects

including stakeholders, financial, social and environmental, learning and growth, and internal business process aspect. There are 13 strategic objectives which are assessed as success criteria and assigned into the five BSC perspectives, including culture (C), system (S), human (H), legislation (L), resources (R), quality (Q), time (T), technology (TE), environment (E), health and safety (HS), business benefit (B), predictability (P), and stakeholders satisfaction (SS).

Figure 1 represents the preliminary strategy map for the coastal urban project that is proposed in this study. This is only the conceptual framework due to the lack of clearly identified relationships between strategic objectives that the proposed Fuzzy DEMATEL method is expected to full fill. The main objective of learning & growth aspect is to identify the infrastructure that a company/ project should develop for its sustainable development. People, systems, and culture are the three main contents that an organization should focus on in terms of learning and growth. Focusing on internal processes within the organization is very important to the organization. Time, quality, technology, project resources and legal are the key success criteria that could measure the effectiveness of the internal process for coastal urban projects. The social and environmental aspects help to show how the organization's objectives are linked to the society and environment. Project effectiveness on social, environmental and financial perspectives are measured by criteria of health and safety, environmental impact, and business performance. In addition, the criterion on the project's predictability

also helps measure the sustainability of the project. The top target of coastal urban projects belongs to the project stakeholders that the most appropriate measure is the satisfaction of stakeholders.

3 Structuring the Strategy Map Using Fuzzy DEMATEL

DEMATEL method based on individual perception (group of people or individual) is employed to identify total causal relations. The method begins with the matrix of the direct relations between the pair of factors. DEMATEL uses a technique to calculate the total relation matrix including the direct as well as indirect influences. Consequently, an Impact-Relation-Map (IRM) which represents the important relationship (direct and indirect) is developed. The input is a matrix of direct relations including the influence of each factor to the others [25].

In the first DEMATEL, the connections of factor variables are evaluated by crisp values [8]. Notwithstanding, in some certifiable applications, human decisions are regularly misty and careful numerical qualities are deficient to gauge the unclear interdependency connections between criteria. Fuzzy logic [34] applies a linguistic scale that refers to the causal relations. This scale is converted into numerical values by applying fuzzy sets, thereby enabling a quantitative strategic map.

The idea of fuzzy sets has been connected to the DEMATEL by numerous specialists. The following procedure of the application of Fuzzy DEMATEL to structure the strategy map for coastal urban projects are inherited from the related studies [1, 28, 30–32] as follows:

- Step 1: Selecting the experts who are decision-makers of coastal urban projects. The q leaders of the project are selected and invited to evaluate the influences between proposed strategic objectives.
- Step 2: Designing the fuzzy linguistic scale. The fuzzy triangular number is employed to convert the linguistic scale for assessment of relationships using a . That is, each qualitative term has three equivalent numerical qualities: minimum (l), intermediate (m), and maximum (i). The scale applied in this study is commonly used in the literature [28]. The fuzzy number (l, m, u) converted from linguistic terms of Null (N), Low (L), Mid-Low (ML), Mid-High (MH), High (H) are respectively $(0, 0, 0)$; $(0, 0, 0.25)$, $(0, 0.25, 0.5)$, $(0.25, 0.5, 0.75)$, $(0.5, 0.75, 1)$.
- Step 3: Measuring the causal relationships and setting up the direct relation matrix. The n strategic goals are located in the ranking matrix rows and columns arranged upwards from the BSC's perspectives in Fig. 1. Every expert is solicited to show the impact level of each objective on the others as far as causality. Unfeasible connections are hindered to ensure that the technique would follow the legitimate conditions that were suggested by Kaplan and Norton.

$$[A^k] = \begin{bmatrix} 0 & a_{12}^k & \cdots & a_{1n}^k \\ a_{21}^k & 0 & \cdots & a_{2n}^k \\ \vdots & \vdots & \vdots & \vdots \\ a_{n1}^k & a_{n2}^k & \cdots & 0 \end{bmatrix} \quad (1)$$

With a_{ij} : direct influence of factor i (row) on factor j (column), $\forall i, j$ and $k = 1, \dots, q$

- Step 4: Building the fuzzy matrices of direct relations using triangular fuzzy numbers. From the experts' qualifications ($k = 1, \dots, q$), the matrix of direct relations $[A^k]$ is actually transferred to 3 fuzzy matrices, in which each composed of the values l, m, u respectively. The fuzzy direct relation matrices are structured as the matrix $[A^k]$ regarding [1] where $a_{ij}^k = (l_{ij}^k, m_{ij}^k, u_{ij}^k)$
- Step 5: Nominalizing the fuzzy matrices of direct relations from $[A^k]$ to $[X^k]$

$$s^k = \text{Min} \left[\frac{1}{\text{Max}_{1 \leq i \leq n} \sum_{j=1}^n a_{ij}^k}, \frac{1}{\text{Max}_{1 \leq j \leq n} \sum_{i=1}^n a_{ij}^k} \right] \quad (2)$$

$$[X^k] = s^k \cdot [A^k] \quad (3)$$

- Step 6: Aggregation of the fuzzy direct relation matrices of q experts using the average value, is calculated by [4] and the fuzzy matrices X^k are transferred to the matrix X as follows.

$$[X] = \begin{bmatrix} X_{11} & X_{12} & \cdots & X_{1n} \\ X_{21} & X_{22} & \cdots & X_{2n} \\ \vdots & \vdots & \vdots & \vdots \\ X_{n1} & X_{n2} & \cdots & X_{nn} \end{bmatrix} \text{ where } X_{ij} = \frac{\sum_{k=1}^q X_{ij}^k}{q} \quad (4)$$

$$[X] = [X_l, X_m, X_u]$$

- Step 7: Calculate the fuzzy matrices of the total relations $[T]$ using [5]

$$[T] = \lim_{w \rightarrow \infty} ([T]^1 + [T]^2 + \dots + [T]^w) = \lim_{t \rightarrow \infty} (\sum_{t=1}^w [T]^t) = [T] \cdot ([I] - [T])^{-1} \quad (5)$$

$$[T_l] = [X_l] \cdot ([I_l] - [X_l])^{-1}; [T_m] = [X_m] \cdot ([I_m] - [X_m])^{-1}; [T_u] = [X_u] \cdot ([I_u] - [X_u])^{-1}$$

- Step 8: Defuzzification of the matrices. This study applies the average method.

- Step 9: Calculating r_i (sum of elements in row i) and c_i (sum of elements in column j)

$$r_i = \sum_{j=1}^n t_{ij} \forall i \quad (6)$$

$$c_j = \sum_{i=1}^n t_{ij} \forall j \quad (7)$$

If $(r_i - c_i) > 0$, it means that factor i impact on other factors; and $(r_i - c_i) < 0$ means that factor i is influenced by the others. Besides, the value of $(r_i + c_i)$ quantifies the magnitude of relationships between factors i with the others.

- Step 10: Construct the Impact-Relation-Map (IRM)

A threshold value is set to determine important relations, thereby building an impact relationship map (IRM). Which elements of the total relation matrix are lower than that threshold number are converted to 0, and IRM is constructed with values greater than or equal to the threshold value.

4 Case Study

A coastal resort project in the central region of Vietnam is selected for the case study. The project includes 118 luxury villas, 2 high-rise apartment buildings, office and commercial center for rent, public area for business (e.g. beach club, pool bar) and condotel with total 15.6 hectares of areas and 1654 billion VND of budget. A group of decision-makers of the project is invited to direct interviews (Step 1). The surveyed group includes one representative of the board of company directors, the head of the project management unit, and one leader of the local government. All of these people have been directly related to the project since the planning phase.

The above-mentioned blurry DEMATEL method is applied with the strategic objectives specified. The decision-maker delivered its own linguistic values after developing the linguistic scale. In this step, the matrix of influence was achieved by surveying the effect of each criterion on each other. The question was, “If strategic objective A is achieved, what would the impact on strategic objective B be”. Table 1 shows the evaluation of one expert using the linguistic scale. Once each expert’s linguistic values were collected, the minimal, intermediate, and maximum matrices were determined. Each of the expert’s three matrices was standardized by the process described in step 5.

The matrix of total aggregate relationships is obtained following the process in step 7 and after defuzzification in step 8 (Table 2)

Figure 2 presents the causality analysis and IRM for the case study. After determining the r and c values of each strategic goal, the result value ($r-c$) of the 13

Table 1 A direct relation matrix

	SS	B	E	HS	P	L	Q	R	T	TE	C	H	S
SS	N	-	-	-	-	-	-	-	-	-	-	-	-
B	H	N	L	ML	MH	-	-	-	-	-	-	-	-
E	H	ML	N	H	ML	-	-	-	-	-	-	-	-
HS	H	ML	MH	N	MH	-	-	-	-	-	-	-	-
P	H	H	H	MH	N	-	-	-	-	-	-	-	-
L	H	MH	MH	ML	ML	N	ML	ML	ML	ML	-	-	-
Q	H	H	H	ML	MH	N	ML	MH	L	-	-	-	-
R	H	MH	MH	ML	ML	MH	MH	N	MH	MH	-	-	-
T	H	H	ML	L	ML	H	MH	H	N	ML	-	-	-
TE	H	MH	MH	ML	ML	MH	MH	MH	N	-	-	-	-
C	H	ML	L	L	L	ML	ML	MH	ML	N	MH	MH	MH
H	H	H	ML	ML	MH	ML	MH	L	H	ML	N	MH	MH
S	H	ML	ML	L	L	0	MH	L	MH	ML	ML	ML	N

Notes Null (N), Low (L), Mid-Low (ML), MidHigh (MH), High (H), Unfeasible relationship (-)

Table 2 The final matrix of total relations after defuzzification

	SS	B	E	HS	P	L	Q	R	T	TE	C	H	S
SS	0	0	0	0	0	0	0	0	0	0	0	0	0
B	0.158	0	0.049	0.041	0.051	0	0	0	0	0	0	0	0
E	0.107	0.068	0	0.097	0.065	0	0	0	0	0	0	0	0
HS	0.097	0.041	0.042	0	0.042	0	0	0	0	0	0	0	0
P	0.097	0.097	0.084	0.042	0	0	0	0	0	0	0	0	0
L	0.120	0.086	0.075	0.030	0.030	0	0.041	0.031	0.092	0.031	0	0	0
Q	0.120	0.107	0.093	0.107	0.041	0.049	0	0.095	0.089	0.059	0	0	0
R	0.107	0.113	0.163	0.031	0.020	0.062	0.116	0	0.086	0.089	0	0	0
T	0.131	0.107	0.058	0.049	0.041	0.101	0.089	0.074	0	0.068	0	0	0
TE	0.097	0.113	0.140	0.113	0.030	0.031	0.137	0.113	0.113	0	0	0	0
C	0.084	0.041	0.056	0.109	0.049	0.045	0.041	0.041	0.062	0.020	0	0.140	0.052
H	0.107	0.134	0.031	0.041	0.089	0.041	0.110	0.032	0.107	0.041	0.118	0	0.086
S	0.073	0.054	0.054	0.045	0.056	0.008	0.062	0.049	0.089	0.113	0.031	0.041	0

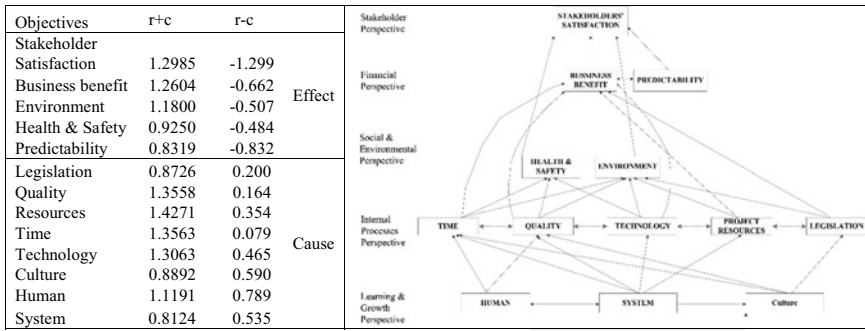


Fig. 2 Causality analysis and Impact Relation Map

strategic objectives in the research project shows that the strategic objectives belong to “learning and growth” and “internal processes” that point to the causal factors; while the remaining strategic objectives in the “social & environmental”, “financial”, and “stakeholders” perspectives are consequential factors. The value ($r + c$) embodies the influence magnitude of each strategic objective. Accordingly, the “Time”, “Project resources”, and “Quality” are underlined as vital strategic drivers. The fulfillment of these objectives is able to help obtain the “Stakeholder Satisfaction”, “Business benefit”, and “Environment” objectives which are “Triple bottom lines” of sustainable development. There are two issues that need to be raised for the IRM development: (1) What are the direction of the relationship arrows between strategic objectives? (2) What relationships are important enough to show in IRM? To solve the second problem, a threshold value needs to be identified to determine which relationship is important enough. In many related studies [1, 4, 11, 28], the threshold value is defined as the average value of all elements in the total matrix. For this case study, the threshold value is 0.043 which is the mean value of the matrix in Table 2. Accordingly, the important relationships with values greater than 0.043 in the total impact matrix are shown in the IRM.

5 Conclusions

This study has exploited the Fuzzy DEMATEL approach into the field of coastal urban project management which still not received adequate research attention in a coastal country like Vietnam. The BSC method is applied to design the conceptual strategy map which presents the 13 strategic objectives in five perspectives, including learning and growth, internal business processes, social and environmental, financial, and stakeholder satisfaction perspectives. The DEMATEL method is applied to produce a total influence matrix (direct and indirect relationships) based on the experts’ opinion on the impact of strategic objectives. To reduce the subjectivity and

vagueness of expert judgments, the fuzzy triangle numbers are applied to convert linguistic feedback to a numerical score. Based on the total relation matrix, important causal relationships are identified and the Impact Relation Map (IRM) is developed. A coastal resort project in Vietnam is selected for the case study.

A 10-step procedure of applied technique is explained and illustrated through the case study. First, the group of decision-makers who are related to the coastal urban project needs to be selected to collect their evaluations on the influences between 13 strategic objectives in their own projects using the linguistic scale. To reduce the vagueness and subjection of judgments, Fuzzy logic is applied using triangular fuzzy number set. The matrices of direct relations are then constructed and aggregated from different experts. DEMATEL method is applied to compute the matrices of total relations and the average value based defuzzification technique is applied to deliver the final matrix of total influences. The values of $(r + c)$ and $(r - c)$ are calculated to identify which relationships belong to causes and effects before the IRM could be built with important relations. The IRM is the base of structuring the strategy map which shows clearly the causal relationships within the strategy map.

The concrete issue is that there will not be a unique strategy map for all coastal urban projects because each project has different characteristics, various inside and outside environment of the company and the project. With the proposed approach in this study, it can be flexibly applied according to diverse projects. Sometimes these 13 strategic objectives cannot be changed all in other projects. This study contributes as a reference process to assist managers to develop and complete strategic maps that are relevant to their coastal urban projects.

Acknowledgements We acknowledge VNUHCM-Ho Chi Minh City University of Technology, and the University of Danang-University of Science and Technology for their provision of resources and collaborative efforts. This work was also supported by The University of Danang, University of Science and Technology, number of Project T2019-02-38.

References

1. Acuña-Carvajal et al (2019) An integrated method to plan, structure and validate a business strategy using fuzzy DEMATEL and the balanced scorecard. *Expert Syst Appl* 122:351–368
2. Altuntas et al (2014) A fuzzy DEMATEL-based solution approach for facility layout problem: a case study. *Int J Adv Manuf Technol* 73(5):749–771
3. Altuntas, Yilmaz (2016) Fuzzy Dematel method to evaluate the dimensions of marketing resources: an application in SMEs. *J Bus Econ Manage* 17(3):347–364
4. Chang et al (2011) Fuzzy DEMATEL method for developing supplier selection criteria. *Expert Syst Appl* 38(3):1850–1858
5. de Andrade Guerra et al (2018) A proposal of a balanced scorecard for an environmental education program at universities. *J Cleaner Prod* 172:1674–1690
6. Falle et al (2016) Sustainability management with the sustainability balanced scorecard in SMEs: findings from an Austrian case study, vol 8
7. Figge et al (2002) The sustainability balanced scorecard – linking sustainability management to business strategy. *Bus Strategy Environ* 11(5):269–284

8. Fontela, Gabus (1974) DEMATEL, innovative methods. Battelle Geneva Research Institute
9. Hansen, Schaltegger (2016) The sustainability balanced scorecard: a systematic review of architectures, vol 133
10. Holton et al (2010) Managing for sustainability: findings from four company case studies in the UK precast concrete industry. *J Cleaner Prod* 18(2):152–160
11. Jassbi et al (2011) A fuzzy DEMATEL framework for modeling cause and effect relationships of strategy map. *Expert Syst Appl* 38(5):5967–5973
12. Joyce (2005) What really works: building the 42 organization. *Organ Dyn* 34(2)
13. Kagioglou et al (2001) Performance management in construction: a conceptual framework. *Constr Manage Econ* 19(1):85–95
14. Kang et al (2015) Corporate social responsibility and sustainability balanced scorecard: the case study of family-owned hotels. *Int J Hospitality Manage* 48:124–134
15. Kaplan, Norton (1992) The balanced scorecard: measures that drive performance. *Harvard Bus Rev* 70(1):71–79
16. Kaplan, Norton (1996) The balanced scorecard: translating strategy into action. Harvard Business School Press, Boston
17. Kaplan, Norton (2004) Strategy maps: converting intangible assets into tangible outcomes. Harvard Business School Press, Boston
18. Kaplan et al (2008) Mastering the management system. Harvard Baccarini, David Bus Rev 86(1):62–77
19. Kuo (2011) Optimal location selection for an international distribution center by using a new hybrid method. *Expert Syst Appl* 38(6):7208–7221
20. Luu et al (2008) Performance measurement of construction firms in developing countries. *Constr Manage Econ* 26(4):373–386
21. Malviya, Kant (2016) Hybrid decision-making approach to predict and measure the success possibility of green supply chain management implementation. *J Cleaner Prod* 135:387–409
22. Niven (2006) Balanced scorecard step-by-step: maximizing performance and maintaining results, 2nd edn. John Wiley & Sons, New York
23. Pekuri et al (2015) Business models and project selection in construction companies. *Constr Innov Inf Process Manage* 15(2)
24. Price, Newson (2003) Strategic management: consideration of paradoxes, processes, and associated concepts as applied to construction. *J Manage Eng* 19(4):183–192
25. Si et al (2018) DEMATEL technique: a systematic review of the state-of-the-art literature on methodologies and applications. *Math Problems Eng* 2018:33
26. Sidiropoulos et al (2004) Applying sustainable indicators to corporate strategy: the eco-balanced scorecard 27(1)
27. Valenzuela, Maturana (2016) Designing a three-dimensional performance measurement system (SMD3D) for the wine industry: a Chilean example, vol 142
28. Valmohammadi (2015) Modeling cause and effect relationships of strategy map using fuzzy DEMATEL and fourth generation of balanced scorecard. *Benchmarking: Int J* 22(6):1175–1191
29. Wheelen, Hunger (2012) Strategic management and business policy: toward global sustainability, 13th edn. Pearson Education, Inc
30. Wu (2012) Constructing a strategy map for banking institutions with key performance indicators of the balanced scorecard. *Eval Program Plann* 35(3):303–320
31. Wu, Lee (2007) Developing global managers' competencies using the fuzzy DEMATEL method. *Expert Syst Appl* 32(2):499–507
32. Wu et al (2011) Performance evaluation of extension education centers in universities based on the balanced scorecard. *Eval Program Plann* 34(1):37–50
33. Yu et al (2007) Comparable performance measurement system for construction companies. *J Manage Eng* 23(3):131–139
34. Zadeh (1965) Fuzzy sets. *Inf Control* 8(3):338–353

Review the Vietnamese Contractor's Roles in Implementing the Prerequisites of LEED v4 BD + C Project



Duy Hoang Pham, Huyn Kyu Shin, and Yong Han Ahn

1 Introduction

Buildings greatly contribute to air pollution, noise pollution, waste pollution, and water pollution. Furthermore, the global construction industry consumes a great number of resources that include 50% of total energy generated, 40% of all raw materials, 70% of all timber, 16% of total water consumption and 35% of CO₂ emissions and so on [4, 18, 19]. Encouragement of Green buildings (GBs) development to become a significant potential solution to improve environmental problems and reducing energy consumption [9].

The low electricity price one of the biggest hindrances to implementing energy efficiency practices in buildings [10, 11]. However, the electricity price has increased by 8.36% and it does not only place significant pressure on the operation cost of the building but it is also a big motivation for Vietnam GBs development. Because of increasing operating costs, and increasing the building users 'demands of life quality, the number of owners who interests in GBs has been increasing [10, 11] which could be shown through the increase in the number of certified GBss in recent years. There is several GBs rating systems such as is LEED (174 projects), EDGE (34 projects), and LOTUS (51 LOTUS projects) and so on (VGBC 2018; EDGE 2019). However, with 174 certificated and registered projects, LEED is the most popular rating system in Vietnam.

Although GBs rating system is the measurement of GBs quality and brings many benefits to the building users [8], it brings more stringent construction requirements and complex building design, which require collaboration by architects, engineers,

D. H. Pham (✉) · H. K. Shin

Department of Architecture Engineering, Hanyang University, ERICA, Ansan 15588,
Republic of Korea

e-mail: phdhoang@gmail.com

Y. H. Ahn

School of Architecture and Architectural Engineering, Hanyang University, ERICA, Ansan
15588, Republic of Korea

and other building consultants due to their complexity [12, 15]. As a result, GCs need and want a better understanding of their roles and responsibilities in LEED projects, while exploring ways to provide a “value-added” service to the projects. To meet the perquisite requests of LEED within the minimum increasing works and cost, the GCs need to gain more knowledge and assessment of their roles on the LEED v4 BD + C project. This paper points the prerequisite roles of general contractors on a LEED v4 BD + C project, analyses the status of the contractor, and summarize LEED impact on their construction management practices. This research was conducted with the help of existing literature and the analyzing survey results from the constructor’ staff.

2 Literature Review

2.1 *Background of Research*

The contractor has a very important contribution to the success of the project, especially in a sustainable building or a success LEED project [14]. Many studies in the field of construction management and sustainable building have examined the roles and contribution of GCs to the success of a LEED project. Korkmaz (2013) studied point out the potential of GCs in the earlier phases of the project. The Cascadia Chapter of the USGBC (2008) identified 17 credits major relative to the GCs and thier response in implementing and documenting. Klehm (2003) study points out GCs’ roles in LEED project are subcontractor management, materials management, and activity management. Syal et al. [20]’s research identified how GCs can understand the impacts of various LEED-NC requirements on their roles. Syal et al. [21] also analyses the role of GCs on LEED NC projects and its impact on their construction management practices. Frattari and Dalprà (2012) study about the roles of the general contractor in sustainable GBs through two LEED case studies in Italy. Kibert (2017) [7] described GBs systems and implementation. Study of Ahn et al. [1] develops an ‘ICP’ including goals of green construction processes, procedure, the roles and responsibilities of the architect, a contractor, and subcontractor through four stages: ‘Site’, ‘Building Envelope’, ‘Interior’, and ‘Close-Out’ of the construction phase. Bayraktar and Owens [2]’ study presents a LEED implementation guide for the AEs, CxA, GCs, and so on to assist them in the certification process. Schaufelberger and Cloud [17] also identify issues relative to the constructor’s role and provide a contractors’ four-step guide. The Washington Department of General Administration [22] published some guidelines regarding reduction of waste from construction projects. Cha et al. [3]’s research developed an assessment tool to measure the level of waste management performance and listed 16 factors in relation to the contractor’s waste management plan and execution approach.

There is a strong need to define the role of GCs and their early involvement in the GBs process [13, 16]. Previous studies have clarified the roles of GCs and these studies provide guidelines for improving the effectiveness of GCs in the LEED

project. Most studies are based on GCs and projects' data in the U.S and other developed countries. However, there are big differences in the contractor's qualifications and local technical code in Vietnam. In addition, several difference roles should be updated in the new LEED v4 version from 2018. Therefore, a study about the roles of GCs in the Vietnam LEED v4 project is necessary to help contractors easily adapt to future projects.

2.2 General Contractor's Roles in Implementing the Prerequisites of LEED v4 BD

By understanding the project goals and aligning his management with them, the GCs ensure that the goals are realized, without much increasing construction costs. To implement a LEED project the GCs are requested to fulfil various construction management functions (Table 1), such as [1] estimation decisions and project cost, [2] scheduling activities, [3] project administration/documentation, [4] contracts and agreements, [5] field operations and subcontractor coordination, and [6] other constructor related processes [1, 5].

Pre-construction phase: Integrated design is a prerequisite for LEED for health-care projects (LEED v4). An IDP team should be established to fulfil the request, with the cooperation of many different stakeholders, including architects, engineers, contractors, owners, building operators, and government agents (LEED V4; Pearce et al. 2012; Lapinski et al. 2011; Klotz et al. 009; Sayce 2007; Bokalders and Block 2010; Shenoy 2009) [13].

The earlier GC can be brought on as part of the project team, the more of an impact their involvement can have on the project schedule and budget [14, 19].

Construction phase: The civil engineer is typically responsible for developing an erosion and sedimentation control (ESC) plan, General LEED Requirements, LEED Product Requirements, Waste Management, and Disposal and Indoor Air Quality Requirements. The GCs can also assist in streamlining construction methods and constructability reviews in order to achieve LEED goals. The GC also reviews carefully and approve all materials before they are installed. They needs to collect actual data, costs, and test methods and procedures. According to LEED v4 (2014), GCs play a role in Construction Activity Pollution Prevention, Construction and Demolition Waste Management Planning. These requirements are related to the current standards in Vietnam. In addition, LEED requirements are more rigorous than these standards (27/TT-BTNMT 2015; 18/NĐ-CP 2015; 02/TT-BXD 2018). Therefore, GCs need to be prepared to comply with LEED. Particularly for Fundamental Commissioning and Verification criteria, contractors only perform the main role when the project <1860 m². It is important that the GCs need to collect the material data sheet and job site photos. Many credits require documentation should be prepared continuously to submittal for LEED certification.

Table 1 General contractor roles in LEED v4 perquisite credits

Credit name	Document	Works description
<i>Integrative process</i>		
Prerequisite integrative project planning and design (healthcare) [6]	<ul style="list-style-type: none"> – Narrative report how credit requirements and action plan from preliminary rating goals 	<ul style="list-style-type: none"> – Construction manager or general contractor join the IDP to support doing the Life cycle cost analyst; construction cost estimator
<i>Sustainable sites</i>		
Construction activity pollution prevention [1–6]	<ul style="list-style-type: none"> – Report of compliance with EPA CGP – Report compliance with any applicable ESC measures 	<ul style="list-style-type: none"> – Developing an erosion and sedimentation control (ESC) plan – Review local code against EPA CGP, evaluate site for ESC plan needs, create and implement esc plan
Environmental site assessment (schools and healthcare) [3, 6]	<ul style="list-style-type: none"> – Phase I, II, III ESA reports – Report of site contamination, remediation... 	<ul style="list-style-type: none"> – The job request an environmental professional consultant, may not GC's role
<i>Water efficiency</i>		
Outdoor water use reduction [3, 6]	<ul style="list-style-type: none"> – Site plan showing vegetated areas; Narrative for plant species and water requirements 	<ul style="list-style-type: none"> – GC collects invoices and installing photos related to plant species, rainwater tank and irrigation systems from landscape contractors
Indoor water use reduction [3, 6]	<ul style="list-style-type: none"> – Product cut-sheets, manufacturers' information 	<ul style="list-style-type: none"> – GC collects invoices and installing photos
Building-level water metering [3, 6]	<ul style="list-style-type: none"> – Meter declaration; Sharing commitment 	<ul style="list-style-type: none"> – GC collects invoices and installing photos
<i>Energy and atmosphere</i>		
Fundamental commissioning and verification Project <1860 m ² [1–6] Project >1860 m ² [4] *GC only can be a CxA for project under 1860 m ²	<ul style="list-style-type: none"> – CxA previous experience; Confirmation of OPR and BOD contents; list of systems to be commissioned; verification of CxA activities and reviews; Cx plan, documentation of testing and verification; CFR, O&M plan X; Cx report 	<ul style="list-style-type: none"> – Contractors create OPR, BOD, and CX plan – Communicate with the contractors to determine the exact schedule for pre-functional inspections to verify proper installation and commissioned systems – Review the functional test scripts, verify proper operating modes, and comment on any modifications to match actual operation the contractors execute the functional testing

(continued)

Table 1 (continued)

Credit name	Document	Works description
Minimum energy performance [6]	– No documents need from the GC	– Support cost estimation and update changes of building envelope drawing
Building-level energy metering [6]	– No documents need from the GC	– There are no GC tasks but it will affect the cost estimates
Fundamental refrigerant management [6]	– No documents need from the GC	– The MEP engineer is typically responsible in refrigerant management
<i>Materials and resources</i>		
Storage and collection of recyclables [6]	– Not relative to the GC	– There are no GC tasks but it will affect the cost estimates
Construction and demolition waste management (CDWM) planning [1–6]	– Construction waste management plan and implement report	– Develop and implement a CDWM plan by identifying construction or demolition material streams for diversion from landfill, then select collection and diversion methods
PBT source reduction—mercury (Healthcare) [3, 6]	– Lighting list that includes mercury content, ballast type and product manufacturers' data	– Collect and check manufacturers' documentation before installation to ensure that only qualifying products and lamps are used
<i>Indoor environmental quality</i>		
Minimum indoor air quality performance [3, 6]	– No documents need from the GC	– Not relative, however the IAQ plan is typically prepared by the GCs or construction manager
Environmental tobacco smoke control [6]	– No documents need from the GC	– Smoke control during the construction phase could get LEED points
Minimum acoustic performance [3, 6]	– Report showing materials with NRC >0.70 (school project only)	– Collect data of materials with NRC information and update the changes in cost estimates

Closing phase: The contractor's most important task is to gather the documents and provide to the LEED consultant for the LEED submission. Such as C&D waste, recycled content materials, regional materials, certified wood, low emitting materials and so on [17].

3 Research Methods

3.1 Question Development

The purpose of this questionnaire survey is to assess the status of Vietnamese GCs' experience in ensuring the prerequisites of the LEED project. The population of the survey is the experts working in the construction field, working at contractors or contractors in the projects. The developed questionnaire was structured into two sections. The first section is the respondents' background information, which included the experience years, field of work, GBs project experience and English barriers. The others section included 22 questions and jobs required to meet the prerequisite credits that are summarized from "LEED v4 Reference guide BD + C (2014)". For each question is the experience of GCs about a task that needs to be done, the survey respondents by five-points evaluating (1-No experience to 5-Much experience).

3.2 Survey Sampling and Data Collection

The population of this study targeted at the GCs' staff and others who work with GCs in the Vietnamese construction site. To determine the sample size, this study used Eq. (1).

$$n = \left[\frac{Zs}{E} \right]^2 \quad (1)$$

where n is sample size; Z = Z-score (e.g., 1.645 for 90% confidence level); s is the sample standard deviation, and E is the error factor. To determine a sample size that is as large as possible, we set a relatively high standard deviation of 4 and a minimum error factor of 1. Hence, the sample size of this study was 44 based on the calculation shown in Eq. (2).

$$n = \left[\frac{1.65 \times 4}{1} \right]^2 = 43.3 \quad (2)$$

To implement the questionnaire, an online survey was first created, which can be accessed through the Google survey. A short description of intent is also attached, which explained the purposes and objectives of the survey and included the link to the questionnaire. In total, 453 emails have been sent to the engineers, who is in the list of graduating student form department of civil engineering in HCMUT and working in the construction field.

4 Research Result

In total, 453 surveys are sent via email, and there are 52 emails are responded. The 64% of survey respondents have less than 3 years of experience, and 44% of respondents come from GCs. Most of the mean values of LEED works are less than three (Experienced—Know and be able to do). The result indicates that the Vietnamese contractors know about LEED projects but there is a lack of experience to meet LEED v4 prerequisites. In the surveyed credits, there are two credits have mean values greater than 3: IP-1: Assist the investor in the integrative design meeting at the beginning phase (3.39) and IQE-2: Environmental tobacco smoke control (3.20). It showed that some large Vietnamese contractors have had smoking management policies in the construction site. In addition, they are willing to assist investors in the integrative design process. The three credits' request with the lowest mean value is EA6: Collecting the documents Fundamental refrigerant management (2.16), MR5: Collecting and check manufacturers' content products mercury documentation (2.10), IQE1: Minimum Indoor Air Quality Performance (2.37). These jobs are not common in most construction projects in Vietnam. Thus, Vietnamese contractors should have several pieces of training for their staffs before beginning a LEED project, especially strictly LEED projects such as hospital and education building (Table 2).

5 Conclusions

The research points out the roles of GCs in the LEED project prerequisites. Comparison and review with local standards are also carried out. Especially the GCs play a major role in the construction activity pollution prevention, construction air quality management and so on. Thus, Vietnamese GCs can understand their scope of LEED works, and identify the solution to reduce the increase of cost and re-works. The research also points to the important role of GCs in participating owner support from the early stage of the project. In addition, previous studies have also shown that inexperienced GCs will significantly increase LEED projects.

The evaluation of the contractor's experience status is assessed through the questionnaire survey. The research revealed that Vietnamese construction companies are currently in the research and implementation phase of LEED and facing the lack of experience in most LEED prerequisites. Therefore, Vietnamese GCs should give LEED training for their staff and refer LEED recommended code such as U.S. local standards and U.S. national standard, ESC request form EPACGP, or using LEED experts in the first projects is essential to completing the project and minimizing the increase in costs.

Table 2 Survey result of LEED perquisite credits work

Name of GC's works	Mean	Name of GC's works	Mean
IP1: Assist the investor in the integrative design meeting at the beginning phase	3.39	EA4: Collecting the documents for minimum energy performance credit	2.61
IP2: Assessing the project life-cycle cost at the beginning of the project	2.92	EA5: Collecting the documents for building-level energy metering	2.59
SS1: Planning the erosion and sedimentation control	2.55	EA6: Collecting the documents fundamental refrigerant management	2.16
SS2: Implementing the ESC plan	2.61	MR1: Storage and collection of recyclables	2.59
SS3: Evaluating the results the erosion and sedimentation control	2.41	MR2: Making a construction and demolition waste management plan	2.80
WE1: Gathering records for irrigation systems, outdoor water saving	2.86	MR3: Implementing a construction and demolition waste management plan	2.69
WE2: Collecting documents (on water flow) for water use equipment	2.88	MR4: Review and report the results of implementing construction waste	2.57
WE3: Collecting the documents for water flow metering devices	2.69	MR5: Collecting and check manufacturers' documentation of mercury content products	2.10
EA1: Planning fundamental Cx and verification	2.55	IQE1: Minimum indoor air quality performance	2.37
EA2: Implementing fundamental Cx and verification	2.43	IQE 2: Environmental tobacco smoke control	3.20
EA3: Support a fundamental Cx contractors	2.53	IQE 3: Collecting data of NRC >0.7 materials	2.63

References

1. Ahn YH, Jung CW, Suh M, Jeon MH (2016) Integrated construction process for green building. *Procedia Eng* 145:670–676
2. Bayraktar ME, Owens CR (2009) LEED implementation guide for construction practitioners. *J Arch Eng* 16(3):85–93
3. Cha HS, Kim J, Han JY (2009) Identifying and assessing influence factors on improving waste management performance for building construction projects. *J Constr Eng Manag* 135(7):647–656
4. Chau CK, Tse MS, Chung KY (2010) A choice experiment to estimate the effect of green experience on preferences and willingness-to-pay for green building attributes. *Build Environ* 45(11):2553–2561
5. Frattari A, Dalprà M, Salvaterra G (2012) The role of the general contractor in sustainable green buildings: the case study of two buildings in the LEED certification in Italy. *Int J Hous Sci Appl* 36(3):139
6. Gluch P (2009) Unfolding roles and identities of professionals in construction projects: exploring the informality of practices. *J Constr Eng Manag* 27(10):959–968
7. Kibert CJ (2016) Sustainable construction: green building design and delivery. Wiley

8. Leland SM, Read DC, Wittry M (2015) Analyzing the perceived benefits of LEED-certified and energy star-certified buildings in the realm of local economic development. *Econ Dev Q* 29(4):363–375
9. Nguyen HT, Gray M (2016) A review on green building in Vietnam. *Procedia Eng* 142:314–321
10. Nguyen HT, Olanipekun AO, Skitmore MTyvima T (2017a) Motivations for green building development in Vietnam. In: Proceedings of 22nd International Conference on Advancement of Construction, pp 459–466
11. Nguyen HT, Skitmore M, Gray M, Zhang X, Olanipekun AO (2017) Will green building development take off? An exploratory study of barriers to green building in Vietnam. *Resour Conserv Recycl* 127:8–20
12. Pulaski MH, Horman MJ, Riley DR (2006) Constructability practices to manage sustainable building knowledge. *J Arch Eng* 12(2):83–92
13. Riley D, Pexton K, Drilling J (2003) Procurement of sustainable construction services in the United States: the contractor's role in green buildings. *Ind Environ* 26(2):66–69
14. Robichaud LB, Anantatmula VS (2010) Greening project management practices for sustainable construction. *J Manag Eng* 27(1):48–57
15. Rohracher H (2001) Managing the technological transition to sustainable construction of buildings: a socio-technical perspective. *Technol Anal Strateg Manag* 13(1):137–150
16. Samaras C (2004) Sustainable development and the construction industry: status and implications. Carnegie Mellon University Retrieved Oct 26, 2007
17. Schaufelberger J, Cloud J (2009) LEED certification: a constructor's perspective. In: Proceedings of 2009 Construction Research Congress, pp 598–607
18. Sev A (2009) How can the construction industry contribute to sustainable development? A Concept Fram Sustain Dev 17(3):161–173
19. Son H, Kim C, Chong WK, Chou JS (2011) Implementing sustainable development in the construction industry: constructors' perspectives in the US and Korea. *Sustain Dev* 19(5):337–347
20. Syal MM, Mago S, Moody D (2007) Impact of LEED-NC credits on contractors. *J Arch Eng* 13(4):174–179
21. Syal M, Li Q, Abdulrahman K, Mago S (2011) Leed® requirements and construction project management. *Int J Constr Proj Manag* 3(3):257
22. Washington State Department of General Administration (2005) Construction Waste Management, Olympia, Wash

Rice Crop Monitoring in the Mekong Delta, Vietnam Using Multi-temporal Sentinel-1 Data with C-Band



Hoang Phi Phung and Lam Dao Nguyen

1 Introduction

Rice is one of the main agricultural crops that plays an important role in food security, especially in the context of climate change, environmental pollution, and population growth. Rice is a staple food for most of the world's population [4], including Vietnam is a developing country with a population of over 96.6 million people [7]. In addition, climate change leads to an increase in extreme weather conditions such as salinization, droughts, and floods, which can destroy rice fields and impact on farmer livelihoods and food security of national. Therefore, there is a need to determine the exact area of rice and seasonal maps with high accuracy and timeliness. This is to provide information for management and ensure a stable supply of rice.

Rice is grown in flooded areas often, change the rice-growing period can change the backscatter coefficient of radar [15]. Based on the characteristics of the backscattered radar signals, rice planted areas can be mapped. SAR data commonly used in monitoring rice paddy is usually C-band [8] and X-band [13]. SAR data of C-band is particularly suitable for rice monitoring and mapping [11, 16], because of the sensitivity of the C-band sensor for plant biomass depends on the type of plant [6]. SAR data used for rice mapping and monitoring such as RADARSAT-1/2 [10], ERS-1/2 [9], ENVISAT ASAR [2], Sentinel-1 [12]. Radar remote sensing is recognized as an effective method to determine the rice map [1]. Although SAR data is not affected by clouds or sunlight, SAR-based methods have not been used to map large-scale rice due to limited availability of data and the cost of buying images [1]. However, Sentinel-1A satellite [16] was launched in 2014 and provides free and

H. P. Phung (✉) · L. D. Nguyen

Ho Chi Minh City Space Technology Application Center—Vietnam National Space

Center—VAST, Ho Chi Minh City, Vietnam

e-mail: hpphung@vnsc.org.vn

H. P. Phung

Graduate University of Science and Technology, VAST, Hanoi, Vietnam

open data access to users with high resolution of 20 m (Interferometric Wide Swath (IW) Mode), repeat cycle of 12 days and wide swath range of 250 km. By 2016, Sentinel-1B satellite [16] was launched to allow images to be obtained with a 6-day repeat cycle in specific areas. Time series of Sentinel-1 data-dense and free access at high spatial resolution offers an opportunity to facilitate monitoring of rice map near-real-time in the study area. Sentinel-1 image data is used in many applications such as rice crop area monitoring [5]. The objective of this research is to monitor rice/non-rice area distribution in the Mekong Delta and to validate the rice crop map using multi-temporal Sentinel-1 satellite data and ground data.

2 Data Used and Research Methods

2.1 Study Area

The Mekong Delta (Fig. 1) includes the provinces of Dong Thap, Long An, Hau Giang, Tien Giang, Vinh Long, Ben Tre, Tra Vinh, Bac Lieu, Soc Trang, Ca Mau, Kien Giang, An Giang, and Can Tho city. The Mekong Delta has a total natural area of 40,548.2 km² accounting for 13% of the natural area of the country [7]. This is an important area of agricultural production in the country that has been facing challenges and difficulties due to climate change and changing land use purposes. Monitoring and management of rice cultivation is not only to ensuring food security but also for sustainable development.

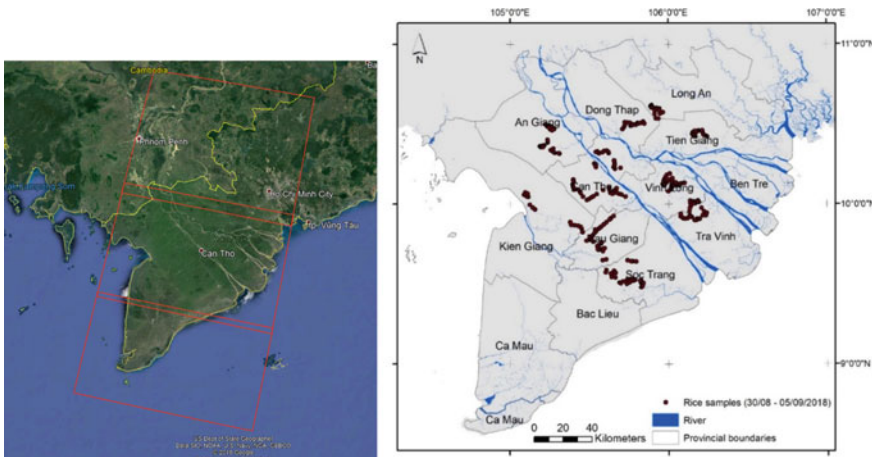


Fig. 1 Sentinel-1 scene frames collected for the Mekong Delta (left), and location map of the validation field samples collected on August 30–September 5, 2018 (right)

2.2 Data Used

Sentinel-1A and 1B satellites were put on orbit on April 3, 2014, and April 25, 2016, respectively. SAR integrated radar aperture image acquisition device using C band [14]. Interferometric Wide (IW) mode acquires data with a 250 km swath at 5 m by 20 m spatial resolution (single look). The incidence angle of the IW acquisition mode ranges from 29° to 46°. This study used Sentinel-1 GRD mode data from November 1, 2017, to December 30, 2018, acquired in the Mekong Delta, Vietnam.

The field data collected in the Mekong Delta was used for verifying the results of rice distribution mapping. Field data were collected including information such as sample location coordinates, crop information (single-, double-, and triple-crop rice) provided by farmers. Considering the natural conditions and rice-growing areas of the provinces in the Mekong Delta with a large area of rice cultivation were selected for field data collection (Fig. 1). The results obtained 271 sample points distributed over the selected provinces.

2.3 Methods

Processing steps on the diagram as shown in Fig. 2, including (a) image pre-processing such as SAR image multi-looking, calibration, terrain correction, noise filtering; (b) rice/non-rice classification using temporal change method; (c) mapping the rice cropping system. Sentinel-1 data was processed to convert to the backscatter coefficient (sigma naught), using the processing steps in SNAP toolbox (Sentinel Application Platform). After calibration and terrain correction steps, terrain effects were removed using the DEM (Digital Elevation Model) of Shuttle Radar Topography Mission with a resolution of 1 arc-second.

Based on the model of radar backscattering behavior of VH polarization according to the growth stages of rice, time-series SAR data were used to identify rice and non-rice areas. Sentinel-1 sigma naught values (σ^0) were extracted from samples of different land cover classes such as rice fields, perennials, forest, urban and water. Sigma naught values of paddy fields compared to other land cover classes with a range of amplitude change in backscattering were greater than 5 dB during a crop cycle, while the others had relatively stable backscattering. The temporal variation of radar backscatter for the VH polarization from land cover classes is shown in Fig. 3. The figure shows the use of time series of data that can distinguish rice from others, i.e. perennial, urban and water bodies. Analysis results showed that a temporal change method can be used to classify rice/non-rice.

Accuracy assessment

We conducted an accuracy assessment based on random sampling by remote sensing experts and local travel conditions. The validation field samples were classified into three classes according to classification results, single crop, double crop, and triple

Fig. 2 Flowchart of image processing for rice crop mapping using multi-temporal Sentinel-1 images

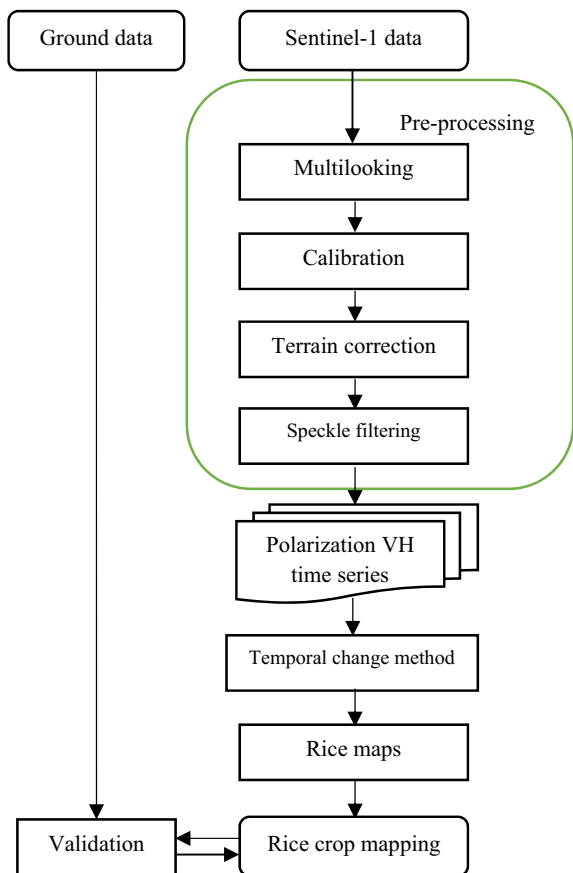
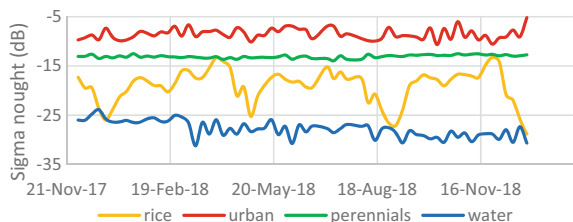


Fig. 3 Temporal variation of Sentinel-1 backscatter for VH polarization from four land cover classes in An Giang province



crop rice. The total number of samples used was 271 sample points and each class should be chosen at the minimum number of 20 samples [3]. All sample points were then used to evaluate the results of rice crop classification. To evaluate classified results, the confusion matrix, classification accuracy, Kappa coefficient, production accuracy, and user accuracy were used for the three classification classes.

3 Results and Discussions

Results of established rice maps for Winter-Spring (WS), Summer-Autumn (SA), and Autumn-Winter (AW) crops in 2018 were combined into the rice cropping system map in the Mekong Delta, Vietnam.

3.1 Rice/Non-rice Maps

The rice/non-rice maps were created from the Sentinel-1 data series collected for the WS, SA and AW 2018 crops in the Mekong Delta. Rely on the crop calendar of the Mekong Delta, the rice/non-rice maps of WS, SA and AW crops were established using Sentinel-1 image data acquired on the period of December 1, 2017—March 25, 2018, March 19–August 4, 2018 and July 5–October 27, 2018, respectively. The results of three rice distribution maps are shown in Fig. 4a–c, respectively.

Fig. 4 Rice map of WS (a), SA (b) and AW (c) crops of 2018 in the Mekong Delta, Vietnam

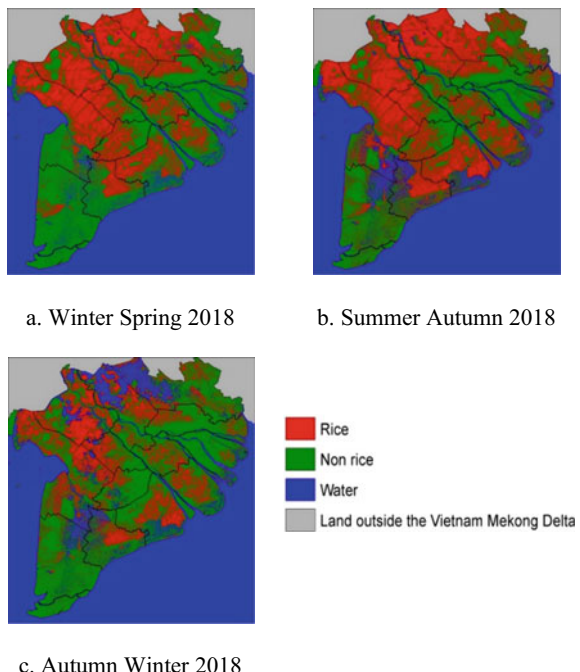
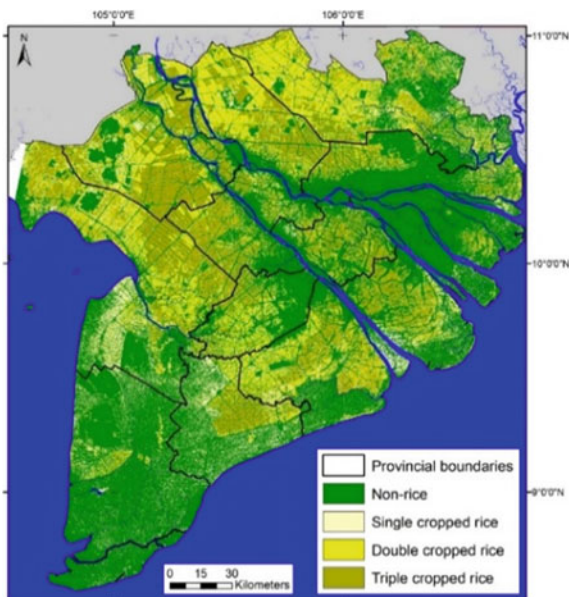


Fig. 5 Rice cropping system map of 2018 in the Mekong Delta



3.2 Rice Cropping System Map

The rice cropping system map (Fig. 5) was produced by combining rice/non-rice maps of WS, SA, and AW 2018 crops. The rice cropping system map for the Mekong Delta consists of three rice classes: single, double and triple cropped rice and non-rice. The classification results show that most of the provinces in the Mekong Delta were cultivated with double or triple crops of rice, of which triple-rice-growing areas are popular in the study area.

3.3 Validation of Rice Cropping System Map

Validation result of the 2018 rice cropping system map using field survey data from August 30 to September 5, 2018. The validation data had a total of 271 sample points distributed throughout the Mekong Delta. Radar images cover all areas of the Mekong Delta provinces except for a small part of Kien Giang province. A confusion matrix is often used as an evaluation method of classification results accuracy. Validation results are presented in the confusion matrix in Table 1. The classification accuracy of the rice cropping system map attained an overall accuracy of 92.6% and a Kappa coefficient of 0.86. The lowest producer's accuracy for double crop class was 88.8% and the lowest user's accuracy for single crop was 72.0%.

Table 1 Confusion matrix of rice cropping system map of 2018 in the Mekong Delta

	Classified data					
Ground data		Single crop	Double crop	Triple crop	Total	User accuracy (%)
Single crop	18	7	0	25	72.0	
	2	71	9	82	86.6	
	0	2	162	164	98.8	
	20	80	171	271		
	90.0	88.8	94.7			
Producer accuracy (%)						

4 Conclusion

The research results have shown that rice-growing areas can be extracted accurately from high spatial resolution Sentinel-1 data series using a multi-temporal method based on its growth stages. The multi-temporal method proved one of the most effective methods for mapping rice distribution areas in the Vietnamese Mekong delta. Applying this method to establish rice crop maps in 2018 using the Sentinel-1 GRD data archived with a spatial resolution of 20 m. The rice map results provide timely and accurate information about rice-growing areas that are important for food security issues.

The classification results of the rice cropping system map for the Mekong Delta have been verified using ground data of 271 sample points collected from August 30, 2018, to September 5, 2018. The validation results of the rice cropping system map proved strongly in mapping rice crops in many different rice_growing regions, with an overall accuracy of 92.6% and a Kappa coefficient of 0.86. The research results showed that the multi-temporal method for classifying rice crops proved to be a suitable method for the study site, Mekong Delta. This study showed the potential application of time series of Sentinel-1 data for rice crop system mapping and monitoring at the regional scale.

Acknowledgements This research is supported by the Project “Nghiên cứu ứng dụng tư liệu viễn thám radar và quang học đa thời gian, đa độ phân giải để theo dõi diễn biến diện tích và ước tính năng suất, sản lượng lúa vùng Đồng bìゝng sông Cửu Long và Đồng bìゝng sông Hồng” (code VT-UD.08/17-20) of Vietnam Academy of Science and Technology.

References

- Bouvet A, Le Toan T, Lam-Dao N (2009) Monitoring of the rice cropping system in the Mekong delta using ENVISAT/ASAR dual polarization data. IEEE Trans Geosci Remote Sens 47:517–526

2. Chen J, Lin H, Pei Z (2007) Application of ENVISAT ASAR data in mapping rice crop growth in Southern China. *IEEE Geosci Remote Sens Lett* 4:431–435
3. Congalton RG, Green K (2009) Assessing the accuracy of remotely sensed data—principles and practices. CRC Press, Taylor & Francis Group, Boca Raton, FL
4. Dobermann A, Fairhurst T (2000) Rice—nutrient disorders and nutrient management. International Rice Research Institute, Manila
5. Ferrant S, Selles A, Le Page M, Herrault PA, Pelletier C, Al-Bitar A, Mermoz S, Gascoin S, Bouvet A, Saqlalli M et al (2017) Detection of irrigated crops from Sentinel-1 and Sentinel-2 data to estimate seasonal groundwater use in South India. *Remote Sens* 9:1119
6. Ferrazzoli P, Paloscia S, Pampaloni P, Schiavon G, Sigismondi S, Solimini D (1997) The potential of multifrequency polarimetric SAR in assessing agricultural and arboreous biomass. *IEEE Trans Geosci Remote Sens* 35:5–17
7. GSO. General Statistics Office of Vietnam (2019) Website: <https://www.gso.gov.vn/>. Access date 03/06/2019
8. Inoue Y, Sakaiya E, Wang C (2014) Capability of C-band backscattering coefficients from high-resolution satellite SAR sensors to assess biophysical variables in paddy rice. *Remote Sens Environ* 140:257–266
9. Kurosu T, Fujita M, Chiba K (1995) Monitoring of rice crop growth from space using the ERS-1 C-band SAR. *IEEE Trans Geosci Remote Sens* 33:1092–1096
10. Li K, Brisco B, Yun S, Touzi R (2012) Polarimetric decomposition with RADARSAT-2 for rice mapping and monitoring. *Can J Remote Sens* 38:169–179
11. Mansaray LR, Huang W, Zhang D, Huang J, Li J (2017) Mapping rice fields in urban Shanghai, Southeast China, using Sentinel-1A and Landsat 8 Datasets. *Remote Sens* 9:257. <https://doi.org/10.3390/rs9030257>
12. Ndiakumana E, Ho Tong Minh D, Thu Dang Nguyen H, Baghdadi N, Courault D, Hossard L, Moussawi IE (2018) Estimation of rice height and biomass using multitemporal SAR Sentinel-1 for Camargue, Southern France. *Remote Sens* 10:1394. <https://doi.org/10.3390/rs10091394>
13. Rossi C, Erten E (2015) Paddy-rice monitoring using TanDEM-X. *IEEE Trans Geosci Remote Sens* 53:900–910
14. Sentinel Online (2019) Sentinel Online technical website. <https://sentinel.esa.int/web/sentinel/missions/sentinel-1>. Access date 03/06/2019
15. Silvestro PC, Pignatti S, Yang H, Yang G, Pascucci S, Castaldi F, Casa R (2017) Sensitivity analysis of the Aquacrop and SAFYE crop models for the assessment of water limited winter wheat yield in regional scale applications. *PLoS ONE* 12:e0187485
16. Torres R, Snoeij P, Geudtner D, Bibby D, Davidson M, Attema E, Potin P, Rommen B, Flouri N, Brown M et al (2012) GMES Sentinel-1 mission. *Remote Sens Environ* 120:9–24

Storage Tank Inspection Based Laser Scanning



L. Truong-Hong, R. Lindenbergh, and P. Fisk

1 Introduction

Recent development of laser scanning technology allows to capture three-dimensional (3D) topographic data of visible surfaces of objects in details with high accuracy in short time. This has enabled various applications of laser scanning data in civil engineering for example building reconstruction [13], construction management [1], infrastructure monitoring and inspection [11]. Particularly, terrestrial laser scanning data associated existing methods have been widely used in identifying damage of structures' surfaces [5]. The highly accurate, dense point cloud can be rich information to automatically inspect damage of a tank associated with its components. That can be an alternative solution to replace this current method, which relies on manual measurements, for example using tapes, or on low sampling data from a total station. However, automatic extracting and detecting damage of the tank are still a challenge task because point clouds corresponding to individual components of the tank have to be extracted from a massive point clouds of the complex structure including the tank components associated with other facilities. Thus, this paper proposes a RANSAC-based method empowered by voxelization to efficiently extract the point cloud of the tank wall and subsequently assess damage of the tank through its deformation.

L. Truong-Hong (✉) · R. Lindenbergh

Department of Geoscience and Remote Sensing, Delft University of Technology, Delft,
The Netherlands

e-mail: l.truong@tudelft.nl

P. Fisk

Ironhide Inspection Inc., Calgary, Canada

2 Related Works

The critical issue in automatic determination of deformation of a tank wall is to extract a point cloud of the tank wall from massive data points of a complex structure consisting of the tank wall and its components (e.g. floor, floating roof, roof, columns, girders, so on), objects surrounding the tank and other facilities (e.g. stair, pipes). In practice, the tank walls mostly appear as a vertical cylinder and are subjected to the surface's damage/deformation after a certain service time. Therefore, this section is focused to survey existing methods for extracting the cylinder from the point cloud.

Most of methods for extracting point cloud representing to a cylinder were based on classification or segmentation of raw point clouds to determine descriptive parameters of the cylinder, which can be Random Sample Consensus (RANSAC) based- and Hough Transform (HT) based-methods [7]. In among of RANSAC based methods, it can highlight the algorithm developed by Schnabel et al. [9] widely popular use in extracting the point cloud of the cylinder. The method estimated a direction of the cylinder's axis as a cross-product of normal vectors of data points, while the center and a radius of the cylinder were determined from the best fit circle of the points on the plane perpendicular to the cylinder's direction. One advantage of the proposed method was a sampling strategy allowing to handle a massive data. However, the method was also required users to tune input parameters (e.g. the minimum points of the estimated cylinder- min_ptc , the maximum distance from the point to the estimated cylinder- ϵ_{max} , and a deviation of points' normal vectors to the cylinder's normal at the points- α) to obtain the best cylinder. Similarly, Tran et al. [10] proposed an iterative algorithm to estimate the cylinder's parameters from a random points associated with their normal vectors, and for each iteration inlier points were remained for a next iteration.

On another hand, Rabbani and Van Den Heuvel [8] proposed a sequential generalized HT to extract a point cloud of a cylinder. The HT was first applied to a Gaussian image of the normal vectors of the points to estimate the direction of a cylinder's axis and the points within the highest cell for voting the direction were then used in a second step. Second, the points were then projected onto the orthogonal plane of the cylinder's direction and the HT was used to estimate the center and radius of the cylinder from these projected points. Additionally, Figueiredo et al. [3] improved HT methods for cylinder detection by introducing a new randomized sampling scheme to create non-uniform orientation Hough accumulators and efficient Hough voting scheme allowing to incorporate curvature information of each cell in the orientation Hough accumulators in the voting scheme. The authors addressed the proposed method can reduce space and executing time.

Although both RANSAC-based and HT-based methods were successful in extracting the cylinder from point clouds, these methods are still problematic with a large data set [6], for example the point cloud of a storage tank is up to hundreds of million points, because these methods are quired normal vectors of the input data. Moreover, it is also difficult to tune many input parameters to obtain the best model, particularly for the tank wall subjected to deformation (including global and local deformations).

As such, this paper proposed a RANSAC-based voxelization method to extract the tank wall, in which the method does not required to compute normal vectors of all data points.

3 Proposed Method

A goal of the proposed method is to automatically extract the point cloud of a tank wall from entire scanning point clouds, which consist of the points of the tank associated with its components (e.g. a floor, floating roof, roof, girders, columns and rafters), other facilities (e.g. stair, pipes), and other objects (e.g. ground objects) surrounding the tank. Subsequently, the tank wall was evaluated through deformation computed from the data points of the tank wall. In practice, the most tank walls appear as a perfectly vertical cylinder, but during service and/or errors from data acquisition the shape of the tank wall may be an inclined and/or imperfect cylinder. In addition, to identify surface damage, the tank was often scanned with a high resolution resulting the point cloud of the tank up to hundreds of million points. To solve these problems, the proposed method involves 4 main steps (Fig. 1) to extract the point cloud of the tank wall. In Step 1, an input point cloud was decomposed into an octree representation and the voxels contain candidate points of the tank wall were extracted based on a deviation angle between the normal vectors of the voxels and a unit vector of the oz axis in Step 2. Subsequently, in Step 3, the RANSAC-based voxelization method was proposed to estimate a fitting cylinder of the tank wall, which can allow to easily to retrieve the points of the tank wall. Finally, Step 4 computes deformation of the tank wall based on its fit cylinder (known as the vertical fit and the best fit cylinders), which is to determine if the tank deformation is exceeded a limitation.

In practice, during capturing a storage tank, the point cloud involves not only the tank's components but also other facilities and environmental objects. An input data points, $\mathbf{P} = (\mathbf{p}_i = \{x_i, y_i, z_i\} \in \mathbb{R}^3, i = [1, N])$ may consist of hundreds of million points. To reduce intensive computation, in Step 1, an octree representation (Fig. 2a)

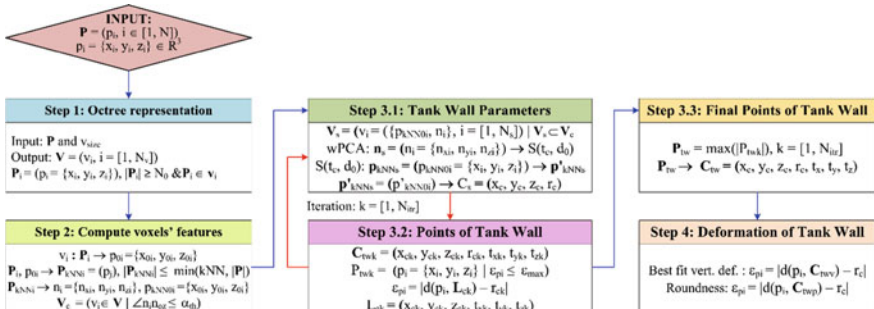


Fig. 1 Proposed workflow to determine deformation of the tank wall

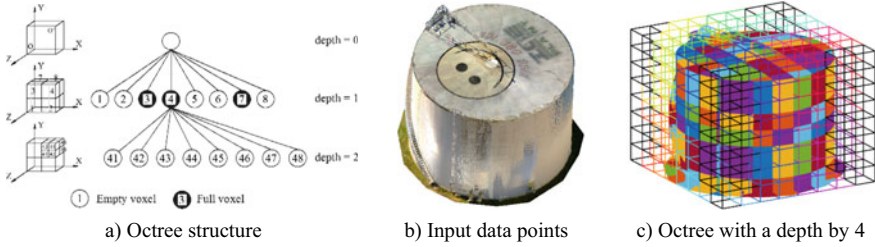


Fig. 2 Octree representation

was employed to recursively subdivide an initial enclosing bounding box of an input point cloud P into the smaller voxels until a terminal condition is reached. In this study, the maximum size of the voxels (v_{size}) on leaf nodes of the octree was used, which is 0.5 m, although several other terminal conditions have been used, for example, a maximum depth or the maximum number of points within the voxel. Each voxel is defined as classification, address and geometry. The voxels are classified as “full” if the voxel contains the number of points equal or larger than a predefined threshold, which is empirically selected as 10 points; otherwise, the voxels were classified as “empty”. Similar to Truong-Hong et al. [12], an address of the voxel is to indicate the relationship between the voxel to its parent voxel and its sibling voxels (Fig. 2a). Moreover, the voxel’s geometry is defined as x-, y-, z-coordinates of two opposite corners of the voxel. A subdivision process is only carried out on the full voxels. Figure 2b, c show the full voxels generated from the point cloud of the exterior tank.

Next, Step 2 is to compute features of the full voxels on leaf nodes of the octree representation to provide information for estimating parameters of a cylinder of a tank wall. First, a normal vector of each full voxel ($\mathbf{v}_i \in \mathbf{V}, i = [1, N_v]$) is computed, which was defined as the normal vector of a local planar surface at the center of the points within the voxel. As such, from the voxel center (p_{0i}) computed the points (\mathbf{P}_v) within the voxel (Eq. 1), the k-nearest neighbor (kNN) of neighbor points (\mathbf{P}_{kNN}) is extracted and the normal vector ($\mathbf{n}_i = \{\mathbf{n}_{xi}, \mathbf{n}_{yi}, \mathbf{n}_{zi}\}$) of the plane through \mathbf{P}_{kNN} is an eigenvector corresponding to the smallest eigenvalue computed from a covariance matrix (Eq. 2) by using a robust principal component analysis rPCA [4]. In this study, kNN by 25 points is empirically used. Notably, for searching the neighbor points, only the points within the voxel are used, which implied $|\mathbf{P}_{kNN}| \leq |\mathbf{P}_v|$. Moreover, after estimating the normal vector \mathbf{n}_i , the new center of the voxel is also updated based on the kNN points (Eq. 1).

$$p_{0i} = \frac{1}{|\mathbf{P}_v|} \sum_{p_j \in \mathbf{P}_v} p_j \quad (1)$$

$$C_{kNN} = \frac{\sum_{p_j \in \mathbf{P}_{kNN}} w(p_j)(p_j - p_{kNN0i})(p_j - p_{kNN0i})^t}{\sum_{p_i \in \mathbf{P}_{kNN}} w(p_i)} \quad (2)$$

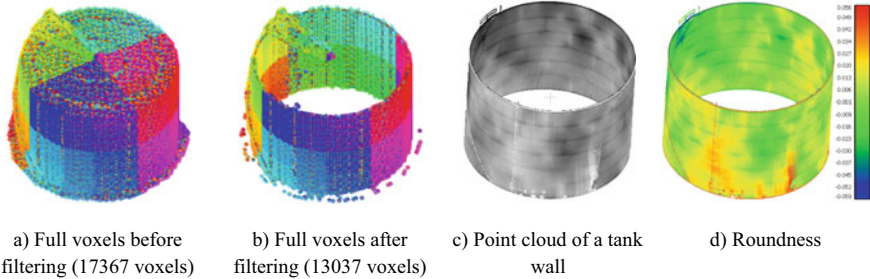


Fig. 3 Extracting the voxels possessed candidate points and resulted point clouds of the tank wall

$$w(p_j) = \exp\left(\frac{-d_{pj}^2}{d_0^2}\right) \quad (3)$$

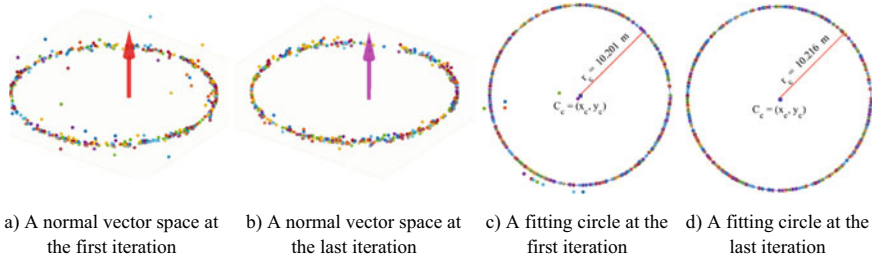
where p_{0i} is a center of the voxel v_i computed from the \mathbf{P}_v , $||$ is the cardinal of the \mathbf{P}_v , C_{kNN} is a covariance matrix computed from P_{kNN} , in which p_{kNN0i} is the centroid of the P_{kNN} computed from Eq. 1, $w(p_j)$ is the weight of each point $p_j \in P_{kNN}$, d_{pj} is the distance between point p_j to a plane through P_{kNN} , and d_0 is set equal to $1/5 \sum d_{pj}$.

By observing the tank configuration, the tank wall is mostly vertical, which is implied if a voxel contains the points of the tank wall, its normal vector is nearly perpendicular to a unit vector $n_{0z} = \{0, 0, 1\}$ of the oz axis. As such, the voxels containing candidate points of the tank wall are filtered based on a deviation angle between the normal vector of the voxel and n_{0z} , which is given in Eq. 4. Resulted filtering irrelevant voxels is shown in Fig. 3.

$$\mathbf{V}_c = (v_i \in \mathbf{V}, i = [1, N_c] \angle n_i, n_{0z} \geq \alpha_{th}) \quad (4)$$

where α_{th} is the angle threshold, which is set 45° . This threshold is selected based on an observation that if the voxels containing the points of both the tank wall and a floor/ground or a roof, the deviation angle may be approximately 45° .

Next, Step 3 is to estimate a cylinder's parameters representing to the tank wall based on the normal vector and center of the voxels \mathbf{V}_c . The cylinder can describe by the cylinder's direction $t_c = \{t_x, t_y, t_z\}$, a point $c_c = \{x_c, y_c, z_c\}$ along the t_c , a radius (r_c). In theory, if there are three points (p_1, p_2, p_3) and their normal vectors (n_1, n_2, n_3) on the cylinder, the direction t_c is a cross-product of a pair of the normal vectors, for example, $t_c = n_1 \times n_2$. Moreover, when projected these points on an orthogonal plane of the t_c , these projected points locate on a circle. As such, the fitting circle through three projected points can give the center c_c and the radius r_c of the cylinder. Thus, the cylinder's parameters were determined based on voxels as following. First, the subset voxels, $\mathbf{V}_s = (v_i = \{p_{kNN0i}, n_i\}, i = [1, N_s] \mid \mathbf{V}_s \subset \mathbf{V}_c \})$ were randomly extracted from the \mathbf{V}_c . The rPCA [4] was employed to estimate the normal vector of the fitting surface through the normal vectors \mathbf{n}_s of the \mathbf{V}_s , which is the direction t_c of the cylinder's axis. The voxel v_{si} can be considered as an outlier voxel if the angle



a) A normal vector space at the first iteration b) A normal vector space at the last iteration c) A fitting circle at the first iteration d) A fitting circle at the last iteration

Fig. 4 Interaction process to estimate the direction, centre and radius of the cylinder

between its normal vector n_{si} and the t_c is larger than a predefined angle threshold (α_{nt}), in which the α_{nt} by 85° was empirically adopted. The process is iteratively removed the outlier voxels until the angle of the t_c from two consecutive iterations is less than a predefined angle by 1° (Fig. 4a, b).

Second, the centers of the inlier voxels ($V_{inlier,s} \subset V_s$) are projected onto the best fit surface along the t_c . The best fit circle (C_s) through the projected points was iteratively generated by using a least squares method, in which the radius and the centroid of C_s are respectively the radius (r_c) and center $c_c = (x_c, y_c, z_c)$ of the cylinder. Notably, any projected point having the fitting error larger than a maximum distance (ε_{max}) from the points to the detected cylinder is eliminated and the convergence is obtained when no the projected point to be eliminated (Fig. 4c, d). Finally, the number of the points within the ε_{max} of the fitting cylinder C_{tw} are used as a score to determine the best fit cylinder having the largest number of points, which is given in Eq. 5.

$$P_{tw} = (p_i | p_i \in P \wedge \varepsilon_{pi} \leq \varepsilon_{max}) \quad (5)$$

where $d(p_i, C_{tw})$ is the distance from the point to the $C_{tw}(c_c, r_c, t_c)$, which is expressed in Eq. 6.

$$\varepsilon_{pi} = d(p_i, C_{tw}) = |d(p_i, L_c) - r_c| \quad (6)$$

where $L_c(c_c, t_c)$ is the line through the center of the fitting cylinder C_{tw} with the direction axis t_c .

In Step 4, two critical types of the tank's deformations need to report: (i) best fit vertical deformation and roundness. The best fit vertical deformation measures as a distance from the points to the tank wall assumed as the perfectly vertical cylinder (C_{twv}), which can be expressed in Eq. 7. The C_{twv} can be defined as a fitting the circle $C(x_c, y_c, z_c, r_c)$ through projection of all points of the tank wall on a horizontal plane for example the xy plane. Moreover, the roundness is defined that the distance from the point to the tank wall assumed as a perfect cylinder (C_{tw}), which is computed based Eq. 6. Notably, the fitting cylinder here can be an inclined cylinder. Figure 3d illustrates the roundness.

$$\varepsilon_{\text{best_fit_vert_def}} = d(p_i, C_{\text{twv}}) = |d(p_i, C) - r_c| \quad (7)$$

4 Experimental Tests

An aim of the experiment is to evaluate the proposed method in extracting and assessing of the tank wall from a massive point cloud acquired from a terrestrial laser scanner. Two tanks are selected to test performance of the proposed methods, and results of the tank wall extraction also compare to ones from RANSAC method proposed by Schnabel et al. [9] plugged in CloudCompare V2.7.0 (CloudCompare). Tank 1 is Tank 67 with a diameter of 18.288 m and height of 12.50 m, located at Regina, Canada while Tank 2 is Tank 2490 with a diameter of 21.336 m and height of 14.63 m, located at Houston, US. Both Tanks were captured by Faro Focus X130 with the sampling step by 6.136 mm at a measurement range by 10 m. After registering the point clouds from different scanning stations, the point clouds are down-sampled with a minimum distance between two adjacent points no more 5 mm. The data sets with x-, y-, and z-coordinates are respectively 33,692,139 points and 22,447,931 points for the Tank 1 and 2 as input data. The proposed method is implemented in Matlab programming language and the tests are processed on Dell Precision Workstation with a main system configuration: Intel(R) Xeon(R) W-2123 CPU @ 3.6 GHz with 32 GB RAM.

Input parameters consisting of the voxel size, $v_{\text{size}} = 0.5$ m, $k_{\text{NN}} = 25$ points, $\alpha_{th} = 45^\circ$, $\alpha_{nt} = 85^\circ$, and $\varepsilon_{\max} = 0.05$ m are used for both Tanks. Moreover, input parameters for the RANSAC method proposed by Schnabel et al. [9] are the $\min_{\text{ptc}} = 10\%$ of size of an input data, the $\varepsilon_{\max} = 0.05$ m, and $\alpha = 10^\circ$. Resulted extraction of data points and deformation of both Tanks are showed in Figs. 5 and 6. A visualization evaluation is showed that the proposed method can extract proper point clouds of the tanks and is comparable with the Schnabel 's method, but resulted based RANSAC [9] includes the data points of a floor, which have to manually indicate to remove it (Fig. 5c). The difference of a tank's diameter from the inventory and ones from

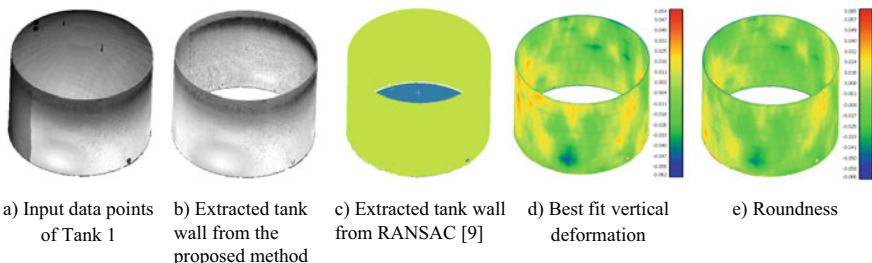


Fig. 5 Resulted extraction of a point cloud of Tank 1 from the proposed method and RANSAC proposed Schnabel et al. [9], and deformation and roundness of the tank from the proposed method

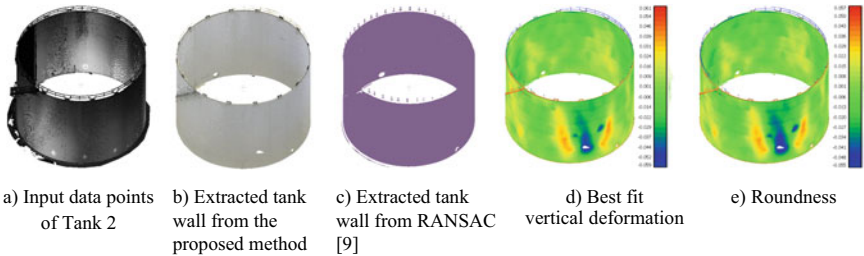


Fig. 6 Resulted extraction of a point cloud of Tank 2 from the proposed method and RANSAC [9], and deformation and roundness of the tank from the proposed method

the proposed method are respectively 0.026 m for Tank 1 (18.288 m vs. 18.262 m) and 0.008 m for Tank 2 (21.336 m vs. 21.344 m). Notably, errors here include errors from a damage of the tank wall, data acquisition and registration and the proposed method.

As the tank wall is assumed as a perfect cylinder when implementing the method to extract the tank wall point cloud, resulted point clouds of adjacent objects of the tank wall are also included, for example, the points of safeguard and ground (Figs. 5b, c, and 6b, c). This issue can be solved when an additional localized filtering is implemented. Moreover, the proposed method may be under-extraction of the tank wall's points when the wall is subjected to deformation larger than the than a maximum distance (ε_{\max}).

The executing time from the proposed method are 697.5 s for Tank 1 and 504.4 s for Tank 2. Comparatively, ones from the RANSAC method proposed by Schnabel et al. [9] are respectively 514.8 s and 335.0 s. However, it is noticed that the RANSAC method was implemented in C++ programming language. Moreover, in the proposed method, only the maximum distance ε_{\max} affects to the results while in the RANSAC method [9] 3 input parameters (\min_ptc , $SS\varepsilon_{\max}$, α) are required to obtain the best result. Finally, by using the RANSAC method [9] for this application, multiple cylinders can be obtained, and additional filtering is needed to determine the correct cylinder of the tank wall, for example, there are 2 cylinders extracted for Tank 1 (Fig. 5c).

5 Conclusions

This paper presents a new, efficient RANSAC-based voxelization method to extract a cylinder representing to a wall of a storage tank from a massive data point cloud. The input data points are decomposed by an octree representation and the voxels containing candidate points of the tank wall are extracted by examining normal vectors of the voxels, which are computed from the kNN points of the voxel center. Next the RANSAC paradigm is applied on a subset voxel to estimate the direction

axis, center, radius of the cylinder. In this step, an outlier removal process is applied to eliminate the outlier voxels. The proposed method is tested on two Tanks scanned from outside and inside. The experimental tests show the points of the tank walls are successfully extracted and comparable with the popular RANSAC method. The results also show that diameters of the extracted cylinders differ from ones derived from an inventory about 0.026 m (Tank 1) and 0.008 m (Tank 2). Moreover, the executing time is respectively 697.5 s and 504.4 s for the data set of 33,692,139 points and 22,447,931 points. However, the point cloud of the tank wall still contains data points of other objects closed to the tank wall, which can be removed by implementing a local outlier filter. Finally, as the tank is often subjected to deformation, selecting an appropriate maximum distance is still difficult.

Acknowledgements This work was funded by the generous support of the European Commission through H2020 MSCA-IF, “*BridgeScan: Laser Scanning for Automatic Bridge Assessment*”, Grant 799149.

References

1. Bosché F, Ahmed M, Turkan Y, Haas CT, Haas R (2015) The value of integrating Scan-to-BIM and Scan-vs-BIM techniques for construction monitoring using laser scanning and BIM: the case of cylindrical MEP components. Autom Constr 49:201–213. <https://doi.org/10.1016/j.autcon.2014.05.014>
2. CloudCompare (Version 2.7.0). Retrieved from <http://www.cloudcompare.org/>
3. Figueiredo R, Dehban A, Moreno P, Bernardino A, Santos-Victor J, Araújo H (2019) A robust and efficient framework for fast cylinder detection. Robot Autonom Syst 117:17–28. <https://doi.org/10.1016/j.robot.2019.04.002>
4. Laefer DF, Truong-Hong L (2017) Toward automatic generation of 3D steel structures for building information modelling. Automation in Construction 74:66–77. <https://doi.org/10.1016/j.autcon.2016.11.011>
5. Laefer DF, Truong-Hong L, Carr H, Singh M (2014) Crack detection limits in unit based masonry with terrestrial laser scanning. NDT E Int 62:66–76. <https://doi.org/10.1016/j.ndteint.2013.11.001>
6. Maalek R, Lichti DD, Walker R, Bhavnani A, Ruwanpura JY (2019) Extraction of pipes and flanges from point clouds for automated verification of pre-fabricated modules in oil and gas refinery projects. Autom Constr 103:150–167. <https://doi.org/10.1016/j.autcon.2019.03.013>
7. Nurunnabi A, Sadahiro Y, Lindenbergh R, Belton D (2019) Robust cylinder fitting in laser scanning point cloud data. Measurement 138:632–651. <https://doi.org/10.1016/j.measurement.2019.01.095>
8. Rabbani T, Van Den Heuvel F (2005) Efficient hough transform for automatic detection of cylinders in point clouds. ISPRS WG III/3, III/4, 3:60–65
9. Schnabel R, Wahl R, Klein R (2007) Efficient RANSAC for point-cloud shape detection. Comput Graph Forum 26(2):214–226
10. Tran T-T, Cao V-T, Laurendeau D (2015) Extraction of cylinders and estimation of their parameters from point clouds. Computers & Graphics 46:345–357. <https://doi.org/10.1016/j.cag.2014.09.027>
11. Truong-Hong L, Laefer D (2015) Documentation of bridges by terrestrial laser scanner. In The IABSE Geneva Conference 2015, Geneva, Switzerland, 22–25 Sep 2015

12. Truong-Hong L, Laefer DF (2014) Octree-based, automatic building façade generation from LiDAR data. *Comput Aided Des* 53:46–61. <https://doi.org/10.1016/j.cad.2014.03.001>
13. Truong-Hong L, Laefer DF, Hinks T, Carr H (2012) Combining an angle criterion with voxelization and the flying voxel method in reconstructing building models from LiDAR data. *Comput-Aided Civ Infrastruct Eng* 28(2):112–129

Studying Wind Flow-Field Around a Triangular Building by CFD and Wind Tunnel



Do N. Ngo, Y. Q. Nguyen, Anh T. Tran, and Hien T. Le

1 Introduction

Studying wind effects on tall building provides essential information for the purposes of designs of structures or natural ventilation of the building. Interaction between wind and building can be studied by experiments in wind tunnels [3, 8, 9], by numerical simulations [4, 10, 11, 13] or by both of them [7]. Those previous studies reported that the cross-sectional shape of the building is one of the most important factors affecting the pressure distribution on the surfaces of the building and the flow structure around the building.

In this studying, we investigated flowfield around a triangular cross-sectional building with a light well on one side and chamfered roof. Baghaei Daemei et al. [3] studied a triangular shaped building with seven different forms to determine the smallest drag coefficient for the design. However, none of their models has a light well.

The flowfield was investigated by numerical simulation with CFD (Computational Fluid Dynamics) technique and compared with results of experiments in a wind tunnel.

D. N. Ngo (✉)

Faculty of Civil Engineering, Ho Chi Minh City University of Technology, VNU-HCM, Ho Chi Minh City, Vietnam

e-mail: 1870018@hcmut.edu.vn

Y. Q. Nguyen

Van Lang University, Ho Chi Minh City, Vietnam

A. T. Tran · H. T. Le

Faculty of Transportation Engineering, Ho Chi Minh City University of Technology, VNU-HCM, Ho Chi Minh City, Vietnam

2 Numerical and Experiment Methods

2.1 Numerical Method

CFD technique was applied to predict flowfield around the building. The air flow was assumed to be steady, incompressible and isothermal which are governed by the continuity and momentum conservation equations [5]. For modeling turbulence, RANS (Reynolds Averaged Navier-Stockes equations) method was used with the following governing equations:

$$\frac{\partial(\rho\bar{u}_i)}{\partial x_i} = 0 \quad (1)$$

$$\frac{\partial(\rho\bar{u}_i)}{\partial t} + \frac{\partial}{\partial x_j} \left(\rho\bar{u}_i\bar{u}_j + \rho\overline{u'_i u'_j} \right) = -\frac{\partial\bar{p}}{\partial x_i} + \frac{\partial\bar{\tau}_{ij}}{\partial x_j} \quad (2)$$

where $\overline{\cdot}$ indicates a time-averaged quantity; $\bar{\tau}_{ij}$ are the mean viscous stress tensor components:

$$\bar{\tau}_{ij} = \mu \left(\frac{\partial\bar{u}_i}{\partial x_j} + \frac{\partial\bar{u}_j}{\partial x_i} \right) \quad (3)$$

The eddy-viscosity model was used for the Reynolds stress $\rho\overline{u'_i u'_j}$ with two equations for the turbulent kinetic energy k and the dissipation ε [5]. Equations (2) and (3) were discretized on an unstructured mesh using Finite Volume Method with the ANSYS Fluent code. Three RANS models: Standard $k-\varepsilon$, $k-\varepsilon$ RNG, $k-\omega$ SST were used to simulate and the results were compared with experiments in this study.

The studied building had a triangular cross section and a chamfered roof. The prototype building was 366-m high and 77-m wide for each of its triangular length. There was a light well on one side of the building. The studied building is scaled to assure the similar conditions as experiments in the wind tunnel. A scaled model of the building was made at a scaling ratio of 1:750 resulting in a studied model of 0.488 m height and 0.1027 m width, as shown in Fig. 1a. The light well is on onside of the building and between the surfaces M3 and M4.

Inside the computational domain, only the building was considered. Surrounding structures were not modeled. As suggested by [6, 12] for computations for single building, the computational domain was extended to 5H to the top and lateral boundaries except for the outflow boundary behind the building where it was set to 15H. Figure 1b shows the size of computational domain.

To reproduce the experiments in the wind tunnel, uniform velocity profile was set at the inlet with a turbulence intensity of 5%. At the lateral and top sides, free stress conditions were used. Zero normal gradients of the flow were assumed at the outflow boundary.

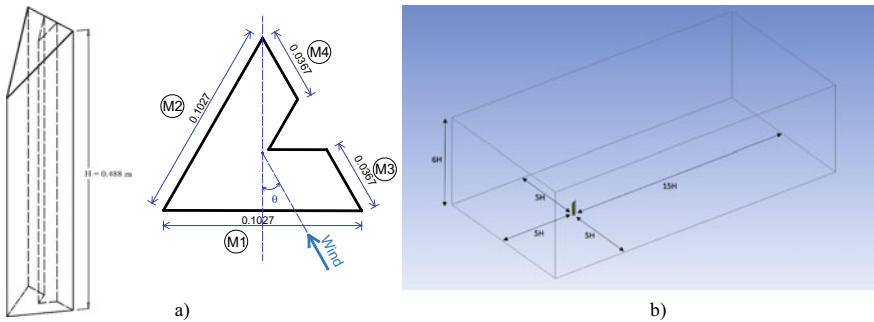


Fig. 1 The studied building: **a)** scaled 3D model of the building and its cross-sectional area with dimensions in meter, **b)** the computational size (H is the building height)

Different mesh resolutions were tested and compared the drag on the building. It was found that a mesh with 10^6 elements or more was sufficient for obtaining a grid-independent drag coefficient.

The drag coefficient is defined as:

$$C_d = \frac{F_d}{\frac{1}{2} \rho V_\infty^2 \cdot A_{ref}} \quad (4)$$

where F_d is the force acting parallel to the wind direction; ρ is the fluid density; V_∞ is the steady wind speed in front of the building, A_{ref} is the reference area which is the frontal area of the building.

2.2 Experiment Method

The experiments were conducted in an open wind tunnel at the Laboratory of Building Physics and Fluid Mechanics of the Ho Chi Minh City University of Technology. The test section of the wind tunnel had an area of $1.0 \text{ m} \times 1.0 \text{ m}$ and a length of 2.0 m . The working wind speed was 6.0 m/s . With the above scaling ratio and the characteristics of the wind tunnel, the Reynolds number based on the height H of the model was 1.83×10^4 and the blockage ratio was 4.98% . These conditions satisfied the recommendations by [1].

The model was placed on the turn table in the test section of the wind tunnel. Different wind angle θ relative to the surface M1 of the model, as indicated in Fig. 1.a, was tested. At each wind angle, pressure on four surfaces of the model, from M1 to M4, was recorded at 27 points on the M1 and M2 faces and 10 points on the M3 and M4 faces together with the static pressure of the wind flow. The wind speed and static pressure was measured at a distance of 0.5 m in front of the model. Figure 2b shows distribution of pressures taps on each face of the model.

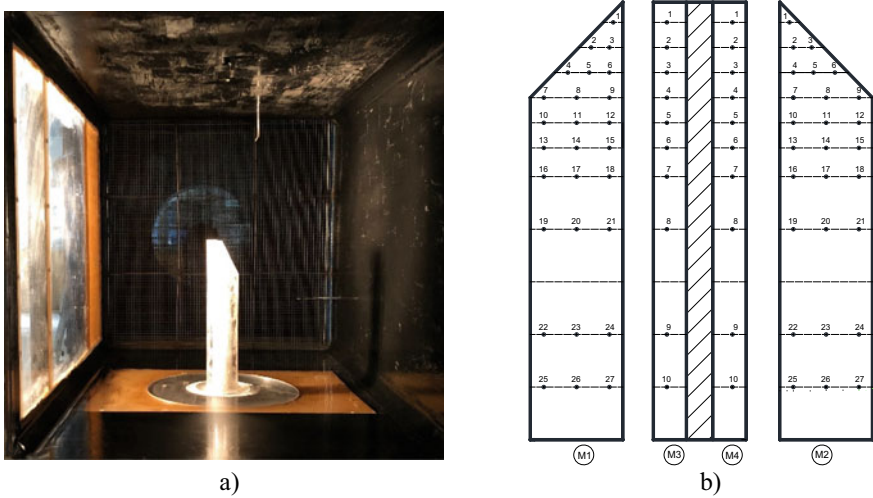


Fig. 2 **a)** Scaled model in the wind tunnel, **b)** distribution of pressure taps on each face

The pressures were recorded by sensors having a resolution of 0.3 Pa and an accuracy of 1%. The sensors were connected to a data logger which had a sampling rate of 1 Hz and recorded signals continuously. The recorded data was analyzed to obtain time-averaged pressure and wind speed. The averaged interval was 5-minute which was found to be sufficient to achieve time-independent statistics.

From the measured data, pressure coefficient C_p at each point on the surfaces of model was obtained:

$$C_p = \frac{p - p_\infty}{\frac{1}{2} \rho V_\infty^2} \quad (5)$$

where p is the measured pressure on the model surface; and p_∞ is the static pressure of the wind flow.

2.3 Results and Discussions

Pressure distribution on the surfaces of the studied building.

For validating the computational model, mean pressure coefficients C_p at 2/3 height of the building at two wind angles: $\theta = 0^\circ$ and $\theta = 120^\circ$ were compared with the experimental data. Figure 3 shows mean pressure coefficients C_p at 2/3 H of the building. The studied building had an equilateral triangular cross-section. Dx is the length of a side. ($Dx = 0.1027$ m).

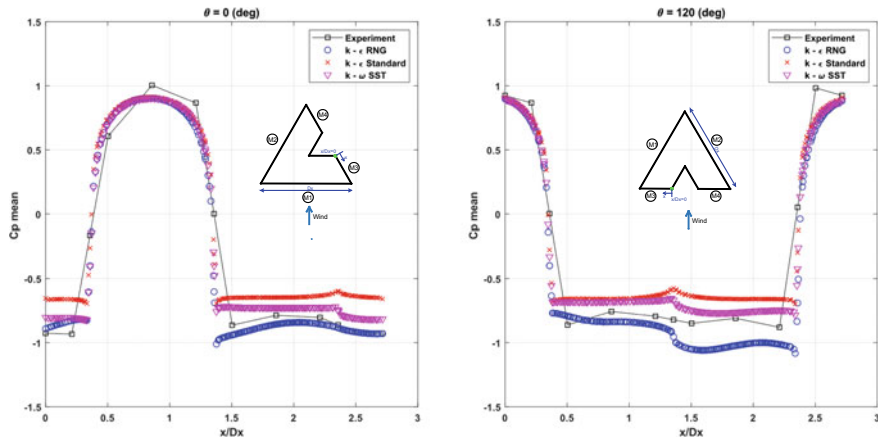


Fig. 3 Mean pressure coefficients C_p at $2/3 H$ of the building

On the front surface of the building at both of wind angles, the present computational results of three RANS models (standard $k-\varepsilon$, $k-\varepsilon$ RNG, $k-\omega$ SST) and the experimental data are in good agreement with minor discrepancy. It is noted that the pressure coefficient distributions from all three RANS models are identical.

There are substantial discrepancies between computational and experimental results on the back and side surfaces. On the back and the side surfaces in the case with the wind angle: $\theta = 0^\circ$, the pressure coefficient distributions predicted by the $k-\varepsilon$ RNG model and the $k-\omega$ SST model are close to those of the measurements. Whereas, the results from the standard $k-\varepsilon$ model and the measurements do not agree well.

In the case with the wind angle: $\theta = 120^\circ$, the pressure coefficient distributions predicted with three RANS models are seen in fairly good agreement with the data of the experiments on the M1 side face. However, there are substantial differences in prediction on the M2 side face among the RANS models. The $k-\omega$ SST model is the closest to the measurements. Discrepancies between computed and experimental data on the leeward sides of the building may be due to the errors in the wind speed measurement and other routine errors. Moreover, the flow structure behind the model is unsteady, which is hard to predict all accurately by steady RANS methods as employed in this study.

Figures 4, 5 and 6 show the distributions of measured pressure coefficient on the surfaces of the model at different wind angle. On each surface, the pressure coefficient C_p varies strongly with the wind angle. It is observed that C_p is positive on the windward surfaces and negative on the leeward sides, as can be expected.

Effects of the light well on pressure distribution can be seen for the case of $\theta = 0^\circ$. The pressure coefficient on the M2 surface was less negative on the M3-M4 surfaces. When the wind flow was normal to a surface ($\theta = 0^\circ$ for M1, $\theta = 240^\circ$ for M2, and $\theta = 120^\circ$ for M3-M4), the pressure coefficient on M1 and M2 have similar values while that on the M3-M4 is sufficiently lower. Therefore, it is expected that

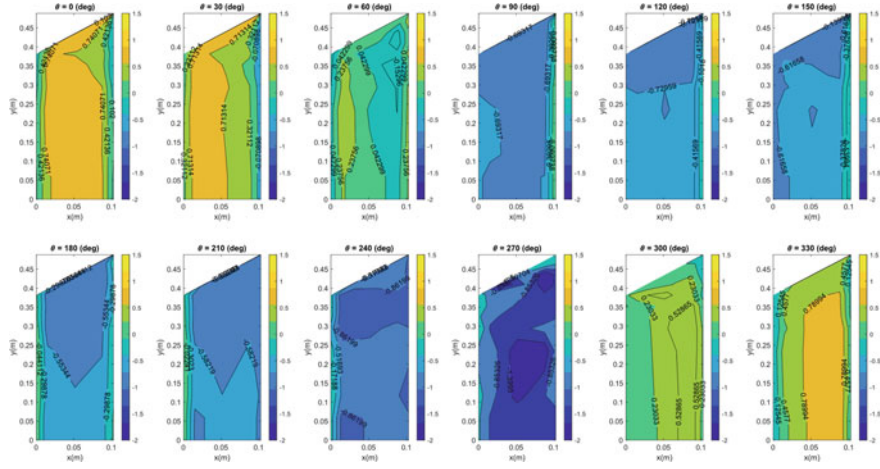


Fig. 4 Distributions of C_p on the M1 surface (experiment)

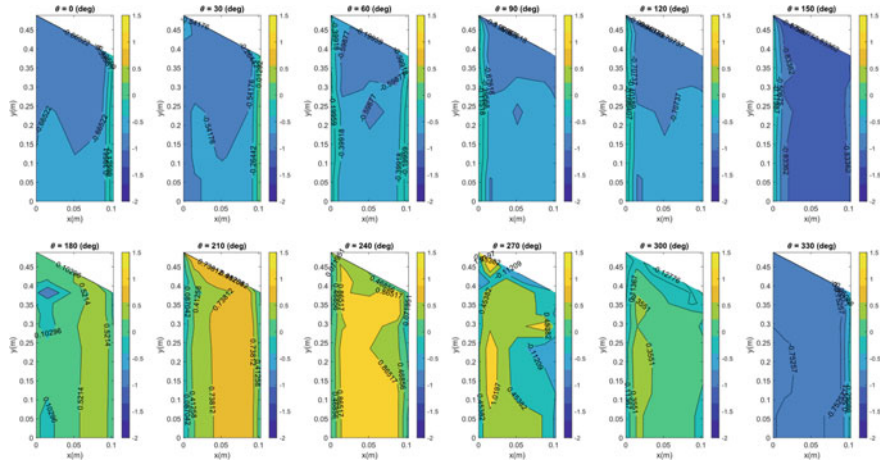


Fig. 5 Distributions of C_p on the M2 surface (experiment)

the presence of the light well and the chamfered roof reduces the pressure on the M3-M4 surfaces where the light well is located.

The distribution of C_p on M1 for $\theta = 0^\circ$ is similar to that on M2 for $\theta = 240^\circ$. This fact shows good repeatability of the measured data, as from the geometry of the building, these two surfaces should have similar aerodynamic behaviors at such wind angles.

One of the intended functions of the light well is for ventilating the building naturally. As the light well was on one side of the building, single-sided natural ventilation mode [2] is expected. The pressure distribution on M3 and M4 should

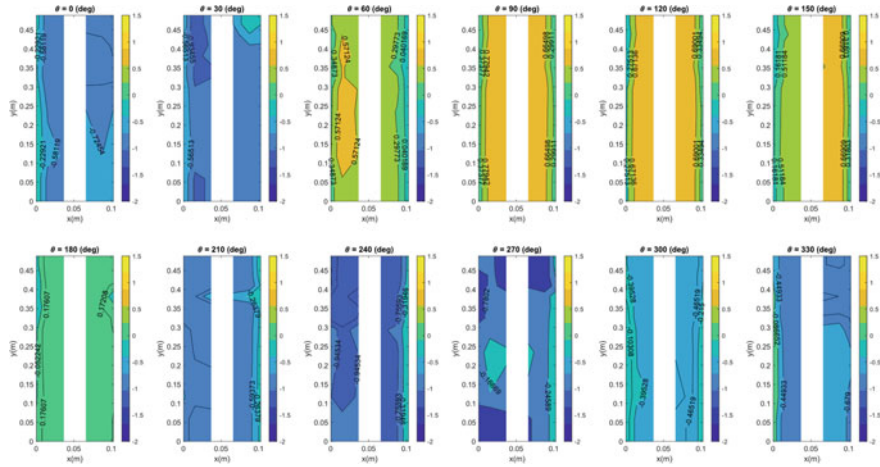


Fig. 6 Distributions of C_p on the M3 and M4 surfaces (experiment)

then have different values so that airflow enters the building on the side with higher pressure and leaves at the other side with lower pressure. From Fig. 6, it is observed that the best wind angle for that purpose is $\theta = 150^\circ$ with maximum difference of C_p between M3 and M4 of about 0.16.

The drag coefficient with different wind angles.

Figure 7 shows the change of drag coefficient C_d with wind angles, which is predicted by $k-\varepsilon$ RNG model, $k-\omega$ SST model and standard $k-\varepsilon$. The computational results of these models are similar to each other, except for small discrepancies with wind angles: $\theta = 0^\circ$, $\theta = 120^\circ$ and $\theta = 240^\circ$. The drag coefficient of the studied building is maximum with wind angle $\theta = 120^\circ$ and minimum with wind angles: $\theta = 60^\circ$, $\theta = 180^\circ$ and $\theta = 300^\circ$. The drag coefficient C_d varies strongly with angle; hence is strongly dependent on the shape of the windward surface.

Flow structure around the building

Figure 8a, b presents the flow structure behind the model visualized by smoke in the wind tunnel and by the CFD model. Vortex shedding can be seen with the smoke as well as the computed flowfield. This phenomenon is also well studied and reported before [4, 8].

Figure 9 shows the streamlines passing the central vertical plane of the model at two wind angles: $\theta = 0^\circ$ and $\theta = 120^\circ$. Different pattern of the wake behind the model can be seen. The difference may be due to two factors: the light well and the chamfered roof.

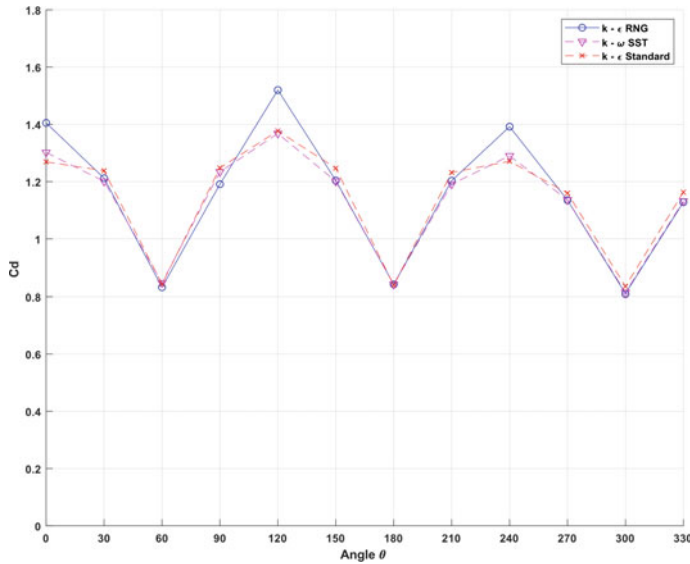


Fig. 7 Drag coefficients C_d with the different wind angles

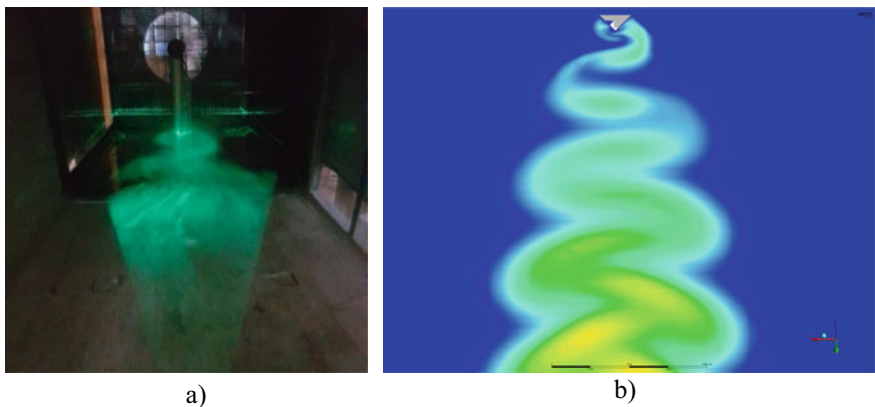


Fig. 8 a) Smoke visualization, b) computed flowfield around the building for the case of $\theta = 0^\circ$

3 Conclusions

By experiments in wind tunnel and by CFD, the flowfield around a triangular cross-sectional building was studied. The results show that the presence of the light well and the chamfered roof reduces the pressure coefficient on the surface of the building and changes the structure of the wake behind the building. The wind angle at which the pressure distribution for the best natural ventilation design of the building with

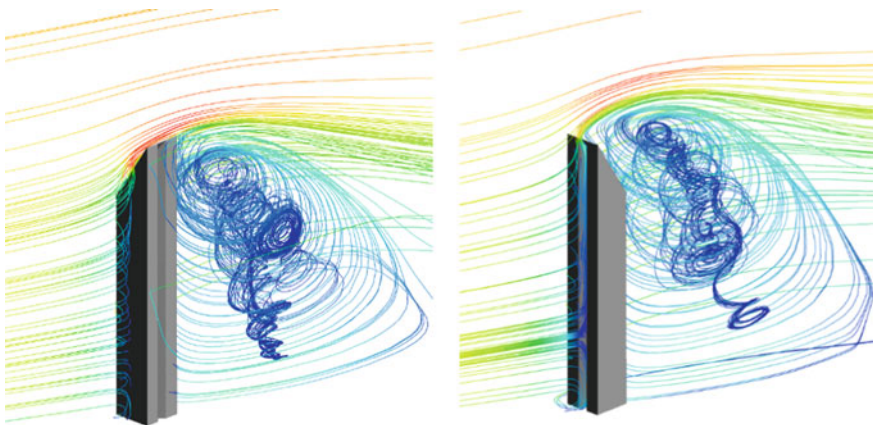


Fig. 9 Computed streamlines in the central vertical plane in the cases of $\theta = 0^\circ$ (left) and $\theta = 120^\circ$ (right)

the light well was found to be $\theta = 150^\circ$. The numerical results show that the $k-\omega$ SST model in three studied RANS models exhibits the best at the prediction of mean pressure coefficients. The drag coefficient of the studied building is maximum with wind angle $\theta = 120^\circ$ and minimum with wind angles: $\theta = 60^\circ$, $\theta = 180^\circ$ and $\theta = 300^\circ$.

Acknowledgements The experiments in this research are supported by the Laboratory of Building Physics and Fluid Mechanics of the Ho Chi Minh City University of Technology, VNU-HCM. P. K. Oanh and N. H. T. Loc (PFIEV 2014) are greatly appreciated for their helping the experiments.

References

1. American Society of Civil Engineers (2012). ASCE/SEI 49-12: wind tunnel testing for buildings and other structures
2. Awbi (2003) Ventilation of buildings. Spon Press
3. Baghaei Daemei A, Khotbehara EM, Nobarani EM, Bahrami P (2019) Study on wind aerodynamic and flow characteristics of triangular-shaped tall buildings and CFD simulation in order to assess drag coefficient. *Ain Shams Eng J*
4. Elshaer A, Aboshosha H, Bitsuamlak G, El Damatty A, Dagnaw A (2016) LES evaluation of wind-induced responses for an isolated and a surrounded tall building. *Eng Struct* 115:179–195
5. Ferziger JH, Peric M (2002) Computational methods for fluid dynamics. Springer
6. Franke J (2007) Introduction to the prediction of wind loads on buildings by computational wind engineering (CWE). In: Stathopoulos T, Baniotopoulos CC (eds) Wind effects on buildings and design of wind-sensitive structures, vol 493. CISM International Centre for Mechanical Sciences, Springer, pp 67–103
7. Hubova O, Macak M, Konecna L, Ciglan G (2017) External pressure coefficients on the atypical high-rise building—computing simulation and measurements in wind tunnel. *Procedia Eng* 190:488–495

8. Kim B, Tse KT, Yoshida A, Tamura Y, Chen Z, Van Phuc P, Park HS (2019) Statistical analysis of wind-induced pressure fields and PIV measurements on two buildings. *J Wind Eng Ind Aerodyn* 188(November 2018):161–174
9. Li Y, Li QS, Chen F (2017) Wind tunnel study of wind-induced torques on L-shaped tall buildings. *J Wind Eng Ind Aerodyn* 167(September 2016):41–50
10. Tamura T, Nozawa K, Kondo K (2008) AJJ guide for numerical prediction of wind loads on buildings. *J Wind Eng Ind Aerodyn* 96(10–11):1974–1984
11. Thordal MS, Bennetzen JC, Koss HHH (2019) Review for practical application of CFD for the determination of wind load on high-rise buildings. *J Wind Eng Ind Aerodyn* 186(October 2018):155–168
12. Tominaga Y, Mochida A, Yoshie R, Kataoka H, Nozu T, Yoshikawa M, Shirasawa T (2008) AJJ guidelines for practical applications of CFD to pedestrian wind environment around buildings. *J Wind Eng Ind Aerodyn* 96(10–11):1749–1761
13. van Hooff T, Blocken B, Tominaga Y (2017) On the accuracy of CFD simulations of cross-ventilation flows for a generic isolated building: comparison of RANS, LES and experiments. *Build Environ* 114:148–165

Variation Order Management in Vietnam Construction Projects



Nam N. N. Tran, Sy T. Do, Thu A. Nguyen, and Long H. Le

1 Introduction

Variations and conflicts in construction projects, at work, and even in our daily lives are very common [1]. Any additions, deletions, or other revisions to project goals and scopes are considered variations, whether they increase or decrease the project cost or schedule [7]. Sun and Meng [10] indicated in construction projects, a change refers to an alteration to design, building work, project program or other project aspects caused by modifications to preexisting conditions, assumptions or requirements.

2 Literature Review

Several papers have been published in all the recognized journals on the subject of variations order and their effects have been described from 1990 to date. Research works on VOs, particularly on high rise building, official buildings and infrastructure projects, have been conducted in many countries such as the UK, the US, South Africa, Iran, Oman, Jordan, Nigeria, Malaysia and Taiwan.

2.1 Category

Marzouk and El-Rasas [8] revealed that “emergent variation” and “anticipated variations” are the most popular categories. Emergent variation arises unexpectedly while anticipated variations are preplanned and occur as predetermined. Based on

N. N. N. Tran (✉) · S. T. Do · T. A. Nguyen · L. H. Le

Department of Construction Engineering and Management, Faculty of Civil Engineering, Ho Chi Minh City University of Technology, VNU-HCM, Ho Chi Minh City, Vietnam
e-mail: tnhatnam@gmail.com

the necessity they can be classified into two types: “required variations” and “elective variations”. Beneficial and detrimental variation orders are clarified based on subsequent effects.

2.2 *Nature of Variation Order*

Various stakeholders involve in a construction project, which result in complex actions, processes and unanticipated results. According to Han et al. [5] variations are unavoidable in projects related to construction. Indeed, variation in orders will undoubtedly occur in projects sometimes even before the contract is signed. Moreover, variations are an unavoidable fact [2], the construction project may have negligible deviations that will lead to significant variations in spite of planning efforts.

2.3 *Model of Change Management*

A number of change management models, processes and outlines have been created to help organizations to minimize changes and improve project performance.

Ibbs et al. [7] introduced some systematic approaches, which have five ideologies: “a balanced change culture, recognition, evaluation, implementation, and continual improvement from experiences”. Love et al. [5] analyzed the impact of change on management system.

According to literature review, no research work has been carried out in Vietnam to identify the causes of variations and to propose a strategic management procedure.

3 Research Methodology

A survey based on wide-ranging literature review was used to collect data for this research. Several different techniques such as the pilot study, interviews and questionnaire (by email and hard copies) were used to collect data for the research. The respondents used a five-point Likert scale to measure the severity of the factors affecting VOs. Employers, consultants, and main/sub-contractors from different construction projects in Vietnam then ranked the VOs concerning severity. The scale and the weights specified to each response are shown in Table 1.

The questionnaire includes 20 factors affecting variation orders. A pilot study of was prepared to verify the completeness of the questionnaire. Six experts in Vietnam’s construction industry with strong practical experience were invited to an empirical interview. The participants include a planning and design director, a project director of

Table 1 Severity weighting scale in the research survey

Severity scale				
No affect	Minor affect	Neutral	Moderate affect	Major affect
1	2	3	4	5

a well-known developer, an international consultant, an engineer of main contractor and a university lecturer.

Respondents are selected from a wide range of professionals engaged in the Vietnam construction sector. The response rate from the owners, project management units, main/sub-contractors and consultants is 25.5%, 6.4%, 42.0%, and 26.1% respectively. The questionnaire were distributed both as hard copy and via email to the construction professionals involved in large projects, including 157 valid responses (42% response rate). The chosen projects are located in Ho Chi Minh, which is undergoing a construction boom. Regarding the number of experience years, 48% of respondents have lesser or equal to five years, 25% of them have between five and 10 years and 27% of them have 10 years or more. These rates reflect the current situation of construction industry in Vietnam: over the recent years, a large number of young engineers who have graduated from their universities are able to meet the requirements of companies. Amongst the respondents, 18% of them participated in the project with scale of less than 100 billion VND; twenty percent in the project with scale of 100–500 billion VND; 15% in the project with scale from 500 to 1000 billion VND; and 17% respondents in the project with scale of over 1000 billion VND.

The SPSS software have been used in analyses, using Cronbach Alpha test (used to verify the result), Kaiser–Meyer–Olkin (KMO) test and Bartlett's test of Sphericity (in order to evaluate the adequacy of the survey data for factor analysis) used in conjunction with EFA to class the roots of variation based on likeness.

4 Result

For this survey, 157 valid responses were obtained. Raw data was coded, entered and analyzed by SPSS v20.0 (Statistical Package for Social Sciences) software for ranking results of 20 factors, top 5 as shown in Table 2. The survey method is done by humans so it is highly subjective. Therefore, an internal consistency of the questionnaire was adopted to test the reliability of the questionnaire. AF15 was rejected due to dissatisfaction (Corrected Item-Total Correlation <0.3, Cristobal et al. [3]). The Cronbach's Alpha coefficient is calculated to be $0.842 > 0.8$ so the measurement scale is appropriate [9].

Checking the appropriateness of collected-data is the first step to run EFA analysis. Quantity of sample competence can be checked by Bartlett test of Sphericity and Kaiser-Meyer-Olkin (KMO). With $KMO = 0.783$ and associated significance =

Table 2 Top critical factors affecting variation order

	N	Mean	Std. Dev	Rank
[AF1. Change of plan]	157	4.51	0.821	1
[AF9. Design change]	157	4.29	0.961	2
[AF12. Design errors]	157	4.10	0.999	3
[AF5. Ambiguous scope of work]	157	4.09	1.021	4
[AF2. Errors in contract documents]	157	3.98	0.990	5

0.0000, the data is adequate. The criteria of selecting factors as individual Eigenvalue greater than 1. Five components are extracted, explained 62.25% of total variance as shown in Table 3.

Group 1: Management-related causes (AF-MNM). The most serious and significant stakeholder of the project is the owner as the originator of the project from the inception to the handover stage. Due to the volatile and complex nature of the construction industry, the likelihoods and risk of a variation, happening in a construction project is extremely influenced by the owner's decisions. The lack of preparation in project planning, the ability to coordinate will all parties in the design phase as well as the ability to monitor and manage the works... greatly affects the variation orders; thereby affecting the schedule, quality and cost of the project. Because of different objects and benefits among the parties involved, variations and conflicts often occur during the course of a construction project. Therefore, the ability to manage the interests, benefits of stakeholders to avoid conflict is even more important.

Group 2: Design related causes (AF-DES). These are changes in design, errors or omissions, owner changing plan or scope, errors in contract documents and so on. Depending on the timing and the extent of the changes, these changes can affect the achievement of the project objectives such as the delivery time frame, budget and quality of product/specific requirements. Han et al [5] revealed "understanding of the overall goals and scope of the project, offering specific suggestions when it makes sense and understanding the deliverables is an important job for the consultant". To mitigate this risk factor, it is necessary to improve the competence and requirement of designers and project management teams [4].

Group 3: Unexpected factors (AF-UNE). The force majeure and government stalking also negatively affected VO. However, these factors can be avoided if in the bidding stage, contract documents are clearly defined, complying with international standards such as FIDIC (International Federation of Consulting Engineers) contracts.

Group 4: Execution related factors (AF-EXE). The contractor changes method statement, replacement of materials and processes that cause VO. The implementation of Fast track construction with poor management ability is a factor that causes variation order.

Group 5: Awareness related factors (AF-AWA). Including AF3—Impedimental decision-making process (loading factor of 0.837) and AF4—Owner's obstinate

Table 3 Exploratory factor analysis result

Group	Code	Factor	Loading factor	Eigen value	% of variance
Management related (AF-MNM)	AF8	Inadequate strategic plan	0.779	4.999	26.310
	AF6	Poor communication	0.735		
	AF17	Poor supervision and site management	0.695		
	AF5	Ambiguous scope of work	0.617		
Design related (AF-DES)	AF9	Design change	0.617	2.782	14.640
	AF12	Design errors	0.695		
	AF1	Change of plan	0.675		
	AF19	Change of standards, regulation	0.603		
	AF2	Errors in contract documents	0.596		
	AF10	Limited knowledge about available materials	0.579		
Unexpected factors (AF-UNE)	AF20	Government stalking	0.809	1.606	8.452
	AF18	Force majeure	0.701		
	AF14	Nonparticipation of contractor in the design phase	0.469		
	AF16	Inefficient RFI process	0.417		
Execution related (AF-EXE)	AF11	Change of method statement	0.731	1.226	6.455
	AF7	Replacement of materials and processes	0.717		
	AF13	Fast track construction	0.708		
Awareness related (AF-AWA)	AF3	Impedimental decision making process	0.837	1.215	6.393
	AF4	Owner's obstinate nature	0.639		
				S %	62.250

nature (0.639). Inefficient decision-making process may result in the delay, triggering the requirement for the change order due to cost additions. These issues greatly affect the work of the construction site, causing obstruction to the work. In this case, the owner must be aware of the importance of making timely decisions, approving timely problems and a way to prevent future complaints and disputes.

5 Variation Order Management

An important aspect of project management is the management of change in construction, as changes create a major cause of variation order, delay and disruption; and both construction constructors usually accept it and owners that change effects are hard to quantify and often lead to disputes.

Analysis of the data also revealed a significant lack of knowledge and experience with the management of change in Vietnam construction projects, which led to several problems that could easily be associated with variation orders. This section outlines the procedures necessary for management of changes. Depending on the timing and extent of the changes, these changes can affect the achievement of the project objectives such as the delivery period, budget and quality of product/specific requirements.

It may be common that some contractors may reserve their claims for variations due to poor contract administration. It is also of the perception traditionally that a few VOs together and negotiating for a lower bulk payment at a later stage may accrue significant savings. It may also be perceived that VO payments can be used as bargaining chips for contractors' efficiency and cooperation, thus explaining deliberate delays in the payout for VOs. Nevertheless, for effective cost control and tracking, prompt payment shall (where possible) be made for the value of work done on site validated by the consultants.

Figure 1 shows the structure of change management starting principles: (1) identify, (2) evaluate and propose, (3) approve, (4) implement and (5) review. Implementation of project change model before project commences is a good practice, active step toward productively managing change.

6 Conclusion

The results indicate that five principle groups that have the most significant impact on change: management-related, design-related, execution-related, awareness and other factors. Among the initial 20 factors, change of plans or scope by owner; factors related to design consultant: changes in design, technical specification; errors and omissions in design by consultant are the three most influential factors. During the literature review, the author found that these three causes are quite similar among developing countries like Vietnam. If operative schemes are used to counter the effect

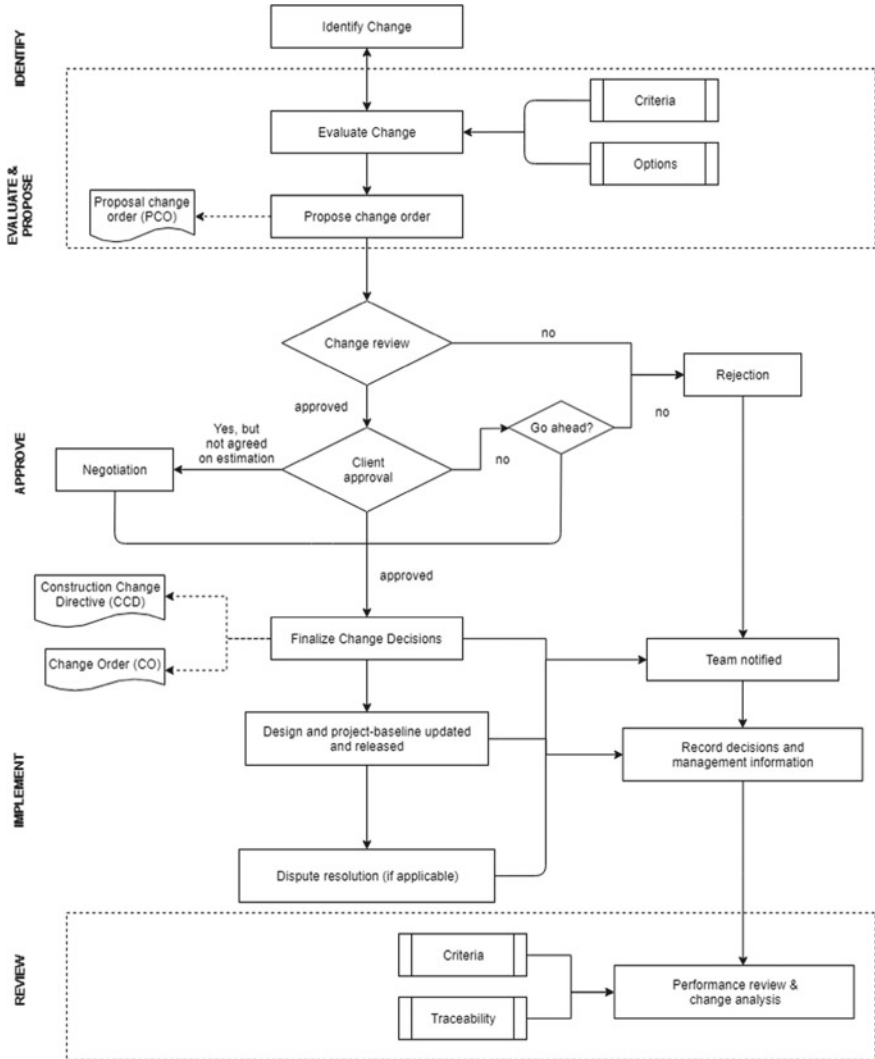


Fig. 1 General change process model. Adapted from Hao et al. [6]

of variation orders, the adverse impacts of this issue can be effectively decreased. The following recommendations from this study are proposed to minimize variation order in construction projects:

- Carrying out a proper tender preparation and pre-qualification exercise prior to the calling of tender
- Allocating adequate time to develop pre-tender planning phase to minimized change probability

- All parties involved in the project before work is started on site require the detailed project plan and scope. Proactivity can help to enhance change management
- All drawings, specification should be completed; tender clarifications can be used for more requirements (if needed) at the tender stage of the project
- Unforeseen and uncommon condition should also be studied, prepared for by all parties
- To ensure the variations are kept within the total construction cost, tracking of VOs is critical. This includes tracking both the committed VOs as well as anticipated VOs
- If the variation is required, it's important to Prioritize the variations to be implemented within the constraints of the budgeted contract sum against the anticipated VO. After that, Value Engineering (VE) should be introduced to reduce cost.

References

1. Arain FM, Low SP (2006) Developers' views of potential causes of variation orders for institutional buildings in Singapore. *Arch Sci Rev* 49(1):59–74
2. Almahmoud ES, Doloi HK, Panuwatwanich K (2012) Linking project health to project performance indicators: Multiple case studies of construction projects in Saudi Arabia. *Int J Proj Manag* 30(3):296–307
3. Cristobal E, Flavian C, Guinaliu M (2007) Perceived e-service quality (PeSQ) Measurement validation and effects on consumer satisfaction and web site loyalty. *Manag serv qual: An Int J* 17(3):317–340
4. Do ST, Veerasak L (2011) Ranking critical risk factors of international construction joint ventures in Vietnam. In: International conference on multi-national joint venture for construction works, 28–29 Sept 2011, Bandung, Indonesia
5. Han S, Love P, Peña-Mora F (2013) A system dynamics model for assessing the impacts of design errors in construction projects. *Math Comput Model* 57(9):2044–2053
6. Hao Q, Shen W, Neelamkavil J, Thomas J (2008) Change management in construction projects
7. Ibbs W, Wong C, Kwak H (2001) Project change management system. *J Manag Eng* 17(3):159–165
8. Marzouk MM, El-Rasas TI (2014) Analyzing delay causes in Egyptian construction projects. *J Adv Res* 5(1):49–55
9. Nunnally JC (1978) Psychometric theory, 2nd edn. McGraw-Hill, New York
10. Sun M, Meng X (2008) Taxonomy for change causes and effects in construction projects. *Int J Proj Manag* 27(6):560–572

Structure Session

Dynamic Analysis of Multi-layer Connected Plate Resting on a Pasternak Foundation Subjected to Moving Load



Tan Ngoc Than Cao, Van Hai Luong, Xuan Vu Nguyen, and Minh Thi Tran

1 Introduction

Static and dynamic analyses of complex continuous structures are of great theoretical and practical necessity for many fields of aeronautics, cosmonautics, civil and mechanical engineering. The complex continuous structures are composed of multi-layer beams or multi-layer plates which are joined by a connected layer. The connected layer can be an elastic, a viscoelastic or a complex layer. With the increasing use of abovementioned structures, many research works have been extensively performed to have a profound understanding of static and dynamic behavior of them. The free vibrations and dynamic responses of a system of connected parallel bar were been studied by Seelig and Hoppmann [9], Saito and Chonan [8], Hamada et al. [4]. The transverse vibrations of rectangular double-plate joined by an elastic layer were examined in the studies of Omiszczuk [7], De Rosa and Lippiello [3]. Nonetheless, to the authors's best knowledge, almost no research work on the dynamic analyses of multi-layer connected rectangular plate resting on a Pasternak foundation subjected to a moving load has been published until now.

Relating to the moving load problems, Koh et al. [5] proposed a Moving Element Method (MEM) for solving one-dimensional train-track problems. The rail beam was discretized into conceptual elements that move together with the moving train/load. That study indicated that the MEM can remedy several drawbacks of the traditional Finite Element Method (FEM) in analysing dynamic responses of infinite structures subjected to moving loads. Indeed, firstly, the moving load position is always kept

T. N. T. Cao

College of Technology, Can Tho University (CTU), Can Tho City, Vietnam

V. H. Luong (✉) · X. V. Nguyen · M. T. Tran

Faculty of Civil Engineering, Ho Chi Minh City University of Technology (HCMUT), Ho Chi Minh City, Vietnam

e-mail: lvhai@hcmut.edu.vn

Vietnam National University Ho Chi Minh City (VNU-HCM), Ho Chi Minh City, Vietnam

unchanged at a particular node in the moving element mesh. As a result, the tracking of moving load position can avoid absolutely. Secondly, the MEM can tackle well the difficulty of the FEM when the moving load approaches the boundary of the finite domain. Thirdly, the number of elements used in the MEM model is completely independent of the distance traversed by the load in the considered time duration. Therefore, the MEM needs lesser elements than the FEM. Subsequently, Cao et al. [1] developed the three dimensional high-speed train-track model using the MEM to analyze dynamic responses of the train-track system. In which, the MEM was extended to establish the coupling moving elements of two rails with 16 degrees of freedom involving all motion components of the train. Most recently, Luong et al. [6] and Cao et al. [2] extended the MEM for static and dynamic analyses of Mindlin plate and composite plate subjected to moving loads, respectively.

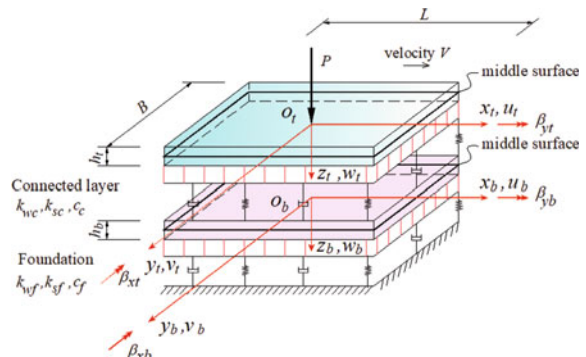
In this paper, the Multi-layer Moving Plate Method (MMPM) is developed to investigate the dynamic responses of multi-layer connected plate resting on a Pasternak foundation subjected to a moving load. The formulations of multi-layer moving plate element mass, damping and stiffness matrices are derived. A parametric study is performed to examine the effects of various parameters on the dynamic responses of multi-layer connected plate structure.

2 Formulation and Methodology

2.1 Weak Form for the Multi-layer Connected Plate Resting on a Pasternak Foundation

Let us consider a model which consists of two plates connected by a Pasternak foundation with the vertical spring stiffness k_{wc} , the shear stiffness k_{sc} and the foundation damping c_c . The upper plate is subjected to a moving load P and the lower plate rests on a Pasternak foundation with the vertical spring stiffness k_{wf} , the shear stiffness k_{sf} and the foundation damping c_f as shown in Fig. 1. It is assumed that both plates

Fig. 1 The model of multi-layer connected plate resting on a Pasternak foundation subjected to a moving load



have the same length L , width B . The upper plate has the thickness h_t and the lower plate has the thickness h_b . The middle (neutral) surfaces of two plates are chosen as the reference planes that occupy the domains $\Omega_t, \Omega_b \subset R^2$.

Based on the first-order shear deformation theory, the displacement field at any point within the upper plate and lower plate are written as

$$\begin{aligned} u_j(x_j, y_j, z_j) &= u_{0j}(x_j, y_j) + z_j \beta_{xj}(x_j, y_j); \quad v_j(x_j, y_j, z_j) \\ &= v_{0j}(x_j, y_j) + z_j \beta_{yj}(x_j, y_j) \quad w_j(x_j, y_j, z_j) = w_{0j}(x_j, y_j) \end{aligned} \quad (1)$$

where the index j is attached to the variables associated with the upper plate ($j = t$) and the lower plate ($j = b$); u_{0j}, v_{0j}, w_{0j} ($j = t, b$) are the displacements in x, y, z direction of the points in middle surfaces of the plates, respectively; β_{xj}, β_{yj} ($j = t, b$) are the vectors of rotations of the plates.

The weak form for the governing equations of the upper plate and the lower plate are written as

$$\begin{aligned} &\int_{\Omega_t} \left\{ (\delta \boldsymbol{\varepsilon}_{mt})^T (\delta \boldsymbol{\kappa}_t)^T (\delta \boldsymbol{\gamma}_t)^T \right\} \begin{bmatrix} \mathbf{D}_{mt} & \mathbf{D}_{mbt} \\ \mathbf{D}_{mbt} & \mathbf{D}_{bt} \\ & \mathbf{D}_{st} \end{bmatrix} \begin{Bmatrix} \boldsymbol{\varepsilon}_{mt} \\ \boldsymbol{\kappa}_t \\ \boldsymbol{\gamma}_t \end{Bmatrix} d\Omega_t \\ &+ \int_{\Omega_t} \delta \mathbf{u}_t^T \mathbf{m}_t \ddot{\mathbf{u}}_t d\Omega_t + \int_{\Omega_t} \delta w_t^T k_{wc} (w_t - w_b) d\Omega_t - \int_{\Omega_t} \delta w_t^T k_{sc} (\nabla^2 w_t - \nabla^2 w_b) d\Omega_t \\ &+ \int_{\Omega_t} \delta w_t^T c_c (\dot{w}_t - \dot{w}_b) d\Omega_t = \int_{\Omega_t} \delta \mathbf{u}_t^T \mathbf{b}_t d\Omega_t \end{aligned} \quad (2)$$

$$\begin{aligned} &\int_{\Omega_b} \left\{ (\delta \boldsymbol{\varepsilon}_{mb})^T (\delta \boldsymbol{\kappa}_b)^T (\delta \boldsymbol{\gamma}_b)^T \right\} \begin{bmatrix} \mathbf{D}_{mb} & \mathbf{D}_{mbb} \\ \mathbf{D}_{mbb} & \mathbf{D}_{bb} \\ & \mathbf{D}_{sb} \end{bmatrix} \begin{Bmatrix} \boldsymbol{\varepsilon}_{mb} \\ \boldsymbol{\kappa}_b \\ \boldsymbol{\gamma}_b \end{Bmatrix} d\Omega_b \\ &+ \int_{\Omega_b} \delta \mathbf{u}_b^T \mathbf{m}_b \ddot{\mathbf{u}}_b d\Omega_b - \int_{\Omega_b} \delta w_b^T k_{wc} (w_t - w_b) d\Omega_b \\ &+ \int_{\Omega_b} \delta w_b^T k_{sc} (\nabla^2 w_t - \nabla^2 w_b) d\Omega_b - \int_{\Omega_b} \delta w_b^T c_c (\dot{w}_t - \dot{w}_b) d\Omega_b \\ &+ \int_{\Omega_b} \delta w_b^T k_{wf} w_b d\Omega_b - \int_{\Omega_b} \delta w_b^T k_{sf} \nabla^2 w_b d\Omega_b + \int_{\Omega_b} \delta w_b^T c_f \dot{w}_b d\Omega_b = 0 \end{aligned} \quad (3)$$

where $\boldsymbol{\varepsilon}_{mj}$, $\boldsymbol{\kappa}_j$ and $\boldsymbol{\gamma}_j$ ($j = t, b$) are the membrane, bending and shear strains of the plates; \mathbf{m}_j ($j = t, b$) are the mass matrices containing the material mass density ρ_j ($j = t, b$) and the plate thickness h_j ($j = t, b$) of the plates; \mathbf{D}_{mj} , \mathbf{D}_{mbj} , \mathbf{D}_{bj} and \mathbf{D}_{sj} ($j = t, b$) are the material constant matrices of the plates. In case of moving load problem, $\mathbf{b}_t = [0 \ 0 \ P\delta(x_t - S)\delta(y_t - 0) \ 0 \ 0]^T$ is the load vector of the upper plate.

2.2 Multi-layer Moving Plate Method (MMPM)

In this section, a new approach, namely Multi-layer Moving Plate Method (MMPM), is developed to study the dynamic response of multi-layer connected plate resting on a Pasternak foundation subjected to a moving load. In this method, the multi-layer moving plate elements consists of two layers of quadrilateral nine-node (Q9) element of the serendipity family as shown in Fig. 2. The node displacement vector of the element is defined as

$$\mathbf{d}^{(e)} = [u_{01} \ v_{01} \ w_{01} \ \beta_{x1} \ \beta_{y1} \ \dots \ u_{018} \ v_{018} \ w_{018} \ \beta_{x18} \ \beta_{y18}]^T_{90 \times 1} \quad (4)$$

Using the shape functions, the displacement, the membrane, bending and shear strain vectors of the upper plate ($j = t$) and lower plate ($j = b$) can be expressed as

$$\mathbf{u}_j = \mathbf{N}_j \mathbf{d}^{(e)}; \quad w_j = \mathbf{N}_{wj} \mathbf{d}^{(e)}; \quad \boldsymbol{\varepsilon}_{mj} = \mathbf{B}_{mj} \mathbf{d}^{(e)}; \quad \boldsymbol{\kappa}_j = \mathbf{B}_{bj} \mathbf{d}^{(e)}; \quad \boldsymbol{\gamma}_j = \mathbf{B}_{sj} \mathbf{d}^{(e)} \quad (j = t, b) \quad (5)$$

where

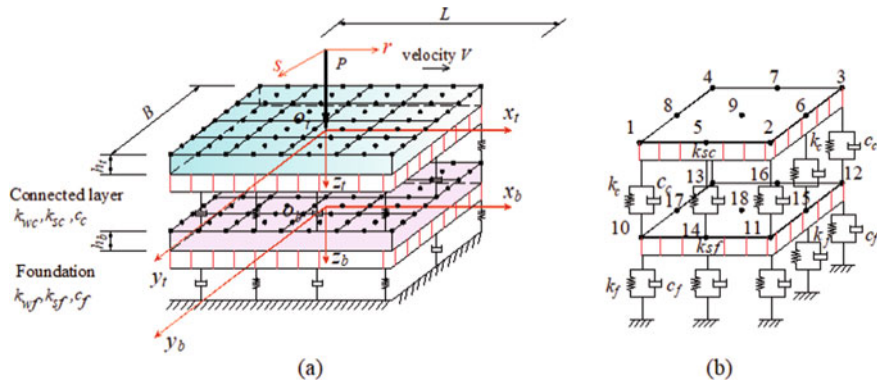


Fig. 2 **a** Discretization of plates into multi-layer moving plate elements; **b** A typical multi-layer moving plate element with 90 DOFs

$$\mathbf{N}_t = \begin{bmatrix} N_i & 0 & 0 & 0 & 0 & 0 & 0 & 0 & 0 \\ 0 & N_i & 0 & 0 & 0 & 0 & 0 & 0 & 0 \\ 0 & 0 & N_i & 0 & 0 & 0 & 0 & 0 & 0 \\ 0 & 0 & 0 & N_i & 0 & 0 & 0 & 0 & 0 \\ 0 & 0 & 0 & 0 & N_i & 0 & 0 & 0 & 0 \end{bmatrix}_{5 \times 90}; \quad ; \quad \mathbf{N}_b = \begin{bmatrix} 0 & 0 & 0 & 0 & 0 & N_i & 0 & 0 & 0 & 0 \\ 0 & 0 & 0 & 0 & 0 & 0 & N_i & 0 & 0 & 0 \\ 0 & 0 & 0 & 0 & 0 & 0 & 0 & N_i & 0 & 0 \\ 0 & 0 & 0 & 0 & 0 & 0 & 0 & 0 & N_i & 0 \\ 0 & 0 & 0 & 0 & 0 & 0 & 0 & 0 & 0 & N_i \end{bmatrix}_{5 \times 90} \quad (6)$$

$$\mathbf{N}_{wt} = [\underbrace{0 & 0 & N_i & 0 & 0}_{5 \times 9(i=1 \div 9)} \quad \underbrace{0 & 0 & 0 & 0 & 0}_{5 \times 9}]_{1 \times 90}; \quad \mathbf{N}_{wb} = [\underbrace{0 & 0 & 0 & 0}_{5 \times 9} \quad \underbrace{0 & 0 & N_i & 0 & 0}_{5 \times 9(i=1 \div 9)}]_{1 \times 90} \quad (7)$$

$$\mathbf{B}_{mt} = \begin{bmatrix} N_{i,x} & 0 & 0 & 0 & 0 & 0 & 0 & 0 & 0 & 0 \\ 0 & N_{i,y} & 0 & 0 & 0 & 0 & 0 & 0 & 0 & 0 \\ N_{i,y} & N_{i,y} & 0 & 0 & 0 & 0 & 0 & 0 & 0 & 0 \end{bmatrix}_{3 \times 90}; \quad ; \quad \mathbf{B}_{mb} = \begin{bmatrix} 0 & 0 & 0 & 0 & 0 & N_{i,x} & 0 & 0 & 0 & 0 \\ 0 & 0 & 0 & 0 & 0 & 0 & N_{i,y} & 0 & 0 & 0 \\ 0 & 0 & 0 & 0 & 0 & 0 & 0 & N_{i,x} & 0 & 0 \end{bmatrix}_{3 \times 90}$$

$$\mathbf{B}_{bt} = \begin{bmatrix} 0 & 0 & 0 & N_{i,x} & 0 & 0 & 0 & 0 & 0 & 0 \\ 0 & 0 & 0 & 0 & N_{i,y} & 0 & 0 & 0 & 0 & 0 \\ 0 & 0 & 0 & N_{i,y} & N_{i,x} & 0 & 0 & 0 & 0 & 0 \end{bmatrix}_{3 \times 90}; \quad ; \quad \mathbf{B}_{bb} = \begin{bmatrix} 0 & 0 & 0 & 0 & 0 & 0 & 0 & N_{i,x} & 0 & 0 \\ 0 & 0 & 0 & 0 & 0 & 0 & 0 & 0 & N_{i,y} & 0 \\ 0 & 0 & 0 & 0 & 0 & 0 & 0 & 0 & 0 & N_{i,y} N_{i,x} \end{bmatrix}_{3 \times 90}$$

$$\mathbf{B}_{st} = \begin{bmatrix} 0 & 0 & N_{i,x} & N_i & 0 & 0 & 0 & 0 & 0 & 0 \\ 0 & 0 & N_{i,y} & 0 & N_i & 0 & 0 & 0 & 0 & 0 \end{bmatrix}_{2 \times 90}; \quad ; \quad \mathbf{B}_{sb} = \begin{bmatrix} 0 & 0 & 0 & 0 & 0 & 0 & N_{i,x} & N_i & 0 & 0 \\ 0 & 0 & 0 & 0 & 0 & 0 & 0 & N_{i,y} & 0 & N_i \end{bmatrix}_{2 \times 90} \quad (8)$$

The MEM was proposed with the idea of attaching the origin of the spatial coordinates system to the moving load. Figure 2 shows a travelling coordinates system (r, s) moving at the same speed as the moving load. The relationship between the moving coordinates (r, s) and the fixed coordinates (x, y) is given by

$$r = x - S; \quad s = y \quad (9)$$

where S is the distance traveled by the moving load at any instant time t .

By using the coordinates transformation, the governing equations in Eqs. (2) and (3) are rewritten in the moving coordinates system (r, s) . Using the shape functions and procedure of writing the weak form in term of the displacement field, the governing equations of the upper and lower plate elements in the moving coordinates system (r, s) are written in short and familiar forms as

$$\mathbf{M}_t^{(e)} \ddot{\mathbf{d}}^{(e)} + \mathbf{C}_t^{(e)} \dot{\mathbf{d}}^{(e)} + \mathbf{K}_t^{(e)} \mathbf{d}^{(e)} = \mathbf{P}_t^{(e)}; \quad \mathbf{M}_b^{(e)} \ddot{\mathbf{d}}^{(e)} + \mathbf{C}_b^{(e)} \dot{\mathbf{d}}^{(e)} + \mathbf{K}_b^{(e)} \mathbf{d}^{(e)} = \mathbf{P}_b^{(e)} \quad (10)$$

where the formulations for the mass $\mathbf{M}_t^{(e)}$, $\mathbf{M}_b^{(e)}$, damping $\mathbf{C}_t^{(e)}$, $\mathbf{C}_b^{(e)}$, stiffness $\mathbf{K}_t^{(e)}$, $\mathbf{K}_b^{(e)}$ matrices of the moving element are given as

$$\begin{aligned} \mathbf{M}_t^{(e)} &= \mathbf{m}_t \int_{\Omega_t^{(e)}} \mathbf{N}_t^T \mathbf{N}_t \det \mathbf{J} d\xi d\eta \\ \mathbf{C}_t^{(e)} &= -2\mathbf{m}_t \dot{S} \int_{\Omega_t^{(e)}} \mathbf{N}_t^T \mathbf{N}_{t,r} \det \mathbf{J} d\xi d\eta + c_c \int_{\Omega_t^{(e)}} \mathbf{N}_{wt}^T \mathbf{N}_{wt} \det \mathbf{J} d\xi d\eta \\ &\quad - c_c \int_{\Omega_t^{(e)}} \mathbf{N}_{wt}^T \mathbf{N}_{wb} \det \mathbf{J} d\xi d\eta \quad \mathbf{K}_t^{(e)} = \int_{\Omega_t^{(e)}} \{ (\mathbf{B}_{mt})^T (\mathbf{B}_{bt})^T (\mathbf{B}_{st})^T \} \\ &\quad \left[\begin{array}{cc} \mathbf{D}_{mt} & \mathbf{D}_{mbt} \\ \mathbf{D}_{mbt} & \mathbf{D}_{bt} \\ \mathbf{D}_{bt} & \mathbf{D}_{st} \end{array} \right] \left\{ \begin{array}{c} \mathbf{B}_{mt} \\ \mathbf{B}_{bt} \\ \mathbf{B}_{st} \end{array} \right\} \det \mathbf{J} d\xi d\eta - \mathbf{m}_t \ddot{S} \int_{\Omega_t^{(e)}} \mathbf{N}_t^T \mathbf{N}_{t,r} \det \mathbf{J} d\xi d\eta \\ &\quad + \mathbf{m}_t \dot{S}^2 \int_{\Omega_t^{(e)}} \mathbf{N}_t^T \mathbf{N}_{t,rr} \det \mathbf{J} d\xi d\eta + k_{wc} \int_{\Omega_t^{(e)}} \mathbf{N}_{wt}^T \mathbf{N}_{wt} \det \mathbf{J} d\xi d\eta \\ &\quad - k_{wc} \int_{\Omega_t^{(e)}} \mathbf{N}_{wt}^T \mathbf{N}_{wb} \det \mathbf{J} d\xi d\eta - k_{sc} \int_{\Omega_t^{(e)}} (\mathbf{N}_{wt}^T \mathbf{N}_{wt,rr} + \mathbf{N}_{wt}^T \mathbf{N}_{wt,ss}) \det \mathbf{J} d\xi d\eta \\ &\quad + k_{sc} \int_{\Omega_t^{(e)}} (\mathbf{N}_{wt}^T \mathbf{N}_{wb,rr} + \mathbf{N}_{wt}^T \mathbf{N}_{wb,ss}) \det \mathbf{J} d\xi d\eta - c_c \dot{S} \int_{\Omega_t^{(e)}} \mathbf{N}_{wt}^T \mathbf{N}_{wt,r} \det \mathbf{J} d\xi d\eta \\ &\quad + c_c \dot{S} \int_{\Omega_t^{(e)}} \mathbf{N}_{wt}^T \mathbf{N}_{wb,r} \det \mathbf{J} d\xi d\eta \quad (11) \\ \mathbf{M}_b^{(e)} &= \mathbf{m}_b \int_{\Omega_b^{(e)}} \mathbf{N}_b^T \mathbf{N}_b \det \mathbf{J} d\xi d\eta \\ \mathbf{C}_b^{(e)} &= -2\mathbf{m}_b \dot{S} \int_{\Omega_b^{(e)}} \mathbf{N}_b^T \mathbf{N}_{b,r} \det \mathbf{J} d\xi d\eta + c_f \int_{\Omega_b^{(e)}} \mathbf{N}_{wb}^T \mathbf{N}_{wb} \det \mathbf{J} d\xi d\eta \\ &\quad + c_c \int_{\Omega_b^{(e)}} \mathbf{N}_{wb}^T \mathbf{N}_{wb} \det \mathbf{J} d\xi d\eta - c_c \int_{\Omega_b^{(e)}} \mathbf{N}_{wb}^T \mathbf{N}_{wt} \det \mathbf{J} d\xi d\eta \end{aligned}$$

$$\begin{aligned}
\mathbf{K}_b^{(e)} = & \int_{\Omega_b^{(e)}} \left\{ (\mathbf{B}_{mb})^T (\mathbf{B}_{bb})^T (\mathbf{B}_{sb})^T \right\} \begin{bmatrix} \mathbf{D}_{mb} & \mathbf{D}_{mbb} \\ \mathbf{D}_{mbb} & \mathbf{D}_{bb} \\ & \mathbf{D}_{sb} \end{bmatrix} \begin{Bmatrix} \mathbf{B}_{mb} \\ \mathbf{B}_{bb} \\ \mathbf{B}_{sb} \end{Bmatrix} \det \mathbf{J} d\xi d\eta \\
& - \mathbf{m}_b \ddot{\mathcal{S}} \int_{\Omega_b^{(e)}} \mathbf{N}_b^T \mathbf{N}_{b,r} \det \mathbf{J} d\xi d\eta + \mathbf{m}_b \dot{\mathcal{S}}^2 \int_{\Omega_t^{(e)}} \mathbf{N}_b^T \mathbf{N}_{b,rr} \det \mathbf{J} d\xi d\eta \\
& + k_{wf} \int_{\Omega_b^{(e)}} \mathbf{N}_{wb}^T \mathbf{N}_{wb} \det \mathbf{J} d\xi d\eta - c_f \dot{\mathcal{S}} \int_{\Omega_b^{(e)}} \mathbf{N}_{wb}^T \mathbf{N}_{wb,r} \det \mathbf{J} d\xi d\eta \\
& - k_{sf} \int_{\Omega_b^{(e)}} (\mathbf{N}_{wb}^T \mathbf{N}_{wb,rr} + \mathbf{N}_{wb}^T \mathbf{N}_{wb,ss}) \det \mathbf{J} d\xi d\eta \\
& + k_{wc} \int_{\Omega_b^{(e)}} \mathbf{N}_{wb}^T \mathbf{N}_{wb} \det \mathbf{J} d\xi d\eta - k_{wc} \int_{\Omega_b^{(e)}} \mathbf{N}_{wb}^T \mathbf{N}_{wt} \det \mathbf{J} d\xi d\eta \\
& - k_{sc} \int_{\Omega_b^{(e)}} (\mathbf{N}_{wb}^T \mathbf{N}_{wb,rr} + \mathbf{N}_{wb}^T \mathbf{N}_{wb,ss}) \det \mathbf{J} d\xi d\eta \\
& + k_{sc} \int_{\Omega_b^{(e)}} (\mathbf{N}_{wb}^T \mathbf{N}_{wt,rr} + \mathbf{N}_{wb}^T \mathbf{N}_{wt,ss}) \det \mathbf{J} d\xi d\eta \\
& - c_c \dot{\mathcal{S}} \int_{\Omega_b^{(e)}} \mathbf{N}_{wb}^T \mathbf{N}_{wb,r} \det \mathbf{J} d\xi d\eta + c_c \dot{\mathcal{S}} \int_{\Omega_b^{(e)}} \mathbf{N}_{wb}^T \mathbf{N}_{wt,r} \det \mathbf{J} d\xi d\eta \quad (12)
\end{aligned}$$

where $\dot{\mathcal{S}}$ and $\ddot{\mathcal{S}}$ the velocity and acceleration of the load, respectively.

The mass, damping and stiffness matrices of the multi-layer moving plate element can be obtained as

$$\mathbf{M}^{(e)} = \mathbf{M}_t^{(e)} + \mathbf{M}_b^{(e)}; \quad \mathbf{C}^{(e)} = \mathbf{C}_t^{(e)} + \mathbf{C}_b^{(e)}; \quad \mathbf{K}^{(e)} = \mathbf{K}_t^{(e)} + \mathbf{K}_b^{(e)}; \quad \mathbf{P}^{(e)} = \mathbf{P}_t^{(e)} + \mathbf{P}_b^{(e)} \quad (13)$$

Assembling all element matrices gives the equation of motion of the multi-layer plate as:

$$\mathbf{M}\ddot{\mathbf{d}} + \mathbf{C}\dot{\mathbf{d}} + \mathbf{K}\mathbf{d} = \mathbf{P} \quad (14)$$

where $\ddot{\mathbf{d}}$, $\dot{\mathbf{d}}$ and \mathbf{d} denote the global acceleration, velocity and displacement vectors of the nodal, respectively; \mathbf{M} , \mathbf{C} and \mathbf{K} the global mass, damping and stiffness matrices, respectively. In the global load vector \mathbf{P} , the component at the node of the upper plate, which is applied load, has the value P of load and other components are zero. The above motion equation can be solved by the Newmark method.

3 Numerical Results

3.1 Static Analysis

For the purpose of verification, the convergence of displacement at centers of upper plate and lower plate was investigated and verified. Two simply supported connected square plates ($L = B = 30$ m, $h = 0.3$ m) subjected to a uniform load $q = 10^4$ N/m² are considered. The material properties and the foundation stiffness are presented in Table 1. The convergence of displacement at centers of the plates against the increase of the foundation stiffness k_{wf} is shown in Table 2. It is noted that as the foundation stiffness increases to infinite, the displacement of the lower plate reaches zero and the response double-plate structure remains only the displacement of the upper plate. The calculated results obtained in this study are compared with those obtained by using the Sap2000 program. The comparisons show that these results agree excellently.

Table 1 Material properties of the plates and foundation stiffness

Young's modulus	Poisson's ratio	Mass density	Foundation stiffness
$E_t = E_b = 3.1 \times 10^{10}$ (N/m ²)	$\nu_t = \nu_b = 0.3$	$\rho_t = \rho_b = 2440$ (kg/m ³)	$k_{wc} = k_{wf} = 1 \times 10^7$ (N/m ³)

Table 2 Covergence of displacement at centers of the plates against the increase of foundation stiffness k_{wf}

Foundation stiffness k_{wf} (N/m ³)	Method	Meshing $N \times N$					
		6 × 6	10 × 10	20 × 20	30 × 30	40 × 40	
1×10^7	MMPM	Upper plate	-2.3871	-2.3054	-2.2829	-2.2804	-2.2798
		Lower plate	-1.2397	-1.1883	-1.1741	-1.1725	-1.1720
1×10^{20}	MMPM	Upper plate	-1.1407	-1.0905	-1.0794	-1.0782	-1.0780
		Lower plate	-1.12×10^{-13}	-1.02×10^{-13}	-1.07×10^{-13}	-1.07×10^{-13}	-1.07×10^{-13}
	Sap2000	Single plate	-1.0731	-1.0750	-1.0771	-1.0779	-1.0779

3.2 Dynamic Analysis

In this section, we now further investigate the performance of the proposed approach for dynamic analysis of the multi-layer connected plate resting on a Pasternak foundation subjected to a moving load. The parameters of the connected layer and the foundation are as follow: $k_{wc} = k_{wf} = 1 \times 10^7 \text{ N/m}^3$, $k_{sc} = k_{sf} = 1 \times 10^5 \text{ N/m}$, $c_c = c_f = 1 \times 10^4 \text{ Ns/m}^3$. A load $P = 10^5 \text{ N}$ moves along the longitudinal mid-line of the upper plate with velocity $V = 20 \text{ m/s}$. Figure 3 shows the displacement at centers of plates against the variations of upper plate thickness and lower plate thickness, respectively. Figure 4 shows the displacement at centers of plates against the variations of foundation stiffness and connected layer stiffness, respectively. The general trend is that when the plate thickness and the foundation stiffness increase, the displacements of two plates decrease. The upper plate thickness has more strong effect than the lower plate thickness. In addition, when the stiffness of the connected layer increases to infinite, the displacement of the upper plate reaches that of the lower plate.

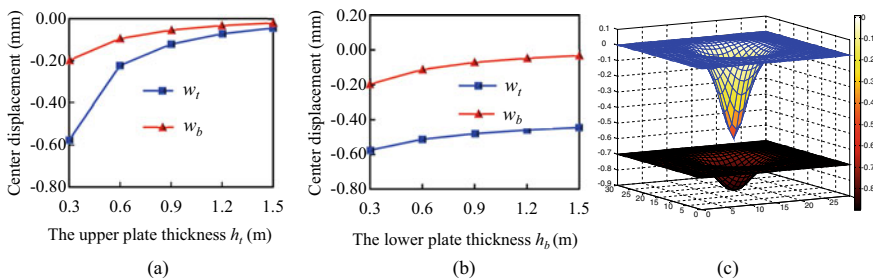


Fig. 3 **a** Displacement at centers of plates against the variation of upper plate thickness, **b** displacement at centers of plates against the variation of lower plate thickness, **c** 3D view of plate displacement

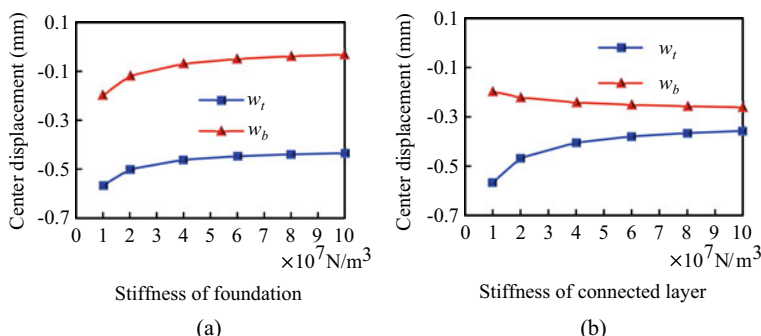


Fig. 4 **a** Displacement at centers of plates against the variation of stiffness of foundation, **b** displacement at centers of plates against the variation of stiffness of connected layer

4 Conclusion

In this paper, a new computational method, namely Multi-layer Moving Plate Method (MMPM), has been developed to investigate the dynamic responses of the multi-layer connected plate resting on a Pasternak foundation subjected to a moving load. The formulations of multi-layer moving plate element mass, damping and stiffness matrices are derived. A parametric study is performed to examine the effects of various parameters on the dynamic responses of multi-layer connected plate structure.

Acknowledgements This research is funded by Vietnam National Foundation for Science and Technology Development (NAFOSTED) under grant number 107.02-2018.14.

References

1. Cao TNT, Reddy JN, Ang KK, Luong VH, Tran MT, Dai J (2018) Dynamic analysis of three-dimensional high-speed train-track model using moving element method. *Adv Struct Eng* 21(6):862–876
2. Cao TNT, Luong VH, Vo HN, Nguyen XV, Bui VN, Tran MT (2018) A moving element method for the dynamic analysis of composite plate resting on a Pasternak foundation subjected to a moving load. *Int J Comput Method* 15(3):1850124 (1-19)
3. De Rosa MA, Lippiello M (2009) Free vibrations of simply supported double plate on two models of elastic soils. *Int J Numer Anal Methods Geomech* 33:331–353
4. Hamada TR, Nakayama H, Hayashi K (1983) Free and forced vibrations of elastically connected double-beam systems. *Trans Jpn Soc Mech Eng* 49:289–295
5. Koh CG, Ong JSY, DKH. Chua Feng J (2003) Moving element method for train-track dynamics. *Int J Numer Methods Eng* 56:1549–1567
6. Luong VH, Cao TNT, Reddy JN, Ang KK, Tran MT, Dai J (2018) Static and dynamic analyses of Mindlin plates resting on viscoelastic foundation by using moving element method. *Int J Struct Stab Dyn* 18(11):1850131(1-20)
7. Oniszczuk Z (1992) Free vibrations of elastically connected rectangular double-plate system. In: Proceedings of the XVth symposium “vibration in physical systems”, Poznán 126
8. Saito H, Chonan S (1968) Vibrations of elastically connected double-beam systems. *Trans Jpn Soc Mech Eng* 34:1898–1907
9. Seelig JM, Hoppmann WH II (1964) Normal mode vibrations of systems of elastically connected parallel bars. *J Acoust Soc Am* 36:93–99

A Proposed Method for Inspecting and Predicting the Seismic Vulnerability of Dam Structures in Korea



Anh-Tuan Cao, Thanh-Tuan Tran, Tahmina Tasnim Nahar, and Dookie Kim

1 Introduction

Seismic loading can significantly affect the dam operation because of inducing the potential failures and damages. The main purpose of this study is to propose a method for checking the operational condition of the dam under seismic effects. The capacity of the Bohyeonsan concrete dam in Korea is calculated and checked after withstanding the Pohang earthquake (2017). Using the seismic source models of the Korean Peninsula, this research defines the magnitude range and the corresponding PGA values to estimate the potential CAV at the dam's site for evaluation. From the earthquake (EQ) data provided by K-water organization, twelve ground motions in Korea are selected to conduct the fragility and CAV analysis, and the seismic risks at the structural location can be estimated based on the value of the capacity CAV_{limit} . There are many seismic influences on dam structure were recorded during history. Reference [7] mentioned that the Lower San Fernando Dam in the USA had a liquefaction phenomenon when withstanding seismic excitation. The Tohoku earthquake with a strong magnitude of 9.0 induced various consequences such as cracking at the gate of Takou Dam etc. Presently, to carry out the post-earthquake inspection for the structure will cost a lot, it becomes a financial burden for the governments if all of the infrastructural facilities in the influential zone are checked. Thus, the idea to make the preliminary evaluation based on the acceleration data obtained from sensors will be promising and it is the motivation for this research.

A.-T. Cao (✉) · T.-T. Tran · T. T. Nahar

Department of Civil Engineering, Kunsan National University, 558 Daehak Ro, Kunsan, Jeonbuk 54150, Republic of Korea

e-mail: anhtuan.hcmut@gmail.com

D. Kim

Department of Civil and Environmental Engineering, Kongju National University, Cheonan, Republic of Korea

2 Seismic Source Models in the Korean Peninsula

More than 2000 ground motions were used to establish these seismic source models by different research teams [6]. Both theories to make the magnitude-frequency relationship in the seismic models and the magnitude-PGA relationship in this study apply the previous researches of Gutenberg-Richter [3, 8]. The magnitude value presents the size of an earthquake, and various areas may have different potential ranges of the magnitude. The graphical models corresponding to different magnitude areas in the Korean peninsula are expressed in Fig. 1.

3 Relation of Magnitude-PGA

The intensity is an indirect expression of the excitation strength, which is assessed upon the human's senses and damages on the structure during the seismic event. In this study, PGA is considered as the important intensity measure (IM) and calculated by equations of Gutenberg- Richter, which are explained by Eqs. 1 and 2. Based on the coordinate of the dam's location in the seismic source models (36.12° N and 128.94° E), the determination of the magnitude and PGA ranges are from 6.3 to 7.1 and 0.14 g to 0.36 g, respectively.

$$M = \frac{2}{3} \times MMI + 1 \quad (1)$$

$$\log_{10}PGA = 0.33 \times MMI - 0.5 \quad (2)$$

4 Validation of the Numerical Model

Belongs to the dam's specification, the total crest length is 250 m and the maximum height is 57 m. There are two sensors installed on the top and the bottom of the dam to record the acceleration, which is shown in Fig. 2. In order to evaluate the behaviors of the dam, ABAQUS is used to simulate the two-dimensional finite element model (FEM), and the Pohang earthquake is used as the input ground motion. Figure 3 describes the numerical model of the critical section corresponding to the location of sensors installation. RSM uses the recorded acceleration data from sensors to optimize the numerical model; it is capable to consider various factors, which affect the structural responses. Different sets of input parameters can be created by the Central Composite Design (CCD) method to make the response surface. Normally, the first and second orders are used for RSM, which are described by mathematical Eqs. 3 and 4.

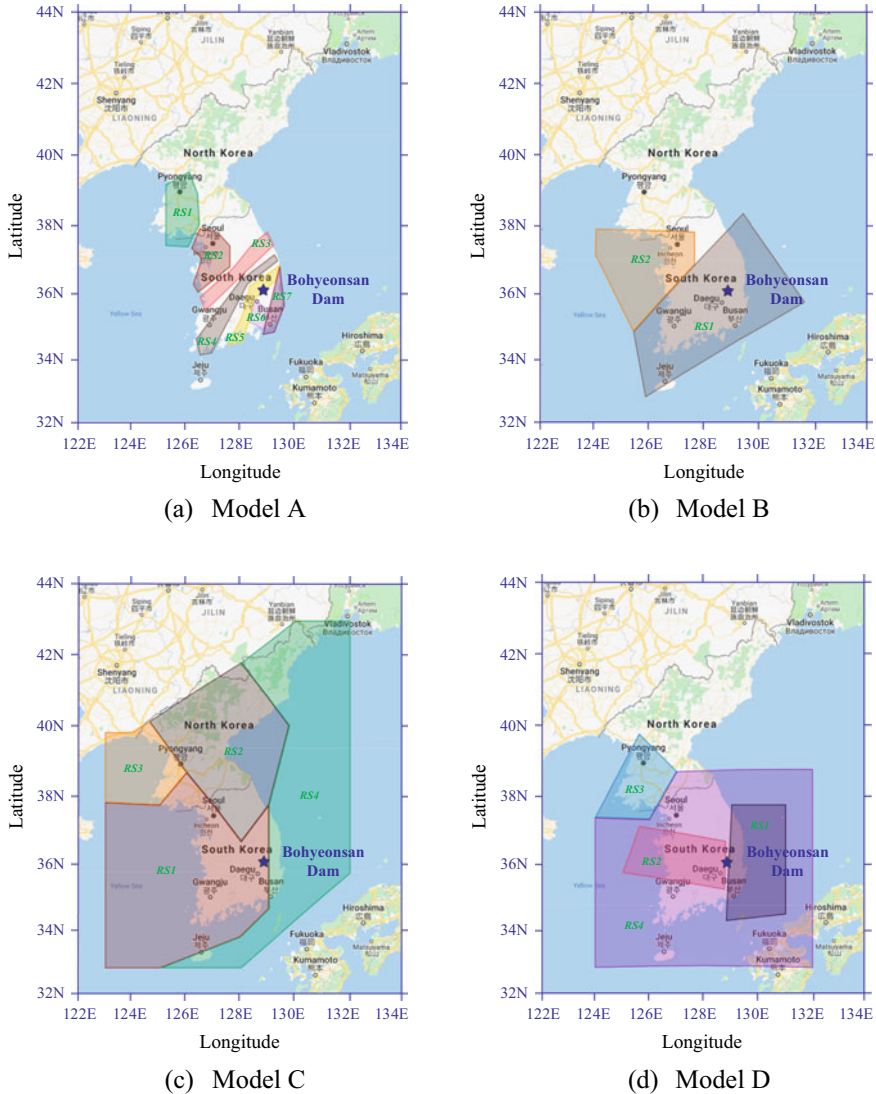


Fig. 1 Seismic source models in the Korean peninsula [2]

First order:

$$t = \gamma_0 + \sum_{i=1}^n \gamma_i a_i + \sum_{i,j=1}^n \gamma_{ij} a_i a_j + \mu \quad (3)$$

Fig. 2 Perspective view of the Bohyeonsan Dam

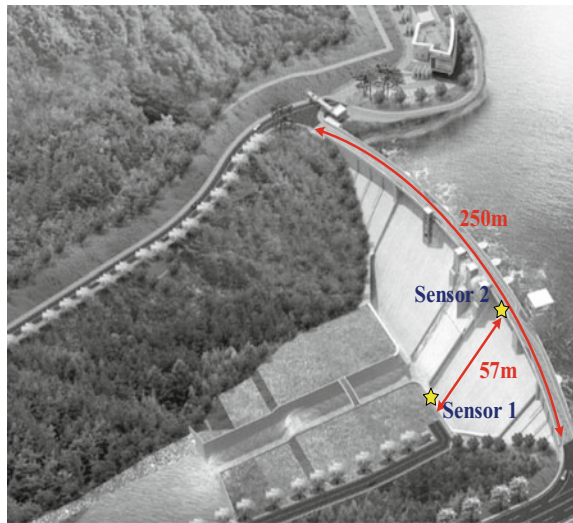
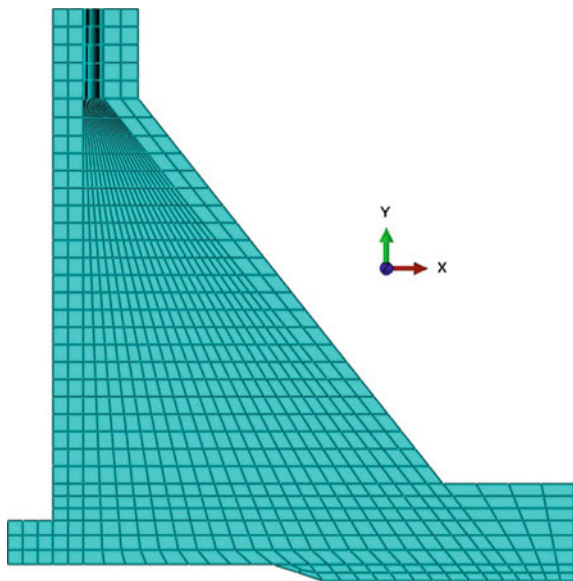


Fig. 3 Plane section of the numerical model



Second order:

$$t = \gamma_0 + \sum_{i=1}^n \gamma_i a_i + \sum_{i=1}^n \gamma_i a_i^2 + \sum_{i,j=1}^n \gamma_{ij} a_i a_j + \mu \quad (4)$$

where γ is the approximate regression coefficient, a_i is the factor ($i, j = 1, 2, 3 \dots, n$) and μ is the offset term. In this case, the second order is adequate for estimating the response surface. The CCD method is used to create the set of experimental models including factorial, axial and center points. The number of the variable sets (N) are calculated by Eq. 5

$$N = 2^n + 2n + c_p \quad (5)$$

where c_p is the number of center-point, and n is the number of the factors (Young's modulus and density). The objective functions are the top acceleration and frequency values in the response spectrum (RS) created from recorded data, which are expressed by Eqs. 6 and 7.

$$F_1 = (FA) \quad (6)$$

$$F_2 = (PA) \quad (7)$$

(PA) is the peak acceleration and (FA) is the value of frequency corresponding to the peak value on the response spectrum. The optimum response is calibrated based on the target values, and the material parameters after optimizing are 0.787 and 2.32 (ton/m³) for Young's modulus ratio (α) and density (ρ), respectively.

5 Fragility and CAV Analysis

5.1 Fragility and CAV Analysis for Dam Structure

PGA is one of the intensity measures (IM) used popularly in the fragility analysis, and the fragility curve assesses the vulnerability of the structure based on the probability of failure. In this research, the tensile strength and relative displacement are considered as the limit states (LS) of the structure.

Reference [5] stated that the mean and standard deviation values are determined by logarithms calculation from the onset of collapse, as explained by Eqs. 8 and 9.

$$\ln \theta = \frac{1}{n} \sum_{i=1}^n \ln IM_i \quad (8)$$

$$\beta = \sqrt{\frac{1}{n-1} \sum_{i=1}^n (\ln(IM_i/\theta))^2} \quad (9)$$

To be more conservative, the dam's high confidence of low probability of failure (HCLPF) point is selected as the smaller value from both fragility curves. HCLPF

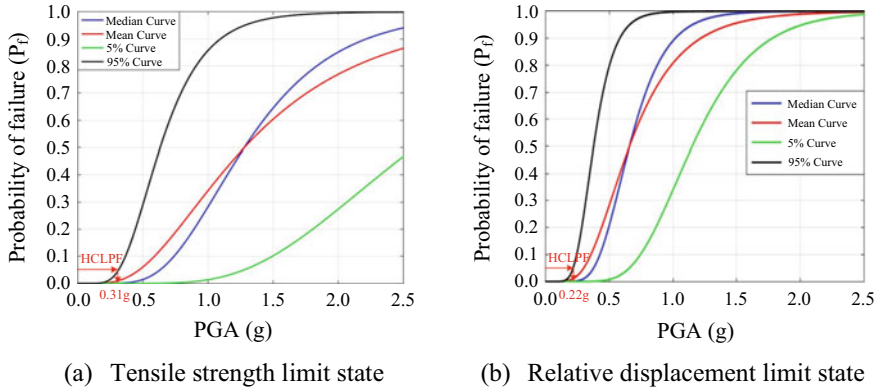


Fig. 4 Fragility curves of the Bohyeonsan Dam

point reflects 95% confidence of 5% probability of exceedance. From Fig. 4, it can be said that the selected HCLPF point comes from the fragility curves of relative displacement, which has the PGA value is 0.22 g and smaller than 0.31 g of the tensile strength curve. The PGA value of HCLPF point is used for defining the CAV capacity of the dam, and the CAV_{limit} will be meaningful with the operators who give the decision whether the dam must be shut down after an earthquake or not. From Eq. 10, the CAV value is calculated as the integral of absolute acceleration in the time domain [1].

$$CAV = \int_0^{t_{\max}} |a(t)| dt \quad (10)$$

where $|a(t)|$ is absolute acceleration value and t_{\max} is the time duration. CAV value increase until t_{\max} , thus the total influences of the earthquake is cumulated. The CAV capacity of the Bohyeonsan Dam is defined conservatively after scaling twelve earthquakes in Korea with the PGA of selected HCLPF point ($\text{PGA} = 0.22 \text{ g}$). According to [4], the CAV limitation is selected as the lowest value from both earthquake horizontal components. To be safer, the arias intensity duration from 5% to 75% is used in this study, which only includes the effective range of each seismic data. Eventually, the capacity $\text{CAV}_{\text{limit}}$ of 0.185 g is obtained from earthquake 6DB in the North-South direction. The failures can occur if any one of CAV value from both free-field horizontal components is greater than $\text{CAV}_{\text{limit}}$, then the structural survey should be carried out or shut down the operation.

Table 1 Design PGA values in Korea

Return period	Level	Design PGA (g)
100	Operational level (OP)	$\text{PGA}_1 = 0.11 \text{ g} \times 0.57 = 0.0627$
200	Immediate occupancy level (IO)	$\text{PGA}_2 = 0.11 \text{ g} \times 0.73 = 0.080$
500	Life safety level (LS)	$\text{PGA}_3 = 0.11 \text{ g} \times 1.0 = 0.11$
1000	Collapse level (CP)	$\text{PGA}_4 = 0.11 \text{ g} \times 1.4 = 0.154$

5.2 CAV Analysis for Dam's Site

In order to conduct the CAV analysis for the dam's site in Korea, the relation between CAV-PGA must be defined. Table 1 shows the design PGA values calculated based on the coefficients of various ground motion levels. The operational, immediate occupancy, life safety, and collapse level corresponding to the return period of 100, 200, 500 and 1000 years, respectively.

The relation CAV-PGA expresses a linear analysis, and the mathematical equation generated from this research is described by Eq. 11. From this equation and the PGA range at the dam's site, the potential CAV range can be estimated from 0.12 to 0.3 g s.

$$\text{CAV} = 0.8394\text{PGA} + 5 \times 10^{-6} \quad (11)$$

5.3 CAV Analysis for the Pohang EQ

The recorded acceleration data taken from the Pohang earthquake event is used to validate the numerical model, thus it is also essential for checking the operational condition of the dam under its effects. Figure 5 shows the CAV values of the Pohang EQ with two horizontal components. The greater value of 0.063 g s comes from East-West direction is selected for comparing with the capacity of the dam.

6 Result Summary

Figure 6 summarizes the total results of CAV calculation for dam structure, the specific location, and the Pohang earthquake. The selected CAV value of 0.063 g s obtained from the Pohang earthquake is smaller than the CAV capacity of the dam is 0.185 g s. Therefore, the operational condition of the dam is not affected after withstanding the Pohang earthquake. Nevertheless, the $\text{CAV}_{\text{limit}}$ of the dam could be smaller than the CAV value at the dam's site ((0.12 g s < 0.185 g s < 0.30 g s), so the potential disasters can happen. It is necessary to raise awareness about the important

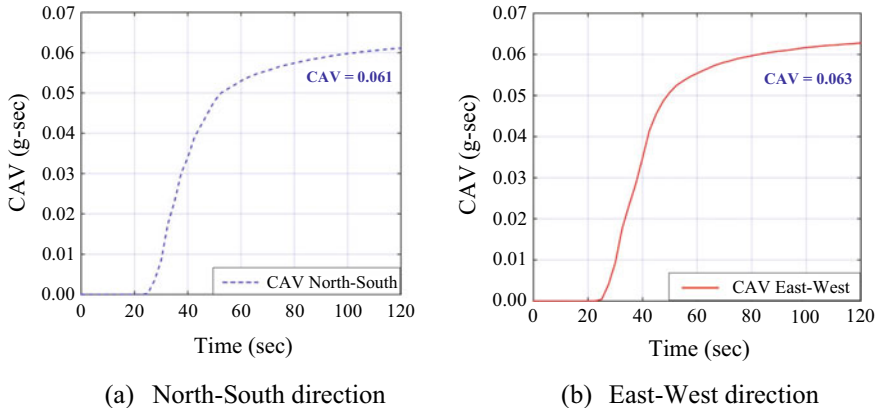
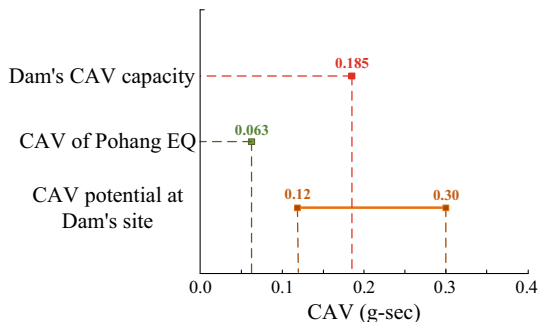


Fig. 5 CAV calculation for the Pohang earthquake

Fig. 6 Cumulative absolute velocity comparison



role of seismic risk assessment for dam structure and prepare for the worst-case to preclude the consequences, which damage the natural environment and social life.

7 Conclusion

Using the proposed method in this study, it is feasible for post-earthquake inspection and predicting the vulnerability of the dams in Korea based on the seismic source models. Within a short time, the dam operators are able to estimate the capacity of the structure and conduct the seismic risk assessment.

The strong point of this method is cost-effective and time-saving. Moreover, the applicability is the most important feature, via the calculation for the Bohyeonsan Dam as an example, the operators can apply for various dams in Korea. Besides that, the user can be flexible for replacing some methods in each step to improve reliability.

For future research, the soil-structure interaction (SSI) and fluid effects can be considered to increase the accuracy of the numerical model. The non-reflecting boundary condition is available in Abaqus for acoustic elements, and the infinite or viscous boundary can be applied for soil. It will be the additional research with full of promise for urgent warning and assessing the characteristics of structures.

Acknowledgements This research was supported by a grant (2017-MOIS31-002) from Fundamental Technology Development Program for Extreme Disaster Response funded by the Korean Ministry of Interior and Safety (MOIS).

References

1. Campbell KW, Bozorgnia Y (2010) Analysis of cumulative absolute velocity (CAV) and JMA instrumental seismic intensity (IJMA) using the PEER-NGA strong motion database. Pacific Earthquake Engineering Center, Berkeley
2. Choun YS, Choi IK, Ohtori Y, Shiba Y, Nakajima M (2003) Korea–Japan Joint Research on Development of Seismic Capacity Evaluation and Enhancement Technology Considering Near-fault Effects. (No. KAERI/RR-2392/2003), Korea Atomic Energy Research Institute
3. Gutenberg B, Richter CF (1944) Frequency of earthquakes in California. Bull Seismol Soc Am 34(4):185–188
4. Hardy G, Merz K, Abrahamson N, Watson-Lamprey J (2006) Program on technology innovation: Use of cumulative absolute velocity (CAV) in determining effects of small magnitude earthquakes on seismic hazard analyses. EPRI, Palo Alto, CA, and the US Department of Energy, Germantown. EPRI report MD, 1014099
5. Ibarra LF, Krawinkler H (2005) Global collapse of frame structures under seismic excitations. Pacific Earthquake Engineering Research Center, Berkeley, CA. pp 29–51
6. Seo JM, Min GS, Choun YS, Choi IK (1999) Reduction of uncertainties in probabilistic seismic hazard analysis. KAERI/CR-65/99
7. Tosun H (2015) Earthquakes and dams. Earthq Eng. <https://doi.org/10.5772/59372>
8. Zanini MA, Hofer L, Faleschini F (2019) Reversible ground motion-to-intensity conversion equations based on the EMS-98 scale. Eng Struct 180:310–320

Analysis of the Relationship Between the Deflection Pattern of a Floating Plate Induced by Moving Load and the Material Angle by Using the Boundary Element-Moving Element Method



Xuan Vu Nguyen, Van Hai Luong, Tan Ngoc Than Cao, and Minh Thi Tran

1 Introduction

Thanks to the endless rise of both the urbanization trend and the climate change, a pressure of expanding urban regions to lessen the situation of overcrowded inhabitants has been necessary now. Consequently, migration is the most vulnerable aspect of today's developing metropolis regions, and the numbers of urban poor populations are increasing. In order to deal with this issue, very large floating structures (VLFSs) has been considered as a relatively promising solution due to the simplicity of their construction and expansion. Such structures are often built on the surface of river, lake or ocean to promote power generation, water distillation, and resource storage. In comparison with ship-like floating structures, they own a relatively small ratio between the depth and dimensions in the plane. Hence, elastic responses are more important than rigid-body motions, in which hydroelastic behavior known as the interaction between fluid and structure is taken as a center stage in designing VLFSs. For hydroelastic analyses, VLFSs are generally assumed to be a homogeneous material with Young's modulus, Poisson's ratio and mass per unit are modified to match to natural frequencies and vibration modes of real structures. Regarding analyses of floating flexible plates subjected to moving load, the structural wave under the impact of a moving excitation with different speeds is generated on the plate [8]. Takizawa [7] conducted an experiment on a sea ice-sheet subjected to a

X. V. Nguyen · V. H. Luong (✉) · M. T. Tran

Faculty of Civil Engineering, Ho Chi Minh City University of Technology (HCMUT), 268 Ly Thuong Kiet Street, Ward 14, District 10, Ho Chi Minh City, Vietnam
e-mail: lvhai@hcmut.edu.vn

Vietnam National University Ho Chi Minh City (VNU-HCM), Linh Trung Ward, Thu Duc District, Ho Chi Minh City, Vietnam

T. N. T. Cao
College of Technology, Can Tho University, Can Tho City, Vietnam

moving excitation of an automobile ski-doo. In that work, parameters representing the characteristic of structural wave including depression depth, depression width, lag, wavelength and propagation speed of the depression were investigated. By utilizing the experimental results, the variation of these parameters with the speed of moving loads was reported in Ref. [7]. In addition, the theoretical relations between the load speed and the structural wave were also presented by Nevel [4], Hosking and Sneyd [3], and Eyre [1]. It can be found that, most of all the aforementioned studies have only focused on the relation between the load speed and structural wave without considering any directional dependence of structural properties. In fact, a VLFS includes different modules where each of them consists of bulkheads, decks and bottom platings [2]. The arrangement of bulkheads in two major directions inevitably leads to the discrepancy between the transversal and longitudinal flexural rigidity. Therefore the orthotropic properties should be included to achieve more accurate hydroelastic analyses. Moreover, the moving direction of loads is not generally parallel to the strong material direction. The angle between these two directions, which is referred to the material angle in this study, should be therefore also considered. In order to tackle the foregoing shortcomings, the dependence of the structural wave on material angle is further investigated in this article. Concerning moving load analyses, the moving element method (MEM) has been successfully implemented to analyze various dynamic problems of structures subjected to moving loads. However, there has been almost no research work on the extension of the MEM for the hydroelastic problems of floating orthotropic plates. In order to fill in this research gaps, the MEM is therefore extended and cooperated with the Boundary Element Method (BEM), named the BEM-MEM, in order to study hydroelastic responses of floating orthotropic plates subjected to moving loads.

The remaining of the paper is organized as follow: in the first half of the article, the proposed computational approach is presented. In the second half, a simulation of an infinite floating composite plate under a moving concentrated force is described. The dynamic amplification factor for displacement, depression width, and drag force are considered in this paper. According to numerical results, the variation of these parameters with material angle is presented and discussed. Generally, the tendencies of variations depend on the magnitude of speed.

2 Theoretical Formulation

The transient problem for an infinite orthotropic elastic plate floating on a still water with the finite depth of H is considered. The z -axis of an orthogonal Cartesian coordinate system is taken as positive vertically upward, with $z = 0$ defined as the plane of the undisturbed free surface, as shown in Fig. 1. The fluid is assumed to be perfect, so it means that a potential flow is assumed. It is also assumed that the fluid vertical motion is small relative to the depth H so that the linear potential theory can be applied for formulating the fluid-domain problem. Since the structural draft is so shallow relative to the dimensions in the plane, it can be treated as zero. The

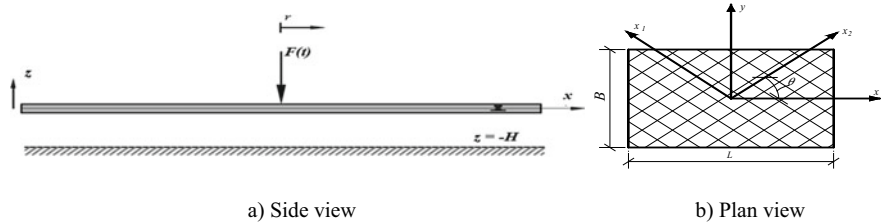


Fig. 1 Depicting the floating plate

transient elastic responses of the plate caused by a dynamic force $F(t)$ moving on the floating plate are investigated.

Based on the abovementioned assumptions, a velocity potential $\phi(x, y, z, t)$ satisfying the Laplace's equation can represent the fluid motion. At the wetted surface, there is no gap between fluid and plate. Assuming that the sea-bottom is flat and the fluid's vertical velocity at the sea-bed is taken equal to zero. Besides, the water's velocity is also assumed to be zero when x and y approach infinity. Concerning the structure, the governing equation of an orthotropic plate based on the Kirchhoff-Love theory of plates is employed in order to describe the motion of the floating structure.

For solving the boundary-value problem, a relative orthogonal Cartesian coordinate system, with its origin taken as attached to the moving load for convenience may be defined as

$$r = x - d; \quad s = y; \quad z = z \quad (1)$$

In view of making a transformation to the moving coordinate system, the governing and boundary equations may be rewritten. With regard to numerical modeling, a truncated area of the infinite domain is defined with the boundaries taken to be adequate far from the moving load such that the deflection, rotation of the plate and the potential, velocity of the fluid are nearly equal to zero. Moreover, in order to reduce the mesh size without disturbing numerical results caused by the reflected wave from the boundaries, an artificial layer is adopted to absorb all outgoing energies. An expression for artificial damping coefficient referred from the working of Nguyen and Duhamel [5] and modified for two-dimensional problem is implemented in this study.

By adopting the Galerkin's approach and the displacement shape function be \mathbf{N} , the element mass, damping and stiffness matrices are represented by \mathbf{M}^e , \mathbf{C}^e , \mathbf{K}^e , respectively.

$$\mathbf{K}_e = \int_{S_e} (\mathbf{B}^T \mathbf{D} \mathbf{B}) dS - m \frac{\partial d}{\partial t} \int_{S_e} \mathbf{N}_{,r}^T \mathbf{N}_{,r} dS - m \frac{\partial^2 d}{\partial t^2} \int_{S_e} \mathbf{N}^T \mathbf{N}_{,r} dS z$$

$$\begin{aligned}
& + \rho g \int_{S_e} \mathbf{N}^T \mathbf{N} dS - \frac{\partial d}{\partial t} c \int_{S_e} \mathbf{N}^T \mathbf{N}_{,r} dS \\
& - \frac{\partial d}{\partial t} \int_{S_e} c_{vd} \mathbf{N}^T \mathbf{N}_{,r} dS - \alpha \int_{S_e} (\mathbf{B}^T \mathbf{D} \mathbf{B}_{,r}) dS
\end{aligned} \tag{2}$$

$$\begin{aligned}
\mathbf{M}_e &= m \int_{S_e} \mathbf{N}^T \mathbf{N} dS, \quad \mathbf{C}_e = c \int_{S_e} \mathbf{N}^T \mathbf{N} dS + \alpha \int_{S_e} (\mathbf{B}^T \mathbf{D} \mathbf{B}) dS \\
& + \int_{S_e} c_{vd} \mathbf{N}^T \mathbf{N} dS - 2m \frac{\partial d}{\partial t} \int_{S_e} \mathbf{N}_{,r}^T \mathbf{N} dS
\end{aligned} \tag{3}$$

where $(\cdot)_{,r}$ denotes partial derivative with respect to r , S_e represents each element on the wetted surface. \mathbf{D} is the elasticity matrix of orthotropic plate and \mathbf{B} represents a matrix of differential operators which can be referred to Szilard [6]. In this study, Hermite shape function is adopted to interpolate the displacement over each element.

By using the high-order BEM, the surface of fluid domain is discretized into a number of boundary elements and the velocity potential is assumed to be linear over each element. By applying the collocation method, the boundary integral equation may be rewritten in the discrete form. Since adopting the shape function \mathbf{N} and the linear panel, the virtual work done by the applied dynamic pressure of water to each of plate elements may be written as

$$\begin{aligned}
& \int_{S_e} \left(\frac{\partial \phi(r, s, 0, t)}{\partial t} + \dot{d}\phi(r, s, 0, t) \frac{\partial \delta w}{\partial r} \right) \delta w \cdot dS \\
& = \delta \mathbf{w}^T \left(\int_{S_e} (\mathbf{N}^T \varphi) dS \cdot \dot{\Phi}^e + \dot{d} \int_{S_e} (\mathbf{B}_{,r}^T \varphi) dS \cdot \dot{\Phi}^e \right) \\
& = \delta \mathbf{w}^T (L_2^e \dot{\Phi}^e + \dot{d} \mathbf{L} \mathbf{d} \mathbf{r}_2^e \Phi)
\end{aligned} \tag{4}$$

where $\delta \mathbf{w} = [\delta w, \delta w_x, -\delta w_y]^T$ is vector containing virtual displacements of nodes on each element, and $j = 1 \dots N$. After assembling the matrices of the model, the governing equation of motion for the combined model of the plate and fluid can be represented as

$$\begin{bmatrix} \mathbf{M} & \mathbf{0} \\ \mathbf{0} & \mathbf{0} \end{bmatrix} \begin{bmatrix} \ddot{\mathbf{w}} \\ \ddot{\Phi} \end{bmatrix} + \begin{bmatrix} \mathbf{C} & \rho \mathbf{L}_2 \\ -\mathbf{G} & \mathbf{0} \end{bmatrix} \begin{bmatrix} \dot{\mathbf{w}} \\ \dot{\Phi} \end{bmatrix} + \begin{bmatrix} \mathbf{K} & -\rho \cdot \dot{d} \cdot \mathbf{L}_{dr2} \\ \dot{d} \cdot \mathbf{G} \mathbf{d} \mathbf{r} & \mathbf{H} \end{bmatrix} \begin{bmatrix} \mathbf{w} \\ \Phi \end{bmatrix} = \begin{bmatrix} \mathbf{P} \\ \mathbf{0} \end{bmatrix} \tag{5}$$

where the structural stiffness, damping and mass matrices are denoted by \mathbf{K} , \mathbf{C} and \mathbf{M} , respectively. The external force vector \mathbf{P} contains mostly zeroes, and non-zero terms in \mathbf{P} is at contact point with the corresponding degree of freedom. Φ is vector

containing potential velocity at the field points and \mathbf{w} denotes to a vector comprising nodal displacements of plate model.

3 Numerical Results

In this section, the BEM-MEM is employed to analyze the hydroelastic responses of a floating orthotropic plate. A model of orthotropic plate floating on calm water with the finite depth and subjected to translating concentrated load is simulated. In the simulation, the wetted surface of the retained fluid domain is rectangular of length 200 m and width 200 m with its center located at the contact point. By adopting the artificial damping layer, the undisturbed condition is assumed to satisfy, and the structural waves cannot reach the far field boundaries. The fluid domain is divided into 6200 linear boundary elements which are assumed to coincide with 6200 structural moving elements of the floating plate. The physical parameters are presented in Table 1 employed in the experiment described in Takizawa [7]. On the other hand, for numerical investigations, the load speed is normalized by the minimum celerity of the free surface of hydroelastic system, $C_{\min} = 1.325(g^3 D / \rho)^{1/8}$ [9].

3.1 The Dynamic Amplification Factor

When the vehicle moves on the floating plate, a depression surrounding the contact point appears and the maximum deflection locates at the center of the depression or depression depth. The relationship between depression depth and load speed has been reported in the previous works [1, 3, 4, 7]. In this section, the dependence

Table 1 The technical parameters of a flexible floating orthotropic plate

Technical parameters	Magnitude	Unit
Young's modulus in x_1 -direction E_1	0.25	GPa
Young's modulus in x_2 -direction E_2	0.5	GPa
Thickness of plate	0.17	m
Poisson's ratio ν_{12}	0.13	
Mass density	0.926	T/m ³
Water depth	6.8	m
Material angle θ	0, 15, 30, 45, 60, 75, 90	degree
Magnitude of moving load	2.35	kN
Speed of moving load	0–11.6 growing in steps of 5.8	m/s

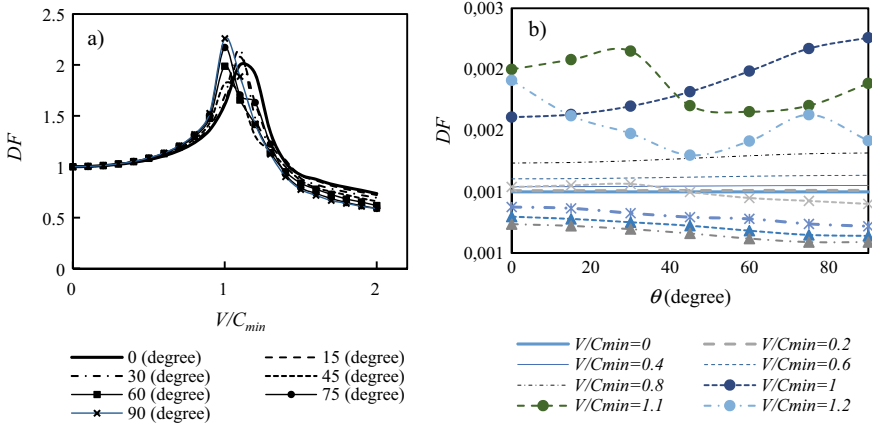


Fig. 2 **a** Variation of DF with speed V/C_{\min} for various θ (degree), **b** variation of DF with θ for various speed V/C_{\min}

of the dynamic amplification factor for displacement (DF), which is ratio between maximum vertical displacement taking account of dynamic effects and those due to static load, on material angle is examined. Namely, with $E_1/E_2 = 0.5$, the DF - θ relation for θ ranging from 0° to 90° growing in steps of 15° is plotted in Fig. 2a. Generally, the tendency of relationships depends on the values of speed that can be listed in three groups. At the $V < 0.5C_{\min}$, deflection pattern of floating plate is symmetric about the contact point and similar to that induced by the static load. Due to the symmetric, the DF is nearly independent on the angle θ . However, with the speed above $0.5C_{\min}$, with the disappearance of the symmetric about the origin, the effect of θ on DF becomes noticeable. Following Fig. 2b, the variation of the DF with the angle θ is presented. At the same V , the relationship between two variables is directly proportional excluding the speeds neighborhood of C_{\min} where the tendencies are complicated. However, when the load moves over the speed of $1.5C_{\min}$, increasing in the angle θ decreases the DF . On the other hand, according to Fig. 2a, for the range of $\theta < 45^\circ$, the critical speed where the peak of DF occurs is greater than that for the rest. It means that with the angle between the velocity vector and the strong material direction below 45° , the critical speed is greater than that for the others.

3.2 Depression Width

The width of the depression curve along the longitudinal centerline is defined as the distance between two points which intersect with the neutral line. The depression width also varies when the speed of load increases. Following Fig. 3, at first, with the speed below C_{\min} the faster the vehicle moves, the more narrow the longitudinal depression width becomes. The minimum value of the depression width occurs at

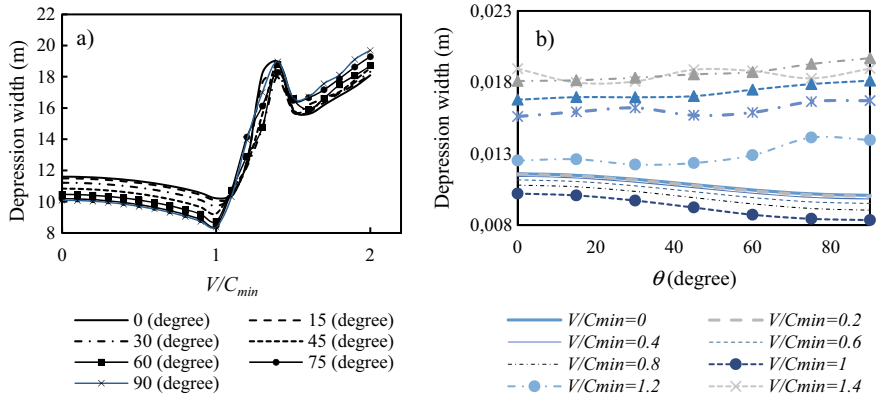


Fig. 3 **a** Variation of the width of depression with speed V/C_{\min} for various θ and **b** variation of the width of depression with θ for various speed V/C_{\min}

the speed of C_{\min} . At the velocities above the critical value C_{\min} , the depression width increases with an increase in the speed and becomes greater than the width induced by the static load. It is noted that there is a slight decrease in the width of depression when the speed ranges from 1.4 to $1.5C_{\min}$.

With $E_1/E_2 = 0.5$, the relationships between the width of depression and the angle θ are presented in Fig. 3. Generally, the tendency of the relationship between the width and the angle θ depends on the speed of load. In the three first stages ($V < 1.2C_{\min}$), at the same V , with an increase in θ , the width decreases; but it increases in the last two stages ($V > 1.2C_{\min}$). It means that from the quasi-static stage to late-transition stage, the dependence of the width on the material angle is similar to the those due to the static load. Rotating the weak material direction toward the direction of velocity reduces the flexural rigidity in the longitudinal direction resulting in a decrease in the depression width. However, in the last two stages (the two-wave stage and single-wave stage), inversely, the width becomes wider when the angle between the velocity and the weak material direction decreases.

4 Conclusions

In this article, the BEM-MEM method has been developed to analyze behavior of floating orthotropic plates under moving load for the first time. The effect of material angle on responses of floating orthotropic plates is examined. Through the present formulations and numerical investigations, several remarkable conclusions are obtained. The effect of the material angle on responses of floating plates changes according to the stage of the velocity. Especially, the influence becomes significant when the speed is larger than the minimum celerity of the free surface of hydroelastic system (C_{\min}). Therefore, naval engineers should take account of the directional-dependent

bending stiffness in the stage of design of VLFSs to obtain an optimized solution with more accurate responses.

Acknowledgements This research is funded by the Vietnam National University Ho Chi Minh City (VNU-HCM) Under Grant No. B2019-20-13: “Development and application of a combined boundary element method and moving element method BEM-MEM for the dynamic analysis of very large floating structures”.

References

1. Eyre D (1977) The flexural motions of a floating ice sheet induced by moving vehicles. *J Glaciol* 19(81):555–570
2. Fujikubo M, Yao T (2001) Structural modeling for global response analysis of VLFS. *Marine Struct* 14:295–310
3. Hosking RJ, Sneyd AD (1966) Waves due Vehicle on floating ice sheets. In: 9th Australasian Fluid mechanics conference, AuckLan, pp 51–54
4. Nevel DE (1970) Moving loads on a floating ice sheet. Cold Regions Research and Engineering Laboratory
5. Nguyen, V. H., & Duhamel, D. (2008). Finite element procedures for nonlinear structures in moving coordinates. Part II: Infinite beam under moving harmonic loads. *Computers and Structures*, 86(21–22), 2056–2063
6. Szilard R (2004) Theories and applications of plate analysis: classical, numerical and engineering methods. Wiley, Hoboken, NJ
7. Takizawa T (1985) Deflection of a floating sea ice sheet induced by a moving load. *Cold Reg Sci Technol* 11:171–180
8. Takizawa T (1988) Response of a floating sea ice sheet to a steadily moving load. *J Geophys Res* 93(5):5100–5112
9. Yeung RW, Kim JW (2000) Effects of a translating load on a floating plate structural drag and plate deformation. *J Fluids Struct* 14(7):993–1011

Case Study on Field Application of Structural Strengthening Technique with Fire-Protection to a Commercial Building



L. X. Binh, V. N. Linh, D. X. Quy, H. V. Quan, H. V. Tuan, and W. K. Ong

1 Introduction

The rapid development of new advanced materials have made it possible to solve difficult and emerging problems. One notable development was the invention of Fibre Reinforced Polymer (FRP) which has seen its wide usage in the field of structural reinforcement. Since its first application in the field of structural reinforcement in the 1980s, this material has gained wide acceptance around the world and also achieved significant progress in solving many modern day structural problems.

In Vietnam, since it was introduced in the early 2000, the application of FRP materials has only gained momentum from 2011. One of the challenges faced is to meet the strength requirements and at the same time to satisfy other requirements in the process of its applications, such as fire resistance. This paper aims to highlight the application of FRP materials in the strengthening of a commercial building in Hanoi and addressing the fire-rating requirement at the same time. Beyond the required strengthening, a full-scale insitu load test was conducted and a separate fire test was carried out to meet the fire-rating requirement of the building. The FRP materials used for this project were supplied by Fyfe Asia and imported through the authorised applicator VSBCO Joint Stock Company. The entire process of the strengthening, testing and the problems encountered are documented in this paper.

L. X. Binh · V. N. Linh · D. X. Quy · H. V. Quan · H. V. Tuan
Faculty of Civil Engineering, University of Transport and Communications, Hanoi, Vietnam

W. K. Ong (✉)
Fyfe Asia Pte. Ltd., Singapore, Singapore
e-mail: weekeongong@aegion.com

2 Background of Project

A 6-storey building in Hoang Mai District, Hanoi, was originally designed to be an apartment building. When the building was only partially completed, there was a sudden change of function of the building by the project investor to convert it to become a commercial building for the display and introduction of products. This change of function resulted in the requirement for strengthening as the building was not designed to support the new higher loadings. The project designer studied various strengthening methods and finally approved the use of FRP materials to strengthen the building. Beyond the strengthening, the building must adhere to the stringent fire-rating requirement with the ability to withstand fire for 90 min for the slabs and 120 min for both the beams and columns.

2.1 *Technique of Strengthening*

As both beams and slabs were found to be deficient, the project designer considered various strengthening techniques based on their advantageous and cost benefits. Conventional techniques of strengthening such as concrete enlargement and steel-plate bonding were considered but were found to be unsuitable due to additional dead loads, higher cost of construction and time consuming. As such, the advanced technique of strengthening using the FRP technology was considered and accepted.

2.2 *Selection Criteria of FRP for Strengthening*

The FRP strengthening system selected for this project comprised of the Carbon FRP composite systems and E-glass FRP composite systems under the TYFO® Fibrwrap® Composite System. It is made up of E-glass fibres and is stitched bonded by a process that is able to assemble a variety of materials into a single composite material. This composite meets the demands of the construction industry for a lightweight, easily applicable, structurally powerful, and reasonably priced retrofit material. This particular system has been thoroughly tested worldwide and conforms to ICBO AC125's [2], ICBO material characterization, stringent system testing, and durability requirements. Under guidelines from ICBO AC125 [2], the system selected must be tested over a long period of time to ensure repeatability and reliability of its composite properties and performance.

In ACI440.2R-2017 [1], there is a specific requirement to only allow for the use of systems in strengthening projects that are fully tested, certified and well-supported with test reports, research papers and other relevant technical documents showing their effectiveness in structural strengthening.

Table 1 Properties of the Carbon FRP and E-glass FRP composite system

Type of FRP composite system	Tensile strength (MPa)	Elastic Modulus (GPa)	Ultimate strain (%)
Tyfo® SEH51A E-glass FRP	575	26.1	2.20
Tyfo® SCH11UP Carbon FRP	1062	102.0	1.05
Tyfo® SCH41 Carbon FRP	986	95.8	1.00

The properties of the FRP are governed by the individual properties of the constituents. In particular, the properties of the unidirectional FRP are substantially higher in the longitudinal direction than in the transverse direction. It is the longitudinal properties of FRP that are mentioned in this literature for comparative purposes. Properties of the Carbon FRP composite systems and E-glass FRP composite systems used in this project are summarized in Table 1.

2.3 Design of FRP for Strengthening

The strengthening to the beams and slabs using FRP strengthening system was targeted to satisfy the required shear, positive and negative moments as provided by the project designer. Following ACI 440.2R-2017 [1], the strengthening design must satisfy the requirement of strain compatibility and force equilibrium with consideration of the tensile force contributions from the existing steel reinforcements and the FRP strengthening system. The deflection of the beams and slabs was checked to satisfy the allowable deflection as required under the code.

2.4 Stringent Project Requirement for Structural and Fire Safety

As this is a high profile project with stringent structural and fire safety requirement as set forth by the project owner and project designer, the scopes of the project required that in situ load test be conducted on the strengthened structural members and fire test must be conducted separately on the fire-protection materials prior to the application of the fire-protection materials for fire-protection to the FRP Composite Systems. The purpose of the load test is to demonstrate the effectiveness of strengthening by the FRP Composite Systems, while also demonstrating good adhesion between RC beams and slabs and FRP material. The requirement for fire-resistant materials for the FRP is to ensure that the structure still works safely with a fire-resistance duration of 120 min.

3 Project Implementation

With a tight project duration of 60 days, the strengthening work to the beams and slabs was carried out with simultaneous action taken to conduct the fire test and in situ load test. The following sections will provide the full account on the full procedure and the result of the fire test and in situ load test.

3.1 Fire Testing for 2-H Fire Rating on FRP Composite Systems

To meet the fire-rating of 120 min, the FRP material is protected by a fire-resistant material called Tyfo® VG. The thickness of the fire-resistant material varies depending on the fire-rating. The thicker the Tyfo® VG the higher the fire resistance. In this project, a thickness of 30 mm is used to satisfy the fire-rating of 120 min. 480 × 480 × 50mm RC slabs with M300 concrete were fabricated with 4 holes in each plate to cater for temperature measurement of the FRP materials by sensors during the fire test (Fig. 1). The RC slabs were enhanced with 2 layers of Tyfo® SCH41 composite in the direction perpendicular to each other and then protected with 30 mm thick of Tyfo® VG material. The Tyfo® VG was installed with a thickness of 5–7 mm each time and built up until a thickness of 30 mm is achieved (Fig. 2). The completed test slab specimens were cured at ambient condition for 72 h before the fire test (Figs. 3 and 4). The temperature is increased in accordance with the specification. The thermal increment is shown in Fig. 5. After test, the results showed that the fire-resistant material has passed the fire test according to TCVN2622-1995, satisfying two criterias of structural integrity and insulation. Integrity requires that the Tyfo® VG does not debond after the test. The insulation requires that the temperature of the FRP does not its critical temperature of 260 °C with the overall average temperature

Fig. 1 Strengthened specimen

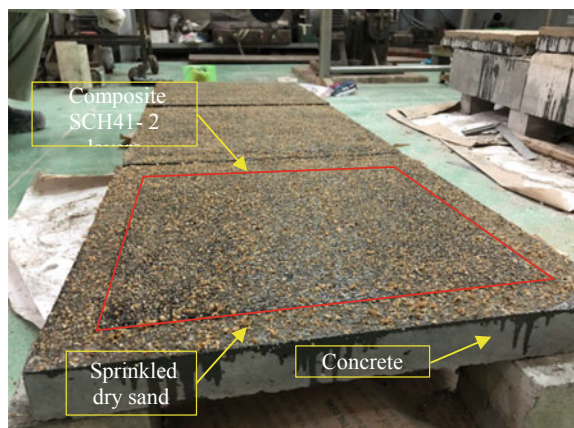


Fig. 2 Fire-proofed strengthened specimen

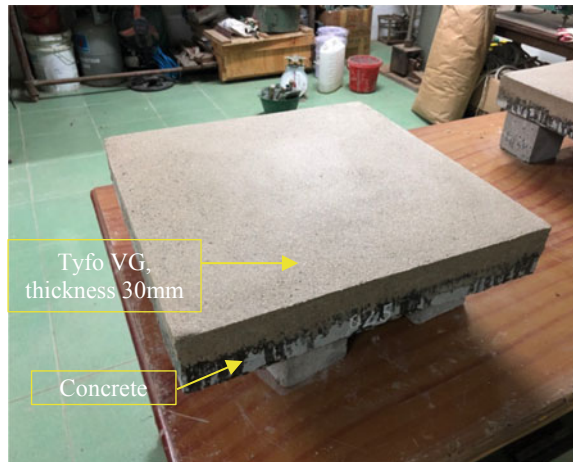


Fig. 3 Specimen is set in the burning room



Fig. 4 Specimen after the test



Fig. 5 Temperature versus time curve

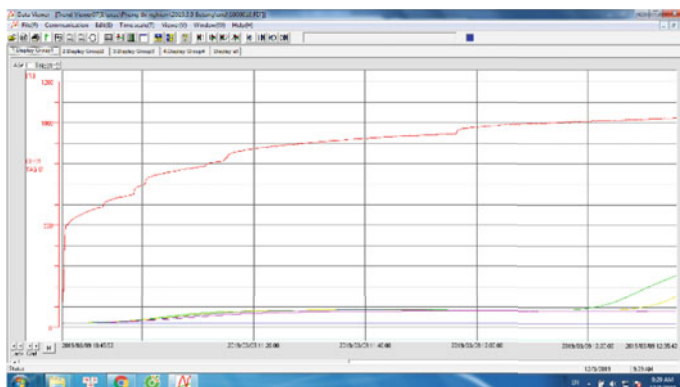
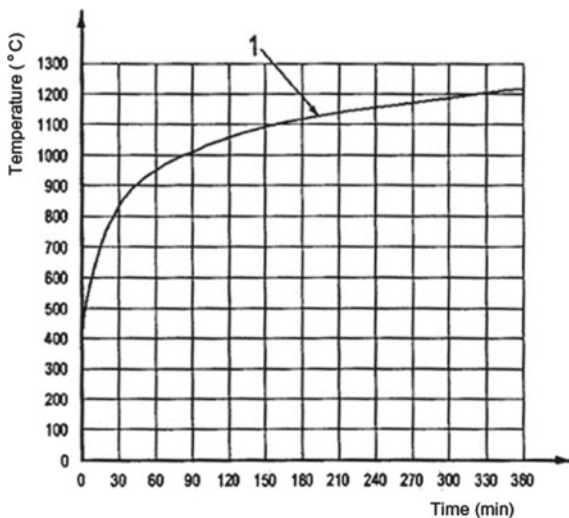


Fig. 6 Temperature recorded by thermal gauges

of the 4 probes below 170 °C. The results showed that after 120 min, the highest recorded temperature was 215 °C with the average as 150 °C (Fig. 6).

3.2 In Situ Load Testing on Beams and Slabs Strengthened By FRP Composite Systems

To verify the effectiveness of strengthening as well as the adhesion quality of FRP used in the project, the pre- and post-load test of the structure were carried out. A RC slab and a RC beam at first floor of the building were selected for the test and their

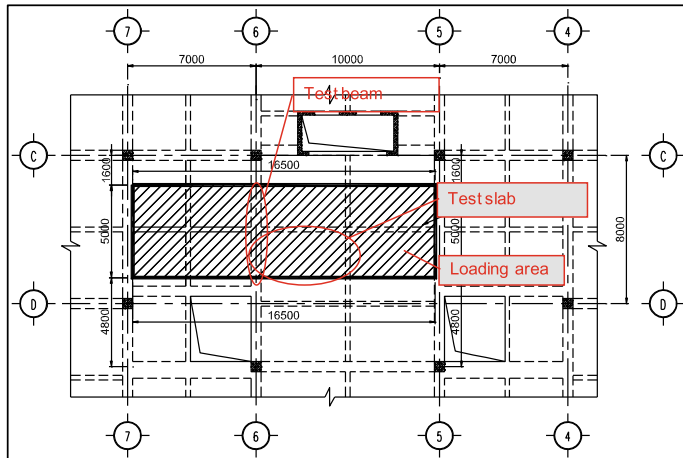


Fig. 7 Layout of load test

location of slab and beam are shown in Fig. 7. The dimension of the beam is $550 \times 600 \times 12,000$ mm and the slab is 4000×5000 mm with thickness of 140 mm. The slab was strengthened with Glass FRP, Tyfo® SEH25A, while the beam was strengthened with Carbon FRP, Tyfo® SCH41. Water was used for the load test by filling a temporary tank of 5000×16500 mm with height 675 mm installed on the first floor of the building. The maximum water height corresponds to the maximum design imposed live load for the structure which is equivalent to the design live load of 700 kg/m^2 . The loading process was carried out over 5 load increments with each increment having a load corresponding to 20% of the maximum load. After each increment, readings from the strain gauges and on the deflection were recorded. Upon achieving the full load for the test, the load was maintained for a duration of 24 h to monitor the variation of deflection and deformation of RC beam and RC slab. The monitoring equipment was set at the middle section of the beam and the slab as shown in Fig. 8.

During the load test preparation, strain gauges were installed before the strengthening to the selected RC beams and RC slabs. Both the deflection and deformation of the beam and slab were measured before and after the strengthening. The details of the installation of measuring devices are shown in Figs. 9 and 10.

Deflection result and the stress versus deformation results of beam and slab before and after strengthening are shown in Tables 2 and 3 respectively. The strain versus load level of concrete and FRP material in the beam and slabs before and after strengthening are shown in Figs. 13 and 14. From the result from Table 2, Figs. 11 and 12, the strengthening to beams and slabs have shown slight improvement to their rigidity. The measurements showed lower deflection in the strengthened beam and slab. From the data in Tables 3 and 4, Figs. 13 and 14, it showed that the stress and deformation values of beam, slab and FRP composites are smaller than the allowable values. The result showed that the FRP material is effective in strengthening the RC

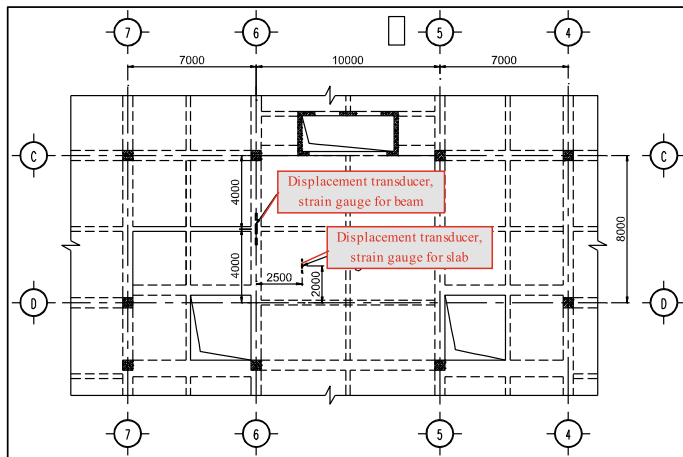


Fig. 8 Location of displacement transducer and strain gauges

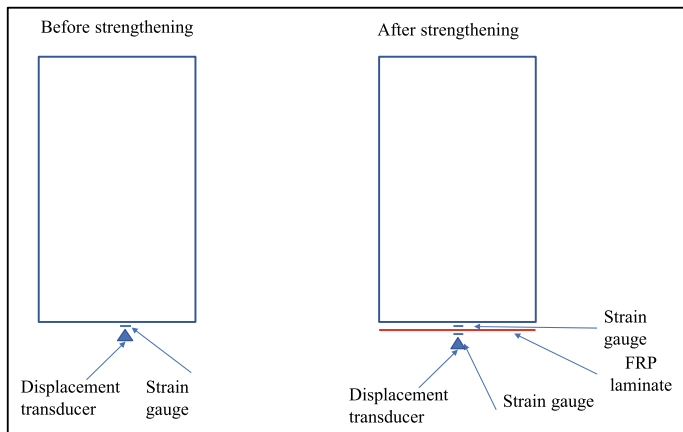


Fig. 9 Location of strain gauge on RC beam before and after strengthening

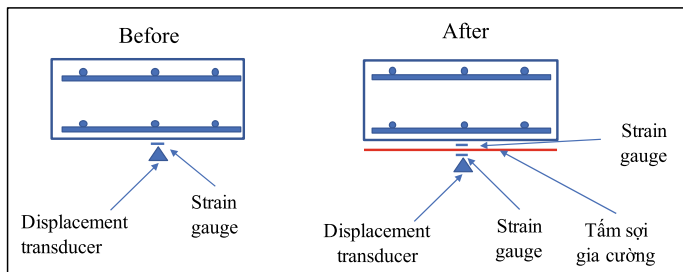


Fig. 10 Location of Strain gauge on slab before and after strengthening

Table 2 Data on deflection of beam and slab before and after reinforcement

Load level (%)	Slab			Beam		
	Before (mm)	After (mm)	Comparison (%)	Before (mm)	After (mm)	Comparison (%)
0	0.00	0.00		0.00	0.00	
20	0.74	0.73	99.3	0.45	0.44	97.8
40	1.53	1.42	92.8	1.03	0.99	95.6
60	2.20	2.11	95.7	1.54	1.49	97.1
80	2.99	2.80	93.6	2.11	2.00	94.8
100	3.82	3.34	87.5	2.65	2.26	85.4

members with reduced deformation. The deformation of FRP and concrete are similar indicating their composite behavior during the load bearing process of the structure. The bonding between FRP and concrete is good.

4 Conclusions

From the result of the insitu load test, the FRP strengthening system has proven effective. The deflections of the strengthened RC members are lower than the unstrengthed at each corresponding increment applied. Experimental results also exhibited the good adhesion properties between FRP materials and concrete indicating good composite action. Fire-resistant material tested as effective in protecting the FRP material against fire at 1000 °C for up to 120 min and also maintaining its integrity and insulating ability to the FRP composite. This method of strengthening has helped in reducing the project time and brought along significant cost savings to the project owner. Through this project and the tests involved, it is a significant milestone achieved in Vietnam to satisfy both strengthening and fire-rating requirements with added benefits from cost and time savings. This approach can be used for structures in petrochemical plants and key government institutions for blast mitigation.

Table 3 Data on deformation of slab and beam

Load level %	Slab			Beam			FRP material SCH41 10 ⁻⁶	Comparison of concrete strain (%)
	Concrete strain before reinforcement 10 ⁻⁶	Concrete strain after reinforcement 10 ⁻⁶	FRP material SEH25A 10 ⁻⁶	Concrete strain before reinforcement 10 ⁻⁶	Concrete strain after reinforcement 10 ⁻⁶	Concrete strain after reinforcement 10 ⁻⁶		
0	(5.04)	(4.66)	(6.96)	92.5	6.35	5.21	2.10	82.0
20	3.30	2.43	2.55	73.7	13.73	12.50	14.38	91.1
40	17.04	13.06	13.75	76.6	22.97	21.30	22.59	92.7
60	34.59	27.20	28.71	78.7	30.42	26.16	27.12	86.0
80	42.76	36.77	38.29	86.0	36.29	33.21	33.56	91.5
100	52.33	44.90	45.64	85.8	40.50	37.23	38.50	91.9

Fig. 11 Displacement versus loading curves of slab

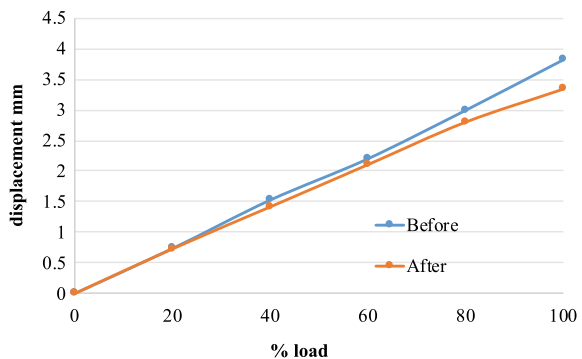


Fig. 12 Displacement versus loading curve of beam

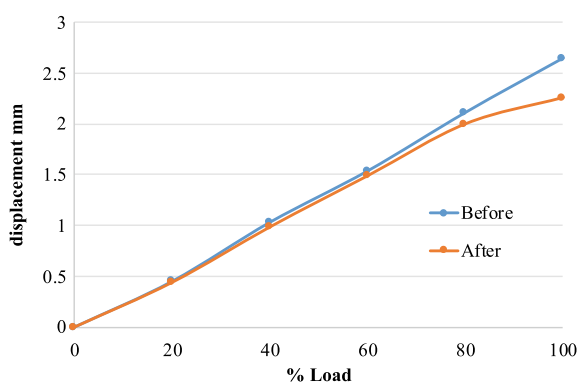


Table 4 Calculation of maximum stress in concrete and FRP material before and after strengthening

Item	Before and after strengthening	Concrete			FRP laminate (SEH25A#/SCH41*)		
		Tensile Modulus (MPa)	Max strain ϵ	Stress $\alpha = E \times \epsilon$ (MPa)	Tensile Modulus (MPa)	Max strain ϵ	Stress $\alpha = E \times \epsilon$ (MPa)
Slab	Before	24,631	52.23×10^{-6}	1.29			
	After	24,631	44.9×10^{-6}	1.10	20,900 [#]	45.64×10^{-6}	0.95
	Allowable value			2.54			417
	Check			OK			OK
Beam	Before	24,631	40.5×10^{-6}	0.99			
	After	24,631	37.2×10^{-6}	0.92	82,000*	38.5×10^{-6}	3.16
	Allowable value			2.54			834
	Check			OK			OK

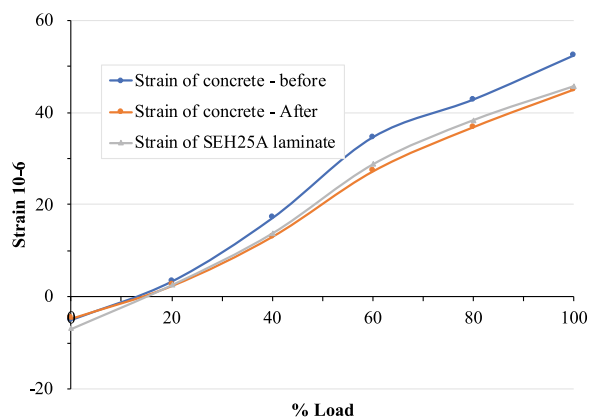
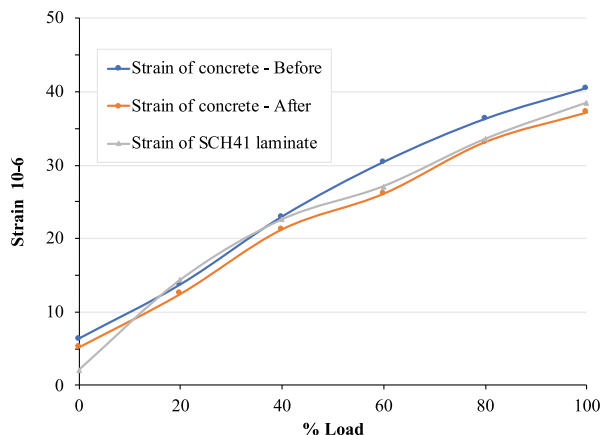
Fig. 13 Comparison of strain of concrete before and after strengthening and SEH25A Laminate

Fig. 14 Comparison of strain of concrete before and after strengthening and SCH41 Laminate



References

1. American Concrete Institute (ACI 440.2R-17) Guide for the design and construction of externally bonded FRP systems for strengthening concrete structures: Reported by ACI Committee 440:3-15. USA (2017)
2. ICC (ICBO) Evaluation Service (AC125) Interim criteria for concrete and reinforced and unreinforced masonry strengthening using fibre-reinforced polymer (FRP), composite system; California: USA (2003)

Damage Detection in Plates with Different Boundary Conditions Using Improved Modal Strain Energy Method



Thanh-Cao Le, Tan-Thinh Nguyen, Thanh-Canh Huynh, and Duc-Duy Ho

1 Introduction

In the last two decades, structural health monitoring (SHM) has been playing a very important role for the safety and sustainable performance of construction structures. The non-destructive detection methods for diagnosing structural failures, especially methods based structural vibration responses, have received the attention of many researchers [2]. Modal strain energy (MSE) is one of the highly effective methods for detecting damages in structures. Stubbs et al. [9] first applied the concept of MSE method to detect the damage of structures based on the changes in modal strain energy of structures. Subsequently, Cornwell et al. [1] extended MSE method for an index of damage in plate-like structure characterized by two-dimensional curvatures. In their method, the fractional strain energy of the plate before and after crack occurrence was used to calculated a damage index which can successfully locate the area with stiffness reduction as low as 10% using relatively few modes. Furthermore, in their experimental validation, two edge cracks with certain severities were identified by damage index. Kim et al. [6] applied the modal strain energy method for simple beam structure and accurately estimated the damage position in the middle and in a quarter span with only two mode shapes. The severity of damage in the beam is also determined accurately. Hu and Wu [4] developed a non-destructive damage detection method using experimental results to detect surface cracks in a thin aluminum plate under a completely free boundary condition. Only few mode shapes of the plate

T.-C. Le · T.-T. Nguyen · D.-D. Ho (✉)

Faculty of Civil Engineering, Ho Chi Minh City University of Technology (HCMUT),
VNU-HCM, Ho Chi Minh City, Vietnam
e-mail: haducduy@hcmut.edu.vn

T.-C. Le

Faculty of Civil Engineering, Nha Trang University, Nha Trang, Vietnam

T.-C. Huynh

Faculty of Civil Engineering, Duy Tan University, Da Nang, Vietnam

before and after occurrence of crack are required to calculate the modal strain energy and damage index. The differential quadrature method used to calculate the second derivative of the mode shapes in strain energy formula by using only displacement data at nodes. Hu et al. [5] detected damage in circular hollow cylinder using modal strain energy and scanning damage index methods. Le and Ho [7] developed modal strain energy method for thin plate under different boundary conditions. In this study, Modal Strain Energy (CDM) was used to calculate the second derivative of the mode shapes. Fu et al. [3] established a two-step procedure using the modal strain energy method for diagnosing plate structures using isotropic homogeneous materials: the first step focuses on detection of damage area; in the second step, the locations and extents of the damages are identified. Loendersloot et al. [8] applied damage index successfully on monitoring of a composite plate with stiffeners.

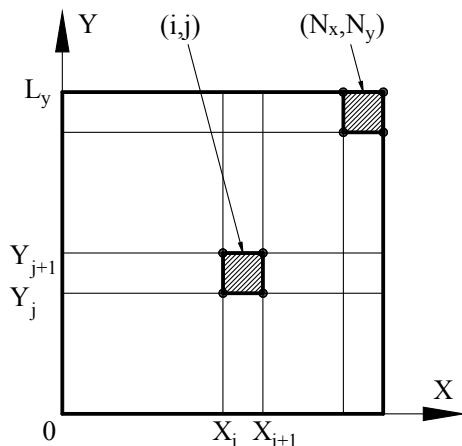
For most of previous proposed studies, MSE is deployed for the structure at global level. This procedure requires a massive displacement data throughout the plate to ensure the accuracy of the diagnosis. It isn't only expensive but also complex in practice. In this study, MSE is improved and applied to the preliminary damaged area. As a result, required data are reduced significantly but still ensure the accuracy of the diagnostic results.

2 Modal Strain Energy-Based Damage Detection Method

2.1 Global Modal Strain Energy Method

For plate structures, the mode shape is characterized by a two-dimensional surface. Considering a plate subdivided into $N_x \times N_y$ sub-regions and each sub-region (i,j) is located by the coordinates of two points (x_i, y_j) and (x_{i+1}, y_{j+1}) as shown in Fig. 1.

Fig. 1 Schematic of plate structure



Model and analysis the free vibration of plate using finite element analysis (FEA) in two states: before and after the occurrence of damage with the different boundary conditions. In this step, the rough model mesh is used for FEA. The outputs of this step are mode shape data of plate in both states.

For a particular mode shape ϕ_k , the modal strain energy of the sub-region (i, j) is determined as follows:

$$U_{k,ij} = \frac{D_{ij}}{2} \int_{y_j}^{y_{j+1}} \int_{x_i}^{x_{i+1}} \left[\left(\frac{\partial^2 \phi_k}{\partial^2 x} \right)^2 + \left(\frac{\partial^2 \phi_k}{\partial^2 y} \right)^2 + 2\nu \left(\frac{\partial^2 \phi_k}{\partial^2 x} \right) \left(\frac{\partial^2 \phi_k}{\partial^2 y} \right) 2(1-\nu) \left(\frac{\partial^2 \phi_k}{\partial x \partial y} \right)^2 \right] dx dy \quad (1)$$

where D_{ij} is the flexural stiffness of the sub-region (i, j) ; ν is the coefficient of Poisson.

Total strain energy of the plate during elastic deformation is given by:

$$U_k = \sum_{i=1}^{N_x} \sum_{j=1}^{N_y} U_{k,ij} \quad (2)$$

The second derivative of the mode shape (mode shape curvature) is also determined by the center differential method (CDM), as follows:

For the midpoints:

- For the nodes N_{ij} in x -direction, where $i = 2, 3, \dots, N_y; j = 2, 3, \dots, N_x$

$$\frac{\partial^2 \phi_{k,ij}}{\partial^2 x} = \frac{\phi_{k,i(j-1)} - 2\phi_{k,ij} + \phi_{k,i(j+1)}}{(s_x)^2} \quad (3)$$

$$\frac{\partial^2 \phi_{k,ij}}{\partial^2 y} = \frac{\phi_{k,(i-1)j} - 2\phi_{k,ij} + \phi_{k,(i+1)j}}{(s_y)^2} \quad (4)$$

where, s_x and s_y are grid space in x -direction and y -direction, respectively.

For boundary points:

- For free and pin boundary conditions:

$$\frac{\partial^2 \phi_{k,1j}}{\partial^2 x} = \frac{\partial^2 \phi_{k,(N_x+1)j}}{\partial^2 x} = 0 \quad (5)$$

$$\frac{\partial^2 \phi_{k,i1}}{\partial^2 y} = \frac{\partial^2 \phi_{k,i(N_y+1)}}{\partial^2 y} = 0 \quad (6)$$

- For fixed boundary condition: the displacement value at the virtual marginal point is determined by extrapolation using 3-level polynomial function. The virtual

marginal point is a grid point combining with a real marginal point and a boundary point to form a smooth curve.

The fractional strain energy the sub-region (i, j) is determined as follows:

$$F_{k,ij} = \frac{U_{k,ij}}{U_k} \quad (7)$$

where $\sum_{i=1}^{N_x} \sum_{j=1}^{N_y} F_{k,ij} = 1$.

Considering m mode shapes, the damage index of the sub-region (i, j) is defined as:

$$\beta_{ij} = \frac{\sum_{k=1}^m F_{k,ij}^*}{\sum_{k=1}^m F_{k,ij}} \quad (8)$$

where, the symbol * denotes damaged state of the structure.

The damage index after normalization is determined as follows:

$$Z_{ij} = \frac{\beta_{ij} - \bar{\beta}_{ij}}{\sigma_{ij}} \quad (9)$$

where $\bar{\beta}_{ij}$, σ_{ij} are mean and standard deviation of the damage indices, respectively.

Compare the damage index with the damage threshold to determine preliminary damaged area. In this study, the damage threshold Z_o , as illustrated in Fig. 2, is defined as the percentage of the largest damage index across the whole plate (Z_{ij}^{\max}). When the damage index of an element is greater than or equal to the damage threshold,

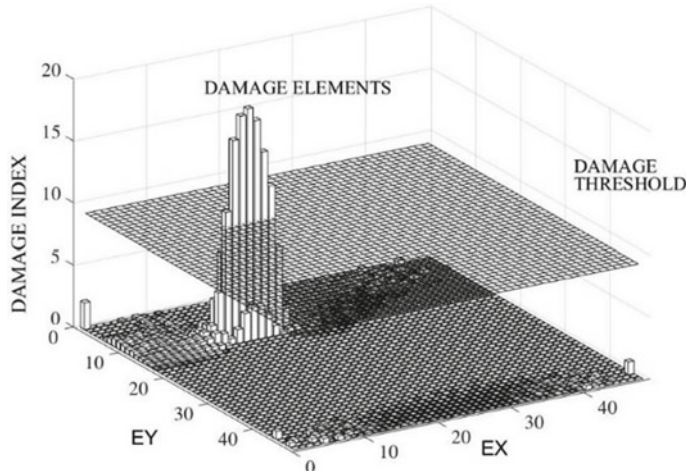


Fig. 2 Illustration of damage threshold

the element is considered to be damaged and shown on the chart; and vice versa, the element is considered undamaged. The locations of cracks are determined based on truncated damage index chart. Preliminary damaged area is a rectangular zone covering the damaged elements.

2.2 Local Modal Strain Energy Method

After deploying the global MSE method on the whole plate structure with low resolution mesh, the preliminary damaged area is determined. Next, the MSE method is applied separately to each of localized failure zones (Fig. 3) with a higher resolution mesh to determine in more detail the location and the severity of the cracks.

The mode shape curvature is also determined by CDM. For the midpoints, Eqs. (3) and (4) are used. For the boundary nodes of the local damaged zone, the mode shape curvature is calculated from the displacement data at the true boundary points of the damaged zone. This is different from the global MSE method, which requires displacement data at virtual marginal points. In order to assess the accuracy of the method, a detect capability index (DCI) is proposed as follows:

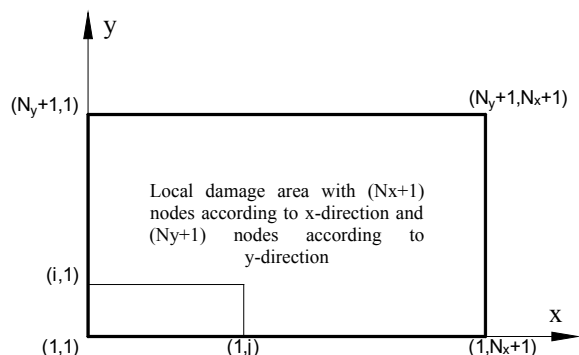
$$\text{DCI} = \frac{L_{\text{pred}}}{L_{\text{real}}} \times 100\% \quad (10)$$

where L_{pred} is the crack's length detected from the damage index chart; L_{real} is the actual crack's length. Based on the DCI index, the damage detection results are evaluated as follows:

- If $0 \leq \text{DCI} < 50\%$: detect capability is bad (B).
- If $50\% \leq \text{DCI} \leq 80\%$: detect capability is moderate (M).
- If $80\% < \text{DCI} \leq 100\%$: detect capability is good (G).

It should be noted that this is a reverse diagnostic problem, without the information of damage. The input data are the mode shape of plate in the two state: before and

Fig. 3 Scheme of local damage area



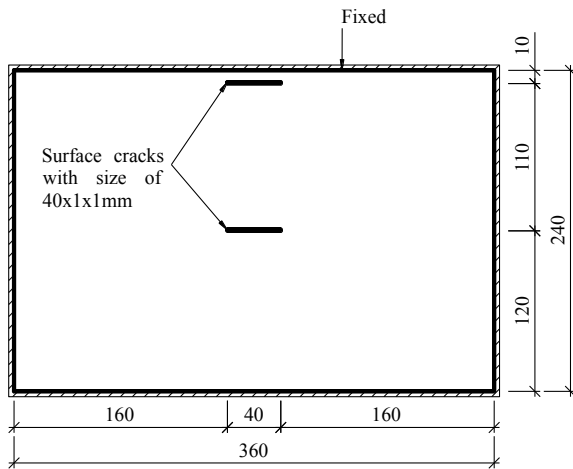


Fig. 4 Rectangular plate with two cracks

after the occurrence of cracks. By applying MSE method (global and local), location and length of the cracks are detected.

3 Numerical Verification

3.1 Properties of Plate

An aluminum plate is $360 \times 240 \times 2$ mm in size, four edges are fixed; there are two cracks with the size of $40 \times 1 \times 1$ mm; one crack is in the middle and another is at the edge of the plate (Fig. 4). Material properties of the plate: mass per unit volume $\rho = 2735 \text{ kg/m}^3$, modulus of elasticity $E = 70 \text{ GPa}$, Poisson's ratio $\nu = 0.33$. The strain energy method is deployed in two steps. In the first step, MSE is applied on whole plate with 10-mm-element mesh to determine the preliminary damaged area. In the next step, MSE is applied on the area determined in first step with a 1-mm-element mesh to determine the position and length of the cracks in more detail.

3.2 Modal Analysis

ANSYS software is used to simulate and analyze free vibration for tested plate structure. Figure 5 shows the first four mode shapes for the undamaged state. The vibration frequency results are summarized in Table 1. When there are damages, the natural frequency decreases lightly.

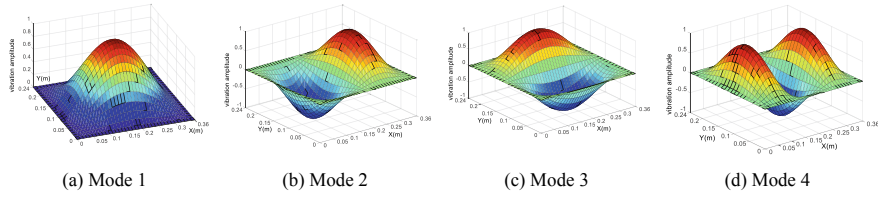


Fig. 5 First four mode shapes

Table 1 Natural frequencies for the first four modes

Mode	Frequency before damage (Hz)	Frequency after damage (Hz)	Difference (%)
1	222.82	220.12	1.21
2	342.43	342.34	0.03
3	547.01	542.9	0.75
4	547.13	546.61	0.10

4 Results and Discussions

4.1 Global Detection

Figure 6 shows the damage index chart Z_{ij} corresponding to the damage threshold $30\%Z_{ij}^{\max}$, where Z_{ij}^{\max} is the maximum damage index. In this study, three types of combination of mode shapes are examined: using only mode shape; combination of two mode shapes and combination of three mode shapes. The global diagnostic results show that two damaged areas are accurately located when using the appropriate damage threshold and mode shapes.

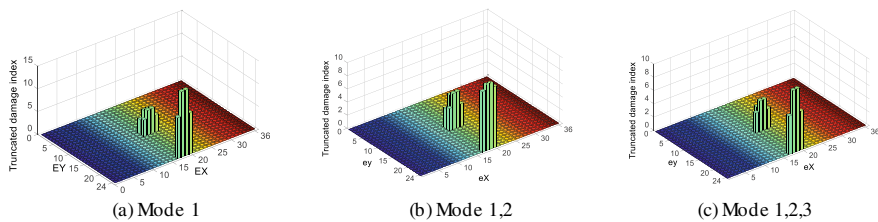


Fig. 6 Damage index charts, threshold $30\%Z_{ij}^{\max}$, 10-mm mesh

4.2 Local Detection

After applying the global MSE method on the whole plate, the preliminary damaged areas are identified as a rectangle with a size of 60×20 mm (Fig. 7). The MSE method is deployed on these areas with the 1-mm grid to evaluate the efficiency in diagnosing of cracks. The diagnosis results are shown in Figs. 8 and 9 and summarized in Tables 2 and 3. It is clear from the results that the MSE method determines accurately the length of the crack when using the appropriate damage threshold.

Fig. 7 Preliminary damaged area detected from global detection, 10-mm mesh

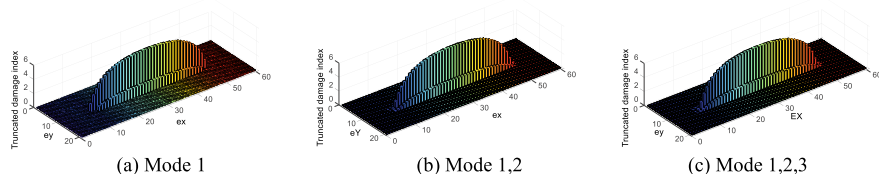
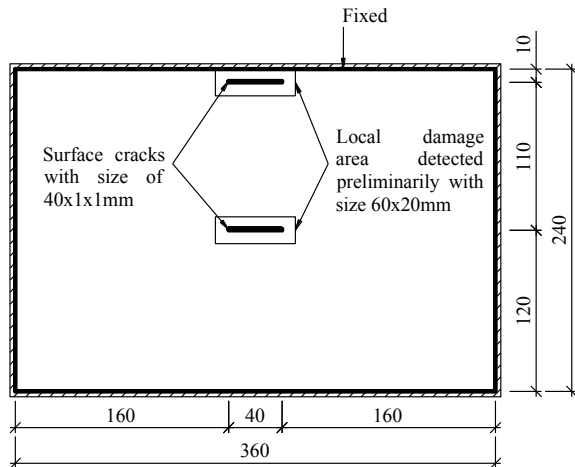


Fig. 8 Damage index charts, threshold $30\%Z_{ij}^{\max}$, 1-mm mesh, boundary crack

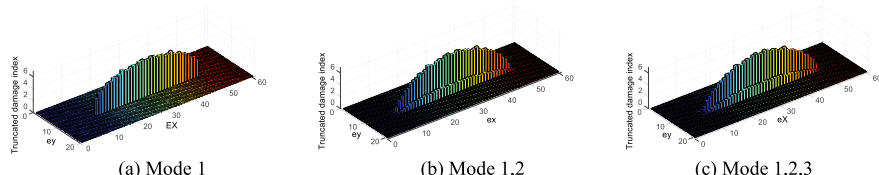


Fig. 9 Damage index charts, threshold $30\%Z_{ij}^{\max}$, 1-mm mesh, middle crack

Table 2 DCI for the boundary crack

Threshold % Z_{ij}^{max} (%)	Mode 1	Mode 2	Mode 3	Mode 4	Mode 1 + 2	Mode 1 + 2 + 3
10	98 (G)	98 (G)	98 (G)	Noise	98 (G)	98 (G)
20	93 (G)	97 (G)	93 (G)	Noise	93 (G)	93 (G)
30	85 (G)	95 (G)	85 (G)	Noise	85 (G)	83 (G)
40	70 (M)	93 (G)	78 (M)	Noise	70 (M)	70 (M)
50	90 (G)	95 (G)	85 (G)	Noise	95 (G)	95 (G)

Table 3 DCI for the middle crack

Threshold % Z_{ij}^{max} (%)	Mode 1	Mode 2	Mode 3	Mode 4	Mode 1, 4	Mode 1, 2, 4	Mode 1, 2, 3
10	93 (G)	87 (G)	58 (M)	95 (G)	95 (G)	94 (G)	90 (G)
20	73 (M)	62 (M)	43 (B)	77 (M)	73 (M)	73 (M)	73 (M)
30	95 (G)	95 (G)	48 (B)	95 (G)	95 (G)	98 (G)	95 (G)
40	90 (G)	80 (G)	43 (B)	95 (G)	90 (G)	90 (G)	88 (G)
50	85 (G)	75 (M)	38 (B)	90 (G)	90 (G)	85 (G)	85 (G)

5 Conclusions

In this study, the MSE method was improved successfully for detecting global and local damage in like-plate structures. From the analysis results, the important conclusions were drawn as follows:

- (1) The proposed method has the ability to accurately detect cracks in like-plate structures with different boundary conditions when using the appropriate mode shapes and threshold. The global step locates the preliminary damaged areas. The local step identifies the exact length of the cracks.
- (2) In the local step, the plate's boundary condition and the modal data at the nodes outside the damaged area don't need to consider. Thus, the displacement data decrease significantly and the analysis time is shortened.
- (3) The using of the three first modes with a damage threshold 10% of the maximum damage index is good enough to accurately detect the location and the length of the cracks in like-plate structures, for both cracks at border and in the middle of the plate.

Acknowledgements This research is funded by Ho Chi Minh City University of Technology (HCMUT) - VNU-HCM, under grant number BK-SDH-2020-1880698.

References

1. Cornwell PJ, Dobeling SW, Farrar CR (1999) Application of the strain energy damage detection method to plate-like structures. *J Sound Vib* 224:359–374
2. Fan W, Qiao P (2011) Vibration-based damage identification methods: a review and comparative study. *Struct Health Monit* 10:83–111
3. Fu YZ, Liu JK, Wei ZT, Lu ZR (2016) A two-step method for damage identification in plates. *J Vib Control* 22(13):3018–3031
4. Hu HW, Wu CB (2008) Nondestructive damage detection of two dimensional plate structures using modal strain energy method. *J Mech* 24:319–332
5. Hu HW, Wu CB, Lu WJ (2011) Damage detection of circular hollow cylinder using modal strain energy and scanning damage index methods. *Comput Struct* 89:149–160
6. Kim JT, Ryu YS, Cho HM, Stubbs N (2003) Damage identification in beam-type structures: frequency-based method versus mode shape-based method. *Eng Struct* 25(1):57–67
7. Le TC, Ho DD (2015) Damage detection in plate-like structures using modal strain energy-based method. *J Constr* 6:100–105
8. Loendersloot R, Ooijevaar TH, Warnet L (2017) Vibration based SHM of a composite plate with stiffeners. In: International conference on noise and vibration engineering, Belgium: ISMA, 2007–2015
9. Stubbs N, Kim JT, Farrar CR (1995) Field verification of a nondestructive damage localization and sensitivity estimator algorithm. In: Proceedings of the 13th international modal analysis conference, pp 210–218

Dynamic Analysis of Beams on Nonlinear Foundation Considering the Mass of Foundation to Moving Oscillator



Trong Phuoc Nguyen and Minh Thi Ha

1 Introduction

Analyzing dynamic behavior of beams on the ground bearing moving loads is one of the topics having been interested in for more than a decade and the special consideration in nonlinear foundation including analytical and numerical solutions has been indicated in many studies as Ding et al. [2], Froio et al. [3], Jorge et al. [4], Rodrigues et al. [10], Younesian et al. [11] and Zhou et al. [12]. Nowadays, the interest has been increasing rapidly thank to the improvement in transport system. This topic is applied in designing building structures like airport runway surface, train rails, bridge structure and horizontal fluid conduit etc. For some types of soil, modern high-speed trains could move at the same speed as the smallest phase velocity of the propagating wave in the elastic substrate [1, 5, 6], displacement due to vibrating causes can be significantly larger due to static load. Therefore, it is interesting to study the dynamic reaction of structures supporting motion mechanical systems to minimize the above-mentioned impacts.

Most models used in reality or research have a common feature not to mention the influence of the mass of foundation during the analysis. But the fact is that the ground has mass, so the mass of foundation will have some influence on the behavior of the structure. Therefore, the problem of analyzing the effect of the mass of foundation on the dynamic behavior of the structure interacting with the foundation is really necessary and deserves attention. But in most studies, this has not been really focused on. Therefore, there have been very few works published in recent years.

T. P. Nguyen (✉)

Faculty of Civil Engineering, Ho Chi Minh City Open University, Ho Chi Minh City, Vietnam
e-mail: phuoc.nguyen@ou.edu.vn

M. T. Ha

Faculty of Civil Engineering, Ho Chi Minh City University of Technology, Ho Chi Minh City, Vietnam

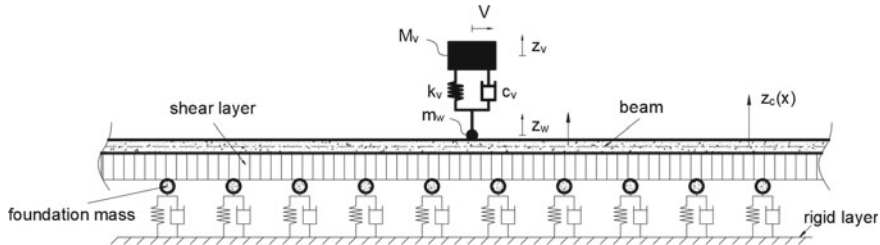


Fig. 1 Problem model

Pham et al. [9] experiments determine the effect of the mass of foundation on the natural frequency of the plate on the elastic foundation, the experimental results show that the mass of foundation involved in vibration is a significant influence on dynamic characteristics of the plate. Nguyen et al. [8] proposed a new model for dynamic analysis of beams on a nonlinear foundation subject to moving mass. This model includes linear and nonlinear Winkler foundation parameters, Pasternak linear foundation parameters, viscous coefficient and special consideration of the influence of the mass of foundation parameters.

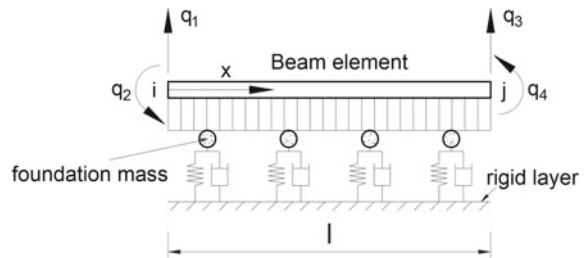
Through what the author has presented above, the problem of considering the effect of the mass of foundation on the behavior of beams is still quite new and there has not been much research on it (Fig. 1).

2 Formulation

Consider a simply supported beam of length L , height h , width b , Young's modulus E , density mass of the beam ρ and the foundation mass m_f . Based on finite element method, the beam is discretized to n element of length l . Each element has two nodes, two degrees of freedom per node as Fig. 2.

The generalized displacements and transverse of the element are as follows

Fig. 2 Beam element



$$\mathbf{q}^e = \{ q_1 \ q_2 \ q_3 \ q_4 \}^T$$

$$z_c(x, t) = \{ N_1(x) \ N_2(x) \ N_3(x) \ N_4(x) \} \begin{Bmatrix} q_1(t) \\ q_2(t) \\ q_3(t) \\ q_4(t) \end{Bmatrix} = \mathbf{N}^e(x) \mathbf{q}^e(t) \quad (1)$$

The total kinetic energy of the beam and foundation of the element

$$T = T_b + T_f = \int_0^l dT_b + \int_0^l dT_f = \frac{1}{2} \int_0^l m_f \dot{z}_c(x, t)^2 dx$$

$$+ \frac{1}{2} \int_0^l \rho A \dot{z}_c(x, t)^2 dx = \frac{1}{2} (\dot{\mathbf{q}}^e)^T \mathbf{M}_b^e \dot{\mathbf{q}}^e + \frac{1}{2} (\dot{\mathbf{q}}^e)^T \mathbf{M}_f^e \dot{\mathbf{q}}^e \quad (2)$$

where, \mathbf{M}_b^e and \mathbf{M}_f^e are the elementary consistent beam's and foundation's mass matrices given as

$$\mathbf{M}_b^e = \int_0^l \mathbf{N}^e(x)^T \rho A \mathbf{N}^e(x) dx = \frac{\rho Al}{420} \begin{bmatrix} 156 & 22l & 54 & -13l \\ 22l & 4l^2 & 13l & -3l^2 \\ 54 & 13l & 156 & -22l \\ -13l & -3l^2 & -22l & 4l^2 \end{bmatrix}$$

$$\mathbf{M}_f^e = \int_0^l \mathbf{N}^e(x)^T m_f \mathbf{N}^e(x) dx \quad (3)$$

The beam elastic strain energy is given as

$$U_b = \frac{1}{2} \int_V \sigma_{xx} \varepsilon_{xx} dV = \frac{1}{2} \int_0^l M \frac{\partial^2 z_c}{\partial x^2} dy = \frac{1}{2} (\mathbf{q}^e)^T \mathbf{K}_b^e \mathbf{q}^e \quad (4)$$

in which \mathbf{K}_b^e is the elementary beam's stiffness matrix as follows

$$\mathbf{K}_b^e = \frac{EI_y}{l^3} \begin{bmatrix} 12 & 6l & -12 & 6l \\ 6l & 4l^2 & -6l & 2l^2 \\ -12 & -6l & 12 & -6l \\ 6l & 2l^2 & -6l & 4l^2 \end{bmatrix} \quad (5)$$

Reaction on each unit of length is $F_f = F_l + F_{nl} = k_l z_c + k_s \nabla^2 z_c + k_{nl} z_c^3$, where k_l is the Winkler linear elastic parameter, k_s is the Pasternak shear layer parameter, and k_{nl} is the nonlinear elastic parameter. So that, elastic strain energy on each unit of length is given as

$$u_f = \int_0^{z_c} F_f dz_c = \frac{1}{2} k_l z_c^2 + \frac{1}{2} k_s \nabla^2 z_c^2 + \frac{1}{4} k_{nl} z_c^4 \quad (6)$$

The elastic strain energy of the foundation and potential of the forces are as follows

$$\begin{aligned} U_f &= \int_0^l u_f dz_c = \int_0^l \left(\frac{1}{2} k_l z_c^2 + \frac{1}{2} k_s \nabla^2 z_c^2 + \frac{1}{4} k_{nl} z_c^4 \right) dz_c \\ &= \frac{1}{2} (\mathbf{q}^e)^T \mathbf{K}_l^e \mathbf{q}^e + \frac{1}{2} (\mathbf{q}^e)^T \mathbf{K}_s^e \mathbf{q}^e + \frac{1}{4} \int_0^l k_{nl} (\mathbf{N}^e(x) \mathbf{q}^e)^4 dz_c \end{aligned} \quad (7)$$

$$V = - \int_0^l f_c \delta(x - x_0) z_c(x, t) dx - (\mathbf{Q}^e)^T \mathbf{q}^e = -f_c \mathbf{N}^e(x_0) \mathbf{q}^e - (\mathbf{Q}^e)^T \mathbf{q}^e \quad (8)$$

where, $\delta(x - x_0) = \begin{cases} 1 & \text{if } x = a \\ 0 & \text{if } x \neq a \end{cases}$ is Dirac's delta function, f_c is the contact reaction force between the moving oscillator and the beam, and \mathbf{Q}^e is the vector of generalized forces. The governing equations of the system can be obtained from the Lagrange equations and Hamilton's principle as

$$\frac{d}{dt} \frac{\partial T}{\partial \dot{\mathbf{q}}^e} - \frac{\partial T}{\partial \mathbf{q}^e} + \frac{\partial(U + V)}{\partial \mathbf{q}^e} = \mathbf{Q}_{nc}^e \quad (9)$$

where $\mathbf{Q}_{nc}^e = -\mathbf{C}^e \dot{\mathbf{q}}^e$, $\mathbf{C}^e = a_0 \mathbf{M}_b^e + a_1 \mathbf{K}_b^e + \mathbf{C}_f^e$, $\mathbf{C}_f^e = \int_0^{l_e} \mathbf{N}^e(x)^T c_f \mathbf{N}^e(x) dx$, $a_0 = 2\xi_f \sqrt{\frac{2k_l}{\rho A}}$; Eq. (9) is derived as

$$(\mathbf{M}_b^e + \mathbf{M}_f^e) \ddot{\mathbf{q}}^e + \mathbf{K}_b^e \mathbf{q}^e + \mathbf{Q}_{nl}^e(q^e) = f_c \mathbf{N}^e(x_0) + \mathbf{Q}^e + \mathbf{Q}_{nc}^e \quad (10)$$

in which $\mathbf{Q}_{nl}^e(\mathbf{q}^e) = \frac{\partial U_f}{\partial \mathbf{q}^e} = \mathbf{K}_l^e \mathbf{q}^e + \mathbf{K}_s^e \mathbf{q}^e + \int_0^l \mathbf{N}^e(x)^T k_{nl} (\mathbf{N}^e(x) \mathbf{q}^e)^3 dx$ is a force vector including the Pasternak and nonlinear elastic parameters; beam's stiffness matrix derives as $\frac{\partial^2 U}{\partial \mathbf{q}^e \partial \mathbf{q}^e} = \mathbf{K}_b^e + \mathbf{K}_l^e + \mathbf{K}_s^e + 3 \int_0^l \mathbf{N}^e(x)^T k_{nl} (\mathbf{N}^e(x) \mathbf{q}^e)^2 \mathbf{N}^e(x) dx$. From Eq. (10), the governing equation of motion is obtained as

$$(\mathbf{M}_b + \mathbf{M}_f) \ddot{\mathbf{q}} + \mathbf{C}_f \dot{\mathbf{q}} + \mathbf{K}_b \mathbf{q} + \mathbf{K}_l \mathbf{q} + \mathbf{K}_s \mathbf{q}$$

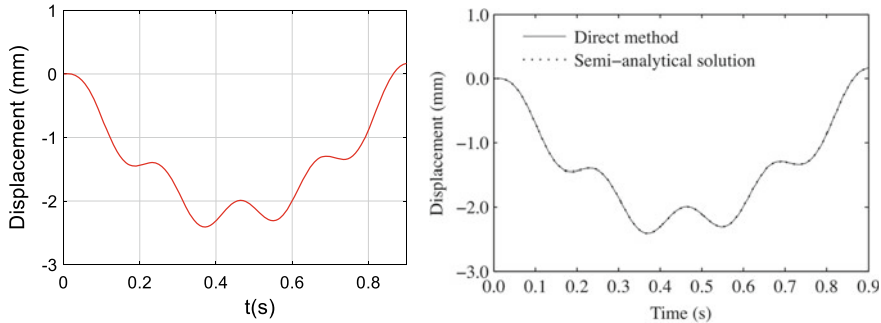


Fig. 3 The displacements of the midpoint of the beam: present (left) and Neves (right)

$$+ \int_0^l \mathbf{N}(x)^T k_{nl}(\mathbf{N}(x)\mathbf{q})^2 \mathbf{N}(x) dx \mathbf{q} = f_c \mathbf{N}(x_0) \quad (11)$$

This equation is solved by the step by step of Newmark algorithm in the time domain based on the program written in MATLAB language.

3 Numerical Results

3.1 Verified Examples

In the first verifiable numerical example, the solutions of displacement at the mid-beam (no foundation) subjected to a moving oscillator along a simple beam with constant velocity are derived and compared with ones of Neves et al. [7]. The results show the agreements expressed in Fig. 3. It can be seen that program using MATLAB code is completely reliable and used to investigate the parameters in the following section.

3.2 Numerical Investigation

In this section, a simple beam of length $L = 5\text{m}$, cross-sectional area $A = 0.1\text{m}^2$, density mass $\rho = 7860\text{kg/m}^3$, Young's modulus $E = 206 \times 10^9\text{N/m}^2$ on the dynamic foundation has $K_L = 50$, $K_S = 1$, $K_{NL} = 10^7$, $c_f = 100\text{Ns/m}^2$, $m_f = \beta\rho$ is used to dynamic analysis. The moving oscillator has dynamic characteristics as damping factor $\zeta_v = 10\%$, velocity $V = 50\text{m/s}$, $\kappa = 0.5$, $\gamma = 0.5$. The dimensionless parameters are defined as $K_L = \frac{k_L L^4}{EI}$, $K_{NL} = \frac{k_{nl} L^6}{EI}$, $K_S = \frac{k_S L^2}{\pi^2 EI}$, $\kappa = (M_v + m_w)/M_b$, $\gamma = \frac{\omega_b}{\omega_h}$. From the Fig. 4 to Fig. 9, the behavior of the beam in this system based

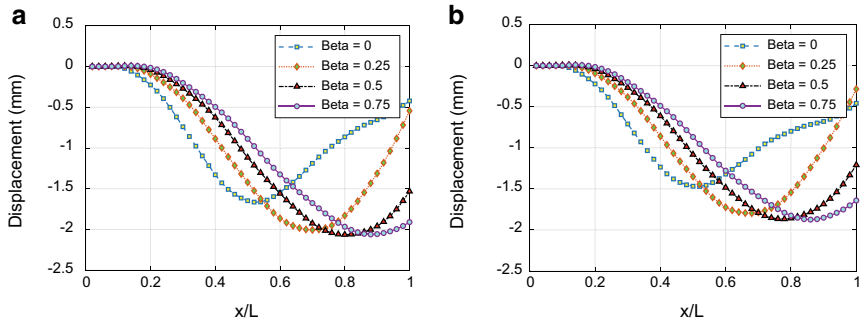


Fig. 4 The displacements of the midpoint: **a** $K_L = 25$, **b** $K_L = 50$

on the time history of vertical deflection at the midpoint and dynamic magnification factor (DMF), defined as the ratio of the maximum dynamic displacement at the midpoint and the maximum static displacement, is determined. The foundation mass has significantly effects on the dynamic response of the beam, shown from Fig. 4 to Fig. 11. In the many cases, the foundation mass is more increasing or decreasing the time history displacement of the beam than without effects of the foundation mass with various parameters. These results can be analyzed as follows. Due to the total mass of the system including the beam, foundation and moving oscillator, increased and the global stiffness remaining constant, then the dynamic properties of the system are also changed as natural frequencies reduced. So that, the dynamic behavior of the structure must be changed in the various of the range of values of velocity. These behavior also depend on the various foundation parameters clearly expressed from Fig. 4 to Fig. 11. Next, the time history of vertical displacement at mid point of the beam due to varying velocity of moving oscillator and multiple moving oscillators is also studied. These responses of the beam are respectively plotted in Figs. 12 and 13 with various of foundation mass, defined as β parameter. Similarly, it can be seen that the dynamic displacement of the beam increased significantly and clearly compared to without effects of the foundation mass.

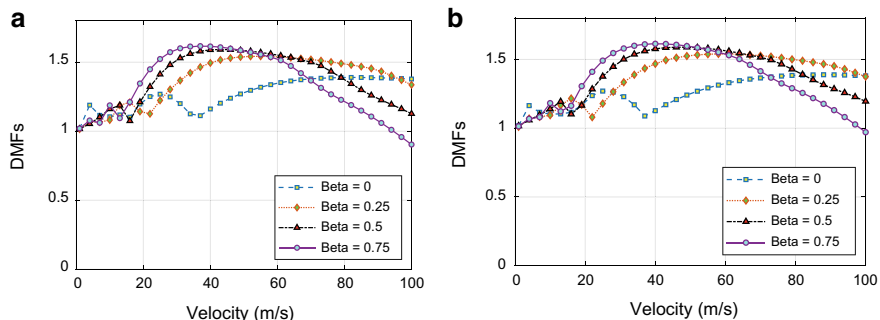


Fig. 5 Dynamic magnification factor: **a** $K_L = 25$, **b** $K_L = 50$

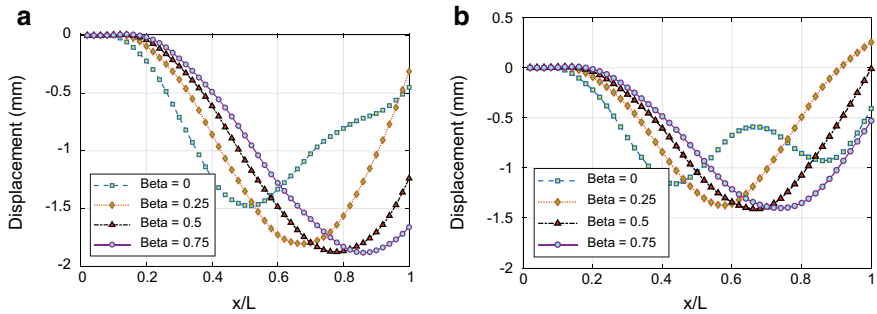


Fig. 6 The displacements of the midpoint: **a** $K_{NL} = 10^5$, **b** $K_{NL} = 10^9$

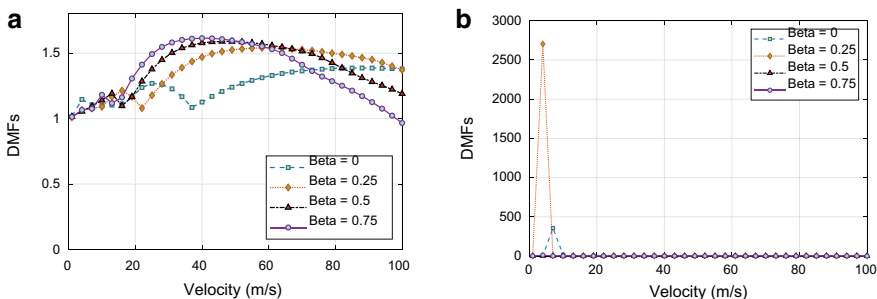


Fig. 7 Dynamic magnification factor: **a** $K_{NL} = 10^5$, **b** $K_{NL} = 10^9$

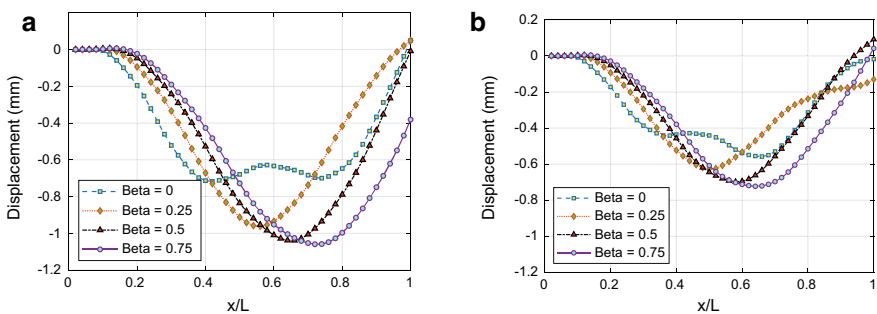


Fig. 8 The displacements of the midpoint: **a** $K_S = 3$, **b** $K_S = 5$

4 Conclusion

The numerical results indicate that the mass of foundation has a certain influence on the dynamic behavior of the beam. The mass of foundation in most cases increases the behavior of beams such as: increase displacement, increase dynamic coefficient.

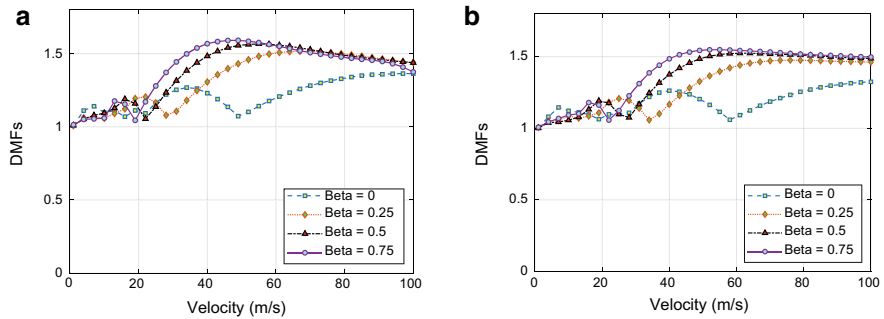


Fig. 9 Dynamic magnification factor: **a** $K_s = 3$, **b** $K_s = 5$

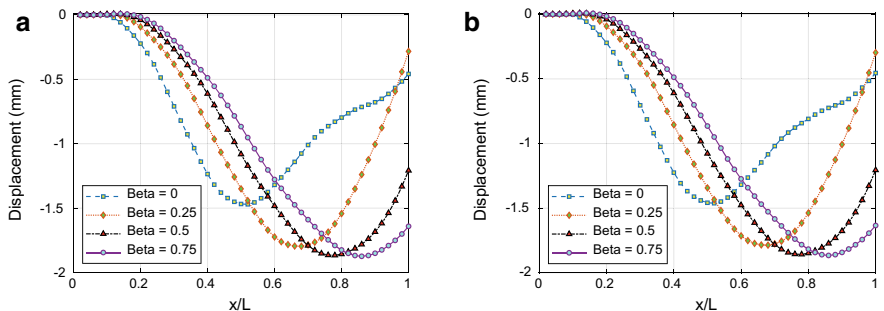


Fig. 10 The displacements of the midpoint: **a** $c_f = 0$ (Ns/m^2), **b** $c_f = 10^3$ (Ns/m^2)

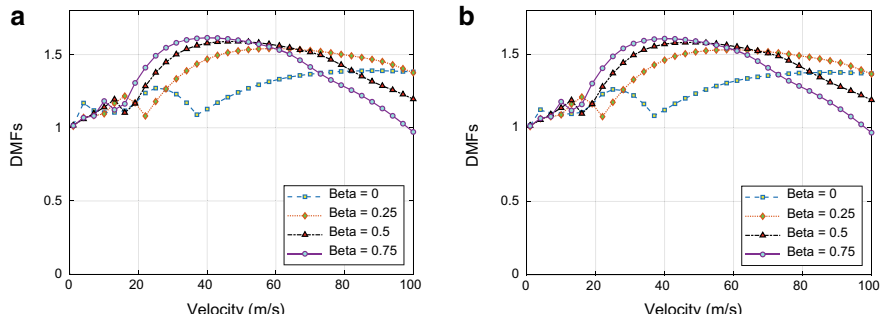


Fig. 11 Dynamic magnification factor: **a** $c_f = 0$ (Ns/m^2), **b** $c_f = 10^3$ (Ns/m^2)

The foundation model is more suitable than the existing foundation models, because the model has considered the influence of the mass of foundation by including the kinetic energy contributing to the total kinetic energy of the system.

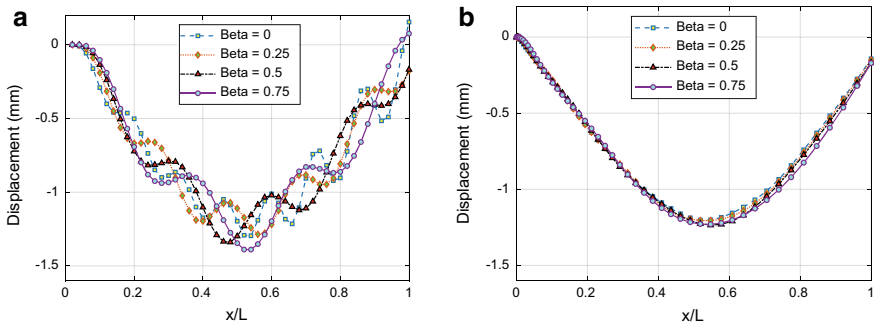


Fig. 12 The displacements of the midpoint: **a** $a = 0$ (m/s^2), $v_0 = 10$ (m/s), **b** $a = 40$ (m/s^2), $v_0 = 0$ (m/s)

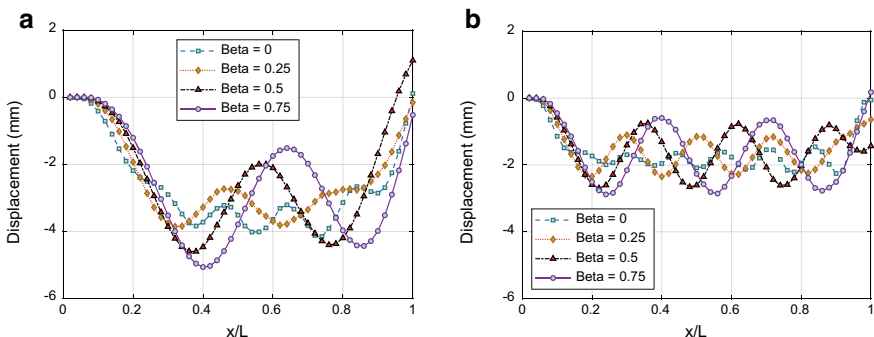


Fig. 13 The displacements of the midpoint: **a** 10 moving oscillators, distance between two oscillators of 1 m, **b** 10 moving oscillators, distance between two oscillators of 2 m

References

- Ansari M, Esmailzadeh E, Younesian D (2011) Frequency analysis of finite beams on nonlinear Kelvin—Voight foundation under moving loads. *J Sound Vib* 330:1455–1471
- Ding H, Shi KL, Chen LQ, Yang SP (2013) Dynamic response of an infinite Timoshenko beam on a nonlinear viscoelastic foundation to a moving load. *Nonlinear Dynamic* 73:285–298
- Froio D, Rizzi E, Simoes FMF, Costa AP (2017) Critical velocities of a beam on nonlinear elastic foundation under harmonic. *Procedia Eng* 199:2585–2590
- Jorge PC, Simoes FMF, Costa AP (2015) Dynamics of beams on non-uniform nonlinear foundations subjected to moving loads. *Comput Struct* 148:26–34
- Metrikine A, Verichev SN (2001) Instability of vibrations of a moving two-mass oscillator on a flexibly supported Timoshenko beam. *Arch Appl Mech* 71(9):613–624
- Morfidis K (2010) Vibration of Timoshenko beams on three-parameter elastic foundation. *Comput Struct* 88:294–308
- Neves S, Azevedo A, Calçada R (2012) A direct method for analyzing the vertical vehicle-structure interaction. *Eng Struct* 34:414–420
- Nguyen TP, Pham DT, Hoang PH (2016) A new foundation model for dynamic analysis of beams on nonlinear foundation subjected to a moving mass. *Procedia Engineering* 142:168–174

9. Pham DT, Hoang PH, Nguyen TP (2018) Experiments on influence of foundation mass on dynamic characteristic of structures. *Struct Eng Mech* 65(5):505–512
10. Rodrigues C, Simoes FMF, Costa AP, Froio D, Rizzi E (2018) Finite element dynamic analysis of beams on nonlinear elastic foundations under a moving oscillator. *Eur J Mech A Solids* 68:9–24
11. Younesian D, Saadatnia Z, Askari H (2012) Analytical solutions for free oscillations of beams on nonlinear elastic foundations using the variational iteration method. *J Theoretical Appl Mech* 50(2):639–652
12. Zhou S, Song G, Wang R, Ren Z, Wen B (2017) Nonlinear dynamic analysis for coupled vehicle-bridge vibration system on nonlinear foundation. *Mech Syst Signal Process Part A* 87:259–278

Energy Simulation and Life Cycle Cost Analysis for Designing Energy Efficient Commercial Buildings in Pakistan



Najam Us Saqib and Salman Azhar

1 Introduction

In the built environment, buildings are one of the main users of energy, right from the start of construction to demolition of the structure. Globally, buildings use 30–40% of the total energy generated and contribute 40–50% to the greenhouse gas emissions [6]. Among the various types of buildings, the commercial buildings consume a considerable amount of energy. Space heating and cooling, lighting, computing, and water heating are the main energy consumption items in the commercial buildings [2].

In Pakistan, the commercial sector is responsible for 7.5% of total energy consumption, whereas domestic sector is the major consumer with 46.4% of total electricity produced. Pakistan is one of the energy deficient countries in the world. There are several energy generation resources in Pakistan but because of the rapid urban development, lack of energy policies and poor planning, Pakistan is facing a major energy shortfall issue. In the peak time, the electricity shortage reaches to 5–7 GW which account for 32% of the total demand of electricity [5]. This shortage is responsible for economic loss as well as social unrest. Recently hundreds of factories have been shut down which lead to the unemployment and economic crisis. Energy consumption in Pakistan is rapidly increasing each year and it is expected to rise 8–10% per year [1].

According to a study conducted by the German Society for International Cooperation (GIZ), Pakistan can save US\$5 billion per year with energy conservation and buildings have the potential to reduce consumption by 30% [4]. There have been some attempts to promote energy efficient design in Pakistan. For example, the National Energy Conservation Center (ENERCON) developed the “Building

N. U. Saqib · S. Azhar (✉)

McWhorter School of Building Science, Auburn University, Auburn, AL, USA
e-mail: salman@auburn.edu

Energy Code of Pakistan" in 1990. This code was mostly based on American Society of Heating Refrigerating and Air-Conditioning Engineers (ASHRAE) standards. The code provided minimum performance standards for building windows and openings, heating, ventilating and air conditioning equipment, and lighting. The Building Energy Code was non-mandatory and over the years did not result in any significant improvements in local design practices. In 2011, ENERCON and Pakistan Engineering Council (PEC) thoroughly revised this code and made it an integral part of the Pakistan Building Code of 1986 (i.e. Energy Provisions-2011). These Energy Provisions shall apply to buildings and building clusters that have a total connected load of 100 kW or greater, or a contract demand of 125 kVA, or a conditioned area of 9690 ft² (900 m²) or unconditioned buildings of covered area of 12,900 ft² (1200 m²) or more. At this point, no published data are available for evaluating the usefulness of these energy provisions.

This research is conducted with a goal of demonstrating the monetary benefits of energy efficient commercial buildings in an effort to convince architects, engineers, and owners to invest in high performance energy efficient buildings. Three recently designed and constructed buildings are chosen as a case study. Energy simulation and Life Cycle Cost Analysis (LCCA) of the "baseline" and "energy efficient" models of these buildings are conducted to identify and recommend best practices. The data generated through these case studies is also used to develop preliminary guidelines for new or existing buildings to make them energy efficient. The results of this research study will be useful for local designers, engineers, constructors, owners, and related government agencies to promote energy efficient buildings in the country.

2 Commercial Building Design and Construction Practices in Pakistan

In Pakistan, most commercial buildings are mix-use consisting of retail spaces on the lower floors and offices and/or multi-family housing units on the upper floors. However, there are several commercial buildings in big cities that are solely used for offices. A typical commercial building has 8–10 floors. All buildings from low-rise to high-rise have a reinforced concrete structure. The main reason is the abundance of cement and cheap labor in Pakistan. Exterior walls are non-loading bearing and generally made up of concrete blocks and are typically 9 inch thick. In most of the buildings, no insulation is used in the construction of walls. A cement and sand mortar, commonly called as 'Plaster' is used on both sides of the walls to make a smooth surface for the paint. Plaster also acts as a waterproofing agent for the walls. Interior walls are also made up of concrete blocks, which act as partition walls as well. Typical thickness of interior wall is 4.5 inches. Floors are commonly made up of reinforced cement concrete with tiles on the top. Most of the buildings have flat roof structure with some amount of heatproof insulation material. Roofs also have a layer of mud over the insulation to develop a slope for rainwater drainage. Clay tiles

are usually placed on the top of the roof. Single glazed windows are typically used in all buildings. Most buildings use individual units for heating and air-conditioning whereas less than 10% are centrally air-conditioned.

3 Research Design and Methodology

Since the intent of the research is to determine the best energy efficient practices for Pakistan, drawings and specifications of various commercial buildings were obtained from the local architects. Case study approach was adopted to compare the energy efficiency of selected buildings and thereby recommend best practices. Figure 1 depicts the research framework.

3.1 Selection of Buildings

After literature review, it was decided to categorize the commercial buildings based on number of floors in order to select a low-rise (up to 5 floors), a medium-rise (up to 10 floors), and a high-rise building (more than 10 floors) in Pakistan. Buildings higher than 15 floors are not designed/permited in most major cities of Pakistan. After careful search, the following three buildings were shortlisted.

1. Building A: State Life Office—Lahore (Basement + 3 Floors)
2. Building B: JF Carpets—Lahore (Basement + 8 Floors)
3. Building C: Mall of Gulberg—Lahore (Basement + Mezzanine + 12 Floors).

State Life Office building has an underground basement and three floors of office space. JF Carpet is a mix-use commercial building with basement parking, 3 floors of retail space, and 5 floors of office space. Mall of Gulberg is also a mix-use building with shops in the basement and mezzanine floors. There are residential units from floor 1 to 12. All three buildings are located in Lahore, Pakistan which has mild-to-strong summer and winter weather. Average summer temperature is 115 °F (45 °C)

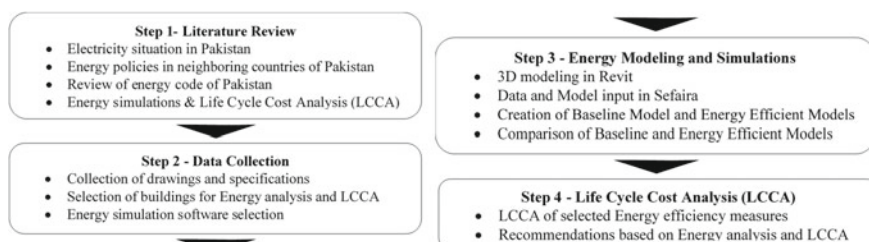


Fig. 1 The research framework

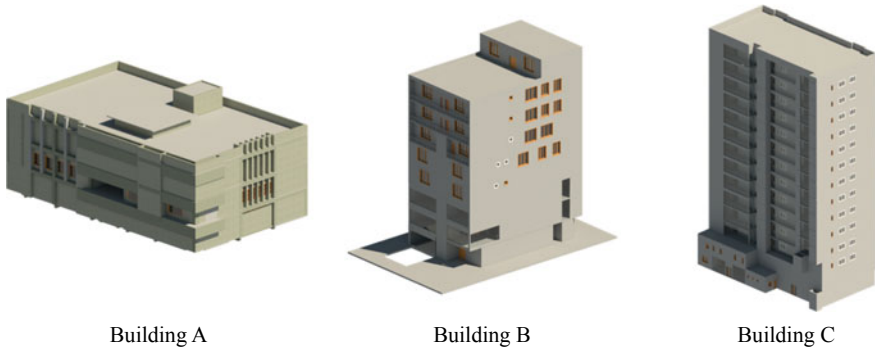


Fig. 2 Shortlisted buildings for energy simulations and LCCA analysis

while the average winter temperature is 41 °F (5 °C). Figure 2 shows the 3D models of the three selected buildings.

3.2 Energy Modeling and Simulation

The Energy modeling is performed in Trimble Sefaira®. The software has Plug-ins for Revit® and SketchUp® that make it easy to do energy modeling and run energy simulation. The selected buildings were modelled in Revit and material properties of various structural and non-structural components and buildings systems (e.g. U or R values, heating and/or cooling loads, etc.) were entered. Next, the operation schedule of each building was defined. More details about this process can be found in Saqib [7]. After the modeling process, energy simulation were run on the baseline design. The simulation provided values of total monthly and yearly energy consumption of the three buildings in kWh. The results were validated against actual electricity bills and minor refinements were made in the models and/or material properties.

After performing energy simulation for the base designs, the following Energy Efficiency Measures (EEMs) were added into the base models one by one: (a) Improved roof and wall insulation; (b) Energy efficient glass for windows; (c) Windows glass color; (d) Windows shading; (e) LED lighting and adjustments in lighting power density; and (f) Addition of occupancy sensors. After reviewing the base simulation results and incorporating EEMs, comparison results were obtained to analyze the effect of each EEM on the energy consumption. Finally, the best EEMs were shortlisted and a set of recommendations is prepared for the designers and constructors.

3.3 Life Cycle Cost Analysis (LCCA)

The LCCA was performed using data from energy simulation of existing and proposed design solutions. The results of the LCCA indicate if a design solution is effective and beneficial over the course of its life cycle. The first step in LCCA is to determine the economic impact of an alternative or improved design. The Life cycle costs include initial cost, energy and water usage costs, operation and maintenance costs, replacement costs, residual value and other costs like taxes etc. After determining all these costs, one can calculate the life cycle cost of a building [3]. For LCCA, the Present Value method was used. In the Present Value method, all present and future costs are converted into baseline of today's costs. Initial costs are expressed as Present Worth. Net present value is the difference between the present value of cash inflows and the present value of cash outflows that occur as a result of undertaking an investment project [3].

The following formula is used for Present Value calculations [3]:

$$PV = \frac{FV}{(1 + i)^n} \quad (1)$$

where:

PV Is Present Value

FV Is Future Value

i Is the interest rate (as a decimal)

n Is the number of years.

The unit rates of all design items were collected from open market and vendors in Pakistan. Typical discount rates used in LCCA range from 3 to 5%. The discount rate used in this research is 5% [8].

4 Results and Discussion

Table 1 shows the energy consumption of the Base Model of three buildings and impact of various Energy Efficiency Measures (EEMs) on the total energy consumption. The numbers in the parenthesis show the percentage energy consumption reduction (if negative) or increase (if positive) for each EEM.

The results indicate that the wall insulation is the best EEM for all three buildings and reduced their energy load from 3.77 to 9.16%. The energy savings are due to reduction in heating, cooling, and fan loads. The total percentage of reduction in energy consumption is low in building 3 (3.77%) as compared to the other two buildings due to its better orientation and use of a thin wall insulation in the original design as compared to first two buildings that have no wall insulation in the original design. The second best EEM is use of energy efficient glass in the windows. All

Table 1 Annual electricity consumption of baseline and energy efficient designs

Energy efficiency measures	Building A	Building B	Building C
Baseline Model Energy Consumption (kWh/yr)	357,345	467,839	1,451,036
Wall Insulation (2" thermopore board, R-value = 5.85 F-ft ² -h/Btu per inch)	324,628 (-9.16%)	438,481 (-6.28%)	1,401,219 (-3.77%)
Roof Insulation (Thermospray, R-value = 6.80 F-ft ² -h/Btu per inch)	352,633 (-1.32%)	464,979 (-0.61%)	1,448,627 (-0.17%)
Energy Efficient Glass (Double Glazed Windows, U-value = 1.3)	345,842 (-3.21%)	435,842 (-6.83%)	1,419,842 (-2.15%)
Window glass colour and shades	350,842 (-1.81%)	460,154 (-1.64%)	1,435,942 (-1.04%)
LED Lighting (replacement of CFLs)	347,816 (-2.26%)	448,765 (-4.07%)	1,430,573 (-1.41%)
Occupancy Sensors (for hallways and less traffic areas)	349,368 (-2.23%)	458,703 (-1.95%)	1,442,419 (-0.59%)
Combined Effect of Top Three EEMs (wall insulation, DG windows, and LED lighting)	316,390 (-11.46%)	424,091 (-9.35%)	1,379,653 (-4.92%)

three buildings used single glazed windows (U value = 5.1) which were replaced with double glazed windows (U value = 1.3) and resulted in energy reduction between 2.15 and 6.83%. The third best EEM is replacement of incandescent and CFL lighting with the LED lighting. It reduced the energy consumption between 1.41 and 4.07%. The other measures also resulted in minor to moderate energy savings. When all measures were combined, the net effect was 11.46% reduction for Building A, 9.35% reduction for Building B, and 4.92% reduction for Building C. It is important to note that Building C was designed based on the latest energy provisions of the Pakistan Building Code and hence showed improved performance as compared to the other two buildings.

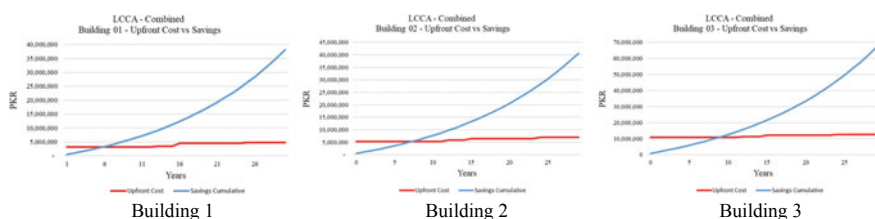
At the end, the combined effect of the three top EEMS (i.e. wall insulation, double glazed windows, and LED lighting) was analyzed through Life Cycle Cost Analysis (LCCA) and results are summarized in Table 2. The LCCA was also performed for other EEMS and results can be found in Saqib [7].

Figure 3 depicts the LCCA results by showing upfront cost versus savings for each building. The LCCA results show that the initial cost of top three EEMs (wall insulation, double glazed windows, and LED lighting) can be recovered in 4.5–9 years and the owner can save substantial money afterwards.

Table 2 Savings from top three energy efficiency measures (determined via LCCA)

Building	Upfront cost (U)		Yearly savings (Y)		Lifetime savings (L)		Net savings N = L-U-replacement	
	PKR	USD*	PKR	USD*	PKR	USD*	PKR	USD*
Building 01	3,231,000	25,202	481,631	3757	38,076,857	296,999	36,517,257	271,797
Building 02	5,271,200	41,116	514,476	4013	40,673,577	317,254	38,978,177	276,138
Building 03	10,776,200	84,055	839,464	6548	66,366,508	517,659	65,070,108	433,604

*Exchange rate, 1US\$ = PKR 128.21

**Fig. 3** LCCA for combined EEMs for the three selected buildings

5 Guidelines for Energy Efficient Buildings in Pakistan

Based on the outcome of this research study, the following preliminary guidelines are proposed:

1. Foam board insulation of at least 2 in. (5 cm) on roof slab and exterior masonry walls should be used. Insulation should be covered with white paint or white tiles for maximum effect.
2. Walls facing sun path should have less window-to-wall ratio. Generally, east and west walls face sun path. Window-to-wall ratio should not exceed 40%.
3. Exterior shading devices or shutters should be used to shade the windows facing sun path. Shutter or moderate size awning should be used on south windows. Vertical fins or shutters should be used in north windows on each side. A louver should be used if natural ventilation is required.
4. Low and wide windows should be designed because they are easier to shade. Windows should be energy efficient. A solar heat gain coefficient of below 0.25 should be specified in the design. Double glazing with low-e coating should be used.
5. Architect should educate clients about possible energy efficient measures. Energy modeling software should be used during the design phase to select the cost-effective energy efficient measures.
6. Living spaces should be designed such that the spaces face cooler façade.

7. Minimum allowable Visual Light Transmittance (VLT) is 0.27. Light control device should be used to turn off the lights within 20 min of occupants leaving the space except general and task lighting.

6 Conclusions

This purpose of this research is to find out best energy efficiency measures for commercial buildings in Pakistan. Energy simulation of three commercial buildings was conducted with different energy efficiency measures. Results showed that the electricity consumption of commercial buildings can be reduced between 5 and 12% by using adequate wall and roof insulation, low-energy windows, and LED lighting. The LCCA showed that the initial cost of these energy efficient measures can be recovered in 4.5–9 years and the owner can save substantial money afterwards. This research results and recommendations can help owners, architects and contractors to better design new commercial buildings or retrofit existing one. This research focused on commercial buildings (mix-use, office) in Pakistan. The next phase of this research will be aimed at institutional and health care buildings.

Acknowledgements This research study is funded by the US Department of State and the Higher Education Commission of Pakistan (HEC) under the joint Pakistan-U.S. Science and Technology Cooperation Program (Phase 6).

References

1. Azad S, Akbar Z (2015) The impediments in construction of sustainable buildings in Pakistan. *Eur Sci J ESJ* 11
2. Bastani MS, Somayeh A (2015) Simulating the impact of feedback on energy consumption and emission production in commercial buildings using agent-based approach. In: AEI 2015 Proceedings. <https://doi.org/10.1061/9780784479070.008>
3. Dell'Isola A (1997) Value engineering: practical applications for design, construction, maintenance & operations. RS Means Company Inc., Kingston
4. ENERCON (2017) <http://www.enercon.gov.pk/home.php> (Accessed 12.13.17)
5. Mirjat NH, Uqaili MA, Harijan K, Valasai GD, Shaikh F, Waris M (2017) A review of energy and power planning and policies of Pakistan. *Renew Sustain Energy Rev* 79:110–127. <https://doi.org/10.1016/j.rser.2017.05.040>
6. Ramesh T, Prakash R, Shukla KK (2010) Life cycle energy analysis of buildings: an overview. *Energy Build* 42:1592–1600. <https://doi.org/10.1016/j.enbuild.2010.05.007>
7. Saqib NU (2018) Energy simulation and life cycle cost analysis of high performance commercial and public buildings in Pakistan, master capstone. Auburn University, AL
8. Trading Economics (2017) Website.: <https://tradingeconomics.com/>

Evaluation of Response Variability of Euler–Bernoulli Beam Resting on Foundation Due to Randomness in Elastic Modulus



Ta Duy Hien and Phu-Cuong Nguyen

1 Introduction

Beams resting on foundations are commonly used in construction. To describe the behaviour between beams and foundation, we can use a linear model, nonlinear model with single-parameter or multiparameter. Many studies have been carried out in relation to the behaviour of beams resting on foundations. Allahkarami et al. [1] studied dynamic responses of curved microbeams resting on a nonlinear foundation. Nguyen and Kim [2, 3] proposed new plastic hinge approaches for nonlinear analysis of space steel frames considering the flexibility of column-base connections. Chakraverty and Jena Subrat [4] used classical beam theory to research the free vibration of carbon nanotubes. Pradhan et al. [5] studied the stability of a tapered beam resting on a Pasternak foundation, Lohar et al. [6] computed the frequencies of non-uniform beams using an analytical method, and Hien and Lam [7] computed displacements, strain and stresses in FG plates on a viscoelastic foundation using an analytical method.

In addition to deterministic problems, some researchers have studied stochastic problems for the static and dynamic stability of beams or frames. Claudio et al. [8] applied the Askey-Wiener scheme to solve Euler-Bernoulli beams with an uncertain elastic modulus, Kim et al. [9] analyzed a semi-rigid steel frame considering the randomness of elastic modulus using a Monte-Carlo simulation, and Hien et al. [10] used Euler-Bernoulli beam theory to calculate the variability of displacements of beams subjected to a moving load.

T. D. Hien (✉)

University of Transport and Communications, Hanoi, Vietnam

e-mail: tdhien@utc.edu.vn

Research and Application Center for Technology in Civil Engineering (RACE), Hanoi, Vietnam

P.-C. Nguyen

Faculty of Civil Engineering, Ho Chi Minh City Open University, Ho Chi Minh City, Vietnam

The paper contents: the finite element of a beam resting on an elastic foundation is given in Sect. 2, Sect. 3 constructs a stochastic finite element method with a weighted integration technique, employs a numerical example and provides a subsequent discussion, Sect. 4 offers conclusions.

2 Stochastic Finite Element Formulation of Euler–Bernoulli Beam

In here, we investigate a beam with a random property of elastic modulus. Beam rest on an elastic foundation, as shown in Fig. 1.

For a Euler–Bernoulli beam, the beam element with four degrees of freedom is suitable for a Euler–Bernoulli beam, as shown in Fig. 2. The transverse displacement $w(x)$ is interpolated by a Hermite function as follows:

$$w(x) = [N_1 \ N_2 \ N_3 \ N_4] \{q\}_e \quad (1)$$

where N_1, N_2, N_3, N_4 are the Hemite function:

$$\begin{cases} N_1 = 1 - 3\left(\frac{x}{L_e}\right)^2 + 2\left(\frac{x}{L_e}\right)^3 & N_2 = \left(x + \frac{x^3}{(L_e)^2} - 2\frac{x^2}{(L_e)}\right) \\ N_3 = 3\left(\frac{x}{L_e}\right)^2 - 2\left(\frac{x}{L_e}\right)^3 & N_4 = \left(\frac{x^3}{(L_e)^2} - \frac{x^2}{(L_e)}\right) \end{cases} \quad (2)$$

and transverse displacement vector of the element:

Fig. 1 Beam on a foundation and uncertain elastic modulus E

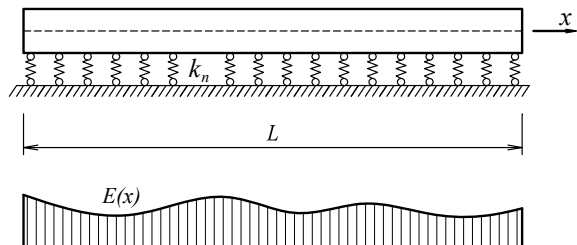
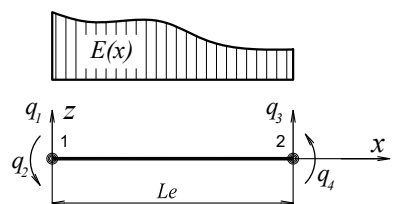


Fig. 2 Beam finite element including random field in elastic modulus



$$\{q\}_e = \begin{Bmatrix} q_1 \\ q_2 \\ q_3 \\ q_4 \end{Bmatrix} \quad (3)$$

Four interpolation function in Eq. (2) are the third polynomials to be of Hermite function.

The bending stiffness matrix can be computed following Yang [11]:

$$[K]_{be} = \int_{V_e} [B]^T [D] [B] dV \quad (4)$$

where B matrix

$$[B] = -z \left[\left(-\frac{6}{(L_e)^2} + \frac{12x}{(L_e)^3} \right) \left(-\frac{4}{(L_e)} + \frac{6x}{(L_e)^2} \right) \frac{6}{(L_e)^2} \left(1 - \frac{2x}{L_e} \right) \left(-\frac{2}{(L_e)} + \frac{6x}{(L_e)^2} \right) \right] \quad (5)$$

In Eq. (4), we note that elastic modulus E is a random field, and it cannot be calculated by deterministic finite element method. The random fields of elastic modulus are represented as follows:

$$E(x) = E_0[1 + r(x)] \quad (6)$$

where $r(x)$ is a Gaussian random field with zero mean.

Substituting Eq. (6) into Eq. (4) and applying the weighted integral method, we obtain:

$$[K]_{be} = \int_{V_e} [B]^T E_0[B] dV + \int_{V_e} r(x)[B]^T E_0[B] dV = [K]_{be}^0 + \sum_{r=1}^{Nr} [C]_r^{(e)} R_r^{(e)} \quad (7)$$

Random variables R_r are represented by integration:

$$R_r^{(e)} = \int_{V_e} x^r r(x) dx \quad (8)$$

For determining the stiffness matrix of a foundation $[K]_{ne}$, the potential energy of the foundation is written as follows:

$$U_F = \frac{1}{2} \int_0^{L_e} k_n [w(x)]^2 dx = \frac{1}{2} \{q\}_e^T [K]_{ne} \{q\}_e \quad (9)$$

Global stiffness matrix of a finite element:

$$[K]_e = [K]_{be} + [K]_{ne} \quad (10)$$

Bending element stiffness matrix $[K]_{be}$ in Eq. (10) contains random variables R_i that is determined from Eq. (8).

Displacement can be approximated as follows:

$$\{U\} = \{U\}_0 + \sum_e^{Ne} \sum_k^{Nr} \frac{\partial \{U\}}{\partial dR_i^{(k)}} R_i^{(k)} \quad (11)$$

Displacement vector $\{U\}$ in Eq. (11) is function of random variables R_i that is determined from Eq. (8).

Mean and covariance of displacement is computed as follows:

$$\begin{aligned} \bar{E}\{U\} &= [K]_0^{-1}\{F\} \\ \text{Covariance}(\{U\}, \{U\}) &= \bar{E}\left\{ (\{U\} - \bar{E}\{U\})(\{U\} - \bar{E}\{U\})^T \right\} \end{aligned} \quad (12)$$

Mean vector and covariance matrix in Eq. (12) can calculate from random variables R_i in Eq. (11). Random variables R_i is defined from (8) as stochastic integration, so computation mean vector and covariance matrix in Eq. (12) are quite difficult. We construct algorism for determining mean vector and covariance matrix in Eq. (12) and programing in Matlab software.

3 Numerical Examples

The simply supported rectangular beam has length $L = 8$ m, the material properties are $E_0 = 35$ GPa, and $v = 0.3$. The cross section of beam: $b = 0.3$ m, $h = 0.5$ m and uniform load on beam $q = 10^4$ N/m. The parameter k_f of an elastic foundation will be used for convenience:

$$k_f = \frac{k_n L^3}{EI} \quad (13)$$

In this example, we assume $k_f = 3$

Formulation for the coefficient of variation of displacement as follows:

$$COV = \frac{\sqrt{Variance(U)}}{mean(U)} \quad (14)$$

We assume that the autocorrelation functions for random field $r(x)$ is:

$$G_R(\xi) = \sigma^2 e^{\left(-\frac{|\xi|}{d}\right)} \quad (15)$$

where $G_R(\xi)$, d , σ are the autocorrelation function, correlation distance and coefficient of variation of a random field.

We use Monte Carlo simulation (MSC) to compare the COV of displacement of a beam with present approach with assumption $\sigma = 0.1$.

We have graphed both the results of the standard deviation (SD) and coefficient of variation (COV) of displacement by correlation distance of random field d parameter as shown in Figs. 3 and 4. As we could see from the graph the SD and COV calculated by Monte Carlo Simulation method is good agreement with results calculated by weighed integral method. The overall behaviour of MSC graph and SFEM graph increase from 0.02 to 0.08. In the last part the SD and COV graph have flatten down, from d equal 10 to 100 the SD and COV only increase from 0.29 to 0.31 and 0.07 to 0.08, respectively. At this stage the two line of graph of the MSC and SFEM have merged with each other to be came one which indicate a highly agreement of two methods.

Fig. 3 Coefficient of variation COV as d

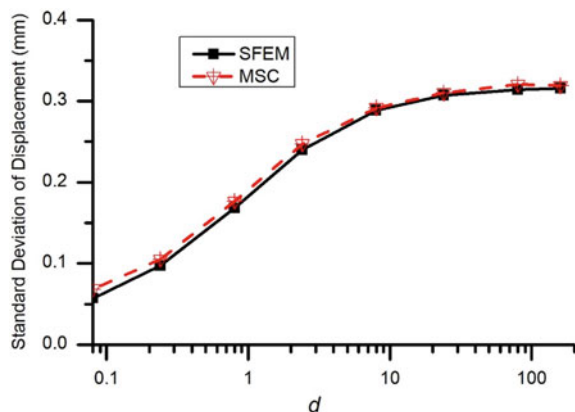
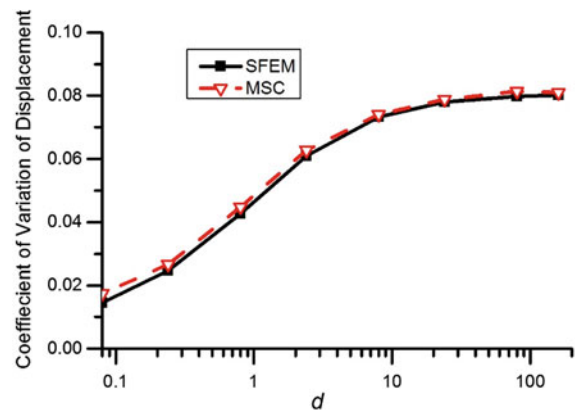


Fig. 4 Coefficient of variation COV as d



4 Conclusions

Mean, standard deviation and coefficient of displacements of Euler–Bernoulli beam lying on an elastic foundation were determined by stochastic finite element method. Weighted integration technique applied to formulate a stochastic finite element. Comparing the *COV* of displacement by the present method and Monte Carlo simulation demonstrated the suitability of the proposed method. The randomness of the elastic modulus was found to have significantly affected the displacements of the beam.

Acknowledgements The authors would like to acknowledge the support from Vietnam National Foundation for Science and Technology Development under grant number 107.01-2017.314.

References

1. Allahkarami F, Saryazdi MG, Nikkhah-Bahrami M (2018) Nonlinear forced vibration of curved microbeam resting on nonlinear foundation using the modified strain gradient theory. *Int Appl Mech* 54(6):718–738
2. Nguyen PC, Kim SE (2017) Investigating effects of various base restraints on the nonlinear inelastic static and seismic responses of steel frames. *Int J Non-Linear Mech* 89:151–167
3. Nguyen PC, Kim SE (2018) A new improved fiber plastic hinge method accounting for lateral-torsional buckling of 3D steel frames. *Thin-Walled Str* 127:666–675
4. Chakraverty S, Jena Subrat K (2018) Free vibration of single walled carbon nanotube resting on exponentially varying elastic foundation. *Curved Layered Struct* 5(1):260
5. Pradhan M, Dash PR, Mishra MK, Pradhan PK (2019) Stability analysis of a tapered symmetric sandwich beam resting on a variable Pasternak foundation. *Int J Acoust Vibr* 24(2):228–240
6. Lohar H, Mitra A, Sahoo S (2018) Free vibration of initially deflected axially functionally graded non-uniform Timoshenko beams on elastic foundation. *Rom J Acoust Vib* 15(2):75–89
7. Hien TD, Lam NN (2018) Vibration of functionally graded plate resting on viscoelastic elastic foundation subjected to moving loads. *IOP Conf Ser Earth Environ Sci* 143:12–24
8. Ávila da Silva Jr, C, Beck A, Rosa E (2009) Solution of the stochastic beam bending problem by Galerkin Method and the Askey-Wiener scheme. *Lat Am J Solids Struct* 6:51–72
9. Kim DY, Noh HC (2013) Probabilistic nonlinear analysis of semi-rigid frames considering random elastic modulus. *J Comp Str Eng Inst Korea* 26(3):191–198
10. Hien TD, Hung ND, Kien NT, Noh HC (2019) The variability of dynamic responses of beams resting on elastic foundation subjected to vehicle with random system parameters. *Appl Math M* 67:676–687
11. Yang TY (1986) Finite element structural analysis. Prentice-Hall

Experimental and Numerical Modal Analysis of Cabinet Facility Considering the Connection Nonlinearity



Thanh-Tuan Tran, Anh-Tuan Cao, Kashif Salman, Phu-Cuong Nguyen, and Dookie Kim

1 Introduction

Nonstructural components (NSCs) are structures, systems and components that are attached to the traditional civil engineering structures such as buildings, hospitals, or nuclear power plants (NPPs). In the nuclear industry, the heavy nonstructural components such as electric cabinets are one of the most popular components that any risk to these equipments will tend to failure which is not desired. Many researchers covered the behavior of the cabinet under different earthquakes excitation through the finite element model or experimental test, etc. [4, 7, 12]. Hur et al. [7] developed several simplified numerical models for cabinets using finite element (FE) methods. In these models, the nonlinear material properties, different force-deformation behavior of connections, and various support boundary conditions ranging from fixed, elasto-plastic to free are considered. In 1999, Gupta et al. [5] proposed a simple method for evaluation of in-cabinet response required for seismic qualification (SQ) of electrical instruments based on a Ritz vector approach. The method was modified later on by Gupta and Yang [6] to overcome certain limitations and to improve the accuracy. Recently, the seismic risk assessments of cabinet facilities in NPP have been performed by developing fragility curves using the lognormal approaches [10, 11].

T.-T. Tran (✉) · A.-T. Cao · K. Salman

Department of Civil Engineering, Kunsan National University, Gunsan, Republic of Korea
e-mail: tranhanhtuan@kunsan.ac.kr

T.-T. Tran

Faculty of Technology and Technique, Quy Nhon University, Quy Nhon, Vietnam

P.-C. Nguyen

Faculty of Civil Engineering, Ho Chi Minh City Open University, Ho Chi Minh City, Vietnam

D. Kim

Department of Civil and Environmental Engineering, Kongju National University, Cheonan, Republic of Korea

Until today, much knowledge and research about connections between framing members or plate and framing members have been investigated. In the nonlinear structural analysis for framed structures, the co-author of this present work, Nguyen and Kim [8, 9] proposed new plastic hinge approaches for nonlinear analysis of space steel frames considering the flexibility of column-base connections and semi-rigid connections. For the cabinet facility, these connectors are used popularly. For example, screws connect frames and plates at each node or the door are also connected to the top and base of the frames by wing screws. Thus, the electrical structure can be failed at the base of the unit or the connecting fasteners between plates and frame members. The failure modes of a fastener, such as pull-out or pull-over, are the most common failure modes of the electric cabinet. Therefore, these connectors should be considered carefully in order to get an accurate model of the cabinet for assessing the seismic risk of structure.

The aims of this study are to develop FE models for cabinet considering the effects of nonlinear behavior of connections. Three models with different type and number of connections corresponding to welding and screw connections between plate and frame members are presented. Dynamic characteristics of cabinets are discussed through shaking table test and numerical model analysis.

2 Numerical Model of Cabinet

2.1 Description of Cabinet

A prototype of the electric cabinet provided by the Korea Electric Power Research Institute (KEPRI) is used in this study. The detailed specifications of the cabinet are shown in Fig. 1. The dimensions of the cabinet are 800 mm wide, 800 mm deep, and 2100 mm height. The total weight is about 290 kg, while the door's weight is around 44 kg for each one. According to the real configuration of the electrical cabinet, the sections of the main-frame and sub-frame are rectangular and C-shape, respectively. The shape of the main cross-sections and their parameters are given in Fig. 1. For the material properties, all frame and plate members are assigned the SS400 steel with 200 GPa of modulus of elastic, 7850 kg/m^3 of density (ρ) and 0.3 of Poisson's ratio (ν).

2.2 Modelling of Nonlinear Behavior

In this research, assuming that the steel panels are connected with the framing members using the screw connections. As shown in Fig. 2b, the connections can be failed

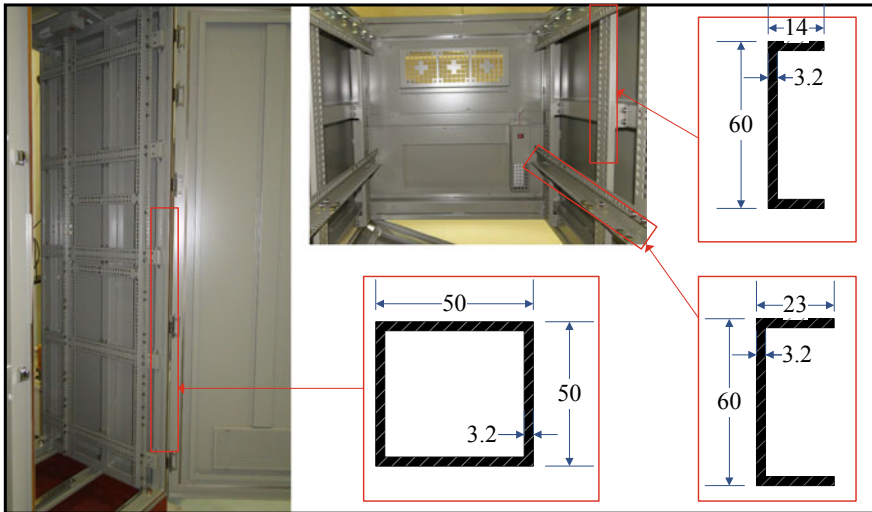


Fig. 1 Test specimen

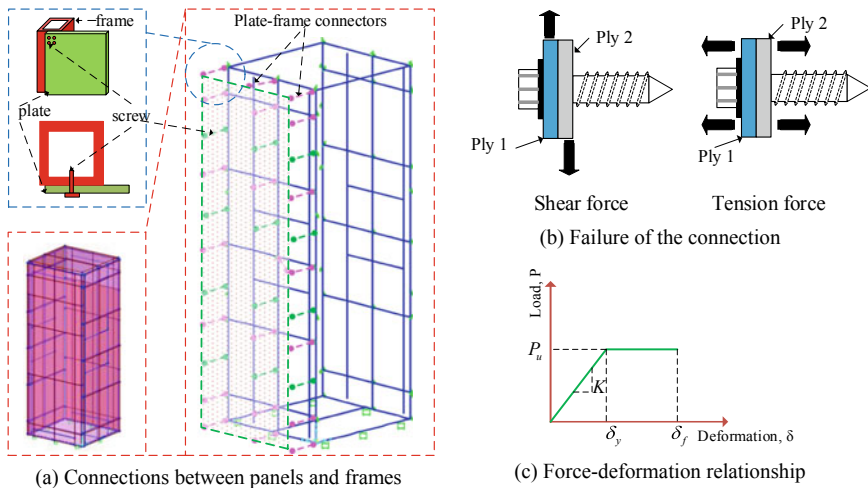


Fig. 2 Model of electric cabinet

under shear, tension or the combination of shear and tension forces. These failure modes depend on the strength and thickness of plates as well as the hole size, spacing, and edge distance of fasteners. In the practice, the force-deformation relationship of screw connections is difficult to quantify; hence, a simple model with bilinear behavior is assumed for these fasteners (Fig. 4c). The shear-force deformation, V_{AISI} , and tensile-force deformation, T_{AISI} , per fastener are calculated as follows [1]:

$$V_{AISI} = \min(4.2\sqrt{t^3 d} F_u, 2.7 t d F_u) \quad (1)$$

$$T_{AISI} = 0.85 t d F_u \quad (2)$$

where d is the nominal diameter of screws; F_u is tensile strength, and t is the thickness of connected members.

The FE model of the cabinet is generated using SAP200 as shown in Fig. 2. In order to get accurately model, the model should be composed close with the real behavior of the cabinet. The vertical and horizontal members are modelled using the frame elements, while panel members are modelled using the shell elements. The connections between the plates and frame are simulated as link elements. These elements consider the stiffness properties of screw fasteners that are explained in Fig. 2c. The hinge connectors between door and frame are also considered to be fixed at five degrees of freedom, whereas shim connectors are considered to be fixed at three translation degrees of freedom. For the support boundary condition, the connection is assumed to be fixed at the base of the cabinet.

In order to consider the effect of connections on the nonlinear behaviour, various models with different fasteners are applied including (Case 1) the welding connections, (Case 2) the screw connections, and (Case 3) adding screws located at the mid-span of each sub-frame. For the nonlinear behavior, the bilinear behavior for the force-deformation curve is applied to the plate-frame connections. The link elements are assigned to transfer the effect of the frame to plate members, as shown in Fig. 2.

3 Experimental Investigation

3.1 Experiment Setup

As shown in Fig. 3, a schematic view of the test setup is presented. The specimen was anchored onto the channels by bolts, and the channels were connected to the shaking table by welding connections. There is no equipment attached to the structure. Three accelerometers are attached to the panel and the position of measuring equipment is illustrated in Fig. 3a. To investigate the dynamic characteristic of the cabinet, the impact hammer test is conducted at the top of the cabinet. Detail of impact force is shown in Fig. 3b.

3.2 Verification of the FE Models

The natural frequencies of the cabinet from the vibration test are determined using the frequency domain decomposition (FDD) method [3]. The FDD is a modal analysis

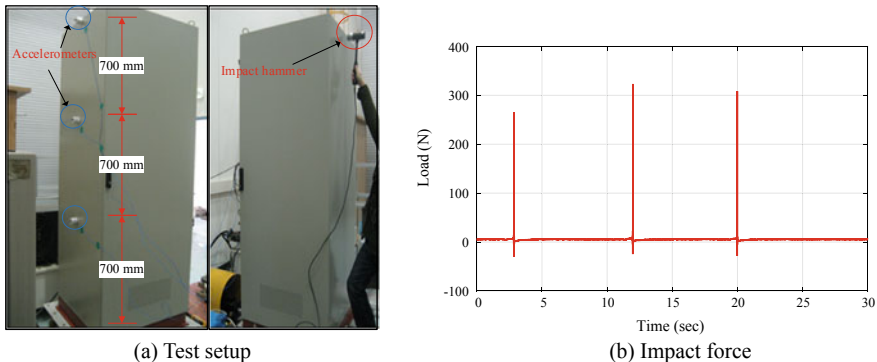


Fig. 3 Test setup and impact force

technique which generates a system realization using the frequency response given multi-output data. This technique involves the main steps which are listed below:

- Compute Power Spectral Density (PSD) matrix $S_{yy}(w)$ from the time series data as follows

$$S_{yy}(w) = U(w)^T \Sigma(w) V(w) \quad (3)$$

where Σ is the diagonal matrix consisting of the singular values (σ_i' s) and U and V are the unitary matrices.

- Perform singular value decomposition of the spectral density matrices.
 - If multiple test setups are available, then average the first singular value of all test setups and average the second.
 - Peak pick on the singular values to estimate the natural frequency.

Based on the FDD technique, the fundamental natural frequencies of the cabinet in front-to-back (FB) and side-to-side (SS) is obtained by the experimental test are shown in Fig. 4.

The experimental analysis using signal processing reveals some of the fundamental solutions for the modal analysis. The recorded response from the accelerometer is studied and the peak picking method was proposed as shown. The selection of peak is considered for the resonant frequencies for both FB and SS direction which contain the higher modal participation ratio. The values of 14.75 and 16.63 Hz in FB and SS direction are obtained in order to calibrate with the numerical models.

Table 1 tabulates the comparisons of natural frequencies from the impact hammer test and FEM. The natural frequencies from the experimental tests are selected from the peaks of the graph in Fig. 4, while the results from the FEM are selected from the modal participating mass ratios (MPMR). Based on the comparisons, the frequencies might have been reasonable because they have a good agreement with each other.

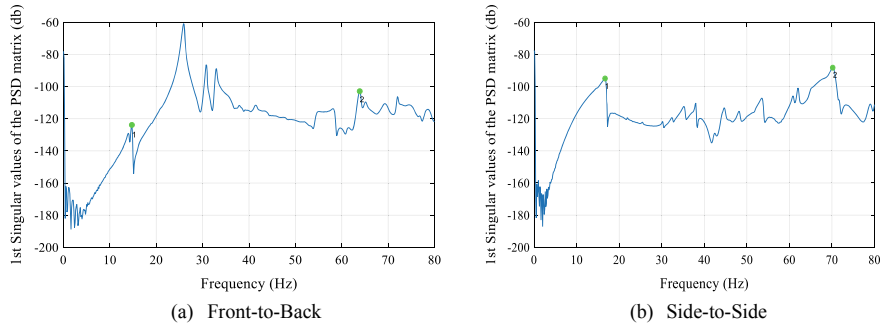


Fig. 4 The fundamental frequencies of the test result

Table 1 The natural frequencies of the cabinet (Hz)

Mode	Mode	Test	FEM		
			Case 1	Case 2	Case 3
Front-to-Back	1	14.75	14.36	14.14	14.18
	2	25.87	23.58	23.02	23.22
Side-to-Side	1	16.63	14.64	14.17	14.26
	2	44.75	41.73	39.24	50.33

3.3 Effects on Structural Dynamic Characteristics

In order to investigate the effects of the connectors on the cabinet response, the modal analysis is conducted for three representative cases. The amplification functions (AFs) are obtained based on the acceleration response of the FE model. According to the definition of NUREG CR-5203 [2], the AF at any designated frequency is the ratio of the corresponding spectral acceleration at the response and the control locations. In this work, the AF is defined as follows:

$$AF(f) = \frac{S_{at}(f, 5\%)}{S_{ab}(f, 5\%)} \quad (4)$$

where $S_{at}(f, \xi)$ and $S_{ab}(f, \xi)$ are the top and bottom response spectrum, ξ is the damping ratio, and f is the frequency.

Figure 5 shows the effects of the connections on the AF of the cabinet. As expected, the frequencies of these models are basically decreased with increasing the stiffness of the structure. This cause the screw connections tend to weaken to the system. For the FB direction, when compared with the first case the peaks in the first mode are shifted about 2.82% (14.14 Hz) and 2.47% (14.19 Hz) for the second case and third case, respectively. The reduction values for case 2 and case 3 are 4.87% (14.26 Hz) and 4.27% (14.35 Hz), respectively for SS direction.

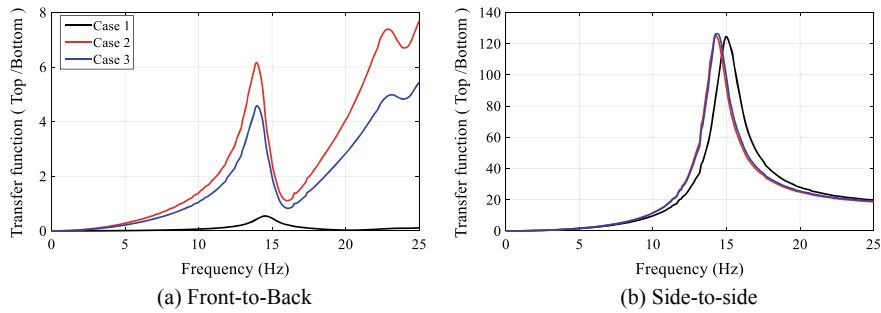


Fig. 5 Frequency response curves of the acceleration for different cases

4 Conclusions

A bilinear force-deformation relationship is proposed in this paper to investigate the nonlinear behavior of the cabinet facility in NPP. Three models with various types of connections are built corresponding to (Case 1) welding connections, (Case 2) the screw connections, and (Case 3) adding screws located at the mid-span of each sub-frame. The model dynamic characteristics are verified using experimental tests. Simulation results show good agreement between the numerical models and the experiments. Moreover, the effects of the connections are investigated. The obtained results indicate that the connectors tend to reduce the frequencies of two translational modes due to the stiffness. The model frequencies increase with the increment of numbers of screw connectors which is an important aspect of cabinet facility.

Acknowledgements This work was supported by the Korea Institute of Energy Technology Evaluation and Planning (KETEP) and the Ministry of Trade, Industry & Energy (MOTIE) of the Republic of Korea (No. 20171510101960).

References

1. AISI (2007) North American standard for cold-formed steel framing-general provisions. S100-07, American Iron and Steel Institute, USA
2. Bandyopadhyay KK, Hofmayer CH, Kassir MK, Pepper SE (1988) Dynamic amplification of electrical cabinets (No. NUREG/CR-5203). Nuclear Regulatory Commission
3. Brincker R, Zhang L, Andersen P (2000) Modal identification from ambient responses using frequency domain decomposition. In: Proceedings of the 18 "International Modal Analysis Conference (IMAC)". San Antonio, Texas
4. Cho SG, Kim D, Chaudhary S (2011) A simplified model for nonlinear seismic response analysis of equipment cabinets in nuclear power plants. Nucl Eng Des 241(8):2750–2757
5. Gupta A, Rustogi SK, Gupta AK (1999) Ritz vector approach for evaluating incabinet response spectra. Nucl Eng Des 190(3):255–272
6. Gupta A, Yang J (2002) Modified Ritz vector approach for dynamic properties of electrical cabinets and control panels. Nucl Eng Des 217(1–2):49–62

7. Hur J, Althoff E, Sezen H, Denning R, Aldemir T (2017) Seismic assessment and performance of nonstructural components affected by structural modeling. *Nucl Eng Technol* 49(2):387–394
8. Nguyen PC, Kim SE (2017) Investigating effects of various base restraints on the nonlinear inelastic static and seismic responses of steel frames. *Int J Non-Linear Mech* 89:151–167
9. Nguyen PC, Kim SE (2018) A new improved fiber plastic hinge method accounting for lateral-torsional buckling of 3D steel frames. *Thin-Walled Struct* 127:666–675
10. Nguyen DD, Thusa B, Han TS, Lee TH (2019) Identifying significant earthquake intensity measures for evaluating seismic damage and fragility of nuclear power plant structures. *Nucl Eng Technol*
11. Tran TT, Cao AT, Nguyen THX, Kim D (2019a) Fragility assessment for electric cabinet in nuclear power plant using response surface methodology. *Nucl Eng Technol* 51(3):894–903
12. Tran TT, Kim D (2019b) Uncertainty quantification for nonlinear seismic analysis of cabinet facility in nuclear power plants. *Nucl Eng Des* 355

Experimental Modelling of Self-excited Responses of a Square Cylinder in Smooth Wind Flow



Cung Huy Nguyen, Van Tan Vu, and Khang Thanh Huong

1 Introduction

It is well-known that a slender structure with squares section is prone to aeroelastic instability including Vortex-induced vibration (VIV) or galloping. Many wind tunnel studies have been carried out to understand these self-excited phenomena and determine the aeroelastic responses of the structure, e.g. Barrero-Gil and Fernandez-Arroyo [1], Freda et al. [2], Kumar and Gowda [3], Lee [4]. In most studies, the structural body is allowed to vibrate in a direction normal to wind. An extensive review of VIV and galloping is referred to Paidoussis et al. [6]. The literature shows that agreement between experiments and theoretical predictions are not always present [2]. In addition, as in real practice, a structure can vibrate in different directions under wind actions, depending on the orientation of the principal axes to the wind. This mean that the aeroelastic instability may still occur in a direction inclined to the wind. That requires further investigations.

The remarks above motivate a study on the self-excited responses of a square-section cylinder prism to wind loads using wind tunnel tests. This paper present such a study to identify the role of the structural axis orientation to the wind. Wind tunnel tests were conducted for the cases of cross-wind and non-cross-wind to evaluate the aeroelastic responses. The experiment result is also compared with the theoretical prediction using quasi-steady theory, which is widely used in previous research and applications.

C. H. Nguyen (✉)

Industrial University of Ho Chi Minh City, Ho Chi Minh City, Vietnam

e-mail: nguyenhuycung@iuh.edu.vn

V. T. Vu

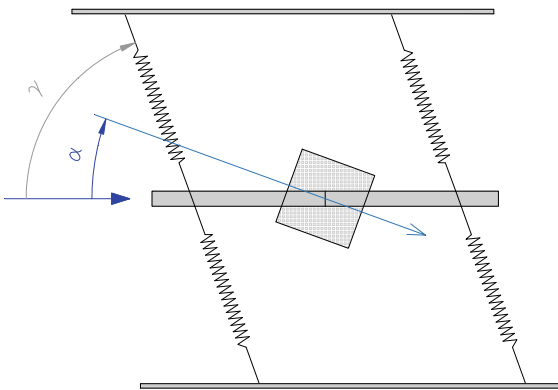
University of Architecture Ho Chi Minh City, Ho Chi Minh City, Vietnam

K. T. Huong

Technology University of Ostrava, Ostrava, Czech Republic

Ton Duc Thang University, Ho Chi Minh City, Vietnam

Fig. 1 Sketch of the vibration model in the experimental setup (α is angle of attack, γ is inclination angle)



2 Wind Tunnel Modeling

2.1 Experimental Setup

Wind tunnel tests on a 140 mm \times 140 mm square section model in smooth flow were conducted in the aeronautical wind tunnel at BMT Fluid Mechanics Ltd, Teddington, UK. The tunnel test section is 2.74 m wide and 2.14 m high. It can run with wind speed varying from 0.2 to 65 m/s. The blockage ratio is very low (<2.5%), so no data correction has been adopted with reference to the blockage ratio.

To study the role of the orientation of the structural axes with respect to the wind direction on the aeroelastic responses and to assess the validity of quasi-steady theory, which is often used in predicting the critical velocity for galloping, dynamic tests were carried out at an angle of attack of $\alpha = 10^\circ$ for two cases of inclination angle γ : $\gamma = 90^\circ$ and $\gamma = 80^\circ$. The first case is the conventional wind tunnel test for transverse vibration. Figure 1 shows the arrangement of the model setup and definition of the two angles. Each end of the model was mounted on a dynamic rig consisting of a system of springs allowing for the vibrations. A laser system with Micro Epsilon opto NCDT lasers was used to measure the vibration responses. To provide additional damping to the system, an electro-magnetic damping system with copper plates moving through magnetic fields was used.

2.2 Experimental Results

Figure 2 shows an example of steady-state responses in 40 s. At a given wind speed, the displacement is determined as the root-mean-square of the 40-s time response. The determination of VIV and galloping responses are based on the steady-state responses.

Fig. 2 Steady-state of the dynamic response

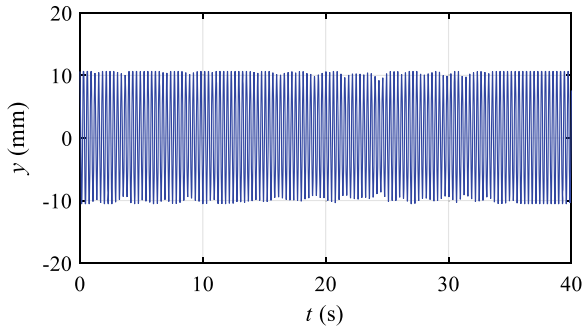


Figure 3 shows the reduced response y_r , defined in Eq. (1) below, divided by Scruton number (Sc) versus the reduced wind speeds U_r , also divided by Sc , for $\gamma = 82^\circ$ and $\gamma = 90^\circ$ at angle of attack $\alpha = 10^\circ$.

$$y_r = \frac{y}{fb}; U_r = \frac{U}{fb} \quad (1)$$

$$Sc = \frac{4\pi\xi m}{\rho b^2} \quad (2)$$

where y , f , b , U , m , ξ , ρ are the root-mean-square response amplitude, structural frequency, width of cross section, mean wind velocity, mass per unit length, structural

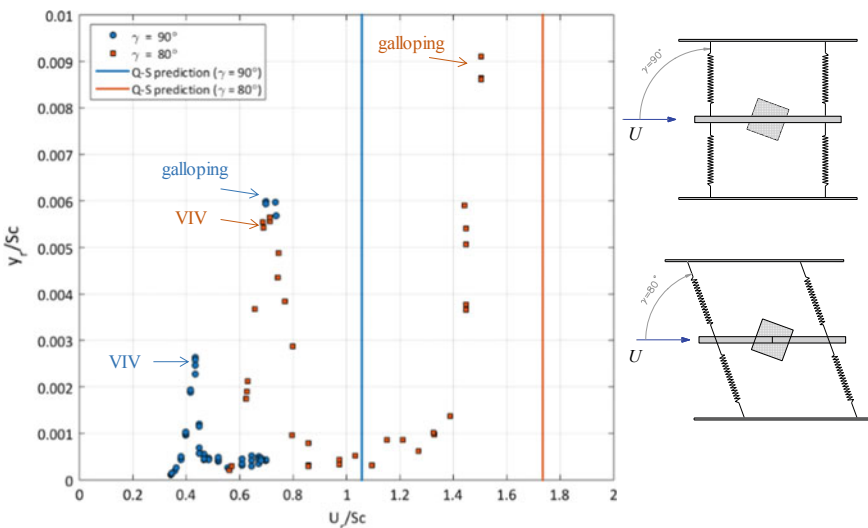


Fig. 3 Normalized galloping hysteresis amplitudes for different orientations of the principal axes, $\gamma = 80^\circ$, $\gamma = 90^\circ$

damping ratio, air density, respectively. For each case, the normalised critical wind velocities $U_{r,cr}$ predicted through quasi-steady (Q-S) theory, based on the following equation [2], are also shown in the figure in order to compare the experiment and theory.

$$U_{r,cr} = -\frac{2Sc}{C_D + C'_L} \quad (3)$$

where C_D and C'_L are the drag coefficient and the prime derivative of lift coefficient with respect to angle of attack and Scuton number, respectively.

It can be seen from Fig. 3 that VIV and galloping occur when wind is normal and incline to the structural axis. It is evident that their responses are different for different inclination angle between the wind direction and the axis. Both VIV and galloping occur at lower wind speeds for $\gamma = 90^\circ$ than for $\gamma = 80^\circ$. The structural responses herein are different between the two cases that is different from the well-known study by Parkinson and Smith [7], which states that, for the same angle of attack, structural damping and frequency, the responses are collapsed in a single curve, i.e. no different response for the two cases. This shows that the structural axis play a significant role in the responses of the structure to wind, particularly in the condition for VIV and galloping occurrence.

Figure 3 also shows the prediction of critical wind speeds for galloping occurrence through the mean of quasi-steady theory. For $\gamma = 90^\circ$, galloping occurs at $U_{cr,r}/Sc = 0.73$, while the theory predicts the galloping occurrence at a higher wind speed with $U_{cr,r}/Sc = 1.06$, i.e. higher 45%. For $\gamma = 80^\circ$, the theory gives a better prediction with $U_{cr,r}/Sc = 1.75$, which is higher 17% than the value given by the test with $U_{cr,r}/Sc = 1.5$. The result reveals that the quasi-steady theory works better for the case of inclined axis to the wind. However, as for both cases the theoretical prediction provides a higher critical wind speeds than the tests, such prediction provides unsafe critical condition for the structural stability. The failure of the use of the quasi-steady theory for galloping prediction was also previously reported in [5].

3 Conclusions

Different from previous wind tunnel experiments for vibration of sectional prism, where solely cross-wind vibrations have been addressed, this paper presents an experimental investigation to study the structural vibration in a non-crosswind direction. This reflect the practice that the structural motion can be in a direction different from transverse wind when its principal axis is not normal to the wind direction. Two dynamic wind tunnel setups have been setup to evaluate the response of a square cylinder to wind, a conventional one to study cross-wind vibration and another to study non cross-wind vibration.

The result shows that the cylinder has different aeroelastic behaviour for different angles between the wind direction and the structural axes. The orientation of structural axis with respect to the wind play an important role for the aeroelastic response of the structure.

Quasi-steady theory overestimates the critical wind velocity for across-wind galloping. When changing the principal axis direction, the theoretical prediction however agrees better with the experimental results. As the quasi-steady theory provides prediction unsafe for the structures, at least for the current study, further studies on the aeroelastic behaviour of square cylinders are required.

Acknowledgements This research is funded by Vietnam National Foundation for Science and Technology Development (NAFOSTED) under grant number 107.04-2017.321.

Wind tunnel data is obtained from the wind tunnel tests conducted at BMT Fluid Mechanics Ltd during the first author's visit at University of Bristol under the support of the Newton Fund (grant number NRCP/1415/292). The author is deeply indebted to Dr Macdonald (University of Bristol) and the BMT team (Mr Stefano Cammelli, Mr. Tomas Krajcovic and Mr. David Hood) for their support.

The second author is thankful to the University of Architecture Ho Chi Minh (UAH) for supporting him to attend to the conference.

References

1. Barrero-Gil A, Fernandez-Arroyo P (2013) Maximum vortex-induced vibrations of a square prism. *Wind Struct Int J* 17(1):107–121
2. Freda A, Carassale L, Piccardo G (2015) Aeroelastic crosswind response of sharp-edge square sections : experiments versus theory. In: Proceedings of the 14th International Conference on Wind Engineering, Porto Alegre, Brazil, 21–26 June 2015
3. Kumar RA, Gowda BHL (2006) Flow-induced vibration of a square cylinder without and with interference 22:345–369
4. Lee BE (1975) The effect of turbulence on the surface pressure field of a square prism. *J Fluid Mech* 69:263–282
5. Nguyen CH, Freda A, Solari G, Federica T (2015) Experimental investigation of the aeroelastic behavior of a complex prismatic element. *Wind Struct Int J* 20(5):683–699
6. Paidoussis M, Price S, De Langre E (2011) Fluid-Structure Interactions: cross-flow-induced instabilities. Cambridge University Press
7. Parkinson G, Smith J (1964) The square prism as an aeroelastic non-linear oscillator. *Q J Mech Appl Math* 17(2):225–239

Free Vibration Analysis of FG Sandwich Plates on Elastic Foundation Using a Refined Quasi-3D Inverse Sinusoidal Shear Deformation Theory



**Tan-Van Vu, Ngoc-Hung Nguyen, Tan-Tai Huynh Nguyen,
Canh-Tuan Nguyen, Quang-Hung Truong, and Ut-Kien Van Tang**

1 Introduction

Sandwich-structured composite is fabricated by some homogeneous elastic layers to reach the desirable mechanical properties, thus it widely used in many engineering applications. However, the sudden change of material properties across the layers may lead to large interlaminar stresses resulting in delamination failures. One can use functionally graded materials (FGM) whose mechanical properties change continuously for the layers in order to overcome this drawback. Recently, the sandwich plate structure resting on elastic foundations have been extensively adopted by many researchers to model various structural engineering problems. The well-known direct applications of these kinds of plates are pavements of highways, airport runways, foundation of storage tanks and building infrastructures.

T.-V. Vu (✉)

Department of Civil Engineering, University of Architecture Ho Chi Minh City, Ho Chi Minh City, Vietnam

e-mail: van.vutan@uah.edu.vn

N.-H. Nguyen

Faculty of Architecture, Thu Dau Mot University, Thu Dau Mot, Binh Duong Province, Vietnam

T.-T. H. Nguyen

Falculty of Civil Engineering, Ho Chi Minh City of Technology and Education, Ho Chi Minh City, Vietnam

C.-T. Nguyen

Faculty of Civil Engineering, Ho Chi Minh City University of Technology, VNU-HCM, Ho Chi Minh City, Vietnam

Q.-H. Truong

Ssangyong Engineering & Construction Co. Ltd., Ho Chi Minh City, Vietnam

U.-K. Van Tang

Gia Khang Thinh Construction Co. Ltd., Ho Chi Minh City, Vietnam

Some authors have studied the free vibration problem of FG sandwich plates on the elastic foundations based on the analytical and numerical methods. In framework of the analytical method, Sobhy [4] employed the sinusoidal shear deformation plate theory to generate the exact solutions of the critical buckling loads and natural frequencies of exponential-law FG sandwich plates under different boundary conditions on the isotropic or orthotropic two-parameter [3] elastic foundations. Akavci [1] employed the hyperbolic shear and normal deformation plate theory to analysis the natural frequencies of the power-law FG sandwich plates. Li et al. [2] utilized the first-order shear deformation theory (FSDT) combined with Fourier-Ritz method to investigate the vibration characteristics of the moderately thick FG sandwich sector plates with general plate boundary conditions. Singh and Harsha [5] have developed inverse hyperbolic shear deformation plate theory for the free vibration and buckling analysis of sigmoidal-law FG sandwich plates using the various boundary conditions. In framework of the numerical method, Tossapanon and Wattanasakulpong [7] employed the spectral method integrated with FSDT to analysis the natural frequencies of FG sandwich plates. Lately, Singh and Harsha [6] employed the stress-function Galerkin method to explain the nonlinear dynamic characteristics of the modified sigmoid-law FG sandwich plates in thermal environment.

To the best of authors knowledge, the natural frequency analysis of the FG sandwich plates resting on elastic foundation by using the moving Kriging interpolation-based element-free Galerkin method has not been presented, yet. So, this paper presents an efficient refined quasi-3D hyperbolic shear deformation theory (R-QSDT) wherein the effect of shear deformation and normal deformation are taken into account with the enhanced moving Kriging interpolation-based (EMKI) element-free Galerkin method [8] to the free vibration analysis of FG sandwich plates resting on the Pasternak's foundation.

2 Theoretical Formulations

A considered rectangular FG sandwich plate of constant thickness h and cross-sectional dimensions a and b is shown in Fig. 1a. It consists of three homogeneous or FGM layers with the same Poisson's ratio ν resting on the Pasternak's foundation. Each FGM layer possessed the effective mechanical properties varied continuously

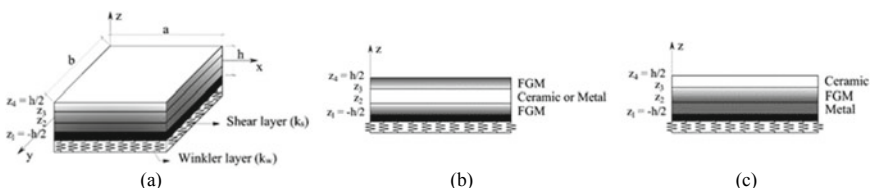


Fig. 1 The FG sandwich plate: **a** Plate geometry in Cartesian coordinate system; **b** Type A; **c** Type B

across the thickness to obey a power-law distribution defined by Eq. (1)

$$P(z) = P_b + (P_t - P_b)V(z) \quad \text{where} \quad V(z) = (0.5 + z/h)^n \quad (1)$$

wherein $P(z)$ is an effective material property such as Young's modulus $E(z)$ or mass density $\rho(z)$; P_t and P_b are the material properties of the layer top and bottom, respectively; $V(z)$ and n are the volume fraction and gradient index, respectively.

2.1 FG Sandwich Plates with Homogeneous Core and FGM Skins (Type A)

The FG sandwich plate-type A consists of a homogeneous core and two skins whose metal-rich at surfaces $z = z_1, z = z_4$ and ceramic-rich at surfaces $z = z_2, z = z_3$, is depicted in Fig. 1b. The volume fraction of the FGM skins can be calculated by Eq. (2)

$$\begin{aligned} V_c^{(1)}(z) &= \left(\frac{z - z_1}{z_2 - z_1} \right)^n, \quad z \in [z_1, z_2]; \quad V_c^{(2)}(z) = 1, \quad z \in [z_2, z_3]; \\ V_c^{(3)}(z) &= \left(\frac{z_4 - z}{z_4 - z_3} \right), \quad z \in [z_3, z_4] \end{aligned} \quad (2a,b,c)$$

where $(z_2 - z_1)$ and $(z_4 - z_3)$ are thicknesses of bottom and top skins, respectively. Thickness index of each plate layers of $(z_4 - z_3)/(z_3 - z_2)/(z_2 - z_1)$ is determined as the different ratios 2/1/2; 2/2/1 and so on.

2.2 FG Sandwich Plate with FGM Core and Homogeneous Skins (Type B)

Figure 1c illustrates the FG sandwich plate-type B consisting of a power-law FGM core and two homogeneous layers. The volume fraction of this FG sandwich can be calculated by Eq. (3)

$$\begin{aligned} V_c^{(1)}(z) &= 0, \quad z \in [z_1, z_2], \\ V_c^{(2)}(z) &= \left(\frac{z - z_2}{z_3 - z_2} \right)^n, \quad z \in [z_2, z_3], \\ V_c^{(3)}(z) &= 1, \quad z \in [z_3, z_4] \end{aligned} \quad (3a,b,c)$$

where $V_c^{(i)}$, ($i = 1, 2, 3$) is the volume fraction function of layer i ; $(z_3 - z_2)$ is the core thickness.

2.3 An Efficient R-QSDT Integrated with EMKI Element-Free Galerkin Method

Let Ω be a domain in \mathbb{R}^2 located in the plate mid-plane. Regarding to the stretching effect in z direction ($\varepsilon_z \neq 0$), the plate displacements u , v and w in the x , y and z directions, respectively can be modeled with only (4) unknown variables [9] as follows:

$$u(x, y, z) = u_0(x, y) - z\partial w_b(x, y)/\partial x + f(z)\partial w_s(x, y)/\partial x \quad (4)$$

$$v(x, y, z) = v_0(x, y) - z\partial w_b(x, y)/\partial y + f(z)\partial w_s(x, y)/\partial y \quad (5)$$

$$w(x, y, z) = w_b(x, y) + w_s(x, y)g(z) \quad (6)$$

One can set up the above equations in the following matrix form

$$\bar{\mathbf{u}} = \bar{\mathbf{u}}_0 + z\bar{\mathbf{u}}_1 + f(z)\bar{\mathbf{u}}_2 + g(z)\bar{\mathbf{u}}_3; \quad \bar{\mathbf{u}}_0 = \{u_0 \ v_0 \ w_b\}^T, \bar{\mathbf{u}}_1 = -\{\partial w_b/\partial x \ \partial w_b/\partial y \ 0\}^T, \bar{\mathbf{u}}_3 = \{0 \ 0 \ w_s\}^T \text{ and } \bar{\mathbf{u}}_2 = \{\partial w_s/\partial x \ \partial w_s/\partial y \ 0\}^T.$$

The strain-displacement relations are given by Eq. (7)

$$\begin{aligned} \bar{\boldsymbol{\varepsilon}} &= \{\varepsilon_x \ \varepsilon_y \ \gamma_{xy} \ \varepsilon_z\}^T = \bar{\boldsymbol{\varepsilon}}_0 + z\bar{\boldsymbol{\varepsilon}}_1 + f\bar{\boldsymbol{\varepsilon}}_2 + g'\bar{\boldsymbol{\varepsilon}}_3; \\ \bar{\boldsymbol{\gamma}} &= \{\gamma_{xz} \ \gamma_{yz}\}^T = [f' + g]\bar{\boldsymbol{\varepsilon}}_s \end{aligned} \quad (7a,b)$$

where

$$\begin{aligned} \bar{\boldsymbol{\varepsilon}}_0 &= \left\{ \begin{array}{c} \partial u_0/\partial x \\ \partial v_0/\partial y \\ \partial u_0/\partial y + \partial v_0/\partial x \\ 0 \end{array} \right\}, \bar{\boldsymbol{\varepsilon}}_1 = -\left\{ \begin{array}{c} \partial^2 w_b/\partial x^2 \\ \partial^2 w_b/\partial y^2 \\ 2\partial^2 w_b/\partial x \partial y \\ 0 \end{array} \right\}, \\ \bar{\boldsymbol{\varepsilon}}_2 &= \left\{ \begin{array}{c} \partial^2 w_s/\partial x^2 \\ \partial^2 w_s/\partial y^2 \\ 2\partial^2 w_s/\partial x \partial y \\ 0 \end{array} \right\}, \bar{\boldsymbol{\varepsilon}}_3 = \left\{ \begin{array}{c} 0 \\ 0 \\ 0 \\ w_s \end{array} \right\}, \bar{\boldsymbol{\varepsilon}}_s = \left\{ \begin{array}{c} \partial w_s/\partial x \\ \partial w_s/\partial y \end{array} \right\} \end{aligned} \quad (8a,b,c,d,e)$$

In which $f = \sin^{-1}(ze^{-2(z/h)^2})$ and $g = f'$, while f' and g' are the first derivatives with respect to z , respectively. The virtual work principle for the free vibration of FGM plate resting on the two-parameter elastic foundation can be stated as:

$$\int_{\Omega} \delta \boldsymbol{\varepsilon}^T \mathbf{D}^e \boldsymbol{\varepsilon} d\Omega + \int_{\Omega} \delta \boldsymbol{\varepsilon}_s^T \mathbf{D}^s \boldsymbol{\varepsilon}_s d\Omega + \int_{\Omega} \nabla^T \delta(w_b + gw_s) k_s \nabla(w_b + gw_s) d\Omega$$

$$\begin{aligned}
& + \int_{\Omega} \delta(w_b + gw_s) k_w (w_b + gw_s) d\Omega + \dots \\
& + \int_{\Omega} \delta \mathbf{u}^T \mathbf{m} \ddot{\mathbf{u}} d\Omega = 0; \quad \mathbf{D}^s = \int_{-h/2}^{h/2} \mathbf{D}_s(z) dz, \\
D_{ij}^s &= \int_{-h/2}^{h/2} (f' + g)^2 G_{ij} dz, \quad \mathbf{G} = \frac{E(z)}{2(1+\nu)} \begin{bmatrix} 1 & 0 \\ 0 & 1 \end{bmatrix} \quad (9a,b,c,d)
\end{aligned}$$

where k_w and k_s are the spring stiffness of Winkler and shear modulus of elastic foundation, respectively. $\nabla^T = [\partial/\partial x \ \partial/\partial y]^T$, $\boldsymbol{\varepsilon} = \{\boldsymbol{\varepsilon}_0 \ \boldsymbol{\varepsilon}_1 \ \boldsymbol{\varepsilon}_2 \ \boldsymbol{\varepsilon}_3\}^T$, $\mathbf{u} = \{\mathbf{u}_0 \ \mathbf{u}_1 \ \mathbf{u}_2 \ \mathbf{u}_3\}^T$; $A_{ij}^e, B_{ij}^e, D_{ij}, C_{ij}, E_{ij}, F_{ij}, L_{ij}, H_{ij}, O_{ij}, P_{ij} = \int_{-h/2}^{h/2} \{1, z, z^2, f, g', zf, zg', f^2, fg', g^2\} Q_{ij} dz$

$$\begin{aligned}
\mathbf{D}^e &= \begin{bmatrix} \mathbf{A}^e & \mathbf{B}^e & \mathbf{C} & \mathbf{E} \\ \mathbf{B} & \mathbf{D} & \mathbf{F} & \mathbf{L} \\ \mathbf{C} & \mathbf{F} & \mathbf{H} & \mathbf{O} \\ \mathbf{E} & \mathbf{L} & \mathbf{O} & \mathbf{P} \end{bmatrix}, \quad \mathbf{Q} = \frac{E(z)}{(1-2\nu)(1+\nu)} \begin{bmatrix} 1-\nu & \nu & 0 & \nu \\ \nu & 1-\nu & 0 & \nu \\ 0 & 0 & (1-2\nu)/2 & 0 \\ \nu & \nu & 0 & 1-\nu \end{bmatrix}, \\
\mathbf{m} &= \begin{bmatrix} I_1 & I_2 & I_4 & I_5 \\ I_2 & I_3 & I_6 & I_7 \\ I_4 & I_6 & I_8 & I_9 \\ I_5 & I_7 & I_9 & I_{10} \end{bmatrix} \quad (10)
\end{aligned}$$

and $\{I_1, I_2, I_3, I_4, I_5, I_6, I_7, I_8, I_9, I_{10}\} = \int_{-h/2}^{h/2} \rho(z) \{1, z, z^2, f, g, zf, zg, f^2, fg, g^2\} dz$;

According to the moving kriging interpolation (MKI), an unknown function $\mathbf{u}^h(\mathbf{x})$ can be generated by the vector valued function $\mathbf{u}(\mathbf{x})$ based on points $\mathbf{x}_i (i \in [1, n_x])$ in a sub-domain $\Omega_x \subseteq \Omega$, where n_x is the total number of the nodes in Ω_x as follows:

$$\mathbf{u}^h(\mathbf{x}) = [\mathbf{p}^T(\mathbf{x}) \mathbf{A} + \mathbf{r}^T(\mathbf{x}) \mathbf{B}] \mathbf{u}(\mathbf{x})$$

or

$$\mathbf{u}^h(\mathbf{x}) = \sum_{I=1}^{n_x} \phi_I(\mathbf{x}) \mathbf{u}_I; \quad \phi_I(\mathbf{x}) = \sum_{j=1}^m p_j(\mathbf{x}) A_{jI} + \sum_{k=1}^n r_k(\mathbf{x}) B_{kI} \quad (11)$$

wherein $\phi_I(x)$ is the moving kriging shape function, $\mathbf{A} = (\mathbf{P}^T \mathbf{R}^{-1} \mathbf{P})^{-1} \mathbf{P}^T \mathbf{R}^{-1}$, $\mathbf{B} = \mathbf{R}^{-1}(\mathbf{I} - \mathbf{P}\mathbf{A})$; \mathbf{I} is unit matrix; vectors $\mathbf{p}^T(\mathbf{x}) = [p_1(\mathbf{x}) \ p_2(\mathbf{x}) \ \dots \ p_m(\mathbf{x})]$ and $\mathbf{r}^T(\mathbf{x}) = [R(\mathbf{x}_1, \mathbf{x}), R(\mathbf{x}_2, \mathbf{x}), \dots, R(\mathbf{x}_n, \mathbf{x})]$ are the polynomial with m basic functions and the correlation function, respectively. In this study, we employed the multi-quadratic correlation function to make the MKI shape function stable [8]. In framework of the enhanced MKI-based meshless method, the plate displacement field can be

approximated by $\mathbf{u}^h = [u^h \ v^h \ w_b^h \ w_s^h]^T$ and $\mathbf{u}_I = [u_I \ v_I \ w_{bI} \ w_{sI}]^T$. Substituting Eq. (11) into Eq. (8), one can obtain:

$$\begin{aligned}\bar{\mathbf{e}}_0 &= \sum_{I=1}^n \mathbf{B}_I^m \mathbf{u}_I, \bar{\mathbf{e}}_1 = \sum_{I=1}^n \mathbf{B}_I^{b1} \mathbf{u}_I, \bar{\mathbf{e}}_2 = \sum_{I=1}^n \mathbf{B}_I^{b2} \mathbf{u}_I \\ \bar{\mathbf{e}}_3 &= \sum_{I=1}^n \mathbf{B}_I^{b3} \mathbf{u}_I, \bar{\mathbf{e}}_s = \sum_{I=1}^n \mathbf{B}_I^s \mathbf{u}_I\end{aligned}\quad (12a,b,c,d,e)$$

wherein

$$\begin{aligned}\mathbf{B}_I^m &= \begin{bmatrix} \phi_{I,x} & 0 & 0 & 0 \\ 0 & \phi_{I,y} & 0 & 0 \\ \phi_{I,y} & \phi_{I,x} & 0 & 0 \\ 0 & 0 & 0 & 0 \end{bmatrix}; \mathbf{B}_I^{b1} = \begin{bmatrix} 0 & 0 & -\phi_{I,xx} & 0 \\ 0 & 0 & -\phi_{I,yy} & 0 \\ 0 & 0 & -2\phi_{I,xy} & 0 \\ 0 & 0 & 0 & 0 \end{bmatrix}; \\ \mathbf{B}_I^{b2} &= \begin{bmatrix} 0 & 0 & 0 & \phi_{I,xx} \\ 0 & 0 & 0 & \phi_{I,yy} \\ 0 & 0 & 0 & 2\phi_{I,xy} \\ 0 & 0 & 0 & 0 \end{bmatrix}; \mathbf{B}_I^{b3} = \begin{bmatrix} 0 & 0 & 0 & 0 \\ 0 & 0 & 0 & 0 \\ 0 & 0 & 0 & 0 \\ 0 & 0 & 0 & \phi_I \end{bmatrix}; \\ \mathbf{B}_I^s &= \begin{bmatrix} 0 & 0 & 0 & \phi_{I,x} \\ 0 & 0 & 0 & \phi_{I,y} \end{bmatrix}\end{aligned}\quad (13a,b,c,d,e)$$

with

$$\begin{aligned}\mathbf{u}_0 &= \sum_{I=1}^n \mathbf{N}_I^0 \mathbf{u}_I, \mathbf{u}_1 = \sum_{I=1}^n \mathbf{N}_I^1 \mathbf{u}_I, \\ \mathbf{u}_2 &= \sum_{I=1}^n \mathbf{N}_I^2 \mathbf{u}_I, \mathbf{u}_3 = \sum_{I=1}^n \mathbf{N}_I^0 \mathbf{u}_I\end{aligned}\quad (14a,b,c,d)$$

and

$$\begin{aligned}\mathbf{N}_I^0 &= \begin{bmatrix} \phi_I & 0 & 0 & 0 \\ 0 & \phi_I & 0 & 0 \\ 0 & 0 & \phi_I & 0 \end{bmatrix}, \mathbf{N}_I^1 = \begin{bmatrix} 0 & 0 & -\phi_{I,x} & 0 \\ 0 & 0 & -\phi_{I,y} & 0 \\ 0 & 0 & 0 & 0 \end{bmatrix}, \mathbf{N}_I^3 = \begin{bmatrix} 0 & 0 & 0 & 0 \\ 0 & 0 & 0 & 0 \\ 0 & 0 & 0 & \phi_I \end{bmatrix}, \\ \mathbf{N}_I^2 &= \begin{bmatrix} 0 & 0 & 0 & \phi_{I,x} \\ 0 & 0 & 0 & \phi_{I,y} \\ 0 & 0 & 0 & 0 \end{bmatrix}; \mathbf{N}_I^3 = \begin{bmatrix} 0 & 0 & 0 & 0 \\ 0 & 0 & 0 & 0 \\ 0 & 0 & 0 & \phi_I \end{bmatrix}\end{aligned}\quad (15a,b,c,d)$$

3 Numerical Results

Example 1 A free vibration analysis of a simply-supported FG square sandwich plate (type A) made of aluminium (Al) and zirconia (ZnO_2) resting on the elastic foundation is considered a benchmark problem to assess the proposed method's accuracy. Young's modulus and density mass for aluminium are $E_m = 70 \text{ GPa}$ and $\rho_m = 2707 \text{ kg/m}^3$, respectively. These mechanical properties of zirconia are $E_c = 151 \text{ GPa}$ and $\rho_c = 3000 \text{ kg/m}^3$. Both aluminium and zirconia have the same Poisson's ratio $\nu = 0.3$. Two parameters of the elastic foundation are $K_w = k_w a^4 / D_c$ and $K_s = k_s a^2 / D_c$ with $D_c = E_c h^3 / 12 / (1 - \nu^2)$, respectively.

The plate natural frequency is normalized by $\bar{\omega} = \omega a^2 / h \sqrt{\rho_0 / E_0}$ with $E_0 = 1 \text{ GPa}$ and $\rho_0 = 1 \text{ kg/m}^3$. Table 1 shows the comparison of the first non-dimensional natural frequencies obtained by the present R-QSDT with 17×17 uniformly nodes with those generated by the quasi-3D hyperbolic shear deformation theory [1] in tabular form. From the results, it is concluded that present results are in good agreement with the Akavcis' results, irrespective of the length-to-thickness ratios, foundation parameters or gradient indices considered. It is worth noting that the plate natural frequency decreases as the gradient index of the FGM layers increases.

Example 2 The effect of the elastic foundation on the natural frequencies of Al/Al_2O_3 simply-supported FG square sandwich plate (type B) with the fixed side-to-thickness ratio $a/h = 5$ is investigated in this example. Young's modulus and density mass for alumina are $E_c = 380 \text{ GPa}$ and $\rho_c = 3800 \text{ kg/m}^3$, respectively. The variations of the first non-dimensional natural frequency of the FG sandwich plate versus the gradient index are depicted in Fig. 2a-d. It is observed that the natural frequency increases with different configuration of sandwich FGM plate as all elastic foundation parameters increase. As increasing the gradient index of the FGM core, the magnitudes of the natural frequency are increasing with the increasing the shear modulus of Pasternak foundation. From the Fig. 2c, d, it can be concluded that the effect of spring stiffness of Winkler foundation on the natural frequency of the plate is insignificant.

4 Conclusions

An EMKI meshless method integrated with a novel R-QSDT for free vibration analysis of FGM sandwich plates resting on the two-parameter elastic foundation is presented. The accuracy of the proposed method is ascertained by comparing its results with existing solutions using the different side-to-thickness ratios, gradient indices and elastic foundation parameters. The foundation parameters effect on the non-dimensional frequency for different configurations of sandwich FGM plates are analysed. It is relevant to notice that the plate natural frequency is increasing with

Table 1 Comparison for the first non-dimensional natural frequency $\bar{\omega}$ of the simply-supported FG square (Al/ZrO_2) sandwich plate (type A)

$\frac{a}{h}$	n	K_w	K_s	2 - 1 - 2	1 - 1 - 1	2 - 2 - 1	1 - 2 - 1
5	0	0	0	1.1912	1.2028	Akavci [1] Present	Akavci [1] Present
				(-0.98) ^a	(-0.98)		(-0.98)
10	10	1.5135	1.5202	1.5135	1.5202		
				(-0.45)	(-0.45)		(-0.45)
10^2	10^2	3.0908	3.0941	3.0908	3.0941		
				(-0.11)	(-0.11)		(-0.11)
2	0	0.9318	0.9211	0.9541	0.9333	0.9755	0.9665
				(1.15)	(2.19)		(0.92)
10	10	1.3341	1.3279	1.3469	1.3334	1.3611	1.3554
				(0.46)	(1.01)		(0.42)
102	102	2.6823	2.6852	2.7579	2.7608	2.7937	2.7973
				(-0.11)	(-0.11)		(-0.13)
10	0	0.8791	0.8685	0.8969	0.8721	0.9215	0.9111
				(1.21)	(2.77)		(1.13)
10	10	1.3045	1.2987	1.3119	1.2970	1.3274	1.3216
				(0.45)	(1.14)		(0.44)
10^2	10^2	2.5044	2.5070	2.6178	2.6206	2.6707	2.6746
				(-0.11)	(-0.11)		(-0.14)
10^2	0	0	1.3404	1.3003	1.3404	1.3003	1.3404
				(2.99)	(2.99)		(2.99)

(continued)

Table 1 (continued)

$\frac{q}{h}$	n	K_w	K_s	2 - 1 - 2	1 - 1 - 1	2 - 2 - 1	1 - 2 - 1
		Akavci [1]	Present	Akavci [1]	Present	Akavci [1]	Present
10^2	10	1.6590 (1.90)	1.6275 (1.90)	1.6590 (1.90)	1.6275 (1.90)	1.6590 (1.90)	1.6275 (1.90)
	10^2	3.3694 (0.37)	3.3570 (0.37)	3.3694 (0.37)	3.3570 (0.37)	3.3694 (0.37)	3.3570 (0.37)
2	0	0.0182	0.9880 (2.97)	1.0428 (3.76)	1.0036 (3.76)	1.0695 (3.00)	1.0374 (3.01)
	10	1.4300 (1.43)	1.4095 (1.43)	1.4444 (1.88)	1.4173 (1.88)	1.4623 (1.53)	1.4399 (1.53)
10^2	10^2	3.3344 (0.17)	3.3287 (0.17)	3.3283 (0.26)	3.3196 (0.26)	3.3300 (0.20)	3.3232 (0.20)
	0	0.9602	0.9319 (2.96)	0.9758 (2.96)	0.9373 (3.95)	1.0062 (3.95)	0.9768 (2.92)
10	10	1.3967	1.3783 (1.32)	1.4029 (1.83)	1.3772 (1.83)	1.4219 (1.39)	1.4022 (1.43)
	10^2	10^2	3.3480 (0.14)	3.3434 (0.23)	3.3332 (0.23)	3.3255 (0.16)	3.3273 (0.17)

^aNumbers in parentheses denotes the percentage error in respect to Akavci's values

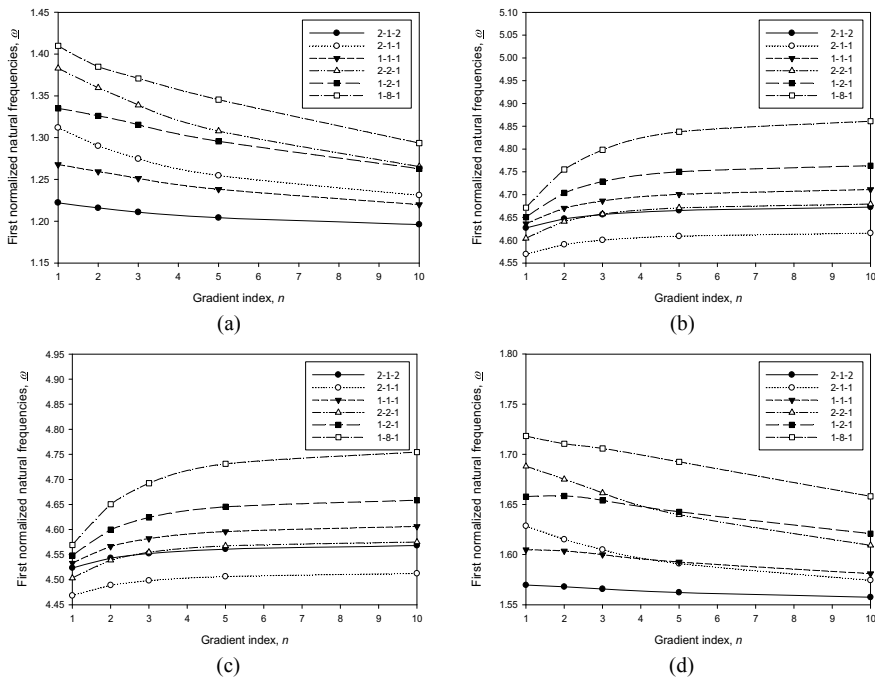


Fig. 2 Effects of foundation parameters on the natural frequency $\bar{\omega}$ for various plate configurations with $a/h = 5$: **a** $K_s = K_w = 0$; **b** $K_s = K_w = 10^2$; **c** $K_s = 10^2$, $K_w = 0$; **d** $K_s = 0$, $K_w = 10^2$

the existence of elastic foundations, and spring stiffness of Winkler's foundation has an insignificant influence on the natural frequency of the sandwich FGM plate.

Acknowledgements This research is funded by Vietnam National Foundation for Science and Technology Development (NAFOSTED) under grant number 107.01-2018.319.

References

1. Akavci SS (2016) Mechanical behavior of functionally graded sandwich plates on elastic foundation. Comp Part B Eng 96:136–152
2. Li H, Pang F, Wang X, Li S (2017) Benchmark solution for free vibration of moderately thick functionally graded sandwich sector plates on two-parameter elastic foundation with general boundary conditions. Shock Vib 35
3. Pasternak P (1954) On a new method of analysis of an elastic foundation by means of two foundation constants. Gosudarstvennoe izdatelstvo literaturi po stroitelstvu i arkhitekturie, Moscow
4. Sobhy M (2013) Buckling and free vibration of exponentially graded sandwich plates resting on elastic foundation under various boundary conditions. Comp Struct 99:76–87

5. Singh SJ, Harsha SP (2018) Exact solution for free vibration and buckling of sandwich S-FGM plates on pasternak elastic foundation with various boundary conditions. *Int J Struct Stab Dyn* 19(3)
6. Singh SJ, Harsha SP (2019) Nonlinear dynamic analysis of sandwich S-FGM plate resting on pasternak foundation under thermal environment. *Euro J Mech - A/Solids* 76:155–179
7. Tossapanon P, Wattanasakulpong N (2017) Flexural vibration analysis of functionally graded sandwich plates resting on elastic foundation with arbitrary boundary conditions: Chebyshev collocation technique. *J Sand Struct Mat*
8. Vu TV, Curiel-Sosa JL, Bui TQ (2018) A refined sin hyperbolic shear deformation theory for sandwich FG plates by enhanced meshfree with new correlation function. *Int J Mech Mat* 15:647–669
9. Zenkour AM (2013) A simple four-unknown refined theory for bending analysis of functionally graded plates. *Appl Math Model* 37:9041–9051

Hydroelastic Analysis of Floating Plates Subjected to Moving Loads in Shallow Water Condition by Using the Moving Element Method



Xuan Vu Nguyen, Van Hai Luong, Tan Ngoc Than Cao, and Minh Thi Tran

1 Introduction

Due to the pressure of intensively growing population and extensively expanding urban areas, many countries with long coastlines and islands have had land reclamation activities from sea as an effective solution. Nonetheless, such works cause negative impacts on the natural environment for both the sea and land ecosystems, and they always require a huge amount of economic costs. In order to tackle such drawbacks, Very Large Floating Structures (VLFSs) have been proposed and broadly employed in practical engineering applications such as airports, storages, facilities, even habitations and so on. For such structures, their thickness is often much smaller than two remaining dimensions. Thus, they are modeled as either thin plates or shells to analyze structural responses. Unlike researching into shell-like structures in “dry” environments where their vibrations have been uncoupled from other elastic structures having mass such as air, water, etc., for the behaviors of floating body under wave actions, their motions and pressure of fluid action the body must be determined concurrently. The displacements of a floating body cause the change of the flow surrounding them. That leads to the change of pressure of fluid in order to satisfy the Bernoulli’s equation and the motions of floating body are also affected due to this change. Especially, in case of VLFSs, the elastic deformation is included in the motion of floating body, this behavior is so-called hydroelastic and is one of key points in designing VLFSs. In this regard, there have been numerous reports to be published

X. V. Nguyen · V. H. Luong (✉) · M. T. Tran

Faculty of Civil Engineering, Ho Chi Minh City University of Technology (HCMUT), 268 Ly Thuong Kiet Street, Ward 14, District 10, Ho Chi Minh City, Vietnam
e-mail: lvhai@hcmut.edu.vn

Vietnam National University Ho Chi Minh City (VNU-HCM), Linh Trung Ward, Thu Duc District, Ho Chi Minh City, Vietnam

T. N. T. Cao
College of Technology, Can Tho University, Can Tho City, Vietnam

by many scholars thus far. For hydroelastic analyses of pontoon-type VLFSs, a comprehensive review was reported in detail by Watanabe et al. [13]. Endo and Kiyokazu [2] proposed the hybrid Boundary Element Method-Finite Element Method (BEM-FEM) for time history analyses. Ismail [3] used the time-domain three-dimensional BEM-FEM for analyzing transient responses of VLFSs subjected to unsteady loads. In addition, a variety of researches on studying behavior of infinitely extended elastic plates under moving loads were also conducted.

For example, Nevel [6] analyzed internal forces of a Kirchhoff-Love plate model-based floating ice-sheet by using the Fourier Transform Method. Furthermore, Takizawa [12] also experimentally examined responses of a floating sea ice sheet under moving load. It can be found that the above problems were only studied within the limit of linearized water wave theory. Nevertheless, for coastal areas, when the wavelength is large compared to the water depth, the linearized shallow-water theory results in a better approximation. For this aspect, Sturova [8] investigated behavior of a circular elastic plate induced by an external load by using a superposition of modal functions. A time-domain method was developed by Sturova [9] to analyze hydroelastic responses of a heterogeneous strip floating on shallow water of variable depth. On the other hand, relating to moving load analyses, behaviors of infinitely extended structures including moving excitations have appealed to many scholars in last decades. Numerous theories using FTM have been developed for traditional structural models such as beam and plate under moving loads or moving frames. However, FTM owns disadvantages when coping with moving dynamic systems of many degrees of freedom (DOFs). To overcomes this drawback, FEM has been considered as an effective method for solving complex dynamic problems. A number of studies based on FEM-model have been employed to analyses dynamic responses of various structural models subjected to moving load such as bridge, train-track, etc. Nonetheless, the FEM also encounters difficulties when the moving load approaches the boundary of the finite domain and travels beyond the boundary. In an effort to overcome the complication encountered by the standard method, Koh et al. [4] proposed a new numerical method called moving element method (MEM) to predict dynamic responses of train-tracks. That study indicated the MEM can remedy several drawbacks of the standard FEM in analyzing dynamic responses of infinite structures subjected to moving loads. For such advantages, Cao et al. [1] proposed the 3D train-track model to analyze dynamic responses of high-speed train using the MEM. Luong et al. [5] succeeded in developing the MEM to static and dynamic analyses of a Mindlin plate resting on a viscoelastic foundation. From the above-mentioned investigations, to the authors' best knowledge, almost no any report relating to hydroelastic analyses of infinite plates floating on shallow water under moving load utilizing the MEM has been published until now. In this work, a novel MEM is firstly proposed to simultaneously discretize both computational domains of fluid and structure into "moving elements" instead of only building the moving element for a structural region as that previously done in existing literature. This not only helps to completely exclude the update procedure of moving loads for each element, but also to narrow the computational domain for lessening number of elements discretized in finite element analyses (FEAs) for the effort savings.

2 Theoretical Formulation

As shown in Fig. 1, an infinite elastic thin plate under moving loads floating over water with the constant depth H , is considered herein. The z -axis of the Cartesian coordinate system is taken as positive vertically upward, with $z = 0$ defined at the plane of the undisturbed free surface. The plate infinitely extends into two directions of the plate plane.

Since the structure's draft is so shallow compared with the rest of dimensions, it can be therefore treated as zero. The interactions between water wave and the body are considered under the assumption of small amplitude shallow water approximation. At the wetted surface, there is no gap between the structure and fluid. Assume that the bottom sea is flat and the fluid is not allowed to pass through the bed, it means that the vertical velocity at the seabed is equal to zero. It is also supposed that the far fields satisfy undisturbed conditions. The reduced system of equations is presented as follow

$$\frac{\partial w}{\partial t} + h \left(\frac{\partial^2}{\partial x^2} + \frac{\partial^2}{\partial y^2} \right) \phi = 0 \quad (1)$$

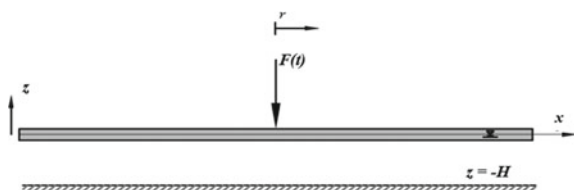
$$\frac{\partial \phi}{\partial x}; \frac{\partial \phi}{\partial y} = 0, x \rightarrow \infty, y \rightarrow \infty \quad (2)$$

$$\begin{aligned} m \frac{\partial^2 w}{\partial t^2} + \alpha \cdot \nabla^4 \left(\frac{\partial w}{\partial t} \right) + c \frac{\partial w}{\partial t} + D (\nabla^4 w) \\ + \rho g w = -\rho \frac{\partial \phi}{\partial t} \Big|_{z=0} + F(t) \delta(x-d) \delta(y) \end{aligned} \quad (3)$$

where $F(t)$ is the magnitude of moving load, $\delta()$ stands for the Dirac's delta function, and d symbolizes the longitudinal displacement of the vehicle at any instant of time, D is the plate rigidity, m is the mass per unit area, ρ is the fluid density, g is the gravitational acceleration, α is the material damping, c is the external damping coefficient and $w(x, y, t)$ denotes to the elastic vertical deflection of the plate. For solving the above boundary-value problem, a relative orthogonal Cartesian coordinate system with its origin coincidentally attached to the moving load is defined as

$$r = x - d; \quad s = y; \quad z = z \quad (4)$$

Fig. 1 The model of a floating plate under moving load



In order to transform the moving coordinate system, the governing and boundary equations can be rewritten as Eqs. (5)–(7). With regard to numerical modelings, a truncation of the infinite domain of the water-plate model is defined. The boundaries are taken to be adequate far from the moving load such that the deflection, rotation of the plate, and the potential, the velocity of the fluid are nearly equal to zero.

$$\begin{aligned} D \left(\frac{\partial^4}{\partial r^4} + 2 \frac{\partial^4}{\partial r^2 \partial s^2} + \frac{\partial^4}{\partial s^4} \right) w + m \left(\left(\frac{\partial d}{\partial t} \right)^2 \frac{\partial^2 w}{\partial r^2} - 2 \frac{\partial d}{\partial t} \frac{\partial^2 w}{\partial r \partial t} + \frac{\partial^2 w}{\partial t^2} - \frac{\partial^2 d}{\partial t^2} \frac{\partial w}{\partial r} \right) \\ + \rho g w + \alpha \nabla^4 \left(\frac{\partial w}{\partial t} - \frac{\partial d}{\partial t} \frac{\partial w}{\partial r} \right) + c \left(\frac{\partial w}{\partial t} - \frac{\partial d}{\partial t} \frac{\partial w}{\partial r} \right) \\ = -\rho \left(\frac{\partial \phi}{\partial t} - \frac{\partial d}{\partial t} \frac{\partial \phi}{\partial r} \right) \Big|_{z=0} + F(t) \delta(r) \delta(s) \end{aligned} \quad (5)$$

$$\frac{\partial w}{\partial t} - \frac{\partial d}{\partial t} \frac{\partial w}{\partial r} + h \left(\frac{\partial^2}{\partial r^2} + \frac{\partial^2}{\partial s^2} \right) \phi = 0 \quad (6)$$

$$\frac{\partial \phi}{\partial r}, \frac{\partial \phi}{\partial s} = 0, r \rightarrow \infty, s \rightarrow \infty \quad (7)$$

However, the higher the velocity of moving load is, the further the structural wave spread out from its origin before decaying to zeros is. Thus, in order to reduce the mesh size without disturbing numerical results caused by the reflected wave from the boundaries, an artificial damping layer is adopted to absorb all outgoing energies. An expression for the artificial damping coefficient, which originally developed by Nguyen and Duhamel [7], is modified for two-dimensional problems, as follows

$$c_{vd}(r, s) = \gamma \left(\frac{|r| - L_{0r}}{\lambda} \right)^4 \cdot H(|r| - L_{0r}) + \gamma \left(\frac{|s| - L_{0s}}{\lambda} \right)^4 \cdot H(|s| - L_{0s}) \quad (8)$$

After discretizing the calculated domain into a finite number of moving elements, according to the principle of virtual work with the virtual displacement of δw , the weak form of the Eq. (5) is derived. Moreover, introducing a variation of velocity potential $\delta\phi$ and integrating the Eq. (6) over the fluid domain lead to the weak formulation for the water. Adopting Galerkin's approach and letting the standard shape function of displacement and potential velocity be \mathbf{N} and $\boldsymbol{\varphi}$, respectively, the element matrices are represented by the following. In this study, the 4-node Hermite shape functions is adopted to interpolate the displacement over each element while 4-node quadrilateral element is applied to the fluid.

$$\begin{aligned} \mathbf{K}_e = \int_{S_e} (\mathbf{B}^T \mathbf{D} \mathbf{B}) dS - m \frac{\partial d}{\partial t}^2 \int_{S_e} \mathbf{N}_{,r}^T \mathbf{N}_{,r} dS - m \frac{\partial^2 d}{\partial t^2} \int_{S_e} \mathbf{N}^T \mathbf{N}_{,r} dS \\ + \rho g \int_{S_e} \mathbf{N}^T \mathbf{N} dS - \frac{\partial d}{\partial t} c \int_{S_e} \mathbf{N}^T \mathbf{N}_{,r} dS \end{aligned}$$

$$-\frac{\partial d}{\partial t} \int_{S_e} c_{vd} \mathbf{N}^T \mathbf{N}_{,r} dS - \alpha \int_{S_e} (\mathbf{B}^T \mathbf{D} \mathbf{B}_{,r}) dS \quad (9)$$

$$\mathbf{M}_e = m \int_{S_e} \mathbf{N}^T \mathbf{N} dS \quad (10)$$

$$\begin{aligned} \mathbf{C}_e &= c \int_{S_e} \mathbf{N}^T \mathbf{N} dS + \alpha \int_{S_e} (\mathbf{B}^T \mathbf{D} \mathbf{B}) dS \\ &+ \int_{S_e} c_{vd} \mathbf{N}^T \mathbf{N} dS - 2m \frac{\partial d}{\partial t} \int_{S_e} \mathbf{N}_{,r}^T \mathbf{N} dS \end{aligned} \quad (11)$$

$$\mathbf{L}_2^e = \int_{S_e} (\mathbf{N}^T \boldsymbol{\varphi}) dS; \mathbf{Ldr}_2^e = \int_{S_e} (\mathbf{N}_{,r}^T \boldsymbol{\varphi}) dS \quad (12)$$

$$\mathbf{Q}_1^e = \int_{S_e} \boldsymbol{\varphi}^T \mathbf{N} dS; \mathbf{Q}_2^e = \int_{S_e} \boldsymbol{\varphi}^T \mathbf{N}_{,r} dS \quad (13)$$

$$\mathbf{H}_{sh}^e = \int_{S_e} h(\boldsymbol{\varphi}_{,r} \boldsymbol{\varphi}_{,r} + \boldsymbol{\varphi}_{,s} \boldsymbol{\varphi}_{,s}) dS \quad (14)$$

where $(,r)$ denotes partial derivative with respect to r , S_e represents each element on the wetted surface and \mathbf{D} is the elasticity matrix and \mathbf{B} represents a matrix of differential operators which can be referred to Szilard [10]. After assembling the matrices of the model, the governing equation of motion for the combined model of the plate and fluid can be represented as follow

$$\begin{bmatrix} \mathbf{M} & \mathbf{0} \\ \mathbf{0} & \mathbf{0} \end{bmatrix} \begin{Bmatrix} \ddot{\mathbf{w}} \\ \ddot{\boldsymbol{\Phi}} \end{Bmatrix} + \begin{bmatrix} \mathbf{C} & \rho \mathbf{L}_2 \\ \mathbf{Q}_1 & \mathbf{0} \end{bmatrix} \begin{Bmatrix} \dot{\mathbf{w}} \\ \dot{\boldsymbol{\Phi}} \end{Bmatrix} + \begin{bmatrix} \mathbf{K} & \rho \frac{\partial d}{\partial t} \mathbf{Ldr}_2 \\ \frac{\partial d}{\partial t} \mathbf{Q}_2 & -\mathbf{H}_{sh} \end{bmatrix} \begin{Bmatrix} \mathbf{w} \\ \boldsymbol{\Phi} \end{Bmatrix} = \begin{bmatrix} \mathbf{P} \\ \mathbf{0} \end{bmatrix} \quad (15)$$

where the structural stiffness, damping and mass matrices are denoted by \mathbf{K} , \mathbf{C} and \mathbf{M} , respectively; \mathbf{H}_{sh} , \mathbf{Q}_1 , \mathbf{Q}_2 , \mathbf{L}_2 and \mathbf{Ldr}_2 are matrices composed by \mathbf{H}_{sh}^e , \mathbf{Q}_1^e , \mathbf{Q}_2^e , \mathbf{L}_2^e and \mathbf{Ldr}_2^e . The external force vector \mathbf{P} contains mostly zeroes, and non-zero terms in \mathbf{P} is at the contact point with the corresponding degree of freedom. $\boldsymbol{\Phi}$ is a vector containing potential velocity at nodal points and \mathbf{w} denotes a vector comprising nodal displacements of the plate model. For solving the coupled systems, the Newmark method can be employed.

3 Numerical Results

The MEM is used to calculate the behavior of a floating plate subjected to moving load in shallow water environment. The proposed approach is verified and its advantages are also highlighted. Physical parameters employed in the experiment of Takizawa [11] are adopted in a series of numerical results. In this work, a sea ice-sheet has the thickness $h = 0.17$ m and the material elastic modulus $E = 500$ Mpa. A snowmobile (235 kg in weight including a driver) has been used as a moving load with the speed change from 0 to 14 m/s. Moreover, the experiment was conducted on calm water with a water depth of 6.8 m. In order to obey the shallow water assumption, the numerical simulations are conducted with a series of reduced water depth ranging from 0.5 to 2 m. For the MEM, the wetted surface of the retained fluid domain is a rectangular with its length being 400 m and its width being 200 m. By adopting the artificial damping layer, the undisturbed condition is assumed to be satisfied at field boundaries. The fluid domain is divided into 25,000 linear moving elements which are assumed to coincide with 25,000 moving Hermite elements of the floating plate.

3.1 Verification

In this part, the accuracy and validation of proposed methodology are verified by comparing its results with those of the FTM. For this aim, the snowmobile is assumed to be a concentrated force moving at a constant velocity of 8 m/s on the plate floating over constant shallow depth of 1 m, it means that only gravity load is considered. For an adequate interval of time, the unsteady-state responses have disappeared, only the steady-state motions remain. This state is called the quasi-static state which is mentioned in the work of Nevel [6]. For the MEM, the derivatives with respect to time in Eq. (15) are vanished, and so no time-integration is needed, although the responses are still dynamic at any fixed point on the floating plate. Figure 2 presents quasi-static solutions obtained by the MEM and the FTM. The overall agreement

Fig. 2 Deflection profile of floating plate at speed of 8 m/s

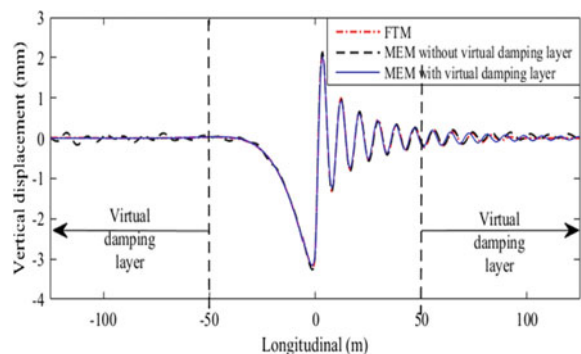
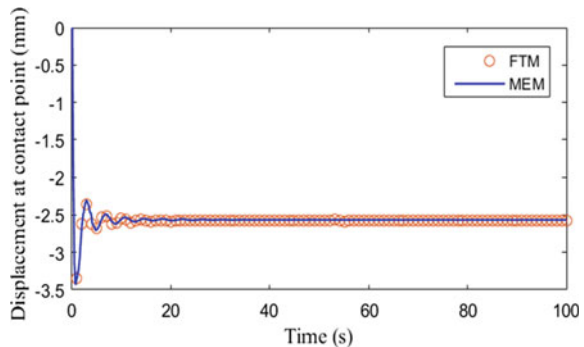


Fig. 3 Time-history of vertical displacement at the contact point



between both methods is quite good. It is noted that the artificial damping layer effectively attenuates the wave propagating away from the contact point. Hence, the only numerical solutions in the monitored zone are valid and agreement with those obtained by FTM. When the model has no artificial damping layer, the reflected wave from the fixed boundaries leads to disturbance in the far field. For time-independent behaviors, the MEM is also adopted to compute dynamic responses of the floating plate. With above load speed, a dynamic analysis is performed with the initial value $\mathbf{w} = \mathbf{w}_t = \Phi = 0$ to determine the vertical displacement at contact point. The equations system is solved with the time step $\Delta t = 0.01\text{s}$ and the total time of simulation is 100s used in the time integration scheme. Figure 3 shows the displacement at the contact point obtained by the MEM in comparison with the FTM. The outcomes gained from both methods are in close agreement with each other.

3.2 Effect of the Water Depth

In this part, the effect of water depth and load speed on responses of the plate taking account dynamic factor is studied. For the floating thin plate, in general, when the vehicle moves on the floating plate, a depression surrounding the contact point appears and the maximum deflection locates at the center of the depression. As can be seen in Fig. 4, with the increase in the speed, at the first, the depression increases and reaches to the maximum value at the speed V_{cr} which is the so-called critical speed. Above this value, the depression rapidly decreases and becomes lower than those of static load at the speed of V_u . Lastly, the depression slightly decreases with the speed above V_u . The depression depth also significantly depends on the water depth. The relationship between two variables with different values of speed is shown in Fig. 5. Generally, the tendency can be divided into three cases. At the speed below 2.5 m/s, the depression depth slightly decreases with an increase in the water depth. Above this value, the depression increases at first and reaches the peak value before the decrease. Lastly, a positive linear relationship, at the high speed above 4 m/s, is confirmed between water depth and depression depth. Concerning critical speed, in

Fig. 4 Variation of maximum displacement with the load speed

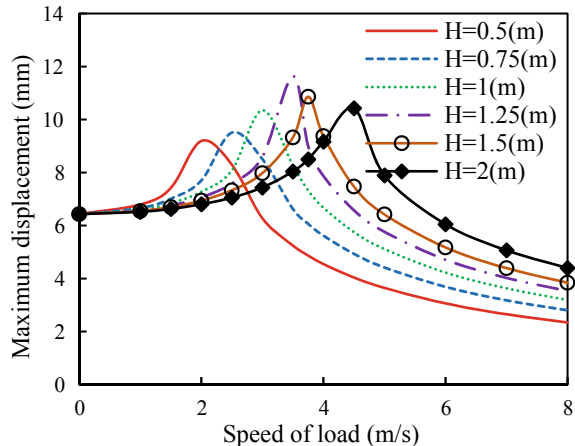
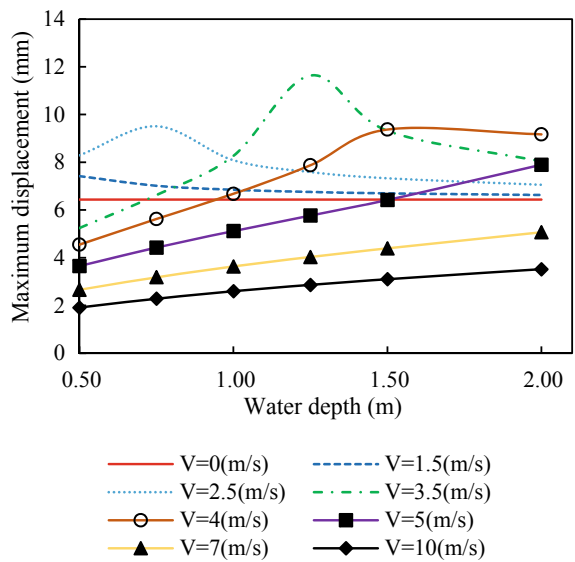


Fig. 5 Variation of maximum displacement with the water depth

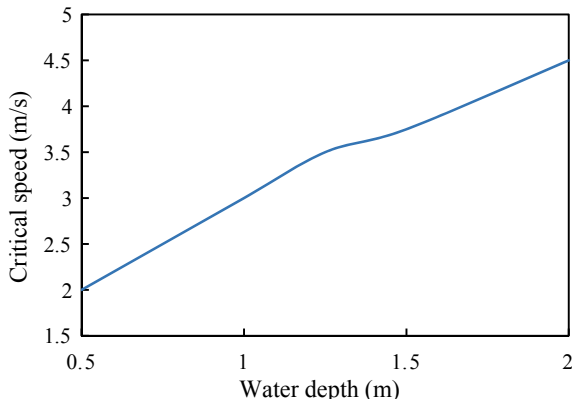


shallow water condition, this quantity increase with water depth, as shown in Fig. 6. A nearly positive linear relationship between them occurs.

4 Conclusions

In this paper, a moving element method has been developed to analyze hydroelastic responses of infinite floating thin plates subjected to moving load in shallow water

Fig. 6 Variation of critical speed with the water depth



condition. In the present methodology, the moving element is simultaneously formulated for both fluid and structure domains, where its coordinate system moves with the same velocity of applied loads. Therefore, the proposed method can completely avoid the update process of loading since the moving load is taken as “stationary” compared with discretized elements. Moreover, this “motionlessness” leads to the independence of computational domain on the distance of moving load. As a result, the method requires fewer number of elements discretized for both fluid and structure than the standard FEM. Through presented formulations and investigated numerical examples, several important remarks are drawn as follows. For the verification, the proposed MEM yields reliable and accurate results against those of the FTM. On the other hand, concerning the effect of seabed in shallow water environment, there is a nearly positive linear relationship between the critical speed and water depth. The numerical investigations also show that the relationship between the water depth and the maximum displacement of the floating plate depends on the load speed.

Acknowledgements This research is funded by the Vietnam National University Ho Chi Minh City (VNU-HCM) Under Grant No. B2019-20-13: “Development and application of a combined boundary element method and moving element method BEM-MEM for the dynamic analysis of very large floating structures”.

References

1. Cao TNT et al (2018) Dynamic analysis of three-dimensional high-speed train-track model using moving element method. *Adv Struct Eng* 21(6):862–876. <https://doi.org/10.1177/1369433217733763>
2. Endo H, Kiyokazu Y (1999) Time history response of a large floating structure subjected to dynamic load. *J Soc Naval Archit Jpn* 86:369–376
3. Ismail RES (2016) Time-domain three dimensional BE-FE method for transient response of floating structures under unsteady loads. *Lat Am J Solids Struct* 13(7):1340–1359. <https://doi.org/10.1590/1679-78251688>

4. Koh CG et al (2003) Moving element method for train-track dynamics. *Int J Numer Meth Eng* 56:1549–1567. <https://doi.org/10.1002/nme.624>
5. Luong VH et al (2018) Static and dynamic analyses of mindlin plates resting on viscoelastic foundation by using moving element method. *Int J Struct Stab Dyn* 18(11):1850131. <https://doi.org/10.1142/s0219455418501316>
6. Nevel DE (1970) Moving loads on a floating ice sheet. *Cold Reg Res Eng lab*
7. Nguyen VH, Duhamel D (2008) Finite element procedures for nonlinear structures in moving coordinates. Part II: Infinite beam under moving harmonic loads. *Comput Struct* 86(21–22):2056–2063. <https://doi.org/10.1016/j.compstruc.2008.04.010>
8. Sturova IV (2003) The action of an unsteady external load on a circular elastic plate floating on shallow water. *J Appl Math Mech* 67(3):407–416. [https://doi.org/10.1016/s0021-8928\(03\)90024-4](https://doi.org/10.1016/s0021-8928(03)90024-4)
9. Sturova IV (2008) Effect of bottom topography on the unsteady behaviour of an elastic plate floating on shallow water. *J Appl Math Mech*. <https://doi.org/10.1016/j.jappmathmech.2008.08.012>
10. Szilard R (2004) Theories and applications of plate analysis: classical, numerical and engineering methods. Wiley, Hoboken, New Jersey
11. Takizawa T (1985) Deflection of a floating sea ice sheet induced by a moving load. *Cold Reg Sci Technol* 11:171–180. [https://doi.org/10.1016/0165-232x\(85\)90015-1](https://doi.org/10.1016/0165-232x(85)90015-1)
12. Takizawa T (1988) Response of a floating sea ice sheet to a steadily moving load. *J Geophys Res* 93(5):5100–5112. <https://doi.org/10.1029/jc093ic05p05100>
13. Watanabe E, Utsunomiya T, Wang CM (2004) Hydroelastic analysis of pontoon-type VLFS: a literature survey. *Eng Struct* 26(2):245–256. <https://doi.org/10.1016/j.engstruct.2003.10.001>

Multi-patch Geometrically Nonlinear Isogeometric Analysis of Spatial Beams with Additive Rotation Updates



Duy Vo, Pruettha Nanakorn, and Tinh Quoc Bui

1 Introduction

Isogeometric analysis (IGA) has become an appealing approach in the field of computational mechanics [6]. Exploiting rational B-spline basis functions for approximations of both geometry and primary variable fields is its fundamental concept. IGA has been successfully applied in several beam formulations for analysis of spatial beam structures, namely, Euler-Bernoulli beam formulations [1, 3, 4, 9] and Timoshenko beam formulations [2, 7, 8, 11]. Better accuracy per degree-of-freedom, due to better approximations of geometry and unknown kinematics using rational B-spline basis functions, has been reported.

In isogeometric Euler-Bernoulli beam formulations, the displacements of the beam axis and the torsional rotation around the beam axis are widely considered as the unknown kinematics [1, 3, 9]. Although this set of unknown kinematics reduces the number of involved discrete variables, the omission of the total cross-sectional rotation along the beam axis results in some drawbacks in practical applications, e.g., the enforcement of rigid connections in multi-patch beam structures. Considering the end total rotations of beams as discrete variables is one way to overcome such difficulties [4]. In the area of geometrically nonlinear analysis, this approach has been successfully implemented for planar beams [10], but the accuracy of the approach for spatial beams still needs further examinations.

In isogeometric Timoshenko beam formulations, the displacements of the beam axis and the total cross-sectional rotation along the beam axis are employed as the

D. Vo (✉) · P. Nanakorn

School of Civil Engineering and Technology, Sirindhorn International Institute of Technology,
Thammasat University, Pathumthani, Thailand
e-mail: duyvo.ce@gmail.com

T. Q. Bui

Department of Civil and Environmental Engineering, Tokyo Institute of Technology, Tokyo, Japan

unknown kinematics by many researchers [2, 7, 8, 11]. The inclusion of the cross-sectional rotation allows geometrically nonlinear analysis of multi-patch beam structures to be performed straightforwardly. Orthogonal tensors are extensively used to represent cross-sectional rotations. Several parameterizations of orthogonal tensors, such as quaternions, rotation vectors, and Euler angles, can be used. Among these parameterizations, rotation vectors are preferable due to simple geometrical meanings. In this paper, rotation vectors are used for the parameterization of rotations. This choice of parameterization allows additive updates to be performed on the rotations. As a result, secondary storage manipulations of the unknown kinematics can be avoided. A well-established example is analyzed, and the computed numerical results are compared with those obtained by the conventional finite element implementation to show the accuracy of the proposed approach.

2 Timoshenko Beam Formulation

2.1 Kinematic Descriptions

Here, the kinematic description of Timoshenko beams is discussed. A global Cartesian coordinate system is spanned by a set of three orthonormal vectors, i.e., \mathbf{e}_1 , \mathbf{e}_2 , and \mathbf{e}_3 . The unstressed configuration is considered as the reference configuration. Any material point can be determined by a set of coordinates, $S^{(1)}$, $S^{(2)}$, and $S^{(3)}$, where $S^{(1)}$ is the coordinate along the beam axis, and $S^{(2)}$ and $S^{(3)}$ are the coordinates along the principal axes of the cross-section at $S^{(1)}$. In this study, $S^{(1)}$ is considered as the arc-length variable of the reference beam axis. The uppercase and lowercase letters are used, respectively, to indicate the quantities in the reference and current configurations. In addition, the repeated indices vary from 1 to 3.

The position vectors of a material point on the beam axis in the reference and current configurations are denoted by $\mathbf{R}_0(S^{(1)})$ and $\mathbf{r}_0(S^{(1)})$. The displacement vector of the material point is obtained as

$$\mathbf{u}_0(S^{(1)}) = \mathbf{r}_0(S^{(1)}) - \mathbf{R}_0(S^{(1)}). \quad (1)$$

The tangent vectors of the beam axis can be computed as

$$\mathbf{A}_1 = \frac{d\mathbf{R}_0(S^{(1)})}{dS^{(1)}} = \mathbf{R}'_0(S^{(1)}); \quad \mathbf{a}_1 = \frac{d\mathbf{r}_0(S^{(1)})}{dS^{(1)}} = \mathbf{r}'_0(S^{(1)}). \quad (2)$$

In this paper, the primes denote the derivatives with respect to $S^{(1)}$.

The unit normal vector \mathbf{N} and the unit bi-normal vector \mathbf{B} of the beam axis in the reference configuration are determined from \mathbf{A}_1 as

$$\mathbf{N} = \frac{\mathbf{A}'_1}{\|\mathbf{A}'_1\|}; \quad \mathbf{B} = \mathbf{A}_1 \times \mathbf{N}. \quad (3)$$

The principal unit vectors, \mathbf{A}_2 and \mathbf{A}_3 , of a cross-section can be determined by a 2D quasi-rotation of \mathbf{N} and \mathbf{B} around \mathbf{A}_1 with an angle ϕ , i.e.,

$$\mathbf{A}_2 = \cos \phi \mathbf{N} + \sin \phi \mathbf{B}; \quad \mathbf{A}_3 = -\sin \phi \mathbf{N} + \cos \phi \mathbf{B}. \quad (4)$$

In the current configuration, the principal unit vectors of a cross-section can be expressed via the following mappings, i.e.,

$$\mathbf{a}_2 = \boldsymbol{\Lambda} \mathbf{A}_2; \quad \mathbf{a}_3 = \boldsymbol{\Lambda} \mathbf{A}_3; \quad (5)$$

where $\boldsymbol{\Lambda}$ is an orthogonal tensor with the following properties, i.e., $\boldsymbol{\Lambda}^T \boldsymbol{\Lambda} = \mathbf{I}$, $\det \boldsymbol{\Lambda} = 1$. Here, \mathbf{I} is the identity matrix of size 3×3 . The tensor $\boldsymbol{\Lambda}$ is frequently referred to as the rotation tensor. In this study, this tensor is parameterized by a rotation vector $\boldsymbol{\theta}$ as

$$\tilde{\boldsymbol{\theta}} = skew(\boldsymbol{\theta}) = \begin{bmatrix} 0 & -\theta_3 & \theta_2 \\ \theta_3 & 0 & -\theta_1 \\ -\theta_2 & \theta_1 & 0 \end{bmatrix}; \quad \boldsymbol{\Lambda} = \mathbf{I} + \frac{\sin \theta}{\theta} \tilde{\boldsymbol{\theta}} + \frac{1 - \cos \theta}{\theta^2} \tilde{\boldsymbol{\theta}} \tilde{\boldsymbol{\theta}}^T; \quad (6)$$

where $\theta = \|\boldsymbol{\theta}\|$, and θ_1 , θ_2 , and θ_3 are the components of $\boldsymbol{\theta}$ in the global Cartesian coordinate system.

By using the principal unit vectors of the cross-section at $S^{(1)}$, any material point on the cross-section can be expressed in the reference and current configurations, respectively, as

$$\mathbf{R}(S^{(1)}, S^{(2)}, S^{(3)}) = \mathbf{R}_0(S^{(1)}) + S^{(2)} \mathbf{A}_2 + S^{(3)} \mathbf{A}_3; \quad (7)$$

$$\mathbf{r}(S^{(1)}, S^{(2)}, S^{(3)}) = \mathbf{r}_0(S^{(1)}) + S^{(2)} \mathbf{a}_2 + S^{(3)} \mathbf{a}_3. \quad (8)$$

Covariant vectors are defined as

$$\mathbf{G}_i = \frac{\partial \mathbf{R}(S^{(1)}, S^{(2)}, S^{(3)})}{\partial S^{(i)}}; \quad \mathbf{g}_i = \frac{\partial \mathbf{r}(S^{(1)}, S^{(2)}, S^{(3)})}{\partial S^{(i)}}; \quad (9)$$

and covariant coefficients are determined from \mathbf{G}_i and \mathbf{g}_i as

$$G_{ij} = \mathbf{G}_i \cdot \mathbf{G}_j; \quad g_{ij} = \mathbf{g}_i \cdot \mathbf{g}_j. \quad (10)$$

Contravariant vectors \mathbf{G}^i are defined to have the following reciprocal relations with the covariant vectors \mathbf{G}_i as

$$\mathbf{G}^j \cdot \mathbf{G}_j = \begin{cases} 1 & \text{if } i = j \\ 0 & \text{if } i \neq j. \end{cases} \quad (11)$$

2.2 Cross-Sectional Resultant Forces

In this study, the Green-Lagrange strain tensor \mathbf{E} is used. Its non-zero components in the contravariant coordinate system $\mathbf{G}^i \otimes \mathbf{G}^j$ are given by

$$\begin{aligned} E_{11} &= \frac{1}{2}(\mathbf{a}_1 \cdot \mathbf{a}_1 - \mathbf{A}_1 \cdot \mathbf{A}_1) + S^{(2)}(\mathbf{a}_1 \cdot \mathbf{a}'_2 - \mathbf{A}_1 \cdot \mathbf{A}'_2) \\ &\quad + S^{(3)}(\mathbf{a}_1 \cdot \mathbf{a}'_3 - \mathbf{A}_1 \cdot \mathbf{A}'_3); \end{aligned} \quad (12)$$

$$E_{12} = \frac{1}{2}[(\mathbf{a}_1 \cdot \mathbf{a}_2 - \mathbf{A}_1 \cdot \mathbf{A}_2) + S^{(3)}(\mathbf{a}_2 \cdot \mathbf{a}'_3 - \mathbf{A}_2 \cdot \mathbf{A}'_3)]; \quad (13)$$

$$E_{13} = \frac{1}{2}[(\mathbf{a}_1 \cdot \mathbf{a}_3 - \mathbf{A}_1 \cdot \mathbf{A}_3) + S^{(2)}(\mathbf{a}_3 \cdot \mathbf{a}'_2 - \mathbf{A}_3 \cdot \mathbf{A}'_2)]. \quad (14)$$

The second Piola-Kirchhoff stress tensor \mathbf{S} is used as the energy conjugate of \mathbf{E} . The components of \mathbf{S} corresponding to the non-zero components of \mathbf{E} are given by

$$S^{11} = E E_{11}; \quad S^{12} = 2 G E_{12}; \quad S^{13} = 2 G E_{13}; \quad (15)$$

where E and G are Young's modulus and the shear modulus, respectively. Note that the components of \mathbf{S} are expressed in the covariant coordinate system $\mathbf{G}_i \otimes \mathbf{G}_j$.

The normal force N^{11} , shear forces N^{12} and N^{13} , bending moments M^{12} and M^{13} , and torsional moment M^{23} are defined as

$$N^{11} = \int_A S^{11} dA; \quad N^{12} = \int_A S^{12} dA; \quad N^{13} = \int_A S^{13} dA; \quad (16)$$

$$M^{12} = \int_A S^{(2)} S^{11} dA; \quad M^{13} = \int_A S^{(3)} S^{11} dA;$$

$$M^{23} = \int_A (S^{(3)} S^{12} - S^{(2)} S^{13}) dA; \quad (17)$$

where A is the cross-sectional area.

2.3 Variations of Kinematics and System Equations

The variation of Λ can be expressed as

$$\delta\Lambda = \widetilde{\delta\mathbf{w}}\Lambda; \quad (18)$$

where $\widetilde{\delta\mathbf{w}} = skew(\delta\mathbf{w})$, and $\delta\mathbf{w}$ is given by Gruttmann et al. [5]

$$\delta\mathbf{w} = \mathbf{T}\delta\boldsymbol{\theta}; \quad \mathbf{T} = \mathbf{I} + \frac{1 - \cos\theta}{\theta^2}\tilde{\boldsymbol{\theta}} + \frac{\theta - \sin\theta}{\theta^3}\tilde{\boldsymbol{\theta}}\tilde{\boldsymbol{\theta}}. \quad (19)$$

This relation links the variation of Λ to the variation of $\boldsymbol{\theta}$. In other words, the rotation can now be characterized by a vector instead of an orthogonal tensor. Thus, in this study, the displacements of the beam axis $\mathbf{u}_0(S^{(1)})$ and the rotation vector $\boldsymbol{\theta}$ are considered as unknown kinematics. The unknown kinematics are approximated by using NURBS curves as

$$\mathbf{u}_0(S^{(1)}) = \sum_{i=1}^n R_{i,p}(S^{(1)})\mathbf{u}_i; \quad \boldsymbol{\theta} = \sum_{i=1}^n R_{i,p}(S^{(1)})\boldsymbol{\theta}_i; \quad (20)$$

where $R_{i,p}(S^{(1)})$ are a rational B-spline basis function of degree p , and n is the number of basis functions. In addition, \mathbf{u}_i and $\boldsymbol{\theta}_i$ are the control variables.

The virtual work principle is written as

$$\begin{aligned} \int_V \delta\mathbf{E} : \mathbf{S} dV &= \int_0^L (\delta\mathbf{u}_0^T \mathbf{F} + \delta\boldsymbol{\theta}^T \mathbf{M}) dS^{(1)} \\ &\quad + \delta\mathbf{u}_0^T(0)\mathbf{f}(0) + \delta\mathbf{u}_0^T(L)\mathbf{f}(L) \\ &\quad + \delta\boldsymbol{\theta}^T(0)\mathbf{m}(0) + \delta\boldsymbol{\theta}^T(L)\mathbf{m}(L) \end{aligned} \quad (21)$$

where V and L are the volume and length of the reference beam configuration. In addition, \mathbf{F} and \mathbf{M} are the distributed force and moment. Moreover, $\mathbf{f}(0)$ and $\mathbf{f}(L)$ are the concentrated forces while $\mathbf{m}(0)$ and $\mathbf{m}(L)$ are the concentrated moments at $S^{(1)} = 0$ and $S^{(1)} = L$, respectively.

By using Eqs. (18)–(20), the required discretized kinematic quantities can be determined. Substitutions of these discretized quantities into Eq. (21) yields the nonlinear equations in terms of the control variables, i.e., \mathbf{u}_i and $\boldsymbol{\theta}_i$. The Newton-Raphson algorithm is used to solve these nonlinear equations.

3 Numerical Results

The proposed beam formulation is used to analyze a circular arch subjected to a lateral force shown in Fig. 1. The arch is fixed at point *A* and pinned at point *B*. A concentrated force *P* is applied at point *C* in the direction of *Z*-axis. The cross-sectional dimensions and material properties are given in the same figure. The arch is split into two segments, i.e., *AC* and *CB*. Each segment is represented by a septic NURBS curve. The total number of control points is 15 (equivalent to 90 degrees of freedom). The enforcement of the rigid connection at point *C* is easily handled in this study because the end cross-sectional rotations of each segment are treated as the degrees of freedom.

For validation, the same arch is also analyzed using MSC Marc-Mentat, a commercial finite element package, since there are no reference results found in the literature. The results, obtained by using 500 B98 two-noded beam elements in Marc-Mentat, are served as the reference solutions. The normalized load-displacement curves of point *C* obtained by the proposed approach and Marc-Mentat are plotted in Fig. 2a. Note that $I = bh^3/12$ is a moment of inertia of the cross-section. Good agreement between the two solutions is observed, revealing the accuracy of the proposed approach. Furthermore, in order to clearly illustrate the perfect enforcement of the rigid connection at *C*, the deformed configurations of the arch at some loading stages are shown in Fig. 2b. It can be seen that the cross-sections of the two segments at the point *C* are always identical during deformation.

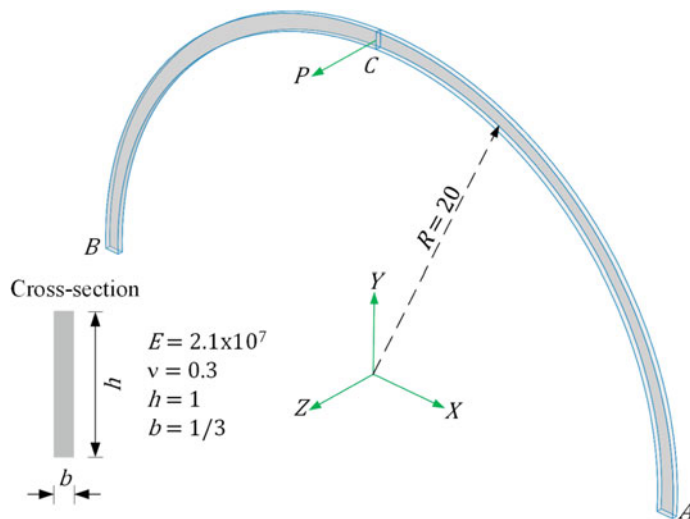


Fig. 1 Circular arch subjected to a lateral concentrated force

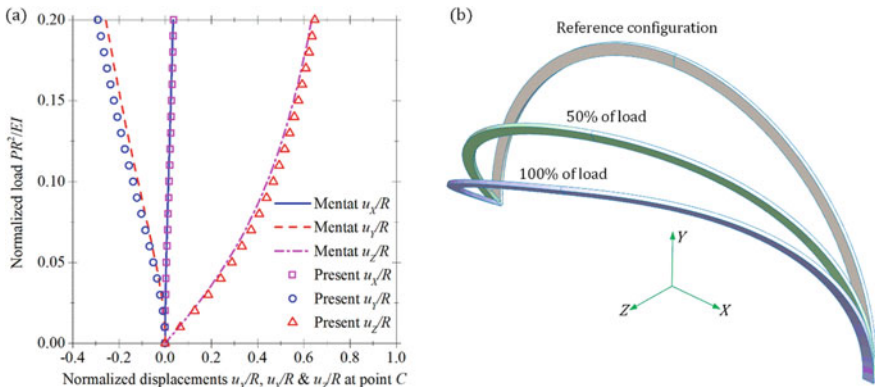


Fig. 2 Circular arch. **a** Normalized load-displacement curves of point C. **b** Deformed configurations

4 Conclusions

In this paper, geometrically nonlinear analysis of multi-patch spatial beam structures is considered. The Timoshenko beam theory is used. The total rotation of a cross-section is represented by an orthogonal tensor which is parameterized by a rotation vector. A relation between the variations of the orthogonal tensor and the rotation vector is utilized. With this relationship, the rotation vector can be included as one of the unknown kinematics, and additive updates of the unknown kinematics become possible. The accuracy of the proposed approach is confirmed through one numerical example of a circular arch. The present approach offers acceptable results when compared with those obtained from the conventional finite element method.

Acknowledgements Scholarships from the ASEAN University Network/Southeast Asia Engineering Education Development Network (AUN/SEED-Net) and Sirindhorn International Institute of Technology (SIIT) for the first author are greatly appreciated.

References

1. Bauer AM, Breitenberger M, Philipp B, Wüchner R, Bletzinger KU (2016) Nonlinear isogeometric spatial Bernoulli beam. *Comput Methods Appl Mech Eng* 303:101–127
2. Choi M-J, Cho S (2019) Isogeometric configuration design sensitivity analysis of geometrically exact shear-deformable beam structures. *Comput Methods Appl Mech Eng* 351:153–183
3. Greco L, Cuomo M (2013) B-Spline interpolation of Kirchhoff-Love space rods. *Comput Methods Appl Mech Eng* 256:251–269
4. Greco L, Cuomo M (2014) An implicit G1 multi patch B-spline interpolation for Kirchhoff-Love space rod. *Comput Methods Appl Mech Eng* 269:173–197
5. Gruttmann F, Sauer R, Wagner W (2000) Theory and numerics of three-dimensional beams with elastoplastic material behaviour. *Int J Numer Meth Eng* 48(12):1675–1702

6. Hughes TJR, Cottrell JA, Bazilevs Y (2005) Isogeometric analysis: CAD, finite elements, NURBS, exact geometry and mesh refinement. *Comput Methods Appl Mech Eng* 194(39–41):4135–4195
7. Marino E (2016) Isogeometric collocation for three-dimensional geometrically exact shear-deformable beams. *Comput Methods Appl Mech Eng* 307:383–410
8. Marino E (2017) Locking-free isogeometric collocation formulation for three-dimensional geometrically exact shear-deformable beams with arbitrary initial curvature. *Comput Methods Appl Mech Eng* 324:546–572
9. Radenković G, Borković A (2018) Linear static isogeometric analysis of an arbitrarily curved spatial Bernoulli-Euler beam. *Comput Methods Appl Mech Eng* 341:360–396
10. Vo D, Nanakorn P (2020) Geometrically nonlinear multi-patch isogeometric analysis of planar curved Euler-Bernoulli beams. *Comput Methods Appl Mech Eng* 366:113078
11. Weeger O, Yeung S-K, Dunn ML (2017) Isogeometric collocation methods for Cosserat rods and rod structures. *Comput Methods Appl Mech Eng* 316:100–122

Optimal Compensation of Axial Shortening in Tall Buildings by Differential Evolution



Duc-Xuan Nguyen and Hoang-Anh Pham

1 Introduction

In tall buildings, large axial shortenings occur in vertical elements like columns and walls since these elements carry huge vertical loads from many floors [4]. The amount of axial shortenings among the members is usually not the same because of the difference in stress levels and other aspects such as reinforcement ratios and volume-surface ratios. The difference in axial shortening of vertical members can result in redistribution of loads between vertical members and additional forces in horizontal elements. Besides effecting on structural elements, differential axial shortenings can also cause damages in nonstructural elements such as the interior partitions, cladding systems, and plumbing systems. Therefore, differential axial shortening is of primary concern in the structural design of tall buildings [1, 3].

To avoid negative effects on structural and nonstructural elements of the building, differential axial shortenings of vertical elements should be minimized. In the design stage, this can be carried out by achieving uniformity of compressive stress within vertical elements, increasing the stiffness of horizontal members [6], and increasing axial stiffness of vertical elements anticipated to be subjected to large magnitude of shortening (e.g. by means of providing additional reinforcement) [5]. Nevertheless, such approaches in the design stage may not guarantee that differential axial shortening can be fully controlled due to many other design aspects to be considered. An effective means for reducing differential shortening is to compensate for the change in lengths of the vertical elements at the construction stage. For example, during the construction of columns, the concrete can be ‘overcast’ to accommodate the anticipated axial shortening. In this approach, floors are often grouped and an

D.-X. Nguyen

Faculty of Civil Engineering, Vinh University, Vinh, Vietnam

H.-A. Pham (✉)

Department of Structural Mechanics, National University of Civil Engineering, Hanoi, Vietnam

e-mail: anhph2@nuce.edu.vn

equal compensation amount will be applied for every floor in a group [7–9, 11]. By restricting the errors between the calculated differential shortening and the compensation amount, the differential shortening can be controlled [9–11]. In practice, the number of lumped groups should be minimized for the sake of simplification of the compensation task.

In this study, the moving-optimal compensation method (MOC) is established to determine the optimal number of lumped groups as well as the optimal correction amounts for the compensation of differential axial shortening of the vertical elements in tall buildings. Instead of solving the optimization problem as a whole, which may be very costly, the current method successively solves a sequence of smaller optimization problems by a differential evolution algorithm. The method is examined for the compensation of the differential shortening of vertical elements in a 70-story building. The efficiency of MOC is compared with those of two other methods, including the optimal compensation technique (OC) [9] and the moving average correction technique (MAC) [11].

2 Compensation Strategy

2.1 Formulation of Moving Optimal Compensation

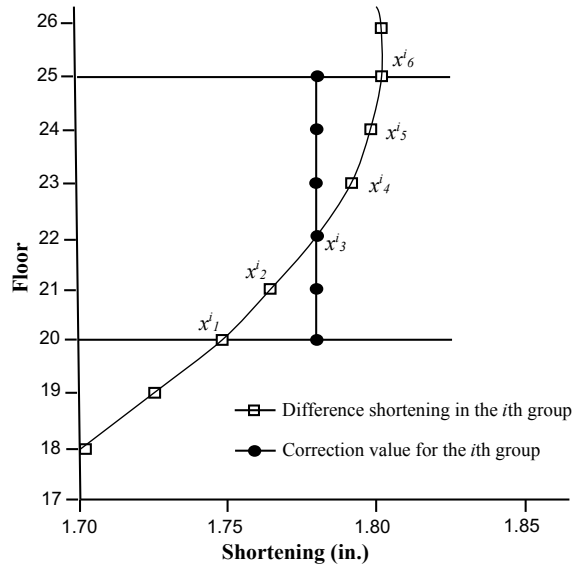
The moving optimal compensation method (MOC) in this study has a strategy similar to that of the MAC method proposed by Parket al. [11]. The floors are divided into groups with an equal correction amount for every floor in a group as described in Fig. 1. In Fig. 1, x_j^i is the calculated shortening of a vertical element of the j th floor in i th group.

To simplify the compensation or the construction process in practice, the number of lumped groups should be minimized. This can be achieved by maximizing the number of floors, N_i , in each group. On the other hand, there will be errors between the compensation amounts and the prediction amounts. The correction amount, δ_i , used for the i th group, therefore, should be chosen such that the cumulative error between the predicted differential shortening and the correction amounts is minimum. Thus, the objective function for the optimal compensation of the i th group is formulated in the following form:

$$\text{Minimize } f(N_i, \delta_i) = -N_i + w \times \left| \sum_{k=1}^{i-1} \varepsilon_k + \sum_{j=1}^{N_i} (x_j^i - \delta_i) \right| \quad (1)$$

where w , ($w \geq 1$) is a weighted factor; ε_k is the cumulative error between the compensation amount and the predicted differential shortening in the k th group

Fig. 1 Concept of the moving average correction method [11]



$$\varepsilon_k = \sum_{j=1}^{N_i} (x_j^k - \delta_k), k = 1, \dots, i-1 \quad (2)$$

To control the slab tilt caused by the axial shortenings, an allowable error value, θ_i , is introduced [9]. Moreover, the cumulative error is limited to a tolerance, ϵ_i . These constraints are written in the following forms [11]:

$$|x_j^i - \delta_i| \leq \theta_i \quad (3)$$

$$\left| \sum_{k=1}^{i-1} \varepsilon_k + \sum_{l=1}^j (x_l^i - \delta_i) \right| \leq \epsilon_i \quad (4)$$

The optimal number of floors, N_i , together with the correction amount δ_i for the i th group is determined by solving the above constrained optimization problem. The steps of the moving optimal compensation method are as followings:

1. Predict the differential shortenings of vertical elements and set the tolerances for the compensation errors, θ_i and ϵ_i .
2. Solve the optimization problem described in Eq. 1 with the constraints in Eq. 3 and Eq. 4 to obtain the optimal number of floors, N_i , and the optimal correction amounts, δ_i , for the i th group.
3. Set $i = i + 1$, and move to the next group.

The optimal compensation solutions are found by using differential evolution (DE) [12]. DE is simple, easy to use and applicable for different optimization problems. The basics of DE are described in the following.

2.2 Differential Evolution

DE utilizes a population of N_P candidate vectors of the design variables, $\mathbf{a}_k, k = 1, \dots, N_P$ (individuals), and an individual is defined as $\mathbf{a}_k = a_{k1}, a_{k2}, \dots, a_{kD}$, where $a_{ki}, i = 1, \dots, D$ are D design variables.

Initially, a population is randomly sampled from the solution space. For each individual \mathbf{a}_k (named the target vector) of the current population, a trial vector \mathbf{c}_k is generated by the ‘mutation’ and ‘crossover’ operators as follows.

Mutation: A mutant vector \mathbf{b}_k is first created as:

$$\mathbf{b}_k = \mathbf{a}_{r1} + F \times (\mathbf{a}_{r2} - \mathbf{a}_{r3}) \quad (5)$$

where \mathbf{a}_{r1} , \mathbf{a}_{r2} and \mathbf{a}_{r3} are different individuals randomly chosen from the population; F is a scaling factor chosen in the interval $[0, 1]$.

Crossover: the mutant vector is then exchanged with the target vector \mathbf{a}_k , producing the trial vector \mathbf{c}_k as:

$$c_{ki} = \begin{cases} b_{ki} & \text{if } (\text{rand}[0, 1] \leq C_r) \text{ or } r = i \\ a_{ki} & \text{otherwise} \end{cases} \quad (6)$$

where r is a randomly chosen integer in the interval $[1, D]$; C_r is the crossover parameter given in the interval $[0, 1]$.

Then, the trial vector \mathbf{c}_k is compared with the target vector \mathbf{a}_k and the better one will survive in the next generation. The evolution stops when a termination criterion is satisfied.

2.3 Handling Constraints and Comparison of Solutions

The considered optimization problem has inequality constraints, which can be expressed in the form

$$c_j(\mathbf{a}_k) \leq 0, j = 1, \dots, n_C \quad (7)$$

where n_C is the number of constraints and $c_j(\mathbf{a}_k)$ is the j th constraint function. The constraint violation of an individual \mathbf{a}_k is given by

$$C_k = \max \left\{ \max_j \{0, c_j(\mathbf{a}_k)\} \right\}, j = 1, \dots, n_C \quad (8)$$

Deb's rules [2] are applied in this constrained optimization problem to compare two individuals. Deb's constraint rules are described as:

1. A feasible individual is better than any infeasible one.
2. Of two feasible individuals or two individuals with equal constraint violations, the smaller objective function value is the better.
3. Of two infeasible individuals, the smaller constraint violation is the better.

3 Illustration Example

In this section, a 70-story building [4] is considered to demonstrate the performance of the moving-optimal compensation method. Figure 2 shows the typical floor plan of the building. The differential shortening between the interior wall and the exterior column given in references [9, 11] is used as input data. The shortening of columns and walls includes both elastic and inelastic (creep and shrinkage) shortenings. The performance of the proposed method is compared with those of two other methods, the OC using simulated annealing (SA) [9] and the MAC method [11].

For the comparison, in the MOC method, the tolerance of 0.4 in is also given for both the compensation error and the cumulative correction error. Figure 3 depicts the compensation curves of the considered methods. The correction values for each group from the three methods are given in Table 1. The compensation error curves are depicted in Fig. 4 and the cumulative compensation error curves are shown in Fig. 5. It is seen from these results that the differential shortening values at every floor are controlled within the 0.4 in. limit. Considering the maximum accumulated compensation error, the OC using SA results in 1.07 in. on the 47th floor, whereas,

Fig. 2 Typical layout of the 70-storey building [4]

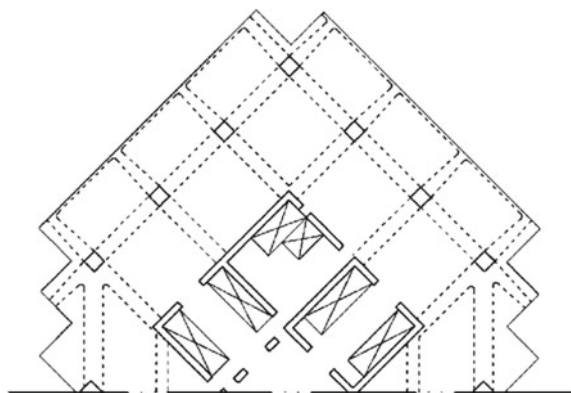


Fig. 3 Comparison of compensation curves from different correction methods for a 70-story building

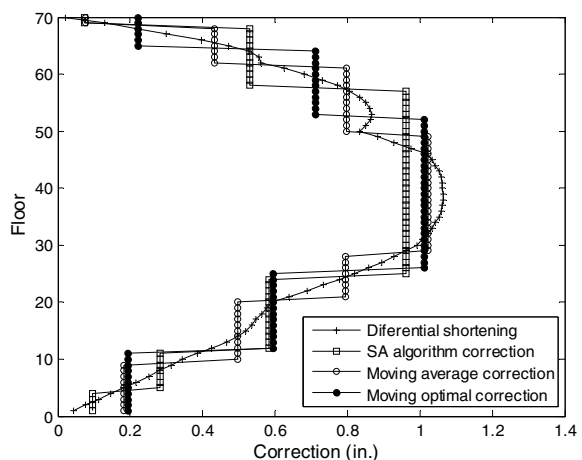


Table 1 Comparison of compensation solutions of different methods

OC with SA			MAC			MOC		
Group	Floor	Correction (in.)	Group	Floor	Correction (in.)	Group	Floor	Correction (in.)
1	1–4	0.096	1	1–9	0.182	1	1–11	0.192
2	5–11	0.282	2	10–20	0.496	2	12–25	0.596
3	12–24	0.582	3	21–28	0.794	3	26–52	1.012
4	25–57	0.962	4	29–49	1.023	4	53–64	0.712
5	58–68	0.530	5	50–61	0.798	5	65–70	0.221
6	69–70	0.075	6	62–68	0.433	–	–	–
–	–	–	7	69–70	0.076	–	–	–

Fig. 4 Compensation errors from different correction methods for a 70-story building

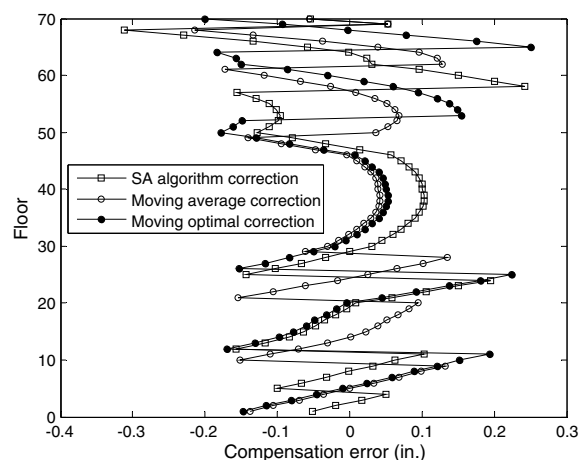
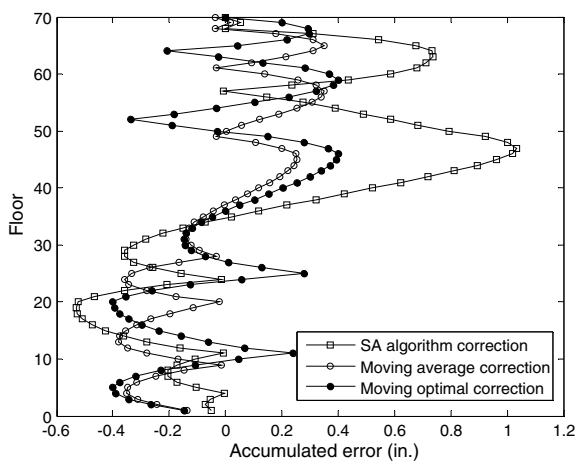


Fig. 5 Accumulated compensation errors from different correction methods for a 70-story building



the MOC method gives 0.4 in. at the 46th and 59th floors, which is similar to the MAC does (0.38 in. on the 65th floor).

The advantage of the MOC method is that it can give a smaller number of lumped groups in comparison with the OC using SA and the MAC methods. For this example, the number of lumped groups of the MOC method is five, whereas those of the OC using SA and the MAC method are six and seven, respectively. Another benefit of the proposed method is the low computational cost to produce the optimal solution since, in the moving optimization compensation, the optimization problem is performed in a sequence of small optimization problems with only two variables.

4 Conclusion

The moving optimal compensation method (MOC) for controlling the differential shortening of the vertical members in tall buildings is presented in this paper. Different from the existing methods, the proposed method determines the optimal compensation solution including the number of floor groups, the number of floors in each group and the average correction amount for each floor by solving a sequence of small optimization problems. The classical differential evolution algorithm is utilized as the optimizer. The MOC method is examined with a 70-story building example and its performance is compared with those of two existing methods previously reported in the literature. It is demonstrated that a smaller number of compensation groups can be found by the proposed method. By using the MOC method, the optimal solution for the compensation purpose can be derived systematically with low computational cost.

References

1. Cagnino A, Debernardi PG, Guiglia M, Taliano M (2012) Axial shortening compensation strategies in tall buildings. a case study: the new piedmont government office tower. *Struct Eng Int* 22(1):121–129
2. Deb K (2000) An efficient constraint handling method for genetic algorithms. *Comput Method Appl M* 186(2–4):311–338
3. Fan F, Wang H, Zhi X, Huang G, Zhu E, Wang H (2013) Investigation of construction vertical deformation and pre-deformation control for three super high-rise buildings. *Adv Struct Eng* 16(11):1885–1897
4. Fintel M, Ghosh SK, Iyengar H (1987) Column shortening in tall structures: prediction and compensation. *Portland Cement Assn*
5. Kim HS (2015) Optimum distribution of additional reinforcement to reduce differential column shortening. *Struct Des Tall Spec* 24(10):724–738
6. Kim HS (2017) Effect of outriggers on differential column shortening in tall buildings. *Int J High-Rise Build* 6(1):91–99
7. Kim YM (2008) Optimal compensation of differential column shortening in tall buildings for multi column groups. *J Comput Struct Eng Inst Korea* 21(2):189–197
8. Kim YM (2011) The optimal column grouping technique for the compensation of column shortening. *J Comput Struct Eng Inst Korea* 24(2):141–148
9. Park HS (2003) Optimal compensation of differential column shortening in high-rise buildings. *Struct Des Tall Spec* 12(1):49–66
10. Park SW, Choi SW, Park HS (2010) Average correction for compensation of differential column shortening in high-rise buildings. *J Comput Struct Eng Inst Korea* 23(4):395–401
11. Park SW, Choi SW, Park HS (2013) Moving average correction method for compensation of differential column shortenings in high-rise buildings. *Struct Des Tall Spec* 22(9):718–728
12. Storn R, Price K (1997) Differential evolution—a simple and efficient heuristic for global optimization over continuous spaces. *J Global Optim* 11(4):341–359

Postbuckling Isogeometric Analysis of Functionally Graded Carbon Nanotube-reinforced Composite Shells Under Combined Loading



Tan N. Nguyen, Pham Toan Thang, Dieu Thanh Thi Do, Seunghye Lee,
and Jaehong Lee

1 Introduction

The discovery of carbon nanotubes (CNTs) [1] has made a great stride for materials science. Nowadays, carbon nanotubes have been drawing a great interest by their notable electrical, thermal and mechanical characteristics [2]. From the structural point of view, carbon nanotubes are impressive by their high strength, stiffness, aspect ratio and low density. Hence, CNTs can be considered as a good candidate for composite structures. In practice, shells are widely used to manufacture and construct the important and complicated components such as shells of ships, roofs of buildings and wings of airplanes, etc. For these reasons, behaviors of FG-CNTRC shells need to be studied particularly.

To overcome some disadvantages of analytical approaches, many numerical methods have been investigated for analyses of shells such as finite element method (FEM) [3], meshless method [4, 5] and an isogeometric meshless coupling approach [6], etc. In attempts to develop the advanced numerical methods, isogeometric analysis (IGA) or NURBS-based finite element analysis was proposed by Hughes et al. [7]. As an advantage of this method, NURBS basis functions possess high derivatives that allows convenience combinations with most of shell theories. In IGA, both exact geometry and approximated solutions are obtained from the same basis functions. Therefore, geometric data from computer-aided design (CAD) can be used directly for numerical simulation. It is asserted that the main procedures of IGA and FEM are same. Hence, isogeometric analysis can be considered as an unified approach that bridges the existing gap between CAD and FEM. This opens a new way for computational mechanics, especially for industrial problems with arbitrary geometries and required high accuracy. An overview and computer implementation aspects of IGA were presented in [8]. For linear analyses of shells, IGA has been successfully

T. N. Nguyen · P. T. Thang · D. T. T. Do · S. Lee · J. Lee (✉)

Department of Architectural Engineering, Sejong University, 209 Neungdong-ro, Gwangjin-gu, Seoul 05006, Republic of Korea
e-mail: jhlee@sejong.ac.kr

investigated for isotropic thin shells [9] and composite thick shells [10, 11]. In addition, it has been extensively studied for nonlinear problems [12, 13], optimization problems [14] of isotropic shells. It should be emphasized that the application of IGA to nonlinear analyses of FG-CNTRC shells is limited.

In this work, the shell formulation for postbuckling analysis of functionally graded carbon nanotube-reinforced composite shells based on isogeometric analysis and first-order shear deformation shell theory (FSDT) is proposed. The nonlinearity of shells is formed in the Total Lagrangian approach considering the von Karman assumption. The nonlinear equation is numerically solved by using a modified Riks method. In the present formulation, the effective material properties are estimated via the rule of mixture. Exact geometries of shells are modeled based on the advantage of isogeometric analysis. Several examples are given to confirm the high reliability of the proposed formulation. The outline of this paper is organized as follows. Section 2 mentions the FG-CNTRC shell formulation based on NURBS and FSDT. Numerical results are provided and discussed in Sect. 3. The paper is closed with some notable conclusions in Sect. 4.

2 Formulation Using NURBS and FSDT

2.1 A Brief Introduction to NURBS Basis Functions

The aim of this subsection is to introduce briefly NURBS basis functions. The details as well as an open isogeometric analysis source code can be found in [8]. First, we consider a knot vector $\Xi = \{\xi_1, \xi_2, \dots, \xi_{n+p+1}\}$ with $\xi_i \in R$ and $i = 1, \dots, n+p+1$. When the first and last knots are repeated $p+1$ times, the knot vector is called open. The characteristic of a B-spline basis function is C^∞ continuous inside a knot span and C^{p-1} continuous at each knot. The B-spline basis functions in one-dimensional parametric space $N_{i,p}(\xi)$ are expressed based on Cox-De Boor recursive formula as follows

$$N_{i,p}(\xi) = \frac{\xi - \xi_i}{\xi_{i+p} - \xi_i} N_{i,p-1}(\xi) + \frac{\xi_{i+p+1} - \xi}{\xi_{i+p+1} - \xi_{i+1}} N_{i+1,p-1}(\xi) \\ \text{as } p = 0, N_{i,0}(\xi) = \begin{cases} 1 & \text{if } \xi_i \leq \xi < \xi_{i+1} \\ 0 & \text{otherwise} \end{cases} \quad (1)$$

Next, two knot vectors $\Xi = \{\xi_1, \xi_2, \dots, \xi_{n+p+1}\}$ and $\mathbf{H} = \{\eta_1, \eta_2, \dots, \eta_{m+q+1}\}$ are considered. The B-spline basis functions in two-dimensional parametric space are obtained via a tensor product of basis functions in parametric dimensions ξ and η as follows

$$N_A^b(\xi, \eta) = N_{i,p}(\xi) M_{j,q}(\eta) \quad (2)$$

Thanks to considering the weight w for each control point, the non-uniform rational B-spline (NURBS) basic functions can be used to describe exactly the curved and complex geometries such as: spheres, ellipsis, circles, etc. Therefore, the NURBS functions are calculated as [7]

$$N_A(\xi, \eta) = \frac{N_A^b w_A}{\sum_{I=1}^{m \times n} N_I^b(\xi, \eta) w_I} \quad (3)$$

It should be noted that when all the weights of control points are equal, the B-spline and NURBS functions are identical.

2.2 Formulation Using NURBS and FSST

In this paper, the modified Riks method which consists of a series of linear solutions is used to solve the nonlinear equation. To implement the modified Riks method for postbuckling problems, an iterative procedure is carried out for all load increments as follows

$$\mathbf{K}_T(\mathbf{q}_m) \Delta^i \mathbf{q}_m = {}^i \mathbf{F}_{\text{ext},m} - {}^i \mathbf{F}_{\text{int},m} \quad (4)$$

in which, the tangent stiffness matrix of shells

$$\begin{aligned} \mathbf{K}_T &= \int_{\Omega} \left[\begin{Bmatrix} \mathbf{B}_A^L \\ \mathbf{B}_A^b \\ \mathbf{B}_A^s \end{Bmatrix} + \begin{Bmatrix} \mathbf{B}_A^N \\ \mathbf{0} \\ \mathbf{0} \end{Bmatrix} \right]^T \begin{Bmatrix} \mathbf{A} & \mathbf{B} & \mathbf{0} \\ \mathbf{B} & \mathbf{D}^b & \mathbf{0} \\ \mathbf{0} & \mathbf{0} & \mathbf{D}^s \end{Bmatrix} \left[\begin{Bmatrix} \mathbf{B}_A^L \\ \mathbf{B}_A^b \\ \mathbf{B}_A^s \end{Bmatrix} + \begin{Bmatrix} \mathbf{B}_A^N \\ \mathbf{0} \\ \mathbf{0} \end{Bmatrix} \right] d\Omega \\ &\quad + \int_{\Omega} (\mathbf{B}_A^g)^T \begin{bmatrix} N_x & N_{xy} \\ N_{xy} & N_y \end{bmatrix} \mathbf{B}_A^g d\Omega \end{aligned} \quad (5)$$

and the external and internal load vectors

$$\begin{aligned} {}^i \mathbf{F}_{\text{ext},m} &= ({}^i \lambda_m + \Delta^i \lambda_m) \int_{\Omega} f_0 \left\{ 0 \ 0 \ N_A \ 0 \ 0 \right\}^T d\Omega \\ &= ({}^i \lambda_m + \Delta^i \lambda_m) \mathbf{F}_0 \end{aligned} \quad (6)$$

$${}^i \mathbf{F}_{\text{int},m} = {}^i \mathbf{K}_m^i \mathbf{q}_m \quad (7)$$

in which

$$^i \mathbf{K}_m = \int_{\Omega} \left[\begin{Bmatrix} \mathbf{B}_A^L \\ \mathbf{B}_A^b \\ \mathbf{B}_A^s \end{Bmatrix} + \begin{Bmatrix} \mathbf{B}_A^N \\ \mathbf{0} \\ \mathbf{0} \end{Bmatrix} \right]^T \begin{bmatrix} \mathbf{A} & \mathbf{B} & \mathbf{0} \\ \mathbf{B} & \mathbf{D}^b & \mathbf{0} \\ \mathbf{0} & \mathbf{0} & \mathbf{D}^s \end{bmatrix} \left[\begin{Bmatrix} \mathbf{B}_A^L \\ \mathbf{B}_A^b \\ \mathbf{B}_A^s \end{Bmatrix} + 0.5 \begin{Bmatrix} \mathbf{B}_A^N \\ \mathbf{0} \\ \mathbf{0} \end{Bmatrix} \right] d\Omega \quad (8)$$

For each load increment, the iteration is repeated until the convergence criterion based on the residual load vector is satisfied as follows

$$\frac{\|{}^i \lambda_m \mathbf{F}_0 - {}^i \mathbf{F}_{\text{int},m}\|}{\|({}^i \lambda_m + \Delta {}^i \lambda_m) \mathbf{F}_0\|} < 10^{-8} \quad (9)$$

3 Results and Discussions

In this paper, we use four types of CNTs distributions: UD, FG-V, FG-O, FG-X as described in Fig. 1. A hinged (HFHF) FG-CNTRC cylindrical panel under a central point load as shown in Fig. 2 is first considered. The geometric data is given as: the thickness $h = 12.7$ mm, $L = B = 508$ mm and the radius $R = 2540$ mm. In this study, the armchair (10) SWCNTs and Poly-methyl methacrylate (PMMA) are chosen as

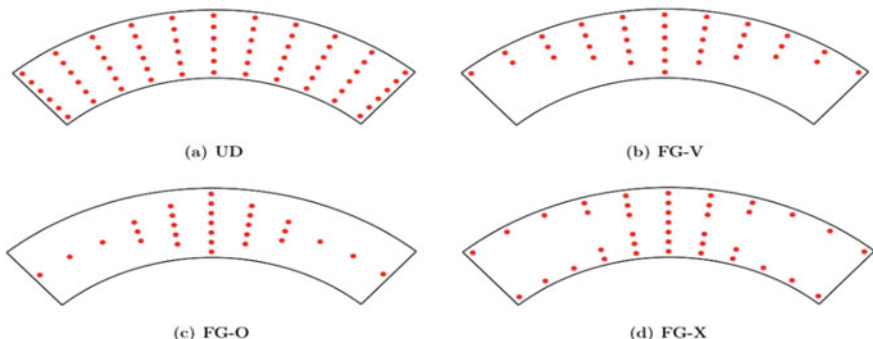


Fig. 1 Four types of CNTs distributions

Fig. 2 A hinged (HFHF) cylindrical panel under a central point load

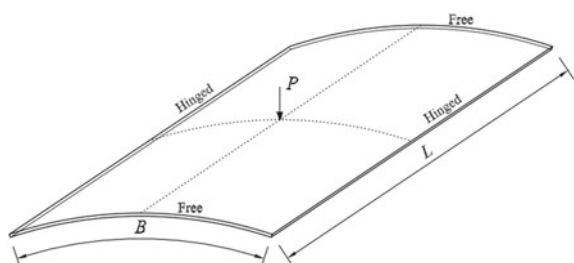
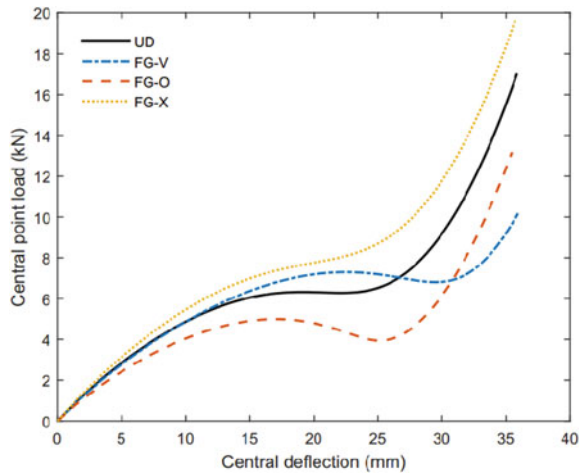


Fig. 3 Central deflections of HFHF FG-CNTRC cylindrical panels with $h = 12.7$ mm, $V_{CNT}^* = 0.11$, circumferential reinforcement



the reinforcements and the matrix material for FG-CNTRC shells, respectively. Effect of CNTs distribution on response of the panel with volume fraction $V_{CNT}^* = 0.11$ and circumferential reinforcement by CNTs is investigated and presented in Fig. 3. It is clear that CNTs distribution significantly influences postbuckling strength and stability of the panel. It is noted that the FG-X panel only experiences nonlinear bending behavior and is stable during loading.

Next, a CCSS FG-CNTRC cylindrical panel under axial compression as shown in Fig. 4 is considered. The geometric data is given as: the thickness $h = 3.175$ mm, $L = B = 508$ mm and the radius $R = 2540$ mm. Figure 5 confirms that FG-X and FG-O are the best and worst distributions that give the highest and lowest nonlinear bending strengths, respectively.

Fig. 4 A clamped-simply-clamped-simply (CCSS) cylindrical panel under axial compression

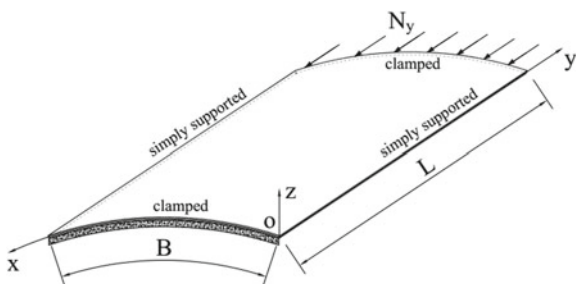
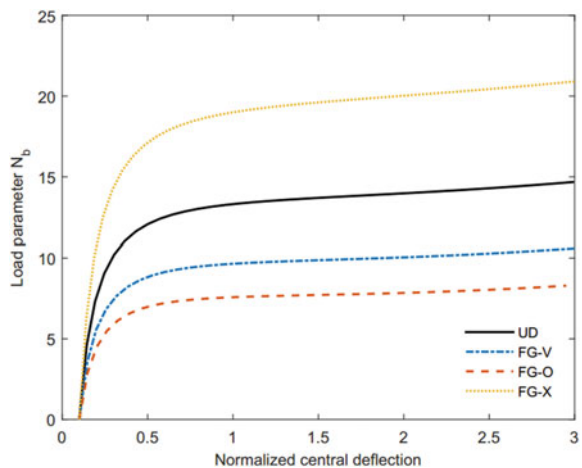


Fig. 5 Effect of CNTs distribution on load-deflection curves of FG-CNTRC panels, $V_{CNT}^* = 0.11$, longitudinal reinforcement



4 Conclusions

Postbuckling analysis of functionally graded carbon nanotube-reinforced composite (FG-CNTRC) shells has been carried out. In the present approach, exact geometries and approximated solutions of shells were obtained by using non-uniform rational B-Spline (NURBS) basis functions. The nonlinearity of shells was formed in the Total Lagrangian approach considering the von Karman assumption. The incremental solutions were achieved by using a modified Riks method. The effective material characteristics were computed via the rule of mixture. It is found that CNTs distribution and loading significantly affect the nonlinear behaviors of panels.

Acknowledgements This research was supported by grants (NRF-2017R1A4A1015660, NRF-2018R1C1B6004751) from NRF (National Research Foundation of Korea) funded by MEST (Ministry of Education and Science Technology) of Korean government.

References

1. Iijima S (1991) Helical microtubules of graphitic carbon. *Nature* 354(6348):56–58
2. Dang LM, Min K, Lee S, Han D, Moon H (2020) Tampered and computer-generated face images identification based on deep learning. *Appl Sci* 10(2):505
3. Kanok-Nukulchai W (1979) A simple and efficient finite element for general shell analysis. *Int J Numer Meth Eng* 14(2):179–200
4. Nguyen TN, Thai CH, Nguyen-Xuan H (2016) A novel computational approach for functionally graded isotropic and sandwich plate structures based on a rotation free meshfree method. *Thin-Walled Struct* 107:473–488
5. Thai CH, Nguyen TN, Rabczuk T, Nguyen-Xuan H (2016) An improved moving Kriging meshfree method for plate analysis using a refined plate theory. *Comput Struct* 176:34–49

6. Li Y, Wang H, Dang LM, Sadeghi-Niaraki A, Moon H (2020) Crop pest recognition in natural scenes using convolutional neural networks. *Comput Electron Agric* 169:105174
7. Hughes TJR, Cottrell JA, Bazilevs Y (2005) Isogeometric analysis: CAD, finite elements, NURBS, exact geometry and mesh refinement. *Comput Methods Appl Mech Eng* 194(39):4135–4195
8. Nguyen VP, Anitescu C, Bordas SPA, Rabczuk T (2015) Isogeometric analysis: an overview and computer implementation aspects. *Math Comput Simul* 117:89–116
9. Hassan SI, Dang LM, Mahmood I, Im S, Choi C, Kang J, Park YS, Moon H (2019) Underground sewer pipe condition assessment based on convolutional neural networks. *Autom Constr* 106:102849
10. Nguyen TN, Thai CH, Nguyen-Xuan H, Lee J (2018) NURBS-based analyses of functionally graded carbon nanotube-reinforced composite shells. *Compos Struct* 203:349–360
11. Nguyen TN, Thai CH, Nguyen-Xuan H, Lee J (2018) Geometrically nonlinear analysis of functionally graded material plates using an improved moving Kriging meshfree method based on a refined plate theory. *Compos Struct* 193:268–280
12. Nguyen TN, Thai CH, Luu AT, Nguyen-Xuan H, Lee J (2019) NURBS-Based postbuckling analysis of functionally graded carbon nanotube-reinforced composite shells. *Comput Methods Appl Mech Eng* 347:983–1003
13. Nguyen TN, Lee S, Nguyen-Xuan H, Lee J (2019) A novel analysis-prediction approach for geometrically nonlinear problems using group method of data handling. *Comput Methods Appl Mech Eng* 354:506–526
14. Nguyen TN, Nguyen-Xuan H, Lee J (2020) A novel data-driven nonlinear solver for solid mechanics using time series forecasting. *Finite Elem Anal Des* 171:103377

Safety of Structures in Fire



Asif S. Usmani

1 Introduction

This paper presents a summary of ongoing research at Hong Kong Polytechnic University in the context of the rapidly changing nature of urban environments, especially in Asia where rampant urbanization and high population density regions are leading to the proliferation of dense vertical cities. A high density of population increases the risk from disasters such as earthquake, fire, typhoon, and so on. Structural engineering curricula worldwide include elements where extreme loadings such as earthquake and wind are discussed with students. Often experimental facilities are also available at well-resourced institutions, such as shake tables and wind tunnels, where the effects of these loads may be illustrated to students using suitable laboratory scale models, both in theory and practice. While the risk of earthquakes and high winds are not of uniform severity across the globe, the risk of severe fires exists nearly uniformly in built environments everywhere, however it is rare to find this subject in structural engineering curricula except in a handful of institutions worldwide. It is the same story when it comes to research. International building codes and standards provide a level of guidance, which essentially perpetuates the century old practice of subjecting structural components to a prescribed temperature time curve, called “standard fire”, that is based on how a fire burns in a small compartment. Certain indicators, such as temperature of the component or its deflection after a period of exposure to the standard fire determines “failure”. This period of exposure is termed as the “fire resistance” of the structure that contains the component. For steel framed structures this usually amounts to restricting the temperature of all steel members to 550 °C, at which the roughly half of the steel strength at ambient still remains. While this approach has proved to be generally conservative, it is fundamentally unscientific from both the perspective of the loading (the fire) and the structural response

A. S. Usmani (✉)

Faculty of Construction and Environment, Hong Kong Polytechnic University, Hong Kong,
S.A.R., China

e-mail: asif.usmani@polyu.edu.hk

to the loading. Building and infrastructure fires hardly ever correspond to standard fires and the overall response of a highly statically indeterminate structural frame does not depend upon the failure of a single component. Furthermore, the nonlinear structural response of a building frame depends highly upon the temperature history that its components have been exposed to, as shown in Usmani et al. [24]. The main consequence of the continued prevalence of this prescriptive approach is that there is no real quantification of the either the fire or the actual structural response that is likely to occur under realistic fire scenarios. As mentioned earlier, the current approaches are generally conservative and generally lead to waste of resources by often applying fire protection to components where it is not required. However, the greater threat to the safety of modern urban infrastructure come from cases where the assumptions associated with prescriptive approaches lead to unsafe designs by ignoring structural failures that may occur as a result of possible fire scenarios and structural responses that are never considered at the design stage. The most extreme example of such failures is the collapse of WTC 1, 2 and 7 on 11 September 2001 in New York [25], however there have been many other such cases (Gretzenbach, Switzerland, Windsor Tower Madrid and Plasco Tower, Iran).

The author has worked in this field for over two decades (most of this time spent at University of Edinburgh, UK), with the primary aim of improving the fundamental understanding of the mechanics of structural response to real fires using analytical, experimental and computational research. The understanding so developed has enabled better quantification of both the fire load and structural response so that performance based approaches may be used more widely in the engineering of structural fire resistance [19]. This paper provides an overview of the some of key developments along the way and also provides the reader with the direction this work has taken in recent years and what are the likely developments to be undertaken in the near future.

2 Understanding Thermomechanical Response and the Cardington Fire Tests

The six fire tests carried out in Cardington (UK) have been a seminal contribution to the research devoted to understanding the response of steel framed composite structures to fire. The tests happened in the mid-1990s and have ever since been an excellent resource for new researchers entering this field. This was the case for the author who had the good fortune to begin his research career in this field in UK while these tests were being conducted. A proposal for a project to carry out computational simulations of these tests to UK Government was successful and produced a large volume of work with provided new insights into the steel frame composite frame response to fire [23]. The key findings from these tests could be summarised as follows:

- (1) The geometrical deformations as a result of thermal elongations and thermal bowing of individual structural components dominated structural response until the point where local or global structural collapse becomes likely or imminent [24, 27].
- (2) Traditional approaches have always emphasized material strength at elevated temperatures as the critical criterion in structural fire resistance design. This has resulted in the blind application of fire protection on every structural steel component, with no regard to the actual need for that protection. The Cardington tests were carried out with either none or only partially protected steel components without any failures, exposing the poor justification for solely material strength based arguments for structural fire resistance [6, 7].
- (3) The tests also showed that the composite floor systems in steel framed construction could adopt highly deflected shapes that was helpful for the floor system to continue carrying the loads on it using the tensile membrane mechanism [1].

3 Progressive Collapse of Framed Structures and September 11, 2001 WTC Disaster

Whereas the Cardington tests created the impression that steel framed structures had a robust performance in fire as none of the tests exhibited any danger of global or progressive collapse of the structure. There were significant local deformations in members, however the overall structural response remained stable in all six tests. In this context the author was shocked by the collapse of three tall steel framed composite buildings after the September 11, 2001 terrorist attacks. This event spurred the author's research group to investigate the collapse of the two WTC towers as these were buildings were relatively simple structurally (a perimeter tube frame and a stiff steel core connected by a relatively light truss floor system). A range of 2D and 3D simulations were carried out by applying fires simultaneously one single and multiple floors (as multiple floor fires were clearly visible in videos of the event). This resulted in the discovery of two collapse mechanisms, weak-floor and strong-floor collapse [4, 5, 15, 16, 25]. These were also shown to be generic failure mechanisms that could potentially occur in multi-storey steel framed structures where fires may spread vertically over multiple storeys, which are not so rare an occurrence. These collapse mechanisms can be designed out using simple analytical approaches [18], however as there is no regulatory requirement to do so, there is no obligation for the highly cost-conscious construction industry to carry out simple checks indicated in Lange et al. [18]. Such a laissez faire approach to safety would not be possible in some other industries, such as automotive or aviation.

4 Development of an Integrated Approach to Simulation of Structures in Fire

Most of the early work of the author and his research students relied upon commercial finite element simulation package ABAQUS. However, over time the use of proprietary black box codes began to pose severe limitations to the simulation capability required. As mentioned earlier, the structural response depends greatly on the thermal history of the structural components. It was found difficult to apply steep enough thermal gradients in ABAQUS, especially in concrete members. The application of spatially non-uniform temperatures as a result of realistic fire scenarios (such as from an experiment or CFD simulation) is also exceptionally tedious. However, the greatest limitation is developing new elements and material models for improving the quality or efficiency of the structural simulations. Current work in the group is focusing on developing an integrated simulation environment for structural fire response simulations based on the open source software framework OpenSEES [8, 9]. The most recent versions of the development can be downloaded from the project Github website [20]. The open source and freely available CFD tool for fire simulation developed by NIST is being coupled to OpenSEES so that realistic fire simulations could be seamlessly performed from; fire scenario; to boundary heat fluxes applied to structural components; followed by automated heat transfer simulation in the solid; and computing the thermomechanical response of the structure as schematically illustrated in Fig. 1. Development of such a tool will provide researchers and practitioners a free, powerful and industry leading tool for simulation of structural response to real fires, enabling wider adoption of performance based engineering (PBE) approaches for structural fire resistance design [19].

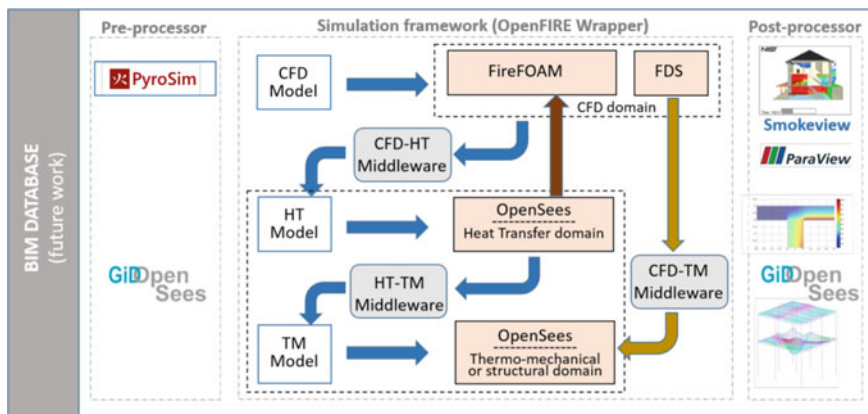


Fig. 1 Schematic of integrated computational environment of simulation of structures in fire

5 Other Important Developments

In addition to the key stages of development of a new framework for safety of structures in fire described above there are a number of other developments taking place simultaneously that are worth noting. Some of the most important ones are described in the following subsections.

5.1 *Theoretical Solutions of Thermo-mechanical Response of Structural Elements in Fire*

Much of the work described in this paper relies upon computational simulation. Large nonlinear finite element simulations are now routine in design and assessment of major infrastructure projects against hazards such as earthquake or wind but they are still a rare occurrence for assessing whole structural response in fire. Before such practice does become routine, simulation tools must be “verified” and “validated”. The former process ensures that a simulation tool is able to represent the various mathematical models (such finite element and material formulations; solution procedures; boundary and other constraint handling procedures and so on) that it is based upon. The latter process determines if the tool is able to reasonably represent real physical behaviour that it is intended to simulate, as observed in experiments conducted on materials, components and structural systems at various scales, such as the Cardington fire tests described above. The verification process requires checking computational solutions against analytical and closed-form theoretical solutions of the governing equations, ideally obtained using non-numerical approaches. This work has resulted in a number of such fundamental solutions to be developed for beams, plates and shells as reported in [12–14, 26].

5.2 *New Element and Material Model Development for OpenSEES*

The integrated structures in fire simulation environment mentioned earlier is being developed using the open source software framework OpenSEES, which has required developing many material models and elements in order to carry out thermo-mechanical response simulation of structures in fire. Most of the early development work has been added to the main OpenSEES release maintain at University of California, Berkeley (OpenSEES, Berkeley [21], however the most recent development in structures in fire can be downloaded from OpenSEES [20]. Recent developments include work on developing new models for structural and stainless steels in fire [28], with the ability to simulate the Bauschinger effect and the combined isotropic and kinematic hardening behavior observed at elevated temperatures. Jiang and Usmani

[10] developed “force-based” elements in addition to the “displacement-based” elements that had been adapted earlier for simulation of beams in fire in OpenSEES. Considerably fewer force-based elements produce results of the same accuracy at much lower computational cost.

5.3 Development of Realistic Fire Models

The greatest uncertainty in the simulations of structures in fire arises from the fire loading. No two full-scale fires in a building or other infrastructure facility can be exactly the same, even in carefully controlled laboratory conditions. As discussed earlier, much of this uncertainty is currently ignored and simplified fire models are used for nearly all structural fire resistance design around the world. The author and his students proposed alternatives in the past, and more recently to enable more realistic fire conditions to be considered in the context of PBE [3]. The latter paper proposes a new class of “travelling fire” that mimics the behavior of a fire in a large compartment, which tends to spread from its original location to other locations within the compartment, even after it has “burnt out” at the original location. This work takes into account the variability in the spread of the fire caused by the distribution of the fuel and ventilation in the compartment; the accumulation and variation in the smoke layer on the ceiling and the resultant changes in emissivity. The proposed new method also accounts for energy conservation.

5.4 Multi-hazard Fire Following Earthquake Simulation

Urban fires occur as largely random events in buildings or other infrastructure for a variety of reasons and usually act alone. However, on occasion fires can be the result of other hazards, such as earthquake, blast, lightning and so on and in some cases fires may also generate other hazards, such as explosions or structural collapses. While currently there is no requirement to consider multi-hazard scenarios in the design of structures, it may in certain cases still be prudent to do so, such as in seismically active zones of the world. The author led a project on experimental investigation of full-scale reinforced concrete structural frames, which were first damaged by applying large lateral cyclic loads to simulate seismic damage in the frames and then subjected the frame to a compartment fire reaching over 1000 °C [22]. The experimental programme enabled the comparison and quantification of fire damage to previously undamaged frames against fire damage in seismically damaged frames. Further work has been done on understanding the damage to cementitious fire protection on steel frames under moderate earthquakes and the resultant loss of fire resistance. This was based on experiments conducted on damage mechanisms of cementitious coatings [2], which were used to specify threshold strains at which coating damage was likely. Steel structural frames were then subjected to an earthquake

time histories that produced storey drifts consistent to moderate damage levels. The maximum outer surface strain histories in columns and beams as a result of the earthquake loading were compared to the damage threshold strains to determine the extent of coating damage. The damaged frame was then subjected to fire loading and its remaining fire resistance determined [29].

5.5 *Hybrid Simulation Approach for Structures in Fire*

Testing large structural systems in full scale is usually unfeasible given the enormous resources just one such experiment may consume. Hybrid simulations approaches were introduced in earthquake engineering based on breaking up a large system into numerical and physical components, which would allow the usually much smaller physical component(s) to be tested in labs while virtually connected in real time to the rest of the system (modelled numerically) through actuators and control systems. This approach has not been used in fire other than in very rudimentary forms. The author's group has been working on a virtual hybrid approach to develop this methodology to be eventually exploited for structures in fire simulation [11]

Acknowledgements The work reported here contains contributions of a very large number of the authors' students, post-doctoral researchers and colleagues, many (but by no means all) of their names appear in the references cited below.

References

1. Cameron N, Usmani A (2005) A new design method to determine the membrane capacity of laterally restrained composite floor slabs in fire, part 1: theory and method and part 2: validation. *Struct Eng* 83(19):28–39
2. Chen S, Jiang L, Usmani A, Li GQ, Jin C (2015) Damage mechanism investigation of spray-applied fire-resistive materials on axially loaded steel Members. *Construct Build Mater* 90:18–35
3. Dai X, Welch S, Usmani A (2017) A critical review of “travelling fire” scenarios for performance-based structural engineering. *Fire Saf J* 91:568–578
4. Flint G, Usmani A, Lamont S, Torero J, Lane B (2006) Effect of fire on composite long span truss floor systems. *J Constr Steel Res* 62:303–315
5. Flint G, Usmani A, Lamont S, Torero J, Lane B (2007) Structural response of tall buildings to multiple floor fires. *J Struct Eng ASCE* 133(12):1719–1732
6. Gillie M, Usmani A, Rotter J (2001) A structural analysis of the first Cardington test. *J Constr Steel Res* 57(6):581–601
7. Gillie M, Usmani A, Rotter J (2002) Structural analysis of the Cardington British steel corner test. *J Constr Steel Res* 58(4):427–442
8. Jiang J, Jiang L, Kotsos P, Zhang J, Usmani A, McKenna F, Li GQ (2013) OpenSees software architecture for the analysis of structures in fire. *J Comput Civil Eng ASCE* 29(1)
9. Jiang J, Usmani A (2013) Modeling of steel frame structures in fire using OpenSees. *Comput Struct* 118:90–99

10. Jiang L, Usmani A (2018) Computational performance of beam-column elements in modelling structural members subjected to localised fire. *Eng Struct* 156:490–502
11. Khan M, Jiang L, Cashell K, Usmani A (2018) Analysis of restrained composite beams exposed to fire using a hybrid simulation approach. *Eng Struct* 172:956–966
12. Khazaienejad P, Usmani A, Laghrouche O (2014) An analytical study of the nonlinear thermo-mechanical behaviour of thin isotropic rectangular plates. *Comput Struct* 141:1–8
13. Khazaienejad P, Usmani A, Laghrouche O (2015) Temperature-dependent nonlinear behaviour of thin rectangular plates exposed to through-depth thermal gradients. *Compos Struct* 132:65–664
14. Khazaienejad P, Usmani A (2016) Temperature-dependent nonlinear analysis of thin shallow shells: a theoretical approach. *Compos Struct* 141:1–13
15. Kotsovinos P, Jiang Y, Usmani A (2013) Effect of vertically travelling fires on the collapse of tall buildings. *Int J High-Rise Build* 2:49–62
16. Kotsovinos P, Usmani A (2013) The World Trade Center 9/11 disaster and progressive collapse of tall buildings. *Fire Technol* 49:741–765
17. Lamont S, Lane B, Flint G, Usmani A (2006) Behaviour of structures in fire and real design—a case study. *J Fire Prot Eng* 16:5–35
18. Lange D, Roben C, Usmani A (2012) Tall building collapse mechanisms initiated by fire: mechanisms and design methodology. *Eng Struct* 36:90–103
19. Lange D, Devaney S, Usmani A (2014) An application of the PEER PBEE framework to structures in fire. *Eng Struct* 66:100–115
20. OpenSEES for Fire (2019) <http://openseesforfire.github.io/>
21. OpenSEES Berkeley (2019) <http://opensees.berkeley.edu/>, 2019
22. Sharma U, Kamath P, Kumar P, Bhargava P, Usmani A, Singh B, Singh Y, Torero J (2015) Full scale fire test on an earthquake-damaged reinforced concrete frame. *Fire Saf J* 73:1–19
23. Usmani A (2000) Cardington PiT project reports (2000) <https://www.eng.ed.ac.uk/research/projects/cardington-test-reports-pit-project>
24. Usmani A, Rotter J, Lamont S, Sanad A, Gillie M (2001) Fundamental principles of structural behaviour under thermal effects. *Fire Saf J* 36:721–744
25. Usmani A, Chung Y, Torero J (2003) How did the WTC towers collapse? A New Theory *Fire Saf J* 38:501–533
26. Usmani A, Cameron N (2004) Limit capacity of laterally restrained reinforced concrete floor slabs in fire. *Cement Concr Compos* 26(2):127–140
27. Usmani A (2005) Understanding the response of composite structures to fire. *Eng J Am Inst Steel Construct Inc.* 42(2):83–98
28. Zhou M, Cardoso R, Bahai H (2019) A new material model for thermo-mechanical analysis of steels in fire. *Int J Mech Sci* 159:467–486
29. Zhou M, Jiang L, Chen S, Cardoso R, Usmani A (2019b) Remaining fire resistance of steel frames following moderate earthquake—a case study. *J Construct Steel Res* in press

Stochastic Modelling for Service Life Prediction of Underground Tunnels Subjected to Water Ingress



Hassan Baji and Hamid Reza Ronagh

1 Introduction

In most of the deterioration processes in concrete structures, water is either the main damaging substance or the substance by which other harmful agents such as chloride and sulphate ingress in concrete initiating other degradation processes e.g. corrosion. For underground tunnel linings, inspection results have shown that most of the current tunnels suffer from different damages induced by water infiltration [8] costing the operating agencies considerable financial burden to repair and remedy these damages. Therefore, resistance to water ingress can be used as a key indicator in determining durability of concrete structures. Using hydraulic properties of concrete, which depend on water flow type, resistance of concrete to water ingress can be quantified. Types of water flow in concrete material are generally categorized as saturated and unsaturated [3]. In saturated flow, which assumes that entire pores in concrete medium are filled with water, Darcey's law is used to establish the governing equations. In this case, concrete permeability coefficient or conductivity is used to measure water resistance of concrete. Flow of water in unsaturated concrete medium is governed by Fick's second law, in which sorptivity coefficient is employed as an indicator to measure water resistance [6].

In performance-based, water/ion transport properties of concrete are usually used in durability design and service life prediction of concrete structures. Ho and Chirgwin [4] proposed the concrete sorptivity as an indicator to measure concrete resistance to water ingress. Alexander [1] proposed an engineering approach for durability design of concrete structures based on oxygen permeability, hydraulic sorptivity and chloride diffusion as the durability indices. Murata et al. [7] proposed a design method

H. Baji (✉)

School of Engineering and Technology, Central Queensland University, Cairns, Australia
e-mail: h.baji@cqu.edu.au

H. R. Ronagh

Centre for Infrastructure Engineering, Western Sydney University, Sydney, Australia

in which Darcey's law was used to approximate the water front in concrete under hydraulic pressure and predict service life of concrete structures subjected to water infiltration. In line with the load and resistance factor design method, Murata et al. [7] proposed resistance reduction factors to be applied on conductivity and diffusivity of concrete material, while as a load factor, the hydraulic pressure is increased. Lockington et al. [6] employed a similar criterion. However, they used the sorptivity to find the water front location. In any service life prediction, a probabilistic-based framework in which the uncertainties are considered is essential [5]. Probabilistic methods, in which spatial and temporal variation of seepage as a random process are considered, have rarely been employed in formulation of design framework for durability design and service life prediction of concrete structures.

In this paper, using the Gamma process and copulas, a probabilistic procedure to account for temporal and spatial variabilities of seepage process is employed. To formulate the water ingress in concrete, a simple approximate method proposed by Murata et al. [7] is employed. From the proposed probabilistic procedure, the extent of wetted area on the surface of structures subjected to water pressure, e.g. tunnel lining, and its likelihood can be determined. An illustrative example is used to demonstrate applicability of the procedure.

2 Methodology

2.1 Limit State

Because of infinite water supply through underground water, estimation of water inflow is one of the main challenges in assessment of underground structures. In case of presence of constant water source outside the underground structure, e.g. tunnel, water seeps through the lining protecting the underground structure. A typical tunnel lining with circular cross-section and a uniform thickness, D , is shown in Fig. 1. The tunnel is subjected to piezometric water pressure of P_w .

At a certain point on the surface of the tunnel, see point "O" in Fig. 1, the time it takes water to travel through the entire lining thickness can be used as measure to quantify service life of structure. If it is assumed that the time required for water to pass through the lining thickness marks the useful service life of tunnel, the following limit state can be formulated to probabilistically evaluate the service life,

$$g = X(t) - D \quad (1)$$

where t represents time and X represents the water front depth. The time at which X exceeds D marks the end of service life of structure according to the assumed criterion. To find location of water front X , Murata et al. [7] used Darcey's law proposing the following expression,

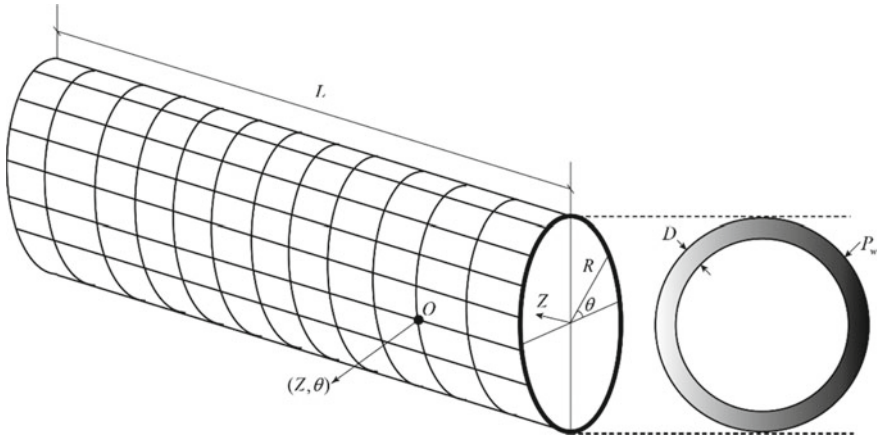


Fig. 1 Geometry of a typical shield tunnel

$$X(t) = \sqrt{2P_w K_c t} \quad (2)$$

where K_c is the hydraulic conductivity of concrete and P_w is the pressure difference on both sides of lining thickness. Effective hydraulic conductivity of concrete can be related to hydraulic properties of its constituents that are the mortar, aggregates and the interfacial transition zone (ITZ). Baji et al. [2] proposed the following analytical model for the effective hydraulic conductivity of concrete,

$$K_c \approx K_m \left(1 - 1.4123\varphi + 0.419\varphi^2 \right) + 1.4665 \left(1.6853\varphi - \varphi^2 \right) \left[1.2 \left(\frac{2K_i d_i}{K_m a_{\max}} \right) - \left(\frac{2K_i d_i}{K_m a_{\max}} \right)^2 \right] \quad (3)$$

where φ is the coarse aggregate volume fraction and K_m is the hydraulic conductivity of mortar. K_i and d_i are the hydraulic conductivity and thickness of the ITZ. a_{\max} is the maximum aggregate size [defined as the maximum radius of aggregate in Eq. (3)].

Probabilistically, the water front $X(t)$ can be represented with a random process. By having statistics of the basic random variables, e.g. K_m , K_i , d_i , etc., some information on the probabilistic nature of this process can be acquired. Having a probabilistic model for $X(t)$, and by using Eq. (1), tunnel service life based on the water seepage criterion can be calculated. In the method proposed in this paper, water seepage at different points on the tunnel surface follow an identical random process. Using copulas, these random processes are correlated. The probabilistic analysis will also be used to evaluate extent of water seepage on the surface of tunnel. In what follows details of consideration of temporal and spatial variation will be given.

2.2 Temporal Variation of Seepage

To account for temporal variability, random process is used to model evolution of water front. One of the most common stochastic processes which has been successfully employed in Civil Engineering applications is the Gamma process [9]. With the Gamma process, the water front location x at time t , follows a Gamma density function as follows,

$$f_{X(t)}(x) = Ga[x|\lambda(t), \beta] = \frac{\beta^{\lambda(t)}}{\Gamma[\lambda(t)]} \delta^{\lambda(t)-1} e^{-\beta x} \quad (4)$$

where $\lambda(t)$ and β are parameters of the Gamma random process and Γ is the gamma function. Parameters of the Gamma process can be determined from collected data over time by using a common statistical method such as maximum likelihood estimation or the method of moments.

2.3 Spatial Variation of Seepage

A copula is a tool to consider dependency between different random variables for which the individual probability density functions are known. According to Sklar's theorem any multivariate joint distribution with n elements can be written in terms of univariate marginal distribution functions, F_i , and a copula, C , which describes the dependence structure between the variables.

$$F[x_1, x_2, \dots, x_n] = C[F_1(x_1), F_2(x_2), \dots, F_n(x_n)] \quad (5)$$

where F_i shows the joint probability density function. x_i values represent the water front increment at different points on the surface of tunnel (see Fig. 1). Here Gaussian copula, C^G , which is formulated as follows is used,

$$C^G[u_1, u_2, \dots, u_{n_\theta}; \rho] = \Phi_\rho[\Phi^{-1}(u_1), \Phi^{-1}(u_2), \dots, \Phi^{-1}(u_{n_\theta})] \quad (6a)$$

$$\Phi_\rho[\Phi^{-1}(u_1), \Phi^{-1}(u_2), \dots, \Phi^{-1}(u_{n_\theta})] = \int_{-\infty}^{\Phi^{-1}(u_1)} \dots \int_{-\infty}^{\Phi^{-1}(u_{n_\theta})} \frac{1}{(2\pi)^{n/2} |\rho|^{1/2}} \exp\{-X^T \rho^{-1} X\} dX \quad (6b)$$

where Φ is the standard multivariate Gaussian distribution and ρ is the correlation matrix. u_i are uniformly distributed random variables between 0 and 1. By applying an inverse of F_i (Gamma in this study) to the generated copula u_i values, one can obtain realizations of x_i values at each different time point. In this paper, it is assumed that the correlation between the water front of any pair of points on the tunnel surface follows an exponential function as follows,

$$\rho_{XX}(i, j) = \exp \left[-\frac{\sqrt{(R\theta_j - R\theta_i)^2 + (Z_j - Z_i)^2}}{L_c} \right] \quad (7)$$

The coordinates Z and θ for points i and j are taken from the global coordinate system shown in Fig. 1. L_c is the correlation length that controls the strength of correlation amongst different points on the tunnel surface. Components of the autocorrelation function ρ_{XX} constitute the correlation matrix ρ in Eq. (6b).

2.4 Simulation

The Monte Carlo simulation technique is employed to generate a large pool of samples based on the proposed probabilistic procedure. The algorithm of simulation can be summarized as follows:

- (1) Discretise the tunnel surface into $n_Z \times n_\theta$ elements, where n_Z and n_θ are number of divisions in Z and θ directions (see Fig. 1);
- (2) Discretise the time interval $[0, t]$ into small time steps, Δt_i , where $i = 1:n_t$;
- (3) Based on the discretised points, use Eq. (7) to construct the spatial correlation matrix;
- (4) At each time interval, using the Gaussian copula shown in Eq. (6a, 6b), simulate correlated Gamma-distributed random variables representing the water front increment, Δx_i , at each step;
- (5) Accumulate the Δx_i values to get the water front at each discretised time;
- (6) Using the limit state shown in Eq. (1), evaluate whether the limit state is violated or not;
- (7) Repeat steps (4–6) for adequately large number of simulations;
- (8) Process the simulation results and find the extent and likelihood of seepage-induced damage on the tunnel surface;

In the next section, using an illustrative example, application of the above steps is presented.

3 Illustrative Example

A typical underground shield tunnel with circular cross-section is considered as an example to show applicability of the proposed stochastic procedure. Geometric and material specifications of the considered tunnel are shown in Table 1. Refer to Fig. 1 for graphical representation of the graphical specifications. Ignoring the change of water pressure due to height difference on the tunnel surface, it is assumed that the outer surface of the tunnel is subjected to an equivalent hydraulic pressure of 3

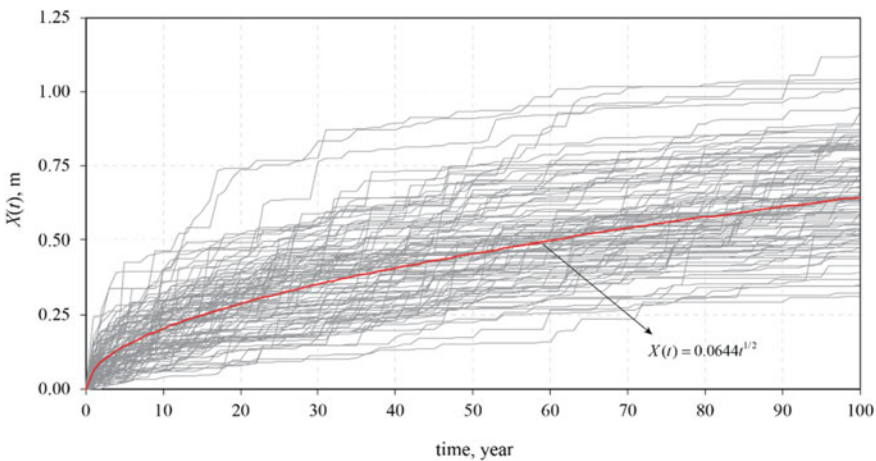
Table 1 Specifications of the considered underground tunnel

L (m)	R (m)	D (m)	P_w (m)	φ (-)	K_m (m/s)	K_i (m/s)	d_i (mm)	a_{\max} (mm)
10	3.0	0.50	3.0	0.50	5×10^{-11}	$10 \times K_m$	0.02	10

metres. According to the limit state defined in Eq. (1), once the water front reaches the inner surface of tunnel, state of failure is deemed to occur.

Tunnel surface is discretised in such a way that the size of discretised elements is around the lining thickness, $D = 0.50$ m, resulting in a 20 (longitudinal) \times 36 (circumferential) grid. The tunnel is analysed over a 100-year period. One-year time steps are used for simulation. By having statistics of the basic random variables, random variation of the water front as a stochastic process can be evaluated. However, realistic probabilistic models for the basic random variables used in this study are not readily available [5]. Therefore, without the loss of generality and for convivence, it is assumed that the time dependent function in Eq. (2) represents the mean of the process and the coefficient of variation of the process at 50-year is 0.30. This results in $\lambda(t) = 1.57t^{1/2}$ and $\beta = 0.041$ as parameters of the Gamma process representing the water front. The correlation length L_c is taken as 10 times the thickness of lining. In Fig. 2, typical simulation results for the water front process, X , is shown. For clarity, only 100 simulations are shown.

By having the parameters of Gamma distribution and the correlation structure of copula, temporal evolution of water front can be evaluated. In Fig. 3a-d, a typical evolution of water front at four different times is shown. For better graphical representation, the cylindrical tunnel surface is flattened. As it can be seen the areas over which the water front exceeds the lining thickness increases with time.

**Fig. 2** Typical realizations of Gamma process for water front

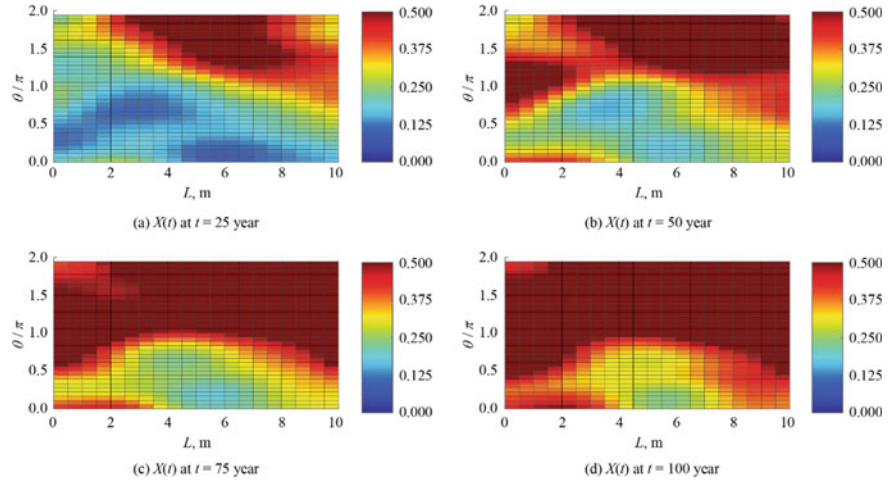


Fig. 3 Evolution of water front for a typical simulated sample

To extract statistics of the water front process, 10,000 simulations are generated. The simulated samples can be used to evaluate extent of damage, here damage is defined as seepage, over the tunnel surface. An important reliability analysis result is the probability that the damage area exceeds a certain specified level. In Fig. 4, based on four different area extent limits, the results are shown.

As results of Fig. 4 show, extent and likelihood of damaged area increase with time. These results can be used for service life prediction of tunnels subjected to water seepage. For instance, choosing an acceptable extent of damage of 50% and an acceptable probability of 0.20, service life of the considered tunnel is around 50 years.

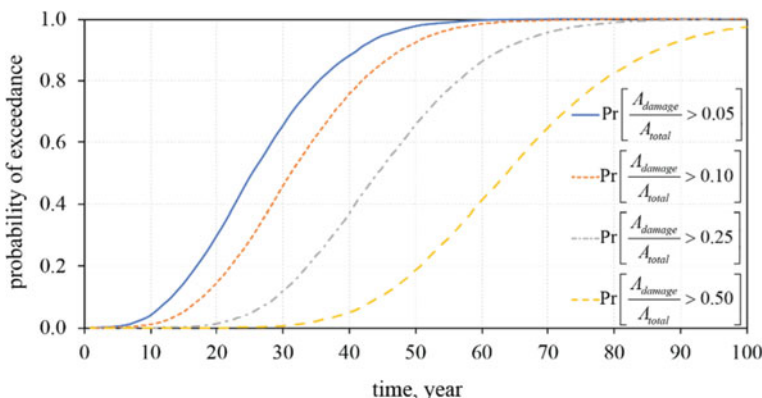


Fig. 4 Probability of damaged area exceeding different levels

4 Conclusion

In this paper, a stochastic procedure in which temporal and spatial variability of seepage process can be considered is employed. Gamma process and copulas are used to account for the temporal and spatial variabilities, respectively. A simple model from the literature was used to calculate the water front coordination. Simulation based on the Monte Carlo technique is used to derive statistics of the random process. An illustrative example of a typical underground tunnel was used to demonstrate applicability of the presented method. The results showed that the extent and likelihood of water seepage-induced damage increase with time. Based on 50% extent of seepage-induced damage and acceptable probability of failure of 0.20, service life of tunnel is around 50 years, while for 0.05 extent of damage service life is around 16 years. These results can be used as a useful tool in service life prediction of underground tunnels.

References

1. Alexander MG (2004) Durability indexes and their use in concrete engineering. In: International RILEM symposium on concrete science and engineering: a tribute to Arnon Bentur, Illinois, USA, pp 9–22
2. Baji H, Yang W, Li CQ, Shi W (2019) Analytical models for effective hydraulic sorptivity, diffusivity and conductivity of concrete with interfacial transition zone. *Constr Build Mater* 225:555–568
3. Hall C (1989) Water sorptivity of mortars and concretes: a review. *Magazine Concrete Res* 41(147):51–61
4. Ho DWS, Chirgwin GJ (1996) A performance specification for durable concrete. *Constr Build Mater* 10(5):375–379
5. Li CQ, Baji H, Yang S (2018) Probabilistic study on hydraulic conductivity of concrete at mesoscale. *ACI Mater J* 115(5):717–725
6. Lockington D, Leech C, Parlange J, Dux P (2002) The sorptivity test and predicting resistance to water absorption in concrete. In: Concrete Materials and Construction, Dundee, Scotland, pp 9–11
7. Murata J, Ogihara Y, Koshikawa S, Itoh Y (2004) Study on watertightness of concrete. *ACI Mater J* 101(2):107–116
8. Richards J (1998) Inspection, maintenance and repair of tunnels: international lessons and practice. *Tunn Undergr Space Technol* 13(4):369–375
9. van Noortwijk JM (2009) A survey of the application of gamma processes in maintenance. *Reliab Eng Syst Saf* 94(1):2–21

Structural Damage Detection in Space Frames Using Modal Strain Energy Method and Genetic Algorithm



Quang-Huy Le, Van-Phuong Huynh, Minh-Tuan Ha, and Duc-Duy Ho

1 Introduction

During the last three decades, there are concepts to develop a system for structural health monitoring (SHM) including impedance-based methods, vision-based methods, and vibration-based methods, which have been motivating researchers to work on. Across the disciplines of SHM, vibration-based damage detection methods are widely adopted due to the sensitivity of the structural vibration characteristics according to the changes in structure. Basically, in the categories of vibration-based damage detection, vibration characteristics of the structure can be extracted to develop the approaches, which consist of natural frequency-based methods, mode shape-based methods, mode shape curvature-based methods, strain mode shape-based methods, dynamically measured flexibility-based methods, matrix update-based methods, non-linear methods, ... [3–5].

This study attempts to develop a structural damage detection method, in which the sensibility of the MSE is utilized, combined with the GA to detect location and extent of damages. The ultimate aim of this study is to provide a solution to identify specific locations of the damages within structure, then the extents of those damages are determined. The general idea is to step-by-step narrow the detecting domain of damages; therefore, the calculation volume can consequently reduce, which in turn

Q.-H. Le

Faculty of Civil Engineering, Ho Chi Minh City University of Transport, Ho Chi Minh City, Vietnam

V.-P. Huynh · D.-D. Ho (✉)

Faculty of Civil Engineering, Ho Chi Minh City University of Technology (HCMUT), VNU-HCM, Ho Chi Minh City, Vietnam

e-mail: haducduy@hcmut.edu.vn

M.-T. Ha

Faculty of Civil Engineering, Ho Chi Minh City University of Technology (HUTECH), Ho Chi Minh City, Vietnam

improves the accuracy of the method. The proposed method is numerically validated with a complete real scale space frame structure.

2 Theory of Damage Detection Method

2.1 Modal Strain Energy

The MSE method was first developed by Stubbs and Farrar [7], which was used for various later research studies. The method was applied to an Euler-Bernoulli continuous beam for the early period, which was to recognize the changes in bending stiffness [1]. Generally, the strain energy of a structure respective to the mode shape displacements are defined to be MSE. In finite element method, the mode shape is represented via a set of nodal displacements in discrete form. Corresponding to the mode shape nodal displacements obtained from the finite element method, the MSE of *j*th element for *i*th mode is formulated as:

$$\text{MSE}_{ij} = \Phi_i^T \mathbf{K}_j \Phi_i \quad (1)$$

where MSE_{ij} is the MSE of *j*th element for *i*th mode, Φ_i is the *i*th mode shape, and \mathbf{K}_j is the stiffness matrix of the *j*th element in global coordinates.

2.2 Damage Assumption

In this study, as mentioned in previous section, the states of structure, which include both being in healthy and being in damaged, are numerically simulated by means of finite element method. Therefore, the issue of how to develop an adequate model consisting of appropriate figures should be paid proper attention. To design an appropriate model for the investigation, it is necessary to formulate the correlation in stiffness reduction between a (some) specific point(s) and the general beam, i.e. in case one or some positions along the beam experience α_i (%) of stiffness reduction, the stiffness of the general beam should be considered as how much percentage (α) of degradation. The idea given in this study is that the displacement of the beam is used to determine that consequent decrease of the stiffness.

2.3 Modal Strain Energy-Based Damage Detection Method

In this study, by inheriting previous studies, unhealthy element leads to some changes in structural stiffness Barroso and Rodriguez [2], in which damage is considered as

the reduction of the structural stiffness. As denoted in the previous section, for the i th mode shape and j th element, the MSE of healthy and damaged state of structure are given as:

$$\text{MSE}_{ij}^h = \Phi_i^{hT} \mathbf{K}_j \Phi_i^h \quad (2)$$

$$\text{MSE}_{ij}^d = \Phi_i^{dT} \mathbf{K}_j \Phi_i^d \quad (3)$$

where Φ_i^h ; Φ_i^d are the nodal displacement vectors of healthy and damaged state respectively at the i th mode shape; \mathbf{K}_j is the stiffness matrix of the j th element in global coordinate. Note that the value of MSE_{ij}^d is approximated by the healthy stiffness matrix \mathbf{K}_j , and the letters of “ h ” and “ d ” are denoted to express the “healthy” and “damaged” states of structure respectively.

When damages occur, the structural stiffness of the element reduces, which results in the change in the value of the elemental MSE. Utilizing that change, damage can be recognized by an index which is formulated from the change. So far, there were a number of formulas developed as the index to detect the damages. For frame structure, the index namely modal strain energy based index—MSEBI, which was proposed by Seyedpoor [6], shows highly effective performance. The expressions of the MSEBI are presented as follow:

The sum of the MSE for the i th mode shape,

$$\text{MSE}_i = \sum_{j=1}^n \text{MSE}_{ij} \quad (4)$$

The MSE of the j th element at the current considering mode shape i th is normalized according to the sum of the MSE,

$$n\text{MSE}_j = \frac{\text{MSE}_{ij}}{\text{MSE}_i} \quad (5)$$

The average value of the expression (5) according to the first m mode shapes is given,

$$n\overline{\text{MSE}}_j = \frac{1}{m} \sum_{i=1}^m n\text{MSE}_j \quad (6)$$

By the above-given expressions, the value of MSEBI is described as below,

$$\text{MSEBI}_j = \max \left\{ 0; \frac{n\overline{\text{MSE}}_j^d - n\overline{\text{MSE}}_j^h}{n\overline{\text{MSE}}_j^h} \right\} \quad (7)$$

The expression (7) provides the recognition of the damage, in which the probable damaged element will give the positive value, and the value of zero represents the undamaged element.

Among above expressions, m is given as the first number of mode shape, n is the total element number of the structure; i and j are denoted for the i th mode shape and j th element respectively.

2.4 Genetic Algorithm

Objective function

In practice, structural damage is represented by a reduction of structural stiffness. Therefore, the relation of structural stiffness between undamaged and damaged element is given through the following equation,

$$(EI)_j^s = (1 - \alpha_j)(EI)_j^0 \quad (8)$$

where $(EI)_j^0$, $(EI)_j^s$ are the structural stiffness of the j th element corresponding to undamaged and damaged state, and α_j is the percentage of the structural stiffness reduction of the j th element.

A vector of α representing the stiffness reduction of k probable damaged elements, which are identified by the MSEBI described in the previous section, is expressed as,

$$\alpha = \{\alpha_1 \ \alpha_2 \dots \alpha_k\} \quad (9)$$

An objective function is defined by setting a function whose value goes to zero when its variables vector proceeds to the desired solution. The vector (9) is the designed variables vector which is denoted as α^s . In this paper, the objective function is developed based on the difference in the MSE as follows,

$$\text{OF}(\alpha^s) = \min \sum_{i=1}^m \sum_{j=1}^n \left| \frac{\Phi_i^{dT} \mathbf{K}_j \Phi_i^d - \Phi_i^T(\alpha^s) \mathbf{K}_j \Phi_i(\alpha^s)}{\Phi_i^{dT} \mathbf{K}_j \Phi_i^d} \right| \quad (10)$$

$$\alpha^s = \{\alpha_1^s \ \alpha_2^s \dots \alpha_n^s\} \in [0, 1]^n$$

where Φ_i^* is the i th mode shape; m is the number of modes considered; n is the total number of elements; and the superscript d expresses the damaged state.

Single-objective genetic algorithm

In this study, the GA is utilized as an optimization tool to find out the solution of the designed variables vector which satisfies the objective function via a defined fitness limit value. The initial input parameters for the algorithm are set as: fitness evaluation function— $\text{OF}(\alpha^s)$, presented in the Eq. (10); bound constrains— $\alpha^s \in$

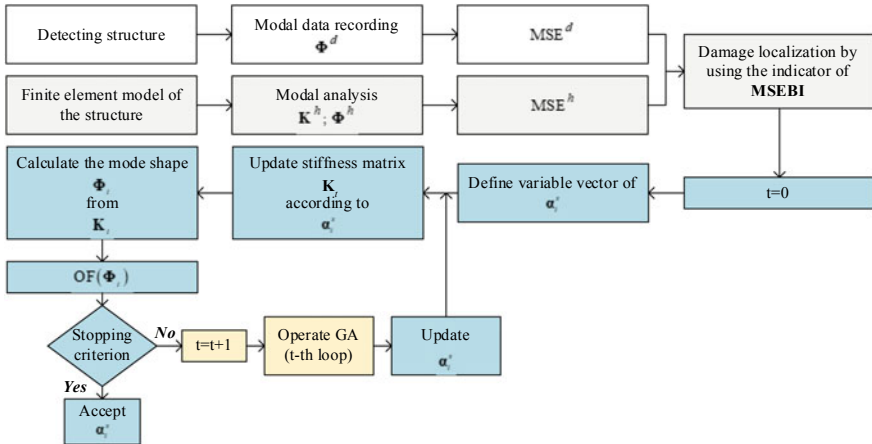


Fig. 1 The overall procedure of the proposed method

[0, 1]; population size—200; stall generation—1; max generation—5000; fitness limit—0.01.

Overall procedure of the modal strain energy-based damage detection method
The overall procedure illustrating the proposed method is described in Fig. 1.

3 Numerical Verification

3.1 Model Properties

The finite element (FE) model used to validate the proposed method is a 4-story irregular 3D frame structure whose details are presented in the Fig. 2, Tables 1 and 2.

3.2 Damage Scenarios

The damaged state of the structure with local locations is assumed to be a total of 7 positions, located on the 1st, 15th, 48th, and 63rd bar (Fig. 2). The damages are positioned randomly and irregularly to acquire the objectivity for the investigation. By FE method, damage bar is meshed into 10 sub-elements, then reduction of stiffness is assigned to the assumed damaged position (Tables 3 and 4). The meshed model is shown in the Fig. 3.

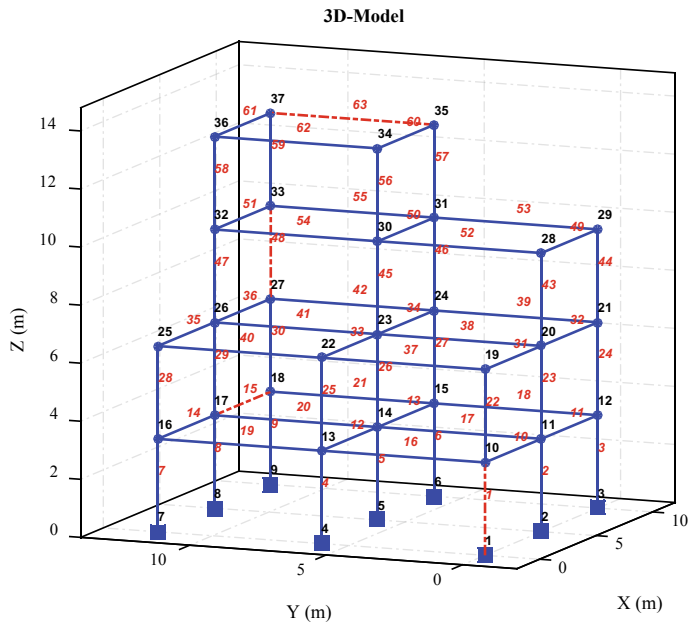


Fig. 2 3D frame's FE model

Table 1 Material and section properties

	Beam	Column
E (kN/m^2)	32.5×10^6	32.5×10^6
Mass (T/m^3)	2.500	2.500
Poisson	0.2	0.2
Section width (m)	0.3	0.3
Section height (m)	0.5	0.5

Table 2 Geometric properties

Directions	Length (m)
X	5.0
Y	6.0
Z	3.2

3.3 Global Damage Detection

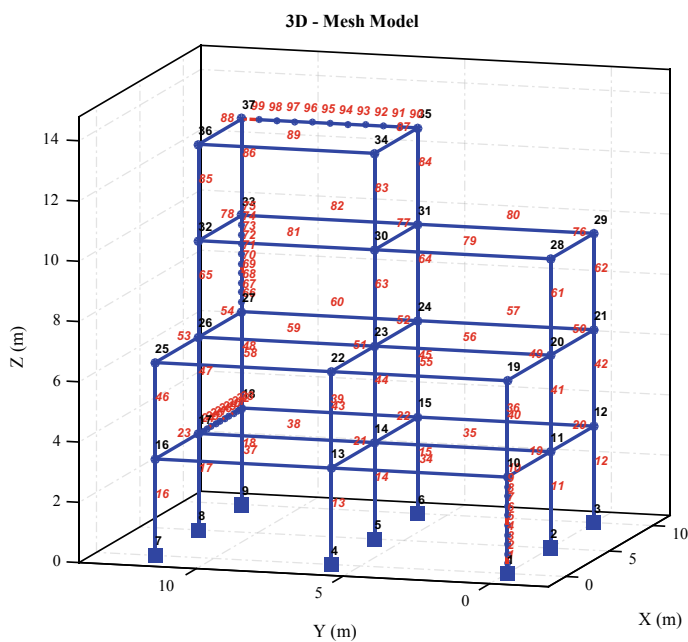
In this stage, bars probably witnessing damage are diagnosed based on the indicator of MSEBI. By evaluating the values of the MSEBI, possible damaged bars are detected and illustrated in the Fig. 4. Considering the outcome, bars with damage are all detected; furthermore, result in higher values of the MSEBI than the other bars.

Table 3 Degradation scenario of elements

Element	Severity (%)
2	38
6	45
26	30
29	48
31	35
70	42
99	40

Table 4 Degradation scenario of bars

Bar	Severity (%)
1	15.2
15	14.7
48	11.2
63	9.5

**Fig. 3** 3D frame's meshed model

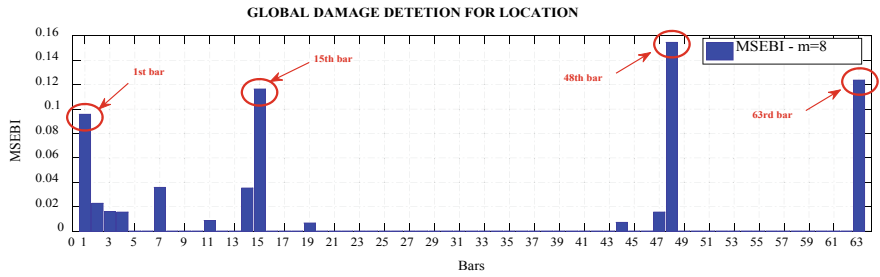


Fig. 4 Global damage detection for location

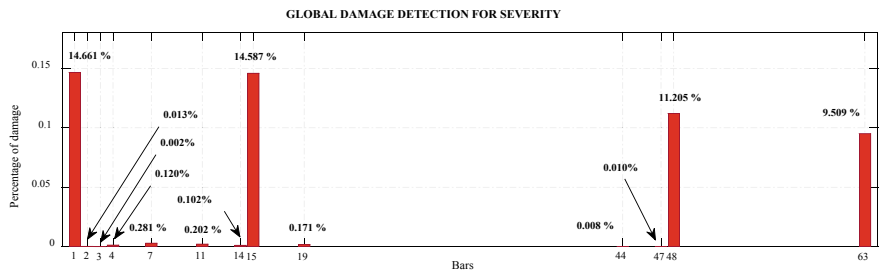


Fig. 5 Global damage detection for severity

Therefore, the MSEBI with exceptional value reveals high probability of damage. However, to ensure the reliability of the work, all bars with positive value of the MSEBI should be taken into consideration for the next stage.

The damage severities are determined and shown in the Fig. 5. The best solution gives the objective function the value of 0.0099. All the assumed damaged bars are accurately detected with highly exact ratio of the stiffness reduction compared to the scenario. The undamaged bars are accompanied with minor values of just over zero.

3.4 Local Damage Detection

In this stage, the MSEBI is generated in scope of each bar, i.e. the j^{th} index in the formulas (presented in the Sect. 2.3) varies from k to l , where k and l are the index of the starting and ending element in each considering bar. The previous stage shows that the damaged bars include the 1st, 15th, 48th, and 63rd bar, which are going to be detected for local damages. The outcome of the diagnosis is presented in Fig. 6. The proposed method gives accurate result in which all the local damage locations of each bar are detected.

To determine the extent of the identified damages, a vector storing variables representing the damage severities is defined. The numerical result of the damage severities

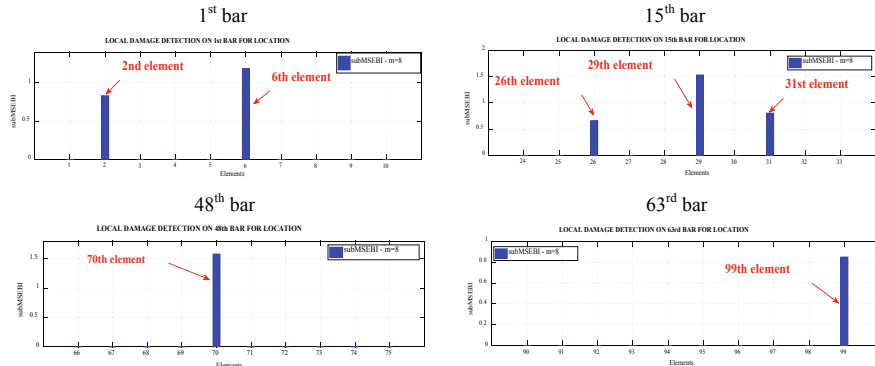


Fig. 6 Local damage detection for location

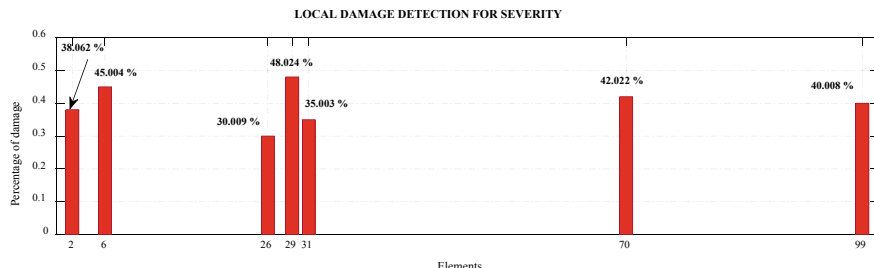


Fig. 7 Local damage detection for severity

determination is pointed out in Fig. 7. The optimal solution satisfies the fitness limit at value of 0.0096.

4 Conclusions

In this study, a two-stage damage detection method using MSE method, combined with the GA, is proposed and successfully applied to space frame structure. From the analysis results, several conclusions were drawn: (i) the proposed method gives accurate outcome in both global and local damage detection for space frame structure. (ii) the GA provides high efficiency in determining the extent of the damages. (iii) the MSE is good selection for the objective function. (iv) the GA shows good performance with the proposed method due to the lower number of variables than the single stage damage detection method.

Acknowledgements This research is funded by Ho Chi Minh City University of Technology (HCMUT)—VNU-HCM, under grant number T-KTXD-2019-13.

References

1. Balageas D, Fritzen CP, Güemes A (2006) Structural health monitoring, 1st edn. ISTE Ltd, London W1T 5DX, UK
2. Barroso LR, Rodriguez R (2004) Damage detection utilizing the damage index method to a benchmark structure. *J Eng Mech* 130(2):142–151
3. Doebling SW, Farrar CR, Prime MB, Shevitz DW (1996) Damage identification and health monitoring of structural and mechanical systems from changes in their vibration characteristics: A literature review. Los Alamos National Laboratory
4. Fan W, Qiao P (2011) Vibration-based damage identification methods: a review and comparative study. *Struct Health Monitoring* 10(1):83–111
5. Fanning P, Carden EP (2004) Vibration based condition monitoring: a review. *Struct Health Monitoring* 3(4):355–377
6. Seyedpoor SM (2012) A two-stage method for structural damage detection using a modal strain energy based index and particle swarm optimization. *Int J Nonlinear Mech* 47(1):1–8
7. Stubbs N, Farrar CR (1995) Field verification of a nondestructive damage localization and severity estimation algorithm. In: Proceedings of the 13th international modal analysis conference (IMAC XIII) 182:210–218

Structural Damage Detection Using Model Order Reduction and Two-Stage Method



Qui X. Lieu, Phu-Cuong Nguyen, Seunghye Lee, Jaehong Lee,
and Van Hai Luong

1 Introduction

In general, real engineering structures may exist local damage of a certain structural part or the damage of the whole structure. Such damage can occur with various scenarios such as ageing, environment effects, sudden accidents and so on. Accordingly, the so-called structural health monitoring (SHM) or damage identification has been extensively developed and has captured a huge attention of many scholars owing to its essential usefulness. A large number of methodologies have been therefore proposed to detect the location and severity of damage in a structural system and could be easily found in open literature. Among them, the inverse optimization-based damage detection paradigm is one of the most popular ones. A variety of metaheuristic optimization algorithms have been also utilized to resolve such optimization problems such as differential evolution (DE) [2], particle swarm optimization (PSO) [9], ant colony optimization (ACO) [8], improved charged system search (CSS) [1], etc. However, a considerable amount of computational attempts are required in the optimization process due to utilizing a large number of design variables to define all

Q. X. Lieu (✉) · V. H. Luong

Faculty of Civil Engineering, Ho Chi Minh City University of Technology (HCMUT), 268 Ly
Thuong Kiet Street, Ward 14, District 10, Ho Chi Minh City, Vietnam
e-mail: lieuxuanqui@hcmut.edu.vn

Vietnam National University Ho Chi Minh City (VNU-HCM), Linh Trung Ward, Thu Duc
District, Ho Chi Minh City, Vietnam

P.-C. Nguyen

Faculty of Civil Engineering, Ho Chi Minh City Open University, Ho Chi Minh City, Vietnam

S. Lee · J. Lee

Deep Learning Architecture Research Center, Sejong University, 209 Neungdong-ro,
Gwangjin-gu, Seoul 05006, Republic of Korea
e-mail: jhlee@sejong.ac.kr

healthy and damage elements. In order to lessen the problem dimension, healthy elements are eliminated first, whilst only keeping suspected ones for the performance of inverse optimization problems. This technique is the so-called two-stage damage identification approach [9], and it has also proven to be effective and robust in many publications.

Obviously, fully measuring all degrees of freedom (DOFs) of a certain structure, especially for large-scale ones, often encounters the difficulties, even impossible in many cases owing to the lack of measurement sensors and extremely expensive experiment costs. Many model order reduction techniques have been thus suggested to reduce a measured number of DOFs such as Guyan's method, the first and second-order Neumann series expansion [11] and so on.

In this paper, an inverse optimization-driven damage assessment approach for truss structures with a limited number of sensors is presented. In which, the second-order Neumann series expansion is utilized as a model order reduction strategy to condense the structural physical features due to limited sensors. By applying this technique, unmeasured information of eigenvectors is obtained. Subsequently, a two-stage method is built to detect the site and extent of multiple damage. In the first stage, the location of suspected elements is determined by means of modal strain energy based index (MSEBI). Meanwhile the AHEFA [3] is employed as an optimizer in the remaining step with the aim of precisely computing the damage severity of those elements and liquidating false evaluations collected from the previous step. The capability of the present methodology is tested via a benchmark 31-bar planar truss.

The rest of the article is arranged as follows. The next Section briefly presents the theoretical formulation of a second-order Neumann series expansion-relied model order reduction and MSEBI. Section 3 states the inverse optimization-based damage identification problem and optimization algorithm. A 31-bar truss is investigated in Sect. 4 to verify the accuracy and effectiveness of the suggested methodology. Ultimately, several important conclusions are provided in Sect. 5.

2 Theoretical Formulation

2.1 Model Order Reduction

Among the afore-discussed model order reduction techniques, the second-order Neumann series expansion [11] is adopted in this work owing to its good accuracy in many cases. Below concisely exhibits this strategy.

In general, the free vibration problem can be expressed as follows

$$\mathbf{K}\boldsymbol{\phi}_i = \omega_i^2 \mathbf{M}\boldsymbol{\phi}_i, \quad i = 1, 2, \dots, n_{\text{dof}}, \quad (1)$$

where \mathbf{K} and \mathbf{M} denote the global stiffness and lump mass matrices, respectively; ω_i and $\boldsymbol{\phi}_i$ are the i th natural frequency and mode shape vector of the structure, respectively, and n_{dof} symbolizes the total degrees of freedom (DOFs) of the structure.

The above equation can be rewritten in terms of another form as follows

$$\begin{bmatrix} \mathbf{K}_{mm} & \mathbf{K}_{ms} \\ \mathbf{K}_{sm} & \mathbf{K}_{ss} \end{bmatrix} \begin{Bmatrix} \boldsymbol{\phi}_m \\ \boldsymbol{\phi}_s \end{Bmatrix} = \omega_i^2 \begin{bmatrix} \mathbf{M}_{mm} & \mathbf{M}_{ms} \\ \mathbf{M}_{sm} & \mathbf{M}_{ss} \end{bmatrix} \begin{Bmatrix} \boldsymbol{\phi}_m \\ \boldsymbol{\phi}_s \end{Bmatrix}, \quad (2)$$

where m is the master DOFs measured by sensors, whilst s implies unmeasured DOFs named as a slave.

Equation 2 can be expressed in the following compact matrix form

$$\mathbf{K}_R \boldsymbol{\phi}_m = \omega_i^2 \mathbf{M}_R \boldsymbol{\phi}_m, \quad (3)$$

where \mathbf{K}_R and \mathbf{M}_R are the reduced global stiffness and mass matrices, respectively, and given by

$$\mathbf{K}_R = \mathbf{T}^T \mathbf{K} \mathbf{T}, \quad \mathbf{M}_R = \mathbf{T}^T \mathbf{M} \mathbf{T}, \quad (4)$$

where \mathbf{T} denotes the transformation matrix, given as

$$\mathbf{T} = \begin{bmatrix} \mathbf{I}_{mm} \\ -[\mathbf{B}_1 + \mathbf{K}_{ss}^{-1} \mathbf{M}_{ss} (\mathbf{A}_1 \mathbf{A}_4 + \mathbf{A}_1 \mathbf{A}_5)]^{-1} [\mathbf{B}_2 + \mathbf{K}_{ss}^{-1} \mathbf{M}_{ss} (\mathbf{A}_1 \mathbf{A}_2 + \mathbf{A}_1 \mathbf{A}_3)] \end{bmatrix}, \quad (5)$$

in which

$$\begin{aligned} \mathbf{A}_1 &= \mathbf{K}_{ss}^{-1} \mathbf{M}_{ss} \mathbf{K}_{ss}^{-1} \mathbf{K}_{sm} \mathbf{M}_{mm}^{-1}; & \mathbf{A}_2 &= \mathbf{K}_{mm} \mathbf{M}_{mm}^{-1} \mathbf{K}_{mm}, \\ \mathbf{A}_3 &= \mathbf{K}_{ms} \mathbf{M}_{ss}^{-1} \mathbf{K}_{sm}; & \mathbf{A}_4 &= \mathbf{K}_{mm} \mathbf{M}_{mm}^{-1} \mathbf{K}_{ms}, \\ \mathbf{A}_5 &= \mathbf{K}_{ms} \mathbf{M}_{ss}^{-1} \mathbf{K}_{ss}; & \mathbf{B}_1 &= \mathbf{I}_{ss} + \mathbf{A}_1 \mathbf{K}_{ms}, \\ \mathbf{B}_2 &= \mathbf{K}_{ss}^{-1} \mathbf{K}_{sm} + \mathbf{A}_1 \mathbf{K}_{mm}. \end{aligned} \quad (6)$$

Finally, the i th mode shape vector with respect to slave DOFs $\boldsymbol{\phi}_{i,s}$ can be easily computed by

$$\boldsymbol{\phi}_{i,s} = -[\mathbf{B}_1 + \mathbf{K}_{ss}^{-1} \mathbf{M}_{ss} (\mathbf{A}_1 \mathbf{A}_4 + \mathbf{A}_1 \mathbf{A}_5)]^{-1} [\mathbf{B}_2 + \mathbf{K}_{ss}^{-1} \mathbf{M}_{ss} (\mathbf{A}_1 \mathbf{A}_2 + \mathbf{A}_1 \mathbf{A}_3)] \boldsymbol{\phi}_{i,m}. \quad (7)$$

2.2 Modal Strain Energy Based Index

In the first step of the two-stage approach, modal strain energy based index (MSEBI) [9] is employed to detect the location of doubtful damage elements of a structure. In order to calculate this indicator, modal shape vectors obtained by Eq. 1 are demanded. It is apparent that the meaning of model shape vectors attained from the above equation is analogous to that of displacements given in static problems, and thus each of all elements exists a strain energy which is the so-called modal strain energy (MSE) in this case. From this observation, the e th MSE with regard to the i th mode shape can be defined as follows

$$\mathcal{U}_i^e = \frac{1}{2} (\boldsymbol{\phi}_i^e)^T \mathbf{K}^e \boldsymbol{\phi}_i^e, \quad (8)$$

where \mathbf{K}^e is the stiffness matrix of the e th element, and $\boldsymbol{\phi}_i^e$ stands for the mode shape vector of the e th element corresponding to the i th mode.

The e th MSE is often normalized for the computational convenience as follows

$$\bar{\mathcal{U}}_i^e = \frac{\mathcal{U}_i^e}{\sum_{e=1}^n \mathcal{U}_i^e}. \quad (9)$$

For taking account of the first m mode shapes, the e th normalized MSE in Eq. 9 is given as

$$\bar{\mathcal{U}}^e = \frac{\sum_{i=1}^m \bar{\mathcal{U}}_i^e}{m}. \quad (10)$$

When damage occurs at a certain local position or the total structure, the global stiffness matrix becomes weaker. Assume that the global mass matrix still remains constant. The mode shape vectors obtained from Eq. 1 may have a larger magnitude, and this causes a corresponding raise of $\bar{\mathcal{U}}^e$. Accordingly, by comparing in pairs of the item given in Eq. 10 for a healthy element $\bar{\mathcal{U}}^{e,h}$ and a corresponding damage one $\bar{\mathcal{U}}^{e,d}$, the damage appearance of a certain element can be detected by the so-called MSEBI as follows

$$I_{\text{MSE}}^e = \begin{cases} \frac{\bar{\mathcal{U}}^{e,d} - \bar{\mathcal{U}}^{e,h}}{\bar{\mathcal{U}}^{e,h}} > 0, & \text{damaged element,} \\ \frac{\bar{\mathcal{U}}^{e,d} - \bar{\mathcal{U}}^{e,h}}{\bar{\mathcal{U}}^{e,h}} \leq 0, & \text{healthy element,} \end{cases} \quad (11)$$

where $\bar{\mathcal{U}}^{e,d}$ can be gained from experimental data, while $\bar{\mathcal{U}}^{e,h}$ can be directly given from simulation modelings such as analytical and numerical ones.

3 Inverse Optimization-Based Damage Detection

3.1 Problem Statement

In the remaining step of the two-stage method, the damage severity of those suspected elements determined in the former stage is accurately estimated by solving an inverse optimization problem. The mathematical statement of this problem is given by

$$\begin{aligned} \text{Min : } f_{MDLAC}(\mathbf{x}) &= -\frac{|\Delta\omega^T \delta\omega|^2}{(\Delta\omega^T \Delta\omega)(\delta\omega^T \delta\omega)}, \\ \text{St : } &\left\{ \begin{array}{l} [\mathbf{K}(\mathbf{x}) - \omega_i^2 \mathbf{M}] \phi_i = \mathbf{0}, \quad i = 1, 2, \dots, p, \dots, n_{dof}, \\ x_{LB,j} \leq x_j \leq x_{UB,j}, \quad j = 1, 2, \dots, d, \end{array} \right. \end{aligned} \quad (12)$$

where $f_{MDLAC}(\mathbf{x})$ is the multiple damage location assurance criterion (MDLAC) objective function [10], $\mathbf{x} = \{x_1, x_2, \dots, x_j, \dots, x_d\}$ is the design variable vector with d being the number of variables, x_j is given by

$$x_j = \frac{E - E_j}{E_j}, \quad (13)$$

in which E and E_j are the intact and actually damaged Young's moduli, respectively. Moreover $\Delta\omega = \{\Delta\omega_1, \Delta\omega_2, \dots, \Delta\omega_i, \dots, \Delta\omega_p\}^T$ and $\delta\omega = \{\delta\omega_1, \delta\omega_2, \dots, \delta\omega_i, \dots, \delta\omega_p\}^T$ are respectively the vectors depicting the relative change of the first p natural frequencies in the damaged and predicted structures against those of the healthy one, where $\Delta\omega_i$ and $\delta\omega_i$ are respectively given by

$$\Delta\omega_i = \frac{\omega_i^h - \omega_i^d}{\omega_i^h}, \quad \delta\omega_i = \frac{\omega_i^h - \omega_i(\mathbf{x})}{\omega_i^h}, \quad i = 1, 2, \dots, p, \quad (14)$$

in which ω_i^h , ω_i^d and $\omega_i(\mathbf{x})$ symbolize the i th natural frequency of the healthy, damaged and predicted structures, respectively.

3.2 Optimization Algorithm

The AHEFA was successfully developed for size and shape optimization of truss structures in an authors' previously published study [3]. In addition, its efficiency and reliability for optimization of functionally graded (FG) plates [4–6], and reliability-based design optimization (RBDO) of FG plates [7] have been also proven. Herein, this algorithm is adopted as an optimizer.

4 Numerical Examples

A benchmark 31-bar planar truss as shown in Fig. 1 is tested in this Section. All elements are of the same material density $\rho = 2770 \text{ kg/m}^3$ and Young's modulus $E = 70 \text{ GPa}$. Furthermore, the cross-sectional area is taken as 0.01 m^2 . Table 1 presents two different damage cases. The first five mode shapes are considered for the damage presence diagnosis in the first stage ($m = 5$) as well as the objective estimation in the second stage ($p = 5$). Results obtained by the AHEFA are compared with the DE and firefly algorithm (FA) for comparison and verification. The population size is set to be 20. When either the absolute diversity of the best and mean value of the objective function is less than 10^{-6} or 1000 iterations are performed, the optimization process is ended. Each case runs 10 independent times. Only the best value of design variables (Best), the corresponding number of finite element analyses (No. FEAs) of the best instance and standard deviation (SD) are reported for comparison. Suppose that only six sensors at nodes 3, 4, 5, 9, 11 and 13 are placed for the measurement of vertical DOFs. Code structures are done employing Python 3.6 on a laptop computer with CoreTM i7-2670QM CPU@2.20 GHz, 8.00 GB RAM, and Windows 7[®] Professional (64-bit operating system).

After the first stage is done, only the elements 1, 2 and 4 for case 1 and 11, 16, 21, 25 and 26 for case 2 are detected as suspiciously damaged ones. Herein, only elements whose indexes are more than 0.05 are considered as suspected ones. Obtained damage identification results are reported in Table 2. As found, all algorithms accurately detect the damage site and extent for case 1. In case 2, false damage signs of elements 16, 21 and 26 are eliminated with a fairly small damage ratio. Note that the AHEFA always requires the least computational cost in all illustrated instances. Figures 2 and 3 show the convergence histories with the best run for cases 1 and 2. Note that only a first number of iterations of the convergence histories of the DE and the FA are

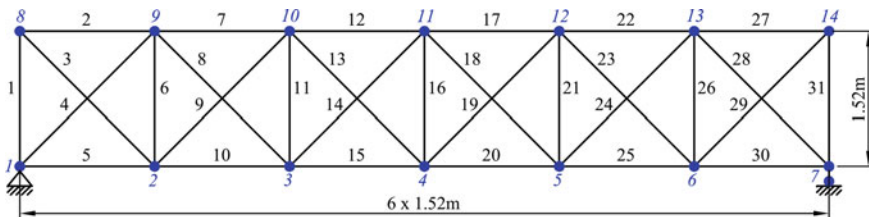


Fig. 1 The 31-bar planar truss

Table 1 Two different damage scenarios

Case	1		2	
Element	1	2	11	25
Damage ratio	0.3	0.2	0.25	0.15

Table 2 Damage detection results obtained by three different optimization algorithms

Case	Element	DE			FA			AHEFA		
		Best	SD	No. FEAs	Best	SD	No. FEAs	Best	SD	No. FEAs
1	1	0.299	0	1140	0.3	0	6500	0.3	0	740
	2	0.199	0		0.2	0		0.2	0	
	4	0	0		0	0		0	0	
2	11	0.272	0.024	2640	0.282	0.021	5120	0.265	0.034	1540
	16	0.009	0.022		0.021	0.341		0.006	0.028	
	21	0.001	0.013		0.010	0.596		0.005	0.029	
	25	0.168	0.224		0.178	0.092		0.163	0.033	
	26	0.006	0.010		0.001	0.276		0.002	0.066	

Fig. 2 The convergence histories for case 1 with three different optimization algorithms

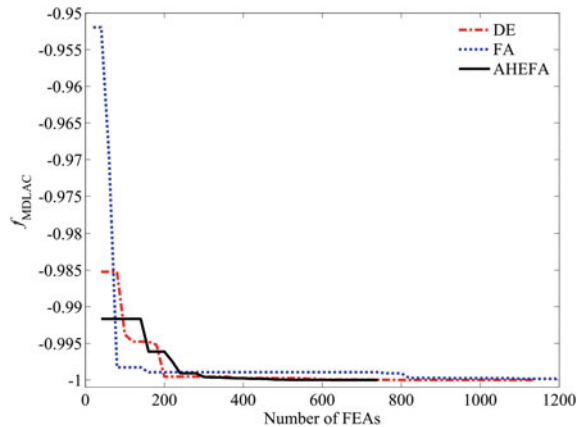
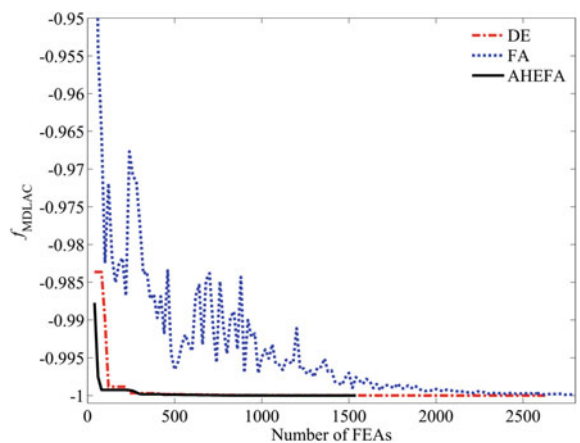


Fig. 3 The convergence histories for case 2 with three different optimization algorithms



depicted for visualization. As observed, the AHEFA always has a better convergence than the others.

5 Conclusions

In the article, an inverse optimization-based two-stage damage identification paradigm with limited sensors employing the AHEFA is first introduced to truss structures. In which, a second-order Neumann series expansion-based model order reduction technique is utilized to compact structural physical properties. In the first step of the two-stage method, distrustfully damaged elements are recognized via the MSEBI. In the remaining one, the AHEFA is utilized to solve an inverse optimization problem for precisely computing the damage extent of suspected elements captured

in the preceding step. The obtained outcomes of the proposed methodology have illustrated its effectiveness and reliability for multiple damage scenarios. Accordingly, the current paradigm can be easily extended to damage diagnosis of various practical engineering structures such as nonlinear elastic-plastic steel frames, FG plates, shells and so on.

Acknowledgements This was supported by a grant (NRF-2018R1A2A1A05018287) from NRF (National Research Foundation of Korea) funded by MEST (Ministry of Education and Science Technology) of Korean government.

References

1. Kaveh A, Zolghadr A (2015) An improved CSS for damage detection of truss structures using changes in natural frequencies and mode shapes. *Adva Eng Soft* 80:93–100
2. Kim NI, Kim S, Lee J (2019) Vibration-based damage detection of planar and space trusses using differential evolution algorithm. *Appl Acoustic* 148:308–321
3. Lieu QX, Do DTT, Lee J (2018) An adaptive hybrid evolutionary firefly algorithm for shape and size optimization of truss structures with frequency constraints. *Comput Struct* 195:99–112
4. Lieu QX, Lee J (2017) Modeling and optimization of functionally graded plates under thermo-mechanical load using isogeometric analysis and adaptive hybrid evolutionary firefly algorithm. *Compos Struct* 179:89–106
5. Lieu QX, Lee J, Lee D, Lee S, Kim D, Lee J (2018) Shape and size optimization of functionally graded sandwich plates using isogeometric analysis and adaptive hybrid evolutionary firefly algorithm. *Thin-Walled Struct* 124:588–604
6. Lieu QX, Lee J (2019) An isogeometric multimesh design approach for size and shape optimization of multidirectional functionally graded plates. *Comput Methods Appl Mech Eng* 343:407–437
7. Lieu QX, Lee J (2019) A reliability-based optimization approach for material and thickness composition of multidirectional functionally graded plates. *Compos B Eng* 164:599–611
8. Majumdar A, Maiti DK, Maity D (2012) Damage assessment of truss structures from changes in natural frequencies using ant colony optimization. *Appl Math Comput* 218:9759–9772
9. Seyedpoor SM (2012) A two stage method for structural damage detection using a modal strain energy based index and particle swarm optimization. *Int J Non-Linear Mech* 47:1–8
10. Seyedpoor SM (2015) An efficient method for structural damage detection using a differential evolution algorithm-based optimisation approach. *Civ Eng Environ Syst* 32:230–250
11. Yang QW (2009) Model reduction by Neumann series expansion. *Appl Math Model* 33:4431–4434

The Application of Basalt Fiber Fabric to Reinforce the Structures in the Construction Industry



Thi Ngoc Quyen Nguyen

1 Introduction

1.1 *Introduction of Basalt—BCF Fibers*

Basalt fiber (BCF—continuous basalt fiber) is made from extremely smooth Basalt fiber, including minerals such as plagioclase, pyroxene and olivine. They have advantages like glassfiber but Basalt fiber has better mechanical properties and cheaper. The researching about BCF fiber start from 1960s in Soviet Union, then in 1972, the Basalt fiber was produced to make bulletproof vest for infantry by Soviet defense ministry by 1985, in Ukraine (belonging to the Soviet Union), there were established factories producing special insulating materials BIEREQIE. Nowadays, basalt fiber (BCF) has been commercialized and widely used as a fireproof material in aerospace and automotive industry and can also be used as a synthetic material to produce products, products in other industries. Especially most recently applied as bearing materials to replace other materials like steel, alloy, ..., in the construction industry in advanced countries around the world.

1.2 *Basalt Fiber Production Process (BCF)*

From the source, basalt rocks are carefully selected, washed, crushed and then melted to form a fiber [1]. High basaltic acid (silica content is above 46%) and low iron content are considered to be the best raw materials for BCF fiber production [2]. Unlike the production of other synthetic materials (e.g. glass fiber, carbon fiber),

T. N. Q. Nguyen (✉)

Faculty of Architecture and Arts, Ho Chi Minh City University of Technology (HUTECH), Ho Chi Minh City, Vietnam

e-mail: ntn.quyen@hutech.edu.vn

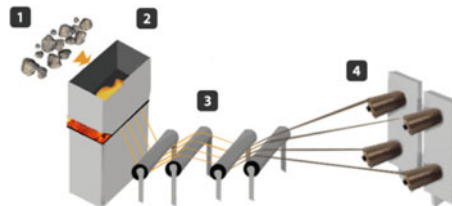


Fig. 1 Illustration of production steps of basalt fiber (BCF-continuous basalt fiber). *Note* 1. The only raw material: Basalt. 2. Basalt is melted at a temperature of 1500 °C (higher than glass). 3. BCF spun process. 4. Finished products are basalt-BCF rolls, which are then supplied to produce fabrics or materials for other industries including construction

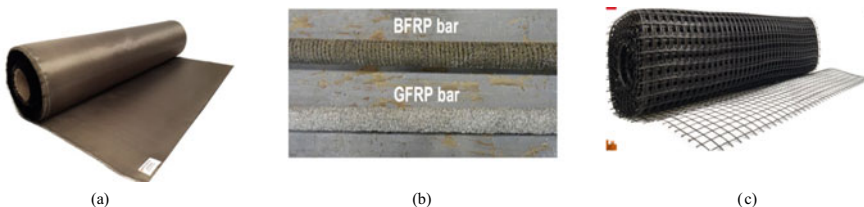


Fig. 2 Products of basalt fiber. **a** Woven fabrics of BCF which are used in the automobile industry. **b** Polymer rods combined with basalt fiber (BFRP) are more effective in reinforcing concrete structures than glass fibers (GFRP). **c**. BCF reinforced wire mesh application in soil treatment and basement in construction

basically producing simpler BCF fibers, no materials are added and basalt is heated only once, then the formation of BCF is done by “cold technology” with lower energy costs (Fig. 1).

1.3 Products Made from Basalt Fiber—(BCF-Continuous Basalt Fiber)

See Fig. 2 and Table 1.

1.4 Composite Materials Which Are Made of Basalt Fiber

Basalt fiber can be used as reinforced reinforcement materials for reinforced concrete structures, there are two types: synthetic fiber reinforced (BFRP), or cement (BFRCM) (see Fig. 3). These types have very different geometry and fiber structure. Continuous fibers, featured by a woven or nonwoven structure (e.g. fabric), which are impregnated with polymer resins (e.g. epoxy, polyester or vinylester) to form a

Table 1 Comparison of mechanical properties of BCF basalt fibers with other materials [4]

Speciality	Unit	Glassess		Aramid Fiber (Kevlar)	Carbon		Polyester	Metal		
		E	S		HS	HM		Aluminum	Titanium	Steel
Specific gravity	g/cm ³	2.54	2.46	1.46	1.76	1.8	1.38	2.8	4.5	7.8
Elastic module	GPa	72	87	124	235	338	14	72	110	207
Tensile strength	MPa	3400	4600	3600	3500	2480	1200	460	930	620
Elongation at break	%	4.8	5.4	2	1.2	0.5	13.5	8	16	23
Coefficient of thermal expansion	10 ⁶ m/mK	5	2.4	-3.5	-0.36	-0.54	60	23.4	10.1	10.8

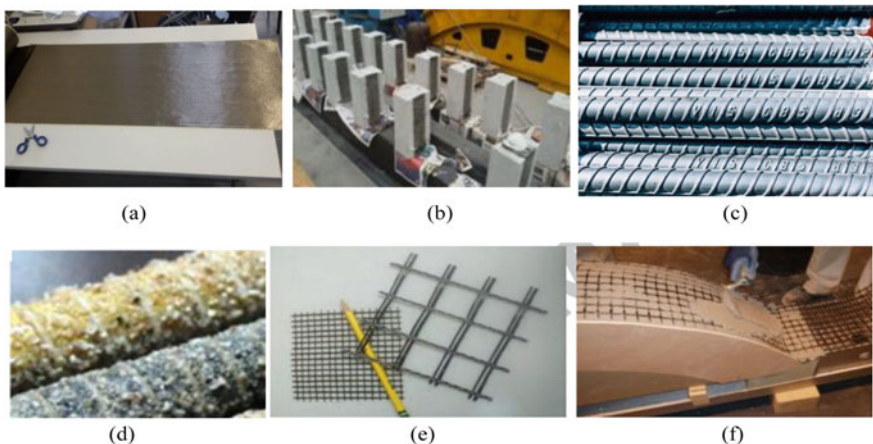


Fig. 3 The composite material reinforced with basalt fiber (BCF) and applications of BCF in construction. **a** Basalt-BFRP fiber material; **b** examples illustrating concrete reinforced with BFRP panels; **c** plain steel bars; **d** BFRP Basalt-coated steel; **e** basalt-coated wire mesh; **f** basalt fiber cement grid (BFRCM)

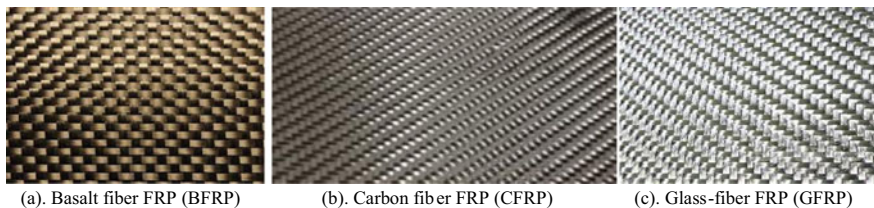
new material, the total fiber reinforced sheet FRP. In addition, FRP can also be used to produce composite rods, composed of continuous fibers arranged along the rod axis. These types of composite bars can be substituted for tensile working steel bars in reinforced concrete structures. In some cases, the continuous yarn can be arranged in the form of an open mesh, woven into fabric and embedded in a cement mixture to form a fiber reinforced cement net (FRCM). Basalt composite materials can also be created by cutting BCF fibers into shorter fibers and mixing them with concrete mixes to create high strength reinforced fiber (FRC) in construction.

1.5 Analysis of Mechanical Properties of Reinforced Basalt Fiber Sheet Origin (BFRP)

To compare the mechanical properties of basalt synthetic FRP synthetic fiber (BFRP) and other fibrous materials such as glass fiber reinforced polymer (GFRP) or carbon fiber reinforced polymer (CFRP), researchers around the world have done many experiments on the plates in Fig. 4.

From the results of the experimental results, it is show that the strength and elasticity of the BFRP basalt fiber layers are usually higher than the glass fiber polymer GFRP when the test components have the same fiber content and the same polymer resins. The data on tensile, compressive and bending strength is shown in Tables 2, 3 and 4.

Two authors, Dorigato and Pegoretti [3], experimented on pulling BFRP basalt fiber reinforced sheets and GFRP glass fiber base (with the same bidirectional fabric

**Fig. 4** Illustration of FRP fiber reinforced fabrics in material mechanical tests**Table 2** The comparison of mechanical properties of basalt FRP and glass fiber-based polymer (GFRP) or carbon fiber-reinforced (CFRP) materials, symbols used in the table

No. (sample for experiment)	Sorting type	Fiber type F	Plastic	t (mm)	f_w (%)	f_v (%)
1-[3]	Two-dimensional fabric	B	Epoxy	3.00	53.38	–
2-[3]	Two-dimensional fabric	E-G	Epoxy	3.00	57.76	–
3-[4]	Unidirectional fabric	C	Epoxy	–	–	50.0
4-[4]	Unidirectional fabric	PBO	Epoxy	–	–	50.0

N: receipt number format for each reference; F: fiber's type (B: Basalt; C: carbon; G: glass; E-G: non-alkali glass; PBO: polyparaphenylenl benzobisoxazole); t: sheet thickness for testing; f_w : fiber weight ratio; f_v : density ratio of fiber volume [5]

Table 3 Mechanical characteristic data in the tensile strength tests of FRP fiber reinforced sheets corresponding to the material components are given in Table 2

No. (sample for experiment)	f_{ut} (MPa)	E_t (GPa)	ε_u (mm)
1-[3]	330 ± 17	–	–
2-[3]	250 ± 14	–	–
3-[4]	258 ± 6.12	24.2	1.74
4-[4]	250 ± 5.86	26.6	1.6

Symbols used in Table 3: N: number identification for each reference, f_{ut} : tensile strength limit; E_t : modulus of elasticity of materials; ε_u extreme deformation [5]

Table 4 Mechanical characteristic data in the compressive strength test of FRP synthetic fiber reinforced sheets corresponding to the material components are given in Table 2

No. (sample for experiment)	f_{uc} (MPa)	E_c (GPa)
1-[3]	300.0 ± 17.0	–
2-[3]	170.0 ± 8.0	–
3-[4]	280.0 ± 20.0	22.2 ± 1.4
4-[4]	174.0 ± 15.0	13.5 ± 2.3

The symbols used in Table 4 are: N: identifier for each reference, f_{uc} : compression strength limit; E_c : elastic material compression module [5]

Table 5 Tensile strength of reinforcement according to TCVN 5574: 2012

Steel group		Reinforced R_s (Mpa)	Rebar stirrup R_{sw} (Mpa)
CI, A-I	6–8	225	175
CII, A-II	10–40	280	225
CIII, A-III diameter, mm	10–40	365	285

Table 6 Modulus of elasticity of some types of reinforcement according to TCVN 5574: 2012

Steel group	E_s (Mpa)
CI, A-I, CII, A-II	210,000
CIII, A-III	200,000

structure and the same fiber weight ratio, epoxy impregnated content the same) proved that they have similar durability. Also in this experiment, if the increase of about 7% of the basalt fiber mass, the tensile strength will increase by 17% and the elastic module will increase by about 20% compared to the previous experiments. Similarly, experimenting with basalt fiber BFRP panels with smaller structure and fiber content of over 60%, the result of tensile test is 14% lower than that of the same type structure but using carbon fiber CFRP (see Table 3).

From the above experiments, it is shown that textile materials from fibers such as GFRP glass, carbon fiber CFRP, especially BFRP basalt fiber have very high mechanical properties even when compared with traditional materials. Tensile and compressive systems are steel and concrete in construction (Table 5). Therefore, it is absolutely safe to use FRP fiber reinforced materials such as GFRP, CFRP, especially BFRP to enhance repair or enhance the strength, bearing capacity of the structure in Vietnam (see Tables 5, 6, 7 and 8).

2 Applications of Combined Bazan Yarn (BFRP) in Construction Industry

In the field of construction, FRP reinforced polymer reinforced fiber in the form of stickers or wrap is used a lot in repairing or improving bearing capacity for structures like reinforced concrete (RC), concrete piles or brick masonry, etc. The carbon fiber reinforced sheets CFRP is used to reinforce the structure of beams, plates in transportation works, wharves because the carbon fiber is 5 times stronger than steel, twice as hard as steel, but weighs only about 2/3 steel. The GFRP fiberglass-reinforced sheet is flexible, easy to bend, (for example, glass fiber (Pilemedic, Pilejax) is often used to reinforce the piles below the average water level. Particularly BFRP Basalt-based polymer fabrics mostly used such as civil constructions, wharves, traffic, irrigation should be reinforced, upgraded and renovated because of diversified products, durable and cheaper than CFRP, GFRP (see Fig. 5).

Table 7 Computational strength of heavy concrete R_b , R_{bt} according to TCVN 5574: 2012

		Compression level of concrete (Mpa)									
	B12,5	B15	B20	B25	B30	B35	B40	B45	B50	B55	B60
R_b	7.5	8.5	11.5	14.5	17.0	19.5	22.0	25.0	27.5	30.0	33.0
R_{bt}	0.66	0.75	0.90	1.05	1.20	1.30	1.40	1.45	1.55	1.60	1.65

Table 8 The modulus about elasticity of heavy concrete according to TCVN 5574: 2012

$E_b \times 10^3$	Compression level of concrete E_b (Mpa)					
	B12.5	B15	B20	B25	B30	B35
21	23	27	30	32.5	34.5	36
23	25	28	31	33.5	35.5	37.5
25	27	30	33	35.5	38	39.5
27	29	32	35	37.5	40	40

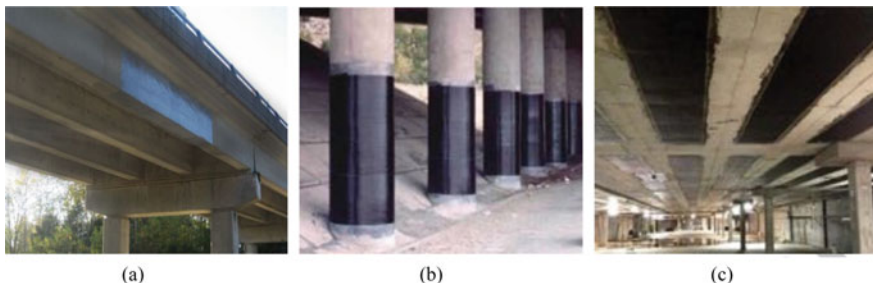


Fig. 5 Typical applications for structural reinforcement with BFRP Basalt fiber-reinforced fiber sheets in the form of construction plasterboard or wrap. **a** Reinforcing bridge, **b** reinforcing columns, **c** upgrading existing beams and floors

3 Procedure for Repairing Concrete Structure by Steel Boosting Method Bazan—BFRP

1. Survey and determine the extent of damage;
2. Demolition of damaged concrete;
3. Cleaning reinforcement, sweeping corrosion inhibitors;
4. Scan the old concrete binder with epoxy adhesive that has the characteristics in Table 9;
5. Spraying concrete or plastering with high strength mortar;
6. Reinforcing beams by gluing basalt fibers BFRP;
7. Complete, test, acceptance.

From the data in Table 9, we see that the compressive strength, tensile strength, elastic modulus of Epoxy glue (according to ASTM D695) are higher than the corresponding results of the concrete structure material or brick masonry (objects need to be reinforced, upgraded or repaired after a period of use). This is reasonable, since the strength of the bonds (particularly epoxy glue and BFRP adhesive) in the structure must be more durable than the structure itself when subjected to impact loads (Fig. 6).

Table 9 Mechanical properties of epoxy according to ASTM D695

Mechanical characteristics	Value
Compressive strength (MPa)	65.54
Tensile strength (MPa)	25.21
Elastic modulus (GPa)	04.58



Fig. 6 Illustration of steps for reinforcing reinforced concrete columns with basalt-BFRP fiber reinforced material

4 Conclusion

The article gave an overview of the origin of FPR synthetic fiber materials such as glass fiber reinforced glass GFRP, carbon fiber reinforced CFRP and special BFRP basalt fiber core and their mechanical properties. The material has its advantages and disadvantages, as well as its range of uses.

BFRP Basalt fiber has more advantages than FRP-based materials in strengthening the structure, the areas of BFRP fiber application are very wide such as upgrading and repairing civil constructions, transport works, bridges, ports... In addition, compared with traditional repair solutions such as chisels, reinforced implants for beams, columns for very dangerous and not high reliability, this technology is very safe. However, there should be further studies to complete the testing standards, design manuals, construction procedures of FPR materials in general as well as materials of basalt fiber BFRP in particular.

With abundant basalt resources, Vietnam can produce synthetic basalt-based fibers (BFRP) or basalt-covered reinforcement (BFRP bars) to replace imported FRP fiber materials. In addition, the local labor force is also a favorable condition for the textile and chemical industry to develop production of basalt synthetic fiber products.

References

1. Vinson JR, Sierakowski RL (1986) The behavior of structures composed of composite materials. Martinus Nijho, Dordrecht
2. Jamshaid H, Mishra R (2016) A green material from rock: basalt fiber—a review. *J Text* 107(7):923–937
3. Dorigato A, Pegoretti A (2012) Fatigue resistance of basalt fibers-reinforced laminates. *J Compos Mater* 46(15):1773–1785
4. Brandt AM (2008) Fibre reinforced cement-based (FRC) composites after over 40 years of development in building and civil engineering. *Composite Struct* 86:3–9
5. Monaldoa E, Nerillia F, Vairo G (2019) Basalt-based fiber-reinforced materials and structural applications in civil engineering. *Compos Struct* 214:246–263

The Impacts of Different Structural Design Alternatives on the Embodied Emissions of Flat Plate Buildings



Tran Mai Kim Hoang Trinh, Sanaul Chowdhury, Jeung-Hwan Doh,
and Cai Shunyao

1 Introduction

The building sector plays a crucial role in the economic growth of a nation. However, it has been long blamed as one of the major contributors of the worsening environment [5]. Currently, construction material consumption is greater than any time in history. Worldwide, the annual usage of concrete continuously increases, approaching 20,000 million metric tons [7] and the cement industry solely contributes 7% to the global CO₂ emissions [4]. Thus, it is urgent for the entire industry to formulate effective strategies and implementation plans to accommodate sustainable design and construction.

Recently, sustainable development principles have been increasingly adopted in the design procedure with the purpose of reducing environmental impacts generated during both the construction and operation phases of buildings. Since the OE has been shown to occupy the largest share of the building's lifecycle energy [1], EE incurred in the material production and the construction process is largely overlooked [9]. Consequently, in current building design procedure, structural engineers often play a limited role in the overall sustainability of the project, with environmentally-sensitive decisions usually laying in the hands of architects and clients [8].

Recent studies have highlighted the cooperation of multi-disciplinary professions in the delivery of long-term sustainable projects. In fact, structural engineers are capable of adopting sustainable design solutions by improving structural effectiveness of a building, while concurrently maintaining all technical requirements. Considering a flat plate building, this research aims to quantify the contribution of vertical and horizontal load-resisting systems with respect to various design parameters, thereby revealing their interaction in terms of environmental impacts. The outcomes will help

T. M. K. H. Trinh · S. Chowdhury (✉) · J.-H. Doh · C. Shunyao
School of Engineering and Built Environment, Griffith University, Gold Coast, QLD, Australia
e-mail: s.h.chowdhury@griffith.edu.au

identifying the factors that should be given more attention in the pre-design stage of a sustainable building.

2 Research Methodology

2.1 Research Methodology

To attain the abovementioned objectives, a multi-stage approach based on quantitative analysis was established (Fig. 1). In general, this methodology was composed of two major phases: Structural Design and Environmental Impact Assessment. During the first phase, all case study buildings were designed in accordance with AS3600-2009—Concrete Structures [11] and AS1170-2002—Design Loading Actions [10]. The commercially available software package, RAPT, was utilized to verify the manual calculations and generate the detailed reinforcement layout for slab systems. On the other hand, columns were designed and inspected using an Excel spreadsheet to create the Interaction Diagram and determine the suitable longitudinal reinforcement arrangement. Once the final designs of both slabs and columns were verified, a Bill of Quantities (BOQ) specifying the total steel and concrete consumption was created to quantify the embodied impacts.

Among three types of methods used for embodied emissions estimations [6], quantification based on the quantities of construction materials was adopted. To apply this approach, appropriate EE unit rates of different building materials were required. Through a thorough investigation, EE intensities published by Crawford [3] were selected due to its highly accurate and comprehensive quantification methodology and its representative characteristics of Australian building industry. The EE coefficients of various kinds of concrete and steel were summarized in Table 1. Since there is currently no study considering the EE of high strength concrete, an extrapolated value from available data was utilized in this research.

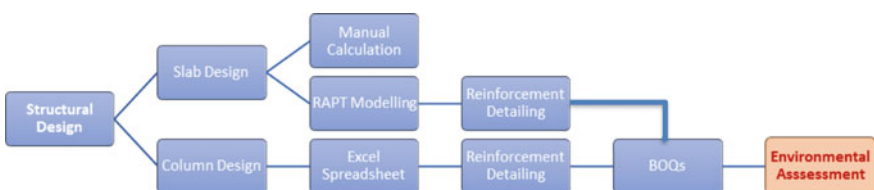


Fig. 1 The multi-stage methodology of structural design and environmental impact assessment

Table 1 EE coefficients for steel and concrete of different strengths

Building materials	EE intensities
Concrete (32 MPa)	5810 (MJ/m ³)
Concrete (40 MPa)	6750 (MJ/m ³)
Concrete (50 MPa)	8550 (MJ/m ³)
Concrete (65 MPa)	12,320 (MJ/m ³)
Concrete (100 MPa)	26,509.3 (MJ/m ³)
Steel reinforcement	85.46 (MJ/kg)

2.2 Structural Parameters

The 11-storey office building with car parks on the ground floor and ten floors of commercial space is indicative of current construction practices in the South East Queensland (SEQ) region of Australia. Simple flat plate construction arranged in a square grid with varying number of spans was applied for the typical floors and roof. The building's external dimensions were kept constant at 40.5 m by 40.5 m with a fixed floor-to-floor height of 3.5 m, allowing for accurate comparisons between design alternatives. The column's size was initially fixed as 500 mm by 500 mm with the column concrete strength of 100 MPa, to sufficiently resist the combined compression and bending effect. According to Cement and Concrete Association of Australia [2], the most economical span for reinforced concrete flat plate is between 6 and 8 m, therefore, the span lengths examined in this study were 5.71, 6.67, and 8 m—corresponding to seven, six, and five slab spans per design strip.

3 Structural Analysis Results

3.1 Case Study 1: The Impact of Different Concrete Strength and Column Spacing

Table 2 describes the impact of varying concrete strength on the total concrete volume and steel mass of the examined structures. As the concrete strength increased, the slab thickness steadily reduced leading to an overall reduction in concrete volume. Interestingly, while considerable and consistent reductions by 6–18% were observed for 6.67- and 8-m spacing scenarios, rising concrete strength had a lower influence on the concrete volume of buildings with shorter slab spans. For 5.71-m span, when more columns and higher strength of concrete were provided, the effect of punching shear failure reduced, and it was the structural adequacy and durability requirements that governed the slab thickness, leading to a smaller reduction in the overall concrete volume.

In contrast, the relationship between the concrete strength and the total steel mass was more complicated. As the column concrete strength remained constant at

Table 2 Case study 1: building's bill of quantities

5.71 m span	Concrete volume (m^3)				Steel mass (tons)			
f'_c (MPa)	32	40	50	65	32	40	50	65
Slab	4149.83	3879.19	3662.68	3608.55	213.42	216.17	229.04	246.39
Column	213.42	216.17	229.04	246.39	54.16	54.16	54.16	54.16
Total	4363.25	4095.36	3891.72	3854.94	267.58	270.33	283.19	300.55
6.67 m span	Concrete volume (m^3)				Steel mass (tons)			
f'_c (MPa)	32	40	50	65	32	40	50	65
Slab	5142.18	4727.20	4420.47	4095.70	257.60	250.68	262.97	280.78
Column	433.22	436.32	438.61	441.04	41.47	41.47	41.47	41.47
Total	5575.40	5163.52	4859.08	4536.74	299.06	292.14	304.44	322.24
8 m span	Concrete volume (m^3)				Steel mass (tons)			
f'_c (MPa)	32	40	50	65	32	40	50	65
Slab	6549.52	6098.45	5683.47	5250.44	310.56	313.04	315.32	317.69
Column	316.26	306.57	319.01	336.81	107.93	94.44	67.46	48.96
Total	6865.78	6405.02	6002.48	5587.25	418.49	407.48	382.78	366.65

100 MPa, which in itself was sufficient to resist combined axial loading and bending, the minimum vertical reinforcement was selected to avoid redundant design in all cases. In other words, the variation in the steel consumption stemmed from the change in slab reinforcement. While the steel mass grew slowly by 1.0–12.3% and 1.8–7.8%, respectively for 5.71- and 6.67-m span lengths, the 8-m spacing buildings experienced a decline from 5.5 to 9.1%. In this scenario, 100-MPa concrete strength was not solely adequate for the interactive compression and bending effect applied on the column; therefore, the vertical reinforcement must increase to withstand the transferred loadings from the floor systems. As a result, a dramatically descending trend in the column steel reinforcement were observed with the rise in slab concrete strength (thinner slab depths), thereby the reduction in overall steel demand.

On another aspect, both concrete volume and steel consumption of the investigated structures rose with the larger column spacing. Specifically, for 32–50 MPa, the concrete volume climbed up by 14–18% and 41–45%, respectively, for 6.67- and 8-m span length. However, regarding 65-MPa options, the growth in concrete volume was reduced to 8.3% (6.67-m) and 32.9% (8-m), indicating the lower impact of column spacing on concrete volume when adopting significantly higher concrete strength. Obviously, the larger the span length, the thicker the slab thickness became to reduce the maximum bending moment and deflection, resulting in the overall increase of

concrete volume. Along with the rise in slab thickness and concrete strength, the minimum slab reinforcement required for crack control also proportionally increased. The same growing pattern was observed for the steel demand, with 7.2–11.8% and 28.4–58.5% for 6.67-m and 8-m spacing, respectively. Again, the use of 65-MPa concrete strength greatly reduced the effect of column spacing on the steel mass. As the concrete strength increased, a thinner slab could be adopted, providing adequate punching shear strength and satisfying deflection limit. This largely diminished the vertical loadings exerted on the columns, thereby reducing the column vertical reinforcement and limiting the growth of total steel consumption in 65-MPa case buildings.

3.2 Case Study 2: The Impact of Column's Size

To investigate the influence of column's size on the building's total embodied impacts, while the slab depths estimated in Case Study 1 were kept constant, the column's dimensions were minimized to attain adequate punching shear and column strength. Two slab spans (5.71 and 8 m) and four slab concrete strengths (32, 40, 50, and 65 MPa) were concurrently considered to verify the analysis and observe the changing tendency.

Case Study 2.1: 5.71-m Slab Span

Table 3 presents an opposite trend between the concrete volume and steel demand of all optimized buildings compared with Case Study 1's counterparts. In general, the concrete volume reduced consistently between 7.3 and 8.7%, with the decrease of column size and varying concrete strength. On the other hand, the steel consumption

Table 3 Case Study 2: Building's Bill of Quantities

5.71 m span	Concrete volume (m^3)				Steel mass (tons)			
f'_c (MPa)	32	40	50	65	32	40	50	65
Slab	4149.83	3879.19	3662.68	3608.55	226.59	231.19	246.10	261.36
Column	231.33	223.68	215.92	216.12	71.95	71.95	71.95	71.95
Total	4381.16	4102.87	3878.60	3824.67	298.55	303.15	318.05	333.31
8 m span	Concrete volume (m^3)				Steel mass (tons)			
f'_c (MPa)	32	40	50	65	32	40	50	65
Slab	6549.52	6098.45	5683.47	5250.44	316.26	307.90	320.23	338.38
Column	310.56	300.64	293.02	285.51	107.93	104.45	94.44	94.44
Total	6860.08	6399.09	5976.49	5535.95	424.19	412.35	414.67	432.82

witnessed a small rise of 10.9–12.3% in all cases. The reason could be the decrease in column's dimension resulting in lower stiffness of the column, causing lesser bending moments transmitted from the slab system to the columns. As such, the slab system had to endure larger bending moments, thereby requiring more steel reinforcement. Also, since the column's size was minimized, the area of concrete resisting vertical loadings diminished, which resulted in more longitudinal reinforcement to strengthen the column under compression and bending interaction.

Case Study 2.2: 8-m Slab Span

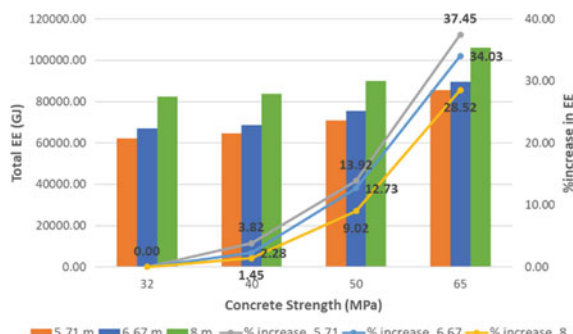
In this scenario, the effect of column optimisation was insignificant. While the steel demand kept growing gradually from 2.83 to 12.2%, the reductions in total concrete volume were minimal, below 1%. Due to the fact that the 8-m column distance resulted in massive vertical loadings applied on columns, the column's size accordingly could not be minimized to the extent that was observed in 5.71-m span buildings. Further, because the column's concrete volume itself was roughly adequate to resist the compressive loadings, the impact of vertical steel reinforcement was reduced, leading to the decrease of total steel mass.

4 Environmental Impact Assessment

4.1 Case Study 1

Generally, the total EE of studied buildings increased with the rise in concrete strengths for slabs. For all three column arrangements, the relationship between the overall EE and slab concrete strength remained unchanged with the lowest and largest figures belonging to 32 and 65 MPa, respectively (Fig. 2). While the overall EE of all 40-MPa case buildings rose marginally by 1.45–3.82%, 65-MPa counterparts experienced a considerable increase of 28.52–37.45%. The observed pattern could be attributed to the use of more energy-intensive high strength concrete along with

Fig. 2 The relationship between the total EE and the slab concrete strength



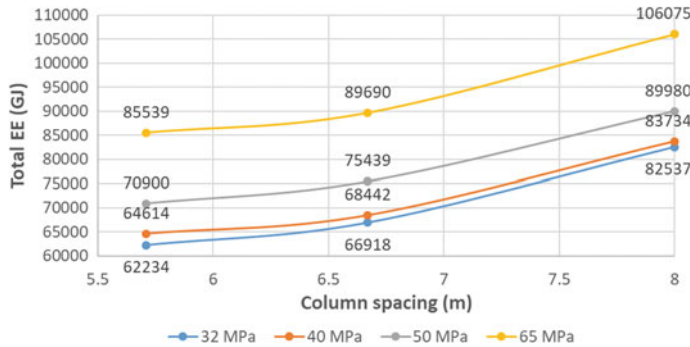


Fig. 3 The relationship between the total EE and the column spacing

the growth in steel demand for slab reinforcement. Interestingly, despite the reduction in both concrete volume and steel mass, the overall EE of 65-MPa structures was greater than those using lower concrete strength, considering the 8-m spacing. Therefore, the trade-offs between material saving and material energy-intensiveness are highlighted in the decision towards sustainable designs and solutions.

As clearly outlined in Fig. 3, the total EE increased with the rise in column spacing. Specifically, the EE increased by 4.85–7.53% and up to 24–32.62% for 6.67- and 8-m slab spans. A rapid growth observed for the 8-m options was due to the thicker slab thickness and the increase of column steel reinforcement. As explained above, lengthen column spacing to 8 m caused considerably thicker slab depths and extensive vertical loadings applied on the columns. Since the 100-MPa concrete strength was no more sufficient for the column strength, the reinforcing steel must increase to resist the loading and bending moment interaction.

4.2 Case Study 2

Figure 4 compares the overall EE of all optimized buildings with Case Study 1's counterparts. Despite the higher steel mass consumed in Case Study 2's structures, their overall EE values were smaller than those of Case Study 1. Even though the volume of concrete for columns reduced marginally, the use of very high carbon-intensive material, 100 MPa, intensified the total reduction in the embodied impacts of concrete. Regarding 8-m slab span, the benefits of column optimization disappeared. The column optimization in this scenario had a counter-productive effect on the overall EE of the structure. Due to the predominant increase of steel consumption, all optimized buildings experienced a slight increase of at most 3% in the total EE, indicating that the use of minimum column's size and minimum slab depth did not necessarily mean a reduction in the overall EE, which was rather based on the column arrangement. Consequently, a comprehensive optimization approach should

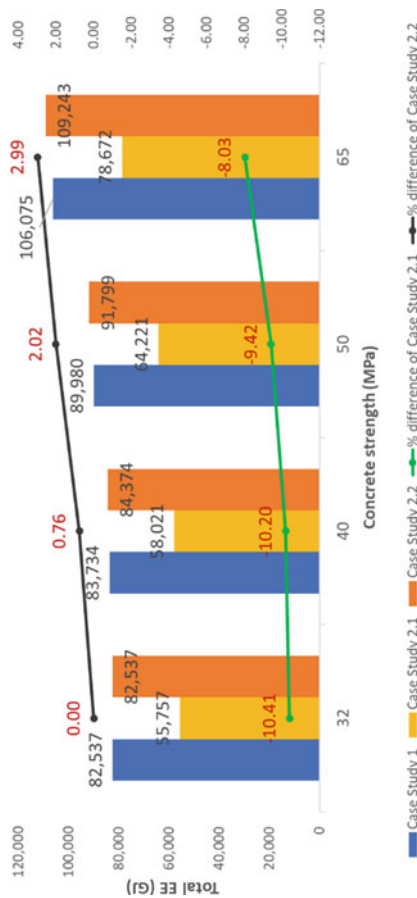


Fig. 4 The total EE of Case Study 2's buildings compared with Case Study 1's counterparts

be developed to find an optimal combination of solutions through which the least environmental impact is achieved.

5 Conclusion

Results of the comparison of distinctive design alternatives has exemplified the degree of possible impacts and improvements of structural efficiency. As presented in this paper, the minimum slab thickness together with minimum column's size was not always the most sustainable option, which depends on different plan layouts and concrete strength. Noticeably, not only did span length greatly influence the achieved reductions in material savings and EE, it also had a considerable effect on the relative contribution of slab and column systems. However, it should be emphasised that material saving does not necessarily mean more environmentally-sensitive solution. There is always a compromise between options, in terms of material savings and material energy-intensity. Therefore, a more comprehensive methodology, which enables to find the most sustainable combination of design solutions, is highly sought for.

References

1. Biswas WK (2014) Carbon footprint and embodied energy consumption assessment of building construction works in Western Australia. *Int J Sustain Built Environ* 3(2):179–186. <https://doi.org/10.1016/j.ijjsbe.2014.11.004>
2. Cement and Concrete Association of Australia (2003) Guide to long-span concrete floors. TechMedia Publishing Pty Ltd.
3. Crawford R (2011) Life cycle assessment in the built environment. Taylor & Francis
4. Flower DJ, Sanjayan JG (2007) Green house gas emissions due to concrete manufacture. *Int J Life Cycle Assess* 12(5):282
5. Gong X, Nie Z, Wang Z, Cui S, Gao F, Zuo T (2012) Life cycle energy consumption and carbon dioxide emission of residential building designs in Beijing. *J Ind Ecol* 16(4):576–587
6. Jiao S, Cao M, Li Y (2011) Impact research of solid waste on the strength of low carbon building materials. Paper presented at the Electrical and Control Engineering (ICECE), 2011 International Conference on
7. Mehta PK, Meryman H (2009) Tools for reducing carbon emissions due to cement consumption. *Structurae* 1(1):11–15
8. Miller D, Doh JH (2015) Incorporating sustainable development principles into building design: a review from a structural perspective including case study. *Struct Design Tall Special Build* 24(6):421–439
9. Monahan J, Powell JC (2011) An embodied carbon and energy analysis of modern methods of construction in housing: a case study using a lifecycle assessment framework. *Energy Build* 43(1):179–188. <https://doi.org/10.1016/j.enbuild.2010.09.005>

10. Standards Association of Australia (2009) Australian/New Zealand Standard—structural design actions part 1: permanent, imposed and other actions (AS Standard No. 1170.1-2002). Standards Australia International, Sydney
11. Standards Association of Australia (2010) Australian standard: concrete structures (AS Standard No. 3600:2009). Retrieved from <https://infostore.saiglobal.com/en-au/standards/as-3600-2009-1382662/>

The Reduction of Vibration of Multiple Tuned Mass Dampers in Continuous Beam Traversed by Moving Loads



Trong Phuoc Nguyen and Duy Thoai Vo

1 Introduction

The continuous beam traversed by the moving loads has been attracted significant attention for mitigating vibration. By using the Tuned Mass Damper (TMD), the theoretical analyses and experimental researches have been shown that equipment is an effective in reducing the vibration of structures. Principle of using TMD is reduced structural vibration energy, it's worked by transferring many of vibration energy from structure to the TMD.

TMD has been broadly studied and applied to restrain agents induced vibrations. The efficiency of this device depending on various parameters of their state and main structures in control the external vibration has been studied [1]. Wang et al. [9] deals with the applicability of passive TMDs to suppress train-induced vibration on Taiwan High-Speed Railway bridge, the numerical results for a moderately long bridge under train induced vibration showed that the TMD was reduced up to about 40% of vertical acceleration. [3] studied about the Multiple Tuned Mass Dampers (MTMDs), which is developed to reduce the dynamic responses of high-speed railway bridges. The maximum vertical acceleration of the bridge was reduced up to 57% for a 2% MTMD mass ratio. Li et al. [2] compared a single TMD to the MTMD. With the same total mass ratio, the MTMD were more effective to reduce the footbridge peak root-mean-square acceleration. Due to the optimal MTMD system with 5 TMDs and 2% total mass ratio, the footbridge peak root-mean-square acceleration was approximately reduced to 20% original magnitude corresponding to the uncontrolled footbridge [2]. Several researchers have studied its practical applications in

T. P. Nguyen (✉)

Faculty of Civil Engineering, Ho Chi Minh City Open University, Ho Chi Minh City, Vietnam
e-mail: phuoc.nguyen@ou.edu.vn

D. T. Vo

Dai Phuc CDI Co., Ltd., 219/51 Tran Hung Dao Str., Co Giang Ward, District 1, Ho Chi Minh City, Vietnam

suppressing vibration because of wind force, earthquake, vehicle passing on, even human-induced vibrations of bridge [7–10].

However, when studying the TMD structure system applying to the bridge structure, there are many problems to resolve, the more to be closed realistic model, the more parameters it gets. The results obtained to demonstrate that the MTMDs has significantly effectiveness in dynamic responses.

2 Formulation

TMDs are system added to reduce dynamic response as Fig. 1 depending on the first mode of vibration. The properties of TMD system proposed by Tsai and Lin [6]—defined as follows

$$\mu = \frac{m_d}{m} \quad (1)$$

$$\xi_{d,opt} = \sqrt{\frac{3\mu}{8(1+\mu)(1-0.5\mu)}} + (0.15\xi - 0.17\xi^2) + (0.163\xi - 4.980\xi^2)\mu \quad (2)$$

$$\gamma_{opt} = \left(\frac{\sqrt{1-0.5\mu}}{1+\mu} + \sqrt{1-2\xi^2} - 1 \right) - (2.375 - 1.034\sqrt{\mu} - 0.426\mu)\xi\sqrt{\mu} \\ - (3.730 - 16.903\sqrt{\mu} - 20.496\mu)\xi^2\sqrt{\mu} \quad (3)$$

where μ is the mass ratio (m_d mass of TMD and m mass of structure), $\xi_{d,opt}$ is the damping ratio of TMD, ξ is the damping ratio of structure, and γ_{opt} is the frequency ratio. From the optimal parameters of the TMD, the characteristics of the TMD can be found through the frequency ratios of TMD as follows: $\omega_d = \gamma \times \omega$, $k_d = \omega_d \times m_d$, $c_d = \xi_d \times 2 \times \omega_d \times m_d$, in which ω is frequency of the main structure.

Figure 1 described in detail the force components, that affect the mass of TMD (m_d). The transposed structure causes the external force, which operates to the TMD,

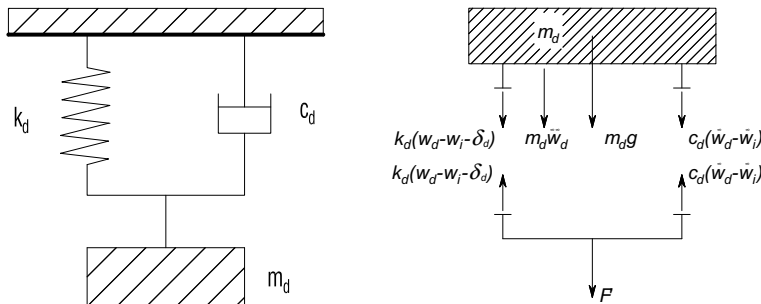


Fig. 1 TMD system and structure

the fluctuation of TMD system cause reacting force, which reduce the structural displacement, thereby reducing the absolute displacement. Where m_d is mass of TMD, w_d is vertical displacement of TMD, k_d is stiffness of TMD, c_d is the damping coefficient of TMD, w_i is the displacement of TMD at the position. The F' is the interacting force at the position of the bridge beam and TMD. The equation of motion of TMD is given as

$$-m_d g - m_d \ddot{w}_{di} - c_d (\dot{w}_{di} - \dot{w}_i) - k_d (w_{di} - w_i - \delta_d) = 0 \quad (4)$$

$$-F' + c_d (\dot{w}_{di} - \dot{w}_i) + k_d (w_{di} - w_i - \delta_d) = 0 \quad (5)$$

where δ_d is the static displacement, determined by the equation $k_d \delta_d = m_d g$. From Eqs. (4) and (5), the interacting force equation between TMD and bridge beam can be also expressed as

$$F' = -m_d g - m_d \ddot{w}_{di} \quad (6)$$

where $m_d g$ is the TMD static component, $m_d \ddot{w}_{di}$ is the effect of TMD inertia. Hence the vertical displacement at the position, where applied TMD system to the structure, is defined as

$$w_i(t) = v(x_i, t) \quad (7)$$

$$\dot{w}_i(t) = \frac{\partial v}{\partial t} \quad (8)$$

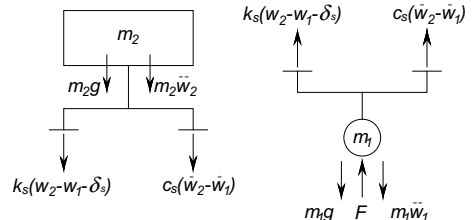
Figure 2 described in detail the acting force components, which operates to the moving load, the $F'(t)$ is the interacting force at the position, where the wheel of moving load contact with bridge beam.

The governing equations of motion are expressed as

$$-m_2 g - m_2 \ddot{w}_2 - k_s (w_2 - w_1 - \delta_s) - c_s (\dot{w}_2 - \dot{w}_1) = 0 \quad (9)$$

$$-m_1 g - m_1 \ddot{w}_1 + k_s (w_2 - w_1 - \delta_s) + c_s (\dot{w}_2 - \dot{w}_1) + F = 0 \quad (10)$$

Fig. 2 The balance diagram of the mass m_1 and m_2



where δ_s is the spring static movement of moving load, $k_s \delta_s = m_2 g$. From Eqs. (9) and (10), the interacting force of the load and bridge can be also obtained as

$$F = (m_1 + m_2)g + m_1 \ddot{w}_1 + m_2 \ddot{w}_2 \quad (11)$$

therein, $(m_1 + m_2)g$ is the static component of contact force, $m_1 \ddot{w}_1 + m_2 \ddot{w}_2$ describes the inertia effect. The equation of motion of the structure including beam, TMD and moving load is obtained as

$$\begin{aligned} & \left[M_b + m_1 N^T N \quad m_2 N^T \quad m_{d1} N_0^T \quad \cdots \quad m_{dn} N_0^T \right] \begin{Bmatrix} \ddot{q} \\ \ddot{w}_2 \\ \ddot{w}_{d1} \\ \vdots \\ \ddot{w}_{dn} \end{Bmatrix} \\ & + \left[C_b + 2m_1 v_m N^T N_x \quad 0 \quad 0 \quad \cdots \quad 0 \right. \\ & \quad \left. -c_s N \quad c_s \quad 0 \quad \cdots \quad 0 \right] \begin{Bmatrix} \dot{q} \\ \dot{w}_2 \\ \dot{w}_{d1} \\ \vdots \\ \dot{w}_{dn} \end{Bmatrix} + \cdots \\ & + \left[K_b + m_1 v_m^2 N^T N_{xx} + m_1 a_m N^T N_x \quad 0 \quad 0 \quad \cdots \quad 0 \right. \\ & \quad \left. -k_s N - c_s v_m N_x \quad k_s \quad 0 \quad \cdots \quad 0 \right] \begin{Bmatrix} q \\ w_2 \\ w_{d1} \\ \vdots \\ w_{dn} \end{Bmatrix} \\ & = \left\{ \begin{array}{l} -N^T(m_1 + m_2)g - \sum_{n=0}^n N_0^T m_{dn} g \\ 0 \\ 0 \\ \vdots \\ 0 \end{array} \right\} \end{aligned} \quad (12)$$

3 Numerical Results

In order to verify the reliability of the MATLAB program established in this paper, the results of vertical displacement and the displacement coefficient at mid-beam points of similar models with Neves et al. [4] and Olsson [5] are compared in Figs. 3

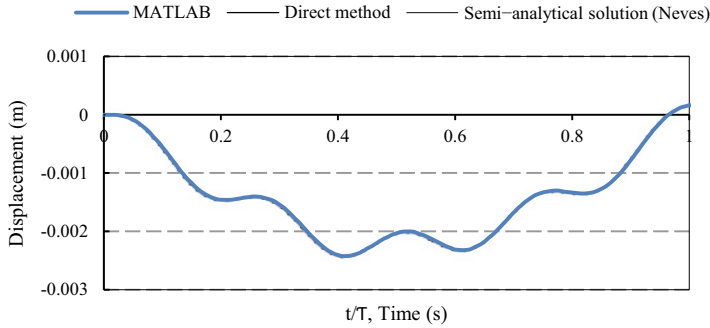


Fig. 3 Comparing the displacement results with the similar model of Neves et al. [4]

and 4; it can be seen that the responses from the present study are agreement with previous studies.

Considering a continuous beam in Fig. 5, having a length $L = 30$ m, sectional area $F = 0.6 \text{ m}^2$, inertia moment $I = 0.012 \text{ m}^4$, elastic modulus $E = 2 \times 10^{10} \text{ N/m}^2$, beam density $\rho = 2500 \text{ kg/m}^3$, damping ratio $\xi_b = 2\%$; the moving load, which having wheel mass $m_1 = 2500 \text{ kg}$, trunk mass $m_2 = 30000 \text{ kg}$, the spring stiffness $k_s = 8.63 \times 10^6 \text{ N/m}$, damping parameter $c_s = 8.14 \times 10^4 \text{ N/m}$, viscous damping parameter ξ_v ; and the MTMD, which having frequency ω_d , mass ratio μ , damping frequency ratio γ_{opt} . Where m is the mass of a bridge beam, ω is the first frequency of bridge beam. The dynamic coefficient of displacement $DAFu$ and $DAFm$ at the position are defined as the ratio of the maximum dynamic displacement and moment to the maximum static displacement and moment respectively.

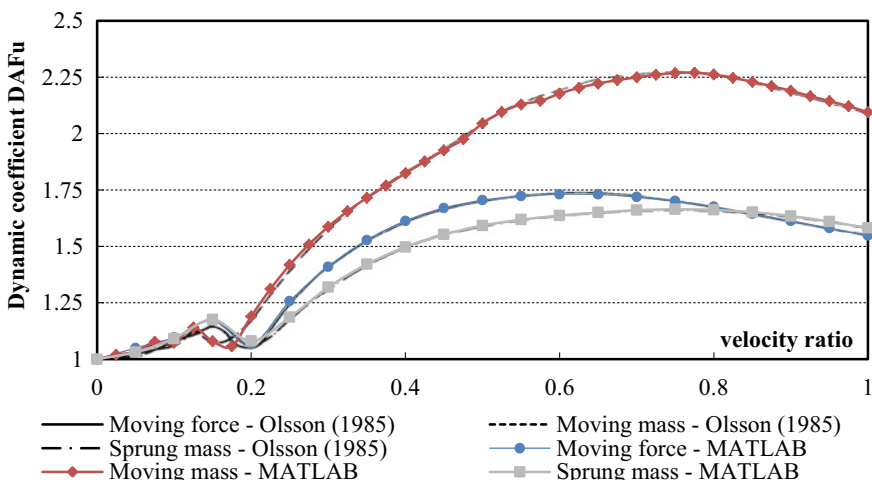


Fig. 4 Comparing the displacement results with the similar model of Olsson [5]

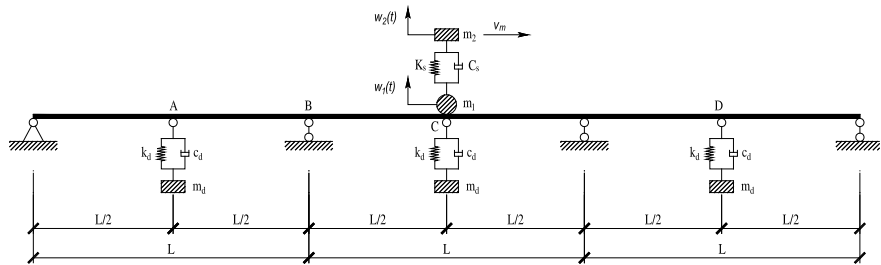


Fig. 5 The moving load—continuous beam—MTMD system

Tables 1 and 2 are described the dynamic response of the beam changed. The “critical” velocity of moving load in this beam are approximately as 30 and 70 m/s, the dynamic response increasing to “peak” expressed in Figs. 6 and 7. When the mass ratio μ increases from 0 to 5%, the dynamic coefficients of displacement and moment at A, C, D are also decreased; it can be seen that the MTMD has significantly effectiveness in dynamic responses of the dynamic response of the beam.

Table 1 Dynamic coefficient of displacement at the midpoint of beams

Velocity (m/s)	Position	$\mu = 0\%$ (a)	$\mu = 5\%$ (b)	(a) versus (b) (%)
30	A	3.7520	2.8614	-31.12
	C	3.7961	3.6459	-4.12
	D	5.2053	4.3279	-20.27
70	A	2.6601	2.2503	-18.21
	C	2.8971	2.2881	-26.61
	D	3.8149	3.2397	-17.75

Table 2 Dynamic coefficient of moment at the midpoint of beams

Velocity (m/s)	Position	$\mu = 0\%$ (a)	$\mu = 5\%$ (b)	(a) versus (b) (%)
30	A	2.9035	2.4016	-20.90
	C	2.8035	2.7280	-2.77
	D	4.4639	3.9987	-11.64
70	A	2.1184	1.9602	-8.07
	C	2.5526	1.8508	-37.92
	D	4.2146	3.5118	-20.01

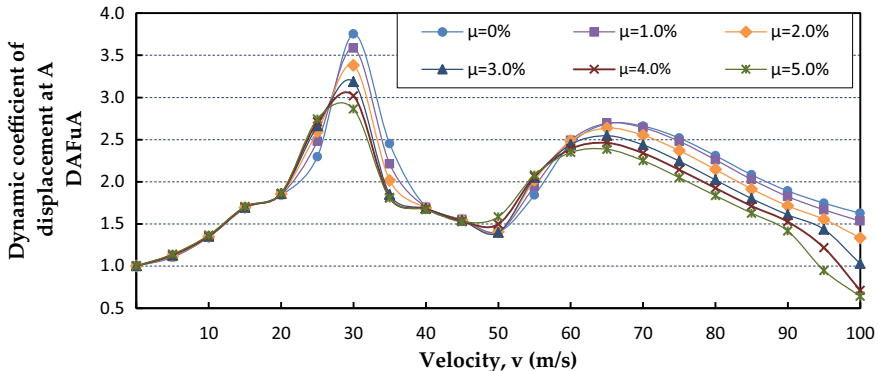


Fig. 6 The dynamic coefficients of displacement at A, while TMDs at A

4 Conclusion

From the results of this study, the following conclusions are written as follows

- The reduction of vibration of the beam depends on TMD and moving load as the number of TMD, the number of span beams, the number of moving loads. The numerical results also confirm that these parameters are sensitively influenced.
- The efficiency of the MTMD also depends on TMD properties. The influence of the parameters is different corresponding with each the mass ratio.
- In addition, the parameters of the moving load axle are less influential, so not be considered in this problem. The parameters of moving loads and the beam are constant during the investigation of the problem.

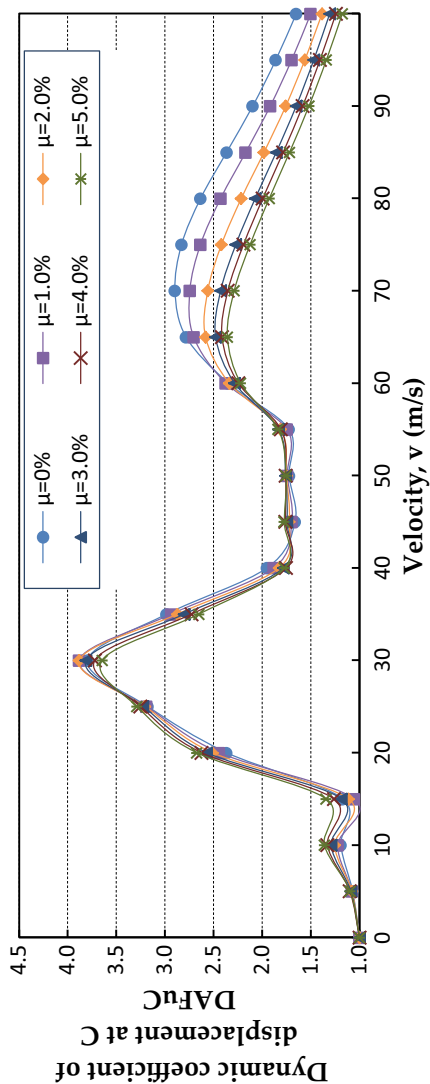


Fig. 7 The dynamic coefficients of displacement at C, while TMDs at C

References

1. Ben Mekki O, Bourquin F, Maceri F (2012) Control of bridge structures with semi-active tuned mass damper. In: Frémond M, Maceri F (eds) Mechanics, models and methods in civil engineering. Lecture notes in applied and computational mechanics, vol 61. Springer, Berlin, Heidelberg, pp 453–464
2. Li Q, Fan J, Nie J, Li Q, Chen Y (2010) Crowd-induced random vibration of footbridge and vibration control using multiple tuned mass dampers. *J Sound Vib* 329:4068–4092
3. Lin C, Wang F, Chen L (2005) Train-induced vibration control of high-speed railway bridges equipped with multiple tuned mass dampers. *J Bridge Eng* 10(4):398–414
4. Neves SGM, Azevedo AFM, Calçada R (2012) A direct method for analyzing the vertical vehicle—structure interaction. *Eng Struct* 34:414–420
5. Olsson M (1985) Finite element, modal co-ordinate analysis of structures subjected to moving loads. *J Sound Vib* 99(1):1–12
6. Tsai HC, Lin GC (1993) Optimum tuned-mass dampers for minimizing steady state response of support-excited and damped systems. *Earthquake Eng Struct Dynam* 22:957–973
7. Tubino F, Piccardo G (2015) Tuned mass damper optimization for the mitigation of human-induced vibrations of pedestrian bridges. *Meccanica* 50:809–824
8. Ubertini F, Comanducci G, Laflamme S (2015) A parametric study on reliability-based TMD design against bridge flutter. *J Vib Control* 1–17
9. Wang H, Tao T, Cheng H, He X (2014) Simulation study on train-induced vibration control of a long-span steel truss girder bridge by tuned mass dampers. *Math Problems Eng* 2014: 12, Article ID 506578. <https://doi.org/10.1155/2014/506578>
10. Xing C, Wang H, Li A, Xu Y (2014) Study on wind-induced vibration control of a long-span cable-stayed bridge using tuned mass damper type counterweight. *J. Bridge Eng* 19:141–148

Topology Optimization of Two-Dimensional Trusses Using Improved Particle Swarm Optimization



Phirun Hou and Pruettha Nanakorn

1 Introduction

When stability and displacement constraints are considered, truss topology optimization problems become nonlinear programming problems, which usually contain many local optimal solutions. For this reason, they require robust optimization methods that can efficiently find global optimal solutions. Metaheuristic optimization methods are good candidates for solving truss topology optimization problems [3, 6, 7]. Metaheuristic optimization methods use many search points, and can, therefore, avoid being trapped in local optimal regions. Moreover, unlike gradient-based optimization methods, metaheuristic methods do not need gradient information to perform their search. Unfortunately, most truss optimization problems contain large sets of possible designs. Consequently, it is still difficult to successfully solve these problems with the existing metaheuristic optimization techniques.

In this study, an improved particle swarm optimization (PSO) algorithm is proposed to solve topology optimization problems of 2D trusses. In the proposed algorithm, a two-phase strategy is utilized. In the first phase, each particle updates its location based on the PSO technique. In the second phase, a particle moves toward or away from another randomly selected particle, depending on their relative merits. To demonstrate the effectiveness of the proposed technique, two benchmark problems of 2D trusses are solved and the obtained results are compared with those obtained from the conventional PSO and those reported in the literature.

P. Hou · P. Nanakorn (✉)

School of Civil Engineering and Technology, Sirindhorn International Institute of Technology,
Thammasat University, Pathumthani 12120, Thailand
e-mail: nanakorn@siit.tu.ac.th

2 Improved Particle Swarm Optimization

PSO has some disadvantages when used to solve large problems, particularly structural optimization problems. In large problems, the conventional PSO tends to be quickly trapped in local optimal regions [1, 2, 5]. To remove this shortcoming, the proposed algorithm introduces the concept of exchanging information among particles from different regions. The proposed algorithm updates the population of particles in two phases. In the first phase, the conventional PSO technique is employed. In the second phase, each particle considers a random particle. If the random particle is better than the particle itself, the particle moves toward the random particle. Otherwise, it moves away in the opposite direction.

In PSO, a particle updates its position using three main directions, i.e. its current trajectory, the direction toward the best position it has ever experienced, and the direction toward the best position the whole population has ever known. The update equations in the first phase are expressed as follows:

$$V_{id}^{k+1} = W \times V_{id}^k + C_1 \times R_{1id} \times (Pb_{id}^k - X_{id}^k) + C_2 \times R_{2id} \times (Gb_d^k - X_{id}^k) \quad (1)$$

$$X_{id,I}^k = X_{id,I}^k + V_{id,I}^{k+1} \quad (2)$$

$$W = W_{\max} - \frac{(W_{\max} - W_{\min}) \times k}{T} \quad (3)$$

where V_{id}^k and X_{id}^k represent the velocity and position in dimension d of particle i at iteration k before the first phase while $X_{id,I}^k$ represents the updated position after the first phase. In addition, Pb_{id}^k is the position in dimension d of the best solution that particle i has ever experienced, called the particle best of particle i , while Gb_d^k represents the position in dimension d of the best solution that the whole population has ever experienced, called the global best. Moreover, R_{1id} and R_{2id} are uniform random numbers on $[0, 1]$. The coefficients C_1 , C_2 , W_{\min} , and W_{\max} are user-defined constants while T denotes the maximum iteration number. In this study, C_1 , C_2 , W_{\min} , and W_{\max} are set to 2, 2, 0.4, and 0.9, respectively.

The positions obtained from the first phase are updated further in the second phase. Particle i interacts with a random particle j in the population. Particle i updates its location by comparing its augmented objective function value, to be defined in the next section, with that of particle j , where $i \neq j$. For a minimization problem, the update equations in the second phase are given as

$$X_{id}^{k+1} = X_{id,I}^k + R_{id}(X_{jd,I}^k - X_{id,I}^k) \quad \text{If } Obj(X_{id,I}^k) > Obj(X_{jd,I}^k) \quad (4)$$

$$X_{id}^{k+1} = X_{id,I}^k + R_{id}(X_{id,I}^k - X_{jd,I}^k) \quad \text{If } Obj(X_{id,I}^k) < Obj(X_{jd,I}^k) \quad (5)$$

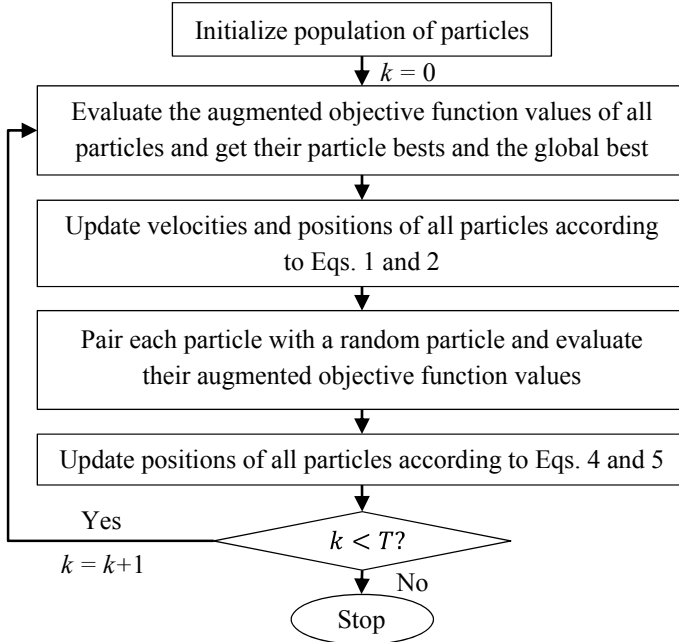


Fig. 1 Flowchart of the proposed PSO algorithm

Here, Obj denotes the augmented objective function to be minimized. In addition, R_{id} is a uniform random number on $[0, 1]$. Note that, if $Obj(X_{id,I}^k) = Obj(X_{jd,I}^k)$, a new random particle j is selected until $Obj(X_{id,I}^k) \neq Obj(X_{jd,I}^k)$. The flowchart of the proposed algorithm is shown in Fig. 1.

3 Truss Topology Optimization

In this study, the objective of a truss topology optimization problem is to minimize the weight of a truss. Here, the ground structure approach is utilized in defining all possible trusses in a search space. This approach is quite effective when used in problems that are not large. When many nodes are used in a ground structure, the size of the resulting search space increases significantly and the problem becomes difficult to solve. In this study, an element-removal algorithm used in the work by Shakya et al. [6] is used to alleviate the problem of large search spaces. In the element-removal algorithm, unwanted elements are removed during the decoding process in order that more feasible structures are obtained.

In this study, a truss topology optimization problem is written as

$$\text{Minimize } w = \sum_{i=1}^M \rho_i L_i A_i \quad (6)$$

Subjected to G_1 : Truss is kinematically stable

$$\begin{aligned} G_2 : \sigma_i - \sigma_{a,i} &\leq 0 \quad i = 1, 2, \dots, m \\ G_3 : \delta_i - \delta_{a,i} &\leq 0 \quad i = 1, 2, \dots, ndof \end{aligned} \quad (7)$$

where M is the number of possible elements from the ground structure, while m and $ndof$ denote, respectively, the real number of elements and the real number of displacement degrees of freedom of the truss. In addition, ρ_i , L_i , and A_i denote the weight density, length, and cross-sectional area of element i of m elements. Subsequently, w is the weight of the truss. Moreover, σ_i and $\sigma_{a,i}$ represent the stress of element i and its allowable value, while δ_i and $\delta_{a,i}$ denote the displacement degree of freedom i and its allowable value. Constraints that are automatically satisfied by appropriate choices of input data, such as the ranges of sectional areas, are not included as constraints.

In the optimization process, the area of an element in the employed ground structure can be zero, which simply means that the element is not present. In this way, different topologies of trusses can be built from the ground structure, including those that are not kinematically stable. In this study, infeasible solutions are penalized by augmenting the original objective function w to obtain an augmented objective function Obj , to be minimized, i.e.

$$Obj = \begin{cases} 10^{15} & \text{If the constraint } G_1 \text{ is violated} \\ w + 10^5 \sum_{\substack{i=1 \\ ndof}}^m \max(0, \sigma_i - \sigma_{a,i}) & \text{Otherwise} \\ + 10^5 \sum_{i=1}^{ndof} \max(0, \delta_i - \delta_{a,i}) \end{cases} \quad (8)$$

4 Results

Two benchmark problems of 2D trusses are used to investigate the effectiveness of the proposed algorithm. The results of the proposed algorithm are compared with those obtained by the conventional PSO and those in the literature. All problems solved in this study employ 10 particles. The numbers of iterations used are 200 and 100 for Problems 1 and 2, respectively. Each problem is run for 100 times. The codes of the conventional and proposed PSO algorithm are written in C++, and a computer having Intel Core i7-6700HQ Processor and 16 GB RAM is used.

4.1 Problem 1

The ground structure in Fig. 2, having 10 nodes and 45 elements, is considered [3, 7]. In this study, the symmetry of the problem is not assumed. The weight density $\rho = 0.1\text{lb/in}^3$, Young's modulus $E = 10^4\text{ksi}$, the allowable stress $\sigma_a = \pm 25\text{ksi}$, and the allowable displacement $\delta_a = \pm 2\text{in}$ are used. In addition, A_{\min} and A_{\max} are equal to 0.09 and 1.0 in^2 , respectively. However, in the optimization process, the area design variable of an element is set to vary from -1.0 to 1.0 in^2 . When its value is lower than $A_{\min} = 0.09\text{ in}^2$, the area of the element is considered to be zero.

Table 1 shows the results obtained by the conventional and proposed PSO algorithms, which yield, respectively, the best weights of 44.0440 and 44.0000 lb. The basic best topology for this problem is shown in Fig. 3. As shown in Table 1, the best result obtained from the proposed algorithm does not have member 7 in Fig. 3. In addition, it is better than the result by Deb and Gulati [3] and slightly heavier than the result by Wu and Tseng [7]. However, the number of merit function evaluations (FE), which is the number of the evaluations of the employed merit functions, for the proposed algorithm is significantly less than that for AMPDE by Wu and Tseng [7]. Note that the number of merit function evaluations for the proposed PSO is

Fig. 2 Ground structure of Problem 1

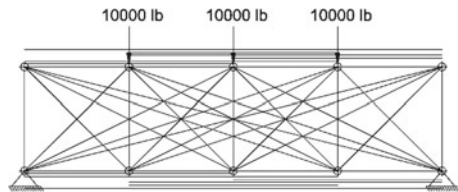


Table 1 Results for Problem 1

Member	Area (in^2)			
	Deb and Gulati [3]	Wu and Tseng [7]	This study	
	GA	AMPDE	PSO	Proposed PSO
1	0.566	0.566	0.5664	0.5657
2	0.477	0.447	0.4474	0.4472
3	0.477	0.447	0.4475	0.4472
4	0.566	0.566	0.5657	0.5657
5	0.082	0.09	0.4022	0.4000
6	0.080	0.09	0.4002	0.4000
7	0.321	0.31	—	—
Weight (lb)	44.033	43.99	44.0440	44.0000
Max σ (ksi)	—	25.000	24.9973	25.0000
Max δ (in)	—	1.108	1.2494	1.2500
FE	—	30,800	2000	4000

Fig. 3 Basic best topology of Problem 1

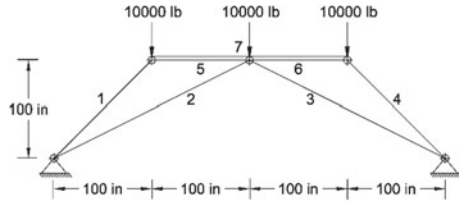
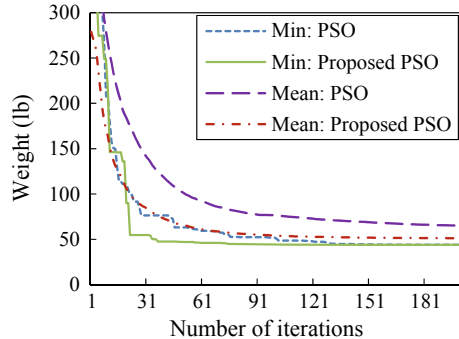


Fig. 4 Convergences of Problem 1



twice as big as that of the conventional PSO because the proposed algorithm has two phases, instead of one. Figure 4 shows example convergences obtained by the conventional and proposed PSO algorithms. The convergence of the proposed PSO algorithm is much faster than that of the conventional PSO algorithm. Table 3 shows the statistics of the solutions of the 100 runs obtained by both algorithms, including the minimum weight, the maximum weight, the average weight, the standard deviation (SD), and the average run time. It can be seen from Table 3 that the proposed algorithm performs better than the conventional algorithm for this problem. However, extra computational time is needed for the proposed PSO algorithm because of its additional merit function evaluations.

4.2 Problem 2

The ground structure in Fig. 5, having 12 nodes and 66 elements, is considered [4]. In this study, the symmetry of the truss along the middle horizontal line is considered. As a result, the number of design variables is reduced from 66 to 38. The material properties are the same as those in Problem 1. In this problem, the allowable stress $\sigma_a = \pm 5000$ psi and the allowable displacement $\delta_a = \pm 0.6$ in are used. In addition, A_{\min} and A_{\max} are equal to 0.09 and 35 in², respectively. In the optimization process, the area design variable of an element is set to vary from -35 to 35 in². When its value is lower than $A_{\min} = 0.09$ in², the area of the element is considered to be zero.

Fig. 5 Ground structure of Problem 2

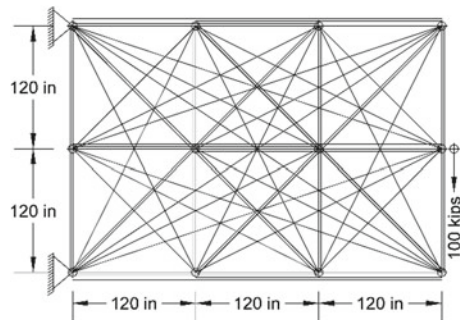


Table 2 shows the results obtained by the conventional and proposed PSO algorithms, which yield the same best weight of 2400.0000 lb. The best topology obtained by the proposed algorithm is shown in Fig. 6. As shown in Table 2, the best result obtained in this study is slightly better than the result by Faramarzi and Afshar [4]. The best topology obtained by Faramarzi and Afshar [4] is shown in Fig. 7. In addition, the number of merit function evaluations for the proposed algorithm is less than that for CA-LP by Faramarzi and Afshar [4]. Although the best weights by Faramarzi and Afshar [4] and by this study are virtually the same, the obtained topologies are significantly different. This shows that the optimization problem has more than one optimal region, and there are at least two optimal topologies that have similar weights. Figure 8 shows example convergences obtained by the conventional and proposed PSO algorithms. The convergence of the proposed PSO algorithm is much faster than that of the conventional PSO algorithm. The statistics of the results

Table 2 Results for Problem 2

Member	Area (in^2)		
	Faramarzi and Afshar [4]	This study	
	CA-LP	PSO	Proposed PSO
1	20.000	31.6228	31.6228
2	9.0597	31.6228	31.6228
3	8.9442	—	—
4	3.1423	—	—
5	7.0263	—	—
6	20.000	—	—
7	6.2845	—	—
8	17.8885	—	—
Weight (lb)	2400.001	2400.0000	2400.0000
Max σ (psi)	5000.000	5000.0000	5000.0000
Max δ (in)	0.5999	0.6000	0.6000
FE	2230	1000	2000

Fig. 6 Best topology of Problem 2 obtained by this study

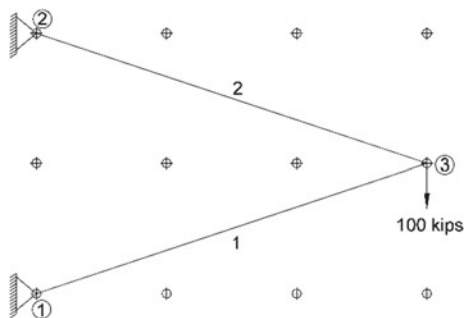


Fig. 7 Best topology of Problem 2 obtained by Faramarzi and Afshar [4]

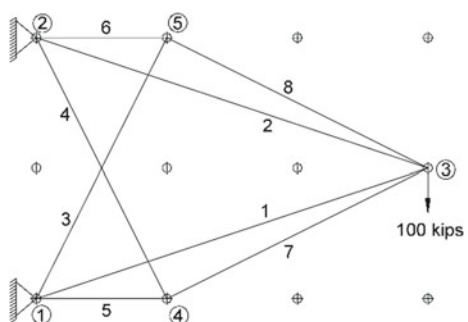
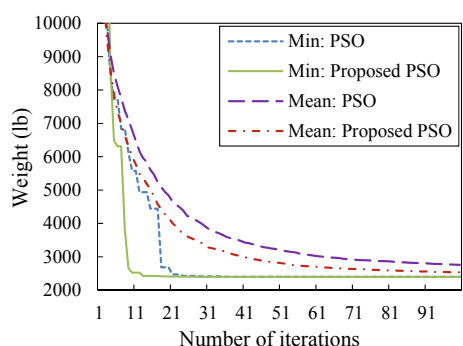


Fig. 8 Convergences of Problem 2



in Table 3 show that, for this problem, the proposed algorithm still performs better than the conventional PSO. Similar to Problem 1, extra computational time is needed for the proposed PSO algorithm.

Table 3 Statistics of 100 run solutions

Problem	Algorithm	Min weight (lb)	Max weight (lb)	Average weight (lb)	SD (lb)	Average time (s)
Problem 1	PSO	44.0440	132.0382	65.1183	17.6748	0.80
	Proposed PSO	44.0000	92.9274	51.3294	10.7804	1.45
Problem 2	PSO	2400.0000	5281.7500	2761.3250	521.6961	0.47
	Proposed PSO	2400.0000	3694.7032	2534.9049	274.3869	0.85

5 Conclusions

This study presents an improved PSO algorithm by adding an effective particle-interaction strategy to improve the degree of exploitation of good solutions in PSO. The proposed algorithm is divided into two phases. The first phase is simply the conventional PSO algorithm. In the second phase, a particle compares itself with a randomly selected particle and moves toward or away from that particle, depending on their relative merits. If the randomly selected particle is better than the particle being considered, the particle will move toward this randomly selected particle. Otherwise, it will move away in the opposite direction. Two benchmark problems of 2D trusses are solved. The obtained results show that the proposed algorithm is superior to the conventional PSO algorithm in terms of both the quality and uniformity of the results. The proposed algorithm is also found to have faster convergence rates than the conventional algorithm. The obtained results also show that the proposed algorithm provides comparable results with those in the literature. Since the proposed PSO algorithm has two phases, the number of merit function evaluations is two times of the conventional PSO algorithm. Thus, the proposed PSO algorithm requires longer computational time than the conventional one. Nevertheless, the increased computational time is worthwhile.

Acknowledgements A scholarship under the Program of Thai Royal Scholarship for Cambodia by Sirindhorn International Institute of Technology (SIIT) for the first author is greatly appreciated.

References

1. Abdouleh Z, Gastli A, Ben-Brahim L, Haouari M, Al-Emadi NA (2017) Review of optimization techniques applied for the integration of distributed generation from renewable energy sources. *Renew Energy* 113:266–280
2. Adrian AM, Utamima A, Wang KJ (2015) A comparative study of GA, PSO and ACO for solving construction site layout optimization. *KSCE J Civ Eng* 19(3):520–527
3. Deb K, Gulati S (2001) Design of truss-structures for minimum weight using genetic algorithms. *Finite Elem Anal Des* 37(5):447–465

4. Faramarzi A, Afshar MJSI (2012) Application of cellular automata to size and topology optimization of truss structures. *Sci Iran* 19(3):373–380
5. Li M, Du W, Nian F (2014) An adaptive particle swarm optimization algorithm based on directed weighted complex network. *Math Problems Eng* 2014
6. Shakya A, Nanakorn P, Petprakob W (2018) A ground-structure-based representation with an element-removal algorithm for truss topology optimization. *Struct Multidiscip Optim* 1–19
7. Wu CY, Tseng KY (2010) Truss structure optimization using adaptive multi-population differential evolution. *Struct Multidiscip Optim* 42(4):575–590

Transverse Galloping Analysis of a Sculptural Column



Cung Huy Nguyen, Tai Dinh Truong, Kha Dinh Nguyen, and Van Hai Luong

1 Introduction

Vertical slender structures can be suffered from galloping instability, an aeroelastic instability phenomenon causing large amplitudes of vibration due to the interaction between wind and structures. Galloping can occur when the total of aerodynamic and structural damping becomes negative.

Galloping is an interesting topic that has been attracted researchers to investigate since over 90 years ago. However, the phenomenon is not entirely understood. The very first investigation of this issue was presented by Glauert [4] and then by Den Hartog [2] with a criterion for the critical condition for one degree of freedom (1DOF) transversal galloping. Those studies showed that the galloping occurs in the crosswind direction when the aerodynamic damping is negative. This criterion is referred to as Glauert-Den Hartog's criterion, which has become an important tool in engineering application.

Following the studies of Glauert and Den Hartog, many models have been proposed to extend their theory. Extensive review on across-wind galloping can be found in a review by Paidoussis et al. [7].

It is important to note that, in the literature, most of analyses have been carried out for structures with a hypothesis that the aerodynamic coefficients, mean wind velocity, mass per unit length, size of cross sections are constant along the structure. This assumption is not actually the case when those parameters, in reality, usually vary along the structure. In other words, the common analyses can lead to significant error.

C. H. Nguyen (✉)

Department of Civil Engineering, Industrial University of Ho Chi Minh City, Ho Chi Minh City, Vietnam

e-mail: nguyenhuytung@iuh.edu.vn

T. D. Truong · K. D. Nguyen · V. H. Luong

Faculty of Civil Engineering,

Ho Chi Minh City University of Technology, VNU-HCM, Ho Chi Minh City, Vietnam

This paper aims to develop a theoretical framework of transverse galloping analysis of vertical structures. The variation of mean wind, aerodynamic coefficients, and mass per unit length along the structure are taken into account. Furthermore, particular cases commonly used in practice that analytical solutions can be derived are discussed. The theory is then illustrated through an application for a real structures, in which aerodynamic coefficients are obtained from wind tunnel tests. Critical remarks are finally discussed.

2 Critical Galloping Wind Speed Formulation

Considering a vertical structure with height H subjected to the distributed external load $f(z, t)$. The equation of motion is given by Clough and Penzien [1]:

$$EI(z) \frac{\partial^4 q(z, t)}{\partial z^4} + m(z) \frac{\partial^2 q(z, t)}{\partial t^2} = f(z, t) \quad (1)$$

where E, I, m, q, z, t are Young modulus, moment of inertia, mass per unit length, structural displacement, axial coordinate variable, time variable, respectively.

The equation can be decoupled as follows:

$$\ddot{p}_k(t) + \omega_k^2 p_k(t) = \frac{1}{m_k} f_k(t) \quad (2)$$

where ω_k, p_k, m_k and $f_k(t)$ are the angular natural frequency, generalized coordinate, generalized mass and generalized force, respectively, related to mode k -th with the mode shape ψ_k :

$$\left\{ \begin{array}{l} m_k = \int_0^H m(z) \psi_k^2(z) dz \\ f_k(t) = \int_0^H \psi_k(z) f(z, t) dz \end{array} \right. \quad (3)$$

It is well-known that for slender vertical structures, only the first mode of vibration is important. Then the modal equation of motion Eq. (3) can be rewritten by adding the damping term with damping ratio ξ :

$$\ddot{p}_1(t) + 2\xi\omega_1\dot{p}_1(t) + \omega_1^2 p_1(t) = \frac{1}{m_1} f_1(t) \quad (4)$$

To formulate the critical galloping wind speed, the external wind load due to self-excited wind load is given by Nguyen and Macdonald [6]:

$$f(t) = -\frac{1}{2}\rho \int_0^H b(z)U(z)[C_D(z) + C'_L(z)]\psi_1(z)\dot{p}_1(t)dz \quad (5)$$

where C_D , C'_L , U , b and ρ are the drag coefficient, derivative of lift coefficient, mean wind profile, width of structure and air density, respectively. The mean wind profile, which is varying along structural height, can be expressed through the mean wind speed at a reference height z_e [6]:

$$U(z) = U(z_e) \frac{\mu(z)}{\mu(z_e)} \quad (6)$$

where $\mu(z)$ is wind profile function, followed by a power law or logarithm law [8].

Substituting Eq. (6) into Eq. (5) and Eq. (5) into Eq. (4), it yields:

$$\ddot{p}_1(t) + 2\omega_1 \left[\xi_k + \frac{\rho b(z_e) c_a U(z_e)}{4m_{eq}\omega_1} \right] \dot{p}_1(t) + \omega_1^2 p_1(t) = 0 \quad (7)$$

where m_{eq} and c_a are the equivalent mass and non-dimensional aerodynamic damping coefficient, respectively:

$$m_{eq} = \frac{m_1}{\int_0^H \psi_1^2(z)dz} \quad (8)$$

$$c_a = \frac{\int_0^L b(z)\mu(z)[C_D(z) + C'_L(z)]\psi_1^2(z)dz}{b(z_e)\mu(z_e) \int_0^H \psi_1^2(z)dz} \quad (9)$$

The structure is unstable (galloping occurrence) if its total damping, i.e. $\left[\xi_k + \frac{\rho b(z_e) c_a U(z_e)}{4m_{eq}\omega_1} \right]$, is negative. This means that galloping can occur if the following necessary and sufficient conditions are satisfied, respectively:

$$c_a < 0 \quad (10)$$

$$U(z_e) > U_{cr}(z_e) \quad (11)$$

where $U_{cr}(z_e)$ is the critical galloping speed at the reference height z_e :

$$U_{cr}(z_e) = \frac{4m_{eq}\omega_1\xi}{\rho b(z_e)c_a} \quad (12)$$

The necessary condition for galloping occurrence given in Eq. (10), showing the negative condition of the aerodynamic damping coefficient c_a , the first check if a structure is potentially unstable. The galloping instability sufficiently the wind velocity is $U(z_e)$ higher than a critical value $U_{cr}(z_e)$. The galloping conditions given in Eqs. (10), (11), along with the non-dimensional terms in Eqs. (8), (9), are derived for a general case where both structure and wind profile are not uniform. It is worth to relate the general case to the following particular cases commonly used in practice:

1. **Case 1:** wind profile is not uniform; the structure is uniform, i.e. m, b, C_D, C'_L are constant along the height:

In this case, Eqs. (8)–(11) and Eq. (12) reduce as:

$$m_{eq} = m \quad (13)$$

$$c_a = \frac{(C_D + C'_L) \int_0^L \mu(z) \psi_1^2(z) dz}{\mu(z_e) \int_0^H \psi_1^2(z) dz} \quad (14)$$

$$C_D + C'_L < 0 \quad (15)$$

$$U_{cr}(z_e) = \frac{4m\omega_1\xi}{\rho b c_a} \quad (16)$$

2. **Case 2:** wind profile and structure are uniform, i.e. U, m, b, C_D, C'_L are constant along the height

In this case, the critical wind speed is constant along the height, denoting as U_{cr} . Moreover, Eqs. (14) and (16) significantly simplify as follows:

$$c_a = C_D + C'_L \quad (17)$$

$$U_{cr} = \frac{4m\omega_1\xi}{\rho b(C_D + C'_L)} \quad (18)$$

It can be realise that Eqs. (15) and (18) are the well-known Glauert-Den Hartog criterion for galloping occurrence [2, 4], which means that the galloping criterion given in Eqs. (10), (11), along with the uses of Eqs. (8), (9), is a generalisation of the Glauert-Den Hartog criterion. This generalised criterion therefore can be considered as the rigorous solution for the transverse galloping problem. It can be also seen that the Glauert-Den Hartog criterion is independent from the structural mode shape. The criterion is widely used in engineering practice and many design wind codes, e.g. Eurocode. It should be emphasised that such wide use is even applied for both uniform and non-uniform structures to evaluate the stability of the structure. Strictly speaking, this treatment is incorrect due to the nature of non-uniform wind. For uniform structures, although the necessary Glauert-Dean Hartog's condition is correct to predict then angle of attack for galloping occurrence, i.e. wind direction,

as shown in Eq. (15), the criterion is incorrect to predict the critical velocity since it excludes the mode shape and variation of the mean wind. As seen from Eqs. (14) and (16), the mode shape and wind profile function play a role to the critical velocity. For non-uniform structures, the Glauert-Dean Hartog's condition given by Eq. (15) is even inappropriate since variation of the structural parameters along the height must be considered as shown in Eq. (9).

3 Numerical Example

To illustrate the theory developed in the previous section, an application to the famous sculpture “Endless Column” in Romania is considered (Fig. 1a). The column, also known as Brancusi column, is considered to be an extraordinarily valuable artistic and technical work. Although it is very slender, it has never been suffered from any clear instability. This has attracted many investigations for its stability.

In this paper, applying the proposed theory, the galloping analysis is carried out. The parameters used for the analysis is shown in Table 1, obtained from Dragomirescu et al. [3], Lungu et al. [5].

The drag and lift aerodynamic coefficients for different angles of attack α are determined from wind tunnel tests, which is reported in Lungu et al. [5], and are redrawn herein in Fig. 1b.

As the structure can be considered as uniform, Eqs. (15), (16) are used to evaluate the condition for galloping occurrence of the column. Figure 2a shows the value of the aerodynamic damping coefficients against the angle of attack. The derivative of the lift coefficient is estimated through a spline fitting the aerodynamic coefficients. The shadows correspond to the negative values of the aerodynamic damping coefficients, showing the wind directions that galloping potentially occurs. It can be seen that the

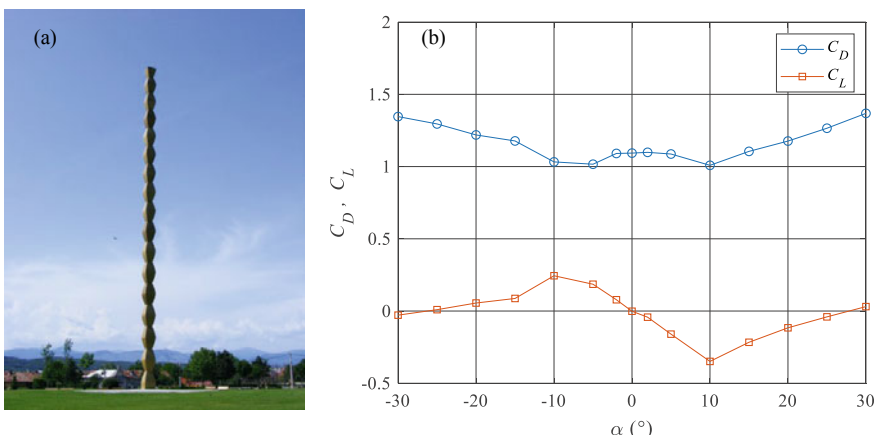
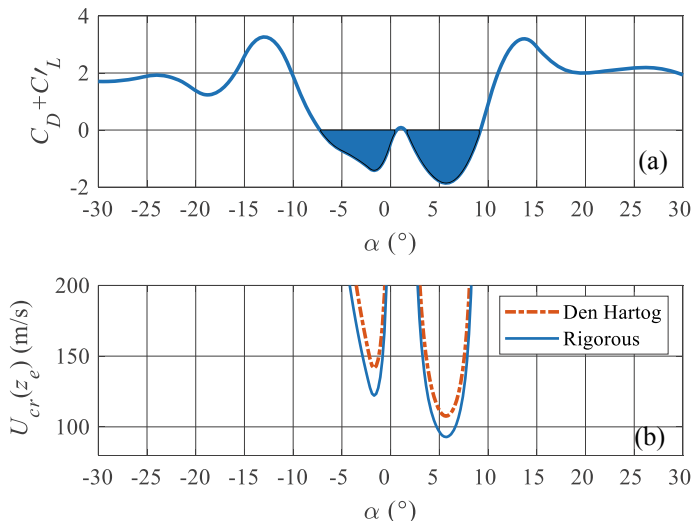


Fig. 1 a The “Endless Column” (source www.romania-insider.com); b aerodynamic coefficients

Table 1 Input values for galloping analysis

Parameter	Value
Total weight M	31,000 (kg)
Natural frequency n	0.513 (Hz)
Damping ratio ξ	0.016
Air density ρ	1.225 (kg/m ³)
Height H	29 (m)
Sectional width b	0.9 (m)
Roughness length z_o	0.05 (m)
Reference height z_e	10 (m)

**Fig. 2** **a** Aerodynamic damping coefficient; **b** critical velocity at reference height

column is prone to galloping for a range of angle of attack from -7° to 9° . Outside this zone, the column is stable.

For the galloping zone, i.e. the shadow areas, Fig. 2b shows the critical galloping wind speeds at the reference height, using the Glauert-Den Hartog criterion given by Eq. (18) and the rigorous criteria given by Eq. (16). The speeds higher than 200 m/s are excluded from the figure as they are too high to happen in reality. Using the Glauert-Den Hartog criterion, the minimum critical wind speed is 107.6 m/s at angle of attack 5.7° . Meanwhile, the rigorous criteria provides the minimum value 92.8 m/s as the same angle of attack. So, the two criteria provide the same prediction of the wind direction leading to worst galloping. However, the Glauert-Den Hartog criterion overestimates 16% the critical wind speed. Another comparison at angle of attack

1.7° shows that the Glauert-Den Hartog criterion can overestimate 23% the critical wind speed. Such overestimations provide unsafe prediction of the occurrence of galloping.

4 Conclusions

The paper presents a generalisation of the well-known Glauert-Den Hartog theory for galloping analysis of vertical slender structures. The conditions for the occurrence of galloping are derived for the general case, which takes into account the non-uniform wind, structural mode shapes and the variation along the structure of structural parameters, such as mass per unit length and the dimension of the structural cross section.

The proposed theory is applied for assessing the galloping instability of a real structure. The rigorous galloping criterion is compared with the widely used Glauert-Den Hartog's criterion. It is shown that using the Glauert-Den Hartog's criterion can overestimate the critical wind speed that is unsafe for structure. The reduction of critical wind speeds using the rigorous criterion highlights the importance of mode shape and the variation of the mean wind speeds. Although the rigorous critical wind speeds are relatively high, showing a great aerodynamic efficiency of the structure, the different values from the two criteria provide an evidence that using the Glauert-Den Hartog's criterion can lead to results unsafe for structures.

As a result of those findings, potential ideas for future works can be drawn. First, it is necessary to apply the proposed criterion for other slender structures to test the applicability of the Glauert-Den Hartog's criterion. It is also noteworthy to validate the proposed theory through wind tunnel tests. Finally, the proposed criterion for galloping could be formulated in closed forms that provides a useful tool for structural engineers.

Acknowledgements This research is funded by Vietnam National Foundation for Science and Technology Development (NAFOSTED) under grant number 107.04-2017.321.

References

1. Clough RW, Penzien J (2003) Dynamics of structures, 3rd edn. Computers & Structures, Inc., California
2. Den Hartog JP (1932) Transmission line vibration due to sleet. Trans Am Inst Electr Eng 51:1074–1076
3. Dragomirescu E, Yamada H, Katsuchi H (2009) Experimental investigation of the aerodynamic stability of the “Endless Column”, Romania. J Wind Eng Ind Aerodyn 97(9–10):475–484
4. Glauert BH (1919) The rotation of an aerofoil about a fixed axis. Report and Memoranda, No. 595, British Advisory Committee for Aeronautics (ARC), (R and M No. 595), pp 443–447

5. Lungu D, Solari G, Bartoli G, Righi M, Vacareanu R, Villa A (2002) Reliability under wind loads of the Brancusi endless column, Romania. *Int J Fluid Mech Res* 29(3–4):323–328
6. Nguyen CH, Macdonald JHG (2018) Galloping analysis of a stay cable with an attached viscous damper considering complex modes. *J Eng Mech* 144(2):04017175
7. Paidoussis M, Price S, De Langre E (2011) Fluid-structure interactions: cross-flow-induced instabilities. Cambridge University Press, Cambridge
8. Simiu E, Scanlan RH (1996) Wind effects on structures—fundamentals and applications to design. Wiley, Hoboken

Two-Dimensional Truss Topology Design by Reinforcement Learning



S. Sahachaisaree, P. Sae-ma, and P. Nanakorn

1 Introduction

1.1 Background in Structural Design

A truss design task consists of the selection of the topology and members of the truss. Designing a truss, even a complex one, may not seem to be a difficult task. However, finding optimal designs of trusses is in fact not straightforward. Design choices of topologies, members, and materials play important roles in the economy and structural capability of trusses. In general, the design of a structure must consider, in addition to its stability, stresses and displacements that can happen in the structure to ensure its safety and serviceability. At the same time, the design must also consider the resulting cost. The optimal design targets the best performance at a reasonable price. Traditionally, designers obtain the optimal design of a structure by the trial and error method, coupled with designers' experience. This traditional design method has been recently supplemented by the use of design algorithms. This is fundamentally done by considering structural design problems as optimization problems and using optimization algorithms to solve the corresponding optimization problems.

Metaheuristic algorithms are those algorithms that rely on sets of heuristics in performing searches. Metaheuristic algorithms usually require no derivatives of the objective functions. As a result, they can be more suitable for real-world problems than gradient-based algorithms. The heuristics used in metaheuristic algorithms are usually nature-inspired. Currently, metaheuristic algorithms, such as genetic algorithms, ant colony optimization, particle swarm optimization, firefly algorithms, are

S. Sahachaisaree (✉) · P. Sae-ma · P. Nanakorn

School of Civil Engineering and Technology, Sirindhorn International Institute of Technology,
Thammasat University, P.O. Box 22, Thammasat-Rangsit Post Office, Pathumthani 12121,
Thailand

e-mail: somporn.sahachaisaree@gmail.com

popularly used in truss topology optimization [4, 6, 8]. Unfortunately, there is no algorithm that can perform perfectly in every specific case [14].

1.2 Artificial Intelligence and Reinforcement Learning

The artificial intelligence research has a limited number of applications in the field of structural design. Its applications have been successful in other civil engineering fields that need to deal with problems with data uncertainties such as structural health monitoring, construction management, and mechanical properties of materials [9]. Most of these applications use some variants of multi-layer perceptron to deal with classification tasks, regression tasks, etc.

Structural design tasks are tasks that designers have to perform under specific rules. Good designers are those who understand the rules well and can achieve the design objectives without breaking these rules. One area of artificial intelligence that focuses on how computers can be taught to perform certain tasks effectively under given rules is reinforcement learning (RL). Learning through reinforcement in computer science is a programming paradigm inspired by the behaviorist theory of reinforcement. In RL, the learner or decision maker is called artificial intelligent agent, or agent in short. An agent interacts with a separate entity called environment through selecting actions. In turn, environment reacts to that action by presenting a new situation, called state, and giving a corresponding reward. This cycle recurs continually. A series of agent-environment interactions allows the agent to improve itself. After learning from some experiences, the agent behaves better and attains higher cumulative reward through its choice of actions. In summary, an RL algorithm is an optimization algorithm that seeks optimal policies to achieve maximum cumulative rewards. One of the most successful artificial intelligence applications that represents capability of RL is AlphaGo Zero [12]. AlphaGo Zero is a Go-playing agent that can learn the principles of playing various game strategies efficiently and expertly.

AlphaGo Zero is an inspirational achievement in the RL field. With that, this study aims to create environments for an RL agent to learn to be a truss topology designer. In the proposed methodology, topology design of simple 2D trusses is formulated, based on OpenAI Gym API [2], as a game, called “TrussGame.” The game consists of a grid board and player’s actions, which include adding nodes, adding truss members, and passing. An RL agent is then created, using OpenAI Spinning Up [1], for the game and is trained to play the game via the RL process. It is expected that, after the training, the agent becomes an expert that can instantaneously design the topologies of simple 2D trusses. Note that, in this study, the objective of topology design is limited to finding the optimal stable topologies of simple 2D trusses without consideration of their member sizes.

2 Theoretical Background

This section presents brief RL backgrounds related to the methodology of this study. More details can be found in the book by Sutton and Barto [13].

2.1 Markov Decision Processes

The term “Markov decision process” originated from the study on finding optimal return functions in dynamic programming. Dynamic programming is widely known as the very first method that can solve Markov decision processes (MDPs), but with the requirement of knowledge of MDP environment dynamics. Finite MDPs are formulations of stochastic optimal control problems where objectives are to maximize return G defined by

$$G_t \equiv R_{t+1} + R_{t+2} + R_{t+3} + \dots + R_T \quad (1)$$

by wandering through a finite trajectory, expressed as

$$S_0, A_0, R_1, S_1, A_1, R_2, \dots, A_{T-1}, R_T, S_T. \quad (2)$$

The above trajectory is a sequence of states S_t , actions A_t , and rewards R_{t+1} . The subscript t , where $t = 0, 1, \dots, T$, denotes the time step. The Markov property holds for MDPs; namely, the state transition probabilities are functions of the current state. In other words, only the information of the current state is necessary for the decision making at the present time step.

2.2 Policies

Define a policy π that is a mapping from states to action selection probabilities as

$$\pi(a|s) \equiv \mathbb{P}[A_t = a | S_t = s] \quad (3)$$

where $\forall s \in \mathcal{S}, \forall a \in \mathcal{A}(s)$. In addition, \mathcal{S} denotes the set of all states, while $\mathcal{A}(s)$ denotes the set of all possible actions at s . Moreover, \mathbb{P} is a probability distribution function. The probability distribution over actions varies according to the state s . In this way, a policy stochastically directs an agent to a subsequent state based upon the current state information. This policy notion is the heart of the policy gradient reinforcement learning methods. The RL agent embeds its knowledge from its experience, stored in parameter vector $\theta \in \mathbb{R}^d$, which is used as a parameter of π , i.e.

$$\pi(a|s, \theta) \equiv \mathbb{P}[A_t = a | S_t = s, \theta_t = \theta]. \quad (4)$$

An optimal policy is a mapping from states to action selection probabilities such that the expected cumulative reward of any finite trajectory is optimal. Accordingly, rewards are crucial to how state-action pairs are valued. They are the basis for differentiation between favorable and unfavorable states and guide the direction of the policy towards its improvement. Finding the optimal policies is the ultimate goal in RL problems.

2.3 Actor-Critic Policy Gradient Methods

To train a parameterized policy, a gradient ascent step with respect to policy parameter θ is taken on the performance measure function $J(\theta_t)$, i.e.

$$\theta_{t+1} = \theta_t + \alpha \nabla_\theta J(\theta_t); \quad \nabla_\theta J(\theta) \equiv \nabla_\theta v_{\pi_\theta}(s_0). \quad (5)$$

Here, α is the policy network learning rate, and $v_{\pi_\theta}(s_0)$ denotes the initial state-value function under $\pi(a|s, \theta)$. Note that the initial state-value function is the expected return of the initial state s_0 , and α denotes the learning rate. The actor-critic policy gradient model is nowadays considered as the de facto standard for policy gradient frameworks. The parameterized policy described above is in fact the actor. A value function approximator, called a critic, can be used to improve estimates of the gradient by bootstrapping. Using the estimate of the subsequent value function to evaluate the current value function, or bootstrapping the value function, introduces bias and reduces the variance of the value function, which is beneficial to the convergent speed.

3 Methodology

3.1 TrussGame Environment

Environment Dynamics

In TrussGame environment, a grid, whose points are the potential positions of nodes, must be initially defined. A game is set for the player by placing some supports and forces on selected grid points. Nodes are also placed on these selected grid points. A state of truss is defined by the spatial configuration of nodes, truss members, and boundary conditions. To transit to a new state, an action that can be either node adding or member adding is to be made. A member can be added only between two existing nodes. An episode in TrussGame has two phases, i.e.

Episode:

First phase:

Choices of action for state transit: Add a node on a grid point that does not have a node
or
Stop node adding and move to the second phase

Second phase:

Choices of action for state transit: Add a member between two existing nodes that do not have a member
or
Stop member adding and terminate the episode

Rewards

The definition of rewards is crucial because proper valuation of state-action pairs allows learning to reach optimal truss topologies. Truss topologies created by the agent should be stable. For this reason, a penalty for an unstable truss must be transmitted to the agent each time it takes a wrong action. To achieve this, a reasonable terminal penalty for unstable truss topologies is set. In addition, trusses with the optimal weights are the ultimate aim of TrussGame. Since the total length of all members in a truss reflects the weight of the truss, when a member is added, a penalty equal to the length of the added member can be set. In the scope of this study, there is no consideration of stresses or displacements. In summary, the rewards are set as follows:

Adding a member : Reward = $-1 \times$ Length of the added member

Unstable truss at the end of an episode: Reward = A big negative number

State Representation

A state of truss must encompass all necessary information for satisfying the Markov property. For efficiency, the containers of state information are selected to be graphics. Simply speaking, this agent-environment interaction can be seen as a 1-player board game. Truss elements and nodes are what the RL agent plays with on the board to win the game.

3.2 Actor-Critic Networks

Modern RL techniques, both value-based and policy-based, can solve large problems owing to the use of some function approximators. In this case, the graphical state representation narrows the options to using a kind of neural network that is capable of learning image representation.

Convolutional neural networks (CNN) are commonly applied to analyze visual imagery, and they are one of the classes of deep neural networks [5]. The use of CNN in RL as function approximators has been extensive [3, 7, 12]. Similar to feedforward networks, the CNN architecture consists of an input layer, multiple hidden layers,

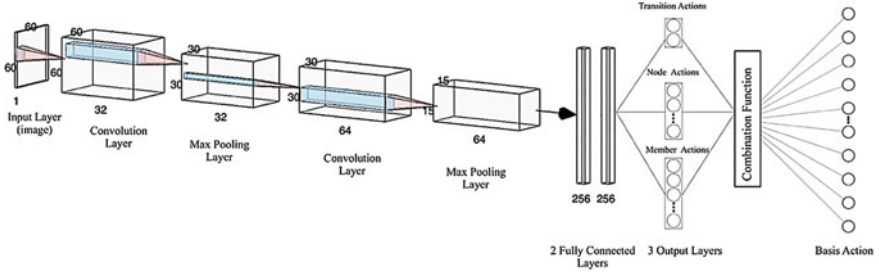


Fig. 1 Policy network architecture for TrussGame environment

and an output layer. CNNs built by using the TensorFlow machine learning library are employed in this study.

The actor needs not only to learn representations of trusses, but also perform complex actions in the TrussGame environment. An action factorization technique by Sharma et al. [11] is adopted for factoring action space into phase transition, node adding and member adding spaces. The critic is created separately having the same architecture but with only 1 scalar output for state-value function estimates. A simple vanilla policy gradient algorithm is used merely to demonstrate an empirical proof of the concept. Note that generalized advantage estimation [10] is used for the policy gradient calculation. The neural network architecture for both policy and value function is shown in Fig. 1.

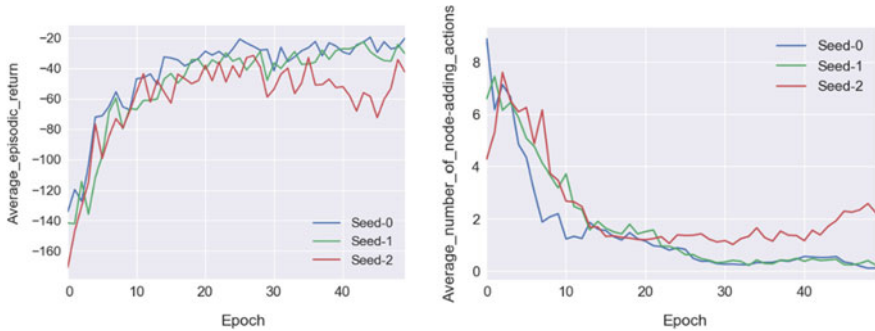
4 Results and Discussion

An example game having 4×4 grid lines is used to demonstrate the concept of TrussGame. The indexes of the grid lines in each direction are from 0 to 3. By using the TrussGame environment, in every episode, a pinned support and a roller support are provided at the (0, 0) and (3, 0), respectively. A random number of applied-force nodes between 1 and 4 are generated on the grid points under uniform probability distribution. If a randomized force coincides with an existing support or an existing force, the force is nullified. All this information in total makes up an initial state. The agent is trained by using the hyperparameters given in Table 1. In addition to the common performance measure in RL, the nodes added by the agent are counted and averaged over each epoch as shown in Fig. 2. The descent of the average number of added nodes per epoch and the ascent of the average episodic return per epoch show the convergence to more optimal policies.

Figure 3 shows the first 15 episodes of some example epochs. Note that epoch 49 is the last training epoch. It can be seen that the global optimal policy has not been achieved yet at the last epoch. At that capability, the agent still mostly inputs too many truss elements than it is necessary to form a stable truss. Nevertheless, in the later epochs, the performance of the agent improves, and it can obtain stable

Table 1 Test hyperparameters

Parameter	Value	Parameter	Value
Image size	60×60	Discount factor (γ)	0.99
Reward for instability	-200	Trace-decay parameter (λ)	0.97
Number of epochs	50	Policy network learning rate (α)	$3e-5$
Number of actions per epoch	1000	Value network learning rate	0.001
Value network iterations per epoch	80	Activation function in fully-connected layers	Hyperbolic tangent

**Fig. 2** Learning performances of three runs with different random-number-generator seeds

trusses with less members. For this demonstration problem, it is best for the agent to transit directly to the member-adding phase without adding any node, in most game episodes. However, never adding any node does not constitute the true optimal policy because of some “special episodes” where all forces are between the two supports. The first episode of epoch 49 in Fig. 3 is a special episode. For special episodes, node adding by the agent is necessary for obtaining stable trusses. The agent seems not able to grasp this fact.

5 Conclusions

This paper presents a framework for creating a design automation system using RL. Instead of directly optimizing a structure under objective and constraint functions, a different approach is proposed. The framework encompasses formulating a design environment, followed by creating a policy function and optimizing the policy to take good design actions. This approach can be extremely more time-efficient than the conventional optimization approach. Notwithstanding all limitations presented, a better performance may be achieved using an RL algorithm that is more advanced. Advanced RL algorithms will allow more design decisions or complexities, such as

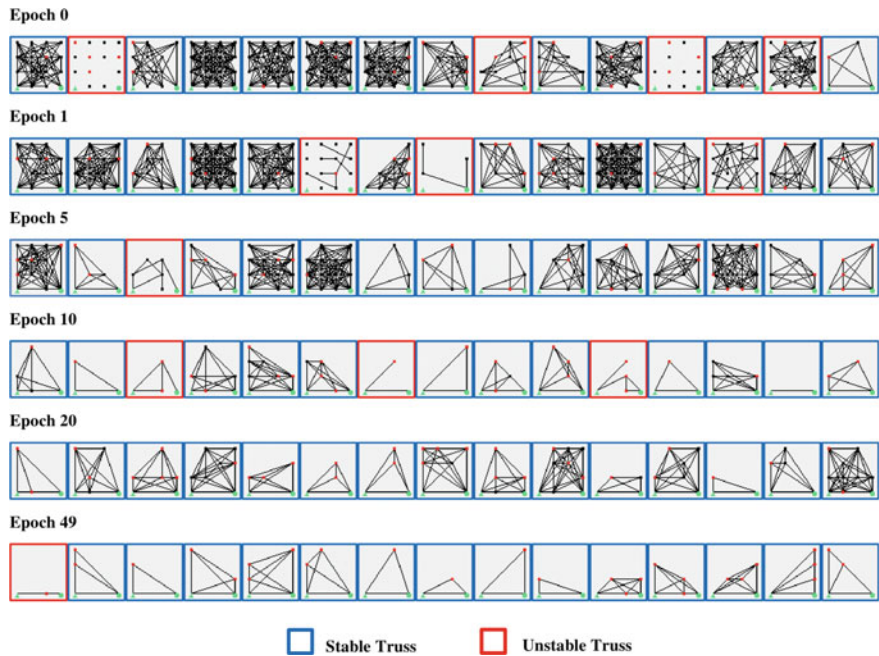


Fig. 3 First 15 episodes of some example epochs (applied forces in red)

stress and displacement constraints to be considered. The concept demonstrated in this paper can also be extended to other types of design task where MDPs can be formulated.

References

1. Achiam J (2019) Spinning up documentation, release. OpenAI
2. Brockman G, Cheung V, Pettersson L, Schneider J, Schulman J, Tang J, Zaremba W (2016) OpenAI gym. arXiv e-prints
3. De Bruin T, Kober J, Tuyls K, Babuska R (2018) Integrating state representation learning into deep reinforcement learning. IEEE Robot Autom Lett 3(3):1394–1401
4. Kaveh A (2014) Advances in metaheuristic algorithms for optimal design of structures, vol 9783319055497
5. Lecun Y, Bengio Y, Hinton G (2015) Deep learning. Nature 521(7553):436–444
6. Luh GC, Lin CY (2009) Structural topology optimization using ant colony optimization algorithm. Appl Soft Comput J 9(4):1343–1353
7. Mnih V, Kavukcuoglu K, Silver D, Graves A, Antonoglou I, Wierstra D, Riedmiller M (2013) Playing Atari with deep reinforcement learning. arXiv e-prints
8. Perez RE, Behdinan K (2007) Particle swarm approach for structural design optimization. Comput Struct 85(19–20):1579–1588
9. Salehi H, Burgueño R (2018) Emerging artificial intelligence methods in structural engineering. Eng Struct 171:170–189

10. Schulman J, Moritz P, Levine S, Jordan M, Abbeel P (2015) High-dimensional continuous control using generalized advantage estimation. arXiv e-prints
11. Sharma S, Suresh A, Ramesh R, Ravindran B (2017) Learning to factor policies and action-value functions: factored action space representations for deep reinforcement learning. arXiv e-prints
12. Silver D, Schrittwieser J, Simonyan K, Antonoglou I, Huang A, Guez A, Hassabis D (2017) Mastering the game of Go without human knowledge. *Nature* 550(7676):354–359
13. Sutton RS, Barto AG (2018) Reinforcement learning: an introduction. MIT Press, Cambridge
14. Wolpert DH, Macready WG (1997) No free lunch theorems for optimization. *IEEE Trans Evol Comput* 1(1):67–82

Updating the Reliability of Aging Miter Gates in the Presence of Corrosion and Fatigue



Thuong Van Dang, Quang Anh Mai, Pablo G. Morato, and Philippe Rigo

1 Introduction

Hydraulic steel structures deteriorate due to the aging of their components and cyclic loading within operations. Aging hydraulic gates are exposed to different levels of deterioration mainly from fatigue and corrosion. This degradation influences the integrity and life cycle costs of hydraulic steel structures. As a consequence, the studies involved in reducing the detrimental effect of structural deterioration under the effect of corrosion and fatigue are crucial. In general, the effect of corrosion to a miter gate consists of a number of factors, for instance, coating protection, temperature, humidity, constant wet/dry cycling, immersion in fresh or saline water. Fatigue is the initiation and developing of cracks to failure. There are parameters influence fatigue crack growth, for example, initial crack, stress range, geometry factor. These factors need to be considered during structural performance degradation. For ship structures, the probabilistic model for corrosion is suggested [1, 2]. The studies focus on considering the influence of fatigue and corrosion on ship hull structures presented [3–5]. This research aims to provide an approach for calculating the reliability of hydraulic steel structures to give strategies and solutions to alleviate adverse effects of corrosion and fatigue. Updating failure probability of aging miter gates under the effect of fatigue and corrosion are performed. An example of assessment and updating the reliability of vulnerable members about fatigue and corrosion (e.g., a welded joint) is used in the illustration.

T. V. Dang (✉) · Q. A. Mai · P. G. Morato · P. Rigo
Faculty of Applied Sciences, University of Liege, Liege, Belgium
e-mail: dangvanthuong@doct.uliege.be; thuongdv@tlu.edu.vn

2 Corrosion Model

In hydraulic steel structures, corrosion is a deterioration process of metal alloy structure through the oxidizes. The corrosion process may affect the chemical, physical properties and mechanical behavior of material that lead to a decrease in the fatigue life of the structure. The major degrading effects of corrosion on structural members are thickness loss, accumulation of corrosive products around joint components and may cause stress concentrations at local details. This section considers a common type of corrosion, general corrosion. It causes a decrease of section modulus by thinning cross-section of structural components. As a result, general corrosion mitigates the capacity of hydraulic steel structures to withstand the loading during the operation. Different patterns of general corrosion development have been proposed [1, 6]. The most commonly used model is presented in Eq. 1.

$$a_{rt} = C_1(t - t_0)^{C_2} \quad (1)$$

where a_{rt} is the cross-section decrease (mm), t is the time (year), C_1 is the annual corrosion rate (mm/year) while C_2 is a constant between 1/3 and 1. Initial corrosion protection time, t_0 (year). Depending on the type and quality of the corrosion protection, it may take values from 15 to 20 years [7].

3 Fatigue Model

One of the two main approaches for assessing fatigue strength is S-N model. This is the main tool to analyze and predict the fatigue resistance for structural members. It is evolved from S-N curves and Miner's rule [8]. The safety margin in S-N model is expressed as Eq. 2.

$$g = \Delta - n \frac{B_s^{m_{SN}} \Delta \sigma^{m_{SN}}}{C_{SN}} \quad (2)$$

where Δ is the damage criteria, $\Delta\sigma$ is stress-range, n is the number of lockages per year [9], B_s is uncertainty on the calculation of fatigue loading, C_{SN} and m_{SN} are parameters of material, respectively. In this study, the cover-plate weld details found fittest to the type E category by AASHTO, where severe fatigue cracks have been observed [10]. The variables in the S-N model are shown in Table 1.

The other approach to assess fatigue strength is the FM model. This model can be used to estimate the fatigue crack growth. The most common crack propagation model described by Paris-Erdogan equation [11]:

$$\frac{da}{dN} = C(Y \Delta \sigma \sqrt{\pi a})^m \quad (3)$$

Table 1 Variables utilized in S-N model

Variables	Distribution	Mean	Cov
n	Deterministic	3660	
Δ	Lognormal	1.0	0.3
m_{SN}	Deterministic	3	
$\Delta\sigma$	Deterministic	83	
B_s	Lognormal	1	0.40
C_{SN}	Lognormal	3.61×10^{11}	0.01

where da/dN is the fatigue crack growth under a load cycle N, model parameters C and m determined by empirical, geometry function Y is assumed constant. The integration of Eq. 3 ($m \neq 2$) obtains crack growth equation:

$$a_t = [a_0^{1-\frac{m}{2}} + \left(1 - \frac{m}{2}\right)CB_S^m Y^m \Delta\sigma^m \pi^{m/2} nt]^{2/(2-m)} \quad (4)$$

where a_0 is the initial crack depth.

The failure event is defined by the limit state function:

$$g = a_c - a_t \quad (5)$$

where a_c represents the critical crack depth. The failure occurs if $g \leq 0$. The calibration models of the FM to the S-N are performed to get a similar reliability index. Monte Carlo simulation is a technique to model the probability of various outcomes. This method has been successfully applied for risk and uncertainty of different fields. In this paper, it is used to determine the reliability index for the FM model. The FM model is calibrated to the S-N model by a least-squares fitting in reliability index space (β), as described by Eq. 6.

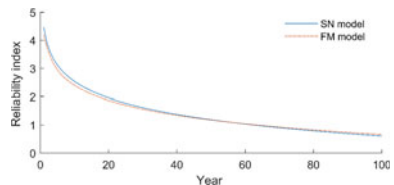
$$\min \sum_{t=1}^T (\beta_{SN}(t) - \beta_{FM}(t, x_1, x_2, x_3))^2 \quad (6)$$

where β_{SN} is the reliability index, calculated utilizing the S-N model; β_{FM} is the reliability index, calculated utilizing the FM model. Three parameters x_1, x_2, x_3 represent initial crack size, fatigue coefficient parameter and geometry function. The calibrated outcome is shown in Table 2 and the result is illustrated in Fig. 1.

Table 2 Parameters used in the FM model

Parameters	Distribution	Mean	Cov
a_0	Exponential	0.2142	
a_c	Deterministic	25	
$\Delta\sigma$	Deterministic	83	
Y	Lognormal	1	0.12
C	Normal	2.3×10^{-12}	0.12
m	Deterministic	3	
B_s	Lognormal	1	0.40
n	Deterministic	3660	

Fig. 1 Calibrated result between FM model and the SN model



4 Reliability Assessment Regarding the Influences of Fatigue and Corrosion

The reliability assessment is performed regarding the influences of corrosion and fatigue. In general, the effects of corrosion on the surface of structural components start to regard after aging miter gate coating broke down. It is assumed the coating protection time t_0 equal to 15 years. The corrosion implies a thickness reduction (see Sect. 2). Hence, the stress level and crack growth parameter are raised and the resistance is decreased. The influence of corrosion on the characteristic of the material is considered by providing a correction factor C_{corr} . This factor has been suggested as a constant, which is greater than 1.0 [3, 5]. In this study, C_{corr} is considered as a function, it depends on the thickness of the plate t_{ref} , annual corrosion rate and time service [12], which is expressed as Eq. 7.

$$C_{corr} = \frac{t_{ref}}{t_{ref} - 2C_1 t^{0.667}} \quad (7)$$

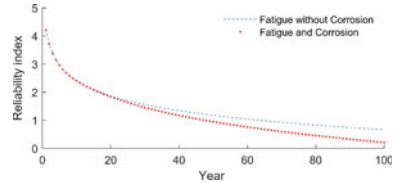
where C_1 equals 0.03 mm/year represents annual corrosion rate (see Sect. 2) and t is the time (year).

The effect of corrosion on stress range is defined as a function F_s . This function has been derived based on test data [12], which can be expressed by Eq. 8.

$$F_s = 1 + 0.033t^{0.5} \quad (8)$$

where t again is the time in years.

Fig. 2 Reliability index in the two cases



Subsequently, the crack depth of Eq. 4 is given by Eq. 9.

$$a_t = \left\{ a_{t-1}^{1-\frac{m}{2}} + \left(1 - \frac{m}{2}\right) CC_{corr} [F_s \Delta \sigma]^m Y^m \pi^{m/2} n \right\}^{2/(2-m)} \quad (9)$$

The limit state function follows Eq. 5 then gives by Eq. 10.

$$g = a_c - a_{rt} - a_t \quad (10)$$

Using the FM model, Fig. 2 shows the comparison between the two cases: reliability without corrosion (based on fatigue) and reliability in the presence of fatigue and corrosion. It is seen that corrosion significantly affects the aging structure if the coating is not properly maintained. This influence is really important for hydraulic steel structures that the design life is normally from 70 years [13] to 100 years [14].

5 Updating Reliability for a Welded Joint Based on Inspection Outcomes

The inspection quality of cracks in hydraulic steel structures is described by the probability of detection (POD) or the probability of non-detection (PND) curves. In a study about welded steel structure [15] proposed a PND curve as a lognormal distribution,

$$PND = 1 - \Phi \left[\frac{\ln \left(\frac{a}{a_d} \right)}{\xi_d} \right] \quad (11)$$

where a_d is the median flaw detection and ξ_d takes a value 0.5. This study uses a median surface flaw detected with visual inspection methods in field inspection, a_d equals 3 mm [16].

The inspection of a miter gate is required after approximately 5–10 year periods [17]. Inspection results (and repairs if any) provide information to update the failure probability or reliability for a component/structure. Dang et al. [18] demonstrates a

Fig. 3 Updating annual failure probability with the maximum allowable annual $P_f = 1.4 \times 10^{-3}$

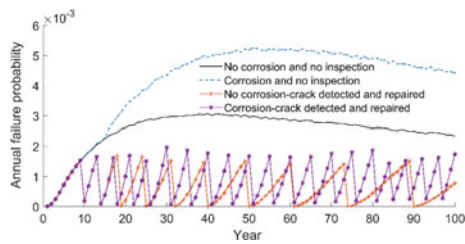
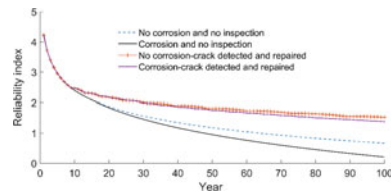


Fig. 4 Updating reliability with the maximum allowable annual $P_f = 1.4 \times 10^{-3}$



comprehensive analysis of optimizing the total expected costs of a miter gate. Mahmoud et al. [19] presented a method to optimize life-cycle cost for a miter gate considering fatigue and fracture. However, the influence of corrosion is not mentioned. To illustrate the effect of corrosion in condition-based maintenance optimization of lock gates, the updating reliability of a miter gate welded joint is performed in different strategies. This study utilizes the maximum allowable probability of failure is $P_f = 1.4 \times 10^{-3}$ [20] and an assumption detected cracks during the inspection are repaired. Figure 3 shows the results of annual failure probability curves in other cases. According to this figure, when the coating is well preserved before it breaks down (every 15 years), it implies “no corrosion”. Annual failure probability reduces significantly, comparison between the case “no corrosion and no inspection” and “corrosion and no inspection”. And then the number of inspections and repairs with the case “no corrosion-crack detected and repaired” is also lower. In other words, if we want to obtain a similar reliability index after updating using inspection outcomes (see Fig. 4) while the coating is not protected (corrosion), the number of inspections and repairs needs to be higher.

6 Conclusions

There is presently a large amount of navigation lock gates in the inland waterway system. After many decades in operation, a lot of aging lock gates exposed the deterioration under the impact of fatigue and corrosion. Therefore, it is required to establish inspection and repair planning for these structures. The outcomes of inspection and repair can be used for assessment and updating the reliability of the structures. In this work, a practical method for reliability assessment and updating the reliability of a miter gate welded joint has been presented. The reliability updating method

presented here can be used for risk-based maintenance optimization of navigation lock gates where coating, inspection, repair cracks and failure costs are considered.

Acknowledgements The authors gratefully acknowledge the financial support through the Wallonie-Bruxelles International (WBI), Belgium.

References

1. Paik JK, Kim SK, Lee SK (1998) Probabilistic corrosion rate estimation model for longitudinal strength members of bulk carriers. *Ocean Eng* 25(10):837–860
2. Melchers RE (2003) Probabilistic models for corrosion in structural reliability assessment—Part 1: empirical models. *J Offshore Mech Arct Eng* 125(4):264
3. Akpan UO, Koko TS, Ayyub B, Dunbar TE (2002) Risk assessment of aging ship hull structures in the presence of corrosion and fatigue. *Mar Struct* 15(3):211–231
4. Soares CG, Garbatov Y (1999) Reliability of maintained ship hulls subjected to corrosion and fatigue under combined loading. *J Constr Steel Res* 52(1):93–115
5. Kwon K, Frangopol DM (2012) System reliability of ship hull structures under corrosion and fatigue. *J Ship Res* 56(4):234–251
6. Melchers RE (1999) Corrosion uncertainty modelling for steel structures. *J Constr Steel Res* 52:3–19
7. Daniel R, Paulus T (2018) Lock gates and other closures in hydraulic projects. Butterworth-Heinemann, Oxford
8. Miner MA (1945) Cumulative damage in fatigue. *J Appl Mech* 12:159–164
9. McAllister TP, Ellingwood BR (2001) Evaluation of crack growth in miter gate weldments using stochastic fracture mechanics. *Struct Saf* 23(4):445–465
10. AASHTO, AWS D1.5. (1995) Bridge welding code
11. Paris P, Erdogan F (1963) A critical analysis of crack propagation laws. *J Basic Eng* 85(4):528–533
12. USACE-ETL-1110-2-566 (2010) Advanced reliability analysis of fatigue cracking in horizontally framed miter gates
13. Stahlwasserbauten-DIN 19704 (1998) DIN 19704-hydraulic steel structures
14. USACE-ETL-1110-2-584 (2014) ETL 1110-2-584 design of hydraulic steel structures
15. McAllister TP (1999) Assessing reliability of highly redundant welded steel frame structures. Johns Hopkins University
16. McAllister TP, Ellingwood BR (2001) Reliability-based condition assessment of welded miter gate structures. *J Infrastruct Syst* 7(3):95–106
17. Eick BA et al (2018) Automated damage detection in miter gates of navigation locks. *Struct Control Health Monit* 25(1):1–18
18. Dang TV, Mai QA, Morato PG, Rigo P (2019) Optimal inspection and repair scheduling for mitre lock gates. *Marit Eng* 1–9
19. Mahmoud H, Chulahwat A, Riveros G (2018) Fatigue and fracture life-cycle cost assessment of a miter gate with multiple cracks. *Eng Fail Anal* 83:57–74
20. Dang TV, Mai QA, Morato PG, Rigo P (2019) Updating the failure probability of miter gates based on observation of water levels. In: Mechanical fatigue of metals. Springer International Publishing, Cham, p 8

Vibration Analysis in Designing Post-tensioned Slabs



Ha Thu Tran and Hung Manh Tran

1 Introduction

The post-tensioned (PT) slabs now are using popularly in Vietnam. It is applied not only in offices, residential but also in factories and commercial centers. However there still a problem that client concern about PT slabs and may feel uncomfortable when choosing this option. It is the floor's vibration caused by footfalls or running machines. Actually, this problem will not be seriously if engineers carry out the vibration analysis at the beginning of the design stage and determine whether a floor meets the serviceability requirements for vibration using conservative values or whether a more detailed analysis is considered. Through this article, the author shows the analysis vibration for some kinds of real and finished post-tension slabs in Vietnam then giving the proposal about which slab type should be determined vibrations guaranteeing the comfort of occupants.

2 The Process of the Vibration Analysis

In general, the vibration response of a concrete floor is attributed to 2 groups as direct and indirect reasons. Direct reasons are consequence of foot drop or vibration due to operation of machinery located on slabs and indirect reasons are vehicular traffic outside the building or vibration due to earthquake, wind or other impact forces. The scope of this article is design for vibration caused by footfalls or running machines inside the building.

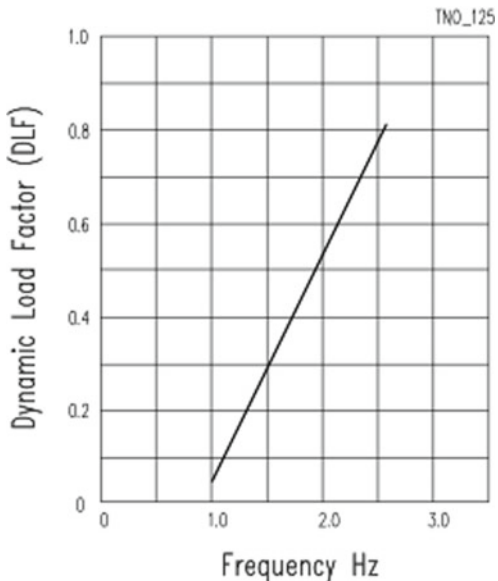
H. T. Tran (✉)

ARES Optimal Building Solution Joint Stock Company, Hanoi City, Vietnam
e-mail: hatran.aresco@gmail.com

H. M. Tran

University of Canterbury, Christchurch 8041, New Zealand

Fig. 1 Dynamic load factor for first harmonic of walking force



To determine the vibration, it is the most important to identify the vibration source, the vibration transmission path and the vibration characteristics of a floor at design stage and then determining whether or not the vibration response is acceptable.

2.1 *The Vibration Sources*

The vibration source is the foot drop of walking people or the vibration from operating machines. For offices, residential and commercial center, the vibration from footfalls will be concerned and for some factories the vibration from running machines will be concerned. Of course, the force of vibration is different among individuals but typically the walking frequency 1.8–2.1 Hz is recommended [1]. Average value 2 Hz can be used for most cases. For factories, frequency of machines when it works must be given to engineers. Figure 1 from reference [1] recommends an approximate guideline for determining Dynamic Load Factor (DLF) as a function of a person's walking frequency.

2.2 *The Vibration Transmission Path*

The transmission path of vibration are mass, stiffness and damping. The mass is self-weight of a floor and its superimposed loads. The stiffness of a floor also effects on

Table 1 Recommended damping factors for different occupancies

Occupancy	Damping factor (β)
Bare concrete floor	0.02
Furnished, low partition	0.03
Furnished, full height partition	0.05
Shopping malls	0.02

vibration, they are modulus of Elasticity, cracks (if any) and post-tensioning. Damping is determined when a floor is finished and in using. As reference [2] damping factors suggested are listed in Table 1.

2.3 The Vibration Characteristics of a Floor

Determining vibration characteristics is finding the natural frequency of a floor system and the peak acceleration. Using ADAPT FLOOR PRO, a specific software for PT slab design and can also analysis the vibration period, to find the first frequency of a floor. And to evaluate the vibration of a floor [3, 4] gives the following formulation:

$$\frac{a_p}{g} \leq \frac{P_0 e^{-0.35fn}}{\beta W} \quad (1)$$

where:

- a_p peak acceleration;
- g gravitation acceleration (9.81 m/s^2);
- P_0 constant force representing the walking force;
- β damping factor, recommended in Table 1;
- W weight of a floor and effective loads;
- fn first natural frequency.

2.4 The Acceptability of Vibration

It is the fact that in Vietnam now there isn't a standard about vibration caused by footfalls inside the buildings. There is only a national code [5] giving allowance values of vibration caused by individuals or groups that have effect on human living areas. Table 2 giving the maximum allowance acceleration according to this code. For more detail and focus directly on perception of vibration caused by walking, the Applied Technology Council [4] recommends the threshold of human sensitivity to vertical vibration as shown in Fig. 2. The data from investigators shows that human is

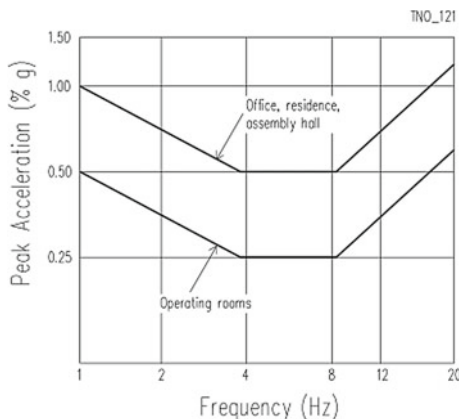
Table 2 The maximum allowance of acceleration for commercial activities

Living area	Acceleration (m/s^2)
Special area (from 21 p.m. to 6 a.m.)	0.006
Special area (from 6 a.m. to 21 p.m.)	0.010
Normal area (from 21 p.m. to 6 a.m.)	0.010
Normal area (from 6 a.m. to 21 p.m.)	0.030

where:

Special areas are hospitals, libraries, schools, churches, pagodas
Normal areas are residential, hotels, offices, factories

Fig. 2 Threshold of human sensitivity to vertical vibration (ACT)



most sensitive to vibration for frequencies between 4 and 8 Hz. Larger acceleration values can be tolerated at higher or lower frequencies.

2.5 The Six-Step Process for Carrying Out Footfall Vibration Analysis

From above explanation, [6] suggested that the process of footfall vibration analysis can be expressed in six following steps:

1. Finding the first natural frequency (f_n)
2. Exciting force of vibration (P_0). P_0 is equal to DFL multiplies with the weight of walking person
3. Selecting floor type for damping ratio (β)
4. Calculating modal mass W (weight of vibrating floor)
5. Determining peak acceleration ratio caused by footfall (a_p/g)
6. Comparing with the allowance values.

3 The Real Examples of Vibration Analysis in Vietnam

The author has carried out vibration analysis for 3 types of floor as a commercial centre, a school and a factory. The result is shown in Table 3 (Figs. 3, 4, 5 and 6).

According to formula (1), we can calculate the peak acceleration and we compare with the standard of ACT (as above diagram) or Vietnamese Code (Table 2) and then from Table 3 we can see all vibration are in allowable range.

Table 3 The result of vibration analysis

No	Project name	f_n (Hz)	P_0 (lb)	β	W (kip)	ap/g (%)	Evaluation (ACT)
1	DHS Centre	5.28	82.15	0.02	201.80	0.32	OK
2	KD School	5.52	82.15	0.02	159.05	0.37	OK
3	SPD Factory	5.71	82.15	0.02	189.26	0.29	OK

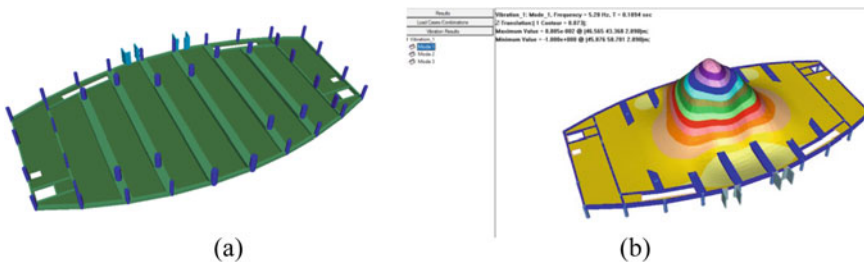


Fig. 3 Vibration analysis for project Dai Hoang Son centre. **a** 3D structural model of the slab; **b** first natural mode of the slab

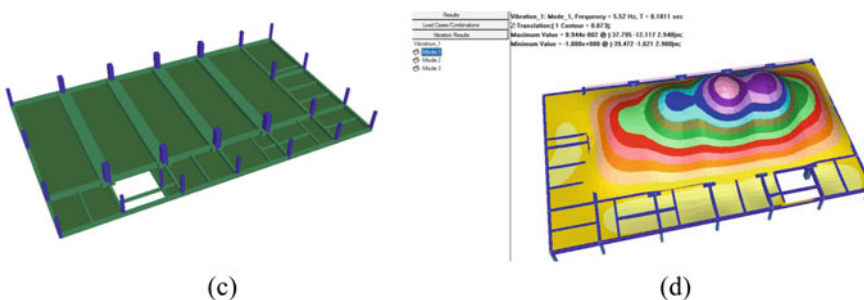


Fig. 4 Vibration analysis for project Dich Vong school. **a** 3D structural model of the slab; **b** first natural mode of the slab

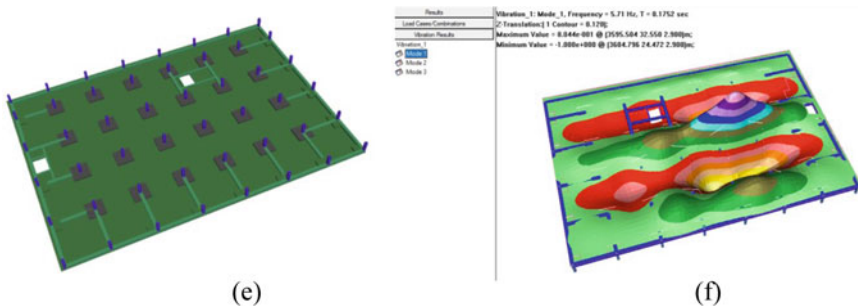


Fig. 5 Vibration analysis for project Spindex factory. **a** 3D structural model; **b** first natural mode of the slab

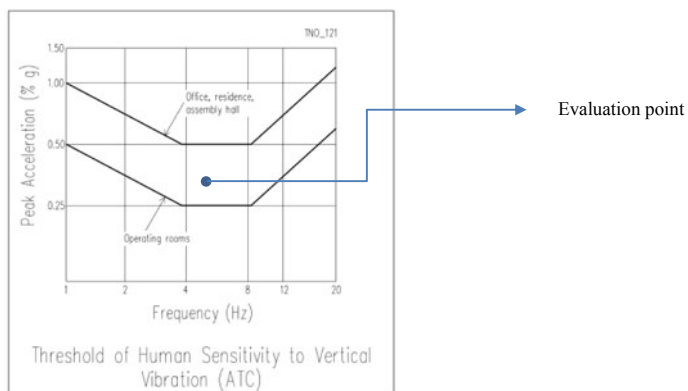


Fig. 6 Threshold of Human sensitivity to vertical vibration (ACT)

4 Conclusion

Through the analysis above, almost investigating projects are satisfied about vibration caused by footfall of one person with the rather small force of vibration. But actually, in fact we can meet the case of resonance and it makes the vibration increase to many times. Therefore, the authors would like to propose that vibration analysis has to be checked and designed at the beginning of project, especially for hospitals, commercial centres, schools and some kinds of factories so that we have the overall view of designing and we can choose the best slab option for the project.

References

1. TR43 (2005) Post-tensioned concrete floors: design handbook, 2nd edn. The Concrete Society, Surrey GU17 9AB, UK
2. Allen DE, Murray TM (1993) Design criterion for vibrations due to walking. Eng J 30(4):117–129
3. AISC/CISC (1997) Steel design guide series 11, floor vibrations due to human activity. American Institute of Steel Construction, Chicago, IL
4. ATC (1999) ATC design guide 1. Minimizing floor vibration. Applied Technology Council, Redwood City, CA, 49 p
5. QCVN 27 (2010) National technical regulation on vibration. Ministry of Natural Resources and Environment
6. ADAPT TN290 (2010) Vibration design of concrete floors for serviceability. ADAPT Corporation, Redwood City, CA. www.adaptsoft.com, p 20